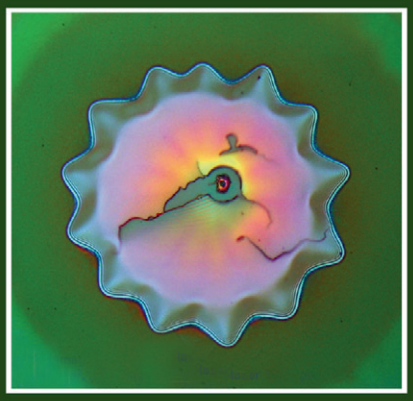
WOODHEAD PUBLISHING SERIES IN ELECTRONIC AND OPTICAL MATERIALS



Optical Thin Films and Coatings

From Materials to Applications

Second Edition

Edited by Angela Piegari and François Flory

WP
WOODHEAD PUBLISHING

Optical Thin Films and Coatings

Related titles

Handbook of Thin Film Deposition
(ISBN: 978-1-4377-7873-1)

Thin Film Coatings for Biomaterials and Biomedical Applications
(ISBN: 978-1-78242-453-6)

Metallic Films for Electronic, Optical, and Magnetic Applications, Structure, Processing and Properties
(ISBN: 978-0-85709-057-7)

Modern Plasmonics by Part of the Handbook of Surface Science
(ISBN: 978-0-444-59526-3)

Woodhead Publishing Series in Electronic and Optical Materials

Optical Thin Films and Coatings

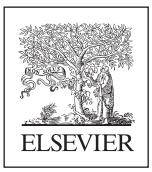
From Materials to Applications

Second Edition

Edited by

Angela Piegari

François Flory



WP
WOODHEAD PUBLISHING
An imprint of Elsevier

Woodhead Publishing is an imprint of Elsevier
The Officers' Mess Business Centre, Royston Road, Duxford, CB22 4QH, United Kingdom
50 Hampshire Street, 5th Floor, Cambridge, MA 02139, United States
The Boulevard, Langford Lane, Kidlington, OX5 1GB, United Kingdom

Copyright © 2018 Elsevier Ltd. All rights reserved.

No part of this publication may be reproduced or transmitted in any form or by any means, electronic or mechanical, including photocopying, recording, or any information storage and retrieval system, without permission in writing from the publisher. Details on how to seek permission, further information about the Publisher's permissions policies and our arrangements with organizations such as the Copyright Clearance Center and the Copyright Licensing Agency, can be found at our website: www.elsevier.com/permissions.

This book and the individual contributions contained in it are protected under copyright by the Publisher (other than as may be noted herein).

Notices

Knowledge and best practice in this field are constantly changing. As new research and experience broaden our understanding, changes in research methods, professional practices, or medical treatment may become necessary.

Practitioners and researchers must always rely on their own experience and knowledge in evaluating and using any information, methods, compounds, or experiments described herein. In using such information or methods they should be mindful of their own safety and the safety of others, including parties for whom they have a professional responsibility.

To the fullest extent of the law, neither the Publisher nor the authors, contributors, or editors, assume any liability for any injury and/or damage to persons or property as a matter of products liability, negligence or otherwise, or from any use or operation of any methods, products, instructions, or ideas contained in the material herein.

Library of Congress Cataloging-in-Publication Data
A catalog record for this book is available from the Library of Congress

British Library Cataloguing-in-Publication Data
A catalogue record for this book is available from the British Library

ISBN: 978-0-08-102073-9 (print)
ISBN: 978-0-08-102099-9 (online)

For information on all Woodhead publications
visit our website at https://www.elsevier.com/books-and-journals



Publisher: Matthew Deans
Acquisition Editor: Kayla Dos Santos
Editorial Project Manager: Carlos Rodriguez
Production Project Manager: Swapna Srinivasan
Cover Designer: Miles Hitchen

Typeset by SPi Global, India

Contents

Contributors xix
Preface to the First Edition xxiii
Preface xxvii

PART I DESIGN AND MANUFACTURING OF OPTICAL THIN FILMS AND COATINGS

CHAPTER 1 Recent developments in deposition techniques for optical thin films and coatings 3
H. Angus Macleod

1.1 Introduction 3
1.2 Early Processes for the Deposition of Optical Coatings 4
1.3 The Energetic Processes 6
1.3.1 Ion-Assisted Deposition 6
1.3.2 Ion Plating 8
1.3.3 Sputtering 10
1.4 Cathodic Arc Evaporation 15
1.5 Pulsed Laser Deposition 15
1.6 Chemical Vapor Deposition 16
1.7 Atomic Layer Deposition 17
1.8 Sol-Gel Processes 18
1.9 Etching 18
1.10 Other Techniques 19
1.11 Conclusion 19
References 20

CHAPTER 2 Design of complex optical coatings 25
Pierre G. Verly, Daniel Poitras

2.1 Introduction 25
2.2 Modern Numerical Thin Film Synthesis Techniques 27
2.2.1 Fourier Transform Method 27
2.2.2 Inhomogeneous Refinement 30
2.2.3 Needle Method 32
2.2.4 Global Optimization 34
2.3 Manufacturability Issues 37
2.4 Hybrid Design 40
2.4.1 Waveguide Facet Coatings 41

2.4.2 Structured Coatings 44
2.4.3 Solar Cells 48
2.5 Conclusion 52
References 53
Further Reading 64

CHAPTER 3 Optical monitoring strategies for optical coating manufacturing 65
Alexander V. Tikhonravov, Michael K. Trubetskov, Tatiana V. Amotchkina

3.1 Introduction 65
3.2 Classification of Optical Monitoring Strategies 67
3.3 Turning Point Optical Monitoring and Error Self-Compensation Effect 69
3.4 Level Monitoring: Passive and Active Monochromatic Monitoring Strategies 75
3.5 Monitoring by Swing Values 85
3.6 Direct Broadband Optical Monitoring 89
3.7 Indirect Optical Monitoring Strategies 92
3.8 Conclusion 97
References 99

CHAPTER 4 Production strategies for high-precision optical coatings 103
Henrik Ehlers, Detlev Ristau

4.1 Introduction 103
4.2 Basic Concept of Deterministic Production 105
4.3 Optical Broadband Monitoring 107
4.4 Hybrid Thickness Monitoring Concepts 112
4.5 Virtual Deposition System 114
4.5.1 Deposition System 115
4.5.2 Online Measurement System 116
4.5.3 Process-Tracing Algorithm 116
4.5.4 Application Example for a VDP Analysis 117
4.6 Direct Online Correction Tools 118
4.7 Design Stability in Production Processes 120
4.8 Deposition Control of Coating Systems with Continuous Refractive Index Variation 125
4.8.1 Production of Material Mixtures 126
4.8.2 Deposition Control of Rugate Filters 132
4.9 Conclusion 135
References 136
Further Reading 140

PART II UNCONVENTIONAL FEATURES OF OPTICAL THIN FILMS AND COATINGS

CHAPTER 5 Complex materials with subwavelength inclusions for optical thin film applications 143
Anna Sytchkova

5.1 Introduction 143
5.2 Physics of Some Classes of Novel Materials with Subwavelength Inclusions 145
5.3 Ceramic Matrix With Embedded Nanostructures 147
5.3.1 Materials With Quantum Dots 148
5.3.2 Nanoclusters in Periodic Arrays (Metamaterials) 149
5.3.3 Effect of Small Random Disorders and Imperfections in Metamaterials 154
5.3.4 Composites of Random Elements 154
5.3.5 Coatings Containing Thin and Ultrathin Metal Layers and Coatings Containing Metasurfaces 155
5.4 Searching for Alternative Materials for Resonating Inclusions 156
5.4.1 Alloys and Intermetallics: Novel Metal Materials 157
5.4.2 Semiconductors and Dielectrics 160
5.5 Characterization of Novel Materials with Subwavelength Inclusions 162
5.5.1 Optical Characterization Techniques for Complex Materials 163
5.5.2 Local Properties of Nanostructured Materials 165
5.5.3 Effective Macroscopic Parameters 166
5.5.4 Complex Materials and Ultrathin Metals in Multilayers. 168
5.6 Conclusions 172
References 173

CHAPTER 6 Scattering properties of random structures in thin films 187
Gerard Berginc, Alexei A. Maradudin

6.1 Introduction 187
6.2 Numerical Solution of Reduced Rayleigh Equations for Scattering of Light From Dielectric Films With 1D Rough Surfaces 189
6.2.1 A Film With a 1D Randomly Rough Vacuum-Dielectric Interface Deposited on the Planar Surface of a Perfect Conductor 190

6.2.2 A Film With a Planar Vacuum-Dielectric Interface Deposited on a 1D Randomly Rough Perfectly Conducting Surface 196
6.3 Reduced Rayleigh equations for the scattering of P- and S-Polarized Light From, and Its Transmission through, a Film With Two 1D Rough Surfaces 200
6.3.1 p-Polarization 203
6.3.2 s-Polarization 207
6.3.3 Results 209
6.4 Numerical Solution of the Reduced Rayleigh Equation for the Scattering of Light From a 2D Randomly Rough Penetrable Surface 213
6.5 Scattering of Light From a Dielectric Film With a 2D Randomly Rough Surface Deposited on a Planar Metal Substrate 216
6.5.1 Scattering of Light From a Dielectric Film With a 2D Randomly Rough Surface Deposited on a Planar Metal Substrate 218
6.5.2 A Dielectric Film With a Planar Interface With a Dielectric Superstrate and a 2D Randomly Rough Interface With a Dielectric Substrate 224
6.6 Analytical Methods for the Scattering From a 3D Film With Randomly Rough Surfaces 229
6.6.1 Definition of the Scattering Matrix 230
6.6.2 The SSA and the SPM for a 2D Rough Surface 233
6.6.3 The SSA and the SPM for Slabs With Randomly Rough Boundaries 240
6.6.4 Conclusions 247
6.7 Theoretical Methods for the Scattering of Polarized Light From Randomly Rough Interfaces and Random Media 247
6.7.1 Specific Intensity and Cross Section 248
6.7.2 Specific Intensity and Bethe-Salpeter Equations 253
6.7.3 Effective Permittivity 255
6.7.4 Expression of the Intensity Operator $\overline{\boldsymbol{P}}^{11}$ 256
6.7.5 Expression for the Incoherent Intensity and the Green Tensors $\overline{\boldsymbol{P}}^{11}$ 259
6.7.6 Coherent Backscattering 265
6.7.7 Conclusion 273
6.8 Applications 273
6.9 Conclusion 281
Appendix 281

A.1 Definitions of the Scattering Matrices for a Single Rough Surface 281
A.2 Mueller Matrix and Tensor 282
Acknowledgments 284
References 284
Further Reading 289

CHAPTER 7 Optical properties of thin film materials at short wavelengths 291
Juan I. Larruquert

7.1 Introduction 291
7.2 Material Behavior Over the Spectrum 291
7.3 Reflection and Transmission in Absorbent Materials 294
7.3.1 Roughness and Scattering 296
7.4 The Optical Constants of Materials at Short Wavelengths 299
7.4.1 Interaction Mechanisms Between Photons and Matter 299
7.4.2 Transparency Cutoff of Dielectrics 300
7.4.3 Free Electron Metals 301
7.4.4 Tightly Bound Electrons: Atomic Scattering Factors 303
7.4.5 Absorption Edges 306
7.4.6 Optical Properties at Higher Energies 309
7.5 Link Between n and k: Kramers-Kronig Analysis 314
7.6 Experimental Determination of Optical Constants 315
7.7 Specifics of Optical Coatings at Short Wavelengths 318
7.7.1 Transmission Filters 318
7.7.2 High-Reflectance Coatings 321
7.7.3 Linear Polarizers and Phase Retarders 332
7.8 Conclusion 341
Acknowledgements 342
References 342

CHAPTER 8 Controlling thermal radiation from surfaces 357
Carl G. Ribbing

8.1 Introduction 357
8.2 Blackbody Radiation 359
8.3 Emissivity 362
8.4 Optically Selective Coatings 367
8.4.1 Coatings for Thermal Solar Collectors 367
8.4.2 Energy-Efficient Window Coatings 374

8.4.3 Coatings for Control of Radiative Exchange With the Atmosphere 377
8.5 Conclusion 384
References 385
Further Reading 387

CHAPTER 9 Color in optical coatings 389
Claudio Oleari

9.1 Introduction 389
9.2 The Development of the Understanding of Interference Color 390
9.2.1 Isaac Newton (1642–1727) 390
9.2.2 Thomas Young (1773–1829) 392
9.2.3 Leopoldo Nobili (1784–1835) 393
9.2.4 David Brewster (1781–1868) 394
9.2.5 Auguste Michel-Lévy (1844–1911) 394
9.2.6 J.F. Gabriel Lippmann (1845–1921) 398
9.2.7 Soap Bubbles 398
9.2.8 Lens Optical Coatings 398
9.2.9 Thin Film Anticounterfeiting Coatings 399
9.3 Overview of Basic Colorimetry 399
9.3.1 Psychophysical Colorimetry of Color Stimuli 400
9.3.2 Psychophysical Colorimetry of Light Sources and Nonself-Luminous Surfaces 406
9.3.3 Psychometric Colorimetry 408
9.4 Optical Coating Colorimetry 410
9.4.1 Gonio-Apparent Color Measurement 411
9.4.2 Optical Coating Color 413
9.5 Conclusion 419
Acknowledgments 419
References 419
Further Reading 421

PART III NOVEL MATERIALS FOR OPTICAL THIN FILMS AND COATINGS

CHAPTER 10 Organic optical coatings 425
Thomas Neubert, Michael Vergöhl

10.1 Introduction 425
10.2 Specific Properties of Organic Layers 426
10.3 Optical Coatings With Organic Layers 429

10.4 Deposition Techniques 429
10.4.1 Thermal Evaporation 430
10.4.2 Sputter Deposition 432
10.4.3 Plasma-Enhanced Chemical Vapor Deposition (PECVD) 434
10.4.4 Nonplasma-Activated Chemical Vapor Deposition 438
10.4.5 Adhesion Improvement by Plasma Treatment 441
10.5 Composites 441
10.6 Conclusion 443
References 443

CHAPTER 11 Surface multiplasmonics with periodically nonhomogeneous thin films 449
Muhammad Faryad, Akhlesh Lakhtakia

11.1 Introduction 449
11.2 Historical Development 450
11.3 Periodically Nonhomogeneous Dielectric Materials 452
11.3.1 Rugate Filters 452
11.3.2 Sculptured Nematic Thin Films 452
11.4 Canonical boundary-value problem 454
11.4.1 Theoretical Formulation 454
11.4.2 Metal/Rugate-Filter Interfaces 457
11.4.3 Metal/SNTF Interface 460
11.5 Grating-coupled configuration 462
11.5.1 Metal/Rugate-Filter Interface 462
11.5.2 Metal/SNTF Interface 467
11.6 Turbadar–Kretschmann–Raether Configuration 471
11.6.1 Metal/Rugate-Filter Interface 471
11.6.2 Metal/SNTF Interface 476
11.7 General Remarks 477
11.8 Suggestions for Future Work 479
11.8.1 Excitation of Multiple SPP Waves With Finite Sources 479
11.8.2 Compound Surface-Relief Gratings 479
11.8.3 Effects of Multiple SPP Waves on the Efficiency of Thin-Film Solar Cells 480
11.9 Resources 480
References 480

CHAPTER 12 Optical thin films containing quantum dots 487
François Flory, Yu-Jen Chen, Hung-Ju Lin

12.1 Introduction 487
12.2 Modeling 488
12.3 Electronic Properties of Quantum Wells and the Effective Mass Model 489
12.4 Electronic Properties of Quantum Dots 493
12.4.1 Optical Properties 494
12.5 Properties of Thin Films Containing Quantum Dots 495
12.5.1 Realization 495
12.5.2 Characterization 497
12.6 Applications 505
12.6.1 Hybrid Organic/Quantum Dot Solar Cells 505
12.6.2 Lighting and Displays 507
12.7 Optical Interference Coatings Containing Quantum Dots 508
12.8 Conclusion 509
Acknowledgments 510
References 510
Further Reading 512

PART IV APPLICATIONS OF OPTICAL THIN FILMS AND COATINGS

CHAPTER 13 Optical coatings on plastic for antireflection purposes 517
Ulrike Schulz, Robert W. Schaffer

13.1 Introduction 517
13.2 Transparent Polymer Materials for Optics 517
13.3 Plastics in Vacuum Coating Processes 520
13.3.1 Interaction With Emissions From Plasma 520
13.3.2 Thermal and Stress-Related Effects 522
13.3.3 Water Absorption and Desorption 523
13.3.4 General Considerations for Plasma-Assisted Vacuum Coating Processes 525
13.4 Antireflection Methods 526
13.4.1 Vacuum Deposited Antireflective Coatings 526
13.4.2 Antireflective Structures 528
13.4.3 Wet-Chemical AR Coatings on Plastics 531
13.5 Conclusion 532

13.6 Sources of Further Information and Advice 533
References.....533
Further Reading 537

CHAPTER 14 Protective coatings for durability enhancement of optical surfaces.....**539**
Tjhay W. Boentoro, Bernd Szyszka, Ludvik Martinu

14.1 Introduction.....539
14.2 Plasma- and Ion-Based Deposition of Functional Coatings.....540
14.3 Testing Methods 544
14.3.1 Taber Abraser Test of Abrasion Resistance 545
14.3.2 Sand Trickling Test 546
14.3.3 Scratch Test 546
14.3.4 Crack Onset Strain.....547
14.3.5 Adhesion Tests.....547
14.3.6 Weathering Test.....549
14.3.7 Characterization of the Optical Properties.....550
14.3.8 Haze 551
14.4 Coating Concepts.....551
14.4.1 Coating Systems on Glass Substrate.....552
14.4.2 Coating System on Polycarbonate Substrate 552
14.4.3 Numerical Simulation.....553
14.4.4 Multifunctional Coatings.....553
14.5 Examples of Protective Coating Applications 556
14.5.1 Low-E Coatings on Windshield 556
14.5.2 Polycarbonate in Automotive Glazing 557
14.6 Conclusion 559
References.....561

CHAPTER 15 Optical coatings for displays and lighting.....**565**
Cheng-Chung Lee, Chien-Cheng Kuo

15.1 Introduction.....565
15.2 Optical Coatings for Flat Panel Display (FPD) 566
15.3 Optical Coatings for Projectors 568
15.4 Optical Coatings for Projectors Using Light-Emitting Diode (LED) Light Source.....571
15.5 Optical Coating for Automobiles Head Up Display (HUD) 583
15.6 Optical Coatings for LEDs.....586
15.7 Conclusion 589
Acknowledgments 591
References.....591
Further Reading 594

CHAPTER 16 Innovative approaches in thin-film photovoltaic cells 595
Nicolas Barreau, David Duche, Carmen M. Ruiz, Ludovic Escoubas, Jean-Jacques Simon, Judikael Le Rouzo, Veronica Bermudez

16.1 Introduction 595
16.2 Inorganic Nanostructures for Photovoltaic Solar Cells 599
16.2.1 New Concepts of Solar Cells 599
16.2.2 Light Trapping and Photo-Carrier Collection 600
16.2.3 Quantum Dots and Nanowires Included in Thin-Film Solar Cells 601
16.3 Organic Thin-Film Solar Cells 604
16.3.1 Working Principles of an Organic Solar Cell 605
16.3.2 Light Trapping Strategies for Organic Solar Cells (OSCs) 608
16.4 Chalcogenide Materials in Thin-Film Solar Cells 611
16.4.1 The Substrates 612
16.4.2 The Device Stack for Cells 613
16.4.3 State-of-the-Art Technologies at Industry Level 617
16.4.4 Novel Chalcogenide Absorbers 617
16.4.5 Vacuum-Free Deposition 618
16.5 Organometallic Perovskite-Based Solar Cells 618
16.6 Conclusion 623
References 624
Further Reading 632

CHAPTER 17 Optical coatings for security and authentication devices 633
Bill Baloukas, Ludvik Martinu

17.1 Introduction 633
17.2 Basic Principles and Structures Currently Applied 634
17.2.1 All-Dielectric Filters 636
17.2.2 Metal-Dielectric Filters 638
17.2.3 Optically Variable Pigments 643
17.3 Specific Optical Effects Suitable for Security Devices 644
17.3.1 Metamerism 644
17.3.2 Magnetic Films 648
17.3.3 Combining Interference and Diffraction 649
17.3.4 Other Color Shifting Technologies 651
17.4 Active Devices 652
17.4.1 Application of Active Materials 652
17.4.2 Electrochromic Devices 654

17.5 Film Functionality and Structurally Controlled Optical Coatings 656
17.6 Conclusion 658
References 659

CHAPTER 18 Optical coatings for high-intensity femtosecond lasers 667
Volodymyr Pervak

18.1 Introduction to the Field of Ultrafast Optics 667
18.2 Mirror Design Approaches 669
18.2.1 Dispersive Mirrors 669
18.2.2 Resonant Structure or Gires-Tournois Interferometer Mirror 670
18.2.3 Double-Chirped Mirrors 671
18.2.4 Brewster-Angle CM 672
18.2.5 Back-Side-Coated CM 673
18.2.6 Tilted-Front-Interface CM 673
18.2.7 Complementary Pairs of CMs 674
18.2.8 The Time-Domain DM 676
18.2.9 Double-Angle DM 677
18.2.10 Pulse Compression and Analysis 677
18.3 The Highest Possible Value of GDD 678
18.4 Production of DM 679
18.5 Pulse Compression With DM 680
18.6 Measurement of Group Delay With White Light Interferometer 684
18.7 Application of DM in the High-Intensity Lasers 687
18.8 Conclusions 691
References 691

CHAPTER 19 Optical coatings for large facilities 697
Catherine Grèzes-Besset, Grégory Chauveau, Laurent Pinard

19.1 Introduction 697
19.2 Domains of Applications and Major Programs 697
19.2.1 Scientific Large Instruments 698
19.2.2 Laser 699
19.2.3 Space 701
19.2.4 Astronomy 702
19.2.5 Solar Plants 702
19.3 Review of Technological Solutions 703
19.3.1 Thermal and Electron Gun Evaporation 703
19.3.2 Sputtering 704

19.4 Thin-Film Uniformity: Key Problem 706
19.5 Focus on Large Magnetron Sputtering Facility 708
19.6 Highlights on Two Major Programs 711
19.6.1 Focus on LMJ 711
19.6.2 Focus on Virgo 713
19.7 Conclusion 715
References 715
Relevant Websites 718
Further Reading 718

CHAPTER 20 Optical coatings for automotive and building applications 719
Chris H. Stoessel

20.1 Introduction 719
20.2 The Role of Thermal Control in Glazing 720
20.2.1 Building Window Energy Efficiency 721
20.2.2 Automotive Window Energy Efficiency 722
20.3 Window Coating Types by Functionality 723
20.3.1 Low Emissivity 723
20.3.2 Spectral Selectivity (Infrared Reflecting, Ultraviolet Blocking) 724
20.3.3 Antiglare 726
20.4 Glazing Types: Monolithic, Laminated, and Multicavity Glazing Designs 726
20.5 Coatings on Glass Substrates 727
20.5.1 Low-Emissivity Coatings 727
20.5.2 Antiglare 728
20.6 Coatings on Polymer Substrates 729
20.6.1 Films for Laminates 730
20.6.2 Films for Multicavity Glazing Applications 731
20.6.3 Applied Window Film Products for Retrofit Applications 731
20.7 Special Considerations for Applications 731
20.7.1 Automotive Applications 732
20.7.2 Building Applications 734
20.8 Conclusion 736
20.9 Future Trends 737
20.10 Sources of Further Information and Advice 738
Acknowledgments 738
References 738

CHAPTER 21 Transparent conductive thin films 741
Clark I. Bright

21.1 Introduction 741
21.1.1 Transparent Conductive Oxides 742
21.1.2 Transparent Metallic Thin Films 744
21.2 Conductivity Fundamentals 746
21.2.1 Metals 746
21.2.2 Doping 747
21.2.3 Optical Properties Related to Conductivity 748
21.3 Control of Optoelectronic Properties 753
21.4 Beyond Optoelectronic Properties 754
21.5 Traditional Applications 755
21.5.1 Heaters 755
21.5.2 Electromagnetic Interference Shielding 757
21.5.3 Antistatic Films 757
21.5.4 Transparent Electrodes 757
21.5.5 Energy-Efficient Windows 764
21.6 Recent Applications 767
21.6.1 Conductive AR 767
21.6.2 Touch Sensors 770
21.6.3 OLED Lighting 773
21.6.4 Transparent Oxide Electronics 774
21.7 Future Applications 775
21.7.1 Beyond TFT 775
21.7.2 Transparent OLED 776
21.7.3 Transparent PV (Solar) Cells 777
21.7.4 Transparent Electrochromic Windows 778
21.8 Conclusion 779
21.8.1 Future Developments and Outlook for *n*-Type TCTF ... 780
21.8.2 Future Developments and Outlook for *p*-Type TCTF ... 782
21.8.3 Other Review Articles 783
References 784
Sources of Further Information and Advice 788
Further Reading 788

CHAPTER 22 Optical coatings in the space environment 789
Denny Wernham, Angela Piegari

22.1 Introduction 789
22.2 The Space Environment 789
22.2.1 General Overview of Optics in Space 790

22.2.2 Impact of Space Vacuum 791
22.2.3 Thermal Cycling in Vacuum 794
22.2.4 Solar Irradiance 798
22.2.5 Particulate Radiations 799
22.2.6 Atomic Oxygen 801
22.3 Contamination 801
22.3.1 Terrestrial Contamination 801
22.3.2 Space Contamination Effects 804
22.4 Product Assurance for Space Coatings 806
22.4.1 End to End Traceability 806
22.4.2 Process Control 807
22.4.3 Nonconformance Control 807
22.4.4 Space Qualification 808
22.5 Conclusion 809
Acknowledgments 809
References 810

Index 813

Contributors

Tatiana V. Amotchkina
Ludwig-Maximilians-Universität München, Garching, Germany

Bill Baloukas
Department of Engineering Physics, Polytechnique Montréal, Montreal, QC, Canada

Nicolas Barreau
Nantes University, CNRS, Institut des Matériaux Jean Rouxel (IMN), (UMR6502), Nantes, France

Gerard Berginc
Thales, La Défense, France

Veronica Bermudez
Nexcis, Rousset, France

Tjhay W. Boentoro
Fraunhofer Institute for Surface Engineering and Thin Films—IST, Braunschweig, Germany

Clark I. Bright
Bright Thin Film Solutions LLC, Tucson, AZ, United States

Grégory Chauveau
CILAS, Aubagne, France

Yu-Jen Chen
National Central University, Taoyuan, Taiwan

David Duche
Aix-Marseille University, University Toulon, CNRS, IM2NP, Marseille, France

Henrik Ehlers
Laser Zentrum Hannover, Hannover, Germany

Ludovic Escoubas
Aix-Marseille University, University Toulon, CNRS, IM2NP, Marseille, France

Muhammad Faryad
Department of Engineering Science and Mechanics, The Pennsylvania State University, University Park, PA, United States

François Flory
Ecole Centrale Marseille, Marseille, France

Catherine Grèzes-Besset
CILAS, Aubagne, France

Chien-Cheng Kuo
National Central University, Taoyuan City, Taiwan

Akhlesh Lakhtakia
Department of Engineering Science and Mechanics, The Pennsylvania State University, University Park, PA, United States

Juan I. Larruquert
Institute of Optics-Spanish National Research Council, Madrid, Spain

Judikael Le Rouzo
Aix-Marseille University, University Toulon, CNRS, IM2NP, Marseille, France

Cheng-Chung Lee
National Central University, Taoyuan City, Taiwan

Hung-Ju Lin
National Central University, Taoyuan, Taiwan

H. Angus Macleod
Thin Film Center Inc., Tucson, AZ, United States

Alexei A. Maradudin
University of California, Irvine, CA, United States

Ludvik Martinu
Department of Engineering Physics, Polytechnique Montréal, Montreal, QC, Canada

Thomas Neubert
Fraunhofer Institute for Surface Engineering and Thin Films—IST, Braunschweig, Germany

Claudio Oleari
University of Parma, Parma, Italy

Volodymyr Pervak
Ludwig-Maximilians-University, Munich, Germany

Angela Piegari
Optical Coatings Group, ENEA, Rome, Italy

Laurent Pinard
Lyon I University—CNRS-IN2P3, Lyon, France

Daniel Poitras
National Research Council of Canada, Ottawa, ON, Canada

Carl G. Ribbing
Uppsala University, Uppsala, Sweden

Detlev Ristau
Laser Zentrum Hannover, Hannover, Germany

Carmen M. Ruiz
Aix-Marseille University, University Toulon, CNRS, IM2NP, Marseille, France

Robert W. Schaffer
Evaporated Coatings Inc., Willow Grove, PA, United States

Ulrike Schulz
Fraunhofer Institute of Applied Optics and Precision Engineering IOF, Jena, Germany

Jean-Jacques Simon
Aix-Marseille University, University Toulon, CNRS, IM2NP, Marseille, France

Chris H. Stoessel
Southwall Technologies (a Subsidiary of Eastman Chemical Co.), Palo Alto, CA, United States

Anna Sytchkova
ENEA Optical Components Group, Rome, Italy

Bernd Szyszka
TU Berlin, Institute for High Frequency and Semiconductor System Technologies, Berlin, Germany

Alexander V. Tikhonravov
Moscow State University, Moscow, Russia

Michael K. Trubetskov
Max-Planck Institute of Quantum Optics, Garching bei München, Germany

Michael Vergöhl
Fraunhofer Institute for Surface Engineering and Thin Films—IST, Braunschweig, Germany

Pierre G. Verly
National Research Council of Canada, Ottawa, ON, Canada

Denny Wernham
The European Space Agency (ESA), Noordwijk, The Netherlands

This page intentionally left blank

Preface to the First Edition

The field of optical coatings was thoroughly investigated in the last century and the optical effects of thin films were known even before then, as described by Newton and other scientists in the eighteenth century.The antireflection effect of a single layer on glass was first discovered by Fraunhofer in 1817 but the real development of simple antireflection coatings using vacuum deposition techniques was made in the 1930s, both in Europe and the United States. The understanding of optical interference in thin films and the development of the formalism for the propagation of electromagnetic waves through a layered medium paved the way for designing and producing multilayer coatings in the years following. The deposition under vacuum of metal films for obtaining high-reflectance mirrors was also developed at the industrial level in the first half of the twentieth century, even though mirrors were known long before that, and metal-dielectric filters started to be produced at that time as well.

Since then, much progress has been made in coating design, owing to both the fast development of computers and the implementation of dedicated software. At the same time, the improvements in the technologies for deposition of thin films have allowed ever more reliable coating manufacturing. Nowadays optical coatings are considered an important sector of optical components and often they represent the critical part of entire optical systems, therefore significant efforts are dedicated to improve their performance. Applications can be found in many areas: lasers, smart windows, clean energy, environmental monitoring, telecommunications, astronomy, aerospace, displays and lighting, and anti-counterfeiting devices are only some examples of a long list. As there is an increasing demand for optics in many fields, the range of applications for optical thin films and coatings is widening more and more.

Thin-film optical coatings is an active field of research and innovative breakthroughs are continuously being made, especially in investigations on new materials and structuring of the coating morphology. The development of heterogeneous nanostructures is enlarging the use of thin films and this area is now part of nanophotonics.

A number of books have already been published on both optical coating design and thin-film deposition techniques, as well as on characterization methods, and there is a vast literature on these topics. Thus we decided to dedicate this book mainly to developments on thin-film materials and applications, for optics and related fields.

The book is divided in four parts. The initial chapters in Part I are devoted to classical topics and give a short review of each subject, including new advances. A survey of deposition techniques for optical thin films opens the book (Chapter 1), followed by a description of the methods of design of complex optical coatings (Chapter 2), these being two subjects of central relevance in each approach to optical coatings. Then, the monitoring of coating fabrication (Chapter 3) and the

production technologies for high-precision coatings (Chapter 4) are described, with a look at historical developments and new strategies.

Part II is dedicated to some special features of optical thin films and coatings, like plasmonic effects for optical applications (Chapter 5), scattering in random structures (Chapter 6), thin film properties at short wavelengths (Chapter 7), thermal radiation control (Chapter 8) and color effects (Chapter 9).

Part III follows with some recent developments on film materials, starting with organic films and coatings (Chapter 10); then an overview of surface multiplasmonics with non-homogeneous thin films is given (Chapter 11) and finally a description of optical films containing quantum dots (Chapter 12) closes this part of the book.

The chapters from 13 to 22, in Part IV, are dedicated to applications and represent almost half of the book. They cover different fields, even though they are not exhaustive of all possible areas in which optical thin films can be useful. This last part of the book starts with antireflection coatings on plastic (Chapter 13) and protective coatings for optical surfaces (Chapter 14), then continues with applications in displays and lighting (Chapter 15), photovoltaic cells (Chapter 16) and security devices (Chapter 17). The next two chapters (Chapter 18 and Chapter 19) are dedicated, respectively, to the application of coatings in high-intensity femtosecond lasers and to coatings in large facilities involving lasers and space.

The last chapters give an overview on automotive and building applications (Chapter 20), transparent conductive coatings (Chapter 21) and the behavior of optical coatings in space (Chapter 22).

It is difficult to include in a single book all the interesting applications, such as for example: optical sensors, optical coatings for telecommunications, optics for art conservation, biological and medical applications, and more. Therefore a selection has necessarily been made. Moreover, characterization methods are not specifically dealt with, even though they are of great importance in this field not only to control the optical properties but also to test the environmental resistance of coatings; there are many types of characterization methods for thin films and coatings and some of them are described in different chapters.

The diffusion nowadays of multimedia and the possibility of downloading from the web single chapters of the book, means that each chapter should be self-contained. As a consequence, some overlaps can be found between several chapters. For example optical monitoring strategies are described in both Chapters 3 and 4, plasmonics is present in the title of Chapters 5 and 11, organic thin films are mentioned in Chapters 10 and 16 and solar cells in Chapters 2 and 16, transparent conductive coatings appear in Chapters 20, 21 and others as well. However, even when similar topics are described by more than one author, the approach is substantially different and complementary. More details can be found in the contents of each chapter, which will be accessible through the web.

The authors come from both research institutes and industry, thus a combination of theoretical contributions and practical views can be seen throughout the whole book. All contributors are renowned specialists in their fields and many of them, as well as the editors, have been working in the area of optical thin films for more

than thirty years. Several chapters are authored by experts who took part in the early developments in the specific sectors, and published many fundamental works.

We hope the book will be useful for scientists and technical people, providing an overview of the key role of optical coatings in different fields and stimulating the reader's interest to go deeper in each topic, taking advantage of the bibliographic material in all chapters.

The potential readers of this book may be physicists, chemists and engineers, including senior students, interested in both research developments and practical applications. Newcomers to the field of optical thin films and coatings could be attracted by the extremely wide range of applications, while specialists of a particular field could find information on the new trends in their area of interest.

We wish to thank all authors for their valuable contributions and efforts and we are also grateful to the Publishers for their assistance during the preparation of the book.

Angela Piegari
Rome, Italy

François Flory
Marseille, France
March 2013

This page intentionally left blank

Preface

The second edition of the book comes 5 years after the first edition, and this work would not have been possible without the support of Elsevier Publisher, especially Kayla Dos Santos who asked us to review the book 2 years ago and followed all the steps till the publication, together with her collaborators.

In the recent years, the field of optical coatings expanded, however, the topics included in the first edition are still valid, with some chapters dedicated to traditional subjects, some others devoted to new materials and features, and many chapters covering specific applications. We decided to leave the structure of the book unchanged and divided it into four parts, with 22 chapters grouped in the following areas: (I) design and manufacturing of optical thin films and coatings, (II) unconventional features of optical thin films and coatings, (III) novel materials for optical thin films and coatings, and (IV) applications of optical thin films and coatings.

In this edition most of the chapters have been revised, adding recent developments and updating the bibliography. Only two chapters have been reprinted without variations (Coatings for lighting and thermal radiation control) because the authors were no longer available; nevertheless we preferred to keep the original writings of these chapters because their contents are still of interest to our community. In spite of including additional material, the book is far from complete; there are several other interesting subjects in the field of optical thin films and coatings. Books dedicated to specific aspects are available and also the topics included in this book could be analyzed in greater detail using the bibliography reported in each chapter.

In a few chapters of this edition, new names were added to the list of original contributors, being the revision made by new authors. We wish to thank especially the new contributors because they accepted the difficult task of acting on a text written by others.

We are deeply grateful to all the authors for dedicating time and efforts to revise their chapters; we also wish to acknowledge the helpful support of the Elsevier staff and thank all readers of the book.

Angela Piegari
François Flory

This page intentionally left blank

PART

I

Design and manufacturing of optical thin films and coatings

This page intentionally left blank

CHAPTER

1 Recent developments in deposition techniques for optical thin films and coatings

H. Angus Macleod
Thin Film Center Inc., Tucson, AZ, United States

1.1 INTRODUCTION

A thin-film optical coating is a treatment intended to modify, in a prescribed way, the properties of the surface that supports it, and the deposition of the coating, therefore, begins with this surface. Although the coating may be expected to present a range of different properties, environmental, thermal, chemical, even acoustical, the primary objective is most frequently a set of desired specular optical properties that alter the quality of the light manipulated by the surface but leave its direction unchanged. This is the nature of the bulk of the coatings considered in this book. A glance at the chapter headings will demonstrate the enormously wide range of possible coating types. For such coatings, the surface must be smooth in optical terms. In other words, departures from perfection should be of a size that is orders of magnitude less than the wavelength of the light. We assume that this is the case. Our coatings then consist of one or more thin layers of chosen materials that together exhibit the properties that we require, usually by a combination of interference and the intrinsic properties of the materials. Sometimes the materials may themselves be altered from their natural state by engineering their microstructure and this is dealt with elsewhere in this book.

The forces that hold thin films together and attach them to their surfaces are all short range, from one atom to the next. These forces are exceedingly strong but have quite short range and so a monomolecular layer of contaminant can block the bonds completely. Thus, not only is the smoothness of the surface important but its cleanliness is even more so.

There are so many processes that are or have been used for the deposition of optical coatings that a complete list is beyond us. Probably one of the earliest was the production of mirrors during the later Roman Empire by pouring molten lead over glass. Enough lead adhered to the glass to increase considerably its reflectance but the glass tended to shatter under this treatment and so the mirrors were small and irregularly shaped. An improved technique originating in the 15th century was a tin

Optical Thin Films and Coatings. https://doi.org/10.1016/B978-0-08-102073-9.00001-1
Copyright © 2018 Elsevier Ltd. All rights reserved.

amalgam coating that, coupled with the enormous simultaneous improvements in the quality of flat glass, allowed mirrors of essentially modern quality to be produced. Chemical silvering was developed in the middle of the 19th century and was the preferred technique for front-surface mirrors until the 1930s. At the same time, great progress was made in photographic processes culminating in the Lipmann emulsion that, when developed, was essentially a thin-film interference filter. Artificial tarnishing of glass surfaces to reduce their reflectance was also practiced to an extent in the 19th century. However, apart from the front-surface mirror coatings, there was little need for optical coatings until the increasing complexity of optical instruments and systems in the early 20th century demanded improved surface properties, especially the reduction of reflectance that greatly improved transmittance at the same time as removing glare and ghost images. Vacuum deposition was generally adopted as the preferred process. By the middle of the 20th century, the field of optical coatings was growing rapidly. Much was happening in optics, but the advent of the laser was probably the most significant event and lasers need coatings. The unprecedented expansion of optics in the second half of the 20th century took optical coatings with it and the expansion still continues in the 21st century.

Today, vacuum deposition is still the major process for the production of optical coatings but while thermal evaporation has been the primary process for many years, we are now seeing much more use of alternative vacuum processes and even some processes that do not depend on vacuum.

1.2 EARLY PROCESSES FOR THE DEPOSITION OF OPTICAL COATINGS

In 1912, Pohl and Pringsheim published a paper on the deposition of metallic mirrors through a process they called vacuum distillation (Pohl and Pringsheim, 1912). This laid out the principles of what became known as thermal evaporation. Thermal evaporation is quite simple. Material is heated under vacuum until it boils, and the resulting vapor then condenses on the substrates to be coated, which are held at temperatures well below the freezing temperature of the evaporated material. The material, the evaporant, immediately forms a thin solid film. Although Pohl and Pringsheim's paper dealt with metals, it was clear that dielectrics and semiconductors could be equally well deposited by this technique. The technique became quite generally used for optical coatings in the 1930s and it is still of considerable importance. The thickness of the deposited film tends to follow the same rules as illumination, inverse square law coupled with the cosines of incident and emission angles, and the uniformity required for any but the simplest single-layer antireflection coatings requires movement of the substrates during deposition to even out the layer thickness. The movement is usually fairly simple involving single or double rotation of the structure holding the substrates.

Early dielectric coatings produced by the thermal evaporation technique exhibited two serious problems. They were not particularly resistant to abrasion, and their

spectral characteristics tended to be slightly unstable, usually settling down after a shift to longer wavelengths. This behavior was often termed settling. In the 1940s, it was found possible to improve considerably the abrasion resistance by heating the substrates during deposition (Lyon, 1946) and so that was the first major development in the technique. Radiant heating is normal.

The early evaporation sources were crucibles of refractory metal, like molybdenum, tantalum, or tungsten, heated by passing a current through them. The sources tended to be elongated with lands at the ends for attaching electrodes. The appearance was similar to that of a boat and so the sources, inevitably, are known as boats. Boat sources are still used, but often suffer from corrosive interaction with the heated charge. They are also often run at temperatures close to their melting points when they can distort and change the distribution of vapor. There has therefore been a gradual shift towards electron-beam heating. The electron-beam source normally consists of a metallic crucible, usually copper, with perhaps a suitable lining, which is water cooled. The charge in the crucible is heated by directing a beam of energetic electrons onto it. Beam current can be several ampères and the voltage several kilovolts and so the heat delivered to the charge is massive and capable of melting virtually anything. Interaction with the crucible is inhibited by its water cooling. The electron source is a hot filament that would also suffer from corrosion were it exposed to the evaporant. It is therefore buried in the structure of the source and the electron beam is bent through at least 180° by the magnetic field of a, usually permanent, magnet with pole pieces that run along the side of the source. This helps to focus the beam. Additional, small, electromagnets are frequently included to vary the beam position and the pattern of its movement over the surface of the charge. Although the electron-beam source is rather more expensive than the boat source, it has reached the stage of development where its stability and reliability keep the running costs low and the yield of acceptable products high.

Experiments on both metals and dielectrics by Movchan and Demchishin (1969) in the late 1960s eventually showed that the important parameter in this heating was the ratio of the temperature of the substrate to the melting temperature of the evaporant. Evaporated thin films have a columnar microstructure and the packing of the columns is of critical importance in determining the film properties. Movchan and Demshishin identified three growth zones. Zone One with a ratio for dielectrics below around 0.22–0.26 gives loose dendritic columns with poor mechanical properties, particularly abrasion resistance. A larger ratio of roughly up to 0.45–0.5 yields Zone Two, where the columnar structure becomes very close packed with improved abrasion resistance and stability. With ratios above around 0.5, we have Zone Three where the columns tend to be replaced with what appear to be small recrystallized grains. For optical coatings, Zone Two is much to be preferred. Films produced in Zone Three usually show significant scattering losses and, in any case, the temperature required for the many refractory materials that are employed is too high for normal deposition equipment. This structural zone model is of enormous help in understanding film properties and it has been developed and elaborated (Thornton, 1974) over the years and is still a topic of investigation (Anders, 2010). For instance,

the importance of the energy of the arriving evaporant has been recognized. A transition zone between Zone One and Zone Two has been identified (Thornton, 1974).

By the end of the 1970s, capillary condensation of atmospheric moisture in the pores in between the columns had been shown to be the major cause of the drifting or settling of the optical coatings (Koch, 1965; Macleod and Richmond, 1976; Ogura and Macleod, 1976; Lee, 1983). There were some hints (Motovilov et al., 1974; Hirsch and Varga, 1978) that what were later classified as the energetic processes might offer some improvement.

1.3 THE ENERGETIC PROCESSES

The energetic processes are so-called because they involve the addition of kinetic energy to the condensation process. This additional energy can be supplied in different ways. It may be that of the evaporant itself or may be derived from bombardment by specially generated beams of energetic ions. The energetic processes share the property of increasing the solidity, density and, often, adhesion of the growing films.

Movchan and Demchishin had explained the origin of the universal columnar structure of thermally evaporated thin films as the limited mobility of the condensing species, and this has been confirmed by computer modeling that began with the pioneering work of Dirks and Leamy (1977) and has been detailed by Jacobson (1988). The original ideas of the possible mechanism for the densification inherent in the energetic processes were that the bombardment somehow increased the mobility of the condensing material, perhaps through a form of annealing due to thermal spikes caused by the collisions (Hirsch and Varga, 1980). However, computer simulations tended to show that the densification was due to momentum transfer rather than thermal spikes (Müller, 1986a,b), although thermal spikes could contribute to a sealing of some of the porous voids in the films. Experiments then confirmed that the primary mechanism for densification is momentum transfer (Targove and Macleod, 1988; Targove et al., 1988).

1.3.1 ION-ASSISTED DEPOSITION

The simplest of the energetic processes is termed ion-assisted deposition, or IAD. This is thermal evaporation with additional ion bombardment of the growing film (Fig. 1.1). Broad-beam ion sources had been developed originally by NASA as possible propulsion engines for outer space. They were rapidly adopted by industry, primarily for ion-beam etching in the semiconductor industry, and so were readily available for incorporation in optical coating machines (Harper et al., 1982; Kaufman et al., 1982a,b). The broad-beam sources, mainly of the Kauffmann type, could be incorporated into thermal evaporation machines with little modification. The ions extracted from the source, with energy usually around a few hundred electron volts, are positive and so would rapidly charge any dielectric material

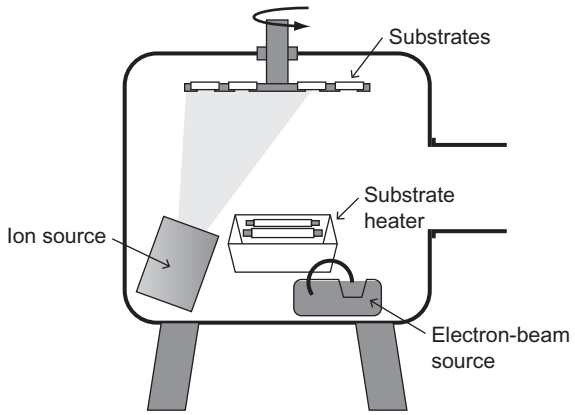


FIG. 1.1

Sketch of a typical arrangement for ion-assisted deposition. The broad-beam ion source does not always irradiate the entire substrate carrier but the rotating substrate carrier moves the substrates through the ion beam each rotation.

Courtesy of Thin Film Center.

preventing further bombardment. Sufficient electrons to neutralize this charge are therefore added to the extracted beams yielding what is usually termed a neutral ion beam. In the early work, mostly argon was used as the bombarding species but, as we shall see, a much wider range is used today. It was soon demonstrated that the bombardment in ion-assisted deposition could so improve the solidity of films as to remove completely their moisture sensitivity (Martin et al., 1983). The absence of moisture-induced shifts and, also because of the high packing density, the more stable optical constants were major reasons for the rapid adoption of ion-assisted deposition by industry.

There are several advantages in ion-assisted deposition over many of the other energetic processes. Probably the most significant, at least in the early days, is not so much a technical as a financial one. Conversion from thermal evaporation, the almost universal technique for optical coatings at that time, was relatively inexpensive. It consisted of the addition of an ion source with its associated power supply and so did not involve the scrapping of an existing, expensive machine. A second, technical advantage is that the bombardment parameters can be adjusted completely independently of the other deposition parameters. The Kaufman source with its extraction grid yields a quite tight distribution of ion energies, making it especially attractive for research.

The refractory oxides represent a very important class of materials. There is a general tendency for these materials to lose some oxygen in the evaporation process and the resulting vacancies cause absorption. The oxygen can be restored by adding oxygen to the background atmosphere of the machine in a process termed reactive evaporation. Reactive evaporation can even produce stoichiometric oxides by the

evaporation of metals in an oxygen atmosphere. A fine degree of judgment is called for in the reactive process. Not enough oxygen and the absorption remains, although reduced; too much oxygen and the packing of the thin film suffers with all the accompanying consequences. Then many nitrides, particularly of silicon and aluminum, are useful optical materials, but straightforward reactive evaporation fails. The nitrogen is not sufficiently reactive.

The reactivity of oxygen and nitrogen can be greatly increased by passing it through the ion source. Pure oxygen can be rather too reactive when in the ionization chamber of the source so that it reacts with its structure and especially with the hot filament of the Kaufman type. Oxygen, if it is to be passed through the ion source, is usually diluted by mixing it with the argon stream. Nitrogen, however, derives great benefit from passage through the source and becomes sufficiently reactive to produce highly transparent and high-quality nitride films (Netterfield et al., 1986; Targove et al., 1987; Hwangbo et al., 1989).

There are many variants of what is essentially ion-assisted deposition that differ principally in the details of the design of the source. An ion source is one in which ions, usually positive ions, are extracted, often by means of a grid, and that has been the primary thrust of the description so far. A plasma source is one in which the entire plasma is permitted to emerge from the source. The electrons in the plasma are very mobile and tend to escape leaving a positively charged plasma that repels the positive ions so that they then bombard the growing film. This is usually termed plasma ion-assisted deposition to distinguish it from ion-assisted deposition.

The major recent development is a move to radio frequency (13.56 MHz) (Anders, 2005; Hagedorn et al., 2008) or even microwave (2.45 GHz) (Sakudo, 1998; Anders, 2005) excitation of the plasma in the source. This reduces the level of impurities in the ion beam and also permits much longer operation of the source before any necessary maintenance.

The fluorides with their enormously wide range of transparency from the far infrared to the extreme ultraviolet are very attractive thin-film materials that are much used. Unfortunately, the bombardment inherent in the energetic processes tends to damage the material by preferential removal of fluorine. Small losses of fluorine can be tolerated because the vacancies are usually healed by oxygen and optical absorption is then minimized. With larger fluorine loss, however, an oxyfluoride can form that has normally rather poorer durability, more constricted regions of transparency, and elevated refractive index. All this implies that bombardment of the fluorides in energetic deposition must be severely limited. Gentle bombardment is beneficial and has been shown to improve adhesion, increase packing density, and inhibit oxidation but not nearly to the extent of the improvements found in the oxides and nitrides (Saxe, 1985; Messerly, 1987; Targove, 1987).

1.3.2 ION PLATING

Ion plating is a somewhat imprecise term used for a variety of processes. In its original form, it was intended to replace electroplating (Mattox, 1967) and it has achieved a high degree of success in that role. In that application, it consists of a

thermal evaporation source and a metallic substrate holder with a glow discharge between them sustained by several thousand volts, the anode being the source and the cathode the substrate holder, an arrangement known as high-voltage ion plating. The original idea was that the positive ions would be attracted from the plasma to bombard and coat the substrates. Hard, tough deposits with excellent throw are, in fact, produced. It is now clear that the process is much more complex (Mattox, 1979) and there can be large differences between the various forms of implementation. The degree of ionization in high-voltage ion plating is usually quite small and the major effect is the bombardment of the growing film by energetic particles, mostly neutral and that have gained energy from collisions in the discharge. These energetic particles, largely of the evaporant, form the growing film and, in transferring momentum, compact it as in ion-assisted deposition. The improved throwing power appears to be largely because of the accompanying gas scattering. This high-voltage form of ion plating has not been much used for optical coatings although Reid and colleagues did produce remarkably tough zinc sulfide layers for use in the infrared (Reid et al., 1979).

Reactive low-voltage ion plating (Moll et al., 1986; Pulker, 1992; Pulker and Guenther, 1995) is a more common ion-plating system for optical coating deposition (Fig. 1.2). It consists of a thermal evaporation machine with an electron-beam source containing a metal or suboxide that is sufficiently conducting. This source is insulated from the structure of the machine and is connected to the positive pole of a

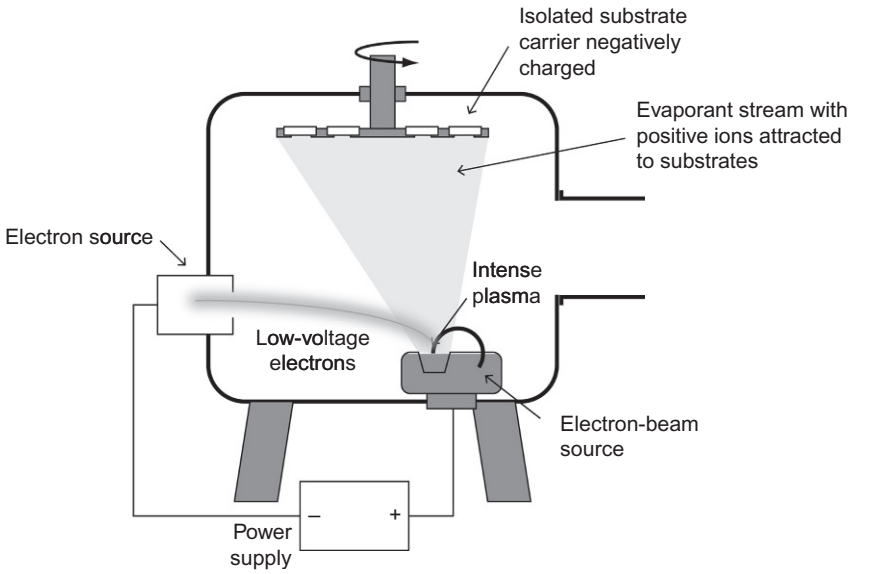


FIG. 1.2

Reactive low-voltage ion plating.

After Pulker, H.K., Guenther, K.H., 1995. Reactive physical vapor deposition processes. In: Flory, F.R. (Ed.) Thin Films for Optical Systems. New York, Basel, Hong Kong: Marcel Dekker, Inc. Courtesy of Thin Film Center.

DC power supply that provides large current at a few hundred volts. The negative side of the power supply is connected to a plasma chamber, also isolated from the machine, which provides an intense beam of low-voltage electrons. These are attracted to the electron-beam source, where an intense plasma forms above the evaporating surface. The substrate carrier is also electrically isolated from the machine, and the electrons that are very mobile, charge it negatively, attracting positive ions from the plasma. These positive ions consist of source material and they impinge on, and form part of, the growing film with all the densification that comes from the transfer of momentum. For transparent films, additional oxygen is added to the plasma to make the process reactive. Alternatively, nitrogen can be added either to create an oxynitride or a nitride, all with excellent optical properties (Bovard et al., 1989).

1.3.3 SPUTTERING

Sputtering is probably the oldest of the energetic processes. It dates back to the middle of the 19th century (Grove, 1852) but it was not much used in the production of optical coatings until the second half of the 20th century. In its simplest form, it consists of an evacuated chamber containing a metallic anode and cathode. These are so arranged as to maintain a glow discharge in the residual gas in a chamber. A voltage of a few kV, together with a pressure of around 1 Pa or greater (0.01 mbar), gives a very rough idea of what might be required. Positive ions from the discharge are attracted to the cathode and bombard it with elevated energy. Transfer of momentum from the bombarding ions to the molecules of the cathode causes collision cascades that end with the ejection of molecules from the cathode with considerable kinetic energy. Although it is not always possible, for best results the atomic weight of the bombarding species should be similar to that of the target material maximizing the momentum transfer. There is only quite small ionization of the sputtered material and, ideally, these molecules travel in straight lines to impinge on the anode, or substrate, and form there a thin solid film. The momentum transfer from the arriving material promotes a dense microstructure in the film.

There are some problems that cause departure from the ideal situation. The first is that, as described, the process works only for conducting metals. If we replace the metallic anode and cathode with dielectrics, then the surfaces quickly charge and inhibit any further sputtering. To prevent this suppression of the sputtering process, the surfaces must be discharged. The capacitance of a dielectric surface is minuscule and the rate of charging exceptionally high. Since the rate of discharging must be equally high, we are led to the process known as radio frequency in which the plasma is created by a radio frequency field rather than zero frequency. The process works well and has been and is used for optical coating deposition. However, there are many more problems associated with radio frequency processes than with zero frequency and so in optical coating the process tends to be used in special cases rather than applied generally.

A second problem is that, with the simple system described, the plasma is in the way of the sputtered material. The resultant scattering reduces the energy of the condensing material and, therefore, acts against the desired densification. Magnetron sputtering (Kelly and Arnell, 2000) can achieve an order of magnitude lower pressure, say 0.1 Pa (0.001 mbar) compared with the 1 Pa or greater in traditional sputtering together with a reduction in the necessary voltage to some hundreds of volts instead of some kilovolts. In magnetron sputtering, the electrons are forced into cycloidal paths by the addition of a magnetic field. Permanent magnets with alternating poles are fixed behind the cathodes (usually plane) so that at a short distance, 10–20 mm perhaps, above the cathode surface the electric field and the magnetic field are crossed (Fig. 1.3). In that region, the plasma forms because of the enhanced ionization due to the longer cycloidal path of the electrons. The plasma is somewhat limited in its extent and so too is the erosion region. On plane rectangular cathodes, the erosion region looks like a map of a racetrack and so the term 'racetrack' is normally used to describe it.

Reactive sputtering represents a way of overcoming the problem of dielectrics. Many dielectrics are metal oxides or sometimes metal nitrides. In such cases, the cathode can be left as the desired metal and reaction can be arranged by adding the necessary oxygen or nitrogen to the background gas. The discharge activates the reacting gas so that its reaction with the growing film is virtually complete and high-quality dielectrics result. Unfortunately, the process is not as successful with fluorides. Fluorine is preferentially sputtered and lost, either from the growing film or from a fluoride target, just as in the ion-assisted processes. Although reactive processes involving added fluorine and fluorine compounds have been pursued in the research laboratory with some degree of success, such processes have not so far been seen as sufficiently reliable to be adopted generally in production.

Unfortunately, in reactive sputtering, the reacting gas tends to react not simply with the growing film but with the sputtering target as well. In magnetron sputtering, this results in a build up of insulating material known as target poisoning. In the

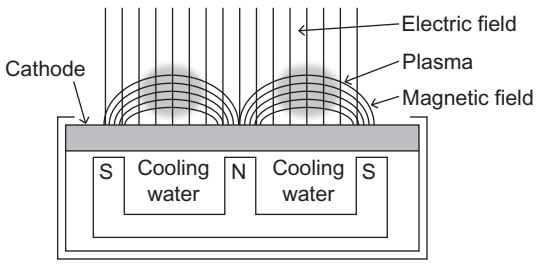


FIG. 1.3

Schematic cross-section of a planar magnetron cathode showing the crossed electric and magnetic fields with the resulting plasma. The area of the cathode under the plasma is the part mainly eroded and is known as the racetrack because of its shape.

Courtesy of Thin Film Center.

racetrack, any insulating material is rapidly removed by the bombardment. It does cause some hysteresis in the electrical characteristics that has to be dealt with in the control system, but it is outside the racetrack that serious problems occur. The thin dielectric layer acts as a capacitor that charges up as the positive ions arrive. Because the coating is thin, the capacitance is high and the charge represents considerable energy. This energy is released from time to time in a capacitor failure and the very high stored energy causes an arc that is frequently powerful enough to melt local regions of the cathode, causing ejection of metallic globules, many of which arrive at the substrate. Fortunately, the high capacitance implies a long time constant so that discharging the capacitors can be carried out at relatively low frequencies, a few tens of kilohertz. Special power supplies that periodically reverse their polarity to discharge the capacitors represent one common solution. Recently, however, a technique known by several different terms has gained much ground in optical coating. Mid-frequency sputtering, or dual magnetron sputtering, involves two similar magnetrons attached to opposite sides of a power supply operating at around 40 kHz. This implies that every half cycle the rôles of the magnetrons switch from cathode to anode and vice versa. This effectively discharges the capacitors and solves another problem that can occur with reactive sputtering known as the disappearing anode. The anode in the normal sputtering process is often the structure of the machine or, sometimes, a rod or similar element introduced to act as anode. The anode gradually becomes coated with an insulating film just like the regular substrates and its effectiveness eventually vanishes. In mid-frequency sputtering, the alternate target is the anode, and so the problem is solved. Mid-frequency sputtering was introduced originally for coating large areas, usually of glass, but in the past decade it has been adopted by precision optical coating.

Target poisoning can be eliminated by scrubbing the whole surface of the cathode by the ions from the plasma. This implies moving the plasma, or moving the surface, or both. In the cylindrical rotating magnetron source, the target becomes cylindrical and is rotated around the permanent magnets. This has the additional advantage of smoothing out the eroded area so that the racetrack disappears and cathode utilization is much more efficient. Small cylindrical magnetrons have penetrated into the precision optical field, particularly in the mid-frequency configuration. Although they do not suffer from the poisoning effects of reactive deposition, they can experience the disappearing anode and this is eliminated by the mid-frequency technique.

A paper describing a process called alternating ion plating (Fig. 1.4) appeared in 1975 (Schiller et al., 1975). Although, at the time, it was not aimed at optical coatings and did not attract any unusual level of interest, nevertheless its effect on the field has been fundamental and far-reaching. The idea is simple. The plasma treatment of the growing film that exists in ion plating, ion-assisted deposition, sputtering, and other reactive energetic processes, interferes with the deposition process. Since the effect of the ion bombardment reaches a certain, small depth in the film it would be better to add an increment of film, bombard it, add another increment, and bombard that and so on. Provided the increments are small enough, the effect will be the same as the continuous process. This technique can readily be implemented by mounting

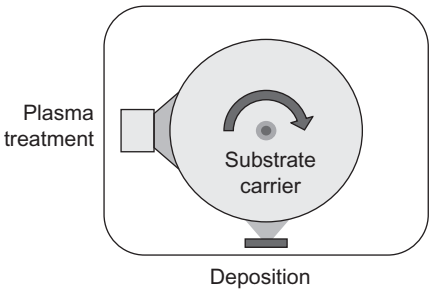


FIG. 1.4

The arrangement of source and treatment stations in alternating ion plating. The substrate carrier rotates rapidly past each so that as each small increment of film is added it is immediately treated but the two stages are separated so that they do not interfere with each other.

Source: After Schiller, S., Heisig, U., Goedicke, G., 1975. Alternating ion plating—a method of high-rate ion vapor deposition. J. Vac. Sci. Technol., 12, 858–864. Courtesy of Thin Film Center.

the substrates on a cylindrical drum and rotating the drum so that the substrates pass the source and then pass the treatment stage and so on. This geometry with its different treatment stages has been widely adopted for the energetic processes.

Radical-assisted sputtering (RAS) is a particularly interesting new process (developed by Shincron Co. Ltd.) that uses this geometry (Song et al., 2000; Nagae et al., 2001; Song and Sakurai, 2004). Here, the treatment phase applies atomic oxygen to the growing film. The oxygen is exceedingly reactive and the oxidation, therefore, very efficient. Films of exceptionally high optical quality are produced.

Closed-field magnetron sputtering (Applied Multilayers LLC) uses a similar cylindrical intermittent deposition system but here the plasma treatment exists around the entire cylinder. This is achieved by arranging the ring of magnetron targets around the cylinder so that the permanent magnets show alternating poles. If one magnetron shows NSN, that next to it will show SNS and so on. This creates a magnetic confinement system that spreads the plasma right round the cylindrical substrate carrier and so the plasma treatment is exceedingly efficient. High-quality optical coatings have been demonstrated (Gibson et al., 2008a,b).

Intermittent deposition and treatment can also be achieved with a flat circular substrate carrier. The advantage here is that with a horizontal carrier the substrates can be held in place by gravity, to face the lower sources and plasma stages in the usual way. It is then a much more straightforward operation to load the carrier robotically without exposing it to the atmosphere. This is the principle of the Helios sputtering system (Leybold Optics GmbH).

A recent variant of magnetron sputtering is known as high power impulse magnetron sputtering with a somewhat variable acronym but usually HIPIMS (Kelly and Bradley, 2009). Here, the process is pulsed at such high pulse power that a highly

ionized metal flux results that has been likened to the output of a cathodic arc. The resulting films possess improved adhesion and are dense and smooth and exhibit, at low temperatures, structures that are associated with much higher temperatures. The pulsing is at a quite low frequency, generally less than 1 kHz, and the pulse duration of a few hundred microseconds does not overheat the targets so that even quite thermally sensitive substrates can be coated. Although the process has not so far been much employed in optical applications, there is evidence that suggests it should offer advantages there also. Titanium dioxide, for example, sputtered from a ceramic $TiO_{1.8}$ target has been shown to exhibit higher refractive index than with competing processes. Sarakinos and colleagues achieved indices of 2.45 and 2.48 at 550 nm compared with 2.38 in DC magnetron sputtering (Sarakinos et al., 2007).

Ion-beam sputtering solves many of the problems associated with the different sputtering processes by using a neutral ion beam derived from a broad-beam source to sputter the target material. Purely dielectric material can be sputtered in this way because there is no target-charging problem. That the plasma from which the ions are derived is in a separate chamber, the body of the ion source, implies that the intervening plasma of the usual sputter process is completely removed. Travel of sputtered material from target to substrate is therefore completely unimpeded. The result is films of exceptionally high quality. Often, a second ion source is used directly to bombard the growing film in what is termed dual ion-beam sputtering (Fig. 1.5). This second ion treatment is primarily for additional control of the film properties, particularly intrinsic stress. The process is rather slower than the other forms of sputtering and the useful coated area somewhat smaller, but because of

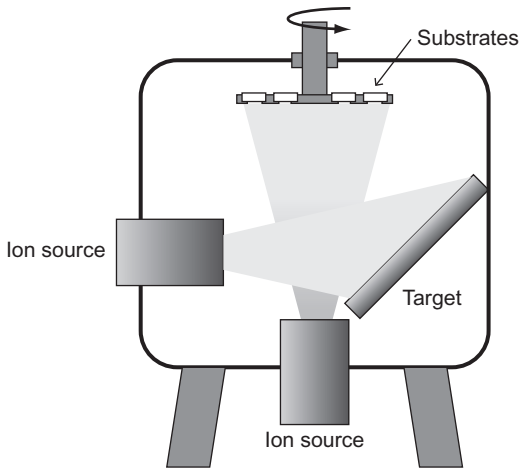


FIG. 1.5

Schematic representation of a dual ion-beam sputtering machine. One ion source bombards the target and is responsible for the sputtering. The second ion beam (vertical in the arrangement illustrated) directly bombards the growing film.

Courtesy of Thin Film Center.

the high quality of the films and its intrinsic accuracy, it has become one of the more important processes for high-performance coatings.

1.4 CATHODIC ARC EVAPORATION

Cathodic arc evaporation (Martin et al., 1991) involves a low-voltage and high-current arc that is struck between an electrode and a conducting cathode. The cross-sectional area of the arc is small and so, therefore, is the area of its impingement on the cathode resulting in a very high local temperature that can be as high as 15,000°C. Evaporated material leaves the cathode with very high energy and is also highly ionized. The cathode spot moves over the surface of the cathode, often in what seems like a random motion. Sometimes, a magnetic system may be employed to move the spot in a regular raster scan.

The main application of the process has been in the coating of cutting tools and there it has been very successful. It has not significantly penetrated the optical thin-film field as yet although the few results reported have been impressive (n of 2.735 for TiO_2 at 633 nm for example (Martin et al., 1991)). A common problem with the simple cathodic arc is the ejection of molten droplets of material that, if permitted to reach the growing film, will act as scattering defects, a major problem for optical applications. For optical purposes, therefore, the evaporated material can be passed through a filter that, relying on the charged nature of the evaporant, magnetically alters its direction to separate it from the unwanted particles (Fulton, 1999). An interesting arrangement adds ion bombardment to the process in the manner of ion-assisted deposition. The process is known as ion-assisted filtered cathodic arc evaporation (IFCAD) (Fulton, 1999).

1.5 PULSED LASER DEPOSITION

High target temperatures over a limited area are also achievable by irradiation by pulsed high-power lasers. The acronym appears to have settled down to pulsed laser deposition (PLD), corresponding to the title of this section. Probably the earliest use of this technique in connection with optical coatings was that of Smith and Turner in 1965 (Smith and Turner, 1965), who used a pulsed ruby laser. They had hoped that the stoichiometry of various semiconductor compounds and alloys might be maintained in the resulting films but only a few of their materials showed the same composition as the sources. This may have been partly due to their use of targets of powder in crucibles and perhaps the lower pulse energy available at that time. Difficulties were experienced with materials transparent in the visible region. Not surprisingly, they found that some absorption at the ruby laser wavelength was required and some of the powders had to be mixed with a small amount of carbon to achieve this.

The laser, even in recent studies, must be placed outside the chamber and its output introduced through an optical system the final element of which, frequently a mirror, is exposed to the evaporant. Coating can be a problem and sometimes the element is arranged to rotate from time to time to expose once again a clear aperture. Smith and Turner reported that they found that their pulses caused the deposited material to re-evaporate, clearing the aperture quite effectively.

Since then, all kinds of high-power lasers have been employed from the ultraviolet to the far infrared. The high fields associated with the very high power and short pulses overcome the transparency problem by simply causing breakdown in the target material and PLD is now a quite viable technique for the deposition of all kinds of optical coatings (Cheung et al., 1992). It has not, however, reached the mainstream and is used primarily for those rather special applications where it has advantages over other techniques. The process can be manipulated to achieve excellent stoichiometry of otherwise difficult alloys, and films can exhibit high optical performance. Recent reports, for example, have concerned zirconium dioxide and hafnium dioxide with excellent transparency (Tang et al., 2010; Zhang et al., 2011) and vanadium dioxide (Briggs et al., 2010) a thermally switched agile material exhibiting semiconductor properties below the transition temperature of approximately 68°C and metallic properties above.

1.6 CHEMICAL VAPOR DEPOSITION

In chemical vapor deposition (CVD), precursors interact chemically to produce the final thin-film product (Choy, 2003). The precursors are transported into a reaction chamber entrained in a carrier gas stream. In this reactor vessel they are induced to react, the reaction product—the thin-film material—being added to the growing film. In traditional CVD, the reaction was triggered by a hot substrate and this technique is still occasionally used. A problem with this process is that an efficient reaction will usually produce material at too fast a rate to be accommodated by the growing film resulting in a rather loose deposit with little mechanical strength and poor optical properties. Thermal CVD, therefore, prefers reactions that are not too favorable. Since impurities in such cases often exhibit faster reactions, traditional thermal CVD required reactants of very high purity.

A more usual approach nowadays is to use more efficient reactants but to arrange triggering of the reaction in short pulses (Segner, 1995). The interval between pulses permits the necessary accommodation of the material in the film resulting in high optical quality and high packing density. Although it has been shown possible to pulse the entry of the reactants into a thermal CVD process (Westmoreland, 1993; Choy, 2003), the preferred technique is to trigger the reaction by a pulsed radio frequency or microwave frequency plasma. The process is known by various names with their different acronyms. Plasma impulse chemical vapor deposition (PICVD) is a common designation.

An interesting combination of microwave and radio frequency excitation of the plasma in the production of a narrowband rejection filter entirely of silicon nitride with packing density variation to change the index is described in Vernhes et al. (2004).

Uniformity in CVD is largely a function of the flow pattern in the reactor and usually each different substrate shape requires a different reactor design. This limits the usefulness of CVD in small batch production. It is primarily used, therefore, for long production runs of identical products where the reactor design is stable. A good example is the production of cold mirrors. The 50-mm parabolic reflectors that surround quartz halogen projection lamps carry a cold mirror and, although the reflector-source combination was originally intended for projectors it has found its way into almost all forms of lighting. The market is estimated to be in the hundreds of million parts per year and so the cold mirror represents the kind of long production run that is ideal for CVD. See Bach and Krause (1997) for an account of the process developed by the Schott Group.

1.7 ATOMIC LAYER DEPOSITION

A related process is atomic layer deposition (ALD) (Alasaarela et al., 2009; Maula et al., 2009). Here, the precursors are introduced in alternate pulses into the reactor. Each pulse results in a thin layer over the substrates. The vapor pressure of the material is such that evaporation of any excess leaves what can be roughly considered as a monomolecular layer behind. The second precursor then reacts with the material on the substrate, excess again evaporating away. The process is slow because the reactor has to be purged between each precursor pulse but it has the enormous advantage of being able to coat quite complex shapes with a high degree of uniformity. Since the thickness increments, although small, are quite regular, the control of layer thickness becomes one of counting cycles and complete automation is straightforward and normal.

Titanium oxide is readily deposited using precursors of $TiCl_4$ and water, and Al_2O_3 using trimethylaluminum (TMA: $Al_2(CH_3)_6$) and water (Maula et al., 2009) and good optical quality is achieved. SiO_2 has been rather more difficult. A good reliable process similar to the TiO_2 and Al_2O_3 processes would probably trigger much greater use in optics. Some success has been achieved with SiO_2 films doped with Al_2O_3 in a rather complex arrangement using TMA and tris(tert-butoxy)silanol ($(Bu^tO)_3SiOH$). The index is only slightly elevated over pure SiO_2 (Hausmann et al., 2002). A quite recent report is particularly encouraging (Pfeiffer et al., 2016). Successful deposition of multilayer antireflection coatings has been achieved with HfO_2 and SiO_2 as thin-film materials. Tetrakis-[dimethylamido]-hafnium (TDMAH) together with plasma-activated oxygen yielded the hafnium dioxide while tris-[dimethylamino]-silane (3DMAS) also with plasma-activated oxygen gave the SiO_2. However, in the same contribution single-layer SiO_2 experiments gave even better results from the point of view of film properties using a commercial precursor, AP-LTO®330, a product

of Air Products and Chemicals, Inc. of Allentown, PA, together with O_3 as the oxygen source and a substrate temperature of 200°C.

1.8 SOL-GEL PROCESSES

Sol-gel processes, as the name suggests, involve a solution that is transformed into a gel and then deposited on a surface (Thomas, 1993). The starting material is a metal alkoxide dissolved in a suitable solvent, often ethanol. The addition of a little water hydrolyzes the material so that it forms a polymeric material, helped usually by making the solution slightly acidic. The resulting material is a loose gel with liquid-filled pores that can be applied to a surface by dipping. Removal of the liquid and densification of the material is achieved by heat treatment; the higher the temperature, the denser the resulting film. Temperatures of 600°C, sometimes even up to 1000°C, may be employed if complete densification is required. However, often lower temperatures are used so as to maintain some prestructure with the idea of reducing the index of the film making it more suitable as an antireflection coating. TEOS (tetraethylorthosilicate, $Si(OC_2H_5)_4$) for silica films and titanium tetraethoxide [$Ti(OC_2H_5)_4$] for titanium oxide are typical starting materials. Multilayer coatings can be produced but mixing of materials is a problem that implies at least drying in between each deposition and so the most usual coating is an inhomogeneous single layer of porous silica, the inhomogeneity improving the antireflecting performance.

There are two main reasons why this process is of interest. First, discrete layer broad-band antireflection coatings for silica present considerable difficulties because of the lack of very low index materials. Second, the laser damage threshold of sol-gel materials is found to be exceptionally high (Thomas, 1993).

A serious disadvantage that limits their use as antireflection coatings is that in uncontrolled environments, the pores take up moisture and other contaminants so that their index can vary with time. They are much used in connection with very large lasers operated in tightly controlled environments.

1.9 ETCHING

The oldest process of all is not a deposition process but a removal one. In the early 1800s, Fraunhofer (1888) reported a reduction in the reflectance of glass surfaces after an acid treatment intended to mimic the corrosive effect of the environment. Then in 1904, Taylor patented (Taylor, 1904) an etching process for the reduction of surface reflection. The etching process was revisited from time to time with Minot (1976) achieving spectacularly broad coatings on borosilicate glasses by first applying a high temperature soak to separate the glass components followed by an acid treatment to leach out all but the silica skeleton that then formed a coating with low reflectance over the region 350 nm to 2.5 μm. Later, Spiller et al. (1980) in 1980

published an account of how bombardment of plastic surfaces by energetic (2 MeV) ions of helium or carbon followed by etching by a solution of NaOH produced arrays of needle-like features that acted as efficient antireflection coatings. Recently, Schulz et al. (2007, 2011) have revived the idea of etching techniques in a particularly simple yet effective plasma surface treatment for plastic materials. PMMA, for example, is a particularly frustrating plastic to coat and this new treatment handles PMMA very well. The surfaces are treated with an argon-oxygen plasma in a machine normally used for plasma ion-assisted deposition. The latest work has included hybrid coatings where inorganic layers make up part of a multilayer antireflection coating with a final organic layer, melamine, plasma treated to give the low index, 1.2, necessary for low reflectance over a wide-angle range.

1.10 OTHER TECHNIQUES

We have covered the principal techniques that are currently used for optical coating deposition but there are so many more that, depending on circumstances, are occasionally employed that it is impossible to cover them all in a chapter of this length. Glancing angle deposition (GLAD) is a variant of thermal evaporation where the angle of incidence of the vapor on the substrate surface is deliberately made very high. This produces a pronounced columnar structure with very low packing density. The films are weak mechanically but exhibit a very low index of refraction that can be particularly useful in antireflection coatings (Woo et al., 2007) but is essentially limited to internal surfaces free from environmental disturbance. The films can also exhibit a pronounced birefringence, potentially useful in polarization-sensitive applications. Other techniques include spinning, spraying, plasma polymerization, electroplating, electrophoresis, anodization, Langmuir-Blodgett techniques involving picking up a floating monomolecular layer, molecular beam epitaxy, and even processes based on the Lipmann emulsion (Ives, 1917). These are just some of them.

1.11 CONCLUSION

We can recognize the beginnings of the field of optical coatings in early metallic coatings for mirrors but it was the 20th century and the development of vacuum processes, particularly thermal evaporation, that permitted the enormous and necessary expansion of optical coatings into virtually every aspect of optics. Thermal evaporation is still an important process but it has been joined by an array of different techniques, so broad as to make a complete account of every single process currently used in some way for optical coatings, impossibly large. This chapter has emphasized the more usual techniques but has also attempted to mention some that, although much less frequently met with in practice, nevertheless have clear potential. The major trend that can be recognized in all this is the proliferation of techniques, all of which bring their different advantages that lend them to particular optical coating

needs. The one thing that can be said with certainty is that there is no one single best technique. The demands of the particular application are the primary driver for the choice of method. Looking into the future is an uncertain activity, but we can surely expect continuous development and extension of the deposition processes to meet the ever-increasingly demanding needs of optics as a whole.

REFERENCES

Alasaarela, T., Maula, J., Sneck, S., 2009. Optical coating of glass tubes by atomic layer deposition. 52nd Annual Technical Conference Proceedings, Santa Clara. Society of Vacuum Coaters, pp. 478–482.

Anders, A., 2005. Plasma and ion sources in large area coatings: A review. Surf. Coat. Technol. 200, 1893–1906.

Anders, A., 2010. A structure zone diagram including plasma-based deposition and ion etching. Thin Solid Films 518, 4087–4090.

Bach, H., Krause, D. (Eds.), 1997. Thin Films on Glass. Springer-Verlag, Berlin, Heidelberg.

Bovard, B.B., Ramm, J., Hora, R., Hanselmann, F., 1989. Silicon nitride thin films by low voltage reactive ion plating: optical properties and composition. Appl. Opt. 28, 4436–4441.

Briggs, R.M., Pryce, I.M., Atwater, H.A., 2010. Compact silicon photonic waveguide modulator based on the vanadium dioxide metal-insulator phase transition. Opt. Express 18, 11192–11201.

Cheung, J.T., Sankur, H., Chang, T., 1992. Applications of pulsed laser deposition to optics. Opt. Photonics News 3, 24–27.

Choy, K.L., 2003. Chemical vapour deposition of coatings. Prog. Mater. Sci. 48, 57–170.

Dirks, A.G., Leamy, H.J., 1977. Columnar microstructure in vapor-deposited thin films. Thin Solid Films 47, 219–233.

Fraunhofer, J.V., 1888. Versuche über die Ursachen des Anlaufens und Mattwerdens des Glases und die Mittel, denselben zuvorzukommen. In: Joseph von Fraunhofer's Gesammelte Schriften. Verlag der Koniglich Bayerischen Akademie der Wissenschaften, München.

Fulton, M.L., 1999. New ion-assisted filtered cathodic arc deposition (IFCAD) technology for producing advanced thin-films on temperature-sensitive substrates. Proc. SPIE 3789, 29–37.

Gibson, D.R., Brinkley, I., Waddell, E.M., Walls, J.M., 2008a. Closed field magnetron sputtering: new generation sputtering process for optical coatings. Proc. SPIE 7101 (710108), 1–12.

Gibson, D.R., Brinkley, I.T., Waddell, E.M., Walls, J.M., 2008b. In: Closed Field Magnetron Sputter Deposition of Carbides and Nitrides for Optical Applications. 51st Annual Technical Conference Proceedings. Society of Vacuum Coaters, Chicago.

Grove, W.R., 1852. On the electro-chemical polarity of gases. Philos. Trans. R. Soc. B142, 87–101.

Hagedorn, H., Klosch, M., Reus, H., Zoeller, A., 2008. Plasma ion-assisted deposition with radio frequency powered plasma sources. Proc. Soc. Photo-Opt. Instrumen. Eng. 7101, 710109-11 to 710109-6.

Harper, J.M.E., Cuomo, J.J., Kaufman, H.R., 1982. Technology and applications of broad-beam ion sources used in sputtering. Part II. Applications. J. Vac. Sci. Technol. 21, 737–756.
Hausmann, D., Becker, J., Wang, S., Gordon, R.G., 2002. Rapid vapor deposition of highly conformal silica nanolaminates. Science 298, 402–406.
Hirsch, E.H., Varga, I.K., 1978. The effect of ion irradiation on the adherence of germanium films. Thin Solid Films 52, 445–452.
Hirsch, E.H., Varga, I.K., 1980. Thin film annealing by ion bombardment. Thin Solid Films 69, 99–105.
Hwangbo, C.K., Lingg, L.J., Lehan, J.P., Macleod, H.A., Suits, F., 1989. Reactive ion-assisted deposition of aluminum oxynitride thin films. Appl. Opt. 28, 2779–2784.
Ives, H.E., 1917. Lippmann color photographs as sources of monochromatic illumination in photometry and optical pyrometry. J. Opt. Soc. Am. 1, 49–63.
Jacobson, M.R. (Ed.), 1988. Modeling of optical thin films. Proc. SPIE 821, 233.
Kaufman, H.R., Cuomo, J.J., Harper, J.M.E., 1982a. Technology and applications of broad-beam ion sources used in sputtering. Part I. Ion source technology (note: Part II listed under harper). J. Vac. Sci. Technol. 21, 725–736.
Kaufman, H.R., Harper, J.M.E., Cuomo, J.J., 1982b. Developments in broad-beam, ion-source technology and applications. J. Vac. Sci. Technol. 21, 764–767.
Kelly, P.J., Arnell, R.D., 2000. Magnetron sputtering: a review of recent developments and applications. Vacuum 56, 159–172.
Kelly, P.J., Bradley, J.W., 2009. Pulsed magnetron sputtering—process overview and applications. J. Optoelectron. Adv. Mater. 11, 1101–1107.
Koch, H., 1965. Optische Untersuchungen zur Wasserdampfsorption in Aufdampfschichten (inbesondere in MgF2 Schichten). Phys. Status Solidi 12, 533–543.
Lee, C.C., 1983. Moisture Adsorption and Optical Instability in Thin Film Coatings. PhD Dissertation, University of Arizona.
Lyon, D. A. (1946). Method for coating optical elements. US patent 2,398,382. April 16, 1946.
Macleod, H.A., Richmond, D., 1976. Moisture penetration patterns in thin films. Thin Solid Films 37, 163–169.
Martin, P.J., Macleod, H.A., Netterfield, R.P., Pacey, C.G., Sainty, W.G., 1983. Ion-beam-assisted deposition of thin films. Appl. Opt. 22, 178–184.
Martin, P.J., Netterfield, R.P., Kinder, T.J., Descôtes, L., 1991. Deposition of TiN, TiC, and TiO_2 films by filtered arc evaporation. Surf. Coat. Technol. 49, 239–243.
Mattox, D.M., 1967. Apparatus for coating a cathodically biassed substrate from plasma of ionized coating material. USA patent 3,329,601.
Mattox, D.M., 1979. Mechanisms of Ion Plating. In: Proceedings of International Conference on Ion Plating and Allied Techniques (IPAT 79), London. CEP Consultants Ltd., Edinburgh.
Maula, J., Alasaarela, T., Sneck, S., 2009. Atomic layer deposition (ALD) for optical coatings. 52nd Annual Technical Conference Proceedings, Santa Clara. Society of Vacuum Coaters, pp. 486–491.
Messerly, M.J., 1987. Ion-Beam Analysis of Optical Coatings. PhD Dissertation, University of Arizona.
Minot, M.J., 1976. Single-layer, gradient refractive index antireflection films effective from 0.35 to 2.5 micrometers. J. Opt. Soc. Am. 66, 515–519.

Moll, E., Pulker, H.K., Haag, W., 1986. Method and apparatus for the reactive vapor deposition of layers of oxides, nitrides, oxynitrides and carbides on a substrate. USA patent 4,619,748. October 28, 1986.

Motovilov, O.A., Lavrischev, A.P., Smirnov, A.N., 1974. Stable narrow-band interference filters for the visible region. Sov. J. Opt. Technol. 41, 278–279.

Movchan, B.A., Demchishin, A.V., 1969. Study of the structure and properties of thick vacuum condensates of nickel, titanium, tungsten, aluminium oxide and zirconium dioxide. Fiz. Met. Metalloved. 28, 653–660.

Müller, K.-H., 1986a. Model for ion-assisted thin-film densification. J. Appl. Phys. 59, 2803–2807.

Müller, K.-H., 1986b. Monte Carlo calculation for structural modifications in ion-assisted thin film deposition due to thermal spikes. J. Vac. Sci. Technol. A 4, 184–188.

Nagae, E., Sakurai, T. and Matsumoto, S. (2001). RAS (radical assisted sputtering) system and its application on depositing optical thin films. Topical Meeting on Optical Interference Coatings, Banff, Canada. Optical Society of America, MB5.

Netterfield, R.P., Martin, P.J., Sainty, W.G., 1986. Synthesis of silicon nitride and silicon oxide films by ion-assisted deposition. Appl. Opt. 25, 3808–3809.

Ogura, S., Macleod, H.A., 1976. Water sorption phenomena in optical thin films. Thin Solid Films 34, 371–375.

Pfeiffer, K., Shestaeva, S., Bingel, A., Munzert, P., Ghazaryan, L., Helvoirt, C., et al., 2016. Comparative study of ALD SiO_2 thin films for optical applications. Opt. Mater. Expr. 6, 660–670.

Pohl, R., Pringsheim, P., 1912. Über der Herstellung von Metallspiegeln durch Destillation im Vakuum. Verh. Dtsch. Phys. Ges. 14, 506–507.

Pulker, H.K., 1992. Ion plating as an industrial manufacturing method. J. Vac. Sci. Technol. 10, 1669–1674.

Pulker, H.K., Guenther, K.H., 1995. Reactive physical vapor deposition processes. In: Flory, F.R. (Ed.), Thin Films for Optical Systems. Marcel Dekker, Inc., New York, Basel, Hong Kong.

Reid, I.M., Macleod, H.A., Henderson, E., Carter, M.J., 1979. The Ion Plating of Optical Thin Films for the Infrared. Proceedings of International Conference on Ion Plating and Allied Techniques (IPAT 79), London, July 1979. CEP Consultants Ltd., Edinburgh.

Sakudo, N., 1998. Microwave ion sources for material processing. Rev. Sci. Instrum. 69, 825–830.

Sarakinos, K., Alami, J., Wuttig, M., 2007. Process characteristics and film properties upon growth of TiO_x films by high power pulsed magnetron sputtering. J. Phys. D 40, 2108–2114.

Saxe, S.G., 1985. Ion-Induced Processes in Optical Coatings. PhD Dissertation, University of Arizona.

Schiller, S., Heisig, U., Goedicke, G., 1975. Alternating ion plating—a method of high-rate ion vapor deposition. J. Vac. Sci. Technol. 12, 858–864.

Schulz, U., Munzert, P., Leitel, R., Wendling, I., Kaiser, N., Tünnermann, A., 2007. Antireflection of transparent polymers by advanced plasma etching procedures. Opt. Expr. 15, 13108–13113.

Schulz, U., Präfke, C., Gödeker, C., Kaiser, N., Tünnermann, A., 2011. Plasma etched organic layers for antireflection purposes. Appl. Opt. 50, C31–C35.

Segner, J., 1995. Plasma impulse chemical vapor deposition. In: Flory, F.R. (Ed.), Thin Films for Optical Systems. Marcel Dekker, Inc., New York, Basel, Hong Kong, pp. 203–229.
Smith, H.M., Turner, A.F., 1965. Vacuum deposited thin films using a ruby laser. Appl. Opt. 4, 147–148.
Song, Y., Sakurai, T., 2004. High-rate, low-temperature radical-assisted sputtering coater and its applications for depositing high-performance optical filters. Vacuum 74, 409–415.
Song, Y., Sakurai, T., Maruta, K., Matusita, A., Matsumoto, S., Saisho, S., Kikuchi, K., 2000. Optical and structural properties of dense SiO_2, Ta_2O_5 and Nb_2O_5 thin-films deposited by indirectly reactive sputtering technique. Vacuum 59, 755–763.
Spiller, E., Haller, I., Feder, R., Baglin, J.E.E., Hammer, W.N., 1980. Graded-index AR surfaces produced by ion implantation on plastic materials. Appl. Opt. 19, 3022–3026.
Tang, W.T., Ying, Z.F., Hu, Z.G., Li, W.W., Sun, J., Xu, N., Wu, J.D., 2010. Synthesis and characterization of HfO_2 and ZrO_2 thin films deposited by plasma assisted reactive pulsed laser deposition at low temperature. Thin Solid Films 518, 5442–5446.
Targove, J.D., 1987. The Ion-Assisted Deposition of Optical Thin Films. PhD Dissertation, University of Arizona.
Targove, J.D., Macleod, H.A., 1988. Verification of momentum transfer as the dominant densifying mechanism in ion-assisted deposition. Appl. Opt. 27, 3779–3781.
Targove, J.D., Lingg, L.J., Lehan, J.P., Hwangbo, C.K., Macleod, H.A., Leavitt, J.A., Mcintyre Jr., L.C., 1987. In: Preparation of aluminum nitride and oxynitride thin films by ion-assisted deposition. Materials Modification and Growth using Ion Beams Symposium, Anaheim, CA, USA. Materials Research Society, Pittsburgh, PA, pp. 311–316.
Targove, J.D., Lingg, L.J., Macleod, H.A., 1988. Verification of momentum transfer as the dominant densifying mechanism in ion-assisted deposition. In: Optical Interference Coatings. Optical Society of America, Tucson, AZ, pp. 268–271.
Taylor, H.D., 1904. Lenses. United Kingdom patent 29561.
Thomas, I.M., 1993. Sol-gel coatings for high power laser optics: past present and future. Proc. SPIE 2114, 232–243.
Thornton, J.A., 1974. Influence of apparatus geometry and deposition conditions on the structure and topography of thick sputtered coatings. J. Vac. Sci. Technol. 11, 666–670.
Vernhes, R., Zabeida, O., Klemberg-Sapieha, J.E., Martinu, L., 2004. Single-material inhomogeneous optical filters based on microstructural gradients in plasma-deposited silicon nitride. Appl. Opt. 43, 97–103.
Westmoreland, D. (1993). CVD method for semiconductor manufacture using rapid thermal pulses. USA patent 5,227,331. July 13, 1993.
Woo, S.-H., Park, Y.J., Chang, D.-H., Sobahan, K.M.A., Hwangbo, C.K., 2007. Wideband antireflection coatings of porous MgF2 films by using glancing angle deposition. J. Korean Phys. Soc. 51, 1501–1506.
Zhang, W., Gan, J., Hu, Z., Yu, W., Li, Q., Sun, J., Xu, N., Wu, J., Ying, Z., 2011. Infrared and Raman spectroscopic studies of optically transparent zirconia (ZrO_2) films deposited by plasma-assisted reactive pulsed laser deposition. Appl. Spectrosc. 65, 522–527.

This page intentionally left blank

CHAPTER

Design of complex optical coatings

2

Pierre G. Verly, Daniel Poitras
National Research Council of Canada, Ottawa, ON, Canada

2.1 INTRODUCTION

Optical thin films are important in nearly all technological fields dealing with light, from scientific instrumentation to communications, data processing, energy, medicine, consumer goods, anti-counterfeiting, and so forth. The design aspect, supported by remarkable advances in thin film deposition, plays a key role. If some relatively simple optical filters are commonly found in mass produced goods, for example antireflection (AR) coatings for ophthalmic glasses, others require complex multilayer systems that are difficult to design and fabricate. Interference filters consisting of hundreds and even thousands of layers are now commercially available, or have been made. Fig. 2.1 shows the performance of a 153-μm-thick filter consisting of 1839 layers, of which 540 are less than20 nm thick. It was deposited on a sapphire substrate specifically for a NASA space mission, and had to block light from 0.725 to 4.5 μm while maintaining more than 85% transparency from 0.4 to 0.66 μm (Hendrix, 2017). Such filters are the cutting edge of current technology because of manufacturing difficulties such as the presence of thin layers that are difficult to control with precision.

The field of optical thin films is documented by an extensive literature. Besides papers, quite a few books and chapters are dedicated to the design aspect, with major contributions by pioneers in the field (Thelen, 1989; Furman and Tikhonravov, 1992; Willey, 1996; Kochergin, 2003; Baumeister, 2004; Macleod, 2010; Cushing, 2011; for early critical papers, see also Jacobson, 1990). Powerful software is available either commercially or under open source license (Larouche and Martinu, 2008). Institutions often develop their own code (Dobrowolski, 1997; Kruschwitz, 2003; Larouche and Martinu, 2008). Thin films, design courses, and short courses are regularly scheduled in universities or at conferences. The Optical Society of America (OSA), the International Society for Optical Engineering (SPIE), and the Society of Vacuum Coaters (SVC) are among the most important scientific societies in the field.

Thin film design is roughly divided into two categories: refinement and synthesis (the distinction between the two is not black and white and there is no firm agreement

Optical Thin Films and Coatings. https://doi.org/10.1016/B978-0-08-102073-9.00002-3
Copyright © 2018 Elsevier Ltd. All rights reserved.

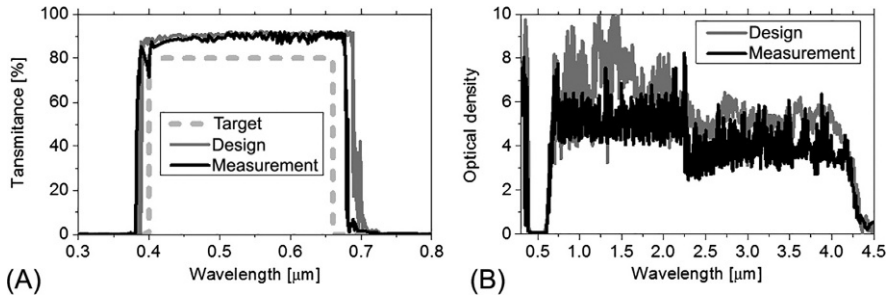


FIG. 2.1

Design (gray) and measured (black) performance of a high-performance blocker filter developed for a NASA space mission: (A) passband (dashed) below 0.725 μm; and (B) blocking region above 0.725 μm.

Adapted from Hendrix, K., 2017. Linear variable filters for NASA's OVIRS instrument: pushing the envelope of blocking. Appl. Opt. 56, C201–C205, with permission of the Optical Society of America.

on the definitions). Typically, *refinement* refers to a situation where a good starting design is optimized using a suitable numerical algorithm. The sequence of layers is usually selected from the start and the optimization is applied to the layer thicknesses. The starting designs are typically approximate solutions of the problem obtained from basic principles or previous experience, by semi-analytical methods or otherwise. *Synthesis* is more flexible and requires less a priori knowledge of the solution. For example, it is possible to start the synthesis of complex multilayer or rugate filters (having gradual refractive index variation with thickness as opposed to abrupt steps in conventional multilayers) from a single homogeneous layer. Refinement is frequently part of the synthesis process but not always.

Synthesis techniques can be purely numerical, analytical or semi-analytical. Examples of semi-analytical approaches are those based on equivalent layers, buffer layers, polynomial synthesis, effective interfaces, or admittance diagrams (Thelen, 1989; Macleod, 2010; Cushing, 2011; Baumeister, 2004). The designs obtained in this way are frequently composed of groups of quarter-wave layers (with an optical thickness nt equal to a quarter wavelength, where n is the refractive index and t the thickness). Such filters are often easier to manufacture than highly optimized purely numerical designs, because they rely on layers that are easier to control using conventional quarter-wave optical monitoring methods. Quite sophisticated filters can be designed in this way. Some simple problems have purely analytical solutions, such as AR coatings with a gradual refractive-index variation, but they can lead to impractical solutions due to the presence of materials not typically available in nature.

Early numerical synthesis approaches include Dobrowolski's comprehensive search, gradual evolution, and minus filter methods (Dobrowolski, 1965, 1981, 1997), Southwell's flip-flop technique (Southwell, 1985) and Tang's statistical search (Tang and Zheng, 1982). *Comprehensive search* systematically explores

the parameter space of a small set of layer thicknesses and materials. *Gradual evolution* consists in successively adding new groups of layers generated in this way to a design solution under construction. In the *flip-flop* technique, a design composed of two dielectric materials is subdivided into many thin layers: the refractive index of each layer is then iteratively flipped and the best configuration is retained. Dobrowolski generalized this approach to three materials including the possibility of metals (Dobrowolski and Kemp, 1992). Tang's *statistical search* is an early global optimization approach where the designs are generated by statistical sampling of the layer parameter space. The sampling is limited to regions where the merit value characterizing the residual spectral errors stays below a certain level, which is progressively decreased toward, in principle, the lowest minimum.

Thin film design and fabrication are highly interdependent. For practical results, the designers must take into account the fabrication limitations, which in turn depend on the deposition and film growth monitoring technique, the optical, mechanical and thermal properties of the coatings and so forth. The stability and control of the film thicknesses and materials constants are often critical issues. This is complicated by the fact that, for example, the error sensitivity of some layers can be highly dependent on their environment, between the time that they are deposited and the final product, which can make them difficult to control.

This paper is organized into three main sections. Section 2.2 is concerned with three of the most successful numerical thin film synthesis approaches and with global optimization. Section 2.3 deals with the manufacturability of complex filter designs, or the reduction of their sensitivity to deposition errors. Section 2.4 gives examples of hybrid design—waveguide coatings, filters with structured films, and solar cells—where the interference in the coating is not the only concern, or where the geometry of the problem significantly complicates the modeling. Finally, other topics of interest and an outlook on future research are presented in the conclusion.

2.2 MODERN NUMERICAL THIN FILM SYNTHESIS TECHNIQUES

This section describes three of the most successful numerical thin film synthesis approaches and gives an outline of global optimization.

2.2.1 FOURIER TRANSFORM METHOD

The Fourier transform (FT) method is probably the first truly successful approach for generating practical dielectric filter designs with arbitrary spectral shape specifications. A similar approach was used for many years for the synthesis of inhomogeneous transmission lines (Bolinder, 1950), the application to thin films beginning in the 1960s and 1970s (Delano, 1966, 1967; Sossi, 1974; Dobrowolski and Lowe, 1978). As its name suggests, the approach is based on an approximate FT relationship,

$$1\mathrm{n}\left[\frac{n(x)}{n_0}\right] = \frac{j}{\pi}\int \frac{\widetilde{Q}(\sigma)}{\sigma} e^{-j2\pi\sigma x}\mathrm{d}\sigma \tag{2.1}$$

between the logarithm of a refractive index profile $n(x)$ and a complex spectral function $\widetilde{Q}(\sigma)$, usually expressed in terms of transmittance or reflectance. The variable

$$x \equiv 2\int_0^z n(z)\mathrm{d}z \tag{2.2}$$

is an optical thickness coordinate measured from the center of the system (otherwise the phase term must be shifted), z is the usual physical thickness, $\sigma = 1/\lambda$ is the wavenumber (inverse wavelength), and n_0 is a constant used to shift the refractive indices profile in a realistic range. In principle, the method works with non-absorbing and nondispersive materials only, but there are ways to partially overcome this limitation. Although the approach was primarily intended for filters with a gradual variation of the refractive index (e.g., inhomogeneous coatings, rugate filters), it can easily be adapted to conventional multilayers composed of homogeneous films. For simplicity, in the following discussion, we will assume that the light is incident at a normal angle (at oblique incidence, n should be replaced by an admittance $n{\cdot}\cos\theta$ or $n/\cos\theta$, for s- or p-polarized light, respectively, with θ the angle of propagation, and x by an effective thickness $x{\cdot}\cos\theta$).

It has been shown from Maxwell's equations that the reflection and transmission coefficients (for the field amplitude) of a film of continuously varying refractive index obey a Ricatti differential equation (Sossi and Kard, 1968; Jacobsson, 1966). Iterative solutions lead to the following expression for the complex transmission coefficient $t(\sigma)$ in terms of an infinite series of nested integrals:

$$\frac{1}{t(\sigma)} = e^{-j2\pi\sigma x}\left\{1 + \int_0^x \mathrm{d}\widetilde{Q}(x_1\sigma)\int_0^{x_1}\mathrm{d}\widetilde{Q}^*(x_2\sigma) + \int\int\int\int\cdots + \cdots\right\}, \tag{2.3}$$

where $\mathrm{d}\widetilde{Q}(x, \sigma)$ is the integrand of

$$\widetilde{Q}(\sigma) = \int \frac{1}{2n}\frac{\mathrm{d}n}{\mathrm{d}x} e^{j2\pi\sigma x}\mathrm{d}x, \tag{2.4}$$

and $\mathrm{d}\widetilde{Q}^*(x, \sigma)$ is its complex conjugate; n is assumed real, i.e., non-absorbing, and independent of σ, i.e., nondispersive. Physically, the integrals in Eq. (2.3) represent internal reflections in the graded index film ($1/n{\cdot}\mathrm{d}n/\mathrm{d}x$ is the infinitesimal expression of the Fresnel reflection coefficient). There is a similar expression for r/t where r is the field amplitude reflection coefficient. Both $1/t$ and r/t are functions with special mathematical properties in thin film theory (for further detail, see Furman and Tikhonravov, 1992; Tikhonravov, 1993).

Eqs. (2.3) and (2.4), and their equivalent for r/t, establish a relationship between $\widetilde{Q}(\sigma)$ and the spectral properties of the film. In the Fourier transform method, it is usually assumed that $\widetilde{Q}(\sigma)$ is small so that the terms of second order or higher are neglected. This means that multiple internal reflections are ignored; two are retained in the calculation of the transmitted light, one for the reflected light.

The dependency of $\widetilde{Q}(\sigma)$ (commonly known as the "Q-function") on the spectral transmittance and reflectance is not trivial. Several simplified analytical forms have been proposed, such as (Delano, 1967; Sossi, 1974; Bovard, 1988; Verly et al., 1989):

$$\begin{aligned} Q &= \sqrt{1-T} = \sqrt{R}\,, \\ Q &= \sqrt{\frac{1}{T-1}}\,, \\ Q &= \sqrt{\mathrm{In}\left(\frac{1}{T}\right)}\,, \\ \widetilde{Q} &= \frac{r}{t}\,, \end{aligned} \tag{2.5}$$

where $R = rr^*$ is the reflectance and T the transmittance of the coating (for the light power). Q is the modulus of the complex Q-function expressed as

$$\widetilde{Q}\,(\sigma) = Q(\sigma)e^{j\varphi(\sigma)}. \tag{2.6}$$

It is easy to verify that the different forms of Q agree when R is small but diverge otherwise, sometimes a lot. The last form in Eq. (2.5), sometimes called Delano's Q-function, is complex and suggests that the phase φ should approximately be equal to $\arg(r/t)$. However, the phases are often unspecified in a design problem, especially in this form. This is a degree of freedom that can be exploited, in particular to control the shape of the index profile, an important consideration in the presence of index constraints. Filters of surprisingly high reflectance can be designed by proper choice of the Q-function and its phase (Verly et al., 1989; Verly, 2011).

In principle, Eq. (2.1) provides a very simple way of synthesizing a dielectric filter with arbitrary transmittance or reflectance specification. However, there are difficulties, starting with the approximate nature of the analytical Q-functions. In addition, a sufficient part of the spectral region where the reflectance is nonzero must be known (as with the Kramers–Kronig relations). For example, it is not possible to design an AR coating just by specifying that the reflectance should be zero in some wavelength region. The reflectance of most coatings, in particular when they are not immersed, is nonzero outside the main region of interest. Finally, errors are introduced when constraints are imposed on the refractive indices and overall thickness. The Q-phase $\varphi(\sigma)$ can help address this particular problem (Verly and Dobrowolski, 1990; Druessel et al., 1993). Surprisingly good rugate reflectors can be designed by Q-phase optimization alone (Verly, 2011).

Several variants of an iterative procedure have been proposed to compensate some of the limitations (Sossi, 1974; Fabricius, 1992b; Cheng et al., 2008a). The approach implemented at the *National Research Council of Canada* (NRC) applies successive corrections to the complex Q-function (Verly and Dobrowolski, 1990):

$$\widetilde{Q}_{i+1} = \widetilde{Q}_i + \Delta\widetilde{Q}_i,$$

$$\begin{aligned} &\text{with} \\ &\Delta\widetilde{Q}_i = \{Q_i[T_D - Q_i(T_i)]\}e^{j\psi_i}\,, \\ &\psi_i = \arg\left(\frac{r_i}{t_i}\right)\,, \end{aligned} \tag{2.7}$$

where T_D is the specified target transmittance and T_i, t_i, and r_i are calculated values obtained from the $n(x)$ found at that point. The calculations are performed by the standard matrix approach after subdividing $n(x)$ in thin layers. The progress is monitored through a standard merit function, for example, the root-mean-square (RMS) residual transmittance error. The material dispersion and losses that are ignored in the Fourier transforms can be introduced in the matrix calculations (Fabricius, 1992a; Bulkin et al., 1996; Verly, 2008). A scaling procedure can also be applied to the target transmittance (Bovard, 1993; Poitras et al., 2002; Larouche and Martinu, 2007).

Eq. (2.7) increments the Q-phase $\varphi(\sigma)$ in a direction consistent with Delano's Q-function r/t. Numerical experimentation shows that using $\arg(r/t)$ of a good solution as an initial Q-phase consistently yields good results. However, as mentioned, this phase is usually unknown at first. Multiple filter solutions of essentially the same reflectance in the region of interest but different phases are usually possible, from which the most suitable for fabrication can be selected (Verly and Dobrowolski, 1990; Verly et al., 1993). Alternatively, it is possible to bypass the initial phase issue and start the iterations from a completely arbitrary starting design, for example, a constant refractive index. It is also possible to refine $\Delta\widetilde{Q}$ or $\widetilde{Q}$ in Eq. (2.7) for improved accuracy (Verly, 1996, 2011).

Despite its limitations, the Fourier transform method can quickly generate useful inhomogeneous and multilayer designs. Fig. 2.2 gives an example of a rugate filter that was designed in this way and fabricated (Cheng et al., 2008b). Typically, the synthesized solutions gradually evolve in quasi-multilayers (i.e., with some graded index sections) when the refractive index (or admittance) modulation reaches the limits imposed by available materials (Verly et al., 1992; Verly, 1996). This is in agreement with the 'Maximum Principle' stating that the optimum solutions for this type of problems should involve no more than two materials (Furman and Tikhonravov, 1992). The hybrid solutions can easily be converted to true multilayer and/or used as advanced starting designs for conventional refinement.

Finally, the design approach has interesting byproducts and benefits from Fourier techniques used in other fields. In particular, frequency filtering provides useful insight in the spectral contributions of different parts of a design (Verly, 1995, 2011). The elimination of the high (spectral and spatial) frequencies contributions also helps reduce the number of thin layers that are notoriously difficult to deposit. It is possible to synthesize surprisingly good AR coatings simply by eliminating the Fourier frequencies of an arbitrary starting design in the desired spectral region (Verly, 1994, 2009). Other byproducts include the thickness estimation of reflecting filters (Verly, 2007) and thin film characterization (Swart and Lacquet, 1990; Verly, 1998a).

2.2.2 INHOMOGENEOUS REFINEMENT

Unfortunately, the Fourier transform method only applies to light incident at a single angle, in a single polarization. The approach discussed in this section removes this limitation; the solutions are simply subdivided into thin layers whose refractive

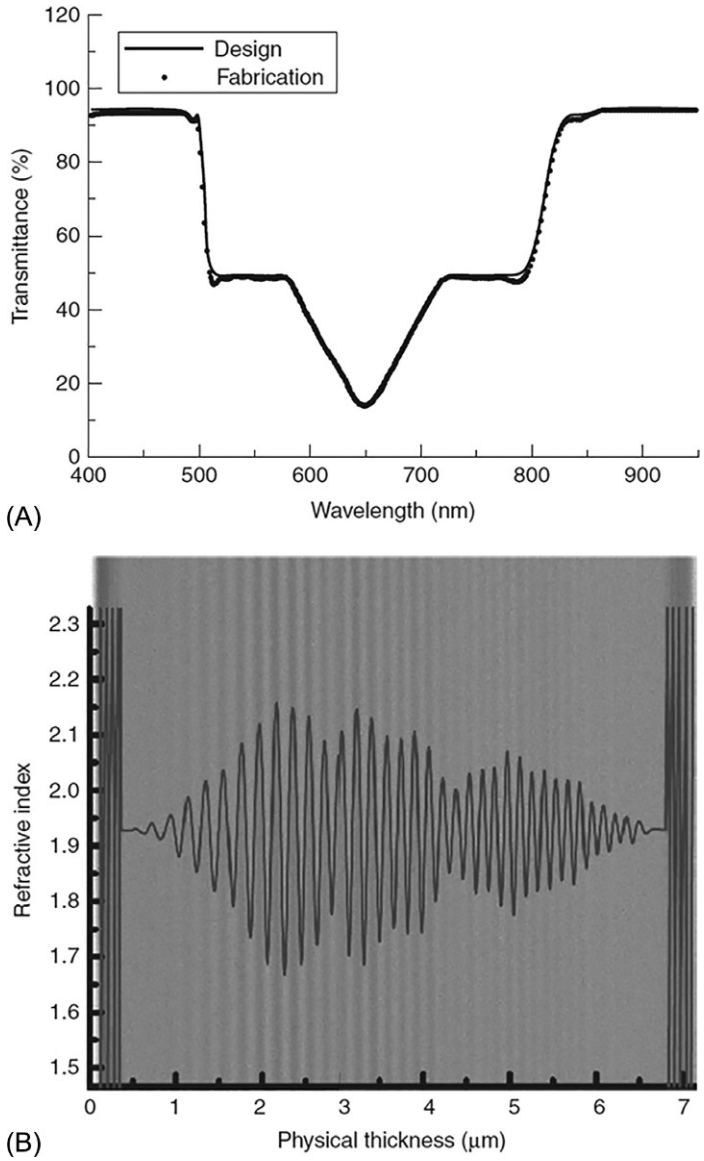


FIG. 2.2

(A) Comparison of the designed and measured transmittance of a rugate filter designed by the Fourier transform method (Cheng et al., 2008b). (B) The calculated refractive index profile is superposed on a SEM picture. The filter is immersed between two quartz plates. Discrete layers at both ends suppress the ripples due to the reflections at the outer interfaces.

Reproduced with permission of the SPIE.

indices and optional thicknesses are refined (Snedaker, 1982; Verly et al., 1997; Verly, 1998b; Tikhonravov et al., 2006). This is an example where the distinction between refinement and synthesis is somewhat ambiguous. However, in this case the starting design can be quite elementary. Apart from a rough estimation of the overall optical thickness, no special assumption is needed about the number of layers, the sequence of materials, and so forth. The thickness estimation can be progressively adjusted if necessary. As with the Fourier approach, the solutions typically start as mostly inhomogeneous and progressively evolve into hybrid multilayers.

This approach is mostly used for the synthesis of all-dielectric filters. Material dispersion and losses can be introduced by considering the film materials as adjustable mixtures. In principle, it is also possible to optimize the extinction coefficient k and the refractive index n of each layer independently (in absorbing materials the refractive index is expressed in complex form as $n-jk$). However, the practical realization of the resulting virtual materials may be a challenge, or even physically impossible, if not compliant with Kramers–Kronig's relations. This optimization option exists in commercial design software. Owing to the large number of parameters typically involved, special consideration has to be given to the speed and accuracy of the calculations. In the NRC implementation, all the gradient values used in the optimization routines are calculated from exact analytical formulas and the code is structured so that repetitive matrix calculations are avoided.

Fig. 2.3 gives an example of a broadband wide-angle, non-polarizing antireflection coating synthesized for angles of incidence $\theta = 0°$, 30°, 45°, 60°, and 70° in air (Verly, 1998b). The refractive index profile represented by a dashed line is strongly inhomogeneous. This is understandable since the maximum contrast of the materials p-polarization admittance $n/\cos\theta$ across the coating is obtained with intermediate refractive indices when $\theta > 40°$. The index profile shown as a solid line has been converted to a five-material multilayer of nearly the same reflectance.

With some precautions, the synthesis of purely inhomogeneous (nonhybrid) filters is also possible. As seen in Fig. 2.3, homogeneous layers are introduced when the refractive-index or admittance modulation reaches its prescribed limits. In Tikhonravov et al. (2006), a regularization term is added to a standard merit function (RMS reflectance) to maintain the smoothness of the refractive index. An additional penalty term forces the refractive indices to stay within bounds. A compromise is necessary between the index smoothness and the optical performance. A simple alternative approach based on a combination of inhomogeneous refinement and Fourier techniques is described in Verly (2008).

2.2.3 NEEDLE METHOD

The *needle method* is probably the most popular and most successful thin film synthesis technique since the early 1990s (Furman and Tikhonravov, 1992; Sullivan and Dobrowolski, 1996; Tikhonravov et al., 1996). Briefly, it consists in inserting very thin layers (needles) in a multilayer system that is subsequently reoptimized in order to improve its spectral performance. The optimum needle materials and positions are

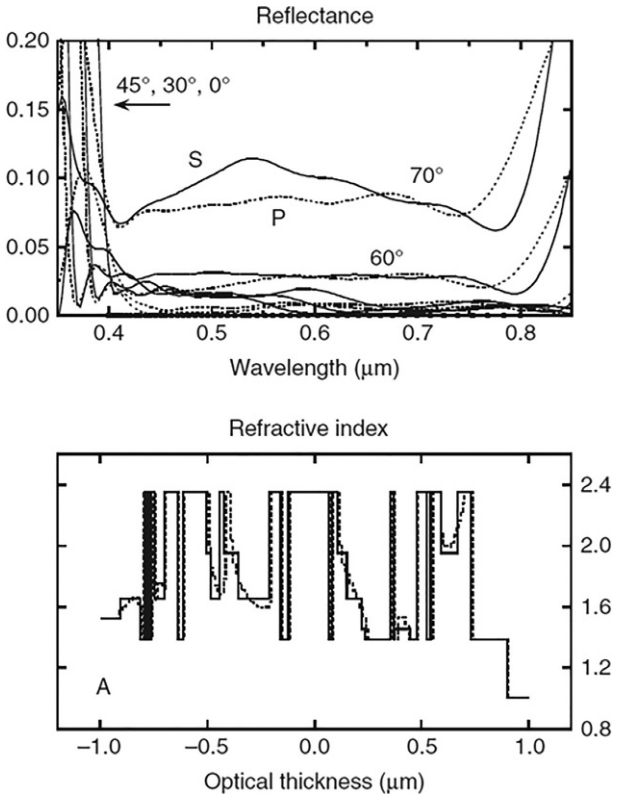


FIG. 2.3

Broadband, wide-angle, nonpolarizing AR coating designed by inhomogeneous refinement for 0°, 30°, 45°, 60°, and 70° angles of incidence in air. Bottom: semi-rugate and five-material multilayer solutions (Verly, 1998b). Top: reflectance in the s and p polarizations of the semi-rugate solution.

Reproduced with permission of the Optical Society of America.

obtained from a perturbation function. The modified multilayer is then refined and the whole procedure repeated as needed. In the so-called *gradual evolution mode* (not to be confused with Dobrowolski's approach mentioned previously), the designs overall thickness is artificially increased when no further progress can be made otherwise. A layer of compatible material is appended, usually on the substrate side, opening new options for additional needles.

A variant of the needle method has been proposed where the needle refractive indices are refined as well (Verly, 2001). The optimum needle indices are calculated by parabolic interpolation (over three points), so that the perturbation function for the determination of the needle positions has to be calculated only twice (for two needle indices, the third one being the unperturbed layer index). Hybrid solutions similar to

those obtained by inhomogeneous refinement have been observed. The two approaches behave differently and tend to complement each other. For example, *inhomogeneous refinement* quickly converges to a solution similar to the final design, while the *needle method* tends to be more efficient for design tuning near the end of the process.

A disadvantage of the needle approach is the frequent proliferation of undesirable thin layers in the nanometer range. Simple procedures for their removal have been described and are implemented in commercial software (Tikhonravov and Trubetskov, 2007). Frequently, trade-offs must be made between the spectral performance and the minimum acceptable layer thickness.

Larouche and Martinu (2006) proposed an approach similar to the needle method, where instead of needles small index steps are inserted in appropriate positions, and both the refractive indices and thicknesses are refined. The justification is that it is sometimes easier to fabricate thicker layers of intermediate indices (i.e., using plasma deposition) than thin layers of two materials. Under suitable conditions, multi-material solutions can be converted to two materials by a standard Herpin transformation (Dobrowolski and Piotrowski, 1982).

Southwell recently published a new version of the flip-flop method (Southwell, 2013) that shows similarities with the needle method. He pointed out the main advantage and disadvantage of the original version, namely, its speed of convergence and its tendency to be trapped in a local solution. He suggested ideas for improvement, in particular the introduction of a "flip-flop Q-function" to optimize the position of the flipped layer in the stack. It turns out that this function is proportional to the needle method's perturbation function, making the two approaches comparable in terms of efficiency.

2.2.4 GLOBAL OPTIMIZATION

Global optimization is an important subfield of numerical analysis where the objective is to find the lowest minimum (or highest maximum) of a function in a complicated parameter landscape generally comprising many local minima (or maxima) (Rinnooy Kan and Timmer, 1987; Schoen, 1991; Panos et al., 2002). Such calculations are common in areas requiring complex mathematical modeling or large data analysis, such as molecular dynamics, image and pattern recognition, artificial intelligence, traffic control, environmental and risk management, finances, etc.

Many global search strategies exist, and have in common that none of them descend directly toward an accessible minimum; they all involve possible uphill steps to increase the chances of finding a lower minimum elsewhere. Conceptually, the simplest strategy is to look at all the possibilities in the parameter space. However, this approach quickly becomes impractical as the number of parameters increases. Statistical searches are more effective but the global minimum is then found with a finite probability (Cox and John, 1992).

Global optimization has had a limited but growing popularity in thin films since its introduction in the field several decades ago (Dobrowolski, 1965; Tang and

Zheng, 1982; Wild and Buhay, 1986). There is still a common perception that it requires lengthy calculations and is slow compared to other synthesis methods. In addition, the solutions are global in a parameter space that has to be carefully set up and may necessitate progressive adjustments (e.g., tolerances or number of layers). Nevertheless, interesting results have been obtained, and the constant advances in computing power make it more and more attractive. Several global approaches successfully applied to thin films are briefly described below; all of them are stochastic (i.e., based on random parameter moves).

Simulated annealing is a method inspired from the metallurgical process of heating a metal to a high temperature and progressively cooling it down to allow a rearrangement of its atomic structure (Schoen, 1991; Boudet et al., 1996). Uphill moves $\Delta MF > 0$ in the parameter space around a minimum are allowed with a probability modeled with a Boltzmann distribution,

$$p = \exp\left(-\frac{\Delta MF}{kT}\right), \tag{2.8}$$

where ΔMF is the change in the merit value, k is Boltzmann's constant, T the temperature, and p must be greater than a random number between 0 and 1. Downhill moves $\Delta MF < 0$ are always accepted. For a given T, the algorithm can thus freely move among minima of depths less than approximately kT. T is initially set to a high value and progressively decreased according to an annealing schedule (or cooling strategy). If after reoptimization a low MF minimum is found, it becomes the new current minimum.

The approach is computationally intensive and sensitive to the adopted cooling strategy and the way of proposing the random moves (Morf and Kunz, 1988; Hobson and Baldwin, 2004). A zone melting approach has been proposed where the annealing is successively applied to parts of the design (Morf and Kunz, 1990), reducing the size of the parameter space. Modifications are possible where the random searches are biased according to the topography from previous history, or where it is made more difficult to wander away from a deeper minimum (Dobrowolski and Kemp, 1990; Cheng et al., 2006). A more general Markov-Chain Monte Carlo (MCMC) method, for which simulated annealing forms a particular case, has also been used with success to design optical coatings. It allows an easy determination of the robustness of the selected design to experimental errors (Hobson and Baldwin, 2004). More recently, the same technique was used to design a beam splitter in a device that efficiently uses the energy from solar light by combining photovoltaic and thermal solar energy extraction (Jiachen et al., 2015).

Genetic algorithms imitate the evolution of living populations in nature (Eisenhammer et al., 1993; Rabinovitch and Toker, 1994; Martin et al., 1995). Successive generations of individuals (designs) are produced by operators that mimic genetic mechanisms: (i) *selection*, where clones of randomly selected individuals are generated with a probability that depends on their merit value (reproduction of the fittest); (ii) *recombination*, or *cross-over*, where random individuals share their genes (e.g., layer thicknesses); (iii) *mutation*, where some individuals suffer random

perturbations of their genes. Several variants of this general scheme exist (Oulton and Adjiman, 2006; Shokooh-Saremi and Magnusson, 2007). In memetic optimization, for example, the new individuals are subjected to a quick partial refinement claimed to increase substantially the computation speed (Yakovlev and Tempea, 2002).

Genetic algorithms have been applied to the design of filters with increasing complexity over the years: X-ray coatings (Binda and Zocchi, 2004; Al-Marzoug and Hodgson, 2008; Wang, 2008), broadband omni-directional reflectors and antireflection coatings (Jiang et al., 2008; Poxson et al., 2009; Xu, 2010; Chiadini et al., 2017), solar cells (Schubert et al., 2008), dispersive mirrors for femtosecond lasers (Yakovlev and Tempea, 2002), polarizing beam splitters (Shokooh-Saremi et al., 2004), narrow-angular absorbers (Granier et al., 2014), etc. The choice of a proper starting design and a limitation of the number of optimized parameters can be critical. Computation time is not always disclosed, but Jiang et al. (2008) reported times on the order of a hundred hours on a PC computer (Pentium 4 Intel 3.0 GHz, 2.0-Gb RAM, using Matlab). An interesting study of the effect of different genetic algorithm parameters on the design of an AR coating (Patel and Kheraj, 2015) has shown that a random cross-over helped speed the convergence of the method, and sporadic random layer thickness re-initialization (equivalent to a complete mutation of a random layer from a random design in the population) helped avoid being trapped in a local minimum.

Clustering methods coupled with local searches are claimed to be among the best for global optimization (Schoen, 1991; Maroosi and Amiri, 2010); they essentially consist in regrouping randomly generated starting designs according to regions of attraction of local minima. The locations and shapes of these regions of attraction are identified. A new local search is pursued only if it does not belong to an existing region of attraction. These sampling, clustering, and local search steps are repeated until no better minimum can be found.

Different clustering approaches are possible (Abul Hasan and Ramakrishnan, 2011). One approach inspired from respiratory system modeling (Csendes et al., 1986) has been applied with success to optical thin film design synthesis. Several complex designs obtained in this way, in combination with a needle method, placed highly in successive thin film design contests organized at the Topical meeting on Optical Interference Coatings (OIC), a key conference in the field. The designs were for a wideband wide-angle AR coating with robustness to simulated manufacturing errors, a minimum-shift immersed short-pass filter and a non-polarizing filter (Tilsch and Hendrix, 2008; Hendrix and Oliver, 2011). The designs consisted of up to 214 layers of several materials selected from a list. A metal-dielectric filter design showing three different colors in transmission and reflection from the front and the back sides was also reported and fabricated (Badoil et al., 2008; Dobrowolski et al., 2008). However, it is worth mentioning that submitted designs of comparable and sometimes better performance were obtained by more conventional thin film synthesis techniques. More recently, Lemarchand (2014) demonstrated that the clustering method can be used to deliver solutions that are close to a global minimum, as well

as providing a portfolio of local solutions when applied to a starting solution with a set number of layers and materials.

Particle swarm optimization (*PSO*) is a robust evolutionary strategy inspired by the social behavior of animal species living in large colonies like birds, ants, or fish. It is interesting that it was first proposed not by mathematicians, but by a social psychologist and an electrical engineer (Kennedy and Eberhart, 1995). The algorithm finds the optimal solution by moving the particles (designs) in the search space. Each particle is first assigned a random position and velocity, which are then varied using an acceleration with three components: an attraction to the best historical position visited by the particle, an attraction to the current best particle in the group, and the previous velocity vector of the particle (inertia). The particle velocity is thus progressively deflected by adding to it random-length components in the direction of the best locations. The particle inertia part of the speed is given a progressively decreasing weight with respect to the changes learned from previous experience.

The application of this technique to thin films appears to be fairly recent. A solar absorber designed in this way was submitted to the thin film design contest of the OIC 2010 conference (Hendrix and Oliver, 2011). The designers mentioned that they let a PC computer with dual quadcore Xeon processors run for 2 months. The design of interference filters or solar cells with diffracting structures is also reported in the recent literature (Shokooh-Saremi and Magnusson, 2007; Mutitu et al., 2008; Pond and Kawano, 2010). Pond reported the optimization of two different types of solar cells by PSO in conjunction with FDTD (finite-difference time-domain) computations: a plasmonic thin film silicon cell with a metal-island film and an organic cell where one interface of the active layer is patterned with a grating. A 15% performance improvement over the unpatterned case was observed. A related global optimization method recently applied to thin films is the teaching–learning-based optimization (TLBO), where a group of designs (learners) is educated (equivalent to a mutation, or a particle position change) first by a teacher (best design so far), and then by co-learners randomly influenced by better learners. It is interesting that only one input parameter is controlled by the user, namely, the learners'group size. The approach has recently been applied to the design of AR coatings and shown faster convergence than a genetic algorithm with the same population (learners) size (Patel et al., 2017).

Global optimization is also used in the analysis of ellipsometric or spectrophotometric data for the characterization of thin films optical constants (Djurisic et al., 2000; Gao et al., 2011). Gao's paper gives an interesting comparison of several global approaches and links to open-source software.

2.3 MANUFACTURABILITY ISSUES

With current software and proper know-how, it is often relatively straightforward to find solutions to thin films design problems when the only concern is the spectral performance. It is however more interesting and useful to find solutions that are

at the same time simple and resilient to manufacturing errors. Apart from random or systematic errors created by small imperfections of the deposition equipment (rate fluctuations, shutter delays, etc.), thickness errors are strongly dependent on the film growth monitoring method and sometimes the layer environment. For example, in optical monitoring, the signal sensitivity to errors in a particular layer can increase drastically between the deposition time and finished product (Poitras, 2005). Some monitoring approaches have inherent error compensation mechanisms that prevent the accumulation of thickness errors; this effect, well known in the case of single wavelength monitoring (Macleod and Pelletier, 1977), has been demonstrated more recently for particular cases of direct broadband monitoring (Tikhonravov et al., 2011, 2017). Several automated deposition processes reoptimize the rest of the system in real time when errors are detected in the deposited layers (Sullivan et al., 2000; Wilbrandt et al., 2010). Taking into account the error sensitivity at the design stage is not easy and requires a good understanding of the deposition process.

The most common practice to address robustness issues is to generate a design for pure spectral performance and check its error sensitivity at the end. The easiest way is to add or substract uncorrelated random errors to the layer thicknesses and/or indices. More sophisticated simulations add the random errors to parameters more representative of the deposition process, such as a simulated monitoring signal, deposition rate(s), shutter delay(s), etc. (Tikhonravov and Trubetskov, 2005).

Designs generated by analytical procedures are commonly perceived to be more robust than purely numerical constructions. Solutions that fulfill the specifications without too much tweaking are often preferred when sophisticated deposition automation is not available. Sometimes simple measures like suppressing thin layers, switching materials, or even reversing a design to put the sensitive layers at the end improve the robustness.

The most direct way of reducing the error sensitivity at the design stage is to add a penalty term to the merit function (Dobrowolski, 1981; Dobrowolski et al., 1989):

$$MF = MF_0 + \alpha \sum_t w_i \frac{\partial MF}{\partial x_i}. \tag{2.9}$$

In this equation, MF_0 is the unperturbed merit value, the w_i's are weights representing the expected error levels on the layer construction parameters x_i, and α is an adjustable constant ($0 < \alpha < 1$) used to control trade-offs between the spectral performance and the error control. Tikhonravov et al. (2003) proposed a variant where a second-order term is added to the Taylor series. This second-order equation can be simplified so that

$$MF = MF_0 + a_2 \sum_i \left(w_i \frac{\partial MF}{\partial x_i} \right)^2. \tag{2.10}$$

Eq. (2.10) is implemented in commercial software and has successfully been used in the desensitization of challenging filters (Pervak et al., 2007).

To our knowledge, Zheng and Tang (1987) were the first to report an automatic design technique simulating an actual deposition environment. In their work, a penalty term proportional to $(1 - Y)$ is added to the merit function, where Y is a yield, or

proportion of randomly perturbed designs that are within specifications. The random errors were applied to simulated monitoring signals in reflection and transmission. The designs were generated using the global optimization approach mentioned earlier (Tang and Zheng, 1982).

Other types of statistical calculations have been reported, frequently in combination with global optimization. Greiner (1996) applied a genetic algorithm to a noisy merit function (statistical average) to desensitize an AR coating with respect to reflectance and color variation. Similarly, Wiesmann et al. (1998) applied an evolutionary algorithm to improve the robustness of a color filter. Yakovlev and Tempea (2002) generated chirped mirrors for dispersion control in femtosecond lasers by using a memetic algorithm; the robustness of a few selected designs was improved by a perturbative gradient descent (a gradient for noisy functions) similar to one used for feedback control in adaptive optics. Nohadani et al. (2008) desensitized a double-chirped 208-layer mirror pair for use in a few-cycle Ti:sapphire mode locked laser; they minimized the worst-case scenario corresponding to random parameters changes within a certain radius of a central design. In a subsequent paper, the design with the best yield was identified on the optimization path followed when the robust design was reoptimized in a standard way, without the error considerations (Birge et al., 2011).

A different approach was also proposed where multiple designs located in a small neighborhood of a pivotal design were simultaneously synthesized by a modified needle method (Pervak et al., 2009, 2011; Trubetskov and Tikhonravov, 2010). The collection of designs, called a *cloud*, was subjected to small random errors and refreshed from time to time. The needle(s) were inserted in each design. The method was successfully applied to different types of filters including challenging dispersion compensating mirrors for ultrafast optics. As a bonus, it was found that the peaks of the electric field intensity were reduced, potentially improving the laser damage threshold of the mirrors.

Another development proposed by Tikhonravov and Trubetskov (2012) involved performing stochastic optimization procedures on selected starting designs, under suitable thickness constraints. The approach generated a portfolio of robust designs from which the most promising were selected. The selection involved a thorough simulation of the fabrication taking into account the specific thickness monitoring method, a step that is sometimes called *preproduction investigation*, *virtual deposition*, or *computational manufacturing* (Ehlers et al., 2010; Amotchkina et al., 2012; Wilbrandt et al., 2010). This exercise not only helped selecting the most robust design, but also provided valuable information for design re-engineering, and for adopting a suitable thickness monitoring strategy.

Three editions of a thin film design contest organized at the topical meeting on Optical Interference Coatings (OIC) highlighted the difficulties of reducing the error sensitivity of challenging designs (Baumeister, 2000; Thelen et al., 2002; Tilsch et al., 2006). The proposed challenges were a dual band AR coating for the visible and the near infrared, a gain flattening filter for erbium-doped fiber amplifiers (EDFA) and a broadband, broad-angle AR (BBAAR) coating subjected to simulated manufacturing errors. Constraints were imposed on the available materials (up to

five), the maximum number of layers, maximum overall thickness, and the minimum layer thickness. Approaches based on the needle method, global optimization, and undisclosed proprietary software were applied.

Gain flattening filters are challenging to design because the specified spectral curve has sharp variations in a narrow spectral region requiring many precisely deposited layers. The filter proposed at the OIC had to flatten the EDFA gain to a fraction of a decibel and the yield had to be maximized when the filter was submitted to simulated random thickness errors (Thelen et al., 2002). Verly (2002) observed that thicker, loosely optimized solutions were the most stable. A correlation was found between the convergence speed and the error stability. Efforts were made to maintain a high convergence rate by limiting the optimization to the most effective layers. A standard merit function was used. The error stability was monitored through the convergence and by regularly checking that the error sensitivity did not shift to resonant cavities in the design. The best solution achieved a 98% yield with 152 layers of SiO_2 and Ta_2O_5.

In parallel with the design contest, a manufacturing contest is also proposed at the OIC to highlight the challenges in the design and fabrication of robust complex filters. The 2016 edition highlighted the difficulties posed by the presence of thin metal layers. The results strongly suggested a variation of their optical constants with thickness, which is difficult to model precisely (Poitras et al., 2017).

Mechanical and thermomechanical properties are other important factors for some applications. A recent example was given by de Denus-Baillargeon et al. (2014), who presented a stress-compensated astronomical filter. The mechanical properties limit the parametersspace available to the designer, such as the maximum layer thickness or number of layers (Tikhonravov et al., 2014). Thin intermediate layers may have to be used to reduce the internal stress, avoid delamination, or crystallization inside the films. Specific materials or materials combination help for stress compensation, thin bonding layers improve adhesion, optical losses may have to be minimized, etc. A new milestone was recently reached with the successful realization of high-performance mirrors for gravitational wave detectors (Pinard et al., 2017).

The laser damage threshold is a related topic of critical importance in the field of high-power lasers. The materials and designs are specific to the source characteristics. Recently, the interest in ultra-short pulses has added phase-dispersion properties controlled over a wide range of wavelengths to the specifications (Fattahi et al., 2014; Razskazovskaya et al., 2016; Bellum et al., 2017).

Such phase specifications magnify the manufacturing issues. Considerations include the thickness nonuniformity, nonplanarity, and roughness (Piegari and Sytchkova, 2016).

2.4 HYBRID DESIGN

This section gives some examples of hybrid situations where factors beyond the usual optical interference in planar thin film stacks are involved.

2.4.1 WAVEGUIDE FACET COATINGS

Coatings are frequently applied to the end facets of optoelectronic devices such as semiconductor lasers, optical amplifiers, and super-luminescent light emitting diodes. This is an interesting design problem because the light incident on the coating is a waveguide mode instead of the usual plane wave. A simplified two-dimensional geometry of the problem is schematically illustrated in Fig. 2.4. The guided mode has a characteristic transverse light distribution concentrated in the waveguide core and an axial propagation constant determined by the waveguide geometry. Once it exits the waveguide, the light diffracts. The returning light spot that has to be coupled back in the waveguide is distorted and excites a superposition of the supported guided and radiation modes (forming a complete set of orthogonal functions). The quantity of interest is the mode reflectance, or fraction of the light coupled back to the same guided mode as the incident light, but propagating in the reverse direction. Fig. 2.5 shows the important difference between the modal and plane-wave reflectances of a narrowband metal-dielectric reflector. The coating, loosely described as Sub | 1.9 L(1.3 nm M)0.1 L(HL)^9 | air (where L, H, M represent SiO_2, TiO_2, and Inconel layers, respectively), is deposited on the end facet of an InAs/InP-based waveguide of 0.35 μm core thickness. The plane wave is assumed to be at normal incidence from an InP medium, and the mode incident from the waveguide side in the TE (transverse electric) polarization. Rigorous calculations of the mode reflectance are possible but time-consuming, especially in optimization algorithms. Approximate approaches deliver good results when suitable conditions are met.

Vassallo (1985, 1988) proposed an approach where a thin fictitious layer of constant index n_{eq} is inserted between the waveguide facet and the coating. When n_{eq} is properly chosen, the mode enters the thin layer without reflection or distortion

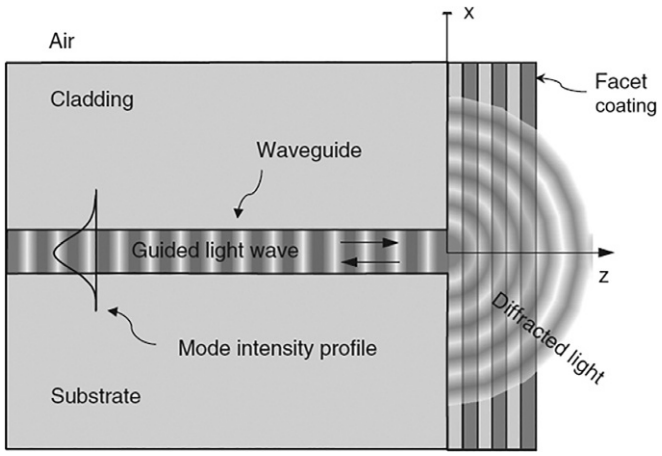


FIG. 2.4

Simplified representation of a waveguide facet coating.

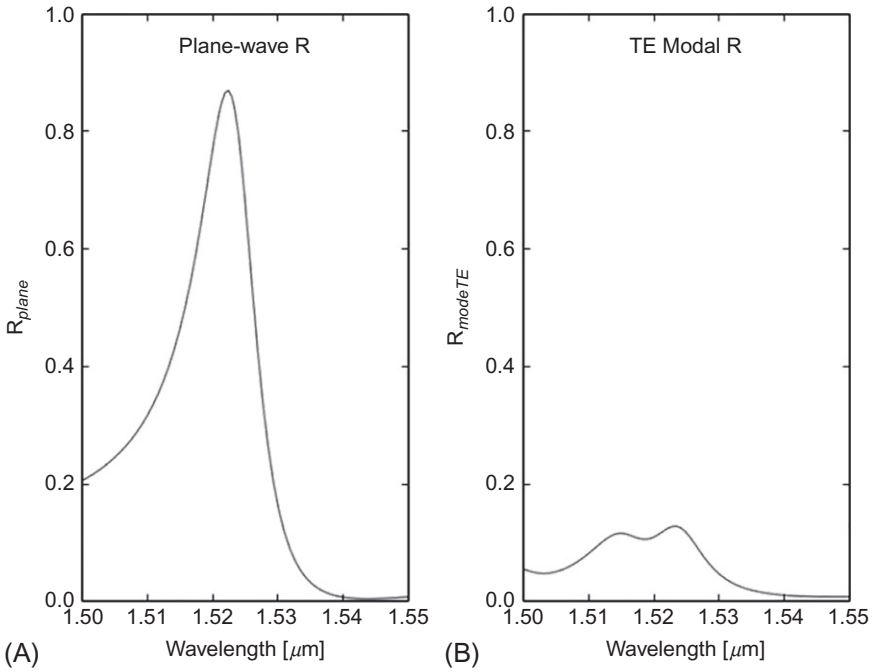


FIG. 2.5

Limitation of the plane-wave approach for facet coatings: case of a narrowband metal-dielectric reflector. (A) plane-wave reflectance; (B) TE mode reflectance.

and becomes a diffracting cone of light, a more conventional geometry for thin film calculations. Assuming for simplicity a TE mode in the geometry of Fig. 2.4, the matching condition is

$$n_{\text{eq}}^2 = \frac{\int n^2(x)|E_0(x)|^2 \mathrm{d}x}{\int |E_0(x)|^2 \mathrm{d}x}, \tag{2.11}$$

where $E_0(x)$ is the modal electric field profile pointing in the y direction and $n(x)$ is the refractive index depth profile of the waveguide. The cone of light is converted to a superposition of plane waves by a Fourier transform:

$$E_0(x) = \int \hat{E}_0(k_x) e^{jk_x x} \mathrm{d}k_x, \tag{2.12}$$

where k_x is the transverse propagation constant in the x direction in medium n_{eq}. The total reflected field $E_r(x)$ at the facet is the superposition of the individual reflected plane waves. The mode reflectance is then found by projecting $E_r(x)$ on the mode of interest (using the mode orthogonality):

$$R_{\text{mode}} = \frac{\int E_r(x)E_0^*(x)\mathrm{d}x}{\int |E_0(x)|^2 \mathrm{d}x}. \tag{2.13}$$

Generalizations to transverse magnetic (TM) modes (H field in the direction of the y axis) and 3D geometries have been published (Vassallo, 1988, 1990). Using angled facets is another way of reducing the mode reflectance further, but the transmitted light is deflected, which is not always acceptable. This theory is valid in the case of small $\mathrm{d}n(x)$ (a weakly guiding mode).

Kendall proposed a modification where the waveguide radiation modes are included to ensure better field matching at the facet (Kendall et al., 1993; Xu et al., 1995; Reed et al., 1996). The radiation modes are approximated by a superposition of plane waves in a homogeneous medium of appropriate refractive index (free-space radiation modes). Improved results are reported. This theory also requires waveguides with a small $\mathrm{d}n(x)$.

Vukovic studied waveguides buried at a shallow depth where the small $\mathrm{d}n(x)$ assumption is no longer valid because the thin cladding does not completely isolate the modal field from the air above and the top corner of the coated facet generates nonnegligible diffraction effects (Vukovic et al., 1998, 2000). A modification of Kendall's model is proposed where the homogeneous medium for the free-space radiation modes is split in two half spaces.

Orobtchouk et al. (1997) developed a model where the small $\mathrm{d}n(x)$ assumption is not necessary. The plane waves in the modal field decomposition all have the same longitudinal wave vector $k_z = Nk_0$ where $k_0 = 2\pi/\lambda$ is the free-space wavenumber and N the mode effective index. Each plane wave i is assumed to propagate in a different medium of equivalent index $n_{\text{eq,i}}$ satisfying

$$n_{eq,i}^2 k_0^2 = k_{x,i}^2 + k_z^2, \tag{2.14}$$

where $k_{x,i}^2$ is the wave vector component along the $x_i$axis. There is no diffraction. The plane wave superposition reverts to the mode at any point along the waveguide axis. The approach is applicable to tilted facets and sharp bends in 3D waveguides of high-index contrast.

Rigorous calculations in 3D geometries greatly increase the computation time. At this time they can hardly be used for thin films design, as opposed to some of the techniques mentioned above. Parallel computations using multi-core CPUs or multiple computers make the situation more tractable (Labukhin and Li, 2005). Different approaches based on FDTD calculations, mode matching, beam propagation method, etc., have been published (Vassallo, 1997, 1998; Wiechmann et al., 2003; Obayya, 2006; Schmid et al., 2007; Strain and Sorel, 2010). An open-source software tool, CAMFR (CAvity Modeling FRamework, available from http://camfr.sourceforge.net), offers a fast and still rigorous alternative to FDTD. It is convenient for checking the modal reflectance of designs generated with more approximate approaches (Bienstman and Baets, 2001; Bienstman, 2001). It is based on field-mode matching, where the fields, expressed as superpositions of modes of successive waveguide sections, are matched at the interfaces.

Finally, it should be noted that the design of waveguide facet coatings generally imposes a limit on the total thickness of the coating. There are two main reasons: (i) to maintain the mechanical integrity of a coating that has to adhere to a tiny device that often has to be diced and handled with tweezers, and (ii) because of diffraction, the fraction of the light reflected back into the mode of interest decreases as the light penetrates deeper inside the coating.

2.4.2 STRUCTURED COATINGS

Achieving narrow spectral bands in reflection is notoriously more difficult than in transmission for thin films. The opposite is true when resonant gratings are incorporated in a multilayer stack (Vincent and Nevière, 1979; Wang et al., 1990; Magnusson and Wang, 1992). Hybrid filters of this type have attracted interest for several decades (Moharam and Gaylord, 1981; Wang and Magnusson, 1993; Rigneault et al., 1999; Escoubas et al., 2001; Boyko et al., 2008; Sergeant et al., 2009; Wang and Menon, 2012) and have proven to be essential for use in some X-ray regions (e.g., Rife et al., 1989;Yang et al., 2017a,b;). The multilayer portion of the gratings is often limited to a quarter-wave stack, sometimes defined at a grazing angle. In their simplest expression, the filters consist of a single layer with a lateral periodic refractive index variation. For simplicity, let us consider the two-dimensional geometry of Fig. 2.6. The periodicity splits the incident plane wave

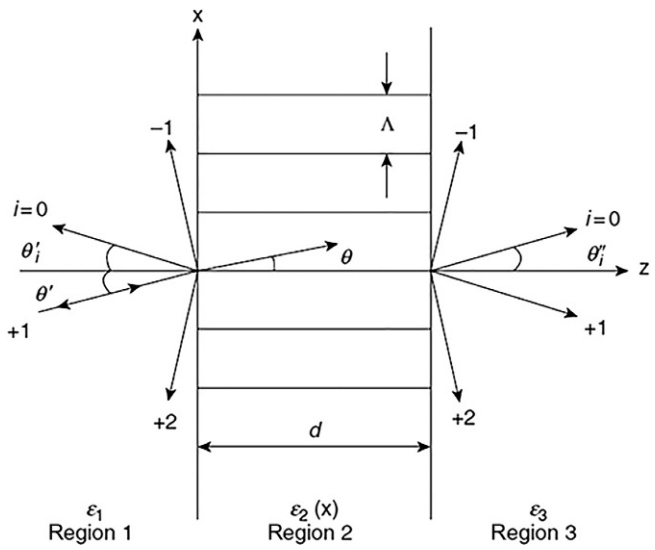


FIG. 2.6

Planar grating diffraction model showing the reflected and transmitted harmonics. The 0th harmonics are the specularly reflected and transmitted waves.

Reproduced with permission of the Optical Society of America (Wang, S.S., Magnusson, R., Bagby, J.S., Moharam, M.G., 1990. Guided-mode resonances in planar dielectric-layer diffraction gratings, J. Opt. Soc. Am. A 7, 1470–1474).

in multiple harmonics that propagate at angles determined by Bragg's condition or decay exponentially in the z direction. In homogeneous media or layers, the harmonics are plane waves with propagation constants in the x and z directions given by

$$\begin{aligned} k_{xm} &= k_x + mK, \quad \vec{m} = 0,1,2,3,\ldots \\ k_{zm} &= \pm\sqrt{n^2k^2 - k_{xm}^2}, \\ k_x &= k_0 \sin\theta_0, \\ K &= \frac{2\pi}{\Lambda}, \end{aligned} \tag{2.15}$$

where k_x belongs to the incident light, K is the grating constant, Λ the grating period, n the refractive index, k_0 the vacuum wave vector, and θ_0 the angle of incidence in air. In the grating layer, the harmonics coupled with the periodicity have a varying amplitude $S_m(z)$. The problem is solved by substitution of the electromagnetic fields (sum of harmonics, also called a Bloch wave) in Maxwell's equations and applying the boundary conditions. The differential equations can be solved numerically (FDTD, etc.) or by a rigorous coupled wave approach, where the problem is reduced to a set of coupled differential equations. For a sinusoidal grating of relative permittivity $\varepsilon(x) = \varepsilon_0 + \Delta\varepsilon$ and $\cos(Kx) = n^2(x)$, one has (Moharam and Gaylord, 1981; Wang et al., 1990)

$$\frac{d^2S_m}{dz^2} = A_m\frac{dS_m}{dZ} + B_mS_m + C_m(S_{m-1} + S_{m+1}), \tag{2.16}$$

where A_m, B_m, and C_m are constants depending on the geometry and C_m describes the coupling between adjacent harmonics, proportional to $\Delta\varepsilon/\varepsilon_0$.

A situation of particular interest occurs when the ± 1 harmonics of a plane wave arriving at normal incidence ($\theta_0 = 0$) are coupled to counter-propagating guided modes of the grating layer ($+x$ and $-x$ directions). For weak gratings ($\Delta\varepsilon/\varepsilon \ll 1$), the mode is essentially the same as in a homogeneous layer of average index. The mode's propagation constant k_x must satisfy the waveguide dispersion equation, a transverse resonance condition for the plane wave trapped by total internal reflection in the guiding layer (the round trip phase shift in the z direction must be a multiple of 2π radians).

According to Eq. (2.15), the guided harmonics are such that $k_{x1} = -kx_{,-1} = K$. They are coupled to each other (reflected in the x direction) by a second-order Bragg condition and coupled to plane waves radiating power in the z direction by a first-order Bragg condition. Such waveguide modes losing energy as they propagate are called leaky modes. The net result of these resonances is a rapid variation of the transmittance or reflectance of the grating layer for light propagating in the z direction as the wavelength (or angle of incidence) is varied. The situation is subtle: slow leaks are essential in order to generate enough guided light; the leaks increase the imaginary part of k_{xm} and create a stop band in the k_{xm} vs k Brillouin diagram. The grating reflectance has narrow peaks at wavelengths near the edges of this stop band (not the middle, where the leak would be too large). The peak at one edge disappears for symmetry reasons when the incident light is at normal incidence and the grating is

symmetrical (Vincent and Nevière, 1979); otherwise, there are two peaks (Avrutskii et al., 1986; Ding and Magnusson, 2004b). This property is used to design filters with more complex spectral shapes.

Strong coupling increases the leaks and broadens the peak(s). The shape of the spectral variations also depends on the layer structure in which the grating is embedded. Narrowband reflection filters are obtained when the grating is embedded in an AR coating. The AR provides the low reflectance background and the grating provides the narrow reflectance peak (Magnusson and Wang, 1992; Lemarchand et al., 1997).

Designs are possible where the gratings have more elaborate periodicities, multiple gratings are stacked, the light couples to more than one waveguide mode, or a combination of these effects (Shin et al., 1998). Different types of filters have been demonstrated including narrowband reflectors with reduced angular sensitivity (Lemarchand et al., 1998), bandpass filters, polarizers and polarization-independent filters (Ding and Magnusson, 2004a; Shokooh-Saremi and Magnusson, 2010b), wideband reflectors (Shokooh-Saremi and Magnusson, 2010a). Fig. 2.7 illustrates two wideband resonant grating filters. Besides filters, the applications include optoelectronic devices, ultrasensitive bio- or chemical sensors, absorption enhancement

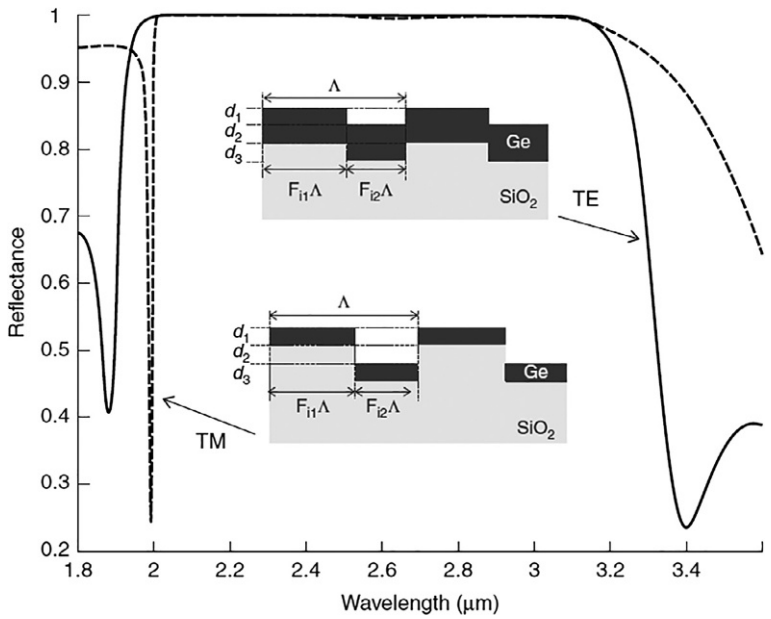


FIG. 2.7

Wideband reflectance spectrum of two Ge/SiO_2 resonant grating filters, respectively, in the TE and TM polarizations (Shokooh-Saremi and Magnusson, 2010a). The triple-level grating geometries are sketched in the inset. TE and TM refer to the polarization of the guided light (E or H field parallel to the grating lines).

Reproduced with permission of the Optical Society of America.

in solar cells, security devices, tunable filters, display components, etc. (Magnusson et al., 2003; Ding and Magnusson, 2004a).

The two-dimensional weak grating model presented above has the advantage of providing physical insight. Strong gratings and 3D geometries (photonic crystals) significantly complicate the situation and require rigorous vectorial calculations.

For decades, periodic two-dimensional meshes and crossed patterns made through metal sheets (inductive grids) or metal-coated on plastic (capacitive grids), in single or multilayer configurations, have been used as filters for far-IR and THz applications (Ulrich, 1967, 1968; Dobrowolski, 1995; Smith et al., 2003). Their design is inspired from the microwave waveguide filters theory and from optical interference approaches, such as those described by Holah and Smith (1972). These mesh filters can be seen as the predecessors of the metamaterial- and plasmonic-material-based devices that have been the object of keen interest in recent years and have shown novel optical properties (for recent reviews see Monticone and Alù, 2017; Urbas et al., 2016; Chen et al., 2016). Metamaterials design methods are outside the scope of this chapter and usually involve FDTD or other rigorous approaches. Nevertheless, at least two points are worth mentioning from an optical coating perspective: (i) similarly to metal meshes for long-wavelength applications, it is fair to think that metamaterial can be used in multilayer configurations and benefit (at least partly) from optical coating design techniques, and (ii) metamaterials and plasmonic materials open the possibility of novel effective optical constants for the realization of innovative or currently unrealistic designs.

For example, some recently proposed high-performance AR and black coatings require materials with unrealistic optical constants and dispersions; attempts have been made to engineer metamaterials and plasmonic materials meeting the requirements (Kim and Park, 2013; Hedayati et al., 2014). This transfer of design parameters from thickness-value and material-choice to material engineering follows the same line of thought as the realization of inhomogeneous coatings "directly" from experimental parameters controlling the composition of the coatings material (Becker et al., 2014). The introduction of metal nanostructures, organized or randomly distributed on a surface or in a cement, allows optical constants with abnormal dispersions to be tuned. The combination of such metasurfaces in simple multilayers has been explored in some devices; Fig. 2.8 shows a micrograph of such a device capable of producing phase holograms; one can clearly see two laterally graded metasurface layers (Larouche et al., 2012).

Apart from AR surfaces, nanostructured materials open new opportunities for the control of light, particularly of its angular behaviour, polarization, and phase (Shen et al., 2016; Zhang et al., 2016). Counterintuitive results are possible, such as negative refraction. Fig. 2.9 shows three recent examples of remarkable devices involving metasurfaces: (a) a high reflectance polarization conversion thin layer (Yang et al., 2014), (b) a bi-metasurface mirror that retro-reflects a light beam incident at an oblique angle (Arbabi et al., 2017), and (c) a thin multilayer–metasurface device that performs analog mathematical operations (i.e., Fourier transform, derivatives) on a light beam profile (Silva et al., 2014).

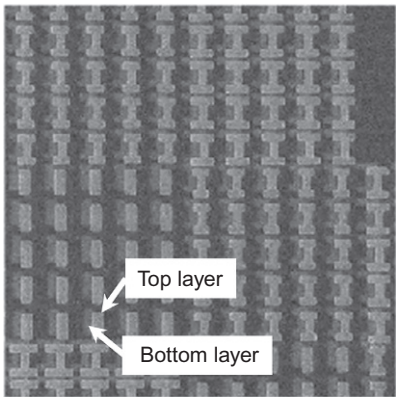


FIG. 2.8

SEM picture of a multilayer–metasurface device with laterally graded dimensions. The device produced an IR phase hologram.

Adapted from Larouche, S., Tsai, Y.-J., Tyler, T., Jokerst, N.M., Smith, D.R., 2012. Infrared metamaterial phase holograms, Nat. Mater., 11, 450–454, with permission of Nature Publishing Group.

2.4.3 SOLAR CELLS

Solar cells are a subject of sustained research, motivated by the need of developing renewable and less polluting energy sources. It is recognized that thin film cells are less expensive to produce than crystalline ones but have more limitations in terms of charge generation and transport. The material properties, fabrication limitations, and light trapping strategies have a profound influence on their design.

The main components of a solar cell are: (i) an active layer where light is absorbed and electric charges are generated, and (ii) electrodes to collect the charges. One electrode is transparent [e.g. indium tin oxide (ITO)], while the other is usually opaque metal. Interfacial layers are often necessary to facilitate charge transport and for other reasons. The energy levels of the layer materials are arranged so that the electrons and holes separate and drift to their collection sites before they have time to recombine. In solar cells based on organic polymers, the charges are generated in the form of bound electron–hole pairs called excitons. The charges are separated at the junction between a hole-transporting (donor-like) and an electron–transporting (acceptor-like) material. This interface must be in close proximity to the light absorption sites because the exciton diffusion length is very short, on the order of 10–20 nm only (Duché et al., 2012). The mobility of the separated charges is about 10 times higher. An effective strategy consists in blending the donor and acceptor materials on a fine scale in order to form narrow elongated pathways leading to the collection sites (bulk-heterojunction materials). The efficiency of the photon-to-collected-charge conversion can be highly nonuniform along the depth of the active layer(s), leading to semi-active or dead regions. Fabrication constraints such as suitable layer

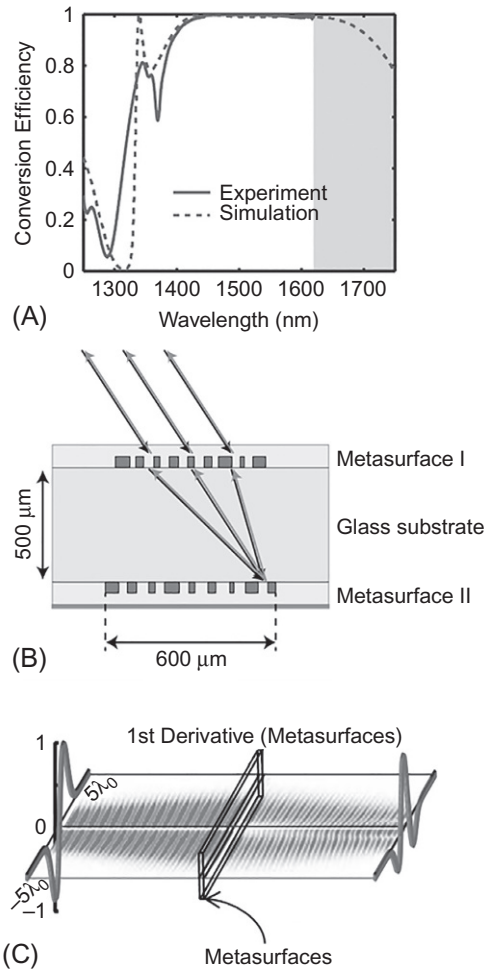


FIG. 2.9

Three examples of novel metasurface devices: (A) polarization convertor, (B) retroreflector at oblique incidence, and (C) first derivative operator metasurface.

(A) Adapted from Yang, Y., Wang, W., Moitra, P., Kravchenko, I.I., Briggs, D.P., Valentine, J., 2014. Dielectric meta-reflectarray for broadband linear polarization conversion and optical vortex generation. Nano Lett. 14, 1394–1399. Copyright 2014 American Chemical Society; (B) Adapted from Arbabi, A., Arbabi, E., Horie, Y., Kamali, S.M., Faraon, A., 2017. Planar metasurface retroreflector. Nat. Photonics 11, 415–420, with permission of Nature Publishing Group; (C) Adapted from Silva, A., Monticone, F., Castaldi, G., Galdi, V., Alù, A., Engheta, N., 2014. Performing mathematical operations with metamaterials. Science 343, 160–163, with permission of AAAS.

materials, roughness, homogeneity, reproducibility, limits on the acceptable thicknesses, cost considerations, and so forth put severe constraints on the design possibilities. Serious consideration must be given to these issues when the optical interference is optimized.

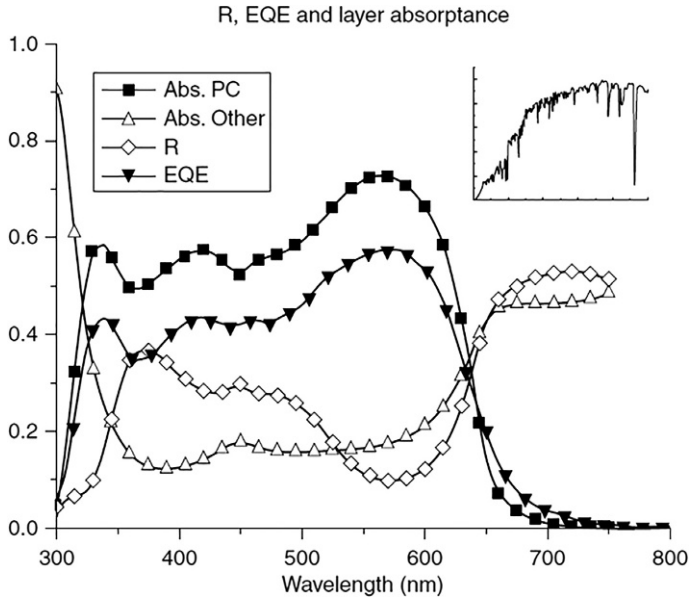


FIG. 2.10

Simulation of the absorption in the organic bulk-heterojunction solar cell described in the text. (Abs. PC): absorptance of the active PCDTBT:$PC_{60}BM$ layer of 75 nm thickness; (Abs. Other): cumulative absorptance of the other layers and the glass substrate; (R): reflectance; (EQE): measured external quantum efficiency. The inset shows the AM 1.5 solar photon flux in the same wavelength range.

Adapted from Chu, T.-Y., Alem, S., Verly, P. G., Wakim, S., Lu, J., Tao, Y., Beaupré, S., Leclerc, M., Belanger, F., Desilets, D., Rodman, S., Waller, D., Gaudiana, R., 2009. Highly efficient polycarbazole-based organic photovoltaic devices, Appl. Phys. Lett., 95, 063304-3, with permission of AIP Publishing.

Fig. 2.10 illustrates the simulation of an organic bulk-heterojunction cell with the following structure:

> Glass/ITO (150 nm)/PEDOT:PSS (50 nm)/PCDTBT:$PC_{60}BM$ (75 nm)/Lithium fluoride (LiF) (1 nm)/Al,

and a comparison with experimental results (Chu et al., 2009). The second and third layers are polymers processed from solution and spun-coated on commercially supplied ITO-on-glass. The PCDTBT:$PC_{60}BM$ is a blend of a donor and acceptor material forming the active layer. The PEDOT:PSS and the LiF are interfacial layers. The simulated absorptance of the active layer (absorbed photon per incident photon) is roughly proportional to the measured EQE (*external quantum efficiency*, or collected electron per incident photon). The ratio of these two quantities (defined as *internal quantum efficiency* or IQE) characterizes the efficiency of the absorbed photon to charge conversion. The calculated reflectance and the cumulative absorptance in the remaining material of the cell (glass substrate and other layers) represent

together the light that does not participate in the current generation. In this case, only the active layer thickness was optimized due to fabrication constraints. The figure inset shows that the photon flux in the AM 1.5 solar spectrum (plotted in the same wavelength range) drops rapidly for wavelengths below 450 nm where the active layer still absorbs.

Fig. 2.11 illustrates the effect of varying the active-layer thickness on the measured short-circuit current J_{sc} and the simulated *solar photon absorption* (SPA) in the active layer:

$$\mathrm{SPA} = \frac{\int S(\lambda)A(\lambda)\mathrm{d}\lambda}{\int S(\lambda)\mathrm{d}\lambda}. \tag{2.17}$$

In this equation, $A(\lambda)$ is the layer absorptance and $S(\lambda)$ the solar photon spectrum. The fluctuations of the SPA with thickness are due to the optical interference. The current and SPA follow similar trends near the first maximum of the curves. The arrow corresponds to the cell simulated in Fig. 2.10. The second, higher SPA maximum visible in the inset and corresponding to a larger thickness was ruled out because of charge transport issues through thick layers. A similar cell with thinner PEDOT:PSS (preferred from an optical perspective) achieved a respectable measured power conversion efficiency (PCE) of 5.7%.

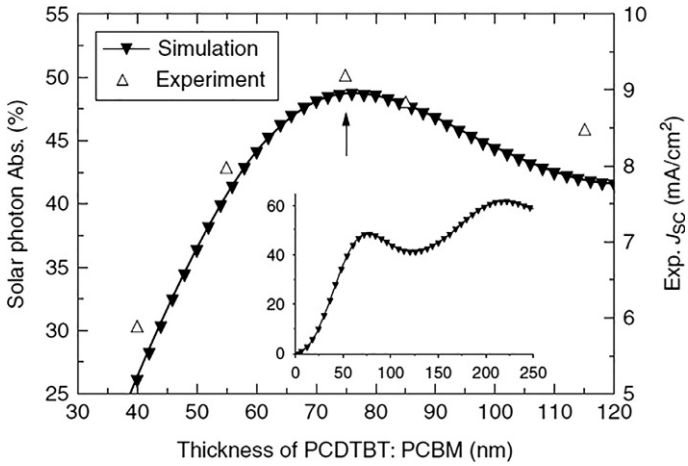


FIG. 2.11

Effect of changing the active layer thickness on the measured short circuit current and simulated solar photon absorption (SPA) in the active layer of the cell described in Fig. 2.10 (arrow). The inset shows the first two maxima of the SPA curve plotted in an extended thickness range.

Adapted from Chu, T.-Y., Alem, S., Verly, P. G., Wakim, S., Lu, J., Tao, Y., Beaupré, S., Leclerc, M., Belanger, F., Desilets, D., Rodman, S., Waller, D., Gaudiana, R., 2009. Highly efficient polycarbazole-based organic photovoltaic devices, Appl. Phys. Lett., 95, 063304-3, with permission of AIP Publishing.

These cells have stability issues associated with the degradation of the electrodes over time. Significant improvements are possible by inverting the layer structure of the cells, with the current direction reversed (Chu et al., 2012):

Glass/ITO/ZnO–NC/PDTSTPD–$PC_{71}BM$/Molybdenum oxide (MoOx)/Ag.

The ZnO–NC is a nanocrystal film acting as an electron transporting layer. A measured PCE of 6.7% is reported. The materials characterization, design, and simulation of such cells can represent a challenge (Ameri et al., 2008).

Efforts are under way to extend the absorption of organic solar cells in the infrared. One way to do this is by stacking two or more cells that absorb light in different wavelength regions (Persson and Inganäs, 2006; Kim et al., 2007; Dennler et al., 2008; Ameri et al., 2009). The cells should be balanced because the current is limited by the weakest link.

Bilayer geometries where the donors and acceptors are in separate layers are also investigated. The very narrow active region requires careful optimization of the optical interference and a good understanding of the charge generation and transport properties. The quantity maximized in the design is the current J_{sc}, calculated from differential equations taking into account the charge generation rate (absorbed photons), recombination (lifetime), as well as diffusion and drift due to charge density variations and built-in electric fields (Pettersson et al., 1999; Monestier et al., 2008). Bulk-heterojunction cells also benefit from such calculations (Monestier et al., 2007; You and Zhang, 2009).

Ways of trapping the light in the active layer are investigated, especially when its thickness is reduced to promote the charge transport properties. A common strategy is to scatter the light into guided modes of the cell structure by means of gratings, photonic crystal structures, or random roughness (Zeng et al., 2006; Mutitu et al., 2008; Seassal et al., 2008; Escoubas et al., 2011; Raman et al., 2011; Duché et al., 2012; Wang and Menon, 2013; Shen et al., 2014; Kubota et al., 2016). The dimensions of the scatterers can be optimized in order to generate resonances in the spectral regions where the intrinsic absorption of the active material is weak. A high density of Bloch modes is necessary to ensure that the improvements are not limited to a narrow spectral region. Plasmonic structures made of metallic nanoparticles are also investigated for their ability to generate high electromagnetic fields in the vicinity of the metal (Catchpole and Polman, 2008; Flory et al., 2011; Vedraine et al., 2011). Dicroic filters or beam splitters have been designed to improve the performance of solar cells by splitting the spectrum and redirecting light toward matched photovoltaic cells or thermal collectors (Jiachen et al., 2015; Maragliano et al., 2016).

2.5 CONCLUSION

It is frequently heard that thin film design is the easy part of the work. A number of proven design techniques and breakthroughs such as the needle method greatly facilitate the designer's task. Nevertheless, there are still many challenges. It has become

a tradition at the topical meeting on Optical Interference Coatings organized by the OSA to propose cutting-edge design and manufacturing problems to the thin films community (for design problems, see Thelen and Langfeld, 1992; Baumeister, 2000; Thelen et al., 2002; Tilsch et al., 2006; Tilsch and Hendrix, 2008; Hendrix and Oliver, 2011; Hendrix et al., 2014; Kruschwitz et al., 2017).

This chapter reviews tools that are available for the solution of difficult design problems and presents some situations outside the classical framework. The desensitization to manufacturing errors is an important topic of practical interest requiring a good understanding of the deposition process. Attempts have been made at simulating the effect of realistic deposition errors (monitoring signals, rate fluctuations, or other relevant parameters) on designs optimized mostly for spectral performance. Other approaches incorporate simplified deposition error models in the design algorithms. It is difficult to do both at the same time and this is still largely an open question.

The chapter also presents examples of hybrid situations where more than the interference in the coating is involved, or where the geometry of the problem significantly complicates the modeling, such as waveguide coatings, resonant grating filters, and solar cells. Solar cells in particular are a subject of intense research. Rigorous modeling has to take into account charge generation and transport issues, accidental scattering or intentional diffraction by photonics structures, and so forth, in addition to the optical interference. Many questions are still unanswered.

The availability of parallel computing stimulates interest in computer-intensive modeling. Clearly, design requires many times more computing power than the simulation of an already known structure. There is no doubt that this is a direction for the future. Metamaterials, novel material mixtures, cermets, photonic crystals and devices, exotic wavelength regions, birefringence, and so forth open opportunities of interesting design work.

REFERENCES

Abul Hasan, M., Ramakrishnan, S., 2011. A survey: hybrid evolutionary algorithms for cluster analysis. Artif. Intell. Rev. 36, 179–204.

Al-Marzoug, S.M., Hodgson, R.J., 2008. Optimization of multilayer mirrors at 13.4 nm with more than two materials. Appl. Opt. 47, 2155–2160.

Ameri, T., Dennler, G., Waldauf, C., Denk, P., Forberich, K., Scharber, M.C., Brabec, C.J., Hingerl, K., 2008. Realization, characterization, and optical modeling of inverted bulk-heterojunction organic solar cells. J. Appl. Phys. 103, 084506_1–084506_6.

Ameri, T., Dennler, G., Lungenschmied, C., Brabec, C.J., 2009. Organic tandem solar cells: a review. Energy Environ. Sci. 2, 347–363.

Amotchkina, T.V., Schlichting, S., Ehlers, H., Trubetskov, M.K., Tikhonravov, A.V., Ristau, D., 2012. Computational manufacturing as a tool for the selection of the most manufacturable design. Appl. Opt. 51, 8677–8686.

Arbabi, A., Arbabi, E., Horie, Y., Kamali, S.M., Faraon, A., 2017. Planar metasurface retroreflector. Nat. Photonics 11, 415–420.

Avrutskii, I.A., Golubenko, G.A., Sychugov, V.A., Tishchenko, A.V., 1986. Spectral and laser characteristics of a mirror with a corrugated waveguide on its surface. Sov. J. Quantum Electron. 16, 1063.

Badoil, B., Lemarchand, F., Cathelinaud, M., Lequime, M., 2008. Manufacturing of an absorbing filter controlled with a broadband optical monitoring. Opt. Express 16, 12008–12017.

Baumeister, P., 2000. Evaluation of the solutions for two design problems presented at the 1998 optical interference coatings conference. Appl. Opt. 39, 2230–2234.

Baumeister, P.W., 2004. Optical Coating Technology. SPIE Press, Bellingham, WA.

Becker, H., Tonova, D., Sundermann, M., Ehlers, H., Günster, S., Ristau, D., 2014. Design and realization of advanced multi-index systems. Appl. Opt. 53, A88–A95.

Bellum, J.C., Winstone, T.B., Field, E.S., Kletecka, D.E., 2017. Broad bandwidth high reflection coatings for petawatt class lasers: femtosecond pulse laser damage tests, and measurement of group delay dispersion. Proc. SPIE 10084, J1–J10.

Bienstman, P., 2001. Rigorous and efficient modelling of wavelength scale photonic components. Ph.D. Thesis, Ghent University (May 2001).

Bienstman, P., Baets, R., 2001. Optical modelling of photonic crystals and VCSELs using eigenmode expansion and perfectly matched layers. Opt. Quant. Electron. 33, 327–341.

Binda, P.D., Zocchi, F.E., 2004. Genetic algorithm optimization of X-ray multilayer coatings. In: Advances in Computational Methods for X-Ray and Neutron Optics. 5536. Proc SPIE—The International Society for Optical Engineering, Denver (CO), pp. 97–108.

Birge, J.R., Kärtner, F.X., Nohadani, O., 2011. Improving thin-film manufacturing yield with robust optimization. Appl. Opt. 50, C36–C40.

Bolinder, F., 1950. Fourier transforms in the theory of inhomogeneous transmission lines. Proc. IRE 38, 1216–1224.

Boudet, T., Chaton, P., Herault, L., Gonon, G., Jouanet, L., Keller, P., 1996. Thin-film designs by simulated annealing. Appl. Opt. 35, 6219–6226.

Bovard, B.G., 1988. Fourier transform technique applied to quarterwave optical coatings. Appl. Opt. 27, 3062–3063.

Bovard, B.G., 1993. Rugate filter theory: An overview. Appl. Opt. 32, 5427–5442.

Boyko, O., Lemarchand, F., Talneau, A., Fehrembach, A.-L., Sentenac, A., 2008. Resonant gratings for narrow band pass filtering applications. In: Advances in Optical Thin Films III.Glasgow, Proc SPIE—The International Society for Optical Engineering. 7101, pp. 71011B–9.

Bulkin, P.V., Swart, P.L., Lacquet, B.M., 1996. Fourier-transform design and electron cyclotron resonance plasma-enhanced deposition of lossy graded-index optical coatings. Appl. Opt. 35, 4413–4419.

Catchpole, K.R., Polman, A., 2008. Plasmonic solar cells. Opt. Express 16, 21793–21800.

Chen, H.-T., Taylor, A.J., Yu, N., 2016. A review of metasurfaces: Physics and applications. Rep. Prog. Phys. 79,076401 (40pp).

Cheng, X., Wang, Z., Zhang, Z., Wang, F., Chen, L., 2006. Design of X-ray supermirrors using simulated annealing algorithm. Opt. Commun. 265, 197–206.

Cheng, X., Fan, B., Dobrowolski, J.A., Wang, L., Wang, Z., 2008a. Gradient-index optical filter synthesis with controllable and predictable refractive index profiles. Opt. Express 16, 2315–2321.

Larouche, S., Martinu, L., 2008b. OpenFilters: open-source software for the design, optimization, and synthesis of optical filters. Appl. Opt. 47, C219–C230.

Chiadini, F., Fiumara, V., Scaglione, A., 2017. Design of bioinspired chirped reflectors using a genetic algorithm. Proc. SPIE, 10162, 101620T-1–7.

Chu, T.-Y., Alem, S., Verly, P.G., Wakim, S., Lu, J., Tao, Y., Beaupré, S., Leclerc, M., Belanger, F., Desilets, D., Rodman, S., Waller, D., Gaudiana, R., 2009. Highly efficient polycarbazole-based organic photovoltaic devices. Appl. Phys. Lett. 95. 063304–3.

Chu, T.Y., Tsang, S.W., Zhou, J., Verly, P.G., Lu, J., Beaupré, S., Leclerc, M., Tao, Y., 2012. High-efficiency inverted solar cells based on a low bandgap polymer with excellent air stability. Sol. Energy Mater. Sol. Cells 96, 155–159.

Cox, D.D., John, S., 1992. A statistical method for global optimization. In: Proc. IEEE Int. Conf. on Systems, Man and Cybernetics. 2, pp. 1241–1246, 18–21 Oct. 1992, Chicago IL.

Csendes, V., Daroczy, B., Hanos, Z., 1986. Nonlinear parameter estimation by global optimization: comparison of local search methods in respiratory system modelling. In: Prékopa, A., Szelezsáan, J., Strazicky, B. (Eds.), System Modeling and Optimization. Springer Verlag, Berlin, pp. 188–192.

Cushing, D., 2011. Enhanced Optical Filter Design. SPIE Press, Bellingham (WA).

de Denus-Baillargeon, M.M., Schmitt, T., Larouche, S., Martinu, L., 2014. Design and fabrication of stress-compensated optical coatings: Fabry–Perot filters for astronomical applications. Appl. Opt. 53, 2616–2624.

Delano, E., 1966. Fourier Methods of Synthesis for Optical Multilayer Filters. Ph.D. Thesis, Institute of Optics, University of Rochester. (available online from University of Rochester).

Delano, E., 1967. Fourier synthesis of multilayer filters. J. Opt. Soc. Am. 57, 1529–1532.

Dennler, G., Scharber, M.C., Ameri, T., Denk, P., Forberich, K., Waldauf, C., Brabec, C.J., 2008. Design rules for donors in bulk-heterojunction tandem solar cells? Towards 15% energy-conversion efficiency. Adv. Mater. 20, 579–583.

Ding, Y., Magnusson, R., 2004a. Resonant leaky-mode spectral-band engineering and device applications. Opt. Express 12, 5661–5674.

Ding, Y., Magnusson, R., 2004b. Use of nondegenerate resonant leaky modes to fashion diverse optical spectra. Opt. Express 12, 1885–1891.

Djurisic, A.B., Fritz, T., Leo, K., Li, E.H., 2000. Improved method for determination of optical constants of organic thin films from reflection and transmission measurements. Appl. Opt. 39, 1174–1182.

Dobrowolski, J.A., 1965. Completely automatic synthesis of optical thin film systems. Appl. Opt. 4, 937–946.

Dobrowolski, J.A., 1981. Versatile computer program for absorbing optical thin-film systems. Appl. Opt. 20, 74–81.

Dobrowolski, J.A., 1995. Chapter 42 of Handbook of Optics, second ed. vol. 1. McGraw-Hill, New York.

Dobrowolski, J.A., 1997. Numerical methods for optical thin films. Opt. Photonics News 8, 24–33.

Dobrowolski, J.A., Kemp, R.A., 1990. Refinement of optical multilayer systems with different optimization procedures. Appl. Opt. 29, 2876–2893.

Dobrowolski, J.A., Kemp, R.A., 1992. Flip-flop thin-film design program with enhanced capabilities. Appl. Opt. 31, 3807–3812.

Dobrowolski, J.A., Lowe, D., 1978. Optical thin film synthesis program based on the use of Fourier transforms. Appl. Opt. 17, 3039–3050.

Dobrowolski, J.A., Piotrowski, S.H.C., 1982. Refractive index as a variable in the numerical design of optical thin film systems. Appl. Opt. 21, 1502–1511.

Dobrowolski, J.A., Ho, F.C., Belkind, A., Koss, V.A., 1989. Merit functions for more effective thin film calculations. Appl. Opt. 28, 2824–2831.

Dobrowolski, J.A., Browning, S., Jacobson, M., Nadal, M., 2008. 2007 topical meeting on optical interference coatings: manufacturing problem. Appl. Opt. 47, C231–C245.

Druessel, J., Grantham, J., Haaland, P., 1993. Optimal phase modulation for gradient-index optical filters. Opt. Lett. 18, 1583.

Duché, D., Escoubas, L., Simon, J.J., Gourgon, C., Masclaux, C., Torchio, P., Le Rouzo, J., Flory, F., 2012. Photonic crystals for improving light absorption in organic solar cells. In: Freundlich, A., Guillemoles, J.F. (Eds.), Physics, Simulation, and Photonic Engineering of Photovoltaic Devices. first ed. 8256. SPIE, San Francisco, California 82561K-8.

Ehlers, H., Schlichting, S., Schmitz, C., Ristau, D., 2010. Hybrid process control for precision optics enhanced by computational manufacturing. In: Optical Interference Coatings. OSA Technical Digest, paper TuC6.

Eisenhammer, T., Lazarov, M., Leutbecher, M., Schöffel, U., Sizmann, R., 1993. Optimization of interference filters with genetic algorithms applied to silver-based heat mirrors. Appl. Opt. 32, 6310–6315.

Escoubas, L., Flory, F.O., Lemarchand, F., Drouard, E., Roux, L., Tisserand, S., Albrand, G., 2001. Fabry-Perot multilayers for enhancing the diffraction efficiency of ion-implanted gratings. Appl. Opt. 40, 1587–1592.

Escoubas, L., Simon, J.J., Torchio, P., Duché, D., Vedraine, S., Vervisch, W., Le Rouzo, J., Flory, F., Rivière, G., Yeabiyo, G., Derbal, H., 2011. Bringing some photonic structures for solar cells to the fore. Appl. Opt. 50, C329–C339.

Fabricius, H., 1992a. Gradient-index filters: conversion into a two-index solution by taking into account dispersion. Appl. Opt. 31, 5216–5220.

Fabricius, H., 1992b. Gradient-index filters: designing filters with steep skirts, high reflection, and quintic matching layers. Appl. Opt. 31, 5191–5196.

Fattahi, H., Barros, H.B., Gorjan, M., Nubbemeiyer, T., Alsaif, B., Teisset, C.Y., Schultze, M., Prinz, S., Haefner, M., Ueffing, M., Alismail, A., Vamos, L., Schwarz, A., Pronin, O., Brons, J., Geng, X.T., Arisholm, G., Ciappina, M., Yakovlev, V.S., Kim, E.-E., Azzeer, A.M., Karpowicz, N., Sutter, D., Major, Z., Merzger, T., Krausz, F., 2014. Review article: third-generation femtosecond technology. Optica 1, 45–63.

Flory, F., Escoubas, L., Berginc, G., 2011. Optical properties of nanostructured materials: a review. J Nanophotonics. 5. 052502–1.

Furman, S.A., Tikhonravov, A.V., 1992. Optics of Multilayer Systems. Gif-sur-Yvette (France), (Editions frontiere).

Gao, L., Lemarchand, F., Lequime, M., 2011. Application of global optimization algorithms for optical thin film index determination from spectro-photometric analysis. In: Lequime, M., MacLeod, H.A., Ristau, D. (Eds.), Advances in Optical Thin Films IV.Marseille, France, Proc SPIE 8168, 81680B1–17.

Granier, C.H., Afzal, F.O., Lorenzo, S.G., Reyes, M., Dowling, J.P., Veronis, G., 2014. Optimized aperiodic multilayer structures for use as narrow-angular absorbers. J. Appl. Phys. 116. 243101-1–10.

Greiner, H., 1996. Robust optical coating design with evolutionary strategies. Appl. Opt. 35, 5477–5483.

Hedayati, M.K., Fahr, S., Etrich, C., Faupel, F., Rockstuhl, C., Elbahri, M., 2014. The hybrid concept for realization of an ultra-thin plasmonic metamaterial antireflection coating and plasmonic rainbow. Nanoscale 6, 6037–6045.

Hendrix, K., 2017. Linear variable filters for NASA's OVIRS instrument: pushing the envelope of blocking. Appl. Opt. 56, C201–C205.

Hendrix, K., Oliver, J., 2011. Optical interference coatings design contest 2010: solar absorber and Fabry-Perot etalon. Appl. Opt. 50, C286–C300.
Hendrix, K., Kruschwitz, J.D.T., Keck, J., 2014. Optical interference coatings design contest 2013: Angle-independent color mirror and shortwave infrared/midwave infrared dichroic beam splitter. Appl. Opt. 53, A360–A376.
Hobson, M.P., Baldwin, J.E., 2004. Markov-chain Monte Carlo approach to the design of multilayer thin-film optical coatings. Appl. Opt. 43, 2651–2660.
Holah, G.D., Smith, S.D., 1972. Multi-element mesh interference filters for the infrared. J. Phys. D. Appl. Phys. 5, 496–509.
Jacobson, M.R. (Ed.), 1990. Selected Papers on Design of Optical Coatings. SPIE Press, Bellingham (WA).
Jacobsson, R., 1966. Light reflection from films of continuously varying refractive index. Prog. Opt. 5, 247–286.
Jiachen, W., Lee, S.B., Lee, K., 2015. Design of broadband multilayer dichroic coating for a high-efficiency solar energy harvesting system. Appl. Opt. 54, 4805–4811.
Jiang, L., Zheng, G., Shi, L., Yuan, J., Li, X., 2008. Broad omnidirectional reflectors design using genetic algorithm. Opt. Commun. 281, 4882–4888.
Kendall, P.C., Roberts, D.A., Robson, P.N., Adams, M.J., Robertson, M.J., 1993. Semiconductor laser facet reflectivities using free-space radiation modes. Optoelectronics, IEE Proc J 140, 49–55.
Kennedy, J., Eberhart, R., 1995. Particle swarm optimization. In: IEEE Proc, International Conference on Neural Networks. 4, pp. 1942–1948.
Kim, J.Y., Lee, K., Coates, N.E., Moses, D., Nguyen, T.-Q., Dante, M., Heeger, A.J., 2007. Efficient tandem polymer solar cells fabricated by all-solution processing. Science 317, 222–225.
Kim, K.H., Park, Q.-H., 2013. Perfect anti-reflection from first principles. Sci. Rep. 3, 1–5.
Kochergin, V., 2003. Omnidirectional Optical Filters. Kluwer Academic Publishers, Norwell, MA.
Kruschwitz, J.D.T., 2003. Software tools speed optical thin-film design. Laser Focus World 39 (6), 157–166.
Kruschwitz, J.D.T., Pervak, V., Keck, J., Bolshakov, I., Gerig, Z., Lemarchand, F., Sato, K., Southwell, W., Sugiura, M., Trubetskov, M., Yuan, W., 2017. Optical interference coating design contest 2016: A dispersive mirror and coating uniformity challenge. Appl. Opt. 56, C151–C162.
Kubota, S., Kanomata, K., Ahmmad, B., Mizuno, J., Hirose, F., 2016. Optimized design of moth eye antireflection structure for organic photovoltaics. J. Coat. Technol. Res. 13, 201–210.
Labukhin, D., Li, X., 2005. Three-dimensional finite-difference time-domain simulation of facet reflection through parallel computing. J. Comput. Electron. 4, 15–19.
Larouche, S., Martinu, L., 2006. A new step method for the synthesis of optical filters with arbitrary indices. In: 49th Annual Technical Conference Proceedings, Soc. Vacuum Coaters 49, pp. 305–308.
Larouche, S., Martinu, L., 2007. Dispersion implementation in optical filter design by the Fourier transform method using correction factors. Appl. Opt. 46, 7436–7441.
Larouche, S., Martinu, L., 2008. OpenFilters: open-source software for the design, optimization, and synthesis of optical filters. Appl. Opt. 47, C219–C230 (the open source software is available at: http://larfis.polymtl.ca/index.php/en/links/openfilters)

Larouche, S., Tsai, Y.-J., Tyler, T., Jokerst, N.M., Smith, D.R., 2012. Infrared metamaterial phase holograms. Nat. Mater. 11, 450–454.

Lemarchand, F., 2014. Application of clustering global optimization to thin film design problems. Opt. Express 22, 5166–5176.

Lemarchand, F., Giovannini, H., Sentenac, A., 1997. Interest of hybrid structures for thin-film design: Multilayered subwavelength microgratings. In: Hall, R.L. (Ed.), Optical Thin Films V: New Developments.San Diego (CA), Proc SPIE—The International Society for Optical Engineering. 3133, pp. 58–64.

Lemarchand, F., Sentenac, A., Giovannini, H., 1998. Increasing the angular tolerance of resonant grating filters with doubly periodic structures. Opt. Lett. 23, 1149–1151.

Macleod, H.A., 2010. Thin-Film Optical Filters, fourth ed. CRC Press, New York.

Macleod, H.A., Pelletier, E., 1977. Error compensation mechanisms in some thin-film monitoring systems. Optica Acta 24, 907–930.

Magnusson, R., Wang, S.S., 1992. New principle for optical filters. Appl. Phys. Lett. 61, 1022–1024.

Magnusson, R., Ding, Y., Lee, K. J., Shin, D., Priambodo, P. S., Young, P. P. and Maldonado, T. A., 2003. Photonic devices enabled by waveguide-mode resonance effects in periodically modulated films, In: Eldada, L. A. (Ed.), Nano and Micro-Optics for Information Systems, San Diego (CA), Proc SPIE 5225, 20–34.

Maragliano, C., Apostoleris, H., Bronzoni, M., Rampino, S., Stefancich, M., Chiesa, M., 2016. Efficiency enhancement in two-cell CIGS photovoltaic system with low-cost optical spectral splitter. Opt. Express 24, A222–A233.

Maroosi, A., Amiri, B., 2010. A new clustering algorithm based on hybrid global optimization based on a dynamical systems approach algorithm. Expert Syst. Appl. 37, 5645–5652.

Martin, S., Rivory, J., Schoenauer, M., 1995. Synthesis of optical multilayer systems using genetic algorithms. Appl. Opt. 34, 2247–2254.

Moharam, M.G., Gaylord, T.K., 1981. Rigorous coupled-wave analysis of planar-grating diffraction. J. Opt. Soc. Am. 71, 811–818.

Monestier, F., Simon, J.J., Torchio, P., Escoubas, L., Flory, F., Bailly, S., De Bettignies, R., Guillerez, S., Defranoux, C., 2007. Modeling the short-circuit current density of polymer solar cells based on P3HT:PCBM blend. Sol. Energy Mater. Sol. Cells 91, 405–410.

Monestier, F., Simon, J.J., Torchio, P., Escoubas, L., Ratier, B., Hojeij, W., Lucas, B., Moliton, A., Cathelinaud, M., Defranoux, C., Flory, F., 2008. Optical modeling of organic solar cells based on CuPc and C60. Appl. Opt. 47, C251–C256.

Monticone, F., Alù, A., 2017. Review: Metamaterial, plasmonic and nanophotonic devices. Rep. Prog. Phys. 80. 036401 (37pp).

Morf, R., Kunz, R.E., 1988. Dielectric filter optimization by simulated thermal annealing. In: Thin films technologies III.Bellingham (WA), Proc SPIE—The International Society for Optical Engineering. 1019, pp. 211–217.

Morf, R.H., Kunz, R.E., 1990. Dielectric filter optimization by simulated thermal annealing: A simulated zone-melting approach. In: Optical Thin Films and Applications. Bellingham (WA), Proc SPIE—The International Society for Optical Engineering, 1270, pp. 11–17.

Mutitu, J.G., Shi, S., Chen, C., Creazzo, T., Barnett, A., Honsberg, C., Prather, D.W., 2008. Thin film solar cell design based on photonic crystal and diffractive grating structures. Opt. Express 16, 15238–15248.

Nohadani, O., Birge, J.R., Kartner, F.X., Bertsimas, D.J., 2008. Robust chirped mirrors. Appl. Opt. 47, 2630–2636.

Obayya, S.S.A., 2006. Scalar finite-element analysis of optical-fiber facets. J. Lightwave Technol. 24, 2115–2121.
Orobtchouk, R., Laval, S., Pascal, D., Koster, A., 1997. Analysis of integrated optical waveguide mirrors. J. Lightwave Technol. 15, 815–820.
Oulton, R.F., Adjiman, C.S., 2006. Global optimization and modeling techniques for planar multilayered dielectric structures. Appl. Opt. 45, 5910–5922.
Panos, M., Pardalos, H., Romeijn, E., 2002. Handbook of Global Optimization. vol. 2. Kluwer Academic Publishers, Dordrecht.
Patel, S.J., Kheraj, V., 2015. Optimization of the genetic operators and algorithm parameters for the design of a multilayer anti-reflection coating using the genetic algorithm. Opt. Laser Technol. 70, 94–99.
Patel, S.J., Toshniwal, A., Kheraj, V., 2017. A novel teaching-learning based optimization approach for design of broad-band anti-reflection coatings. Swarm Evol. Comput. 34, 68–74.
Persson, N.-K., Inganäs, O., 2006. Organic tandem solar cells—Modelling and predictions. Sol. Energy Mater. Sol. Cells 90, 3491–3507.
Pervak, V., Tikhonravov, A.V., Trubetskov, M.K., Naumov, S., Krausz, F., Apolonski, A., 2007. 1.5-Octave chirped mirror for pulse compression down to sub-3 fs. Appl. Phys. B Lasers Opt. 87, 5–12.
Pervak, V., Trubetskov, M., Tikhonravov, A., 2009. Design consideration for high damage threshold UV-Vis-IR mirrors. In: Exarhos, G.J., Gruzdev, V.E., Ristau, D., Soileau, M.J., Stolz, C.J. (Eds.), Laser-Induced Damage in Optical Materials.Bellingham (WA), Proc SPIE—The International Society for Optical Engineering. 7504, 75040A1–10.
Pervak, V., Trubetskov, M.K., Tikhonravov, A.V., 2011. Robust synthesis of dispersive mirrors. Opt. Express 19, 2371–2380.
Pettersson, L.A.A., Roman, L.S., Inganas, O., 1999. Modeling photocurrent action spectra of photovoltaic devices based on organic thin films. J. Appl. Phys. 86, 487–496.
Piegari, A., Sytchkova, M., 2016. Phase distortion and thickness variation in the design of optical coatings. In: International Conference on Space Optics, Biarritz, France, 18–21 October. 2016.
Pinard, L., Michel, C., Sassolas, B., Balzarini, L., Degallaix, J., Dolique, V., Flaminio, R., Forest, D., Granata, M., Lagrange, B., Straniero, N., Teillon, J., Cagnoli, G., 2017. Mirrors used in the LIGO interferometers for first detection of gravitational waves. Appl. Opt. 56, C11–C15.
Poitras, D., 2005. Dealing with sensitivity variations during the manufacture of optical coatings. In: SVC, Society of Vacuum Coaters—48th Annual Technical Conference, Denver, CO, United States, 23–28 April. 2005, pp. 354–358.
Poitras, D., Larouche, S., Martinu, L., 2002. Design and plasma deposition of dispersion-corrected multiband rugate filters. Appl. Opt. 41, 5249–5255.
Poitras, D., Li, L., Jacobson, M., Cooksey, C., 2017. Manufacturing problem contest [invited]. Appl. Opt. 56, C1–C10.
Pond, J., Kawano, M., 2010. Virtual prototyping and optimization of novel solar cell designs. In: Schriemer, H.P., Kleiman, R.N. (Eds.), Photonics North 2010.Bellingham (WA), Proc SPIE—The International Society for Optical Engineering. 7750, 775028-1–6.
Poxson, D.J., Schubert, M.F., Mont, F.W., Schubert, E.F., Kim, J.K., 2009. Broadband omnidirectional antireflection coatings optimized by genetic algorithm. Opt. Lett. 34, 728–730.
Rabinovitch, K., Toker, G., 1994. Genetic algorithm and thin-film design. In: Proc SPIE 2262, pp. 163–174.

Raman, A., Yu, Z., Fan, S., 2011. Dielectric nanostructures for broadband light trapping in organic solar cells. Opt. Express 19, 19015–19026.

Razskazovskaya, O., Hassan, M.T., Luu, T.T., Goulielmakis, E., Pervak, V., 2016. Efficient broadband highly dispersive HfO_2/SiO_2 multilayer mirror for pulse compression in near ultraviolet. Opt. Express 24, 13628–13633.

Reed, M., Benson, T.M., Kendall, P.C., Sewell, P., 1996. Antireflection-coated angled facet design. IEE Proc. Optoelectron. 143, 214–220.

Rife, J.C., Hunter, W.R., Barbee Jr., T.W., Cruddace, R.G., 1989. Multilayer-coated blazed grating performance in the soft x-ray region. Appl. Opt. 28, 2984–2986.

Rigneault, I., Lemarchand, F., Sentenac, A., Giovannini, H., 1999. Strong extraction coefficient for sources located inside waveguide grating structures. J. Opt. A Pure Appl. Opt. 1, 507–511.

Rinnooy Kan, A., Timmer, G., 1987. Stochastic global optimization methods part I: clustering methods. Math. Program. 39, 27–56.

Schmid, J.H., Cheben, P., Janz, S., Lapointe, J., Post, E., Xu, D.X., 2007. Gradient-index antireflective subwavelength structures for planar waveguide facets. Opt. Lett. 32, 1794–1796.

Schoen, F., 1991. Stochastic techniques for global optimization: a survey of recent advances. J. Glob. Optim. 1, 207–228.

Schubert, M.F., Mont, F.W., Chhajed, S., Poxson, D.J., Kim, J.K., Schubert, E.F., 2008. Design of multilayer antireflection coatings made from co-sputtered and low-refractive-index materials by genetic algorithm. Opt. Express 16, 5290–5298.

Seassal, C., Park, Y., Fave, A., Drouard, E., Fourmond, E., Kaminski, A., Lemiti, M., Letartre, X., Viktorovitch, P., 2008. Photonic crystal assisted ultra-thin silicon photovoltaic solar cell. In: Gombert, A. (Ed.), Photonics for Solar Energy Systems II.Bellingham (WA), Proc SPIE—The International Society for Optical Engineering. 7002, 700207-1–8.

Sergeant, N.P., Agrawal, M., Peumansa, P., 2009. Design of selective coatings for solar thermal applications using subwavelength metal-dielectric structures. In: Tsai, B.K. (Ed.), Optical Modeling and Measurements for Solar Energy Systems III.Bellingham (WA), Proc SPIE—The International Society for Optical Engineering. 7410, 74100C1–10.

Shen, B., Wang, P., Menon, R., 2014. Optimization and analysis of 3D nanostructures for power-density enhancement in ultra-thin photovoltaics under oblique illumination. Opt. Express 22, A311–A319.

Shen, Y., Hsu, C.W., Yeng, Y.X., Joannopoulos, J.D., Soljačić, M., 2016. Broadband angular selectivity of light at the nanoscale: Progress, applications and outlook. Appl. Phys. Rev. 3. 011103. (also arXiv:1512.02761v1).

Shin, D., Tibuleac, S., Maldonado, T.A., Magnusson, R., 1998. Thin-film optical filters with diffractive elements and waveguides. Opt. Eng. 37, 2634–2646.

Shokooh-Saremi, M., Magnusson, R., 2007. Particle swarm optimization and its application to the design of diffraction grating filters. Opt. Lett. 32, 894–896.

Shokooh-Saremi, M., Magnusson, R., 2010a. Leaky-mode resonant reflectors with extreme bandwidths. Opt. Lett. 35, 1121–1123.

Shokooh-Saremi, M., Magnusson, R., 2010b. New nonpolarizing resonant beam splitters. IEEE Photonics J. 2, 670–676.

Shokooh-Saremi, M., Nourian, M., Mirsalehi, M.M., Keshmiri, S.H., 2004. Design of multilayer polarizing beam splitters using genetic algorithm. Opt. Commun. 233, 57–65.

Silva, A., Monticone, F., Castaldi, G., Galdi, V., Alù, A., Engheta, N., 2014. Performing mathematical operations with metamaterials. Science 343, 160–163.

Smith, H.A., Rebbert, M., Sternberg, O., 2003. Designer infrared filters using stacked metal lattices. Appl. Phys. Lett. 82, 3605–3607.
Snedaker, C.G., 1982. New numerical thin-film synthesis technique. J. Opt. Soc. Am. 72, 1732.
Sossi, L., 1974. A method for the synthesis of multilayer dielectric interference coatings. Eesti NSV Tead. Akad. Toim. Fuus. Mat. 23, 229–237.
Sossi, L., Kard, P., 1968. On the theory of the reflection and transmission of light by a thin inhomogeneous dielectric film. Eesti NSV Tead. Akad. Toim. Fuus. Mat. 17, 41–48.
Southwell, W.H., 1985. Coating design using very thin high- and low-index layers. Appl. Opt. 24, 457–460.
Southwell, W.H., 2013. Flip-flop coating synthesis revisited. Appl. Opt. 53, A179–185.
Strain, M., Sorel, M., 2010. Curved facet 90° turning mirrors for integrated optical technologies. Electron. Lett. 46, 360–362.
Sullivan, B.T., Dobrowolski, J.A., 1996. Implementation of a numerical needle method for thin-film design. Appl. Opt. 35, 5484–5492.
Sullivan, B.T., Clarke, G.A., Akiyama, T., Osborne, N., Ranger, M., Dobrowolski, J.A., Howe, L., Matsumoto, A., Song, Y., Kikuchi, K., 2000. High-rate automated deposition system for the manufacture of complex multilayer coatings. Appl. Opt. 39, 157–167.
Swart, P., Lacquet, B., 1990. A new algorithm for layer thickness and index step estimation in multi-layer hetero-epitaxial structures. J. Electron. Mater. 19, 1383–1394.
Tang, J.F., Zheng, Q., 1982. Automatic design of optical thin-film systems—Merit function and numerical optimization method. J. Opt. Soc. Am. 72, 1522–1528.
Thelen, A., 1989. Design of Optical Interference Coatings. McGraw Hill, New York.
Thelen, A., Langfeld, R., 1992. Coating design contest: Antireflection coating for lenses to be used with normal and infrared photographic film. In: Thin films for optical systems. Bellingham (WA), Proc SPIE—The International Society for Optical Engineering. 1782, pp. 552–601.
Thelen, A., Tikhonravov, A.V., Trubetskov, M.K., Tilsch, M., Brauneck, U., 2002. Topical meeting on optical interference coatings (OIC 2001): Design contest results. Appl. Opt. 41, 3022–3038.
Tikhonravov, A.V., 1993. Some theoretical aspects of thin-film optics and their applications. Appl. Opt. 32, 5417–5426.
Tikhonravov, A.V., Trubetskov, M.K., 2005. Computational manufacturing as a bridge between design and production. Appl. Opt. 44, 6877–6884.
Tikhonravov, A.V., Trubetskov, M.K., 2007. Modern status and prospects of the development of methods of designing multilayer optical coatings. J. Opt. Technol. 74, 845–850.
Tikhonravov, A.V., Trubetskov, M.K., 2012. Modern design tools and a new paradigm in optical coating design. Appl. Opt. 51, 7319–7332.
Tikhonravov, A.V., Trubetskov, M.K., Debell, G.W., 1996. Application of the needle optimization technique to the design of optical coatings. Appl. Opt. 35, 5493–5508.
Tikhonravov, A.V., Trubetskov, M.K., Amotchkina, T.V., Tikhonravov, A.A., 2003. Application of advanced optimization concepts to the design of high quality optical coatings. In: Righini, G.C., Consortini, A. (Eds.), 19th Congress of the International Commission for Optics: Optics for the Quality of Life, Bellingham (WA), Proc SPIE 4829, pp. 1061–1062.
Tikhonravov, A.V., Trubetskov, M.K., Amotchkina, T.V., Kokarev, M.A., Kaiser, N., Stenzel, O., Wilbrandt, S., Gäbler, D., 2006. New optimization algorithm for the synthesis of rugate optical coatings, Appl. Opt. 45, 1515–1524.

Tikhonravov, A.V., Trubetskov, M.K., Amotchkina, T.V., 2011. Investigation of the error self-compensation effect associated with broadband optical monitoring. Appl. Opt. 50, C111–C116.

Tikhonravov, A.V., Zhupanov, V.G., Fedoseev, V.N., Trubetskov, M.K., 2014. Design andproduction of antireflection coating for the 8–10 μm spectral region. Opt. Express 22, 32174–32179.

Tikhonravov, A.V., Kochikov, I.V., Yagola, A.G., 2017. Error self-compensation mechanism in the optical coating production with direct broad band monitoring. Opt. Express 25, 27225–27233.

Tilsch, M., Hendrix, K., 2008. Optical interference coatings design contest 2007: triple band-pass filter and nonpolarizing beam splitter. Appl. Opt. 47, C55–C69.

Tilsch, M., Hendrix, K., Verly, P.G., 2006. Optical interference coatings design contest 2004. Appl Opt-OT 45, 1544–1554.

Trubetskov, M.K., Tikhonravov, A.V., 2010. Robust synthesis of multilayer coatings. In: Optical Interference Coatings. Optical Society of America, OSA Technical Digest, TuA4–1:3.

Ulrich, R., 1967. Far-infrared properties of metallic mesh and its complementary structure. Infrared Phys. 7, 37–55.

Ulrich, R., 1968. Interference filters for the far infrared. Appl. Opt. 7, 1987–1996.

Urbas, A.M., et al. (34 authors), 2016. Roadmap on optical metamaterials. J. Opt. 18, 093005 (53pp).

Vassallo, C., 1985. Rigorous and approximate calculations of antireflection layer parameters for travelling-wave diode laser amplifiers. Electron. Lett. 21, 333–334.

Vassallo, C., 1988. Reflectivity of multidielectric coatings deposited on the end facet of a weakly guiding dielectric slab waveguide. J. Opt. Soc. Am. A 5, 1918–1928.

Vassallo, C., 1990. Theory and practical calculation of antireflection coatings on semiconductor laser diode optical amplifiers. IEE Proc Part J, Optoelectronics 137, 193–202.

Vassallo, C., 1997. Difficulty with vectorial BPM. Electron. Lett. 33, 61–62.

Vassallo, C., 1998. Finite-difference derivation of the reflectivity at output facets of dielectric waveguides with a highly diverging output beam. J. Opt. Soc. Am. A 15, 717–726.

Vedraine, S., Torchio, P., Duche, D., Flory, F., Simon, J.-J., Le Rouzo, J., Escoubas, L., 2011. Intrinsic absorption of plasmonic structures for organic solar cells. Sol. Energy Mater. Sol. Cells 95 (1), S57–S64.

Verly, P.G., Fourier transform technique with frequency filtering for antireflection coating design, 1994. Bellingham (WA), Proc SPIE 2253, pp. 161–167.

Verly, P.G., 1995. Fourier transform technique with frequency filtering for optical thin-film design. Appl. Opt. 34, 688–694.

Verly, P.G., 1996. Fourier transform technique with refinement in the frequency domain for the synthesis of optical thin films. Appl. Opt. 35, 5148–5154.

Verly, P.G., 1998a. Fourier transform approach for thin film characterization. In: Technical Digest, Topical Meeting on Optical Interference Coatings, Washington D.C., Optical Society of America, OSA Technical Digest Series TUB1 1–2.

Verly, P.G., 1998b. Optical coating synthesis by simultaneous refractive-index and thickness refinement of inhomogeneous films. Appl. Opt. 37, 7327–7333.

Verly, P.G., 2001. Modified needle method with simultaneous thickness and refractive-index refinement for the synthesis of inhomogeneous and multilayer optical thin films. Appl. Opt. 40, 5718–5725.

Verly, P.G., 2002. Design of a robust thin-film interference filter for erbium-doped fiber amplifier gain equalization. Appl Opt-OT 41, 3092–3096.
Verly, P.G., 2007. Fourier transform approach for thickness estimation of reflecting interference filters. 2. Generalized theory. Appl. Opt. 46, 76–83.
Verly, P.G., 2008. Hybrid approach for rugate filter design. Appl. Opt. 47, C172–C178.
Verly, P.G., 2009. Antireflection coating design by Fourier frequency filtering with frequency range adjustments. In: 52nd Annual Technical Conference Proceedings, Society of Vacuum Coaters, 35–39.
Verly, P.G., 2011. Optimum phase for rugate filter synthesis by Fourier transforms. Appl. Opt. 50, C124–C128.
Verly, P.G., Dobrowolski, J.A., 1990. Iterative correction process for optical thin film synthesis with the Fourier transform method. Appl. Opt. 29, 3672–3684.
Verly, P.G., Dobrowolski, J.A., Wild, W.J., Burton, R.L., 1989. Synthesis of high rejection filters with the Fourier transform method. Appl. Opt. 28, 2864–2875.
Verly, P.G., Dobrowolski, J.A., Willey, R.R., 1992. Fourier-transform method for the design of wideband antireflection coatings. Appl. Opt. 31, 3836–3846.
Verly, P.G., Tikhonravov, A.V., Poezd, A.D., 1993. Multiple solutions to the synthesis of graded index optical coatings. In: Dobrowolski, J.A., Verly, P.G. (Eds.), Inhomogeneous and Quasi-Inhomogeneous Coatings.Bellingham (WA), Proc SPIE—The International Society for Optical Engineering. 2046, pp. 9–16.
Verly, P.G., Tikhonravov, A.V., Trubetskov, M.K., 1997. Efficient refinement algorithm for the synthesis of inhomogeneous optical coatings. Appl. Opt. 36, 1487–1495.
Vincent, P., Nevière, M., 1979. Corrugated dielectric waveguides: a numerical study of the second-order stop bands. Appl. Phys. A Mater. Sci. Process. 20, 345–351.
Vukovic, A., Sewell, P., Benson, T.M., Kendall, P.C., 1998. Degraded facet performance caused by edge proximity. Electron. Lett. 34, 1939–1940.
Vukovic, A., Sewell, P., Benson, T.M., Kendall, P.C., 2000. Advances in facet design for buried lasers and amplifiers. IEEE J. Sel. Top. Quantum Electron. 6, 175–184.
Wang, Z., 2008. 'Non-periodic multilayer coatings in EUV, soft X-ray and X-ray range, In: Kaiser Norbert, Lequime Michel and Macleod, H. A. (Eds.), Advances in Optical Thin Films III, Bellingham (WA), Proc SPIE 7101, 710110-1–10.
Wang, S.S., Magnusson, R., 1993. Theory and applications of guided-mode resonance filters. Appl. Opt. 32, 2606–2613.
Wang, P., Menon, R., 2012. Simulation and optimization of 1-D periodic dielectric nanostructures for light-trapping. Opt. Express 20, 1849–1855.
Wang, P., Menon, R., 2013. Optimization of periodic nanostructures for enhanced light-trapping in ultra-thin photovoltaics. Opt. Express 21, 6274–6285.
Wang, S.S., Magnusson, R., Bagby, J.S., Moharam, M.G., 1990. Guided-mode resonances in planar dielectric-layer diffraction gratings. J. Opt. Soc. Am. A 7, 1470–1474.
Wiechmann, S., Heider, H.J., Müller, J., 2003. Analysis and design of integrated optical mirrors in planar waveguide technology. J. Lightwave Technol. 21, 1584.
Wiesmann, D., Hammel, U., Bäck, T., 1998. Robust Design of Multilayer Optical Coatings by means of evolutionary algorithms. IEEE Trans. Evol. Comput. 2, 162–167.
Wilbrandt, S., Stenzel, O., Kaiser, N., 2010. All-oxide broadband antireflection coatings by plasma ion assisted deposition: Design, simulation, manufacturing and re-optimization. Opt. Express 18, 19732–19742.
Wild, W.J., Buhay, H., 1986. Thin-film multilayer design optimization using a Monte Carlo approach. Opt. Lett. 11, 745–747.

Willey, R.R., 1996. Practical Design and Production of Optical Thin Films. 56M. Dekker, New York.
Xu, J., 2010. Optimization of construction of multiple one-dimensional photonic crystals to extend bandgap by genetic algorithm. J. Lightwave Technol. 28, 1114–1120.
Xu, J., Yevick, D., Gallant, M., 1995. Approximate methods for modal reflectivity at optical waveguide facets. J. Opt. Soc. Am. A 12, 725–728.
Yakovlev, V., Tempea, G., 2002. Optimization of chirped mirrors. Appl. Opt. 41, 6514–6520.
Yang, Y., Wang, W., Moitra, P., Kravchenko, I.I., Briggs, D.P., Valentine, J., 2014. Dielectric meta-reflectarray for broadband linear polarization conversion and optical vortex generation. Nano Lett. 14, 1394–1399.
Yang, X., Kozhevnikov, I.V., Huang, Q., Wang, H., Hand, M., Sawhney, K., Wang, Z., 2017a. Analytic theory of alternate multilayer gratings operating in single-order regime. Opt. Express 25, 15987–16001.
Yang, X., Wang, H., Hand, M., Sawhney, K., Kaulich, B., Kozhevnikov, I.V., Huang, Q., Wang, Z., 2017b. Design of a multilayer-based collimated plane- grating monochromator for tender X-ray range. J. Synchrotron Radiat. 24, 168–174.
You, H.L., Zhang, C.F., 2009. Influence of optical interference and carrier lifetime on the short circuit current density of organic bulk heterojunction solar cells. Chinese Phys. B 18, 349–356.
Zeng, L., Yi, Y., Hong, C., Liu, J., Feng, N., Duan, X., Kimerling, L.C., Alamariu, B.A., 2006. Efficiency enhancement in Si solar cells by textured photonic crystal back reflector. Appl. Phys. Lett. 89, 111111–111113.
Zhang, L., Mei, S., Huang, K., Qiu, C.-W., 2016. Advances in full control of electromagnetic waves with metasurfaces. Adv. Optical Mater 4, 818–833.
Zheng, Y.-F., Tang, J.-F., 1987. New automatic design technique for optical coatings. Appl. Opt. 26, 1546–1549.

FURTHER READING

Hendrix, K.D., Hulse, C.A., Ockenfuss, G.J., Sargent, R.B., 2008. Demonstration of narrowband notch and multi-notch filters. In: Kruschwitz, J.D.T., Ellison, M.J. (Eds.), Advances in Thin-Film Coatings for Optical Applications V.San Diego (CA), Proc SPIE—The International Society for Optical Engineering. 7067, 706702–14.
Razskazovskaya, O., Krausz, F., Pervak, V., 2017. Review article: multilayer coatings for femto- and attosecond technology. Optica 4, 129–138.
The LIGO Scientific Collaboration, 2015. Advanced LIGO. Classical Quantum Gravity. 32. 74001 (41pp).

CHAPTER

Optical monitoring strategies for optical coating manufacturing

3

Alexander V. Tikhonravov*, Michael K. Trubetskov†, Tatiana V. Amotchkina‡

Moscow State University, Moscow, Russia Max-Planck Institute of Quantum Optics, Garching bei München, Germany† Ludwig-Maximilians-Universität München, Garching, Germany‡*

3.1 INTRODUCTION

The amazing progress achieved in theoretical design of optical coatings has made a reliable monitoring of thin film multilayer deposition necessary as a key element in optical coating design-production chains. The introduction of new energetic and highly stable deposition processes allows, in some application areas, monitoring of thin film thicknesses by time (Pervak et al., 2007). Quartz crystal monitoring of thin film coating production is also widely employed in the case of various deposition processes (Macleod, 2001). Nevertheless, the interest in optical monitoring strategies has only been increased with new developments in deposition technologies. This is obviously connected to the fact that such strategies monitor optical thicknesses of coating layers and not their physical thicknesses. Macleod (1981) states that this had always been considered as a strong argument in support of optical monitoring strategies. Indeed, an attentive study of the basics of thin film theory shows that only thin film optical thicknesses are physically sensible and are entirely responsible for the optical properties of a dielectric coating (Furman and Tikhonravov, 1992).

Optical monitoring of thin film coating production has almost as long a history as thin film optics itself. Macleod (2001, p. 500) mentions an early article devoted to this subject (Banning, 1947) where a table allowing the monitoring of film optical thickness in quarter-wave units by a color of reflected light was presented. Practically all early works on optical monitoring were connected to the production of multilayers with quarter-wave optical thicknesses of their layers. For such multilayers, reflectance/transmittance is monitored at a central wavelength, which is four times quarter-wave optical thickness. A monitoring signal reaches its maxima or minima exactly at an instant when a new quarter-wave portion of layer optical thickness is deposited. Monitoring of reflectance/transmittance extrema in early days of thin film optics was done by a vacuum plant operator and a 5% accuracy of layer thickness monitoring was typical for a trained operator (Macleod, 2001, p. 503).

Optical Thin Films and Coatings. https://doi.org/10.1016/B978-0-08-102073-9.00003-5
Copyright © 2018 Elsevier Ltd. All rights reserved.

Reflectance/transmittance extrema are often referred to as turning points of monitoring signal and the optical monitoring technique in which a layer deposition is terminated at an extremum of monitoring signal is usually called turning value monitoring (Macleod, 2001) or turning point monitoring (Baumeister, 2004).

A great advantage of this technique is the existence of a strong error self-compensation effect associated with direct optical monitoring of narrow band pass filters at their central wavelengths (Bousquet et al., 1972; Macleod, 1972). This effect was discovered both empirically and by means of computer simulations. Macleod (1972) wrote that "The results of the first computer runs were very surprising. Turning value monitoring gave the enormous thickness errors which were expected, but the computed performance of the filters was found still to be satisfactory." A physical explanation for the error self-compensation effect was provided only three decades later when the interest in turning point monitoring was revived in connection with a boom in production of filters for wavelength division multiplexing (WDM) applications (Tikhonravov and Trubetskov, 2002).

Turning point optical monitoring is useful for the production of multilayers with quarter-wave layer optical thicknesses but it has no obvious and physically sensible advantage in the case of multilayers with nonquarter-wave optical thicknesses. For such multilayers, the so-called level monitoring is often used (Macleod, 1981; Zhao, 1985). When level monitoring is applied, the layer deposition is terminated if reflectance/transmittance at a specially chosen monitoring wavelength reaches a certain theoretically predicted level, which is called termination level. There is a great variety of monochromatic monitoring (MM) strategies exploring level monitoring. These strategies may employ direct monitoring of one of the samples produced in a vacuum chamber or may use separate monitoring chips for indirect monitoring of a coating production. They may differ in specifications of sequences of monitoring wavelengths for various layers of a coating and they may explore corrections of termination levels in a course of coating production. The most promising trends in current developments of MM strategies are considered in this chapter.

Currently broadband optical monitoring attracts the attention of optical coating engineers. The first broadband monitoring (BBM) systems were used for optical coating production in the late 1970s (Vidal et al., 1978, 1979; Vidal and Pelletier, 1979). In these early works, considerable efforts were applied to overcome problems connected with insufficient performances of computers and spectrophotometric instrumentation of those days. Tremendous progress in modern computers performance and the development of photodiode arrays and CCD (charge-coupled device) detectors opened new horizons for applications of BBM systems. An attractive feature of broadband optical monitoring is its much lower sensitivity to random errors in measurement data as compared to monochromatic optical monitoring (Tikhonravov et al., 2006a). Several authors also supposed that some sort of error self-compensation effect is inherent in broadband optical monitoring (Vidal et al., 1978; Macleod, 1981) and indeed the existence of this effect was theoretically demonstrated (Tikhonravov et al., 2011). One of the most recent publications (Zhupanov et al., 2017) demonstrates that broadband optical monitoring may provide a very strong error self-compensation effect.

The most part of modern broadband optical monitoring devices are intended for direct monitoring of one of the samples produced in a vacuum chamber (Ristau et al., 2006, 2008; Stenzel et al., 2008). Along with many attractive features, direct optical monitoring may also have a serious disadvantage connected with the cumulative effect of thickness errors that reduces an accuracy of layer thickness monitoring when the number of deposited layers becomes big enough (Macleod, 2001, p. 509). To prevent the accumulation of errors with the growing number of deposited layers, indirect BBM systems with several monitoring chips can be used (Li and Yen, 1989; Sullivan and Dobrowolski, 1992; Zhupanov et al., 2009). Pro *et* contra of various broadband optical monitoring approaches are discussed in this chapter.

A choice of monitoring technique and selection of monitoring strategy for optical coating production is very much application-dependent. This was clearly demonstrated by Sullivan and Dobrowolski (1992, 1993). Nowadays there is much broader choice of optical monitoring instrumentation, optical monitoring approaches, and optical monitoring algorithms for processing online monitoring data than two decades ago. Knowing the advantages and disadvantages of different optical monitoring strategies is a key to choosing a strategy that is most suitable for a particular application.

3.2 CLASSIFICATION OF OPTICAL MONITORING STRATEGIES

It is evident from the introduction to this chapter that there are a great number of optical monitoring strategies. The classification of the main types of these strategies is useful for a better orientation in their variety (Macleod, 1981; Willey, 1989; Sullivan and Dobrowolski, 1992). A primary subdivision is MM and BBM strategies. It is then essential to distinguish between direct and indirect strategies. In the case of direct monitoring, reflectance/transmittance measurements are performed on at least one of the coatings to be produced while, in the case of indirect monitoring, layer thicknesses are monitored on one or several separate witness chips. As pointed out by Macleod (1981), the main advantage of direct monitoring strategies is that the deposition on exactly one of the production samples is monitored. Another advantage of the direct BBM is the error self-compensation effect. It was recently shown (Zöller et al., 2013) that the direct MM can also provide this effect. In this chapter, we pay special attention to the basic ideas and properties of direct MM and BBM strategies because these ideas and properties also form a basis for indirect optical monitoring strategies.

The classification of optical monitoring strategies is illustrated in Fig. 3.1. As discussed in the Introduction, direct MM strategies are subdivided into turning point optical monitoring and level monitoring. It was also proposed to divide level-monitoring strategies further into passive and active ones (Tikhonravov et al., 2006b). The term passive is applied to those strategies that are entirely specified prior to starting the coating deposition and in which neither the sequence of monitoring wavelengths nor the termination levels are changed in the course of the coating production. In contrast, active strategies can use information obtained during the coating

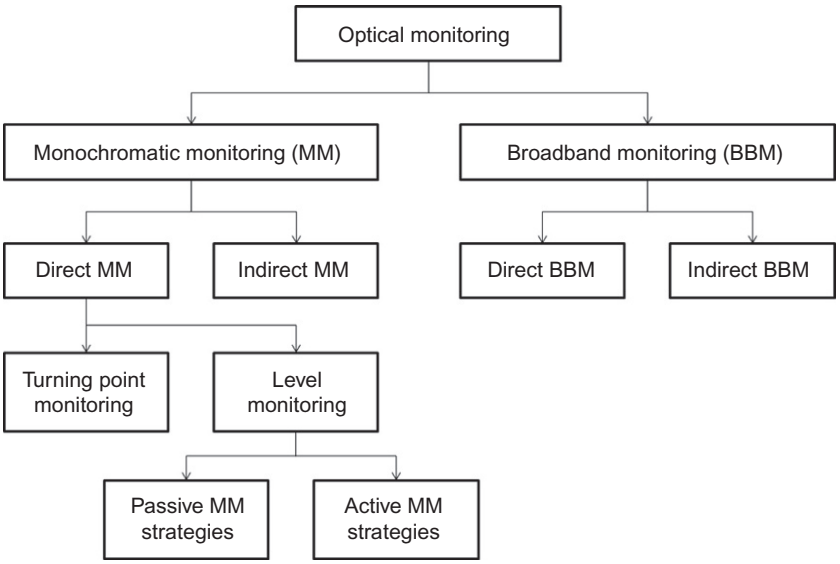


FIG. 3.1

Schematic illustrating main subdivisions of optical monitoring.

deposition to correct the course of a monitoring process. For example, reflectance/transmittance extrema passed during a layer deposition can be used for correcting reflectance/transmittance levels used for terminating layer depositions (Zhao, 1985; Laan, 1986). Monitoring strategies involving online reoptimizations of coating designs (Holm, 1978; Li and Yen, 1989; Sullivan and Dobrowolski, 1992) should also be considered as active strategies.

All monitoring strategies have their advantages and disadvantages. The main advantages of direct optical monitoring have been already mentioned but now it is necessary to discuss the main problem connected with this type of monitoring. Unfortunately, practically all direct monitoring strategies may give rise to a strong cumulative effect of thickness errors. This is connected to the fact that small errors in early layers affect monitoring of later layers (Macleod, 2001, p. 506). A detailed study of cumulative effect of thickness errors has been performed both for monochromatic (Tikhonravov et al., 2006b) and broadband (Tikhonravov et al., 2006a) optical monitoring and it was shown that total errors in layer thicknesses may be many times higher than direct errors in layer thicknesses made during the depositions of individual layers. With the total number of coating layers exceeding two to three dozen, the cumulative effect may lead to a total failure of the monitoring process.

The main reason for using indirect monitoring strategies is to prevent a rapid development of the cumulative effect of thickness errors due to limiting numbers of layers deposited on separate witness chips. At the same time, there is a principal objection towards indirect strategies connected with the fact that layers on witness

chips do not have exactly the same thicknesses as layers on produced coatings (Macleod, 2001, p. 507). All indirect monitoring strategies require accurate calibration of optical monitoring devices. The ratio of the layer thickness on witness chip to the layer thickness on produced sample is called calibration factor. Calibration factors are typically different for different thin film materials. They are also different for different deposition plants and different monitoring arrangements. For this reason, they should be accurately determined for each specific production environment.

A commonly used approach to determine calibration factors is a preliminary deposition of relatively thick single layers of all thin film materials that will be used for coating production. Optical characterization of single layers on witness chips and produced samples is then performed in order to determine thicknesses of these layers. It was shown in studies devoted to optical characterization that thin film optical thickness is always determined with much better accuracy than thin film physical thickness (Tikhonravov et al., 2003). Thus, it is better to specify calibration factors in terms of layer optical thicknesses rather than in terms of layer physical thicknesses. Such definition of calibration factors is also correspondent with the essence of optical monitoring.

It is necessary to add one more note on the determination of calibration factors. Unfortunately, these factors are not always stable and may vary from one deposition run to another and even more, they can vary during a single deposition run (Zhang et al., 2015). For this reason, it may be useful to perform a permanent refinement of calibration factors. This can be done with the help of reverse engineering software based on the post-production optical characterization of produced optical coatings (Oliver et al., 2001; Friedrich et al., 2010; Zhang et al., 2015).

3.3 TURNING POINT OPTICAL MONITORING AND ERROR SELF-COMPENSATION EFFECT

Schematic of a possible arrangement for turning point optical monitoring is presented in Fig. 3.2.

Consider monitoring of a simple Fabry–Perot filter having 19 layers and described by the design formula *HLHLHLHLH2LHLHLHLHLH*. Assume for calculations that refractive indices of high (H) and low (L) index layers are 2.065 and 1.465, respectively. The filter is supposed to be deposited on a glass substrate. Let the filter central wavelength be equal to 1550 nm. Fig. 3.3 shows how the filter transmittance at the central wavelength of 1550 nm is expected to vary versus the optical thickness of deposited filter in the absence of measurement and production errors.

When the first high index quarter-wave layer is deposited, the filter transmittance varies from its maximum to the minimum value, which is achieved exactly when a layer with quarter-wave optical thickness is deposited. The monitoring signal extremum values are referred to as turning points. For the next low index layer, the filter transmittance varies from the achieved minimum value to the maximum value,

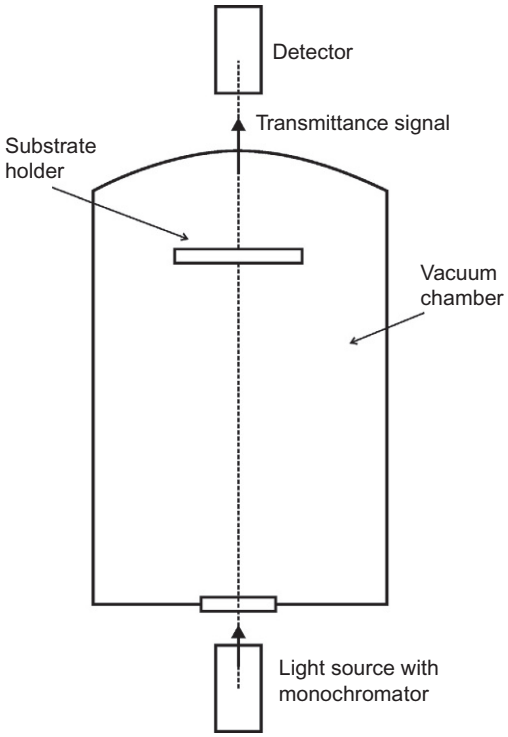


FIG. 3.2

Schematic illustration of a possible arrangement for turning point optical monitoring.

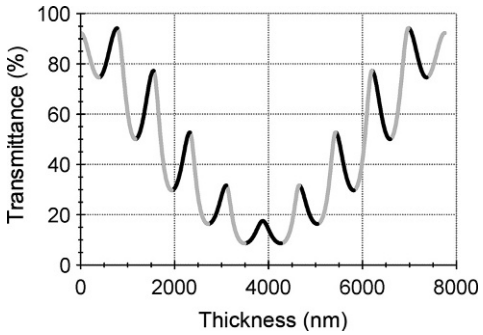


FIG. 3.3

Transmittance of the 19-layer Fabry–Perot filter vs optical thickness of this filter: filter central wavelength is 1550 nm.

which again corresponds to the instant when the next quarter-wave portion of optical thickness is deposited. The layer number 10 is the so-called spacer layer for which optical thickness is two-quarter waves. For this reason, the deposition of this layer should be terminated when the second turning point of the monitoring signal (transmittance minimum) is achieved.

The essence of turning point monitoring is terminating layer depositions at instants when monitoring signal extrema are achieved. Due to inevitable errors in measurement data it is rather difficult to determine instants corresponding to these extrema accurately. In order to raise the accuracy of turning point determination, a special processing of measurement data can be applied. Giacomo and Jacquinot (1952) were first to apply such processing on instrumentation level. They developed a system for measuring reflectance derivative versus wavelength instead of reflectance. At turning points, this derivative goes through zero and varies most rapidly, which helps one to determine termination instants more accurately.

At present, for raising the accuracy of turning point determination a computational processing of measurement data is usually applied. With all possible precautions for raising the accuracy of turning point determination, relative accuracy of layer thickness control could not be better than one or several percent. If thickness errors of such level were not correlated by the monitoring procedure, then it would be impossible to produce practically all narrow band pass filters for modern applications. Turning point monitoring has a special meaning for production of various filters for WDM applications. All these filters are multicavity resonance multilayer structures. For this reason, a physical mechanism of the error self-compensation effect is considered for the general case of a filter with multiple spacer layers or, which is the same, with multiple resonance cavities.

A general schematic of multicavity narrow band pass filter is presented in Fig. 3.4. This filter has q spacer layers marked as $S_1, \ldots, S_q$ and $q+1$ quarter-wave mirrors marked as $M_1, \ldots, M_{q+1}$. Optical thicknesses of spacer layers are integer times half wave optical thickness. Respective integers are called orders of spacer layers. All filters of the presented type are resonance structures with multiple resonance cavities formed by spacer layers and mirrors surrounding these layers (Thelen, 1989; Baumeister, 2004). It is known from the theory (Baumeister, 2004) that the filter spectral transmittance near the filter central wavelength is entirely specified by the number of filter cavities (spacer layers), reflectivities of filter mirrors, and phase properties of filter cavities. For the filter central wavelength, the full change of the phase for the wave making a full circle inside a spacer layer is integer times

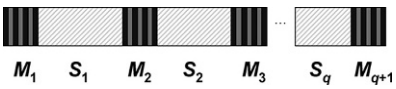


FIG. 3.4

A general schematic of multicavity narrow band pass filter.

2π. This is a condition of resonance inside a spacer layer. The filter spectral performance is destroyed as soon as the resonance condition is destroyed in at least one of the spacer layers.

The full change of the phase for the wave making a full circle inside a spacer layer is specified by the optical thickness of this spacer layer and phase shifts on reflection from surrounding mirrors. Even small errors in the optical thickness of a spacer lead to violating the resonance condition and as a sequence to the degradation of filter spectral performance. This fact was discovered computationally for Fabry–Perot filters many years ago (Lissberger, 1959).

Consider now errors in thicknesses of quarter-wave mirrors. It is known from the theory (Furman and Tikhonravov, 1992) that these errors have only a very small effect on the mirror reflectivity near the mirror central wavelength. At the same time, these errors change the phase shift on reflection significantly. This means that they also affect phase properties of filter cavities. A general conclusion is that thickness errors affect spectral performance of the filter through violating resonance conditions in filter cavities.

It was rigorously proved (Tikhonravov and Trubetskov, 2002) that terminating layer depositions at turning points adjusts errors in thicknesses of filter layers so that resonance conditions in filter cavities are fulfilled. Thus, from a physical point of view the error self-compensation effect is nothing else but maintaining phase properties of filter cavities. It is clear therefore that an accurate control of turning points for mirror layers following spacer layers is especially important. The highest effect on phase properties is caused by variations of thicknesses of layers that follow immediately after spacer layers.

To illustrate the error self-compensation effect, consider a four-cavity filter for WDM applications. This filter uses the same high index and low index materials as the Fabry–Perot filter discussed above. It has 122 layers and is described by the design formula $(HL)^7\ 6H(LH)^{14}\ L16H(LH)^{14}\ L16H(LH)^{14}\ L6H(LH)\ 7L0.385H1.283L$. Note that only the last two design layers are nonquarter-wave layers. They serve as an antireflection coating at the top of the WDM filter design.

The spectral transmittance of ideal filter with no errors in layer thicknesses is shown in Fig. 3.5A. Fig. 3.5B shows what happens with the filter transmittance when there is only one +3% relative error in the thickness of the layer number 12. Additional +0.5% error in the thickness of the first spacer layer (layer number 15) leads to a full degradation of the filter transmittance near 1550 nm (see Fig. 3.5C). Fig. 3.5D shows that both errors in layers number 12 and 15 can be entirely compensated by a proper variation of the thickness of layer number 16 that follows immediately after the spacer layer (thickness of this layer was reduced for 5.7%). Turning point optical monitoring performs such compensation automatically.

It is clear from a physical point of view that spectral performance of a narrow band pass filter is most sensitive to errors in thicknesses of spacer layers and nearby mirror layers. This fact is confirmed by the computational error analysis. Let us apply equal relative errors to all filter layers one by one. For each test, we calculate root mean square deviations of the transmittances of filters with thickness errors from the

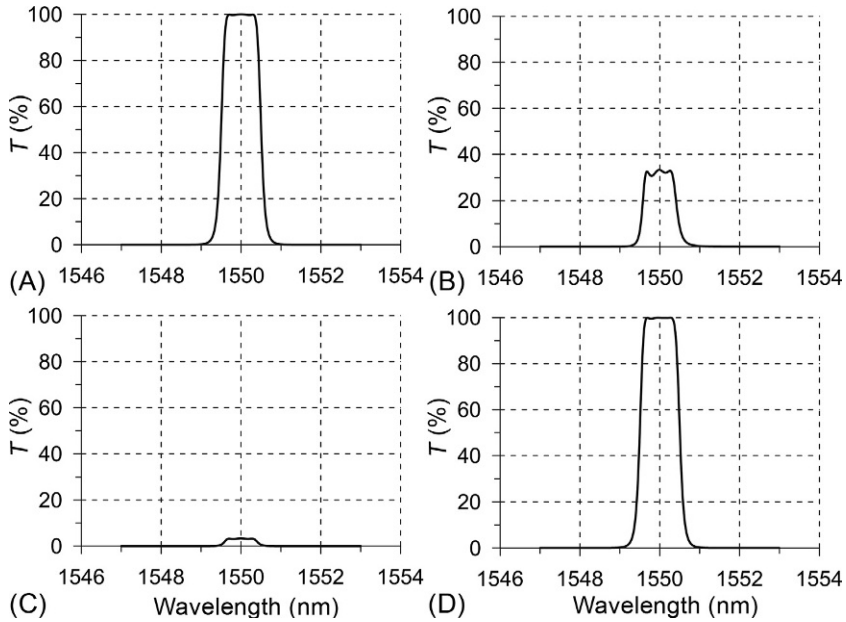


FIG. 3.5

Illustration of the error self-compensation effect: (A) transmittance of the ideal four-cavity WDM filter with no errors in layer thicknesses; (B) transmittance of the same filter with only one +3% relative error in the thickness of the layer number 12; (C) transmittance of the same filter with +3% relative error in the thickness of layer number 12 and +0.5% error in the thickness of the first spacer layer (layer number 15); (D) transmittance of the same filter when +3% error in the thickness of layer number 12 and +0.5% error in the thickness of the layer number 15 are compensated by −5.7% error in the thickness of the layer number 16.

transmittance of ideal filter with no errors. Denote these r.m.s. deviations as D_1, D_2, …, D_m, where m is the total number of filter layers. Let $D_{\max}$ be their maximum value. We assign 100% sensitivity to the layer with $D_{\max}$ deviation. All other layers are ranged with respect to this layer so that their sensitivities are taken equal to $D_j/D_{\max} \cdot 100\%$ where j is the layer number.

Fig. 3.6 presents results of the error sensitivity analysis for the 122-layer WDM filter considered above. One can see that indeed most sensitive to thickness errors are spacer layers (layers number 15, 45, 75, and 105) and nearby mirror layers. Fortunately, turning point optical monitoring provides a self-compensation of errors in thicknesses of these layers. It is also worth noting that errors in layers located far from spacer layers are not that critical. This note may be useful for planning monitoring strategy for multicavity WDM filters.

Fig. 3.7 presents transmittance of the discussed four-cavity WDM filter at its central wavelength for the first 32 layers of this filter. One can see that the variation of monitoring signal for the layer number 30 is very small. During the deposition of this

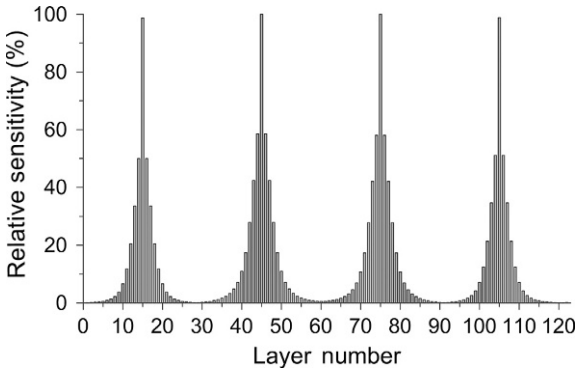


FIG. 3.6

Error sensitivity analysis for the 122-layer four-cavity WDM filter.

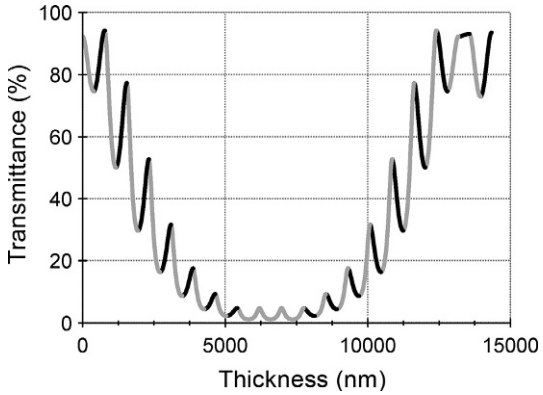


FIG. 3.7

Transmittance of the four-cavity WDM filter versus optical thickness of the first 32 layers of this filter.

layer the filter transmittance varies only for 0.8% from the minimum value of 92.3% to the maximum value of 93.1%. In the presence of measurement errors, it is very difficult to monitor thicknesses of such layers optically. It is however not necessary to deposit all filter layers using turning point optical monitoring. Instead of this, mixed monitoring strategy can be used.

Note that layer number 30 is located exactly between two filter spacer layers (see Fig. 3.6). Intermediate layers of this type are often referred to as coupling layers (Macleod, 2001, p. 518). It can be seen from Fig. 3.6 that a thickness error in this layer is not critical. Instead of using an optical monitor, one can control the deposition of coupling layers using time monitoring or quartz crystal monitoring. These

types of monitoring can also be used for the deposition of the last two layers of the considered filter. Recall that these are nonquarter-wave layers serving as an antireflection coating.

3.4 LEVEL MONITORING: PASSIVE AND ACTIVE MONOCHROMATIC MONITORING STRATEGIES

The discussing of level monitoring starts with the definition of passive monitoring strategies. Recall that this term is applied to those strategies that are entirely specified prior to starting the deposition process and neither sequences of monitoring wavelengths nor termination levels can be changed in the course of the coating production. A passive level-monitoring strategy is entirely specified by a monitoring spreadsheet where monitoring wavelengths and termination levels are indicated for all coating layers. Examples of monitoring spreadsheets corresponding to different monitoring strategies are provided below.

In this section, monitoring spreadsheets for two model design examples are considered. These examples are related to a hot mirror with high transmittance in visible and high reflectance in the infrared spectral band up to 1200 nm. Spectral transmittances of the designs are shown in Figs. 3.8A and 3.9A. Optical thicknesses of design layers are presented in Figs. 3.8B and 3.9B. Odd layers of both designs are high index layers with refractive indices 2.35 and even layers are low index layers with refractive indices 1.45. Refractive index of the substrates is 1.52. Discussion of modern design approaches is beyond the scope of this chapter but it is necessary to make one note in the contest of choosing monitoring strategies. In many cases, modern design techniques enable obtaining multiple solutions to a design problem (Tikhonravov et al., 2007a). Multiple solutions with excellent and almost equivalent spectral properties may have very different structural properties. This fact is illustrated by Figs. 3.8 and 3.9. The first design depicted in Fig. 3.8B has several thin

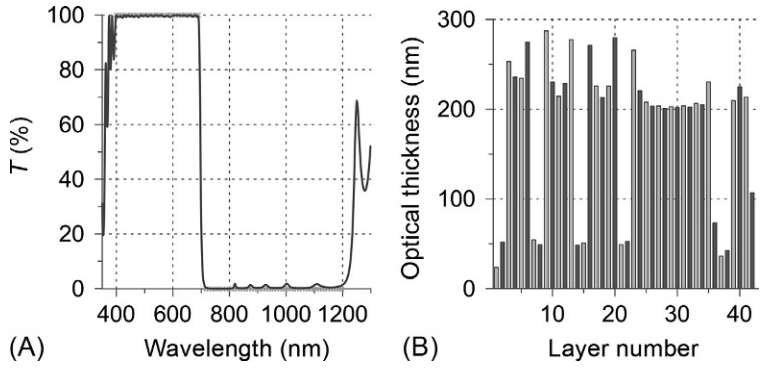


FIG. 3.8

Spectral transmittance (A) and layer optical thicknesses (B) of the 42-layer hot mirror design.

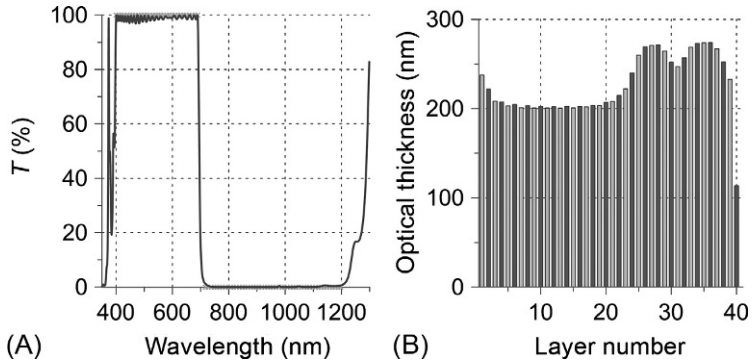


FIG. 3.9

Spectral transmittance (A) and layer optical thicknesses (B) of the 40-layer hot mirror design.

layers with optical thicknesses of about 20–50 nm while optical thicknesses of nearly all layers of the second design are higher than 200 nm and only the last layer has optical thickness of 113.6 nm (see Fig. 3.9B). It will be seen that the application of some monitoring strategies requires specific structural properties of a design. Thus, an optimal choice of monitoring strategy is always correlated with a choice of optical coating design.

Table 3.1 presents the first eight rows of the monitoring spreadsheet for the 42-layer hot mirror design. The monitoring signal is coating transmittance at normal incidence. The first column of the table shows layer numbers starting from the substrate, the second column indicates abbreviations for layer refractive indices (H = high and L = low indices), and the third column gives physical thicknesses of layers. Columns 4–6 can be used for specifications of indirect monitoring strategies and will be discussed in Section 3.7. Monitoring wavelengths for coating layers are indicated in the seventh column. In this particular case, we have the same monitoring wavelength of 700 nm for all coating layers. The eighth column presents theoretically predicted variations of monitoring signal during layer depositions. The first values in all rows of this column are transmittance levels at the starts of layer deposition. The last values are transmittance levels at the ends of layer depositions, that is, termination levels. In some rows, there are also bold values in between the above ones. These are minima and maxima transmittance levels that are expected to be achieved during layer depositions. A special meaning of these values will be discussed later in this section in connection with active monitoring strategies. A trace of the monitoring signal for the first eight layers corresponding to Table 3.1 is shown in Fig. 3.10.

Difficulties associated with optical monitoring of thin layers are clearly seen from Fig. 3.10. One can see that variations of the monitoring signal for the layer numbers 1, 2, 7 are less than 2%. In the presence of measurement errors, it is difficult to monitor such small variations reliably and hence high errors in thicknesses of these layers are possible. Thus, in general, designs with no thin layers are preferable for

Table 3.1 Monitoring spreadsheet for the 42-layer hot mirror design: rows corresponding to the first eight layers are shown

#	Material	Ph.th. (nm)	Chip	Layer number	Correction factor	Wavelength (nm)	Response (%)
1	H	10.03	1	1	1.0	700	91.8 90.3
2	L	35.66	1	2	1.0	700	90.3 88.6
3	H	107.7	1	3	1.0	700	88.6 **71.2** 78.6
4	L	162.5	1	4	1.0	700	78.6 **94.8** 85.3
5	H	99.77	1	5	1.0	700	85.3 **53.9** 75.3
6	L	189.3	1	6	1.0	700	75.3 **91.7** 70.3
7	H	23.12	1	7	1.0	700	70.3 **69.0** 69.7
8	L	33.74	1	8	1.0	700	69.7 73.9

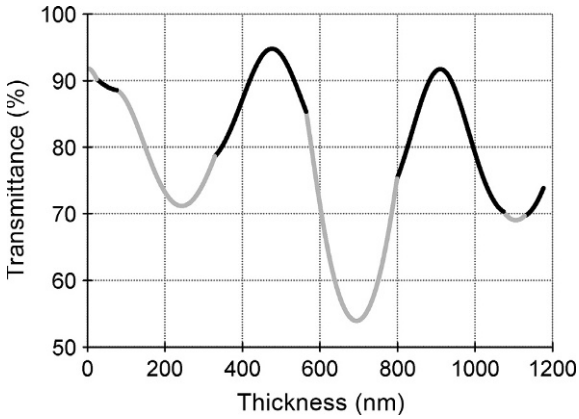


FIG. 3.10

Monitoring signal (normal incidence transmittance) for the first eight layers of the 42-layer hot mirror: monitoring wavelength is 700 nm.

applying optical monitoring strategies. For this reason, in the following part of this section, we proceed with the discussion of optical monitoring strategies using the 40-layer hot mirror design with no thin layers as an example.

The choice of a sequence of monitoring wavelengths for all coating layers is one of the key issues in specifying optical monitoring strategy. One of the rigorously defined monitoring strategies is based on the choice of the so-called most sensitive monitoring wavelengths (Holm, 1978; Sullivan and Dobrowolski, 1992). The most sensitive wavelength is the wavelength from a monitoring spectral band where the derivative of monitoring signal versus layer thickness achieves its maximum value at the end of layer deposition. A sequence of the most sensitive monitoring wavelengths can be easily calculated for a given coating design.

Table 3.2 presents the first eight rows of the monitoring spreadsheet corresponding to the strategy based on the choice of the most sensitive wavelengths for the 40-layer hot mirror design. Columns of the Table 3.2 are used as discussed above for Table 3.1. As above, the monitoring signal is the coating transmittance at normal incidence. The most sensitive monitoring wavelengths for coating layers were chosen in the monitoring spectral band from 400 to 900 nm. A trace of the monitoring signal for the first eight design layers is shown in Fig. 3.11. One can see that the monitoring signal is now discontinuous. All discontinuities correspond to layer boundaries and are attributed to changing the monitoring wavelength from layer to layer (see Table 3.2).

The discussed strategy is based on the assumption that choosing the most sensitive monitoring wavelength allows minimizing thickness errors caused by errors in measurement data. This is however true only to a certain extent. Let us perform a simplified consideration of thickness errors, which nevertheless allows revealing the main problem associated with direct optical monitoring. Consider only random

Table 3.2 Monitoring spreadsheet for the 40-layer hot mirror design: monitoring strategy based on the choice of the most sensitive wavelength, rows corresponding to the first eight layers are shown

#	Material	Ph.th. (nm)	Chip	Layer number	Correction factor	Wavelength (nm)	Response (%)
1	H	101.1	1	1	1.0	400	91.8 **65.7** **91.8** 81.8
2	L	152.9	1	2	1.0	700	71.5 **91.9** 82.5
3	H	88.65	1	3	1.0	652	80.4 **52.7** 74.6
4	L	142.9	1	4	1.0	713	52.4 **76.4** 64.5
5	H	86.38	1	5	1.0	666	71.3 **46.1** 69.6
6	L	141.0	1	6	1.0	698	45.3 **67.4** 52.5
7	H	85.55	1	7	1.0	672	65.5 **42.5** 66.9
8	L	140.1	1	8	1.0	688	47.1 **67.7** 50.2

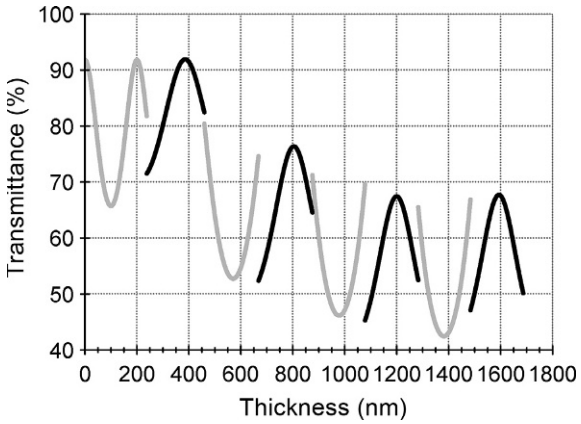


FIG. 3.11

Monitoring signal (normal incidence transmittance) for the first eight layers of the 40-layer hot mirror: monitoring strategy based on the choice of the most sensitive wavelength.

errors in transmittance measurement data and neglect all other factors that may cause errors in layer thicknesses. Suppose that at the end of the first layer deposition the measured transmittance error is $\delta T^{(1)}_{\text{meas}}$. This error will cause an error in the thickness of the first layer, which is (Tikhonravov et al., 2006b)

$$\delta d_1 = -\left[\frac{1}{\partial T^{(1)}/\partial d_1}\right]\delta T^{(1)}_{\text{meas}} \tag{3.1}$$

Here, $\partial T^{(1)}/\partial d_1$ is the derivative of the transmittance of the first coating layer versus its thickness at the end of a layer deposition.

In the case of random measurement errors, it is natural to suppose that they are distributed by the normal law. Denote σ_{meas} as a standard deviation of random errors in transmittance data. For the sake of simplicity assume that this value depends neither on the monitoring wavelength nor on the monitoring time. We shall refer to σ_{meas} as level of errors in measurement data. It follows from Eq. (3.1) that the expected thickness error is also a random error distributed by the normal law. Its mean value is zero and its standard deviation is

$$\sigma_1 = \left|\frac{1}{\partial T^{(1)}/\partial d_1}\right|\sigma_{\text{meas}} \tag{3.2}$$

The value σ_1 and analogous values below will be called expected levels of errors in layer thicknesses. One can see that the expected error in the thickness of the first layer is minimized when the monitoring wavelength for this layer is chosen so as to maximize the modulus of the transmittance derivative $\partial T^{(1)}/\partial d_1$. This is nothing else but the choice of the most sensitive monitoring wavelength.

The monitoring strategy based on the choice of the most sensitive monitoring wavelength would be the best level-monitoring strategy if there were no influence

of errors in preceding layers on the accuracy of subsequent layers monitoring. Unfortunately, in the case of direct optical monitoring, errors in all preceding layers affect monitoring of all subsequent layers. As an example, consider monitoring of the second layer. The expected error in the thickness of the second layer is expressed by the equation (Tikhonravov et al., 2006b):

$$\delta d_2 = -\left[\frac{1}{\partial T^{(2)}/\partial d_2}\right]\left[\delta T^{(2)}_{\text{meas}} + \frac{\partial T^{(2)}}{\partial d_1}\delta d_1\right] \tag{3.3}$$

Here, $\delta T^{(2)}_{\text{meas}}$ is the measurement error at the end of the second layer deposition, $\partial T^{(2)}/\partial d_1$ and $\partial T^{(2)}/\partial d_2$ are derivatives of the transmittance of the two-layer system vs thicknesses of the first and second layers that are also calculated at the end of the second layer deposition.

Eq. (3.3) is basically different from Eq. (3.1) because now an additional term in the second brackets representing the influence of the first layer error on the accuracy of monitoring of the second layer is present. Suppose that at the monitoring wavelength the modulus of the derivative $\partial T^{(2)}/\partial d_1$ is large. This means that there is a strong influence of errors in the first layer on the quality of monitoring of the second layer. In this situation, the choice of the most sensitive monitoring wavelength, i.e., the wavelength corresponding to the largest modulus of the derivative $\partial T^{(2)}/\partial d_2$ is not necessarily the best choice.

Eq. (3.3) represents what is called a cumulative effect of thickness errors. A detailed investigation of this effect was performed by Tikhonravov et al. (2006b). Results of this study enable estimating the cumulative effect of thickness errors for any direct MM strategy. Fig. 3.12 shows expected levels of errors in the thicknesses of layers of the 40-layer hot mirror design when the monitoring strategy based on the choice of the most sensitive monitoring wavelengths is applied.

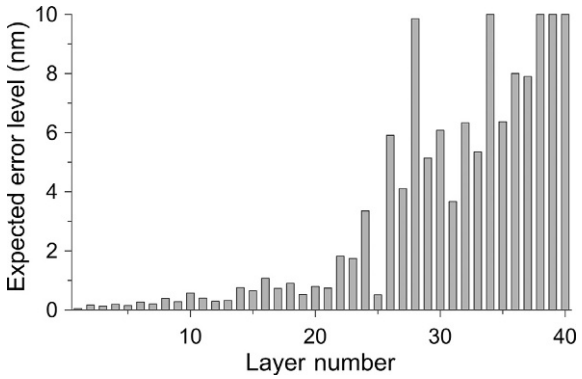


FIG. 3.12

Expected levels of errors in thickness of layers of the 40-layer hot mirror in the case of monitoring strategy based on the choice of the most sensitive monitoring wavelengths: the level of random errors in transmittance data is 0.05%.

The level of random errors in transmittance data for this figure is equal to 0.05%. One can observe a rapid development of the cumulative effect with the growing number of coating layers. Note that for the last layers the expected errors were truncated at the 10 nm level.

Starting from the second layer, instead of choosing the most sensitive monitoring wavelength one can try to choose for each coating layer a compromise wavelength that will minimize the cumulative effect of thickness errors. The algorithm for calculating such compromise wavelengths has been developed (Tikhonravov et al., 2006b) and the respective strategy is referred to as the strategy aimed at minimizing the cumulative effect.

Fig. 3.13 presents a monitoring signal for the first eight layers of the 40-layer hot mirror design when the monitoring strategy aimed at minimizing the cumulative effect is applied. The compromise monitoring wavelengths for this strategy have been chosen in the monitoring spectral band from 400 to 900 nm. One can see that starting from the second layer the monitoring signal in Fig. 3.13 differs from that in Fig. 3.11, which is connected with different choices of monitoring wavelengths.

Fig. 3.14 shows expected levels of errors in the layer thicknesses of the 40-layer hot mirror design when the monitoring strategy aimed at minimizing the cumulative effect of thickness errors is applied. The level of random errors in transmittance data for this figure is as before, 0.05%. One can see that expected thickness errors are much smaller than in the case of monitoring strategy based on the choice of the most sensitive wavelengths. Nevertheless, the development of the cumulative effect of thickness errors is still observed for the last coating layers.

Above only one factor causing errors in thicknesses of deposited coatings was considered. In fact there are a variety of factors that may cause production errors

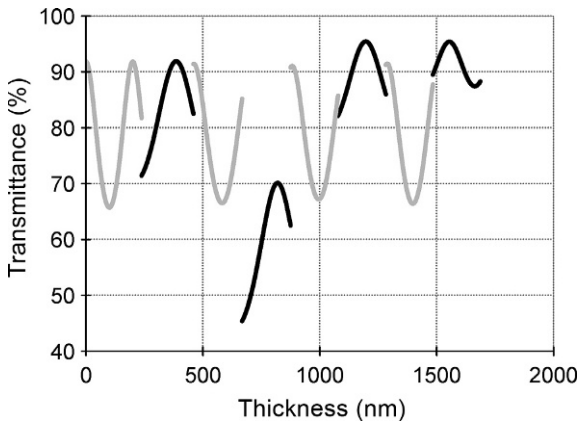


FIG. 3.13

Monitoring signal (normal incidence transmittance) for the first eight layers of the 40-layer hot mirror: monitoring strategy aimed at minimizing the cumulative effect of thickness errors.

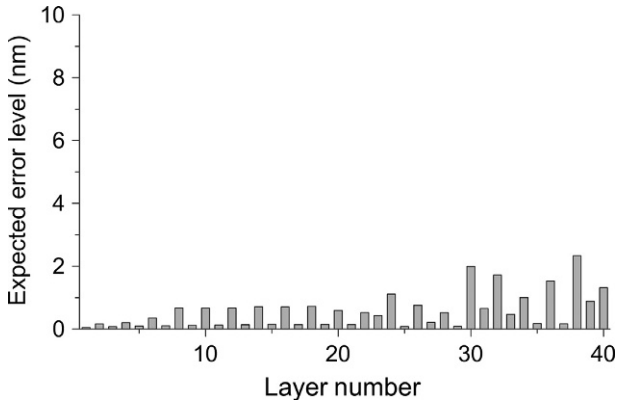


FIG. 3.14

Expected levels of errors in thickness of layers of the 40-layer hot mirror in the case of monitoring strategy aimed at minimizing the cumulative effect of thickness errors: the level of random errors in transmittance data is 0.05%.

(Van der Laan, 1986; Tikhonravov and Trubetskov, 2005). These are deviations of the refractive indices of thin film materials from layer to layer, bulk inhomogeneities of coating layers, thickness errors caused by inaccuracies in delays of closing shutters terminating layer depositions, etc. The cumulative effect of thickness errors may cause a rapid growth of thickness errors. As a result, a real monitoring signal may be quite different to that predicted by the monitoring spreadsheet. Additionally, calibration drifts of optical monitoring devices and fluctuations of a monitoring signal caused by fluctuations in light intensities due to various factors may also cause deviations in a monitoring signal. Active MM strategies may help to overcome these problems.

One of the first active monitoring strategies was discussed by Van der Laan (1986). It was proposed to use monitoring signal extrema registered during layer depositions for the online correction of termination levels. In fact, all active optical monitoring strategies explore this idea of using monitoring signal extrema for correcting termination levels.

Different active monitoring strategies differ in algorithms for correcting termination levels. A substantial progress in these algorithms has been achieved in recent years (Lee et al., 2005; Chun et al., 2006; Tikhonravov and Trubetskov, 2007; Tikhonravov et al., 2007b). Detailed descriptions of mathematical formulas of these algorithms are rather complicated and an interested reader is addressed to the original works. Here only a short description of main ideas of one of these algorithms is provided (Tikhonravov and Trubetskov, 2007). The main feature of this algorithm is that it allows one to eliminate entirely a cumulative effect of thickness errors. Under certain conditions a thickness of any new layer can be monitored independently of thickness errors made in preceding layers.

Consider monitoring of a coating layer with an optical thickness that is big enough for registering one or several monitoring signal extrema during a layer deposition. A schematic of monitoring signal for such layer is presented in Fig. 3.15. In this figure, monitoring signal extrema are denoted as $T_{e,\,1}$, …, $T_{e,\,3}$, T_{in}, and T_{fin} are monitoring signals at the start and at the end of layer deposition, h_{in} is a portion of layer optical thickness deposited at an instant when the first monitoring signal extremum is registered, and h_{fin} is a portion of layer optical thickness deposited between the instant corresponding to the last registered monitoring signal extremum and the end of layer deposition.

Due to errors in thicknesses of previously deposited layers, all monitoring signal values indicated in Fig. 3.15 may be quite different from the respective values indicated in the monitoring spreadsheet specified before the coating deposition. The goal is to correct the termination level T_{fin} so that an optical thickness of the considered layer can be controlled accurately and independently of thickness errors in preceding layers.

Portions of layer optical thickness deposited between two instants corresponding to two adjacent monitoring signal extrema are all equal to a quarter of monitoring wavelength. Therefore, the layer optical thickness h can be represented in the form

$$h = h_{\text{in}} + (m-1)\frac{\lambda}{4} + h_{\text{fin}} \tag{3.4}$$

where m is the number of monitoring signal extrema registered during the layer deposition.

Now it is possible to outline the main steps of the termination level correction algorithm. It is rigorously proved (Tikhonravov and Trubetskov, 2007) that knowing initial monitoring signal value T_{in} and the first monitoring signal extremum $T_{e,\,1}$

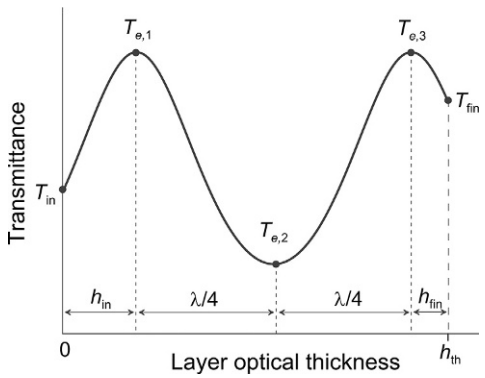


FIG. 3.15

Monitoring signal for a coating layer with several signal extrema passed during a layer deposition.

enable calculating the initial portion of layer optical thickness h_{in}. As soon as this value is known, the final portion of layer optical thickness h_{fin} providing the required layer optical thickness h is calculated from Eq. (3.4). Knowing this value and the value of the last registered monitoring signal extremum $T_{e,3}$ a new termination level T_{fin} can be calculated. The calculation of a new termination level can be performed online immediately after registering the last monitoring signal extremum.

It is seen from the above considerations that for the application of the described algorithm at least one monitoring signal extremum should be registered during the layer deposition. This requires that all coating layers have sufficient optical thicknesses. This demand relates to all active MM strategies. For this reason, optical coating designs with no thin layers may be preferable from the production point of view. One can see in Figs. 3.11 and 3.13 that the 40-layer hot mirror design has layers that are thick enough to achieve monitoring signal extrema during layer depositions.

3.5 MONITORING BY SWING VALUES

Monitoring by a signal swing is a specific form of the level monitoring that possesses features of active monitoring strategies. Denote as V a monitoring signal, for example, a transmittance monitoring signal during a layer deposition. Fig. 3.16 illustrates the definition of the signal swing. The equation for the swing value S is as follows:

$$S = \frac{V - V_{\text{last extr}}}{V_{\text{prev extr}} - V_{\text{last extr}}} \tag{3.5}$$

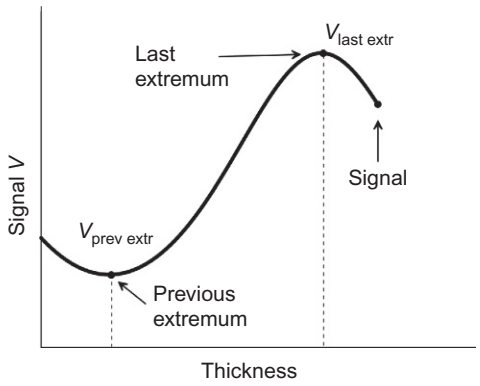


FIG. 3.16

To the definition of monitoring swing value.

Here, V_{lastextr} and V_{prevextr} are two last monitoring signal extrema registered during the layer deposition (see Fig. 3.16). Note that signal swing value is typically specified in percentage.

In monitoring by swing values, layer depositions are terminated when swing reaches specified final swing values. These values are calculated using the respective signal termination levels. An obvious advantage of this type of monitoring is that neither constant signal drifts nor constant in time calibration errors affect accuracy of monitoring by swing values. Indeed, suppose that there is some constant signal drift that influences all signal values in Eq. (3.5) equally. It is obvious that swing values are not affected:

$$S = \frac{(V+\beta) - (V_{\text{last extr}} + \beta)}{(V_{\text{prev extr}} + \beta) - (V_{\text{last extr}} + \beta)} = \frac{V - V_{\text{last extr}}}{V_{\text{prev extr}} - V_{\text{last extr}}} \tag{3.6}$$

The same is true in the case of constant in time calibration errors that cause multiplication of all signal swing values in Eq. (3.5) by the same factor:

$$S = \frac{\alpha V - \alpha V_{\text{last extr}}}{\alpha V_{\text{prev extr}} - \alpha V_{\text{last extr}}} = \frac{V - V_{\text{last extr}}}{V_{\text{prev extr}} - V_{\text{last extr}}} \tag{3.7}$$

One can see from Eqs. (3.6) and (3.7) that in the case of errors of the considered types signal termination levels are automatically corrected if terminations of layer depositions are accomplished according to the specified final swing values. It should be noted that the advantage of monitoring by swing values could be realized in the case of coatings with thick layers when at least one signal extremum is registered during layer deposition.

The concept of swing values is important for specification of all active MM strategies that explore corrections of termination levels based on registered extrema of the monitoring signal. Based on this concept, a special algorithm for automatic construction of MM strategies has been recently proposed (Trubetskov et al., 2015). Along with the demands for signal swing values additional important practical demands are also incorporated in this algorithm.

To outline the main ideas of the algorithm it is necessary to introduce some definitions. Primarily, the initial and final signal swing values for all coating layers are introduced:

$$\begin{aligned} S_{\text{in}} &= \begin{cases} \dfrac{V_{\max} - V_{\text{in}}}{A}\,100\% & \text{if the first extremum is maximum,} \\ \dfrac{V_{\text{in}} - V_{\min}}{A}\,100\% & \text{otherwise,} \end{cases} \\ S_{\text{fin}} &= \begin{cases} \dfrac{V_{\max} - V_{\text{fin}}}{A}\,100\% & \text{if the last extremum is maximum,} \\ \dfrac{V_{\text{fin}} - V_{\min}}{A}\,100\% & \text{otherwise.} \end{cases} \end{aligned} \tag{3.8}$$

Here, V_{in} is the monitoring signal at the start of layer deposition, V_{fin} is the termination level for the monitoring signal. If at least one signal extremum is achieved during the layer deposition then the terms "first extremum" and "last extremum" are related to the respective signal extrema ordered in the direction of the layer growth. In the case of a thin layer, it is necessary to consider respective virtual extrema that could be achieved if the thickness of this layer would be continuously increased. The amplitude of the monitoring signal A in the denominators of Eq. (3.8) ratios is defined as the difference between signal maximum and minimum values:

$$A = V_{max} - V_{min}. \tag{3.9}$$

Another important parameter is the difference between the termination level and the next signal extremum E_{next} that could be achieved if the layer thickness is further increased (this is a virtual extremum):

$$\Delta = |V_{fin} - E_{next}|. \tag{3.10}$$

The discussed algorithm may take into account demands for the initial and final swing values: $a_1 \le S_{in} \le a_2$, $b_1 \le S_{fin} \le b_2$ and demands for the two other parameters introduced by Eqs. (3.9) and (3.10): $A \ge \varepsilon$, $\Delta \ge \delta$. It also enables one to specify the number of allowed switches of monitoring wavelength during the coating deposition. This option is necessary if one wants to minimize the number of different monitoring wavelength used by the MM process. Generally, it may not be possible to meet all specified demands simultaneously for all coating layers. In this case, the algorithm chooses monitoring wavelengths so as to satisfy these demands as close as possible in the weighted mean sense (Trubetskov et al., 2015).

As an example of the application of the discussed algorithm the construction of monitoring spreadsheet for the 40-layer hot mirror with no thin layer is considered (see Fig. 3.9). The following requirements are introduced for the final swing value, the amplitude of monitoring signal, and the difference between the termination level and the next signal extremum: $10\% \le S_{fin} \le 90\%$, $A \ge 4\%$, $\Delta \ge 2\%$. The number of possible switches of monitoring wavelength is set equal to 4, i.e., there could be five different monitoring wavelengths during the hot mirror deposition. The first eight rows of the constructed monitoring spreadsheet are presented in Table 3.3 and the transmittance monitoring signal for all 40 hot mirror layers is shown in Fig. 3.17.

The monitoring wavelengths chosen by the algorithm are as follows: 645 nm for the layers 1–22, 405 nm for the layers 23–28, 680 nm for the layers 29–31, 405 nm for the layers 32–37, and 695 nm for the layers 38–40. The discontinuities of monitoring signal observed in Fig. 3.17 are connected with the switches of monitoring wavelength. The specified demands for the final swing value and other parameters are satisfied for almost all layers except for the last one. Only for the last layer the requirement for the final swing value is violated: the final swing is equal to 9.96%, which is slightly lower than the specified limit of 10%.

Table 3.3 Monitoring spreadsheet for the 40-layer hot mirror design: monitoring strategy aimed at optimizing of monitoring by swing values, rows corresponding to the first eight layers are shown

#	Material	Ph.th. (nm)	Chip	Layer number	Correction factor	Wavelength (nm)	Response (%)	Swing (%)
1	H	101.1	1	1	1.0	645	91.8 **65.7** 75.6	37.7
2	L	152.9	1	2	1.0	645	75.6 **93.5** 80.2	67.9
3	H	88.65	1	3	1.0	645	80.2 **54.2** 77.3	56.0
4	L	142.9	1	4	1.0	645	77.3 **92.5** 76.0	79.6
5	H	86.38	1	5	1.0	645	76.0 **56.8** 82.0	65.9
6	L	141.0	1	6	1.0	645	82.0 **94.4** 80.1	79.7
7	H	85.55	1	7	1.0	645	80.1 **60.9** 80.6	59.7
8	L	140.1	1	8	1.0	6645	80.6 **94.5** 82.4	68.7

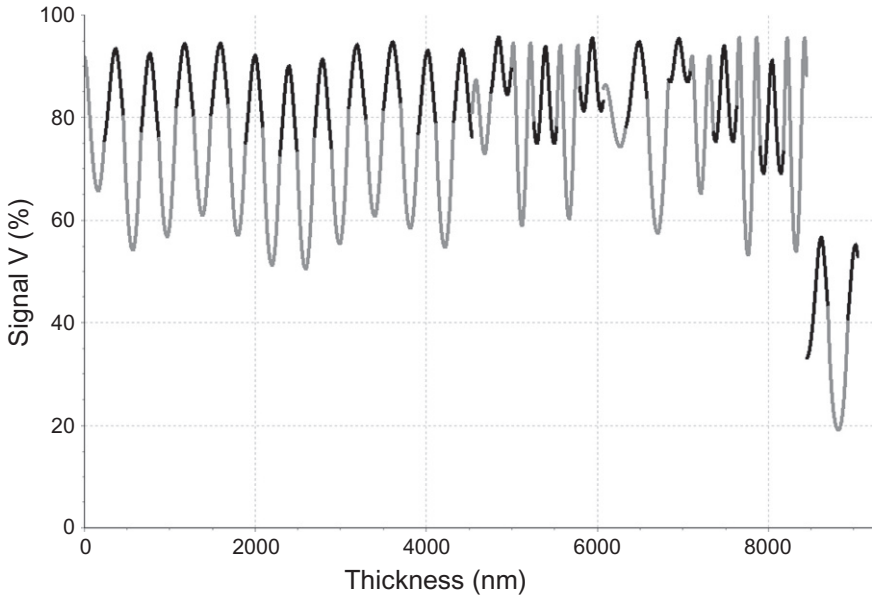


FIG. 3.17

Transmittance monitoring signal for the 40-layer hot mirror without thin layers. The monitoring signal corresponds to the monitoring spreadsheet constructed by the algorithm proposed by Trubetskov et al. (2015).

3.6 DIRECT BROADBAND OPTICAL MONITORING

An obvious trend of recent years is growing interest in direct broadband optical monitoring (BBM). Several research groups in different countries have been reporting a considerable progress in the development of BBM instrumentation and algorithmic tools for processing online monitoring data (Ristau et al., 2008; Friedrich et al., 2010). Evidently, all features of the recently proposed strategies cannot be discussed here. For specific details it is better to refer to original publications as well as to the Chapter 4 of this book where one of these strategies is discussed. This section is focused on basic principles, advantages, and disadvantages of direct BBM strategies.

One of the most attractive features of all BBM techniques is their low sensitivity to random errors in measurement data (Tikhonravov et al., 2002). Tikhonravov et al. (2006a) performed statistical analysis of the influence of errors of different types and, in particular, of random errors in measurement data on the accuracy of layer thickness monitoring. If only random errors in measurement data are considered then an expected level of errors in the thickness of the first layer is

$$\sigma(\beta_1) = \frac{\sigma_{\text{meas}}}{\left[\sum_{\{\lambda_k\}} \left(\partial T^{(1)}/\partial d_1\right)^2\right]^{1/2}} \tag{3.11}$$

Here, $\partial T^{(1)}/\partial d_1$ are the derivatives of the transmittance of the first coating layer versus its thickness calculated at the end of layer disposition for all wavelengths where BBM data are measured. The set of monitoring wavelengths is designated as $\{\lambda_k\}$ and the summation in Eq. (3.11) is performed over all these wavelengths. For simplicity in Eq. (3.11) it is assumed that the level of random errors in measurement data σ_{meas} is the same in the whole monitoring spectral band. As in the previous section it is supposed that random errors have a normal distribution.

Modern monitoring devices record measurement data at hundreds and even thousands of monitoring wavelengths. Thus, there is a great number of terms in the sum of the denominator in Eq. (3.11) and consequently this denominator is many times higher than the denominator in Eq. (3.2) estimating a level of thickness errors in the case of MM data. Analogous results for thickness errors originating from random errors in measurement data are obtained for all other coating layers (Tikhonravov et al., 2006a). Therefore, it is theoretically proved that random errors in measurement data are not as harmful for BBM as for monochromatic optical monitoring.

On the contrary with random errors, systematic errors in measurement data are extremely harmful for all optical monitoring strategies. Such errors are always associated with calibration drifts of optical monitoring devices. Permanent recalibrations of these devices were proved to be necessary for successful application of BBM (Sullivan and Dobrowolski, 1992). It is useful to perform recalibrations before recording every new set of broadband measurement data. For calibrating the spectrometer, it is typical to leave an empty position in the substrate holder and to record signals for this empty position and for an opaque position on the rotating calotte (Ristau et al., 2008).

Along with low sensitivity to random errors there is another attractive feature of direct BBM. Already in the first works devoted to this subject (Vidal et al. 1978, 1979; Vidal and Pelletier, 1979), it was noted that some sort of error self-compensation mechanism is inherent in BBM. An existence of this effect was supposed to be based on results of computer simulations of depositions of relatively simple nonquarter-wave coatings. A detailed investigation of the error self-compensation effect associated with direct broadband optical monitoring was performed recently (Tikhonravov et al., 2011). It was confirmed for coatings of different types (hot mirrors, cold mirrors, band pass filters, narrow band pass filters, multiline filters) that the effect is really present. It was also found that whether the effect is strong or not depends not only on the type of optical coating but also on the choice of specific design of coating of a given type. Thus, it may be useful to perform a preproduction investigation of multiple designs with close spectral properties for choosing one that is most suitable for production with BBM. This issue is discussed in more detail at the end of the section.

It has been recently demonstrated (Zhupanov et al., 2017) that for some types of coatings the effect of error self-compensation provided by BBM is very strong. In this work, the design and production of Brewster angle polarizers based on ZrO2/SiO2 pair of materials is considered. A challenge with the production of such polarizers is connected with the instability of refractive indices of ZrO2 films that are

crystallographically inhomogeneous and feature amorphous, monoclinic, and cubic phases with their growth. Variations of refractive indices of ZrO2 films may also cause high level of thickness errors. In one of the examples provided by Zhupanov et al. (2017) the cumulative effect of thickness errors with the growing number of deposited errors is clearly observed and relative thickness errors in some layers become really high (up to 16%). With thickness errors of this high level one should expect a total failure of polarizer properties. Nevertheless, the polarizer production was successful. The measured p- and s-transmittances of the discussed sample at 55.6 degree of light incidence and 1064 nm wavelength are equal to 98.2% and 0.6%, respectively.

For the discussed sample, normal incidence BBM was performed at 2036 spectral points in the wavelength region from 658 to 1172 nm. This region covers the polarizer's working wavelength of 1064 nm but the polarizer's working angle is quite different and its spectral characteristics are not presented in the measured spectra. Nevertheless, the monitoring procedure correlates thickness errors in such a way that a very strong error self-compensation effect is provided. To confirm this statement, a series of simulation experiments with noncorrelated thickness errors was performed by Zhupanov et al. (2017). Errors in layer thicknesses were specified using Gaussian distributions with zero mathematical expectations and standard deviations equal to modulus of correlated thickness errors observed in the course of deposition with BBM. In 1000 experiments with noncorrelated thickness errors it was found that spectral properties of the polarizer were entirely destroyed.

Obviously, the error self-compensation effect is possible only if thickness errors in coating layers are correlated by monitoring procedure. All direct optical monitoring procedures correlate thickness errors because errors in preceding layers affect the monitoring signal during the monitoring of subsequent layers. These changes of the monitoring signal lead to different thicknesses of subsequent layers preserving to some extent resulting spectral properties of the coating. At some moment, this mechanism stops to work further and the cumulative effect of thickness errors can be observed. A detailed investigation of this effect for the case of direct BBM was presented by Tikhonravov et al. (2006a). In this study, various error factors were considered and formulas allowing preproduction estimation of thickness errors caused by these factors were derived.

As an example, Fig. 3.18 presents expected levels of errors in thicknesses of the 40-layer hot mirror (see Section 3.4) in the case of broadband optical monitoring with transmittance data measured at 501 spectral points in the wavelength range from 400 to 900 nm. For calculating expected levels of thickness errors in Fig. 3.18 only random errors in transmittance data with 0.5% level were specified.

Expected levels of errors in the layer thicknesses of the 40-layer hot mirror design in the case of MM strategy based on the choice of the most sensitive monitoring wavelengths were presented in Fig. 3.12. The level of random errors in transmittance data for this figure was equal to 0.05%. The level of random errors in BBM data in the case of Fig. 3.18 is 10 times higher than this value. At the same time, levels of

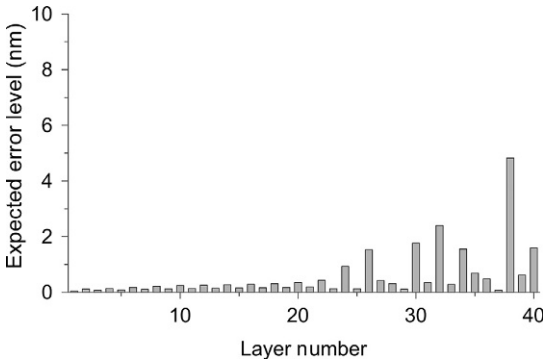


FIG. 3.18

Expected levels of errors in thicknesses of the 40-layer hot mirror in the case of broadband monitoring in the range 400–900 nm: the level of random measurement errors is 0.5%.

thickness errors in Fig. 3.18 are several times less than in Fig. 3.12. This clearly demonstrates the low sensitivity of BBM to random errors in measurement data.

The cumulative effect of thickness errors is clearly observed in Fig. 3.18. It is possible to estimate expected levels of thickness errors also for other factors causing production errors, such as systematic drifts of measurements data, direct thickness errors made in individual layers due to inaccuracies of shutter delays, instabilities of deposition rates, etc. (Tikhonravov et al., 2006a). The cumulative effect of thickness errors is observed in all situations. For the 40-layer hot mirror designs it becomes especially strong after depositing half of its layers.

In the case of direct BBM there are two main approaches to overcoming problems associated with the cumulative effect of thickness errors. The first one is including online reoptimization in optical monitoring strategies (Li and Yen, 1989; Sullivan and Dobrowolski, 1992; Tikhonravov and Trubetskov, 2004; Ristau et al., 2008; Friedrich et al., 2010; Schlichting et al., 2011). The second one is preproduction selection of the most feasible design from a set of possible theoretical solutions (Tikhonravov and Trubetskov, 2002; Friedrich et al., 2010, Amotchkina et al., 2012). Both approaches widely explore such powerful research tool as computational manufacturing of optical coatings (Tikhonravov and Trubetskov, 2005). In fact, computational manufacturing, or numerical simulation of deposition and monitoring processes, was used as a powerful tool for optimizing BBM strategies from the very early days of their development (Vidal et al., 1978).

3.7 INDIRECT OPTICAL MONITORING STRATEGIES

The main reason for using indirect optical monitoring strategies is reducing the number of layers monitored on a single witness chip and, as a consequence, preventing rapid development of cumulative effect of thickness errors caused by monitoring of a

large number of layers on a single substrate (Sullivan and Dobrowolski, 1992). Choosing an optimal indirect monitoring strategy is still an open question because a great variety of such strategies potentially exist. In the case of MM one can vary a number of witness chips being used, number of layers monitored on various chips, and monitoring wavelengths. As an example, only one possible indirect MM strategy is considered in this chapter. This strategy is specified for the 40-layer hot mirror discussed in the previous sections.

Table 3.4 presents the first eight rows of the monitoring spreadsheet corresponding to the indirect strategy using a new witness chip for monitoring of each new pair of high- and low-index layers. The number of the witness chip being used is indicated in the fourth column of the table. The fifth column shows layer numbers on particular chips. The sixth column presents calibration factors for high- and low-index layers. All other columns are used as described above for Tables 3.1 and 3.2.

As in Tables 3.1 and 3.2 the monitoring signal is coating transmittance at normal incidence. The correction factors indicated in the sixth column of Table 3.4 are used to recalculate thicknesses of design layers to the thicknesses of layers on witness chips and then to calculate traces of monitoring signals for all witness chips. These traces for the first four chips are shown in Fig. 3.19.

A strong argument against using indirect monitoring strategies is the necessity to know calibration factors accurately for recalculating thicknesses of coating layers (Macleod, 2001, p. 507). Zöller et al. (2011) have presented a very promising monitoring arrangement that allows one to combine advantages of direct and indirect optical monitoring. A witness chips changer was placed on the rotating substrate holder where produced samples were located. Due to this arrangement a preproduction calibration of witness chips was not required anymore. The changer may have up to four witness chips and can be changed after depositing of a part of coating layers in order to prevent a rapid development of the error accumulation effect. Successful application of this new device with the monochromatic monitor has been demonstrated and it has been indicated that the witness chip changer can be used in combination with broadband optical monitors as well (Zöller et al., 2011).

It is typical for indirect monitoring strategies to use witness chips for monitoring of subsequent groups of coating layers (Li and Yen, 1989; Zöller et al., 2011). This is, however, only one possible approach and other strategies may also be useful. The original indirect BBM strategy where different witness chips are used to monitor not groups of subsequent layers but layers chosen from a design in a special manner has been presented (Zhupanov et al., 2009). An application of this strategy was demonstrated for the 18-layer filter with layer optical thicknesses, as shown in Fig. 3.20. Odd and even layers of the filter are, respectively, titanium dioxide and silica dioxide layers. Theoretical transmittance of the filter is shown by solid curve in Fig. 3.21.

The described monitoring strategy is specified by establishing a correspondence between layers of deposited coating and layers of witness chips used

Table 3.4 Monitoring spreadsheet for the 40-layer hot mirror design: indirect monitoring strategy using a new witness chip for monitoring of each new pair of high and low index layers, rows corresponding to the first eight layers are shown

#	Material	Ph.th. (nm)	Chip	Layer number	Correction factor	Wavelength (nm)	Response (%)
1	H	101.1	1	1	1.05	600	91.8 **65.7** 83.4
2	L	152.9	1	2	1.02	600	83.4 **95.5** 82.1
3	H	88.65	2	1	1.05	600	91.8 **65.7** 75.0
4	L	142.9	2	2	1.02	600	75.0 **93.3** 79.1
5	H	86.38	3	1	1.05	600	91.8 **65.7** 73.6
6	L	141.0	3	2	1.02	600	73.6 **92.8** 79.0
7	H	85.55	4	1	1.05	600	91.8 **65.7** 73.1
8	L	140.1	4	2	1.02	600	73.1 **92.6** 79.1

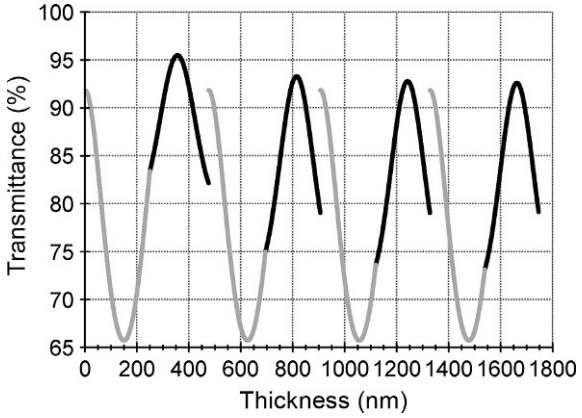


FIG. 3.19

Traces of monitoring signal (transmittance) for the first four witness chips used for indirect monitoring of the 40-layer hot mirror.

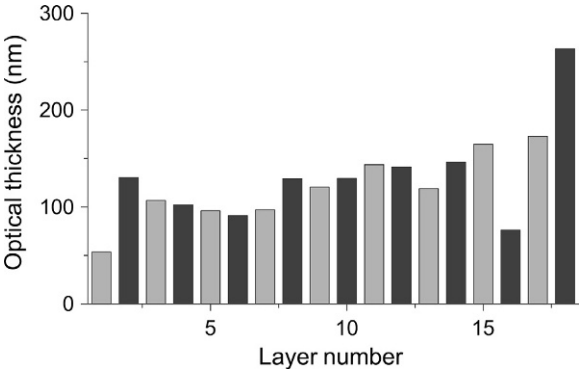


FIG. 3.20

Layer optical thicknesses of the 18-layer filter with TiO_2 odd layers (light bars) and SiO_2 even layers (dark bars).

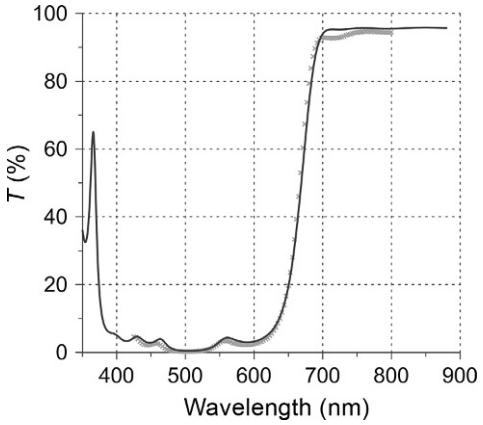


FIG. 3.21

Theoretical transmittance of the 18-layer filter (solid curve) and measured transmittance of the produced filter (crosses).

Table 3.5 Assignment of witness chips for monitoring of different filter layers

T-slide 1	T-slide 2	T-slide 3	T-slide 4
1, H	3, H	11, H	13, H
2, L	5, H	12, L	15, H
4, L	7, H	14, L	17, H
6, L	9, H	16, L	
8, L	18, L		
10, L			

for thickness monitoring. Witness chips are numbered according to an order in which they are brought to a measurement position for the first time. Table 3.5 presents the strategy used for depositing the 18-layer filter. The first witness chip is used for monitoring the first filter layer (high index layer) and then for monitoring five low index layers with numbers 2, 4, 6, 8, and 10. The second witness chip is used for monitoring four high index layers with numbers 3, 5, 7, 9, and so on. In the course of the filter production, the first two layers are monitored using the witness chip 1. For monitoring of the third layer, this chip is replaced by chip 2, but then the witness chip 1 is again placed to the measurement position and is used for monitoring the fourth filter layer. It is clearly seen from Table 3.5 how all subsequent layers are monitored.

Of course, it is possible to assign monitored layers to witness chips in a different way and thus to specify a different monitoring strategy. It was already mentioned that choosing of an optimal strategy is still an open question. Nevertheless, some useful recommendations for specifying strategies of the considered type have been provided (Zhupanov et al., 2009). It is recommended to monitor low index layers not on an uncoated witness chip but on a chip that has been already used for monitoring of a high index layer. This increases the contrast between a refractive index of the low index layer and the effective admittance of an underlying chip. Increasing this contrast facilitates accurate monitoring of thicknesses of low index layers. A deposition of layers of one material on a particular witness chip is also recommended because this also increases an accuracy of optical monitoring. A physical explanation of this fact has been provided by Zhupanov et al. (2009).

Fig. 3.22A–F shows theoretically predicted transmittances (solid curves) and actually measured transmittances of the witness chip 1 at the ends of depositions of filter layers with numbers 1, 2, 4, 6, 8, and 10. The transmittance of the produced 18-layer filter is shown in Fig. 3.21 by crosses.

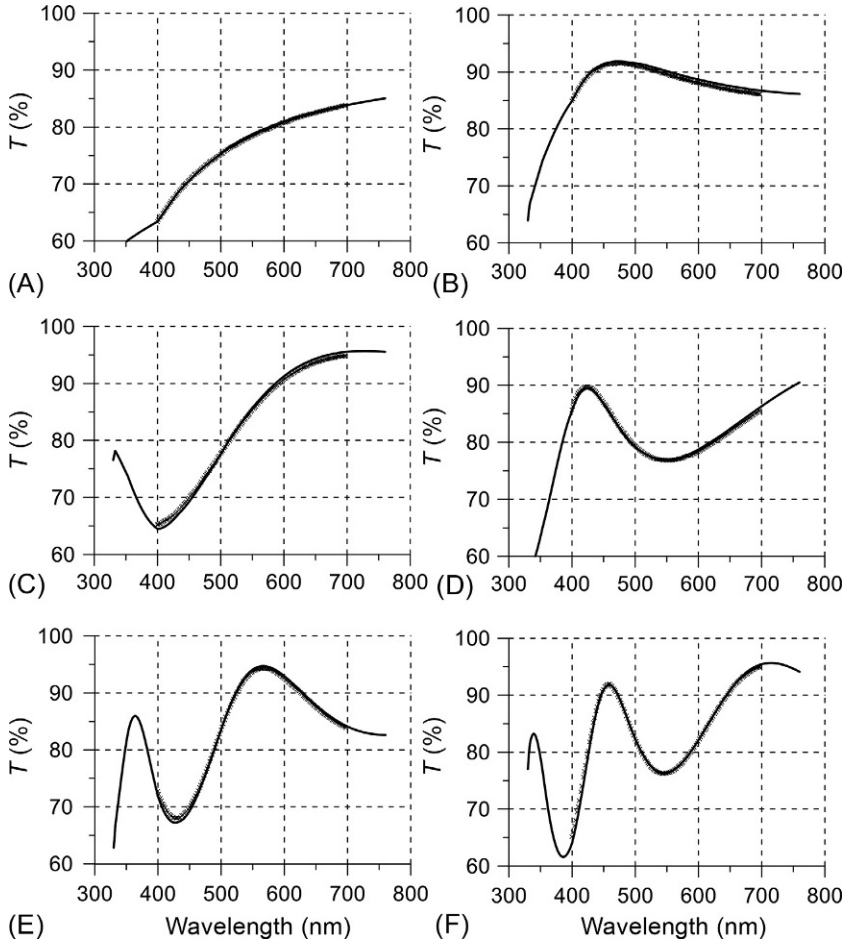


FIG. 3.22

Predicted transmittances (solid curves) and actually measured transmittances (crosses) of the witness chip used for monitoring layers 1, 2, 4, 6, 8, and 10.

3.8 CONCLUSION

Up to now a great variety of optical monitoring strategies have been proposed. Unfortunately, there is no single universal strategy providing an accurate thickness monitoring in all situations. The choice of monitoring approach is dependent on the production environment as well as on the type of optical coating that one wish to produce. The classification of monitoring strategies provided in this chapter may help one to make a proper choice. It is also important to know *pro et contra* of direct

and indirect monitoring approaches, as well as passive and active monitoring strategies. For some types of optical coatings, a choice of monitoring strategy should be correlated with a choice of optimization technique used for constructing an optical coating design. Multicavity narrow band pass filters with steep transmittance slopes are the most obvious examples of such coatings. If one wants to explore the powerful error self-compensation effect associated with turning point optical monitoring of such filters then it is necessary to employ a special optimization technique that allows one to design filters with quarter-wave and multiple quarter-wave optical thicknesses of its layers (Tikhonravov and Trubetskov, 2002).

In this chapter, all main types of optical monitoring strategies based on spectrophotometric measurement data have been discussed. Additionally, it should be mentioned that there are also monitoring approaches based on exploring ellipsometric measurement data. An overview of these approaches was recently provided by Dligatch (2010). The most impressive demonstration of potentialities of in situ ellipsometric monitoring is a successful deposition of a complex notch filter with 79 layers (Dligatch et al., 2004). Nevertheless, monitoring strategies based on in situ ellipsometric data have not been discussed in detail in this chapter for two tightly connected reasons. First, these strategies are used very rarely comparing to the spectrophotometric monitoring strategies. Second, a technical implementation of in situ ellipsometric measurements is more complicated than implementation of in situ photometric measurements because it is necessary to perform a system alignment on a rotating substrate and to overcome problems connected with the substrate wobble (Dligatch et al., 2004).

It has already been mentioned that all monitoring strategies have their advantages and disadvantages. Combining the advantages of different strategies has therefore a great potential for raising the accuracy of thickness monitoring. As an example of combined strategies, monitoring of WDM filters has been discussed. The most part of WDM filter layers can be monitored using turning point monitoring while the coupling layers and the outermost antireflection layers can be monitored using different approaches. In the future, one should expect much wider implementation of combined strategies, in particular, combining BBM approaches with MM approaches.

An essential advantage of in situ ellipsometric measurements is the ability to determine a film refractive index along with a film thickness (Chtanov et al., 2010; Rademacher et al., 2011). The refractive index of films may vary from layer to layer (Dligatch, 2010) and in situ determination of refractive indices may help to raise the accuracy of the optical monitoring. It is therefore important to develop spectrophotometric monitoring strategies and reliable algorithms for the data analysis that can provide the simultaneous in situ determination of layer refractive indices and layer thicknesses. In many application areas there is a great demand for the production of complex optical coatings that require high accuracy monitoring of layer parameters and there is no doubt that a great progress in optical monitoring techniques should be expected in the near future.

REFERENCES

Amotchkina, T., Schlichting, S., Ehlers, H., Trubetskov, M., Tikhonravov, A., Ristau, D., 2012. Computational manufacturing as a tool for the selection of the most manufacturable design. Appl. Opt. 51, 8677–8686.

Banning, M., 1947. Practical methods of making and using multilayer filters. J. Opt. Soc. Am. 37, 792–795.

Baumeister, P., 2004. Optical Coating Technology. SPIE, Washington.

Bousquet, P., Fornier, A., Kowalczyk, R., Pelletier, E., Roche, P., 1972. Optical filters: Monitoring process allowing the auto-correction of thickness errors. Thin Solid Films 13, 285–290.

Chtanov, A., Dligatch, S., Gross, M., 2010. Multi-wavelength laser ellipsometer for in situ monitoring of optical coatings. In: Optical Interference Coatings. OSA Technical Digest (Optical Society of America), paper TuC7.

Chun, C., Kwon Hwangbo, C., Sup Kim, J., 2006. Optical monitoring of nonquarterwave layers of dielectric multilayer filters using optical admittance. Opt. Express 14, 2473–2480.

Dligatch, S., Netterfield, R., Martin, B., 2004. Application of in-situ ellipsometry to the fabrication of multi-layer optical coatings with sub-nanometre accuracy. Thin Solid Films 455–456, 376–379.

Dligatch, S., 2010. In situ ellipsometric monitoring of complex multilayer designs. Chin. Opt. Lett. 8, 44–48.

Friedrich, K., Wilbrandt, S., Stenzel, O., Kaiser, N., Hoffman, K.H., 2010. Computational manufacturing of optical interference coatings: Method, simulation results, and comparison with experiment. Appl. Opt. 49, 3150–3162.

Furman, S., Tikhonravov, A., 1992. Basics of Optics of Multilayer Systems. Edition Frontieres, Gif-sur-Yvette.

Giacomo, P., Jacquinot, P., 1952. Localisation precise d'un maximum ou d'un minimum de transmission en fonction de la longeur d'onde. Application à la prparation des couches minces. J. Phys. Radium 13. 59A–64A.

Holm, C., 1978. Optical thin film production with continuous reoptimization of layer thicknesses. Appl. Opt. 18, 1978–1982.

Laan, C., 1986. Optical monitoring of nonquarterwave stacks. Appl. Opt. 25, 757–760.

Lee, C.-C., Wu, K., Kuo, C.-C., Chen, S.-H., 2005. Improvement of the optical coating process by cutting layers with sensitive monitoring wavelengths. Opt. Express 13, 4854–4861.

Lissberger, P., 1959. Properties of all-dielectric interference filters. I. A new method of calculation. J. Opt. Soc. Am. 49, 121–122.

Li, L., Yen, Y., 1989. Wideband monitoring and measuring system for optical coatings. Appl. Opt. 28, 2890–2894.

Macleod, A., 1972. Turning value monitoring of narrow-band all-dielectric thin-film optical filters. Optica Acta 19, 1–28.

Macleod, A., 1981. Monitoring of optical coatings. Appl. Opt. 20, 82–89.

Macleod, A., 2001. Thin-Film Optical Filters, third ed. Institute of Physics Publishing, Bristol and Philadelphia. Series in Optics and Optoelectronics.

Oliver, J., Tikhonravov, A., Trubetskov, M., Kochikov, I. and Smith, D. (2001), 'Real-time characterization and optimization of e-beam evaporated optical coatings', Optical Interference Coatings (OIC) 2001, OSA Technical Digest Series, ME8.

Pervak, V., Tikhonravov, A., Trubetskov, M., Pistner, J., Krausz, F., Apolonski, A., 2007. Band filters: 2-material technology versus rugate. Appl. Opt. 46, 1190–1193.

Rademacher, D., Vergöhl, M., Richter, U., 2011. In situ thickness determination of multilayered structures using single wavelength ellipsometry and reverse engineering. Appl. Opt. 50, C222–C227.

Ristau, D., Ehlers, H., Gross, T., Lappschies, M., 2006. Optical broadband monitoring of conventional and ion processes. Appl. Opt. 45, 1495–1501.

Ristau, D., Ehlers, H., Schlichting, S., Lappschies, M., 2008. State of art in deterministic production of optical thin films.Proceedings of SPIE7.101, 71010C-1–71010C-13.

Schlichting, S., Heinrich, K., Ehlers, H., Ristau, D., 2011. Online re-optimization as a powerful part of enhanced strategies in optical broadband monitoring. Proc. SPIE. 8168.81681E.

Stenzel, O., Wilbrandt, S., Fasold, D., Kaiser, N., 2008. A hybrid in situ monitoring strategy for optical coating deposition: Application to the preparation of chirped dielectric mirrors. J. Opt. A Pure Appl. Opt. 10, 1–8.

Sullivan, B., Dobrowolski, J., 1992. Deposition error compensation for optical multilayer coatings. I. Theoretical description. Appl. Opt. 31, 3821–3835.

Sullivan, B., Dobrowolski, J., 1993. Deposition error compensation for optical multilayer coatings. II. Experimental results—Sputtering system. Appl. Opt. 32, 2351–2360.

Thelen, A., 1989. Design of Optical Interference Coatings. McGraw-Hill, New York.

Tikhonravov, A., Trubetskov, M., 2002. Automated design and sensitivity analysis of wavelength-division multiplexing filters. Appl. Opt. 41, 3176–3182.

Tikhonravov, A., Trubetskov, M., 2004. On-line characterization and reoptimization of optical coatings. Proc. SPIE 5250, 406–413.

Tikhonravov, A., Trubetskov, M., 2005. Computational manufacturing as a bridge between design and production. Appl. Opt. 44, 6877–6884.

Tikhonravov, A., Trubetskov, M., 2007. Elimination of cumulative effect of thickness errors in monochromatic monitoring of optical coating production: theory. Appl. Opt. 46, 2084–2090.

Tikhonravov, A., Trubetskov, M., Kokarev, M., Amotchkina, T., Duparré, A., 2002. Effect of systematic errors in spectral photometric data on the accuracy of determination of optical parameters of dielectric thin films. Appl. Opt. 41, 2555–2560.

Tikhonravov, A., Trubetskov, M., DeBell, G., 2003. On the accuracy of optical thin film parameter determination based on spectrophotometric data. Proc. SPIE 5188, 190–199.

Tikhonravov, A., Trubetskov, M., Amotchkina, T., 2006a. Investigation of the effect of accumulation of thickness errors in optical coating production using broadband optical monitoring. Appl. Opt. 45, 7026–7034.

Tikhonravov, A., Trubetskov, M., Amotchkina, T., 2006b. Statistical approach to choosing a strategy of monochromatic monitoring of optical coating production. Appl. Opt. 45, 7863–7870.

Tikhonravov, A., Trubetskov, M., DeBell, G., 2007a. Optical coating design approaches based on the needle optimization technique. Appl. Opt. 46, 704–710.

Tikhonravov, A., Trubetskov, M., Amotchkina, T., 2007b. Elimination of cumulative effect of thickness errors in monochromatic monitoring of optical coating production: Theory. Appl. Opt. 46, 6936–6944.

Tikhonravov, A., Trubetskov, M., Amotchkina, T., 2011. Investigation of the error self-compensation effect associated with broadband optical monitoring. Appl. Opt. 50, C111–C116.

Trubetskov, M., Amotchkina, T., Tikhonravov, A., 2015. Automated construction of monochromatic monitoring strategies. Appl. Opt. 54, 1900–1909.
Vidal, B., Fornier, A., Pelletier, E., 1978. Optical monitoring of nonquarterwave multilayer filters. Appl. Opt. 17, 1038–1047.
Vidal, B., Pelletier, V., 1979. Nonquarterwave multilayer filters: Optical monitoring with a minicomputer allowing correction of thickness errors. Appl. Opt. 18, 3857–3862.
Vidal, B., Fornier, A., Pelletier, E., 1979. Wideband optical monitoring of nonquarterwave multilayer filters. Appl. Opt. 18, 3851–3856.
Willey, R., 1989. Optical thickness monitoring sensitivity improvement using graphical methods. Appl. Opt. 26, 729–737.
Zhang, J., Cao, C., Tikhonravov, A., Trubetskov, M., Gorokh, A., Cheng, X., Wang, Z., 2015. Advantages and challenges of optical coating production with indirect monochromatic monitoring. Appl. Opt. 54, 3433–3439.
Zhao, F., 1985. Monitoring of periodic multilayers by the level method. Appl. Opt. 24, 3339–3342.
Zhupanov, V., Klyuev, E., Alekseev, S., Kozlov, I., Trubetskov, M., Kokarev, M., Tikhonravov, A., 2009. Indirect broadband optical monitoring with multiple witness substrates. Appl. Opt. 48, 2315–2320.
Zhupanov, V., Kozlov, I., Fedoseev, V., Konotopov, P., Trubetskov, M., Tikhonravov, A., 2017. Production of Brewster angle thin film polarizers using a ZrO_2/SiO_2 pair of materials. Appl. Opt. 56, C30–C34.
Zöller, A., Hagedorn, H., Weinrich, W., Wirth, E., 2011. Testglass changer for direct optical monitoring. Proc. SPIE. 8168.81681J.
Zöller, A., Boos, M., Goetzelmann, R., Hagedorn, H., Romanov, B., Viet, M., 2013. Accuracy and error compensation with direct monochromatic monitoring. Optical Interference Coatings (OIC) 2013, OSA Technical Digest Series, WB5.

This page intentionally left blank

CHAPTER

Production strategies for high-precision optical coatings

4

Henrik Ehlers, Detlev Ristau
Laser Zentrum Hannover, Hannover, Germany

4.1 INTRODUCTION

Trends in modern photonics clearly indicate the need for optical components with ever increasing quality and demanding spectral transfer properties. In this context, laser technology can be considered as an important pacemaker with an enormous economic and innovation potential. Looking back just two decades into the past, most commercial laser systems contained a few discrete optical components with typical sizes in the centimeter range specified for a single wavelength or constricted spectral range. Nowadays, systems with orders of magnitude of higher performance are assembled to highest compactness with a large variety of special optical components individually tailored in their functioning and geometry to the requirements of the laser and its manufacturing process. This development can be considered as representative for many other fields in modern optics including communication technology, precise measurement methods, or consumer products. As a consequence, new challenges are also imposed on the production of optical coatings in respect to the quality, precision, and difficult specifications covering broader spectral ranges. Moreover, the market position of a modern coating factory will sensitively depend on the flexibility of the implemented production chain and coating processes allowing for the delivery of special coatings in small quantities within short times.

Before this general background, new production strategies have to be implemented in optical coating technology that allow for direct manufacturing in a linear chain. In contrast to conventional production concepts, which are often based on optimization cycles involving several deposition runs until the specified quality is reached, advanced approaches have to combine coating design and evaluation tools with stable and well controlled deposition processes in order to achieve the highest economic efficiency and shortest product development times. Following the line from the customer enquiry to the final product, the first step comprises the selection of materials, process type, and the conception of the coating design. In an innovative fabrication process, the design phase should be followed by an evaluation of the envisioned coating system to exclude problematic designs and to minimize the risk of

Optical Thin Films and Coatings. https://doi.org/10.1016/B978-0-08-102073-9.00004-7
Copyright © 2018 Elsevier Ltd. All rights reserved.

production failures. Apart from conventional evaluation techniques, which just perform an analysis in view of random variations of coating parameters, progressive software environments facilitate an immediate prediction of the coating result. Such virtual deposition programs are based on multiple simulations of the deposition process in combination with the actually applied control systems including optical parameters and major sources of errors observed in routine operation of the individual deposition systems. For the subsequent coating production, stable ion assisted or sputtering processes are suitable which are controlled by precise online monitoring devices. Besides single wavelength optical techniques, the analysis of the transmission or reflection spectra of the growing coating system measured directly on the product over a broad wavelength range within short-time intervals during the coating processes gains importance for achieving the highest precision in layer thickness. These devices, which are often known as optical Broad Band Monitors (BBMs), have become more and more established and allow also for a combination of the in situ analysis with data from additional sensors integrated in the deposition plant to improve the sensitivity and reliability of optical thickness control. Furthermore, they offer the possibility to implement error detection and correction tools which identify upcoming problems in the deposition sequence and even propose adapted design solutions to bring the running deposition process to a successful ending. With this outlined production strategy, optical coating production will move away from the former "black magic art" toward a deterministic manufacturing technique with high efficiency and flexibility. Moreover, by implementing these concepts, optical coating fabrication can be prepared for integration into the upcoming Industry 4.0 production chains with their essential needs for automation and data exchange.

Obviously, present optical coating production still has not reached this ideal situation, and further efforts are necessary in research and industry to master the ever increasing challenges of modern photonics. However, on the basis of advanced measurement devices, fast and inexpensive computer systems, as well as enormous progress in the development of stable ion deposition processes, the fundamental scheme for the deterministic production of optical coatings could be implemented during the last decade. In the following chapter, major aspects of this development are summarized and discussed. In the first part, deterministic production strategies will be outlined in detail, and selected coating processes will be considered in respect to the special requirements of novel thin film production schemes. The following part is dedicated to the technical basis including advanced online monitoring systems in combination with additional sensors and examples for a modern software environment comprising virtual deposition schemes, as well as online error detection and correction tools. The part will be concluded with the discussion of an extended experiment oriented to a demonstration of the advantages of the novel deterministic coating process. The third part highlights some new developments in the field of material mixtures and the related production of rugate filters. A brief review on the production of ternary oxides of reproducible stoichiometry with an adapted ion beam sputtering (IBS) process will be presented. After a glance at the advantages of material mixtures, the production and control of rugate filters will be discussed and illustrated

with a few examples. The chapter will be closed with a summary and outlook on the future prospects of deterministic coating production.

4.2 BASIC CONCEPT OF DETERMINISTIC PRODUCTION

The fundamental idea of deterministic production strategies has already been outlined in the introduction. For further illustration, Fig. 4.1 depicts the major steps of conventional production with iteration cycles in contrast to the novel deterministic approach. The additional ingredients for an implementation of the advanced concept are grouped in the lower half of Fig. 4.1 and incorporate a software environment for the simulation of deposition processes—virtual deposition process (VDP), an advanced monitoring device represented by a BBM system, and the corresponding process-tracing algorithm in conjunction with online error handling tools. In a typical functioning scheme of these units, the BBM system monitors the spectral characteristics of the growing layer system and formats data files for the process-tracing algorithm. The tracing system contains a routine which extracts the thickness and, in some cases, also information on dispersion of the growing single layer in time intervals according to the rotation time of the substrate holder. As an example for detecting the switching point of the current layer, an additional algorithm is integrated that compares the state of the layer to the expected spectral performance for the completed layer or parts of it. Furthermore, data transfer takes place between the process-tracing system and the error analysis as well as correction tools which are also linked to the system control unit of the deposition plant. In case of a deposition failure, the error correction system can automatically modify the sequence of the remaining layers in the process-tracing program to compensate for the detected deviations. A further expansion stage for an improvement in precision and reliability, which is not illustrated in Fig. 4.1, may comprise links of the process-tracing system to other process sensors like a crystal microbalance, mass spectrometer, or plasma monitoring system (Carstens et al., 2016). Combinations of different thickness monitors for enhanced precision in case of demanding multilayers are called hybrid monitoring approaches and will be discussed in more detail in Section 4.4.

Besides the units depicted in Fig. 4.1, the employed deposition processes are of key importance for a successful implementation of deterministic production strategies. Since the applied monitoring concepts are directly targeted on the spectral transfer characteristics of the coating system under the gas atmosphere at low pressure during the running deposition process, a change in the coating properties after venting would reduce the reproducibility. Therefore, conventional thermal evaporation processes, which often suffer from water adsorption effects typical for produced relatively porous coatings, are not well suited to BBM control methods. However, for some special applications, for example, involving fluoride materials for coatings in the deep ultraviolet/vacuum ultraviolet (DUV/VUV)-wavelength range, spectral monitoring offers advantages for the quality management and is occasionally employed in coating production without a link to process control (Ristau et al., 2006).

FIG. 4.1

Production cycle for coated optical components. In many cases, the production cycle has to be performed several times in order to reach the required specifications defined by the client. For the deterministic production of optical coatings, a linear production chain is realized without iteration cycles. The optimization of the coating system is accomplished during the deposition on the basis of adapted in situ monitoring strategies (units in the lower half). *M,*: magnetron sputtering; *LIDT*, laser-induced damage threshold.

In contrast to this, modern ion-assisted deposition (IAD) processes are qualified for manufacturing dense and stable coatings with only small variations in their optical properties. Nowadays, the corresponding commercial deposition plants for precision optics are often equipped with BBM devices directly integrated in the process control scheme, and they already have been routinely employed in industrial production for years (Sullivan, 2010). Sputter processes especially benefit from their intrinsic high process stability and a superior homogeneity of the refractive index in the depth of the layers. As a consequence, simple time control for depositing a defined layer thickness was sufficient for most sputter systems in the past. In conjunction with optical monitoring and particularly BBM devices, sputtering reaches a very high precision in coating thickness down to the level of a single atomic layer.

For example, recent research in magnetron sputtering demonstrated an outstanding reliability of these processes for the production of very complex coating systems including filters for fluorescence spectroscopy and space applications (Lappschies et al., 2011, 2016) or chirped mirrors for ultrashort pulse lasers (Razskazovskaya et al., 2017). In this connection, the enormous capability of magnetron sputtering to produce complex layer stacks of many hundred or even a few thousand single layers (Tilsch et al., 2010; Hendrix, 2017) also has to be mentioned. On the other hand, IBS is known for the production of coatings of excellent optical quality with lowest defect concentration (Pinard et al., 2017). Since the deposition rates are still relatively limited and only a few parameters have to be controlled, IBS concepts are very well suited to sophisticated BBM control techniques and reach an outstanding flexibility as well as precision for manufacturing of complex coating systems (Ristau and Groß, 2005; Ristau, 2010; Günster et al., 2011; Lyngnes et al., 2015). Furthermore, IBS processes could be also extended to the production of coatings with defined material mixtures (Lappschies et al., 2005; Mende et al., 2014) and to rugate filters (Starke and Ristau, 2011; Becker et al., 2014), featuring IBS as an interesting concept for future oriented deterministic coating production concepts. Nevertheless, optical coating processes are treated in the present book in all aspects, and therefore the following part will concentrate on details of the additional components necessary for deterministic production techniques. These will be described for exemplary systems which are being used in industrial production and research of optical thin film systems.

4.3 OPTICAL BROADBAND MONITORING

The technological evolution of monitoring the transfer characteristics of growing coatings during deposition can be traced back to the beginning of the 1970s. At that time, semiautomatic monochromators were coupled to the deposition plant for repetitively measuring the spectral characteristics of a test glass in the center of the substrate holder (Vidal et al., 1978, 1979). This pioneering work of the group at the former Ecole Nationale Superieure de Physique Marseille in France stimulated and was paralleled by several other research activities in Canada (Powell et al., 1986),

the United States (van Milligen and Macleod, 1985), Australia (Netterfield et al., 1988), and Italy (Emiliani et al., 1988) during the 1980s. Limited by the relatively low performance of computer systems available back then, only fractions or selected data points of the measured spectra could be evaluated. An extended analysis of the growing layer system was even more inconvenient, because the deposition processes had to be interrupted to allow for the needed calculation times. However, in the next decade, direct spectral monitoring found first applications in industrial production environments (Bauer and Nüssler, 1994), especially in conjunction with IBS (Tilsch et al., 1994) as a low rate process rendering sufficient time for data processing. In this time period, first control algorithms for a switching of the layers on the basis of the measured spectrophotometric data were also developed, and considerable research work was concentrated on a deeper understanding of the error budgets for a direct spectrophotometric deposition control (Sullivan and Dobrowolski, 1993).

Supported by enormous improvement of compact spectrophotometers with high-speed CCD cameras and the rapid growths of available cost-efficient computer power, new sophisticated online spectrometers could be integrated in deposition systems during the past two decades. These systems feature data acquisition times for a spectrum covering a wavelength range from 230 to 1100 nm in a few milliseconds and therefore allow for a direct monitoring of the actual product synchronized to the rotation of the substrate holder during deposition (Starke et al., 2000; Lappschies et al., 2004b). A typical setup for a BBM device operating in transmission mode is depicted in Fig. 4.2 for an IBS process. In the basic version, measurement radiation is generated by a tungsten lamp and coupled into a fiber that transfers the radiation to the measurement channel in the deposition plant. After collimation by a lens, the radiation passes the product on the moving substrate holder and is guided by a second fiber to the spectrophotometer. Depending on the desired spectral resolution and accuracy, spectrophotometers can be selected from a large variety of commercially available systems. For an economic approach, a compact device with fixed grating and an adapted CCD array detector can be employed, which is directly coupled to a computer system. Recording and data acquisition of spectra can be performed for preselected positions on a fixed radius of the calotte. In this configuration, several products can be monitored and furthermore, an absolute calibration can be performed during each revolution of the calotte. For this purpose, a 100% spectrum of an empty position and a spectrum of an area with zero transmittance are measured and taken as the normalization basis for the product spectra.

In Table 4.1, representative specifications of BBM systems used in industry and research are compiled. The UV-BBM system in column 1 is operated with a D_2-discharge lamp and allows for only relatively long data acquisition times not suited to direct monitoring. However, even though the UV-BBM represented in the second column of Table 4.1 is monitoring a fixed test glass, an improvement in coating precision, especially for coatings used in excimer laser technology, could be achieved (Günster et al., 2001; Ristau and Günster, 2003). In contrast to this, the device mostly favored in industrial production (Table 4.1, "standard") offers sufficient precision

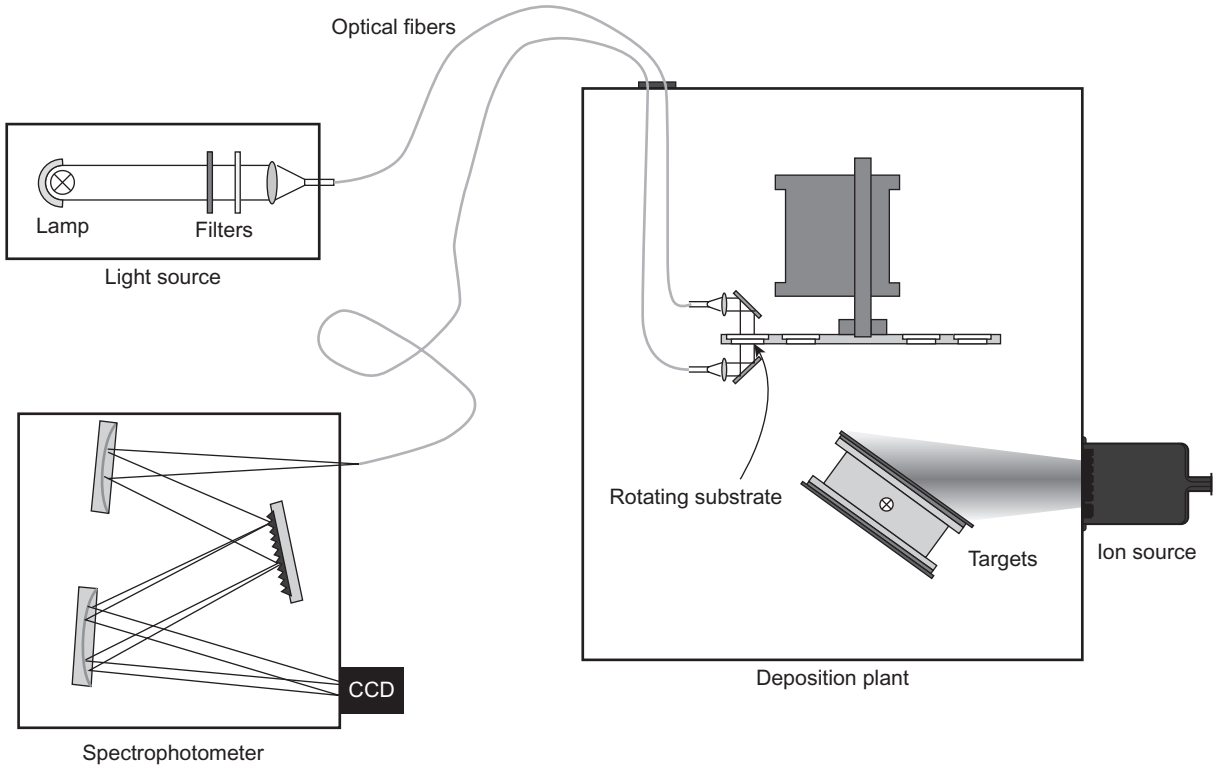


FIG. 4.2

Basic arrangement for an optical broadband monitoring system coupled to a deposition process ion beam sputtering (IBS).

Table 4.1 Selected specifications of typical optical BBM-systems applied in research and industry for deposition control

Specification	UV-BBM in research	BBM-system in industry: standard	BBM-system in industry: extended
Wavelength range (nm)	140–200	350–1050	230–1700
Wavelength resolution (nm)	2	1–1.5	1–5
Accuracy ΔT (%)	1–1.5	<1	<1
Acquisition time (ms)	>100	1–30	1–30

balanced with short data acquisition times. The last column outlines a BBM system with an extended spectral range, which enables an advanced precision and is also available for industrial application. On the one hand, an enhancement in switching accuracy is based on the number of independent data points within the measured spectra, which increases with the spectral range of the measurement device. On the other hand, the extended system provides an insight into additional wavelength ranges, for example, covering spectral target specifications or containing information about the development of optical losses under layer growth. Furthermore, owing to the variety of available spectrometers and light sources, individual adaptions for wider spectral ranges and higher resolutions in the subnanometer range are in use, especially in research environments.

In this context, a further analysis and also experience gained during the application of BBM systems indicate that a major criterion for the accuracy of a BBM-controlled process can be found in the integral variation of the spectra for the respective thickness increments. For example, the sum of the squared variations at all wavelength points in the spectra measured before and after deposition of a certain layer thickness can be considered as a quantity describing the dynamic behavior of the spectra with thickness variation. Obviously, designs with higher spectral dynamics in respect to thickness variations allow for a better switching of the layers than designs with only minute dynamics, where small changes lead to high uncertainties in the thickness values derived from the spectra. This is also a further allegation for an extension of the spectral range for BBM systems which automatically results in covering additional features in the measured spectra, especially if higher orders are taken into account at the short wavelength edge of the detection range. The technical implementation of such BBM systems with measurement ranges extended down to 200 nm in the UV can be only performed with light sources delivering sufficient radiation power in the UV range (Ristau et al., 2008). Nowadays, these systems are also routinely applied in industrial production (Mende et al., 2016). An example of an NIR extended spectrum measured with an advanced BBM operating over a range from 230 to 1700 nm is depicted in Fig. 4.3. This system comprises a combination

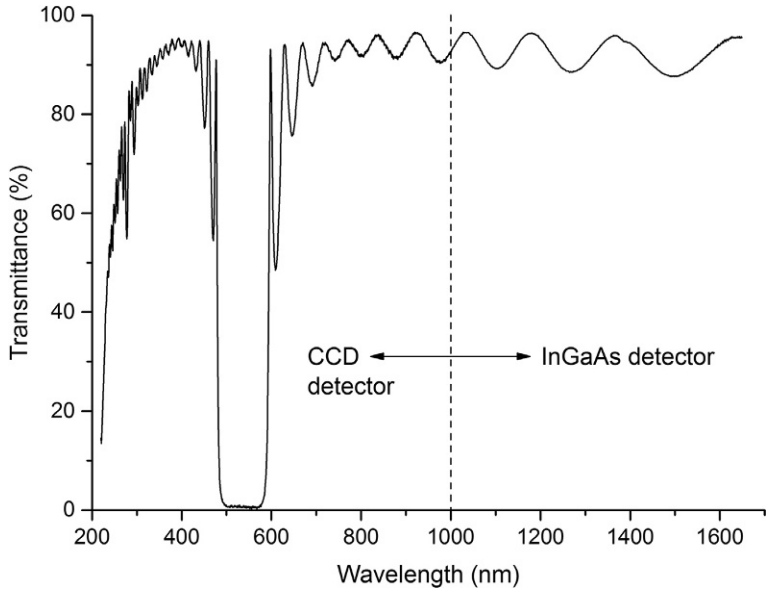


FIG. 4.3

Transmittance spectrum of a multilayer system measured by an advanced BBM system with a detection range from 230 to 1700 nm. The spectral region between 230 and 1000 nm is covered by a CCD array, and the long wavelengths part in the NIR is recorded with an InGaAs array.

of two spectrometer arrangements with a silicon CCD chip and an InGaAs array as detector elements. Technical problems to be solved on the way to BBM featuring more than three octaves in bandwidth from UV to NIR include the adapted splitting and combination of the measurement radiation, the synchronization of spectrometer systems with the motion of the calotte, as well as the calibration of the spectra.

As a further option for an improvement in the precision of BBM devices, measurement channels allowing for the synchronous acquisition of the transmission and reflection of the coating have been investigated. For example, the integration of an Ulbricht sphere in the coating plant can be considered as an interesting approach to mitigate the relatively marked directional variation of the measurement beam reflected by the coating. In the ideal case, the measured power signal of an Ulbricht sphere arrangement is invariant in respect to the direction of incidence tolerating strong geometrical changes in the reflected beam. The additional recording of the reflectance spectra allows for an online determination of optical absorption complementing the thickness calculation algorithms. Multiple measurement channels can be also applied simultaneously for an in situ monitoring of the coating uniformity over the entire substrate holder.

In principle, optical monitoring is not limited to a simple recording of conventional spectra during the deposition. Alternatively, ellipsometric techniques can

be considered that enable the spectrally resolved measurement of the polarization state of light reflected by the growing coatings. Corresponding devices with conventional ellipsometers, as well as specially developed systems, were studied during the past decades. Before this background, the work of E. Masetti dedicated to an arrangement without moving parts in the polarization analyzing channels has to be mentioned (Masetti et al., 1996). The major innovation of this technique was the introduction of special filters separating the polarization modes of the measurement radiation. Ellipsometry as a process control tool for end point detection has been applied, for example, for IAD and magnetron sputtering (Netterfield, 2005; Rademacher et al., 2011). However, most publications in the field of ellipsometric control of deposition processes are dedicated to single wavelength methods, because the practical application of spectrally resolved ellipsometric measurements precludes a static coating sample on account of the long data acquisition times of present ellipsometers. Nevertheless, ellipsometric measurements are successfully applied for in situ refractive index determination of coating materials (Chtanov et al., 2010; Sytchkova et al., 2016).

Recently, a new approach has been demonstrated that opens a way for optical monitoring beyond established transmittance or reflectance measurements (Schlichting et al., 2016). The basic idea is the in situ determination of phase, group delay (GD), and group delay dispersion (GDD) directly on moving substrates by combining the IBS deposition chamber with a Michelson interferometer. This is realized by a fiber based in situ Fourier transform measurement setup enabling GDD precision comparable to common ex situ systems. Phase monitoring is highly advantageous for the production of complex filters with demanding GDD specifications, for example, chirped mirrors. Instead of calculating the GDD indirectly, phase monitoring enables a direct "what you see is what you get" benefit that is comparable to BBM monitoring in case of transmittance or reflectance target specifications. Furthermore, in future, the additional in situ information can be processed for increased coating precision by integrating the system in multimonitoring concepts for enhanced deterministic production solutions. First, experimental applications of the in situ phase monitor for chirped mirror production led to very promising results (Schlichting et al., 2016; Willemsen et al., 2016).

4.4 HYBRID THICKNESS MONITORING CONCEPTS

If highest sensitivity, stability, and reproducibility are demanded, today BBM devices are often connected to other sensors installed in the coating plants. These multisensor approaches result in the need for advanced hybrid monitoring concepts which require adapted control algorithms. In the following, the focus is on in situ layer thickness determination. Therefore, examples aiming mainly at process stability aspects like connections to plasma monitoring or mass spectrometry devices are not considered. Basically, hybrid layer thickness monitoring concepts can be divided into two categories. In the first case, multiple monitoring techniques are applied

sequentially for the end point detection in different layers in one multilayer stack. As a consequence, a strategy defining the optimal monitoring technique for each layer has to be developed prior to the deposition process. Common examples are combinations of optical monitoring and quartz crystal microbalances or time-based thickness monitors. In these approaches, often only critical layers in terms of the precision of the optical monitoring algorithm, for instance, very thin layers, are terminated by nonoptical monitoring systems. It has to be mentioned that in addition to the pure sequential application of the different measurement concepts, cross-system calibrations are possible. For example, the accuracy of the quartz crystal microbalance tooling or the time-based monitor can be enhanced by data of optical measurements of the already finished layers. In the opposite direction, the optical process tracing can be verified by separate consistency checks on the basis of logged data from nonoptically terminated layers. Also, the combination of different optical monitoring systems can be advantageous for the fabrication of some special multilayer designs. For instance, combining broadband monitoring with single wavelength monitoring for terminating selected layers, for example, to overcome resolution limits in case of very thick layers with high frequency ripples in the measured spectra (Lyngnes et al., 2015). In contrast to the previous sequential application of the different monitoring systems, the data of more than one monitoring technique are evaluated simultaneously in the second category of hybrid monitoring approaches. Consequently, in this true hybrid monitoring case, each layer of a multilayer stack is terminated based on an algorithm processing the signals of different monitoring systems. In extension of the example above, a BBM system and a quartz crystal microbalance can be combined in a true hybrid way. For instance, this combination opens up the possibility of guiding the BBM algorithm by the crystal microbalance data in case of critical thicknesses resulting in low spectral dynamics (see Section 4.3). More in detail, the thickness values determined by quartz crystal monitoring influence the starting values for the numerical minimization procedure of the BMM system for fitting the theoretical to the measured transmittance spectra (Ehlers et al., 2010).This hybrid approach is particularly advantageous if minor deviations in the already deposited layers accumulate to larger discrepancies between the measured spectra of the current layer and the theoretical spectra, which are calculated on the basis of error-free thicknesses of the underlying layers (Tikhonravov et al., 2006). In this case, points of ambiguous solutions can occur for the pure BBM tracing algorithm while the layer thickness increases. However, when implementing the hybrid process control, the guiding of the tracing algorithm by the crystal microbalance values allows for passing the described critical positions successfully. Nevertheless, the layer is finally terminated by the high-precision optical BBM system taking advantage of positive effects like error self-compensation (Tikhonravov et al., 2011).

Furthermore, the hybrid combination of different monitoring systems offers the possibility to realize advanced error handling strategies. In such configurations, the operator can often define various individual conditions and actions with a high flexibility. For instance, the deposition process can be adjusted or paused automatically if a certain relative or absolute layer thickness deviation level between different

simultaneously working monitoring systems is exceeded. Also, rules triggered by specific error events can be established to reverse the roles in a master-slave configuration of two monitoring systems, for example, switching to crystal microbalance control if negative rate values are calculated by the BBM algorithm. In addition, thickness levels for switching from crystal microbalance to optical monitoring can be defined to provide a minimum layer thickness for the evaluation of the optical measurements.

In summary, the presented advanced monitoring concepts can enhance precision and yield in the production of complex multilayer stacks without a need for developing design dependent individual monitoring strategies. Practical examples of the benefits of a true hybrid monitoring approach will be given in Section 4.7.

4.5 VIRTUAL DEPOSITION SYSTEM

The evaluation of a synthesized design in respect to its stability in production was always a key issue in optical thin film technology. Typical concepts for a first assessment of the design stability include algorithms performing random variations of the thickness values within predefined limits and a subsequent calculation of the transfer spectra. These algorithms are repeated several times for all layers of the design resulting in estimated confidentiality intervals for the individual thickness values and corresponding tolerance bands for the spectra. More sophisticated techniques also involve variations in the dispersion of the single layers in the design in dependence on their position in the layer structure. Accordingly, a limited comprehension of coating processes can be achieved on the basis of the individual dispersion variations, which are expected to differ significantly, for instance, between conventional evaporation and IBS. Generally, these algorithms form an integral part of modern commercial design synthesis packages and allow for a first estimation of the design stability. However, in most cases, comparisons between the estimated error budget and results observed in practice reveal severe deficiencies of the employed random algorithms. As a consequence, advanced tools, which directly perform a simulation of deposition runs controlled by defined techniques, have been developed during the past few years. Typical approaches consist of an algorithm emulating the deposition plant and a further computer program imitating the control system, which may contain a quartz crystal balance, a single wavelength optical monitor (Zöller et al., 2008), or even a BBM as a measurement system (Ehlers et al., 2010). These simulation tools, often referred to as a "virtual deposition system, VDP" (Ristau et al., 2008) or "computational manufacturing" (Amotchkina et al., 2012), can be devised with high flexibility in respect to the deposition process, the measurement system, or the process-tracing algorithm. In the following, the typical functioning of VDP concepts comprising the emulation of the deposition plant, the online monitoring device, and the process-tracing algorithms will be described for a BBM system as a central

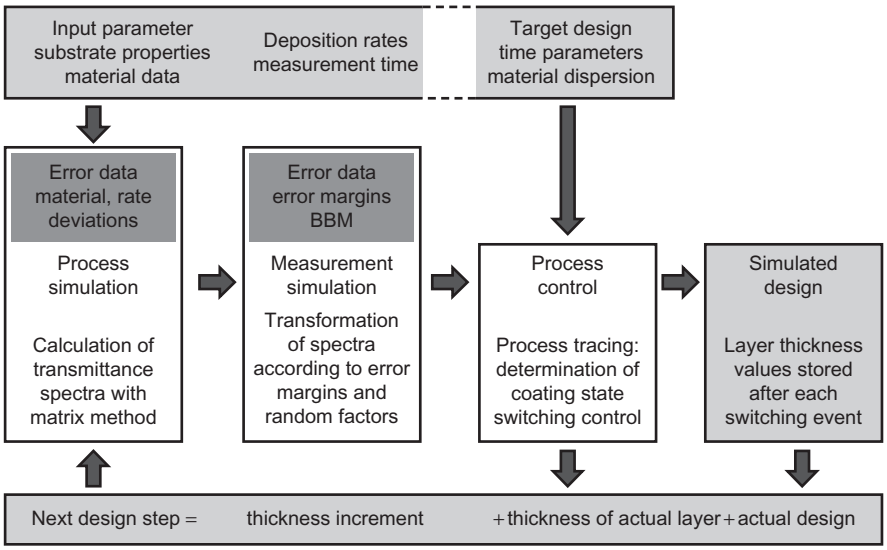


FIG. 4.4

Diagram for a virtual deposition process (VDP) with a BBM system for deposition control. The fundamental structure consists of three units simulating the deposition process and the measurement channel of the online monitoring device. These two parts form the virtual deposition system. The virtual deposition control unit is illustrated in the left half of the diagram for a BBM system.

online monitor (see Fig. 4.4). Finally, results for the dielectric filter system will be illustrated as an example for a typical application (Ehlers et al., 2010, 2011).

4.5.1 DEPOSITION SYSTEM

In a typical VDP concept, the major outcome of the algorithm emulating the deposition system consists of spectra for the different phases of the process. For that reason, the mathematical kernel of the deposition system emulator consists of a layer matrix program calculating spectra for a layer structure formulated according to the progress of the deposition run. At the beginning of the simulation, the first layer of the intended design is considered, and a spectrum is calculated for the first thickness increment from dispersion data of the substrate and the involved layer material. The size of the thickness increment is dependent on the deposition rate and the measurement scheme applied in the control system. In case of a quartz crystal balance, the thickness increment would be defined by the sampling time of the frequency readout. For an optical system operated in the direct monitoring mode, the thickness increment would amount to the deposition rate multiplied by the revolution time of the calotte. Considering these generic relations, the counting basis for the progress of the simulated layer structure is the time interval between the consecutive

measurements of the control system. In the further course of the simulation, the corresponding time counter is continually incremented, and a spectrum is calculated for the layer thickness at each time step. For the first layer, this procedure will be stopped and the reached layer thickness will be stored once the control system has identified the switching point. After that, the second layer data are loaded into the layer matrix program and the spectra are calculated again until the switching point is indicated. This track will be followed until the last layer is simulated, and the result of the VDP-process can be read out as the thickness values stored for each layer at the switching points. The specific properties of the considered deposition processes are accounted for by the input parameters for the deposition emulation routine including variations or trends in the dispersion data and deposition rates of the materials. Also, additional routines are integrated in the program to simulate effects of error sources generated by technical deficiencies in the system. For the highest flexibility and modularity, the deposition emulator is configured to the transmission control protocol/internet protocol (TCP/IP) interface for data communication between the other components of the VDP system.

4.5.2 ONLINE MEASUREMENT SYSTEM

The procedure representing the online measurement system loads the emulated spectra from the deposition system and performs an adapted transformation according to the specific errors of the measurement systems. For instance, prominent errors to be primarily considered for a BBM system include systematic components induced by the limited spectral resolution as well as absolute deviations in the wavelength position and transmittance. Further random variations have to be taken into account representing the noise of the system and aberrations in the calibration routines. The simulation routine for the BBM measurement stamps the effects of the mentioned errors on the ideal spectra calculated by the deposition emulator and formats the data for the subsequent process-tracing algorithm. As a consequence of the TCP/IP interface, the measurement simulation routine can be replaced by any other program module representing a quartz crystal device, single wavelength monitoring, or other specific process observing instruments related to the development of coating design.

4.5.3 PROCESS-TRACING ALGORITHM

If the interfaces of the VDP components are devised in an appropriate way, the respective original process-tracing software package used in the deposition plant can be directly employed. In the case of the BBM system, the corresponding program can be transferred from the deposition plant, where it is operated with the spectrometer system, to the VDP system without any alterations (see process control box in Fig. 4.4). As a consequence, the user interface and all options of the software package are part of the BBM VDP device and can be operated identically to the situation at the real plant. The major functioning of the tracing algorithm is implemented in a least

squares fit algorithm which deduces the actual thickness of the current layer from the measured spectrum (Starke et al., 2000). In the special environment of the VDP system, the measured spectra are given by the data simulated by the VDP online measurement system. Since the process-tracing algorithm is identical to the application tool, all input data describing the target design, the substrate, and the deposition materials are considered in the tracing routines. The current layer thickness calculated by the least squares fit algorithm is compared to the value according to the termination point of the layer during each time step of the VDP routine. At a certain small distance to the target thickness, the control system switches to a time counting mode in order to enable termination of the layer at any instance in between two consecutive time steps of the deposition emulator. After reaching the termination point, the deposition emulator is stopped, and the thickness value, which is corrected by the additional minute amount introduced by the time counting switching mode, is stored as the actual thickness value of simulated design.

4.5.4 APPLICATION EXAMPLE FOR A VDP ANALYSIS

A major prerequisite for an efficient application of VDP procedures is a set of error and material data which has to be gained from the routine operation of the individual deposition plants. In particular, iterative VDP runs can assist the analysis and quantification of production errors and material parameters (Amotchkina et al., 2012). For example, deviations in dispersion and deposition rates are critically dependent on the process concept used for the production of a certain coating design. As a consequence of the relatively low error margins, valid results are expected for stable processes as IAD or IBS. In Fig. 4.5, results for a broadband antireflection design with 16 layers of the materials TiO_2 and SiO_2 are illustrated precluding an IBS process. Target specifications of the design range from 400 to 700 nm. The spectrum calculated directly from the design is depicted by the dashed black curve in Fig. 4.5 and compared to the result of a VDP analysis on the basis of deviation parameters for the employed IBS plant (solid black curves, two simulation runs). Obviously, the VDP analysis leads to small but noteworthy differences in the spectral behavior which are also reflected by the simulated design with some layer thickness values diverging from the target design. Since the observed error margins conform to the specified tolerance band, the coating was produced yielding the in situ spectrum indicated by the gray curve in Fig. 4.5. The good agreement between spectral behavior forecasted by the VDP analysis and the produced layer system clearly demonstrates the versatility of this novel preproduction evaluation tool.

Summarizing, experience gained during several years of application of VDP concepts in research and also in industrial production indicates that the risk for the manufacturing of a certain layer design can be estimated on a reliable basis for a large variety of deposition systems and complex layer designs. In most cases, the produced coating systems deviate only by a small amount from the spectral characteristics forecasted by the VDP analysis, whereas larger differences are often observed for the target designs. For example, experimental investigations even reproduce the

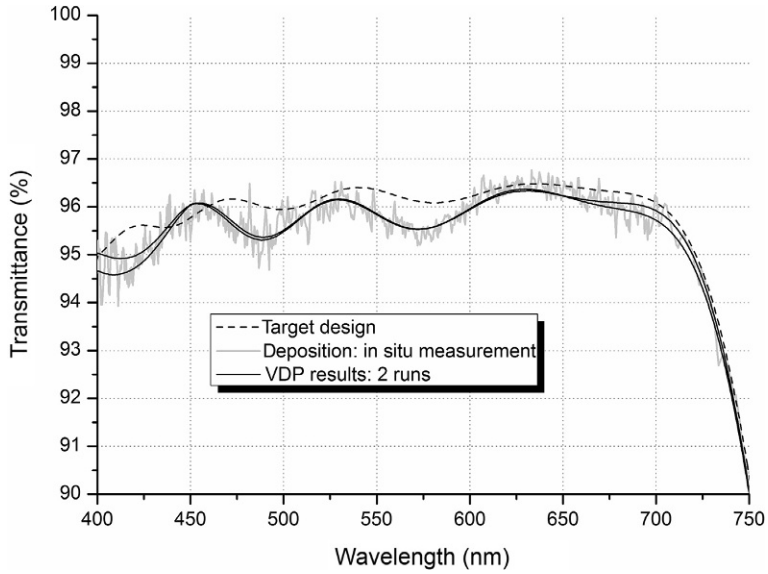


FIG. 4.5

Spectra of a broadband antireflection coating deposited in an ion beam sputtering process with the materials TiO_2 and SiO_2. The spectrum of the target design *(dashed black curve)* is compared to the results of the process simulation using the virtual deposition system (*solid black curves*, two VDP runs) and the produced coating system (in situ spectrum, *gray curve*).

position in a problematic design, where the critical aberration is predicted by the VDP process. A corresponding study will be summarized in a subsequent section of this chapter.

4.6 DIRECT ONLINE CORRECTION TOOLS

Direct online error detection and correction tools complement the described combination of advanced monitoring concepts and virtual deposition systems in an ideal way. The basic idea of a computer based online re-optimization of the layer thicknesses as well as a first implementation in optical coating production can be dated back to the late 1970s (Holm, 1979). In a first step, the evolution of layer thickness errors has to be traced by an error detection tool. In the given case of optical broadband monitoring, the deviations between the measured spectra of the growing layers and the theoretical target spectra have to be evaluated. The necessary calculations can be performed by applying different algorithms, of which two are most common. On the one hand, only the last measured spectrum can be used to calculate the thickness of the corresponding last layer, while the thicknesses of the underlying layers are kept constant. This type of calculation is implemented in the so-called sequential

algorithm. On the other hand, one measured spectrum for each already deposited layer of the growing stack can be evaluated by an algorithm at once to calculate the thicknesses of all deposited layers. This simultaneous analysis of all measurements is done by the so-called triangular algorithm. Owing to the broader experimental database of the triangular algorithm, a better reliability can be expected, which could be demonstrated in an experimental study (Amotchkina et al., 2011).

The above-described approaches provide information about the thickness deviations of the already deposited layers derived from online measurements. Regarding the BBM control, the calculated thicknesses can substitute the theoretical values in the multilayer design to process the remaining layers under conditions as close to reality as possible. However, with respect to the aim of an online correction tool, it is crucial to classify the evaluated errors and to determine a critical error level for an automated intervention. Consequently, in the next step, the impact of the errors on the expected spectral performance of the complete layer system has to be calculated. Depending on the specifications, the need for a re-optimization of the multilayer design has to be checked. In the subsequent re-optimization procedure, the thicknesses of the remaining layers have to be refined, while the thicknesses of the already deposited layers are taken from the previous deviation calculations. If a modified design fulfills all specifications, the process control replaces the original design and the BBM system traces the process on the basis of the new thicknesses for all layers. In rare cases of high deviations, additional layers are required to fulfill the specifications. This further feature can be provided by the online correction tool as a selectable option. Generally comparable to common thin film design software packages, the specifications processed by the correction tool are not limited to transmittance and reflectance values. For instance, absorption, phase, GD, or GDD requirements can also be defined as specific target values for online re-optimization.

Furthermore, the VDP system described in the previous sections can be integrated into the re-optimization procedure to benchmark automatically different refined designs with respect to their design stability within the process. It has to be mentioned that the chosen algorithms in combination with the available hardware have to be fast enough to perform all calculations online, normally before the finish of the current layer.

In addition to the described evaluation of layer thickness deviations, an optional online analysis of deviations in the wavelength dependent refractive indices and extinction coefficients is possible. However, owing to the limited information contained in the measured transmittance data, these online multiparameter fits have to be done carefully. In practice, the re-optimization should be restricted to a layer thickness variation by default, which is no significant limitation in case of stable deposition processes. Nevertheless, in certain cases for selected layer configurations for example, an online refinement of the dispersion data can be advantageous. Altogether, these versatile tools are still under intense development, but already available for industrial production since years (Schlichting et al., 2011; Waldner and Padrun, 2013; Ehlers and Ristau, 2013).

In summary, the direct online correction tools coupled to enhanced BBM systems enable a further increase in yield as well as in precision of complex optical coatings. In most cases, the resulting re-optimized design differs only slightly from the theoretical starting design that would not have been deposited successfully without the application of an online correction tool. A concrete experimental example of re-optimization results will be given in the next section.

4.7 DESIGN STABILITY IN PRODUCTION PROCESSES

In the following, selected results of an experimental study are summarized to give an overview of the potential of different monitoring conditions. The evaluated techniques comprise monitoring by a BBM system and a hybrid BBM configuration as well as the application of a VDP system and a direct online correction tool. All coatings were manufactured by an IAD process on a commercial Leybold SYRUSpro 1100 machine equipped with a Leybold APSpro plasma source.

Following the production chain, the selection of an appropriate design is the first step. Therefore, the VDP system is applied in the beginning to choose the most stable multilayer design. Within the experimental study, a double band-pass filter with transmittance peaks at wavelengths around 600 and 700 nm was chosen as the demonstrator. Initially, two alternative designs for TiO_2/SiO_2 stacks were calculated by a thin film design software. Both of them show nearly identical transmission/reflection in the relevant spectral range from 550 to 800 nm. Furthermore, they similarly include 31 layers with comparable proportions of TiO_2 and SiO_2 as well as a total thickness of $\sim$2.6 µm. Regarding design stability aspects under process conditions, it can be stated that none of the designs contains a layer with a thickness below 30 nm.

In Section 4.5, basic examples of algorithms for design stability analysis were introduced. However, in case of the two given double band-pass filter designs, random variations of the layer thicknesses result in no significant differences. Only a slightly higher stability is predicted for the second design. Also, the analysis of the dynamic behavior of the transmittance spectra with increasing layer thickness reveals no further information. Again, the second design only shows minor advantages over the first one. In contrast, the VDP approach based on the BBM monitoring software results in considerable differences between the two designs. In Fig. 4.6, the simulated transmittance spectra of design 1 are plotted in comparison to the theoretical target spectrum. To take the reproducibility into account, 100 virtual deposition runs were performed. All simulations were done using the SYRUSpro 1100 machine specific error sets and show a high reproducibility with a maximum standard deviation of 0.3% in the transmittance peaks. Therefore, the mean simulated transmittance is depicted in Fig. 4.6. To validate the calculated VPD results, comparable real deposition runs are necessary. In addition, Fig. 4.6 shows the result of three BBM controlled depositions runs for the first design. Obviously, the simulated results are in a good agreement with the measured transmittance data, which indicate good reproducibility, too. Looking at Fig. 4.7, the difference in performance of

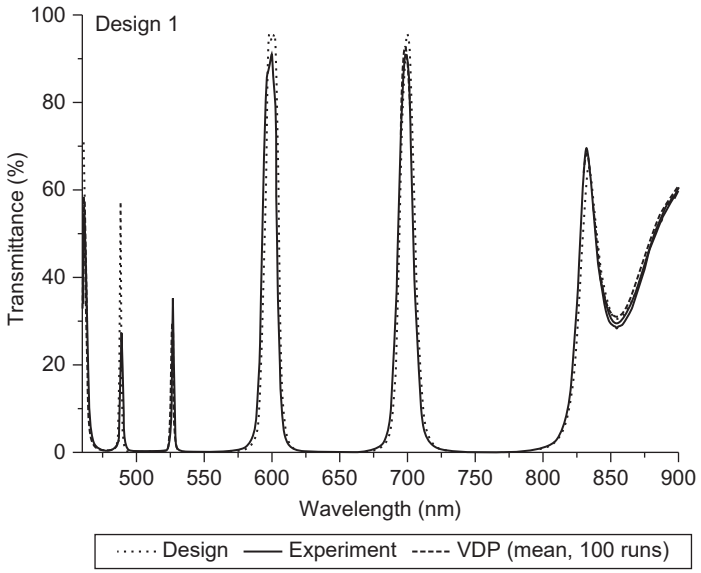


FIG. 4.6

Theoretical transmittance target spectrum of design 1 in comparison to corresponding simulated and measured transmittance spectra.

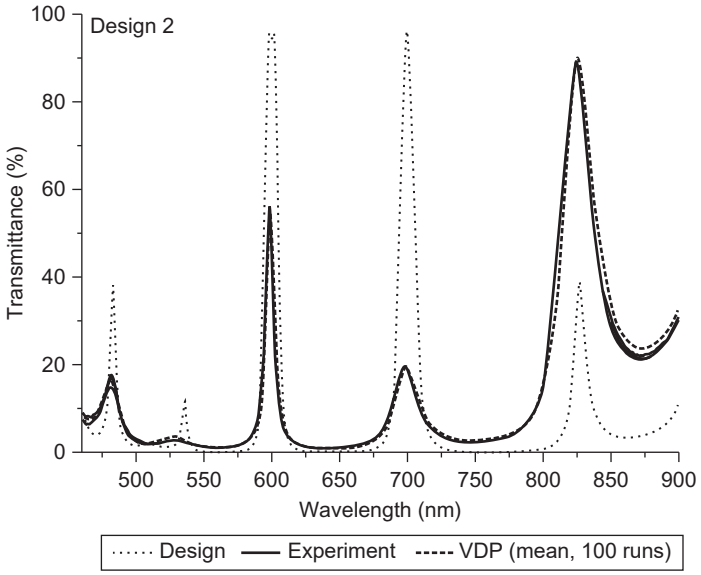


FIG. 4.7

Theoretical transmittance target spectrum of design 2 in comparison to corresponding simulated and measured transmittance spectra.

design 2 compared to design 1 is evident. Again, the theoretical target spectrum and the VDP as well as the experimental results are plotted. Owing to the large target deviations, the second design could be identified as much more unstable under production conditions. This result was predicted by the VDP runs and also confirmed by the real deposition runs. In the given case, the important influence of dominant systematic errors, including error self-compensation and accumulation effects, becomes evident. This can be seen by the high reproducibility of simulation as well as deposition results and the small differences of the corresponding experiments. Consequently, stochastic errors are less significant for the given combination of multilayer designs, deposition process, and thickness monitoring system.

As described above, the intention of this section is to compare different monitoring concepts with respect to their precision and stability in layer thickness control. In production, the first design would most likely be the preferred choice because yield is an important factor. However, in view of this section, a more challenging design is preferable. Therefore, all following examples will refer to the second design and concentrate on the transmittance in the passband centered at a wavelength of about 600 nm. In detail, five different control configurations were applied to evaluate their performance:

1. process monitored by a BBM system (see Section 4.3),
2. process monitored by hybrid combination of a BBM system and a quartz crystal microbalance (see Section 4.4),
3. process monitored by BBM control in combination with a direct online correction tool (see Section 4.6),
4. process monitored by a BBM system after a refinement of deposition and material parameters by a VDP analysis based on the preceding experimental results (see Section 4.5), and
5. process monitored by a simultaneous application of all the above-described tools.

The results of example 1 in Fig. 4.8 are based on the BBM control and therefore Fig. 4.8 shows a detail of Fig. 4.7. Instead of the aimed maximum transmittance of ~95%, only ~55% are reached in the three deposition runs due to strong error accumulation effects resulting from the problematic design. In contrast, Fig. 4.9 documents a much higher transmittance. In this second example, a hybrid BBM monitoring system, which includes a quartz crystal microbalance as described in Section 4.4, was applied. However, deviations of more than 5% from the spectral target deviations are still evident in all three deposition runs. As an optional extension, the connection of the BBM to a direct online correction tool was introduced in Section 4.6. Corresponding results are depicted as example 3 in Fig. 4.10. Again, the transmittance curves of the four experimental runs are much closer to the target transmittance than the results of example 1 and exhibit a high reproducibility. Furthermore, the versatility of the VDP system was applied to perform different parameter refinement simulation runs in example 4. As a database for this analysis, the spectral results from the preceding examples were used. It can be seen in Fig. 4.11 that the VDP refined parameters enabled the BBM without the help of any additional tool to a higher

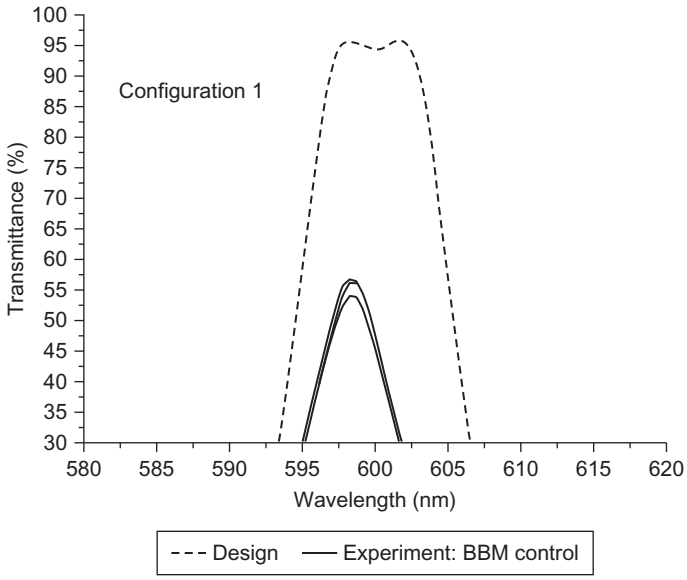


FIG. 4.8

Process monitored by a BBM system (example 1), measured transmittance spectra (three deposition runs) in comparison to the theoretical target spectrum.

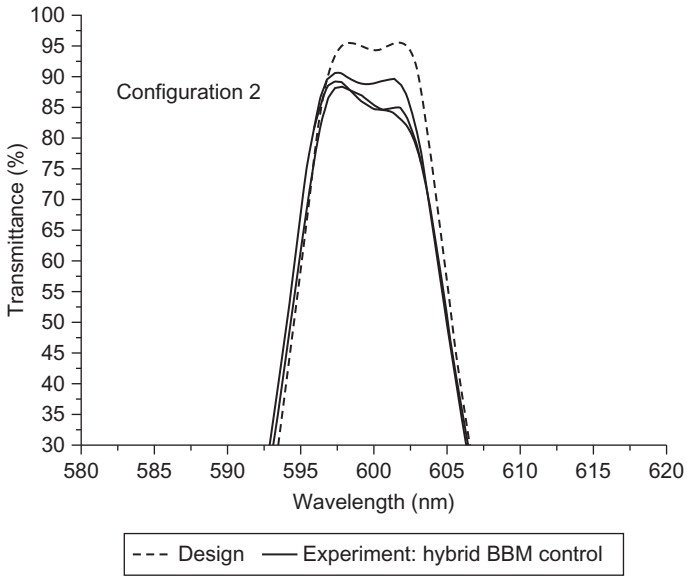


FIG. 4.9

Process monitored by hybrid combination of a BBM system and a quartz crystal microbalance (example 2), measured transmittance spectra (three deposition runs) in comparison to the theoretical target spectrum.

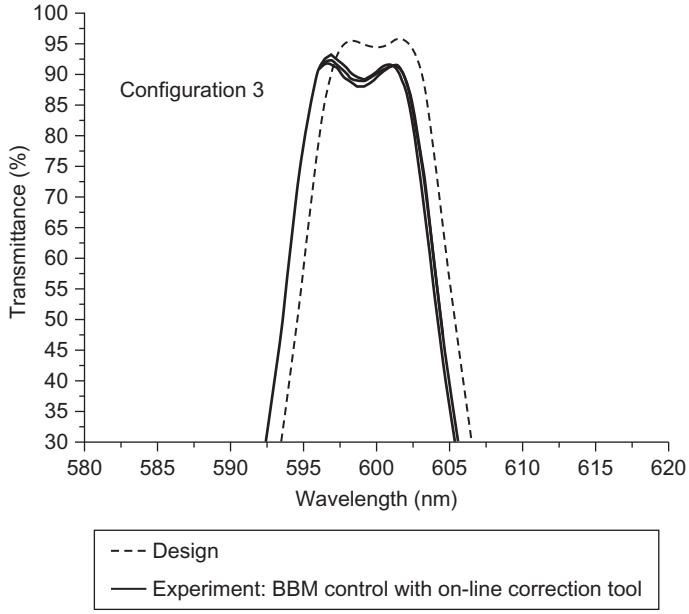


FIG. 4.10

Process monitored by a BBM system with a direct online correction tool (example 3), measured transmittance spectra (four deposition runs) in comparison to the theoretical target spectrum.

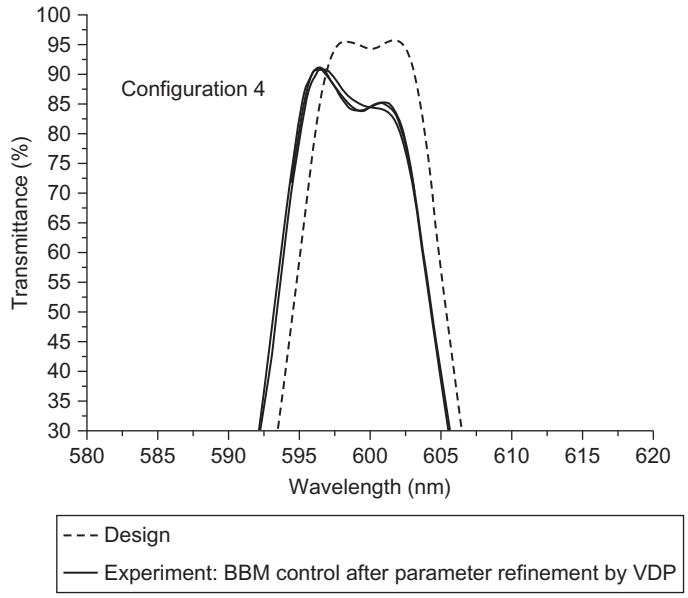


FIG. 4.11

Process monitored by a BBM system after a VDP parameter refinement (example 4), measured transmittance spectra (three deposition runs) in comparison to the theoretical target spectrum.

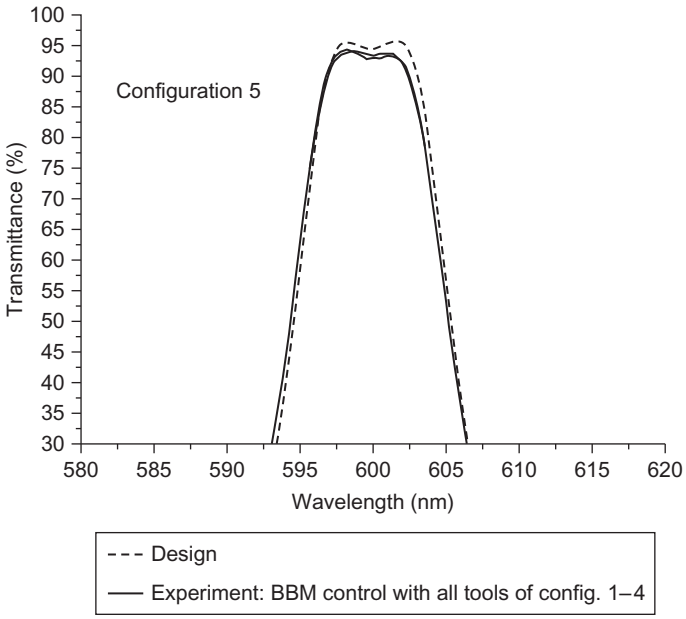


FIG. 4.12

Process monitored by a simultaneous application of all presented tools (example 5), measured transmittance spectra (two deposition runs) in comparison to the theoretical target spectrum.

precision compared to the first runs in Fig. 4.8. Finally, as a state-of-the-art approach, all the above-mentioned tools were simultaneously applied to monitor the deposition in example 5. Consequently, these experiments resulted in the best agreement between measured and calculated transmittance which is shown in Fig. 4.12. In this context, it has to be pointed out again that these small deviations were achieved, although design 2 was identified as very unstable under optical broadband monitoring.

In conclusion, each of the described extensions to pure broadband monitoring allows for a clear improvement in precision and yield. Nevertheless, an advantageous combination of two or more of these tools can even increase these enhancements.

4.8 DEPOSITION CONTROL OF COATING SYSTEMS WITH CONTINUOUS REFRACTIVE INDEX VARIATION

In principle, layer structures comprising a sequence of discrete layers with constant optical properties, which are commonly processed in optical thin film technology, represent only a very special class of coatings. For a more general consideration, functional optical coatings may be understood as a structure with any arbitrary

continuous variation of the refractive index in the depth. In this context, an ideal antireflective coating can be realized on the basis of coating structures with a refractive index decreasing constantly from the substrate value down to the refractive index of the environment. Long before mankind existed, such structures evolved in nature and are presently in the focus of many scientific studies. The "moth eye effect", which was first described by Bernhard (1967), is still among the most prominent topics that can be found and is treated in more detail in Chapter 13 of this book. As a rough estimation, the nanostructure on the cornea of moth eyes can be interpreted as a gradient in density of a transparent material with a pertinent continuous decrease in effective refractive index. The antireflective effect of this system is remarkable in respect to wavelengths covering the entire visible spectral range as well as to the broad regime of angles of incidence.

Besides constant optical performance over broad operation ranges including the suppression of spectral sidebands, additional advantages in temperature and laser stability were expected for gradual systems. Therefore, part of the research work on gradual systems, which can be traced back to the early 1980s (Ristau et al., 1988), is motivated by demands on the laser power handling capability of optical coatings. In this connection, optical coatings with a continuous variation of the refractive index are often referred to as "Rugate Filters," a term initially reserved for structures with a sinusoidal oscillation in refraction. Attempts of closed formulations for the optical transfer properties of the media with a refractive index gradient have been studied since more than one century (Schlick, 1904; Schröder, 1941) and led to different solutions. Besides advanced techniques based on Fourier transformation algorithms (Verly et al., 1989), most of the approaches for the description of the spectral behavior of rugate filters comprise a fractioning of the continuous system in very thin discrete layers with a refractive index given by the average value at the respective position in the structure (Southwell, 1985) and a subsequent calculation of the transfer properties using the common matrix formalism for optical thin films. In contrast to the Fourier transformation methods, this "quasirugate filter" approach integrates the dispersion behavior as well as the absorption losses of the involved coating materials. Furthermore, alternative numerical methods for the design of rugate filters have been proposed that calculate structures with an arbitrary variation of the refractive index taking dispersion and absorption into account (Anzengruber et al., 2012). In practice, the combination of different approaches also can be advantageous, for example, (1) numerical calculation of a rugate filter design, (2) transformation of the gradient design into a quasirugate filter for production (Becker et al., 2014).

4.8.1 PRODUCTION OF MATERIAL MIXTURES

Before the background of the expected superior properties of rugate filters, a large variety of investigations in appropriate production strategies have been performed in optical thin film technology. The fundamental building block is a controllable transition between defined index values within a certain layer thickness. For the technical

implementation of such transitions, mixing of two materials by co-deposition or processes with two reactive gas components can be employed. As a typical concept involving two reactive gases, the production of $(SiO_2) \times (Si_3N_4)_{1-X}$ layers with defined composition ratio x has been studied for sputter processes and found applications for antireflection coatings on laser diode facets (Katagiri and Ukita, 1990) among others. As a consequence of the relatively low flexibility of oxynitrides, the majority of research activities is dedicated to co-deposition processes of ternary oxide compounds that allow for low optical losses and high dynamic ranges in refractive indices. In conventional e-beam deposition systems, switching of the e-beam between two crucibles represents a simple principle where the mixing ratio is adjusted by dwell time of the e-beam on the materials. More advanced concepts involve the application of two separate e-beam evaporation sources with independent rate control (Ristau et al., 1988). In most cases, these co-deposition processes suffer from stoichiometric deficiencies in the compounds induced by the relatively delicate supply of the reactive gas. Also, strong variations in the material composition often cannot be avoided for a small content of one material as a consequence of the poor stability of the evaporation sources operated at their low rate limits. An additional disadvantage can be attributed to the specific emission characteristics of the e-beam sources in conjunction with the low energy of the adatoms forming the co-deposited layer. Electron microscopic investigations in the layer structure of coatings grown on substrates mounted on a rotating calotte reveal the formation of a nanolaminate instead of a homogeneous mixture of the involved materials. This effect is explained by the consecutive adatom fluxes seen by the growing layer passing the emission zones of the two material sources during rotation (Leitel et al., 2005). This problem can be avoided by a geometric superposition of the material fluxes from the material sources. Also, magnetron sputter techniques have been considered for the production of material mixtures and rugate filters (Rickers et al., 2006; Becker et al., 2014) employing two separate sputter sources in an activated reactive process. Major challenges related especially to co-sputtering of oxide materials include the control of the reactive atmosphere to maintain the oxidation state of the two different target surfaces. However, in case of deposition plant concepts based on spatially separated sputter sources, the reactive atmosphere can be adjusted more material-specific.

IBS with a zone target offers several advantages in respect to process stability and quality of the produced coatings (Chao et al., 1999; Lappschies et al., 2005).The fundamental principle of this process strategy is depicted in Fig. 4.13 and comprises the three components of a typical IBS arrangement: ion source, target, and substrate holder. In contrast to conventional IBS systems, the multiple target mount is replaced by a zone target that can be positioned in front of the ion source. In dependence on the position, the ion beam interacts simultaneously with surface areas of the two adjacent materials, and the material composition in the emitted sputter flux is related to the interrogated target area fractions as well as the respective sputtering rates. Consequently, the material composition and the corresponding refractive index of the growing layer can be simply adjusted between the two refractive indices of the

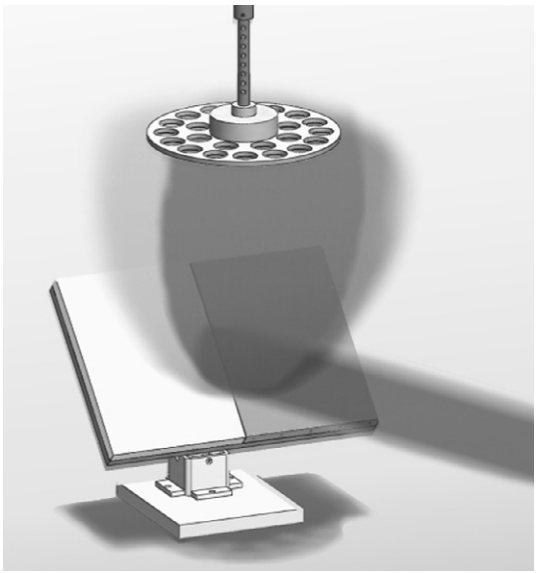


FIG. 4.13

Schematic operation principle of Ion Sputtering Process with a zone target. The ion beam is directed to the target from the lower right corner. The substrate holder is positioned above the target, which can be moved left and right to adjust the mixture ratio of the sputtered materials.

pure target materials by positioning of the target. A more detailed analysis of the layer formation process indicates an inhomogeneous distribution of the two materials in the sputter flux from the target as observed for the competing e-beam and magnetron processes. However, since the material fluxes from the two zones are directly located side by side and the energy of the sputtered adatoms allows for high mobility on the growing layer, a nearly homogeneous intermixing of the two material components is achieved in the layer structure. Selected effective media theories have been applied to model the dependence of the refractive index of produced oxide mixtures on the material composition (Amotchkina et al., 2007; Lappschies, 2009). Among the approaches (see Fig. 4.14) considered for mixed layers of TiO_2/SiO_2, best accordance to the measured refractive index data was found for the Lorentz-Lorenz model. Another interesting observation was a clear variation of the bandgap energy for mixed layers between the values of the pure materials. Opposite to the expectation, defined bandgap energies could be assigned to the mixtures indicating that the produced mixed coatings represent a new class of materials with individual properties. This outcome is supported by extended investigations into the properties of these ternary oxide coatings. For example, laser-induced damage thresholds (LIDTs) of ternary oxides and pure materials were determined in the femtosecond (fs) regime (see Fig. 4.15) with an ultrashort pulse laser system operating at a

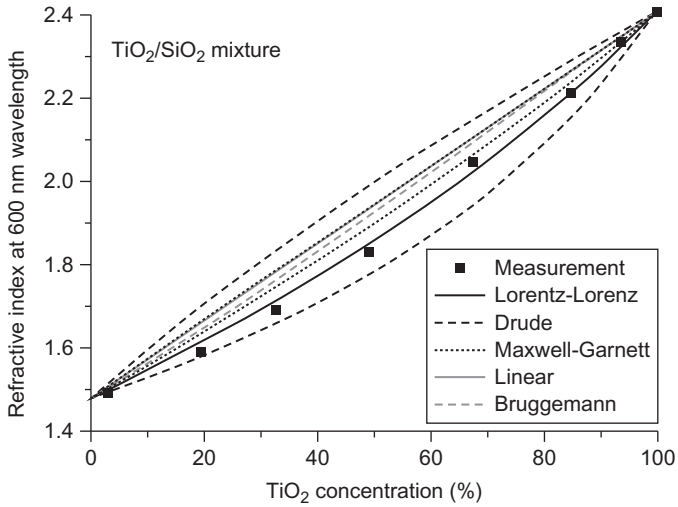


FIG. 4.14

Comparison of results for selected effective media theories (Lorentz-Lorenz, Drude, Maxwell-Garnett, linear model, Bruggemann) to the measured refractive indices of TiO_2/SiO_2-films co-deposited in an IBS process. The concentration of TiO_2 was determined on the basis of EDX measurements (Lappschies, 2009).

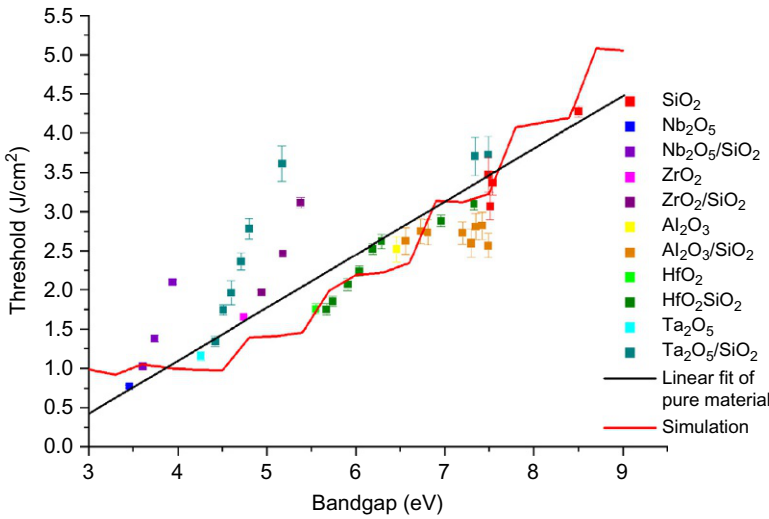


FIG. 4.15

Laser-induced damage thresholds (LIDTs) (measured at a wavelength of 1030 nm, pulse duration of 500 fs, 1-on-1 mode) of pure oxide materials and five ternary oxides with varying composition as a function of bandgap energies. *Black line*: linear fit of pure oxides, *red line*: femtosecond laser damage simulation results.

Adapted from Mangote, B., Gallais, L., Commandré, M., Mende, M., Jensen, L., Ehlers, H., Jupé, M., Ristau, D., Melninkaitis, A., Mirauskas, J., Sirutkaitis, V., Kičas, S., Tolenis, T., Drazdys, R., 2012. Femtosecond laser damage resistance of oxide and mixture oxide optical coatings. Opt. Lett. 37(9).

wavelength of 1030 nm. In contrast to the nanosecond (ns) regime, where laser induced damage phenomena are dominated by inclusions and often exhibit a pronounced statistical behavior, laser induced damage by ultrashort pulses is nearly deterministic in nature and governed by the material properties. Models describing the fs damage mechanisms often involve rate equations for the development of a critical electron density in the conduction band, which are directly related to the bandgap energy of the materials (Jupé et al., 2009). By modeling the LIDT values of the pure materials in respect to their bandgap energy, a specific correlation can be found which is reflected by corresponding measurement values. An example of simulations based on photoionization and avalanche-ionization (Mangote et al., 2012) is shown in Fig. 4.15. The simulation results (red line) are in good agreement with the experimental results for the pure oxides Nb_2O_5, Ta_2O_5, ZrO_2, HfO_2, Al_2O_3, and SiO_2. In case of the ternary oxides, a dependence on the bandgap difference between the two mixed basic materials is observed. For Al_2O_3/SiO_2, and HfO_2/SiO_2, the LIDT behavior is similar to the pure oxide results. In contrast, the mixtures ZrO_2/SiO_2, Ta_2O_5/SiO_2, and Nb_2O_5/SiO_2 with larger bandgap differences show stronger deviations from the predictions of the applied simulation model. Nevertheless, the threshold values of the ternary compounds evidently corroborate the assumption that these mixtures can be considered as a new class of individual materials with adjustable refractive indices and bandgap energies.

This experimental finding is additionally supported by a study of nanolaminates in comparison to co-deposited single layers. As an example (Lappschies et al., 2007), a nanolaminate consisting of 50 alternate thin films of the materials TiO_2 and SiO_2 was produced with an IBS process to form a 2 QWOT (quarter-wave optical thickness) layer for the wavelength 1064 nm. This corresponds to a geometric layer thickness of 4.6 nm for the TiO_2 layer and 7.2 nm for the SiO_2 layer, respectively. The spectrum measured for this nanolaminate is depicted in Fig. 4.16A. In a second experiment, a single layer was deposited with the same material contents ratio as the stack by co-deposition involving the described IBS process with a zone target (Fig. 4.16A). By evaluating the measured spectrum of the co-deposited layer, again the particularity of ternary oxides can be observed. Obviously (see Fig. 4.16A), the transmittance limit of the co-sputtered layer is shifted toward shorter wavelengths, and the spectral behavior of the extinction coefficients (Fig. 4.16B) also indicates that a bandgap shifted by nearly 20 nm into the UV region. This pertinent shift of the bandgap toward shorter wavelengths opens the way toward the improvement of high power laser coating systems for the UV spectral range. For instance, the development of excimer lasers and frequency conversion schemes operating between 240 and 270 nm may significantly benefit from ternary layer materials consisting of the deposition materials HfO_2, Al_2O_3, and SiO_2. By considering also that further experimental results indicated improved temperature stability up to 600 °C of ternary compounds, this new class of materials has a high potential for the optimization of coatings with high LIDTs on the basis of appropriate positioning of ternary compounds in the layer system according to the internal distribution of the electric field strength. Studies (Mende et al., 2011) in such optimization strategies to enhance the power handling capability of high reflectors reveal clear improvements for the wavelength 355 nm of the frequency converted Nd:YAG-laser.

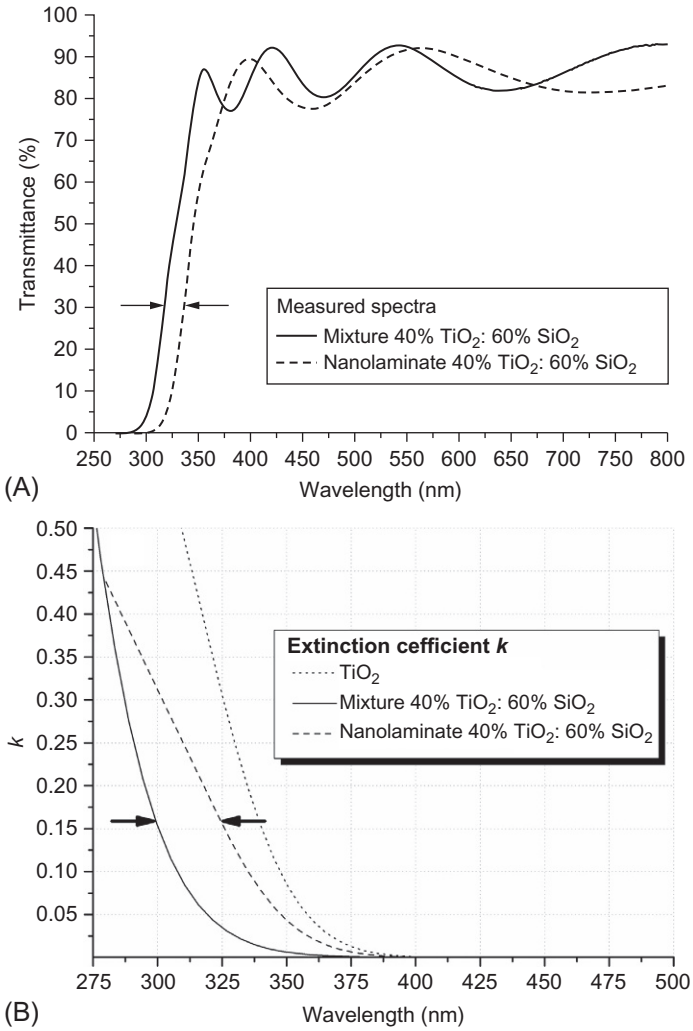


FIG. 4.16

Measured transmittance spectrum of a stack with 50 discrete alternate layers of TiO_2 and SiO_2 (nanolaminate, total thickness 297 nm) compared to a single mixture layer of the same material composition and a thickness of 430 nm (A), both: ion beam sputtering). The related extinction coefficients in comparison to pure TiO_2 are depicted in (B). Both graphs indicate a clear shift of the bandgap to lower wavelengths for the co-deposited layer (Lappschies et al., 2007).

4.8.2 DEPOSITION CONTROL OF RUGATE FILTERS

Before the background of the experimental results for discrete material mixtures, IBS processes with a zone target can be considered as a promising strategy for the reproducible production of rugate filters with complex variations in the refractive index profile. As main ingredients for a stable production of such structures, the thorough control of the refractive indices and the positioning of refractive index values in the depth of the layers have to be harnessed. In principle, an ideally continuous variation of the refractive index can be achieved by a steady motion of the zone target in front of the ion beam. However, such a strategy would imply an absolutely reproducible matching of the attained refractive index values with the target position which cannot be perfectly realized in practice. As a consequence of target erosion and intermediate oxidation effects, minute deviations in the refractive index are observed for a certain position of the zone target. This problem can be solved to an acceptable extent on the basis of the quasirugate deposition technique. In this approach, the continuous variation of the refractive index is approximated by a series of very thin discrete layers with adapted refractive indices (Lappschies et al., 2004a, 2005). An example is illustrated in Fig. 4.17B for a coating to be adapted for laser protection goggles against radiation of the Nd:YAG-laser operating at the wavelength 1064 nm as well as its harmonics at 532 and 355 nm. A rugate filter design was selected because nearly undistorted spectral transmittance had to be reached for the visible range (see Fig. 4.17A). In the present case, the refractive index profile had been resolved into a series of 1854 layers with 726 refractive index steps accumulating to a total thickness of 18.1 μm. Even though the average thickness of the constituent layers is in the range of less than 10 nm, the BBM system described before can be employed for control of the deposition process after adaptation to the zone target option. In contrast to the control of conventional processes, the BBM device moves the zone target to the next position instead of switching a shutter for layer termination. The underlying software algorithms for the determination of the switching point can be directly transferred to the control of rugate filters and allow for a compensation of small variations in the refractive index for each target position. In this configuration, the position control is regularly performed in refractive index steps of typically $\Delta n = 0.05$, which can be adjusted with a reproducibility of approximately $\Delta n \approx 0.02$. Applying this control method, a good agreement between the spectrum of the realized quasirugate filter system and the theoretical spectral performance could be achieved (see Fig. 4.17A). An omnidirectional antireflection coating centered at a wavelength of 800 nm with a spectral bandwidth of 40 nm, which covers an angle of incidence range from 0 to 55 degrees, can be found in (Becker et al., 2014) as a further example for the combination of a quasirugate approach and BBM monitoring.

Finally, a promising material approach for advanced mixture layers and rugate filters is presented. Following the materials commonly used in precision optical coatings, all examples given above are based on metal oxide material mixtures. Metal fluorides are common optical thin film materials, too, and have been mixed with oxides (Mende et al., 2014). However, approaches to novel hybrid materials by

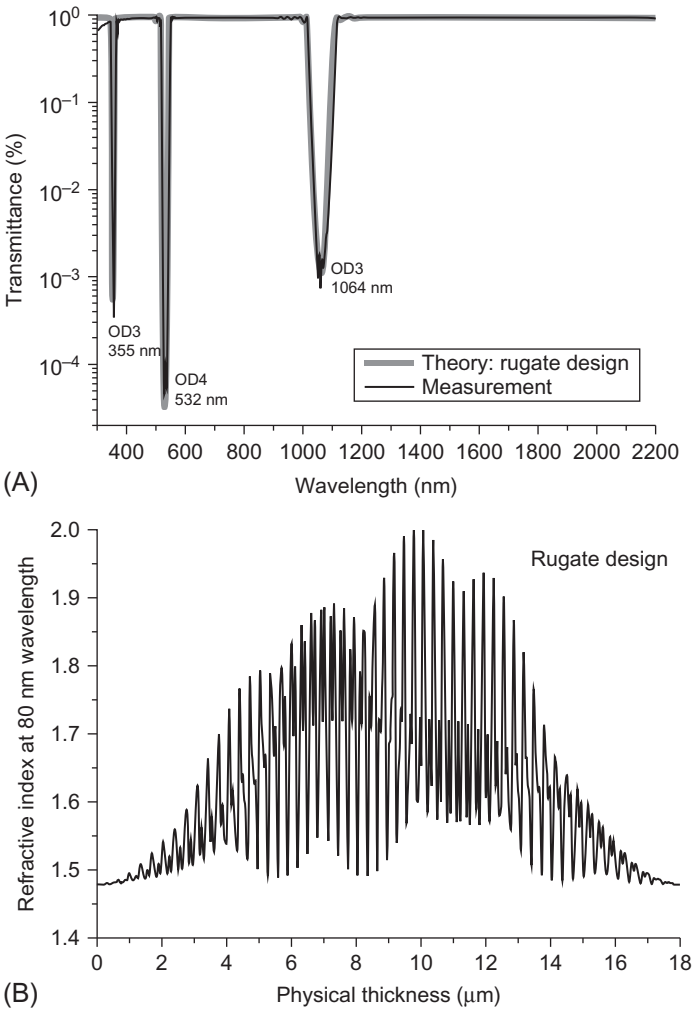


FIG. 4.17

(A) Theoretical and realized spectrum of a quasirugate filter for laser protection goggles. The coating system was produced with an IBS process employing a BBM system for controlling the position of the zone target of Ta_2O_5/SiO_2. (B) The refractive index step function followed by the BBM-tracing algorithm during deposition is illustrated.

combining different material classes also have been published. For instance, the preparation of organic-inorganic coatings by IBS co-sputtering of Al_2O_3 and PTFE from a zone target has been demonstrated (Gauch et al., 2015). In addition to the adjustable refractive index, in particular, the tunable mechanical stress of these materials enables alternative solutions for issues related to the high compressive stress of

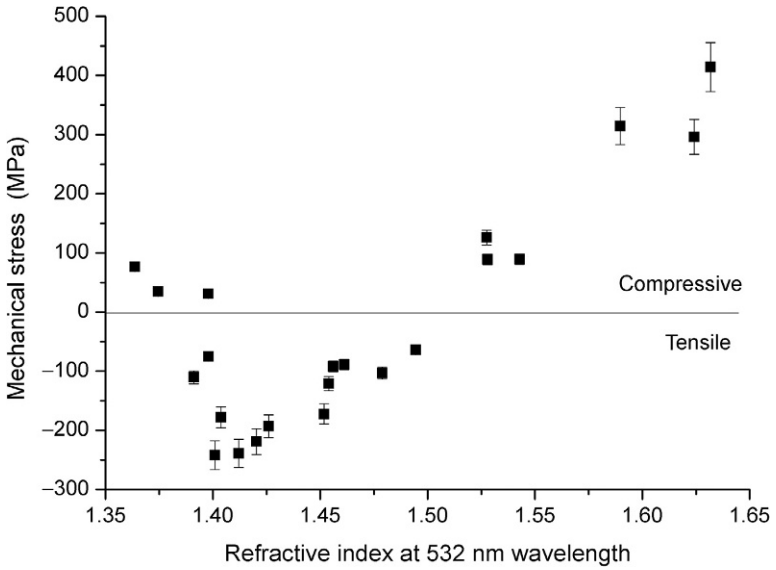


FIG. 4.18

AlOxCyFz composites deposited by IBS: Measured mechanical stress as a function of the refractive index. The C+F content of the evaluated single layers varies between 0% and ~80%. The refractive index increases nearly linearly with decreasing C+F content.

oxide IBS multilayers. Fig. 4.18 shows an example of co-sputtered PTFE and Al_2O_3 resulting in $AlO_xC_yF_z$ composite layers with C+F contents up to ~80%. Increasing the C+F content to these high values decreases the refractive indices below 1.4 at a wavelength of 532 nm. Furthermore, for C+F contents lower than 50% (refractive indices above 1.4), the optical losses are too low to be evaluated by common transmittance and reflectance measurements. In Fig. 4.18, the measured mechanical stress is plotted as a function of the refractive index. In the relevant refractive index range down to 1.4, the high compressive stress of sputtered Al_2O_3 layers decreases at first with increasing C+F content. This nearly linear decrease of compressive stress changes to a nearly linear increase of tensile stress after zero-crossing. In contrast, sputtered metal oxide mixtures still show compressive stress (Stenzel et al., 2011). Thus, by using the novel hybrid materials, advanced sputtered multilayers can benefit from low stress layers as well as from tensile low index layers for stress compensation in combination with compressive high index layers. Looking at rugate filters, an enhancement not only of optical but also of mechanical properties can be addressed. For instance, a continuous transition from pure organic material deposited at an organic surface (high adhesion) to pure oxide at the top of the gradient layer (high mechanical resistivity) works as an advanced protective layer. In summary, multilayer or rugate applications based on organic-inorganic materials could benefit in future from low mechanical stress, low refractive indices (below SiO_2 indices), and high mechanical flexibility, for example, for coatings on polymer foils.

4.9 CONCLUSION

Advanced monitoring and control concepts of high-precision optical coatings gain more and more importance on the way toward deterministic production in modern optical fabrication. The routine implementation of a variety of recently developed control approaches and tools could be realized by intensive research efforts over the last years. In most cases, direct optical in situ measurements, in particular, sophisticated optical BBMs, form the basis of these versatile and modular concepts.

Today, virtual deposition systems often replace classic design stability analysis tools, which are based only on design thickness variations. In contrast, the VDP concepts are process as well as process control specific and reproduce, for example, error accumulation or compensation effects inherently. They are not only advantageous for a reliable preproduction design stability analysis but also as a comprehensive and flexible reverse engineering tool for minimizing process development and error identification times.

Direct online correction tools can be automatically activated if critical layer thickness or dispersion data deviations occur. These software modules initialize design refinement algorithms, which calculate re-optimized designs that differ only slightly from the original target designs in most cases. However, in contrast to the original designs failing in these critical process runs, the automatically re-optimized target designs result directly in a significantly higher rate of yield. In addition, the increased yield is complemented by a gain in precision and flexibility of the manufacturing process.

Advanced hybrid monitoring concepts are a further proven approach to enhance precision and yield for complex multilayer structures. On the one hand, the conventional sequential application of different optical or nonoptical thickness monitoring systems for one multilayer stack can be extended by superior cross calibration routines. On the other hand, recent true hybrid monitoring concepts can evaluate the measured data of more than one system simultaneously for a precise and fail-safe end point detection.

A maximum impact on precision, flexibility, and yield is achieved if the approaches summarized above are combined within a production environment. As shown by the practical examples, even extremely critical multilayer designs can be deposited successfully if multiple advanced monitoring and control concepts are applied. However, this multiconcept approach requires not necessarily a complex hardware basis as could be demonstrated. All discussed approaches allow for rapid manufacturing without the need for developing multilayer design dependent individual monitoring strategies.

Material mixtures produced by co-deposition processes and rugate filters with an arbitrary continuous variation of the refractive index in depth are a particular challenge for adapted production strategies. Ternary oxides as material mixtures represent a new class of materials with individual properties and can be applied to realize rugate filters, which offer new degrees of freedom in the design of optical coatings. However, on the basis of an IBS process with a zone target, quasirugate filters can be successfully manufactured under optical broadband monitoring. In the quasirugate

filters, very thin discrete layers with very small refractive index steps substitute the continuous variation of the refractive index.

Besides further technological improvements in the control devices and software environments, an advanced approach toward deterministic production processes would involve a direct modeling of thin film growth. In this visionary concept, theoretical calculations on the basis of molecular dynamic techniques and quantum mechanics may be employed to determine the structural and optical properties of the growing coating from the specific parameters of a deposition process. Conversely, a forecast of the needed process parameters to achieve a certain set of coating properties may come into reach for harnessing high-quality optical coating production according to future demands.

REFERENCES

Amotchkina, T.V., Ristau, D., Lappschies, M., Jupé, M., Tikhonravov, A.V., Trubetskov, M.K., 2007. Optical properties of TiO2—SiO2 mixture thin films produced by ion-beam sputtering. Optical Interference Coatings. OSA Technical Digest TuA8.

Amotchkina, T.V., Trubetskov, M.K., Pervak, V., Schlichting, S., Ehlers, H., Ristau, D., Tikhonravov, A.V., 2011. Comparison of algorithms used for optical characterization of multilayer optical coatings. Appl. Optics 50, 3389–3395.

Amotchkina, T.V., Schlichting, S., Ehlers, H., Trubetskov, M.K., Tikhonravov, A.V., Ristau, D., 2012. Computational manufacturing as a key element in the design-production chain for modern multilayer coatings. Appl. Optics 51 (31), 7604–7615.

Anzengruber, S.W., Klann, E., Ramlau, R., Tonova, D., 2012. Numerical methods for the design of gradient-index optical coatings. Appl. Optics 51, 8277–8295.

Bauer, H.H., Nüssler, E., 1994. In-situ optical multichannel spectrometer system. SPIE 2253, 423–431.

Becker, H., Tonova, D., Sundermann, M., Ehlers, H., Günster, S., Ristau, D., 2014. Design and realization of advanced multi-index systems. Appl. Optics 53, A88–A95.

Bernhard, C.G., 1967. Structural and functional adaptation in a visual system. Endeavor 26, 79–84.

Carstens, F., Ehlers, H., Ristau, D., 2016. In: Approaches to an adaptive ion-beam sputtering process. Optical Interference Coatings 2016. OSA Technical Digest. WA.4.

Chao, S., Wang, W.-H., Hu, M.-Y., Wang, L.-C., 1999. Characteristics of ionbeam-sputtered high-refractive-index TiO 2-SiO2 mixed films. J. Opt. Soc. Am. A 16 (6), 1477–1483.

Chtanov, A., Dligatch, S., Gross, M., 2010. In: Multi-wavelength laser Ellipsometer for in situ monitoring of optical coatings. O*ptical Interference Coatings*. OSA Technical Digest, p. TuC7.

Ehlers, H., Ristau, D., 2013. Progress in optical monitoring. Optical Interference Coatings. OSA Technical Digest. WB.1.

Ehlers, H., Schlichting, S., Schmitz, C., Ristau, D., 2010. Adaptive manufacturing of high precision optics based on virtual deposition and hybrid process control techniques. Chin. Opt. Lett. 8, 62–66.

Ehlers, H., Schlichting, S., Schmitz, C., Ristau, D., 2011. in: Macleod, A., Lequime, M., Ristau, D. (Eds.), From independent thickness monitoring to adaptive manufacturing:

advanced deposition control of complex optical coatings, [8168–71]. Advances in Optical Thin Films IV Marseille, France, 5–7 September Proceedings of SPIE, Vol. 8168.
Emiliani, G., Piegari, A., Masetti, E., 1988. Fast scan spectrometer for monitoring of thin film optical properties. SPIE 1012, 35–46.
Gauch, M., Ehlers, H., Ristau, D., 2015. In: Properties of transparent organic-inorganic composite coatings prepared by ion beam sputtering of PTFE and Al_2O_3.SPIE Advances in Optical Thin Films V, 9627:96270F.
Günster, S., Kadkhoda, P., Ristau, D., 2001. Online spectrophotometric characterisation of MgF2/LaF3—fluoride multilayer coatings production. In: Proceedings of the Conference on Optical Interference Coatings. OSA Technical Digest, pp. ME9–1.
Günster, S., Ristau, D., Davies, R., 2011. In: Band-pass and OH-suppression filters for the E-ELT: design and prototyping.Proc. SPIE 8168, Advances in Optical Thin Films IV, 81681Y.
Hendrix, K., 2017. Linear variable filters for NASA's OVIRS instrument: pushing the envelope of blocking. Appl. Optics 56, C201–C205.
Holm, C., 1979. Optical thin film production with continuous reoptimization of layer thicknesses. Appl. Optics 18, 1978–1982.
Jupé, M., Jensen, L., Melninkaitis, A., Sirutkaitis, V., Ristau, D., 2009. Calculations and experimental demonstration of multi-photon absorption governing fs laserinduced damage in titania. Opt. Express 17 (15), 12269–12278.
Katagiri, Y., Ukita, H., 1990. Ion beam sputtered (SiO2)X (Si3N4)1-X antireflection coatings on laser facets produced using O 2-N2 discharges. Appl. Optics 29 (34), 5074–5079.
Lappschies, M., 2009. Rugate Filter und Mischschichten für optische Hochleistungskomponenten. dissertation. Leibniz Universität, Hannover.
Lappschies, M., Görtz, B., Ristau, D., 2004a. Application of optical broad band monitoring to quasi-rugate filters by ion beam sputtering. Appl. Optics 45 (7), 1502–1506.
Lappschies, M., Groß, T., Ehlers, H., Ristau, D., 2004b. In: Broadband optical monitoring for the deposition of complex coatings.Proceedings of the Conference on Advances in Optical Thin Films, St. Etienne, France, SPIE, vol. 5250, pp. 637–645.
Lappschies, M., Görtz, B., Ristau, D., 2005. In: Mazuray, L., Wartmann, R. (Eds.), Optical monitoring of rugate filters.Optical Design and Engineering II, Proc. of SPIE, vol. 5963, 1Z1–1Z9.
Lappschies, M., Jupé, M. and Ristau, D. (2007). 'Extension of ion beam sputtered oxide mixtures into the UV spectral range', Optical Interference Coatings, OSA Technical Digest, TuA7.
Lappschies, M., Schallenberg, U., Jakobs, S., 2011. Exclusive examples of highperformance thin-film optical filters for fluorescence spectroscopy made by plasma-assisted reactive magnetron sputtering. In: Lequime, M., Macleod, H.A., Ristau, D. (Eds.), Advances in Optical Thin Films IV.Proceedings of SPIE, vol. 8168 81680Y.
Lappschies, M., Weber, T., Venancio, L. M. and Jakobs, S. (2016). 'Advanced dielectric coatings for the Euclid mission telescope manufactured by the PARMS process', Optical Interference Coatings, OSA Technical Digest, MC.2.
Leitel, R., Stenzel, O., Wilbrandt, S., Gäbler, D., Janicki, V., Kaiser, N., 2005. Fabrication and characterization of rugate structures composed of SiO 2 and Nb2O5. Opt. Precis. Eng. 13 (4), 505–511.
Lyngnes, O., Brauneck, U., Wang, J., Erz, R., Kohli, S., Rubin, B., Kraus, J., Deakins, D., 2015. In: Optical monitoring of high throughput ion beam sputtering deposition.Proc. SPIE 9627, Advances in Optical Thin Films V. 962715.

Mangote, B., Gallais, L., Commandré, M., Mende, M., Jensen, L., Ehlers, H., Jupé, M., Ristau, D., Melninkaitis, A., Mirauskas, J., Sirutkaitis, V., Kičas, S., Tolenis, T., Drazdys, R., 2012. Femtosecond laser damage resistance of oxide and mixture oxide optical coatings. Opt. Lett. 37, 1478–1480.

Masetti, E., Montecchi, M., Larciprete, R., Cozzi, S., 1996. In situ monitoring of film deposition with an ellipsometer based on a four-detector photopolarimeter. Appl. Optics 35 (28), 5626–5629.

Mende, M., Jensen, L.O., Blaschke, H., Ehlers, H., Ristau, D., 2011. In: Macleod, A., Lequime, M., Ristau, D. (Eds.), Laserinduced damage of pure and mixture material high reflectors for 355-nm and 1064-nm wavelength, [8168–73].Conference on Advances in Optical Thin Films IV, Proc. SPIE, vol. 8168, 816821.

Mende, M., Balasa, I., Ehlers, H., Ristau, D., Douti, D., Gallais, L., Commandré, M., 2014. Relation of optical properties and femtosecond laser damage resistance for Al_2O_3/AlF_3 and Al_2O_3/SiO_2 composite coatings. Appl. Optics 53, A383–A391.

Mende, M., Kohlhaas, J., Ebert, W., 2016. High power coatings for line beam laser optics of up to 2-meter in length. In: Proc. SPIE 9730, Components and Packaging for Laser Systems II. 973015.

Netterfield, R.P., 2005. Ellipsometric monitoring of multilayer coatings. In: Proc. SPIE 5870, Advances in Thin-Film Coatings for Optical Applications II. 58700A.

Netterfield, R.P., Martin, P.J., Müller, K.-H., 1988. In-situ optical monitoring of thin film deposition. SPIE 1012, 10–15.

Pinard, L., Michel, C., Sassolas, B., Balzarini, L., Degallaix, J., Dolique, V., Flaminio, R., Forest, D., Granata, M., Lagrange, B., Straniero, N., Teillon, J., Cagnoli, G., 2017. Mirrors used in the LIGO interferometers for first detection of gravitational waves. Appl. Optics 56, C11–C15.

Powell, I., Zwinkels, J.C.M., Robertson, A.R., 1986. Development of optical monitor for control of thin-film deposition. Appl. Optics 25 (20), 3645.

Rademacher, D., Vergöhl, M., Richter, U., 2011. In situ thickness determination of multilayered structures using single wavelength ellipsometry and reverse engineering. Appl. Optics 50 (9), C222–C227.

Razskazovskaya, O., Krausz, F., Pervak, V., 2017. Multilayer coatings for femto- and attosecond technology. Optica 4 (129–138), 1–129.

Rickers, C., Polenzky, C., Vergöhl, M., 2006. Deposition of rugate filters by magnetron sputtering technology.Proceedings of the 6th International Conference on Coatings on Glass and Plastics, 18–22 June 2006, Dresden, Germany.

Ristau, D., 2010. In: Ion beam sputtering—state of the art and industrial application.Proceedings of the 8th International Conference on Coatings on Glass and Plastics, pp. 203–208.

Ristau, D., Groß, T., 2005. In: Mazuray, L., Wartmann, R. (Eds.), Ion beam sputter coatings for laser technology.Optical Design and Engineering II, Proc. SPIE, vol. 5963, pp. 315–326.

Ristau, D., Günster, S., 2003. In: Optimization of optical coatings for the UV/VUV-range.Proceedings of the Conference on Advanced Characterization Techniques for Optics, Semiconductors, and Nanotechnologies, San Diego, USA, SPIE, vol. 5188, pp. 80–95.

Ristau, D., Schink, H., Mittendorf, F., Akhtar, S.M.J., Ebert, J., Welling, H., 1988. In: Bennett, H.E., Guenther, A.H., Newnam, B.E., Soileau, M.J. (Eds.), Laser induced damage of dielectric systems with gradual interfaces at 1.064 μm.Proceedings of the Conference on Laser-Induced Damage in Optical Materials NIST Spec. Publ. No.775, Boulder, USA, 26–28 October, pp. 414–426.

Ristau, D., Groß, T., Lappschies, M., Ehlers, H., 2006. Optical broadband monitoring of conventional and ion processes. Appl. Optics 45 (7), 1495–1501.

Ristau, D., Lappschies, M., Schlichting, S., Ehlers, H., 2008. In: Kaiser, N., Lequime, M., Macleod, H.A. (Eds.), State of the art in deterministic production.Advances in Optical Thin Films III, Glasgow, UK, 2–3 September, Proceedings of SPIE, vol. 710, 71010C–71010C-141.

Schlichting, S., Heinrich, K., Ehlers, H., Ristau, D., 2011. Online re-optimization as a powerful part of enhanced strategies in optical broadband monitoring. Proc. SPIE. 8168. 81681E.

Schlichting, S., Willemsen, T., Ehlers, H., Morgner, U., Ristau, D., 2016. Fourier-transform spectral interferometry for in situ group delay dispersion monitoring of thin film coating processes. Opt. Express 24, 22516–22527.

Schlick, M., 1904. Über die Reflexion des Lichtes in einer inhomogenen Schicht. Dissertation, Berlin.

Schröder, H., 1941. Bemerkung zur Theorie des Lichtdurchgangs durch inhomogene durchsichtige Schichten. Ann. Phys. 5 (39), 55.

Southwell, W.H., 1985. Coating design using very thin high- and low-index layers. Appl. Optics 24 (4), 457.

Starke, K., Ristau, D., 2011. In: Highly stability optical coatings by employing gradient index designs.Proceedings of the 54th Annual Technical Conference Proceedings of the Society of Vacuum Coaters, Chicago, Il, pp. 463–467. ISSN 0737–5921.

Starke, K., Groß, T., Ristau, D., 2000. In: Rapid prototyping of optical thin film filters.Conference Optical and Infrared Thin Films, SPIE. vol. 4094. pp. 83–92.

Stenzel, O., Wilbrandt, S., Schürmann, M., Kaiser, N., Ehlers, H., Mende, M., Ristau, D., Bruns, S., Vergöhl, M., Stolze, M., Held, M., Niederwald, H., Koch, T., Riggers, W., Burdack, P., Mark, G., Schäfer, R., Mewes, S., Bischoff, M., Arntzen, M., Eisenkrämer, F., Lappschies, M., Jakobs, S., Koch, S., Baumgarten, B., Tünnermann, A., 2011. Mixed oxide coatings for optics. Appl. Optics 50, C69–C74.

Sullivan, B.T., 2010. In: An overview of optical monitoring techniques. *Optical Interference Coatings*. OSA Technical Digest. TuC1.

Sullivan, B.T., Dobrowolski, J.A., 1993. Deposition error compensation for optical multilayer coatings: II. experimental results-sputtering system. Appl. Optics 32 (13), 2351.

Sytchkova, A., Vernhes, R., Baloukas, B., Grilli, M.L., Martinu, L., Piegari, A.M., 2016. Ellipsometric monitoring of the refractive index evolution versus temperature for various metal oxides commonly used in interference filters. In: Optical Interference Coatings. OSA Technical Digest (Optical Society of America). paper WC.2.

Tikhonravov, A.V., Trubetskov, M.K., Amotchkina, T.V., 2006. Investigation of the effect of accumulation of thickness errors in optical coating production by broadband optical monitoring. Appl. Optics 45, 7026–7034.

Tikhonravov, A.V., Trubetskov, M.K., Amotchkina, T.V., 2011. Investigation of the error self-compensation effect associated with broadband optical monitoring. Appl. Optics 50, C111–C116.

Tilsch, M., Scheuer, V., Staub, J., Tschudi, T., 1994. Direct optical monitoring instrument with double detection system for the control of multilayer systems from the visible to the near infrared. SPIE 2253, 414–422.

Tilsch, M.K., Grigonis, M., Ockenfuss, G.J., 2010. Manufacturing of precision optical coatings. Chin. Opt. Lett. 8 (Supplement), 38–43.

van Milligen, F.J., Macleod, H.A., 1985. Development of an automated scanning monochromator for monitoring thin films. Appl. Optics 24 (12), 1799.

Verly, P.G., Dobrowolsky, J.A., Wild, W.J., Burton, R.L., 1989. Synthesis of high rejection filters with the Fourier transform method. Appl. Optics 28, 2864–2875.

Vidal, B., Fornier, A., Pelletier, E., 1978. Optical monitoring of nonquarterwave multilayer filters. Appl. Optics 17 (7), 1038.

Vidal, B., Fornier, A., Pelletier, E., 1979. Wideband optical monitoring of nonquarterwave multilayer filters. Appl. Optics 18 (22), 3851.

Waldner, S., Padrun, M., 2013. In: Assessing the suitability of coating designs for in-process reoptimization. Optical Interference Coatings. OSA Technical Digest. WB.7.

Willemsen, T., Schlichting, S., Gyamfi, M., Jupé, M., Ehlers, H., Morgner, U., Ristau, D., 2016. Improved LIDT values for dielectric dispersive compensating mirrors applying ternary composites.Proc. SPIE 10014, Laser-Induced Damage in Optical Materials, 100141Z.

Zöller, A., Boos, M., Hagedorn, H., Romanov, B., 2008. In: Kaiser, N., Lequime, M., Macleod, H.A. (Eds.), Computer simulation of coating processes with monochromatic monitoring.Proceedings of the SPIE, Advances in Optical Thin Films III, vol. 7101, 71010G–71010G-7.

FURTHER READING

Amotchkina, T.V., Schlichting, S., Ehlers, H., Trubetskov, M.K., Tikhonravov, A.V., Ristau, D., 2012b. Computational manufacturing as a tool for the selection of the most manufacturable design. Appl. Optics 51 (36), 8677–8686.

Jasapara, J., Nampoothiri, A.V.V., Rudolph, W., Ristau, D., Starke, K., 2001. Femtosecond laser pulse induced breakdown in dielectric thin films. Phys. Rev. B. 63 (4). 045117.

Jensen, L., Mende, M., Blaschke, H., Ristau, D., Nguyen, D., Emmert, L., Rudolph, W., 2010. In: Exarhos, G.J., Gruzdev, V.E., Menapace, J.A., Ristau, D., Soileau, M.J. (Eds.), Investigations on SiO 2/HfO2 mixtures for nanosecond and femtosecond pulses. Proceedings of the 42nd Annual Symposium on Optical Materials for High Power Lasers, Proceedings of SPIE, vol. 7842.

Nguyen, D.N., Cravetchi, I., Rudolph, W., Jupe, M., Lappschies, M., Starke, K., Ristau, D., 2007. In: Experimental and theoretical studies of subpicosecond laser damage in TixSi1-xO2 composite films.Proceedings of SPIE, Vol. 6720, 64031A.

Ristau, D., 2011. In: Optical thin films with high laser stability. Proceedings of the 54th Annual Technical Conference Proceedings of the Society of Vacuum Coaters, Chicago, IL, pp. 276–282. ISSN-0737–5921.

PART

II

Unconventional features of optical thin films and coatings

This page intentionally left blank

CHAPTER

Complex materials with subwavelength inclusions for optical thin film applications

5

Anna Sytchkova
ENEA Optical Components Group, Rome, Italy

5.1 INTRODUCTION

This chapter was born as an overview of recent results on modeling and characterization of novel materials with plasmonic properties for thin film applications. Since the first edition of the book, time has revealed alternative approaches to engineering of complex material useful to this end. Now the chapter also contains material on resonating inclusions in which functionality is not plasmonic-based, yet keeps its initial main structure.

So we start again with a historical note on the birth of plasmonics: in the beginning of the 1960s, McAlister and Stern (1963) demonstrated that absorption bands in reflection and transmission spectra of very thin metal films illuminated by *p*-polarized light at oblique incidence are due to excited resonances normal to the film plane. Such collective longitudinal optical modes were previously theoretically explained by Ritchie (1957) after the experimental observation of Ferrell in electron energy loss spectroscopy of a thin metal slab (Ferrell, 1958). The so-called Ferrell modes in metals are nowadays also known as volume or bulk plasmons; they are collective oscillations of free electrons at a frequency ω_p that can propagate in a material when its dielectric function $\varepsilon_c(\omega_p)$ approaches zero.

Bulk plasmon is a radiative mode decaying after excitation by spontaneous emission or due to collision damping. However, if coupled to the incident photon, this mode becomes propagating with the wave vector of the photon and forms a so-called plasmon polariton (PP). In continuous metal films (or semiconductor in a free-electron regime), PPs are not forbidden only if they are surface-bound; they are known as surface plasmon polaritons (SPPs) or simply as surface plasmons (SPs). Surface plasmons may exist in a conductor only if its dielectric function ε_c has a negative real part $\varepsilon_c' \equiv \mathrm{Re}\ \varepsilon_c < 0$, and these SPs have a well-pronounced resonance appearance when the optical losses in the material are low, which means when the imaginary part of the dielectric function is small $\varepsilon_c'' \equiv \mathrm{Im}\ \varepsilon_c \ll -\mathrm{Re}\ \varepsilon_c$. In different ranges of the optical spectrum, either metals or semiconductors may satisfy these two criteria simultaneously and thus be good plasmonic materials. Various

Optical Thin Films and Coatings. https://doi.org/10.1016/B978-0-08-102073-9.00005-9
Copyright © 2018 Elsevier Ltd. All rights reserved.

types of collective electron excitations may be rigorously described like the many-body dynamical electronic response of solids to electromagnetic radiation (Pitarke et al., 2007).

SPs can be excited at a plane dielectric-conductor interface by means of matching techniques like prism or grating, and at some well-determined conditions on incidence angle and dielectric function properties of both interfacing materials. With change of the conductor's geometry, that is, when moving from a planar to a spherical shape, the incidence angle ceases to determine resonance excitation for symmetry reasons. Localized SP resonances (LSPRs), known also as localized SPPs, localized SPs, or Mie PPs, can be excited at the surface of metal or semiconductor particles embedded in a less conducting host material even at arbitrary incidence. This phenomenon determines colors of artistic glasses with metal particle suspension, the effect known and exploited since antiquity (Freestone et al., 2007).

Plasmonic conductors shaped into tiny volumes called nanoparticles (NPs) and embedded in dielectric material, or introduced as ultrathin films into multilayers, are the subject of intense research in the past decade and a half (Zhang and Zhang, 2012). If the inclusions are periodically organized, it is common to speak about metamaterials (MMs). Continuously increasing interest in such composites is due to their outstanding capability to concentrate electromechanical energy at optical frequencies onto nanoscale overcoming the theoretical limits for optical confinement valid for electromagnetic energy (Stockman, 2011). Enhancement it enables provides a unique platform for next-generation photonic devices (Maier and Atwater, 2005; Feng and Fainman, 2011) and ensures technological revolution in many fields of life science, for example, Pradeep and Anshup (2009). By variation of NP doping (Luther et al., 2011), size and shape (Kazuma et al., 2009; Kelly et al., 2003), as well as by a suitable choice of host (Kubo et al., 2007), substrate (Sheng and Varadan, 2007), or gain (Nezhad et al., 2004) material, novel artificial materials with particular optical properties may be engineered thanks to a proper tuning of SPs, localized or propagating.

On the other hand, diffracting and scattering properties of NPs may be exploited equally well for NPs composed of dielectric materials; in this case, we deal with so-called all-dielectric MMs. Local phase shift induced by optical resonators, which enables control of light propagation at a nanoscale, may have both pure scattering nature and mixed scattering-plasmonic nature (Genevet et al., 2017; Lalanne and Chavel, 2017). Depending on the application, designers may vary material composition (Yang and Fan, 2017; Zhu et al., 2017) and NP matrix duty cycle (Collin, 2014), profiting from dielectrics' transparency while mitigating or gaining from plasmonic materials' absorption (Boriskina et al., 2017).

Various bottom-up and top-down synthesis methodologies are used for the creation of thin films with NPs, including lithographic techniques (Jain et al., 2007; Pedersen et al., 2007), focused-ion-beam milling (Enkrich et al., 2005), electrochemical methods (Yu et al., 1997), self-assembling from colloidal solutions (Hammond, 2004; Fan et al., 2010), and direct laser writing (Formanek et al., 2006). Physical vapor deposition (PVD) methods are common for many applications too; despite

a relatively poor control of the NP size and spacing they provide, these methods have advantages of being compatible with most substrates of technological interest and with most technologies for nanoplasmonic device manufacturing. The same PVD methods, that is, sputtering (Sytchkova et al., 2013), thermal and electron-beam evaporation (Sahu et al., 2008), laser ablation (Ko et al., 2006), etc. are used for fabrication of multilayer devices with ultrathin metal film with SP properties. An extensive review of different fabrication methods of MMs can be found in Boltasseva and Shalaev (2008).

5.2 PHYSICS OF SOME CLASSES OF NOVEL MATERIALS WITH SUBWAVELENGTH INCLUSIONS

Whether propagating or localized, SPs are waves on the surface of a conductor (metal or semiconductor) interfaced with another less conducting material (semiconductor or dielectric). Therefore, to understand the optical properties of plasmonic media, it is essential to know the physical properties of their basic constituent materials.

Notice that nanostructured inclusions radically change the dispersion relation of the original host material. In fact, thanks to this, MMs are the media with the ad hoc engineered photonic density of states (Jacob et al., 2010).

In the visible and infrared regions, most MMs are strongly dispersive, and the origin of this dispersion is mostly ascribed to the conductor component. Conversely, what dramatically determine the optical performance of a multilayer stack with an ultrathin continuous or semicontinuous layer(s) of a conductor material are the optical properties of the conductor material. Many classical textbooks are dedicated to the optical properties of dielectrics and, as far as the key materials for plasmonic materials are conductors, let us focus our attention on optical features of metals and semiconductors.

Macroscopically, the complex dielectric function $\varepsilon_c(\omega)=\varepsilon_c{}'+\mathrm{i}\varepsilon_c{}''=(n+\mathrm{i}k)^2$ totally describes the electronic response of a conductor to the electromagnetic wave with frequency ω. Here n is the material refractive index and k is its extinction coefficient. The modified Drude approximation is normally used to model the dielectric function of a conductor:

$$\varepsilon_c(\omega)=\varepsilon_\infty-\frac{\omega_p^2}{\omega(\omega+\mathrm{i}\gamma)},\quad \omega_\mathrm{p}^2=\frac{Ne^2}{\varepsilon_0 m^*} \tag{5.1}$$

Here γ is the phenomenological damping term, ω_p is the plasma frequency, N is the conduction electron density, m^* is the effective optical mass of conduction electrons, and ε_0 is the permittivity of vacuum. The offset ε_∞ is "core polarizability" of the material that encompasses contributions due to the interband transitions of bound electrons (single-particle excitations from valence to conduction bands). This term is taken equal to unit for metals in the free-electron regime (classical Drude model), while it is not a unity parameter for the description of conductors at higher frequencies.

As we see, to guarantee a negative dielectric permittivity, the carrier concentration should be high enough. To ensure good plasmonic performance, not only is the sign of $\varepsilon_c{}'$ important, but also the low level of losses, which means high mobility of the carriers and low interband losses (we will consider this issue in detail below). The ideal conductor for plasmonics would have the corresponding indicator maximally left-shifted along the carrier mobility axis and positioned on the horizontal zero-interband-transition plane (Boltasseva and Atwater, 2011), Fig. 5.1.

More precisely, from the point of view of electronic features, for a material to be good for plasmonic applications, it should possess four main properties (Blaber et al., 2010a): (i) the energy bands at the Fermi level must have a gradient sufficiently high to ensure an appropriate ω_p; (ii) all scattering types (including electron-electron, electron-phonon, surface and defect interactions) represented by γ must be low so that $\gamma \ll \omega_p$; (iii) the "core polarizability" ε_∞ must be low; (iv) the ratio ω_g/ω_p, where ω_g is the optical gap, should be proportional to the sharpness of the band edge $\varepsilon_c{}''(\omega_g)$. Notice that interband transitions provoke screening in real conductors, thus shifting the plasma frequency from the value ω_p. Therefore, condition (iv) also means that the screened plasma frequency ω_s should be well separated from the optical gap, that is, the ratio ω_g/ω_s must be low.

A few comments about the physics of all-dielectric MMs. The use of Mie-type resonances in dielectric subwavelength inclusions has been becoming mainstream in metamaterial research for photonic applications (Baranov et al., 2017). Magnetic

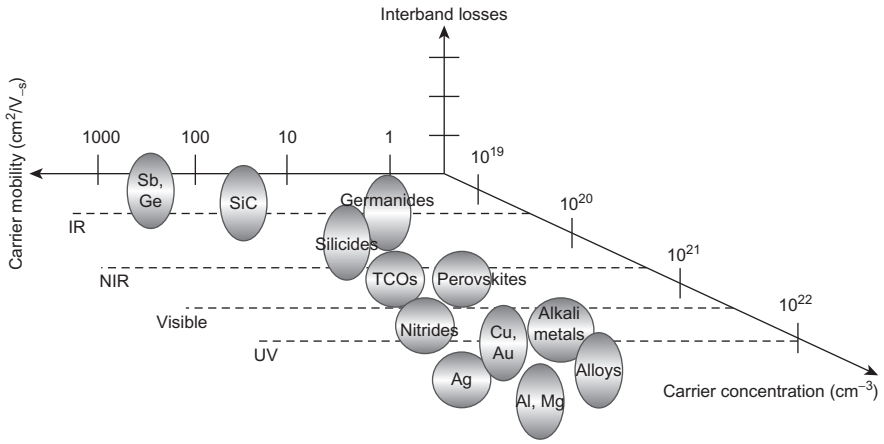


FIG. 5.1

Carrier concentration and mobility, together with interband transition losses, can be optimized by a proper choice of material for a given application. The heights of the bubbles representing the main plasmonic materials indicate their interband losses in the corresponding part of the spectrum.

Figure similar to that in Boltasseva, A., Atwater, H.A., 2011. Low-loss plasmonic metamaterials, Science 331, 290–291. https://doi.org/10.1126/science.1198258. Copyright 2011, AAAS.

response at a nanoscale is emulated through inducing displacement current in high-index dielectric particles, as the displacement current produces a magnetic dipole moment. Different scattering models should be used depending on the ratio between the particle size and the wavelength. If this ratio is much smaller than 1, we talk about Rayleigh scattering. With this ratio increase, the first magnetic type dipole resonance is formed, followed by the first electric type dipole for even higher ratios. For the particles comparable with the wavelength, eigenmodes of higher orders are excited.

The design of the absorption bands of all-dielectric nanostructured materials with regular inclusions like spheres or cylinders is simplified by the fact that the resonance wavelengths can be promptly calculated analytically or numerically. Additionally, all-dielectric structures do not suffer from high absorption typical of plasmonic structures, the problem compromising the applicability of plasmonic structures in the visible. Moreover, fabrication of spherical and cylindrical nanoparticles of high-index dielectrics like silicon may be significantly easier compared to many resonating plasmonic structures, as far as this type of structuring is typical of modern silicon photonics technologies.

To conclude this paragraph, let us recall that all after all, the choice of both material and geometry of nano-inclusions for a given photonic application is dictated by interband transitions in both plasmonic and dielectric resonating nanoparticles (Toudert and Serna, 2017).

5.3 CERAMIC MATRIX WITH EMBEDDED NANOSTRUCTURES

This section considers the influence of geometrical factors on the optical properties of materials with subwavelength inclusions. There are essentially four factors: the size and the shape of inclusions, the particle interdistance, and the type of their distribution within the host material, either periodic or random.

First of all, we shall distinguish between the case of NP inclusions distributed within the volume of the host material, either a bulk or a thin film, and, on the other hand, the case of stratified structures containing layers with NP inclusions or thin metallic layers, in particular, ultrathin (partially) percolated metallic layers. Only the case of metal layers deals with propagating SPs (or SPPs). For all metallic structures, localized SPs (LSPs) are inherent, and for dielectric nanoparticles, localized Mie-type resonances should be considered.

The size scale of subwavelength metal particles determines the theoretical approach proper for calculation of the electromagnetic field in the material. While for the systems with an NP size much smaller than the wavelength of light, but larger than the mean free path of the oscillating electrons (typically about 30–50 nm), the quasi-static approximation may be successfully used to describe the polarizability of a metallic sphere; for smaller or bigger particles, significant corrections are needed. In particular, retardation effects in larger particles bring to a corrected expression (Kuwata et al., 2003) for the material polarizability, while for much smaller NPs a purely classical model is not valid anymore as far as quantum effects begin to set in.

To get an idea what particle sizes we are speaking about, let us refer to silver nanospheres, the simplest NP geometry of most commonly used plasmonic material. For the spheres of radius a such that $10\ \text{nm} < a \ll \lambda$, the quasi-static approach is valid. For larger particles, the phenomena to take into account are the depolarization field inside the NPs on the one hand (Meier and Wokaun, 1983), the radiation damping caused by the radioactive decay of electron oscillations into photons on the other hand (Kokkinakis and Alexopoulos, 1972), as well as nonradiative decay due to intraband excitations within the conduction band and interband transitions (Link and El-Sayed, 2000).

For smaller particles having $a < 10\ \text{nm}$, the so-called "chemical interface damping" due to elastic scattering at the particle surface must be considered (Kreibig and Vollmer, 1995). For even smaller particles with $a \leq 1\ \text{nm}$, a combination occurs of the large concentration of conduction electrons typical of metals ($\upsilon \approx 10^{23}\ \text{cm}^{-3}$) with the small absolute number of electrons $N \approx \upsilon a^3$. This results in comparability of the energy increase of an electron excited by a photon with its kinetic energy, that is, $hc/(\lambda N) \sim k_B T$, where T is the temperature and k_B is the Boltzmann constant. Therefore, for such small particles, plasmons as collective oscillations of electrons cannot adequately represent the mechanisms of light-matter interaction, and multiple-particle excitations should be considered using the language of quantum mechanics (Kreibig and Vollmer, 1995).

Interparticle distance δ scales naturally with the particle size. For well-separated NPs (with $a \ll \delta$), the dipolar approximation is valid for the description of LSP coupling. The dipole interaction has significantly different behavior for the case of closely positioned NPs ($\delta \ll \lambda$) and for the case of well-separated NPs. In the first case, the far field follows δ^{-3} dependence caused by the prevailing near-field character if the interaction and strong field localization in interparticle gaps take place (Krenn et al., 1999), while for well-separated NPs the interference pattern is observable in the near field, the far field behaves with the distance dependence of δ^{-1}, and the interspacing $\delta \sim 3a$ results are sufficient to enter in the regime of essentially isolated NPs (Maier et al., 2002).

5.3.1 MATERIALS WITH QUANTUM DOTS

When the size of NP inclusions in a medium is comparable with the de Broglie wavelength of an electron, it is common to speak about quantum dots (QDs) in a host matrix. Localized SPs of metal QDs are charge density oscillations of metal free electrons in resonance with the driving electromagnetic field of the incident light. For a given host matrix where QDs are embedded, the LSP resonance (LSPR) frequency is tunable by the QD size and geometry, but mainly depends on free electron density of the metal, value modulated by the high-frequency dielectric constant ε_∞ (Pérez-Juste et al., 2005).

QDs are distributed either randomly (Ficcadenti et al., 2009) or periodically (Maier et al., 2003), depending on application; the peculiarity of such nanostructured materials consists in the fact that the SP oscillations should be considered in terms of

quantum mechanics, for example, applying quantum wells as the first theoretical model (Flory et al., 2011a; Flory et al., 2011b). In fact, conventional plasmons in a nanohole array or a metal strip were experimentally proved to possess properties that are essentially quantum, like entanglement (Fasel et al., 2005) and squeezing (Huck et al., 2009). Within the quantum mechanics approach, the squared modulus of the electron wave function provides probability of the electron or hole density distribution. For a series of coupled periodic wells, the energy levels of the single well are split, and we deal with energy bands when the number of coupled wells becomes large. The electrons can be localized or delocalized, like in molecules, if the wells are not equidistant. For nanostructures with elementary geometries that support elementary plasmons, a hybridization model was developed by Prodan et al. (2003) as an electromagnetic analog of molecular orbital theory.

The importance of QD geometries for future nanoscale quantum information processing (Akimov et al., 2007) or fundamental research of quantum effects (Gómez et al., 2010) is determined by the ability of these isolated broadband emitters to interact exceptionally well with plasmons in bigger nanostructures. Near a metallic nanowire, an excited QD with high probability spontaneously emits a single photon into the plasmonic mode and, despite the decoherence expected due to electron collisions, the plasmon will carry the quantum bit of the exciting photon and transmit it in the back-conversion into a photon. Controlled addressing of QDs by nanowire plasmons becomes possible (Gruber et al., 2012). Moreover, the emission wavelength of QDs may be tuned over dozens of nanometers by employing SPPs (Moerland et al., 2012). Furthermore, novel architectures for enhanced three-dimensional quantum confinement like QDs embedded in wells are under extensive study for QD photodetectors for the IR (Sengupta et al., 2012). A short comprehensive overview on new frontiers achievable with quantum plasmonics may be found in Jacob and Shalaev (2011). Most of these effects are important for near-field applications, while in far-field applications appropriate homogenization theories are suitable for description of materials with QD inclusions, as we will see in Sections 5.3.2 and 5.3.3, respectively.

5.3.2 NANOCLUSTERS IN PERIODIC ARRAYS (METAMATERIALS)

Subwavelength resonating structures (plasmonic and not) arranged in periodic arrays act as the functional units of an artificially created medium, called metamaterials (MMs), which has unusual properties in interaction with electromagnetic radiation. When the inclusions are designed in-plane, it is common to talk about a meta-surface (MS). Upon proper engineering, MMs can possess such unattainable in nature behavior like negative refraction index (Anantha Ramakrishna, 2005; Shalaev, 2007), the giant chiral (Plum et al., 2007) and the "trapped rainbow" (Smolyaninova et al., 2012) effects, the electromagnetic cloaking ability (Pendry et al., 2006; Cai and Shalaev, 2010), or the ability to concentrate light extremely (Schuller et al., 2010) and even to funnel energy within a subwavelength slit with no reflection (Argyropoulos et al., 2012), as well as many others. The beginning of theoretical research in the field dates back to the end of the 1960s (Veselago, 1967;

Veselago, 1968), and to date theoretical aspects remain the prevalent subject of publications on metamaterials due mainly to the difficulty in MMs manufacturing. A tremendous variety of geometries have been proposed for MMs depending on applications, from noble-metal nanorods (Link and El-Sayed, 1999; Bogdanov et al., 2015) to nanoholes (Lesuffleur et al., 2006), nanowires (Peng and Kempa, 2012; Rehwald et al., 2007), and to nanorice (Wang et al., 2006) that combines the advantages of noble-metal nanoshells with those of dielectric NPs.

Among the variety of already existing or future applications enabled by MMs, optical filtering takes special place. Perhaps the first types of optical filters essentially using subwavelength structures were diffraction gratings, more generally called nanostructured arrays (Collin, 2014). Depending on the ratio of the grating period d to wavelength λ, the gratings may be classified as diffraction ($d \gg \lambda$), resonating ($d \sim \lambda$), and acting like an effective medium ($d \ll \lambda$). For resonant gratings (our case of interest), depending on the grating filling factor f, three subclasses may be distinguished. Gratings with $f \to 1$ are widely used for coupling to the guided modes when combined with multilayers to create the so-called guided-mode resonance (GMR) effect in periodic layers, as first conceptualized in 1993 (Wang and Magnusson, 1993), and nowadays represents a conventional approach for narrowband filtering, although being a subject of further in-depth research (Bykov et al., 2017). Mathematical description of resonant gratings with $f \to 0$ may be based on approaches valid for coherent multiple scattering. Such structures have been implemented, for example, for creation of extraordinary reflectors (Gomez-Medina et al., 2006). The resonant gratings with $f \sim 0.5$ are commonly known as photonic crystals (PhC) or high-contrast gratings and are widely used in photonic devices for about 20 years, for example, Mateus et al. (2004).

Gratings are a particular case of so-called metasurfaces (MS), the general class of MMs developed in-plane. MS is one of the hottest topics in nano-photonics nowadays, as reviewed, for example, in the above-cited work by Genevet et al. (2017). Recently, a "phase diagram" has been also proposed for terminological classification of MS toward PhC (Rybin et al., 2015).

Besides the aforementioned review by Collin (2014), the use of metal-dielectric 2D gratings for filtering light polarization is well summarized by Sun et al. (2011). Among recent developments in the field of polarization spectral filtering, a multiband stereoMM-based polarization filter may be cited (Shi et al., 2012). It uses chiral structures of twisted asymmetrical split-ring resonators rendering ripple-free transmission peaks of over 60% in a wide GHz range. MMs allow ultrathin polarizers, unachievable by traditional approaches, even at optical frequencies (Ginzburg et al., 2013), and different MM symmetries enable different types of polarization control (Kruk et al., 2015).

Band-pass filtering with MMs is a relatively new vision of the classical problem of spectral selection. At GHz wavelengths, a planar MM was proposed some years ago (Papasimakis et al., 2008) having properties of electromagnetically induced transparency analogously to the classical nonlinear quantum phenomenon. While in the classical approach (Harris et al., 1990) an opaque medium is rendered

transparent in a narrow spectral range utilizing quantum interference of a pump and a probe laser beam tuned at different transitions, in the proposed MM a double fish-scale metallic pattern induces the resonant splitting of the incident radiation, resulting in two separated modes, each corresponding to dipole-like oscillations in both layers of the MM structure. This leads to high-energy concentration between the layers, that is, to trapped-mode resonance. In the far fields, a narrow transmission resonance with long pulse delay is hence observable. However, the in-band transmission level of this MM is about 20% and, combined with high outer-band transmission, this persuades stacking of such planar MM slabs in order to increase the bandwidth and maximum transmitted intensity. The resulting media are appealing candidates for ultracompact broad-band delay lines operating at the prescribed wavelength to employ in the optical communication field.

In the far-infrared (terahertz, THz) range, MM-based filter devices operate by controlling the fundamental inductive-capacitive (LC) resonance in split ring resonator (SRR)-based oscillators. To enhance the sensitivity of the SRRs aiming to have advantages in narrowband filtering, there have been invented different mechanisms to excite sharper LC resonance response with a high-quality factor (Reiten et al., 2011). Very recently, a mirrored arrangement of asymmetric single SRRs (ASRs) was proposed (Al-Naib et al., 2012) that dramatically enhances the quality factor of the LC resonance, so that has the potential to suppress radiation losses in terahertz, microwave, and infrared plasmonic MMs. While in a regular non-mirrored arrangement the surface current modes are all oriented in phase and the light scattered by individual ASRs interferes constructively, in the proposed arrangement the surface currents are oppositely oriented for neighboring ASRs. This leads to the cancellation of the net dipole moment accompanied by destructive interference of the scattered fields. The proposed design outperforms similar non-mirrored super cell geometries by almost three times.

On the other hand, cloaking devices, bandstop filtering, and broadband absorption applications require broad-range filters. Realization of broadband metamaterials in the THz range was proposed either as a multiple stacked MM-layer configuration (Han et al., 2011) or, alternatively, through a planar single layer with nested multiple interconnected rings in succession within a single-gap SRR (Chowdhury et al., 2011). In this latter approach, mode redistribution in the rings results in reduced effective inductance and hence is responsible for the resonance linewidth broadening (by a factor of four in this study, without altering the resonance minima significantly) as well as for the resonance blue shifting. Recently, an ultra-broad 3 dB and sharp-transition band-pass THz filter was projected and realized (Yeh et al., 2012). Essentially, 3D geometries of these structures have ensured transmission over 82%. In this range also, dichroic mirrors were fabricated (Lu et al., 2011), although the employment of MMs for these types of devices is less common.

For the near-infrared (NIR) and visible range, only a very few pioneer works concerning MM-based optical filtering were published recently. This is probably due to the high quality of conventional optical multilayers whose quality is sufficient for many applications. Nonetheless, side ripples and limited acceptance angle may often represent a problem that might be solved using plasmonic MMs. The main reason for

the few results in shorter wavelength ranges is undoubtedly NPs fabrication difficulty, which for the visible should be much smaller than the micron-size inclusions required for the THz range and millimeter-size ones for GHz. As an example, we cite a novel MM polarization spectral filter proposed lately (Zheludev et al., 2011). A metal film patterned at the subwavelength scale has polarization properties enabling a narrow-band ripple-free transmission peak. Isoindex materials for microwaves and NIR were realized, Fig. 5.2. Notwithstanding their low peak transmission value (of only 8% in the NIR), the approach is interesting also due to the omnidirectional character of such a device. Wu and Shvets (2012) have latterly proposed a simple theoretical model for

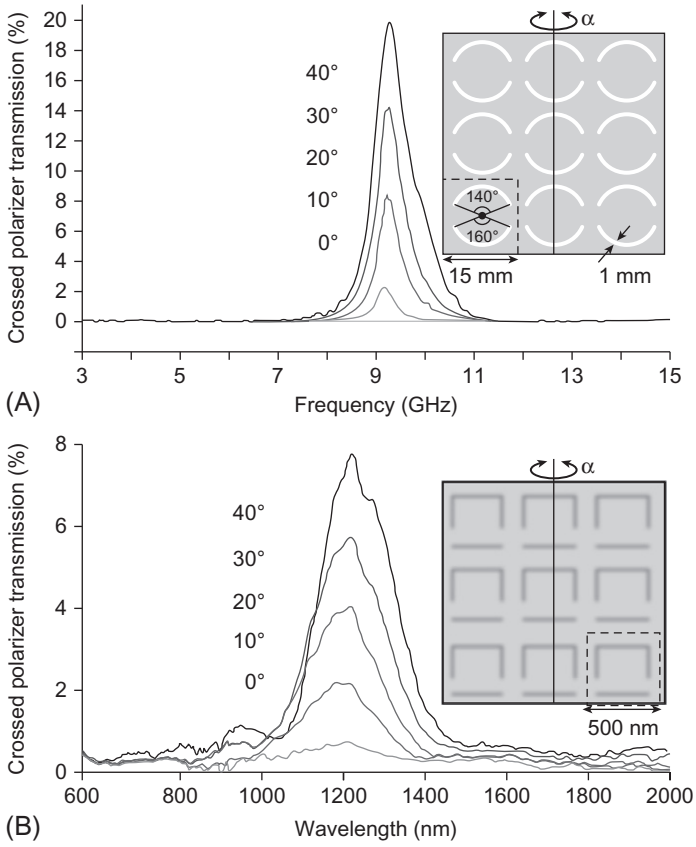


FIG. 5.2

Transmission of MM-based isoindex filters for microwaves (A) and NIR (B) at various incidence angles. The inserts show types of MM patterns.

Reprinted with permission from Zheludev, N.I., Plum, E., Fedotov, V.A., 2011. Metamaterial polarization spectral filter: isolated transmission line at any prescribed wavelength, Appl. Phys. Lett. 99, 171915. https://doi.org/10.1063/1.3656286. Copyright 2011 by the American Institute of Physics.

designing MM-based broadband absorbers in the NIR. It describes the optical response of the coating through the series of circuit models employed for each subunit of the patterned gold on the dielectric surface. Subunit size variety results in almost 100% absorbance over a broad range around 1500 nm. The validity of the proposed model relies on the short propagation range of SPs.

The alignment and control of the distance between the particles represent the main challenge in MMs creation, and from this point of view, "negative" geometries like fishnets (Valentine et al., 2008) are preferable. Nevertheless, since a dozen of years, many successful practical realizations have been achieved and, undoubtedly, plasmonics has been becoming a pervasive technology offering an unprecedented level of synergy between optics and electronics (Chen et al., 2010).

The realm of MMs falls into the three-fourths of possible combinations of signs for real dielectric permittivity and magnetic permeability (Pendry, 2003), Fig. 5.3, where to nonmagnetic optical materials corresponds the dashed line $\mu = 1$. On the other hand, the question on the sign of refractive index is not an evident issue for these materials with a physically unusual behavior. To solve the problem unambiguously, Govyadinov et al. (2007) proposed to firmly link the sign of the refractive index to the wavevector direction for the modes, and derived an approach for imposing causality in active and passive materials.

Vast literature on the subject is available, much of which the reader may find in the reference list to this chapter, including comprehensive monographs and reviews. Here we have referred only to some basic information relevant to the scope of

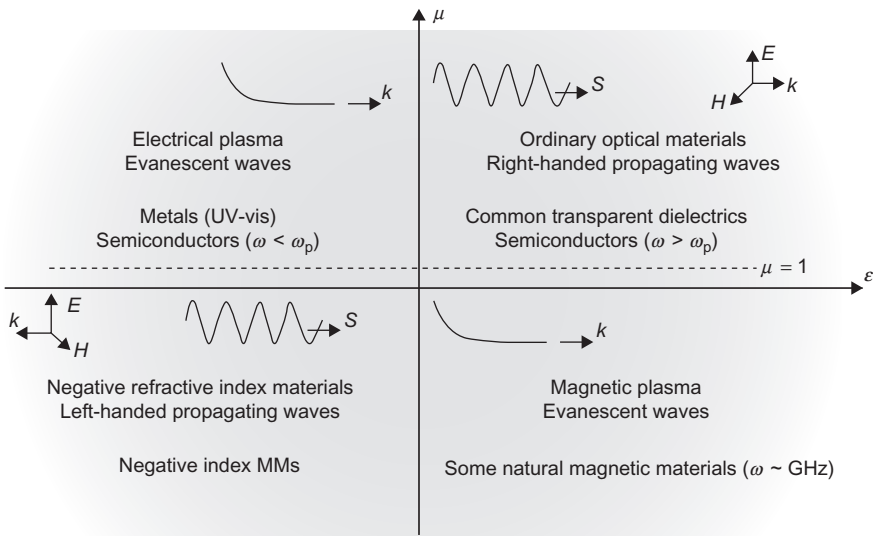


FIG. 5.3

Classification of materials based on their dielectric and magnetic properties. The dashed line corresponds to nonmagnetic materials, $\mu = 1$. S is the Poynting vector.

employment in thin film optics. It should be noted in particular that the inclusions, either "positive" like nanorods or nanoshells, or "negative" like nanoholes, are assumed to be large on the microscale, that is, the first level of homogenization should be allowed that consists of a description of the MM structural units in terms of their bulk dielectric permittivity and magnetic permeability. On the other hand, these structural units are small compared to the wavelength of the optical or microwave range they are thought to be employed in. Therefore, the electromagnetic radiation fails to resolve the MM structure rendering possible the second level of homogenization; hence, the retrieval of the MM effective parameters is based on the optical parameters of the constituent materials, see Section 5.3.2.

5.3.3 EFFECT OF SMALL RANDOM DISORDERS AND IMPERFECTIONS IN METAMATERIALS

Real metamaterials show an optical response different from theoretical metamaterials due to the inherent limitations of the fabrication process. Disorders and imperfections often make the measured losses higher than theoretically predicted. An infinite periodic arrangement of lossless inclusions theoretically cancels out the scattering from each individual NP yielding a perfect lossless metamaterial (Belov and Simovski, 2005), like it should happen in one- or three-dimensional lattices of closely packed NPs (Alù and Engheta, 2007), but the measured permittivity and permeability result is higher either due to deviations of the particle size from the ideal, or, more than that, due to the array alignment deficiency. Experimental efforts in realization of better metamaterials pose a problem of qualitative and quantitative modeling of realistic devices not free from manufacturing imperfections in order to provide an idea of which types of imperfections have the most effect and how the electromagnetic response of the device may be prevented through an improved design. A theory of quantification of the first-order effects of a small random uncontrollable disorder in the periodic arrays of plasmonic NPs has been proposed by Alù and Engheta (2010). They have shown that the main disorder effect consists of additional radiation losses for the guided mode and have proposed an extension of these results to the general class of periodic metamaterials.

5.3.4 COMPOSITES OF RANDOM ELEMENTS

Composites of randomly oriented elements with inclusions of sizes statistically distributed around a chosen design value do not require implementation of expensive manufacturing techniques like focused ion-beam or e-beam lithography. Their relatively low-cost production is useful for many applications where large surfaces should be coated or rather big slabs of 3D material are needed. The PVD methods are widely implemented for creation of such thin film structures.

Many interesting devices created using such comparatively simple approaches are reported in the literature, a significant part of them aimed at improving light energy harvesting or manipulation. For example, an omnidirectional transparent conducting-metal-based plasmonic composite was recently proposed by Elbahri et al. (2011).

The minimization of reflection of the reported coating, composed of a stack of a gold film and a silver/polymer nanocomposite fabricated by sputtering on a glass substrate, is achieved by means of symmetric plasmonic coupling under impedance matching condition in the visible range.

Elezzabi et al. (2009) proposed a random composite governed by nonresonant interactions for which the group refractive index can be increased to be larger than the refractive indices of both the dielectric host material and metal inclusions. Customized novel photonic materials with atypical optical constants may be created easily by mixing two material microparticles. Dense ensembles of subwavelength-sized constituents cannot be described by standard homogenization theories (see Section 5.5.3) and were only qualitatively explained by the authors considering near-field particle-plasmon interaction.

On the other hand, proper processing and deposition method adjustment help to better tailor the size and shape of NPs prepared by sputtering. Bruno et al. (2010) used a two-step sputtering processing to control the nucleation and position of gold NPs on the silicon substrate, thanks to intermediate treatment of the sample with oxygen plasma.

In general, for photonic applications, a theoretical modeling of disorders in MM (plasmonic and non-plasmonic), from strictly periodic through amorphous structures, may enable mitigation of undesirable effects due to the lattice mismatch, hence improving the applicability of disordered systems, even at oblique incidence (Kruk et al., 2015).

5.3.5 COATINGS CONTAINING THIN AND ULTRATHIN METAL LAYERS AND COATINGS CONTAINING METASURFACES

A particular case of periodically alternating layers of a metal with permittivity ε_1 and a dielectric with permittivity ε_2, in fractions f_1 and f_2, respectively, is a simple but important example of an artificial anisotropic composite. Its effective permittivity ε may be calculated by an effective medium approximation model (EMA, see Sections 5.5.3 and 5.5.4) with modification for the shape effect:

$$f_1\frac{\varepsilon_1-\varepsilon}{\varepsilon_1+\xi\varepsilon}+f_2\frac{\varepsilon_2-\varepsilon}{\varepsilon_2+\xi\varepsilon}=0$$

Parameter ξ is the screening factor of the material with respect to the external fields: for the electric field parallel to the layers (p-polarization) $\xi\to\infty$ and $\varepsilon\to\varepsilon_{\parallel}=f_1\varepsilon_1+f_2\varepsilon_2$, while for the electric field perpendicular to the layers (s-polarization) $\xi\to 0$ and $\varepsilon\to\varepsilon_{\perp}=\frac{\varepsilon_1\varepsilon_2}{f_2\varepsilon_1+f_1\varepsilon_2}$. The so-called Wiener bounds (Wiener, 1912) $\varepsilon_{\parallel}$ and $\varepsilon_{\perp}$ are useful for estimation of the possible permittivity values achievable with the given constituent materials in various fractions in a multilayer stack. The extreme values of ε are of great potential interest for photonic nanocircuits (Engheta, 2007), being epsilon-infinity materials perfect conducting wires for optical displacement currents, and epsilon-near-zero (ENZ) media being perfect insulators. Moreover, ENZ materials find a vast field of application for creation of "lenses" that may effectively redirect the energy from a source and reshape the radiation phase pattern on

will, being not limited in shape and size unlike standard lenses (Alù et al., 2007). Covering with ENZ materials may also drastically reduce scattering from dielectric and even conducting objects making these objects practically invisible (electromagnetic cloaking) (Pendry et al., 2006; Cai and Shalaev, 2010).

In interference coatings, single or double metal layers embedded in a particularly designed dielectric stack give rise to so-called induced transmittance filters (Macleod, 2001) suitable for implementation in construction of modern portable spectrometers (Piegari et al., 2008). Reliable deposition of such thin-film devices enables their optimal performance (Sytchkova, 2011) and should take into account not only the process optical monitoring but also the peculiarities of the metal-dielectric interface (Masetti et al., 2004).

Being embedded into multilayer coatings, layers with plasmonic inclusions make possible effective narrowband Fabry-Perot (FP) filtering. Hsu and Wu (2009) reported an FP design with a negative-refractive-index MM and calculated that, unlike conventional FP designs, the spectral response of such a filter strongly depends on the MM layer thickness.

Ultrathin semicontinuous metal films give rise to random metal-dielectric composites with interesting properties. Such composites may be used as transparent electrodes for a wide range of applications (Sytchkova et al.,2013), or make possible surface-enhanced Raman spectroscopy (Brouers et al., 1997), thanks to giant local electric field fluctuations (so-called Anderson localization (Anderson, 1958) or hot spots) that achieve their maximum at a certain pre-percolation state (Krachmalnikov et al., 2010). Random metal-dielectric films have also found vast use in many fields, among which photovoltaics (Atwater and Polman, 2010) should be mentioned. Light-to-current and current-to-light coupling (photon drag effect) in plasmonic systems with thin metal layers, where SPPs are controllable by external dc current (Noginova et al., 2011), may find application in plasmonic nanocircuitry, where advantages of fast photonics are combined with those of compact electronics.

Inclusion of metasurfaces in multilayers has been applied as 1D and 2D metal or dielectric gratings for fine-tuning of transmission of narrowband filters. Since the 1990s (Tibuleac and Magnusson, 1997), the use of periodic diffraction gratings has become a standard tool for very narrowband devices, yet improved continuously (Sakat et al., 2012; Ko and Magnusson, 2016; Fehrembach et al., 2017). The use of both plasmonic (Yokogawa et al., 2012) and later all-dielectric (Horie et al., 2017) gratings hase been proposed for color filters coupled with CMOS devices. The pixilated approach of filters with gratings has been applied also in the infrared (Macé et al., 2017).

5.4 SEARCHING FOR ALTERNATIVE MATERIALS FOR RESONATING INCLUSIONS

Metals are traditional materials used for plasmonic applications, but even those of highest conductivity exhibit high losses in the optical range, and therefore low-loss plasmonic materials research is required (Boltasseva and Atwater, 2011; West et al.,

2010). To determine the proficiency of a material to perform plasmonic application in particular, a series of metrics have been elaborated by Arnold and Blaber (2009). Despite the multiplicity of possible geometries determining a particular quality factor Q, in the quasistatic limit with a presumed low loss level, two main cases may be formulated: for localized SP, $Q_{\mathrm{LSP}} = -\varepsilon_c'/\varepsilon_c'' = k/2n$, and for extended modes, that is, SP polaritons, $Q_{\mathrm{SPP}} = \varepsilon_c'^2/\varepsilon_c'' = k^3/2n$. Therefore, not only the loss issue, that is, the ε_c'' value, is important to render a material good for plasmonic applications, but also an appropriate value of the ε_c'. Thus, the ability to tune the real part of the dielectric permittivity when engineering a novel plasmonic material should be considered simultaneously with the problem of material loss diminishing.

The losses in materials in the optical range are due to interband transitions of electrons to empty levels of higher energy caused by absorption of photons of the incident light. Fig. 5.4 illustrates the impact of interband transitions onto losses in two noble metals, copper and silver (Ehrenreih and Philipp, 1962). For example, in copper, the electrons can either shift from the filled L_3 band to the Fermi surface (peak at 2.1 eV) or undergo $L_2 \rightarrow L_1$ and $X_5 \rightarrow X_{4'}$ transitions (peak at 5.2 eV). Unfortunately, the nanogeometries additionally increase the interband transitions worsening the plasmonic response of the metals. A slightly higher ω_g/ω_s ratio of silver compared to gold and copper ensures better performance of silver nanostructures. For example, in the case of gold, the interband contributions to absorption present in a wide range from 1.8 to 2.35 eV (Balamurugan and Maruyama, 2005) not only red-shift the observable LSPR to 2.4 eV (Alvarez et al., 1997), but also strongly damp, hence broadening the SPR band, Fig. 5.5.

In the past decade, unconventional materials were theoretically studied (Blaber et al., 2010a) to face the problem of interband transitions, and some of the projected doped metals, alloys, and compounds were realized. Loss compensation approaches using layering of metal-dielectric MM have been proposed too (Savelev et al., 2013). For some applications, however, losses are not seen as a critical characteristic of plasmonic nano-inclusions, and can be either well-mitigated or even usefully exploited (Boriskina et al., 2017). Progress in material research for all-dielectric complex materials has enabled metasurfaces with improved properties (Zhu et al., 2017).

5.4.1 ALLOYS AND INTERMETALLICS: NOVEL METAL MATERIALS

Among a vast variety of metals, only those having free electron character are of interest for plasmonic applications, but in nature the choice of free electron metals is extremely limited. Therefore, besides those conventional metals, novel metals are searched for implementation in plasmonic devices, both for reasons of costs and of chemical as well as plasmonic performance.

As far as optical metrics are concerned, there exist superior alternatives to noble metals (gold, silver, and copper) in terms of the dielectric function. Alkali metals would be ideal from the optical performance point of view, but they are chemically reactive, hence problematic to handle, while the durability of a device based on such

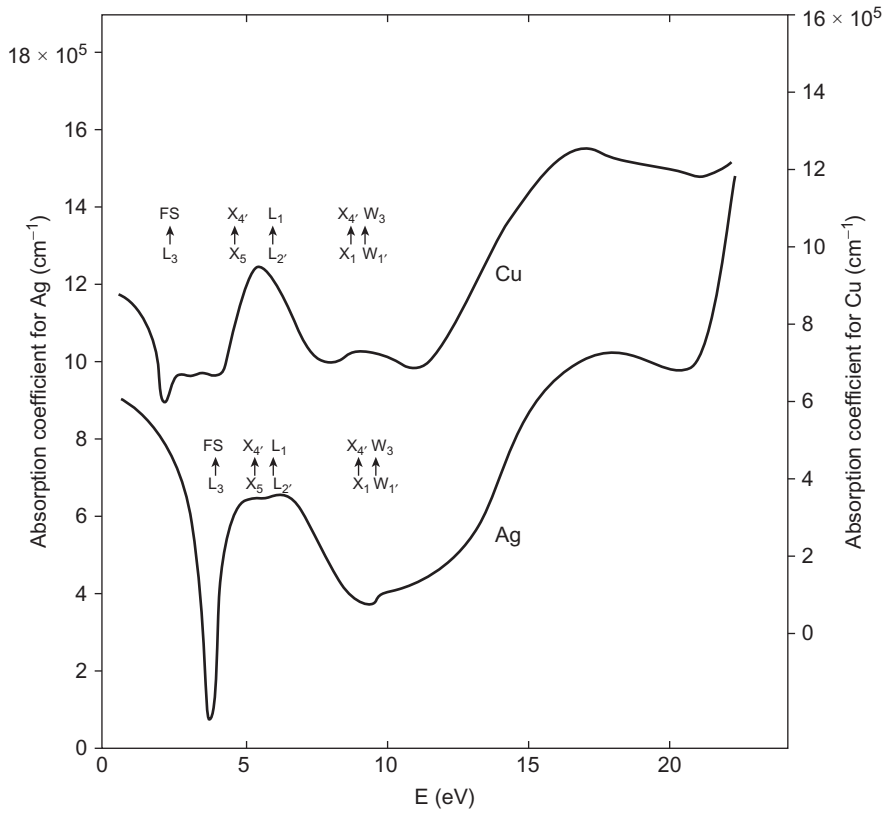


FIG. 5.4

Absorption spectra of copper and silver. Contributions form free-electron losses and interband transition losses are indicated. F.S. stands for "Fermi Surface."

Reprinted with permission from Ehrenreih, H., Philipp, H.R., 1962. Optical properties of Ag and Cu, Phys. Rev. 128, 1622–1629. https://doi.org/10.1103/PhysRev.128.1622. Copyright 1962 by the American Physical Society.

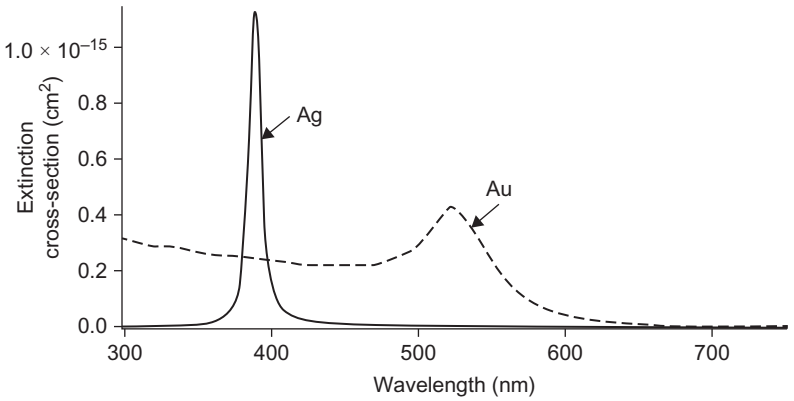


FIG. 5.5

Extinction spectra of silver (solid) and gold (dashed) 20-nm nanospheres in water calculated by the Mie theory.

Figure similar to that in Jain, P.K., El-Sayed, M.A., 2010. Plasmonic coupling in noble metal nanostructures. Chem.Phys. Lett. 487, 153–164. https://doi.org/10.1016/j.cplett.2010.01.062.

materials may be severely compromised. So that the alkali-noble intermetallic compounds, among which potassium gold (KAu) was theoretically demonstrated (Blaber et al., 2010a) to have zero interband losses below its unscreened plasma frequency at 1.54 eV (which, however, is practically worsened down to 0.5 eV by Drude losses). That is why both silver and gold are almost exclusively used in plasmonics nowadays: at the same time, they are more chemically stable (gold is even inert) and have a strong plasmonic performance.

Copper would be a low-cost alternative to gold and silver, thanks also to its ε_c'', comparable with that of gold in the 600–750 nm range, but the ease of copper oxidation dramatically affects the SP modes. Nevertheless, the LSP resonance peak of copper is comparable with that of gold and silver in sharpness and width (Chan et al., 2007).

In the blue and UV range, aluminum is better than noble metals, as its ε_c'' remains relatively low for wavelengths shorter than 200 nm where its ε_c' is negative, while for silver and gold the latter is true only down to 326 nm and 207 nm, respectively. However, again, chemically, aluminum is easily oxidized: the native oxide of 2.5–3 nm red-shifts the LSP resonance frequency from 10.5 to 6.5 eV (Chan et al., 2008). Despite the induced challenges in manufacturing, aluminum has been used in plasmonic devices in the UV-blue range for SPP propagation (Quail et al., 1983) and LSPR employment (Taguchi et al., 2009). Similar behavior of another plasmonic metal interesting for the UV, magnesium, exhibits an SPR peak at 7 eV shifted to 5 eV upon air oxidation.

Among alternative metals being explored for plasmonic applications, gallium was demonstrated to be attractive for employment in quaternary-logical resonatorless optical memory elements (Soares et al., 2006). The SPR of this metal is sufficiently stable against oxidation even in nanoshapes (red shift is about 0.3–0.6 eV) and it yields two plasmon modes, the transverse and longitudinal, that can be tuned in a very wide spectral range, from the UV to the near-IR (Wu et al., 2007). Gallium NPs coupled with some semiconductors enable plasmon-enhanced solid-state devices working in the UV-vis-NIR range, for example, Bao et al. (2006).

Random mixtures of silver, gold, aluminum, and copper were studied by Sharma et al. (Sharma and Mohr, 2008) who suggested the tunability of an SP-based fiber-optic sensor by the non-stoichiometric alloying of Al with its best signal-to-noise ratio and Au with its best sensitivity. Unfortunately, clustering or stoichiometric alloying present in all these alloys originate single electron excitations that have dramatic consequences for the SPR quality.

Blobb et al. (2009) have demonstrated a blue shift of the optical gap of gold by alloying it with cadmium that has caused an improved absorption efficiency of Au-Cd NPs compared to ones of pure Au accompanied, however, by an unwanted disruption in the originally optimal IR behavior of pure gold. In general, by using n-type doping of noble metals by bivalent transition metals, like zinc or cadmium, an increase in plasma frequency may be obtained, hence leading to a shift in the interband transition threshold. Such "band engineering" is considered a promising technique for improvement of noble metals' plasmonic performance for a chosen spectral range.

A comprehensive review of the latest achievements in this field may be found in the work of Blaber et al. (2010b), where noble and transition elementary metals and alloys are compared to binary and ternary intermetallics as well as to silicides. Materials with simple crystal structures and low-lying d electronic states are thought to be the most promising plasmonic alternatives to gold and silver.

As for ultrathin metal layers implemented in plasmonic multilayers, besides doping and alloying, ion sputtering represents a way to modify the surface of a metal film, thus changing its SP properties via induction of magnetic (Liedke et al., 2007) and optical (Oats et al., 2007) anisotropies, structural variation (Toma et al., 2008), and surface morphology modification, in particular by patterning (Everts et al., 2008). Electronic properties of sputtering-modified silver evaporated on the Cu(111) surface were compared with those of the Ar^+-sputtered bulk Ag(100) surface (Politano and Chiarello, 2010). Similar to the above-cited case of Au-Al alloying, a blue shift of the band gap was accompanied by SP broadening due to the induced additional single-particle transitions.

5.4.2 SEMICONDUCTORS AND DIELECTRICS

Generally speaking, the SP tuning is a very attractive issue. One of the most recent works in this field considers a multilayer device which allows the mechanical control of SP propagation properties by means of a simple modification on an inner air gap thickness between two SP-supporting layers, one made of gold and another made of silicon (Armand et al., 2012). It is worth noting, however, that when for the metals such a control is limited to electrical biasing (Chen et al., 2008) or mechanical external forces, the world of semiconductors adds more flexibility in the SP management.

Compound semiconductors may be easily tuned, within certain limits, for a desirable value of the dielectric function. For example, in the case of oxides, such a tuning is possible by doping adjustment or by oxidation state. "Active" tuning by photocarrier generation or by direct dopant injection or by thermal excitation is one more intriguing property of semiconductor-based plasmonic materials. In their pioneer work on this topic, Gómez Rivas et al. (2006) demonstrated such active tuning of the carrier density via modification of the Bragg scattering of terahertz SPPs on an InSb grating by thermal excitation of free carriers. At temperatures lower than 100°C, the SPP propagation was switched off completely at certain frequencies.

Good for plasmonic applications are semiconductors having a high plasma frequency that guarantees $\varepsilon_c' < 0$ in the NIR and visible range, and with a large bandgap that ensures minimum interband transition losses. In semiconductors, interband transitions can be either direct or indirect, depending on the material type. While for direct bandgap semiconductors the bandgap corresponds to the onset of interband transitions, for indirect bandgap semiconductors transitions may be caused by the photons with energies higher than the bandgap by means of various mechanisms of absorption like trap-assisted transitions, transitions between impurity levels, or due to generation of exitons. Any of such mechanisms can be described in terms

of the Lorentz oscillator model: the dielectric function dispersion in the vicinity of the absorption peak due to transition $l \rightarrow k$ is (Jackson, 1998)

$$\varepsilon_{lk}(\omega) = \frac{f_{lk}\omega_{\mathrm{p},lk}^2}{\omega_{lk}^2 - \omega^2 - i\omega\gamma_{lk}} \tag{5.2}$$

where f_{lk} is the oscillator strength, ω_{lk} is the resonant frequency corresponding to the energy difference between the levels, $\omega_{\mathrm{p},lk}$ is the plasma frequency defined similarly to Eq. (5.1) but with N being the concentration of electrons in the lower occupied state. The damping factor γ_{lk} accounts for the peak width. The sum of all allowed Lorentzian terms gives a reasonable approximation for the dielectric function of a semiconductor.

Aside from the optical performance and tunability, compatibility with standard nanofabrication and integration technologies should be taken into account as a factor of suitability of a material for plasmonic applications.

It is easier to find good plasmonic semiconductors at longer wavelengths, where some of them are either intrinsically plasmonic thanks to sufficiently high carrier mobility and concentration, or may exhibit negative real permittivity in phonon resonance (Palik, 1998). For the mid-IR, silicon carbide (Taubner et al., 2006) has been shown to be suitable for superlensing, while some arsenides like highly doped InGaAs and intrinsic AlInAs were used for fabrication of all-semiconductor MM with negative refraction (Hoffman et al., 2007). For the NIR applications, wide-band heavily doped oxides should be considered almost exclusively. They are so-called transparent conductive oxides (TCOs) like ITO (Sn-doped In_2O_3), or AZO and GZO (Al- and Ga-doped ZnO). TCOs are useful for many applications like ENZ materials, MMs with hyperbolic dispersion, and SPP waveguides (Naik and Boltasseva, 2011a).

Pioneer works of Franzen (2008) and Rhodes et al. (2006) opened the way to an extensive study of TCOs like plasmonic materials. In particular, for waveguiding applications, the characteristic penetration depth to the dielectric (d) or conductor (c) medium $l_{d,c} = \mathrm{Im}\left(\frac{\lambda}{2\pi}\sqrt{\frac{\varepsilon_d + \varepsilon_c}{\varepsilon_{d,c}^2}}\right)$ determines the SPP compactness. This means that at telecom wavelengths ($\lambda \sim 1550$ nm), good SPP-supporting materials with planar geometry may appear only with implementation of alternative materials to noble metals like TCOs (Noginov et al., 2011), as for silver and gold SPPs cease to be compact after 539 nm and 660 nm, respectively. Tunability of ITO NPs from 1618 nm to >2200 nm by changing the concentration of Sn doping from 3 to 30 mol% was demonstrated by Kanehara et al. (2009), where the shortest SPR wavelength was reached for the 10% Sn-doping, known as the optimal value of tin solubility in the indium oxide matrix. On the other hand, TCOs start to bring to the visible-range plasmonics their advantageous properties like low losses and optical function flexibility upon doping: a unity-order refractive index change (1.39 at 800 nm) upon the applied external field was reported by Feigenbaum et al. (2010) in TCOs implemented in a metal-oxide-semiconductor heterostructure with conducting oxide as the active material.

Transition-metal nitrides like GaN, TiN, and ZrN may substitute metals traditionally employed in the visible (Naik et al., 2011). The influence of the polarity of hexagonal wurtzite semiconductors (GaN, ZnO, SiC) onto SPR performance of the metal NPs was studied by Wu et al. (2009). Formation, geometry, and dynamics of gallium and gold NPs on the surface of polar semiconductors were shown to be influenced by the interface potential between the substrate and the NPs. Therefore, tailoring of the semiconductor surface charge was indicated as an intrinsic method for tuning the SPR resonance of metal NPs on a polar semiconductor.

Notice that besides noble metal QDs implemented traditionally, semiconductors were also recently reported by Luther et al. (2011) to be employed for plasmonics in the form of QDs. QDs of copper sulfide were shown to exhibit LSPR in the NIR when enough free carriers are introduced via dopants and vacancies. While properties of noble metal QDs may be engineered by their shape and size and then remain locked in permanently, the frequency and intensity of LSPR in semiconductor QDs can be dynamically tuned by doping, temperature, and phase transition.

Semiconductor plasmonics has also developed rapidly for photovoltaics. Gratings of five materials employable for enhancement of broadband absorption of thin-film solar cells, namely, Ag, Au, Al, Si, and SiO_2, were theoretically compared recently (Dühring et al., 2012), and silicon strips were predicted to provide a four-times enhancement of short-circuit current, thanks to much lower ohmic losses.

For metasurfaces based on non-plasmonic types of resonances, selection of materials for subwavelength inclusions has been numerically investigated (Yang and Fan, 2017) for silica, alumina, titania, silicon, and germanium in their transparency ranges. The efficiency of all-dielectric 2D and 3D grating structures of various geometries was shown to improve with increased dielectric function of the inclusions; however, this conclusion is somewhat limited by the use of topology optimization and hence compromised comparability of gratings composed of nano-inclusions of different materials.

5.5 CHARACTERIZATION OF NOVEL MATERIALS WITH SUBWAVELENGTH INCLUSIONS

Characterization of materials refers to probing of internal material structure and properties using external techniques. Interaction of complex materials having sub/wavelength inclusions with external electromagnetic radiation imposes use of suitable measurement techniques as well as adequate data interpretation specific for the case. Depending on the effects under study, near- or far-field material properties should be considered; hence, necessary measurement tools should be applied followed by consistent modeling of microscopic or macroscopic properties of the media. Here we overview the main methods suitable for characterization of such complex materials, including instrumentation and modeling approaches.

5.5.1 OPTICAL CHARACTERIZATION TECHNIQUES FOR COMPLEX MATERIALS

Characterization of a material with nano-inclusions (NPs or thin layers) typically employs tools providing information on the material's optical and morphological (geometrical) features. Depending on if one is interested in near-field or in far-field response of the material, emphasis may be given to this or that characterization method. For geometrical characterization, the prevailing approach is scanning probe microscopy (SPM) with its variants of atomic force microscopy (AFM) and scanning tunneling microscopy (STM). Cross-sectional geometrical analysis of multilayer stacks is possible by means of transmission electron microscopy (TEM). Optical properties of complex materials with plasmonic properties may be measured either by another type of SPM, the scanning near-field optical microscopy (SNOM), or by other microscopies giving access to determination of local parameters, like confocal microscopy and multiphoton microscopy. Surface-enhanced Raman spectroscopy (SERS) should also be mentioned as one of the most popular tools for localized optical characterization.

While a good synthetic description of the most common of the aforementioned measurement techniques (SNOM, SERS, and geometrical methods) applied to materials with subwavelength inclusions may be found in many reviews (see, for example, Fu, 2010), we will focus our attention on the optical methods for macroscopic measurements, as they are more common for the society of optical-coating researchers. In Section 5.5.4, an example of spectral-ellipsometric analysis of a plasmonic structure will be considered, whereas below we will briefly describe the principles of another technique widely employed for SP observation of so-called attenuated total reflectance (ATR) measurement.

Imprints of SPs are observable in the far field as absorption bands in the acquired optical spectra (Zhang et al., 2017) at a proper illumination. To excite an SP at the metal surface, it is necessary to match the wave-vector of the incident light with the wave-vector of surface collective oscillations. In the 1960s, (Otto, 1968; Kretschmann and Raether, 1968) for observation of SPs that exited at the interface between a conductor and a dielectric, Otto and Kretschmann proposed the two optical configurations enabling matching of the wave-vectors by means of a prism put into contact with the studied surface, see Fig. 5.6. Then, in the conditions of total reflectance, at the interface between the prism and the sample, an attenuation of the reflected intensity occurs when the light couples with the surface plasmons of a metal layer covering the sample (Otto configuration) or the prism (Kretschmann configuration). The depth, bandwidth, and shape of the reflectance curve dip are conditioned by the thicknesses of the metal and dielectric layers, the optical constants of the materials, surface roughness, and the sample-prism distance. Enhanced tools combining ATR with ellipsometry (total-internal-reflection ellipsometry, TIRE) may provide higher sensitivity to plasmonic properties of materials (Arwin et al., 2004; Hu et al., 2017).

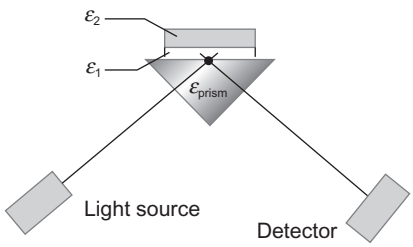


FIG. 5.6

Schematic representation of attenuated total reflectance measurement. To select *p*-polarization, a polarizer is introduced on the path of either the incident or reflected beam (not shown). For the Kretschmann configuration $\varepsilon_1 = \varepsilon_c$ and $\varepsilon_2 = \varepsilon_{gap}$, while for the Otto configuration $\varepsilon_1 = \varepsilon_{gap}$ and $\varepsilon_2 = \varepsilon_c$. The ATR condition is $k_x^2 = k_0^2\left(\frac{\varepsilon_c \varepsilon_{gap}}{\varepsilon_c + \varepsilon_{gap}}\right)$, where k_x is the component of the wave-vector parallel to the surface, and k_0 is the magnitude of the free-space wave vector. Notice that to obtain total reflection conditions the condition $\varepsilon_{prism} > \varepsilon_{gap}$ should be satisfied.

Commercial or *ad hoc* constructed optical benches like spectrophotometers or ellipsometers allow far-field measurements for retrieval of macroscopic optical functions of a composite. It is well known that to retrieve the macroscopic optical functions of natural materials, typically complex amplitude reflection (r) and transmission (t) coefficients are sufficient (Heavens, 1955) and obtainable, for example, from ellipsometric angles Ψ and Δ. For materials with anisotropic properties, the situation is more complicated as for them different polarization states are coupled, and therefore the generalized ellipsometry approach is required, where either the Jones or Mueller matrix is measured (Krasilnikova Sytchkova, 2008). Notice that ellipsometry in its generalized and total-internal-reflection forms (GE and TIRE) enables observation of any plasmonic resonance of a media: volume plasmons (Ferrell modes), SPPs, and LSPRs (Oates et al., 2011). On the other hand, for nonmagnetic ($\mu = 1$) isotropic materials, the refractive index n and extinction coefficient k may be retrieved from relatively simple spectrophotometric measurement of intensity reflectance (R) and transmittance (T), or even from one of them when, for example, the sample is not transparent. In this last case, a Kramers-Kronig analysis should be performed (Roessler, 1965), but the spectral range of the measurement should be sufficiently wide.

In general, nanoscale devices and nanostructured materials often represent a challenge for adequate characterization, particularly if unperturbed near-field effects are of interest. A possibility of representative insight may be offered by shifting prototyping into the microwave regime (Shishkin et al., 2016), if thoroughly respecting scaling factors, both in geometry and dielectric function dispersion ratios for embedded and embedding materials.

5.5.2 LOCAL PROPERTIES OF NANOSTRUCTURED MATERIALS

The analytical solution of Maxwell equations for description of extinction (absorption+scattering) spectra of spherical particles dates back to 1908 (Mie, 1908). Although the famous Mie theory remains of great interest (Kreibig and Vollmer, 1995), new shapes of NPs suitable for various applications make indispensible further development of near-field semi-analytical (Voshchinnikov and Faraonov, 1993) and numerical modeling. Among the most used numerical methods are the Modified Long Wavelength Approximation (MLWA) (Yang et al., 1995), the multiple multipole method (Moreno et al., 2002), the finite-difference time-domain (FDTD) method (Taflove, 1995), and especially the discrete dipole approximation (DDA) (Purcell and Pennypacker, 1973; Kelly et al., 2002). The theoretical advances in this area were reported by Kelly et al. (2003).

The above theories do not, however, consider the particle-particle interaction. To the problem of plasmonic coupling in nanostructures, a large amount of modern studies are dedicated. The polarization, orientation, and distance dependence of the near-field plasmonic coupling was discussed by Jain and El-Sayed (2010) for a series of nanogeometries including nanospheres, nanorods, and nanoshells. The importance of rigorous analytical techniques in studying collective phenomena in complex plasmonic arrays was demonstrated by Natarov et al. (2011) Optical forces between coupled plasmonic NPs near metal interfaces were investigated by Van Vlack et al. (2011) by non-perturbatively calculating the scattering electric field via a Green function technique which includes particle interaction of all orders.

Simplified approximations have also been elaborated. Langguth and Giessen (2011) report a simple and efficient multiple dipole approximation model, which can account for not only SP in single objects, but for their coupling of complex plasmonic systems too. A simple fitting approach to interpret Fano-like spectral features in the nanostructure far-field spectra and to relate them to near-field intensity profiles was proposed by Gallinet and Martin (2011). This approach provides a useful tool for experimental spectra interpretation, as well as for design of plasmonic and photonic devices exploiting the Fano effect.

Quantitative analysis of strong coupling between plasmonic copper nanogap and silicon photonic waveguides was performed by Salas-Montiel et al. (2012). The phenomenon was observed by a near-field scanning optical microscope, and hence modeled to explain the registered signal, providing characteristics such as near-field distribution or effective indices.

Besides the link to macroscopically observable optical features of plasmonic nanostructures, their local properties themselves are of always increasing attraction for the creation of novel devices for time-resolved measurements (Hartland, 2002), surface-enhanced Raman spectroscopy (Hulteen and Van Duyne, 1995), superlenses (Liu et al., 2012), spectroscopy on chip (Smolyaninova et al., 2012), and many others. The sensitivity of plasmonic NPs to local refractive index variation was studied by Piliarik et al. (2011). The first experimental realization and characterization of an MM with sharp topological edge states was done for a bianisotropic metasurface

emulating directly spin-orbit coupling in solids in the GHz regime (Slobozhanyuk et al., 2016). This structure was demonstrated to enable guiding waves through sharp corners, while the proposed measurement approach of near-field scanning was shown to represent a "true open metacrystal" enabling direct near-field mapping.

5.5.3 EFFECTIVE MACROSCOPIC PARAMETERS

Modeling of the optical response to incident electromagnetic radiation of complex materials with plasmonic properties, including MMs and coatings with either composite materials or ultrathin conductor layers, opens possibilities to simulate the behavior of devices based on such materials designed for a wavelength much larger than the mean inclusion size or plasmonic layer thickness. For this purpose, it is indispensable to know the *effective macroscopic* optical functions of such artificial materials, which means solving the inverse problem of determination of the complex effective permittivity ε and the complex magnetic permeability μ from measurement data. Effective macroscopic optical functions are obtainable using so-called homogenization approaches, and in Section 5.3 the approximation limits for such methods were considered.

The two most widely used homogenization models are the Maxwell-Garnett theory (MGT) (Maxwell Garnett, 1904) and Bruggeman effective medium approximation (EMA) (Bruggeman, 1935). These classic homogenization theories are based on the Clausius-Mossotti relation, for example, Jackson (1998), which offers an essential link between macroscopic and microscopic parameters of a medium. Notice that MGT provides a reasonable approximation only for substantially unsymmetrical mixtures where one of the components is treated as a host and the others are low-fraction inclusions. What makes EMA the most well-known mean-field theory, widely used even to modern plasmonic applications, for example, Fu et al. (2009), is that it is applicable to composites with fractions in arbitrary proportion.

Nowadays, the interest in MGT and EMA is justified by their versatility and straightforward applicability to many random geometries for which the experimental observation results are described adequately. For example, an easy-to-handle model based on MGT for layered composites of metal NPs embedded into a dielectric matrix was recently proposed by Protopapa (2009). It allows retrieval of the main features of the inclusions in terms of their shape (in terms of a fitting scalar parameter), size, and geometric distribution with a reasonable experimental agreement (Protopapa et al., 2009). An advanced version of EMA taking into account nonlocal effects neglected by the standard one was proposed by Elser et al. (2007).

The most general effective medium approach was proposed at the end of the 1970s (Bergman, 1978) and known as the Bergman-Milton representation. In this method, the geometrical features of complex plasmonic composites are taken into account not just by a macroscopic depolarization factor, but by defining geometrical functions to which a set of spectral density functions are correlated, and these latest functions are used for the fit (Milton, 2002).

These averaging methods, however, often fail to describe adequately the exotic inclusions in artificial materials (Engheta and Ziolkowski, 2006). For MMs, a

specific protocol for extraction of effective parameters was elaborated by Smith et al. (2002), the authors of the first demonstrated negative-index material, and then improved by them (Smith et al., 2005) and other researchers (Chen et al., 2004). The proposed inversion of the classical relations for the reflection (r) and transmission (t) coefficients in terms of refractive index n and impedance Z ($\varepsilon = n/Z$, $\mu = nZ$) gives for a slab of homogenous material with thickness d:

$$n = \pm\cos^{-1}\left(\frac{1-r^2-t^2}{2t}\right) Z = \pm\sqrt{\frac{(1+r)^2-t^2}{(1-r)^2-t^2}} \tag{5.3}$$

The choice of the sign in these solutions is ruled by the conditions $\mathrm{Re}(Z) > 0$ and $\mathrm{Im}(n) > 0$ for a causal and passive medium.

Similar to the classical approaches, these generalized Clausius-Mossotti methods, however, remain limited to description of a medium by permittivity and permeability, while complex scatterers embedded in MMs have an electromagnetic response that is not sufficiently described with ε and μ tensors. Such bianisotropic media require additional parameters relating the complexity of the electric and magnetic fields in the material, like magnetoelectric coefficients. So that is for an alternative method (Simovski and He, 2003; Fietz and Shvets, 2010) based on averaging of inclusions over a planar sheet with the consequent consideration of a Bloch-lattice-type layer interaction. Therefore, within these approaches, basic passivity and causality constraints (Landau and Lifschitz, 1984) may be easily violated when the optical functions are modeled in the vicinity of inclusion resonances due to a strong spatial dispersion not taken into account properly as demonstrated by Alù (2011a). Analysis (Orlov et al., 2014) of standard approaches for homogenization of metal-dielectric subwavelength multilayers has revealed the risk of false ENZ solutions, if no correction for artifacts is foreseen.

An alternative description of composite media composed from only dielectrics is a Floquet-type representation (Silveirinha et al., 2009) based on the generalized permittivity tensor $\hat{\varepsilon}\left(\omega, \vec{k}\right)$ that is spatially dispersive ($\vec{k}$ is the wave vector). The generalized permittivity tensor includes all polarization effects and hence is suitable for description of artificial or bianisotropic effects including artificial magnetism. To simplify linking these effects with weak spatial dispersion effects, the preferable description of a medium is in terms of local permeability or chirality parameters (Agranovich et al., 2004).

Among other widely used approaches, the bianisotropic parameter retrieval method proposed by Kriegler et al. (2010) should be mentioned. For randomly distributed inclusions, 2D and 3D footprinting methods for geometry modeling followed by finite-difference time domain (FDTD) calculation was shown to yield results in quantitative agreement with the experimentally measured far-field spectra of real samples (Thoreson et al., 2011).

An extension of the rigorous Floquet-type representation to magnetodielectric MMs has been proposed for periodic structures by Alù (2011b). This theory takes into consideration the complex interaction among inclusions via coupling of their polarization properties. The analysis showed that not only magnetoelectric coupling

arising at the inclusion level contributes to bianisotropy description of an MM, but also a weak spatial dispersion effect at the lattice level appearing due to inherent asymmetry introduced by phase propagation across a finite unit cell of the MM. This latter contribution was demonstrated to be inherent to any bianisotropic media and not only to media with asymmetric or noncentered inclusions as previously thought (Marques et al., 2002). Both types of magnetoelectric coupling appear through polarization terms in the expressions for averaged dielectric $\mathbf{D}_{av}$ and magnetic $\mathbf{B}_{av}$ displacements:

$$\mathbf{D}_{av} = \varepsilon_0 \mathbf{E}_{av} + \mathbf{P}_{av} = \varepsilon_{eff} \mathbf{E}_{av} - \left(\chi^e_{eff} + \chi^o_{eff}\right) \boldsymbol{\beta} \times \mathbf{H}_{av} \tag{5.4a}$$

$$\mathbf{B}_{av} = \mu_0 \mathbf{H}_{av} + \mathbf{M}_{av} = \mu_{eff} \mathbf{H}_{av} - \left(\chi^e_{eff} + \chi^o_{eff}\right) \boldsymbol{\beta} \times \mathbf{E}_{av} \tag{5.4b}$$

where $\mathbf{E}_{av}$ and $\mathbf{H}_{av}$ are averaged electric and magnetic fields, $\mathbf{P}_{av}$ and $\mathbf{M}_{av}$ are averaged polarization and magnetic vectors, respectively, $\boldsymbol{\beta}$ is the propagation eigenvector, and ε_0 and μ_0 are the background permittivity and permeability.

The effective parameters χ^e_{eff} and χ^o_{eff} corresponding to the coupling at inclusion and lattice levels, respectively, together with the effective permittivity ε_{eff} and effective permeability μ_{eff}, totally describe the macroscopic response of an MM as a bulk to an arbitrary electromagnetic excitation. The inconsistency and lack of physical meaning for the results obtainable with classic homogenization theories applied to MMs in the way like natural materials are treated (O'Brien and Pendry, 2002; Koschny et al., 2003) were shown to originate from omitting a priori the spatial dispersion contribution χ^o_{eff}, even at the wavelengths where this term is not negligible. A numeric comparison of effective optical parameters for three specific MM geometries has allowed emphasis on the difference of this homogenization approach and other available techniques.

A review (Simovski, 2011) on the methods of electromagnetic characterization and homogenization developed for nanostructured MMs for their linear properties also proposes a concept of *characteristic material parameters* (CMP), which is more restrictive than the concept of effective material parameters. CMP are parameters satisfying basic physical limitations and applicable to different wave processes, satisfying Maxwell's boundary conditions for macroscopic fields at the surface of a material. For effective material parameters, this condition is true with very high accuracy when considering natural materials while it fails for MMs. The pitfalls related to incorrect utilization and interpretation of effective parameters are also explained.

5.5.4 COMPLEX MATERIALS AND ULTRATHIN METALS IN MULTILAYERS

When a plasmonic material is embedded in a multilayer structure, the problem of determination of its effective optical parameters may be posed in two different ways depending on geometrical properties of the coating. Either a total response of the structure may be searched for, if the layers are ultrathin and the coating is intended as an in-one-piece device (Ni et al., 2011), or, in a more classical fashion, each of the composing layers should be treated as a film having own complex dielectric

functions; hence, the rigorous Fresnel coefficient calculus with the matrix method should be used (Macleod, 2001; Hu et al., 2017). In both cases, proper modeling is required for the plasmonic material optical functions as well as its interfaces with adjacent media.

Ni et al. (2011) compare four methods for modeling the dispersion relations of loss-compensated and active hyperbolic metamaterials in which permittivity along one axis is negative, while the permittivities along two other directions are positive. This material is considered as a single slab being in practice composed of ultrathin alternating layers of a metal (20-nm thick silver) and a dielectric (40-nm thick organic dye Rh800 mixed with epoxy). The constituent materials were considered to have a fixed experimentally obtained refractive index and extinction coefficient, while their layers were ideal, that is, isotropic, homogenous, and having plane-parallel surfaces and fixed thicknesses. The rigorous method of matrix calculations providing an exact solution for complex dielectric anisotropic permittivity of the multilayer device was compared in this work with other three methods, namely, spatial harmonic analysis (SHA) (Ni et al., 2010), standard EMA, and a more advanced EMA method (Protopapa et al., 2009) that takes into account the nonlocal effects neglected by the latter. The SHA method was shown to be in perfect agreement with the matrix calculations, both yielding the results of high accuracy for a sufficiently dense numeric mesh. On the other hand, in agreement with their physical nature, hence applicability, the EMA methods provided results with significant errors in effective permittivity calculation for thick layers or for those with high metal-to-dielectric thickness ratio, as well as for oblique incidence. Moreover, while the advanced EMA gave results close to within 3% of the exact values in most considered cases, the standard EMA was shown to produce errors as high as 50% already for the layers as thick as one-twelfth of the wavelength. Both EMA methods overestimate the imaginary parts of the permittivities in the active region of the spectrum for the implemented dye-doped dielectric.

The effect of interface roughness in such hyperbolic MMs may be crucial. For a multilayer metal-insulator stack, Shivanand and Webb (2012) have recently compared the numerically simulated effective parallel and perpendicular dielectric constants and analytical homogenization results as a function of wavelength and number of periods. A 0.2-μm-thick slab made of 10 periods of Ag/ZnO with various roughness values was prepared and analyzed. The homogenized dielectric constants (especially $\varepsilon_{\perp}$) were shown to be very sensitive to interlayer roughness. High roughness hence invalidates the performance of lenses for imaging with subwavelength resolution due to loss of stack anisotropy.

Homogenization with EMA remains the model of choice for reliable characterization of ultrathin metal film materials embedded in dielectric stacks (Sytchkova et al., 2013) or of metal-dielectric composites where a dielectric matrix embeds conductor inclusions (Protopapa, 2009). To simulate the dielectric function of metal nanoinclusions, a nonparametric technique was recently compared with a multiple oscillator technique (Amotchkina et al., 2011). For a description of some types of metal-dielectric composites prepared by e-beam evaporation at different deposition conditions, hence yielding different metal

film granularity, the two approaches, different from both mathematical and physical points of view, were shown to be consistent.

Angularly resolved spectroscopic ellipsometry may be used to provide data for reliable retrieval of a complex dielectric function of a conductor layer with plasmonic features in a stack. Sytchkova et al. (2013) studied the r.f. sputtered transparent electrodes made of silver layers sandwiched between two dielectric layers (aluminum-doped zinc oxide, AZO) and having a thickness varying from 8 to 14 nm obtained at various r.f. power values. Silver films were proposed to be considered to have different effective permittivities upon deposition conditions, see Fig. 5.7, as soon as they had different morphologies too. The refractive index

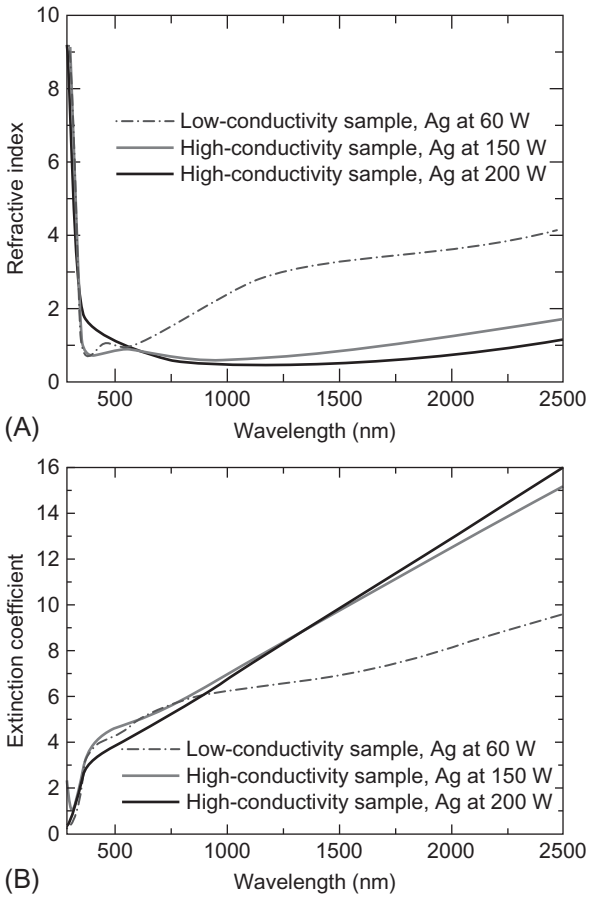


FIG. 5.7

The refractive index and extinction coefficient of silver ultrathin layers within AZO/Ag/AZO transparent electrodes prepared by sputtering at various r.f. power values: 60, 150, and 200 W.

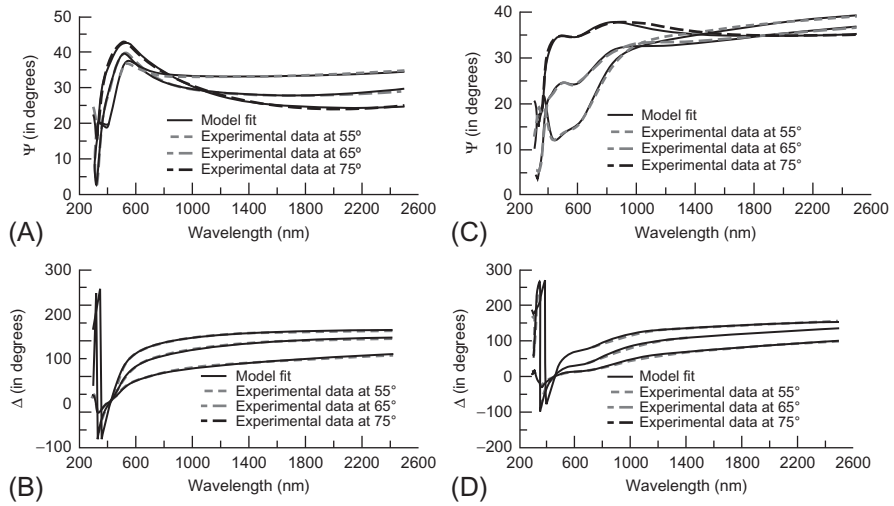


FIG. 5.8

Typical ellipsometric spectra of two AZO/Ag/AZO samples: (A) and (B) are ellipsometric angles for the sample with Ag deposited at 60 W, while (C) and (D) correspond to those of 200 W. Despite the equal nominal thickness of all layers, the graphs show a different character of features corresponding to the different types of absorption bands of SPs.

and extinction coefficient of the silver layers were modeled by an ensemble of Lorentz and Drude oscillators, while the EMA was applied for a description of the rough interfaces with AZO layers. Two examples of ellipsometric spectra for low- and high-energy deposited Ag layers are given in Fig. 5.8, where the imprints of Ferrell modes and SP absorption bands are observable. Indeed, the optical constants of three silver types differ significantly, being that of the 200-W-sample most similar to bulk Ag, whereas the 60-W-sample has LSPR bands in the *k*-curve, corroborated by low conductivity of this partially percolated layer, Fig. 5.7.

For metal films well below the percolation threshold, a similar ellipsometric study was performed earlier by Toudert et al. (2008) for silver nanoclusters sandwiched between two silicon nitride layers. On the basis of their conclusion on the Yamaguchi dipolar model for collective optical response of metal clusters (Yamaguchi et al., 1973), Toudert and coworkers found that the SP spectral position is mainly affected by the average shape of the clusters, while their size, shape, distribution, and electromagnetic interaction appear to have a weaker influence. Haarmans and Bedeaux (1993) showed in fact that noble metal films with particle coverage below 50% are well described by dipole and quadrupole terms in expansion of the problem of interaction between an ensemble of identical particles and incident light. A multipole expansion of this problem has a name of thin island film (TIF) theory and was proposed by Bedeaux and Vlieger (1973). TIF theory was shown (Krasilnikova Sytchkova, 2008) to be the only one correctly evaluating the

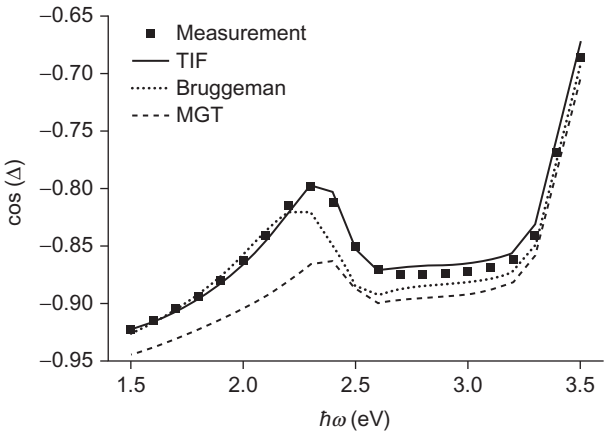


FIG. 5.9

Measured and theoretical dependence of cosine of ellipsometric angle Δ on photon energy for a silicon substrate covered at 12% by 13.6-nm diameter gold colloids. Notice that Bruggemann's EMA predicts a larger red shift of the resonance peak, while MGT forecasts it correctly, but underestimates the overall change in Δ.

Reprinted with permission from Oates, T.W.H., Wormeerter, H., Arwin, H., 2011. Characterization of plasmonic effects in thinfilms and metamaterials using spectroscopic ellipsometry. Prog. Surf. Sci. 86, 328–376. https://doi.org/10.1016/j.progsurf.2011.08.004.

ellipsometric phase (angle Δ) response measured for gold 13.6-nm-NPs on a silicon substrate with a coverage of 12%, if compared to MGT and EMA, Fig. 5.9.

In the infrared region, spectroscopic ellipsometry was employed to study layered structures composed of polar semiconductor materials (Schubert, 2004). GaAs homo- and heterostructures with various types of resonances in the spectral data were studied. Bulk and surface polaritons, together with Fano and Brewster modes, were successfully modeled to fit experimental Ψ and Δ curves.

5.6 CONCLUSIONS

Nanoshaping of any material represents an exciting opportunity for optical engineers. When the NP surface possesses a significant number of free carriers, either electrons or holes, they may work as plasmonic media, and besides the metals, semiconductors, alloys, and intermetallics considered in this review, there exist other categories of alternative plasmonic materials like graphene (Thongrattanarisi et al., 2012), ceramics (Naik and Boltasseva, 2011b), or organic materials (Zhu et al., 2011), which, however, are less advantageous, at least in the present state of the art, in terms of both optical performance and fabrication and integration compatibility (Tassin et al., 2012; Naik et al., 2011). On the other hand, all-dielectric structures based on high-dielectric function inclusions are a valid alternative (Genevet et al., 2017).

Nanotechnology has enabled almost arbitrary control of electromagnetic waves leading to trapped rainbows, superlensing, or anomalous refraction. Moreover, hybrid devices with exotic properties may be engineered when semiconductors and metal NPs are both used, like the invisible photodetector (Fan et al., 2012). Negative index MMs may be engineered to enable nonlinear effects like second-harmonic generation, for example, (Shadrivov et al., 2006) or quadratic and even cubic (Kozyrev et al., 2006) optical parametric amplification, which can be used moreover for loss compensation in MMs (Popov and Shalaev, 2006). Either embedded into multilayer coatings (Hsu and Wu, 2009) or stand-alone deposited on a substrate (Zheludev et al., 2011; Wu and Shvets, 2012), MMs make possible effective narrowband and polarization ripple-free filtering with tunable bandwidth and throughput efficiency anywhere from the optical to microwave range simultaneously operating with a wide acceptance angle. Additionally, plasmonic coupling may be rendered easier than conventional prism and grating approaches using MMs themselves: a gradient-index meta-surface for linking free propagating waves and surface waves was recently proposed (Sun et al., 2012) creating a valid alternative to traditional coupling methods. This material combines a thin gradient-index MM layer with a perfect electric conductor, and such a combination induces a reflection-phase gradient and compensates the momentum mismatch between the two wave types with nearly 100% efficiency. The idea was experimentally confirmed in the microwave range both by near- and far-field measurements and may pave the way for creation of novel types of SP couplers, light absorbers, or antireflection surfaces.

The materials used for all these novel exciting applications require adequate characterization methods both in the near and far fields that we endeavored to overview in this chapter. With the development in the field, new conductors, semiconductors, and dielectrics as well as new characterization methods will arise. Materials from the hottest frontiers of condensed-matter physics might induce further progress in nanophotonics.

REFERENCES

Agranovich, V.M., Shen, Y.R., Baughman, R.H., Zakhidov, A.A., 2004. Linear and nonlinear wave propagation in negative refraction metamaterials. Phys. Rev. B. 69. 165112, https://doi.org/10.1103/PhysRevB.69.165112.

Akimov, A.V., Mukherjee, A., Yu, C.L., Chang, D.E., Zibrov, A.S., Hemmer, P.R., Park, H., Lukin, M.D., 2007. Generation of single optical plasmons in metallic nanowires coupled to quantum dots. Nature 450, 402–406. https://doi.org/10.1038/nature06230.

Al-Naib, I., Singh, R., Rockstuhl, C., Lederer, F., Delprat, S., Rocheleau, D., Chaker, M., Ozaki, T., Morandotti, R., 2012. Excitation of a high-Q subradiant resonance mode in mirrored single-gap asymmetric split ring resonator terahertz metamaterials. Appl. Phys. Lett. 101. 071108, https://doi.org/10.1063/1.4745790.

Alù, A., 2011a. Restoring the physical meaning of metamaterial constitutive parameters. Phys. Rev. B. 83, 081102(R), https://doi.org/10.1103/PhysRevB.83.081102.

Alù, A., 2011b. First-principles homohenization theory for periodic metamaterials. Phys. Rev. B. 84. 075153, https://doi.org/10.1103/PhysRevB.84. 075153.

Alù, A., Engheta, N., 2007. Three-dimensional nanotransmission lines at optical frequencies: A recipe for broadband negative-refraction optical metamaterials. Phys. Rev. B. 75. (1-20) 024304, https://doi.org/10.1103/PhysRevB.75. 024304.

Alù, A., Engheta, N., 2010. Effect of small random disorders and imperfections on the performance of arrays of plasmonic nanoparticles. New J. Phys. 12. 013015, https://doi.org/10.1088/1367-2630/12/1/013015.

Alù, A., Silveirinha, M.G., Salandrino, A., Engheta, N., 2007. Epsilon-near-zero metamaterials and electromagnetic sources: tailoring the radiation phase pattern. Phys. Rev. B. 75. 155410, https://doi.org/10.1103/PhysRevB.75.155410.

Alvarez, M.M., Khoury, J.T., Schaaff, G., Shafigullin, M.N., Vezmar, I., Whetten, R.L., 1997. Optical absorption spectra of nanocrystal gold molecules. J. Phys. Chem. B 101, 3706–3712. https://doi.org/10.1021/jp962922n.

Amotchkina, T.A., Trubetskov, M.K., Tikhonravov, A.V., Janicki, V., Sancho-Parramon, J., Zorc, H., 2011. Comparison of two techniques for reliable characterization of thin metal-dielectric films. Appl. Opt. 50, 6189. https://doi.org/10.1364/AO.50.006189.

Anantha Ramakrishna, S., 2005. Physics of negative refractive index materials. Rep. Prog. Phys. 68, 449–521. https://doi.org/10.1088/0034-4885/68/2/R06.

Anderson, P.W., 1958. Absence of diffusion in certain random lattices. Phys. Rev. 109, 1492–1505. https://doi.org/10.1103/PhysRev.109.1492.

Argyropoulos, C., D'Aguanno, G., Mattiucci, N., Akozbek, N., Bloemer, M.J., Alù, A., 2012. Matching and funneling light at the plasmonic Brewster angle. Phys. Rev. B. 85. 024304, https://doi.org/10.1103/PhysRevB.85.024304.

Armand, D., Taguchi, G., Kadoya, Y., 2012. Mechanical active control of surface plasmon properties. Opt. Express 20, 9523–9534. https://doi.org/10.1364/OE.20.009523.

Arnold, M.D., Blaber, M.G., 2009. Optical performance and metallic absorption in nanoplasmonic systems. Opt. Express 17, 3835–3847. https://doi.org/10.1364/OE.17.003835.

Arwin, H., Poksinski, M., Johansen, K., 2004. Total internal reflection ellipsometry: principles and applications. Appl. Opt. 43 (15), 3028–3036. https://doi.org/10.1364/AO.43.003028.

Atwater, H.A., Polman, A., 2010. Plasmonics for improved photovoltaic devices. Nat. Mater. 9, 205. https://doi.org/10.1038/nmat2629.

Balamurugan, B., Maruyama, T., 2005. Evidence of an enhanced interband absorption in Au nanoparticles: Size-dependent electronic structure and optical properties. Appl. Phys. Lett. 87. 145105 (1-3), https://doi.org/10.1063/1.2077834.

Bao, J., Zimmler, M.A., Capasso, F., Wang, X., Ren, Z.F., 2006. Broadband ZnO single-nanowire light-emitting diode. Nano Lett. 6(2006) 1719–1722. https://doi.org/10.1021/nl061080t.

Baranov, D.G., Zuev, D.A., Lepeshov, S.I., Kotov, O.V., Krasnok, A.E., Evlyukhin, A.B., Chichkov, B.N., 2017. All-dielectric nanophotonics: the quest for better materials and fabrication techniques. Optica 4, 814–825. https://doi.org/10.1364/OPTICA.4.000814.

Bedeaux, D., Vlieger, J., 1973. A phenomenological theory of the dielectric properties of thin films. Physica 67, 55–73. https://doi.org/10.1016/0031-8914(73)90022-0.

Belov, P.A., Simovski, C., 2005. Homogenization of electromagnetic crystals formed by uniaxial resonant scatterers. Phys. Rev. E. 72. 026615, https://doi.org/10.1103/PhysRevE.72.026615.

Bergman, D.J., 1978. Dielectric constant of a composite material—a problem in classical physics. Phys. Rep. 43, 377–407. https://doi.org/10.1016/0370-1573(78)90009-1.

Blaber, M.G., Arnold, M.D., Ford, M.J., 2010a. Designing materials for plasmonic systems: the alkali-noble intermetallics. J. Phys. Condens. Matter. 22. 095501, https://doi.org/10.1088/0953-8984/22/9/095501.

Blaber, M.G., Arnold, M.D., Ford, M.J., 2010b. A review of the optical properties of alloys and intermetallics for plasmonics. J. Phys. Condens. Matter. 22. 143201, https://doi.org/10.1088/0953-8984/22/14/143201.

Blobb, D.A., Zhu, G., Mayy, M., Gavrilenko, A.V., Mead, P., Gavrilenko, V.I., Noginov, M.A., 2009. Engineering of low-loss metal for nanoplasmonic and metamaterials applications. Appl. Phys. Lett. 95. 151102, https://doi.org/10.1063/1.3237179.

Bogdanov, A.A., Shalin, A.S., Ginzburg, P., 2015. Optical forces in nanorod metamaterial. Sci. Rep. 5. https://doi.org/10.1038/srep15846.

Boltasseva, A., Atwater, H.A., 2011. Low-loss plasmonic metamaterials. Science 331, 290–291. https://doi.org/10.1126/science.1198258.

Boltasseva, A., Shalaev, V.M., 2008. Fabrication of optical negative-index metamaterials: recent advances and outlook. Meta 2, 1–17. https://doi.org/10.1016/j.metmat.2008.03.004.

Boriskina, S., Cooper, T., Zeng, L., Ni, G., Tong, J., Tsurimaki, Y., Huang, Y., Meroueh, L., Mahan, G., Chen, G., 2017. Losses in plasmonics: from mitigating energy dissipation to embracing loss-enabled functionalities. Adv. Opt. Photon. 9, 775–827. https://doi.org/10.1364/AOP.9.000775.

Brouers, F., Blacher, S., Lagarkov, A.N., Sarychev, A.K., Gadenne, P., Shalaev, V.M., 1997. Theory of giant Raman scattering from semicontinuous metal films. Phys. Rev. B 55, 13234–13245. https://doi.org/10.1103/PhysRevB.55.13234.

Bruggeman, D.A.G., 1935. Calculation of various physical constants in heterogeneous substances. I. Dielectricity constants and conductivity of mixed bodies from isotropic substances. Ann. Phys. 24, 636–664.

Bruno, G., Bianco, G.V., Giangregorio, M.M., Sacchetti, A., Capezzuto, P., Losurdo, M., 2010. A two-step plasma processing for gold nanoparticles supported on silicon near-infrared plasmonics. Appl. Phys. Lett. 96. 043104, https://doi.org/10.1063/1.3291670.

Bykov, D.A., Doskolovich, L.L., Soifer, V.A., 2017. Coupled-mode theory and Fano resonances in guided-mode resonant gratings: the conical diffraction mounting. Opt. Express 25, 1151–1164. https://doi.org/10.1364/OE.25.001151.

Cai, W., Shalaev, V., 2010. Transformation optics and electromagnetic cloak of invisibility. Chapter 9, In: Optical Metmaterials: Fundamentals and applications. Springer Science +Business Media, LLC, https://doi.org/10.1007/978-1-4419-1151-3_9.

Chan, G.H., Zhao, J., Hick, E.M., Schatz, G.C., Van Duyne, R.P., 2007. Plasmonic properties of copper nanoparticles fabricated by nanosphere lithography. Nano Lett. 7, 1947–1952. https://doi.org/10.1021/nl070648a.

Chan, G.H., Zhao, J., Schatz, G.C., Duyne, R., 2008. Localized surface plasmon resonance spectroscopy of triangular aluminum nanoparticles. J. Phys. Chem. C 112, 13958–13963. https://doi.org/10.1021/jp804088z.

Chen, X.D., Grzegorczyc, T.M., Wu, B.I., Pacheco, J., Kong, J.A., 2004. Robust method to retrieve the constitutive effective parameters of metamaterials. Phys. Rev. E. 70. 016608, https://doi.org/10.1103/PhysRevE.70. 016608.

Chen, H.-T., Lu, H., Azad, A.K., Averitt, R.D., Gossard, A.C., Trugman, S.A., O'Hara, J.F., Taylor, A.J., 2008. Electronic control of extraordinary terahertz transmission through subwavelength metal hole arrays. Opt. Express 16, 7641–7648. https://doi.org/10.1364/OE.16.007641.

Chen, H., Chan, C.T., Shen, P., 2010. Transformation optics and metamaterials. Nat. Mater. 9, 387–396. https://doi.org/10.1038/NMAT2743.

Chowdhury, D.R., Singh, R., Reiten, M., Chen, H.-T., Taylor, A.J., O'Hara, J.F., Azad, A.K., 2011. A broadband planar terahertz metamaterial with nested structure. Opt. Express 19 (17), 15817–15823. https://doi.org/10.1364/OE.19.015817.

Collin, S., 2014. Nanostructure arrays in free-space: optical properties and applications. Rep. Prog. Phys. 77. 126402, https://doi.org/10.1088/0034-4885/77/12/126402.

Dühring, M.B., Mortensen, N.A., Sigmind, O., 2012. Plasmonic versus dielectric enhancement in thin-film solar cells. Appl. Phys. Lett. 100. 211914, https://doi.org/10.1063/1.4719203.

Ehrenreih, H., Philipp, H.R., 1962. Optical properties of Ag and Cu. Phys. Rev. 128, 1622–1629. https://doi.org/10.1103/PhysRev.128.1622.

Elbahri, M., Hedayati, M.K., Chakravadhanula, V.S.K., Jamali, M., Strunkus, T., Zaporojtchenko, V., Faupel, F., 2011. Omnidirectional transparent conducting-metal-based plasmonic nanocomposite. Adv. Mater. 23, 1993–1997. https://doi.org/10.1002/adma.201003811.

Elezzabi, A.Y., Chau, K.J., Baron, C.A., Maraghechi, P., 2009. A plasmonic random composite with atypical refractive index. Opt. Express 17, 1016–1022. https://doi.org/10.1364/OE.17.001016.

Elser, J., Podolskiy, V.A., Salakhutdinov, I., Avrutsky, I., 2007. Nonlocal effects in effective-medium response of nanolayered metamaterials. Appl. Phys. Lett. 90. 191109, https://doi.org/10.1063/1.2737935.

Engheta, N., 2007. Circuits with light at nanoscales: optical nanocircuits inspired by metamaterials. Science 317, 1698–1702. https://doi.org/10.1126/science.1133268.

Engheta, N., Ziolkowski, R.W. (Eds.), 2006. Electromagnetic Metameterials: Physics and Engineering Explorations. John Wiley and Sons, New York.

Enkrich, C., Perez-Willard, R., Gerthsen, D., Zhou, J.F., Koschny, T., Soukoulis, C.M., Wegener, M., Linden, S., 2005. Focused-ion-beam nanofabrication of near-infrared magnetic metameterials. Adv. Mater. 17, 2547–2549. https://doi.org/10.1002/adma.200500804.

Everts, F., Wormeester, H., Poelsema, B., 2008. Optical anisotropy induced by ion bombardment of Ag(001). Phys. Rev. B 78, 155419. https://doi.org/10.1103/PhysRevB.78.155419.

Fan, J.A., Wu, C., Bao, K., Bardhan, R., Halas, N.J., Manoharan, V.N., Nordlander, P., Shvets, G., Capasso, F., 2010. Self-assembled plasmonic nanoparticle clusters. Science 328, 1135–1138. https://doi.org/10.1126/science.1187949.

Fan, P., Chettiar, U.K., Cao, L., Afshinmanesh, F., Engheta, N., Brongersma, M.L., 2012. An invisible metal-semiconductor photodetector. Nat. Photonics 6, 380–385. https://doi.org/10.1038/nphoton.2012.108.

Fasel, S., Robin, F., Moreno, E., Emi, D., Gisin, N., Zbinden, H., 2005. Energy-time entanglement preservation in plasmon-assisted light transmission. Phys. Rev. Lett. 94. 110501, https://doi.org/10.1103/PhysRevLett.94.110501.

Fehrembach, A.-L., Sharshavina, K., Lemarchand, F., Popov, E., Monmayrant, A., Arguel, P., Gauthier-Lafaye, O., 2017. 2×1D crossed strongly modulated gratings for polarization independent tunable narrowband transmission filters. J. Opt. Soc. Am. A 34, 234–240. https://doi.org/10.1364/JOSAA.34.000234.

Feigenbaum, E., Diest, K., Atwater, H.A., 2010. Unity-order index change in transparent conducting oxides at visible frequencies. Nano Lett. 10, 2111–2116. https://doi.org/10.1021/nl1006307.

Feng, L., Fainman, Y., 2011. Manipulation of plasmonics from nano to micro scale. In: Schevts, G., Tsukerman, I. (Eds.), Plasmonics and Plasmonic Metamaterials. World Scientific, Singapore.

Ferrell, R.A., 1958. Predicted radiation of plasma oscillations in metal films. Phys. Rev. 111, 874–881. https://doi.org/10.1103/PhysRev.106.874.

Ficcadenti, M., Pinto, N., Morresi, L., Murri, R., Serenelli, L., Tucci, M., Falconieri, M., Sytchkova, A.K., Grilli, M.L., Mittiga, A., Izzi, M., Pirozzi, L., Jadkar, S.R., 2009. Si quantum dots for solar cell fabrication. Mater. Sci. Eng. B 159–160, 66–69. https://doi.org/10.1016/j.mseb.2008.10.054.

Fietz, C., Shvets, G., 2010. Current-driven metamaterial homogenization. Physica B 495, 2930. https://doi.org/10.1016/j.physb.2010.01.006.

Section 5 inFlory, F., Escoubas, L., Berginc, G., 2011a. Optical properties of nanostructured materials: a review. J. Nanophotonics. 5. 052502, https://doi.org/10.1117/1.3609266.

Flory, F., Chen, Y.-J., Lee, C.-C., Escoubas, L., Simon, J.-J., Torchio, P., Le Rouzo, J., Vedraine, S., Derbal-Habak, H., Shupyk, I., Didane, Y., Ackermann, J., 2011b. Optical properties of dielectric thin films including quantum dots. Appl. Opt. 50, C129. https://doi.org/10.1364/AO.50.00C129.

Formanek, F., Takeyasu, N., Tanaka, T., Chiyoda, K., Ishikawa, A., Kawata, S., 2006. Three-dimensional fabrication of metallic nanostructures over large areas by two-photon polymerization. Opt. Express 14, 800–809. https://doi.org/10.1364/OPEX.14.000800.

Franzen, S., 2008. Surface plasmon polaritons and screened plasma absorption in indium tin oxide compared to silver and gold. J. Phys. Chem. 112, 6027–6032. https://doi.org/10.1021/jp7097813.

Freestone, I., Meeks, N., Sax, M., Higgitt, C., 2007. The Lycurgus cup—a Roman nanotechnology. Gold Bull. 40, 270–277. https://doi.org/10.1007/BF03215599.

Fu, Y., 2010. Subwavelength Optics: Theory and Technology. Bentham Science Publisher, Sharjah.

Fu, J., Park, B., Zhao, Y., 2009. Nanorod-mediated surface resonance sensor based on effective medium theory. Appl. Opt. 48, 4637–4649. https://doi.org/10.1364/AO.48.004637.

Gallinet, B., Martin, O.J.F., 2011. The relation between near-field and far-field properties of plasmonic Fano resonances. Opt. Express 19, 22167–22175. https://doi.org/10.1364/OE.19.022167.

Genevet, P., Capasso, F., Aieta, F., Khorasaninejad, M., Devlin, R., 2017. Recent advances in planar optics: from plasmonic to dielectric metasurfaces. Optica 4 (1), 139–152. https://doi.org/10.1364/OPTICA.4.000139.

Ginzburg, P., Rodríguez Fortuño, F.J., Wurtz, G.A., Dickson, W., Murphy, A., Morgan, F., Pollard, R.J., Iorsh, I., Atrashchenko, A., Belov, P.A., Kivshar, Y.S., Nevet, A., Ankonina, G., Orenstein, M., Zayats, A.V., 2013. Manipulating polarization of light with ultrathin epsilon-near-zero metamaterials. Opt. Express 21, 14907–14917. https://doi.org/10.1364/OE.21.014907.

Gómez Rivas, J., Kuttge, M., Kurz, H., Haring Bolivar, P., Sánchez-Gil, J.A., 2006. Low-frequency active surface plasmon optics on semiconductors. Appl. Phys. Lett. 88. 082106, https://doi.org/10.1063/1.2177348.

Gómez, D.E., Vernon, K.C., Mulvaney, P., Davis, T.J., 2010. Surface plasmon mediated strong exiton-photon coupling in semiconductor nanocrystals. Nano Lett. 10, 274–278. https://doi.org/10.1021/nl903455z.

Gomez-Medina, R., Laroche, M., Sáenz, J.J., 2006. Extraordinary optical reflection from sub-wavelength cylinder arrays. Opt. Express 14, 3730–3737. https://doi.org/10.1364/OE.14.003730.

Govyadinov, A.A., Podolskiy, V.A., Noginov, M.A., 2007. Active metamaterials: Sign of refractive index and gain assisted dispersion management. Appl. Phys. Lett. 91. 191103, https://doi.org/10.1063/1.2800309.

Gruber, C., Kusar, P., Hohenau, A., Krenn, J.R., 2012. Controlled addressing of quantum dots by nanowire plasmons. Appl. Phys. Lett. 100. 231102, https://doi.org/10.1063/1.4725490.

Haarmans, M.T., Bedeaux, D., 1993. The polarizability and the optical properties of lattices and random distributions of small metal spheres on a substrate. Thin Solid Films 224, 117–131. https://doi.org/10.1016/0040-6090(93)90468-5.

Hammond, P.T., 2004. Form and Function in Multilayer Assembly: new Applications at the Nanoscale. Adv. Mater. 16, 1271–1293. https://doi.org/10.1002/adma.200400760.

Han, N.R., Chen, Z.C., Lim, C.S., Ng, B., Hong, M.H., 2011. Broadband multi-layer terahertz metamaterials fabrication and characterization on flexible substrates. Opt. Express 19 (8), 6990–6998. https://doi.org/10.1364/OE.19.006990.

Harris, S.E., Field, J.E., Imamoglu, A., 1990. Nonlinear optical processes using electromagnetically induced transparency. Phys. Rev. Lett. 64, 1107–1110. https://doi.org/10.1103/PhysRevLett.64. 1107.

Hartland, G.V., 2002. Coherent vibrational motion in metal particles: determination of the vibrational amplitude and excitation mechanism. J. Chem. Phys. 116, 8048. https://doi.org/10.1063/1.1469021.

Heavens, O.S., 1955. Optical Properties of Thin Solid Films. Butterworth, London.

Hoffman, A.J., Alekseyev, L., Howard, S.S., Franz, K.J., Wasserman, D., Podolskiy, V.A., Narimanov, E.E., Sivco, D.L., Gmachl, C., 2007. Negative refraction in semiconductor metameterials. Nat. Mater. 6, 946–950. https://doi.org/10.1038/nmat2033.

Horie, Y., Han, S., Lee, J.-Y., Kim, J., Kim, Y., Arbabi, A., 2017. Visible wavelength color filters using dielectric subwavelength gratings for backside-illuminated CMOS image sensor technologies. Nano Lett. 17 (5), 3159–3164. https://doi.org/10.1021/acs.nanolett.7b00636.

Hsu, H.-T., Wu, C.-J., 2009. Design rules for a Fabry-Perot narrow band transmission filter containing a metamaterial negative-index defect. Prog. Electromagn. Res. Lett. 9, 101–107. https://doi.org/10.2528/PIERL09032803.

Hu, G., He, H., Sytchkova, A., Zhao, J., Shao, J., Grilli, M.L., Piegari, A., 2017. High-precision measurement of optical constants of ultra-thin coating using surface plasmon resonance spectral ellipsometry in Otto-Bliokh configuration. Opt. Express 25, 13425–13434. https://doi.org/10.1364/OE.25.013425.

Huck, A., Smolka, S., Lodahl, P., Serensen, A.S., Boltasseva, A., Janousek, J., Andersen, U.L., 2009. Demonstration of quadrature-squeezed surface plasmons in a gold waveguide. Phys. Rev. Lett. 102. 246802, https://doi.org/10.1103/PhysRevLett.102.246802.

Hulteen, J.C., Van Duyne, R.P., 1995. Nanosphere lithography: a materials general fabrication process for periodic particle array surfaces. J. Vac. Sci. Technol. A 13, 1553. https://doi.org/10.1116/1.579726.

Jackson, J.D., 1998. Classical Electrodynamics. Wiley, New York.

Jacob, Z., Shalaev, V.M., 2011. Plasmonics goes quantum. Science 334, 463–464. https://doi.org/10.1126/science.1211736.

Jacob, Z., Kim, J.-Y., Naik, G.V., Boltasseva, A., Narimanov, E.E., Shalaev, V.M., 2010. Engineering photonic density of states using metamaterials. Appl. Phys. B Lasers Opt. 100, 215–218. https://doi.org/10.1007/s00340-010-4096-5.

Jain, P.K., El-Sayed, M.A., 2010. Plasmonic coupling in noble metal nanostructures. Chem. Phys. Lett. 487, 153–164. https://doi.org/10.1016/j.cplett.2010.01.062.

Jain, P.K., Huang, W., El-Sayed, M.A., 2007. On the universal scaling behavior of the distance decay of plasmon coupling in metal nanoparticle pairs: a plasmon ruler equation. Nano Lett. 7, 2080–2088. https://doi.org/10.1021/nl071008a.

Kanehara, M., Koike, H., Yoshinaga, T., Teranishi, T., 2009. J. Am. Chem. Soc. 131, 17736–17737. https://doi.org/10.1021/ja9064415.

Kazuma, E., Matsubara, K., Kelly, K.L., Sakai, N., Tatsuma, T., 2009. Bi- and uniaxially oriented growth and plasmon resonance properties of anisotropic Ag nanoparticles on single crystalline TiO2 surfaces. J. Phys. Chem. Lett. C 113, 4758–4762. https://doi.org/10.1021/jp900749x.

Kelly, K.L., Jensen, T.R., Lazarides, A.A., Schatz, G.C., 2002. Feldhiem, D., Foss, C. (Eds.), Metal nanoparticles: Synthesis, characterization and applications. Marcell-Dekker, New York, p. 89.

Kelly, K.L., Coronado, E., Zhao, L.L., Schatz, G.C., 2003. The optical properties of metal nanoparticles:the influence of size, shape, and dielectric environment. J. Phys. Chem. B 107, 668–677. https://doi.org/10.1021/jp02673y.

Ko, Y.H., Magnusson, R., 2016. Flat-top bandpass filters enabled by cascaded resonant gratings. Opt. Lett. 41, 4704–4707. https://doi.org/10.1364/OL.41.004704.

Ko, S.H., Choi, Y., Hwang, D.J., Grigoropoulos, C.P., Chung, J., Poulikakos, D., 2006. Nanosecond laser ablation of gold nanoparticle films. Appl. Phys. Lett. 89. 141126, https://doi.org/10.1063/1.2360241.

Kokkinakis, T., Alexopoulos, K., 1972. Observation of radiative decay of surface plasmons in small silver particles. Phys. Rev. Lett. 28, 1632–1634. https://doi.org/10.1103/PhysRevLett.28.1632.

Koschny, T., Markos, P., Smith, D.R., Soukoulis, C.M., 2003. Resonant and antiresonant frequency dependence of the effective parameters of metamaterials. Phys. Rev. E. 68. 065602, https://doi.org/10.1103/PhysRevE.68.065602.

Kozyrev, A.B., Kim, H., van der Weide, D.W., 2006. Parametric amplification in left-handed transmission line media. Appl. Phys. Lett. 88. 264101, https://doi.org/10.1063/1.2214136.

Krachmalnikov, V., Castanie, E., Wilde, Y.D., Carminati, R., 2010. Fluctuations of the local density of states probe localized surface plasmons on disordered metal films. Phys. Rev. Lett. 105. 183901, https://doi.org/10.1103/PhysRevLett.105.183901.

Krasilnikova Sytchkova, A., 2008. Measurement of optical constants of thin films by non conventional ellipsometry, photothermal deflection spectroscopy and plasmon resonance spectroscopy. In: Kaiser, N., Lequime, M., Macleod, H.A. (Eds.), Advances in Optical Thin Films III.Proc. of SPIE 7101pp. 7101–7129. https://doi.org/10.1117/12.797660.

Kreibig, U., Vollmer, M., 1995. Optical Properties of Metal Clusters. In: Springer Series in Material Science. 25Springer, Berlin.

Krenn, J.R., Dereux, A., Weeber, J.C., Bourillot, E., Lacroute, Y., Goudonnet, J.P., Schider, G., Gotschy, W., Leitner, A., Aussenegg, F.R., Girard, C., 1999. Squeezing the optical near-field zone by plamon coupling of metallic nanoparticles. Phys. Rev. Lett. 82, 2590–2593. https://doi.org/10.1103/PhysRevLett.82.2590.

Kretschmann, E., Raether, H., 1968. Radiative decay of nonradiative surface plasmons excited by light. Z. Naturforschung 23A, 2135–2136.

Kriegler, C.E., Rill, M.S., Linden, S., Wegener, M., 2010. Bianisotropic photonic metamaterials. IEEE J. Sel. Top. Quant. Electron. 16, 367. https://doi.org/10.1109/JSTQE.2009.2020809.

Kruk, S.S., Poddubny, A.N., Powell, D.A., Helgert, C., Decker, M., Pertsch, T., Neshev, D.N., Kivshar, Y.S., 2015. Polarization properties of optical metasurfaces of different symmetries. Phys. Rev. B 91, 195401. https://doi.org/10.1103/PhysRevB.91.195401.

Kubo, S., Diaz, A., Tang, Y., Mayer, T.S., Khoo, I.C., Mallouk, T.E., 2007. Tunability of the refractive index of gold nanoparticle dispersions. Nano Lett. 7, 3418–3423. https://doi.org/10.21/nl071893x.

Kuwata, H., Tamaru, H., Esumi, K., Miyano, K., 2003. Resonant light scattering from metal nanoparticles: practical analysis beyond Rayleigh approximation. Appl. Phys. Lett. 83, 4625–4627. https://doi.org/10.1063/1.1630351.

Lalanne, P., Chavel, P., 2017. Metalenses at visible wavelengths: past, present, perspectives. Laser Photonics Rev. 11. 1600295, https://doi.org/10.1002/lpor.201600295.

Landau, L., Lifschitz, E., 1984. Electrodynamics of Continuous Media. Butterworth-Heinemann, Oxford.

Langguth, L., Giessen, H., 2011. Coupling strength of complex plasmonic structures in the multiple dipole approximation. Opt. Express 19, 22156–22166. https://doi.org/10.1364/OE.19.022156.

Lesuffleur, A., Kumar, I., Gordon, R., 2006. Enhanced second harmonic generation from nanoscale double-hole arrays in a gold film. Appl. Phys. Lett. 88. 261104, https://doi.org/10.1063/1.2218057.

Liedke, M.O., Liedke, B., Keller, A., Hillebrands, B., Mücklich, A., Facsko, S., Fassbender, J., 2007. Induced anisotropies in exchange-coupled systems on rippled substrates. Phys. Rev. B 75, 220407. https://doi.org/10.1103/PhysRevB.75.220407.

Link, S., El-Sayed, M., 1999. Spectral properties and relaxation dynamics of surface plasmon electronic oscillations in gold and silver nanodots and nanorods. J. Phys. Chem. B 103, 8410–8426. https://doi.org/10.1021/jp9917648.

Link, S., El-Sayed, M.A., 2000. Shape and size dependence of radiative, non-radiative and photothermal properties of gold nanocrystals. Int. Rev. Phys. Chem. 19, 409–453. https://doi.org/10.1080/01442350050034180.

Liu, Z.L., Shalaev, V.M., Kildishev, A.V., 2012. Coupling effect in a near-field object-superlens system. Appl. Phys. A Mater. Sci. Process. 107, 83–88. https://doi.org/10.1007/s00339-012-6780-2.

Lu, M., Li, W., Brown, E.R., 2011. Second-order bandpass terahertz filter achieved by multilayer complementary metamaterial structures. Opt. Lett. 36 (7), 1071–1073. https://doi.org/10.1364/OL.36.001071.

Luther, J.M., Jain, P.K., Ewers, T., Alivisatos, A.P., 2011. Localized surface plasmon resonances arising from free carriers in doped quantum dots. Nature Mat. 10, 361–366. https://doi.org/10.1038/NMAT3004.

Macé, L., Gauthier-Lafaye, O., Monmayrant, A., Camon, H., 2017. Design of angularly tolerant zero-contrast grating filters for pixelated filtering in the mid-IR range. J. Opt. Soc. Am. A 34, 657–665. https://doi.org/10.1364/JOSAA.34.000657.

Macleod, H.A., 2001. Thin Film Optical Filters, third ed. CRC Press, Bristol, Philadelphia ISBN 0750306882, 9780750306881.

Maier, S.A., Atwater, A.H., 2005. Plasmonics: localization and guiding of electromagnetic energy in metal-dielectric structures. J. Appl. Phys. 98. 011101, https://doi.org/10.1063/1.1951057.

Maier, S.A., Brongersma, M.L., Kik, P.G., Atwater, H.A., 2002. Observation of near-field coupling in metal nanoparticle chains using far-field polarization spectroscopy. Phys. Rev. B 65, 193408. https://doi.org/10.1103/PhysRevB.65.193408.

Maier, S.A., Kik, P.G., Atwater, A.H., Meltzer, S., Harel, E., Koel, B.E., Requicha, A.A.G., 2003. Local detection of electromagnetic energy transport below the diffraction limit in metal nanoparticle plasmon waveguides. Nature Mat. 2, 229–232. https://doi.org/10.1038/nmat852.

Marques, R., Medina, F., Rafii-El-Idrissi, R., 2002. Role of bianisotropy in negative permeability and left-handed metamaterials. Phys. Rev. B. 65. 144440, https://doi.org/10.1103/PhysRevB.65.144440.

Masetti, E., Bulir, J., Gagliardi, S., Janicki, V., Krasilnikova Sytchkova, A., Coluzza, C., Di Santo, G., 2004. Ellipsometric and XPS analysis of the interface between silver and SiO2, TiO2 and SiNx thin films. Thin Solid Films 455–456, 468–472. https://doi.org/10.1016/j.tsf.2003.11.244.

Mateus, C.F.R., Huang, M.C.Y., Deng, Y., Neureuther, A.R., Chang, C.J., 2004. Ultrabroadband mirror using low-index cladded subwavelength grating. IEEE Photon. Technol. Lett. 16, 518–520. https://doi.org/10.1109/LPT.2003.821258.

Maxwell Garnett, J.C., 1904. Colours in metal glasses and metallic films. Philos. Trans. R. Soc. Lond. 203, 385–420.

McAlister, A.J., Stern, E.A., 1963. Plasma resonance absorption in thin metal films. Phys. Rev. 132, 1599–1602. https://doi.org/10.1103/PhysRev.132.1599.

Meier, M., Wokaun, A., 1983. Enhanced fields on large metal particles: dynamic depolarization. Opt. Lett. 8, 581–583. https://doi.org/10.1364/OL.8.00058.

Mie, G., 1908. Beitrage zer Optik truber Meiden speziell kolloidaler Metallosungen. Ann. Phys. 25, 377–445.

Milton, G.W., 2002. The theory of composites. In: Cambridge Monographs on Applied and Computational Mathematics. Cambridge University Press, Cambridge.

Moerland, R.J., Recola, H.T., Sharma, G., Eskelinen, A.-P., Väkeväinen, A.I., Törmä, P., 2012. Surface plasmon polariton-controlled tunable quantum-dot emission. Appl. Phys. Lett. 100. 221111, https://doi.org/10.1063/1.4724327.

Moreno, E., Erni, D., Hafner, C., Vahldieck, R., 2002. Multiple multipole method with automatic multipole setting applied to the simulation of surface plasmons in metallic nanostructures. J. Opt. Soc. A 19, 101–111. https://doi.org/10.1364/JOSAA.19.000101.

Naik, G.V., Boltasseva, A., 2011a. A comparative study of semiconductor-based plasmonic metamaterials. Meamaterials 5, 1–7. https://doi.org/10.1016/j.metmat.2010.11.001.

Naik, G., Boltasseva, A., 2011b. Ceramic plasmonic components for optical metameterials. Quantum Electronics and Laser Science Conference (Optical Society of America).

Naik, G.V., Kim, J., Boltasseva, A., 2011. Oxides and nitrides as alternative plasmonic materials in the optical range. Opt. Mat. Express 1, 1090–1099. https://doi.org/10.1364/OME.1.001090.

Natarov, D.M., Byelobrov, V.O., Sauleau, R., Benson, T.M., Nosich, A.I., 2011. Periodically-induced effects in the scattering and absorption of light by infinite and finite gratings of circular silver nanowires. Opt. Express 19, 22176–22190. https://doi.org/10.1364/OE.19.022176.

Nezhad, M.P., Tetz, K., Fainman, Y., 2004. Gain assisted propagation of surface plasmon polaritons on planar metallic waveguides. Opt. Express 12, 4072–4079. https://doi.org/10.1364/OPEX.12.004072.

Ni, X., Liu, Z., Boltasseva, A., Kildishev, A.V., 2010. The validation of the parallel three-dimensional solver for analysis of optical plasmonic bi-periodic multilayer nanostructures. Appl. Phys. A-Mater. 100, 365–374. https://doi.org/10.1007/s00339-010-5865-z.

Ni, X., Ishii, S., Thoreson, M.D., Shalaev, V.M., Han, S., Lee, S., Kildishev, A.V., 2011. Loss-compensated and active hyperbolic metamaterials. Opt. Express. 19. 25242, https://doi.org/10.1364/OE.19.025242.

Noginov, M.A., Gu, L., Livenere, J., Zu, G., Pradhan, A.K., Mundle, R., Bahoura, M., Barnakov, Y.A., Podolskiy, V.A., 2011. Transparent conductive oxides: Plasmonic materials for telecom wavelengths. Appl. Phys. Lett. 99. 021101, https://doi.org/10.1063/1.3604792.

Noginova, N., Yakim, A.V., Soimo, J., Gu, L., Noginov, M.A., 2011. Light-to-current and current-to-light coupling in plasmonic systems. Phys. Rev. B. 84. 035447, https://doi.org/10.1103/PhysRevB.84.035447.

O'Brien, S., Pendry, J.B., 2002. Magnetic activity at infrared frequencies in structured metallic photonic crystals. J. Phys. Condens. Matter 14, 6383. https://doi.org/10.1088/0953-8984/14/25/307.

Oates, T.W.H., Wormeerter, H., Arwin, H., 2011. Characterization of plasmonic effects in thin films and metamaterials using spectroscopic ellipsometry. Prog. Surf. Sci. 86, 328–376. https://doi.org/10.1016/j.progsurf.2011.08.004.

Oats, T.W.H., Keller, A., Facsko, S., Mücklich, A., 2007. Aligned silver nanoparticles on rippled silicon templates exhibiting anisotropic plasmon absorption. Plasmonics 2, 47–50. https://doi.org/10.1007/s11468-007-9025-z.

Orlov, A.A., Yankovskaya, E.A., Zhukovsky, S.V., Babicheva, V.E., Iorsh, I.V., Belov, P.A., 2014. Retrieval of effective parameters of subwavelength periodic photonic structures. Crystals 4, 417–426. https://doi.org/10.3390/cryst4030417.

Otto, A., 1968. Excitation of nonradiative surface plasma waves by the method of frustrated reflection. Z. Physik 216, 398–410.

Palik, E.D., 1998. Handbook of Optical Constants of Solids. Academic Press, San Diego.

Papasimakis, N., Fedotov, V.A., Zheludev, N.I., Prosvirin, S.L., 2008. Metamaterial analog of electromagnetically induced transparency. Phys. Rev. Lett. 101. 253903, https://doi.org/10.1103/PhysRevLett.101. 253903.

Pedersen, R.H., Boltasseva, A., Johansen, D.M., Nielsen, T., Jorgensen, K.B., Leosson, K., Erland, J., Kristensen, A., 2007. Nanoimprinted reflecting gratings for long-range surface plasmon polaritons. Microelectron. Eng. 84, 895–898. https://doi.org/10.1016/j.mee.2007.01.110.

Pendry, J.B., 2003. Focus issue: negative refraction and metamaterials. Opt. Express 11, 639. https://doi.org/10.1364/OE.11.000639.

Pendry, J.B., Schurig, D., Smith, D.R., 2006. Controlling electromagneticfields. Science 312, 1780–1782.

Peng, Y., Kempa, K., 2012. Controlling light propagation with nanowires. Appl. Phys. Lett. 100. 171903, https://doi.org/10.1063/1.4704193.

Pérez-Juste, J., Pastoriza-Santos, I., Liz-Marzán, L.M., Mulvaney, P., 2005. Gold nanorods: Synthesis, characterization and applications. Coord. Chem. Rev. 249, 1870–1901. https://doi.org/10.1016/j.ccr.2005.01.030.

Piegari, A., Bulir, J., Sytchkova, A.K., 2008. Variable narrow-band transmission filters for spectrometry from space. 2. Fabrication process. Appl. Opt. 47, C151–C156. https://doi.org/10.1364/AO.47.00C151.

Piliarik, M., Kvasnicka, P., Galler, N., Kren, J.R., Homola, J., 2011. Local refractive index sensitivity of plasmonic nanoparticles. Opt. Express 19, 9213–9220. https://doi.org/10.1364/OE.19. 009213.

Pitarke, J.M., Silkin, V.M., Chulkov, E.V., Echenique, P.M., 2007. Theory of surface plasmons and surface plasmon polaritons. Rep. Prog. Phys. 70, 1–87. https://doi.org/10.1088/0034-4885/70/1/R01.

Plum, E., et al., 2007. Giant optical gyrotropy due to electromagnetic coupling. Appl. Phys. Lett. 90, 223113. https://doi.org/10.1088/0034-4885/68/2/R06.

Politano, A., Chiarello, G., 2010. Sputtering-induced modification of the electronic properties of Ag/Cu(111). J. Phys. D: Appl. Phys. 43. 085302, https://doi.org/10.1088/0022-3727/43/8/085302.

Popov, A.K., Shalaev, V.M., 2006. Compensating losses in negative-index metamaterials by optical parametric amplification. Opt. Lett. 31, 2169. https://doi.org/10.1364/OL.31.002169.

Pradeep, T., Anshup, 2009. Noble nanoparticles for water purification: a critical review. Thin Solid Films 517, 6441–6478. https://doi.org/10.1016/j.tsf.2009.03.195.

Prodan, E., Radloff, C., Halas, N.J., Nordlander, P., 2003. A hybridization model for the plasmon response of complex nanostructires. Science 302, 419–422. https://doi.org/10.1126/science.1089171.

Protopapa, M.L., 2009. Surface plasmon resonance of metal nanoparticles sandwiched between dielectric layers: theoretical modelling. Appl. Opt. 48, 778–785. https://doi.org/10.1364/AO.48.000778.

Protopapa, M.L., Rizzo, A., Re, M., Pilloni, L., 2009. Layered silvernanoparticles embedded in a BaF2 matrix: optical characterization. Appl. Opt. 48, 6662–6669. https://doi.org/10.1364/AO.48.006662.

Purcell, E.M., Pennypacker, C.R., 1973. Scattering and absorption of light by non- spherical dielectric grains. Astrophys. J. 186, 705–714.

Quail, J.C., Rako, J.G., Simon, H.J., 1983. Long-range surface-plasmon modes in silver and aluminum films. Opt. Lett. 8, 377–379. https://doi.org/10.1364/OL.8.000377.

Rehwald, S., Berndt, M., Katzenberg, F., Schwieger, S., Runge, E., Schierbaum, K., Zerulla, D., 2007. Tunable nanowires: an additional degree of freedom in plasmonics. Phys. Rev. B. 76. 085420, https://doi.org/10.1103/PhysRevB.76.085420.

Reiten, M.T., Roy Chowdhury, D., Zhou, J., Taylor, A.J., O'Hara, J.F., Azad, A.K., 2011. Resonance tuning behaviour in closely spaced inhomogeneous bilayer metamaterials. Appl. Phys. Lett. 98. 131105, https://doi.org/10.1063/1.3566978.

Rhodes, C., Franzen, S., Maria, J.-P., Losego, M., Leonard, D.N., Laughlin, B., Duscher, G., Weibel, S., 2006. Surface plasmon resonance in conducting metal oxides. J. Appl. Phys. 100. 054905, https://doi.org/10.1063/1.2222070.

Ritchie, R.H., 1957. Plasma losses by fast electrons in thin films. Phys. Rev. 106, 1214–1222. https://doi.org/10.1103/PhysRev.106.874.

Roessler, D.M., 1965. Kramers-Kronig analysis of reflection data. Br. J. Appl. Phys. B. 16. 195104, https://doi.org/10.1088/0508-3443/16/8/310.

Rybin, M.V., Filonov, D.S., Samusev, K.B., Belov, P.A., Kivshar, Y.S., Limonov, M.F., 2015. Phase diagram for the transition from photonic crystals to dielectric metamaterials. Nat. Commun. 6, 10102. https://doi.org/10.1038/ncomms10102.

Sahu, D.R., Lin, S.-Y., Huang, J.-L., 2008. Investigation of conductive and transparent Al-doped ZnO/Ag/Al-doped ZnO multilayer coatings by electron beam evaporation. Thin Solid Films 516, 4728–4732. https://doi.org/10.1016/j.tsf.2007.08.089.

Sakat, E., Vincent, G., Ghenuche, P., Bardou, N., Dupuis, C., Collin, S., Pardo, F., Haïdar, R., Pelouard, J.-L., 2012. Free-standing guided-mode resonance band-pass filters: from 1D to 2D structures. Opt. Express 20, 13082–13090. https://doi.org/10.1364/OE.20.013082.

Salas-Montiel, R., Apuzzo, A., Delacour, C., Sedaghat, Z., Bruyant, A., Grosse, P., Chelnokov, A., Lerondel, G., 2012. Quantitative analysis and near-field observation of strong coupling between plasmonic nanogap and silicon waveguides. Appl. Phys. Lett. 100. 231109, https://doi.org/10.1063/1.4725511.

Savelev, R.S., Shadrivov, I.V., Belov, P.A., Rosanov, N.N., Fedorov, S.V., Sukhorukov, A.A., Kivshar, Y.S., 2013. Loss compensation in metal-dielectric layered metamaterials. Phys. Rev. B. 87. 115139, https://doi.org/10.1103/PhysRevB.87.115139.

Schubert, M., 2004. Infrared Ellipsometry on Semiconductor Layer Structures. STMP 209Springer-Verlag, Berlin Heidelberg, pp. 45–65.

Schuller, J.A., Barnard, E.S., Cai, W., Jun, Y.C., White, J.S., Brongersma, M.L., 2010. Plasmonics for extreme light concentration and manipulation. Nat. Mater. 9, 193–205. https://doi.org/10.1038/NMAT2630.

Sengupta, S., Kim, J.O., Barve, A.V., Adhikary, S., Sharma, Y.D., Gautam, N., Lee, S.J., Noh, S.K., Chakrabarti, S., Krishna, S., 2012. Sub-monolayer quantum dots in

confinement enhanced dots-in-a-well heterostructure. Appl. Phys. Lett. 100. 191111, https://doi.org/10.1063/1.4711214.

Shadrivov, I.V., Zharov, A.A., Kivshar, Y.S., 2006. Second-harmonic generation in non-linear left-handed materials. J. Opt. Soc. Am. B 23, 529–534. https://doi.org/10.1364/JOSAB.23.000529.

Shalaev, V.M., 2007. Optical negative-index materials. Nat. Photonics 1, 41–48. https://doi.org/10.1126/science.1139266.

Sharma, A.K., Mohr, G.J., 2008. On the performance of surface plasmon resonance based fibre optic sensor with different bimetallic nanoparticle alloy combinations. J. Phys. D: Appl. Phys. 41. 055106, https://doi.org/10.1088/0022-3727/41/5/055106.

Sheng, Z.Y., Varadan, V.V., 2007. Tuning the effective properties of metamaterials by changing the substrate properties. J. Appl. Phys. 101. 014909, https://doi.org/10.1063/1.2407275.

Shi, J.H., Ma, H.F., Jiang, W.X., Cui, T.J., 2012. Multiband stereomaterial-based polarization spectral filter. Phys. Rev. B. 86. 035103, https://doi.org/10.1103/PhysRevB.86.035103.

Shishkin, I., Baranov, D., Slobozhanyuk, A., Filonov, D., Lukashenko, S., Samusev, A., Belov, P., 2016. Microwave platform as a valuable tool for characterization of nanophotonic devices. Sci. Rep. 6, 35516. https://doi.org/10.1038/srep35516.

Shivanand, A.L., Webb, K.J., 2012. Impact of surface roughness on the effective dielectric constants and subwavelength image resolution of metal–insulator stack lenses. Opt. Lett. 37, 4317. https://doi.org/10.1364/OL.37.004317.

Silveirinha, M.G., Baena, D.J., Jelinek, L., Marques, R., 2009. Nonlocal homogenization of an array of cubic particles made of resonant rings. Meta 3, 115. https://doi.org/10.1016/j.metmat.2009.08.004.

Simovski, C.R., 2011. On electromagnetic characterization and homogenization of nanostructured metamaterials. J. Opt. 13. 013001, https://doi.org/10.1088/2040-8978/13/1/013001.

Simovski, C.R., He, S., 2003. Frequency range and explicit expressions for negative permittivity and permeability for an isotropic medium formed by a lattice of perfectly conducting Ω particles. Phys. Lett. A 311, 254. https://doi.org/10.1016/S0375-9601(03)00494-8.

Slobozhanyuk, A.P., Khanikaev, A.B., Filonov, D.S., Smirnova, D.A., Miroshnichenko, A.E., Kivshar, Y.S., 2016. Experimental demonstration of topological effects in bianisotropic metamaterials. Sci. Rep. 6, 22270. https://doi.org/10.1038/srep22270.

Smith, D.R., Schultz, S., Markos, P., Soukoulis, C.M., 2002. Determination of effective permittivity and permeability of metamaterials from reflection and transmission coefficients. Phys. Rev. B. 65. 195104, https://doi.org/10.1103/PhysRevB.65.195104.

Smith, D.R., Vier, D.C., Koschny, T., Soukoulis, C.M., 2005. Electromagnetic parameter retrieval from inhomogeneous metamaterials. Phys. Rev. E. 71. 036617, https://doi.org/10.1103/PhysRevE.71. 036617.

Smolyaninova, V.N., Smolyaninov, I.I., Kildishev, A.V., Shalaev, V.M., 2012. Trapped rainbow techniques for spectroscopy on chip and fluorescence enhancement. Appl. Phys. B Lasers Opt. 106, 577–581. https://doi.org/10.1007/s00340-011-4856-x.

Soares, B.F., Bashevoy, M.V., Jonsson, F., MacDonald, K.F., Zheludev, N.I., 2006. Polymorphic nanoparticles as all-optical memory elements. Opt. Express. 14. 10652, https://doi.org/10.1364/OE.14.010652.

Stockman, M.I., 2011. Nanoplasmonics: past, present, and glimpse into future. Opt. Express 19, 22029–22106. https://doi.org/10.1364/OE.19.022029.

Sun, Z., Zuo, X., Li, J., 2011. Optical transmission through multilayered ultrathin metal gratings. Plasmonics 6, 745–751. https://doi.org/10.1007/s11468-011-9259-7 And references 1-12 within.

Sun, S., He, Q., Xiao, S., Xu, Q., Li, X., Zhou, L., 2012. A gradient-index meta-surface as a bridge linking propagating waves and surface waves. Nat. Mater. 11, 426–431. https://doi.org/10.1038/NMAT3292.

Sytchkova, A., 2011. Reliable deposition of induced transmission filters with a single metal layer. Appl. Opt. 50, C90–C94. https://doi.org/10.1364/AO.50.000C90.

Sytchkova, A., Grilli, M.L., Rinaldi, A., Vedraine, S., Torchio, P., Piegari, A., Flory, F., 2013. sputtered Al:ZnO-Ag transparent conductor: a plasmonic nanostructure with enhanced optical and electrical properties. J. Appl. Phys. 114, 094509. https://doi.org/10.1063/1.4820266.

Taflove, A., 1995. Computational Electrodynamics: The Finite-Difference Time-Domain Method. Artech House, Boston, p. 509.

Taguchi, A., Hayazawa, N., Furusawa, K., Ishitobi, H., Kawata, S., 2009. Deep-UV tip-enhanced Raman scattering. J. Raman Spectrosc. 40, 1324–1330. https://doi.org/10.1002/jrs.2287.

Tassin, P., Koschny, T., Kafesaki, M., Soukoulis, C.M., 2012. A comparison of grapheme, superconductors and metals as conductors formetamaterials and plasmonics. Nat. Photonics 6, 259–264. https://doi.org/10.1038/nphoton.2012.27.

Taubner, T., Korobkin, D., Urzhumov, Y., Shvets, G., Hillenbrand, R., 2006. Near-field microscopy through a SiC superlens. Science 313, 1595. https://doi.org/10.1126/science.1131025.

Thongrattanarisi, S., Silveiro, I., Garcia de Abajo, F.J., 2012. Plasmons in electrostatically doped graphene. Appl. Phys. Lett. 100. 201105, https://doi.org/10.1063/1.4714688.

Thoreson, M.D., Fang, J., Kildishev, A.V., Prokopeva, L.J., Nyga, P., Chettiar, U.K., Shalaev, V.M., Drachev, V.P., 2011. Fabrication and realistic modeling of three-dimensional metal-dielectric composites. J. Nanophotonics. 5. 051513, https://doi.org/10.1117/1.3590208.

Tibuleac, S., Magnusson, R., 1997. Reflection and transmission guided-mode resonance filters. J. Opt. Soc. Am. A 14, 1617–1626. https://doi.org/10.1364/JOSAA.14.001617.

Toma, A., Šetina Batič, B., Chiappe, D., Boragno, C., Valbusa, U., Godec, M., Jenko, M., Buatier de Mongeot, F., 2008. Patterning polycrystalline thin films by defocused ion beam: The influence of initial morphology on the evolution of self-organized nanostructures. J. Appl. Phys. 104. 104313, https://doi.org/10.1063/1.3021100.

Toudert, J., Serna, R., 2017. Interband transitions in semi-metals, semiconductors, and topological insulators: a new driving force for plasmonics and nanophotonics [Invited]. Opt. Mater. Express 7, 2299–2325. https://doi.org/10.1364/OME.7.002299.

Toudert, J., Babonneau, D., Simonot, L., Camelio, S., Girardeau, T., 2008. Quantitative modeling of surface plasmon resonances of metal nanoclusters sandwiched between dielectric layers: the influence of nanocluster size, shape and organization. Nanotechnology. 19. 125709, https://doi.org/10.1088/0957-4484/19/12/125709.

Valentine, J., Zhang, S., Zentgraf, T., Ulin-Avila, E., Genov, D.A., Bartal, G., Zhang, X., 2008. Three-dimensional optical metametrial with a negative refractive index. Nature 455, 376–379. https://doi.org/10.1038/nature07247.

Van Vlack, C., Yao, P., Hughes, S., 2011. Optical forces between coupled plasmonic nanoparticles near metal surfaces and negative index material waveguides. Phys. Rev. B 83, 245404. https://doi.org/10.1103/PhysRevB.83.245404.

Veselago, V.G., 1967. Usp. Fiz. Nauk 92, 517.

Veselago, V.G., 1968. Sov. Fiz. Usp. 10, 509.

Voshchinnikov, N.V., Faraonov, V.G., 1993. Oprical properties of spheroidal particles. Astrophys. Space Sci. 204, 19–86. https://doi.org/10.1007/BF00658095.

Wang, S.S., Magnusson, R., 1993. Theory and applications of guided-mode resonance filters. Appl. Opt. 32, 2606–2613. https://doi.org/10.1364/AO.32.002606.

Wang, H., Brandl, D.W., Le, F., Nordlander, P., Halas, N.J., 2006. Nanorice: a hybrid plasmonic nanostructure. Nano Lett. 6, 827–832. https://doi.org/10.1021/nl060209w.

West, P.R., Ishii, S., Naik, G.V., Emani, N.K., Shalaev, V.M., Boltasseva, A., 2010. Searching for better plasmonic materials. Laser Photonics Rev. 4, 798–808. https://doi.org/10.1002/lpor.200900055.

Wiener, O., 1912. Die Theorie des Mischkorpers fur das Feld der stationaren Stromung. Abh. Math-Phys. Klasse Königlich Sächsichen Des Wiss 32, 509–604.

Wu, C., Shvets, G., 2012. Design of metamaterial surfaces with broadband absorbance. Opt. Lett. 37, 308. https://doi.org/10.1364/OL.37.000308.

Wu, P., Kim, T.H., Losurdo, M., Bruno, G., Everitt, H.O., Brown, A.S., 2007. Real-time plasmon resonance tuning of liquid Ga nanoparticles by in situ spectroscopic ellipsometry. Appl. Phys. Lett. 90. 103119, https://doi.org/10.1063/1.2712508.

Wu, P.C., Losurdo, M., Kim, T.-H., Giangregorio, M., Bruno, G., Everitt, H.O., Brown, A.S., 2009. Plasmonic gallium nanoparticles on polar semiconductors: Interplay between nanoparticle wetting, localized surface plasmon dynamics, and interface charge. Langmuir 25, 924–930. https://doi.org/10.1021/la802678y.

Yamaguchi, T., Yoshida, S., Kinbara, A., 1973. Anomalous optical absorption of aggregated silver films. Thin Solid Films 18, 63–70. https://doi.org/10.1016/0040-6090(73)90221-6.

Yang, J., Fan, J.A., 2017. Analysis of material selection on dielectric metasurface performance. Opt. Express 25, 23899–23909. https://doi.org/10.1364/OE.25.023899.

Yang, W.H., Schatz, G.C., Van Duyne, R.P., 1995. Discrete dipole approximation for calculating extinction and Raman intensities for small particles with arbitrary shapes. J. Chem. Phys. 103, 869–876. https://doi.org/10.1063/1.469787.

Yeh, T.-T., Genovesi, S., Monorchio, A., Prati, E., Costa, F., Huang, T.-Y., Yen, T.-J., 2012. Ultra-broad and sharp-transition terahertz filters by hybridizing multiple resonance mode in monolithic metamaterial. Opt. Express 20 (7), 7580–7589. https://doi.org/10.1364/OE.20.007580.

Yokogawa, S., Burgos, S.P., Atwater, H.A., 2012. Plasmonic color filters for CMOS image sensor applications. Nano Lett. 12 (8), 4349–4354. https://doi.org/10.1021/nl302110z.

Yu, Y.-Y., Chang, S.-S., Lee, C.-L., Wang, C.R.C., 1997. Gold nanorods: Electrochemical synthesis and optical properties. J. Phys. Chem. B 101, 6661–6664. https://doi.org/10.1021/jp971656q.

Zhang, J., Zhang, L., 2012. Nanostructures for surface plasmons. Adv. Opt. Photon. 4, 157–321. https://doi.org/10.1364/AOP.4.000157.

Zhang, R., Bursi, L., Cox, J.D., Cui, Y., Krauter, C.M., Alabastri, A., Manjavacas, A., Calzolari, A., Corni, S., Molinari, E., Carter, E.A., García de Abajo, F.J., Zhang, H., Nordlander, P., 2017. How to identify plasmons from the optical response of nanostructures. ACS Nano 11 (7), 7321–7335. https://doi.org/10.1021/acsnano.7b03421.

Zheludev, N.I., Plum, E., Fedotov, V.A., 2011. Metamaterial polarization spectral filter: isolated transmission line at any prescribed wavelength. Appl. Phys. Lett. 99. 171915, https://doi.org/10.1063/1.3656286.

Zhu, G., Gu, L., Kitur, J., Urbas, A., Vella, J., Noginov, M., 2011. In: Organic materials with negative and controllable electric permittivity.Quantum electronics and laser science conference" (Optical Society of America).

Zhu, A., Kuznetsov, A., Luk'yanchuk, B., et al., 2017. Traditional and emerging materials for optical metasurfaces. Nanophotonics 6 (2), 452–471. https://doi.org/10.1515/nanoph-2016-0032.

CHAPTER

Scattering properties of random structures in thin films

6

Gerard Berginc*, Alexei A. Maradudin†
*Thales, La Défense, France** University of California, Irvine, CA, United States†*

6.1 INTRODUCTION

The main objective of this chapter is to outline the scattering properties of random structures and to introduce the reader to the phenomena associated with multiple scattering. We consider rough surfaces, random films, and random media with rough boundaries. Our second aim is to bring the advances of scattering modeling from random structures as close as possible to the nontraditional phenomena of scattering properties for polarized electromagnetic waves. Following the fabrication of random structures, their optical scattering properties must be determined. This review will now shift from characterization techniques and coating design to computational and theoretical modeling. Theoretically, the classical optical behavior of a random structure is governed by Maxwell's equations. This chapter outlines improvements in analytic and numerical solutions of Maxwell's equations for random structure scattering and observations of interesting new phenomena. This chapter consists of eight sections. Following the Introduction, Section 6.2 is devoted to numerical solutions of reduced Rayleigh equations for the scattering of light from dielectric films with one-dimensional (1D) rough surfaces. We present solutions for a layered two-dimensional (2D) system with one randomly rough surface. The solution is based on a numerical approach to the solution of the reduced Rayleigh equations. With the method of reduced Rayleigh equations, we can eliminate the field within the scattering medium and simplify the theoretical studies of the light scattering from a structure with rough boundaries. With this new development, satellite peaks that appear on both sides of the well-known enhanced backscattering peak can be investigated with precision for strongly rough surfaces where the small-perturbation method (SPM) is inapplicable. In Section 6.3, we consider a 2D system with two 1D randomly rough surfaces. This challenging and relatively unexplored problem is solved, and multiple-scattering effects such as enhanced backscattering, enhanced transmission, and the existence of satellite peaks are analyzed. In Section 6.4, we present a rigorous calculation of the electromagnetic field scattered from a 2D randomly rough

Optical Thin Films and Coatings. https://doi.org/10.1016/B978-0-08-102073-9.00006-0
Copyright © 2018 Elsevier Ltd. All rights reserved.

surface. Numerical calculations of the scattering of light from this kind of surface have been carried out by a variety of approaches, but such calculations remain time consuming and need improvements. A new approach to the calculation of the light is described in this section. It is based on a purely numerical solution of the reduced Rayleigh equations. The complex problem of the scattering of light from a dielectric film with a 2D randomly rough surface deposited on a planar metal substrate is treated in Section 6.5. In this section, we consider a three-dimensional (3D) system. Until now this system has been solved only by analytic methods. We describe a nonperturbative, purely numerical solution of the reduced Rayleigh equation for the case where the dielectric film has a 2D randomly rough surface and a planar interface with a metallic substrate. Analysis of satellite peaks can be performed. Section 6.6 deals with analytical methods for the scattering of light from a 3D film with randomly rough interfaces. In this section, we introduce the small-slope approximation (SSA) and the SPM for a 2D randomly rough surface. We present the most advanced form of the SPM where the amplitudes of the scattered field are expanded in powers of the surface profile function through terms of third order. The SSA is a new formulation that makes a bridge between the well-known Kirchhoff approximation and the SPM. We give the complete expressions for the scattering matrices and the cross sections for the different polarization states by introducing the Mueller matrices. In this section, we consider a generalization of the SSA to a 3D layer bounded by two randomly rough surfaces which is an unexplored problem. We introduce the development of the SSA series with the third-order SPM kernel. The new terms introduced in the SSA development describe the coupling between the two rough surfaces. With this new formulation, it is now possible to study theoretically the scattering of light from 3D films with rough boundaries for a large spectrum of roughness. In Section 6.7, we make the 3D problem more complex by considering discrete scatterers in the dielectric film. This section is devoted to a theory of transport. In this section, we introduce a new formulation based on a unified Bethe-Salpeter equation which enables obtaining a general expression for the scattered field whatever the choice of the scattering operators used at the randomly rough boundaries. We present a multiple-scattering theory for a random slab bounded by randomly rough surfaces, and we explore the relationships between the different parameters of the random medium and the rough surfaces and the polarized scattered intensity. This section is perhaps the most mathematical one of the chapter, since it contains the derivation and the demonstration of the perturbative solution of the Bethe-Salpeter equation for the polarized scattering from a random slab with a randomly rough surface. This section also treats the coherence effects of multiple scattering and the coupling between the random medium and the rough interfaces. We can observe the effect of backscattering enhancement brought about by the discrete scatterers. The final section contains concluding remarks.

We hope that the topics covered in this chapter will give an overview of new methods in scattering modeling and unconventional features of light behavior in random structures.

6.2 NUMERICAL SOLUTION OF REDUCED RAYLEIGH EQUATIONS FOR SCATTERING OF LIGHT FROM DIELECTRIC FILMS WITH 1D ROUGH SURFACES

In several papers the scattering of light from a layered system, one of whose interfaces is a 1D randomly rough interface, has been studied theoretically. It was found in these studies that if the system supports at least two (and not many more) guided waves at the frequency of the incident light, features can be present in the angular dependence of the intensity of the light scattered incoherently (diffusely) in addition to the well-known enhanced backscattering peak (McGurn et al., 1985; Maradudin et al., 1989), which appears in the retroreflection direction. These features are peaks on both sides of the enhanced backscattering peak, and have come to be called satellite peaks. They are the result of the coherent interference of multiple-scattered guided waves with the frequency of the incident light, but with different wavenumbers, that are excited by the incident light through the roughness of the single rough interface (Freilikher et al., 1994; Sánchez-Gil et al., 1994a, 1996; Wang et al., 1995). These theoretical studies were carried out for the scattering of p- and s-polarized light from a dielectric film with a 1D randomly rough surface, deposited on the planar surface of a perfect conductor (Freilikher et al., 1994; Sánchez-Gil et al., 1994a, 1996; Wang et al., 1995).

Similar effects were found in the angular dependence of the intensity of light transmitted through a multilayer system. The scattering of p-polarized light from, and its transmission through, a thin metal film whose illuminated surface was a 1D randomly rough surface, while its back surface was planar, also displayed satellite peaks (Sánchez-Gil et al., 1994b, 1995) in addition to the enhanced transmission peak in the antispecular direction (McGurn and Maradudin, 1989).

The results of these investigations showed that if the scattering system supports N surface or guided waves, where $N \geq 2$, whose wavenumbers at the frequency ω of the incident light are $q_1(\omega)$, $q_2(\omega)$, …, $q_N(\omega)$, satellite peaks should be seen in the contribution to the mean differential reflection or transmission coefficient from the light scattered incoherently at angles of scattering θ_s or transmission θ_t given by Freilikher et al. (1994) and Sánchez-Gil et al. (1994a, 1995)

$$\sin\theta_{s,t}^{(n,m)} = -\sin\theta_0 \pm \frac{c}{\omega}[q_n(\omega) - q_m(\omega)] \quad (n \neq m), \tag{6.1}$$

where θ_0 is the angle of incidence, c is the speed of light in vacuum, and m and n are integers that label the surface or guided waves, and take the values 1, 2, …, N. The maximum number N of satellite peaks that can be present is twice the number of combinations of N objects taken two at a time, viz., $N_s = 2N!/[(N-2)!2!]$. However, some of the possible combinations may not give rise to a satellite peak. This happens when the absolute value of the right-hand side of Eq. (6.1) is greater than unity. Then the corresponding peak lies in the nonradiative region of the optical spectrum. Moreover, among the real satellite peaks that should appear in the radiative region, not all may be intense enough to be observable.

The methods used in these studies of satellite peaks ranged from small-amplitude perturbation theory (Sánchez-Gil et al., 1994a,b, 1995, 1996) through many-body perturbation theory (Freilikher et al., 1994; Sánchez-Gil et al., 1994a, 1995), the stochastic functional approach (Wang et al., 1995), to computer simulations (Sánchez-Gil et al., 1994a,b, 1995). The small-amplitude perturbation calculations carried out in Sánchez-Gil et al. (1994a,b, 1995, 1996) yielded solutions of the reduced Rayleigh equation for the scattering or transmission problem being studied. In this approach, the electromagnetic field inside the dielectric or metallic film is eliminated from the calculations, so that only a single 1D integral equation for the scattering or transmission amplitude needs to be solved. It is this equation that is solved by small-amplitude perturbation theory.

For scattering from weakly rough surfaces small-amplitude perturbation theory yields good results, but it is inapplicable to scattering from strongly rough surfaces. For such surfaces, computer simulation calculations need to be used, but they yield poor results for weakly rough surfaces. Thus, there is an intermediate range of surface roughness where a different calculational approach is needed. A nonperturbative, purely numerical, solution of the reduced Rayleigh equations is one such approach (Madrazo and Maradudin, 1997; Simonsen and Maradudin, 1999). The numerical approaches to the solution of the reduced Rayleigh equations in Madrazo and Maradudin (1997), Simonsen and Maradudin (1999) were different, and may be of interest in themselves. We describe them in this section, and present some results obtained by their use.

6.2.1 A FILM WITH A 1D RANDOMLY ROUGH VACUUM-DIELECTRIC INTERFACE DEPOSITED ON THE PLANAR SURFACE OF A PERFECT CONDUCTOR

In the first case, we consider the physical system consists of a vacuum in the region $z > h(x)$, a dielectric film whose dielectric constant is ε_d in the region $-d < z < h(x)$, and a perfect conductor in the region $z < -d$ (Fig. 6.1). The surface profile function $h(x)$ is assumed to be a single-valued function of x that is differentiable with respect to x, and constitutes a zero-mean, stationary, Gaussian random process defined by

$$\langle h(x)h(x')\rangle = \sigma^2 w(|x-x'|). \tag{6.2}$$

The angle brackets here denote an average over an ensemble of realizations of the surface profile function, while $\sigma = \langle h^2(x)\rangle^{1/2}$ is the rms height of the surface.

In what follows, we will also need the power spectrum of the surface roughness $g(|k|)$, which is given by the Fourier transform of the surface height autocorrelation function $w(|x|)$:

$$g(|k|) = \int_{-\infty}^{\infty} \mathrm{d}x w(|x|) \exp(-ikx). \tag{6.3}$$

Realizations of the random surface profile are generated by the use of a filtering method based on the power spectrum (Maradudin et al., 1990).

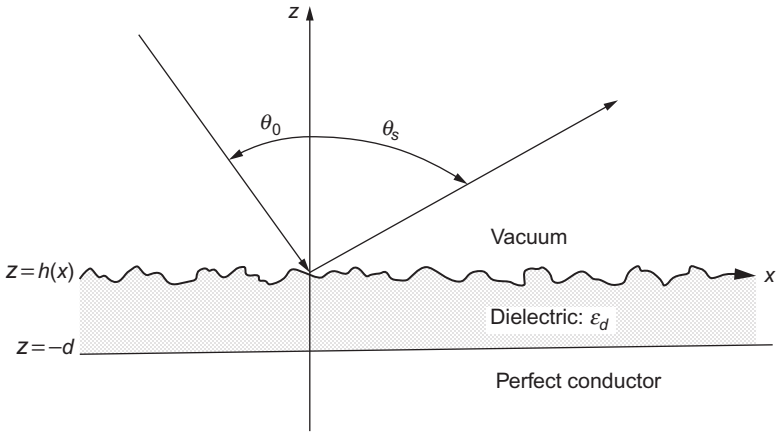


FIG. 6.1

The scattering system studied in Section 6.2.1.

This structure is illuminated from the region $z > h(x)$ by a p- or s-polarized plane wave of frequency ω, whose plane of incidence is the xz plane. There is no cross-polarized scattering in this geometry. The electromagnetic fields in this structure are given by

$$\mathrm{H}(r;t) = \big(0, \Phi_p(x, z|\,\omega), 0\big)\exp(-i\omega t) \tag{6.4a}$$

in p-polarization, and

$$\mathrm{E}(r;t) = (0, \Phi_s(x, z|\,\omega), 0)\exp(-i\omega t) \tag{6.4b}$$

in s-polarization, where $\mathbf{r} = (x, y, z)$. In the region $z > h(x)$, the field amplitude $\Phi_\nu(x, z|=\nu|\,\omega)(\nu = p, s)$ is the sum of an incident field and a Rayleigh expansion of the scattered field,

$$\Phi_v(x, z|\,\omega) = \exp[ikx - i\alpha_0(k, \omega)z] + \int_{-\infty}^{\infty} \frac{\mathrm{d}q}{2\pi} R_v(q|\,k)\exp\lfloor iqx + i\alpha_0(q, \omega)\rfloor z \tag{6.5}$$

where $\alpha_0(q, \omega) = \Big[(\omega/c)^2 - q^2\Big]^{\frac{1}{2}}$, with $\mathrm{Re}\alpha_0(q, \omega) > 0$, $\mathrm{Im}\alpha_0(q, \omega) > 0$. The angles of incidence θ_0 and scattering θ_s are measured counterclockwise and clockwise from the positive z axis, respectively, and are related to the wave numbers k and q by

$$k = \left(\frac{\omega}{c}\right)\sin\theta_0, \quad q = \left(\frac{\omega}{c}\right)\sin\theta_s. \tag{6.6}$$

The scattering amplitude $R_\nu(q|\,k)$ is the solution of the reduced Rayleigh equation (Sánchez-Gil et al., 1994a, 1996),

$$\int_{-\infty}^{\infty} \frac{\mathrm{d}q}{2\pi} M_v^{(+)}(p|\,q)R_v(q|\,k) = -M_v^{(-)}(p|\,k), \tag{6.7}$$

where

$$M_v^{(\pm)}(p|\,q) = e^{i\alpha(p,\,\omega)d}\frac{[pq \mp \alpha(p,\omega)\alpha_0(q,\omega)]^{\mu}}{\alpha(p,\omega)\pm\alpha_0(q,\omega)} I(\alpha(p,\omega)\pm\alpha_0(q,\omega)|\,p-q) - e^{-ia(p,\,\omega)d}\frac{[-pq \pm \alpha(p,\omega)\alpha_0(q,\omega)]^{\mu}}{-\alpha(p,\omega)\pm\alpha_0(q,\omega)} I(-\alpha(p,\omega)\pm\alpha_0(q,\omega)|\,p-q) \tag{6.8}$$

and

$$I(\gamma|\,Q) = \int_{-\infty}^{\infty} \mathrm{d}x\, \exp(-iQx)\exp[i\gamma h(x)]. \tag{6.9}$$

The function $\alpha(q,\ \omega)$ in Eq. (6.8) is defined by $\alpha(q,\omega) = \left[\varepsilon_d(\omega/c)^2 - q^2\right]^{\frac{1}{2}}$, with $\mathrm{Re}\alpha(q,\ \omega)>0$, $\mathrm{Im}\alpha(q,\ \omega)>0$. The exponent μ is unity in the case of p-polarization, and zero in the case of s-polarization.

To solve Eq. (6.6), in Madrazo and Maradudin (1997), a random surface profile function $h(x)$ was first generated numerically by a standard method (Maradudin et al., 1990) for x in the interval $-L/2<x<L/2$. This segment was then replicated periodically to cover the entire x axis. The resulting surface is that of a classical grating with a period L, with a complicated profile within each period. The function $I(\gamma\,|\,Q)$ defined by Eq. (6.9) now becomes

$$I(\gamma|\,Q) = \sum_{s=-\infty}^{\infty} 2\pi\delta(Q-(2\pi s/L))I_s(\gamma), \tag{6.10}$$

where

$$I_s(\gamma) = \frac{1}{L}\int_{-L/2}^{L/2} \mathrm{d}x\, \exp\left(-i\frac{2\pi s}{L}x\right)\exp[i\gamma h(x)]. \tag{6.11}$$

In order that the Floquet-Bloch theorem be satisfied, the scattering amplitude $R_\nu(q\,|\,k)$ must be expressed in the form

$$R_v(q|\,k) = \sum_{s=-\infty}^{\infty} 2\pi\delta(q-k-(2\pi s/L))R_s^{(v)}, \tag{6.12}$$

where $R_s^{(v)}$ is the amplitude of the sth Bragg beam in the diffracted field. On substituting Eqs. (6.10), (6.12) into Eq. (6.7) we obtain the equation satisfied by the $\{R_s^{(v)}\}$,

$$\sum_{n=-\infty}^{\infty} m_{v,m-n}^{(+)}(k_m|\,k_n)R_n^{(v)} = m_{v,m}^{(-)}(k_m|\,k_0),\ m=0,\pm1,\pm2,\ldots \tag{6.13}$$

where we have introduced the notation $k_m = k+(2\pi m/L)$, and

$$m_{v,s}^{(\pm)}(p|\,q) = e^{i\alpha(p,\,\omega)d}\frac{[pq \mp \alpha(p,\omega)\alpha_0(q,\omega)]^{\mu}}{\alpha(p,\omega)\pm\alpha_0(q,\omega)} I_s(\alpha(p,\omega)+\alpha_0(q,\omega)) - e^{-ia(p,\,\omega)d}\frac{[-pq \mp \alpha(p,\omega)\alpha_0(q,\omega)]^{\mu}}{-\alpha(p,\omega)\pm\alpha_0(q,\omega)} I_s(-\alpha(p,\omega)\pm\alpha_0(q,\omega)). \tag{6.14}$$

In the solution of the system of Eq. (6.13) the indices m and n are restricted to take the values 0, ±1, ±2, …, $\pm N$, to produce a finite order matrix equation for the

amplitudes of a finite number of Bragg beams, both propagating and evanescent. The propagating beams are those for which $\alpha_0(k_s, \omega)$ is real.

The Fourier coefficient $I_s(\gamma)$ is calculated by writing it as

$$\begin{aligned} I_s(\gamma) &= \delta_{s,0} + \frac{1}{L}\int_{-L/2}^{L/2} \mathrm{d}x e^{-i\frac{2\pi s}{L}x}\left(e^{i\gamma h(x)} - 1\right) \\ &\cong \delta_{s,0} + \frac{1}{L}\sum_{n=1}^{N}\frac{(i\gamma)^n}{n!}\int_{-L/2}^{L/2}\mathrm{d}x e^{-i\frac{2\pi s}{L}x}h^n(x) \\ &\cong \delta_{s,0} + \sum_{n=1}^{N}\frac{(i\gamma)^n}{n!}A_{sn}, \end{aligned} \tag{6.15}$$

where

$$\begin{aligned} A_{sn} &= \frac{1}{L}\int_{-L/2}^{L/2}\mathrm{d}x e^{-i\frac{2\pi s}{L}x}h^n(x) \\ &\cong \frac{(-1)^s}{l'}\sum_{l=0}^{l'-1}e^{-i(2\pi s l/l')}h^n(x_l). \end{aligned} \tag{6.16}$$

Here $x = -L/2 + l\Delta x$ with $\Delta x = L/l'$. In the calculations carried out in Madrazo and Maradudin (1997) the value of l' used was $l' = 8000$. For values of the rms height of the roughness up to $\sigma = 60\,\mathrm{nm}$, retaining 18 terms in the expansion Eq. (6.15) was sufficient to obtain convergent results.

The differential reflection coefficient, that is, the fraction of the total time-averaged flux incident on the surface that is scattered into the angular interval $\Delta_\theta = \theta_{s+1} - \theta_s \cong \lambda/(L\ \cos\ \theta_s)$ about the direction of the sth diffraction beam is (Madrazo and Maradudin, 1997)

$$\frac{\partial R_v}{\partial \theta_s} = \frac{L}{\lambda}\frac{\cos^2\theta_s}{\cos\theta_0}\left|R_s^{(v)}\right|^2, \tag{6.17}$$

where $\lambda = 2\pi c/\omega$ is the wavelength of the incident light. We see that if $L\ \cos\ \theta_s/\lambda$ is sufficiently large, the scattering angles θ_s can be regarded as being essentially continuously distributed. As we are dealing with scattering from a random surface, it is the average of the mean differential reflection coefficient over the ensemble of realizations of the surface profile that we need to calculate. To study nonspecular effects, it is the contribution to the mean differential reflection coefficient from the light that has been scattered incoherently (diffusely) that is of interest. It is given by Madrazo and Maradudin (1997)

$$\left\langle\frac{\partial R_v}{\partial \theta_s}\right\rangle_{incoh} = \frac{L}{\lambda}\frac{\cos^2\theta_s}{\cos\theta_0}\left[\left\langle\left|R_s^{(v)}\right|^2\right\rangle - \left|\left\langle R_s^{(v)}\right\rangle\right|^2\right]. \tag{6.18}$$

Only propagating beams contribute to this function.

The surface profile function $h(x)$ was generated on the basis of the power spectrum devised by West and O'Donnell (1995) for use in fabricating the weakly rough random surface used in their studies of the enhanced backscattering of p- and

s-polarized light from vacuum-metal interfaces by the surface plasmon polariton mechanism (McGurn et al., 1985). This power spectrum is

$$g(|k|) = \frac{\pi}{k_+ - k_-}[\theta(k-k_-)\theta(k_+-k) + \theta(-k_- - k)\theta(k+k_+)], \tag{6.19}$$

where $\theta(x)$ is the Heaviside unit step function, and

$$k_\pm = k_{sp}(\omega) \pm \frac{\omega}{c}\sin\theta_{\max}. \tag{6.20}$$

Here, $\pm k_{sp}(\omega)$ are the wavenumbers of the forward and backward propagating surface plasmon polaritons at a planar vacuum-metal interface whose frequency is that of the incident field. The significance of the angle $\theta_{\max}$ is that if the angle of incidence θ_0 is in the interval $(-\theta_{\max}, \theta_{\max})$, the incident light can excite both the forward and backward propagating surface plasmon polaritons through the surface roughness. Similarly, if the scattering angle θ_s is in the interval $(-\theta_{\max}, \theta_{\max})$, the excited surface plasmon polaritons will be converted into scattered volume waves in the vacuum region above the surface. Moreover, with this power spectrum, when angles of incidence and scattering satisfy $|q-k| < k_-$, single-scattering processes will not contribute to $\langle \partial R_\nu / \partial\theta_s\rangle_{\text{incoh}}$ (Madrazo and Maradudin, 1997).

The power spectrum Eq. (6.19) was used in the present calculations with values of k_- and k_+ chosen in such a way as to enhance the excitation of selected guided waves supported by the scattering structure.

In Fig. 6.2, we present results of calculations carried out in the manner described. The wavelength of the incident light is $\lambda = 632.8\,\text{nm}$. The period of the rough surface is $L = 160.1\lambda = 101{,}343.3\,\text{nm}$. The number of Bragg beams kept in the solution of the matrix Eq. (6.13) was 801; the number of propagating Bragg beams was 321. The plots were obtained by averaging results from $N_p = 2000$ realizations of the surface profile function. Even with the large number of surface profiles the results obtained (the broken curve in each figure) are noisy. Consequently, they were convolved with a Gaussian function of 1 degree width, and the results are plotted as continuous curves in each figure.

In Fig. 6.2A, $\langle \partial R_p/\partial\theta_s\rangle_{\text{incoh}}$ is plotted as a function of θ_s when p-polarized light is an incident normally ($\theta_0 = 0°$) on the scattering structure. The mean thickness of the dielectric film $d = 380\,\text{nm}$, and its dielectric constant $\varepsilon_d = 5.6644 + i0.1$. In the absence of roughness and absorption this scattering structure supports three guided waves whose wavenumbers are $q_1(\omega) = 2.34(\omega/c)$, $q_2(\omega) = 2.04(\omega/c)$, and $q_3 = 1.32$ (ω/c). The maximum number of satellite peaks possible is therefore six. From Eq. (6.1) it follows that they should occur at scattering angles $\theta_s^{(1,2)} = \pm 17.46$ degrees and $\theta_s^{(2,3)} = \pm 46.05$ degrees, while $\theta_s^{(1,3)}$ is in the nonradiative region.

In obtaining the result plotted in Fig. 6.2A it was assumed that the rms height of the roughness is $\sigma = 30\,\text{nm}$, and the values of k_- and k_+ are $k_- = 1.61(\omega/c)$ and $k_+ = 2.76(\omega/c)$. With these choices for k_- and k_+, the incident light can directly excite only the guided waves with wavenumbers $q_1(\omega)$ and $q_2(\omega)$. Thus, only the satellite peaks at the scattering angles $\theta_s^{(1,2)} = \pm 17.46$ degrees should be present in $\langle \partial R_p/\partial\theta_s\rangle_{\text{incoh}}$. Satellite peaks of these angles are seen in both the raw and smoothed

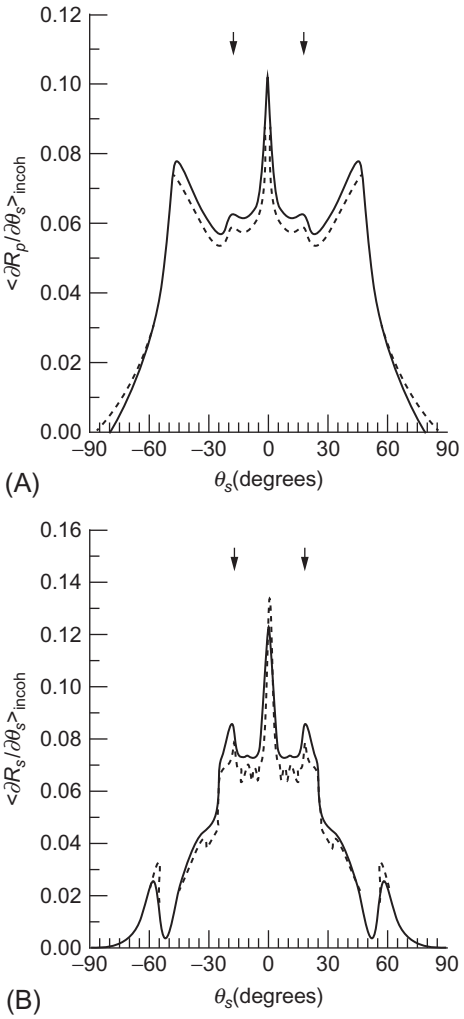


FIG. 6.2

The contribution to the mean differential reflection coefficient from the incoherent component of the scattered light when a plane wave is incident normally from vacuum on the 1D randomly rough surface of a dielectric film deposited on the planar surface of a perfect conductor. (A) p-polarization; (B) s-polarization (Madrazo and Maradudin, 1997).

data in Fig. 6.2A. There is no contribution from single-scattering processes to the result plotted in this figure. The height of the enhanced backscattering peak (at $\theta_s = 0°$) is therefore nearly twice the height of the background at its position, as is expected (Maradudin et al., 1995).

In Fig. 6.2B, we present a plot of $\langle \partial R_s/\partial\theta_s \rangle_{\text{incoh}}$ as a function of θ_s when s-polarized light is incident normally on the scattering structure. The mean thickness

of the dielectric film is now $d = 500\,\text{nm}$. The dielectric constant of the film is $\varepsilon_d = 2.689 + i0.01$. The rms height of the surface is again 30 nm, and the values of k_- and k_+ are $k_- = 0.82(\omega/c)$ and $k_+ = 1.97(\omega/c)$. This structure supports two guided waves whose wavenumbers are $q_1(\omega) = 1.5466(\omega/c)$ and $q_2(\omega) = 1.2423(\omega/c)$ (Sánchez-Gil et al., 1994a), in the absence of roughness and absorption. Thus this power spectrum is nonzero in a range of wavenumbers that contains both $q_1(\omega)$ and $q_2(\omega)$. According to Eq. (6.1) satellite peaks should be present in the result plotted in Fig. 6.2B at scattering angles $\theta_s^{(1,2)} = \pm 17.7$ degrees. Both of these peaks are present in the result presented in this figure, together with a very prominent enhanced backscattering peak. Single-scattering processes do not contribute to $\langle \partial R_s/\partial\theta \rangle_{\text{incoh}}$ for scattering angles $|\theta_s| < 55.1$ degrees. Therefore, the three peaks present in these results are due to multiple-scattering processes.

It should be noted that the satellite peaks present in the mean differential reflection coefficient for s-polarized incident light are stronger and more sharply defined than those in the mean differential reflection coefficient for p-polarized incident light. This may make satellite peaks easier to observe experimentally in s-polarization than in p-polarization.

6.2.2 A FILM WITH A PLANAR VACUUM-DIELECTRIC INTERFACE DEPOSITED ON A 1D RANDOMLY ROUGH PERFECTLY CONDUCTING SURFACE

The second scattering structure we consider consists of a vacuum in the region $z > d$, a dielectric film whose dielectric constant is ε_d in the region $h(x) < z < d$, and a perfect conductor in the region $z < h(x)$ (Fig. 6.3). The surface profile function $h(x)$ possesses the properties described in Section 6.2.1.

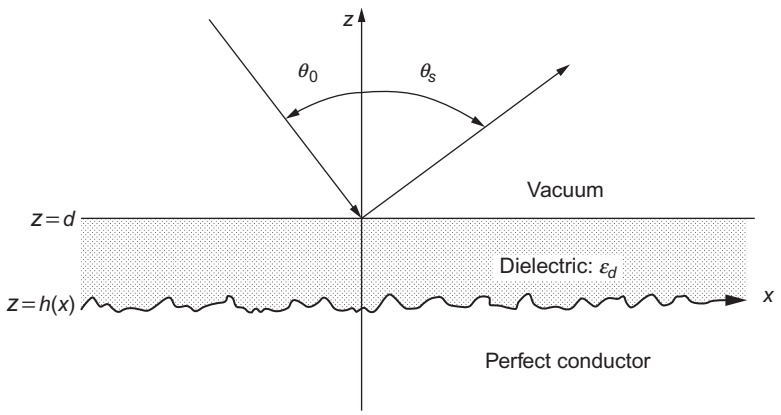


FIG. 6.3

The scattering system studied in Section 6.2.2.

This structure is illuminated from the region $z>d$ by a p- or s-polarized plane wave of frequency ω, whose plane of incidence is the xz plane. The electromagnetic fields in this structure are given by Eqs. (6.4a), (6.4b), and the field amplitude $\Phi_\nu(x, z\,|\,\omega)$ ($\nu=p, s$) entering them in the region $z>d$ is given by Eq. (6.5).

The scattering amplitude $R_\nu(q\,|\,k)$ is the solution of the reduced Rayleigh equation (Simonsen and Maradudin, 1999)

$$\int_{-\infty}^{\infty}\frac{dq}{2\pi}M_\nu^{(+)}(p|\,q)R_\nu(q|\,k)=M_\nu^{(-)}(p|\,k), \tag{6.21}$$

where for p-polarization

$$\begin{aligned}M_p^{(\pm)}(p|\,q)=&\pm e^{\pm i\alpha_0(q,\omega)d}\frac{\varepsilon_d(\omega/c)^2-pq}{\alpha(q,\omega)}\\&\times\left[e^{-i\alpha(q,\omega)d}\frac{\alpha(q,\omega)\pm\varepsilon_d\alpha_0(q,\omega)}{\alpha(q,\omega)}I(\alpha(q,\omega)|\,p-q)\right.\\&\left.+e^{i\alpha(q,\omega)d}\frac{\alpha(q,\omega)\mp\varepsilon_d\alpha_0(q,\omega)}{-\alpha(q,\omega)}I(-\alpha(q,\omega)|\,p-q)\right]\end{aligned} \tag{6.22a}$$

and for s-polarization

$$\begin{aligned}M_s^{(+)}(p|\,q)=&\pm e^{\pm i\alpha_0(q,\omega)d}\left[e^{-i\alpha(q,\omega)d}\frac{\alpha(q,\omega)\pm\alpha_0(q,\omega)}{\alpha(q,\omega)}I(\alpha(q,\omega)|\,p-q)\right.\\&\left.-e^{i\alpha(q,\omega)d}\frac{\alpha(q,\omega)\mp\alpha_0(q,\omega)}{-\alpha(q,\omega)}I(-a(q,\omega)|\,p-q)\right].\end{aligned} \tag{6.22b}$$

The contribution to the mean differential reflection coefficient from the light scattered incoherently from this structure is given in terms of the scattering amplitude $R_\nu(q\,|\,k)$ by

$$\left\langle\frac{\partial R_\nu}{\partial\theta_s}\right\rangle_{incoh}=\frac{1}{L}\left(\frac{\omega}{2\pi c}\right)\frac{\cos^2\theta_s}{\cos\theta_0}\left[\left\langle|R_\nu(q|\,k)|^2\right\rangle-|\langle R_\nu(q|\,k)\rangle|^2\right] \tag{6.23}$$

where L is now the length of the x axis covered by the rough surface. The angles of incidence and scattering, θ_0 and θ_s, respectively, are given in terms of the wavenumbers k and q by Eq. (6.6).

Eq. (6.21) was solved by replacing the infinite limits of integration by finite limits given by $q=\pm Q/2$, where $Q\gg(\omega/c)$. With a finite length of the x axis covered by the rough surface, $L\gg\lambda$, Eq. (6.21) can now be discretized by a standard numerical quadrature scheme, and a system of linear equations is obtained:

$$\frac{h_q}{2\pi}\sum_{n=-N_q/2}^{N_q/2}w_nM_\nu^{(+)}(p_m|\,q_n)R_\nu(q_n|\,k)=M_\nu^{(-)}(p_m|\,k)\;m=-\frac{N_q}{2},\ldots,\frac{N_q}{2}, \tag{6.24}$$

where N_q+1 is the number of discretization points in q space, $h_q=Q/N_q$ is the corresponding discretization length, and $\{w_n\}$ are the weights in the quadrature scheme used. The abscissas $\{q_n\}$ are defined by

$$q_n=nh_q,\quad n=-\frac{N_q}{2},\ldots,\frac{N_q}{2}. \tag{6.25}$$

The quadrature scheme used in these calculations is an $O(h_q^4)$ method with $w_1 = w_N = 3/8$, $w_2 = w_{N-1} = 7/6$, $w_3 = w_{N-2} = 23/24$, and with all the other weights equal to unity (Press et al., 1992a).

The function $I(\gamma\,|\,q)$ is now given by

$$I(\gamma|\,Q) = \int_{-L/2}^{L/2} \mathrm{d}x \exp(-iqx) \exp[i\gamma h(x)]. \tag{6.26}$$

Since we have finite cutoffs of the q integration in Eq. (6.21) at $|\,q\,| = Q/2$, it follows from Eqs. (6.21), (6.22a), (6.22b) that wavenumbers p–q in the range $(-Q, Q)$ are needed in the calculation of this integral. Because this integral is evaluated by discretizing the x variable and using the (discrete) Fourier transform, the value of Q is controlled by the spatial discretization length h_x of the problem. To resolve wavenumbers up to Q one has from the Nyquist sampling theorem (Press et al., 1992b) that the number of spatial discretization points has to satisfy $\pi/h_x \geq Q = h_q N_q$, where we have used Eq. (6.24). In principle, the wavenumber discretization length h_q used in Eq. (6.24) is independent of the one h'_q obtained from the Fourier transform. However, from a numerical point of view it is not very practical to choose different values for h_q and h'_q, and in the present calculations they were assumed to be the same $h'_q = h_q$. The discretization lengths in coordinate and wavenumber space are related by $h_q = 2\pi/Nh_x$, where N is the number of spatial discretization points. If the latter result is used in the inequality $\pi/h_x \geq Q = h_q N_q$, we find that $N \geq 2N_q$. In the present calculations the relation $N = 2N_q$ was assumed for convenience.

To evaluate the integral Eq. (6.26) the integrand was expanded in powers of $h(x)$ and the resulting expression was integrated term by term. For a moderately rough surface this expansion converges quickly. The most attractive feature of this approach, however, is that for a given realization of the surface profile function $h(x)$ the Fourier transforms of $h^n(x)$ needed to calculate $I(\gamma\,|\,q)$ have to be calculated once and for all, and do not have to be recalculated for each value of the variable γ, as would be the case if the expression Eq. (6.26) were to be calculated directly as a Fourier transform.

The calculations were carried out for the scattering of p- and s-polarized light of wavelength $\lambda = 632.8\,\mathrm{nm}$ from a dielectric film whose dielectric constant at this wavelength is $\varepsilon_d = 2.6896 + i0.01$. The mean thickness of the film is $d = 500\,\mathrm{nm}$, and the rms height of the roughness is $\sigma = 30\,\mathrm{nm}$. The length of the x axis covered by the rough surface is $L = 160.1\lambda = 101{,}343.3\,\mathrm{nm}$, the number of spatial discretization points was set to $N = 1604$, so that $N_q = 802$, and ten terms were kept in the expansion for $I(\gamma\,|\,q)$.

The surface roughness was defined by the West-O'Donnell power spectrum, Eq. (6.19), with $k_- = 0.82(\omega/c)$ and $k_+ = 1.97(\omega/c)$. With these values and normal incidence, single-scattering processes do not contribute to $\langle \partial R_\nu / \partial \theta_s \rangle_{\mathrm{incoh}}$ for scattering angles satisfying $|\,\theta_s\,| < 55.1$ degrees. Results obtained for $N_p = 3000$ realizations of the surface profile function were averaged to obtain the contribution to the mean differential reflection coefficient from the light scattered incoherently.

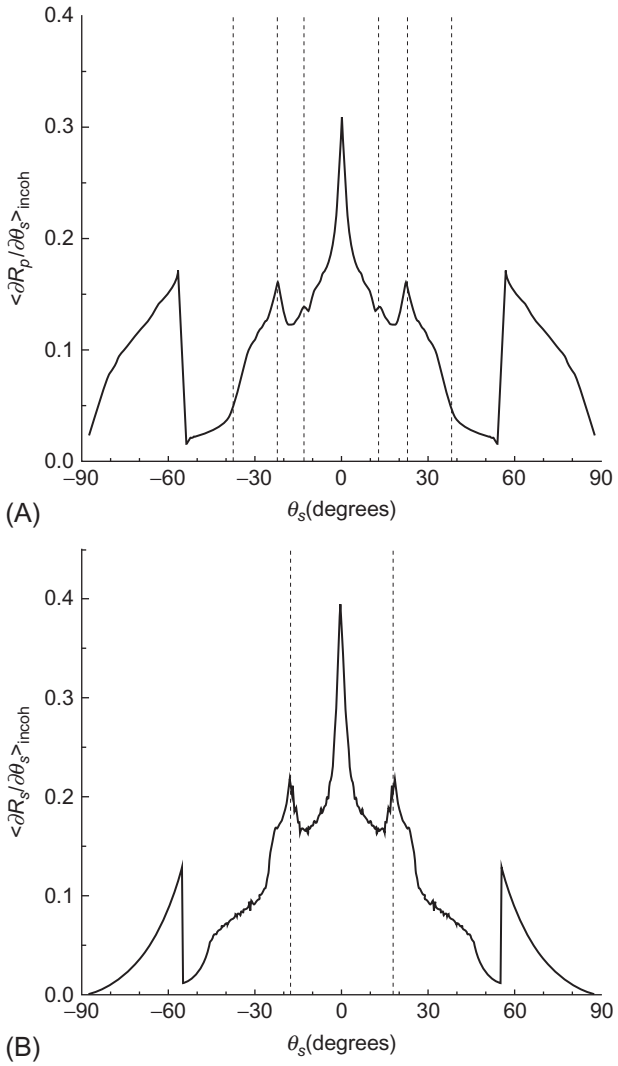


FIG. 6.4

The contribution to the mean differential reflection coefficient from the incoherent component of the scattered light when a plane wave is incident normally from vacuum on the planar surface of a dielectric film deposited on the 1D randomly rough surface of a perfect conductor. (A) p-polarization; (B) s-polarization (Simonsen and Maradudin, 1999).

In Fig. 6.4A we present a plot of $\langle \partial R_p/\partial \theta_s \rangle_{\text{incoh}}$ as a function of θ_s when p-polarized light is incident normally ($\theta_0 = 0$ degrees) on the scattering structure. In the absence of roughness and absorption this structure supports three guided waves (Madrazo and Maradudin, 1997), which according to their dispersion relation

(Madrazo and Maradudin, 1997) have the wavenumbers $q_1(\omega) = 1.6125(\omega/c)$, $q_2(\omega) = 1.3821(\omega/c)$, and $q_3 = 1.0029(\omega/c)$. Therefore, according to Eq. (6.1) there are six possible satellite peaks, and for normal incidence they occur at scattering angles $\theta_s^{(1,2)} = \pm 13.3$ degrees, $\theta_s^{(2,3)} = \pm 22.3$ degrees, and $\theta_s^{(1,3)} = \pm 37.6$ degrees. These angles lie within the angular region within which no single-scattering processes can occur. Therefore if the corresponding peaks are present, they must be multiple-scattering effects. In addition to the well-defined enhanced backscattering peak in the retroreflection direction ($\theta_s = 0$ degrees), the satellite peaks at ± 22.3 degrees are well defined in Fig. 6.4A. The peaks at ± 18.3 degrees though weaker, are clearly seen in this figure. The peaks at ± 37.6 degrees are not visible at all. This may indicate that the coupling of the incident light to the guided mode with wavenumber $q_3(\omega)$ is very weak. This cannot be the complete reason for the absence of these peaks because the peaks at ± 22.3 degrees which also involve the guided wave with wavenumbers $q_3(\omega)$, are observed, and in fact have the strongest intensities. This result can be explained by noting that the mode $q_1(\omega)$ has the largest wavenumber of the three possible guided waves, and therefore is the one that is the most difficult for the incident wave to excite. Therefore, we expect the peaks at ± 37.6 degrees to have a reduced amplitude compared with those at ± 22.3 degrees. The result that the height of the enhanced backscattering peak (at $\theta_s = 0$ degrees) is twice the height of the background at its position is additional evidence that single-scattering processes have not contributed to it (Maradudin et al., 1995).

Turning now to the case of s-polarized incident light, we present in Fig. 6.4B a plot of $\langle \partial R_s/\partial \theta_s \rangle_{\text{incoh}}$ as a function of θ_s when s-polarized light is incident normally on the scattering structure. In the absence of roughness and absorption this structure supports two guided waves with wavenumbers $q_1(\omega) = 1.5466(\omega/c)$ and $q_2(\omega) = 1.2423(\omega/c)$ (Sánchez-Gil et al., 1994a). According to Eq. (6.1) the corresponding satellite peaks are expected to occur at $\theta_s = \pm 17.7$ degrees. These peaks are clearly seen in Fig. 6.4B. They fall within the angular region within which no single-scattering processes are allowed and hence are multiple-scattering effects.

6.3 REDUCED RAYLEIGH EQUATIONS FOR THE SCATTERING OF P- AND S-POLARIZED LIGHT FROM, AND ITS TRANSMISSION THROUGH, A FILM WITH TWO 1D ROUGH SURFACES

Theoretical and computational studies of the scattering of light from a rough surface are significantly simplified if the electromagnetic field within the scattering medium can be eliminated from consideration, so that only the field in the medium of incidence has to be calculated. The method of reduced Rayleigh equations effects this elimination. This method was originally developed for the scattering of p- and s-polarized light from a medium bounded by a 1D rough surface (Toigo et al., 1977) and from a medium bounded by a 2D rough surface (Brown et al., 1984). In the former case a single 1D integral equation for the scattering amplitude is obtained, instead of the pair of coupled 1D integral equations for the scattering

and transmission amplitudes produced by a straightforward application of the Rayleigh method to the scattering problem. In the latter case a 2×2 matrix 2D integral equation is obtained for the amplitudes of the p- and s-polarized components of the scattered field, instead of the set of four coupled integral equations for the amplitudes of the p- and s-polarized components of the scattered and transmitted fields obtained by the application of the Rayleigh method to this scattering problem. The reduction of the number of integral equations that have to be solved in solving a scattering problem by the use of reduced Rayleigh equations is what gives the method its name. Reduced Rayleigh equations have also been derived for the amplitudes of the p- and s-polarized components of the field transmitted through a 1D rough surface (Toigo et al., 1977), or through a 2D rough surface (Greffet, 1988).

Reduced Rayleigh equations have also been used in studies of the scattering of light from, and its transmission through, a film with a rough surface. Reduced Rayleigh equations have been derived for the scattering amplitude in the case of the scattering of p-polarized (Sánchez-Gil et al., 1996) or s-polarized (Sánchez-Gil et al., 1994a) light from a dielectric film deposited on the planar surface of a perfect conductor, when the illuminated surface of the dielectric film is a 1D rough surface. They have also been derived for the scattering amplitude when the illuminated surface of the dielectric film is planar, while the interface between the dielectric film and the perfect conductor is a 1D rough interface (Simonsen and Maradudin, 1999). Reduced Rayleigh equations have been derived for the scattering and transmission amplitudes for p-polarized light incident on a free-standing metal film whose illuminated surface is a 1D rough surface, while its back surface is planar (Sánchez-Gil et al., 1995). Reduced Rayleigh equations have also been obtained for the scattering and transmission amplitudes for four-layer systems in which one of the three interfaces is a 1D rough interface, while the other two interfaces are planar (Leskova et al., 2005).

In the preceding examples of reduced Rayleigh equations for the scattering of light from, or its transmission through, a free-standing or supported film, all of the rough interfaces were 1D. A 2×2 matrix reduced Rayleigh equation was derived for the amplitudes of the p- or s-polarized light scattered from, or transmitted through, a dielectric film, one of whose surfaces is a 2D rough surface, while the other is planar (Soubret et al., 2001a).

In all the film systems cited above, for which reduced Rayleigh equations have been derived, only one of the interfaces was assumed to be rough, while the remaining surfaces or interfaces were assumed to be a planar. The derivation of reduced Rayleigh equations for the amplitudes of light scattered from, or transmitted through, a film bounded by two rough surfaces is a relatively unexplored problem. Such a derivation has been carried out for the case of a dielectric film bounded by two 2D rough surfaces (Soubret et al., 2001b).

Reduced Rayleigh equations for the amplitudes of p- and s-polarized light scattered from, or transmitted through, a film bounded by two 1D rough surfaces have been obtained in two different forms. The first form consists of a pair of coupled 1D integral equations for the scattering and transmission amplitudes (Fitzgerald et al., 2005). This represents a reduction in the number of integral equations that have

to be solved from the four that result from a straightforward application of the Rayleigh method to the solution of the scattering or transmission problem. The second form consists of a single 2D integral equation for the scattering amplitude alone or for the transmission amplitude alone. This represents the maximum possible reduction in the number of integral equations that have to be solved. Such maximally reduced Rayleigh equations have been obtained for the case in which the illuminating light is s-polarized (Leskova and Maradudin, 2008) and for the case in which it is p-polarized (Berginc and Maradudin, 2013). It is to a discussion of this form of reduced Rayleigh equations that this section is devoted.

The optical properties of films with two rough surfaces are of interest for several reasons. When both surfaces are periodically corrugated and anticorrelated ($h_2(x) = -h_1(x)$) they have been used in studies of the transmission of light through them that showed that the extraordinary transmission found for a metal film pierced by a parallel array of slits (Porto et al., 1999) can occur without the presence of complete slits (Fitzgerald et al., 2005; Avrutsky et al., 2000; Baumeier et al., 2006). When both surfaces are randomly corrugated, multiple-scattering effects such as enhanced backscattering or the occurrence of satellite peaks, can be enhanced or diminished by changing the correlations between the surface profile functions on the two surfaces (Leskova and Maradudin, 2008; Berginc and Maradudin, 2013). The derivation of reduced Rayleigh equations for use in calculations of the scattering of light from, and its transmission through, films with these kinds of surface roughness has as its goal the simplification of such calculations.

The physical system we study in this section is depicted in Fig. 6.5. It consists of a dielectric characterized by a dielectric constant ε_2 in the region $z > h_1(x)$, a dielectric characterized by a dielectric constant ε_2 in the region $-H + h_2(x) < z < h_1(x)$, and a

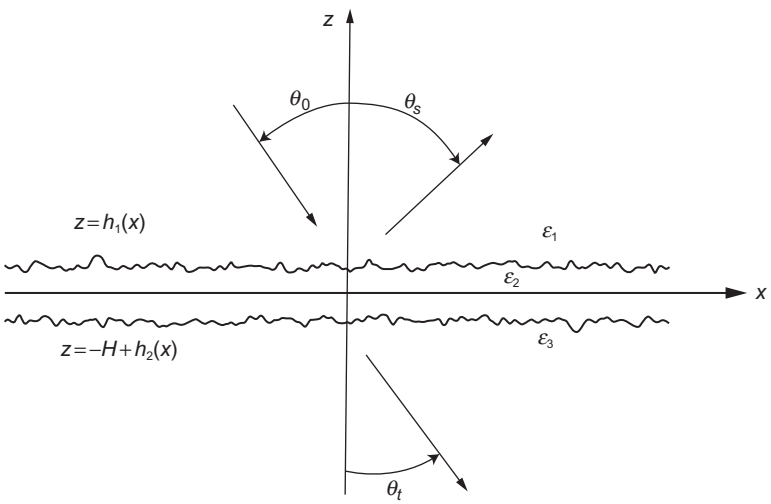


FIG. 6.5

The scattering system studied in Section 6.3.

dielectric characterized by a dielectric constant ε_3 in the region $z<-H+h_2(x)$. One or more of these dielectric constants can be frequency dependent. The surface profile functions $h_1(x)$ and $h_2(x)$ are assumed to be single-valued functions of x that are differentiable. The surface $z=h_1(x)$ is illuminated from the region $z>h_1(x)$ by a p-polarized or by an s-polarized plane wave of frequency ω, whose plane of incidence is the xz plane. There is no cross-polarized scattering in this geometry. We consider these two polarizations in turn.

6.3.1 P-POLARIZATION

In the case of p-polarization it is convenient to work with the single nonzero component of the magnetic field in this structure. It is given in the region $z>h_1(x)_{\max}$ by

$$H_2(x,z|\,\omega)=\exp[ikx-i\alpha_1(k)z]+\int_{-\infty}^{\infty}\frac{dq}{2\pi}R(q|\,k)\exp[iqx+i\alpha_1(q)z]; \tag{6.27}$$

in the region $-H+h_2(x)<z<h_1(x)$ by

$$H_2(x,z|\,\omega)=\int_{-\infty}^{\infty}\frac{dq}{2\pi}\exp(iqx)\{A_1(q|\,k)\exp[i\alpha_2(q)z]+A_2(q|\,k)\exp[-i\alpha_2(q)z]\}; \tag{6.28}$$

and in the region $z<-H+h_2(x)_{\min}$ by

$$H_2(x,z|\,\omega)=\int_{-\infty}^{\infty}\frac{dq}{2\pi}T(q|\,k)\exp[iqx-i\alpha_3(q)z], \tag{6.29}$$

where

$$\alpha_i(q)=\left[\varepsilon_i(\omega/c)^2-q^2\right]^{\frac{1}{2}},\ \mathrm{Re}\alpha_i(q)>0,\ \mathrm{Im}\alpha_i(q)>0,\quad i=1,2,3. \tag{6.30}$$

We have assumed a time dependence $\exp(-i\omega t)$ for the field, but have not indicated this explicitly.

The boundary conditions at the interface $z=h_1(x)$ require the continuity of $H_2(x,\,z\,|\,\omega)$ and $\varepsilon^{-1}\partial H_2(x,\,z\,|\,\omega)/\partial N_1$ across it, where ε is the dielectric constant of the region in which the field is being calculated, and $\partial/\partial N_1=-h'_1(x)\partial/\partial x+\partial/\partial z$, where the prime denotes differentiation with respect to x. Their satisfaction yields the pair of equations

$$\begin{aligned}\exp[ikx-i\alpha(k)(h_1)(x)]+\int_{-\infty}^{\infty}\frac{dq}{2\pi}R(q|\,k)\exp[iqx+i\alpha_1(q)h_1(x)]\\ =\int_{-\infty}^{\infty}\frac{dq}{2\pi}\{A_1(q|\,k)\exp[iqx+i\alpha_2(q)h_1(x)]\\ +A_2(q|\,k)\exp[iqx-i\alpha_2(q)h_1(x)]\}\end{aligned} \tag{6.31}$$

and

$$\begin{aligned}&\frac{1}{\varepsilon_1}\left[-h'_1(x)k-\alpha_1(k)\right]\exp[ikx-i\alpha_1(k)h_1(x)]\\ &\quad+\frac{1}{\varepsilon_1}\int_{-\infty}^{\infty}\frac{dq}{2\pi}\left[-h'_1(x)q+\alpha_1(q)\right]R(q|\,k)\exp[iqx+i\alpha_1(q)h_1(x)]\\ &\quad=\frac{1}{\varepsilon_2}\int_{-\infty}^{\infty}\frac{dq}{2\pi}\left\{A_1(q|\,k)\left[-h'_1(x)q+\alpha_2(q)\right]\exp[iqx+i\alpha_2(q)h_1(x)]\right.\\ &\quad\left.+A_2(q|\,k)\left[-h'_1(x)q-\alpha_2(q)\right]\exp[iqx-i\alpha_2(q)h_1(x)]\right\}\end{aligned} \tag{6.32}$$

The boundary conditions at the interface $z=-H+h_2(x)$ require the continuity of $H_2(x,\ z\,|\,\omega)$ and $\varepsilon^{-1}\partial H_2(x,\ z\,|\,\omega)/\partial N_2$ across it, where $\partial/\partial N_2=-h'_2(x)\partial/\partial x+\partial/\partial z$. Their satisfaction yields a second pair of equations

$$\begin{aligned}&\int_{-\infty}^{\infty}\frac{\mathrm{d}q}{2\pi}\{A_1(q\,|\,k)\exp[iqx+i\alpha_2(q)(-H+h_2(x))]\\&\quad+A_2(q\,|\,k)\exp[iqx-i\alpha_2(q)(-H+h_2(x))]\}\\&\quad=\int_{-\infty}^{\infty}\frac{\mathrm{d}q}{2\pi}T(q\,|\,k)\exp[iqx-i\alpha_3(q)(-H+h_2(x))]\end{aligned}\tag{6.33}$$

and

$$\begin{aligned}&\frac{1}{\varepsilon_2}\int_{-\infty}^{\infty}\frac{\mathrm{d}q}{2\pi}\{A_1(q\,|\,k)\left[-h'_2(x)q+\alpha_2(q)\right]\exp[iqx+i\alpha_2(q)(-H+h_2(x))]\\&\quad+A_2(q\,|\,k)\left[-h'_2(x)q-\alpha_2(q)\right]\exp[iqx-i\alpha_2(q)(-H+h_2(x))]\}\\&\quad=\frac{1}{\varepsilon_3}\int_{-\infty}^{\infty}\frac{\mathrm{d}q}{2\pi}T(q\,|\,k)\left[-h'_2(x)q-\alpha_3(q)\right]\exp[iqx-i\alpha_3(q)(-H+h_2(x))].\end{aligned}\tag{6.34}$$

To obtain a single integral equation for the scattering amplitude $R(q\,|\,k)$ alone, we first multiply Eq. (6.31) by $\varepsilon_2^{-1}[-h'_1(x)p+\alpha_2(p)]\exp[-ipx-i\alpha_2(p)h_1(x)]$, multiplying Eq. (6.32) by $\exp[-ipx-i\alpha_2(p)h_1(x)]$, where p is an arbitrary wavenumber, integrating the resulting equations over x, and adding them, the result obtained is

$$\begin{aligned}&\left(\frac{1}{\varepsilon_2}-\frac{1}{\varepsilon_1}\right)\frac{I_1(\alpha_2(p)+\alpha_1(k)\,|\,p-k)}{\alpha_2(p)+\alpha_1(k)}[\alpha_2(p)\alpha_1(k)-pk]\\&\quad-\left(\frac{1}{\varepsilon_2}-\frac{1}{\varepsilon_1}\right)\int_{-\infty}^{\infty}\frac{\mathrm{d}qI_1(\alpha_2(p)-\alpha_1(q)\,|\,p-q)}{2\pi\qquad\alpha_2(p)-\alpha_1(q)}[\alpha_2(p)\alpha_1(q)+pq]R(q\,|\,k)\\&\quad=\frac{2\alpha_2(p)}{\varepsilon_2}A_1(p\,|\,k),\end{aligned}\tag{6.35}$$

where $(j=1,\ 2)$

$$I_j(\gamma\,|\,Q)=\int_{-\infty}^{\infty}\mathrm{d}x\exp\left[-iQx-i\gamma h_j(x)\right].\tag{6.36}$$

We next multiply Eq. (6.31) by $\varepsilon_2^{-1}[h'_1(x)p+\alpha_2(p)]\exp[-ipx+i\alpha_2(p)h_1(x)]$, multiply Eq. (6.32) by $\exp[-ipx+i\alpha_2(p)h_1(x)]$, integrate the resulting equations over x, and subtract the second from the first, to obtain

$$\begin{aligned}&\left(\frac{1}{\varepsilon_2}-\frac{1}{\varepsilon_1}\right)\frac{I_1(-\alpha_2(p)+\alpha_1(k)\,|\,p-k)}{-\alpha_2(p)+\alpha_1(k)}[\alpha_2(p)\alpha_1(k)+pk]\\&\quad\left(\frac{1}{\varepsilon_2}-\frac{1}{\varepsilon_1}\right)\int_{-\infty}^{\infty}\frac{\mathrm{d}q}{2\pi}\frac{I_1(-\alpha_2(p)-\alpha_1(q)\,|\,p-q)}{-\alpha_3(p)-\alpha_1(q)}[\alpha_2(p)\alpha_1(q)-pq]R(q\,|\,k)\\&\quad=\frac{2\alpha_2(p)}{\varepsilon_2}A_2(p\,|\,k).\end{aligned}\tag{6.37}$$

We continue by multiplying Eq. (6.33) by $\varepsilon_3^{-1}[h_2'(x)p+\alpha_3(p)]\exp[-ipx+i\alpha_3(p)h_2(x)]$, multiplying Eq. (6.34) by $\exp[-ipx-i\alpha_3(p)h_2(x)]$, integrating the resulting equations over x, and adding them. The result obtained is

$$\left(\frac{1}{\varepsilon_2}-\frac{1}{\varepsilon_3}\right)\int_{-\infty}^{\infty}\frac{\mathrm{d}q}{2\pi}\left\{\frac{I_2(\alpha_3(p)-\alpha_2(q)|\,p-q)}{\alpha_3(p)-\alpha_2(q)}[\alpha_3(p)\alpha_2(q)+pq\times A_1(q|\,k)\exp[-i\alpha_2(q)H]\right.$$
$$\left.-\frac{I_2(\alpha_3(p)+\alpha_2(q)|\,p-q)}{\alpha_3(p)+\alpha_2(q)}[\alpha_3(p)\alpha_2(q)-pq]\times A_2(q|\,k)\exp[i\alpha_2(q)H]=0.\right. \tag{6.38}$$

On substituting the expressions for $A_1(q\,|\,k)$ and $A_2(q\,|\,k)$ given by Eqs. (6.35), (6.37), respectively, into Eq. (6.38), we obtain

$$\begin{aligned}
&\int_{-\infty}^{\infty}\frac{\mathrm{d}p}{2\pi}\left\{\frac{I_2(\alpha_3(p)-\alpha_2(q)|\,p-q)}{\alpha_3(p)-\alpha_2(q)}[\alpha_3(p)\alpha_2(q)+pq]\frac{\exp[-i\alpha_2(q)H]}{\alpha_2(q)}\right.\\
&\quad\times\frac{I_2(\alpha_2(q)+\alpha_1(k)|\,q-k)}{\alpha_2(q)+\alpha_1(k)}[\alpha_2(q)\alpha_1(k)-qk]\\
&\quad-\frac{I_2(\alpha_3(p)+\alpha_2(q)|\,p-q)}{\alpha_3(p)+\alpha_2(q)}[\alpha_3(p)\alpha_2(q)-pq]\frac{\exp[i\alpha_2(q)H]}{\alpha_2(q)}\\
&\quad\left.\times\frac{I_1(-\alpha_2(q)+\alpha_1(k)|\,q-k)}{-\alpha_2(q)+\alpha_1(k)}[\alpha_2(q)\alpha_1(k)+qk]\right\}\\
&-\int_{-\infty}^{\infty}\frac{\mathrm{d}q}{2\pi}\int_{-\infty}^{\infty}\frac{dr}{2\pi}\left\{\frac{I_2(\alpha_3(p)-\alpha_2(q)|\,p-q)}{\alpha_3(p)-\alpha_2(q)}[\alpha_3(p)\alpha_2(q)+pq]\right.\\
&\quad\times\frac{\exp[-i\alpha_2(q)H]}{\alpha_2(q)}\frac{I_1(\alpha_2(q)-\alpha_1(r)|\,q-r)}{\alpha_2(q)-\alpha_1(r)}[\alpha_2(q)\alpha_1(r)+qr]\\
&\quad-\frac{I_2(\alpha_3(p)+\alpha_2(q)|\,p-q)}{\alpha_3(p)+\alpha_2(q)}[\alpha_3(p)\alpha_2(q)-pq]\\
&\quad\left.\times\frac{\exp[i\alpha_2(q)H]}{\alpha_2(q)}\frac{I_1(-\alpha_2(q)-\alpha_1(r)|\,q-r)}{-\alpha_2(q)-\alpha_1(r)}[\alpha_2(q)\alpha_1(r)-qr]\right\}R(r|\,k)=0.
\end{aligned} \tag{6.39}$$

Eq. (6.39) is the reduced Rayleigh equation for the scattering amplitude $R(q\,|\,k)$ in p-polarization.

To obtain a single integral equation for the transmission amplitude $T(q\,|\,k)$ alone, we first multiply Eq. (6.31) by $\varepsilon_1^{-1}[h_1'(x)p+\alpha_1(p)]\exp[-ipx+i\alpha_1(p)h_1(x)]$, multiply Eq. (6.32) by $\exp[-ipx+i\alpha_1(p)h_1(x)]$, integrate the resulting equations over x, and subtract the second from the first. The result obtained is

$$\begin{aligned}
2\pi\delta(p-k)\frac{2\alpha_1(k)}{\varepsilon}=\left(\frac{1}{\varepsilon_1}-\frac{1}{\varepsilon_2}\right)\int_{-\infty}^{\infty}\frac{\mathrm{d}q}{2\pi}&\left\{\frac{I_1(-\alpha_1(p)-\alpha_2(q)|\,p-q)}{\alpha_1(p)+\alpha_2(q)}\right.\\
&\times[\alpha_1(p)\alpha_2(q)-pq]A_1(q|\,k)-\frac{I_1(-\alpha_1(p)+\alpha_2(q)|\,p-q)}{\alpha_1(p)-\alpha_2(q)}\\
&\left.\times[\alpha_1(p)\alpha_2(q)+pq]A_2(q|\,k)\right\}.
\end{aligned} \tag{6.40}$$

To obtain $A_1(q|k)$ and $A_2(q|k)$ in terms of $T(q|k)$ we begin by multiplying Eq. (6.33) by $\varepsilon_2^{-1}[h_2'(x)p+\alpha_2(p)]\exp[-ipx+i\alpha_2(p)h_2(x)]$, multiplying Eq. (6.34) by $\exp[-ipx+i\alpha_2(p)h_2(x)]$, integrating the resulting equations over x, and subtracting the second from the first, to obtain

$$\begin{aligned}&\frac{2\alpha_2(p)}{\varepsilon_2}\exp[i\alpha_2(p)H]A_2(p|k)\\&\quad=\left(\frac{1}{\varepsilon_3}-\frac{1}{\varepsilon_2}\right)\int_{-\infty}^{\infty}\frac{dq}{2\pi}\frac{I_2(-\alpha_2(p)+\alpha_3(q)|p-q)}{\alpha_2(p)-\alpha_3(q)}\\&\quad\times[\alpha_2(p)\alpha_3(q)+pq]\exp[i\alpha_3(q)H]T(q|k).\end{aligned}\tag{6.41}$$

We continue by multiplying Eq. (6.33) by $\varepsilon_2^{-1}[h_2'(x)p+\alpha_2(p)]\exp[-ipx+i\alpha_2(p)h_2(x)]$, multiplying Eq. (6.34) by $\exp[-ipx-i\alpha_2(p)h_2(x)]$, integrating the resulting equations over x, and adding them. The result obtained is

$$\begin{aligned}&\frac{2\alpha_2(p)}{\varepsilon_2}\exp[-i\alpha_2(p)H]A_1(p|k)\\&=-\left(\frac{1}{\varepsilon_3}-\frac{1}{\varepsilon_2}\right)\int_{-\infty}^{\infty}\frac{dq}{2\pi}\frac{I_2(\alpha_2(p)+\alpha_3(q)|p-q)}{\alpha_2(p)+\alpha_3(q)}\\&\times[\alpha_2(p)\alpha_3(q)-pq]\exp[i\alpha_3(q)H]T(q|k).\end{aligned}\tag{6.42}$$

Finally, we substitute the expressions for $A_1(q|k)$ and $A_2(q|k)$ given by Eqs. (6.42), (6.41), respectively, into Eq. (6.40), and obtain

$$\begin{aligned}2\pi\delta(p-k)\frac{2\alpha_1(k)}{\varepsilon_1}&=\varepsilon_2\left(\frac{1}{\varepsilon_2}-\frac{1}{\varepsilon_1}\right)\left(\frac{1}{\varepsilon_3}-\frac{1}{\varepsilon_2}\right)\\&\times\int_{-\infty}^{\infty}\frac{dq}{2\pi}\int_{-\infty}^{\infty}\frac{dr}{2\pi}\left\{\frac{I_1(-\alpha_1(p)-\alpha_2(q)|p-q)}{\alpha_1(p)+\alpha_2(q)}[pq-\alpha_1(p)\alpha_2(q)]\right.\\&\times\frac{I_2(\alpha_2(q)+\alpha_3(r)|q-r)}{\alpha_2(q)+\alpha_3(r)}[qr-\alpha_2(q)\alpha_3(r)]\\&\times\exp\{i[\alpha_2(q)+\alpha_3(r)]H\}+\frac{I_1(-\alpha_1(p)+\alpha_2(q)|p-q)}{\alpha_1(p)-\alpha_2(q)}\\&\times[pq+\alpha_1(p)\alpha_2(q)]\frac{I_2(-\alpha_2(q)+\alpha_3(r)|q-r)}{\alpha_2(q)-\alpha_3(r)}\\&\left.\times[qr+\alpha_2(q)\alpha_3(r)]\exp\{-i[\alpha_2(q)-\alpha_3(r)]H\}\frac{T(r|k)}{2\alpha_2(q)}\right\}.\end{aligned}\tag{6.43}$$

Eq. (6.43) is the reduced Rayleigh equation for the transmission amplitude $T(q|k)$ in p-polarization.

Thus, the system of four coupled integral Eqs. (6.31)–(6.34) from which $R(q|k)$ and $T(q|k)$ can be determined has been reduced to a single integral equation for each of these amplitudes. The price we pay for this significant reduction in the number of equations that have to be solved is that the resulting integral equations are 2D integral equations, which makes their numerical solution time consuming.

6.3.2 S-POLARIZATION

In the case of s-polarization we work with the single nonzero component of the electric field in this system. It can be written in the form

$$E_2(x,z|\,\omega) = \exp[ikx - i\alpha_1(k,\omega)z] \times \int_{-\infty}^{\infty} \frac{dq}{2\pi} R(q|\,k)\exp[iqx + i\alpha_1(q,\omega)z] \tag{6.44}$$

in the region $z > h_1(x)_{\max}$,

$$E_2(x,z|\,\omega) = \int_{-\infty}^{\infty} \frac{dq}{2\pi}\exp(iqx)\{A_1(q|\,k)\exp[i\alpha_2(q,\omega)z] + A_2(q|\,k)\exp[-i\alpha_2(q,\omega)z]\} \tag{6.45}$$

in the region $-H + h_2(x) < z < h_1(x)$, and

$$E_2(x,z|\,\omega) = \int_{-\infty}^{\infty} \frac{dq}{2\pi} T(q|\,k)\exp[iqx - i\alpha_3(q,\omega)z] \tag{6.46}$$

in the region $z < -H + h_2(x)_{\min}$.

The boundary conditions at each interface require the continuity of $E_2(x, z\,|\,\omega)$ and its normal derivative across it. This leads to the system of Rayleigh equations for the amplitudes $R(q\,|\,k)$, $A_1(qk)$, $A_2(q\,|\,k)$, and $T(q\,|\,k)$:

$$\begin{aligned}
&\exp[ikx - i\alpha_1(k,\omega)h_1(x)] + \int_{-\infty}^{\infty} \frac{dq}{2\pi} R(q|\,k)\exp[iqx + i\alpha_1(q,\omega)h_1(x)] \\
&\quad = \int_{-\infty}^{\infty} \frac{dq}{2\pi}\{A_1(q|\,k)\exp[iqx + i\alpha_2(q,\omega)h_1(x)] \\
&\qquad + A_2(q|\,k)\exp[iqx - i\alpha_2(q,\omega)h_1(x)]\}
\end{aligned} \tag{6.47}$$

$$\begin{aligned}
&-\left[h_1'(x)k - \alpha_1(k,\omega)\right]\exp[ikx - i\alpha_1(k,\omega)h_1(x)] \\
&+\int_{-\infty}^{\infty} \frac{dq}{2\pi}\left[-h_1'(x)q + \alpha_1(q,\omega)\right]R(q|\,k)\exp[iqx + i\alpha_1(q,\omega)h_1(x)] \\
&= \int_{-\infty}^{\infty} \frac{dq}{2\pi}\left\{A_1(q|\,k)\left[-h_1'(x)q + \alpha_2(q,\omega)\right]\exp[iqx + i\alpha_2(q,\omega)h_1(x)]\right. \\
&\quad \left. + A_2(q|\,k)\left[-h_1'(x)q - \alpha_2(q,\omega)\right]\exp[iqx - i\alpha_2(q,\omega)h_1(x)]\right\}
\end{aligned} \tag{6.48}$$

$$\begin{aligned}
&\int_{-\infty}^{\infty} \frac{dq}{2\pi}\{A_1(q|\,k)\exp[iqx + i\alpha_2(q,\omega)(-H + h_2(x))] \\
&\quad + A_2(q|\,k)\exp[iqx - i\alpha_2(q,\omega)(-H + h_2(x))]\} \\
&= \int_{-\infty}^{\infty} \frac{dq}{2\pi} T(q|\,k)\exp[iqx - i\alpha_3(q,\omega)(-H + h_2(x))]
\end{aligned} \tag{6.49}$$

$$\begin{aligned}
&\int_{-\infty}^{\infty} \frac{dq}{2\pi}\left\{A_1(q|\,k)\left[-h_2'(x)q + \alpha_2(q,\omega)\right]\exp[iqx + i\alpha_2(q,\omega)(-H + h_2(x))]\right. \\
&\quad \left. + A_2(q|\,k)\left[-h_2'(x)q - \alpha_2(q,\omega)\right]\exp[iqx - i\alpha_2(q,\omega)(-H + h_2(x))]\right\} \\
&= \int_{-\infty}^{\infty} \frac{dq}{2\pi} T(q|\,k)\left[-h_2'(x)q - \alpha_3(q,\omega)\right]\exp[iqx - i\alpha_3(q,\omega)(-H + h_2(x))].
\end{aligned} \tag{6.50}$$

To obtain a single integral equation for the scattering amplitude $R(q|k)$ and for the transmission amplitude $T(q|k)$ we carry out the same sequence of multiplications of Eqs. (6.47)–(6.50), integrations over x, and addition or subtraction of the resulting equations, as was done in the case of p-polarization, with one exception. Owing to the absence of dielectric constants multiplying the normal derivatives in the boundary conditions expressing the continuity of the tangential component of the magnetic field across each interface, the factors multiplying Eqs. (6.47)–(6.50) also contain no explicit dielectric constants, the results obtained are (Leskova and Maradudin, 2008)

$$\begin{aligned}
&\int_{-\infty}^{\infty}\frac{\mathrm{d}q}{2\pi}\left\{\frac{I_2(\alpha_3(p,\omega)-\alpha_2(q,\omega)|\,p-q)}{\alpha_3(p,\omega)-\alpha_2(q,\omega)}\frac{\exp[-i\alpha_2(q,\omega)H]}{\alpha_2(q,\omega)}\right.\\
&\quad\times\frac{I_1(\alpha_2(q,\omega)+\alpha_1(k,\omega)|\,q-k)}{\alpha_2(q,\omega)+\alpha_1(k,\omega)}\\
&\quad+\frac{I_2(\alpha_3(p,\omega)+\alpha_2(q,\omega)|\,p-q)}{\alpha_3(p,\omega)+\alpha_2(q,\omega)}\frac{\exp[i\alpha_2(q,\omega)H]}{\alpha_2(q,\omega)}\\
&\quad\left.\times\frac{I_1(-\alpha_2(q,\omega)+\alpha_1(k,\omega)|\,q-k)}{\alpha_2(q,\omega)-\alpha_1(k,\omega)}\right\}\\
&\quad+\int_{-\infty}^{\infty}\frac{\mathrm{d}q}{2\pi}\int_{-\infty}^{\infty}\frac{dr}{2\pi}\left\{\frac{I_2(\alpha_3(p,\omega)-\alpha_2(q,\omega)|\,p-q)}{\alpha_3(p,\omega)-\alpha_2(q,\omega)}\frac{\exp[-i\alpha_2(q,\omega)H]}{\alpha_2(q,\omega)}\right.\\
&\quad\times\frac{I_1(\alpha_2(q,\omega)-\alpha_1(r,\omega)|\,q-r)}{\alpha_2(q,\omega)-\alpha_1(r,\omega)}\\
&\quad+\frac{I_2(\alpha_3(p,\omega)+\alpha_2(q,\omega)|\,p-q)}{\alpha_3(p,\omega)+\alpha_2(q,\omega)}\frac{\exp[i\alpha_2(q,\omega)H]}{\alpha_2(q,\omega)}\\
&\quad\left.\times\frac{I_1(-\alpha_2(q,\omega)-\alpha_1(r,\omega)|\,q-r)}{\alpha_2(q,\omega)+\alpha_1(r,\omega)}\right\}R(r|\,k)=0,
\end{aligned}\tag{6.51}$$

and

$$\begin{aligned}
2\alpha_1(k,\omega)2\pi\delta(p-k)&=(\varepsilon_1-\varepsilon_2)(\varepsilon_2-\varepsilon_3)\left(\frac{\omega}{c}\right)^4\int_{-\infty}^{\infty}\frac{\mathrm{d}q}{2\pi}\int_{-\infty}^{\infty}\frac{\mathrm{d}r}{2\pi}\\
&\quad\times\left\{\frac{I_1(-\alpha_1(p,\omega)-\alpha_2(q,\omega)|\,p-q)}{\alpha_1(p,\omega)+\alpha_2(q,\omega)}\frac{\exp\{i[\alpha_2(q,\omega)+\alpha_3(r)]H\}}{2\alpha_2(q,\omega)}\right.\\
&\quad\times\frac{I_2(\alpha_2(q,\omega)+\alpha_3(r,\omega)|\,q-r)}{\alpha_2(q,\omega)+\alpha_3(r,\omega)}\\
&\quad+\frac{I_1(-\alpha_1(p,\omega)+\alpha_2(q,\omega)|\,p-q)}{\alpha_1(p,\omega)-\alpha_2(q,\omega)}\frac{\exp\{i[-\alpha_2(q)+\alpha_3(r)]H\}}{2\alpha_2(q,\omega)}\\
&\quad\left.\times\frac{I_2(-\alpha_2(q,\omega)+\alpha_3(r,\omega)|\,q-r)}{\alpha_2(q,\omega)-\alpha_3(r,\omega)}\right\}T(r|\,k).
\end{aligned}\tag{6.52}$$

Eqs. (6.51), (6.52) are the reduced Rayleigh equations for the scattering amplitude $R(q|k)$ and the transmission amplitude $T(q|k)$ in s-polarization.

6.3.3 RESULTS

The ability to calculate the scattering and transmission amplitudes $R(q\,|\,k)$ and $T(q\,|\,k)$ is central to the solution of the scattering and transmission problems. This is because the differential reflection and transmission coefficients, which are measurable quantities, are expressed in terms of these amplitudes, respectively.

The differential reflection coefficient $(\partial R/\partial\theta_s)$ is defined such that $(\partial R/\partial\theta_s)d\theta_s$ is the fraction of the total time-averaged incident flux that is scattered into the angular interval $(\theta_s, \theta_s+d\theta_s)$ in the limit as $d\theta_s\to 0$. The differential transmission coefficient $(\partial T/\partial\theta_t)$ is defined such that $(\partial T/\partial\theta_t)d\theta_t$ is the fraction of the total time-averaged incident flux that is transmitted into the angular interval $(\theta_t, \theta_t+d\theta_t)$ in the limit as $d\theta_t\to 0$. For p-polarized light we find that

$$\frac{\partial R_p}{\partial\theta_s}=\frac{\sqrt{\varepsilon_1}}{L_1}\left(\frac{\omega}{2\pi c}\right)\frac{\cos^2\theta_s}{\cos\theta_0}\left|R_p(q|\,k)\right|^2, \tag{6.53}$$

where $k=\sqrt{\varepsilon_1}(\omega/c)\sin\theta_0, q=\sqrt{\varepsilon_1}(\omega/c)\,\sin\theta_s,$ and

$$\frac{\partial T_p}{\partial\theta_t}=\frac{\sqrt{\varepsilon_1}}{L_1}\left(\frac{\omega}{2\pi c}\right)\frac{\cos^2\theta_t}{\cos\theta_0}\left|T_p(q|\,k)\right|^2, \tag{6.54}$$

where $k=\sqrt{\varepsilon_1}(\omega/c)\sin\theta_0, q=\sqrt{\varepsilon_3}(\omega/c)\,\sin\theta_t$. In Eqs. (6.53), (6.54) L_1 is the length of the x axis covered by the rough surface. Here θ_0 is the angle of incidence, measured counterclockwise from the z axis, θ_s is the scattering angle measured clockwise from the z axis and θ_t is the angle of transmission, measured counterclockwise from the negative z axis. For s-polarized light we obtain

$$\frac{\partial R_s}{\partial\theta_s}=\frac{\sqrt{\varepsilon_1}}{L_1}\left(\frac{\omega}{2\pi c}\right)\frac{\cos^2\theta_s}{\cos\theta_0}\left|R_s(q|\,k)\right|^2 \tag{6.55}$$

and

$$\frac{\partial T_s}{\partial\theta_t}=\frac{1}{L_1}\frac{\varepsilon_3}{\sqrt{\varepsilon_1}}\left(\frac{\omega}{2\pi c}\right)\frac{\cos^2\theta_t}{\cos\theta_0}\left|T_s(q|\,k)\right|^2. \tag{6.56}$$

In the case that both surfaces are randomly rough it is the average of each of these coefficients over the ensembles of realizations of the surface profile functions $h_1(x)$ and $h_2(x)$ that we must calculate. The contribution to the mean differential reflection (transmission) coefficient from the incoherent (diffuse) component of the scattered (transmitted) light is then given for p-polarized incident light by

$$\left\langle\frac{\partial R_p}{\partial\theta_s}\right\rangle_{incoh}=\frac{\sqrt{\varepsilon_1}}{L_1}\left(\frac{\omega}{2\pi c}\right)\frac{\cos^2\theta_s}{\cos\theta_0}\left[\left\langle\left|R_p(q|\,k)\right|^2\right\rangle-\left|\left\langle R_p(q|\,k)\right\rangle\right|^2\right] \tag{6.57}$$

$$\left\langle\frac{\partial R_p}{\partial\theta_t}\right\rangle_{incoh}=\frac{\sqrt{\varepsilon_1}}{L_1}\left(\frac{\omega}{2\pi c}\right)\frac{\cos^2\theta_t}{\cos\theta_0}\left[\left\langle\left|T_p(q|\,k)\right|^2\right\rangle-\left|\left\langle T_p(q|\,k)\right\rangle\right|^2\right], \tag{6.58}$$

and for s-polarized incident light by

$$\left\langle \frac{\partial R_s}{\partial \theta_s} \right\rangle_{incoh} = \frac{\sqrt{\varepsilon_1}}{L_1} \left(\frac{\omega}{2\pi c} \right) \frac{\cos^2 \theta_s}{\cos\, \theta_0} \left[\left\langle \left| R_s(q|\, k) \right|^2 \right\rangle - \left| \langle R_s(q|\, k) \rangle \right|^2 \right] \tag{6.59}$$

$$\left\langle \frac{\partial T_s}{\partial \theta_t} \right\rangle_{incoh} = \frac{1}{L_1} \frac{\varepsilon_3}{\sqrt{\varepsilon_1}} \left(\frac{\omega}{2\pi c} \right) \frac{\cos^2 \theta_t}{\cos\, \theta_0} \left[\left\langle \left| T_p(q|\, k) \right|^2 \right\rangle - \left| \langle T_s(q|\, k) \rangle \right|^2 \right]. \tag{6.60}$$

Eqs. (6.39), (6.43) and Eqs. (6.50), (6.52) have not yet been solved by nonperturbative, purely numerical means. Eqs. (6.51), (6.52) have been solved as expansions in powers of the surface profile functions $h_1(x)$ and $h_2(x)$ of the forms

$$\begin{aligned} R(q|\, k) = {} & R_0(k) 2\pi d(q-k) + \sum_i^2 R_i^{(1)}(q|\, k) \hat{h}_i(q-k) \\ & + \sum_{i,j}^2 \int_{-\infty}^{\infty} \frac{dp}{2\pi} R_{ij}^{(2)}(q|\, p|\, k) \hat{h}_i(q-p) \hat{h}_j(p-k) \\ & + \sum_{i,j,m}^2 \int_{-\infty}^{\infty} \frac{dp}{2\pi} \int_{-\infty}^{\infty} \frac{dr}{2\pi} R_{ijm}^{(3)}(q|\, p|\, r|\, k) \hat{h}_j(q-p) \hat{h}_j(p-r) \hat{h}_m(r-k) + \cdots \end{aligned} \tag{6.61}$$

and

$$\begin{aligned} T(q|\, k) = {} & T_0(k) 2\pi \delta(q-k) + \sum_i^2 T_i^{(1)}(q|\, k) \hat{h}_i(q-k) \\ & + \sum_{i,j}^2 \int_{-\infty}^{\infty} \frac{dp}{2\pi} T_{ij}^{(2)}(q|\, p|\, k) \hat{h}_i(q-p) \hat{h}_j(p-k) \\ & + \sum_{i,j,m}^2 \int_{-\infty}^{\infty} \frac{dp}{2\pi} \int_{-\infty}^{\infty} \frac{dr}{2\pi} T_{ijm}^{(3)}(q|\, p|\, r|\, k) \hat{h}_i(q-p) \hat{h}_j(p-r) \hat{h}_m(r-k) + \cdots \end{aligned} \tag{6.62}$$

where the subscripts refer to the surface profile functions $h_1(x)$ or $h_2(x)$, the superscripts denote the order in the expansion, and

$$\hat{h}_j(Q) = \int_{-\infty}^{\infty} dx h_j(x) \exp(-iQx). \tag{6.63}$$

The coefficients in these expansions are lengthy and complicated functions, and will not be presented here. They can be found in Leskova and Maradudin (2008).

To illustrate the preceding results we assume that each surface profile function constitutes a stationary, zero-mean, and Gaussian random process defined by ($j = 1, 2$)

$$\left\langle h_j(x) h_j(x') \right\rangle = \sigma_j^2 w_j(|\, x - x'|\,), \tag{6.64}$$

where the angle brackets denote an average over the ensemble of realizations of the surface profile function, and $\sigma_j = \langle h_j^2(x) \rangle^{1/2}$ s is the rms height of the corresponding

surface. The surface height autocorrelation function $wj(|x|)$ is assumed to have the Gaussian form

$$w_j(|x|) = \exp\left(-\frac{x^2}{a_j^2}\right), \tag{6.65}$$

where the characteristic length a_j is the transverse correlation length of the surface roughness.

In the calculations three cases were considered: (i) $h_1(x)$ and $h_2(x)$ are uncorrelated, so that $\langle h_1(x)h_2(x')\rangle = \langle h_2(x)h_1(x')\rangle = 0$; (ii) $h_1(x)$ and $h_2(x)$ are correlated, $h_2(x) = h_1(x)$; and (iii) $h_1(x)$ and $h_2(x)$ are anticorrelated, $h_2(x) = -h_1(x)$.

It was assumed that the wavelength of the incident light was $\lambda = 632.8\,\text{nm}$, the angle of incidence was $\theta_0 = 5°$, the region $z > h_1(x)$ was glass ($\varepsilon_1 = 2.25$), the region $-H + h_2(x) < z < h_1(x)$ was silicon ($\varepsilon_2 = 11.97 + i0.02$), and the region $z < -H + h_2(x)$ was vacuum ($\varepsilon_3 = 1$). The mean thickness of the silicon film was $H = 650\,\text{nm}$. The rms height of each surface was $\sigma = 5\,\text{nm}$, and the transverse correlation length of the surface roughness was $a = 100\,\text{nm}$ for each surface.

In Fig. 6.6 we present plots of $\langle \partial R_s/\partial\theta\rangle$ as functions of the angle of scattering θ_s, in the cases where the film surface profile functions are (a) uncorrelated, (b)

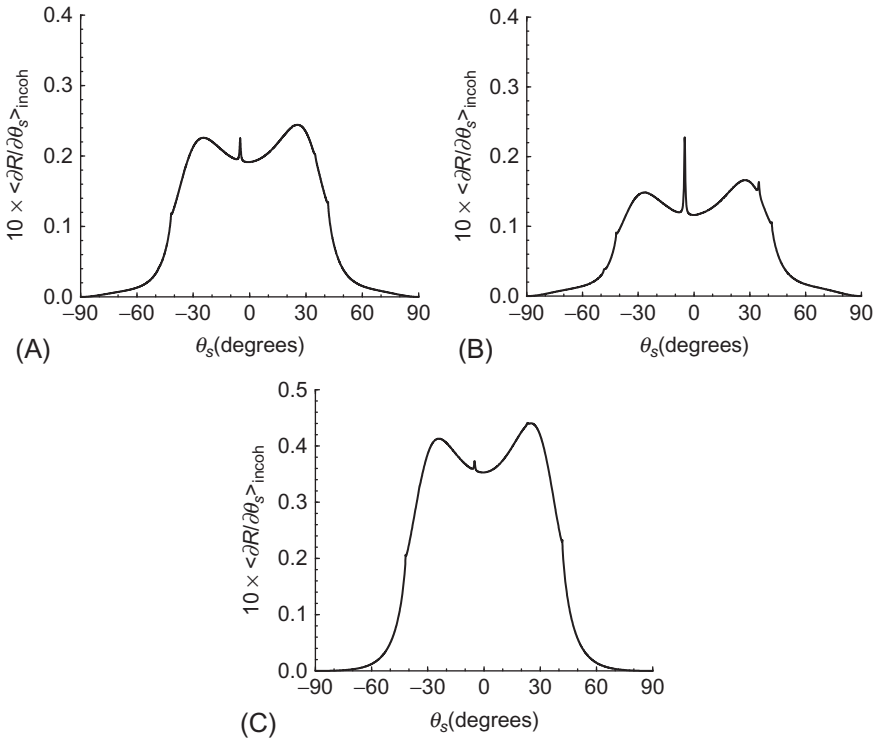


FIG. 6.6

The contribution to the mean differential reflection coefficient from the light scattered incoherently: (A) uncorrelated surface profile functions; (B) correlated surface profile functions; and (C) anticorrelated surface profile functions (Leskova and Maradudin, 2008).

correlated, and (c) anticorrelated. In each of these figures an enhanced backscattering peak (McGurn et al., 1985) is observed at the scattering angle $\theta_s = -5$ degrees. In addition satellite peaks (Freilikher et al., 1994) are present at $\theta_s = -48.15$, -41.8, 34.9, and 41.8 degrees in the case of correlated surface profile functions (Fig. 6.6B). These arise due to the guided waves supported by the scattering structure. Only two of the satellite peaks, at $\theta_s = -41.8$ degrees and 41.8 degrees, survive in the case where the surface profile functions are anticorrelated (Fig. 6.6C), and three of the satellite peaks, at $\theta_s = -41.8$, 34.9, and 41.8 degrees, are present in the case of uncorrelated surface profile functions (Fig. 6.6A). The enhanced backscattering peak is most strongly expressed in the result obtained for the case of correlated surface profile functions.

In Fig. 6.7 we present plots of $\langle \partial R_s / \partial \theta t \rangle$ as functions of the angle of transmission θ_t in the cases where the film surface profile functions are (a) uncorrelated, (b) correlated, and (c) anticorrelated. An enhanced transmission peak (McGurn and Maradudin, 1989) is present in each of these figures. In addition, satellite

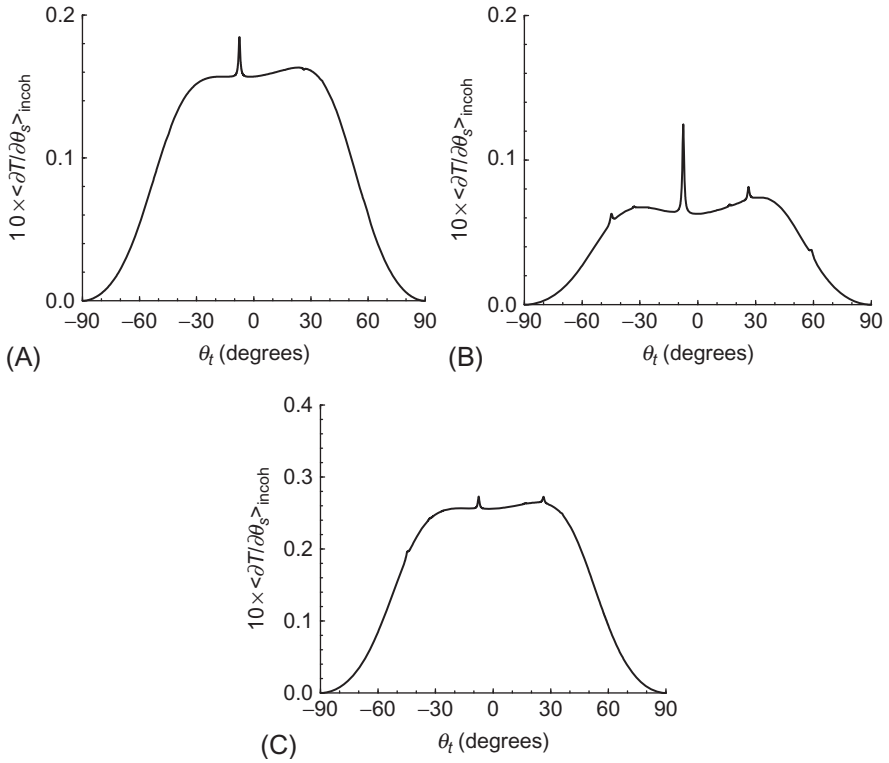


FIG. 6.7

The contribution to the mean differential transmission coefficient from the light transmitted incoherently: (A) uncorrelated surface profile functions; (B) correlated surface profile functions; and (C) anticorrelated surface profile functions (Leskova and Maradudin, 2008).

peaks (Freilikher et al., 1994) are present at $\theta_t = -44.75$, -33.05, 16.54, 26.33, and 58.84 degrees in the case of correlated surface profile functions (Fig. 6.7B). Only the satellite peaks at $\theta_t = -44.75$, 16.54, and 26.33 degrees, survive in the case where the surface profile functions are anticorrelated (Fig. 6.7C). No satellite peaks are observed in the case of the uncorrelated surface profile functions, but a weak satellite dip is present at $\theta_t = 26.33$ degrees (Fig. 6.7A). The strongest enhanced transmission peak is observed in the case where the surface profile functions are correlated.

Thus, in this section we have shown how the sets of four coupled 1D integral Eqs. (6.31)–(6.34), (6.47)–(6.50) from which the scattering amplitudes $R(q|k)$ and transmission amplitudes $T(q|k)$ can be obtained for p- and s-polarized light, respectively, incident on a film bounded by two 1D rough surfaces, can be reduced to a single 2D integral equation for each of these amplitudes. The numerical solution of these equations poses challenging computational problems, but they yield to high-order perturbative solutions as expansions in powers of the surface profile functions, as our illustrative solution shows. It has also been demonstrated that changing the degree of correlation between the two surface profile functions can significantly alter the strength of multiple-scattering effects such as enhanced backscattering and enhanced transmission, and the existence of satellite peaks.

6.4 NUMERICAL SOLUTION OF THE REDUCED RAYLEIGH EQUATION FOR THE SCATTERING OF LIGHT FROM A 2D RANDOMLY ROUGH PENETRABLE SURFACE

A rigorous calculation of the electromagnetic field scattered from a 2D randomly rough surface presents a significant computational challenge. For this reason in the past this problem has been addressed primarily by approximate methods, such as the small-amplitude perturbation theory. In the most advanced form of this method, the amplitudes of the p- and s-polarized components of the scattered field were expanded in powers of the surface profile function through terms of the third order (Soubret et al., 2001a; McGurn and Maradudin, 1996; Johnson, 1999).

However, numerical calculations of the scattering of light from 2D randomly rough, perfectly conducting (Tran et al., 1994; Wagner et al., 1997; Pak et al., 1995; Johnson et al., 1996; Torrungrueng et al., 2000; Soriano and Saillard, 2001; Simonsen et al., 2010a, 2011), and penetrable (Soriano and Saillard, 2001; Tran and Maradudin, 1994; Tsang et al., 1994; Pak et al., 1997; Engheta et al., 1992; Jandhyala et al., 1998; Simonsen et al., 2010b) surfaces have been carried out in recent years, by a variety of approaches. Nevertheless, such calculations remain computationally intensive, and need improvements in the methods used in carrying them out.

In this section, we describe a new approach to the calculation of the angular dependence of the intensity of the light scattered from a 2D randomly rough surface of a penetrable medium in contact with vacuum. It is based on a purely numerical

solution of the reduced Rayleigh equations for the scattering of p- and s-polarized light incident from vacuum on a clean, 2D randomly rough penetrable surface (Leskova et al., 2011).

The physical system we consider here consists of vacuum in the region $z > h(\mathbf{x})$, where $\mathbf{x} = (x, y, 0)$, and the scattering medium, whose dielectric function is $\varepsilon(\omega)$, in the region $z < h(\mathbf{x})$. The surface profile function $h(\mathbf{x})$ is assumed to be a single-valued function of $\mathbf{x}$ that is differentiable with respect to x and y, and constitutes a stationary, zero-mean, Gaussian random process defined by $\langle h(\mathbf{x})h(\mathbf{x}')\rangle = \sigma^2 w(\mathbf{x}-\mathbf{x}')$. The angle brackets here denote an average over the ensemble of realizations of the surface profile function, and $\sigma = \langle h^2(\mathbf{x})\rangle^{1/2}$ is the rms height of the surface.

The numerical generation of each realization of the surface profile function is carried out by a 2D version (Simonsen et al., 2011) of the filtering method used in Maradudin et al. (1990). This method is based on the power spectrum of the surface roughness $g(\mathbf{k})$, where $\mathbf{k} = (k_x, k_y, 0)$, which is defined by

$$g(\mathbf{k}) = \int d^2x w(\mathbf{x}) \exp(-i\mathbf{k}\cdot\mathbf{x}). \tag{6.66}$$

The electromagnetic field in the vacuum region $z > h(\mathbf{x})$ is the sum of an incident and a scattered field $\mathbf{E}(\mathbf{r};\, t) = [\mathbf{E}(\mathbf{r}\,|\,\omega)_{inc} + \mathbf{E}(\mathbf{r}\,|\,\omega)_{sc}] \exp(-i\omega t)$, where $\mathbf{r} = (x, y, z)$,

$$\mathrm{E}(r|\,\omega)_{\mathrm{inc}} = \left\{-\frac{c}{\omega}\left[\alpha_0(k)\hat{\mathbf{k}} + k\hat{\mathbf{e}}_z\right]B_p(\mathbf{k}) + \left(\hat{\mathbf{e}}_z \times \hat{\mathbf{k}}\right)B_x(\mathbf{k})\right\}\exp\left[i\mathbf{k}\cdot\mathbf{x} - i\alpha_0(k)z\right] \tag{6.67a}$$

$$\mathrm{E}(r|\,\omega)_{\mathrm{sc}} = \int \frac{d^2q}{(2\pi)^2}\left\{\frac{c}{\omega}[\alpha_0(\mathbf{q})\hat{\mathbf{q}} - \mathrm{q}\hat{\mathbf{e}}_z]A_p(\mathbf{q}) + (\hat{\mathbf{e}}_z \times \hat{\mathbf{q}})A_s(\mathbf{q})\right\}\exp\left[i\mathbf{q}\cdot\mathbf{x} - i\alpha_0(q)z\right], \tag{6.67b}$$

the subscripts p and s denote the p-polarized and s-polarized components of these fields with respect to the local planes of incidence and scattering, respectively, and $\alpha_0(q) = \left[(\omega/c)^2 - q^2\right]^{\frac{1}{2}}$, with $\mathrm{Re}\alpha_0(q) > 0$, $\mathrm{Im}\alpha_0(q) > 0$.

Maxwell's equations imply a linear relation between the amplitudes $A_\alpha(\mathbf{q})$ and $B_\beta(\mathbf{k})$ of the form ($\alpha, \beta = p, s$).

$$A_\alpha(\mathbf{q}) = \sum_\beta R_{u\beta}(\mathbf{q}|\,\mathbf{k})B_p(\mathbf{k}). \tag{6.68}$$

The scattering amplitudes $R_{\alpha\beta}(\mathbf{q}\,|\,\mathbf{k})$ play a central role in the present approach, because the contribution to the mean differential reflection coefficient from the incoherent (diffuse) component of the scattered light, when incident light of β polarization, whose wave vector has the projection $\mathbf{k}$ on the mean scattering surface, is scattered into light of α polarization, whose wave vector has the projection $\mathbf{q}$ on the mean scattering surface, is given by

$$\left\langle \frac{\partial R_{\alpha\beta}(\mathbf{q}|\,\mathbf{k})}{\partial\Omega_s}\right\rangle_{incoh} = \frac{1}{S}\left(\frac{\omega}{2\pi c}\right)^2 \frac{\cos^2\theta_s}{\cos\theta_0}\left[\left\langle \left|R_{\alpha\beta}(\mathbf{q}|\,\mathbf{k})\right|^2\right\rangle - \left|\left\langle \mathbf{R}_{\alpha\beta}(\mathbf{q}|\,\mathbf{k})\right\rangle\right|^2\right]. \tag{6.69}$$

Here, S is the area of the plane $z = 0$ that is covered by the rough surface, and $\theta_0(\theta_s)$ is the polar angle of incidence (scattering) measured counterclockwise (clockwise) from the z axis.

The scattering amplitudes $R_{\alpha\beta}(\mathbf{q}\,|\,\mathbf{k})$ satisfy the 2×2 matrix integral equation (Brown et al., 1984)

$$\int \frac{d^2q}{(2\pi)^2}\frac{I(\alpha(p)-\alpha_0(q)|\,\mathbf{p}-\mathbf{q})}{\alpha(p)-\alpha_0(q)}\mathbf{M}^{(+)}(\mathbf{p}|\,\mathbf{q})\mathbf{R}(\mathbf{q}|\,\mathbf{k}) = -\frac{I(\alpha(p)+\alpha_0(k)|\,\mathbf{p}-\mathbf{k})}{\alpha(p)+\alpha_0(k)}\mathbf{M}^{(-)}(\mathbf{p}|\,\mathbf{k}), \tag{6.70}$$

where $\alpha(p)=[\varepsilon(\omega)(\omega/c)^2-p^2]^{1/2}$ with $\mathrm{Re}\alpha(p)>0$, $\mathrm{Im}\alpha(p)>0$, and

$$I(\gamma|\,\mathbf{Q}) = \int \mathrm{d}^2x \exp(-i\mathbf{Q}\cdot\mathbf{x})\exp[-i\gamma h(\mathbf{x})]. \tag{6.71}$$

The matrices $\mathbf{M}^{(\pm)}(\mathbf{p}\,|\,\mathbf{q})$ are given by

$$\mathbf{M}^{(\mp)}(\mathbf{p}|\,\mathbf{q}) = \begin{pmatrix} [pq \pm \alpha(p)\hat{\mathbf{p}}\cdot\hat{\mathbf{q}}\alpha_0(q)] & -\dfrac{\omega}{c}\alpha(p)(\hat{\mathbf{p}}\times\hat{\mathbf{q}})_z \\ \pm\dfrac{\omega}{c}(\hat{\mathbf{p}}\times\hat{\mathbf{q}})_2\alpha_0(q) & \dfrac{\omega^2}{c^2}\hat{\mathbf{p}}\cdot\hat{\mathbf{q}} \end{pmatrix}. \tag{6.72}$$

A nonperturbative purely numerical solution of Eqs. (6.70)–(6.72) was obtained in the following way. A realization of the surface profile function was generated by the method described in Simonsen et al. (2011) on a square grid of N_x^2 points within a square region of the xy plane of edge L. The (linear) sampling interval was therefore $\Delta x = L/N_x$. The function $I(\gamma\,|\,\mathbf{Q})$ was then calculated by expanding the integrand in Eq. (6.71) in powers of the surface profile function $h(\mathbf{x})$, and calculating the Fourier transform of $h^n(\mathbf{x})$ by the fast Fourier transform. In evaluating the integral over $\mathbf{q}|$ in Eq. (6.70) the infinite limits were replaced by finite ones, $|q_x|<Q/2$, $|q_y|<Q/2$. The Nyquist sampling theorem (Press et al., 2007a) states that $|q_x|$ and $|q_y|$ cannot be larger than $q_c=\pi/\Delta x=\pi Nx/L$. The components of the vector $\mathbf{Q}=\mathbf{p}-\mathbf{q}$ needed in $\boldsymbol{I}(\gamma\,|\,\mathbf{Q})$, are in the interval $[-Q, Q]$, so that Q was chosen to equal q_c. A square grid with a grid constant $\Delta q=2\pi/L$ was constructed within the square region of the q_xq_y plane where $|q_x|<Q/2$ and $|q_y|<Q/2$. The integral over this region in Eq. (6.70) was carried out by a 2D version of the extended midpoint rule (Press et al., 2007b). The values of $\mathbf{q}$ and $\mathbf{p}$ used in calculating $R_{\alpha\beta}(\mathbf{q}\,|\,\mathbf{k})$ from Eq. (6.70) were given by points on this grid for a given value of $\mathbf{k}$, which was also a point on this grid. The resulting matrix equations were solved by LU factorization and back substitution. The values of $R_{\alpha\beta}(\mathbf{q}\,|\,\mathbf{k})$ and $|R_{\alpha\beta}(\mathbf{q}\,|\,\mathbf{k})|^2$ were then calculated for N_p realizations of the surface profile function. An arithmetic average of the N_p results for each of these functions yielded the averages $\langle R_{\alpha\beta}(\mathbf{q}\,|\,\mathbf{k})\rangle$ and $\langle|R_{\alpha\beta}(\mathbf{q}\,|\,\mathbf{k})|^2\rangle$ from which the mean differential reflection coefficients were calculated according to Eq. (6.69).

To illustrate this approach to the scattering of light from a penetrable surface, it has been applied to the scattering of p- and s-polarized plane waves, whose wavelength is $\lambda=632.8\,\mathrm{nm}$, from a silver surface (Leskova et al., 2011). The dielectric function of silver at this wavelength is $\varepsilon(\omega)=-16.0+i1.088$ (Johnson and Christy, 1972). The roughness of the surface was characterized by a Gaussian power spectrum $g(\mathbf{k})=\pi a^2\exp.(-a^2k^2/4)$, where the transverse correlation length a was given the value $a=\lambda/4$, while the rms height of the surface was $\sigma=\lambda/40$. For the numerical parameters the values $L=15\lambda$ and $N_x=319$ were used, which imply that $Q=6.4(\omega/c)$ and $\Delta x=\pi/Q=0.0781\lambda$.

In Fig. 6.8 we present contributions to the mean differential reflection coefficients from the light scattered incoherently as functions of the polar scattering angle θ_s for the in-plane ($\varphi_s = 0$ degrees) and out-of-plane ($\varphi_s = 90$ degrees) co-polarized (p → p, s → s) and cross-polarized (p → s, s → p) scattering when p- and s-polarized plane waves are incident on the surface at angles of incidence $(\theta_0, \varphi_0) = (25 \text{ degrees}, 0 \text{ degrees})$. An arithmetic average of results obtained for $N_p = 10{,}000$ realizations of the surface profile function was carried out to produce Fig. 6.8. There is no single-scattering contribution to the mean differential reflection coefficient in the cases of in-plane cross-polarized and out-of-plane co-polarized scattering (Tran et al., 1994), and the magnitudes of these contributions are seen to be significantly smaller than they are in the cases of in-plane co-polarized and out-of-plane cross-polarized scattering, which contain contributions from single-scattering processes. A weak enhanced backscattering peak at $\theta_s = -25$ degrees is present in the cases of in-plane scattering, but not in the cases of out-of-plane scattering. It appears as if a rougher surface is needed to produce this peak in results for out-of-plane scattering.

When the imaginary part of the dielectric function of the metal was artificially set equal to zero, it was found that the numerical approach used to solve the reduced Rayleigh equation, Eq. (6.70), conserves energy in the scattering process with an error smaller than 0.5% for the values of the parameters assumed in these calculations.

Thus, nonperturbative, purely numerical solutions of reduced Rayleigh equations open the door to theoretical studies of scattering of electromagnetic waves from weakly rough, 2D randomly rough surfaces that would be difficult to solve by other methods. We will see other examples of the use of this approach in the following section.

6.5 SCATTERING OF LIGHT FROM A DIELECTRIC FILM WITH A 2D RANDOMLY ROUGH SURFACE DEPOSITED ON A PLANAR METAL SUBSTRATE

The scattering of p- and s-polarized light from a metal surface coated with a dielectric film that has a 2D randomly rough interface with a vacuum superstrate and/or a 2D randomly rough interface with a metallic substrate has undergone little theoretical study until now. Reduced Rayleigh equations for the scattering amplitudes have been obtained for films with a single 2D randomly rough surface (Soubret et al., 2003) and for a film with two 2D randomly rough surfaces (Soubret et al., 2001b). However, until now they have been solved only by small-amplitude perturbation theory (Soubret et al., 2001b, 2003). A perturbative solution of this scattering problem, by means of the stochastic functional approach, has been carried out by Kawanishi et al. (1997a).

In this section, we describe a nonperturbative, purely numerical solution of the reduced Rayleigh equation for the case where the dielectric film has a 2D randomly rough interface with a vacuum superstrate and a planar interface with a metallic substrate (Nordam et al., 2012).

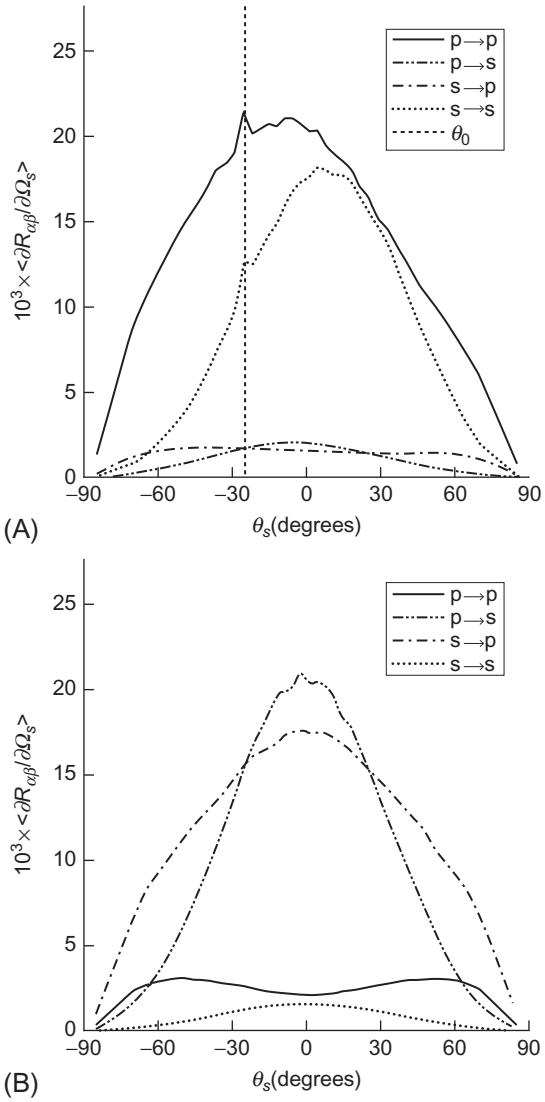


FIG. 6.8

The mean differential reflection coefficients, $\langle \partial R_{\alpha\beta}/\partial \Omega_s \rangle (\beta \to \alpha)$, as functions of the polar scattering angle θ_s. (A) In-plane ($\varphi_s = \varphi_0$) scattering. At $\theta_s = 0$ degrees, from top to bottom the curves correspond to (p → p), (s → s), (p → s), (s → p), scattering. (B) Out-of-plane ($\varphi_s = \varphi_o + 90$ degrees) scattering. At $\theta_s = 0$ degrees, from top to bottom the curves correspond to (p → s), (s → p), (p → p), (s → s) scattering. The wavelength of the incident light is $\lambda = 632.8$ nm. It is incident from vacuum on a 2D randomly rough silver surface ($\varepsilon(\omega) = -16.0 + i1.088$). The roughness of the surface is characterized by a Gaussian power spectrum with a transverse correlation length $a = \lambda/4$ and an rms height $\sigma = \lambda/40$. The angles of incidence are (θ_0, φ_0) = (25 degrees, 0 degrees).

6.5.1 SCATTERING OF LIGHT FROM A DIELECTRIC FILM WITH A 2D RANDOMLY ROUGH SURFACE DEPOSITED ON A PLANAR METAL SUBSTRATE

The system we consider consists of vacuum (ε_1) in the region $z > d + h(\mathbf{x})$; a dielectric film (ε_2) in the region $0 < z < d + h(\mathbf{x})$; and a lossy metal ($\varepsilon_3$) in the region $z < 0$. The surface profile function $h(\mathbf{x})$ is assumed to be a single-valued function of $\mathbf{x}$, that is differentiable with respect to x and y, and constitutes a zero-mean, stationary, isotropic, and Gaussian random process defined by

$$\langle h(\mathbf{x})h(\mathbf{x}')\rangle = \sigma^2 w(\mathbf{x}-\mathbf{x}') \tag{6.73}$$

The angle brackets here and in all that follows denote an average over the ensemble of realizations of the surface profile function, and $\sigma = \langle \xi^2(\mathrm{x})\rangle^{\frac{1}{2}}$ is the rms height of the surface roughness.

The electric field in the vacuum ($z > d + h(\mathbf{x})$) is the sum of an incident and a scattered field, $\mathbf{E}(\mathbf{r};\, t) = [\mathbf{E}(\mathbf{r}\,|\,\omega)_{\mathrm{inc}} + \mathbf{E}(\mathbf{r}\,|\,\omega)_{\mathrm{sc}}]\ \exp.(-i\omega t)$, where $\mathbf{r} = (x,\, y,\, z)$,

$$\mathrm{E}(\mathbf{r}|\,\omega)_{\mathrm{inc}} = \left\{\frac{c}{\omega}\left[\hat{\mathbf{k}}\alpha_1(k) + \hat{\mathbf{e}}_z k\right]B_p(\mathbf{k}) + \left(\hat{\mathbf{e}}_z \times \hat{\mathbf{k}}\right)B_s(\mathbf{k})\right\}\exp\left[i\mathbf{k}\cdot\mathbf{x} - i\alpha_1(k)z\right] \tag{6.74a}$$

$$\mathrm{E}(\mathbf{r}|\,\omega)_{\mathrm{sc}} = \int \frac{d^2\mathbf{q}}{(2\pi)^2}\left\{\frac{c}{\omega}[\hat{\mathbf{q}}\alpha_1(q) + \hat{\mathbf{e}}_z q]A_p(\mathbf{q}) + (\hat{\mathbf{e}}_z \times \hat{\mathbf{q}})A_s(\mathbf{q})\right\}\exp\left[i\mathbf{q}\cdot\mathbf{x} - i\alpha_1(q)z\right]. \tag{6.74b}$$

and the subscripts p and s denote the p-polarized and s-polarized components of these fields with respect to the local planes of incidence and scattering. A caret over a vector indicates that it is a unit vector. The functions $\alpha_i(q)(i = 1, 2, 3)$ are defined by $\alpha_i(q) = \left[\varepsilon_i(\omega/c)^2 - q^2\right]^{\frac{1}{2}}$, with $\mathrm{Re}\alpha_i(q_1) > 0$, $\mathrm{Im}\alpha_i(q) > 0$.

It follows from Maxwell's equations that there is a linear relationship between the amplitudes $A_\alpha(\mathbf{q})$ and $B_\beta(\mathbf{k})$, which we write as ($\alpha,\, \beta = p,\, s$)

$$A_a(\mathrm{q}) = \sum_\beta R_{\alpha\beta}(\mathbf{q}|\,\mathbf{k})B_\beta(k). \tag{6.75}$$

It has been shown by Soubret et al. (2003) that the scattering amplitudes $\{R_{\alpha\beta}(\mathbf{q}\,|\,\mathbf{k})\}$ satisfy the matrix integral equation

$$\int \frac{d^2q}{(2\pi)^2}\mathbf{M}(\mathbf{p}|\,\mathbf{q})R(q|\,\mathbf{k}) = -\mathbf{N}(\mathbf{p}|\,\mathbf{k}). \tag{6.76}$$

The elements of the matrices $\mathbf{M}(\mathbf{p}\,|\,\mathbf{q})$ and $\mathbf{N}(\mathbf{p}\,|\,\mathbf{k})$ in the forms are

$$\begin{aligned} M_{pp}(\mathbf{p}|\,\mathbf{q}) = {} & [pq + \alpha_2(p)(\hat{\mathbf{p}}\cdot\hat{\mathbf{q}})\alpha_1(q)]\Gamma_p(p)\exp\left[-i\{\alpha_2(p) - \alpha_1(q)\}d\right] \\ & \times \frac{I(\alpha_2(p) - \alpha_1(q)|\,(\mathrm{p}-\mathrm{q}))}{\alpha_2(p) - \alpha_1(q)} \\ & + [pq - \alpha_2(p)(\hat{\mathbf{p}}\cdot\hat{\mathbf{q}})\alpha_1(q)]\Delta_p\exp\left[i\{\alpha_2(p) + \alpha_1(q)\}d\right] \\ & \times \frac{\mathrm{I}(-\{\alpha_2(p) + \alpha_1(q)\}|\,\mathbf{p}-\mathbf{q})}{\alpha_2(p) + \alpha_1(q)} \end{aligned} \tag{6.77a}$$

$$M_{ps}(\mathbf{p}|\,\mathbf{q}) = -\frac{\omega}{c}\alpha_2(p)[\hat{\mathbf{p}}\times\hat{\mathbf{q}}]_z\{\Gamma_p(p)\exp[-i\{\alpha_2(p)-\alpha_1(q)\}d]$$
$$\times\frac{I(\alpha_2(p)-\alpha_1(q)|\,(\mathbf{p}-\mathbf{q}))}{\alpha_2(p)-\alpha_1(q)}$$
$$-\Delta_p(p)\exp[i\{\alpha_2(p)+\alpha_1(q)\}d]\frac{I(-\{\alpha_2(p)+\alpha_1(q)\}|\,\mathbf{p}-\mathbf{q})}{\alpha_2(p)+\alpha_1(q)}\} \tag{6.77b}$$

$$M_{ss}(\mathbf{p}|\,\mathbf{q}) = \frac{\omega^2}{c^2}(\hat{\mathbf{p}}\cdot\hat{\mathbf{q}})\left\{\Gamma_s(p)\exp[-i\{\alpha_2(p)-\alpha_1(q)\}d]\frac{I(\alpha_2(p)-\alpha_1(q)|(\mathbf{p}-\mathbf{q})}{\alpha_2(p)-\alpha_1(q)}\right.$$
$$\left.+\Delta_s(p)\exp[i\{\alpha_2(p)+\alpha_1(q)\}d]\frac{I(-\{\alpha_2(p)+\alpha_1(q)\}|\,\mathbf{p}-\mathbf{q})}{\alpha_2(p)+\alpha_1(q)}\right\} \tag{6.77c}$$

and

$$N_{pp}(\mathbf{p}|\,\mathbf{p}) = -\left[pk-\alpha_2(p)\left(\hat{\mathbf{p}}\cdot\hat{\mathbf{k}}\right)\alpha_1(k)\right]\Gamma_p(p)\exp[-i\{\alpha_2(p)+\alpha_1(k)\}d]$$
$$\times\frac{I(\alpha_2(p)+\alpha_1(k)|(\mathbf{p}-\mathbf{k})}{\alpha_2(p)+\alpha_1(k)}$$
$$-\left[pk+\alpha_2(p)\left(\hat{\mathbf{p}}\cdot\hat{\mathbf{k}}\right)\alpha_1(k)\right]\Delta_p(p)\exp[i\{\alpha_2(p)-\alpha_1(k)\}d] \tag{6.78a}$$
$$\times\frac{I(-\{\alpha_2(p)-\alpha_1(k)\}|\,\mathbf{p}-\mathbf{k})}{\alpha_2(p)-\alpha_1(k)}$$

$$N_{ps}(\mathbf{p}|\,\mathbf{q}) = -\frac{\omega}{c}\alpha_2(p)\left[\hat{\mathbf{p}}\times\hat{\mathbf{k}}\right]_z\left\{\Gamma_p(p)\exp[-i\{\alpha_2(p)+\alpha_1(k)\}d]\,\frac{I(\alpha_2(p)+\alpha_1(k)|(\mathbf{p}-\mathbf{k})}{\alpha_2(p)+\alpha_1(k)}\right.$$
$$\left.-\Delta_p(p)\exp[i\{\alpha_2(p)-\alpha_1(k)\}d]\frac{I(-\{\alpha_2(p)-\alpha_1(k)\}|\,\mathbf{p}-\mathbf{k})}{\alpha_2(p)-\alpha_1(k)}\right\} \tag{6.78b}$$

$$N_{sp}(\mathbf{p}|\,\mathbf{k}) = \frac{\omega}{c}\left[\hat{\mathbf{p}}\times\hat{\mathbf{k}}\right]_z\alpha_1(k)\left\{\Gamma_s(\mathbf{p})\exp[-i(\alpha_2(p)+\alpha_1(k)\}d]\right.$$
$$\times\frac{I(\alpha_2(p)+\alpha_1(k)|\,\mathbf{p}-\mathbf{k})}{\alpha_2(p)+\alpha_1(k)} \tag{6.78c}$$
$$\left.+\Delta_s(p)\exp[i\{\alpha_2(p)-\alpha_1(k)\}d]\frac{I(-\{\alpha_2(p)-\alpha_1(k)\}|\,\mathbf{p}-\mathbf{k})}{\alpha_2(p)-\alpha_1(k)}\right\}$$

$$N_{ss}(\mathbf{p}|\,\mathbf{k}) = \frac{\omega^2}{c^2}(\hat{\mathbf{p}}\cdot\hat{\mathbf{k}})\Big\{\Gamma_s(\mathbf{p})\exp[-i(\alpha_2(p)+\alpha_1(k)\}d] \times \frac{I(\alpha_2(p)+\alpha_1(k)|\,\mathbf{p}-\mathbf{k})}{\alpha_2(p)+\alpha_1(k)} + \Delta_s(p)\exp[i\{\alpha_2(p)-\alpha_1(k)\}d]\frac{I(-|\,\{\alpha_2(p)-\alpha_1(k)\}|\,\mathbf{p}-\mathbf{k})}{\alpha_2(p)-\alpha_1(k)}\Big\}. \tag{6.78d}$$

In writing Eqs. (6.77a)–(6.77c), (6.78a)–(6.78d) we have introduced the functions

$$\Gamma_p(p) = \varepsilon_2\alpha_3(p) + \varepsilon_3\alpha_2(p) \tag{6.79a}$$

$$\Delta_p(p) = \varepsilon_2\alpha_3(p) - \varepsilon_3\alpha_2(p) \tag{6.79b}$$

$$\Gamma_s(p) = \alpha_3(p) + \alpha_3(p) \tag{6.80a}$$

$$\Delta_s(p) = \alpha_3(p) - \alpha_2(p) \tag{6.80b}$$

and

$$I(\gamma|\,\mathbf{Q}) = \int d^2x\exp[-i\mathbf{Q}\cdot\mathbf{x}]\exp[-i\gamma h(\mathbf{x})]. \tag{6.81}$$

Realizations of the random surface profile function $h(\mathbf{x})$ were generated numerically by means of a 2D version (Simonsen et al., 2011; Nordam et al., n.d.) of the filtering method used by Maradudin et al. (1990). Eq. (6.76) was then solved by the method described in Section 6.4.

The preceding approach to the study of the scattering of light from a planar metal surface coated with a rough dielectric film has been applied (Nordam et al., 2012) to the scattering of p- and s-polarized plane waves, whose wavelength is $\lambda = 633\,\text{nm}$, incident from vacuum ($\varepsilon_1 = 1$) on a dielectric film ($\varepsilon_2 = 2.6896 + i0.01$) coating a silver surface ($\varepsilon_3 = -18.28 + i0.481$) (Johnson and Christy, 1972). The mean thickness of the film is $d = 0.756\lambda = 478.5\,\text{nm}$. The roughness of the vacuum-dielectric interface was characterized by a 2D version of the West-O'Donnell power spectrum (West and O'Donnell, 1995) given by McGurn and Maradudin (1996)

$$g(\mathbf{k}) = \frac{4\pi}{k_+^2 - k_-^2}\theta(|\,\mathbf{k}| - k_-)\theta(k_+ - |\mathbf{k}|), \tag{6.82}$$

where $\theta(x)$ is the Heaviside unit step function, and $k_- = 0.82(\omega/c)$, $k_+ = 1.97(\omega/c)$. The rms height of the surface roughness was assumed to be $\sigma = \lambda/40 = 15.82\,\text{nm}$.

We will denote by $\langle\partial R\alpha\beta\ (\mathbf{q}|\,\mathbf{k})/\partial\Omega_s\rangle_{\text{incoh}}$ the contribution to the mean differential reflection coefficient when light of β polarization with a projection $\mathbf{k}$ of its wave vector on the mean scattering surface is scattered incoherently into light of α polarization with a projection $\mathbf{q}$ of its wave vector on the mean scattering surface. The contribution to $\langle\partial R\alpha\beta(\mathbf{q}|\,\mathbf{k})/\partial\Omega_s\rangle_{\text{incoh}}$ from light scattered by single-scattering processes (second order in $h(\mathbf{x})$) is proportional to $g(|\,\mathbf{q}-\mathbf{k}\,|)$

where $\mathbf{q}=(\omega/c)\ \sin\theta_s\ (\cos\varphi_s,\ \sin\varphi_s,\ 0)$, $\mathbf{k}=(\omega/c)\ \sin\theta_0(\cos\varphi_0,\ \sin\varphi_0,\ 0)$ (McGurn and Maradudin, 1996). Since the power spectrum Eq. (6.82) is identically zero for $|\mathbf{k}|<k_-$, it follows that there is no contribution to the mean differential reflection coefficient from the light scattered incoherently by single-scattering processes when the wave vectors $\mathbf{q}$ and $\mathbf{k}$ satisfy the inequality $|\mathbf{q}-\mathbf{k}|<k_-$.

In Fig. 6.9A we present the contributions to the mean differential reflection coefficients from the light scattered incoherently as functions of the polar scattering angle θ_s for the in-plane ($\varphi_s=\varphi_0=45$ degrees) co-polarized (p $\rightarrow$ p, s $\rightarrow$ s) and cross-polarized (p $\rightarrow$ s, s $\rightarrow$ p) scattering when a p- or s-polarized plane wave is incident on the dielectric film at angles of incidence (θ_0, φ_0) given by (3.7 degrees, 45 degrees). An arithmetic average of results obtained for $N_p=11{,}165$ realizations of the surface profile function was carried out to produce these figures. In this case of in-plane scattering there is no contribution to the mean differential reflection coefficients for scattering angles in the interval -49.06 degrees $<\theta_s<62.20$ degrees. A well-defined enhanced backscattering peak is present in the retroreflection direction in each of the four curves plotted in this figure. The height of this peak in each case is very close to twice that of the background at its position, which supports the conclusion that it occurs in an angular interval within which single-scattering processes make no contribution to the mean differential reflection coefficients (Shchegrov et al., 2004).

In addition to the enhanced backscattering peaks in Fig. 6.9A additional peaks are seen on both sides of this peak in the s $\rightarrow$ s co-polarized scattering contribution to the mean differential reflection coefficient. These peaks are identified as satellite peaks.

We saw earlier that in the in-plane co-polarized scattering of light of frequency ω from a 1D randomly rough surface of a film system, when the plane of incidence is perpendicular to the generators of the surface, satellite peaks occur at scattering angles given by Eq. (6.1). The scattering angles defined by this equation are expected to give the angles at which satellite peaks occur in the in-plane co-polarized scattering from the two-dimensional randomly rough surfaces of the film system studied here.

It has been found that in the absence of absorption and roughness this film system supports two guided waves in p-polarization, whose wavenumbers are

$$q_1(\omega)=1.4391(\omega/c),\quad q_2(\omega)=1.0119(\omega/c),$$

and two guided waves in s-polarization, whose wavenumbers are

$$q_1(\omega)=1.5467(\omega/c),\quad q_2(\omega)=1.2432(\omega/c).$$

These results predict satellite peaks at scattering angles $\theta_s=-29.46$ degrees and $\theta_s=21.26$ degrees in p-polarization, and at $\theta_s=-21.26$ degrees and $\theta_s=13.82$ degrees in s-polarization. These scattering angles are indicated by vertical dotted lines in this figure. The peaks at $\theta_s=-21.60$ and 13.82 degrees are seen in the s $\rightarrow$ s co-polarized scattering contribution to the mean differential reflection coefficient.

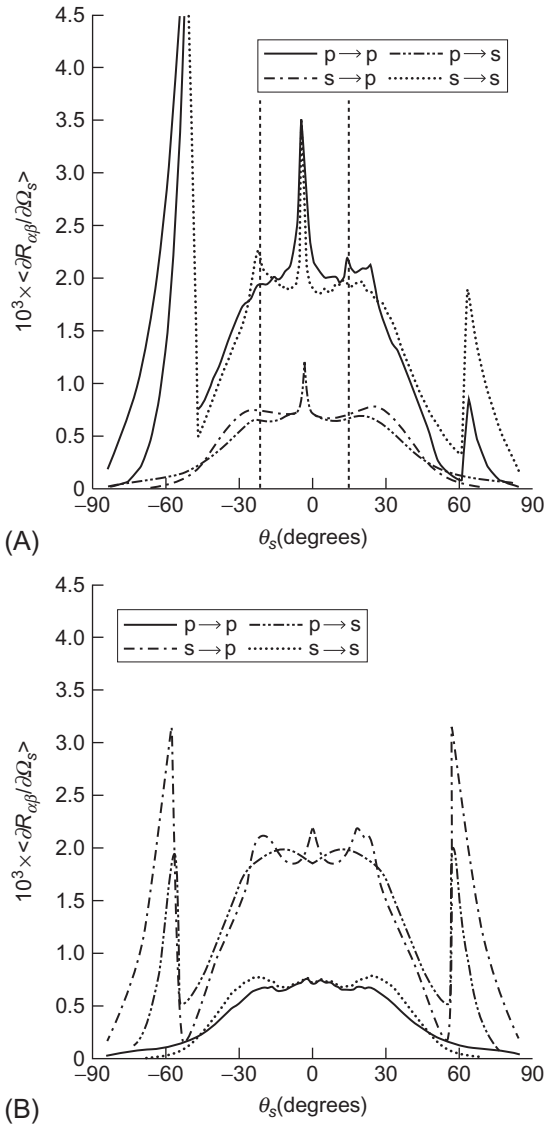


FIG. 6.9

The contributions to the mean differential reflects coefficients as functions of the polar scattering angle θ_s, for the scattering of light incident from vacuum on the 2D randomly rough surface of a dielectric film deposited on a planar silver surface. The wavelength of the incident light is $\lambda = 632.8\,\text{nm}$, the dielectric constant of silver at this wavelength is $\varepsilon_3 = -18.28 + i0.481$, and the angles of incidence are $(\theta_0, \varphi_0) = (3.7\,\text{degrees}, 45\,\text{degrees})$. The dielectric constant of the film is $\varepsilon_2 = 2.6896 + i0.01$, and its mean thickness is $d = 478.5\,\text{nm}$. The roughness of the dielectric surface is characterized by the West-O'Donnell power spectrum, Eq. (6.82), with $k_- = 0.82(\omega/c)$, $k_+ = 1.97(\omega/c)$, and its rms height is $\sigma = 15.82\,\text{nm}$. (A) In-plane ($\varphi_s = \varphi_0$) scattering. At $\theta_s = -25\,\text{degrees}$, from top to bottom the curves correspond to (s→s), (p→p), (s→p), (p→s) scattering. (B) Out-of-plane ($\varphi_s = \varphi_0 + 90\,\text{degrees}$) scattering. At $\theta_s = -25\,\text{degrees}$, from top to bottom the curves correspond to (s→p), (p→s), (s→s), (p→p), scattering.

The satellite peaks predicted to occur at $\theta_s = -29.46$ and 21.26 degrees in the p → p co-polarized contribution to the mean differential reflection coefficient are not visible, presumably because they are too weak to be seen. This result disagrees with those of Soubret et al. (2003), where no satellite peaks were found in the in-plane s → s scattering contribution to the mean differential reflection coefficient when the substrate is a metal, although they are present when the substrate is a perfect conductor. However, the randomly rough surface studied by Soubret et al. (2003) was characterized by a Gaussian power spectrum, not by the 2D West-O'Donnell power spectrum given by Eq. (6.82). This result also disagrees with those of Kawanishi et al. (1997a), where no evidence of satellite peaks was observed in any scattering configuration. In this work, the roughness of the vacuum-film interface was characterized by a Gaussian power spectrum, and the substrate was a perfect conductor. It is shown (Madrazo and Maradudin, 1997) that the use of a Gaussian power spectrum to describe the 1D roughness of a dielectric film on a planar perfectly conducting surface produces weaker satellite peaks than when the roughness is characterized by a West-O'Donnell power spectrum.

Turning now to the results for out-of-plane scattering presented in Fig. 6.9B, we note first that single-scattering processes give no contribution to the mean differential reflection coefficient for -54.83 degrees $< \theta_s <$ 54.83 degrees. A weak enhanced backscattering peak is present in the cross-polarized (p → s, s → p) contributions to the mean differential reflection coefficient. The enhanced backscattering peak in the in-plane p → p scattering turns into the peak in the out-of-plane p → s scattering. Hence, the out-of-plane p → s "enhanced backscattering peak" is simply the shoulder of the in-plane p → p enhanced backscattering peak. From Fig. 6.9A it is seen that the p → p peak is broader than the s → s peak, which means that there is no s → s "backscattering shoulder" in the out-of-plane scattering.

It is important to note that in out-of-plane scattering the dominant contribution to the differential reflection coefficient is due to cross-polarized scattering. Satellite peaks are now present in the p → s scattering contribution, which means that incident p-polarized light excites both of the s-polarized guided waves with wave vectors in the $\varphi_s = \varphi 0 + 90$ degrees direction, which then interferes to produce satellite peaks in out-of-plane scattering. Consequently, the satellite peaks found in the in-plane co-polarized scattering of light from 1D randomly rough surfaces turn into a kind of "satellite ring" formation in scattering from 2D randomly rough surfaces, where part of a ring is co-polarized (s → s, in-plane) and part is cross-polarized (p → s, out-of-plane). We note that the out-of-plane scattering contributions have not been calculated in the earlier perturbative studies of the current problem (Soubret et al., 2003; Kawanishi et al., 1997a).

The main physical result obtained from the calculations described in this section is that satellite peaks can arise in the scattering of light from the film structure studied. This result is in agreement with results of Soubret et al. (2003) but not with those of Kawanishi et al. (1997a). A detailed study of the conditions under which satellite peaks occur in the presence of 2D surface roughness is lacking. Perhaps the computational approach described here will be used to determine them.

6.5.2 A DIELECTRIC FILM WITH A PLANAR INTERFACE WITH A DIELECTRIC SUPERSTRATE AND A 2D RANDOMLY ROUGH INTERFACE WITH A DIELECTRIC SUBSTRATE

In Section 6.5.1 the illuminated surface of the film was assumed to be a 2D randomly rough surface while its back surface was planar. In this section we consider the opposite case, viz., the illuminated surface of the film is planar, while its back surface is a 2D randomly rough surface.

Thus, the scattering system we consider here consists of a dielectric medium whose dielectric constant is ϵ_1 in the region $z>0$, a dielectric medium whose dielectric constant is ϵ_2 in the region $-d+h(\mathrm{x})<z<0$, and a dielectric medium whose dielectric constant is ϵ_3 in the region $z<-d+h(\mathrm{x})$. The dielectric constants ϵ_1, ϵ_2, and ϵ_3 are assumed to be real and positive. The surface profile function $h(\mathrm{x})$ has the properties described in Section 6.5.1.

The interface $z=0$ is illuminated from the region $z>0$ by a plane wave of frequency ω. The electric field in this region is the sum of an incident field and a scattered field, $\mathrm{E}(\mathrm{r};\, t)=[\mathrm{E}(\mathrm{r}\,|\,\omega)_{\mathrm{inc}}+\mathrm{E}(\mathrm{r}\,|\,\omega)_{\mathrm{sc}}]\,\exp.(-i\omega t)$, where

$$\mathrm{E}(\mathrm{r}|\,\omega)_{\mathrm{inc}}=\left[\hat{\mathrm{e}}_p^{(i)}(\mathrm{k})E_{0p}(\mathrm{k})+\hat{\mathrm{e}}_s^{(i)}(\mathrm{k})E_{0s}(\mathrm{k})\right]\exp\left[i\mathrm{k}\cdot\mathrm{x}-i\alpha_1(k)z\right] \tag{6.83a}$$

$$\mathrm{E}(\mathrm{r}|\,\omega)_{\mathrm{sc}}=\int\frac{d^2q}{(2\pi)^2}\left[\mathrm{e}_p^{(s)}(\mathrm{q})A_p(\mathrm{q})+\hat{\mathrm{e}}_s^{(s)}(\mathrm{q})A_s(\mathrm{q})\right]\exp\left[i\mathrm{q}\cdot\mathrm{x}+i\alpha_1(q)z\right], \tag{6.83b}$$

where $\alpha_i(\mathrm{q})=\left[\epsilon_i(\omega/\mathrm{c})^2-q^2\right]^{\frac{1}{2}}(i=1,2,3)$, with $\mathrm{Re}\alpha_i(q)>0$, $\mathrm{Im}\alpha_i(q)>0$, while

$$\hat{\mathrm{e}}_p^{(s)}(\mathrm{k})=\frac{c}{\sqrt{\epsilon_1}\omega}\left[\hat{\mathrm{k}}\alpha_1(k)+\hat{\mathrm{e}}_z k\right] \tag{6.84a}$$

$$\hat{\mathrm{e}}_s^{(i)}(\mathrm{k})=\hat{\mathrm{k}}\times\hat{\mathrm{e}}_z \tag{6.84b}$$

and

$$\hat{\mathrm{e}}_p^{(s)}(\mathrm{q})=\frac{c}{\sqrt{\epsilon_1}\omega}[-\hat{\mathrm{q}}\alpha_1(q)+\hat{\mathrm{e}}_z q] \tag{6.85a}$$

$$\hat{\mathrm{e}}_s^{(s)}(\mathrm{q})=\hat{\mathrm{q}}\times\hat{\mathrm{e}}_z. \tag{6.85b}$$

Maxwell's equations and the boundary conditions at the interfaces $z=0$ and $z=-d+h(\mathrm{x})$ imply linear relations between $A_p(\mathrm{q})$, $A_s(\mathrm{q})$ and $E_{0p}(\mathrm{k})$, $E_{0s}(\mathrm{k})$, which we write as ($\alpha=p,\ s,\ \beta=p,\ s$)

$$A_\alpha(\mathrm{q})=\sum_\beta R_{\alpha\beta}(\mathrm{q}|\,\mathrm{k})E_{0\beta}(\mathrm{k}). \tag{6.86}$$

The equations satisfied by the scattering amplitudes $\{R_{\alpha\beta}(\mathrm{q}\,|\,\mathrm{k})\}$ can be written in the form

$$\int \frac{d^2q}{(2\pi)^2}\mathrm{M}^{+}(\mathrm{p}|\,\mathrm{q})\,\mathrm{R}(\mathrm{q}|\,\mathrm{k}) = -\mathrm{M}^{-}(\mathrm{p}|\,\mathrm{k}),) \tag{6.87}$$

where

$$\mathrm{R}(\mathrm{q}|\,\mathrm{k}) = \begin{pmatrix} R_{pp}(\mathrm{q}|\,\mathrm{k}) & R_{ps}(\mathrm{q}|\,\mathrm{k}) \\ R_{sp}(\mathrm{q}|\,\mathrm{k}) & R_{ss}(\mathrm{q}|\,\mathrm{k}) \end{pmatrix} \tag{6.88}$$

$$\mathrm{M}^{\pm}(\mathrm{p}|\,\mathrm{q}) = \begin{pmatrix} M^{\pm}_{pp}(\mathrm{p}|\,\mathrm{q}) & M^{\pm}_{ps}(\mathrm{p}|\,\mathrm{q}) \\ M^{\pm}_{sp}(\mathrm{p}|\,\mathrm{q}) & M^{\pm}_{ss}(\mathrm{p}|\,\mathrm{q}) \end{pmatrix}. \tag{6.89}$$

The matrix elements $\{M^{\pm}_{\alpha\beta}(\mathrm{p}\,|\,\mathrm{q})\}$ are given by (González-Alcalde et al., 2016)

$$\begin{aligned} M^{\pm}_{pp}(\mathrm{p}|\,\mathrm{q}) = \frac{1}{\alpha_2(q)}\{&I-(\mathrm{p}|\,\mathrm{q})[pq+\alpha_3(p)\hat{\mathrm{p}}\cdot\hat{\mathrm{q}}\alpha_2(q)][\epsilon_1\alpha_2(q)\pm\epsilon_1\alpha_2(q)] \\ &+I_{+}(\mathrm{p}|\,\mathrm{q})[pq-\alpha_3(p)\hat{\mathrm{p}}\cdot\hat{\mathrm{q}}\alpha_2(q)][\epsilon_1\alpha_2(q)\mp\epsilon_2\alpha_1(q)]\} \end{aligned} \tag{6.90a}$$

$$\begin{aligned} M^{\pm}_{sp}(\mathrm{p}|\,\mathrm{q}) = \sqrt{\epsilon_3}\frac{\omega}{c}[\hat{\mathrm{p}}\times\hat{\mathrm{p}}]_3\{&I_{-}(\mathrm{p}|\,\mathrm{q})[\epsilon_1\alpha_2(q)\pm\epsilon_1\alpha_1(q) \\ &-I_{+}(\mathrm{p}|\,\mathrm{q})[\epsilon_1\alpha_2(q)\mp\epsilon_2\alpha_1(q)]\} \end{aligned} \tag{6.90b}$$

$$\begin{aligned} M^{\mp}_{ps}(\mathrm{p}|\,\mathrm{q}) = -\sqrt{\epsilon_1}\epsilon_2\frac{\omega}{c}[\hat{\mathrm{p}}\times\hat{\mathrm{p}}]_3\frac{\alpha_3(p)}{\alpha_2(p)}\{&I_{-}(\mathrm{p}|\,\mathrm{q})[\alpha_2(q)\pm\alpha_1(q)] \\ &+I_{+}(\mathrm{p}|\,\mathrm{q})[\alpha_2(q)\mp\alpha_1(q)]\} \end{aligned} \tag{6.90c}$$

$$\begin{aligned} M^{\pm}_{ss}(\mathrm{p}|\,\mathrm{q}) = \sqrt{\epsilon_1}\epsilon_2\sqrt{\epsilon_3}\left(\frac{\omega}{c}\right)^2\hat{\mathrm{p}}\cdot\hat{\mathrm{q}}\frac{1}{\alpha_2(q)}\{&I_{-}(\mathrm{p}|\,\mathrm{q})[\alpha_2(q)\pm\alpha_1(q)] \\ &+I_{+}(\mathrm{p}|\,\mathrm{q})[\alpha_2(q)\mp\alpha_1(q)]\}. \end{aligned} \tag{6.90d}$$

The functions $I_{\pm}(\mathrm{p}\,|\,\mathrm{q})$ entering Eqs. (6.90a)–(6.90d) are defined by

$$I_{\pm}(\mathrm{p}|\,\mathrm{q}) = \exp\{i[\alpha_3(p)\pm\alpha_2(q)]d\}\frac{I(\alpha_3(p)\pm\alpha_2(q)|\,\mathrm{p}-\mathrm{q})}{\alpha_3(p)\pm\alpha_2(q)}, \tag{6.91}$$

where d is the mean thickness of the film, and

$$I(\gamma|\,\mathrm{Q}) = \int d^2x\ \exp[-i\gamma\zeta(\mathrm{x})]\exp[-i\mathrm{Q}\cdot\mathrm{x}]. \tag{6.92}$$

The contribution to the mean differential reflection coefficient when an incident wave of polarization β whose wave vector has the projection $\mathbf{k}$ on the mean scattering surface is scattered incoherently into a wave of polarization α whose wave vector has the projection $\mathbf{q}$ on the mean scattering surface, within an element of solid angle $d\Omega_s$

about the scattering direction defined by the polar and azimuthal scattering angles (θ_s, ϕ_s), is given by González-Alcalde et al. (2016)

$$\left\langle \frac{\partial R_{\alpha\beta}(\mathbf{q}|\,\mathbf{k})}{\partial \Omega_s} \right\rangle_{incoh} = \frac{\epsilon_1}{S}\left(\frac{\omega}{2\pi c}\right)\frac{\cos^2\theta_s}{\cos\theta_0} \times \left[\left\langle \left|R_{\alpha\beta}(\mathbf{q}|\,\mathbf{k})\right|^2 \right\rangle - \left|\left\langle R_{\alpha\beta}(\mathbf{q}|\,\mathbf{k})\right\rangle\right|^2\right]. \tag{6.93}$$

In this expression S is the area of the plane $z=0$ covered by the random surface, while $\mathbf{k} = \sqrt{\epsilon_1}(\omega/c)\sin\theta_0(\cos\phi_0, \sin\phi_0, 0)$ and $\mathbf{q} = \sqrt{\epsilon_1}(\omega/c)\sin\theta_s(\cos\phi_s, \sin\phi_s, 0)$.

The reflectivity for light of α polarization α incident on the film with a polar angle of incidence θ_0 is

$$\begin{aligned}\mathcal{R}_\alpha(\theta_0) &= |R_\alpha(k)|^2 \\ &= R_\alpha(\sqrt{\epsilon_1}(\omega/c)\sin\theta_0)|^2,\end{aligned} \tag{6.94}$$

where $R_\alpha(k) = \langle R_{\alpha\alpha}(\mathbf{k}\,|\,\mathbf{k})|\cdot$

Realizations of the surface profile function $\zeta(\mathrm{x}_{\|})$ are generated by the filtering method employed in Simonsen et al. (2011), and the reduced Rayleigh Eq. (6.87) is then solved numerically in the manner described in Section 6.4.

Eqs. (6.87)–(6.89) are valid both when the medium of incidence is optically more dense than the substrate ($\epsilon_1 > \epsilon_3$), and when it is optically less dense ($\epsilon_1 < \epsilon_3$). However, here we will consider only the former case, because it is only in that case that interesting effects due to total internal reflection occur.

The preceding results have been applied to the calculation of the mean differential reflection coefficient and the reflectivity when p- and s-polarized plane waves, whose wavelength is $\lambda = 632.8\,\mathrm{nm}$, is incident from a glass prism ($\epsilon_1 = 2.25$) on a photoresist film ($\epsilon_2 = 2.69$), in contact with vacuum ($\epsilon_3 = 1$). The mean thickness of the film is $d = 0.6\,\mu\mathrm{m}$. The roughness of the prism-film interface was characterized by a surface height autocorrelation function $W(|\,\mathbf{x}\,|) = \exp[-(x/a)^2]$, with a transverse correlation length $a = 1.9\,\mu\mathrm{m}$, and an rms height of the interface $\sigma = 22\,\mathrm{nm}$.

In Fig. 6.10 we present plots of numerical results for the contribution to the mean differential reflection coefficient from in-plane co-polarized light scattered incoherently by the rough surface, $\langle \partial R_{\alpha\alpha}/\partial\Omega_s\rangle_{\mathrm{incoh}}$, as a function of the angle of scattering for four values of the angle of incidence in the vicinity of the critical angle for total internal reflection $\theta_c = 41.89$ degrees (González-Alcalde et al., 2016). For polar angles of incidence $\theta_0 \lesssim \theta_0^* = 30$ degrees this function has a structureless form that reflects its proportionality to the power spectrum of the surface roughness $g(|\,\mathbf{q}-\mathbf{k}\,|) = \pi a^2 \exp[-a^2(\mathbf{q}-\mathbf{k})^2/4]$. However, as the angle of incidence is increased toward the critical angle $[\theta_0^* \lesssim \theta < \theta_c]$ peaks gradually start to develop around $\theta_s = \theta_c$ [Fig. 6.10, panels $\theta_0 = 35$, 38 degrees]. Initially, these peaks are more prominent in the results for p-to-p scattering, but for an angle of incidence close to the critical angle $\theta_0 \lesssim \theta_c$, peaks become clearly visible in the results for s-to-s scattering. Finally, for $\theta_0 > \theta_c$, peaks are no longer observed in these numerical results, and the amplitude of the mean differential reflection coefficient decreases as grazing incidence is approached.

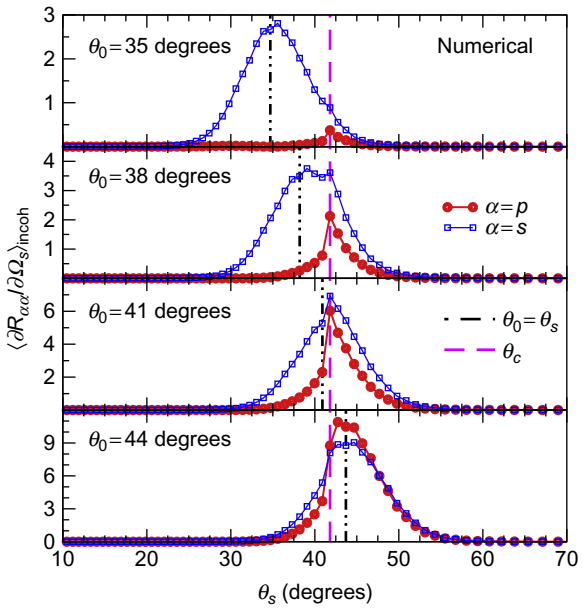


FIG. 6.10

The in-plane angular dependence of $\langle \partial R_{\alpha\alpha}/\partial \Omega_s \rangle_{\text{incoh}}$ for several values of the angle of incidence θ_0, obtained by the numerical simulation approach. The open symbols indicate the datapoints obtained in the simulations, while the lines connecting them are a guide to the eye. Note that the amplitudes of the data vary from panel to panel.

These peaks are the optical analogues of the Yoneda peaks that can arise in the scattering of an electromagnetic field from the rough interface between two dielectric media in the presence of total internal reflection. They are sharp asymmetric peaks occurring at the critical angle for total internal reflection for a fixed angle of incidence in the angular dependence of the intensity of the field scattered back into the medium of incidence when the latter is the optically more dense medium. These peaks were first observed experimentally in the scattering of X-rays incident from air on a metal surface (Yoneda, 1963). They have subsequently been studied theoretically in the context of the scattering of X-rays (Vineyard, 1982; Leskova and Maradudin, 1997), neutrons (Sinha et al., 1988), and light (González-Alcalde et al., 2016; Kawanishi et al., 1997b) from rough surfaces. These peaks are present in the lowest-order nonzero contribution to the mean differential reflection coefficient as an expansion in powers of the surface profile function $\zeta(x)$. They are therefore single-scattering phenomena, not multiple-scattering effects.

The calculations whose results are presented in Fig. 6.10 were carried out in support of experimental studies of the scattering of p- and s-polarized light from a three-medium dielectric structure that is represented by the structure investigated in this section (González-Alcalde et al., 2016). The values of the experimental and

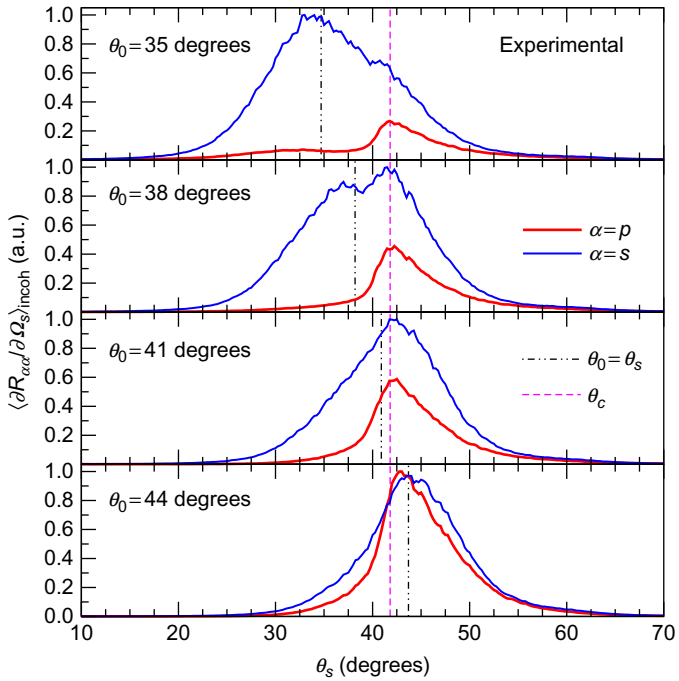


FIG. 6.11

The same as Fig. 6.10, but now presenting the results of experimental measurements. The data sets in each panel were scaled by a common factor so that a unit amplitude corresponds to the maximum value of the corresponding numerical simulation results presented in Fig. 6.10.

roughness parameters describing the structure studied experimentally were the same as the ones assumed in obtaining the results presented in Fig. 6.10. A meaningful comparison of the experimental and computed results could therefore be carried out. In Fig. 6.11, we present experimental results for the contribution to the mean differential reflection coefficient from in-plane co-polarized light scattered incoherently from the rough surface, $\langle \partial R_{\alpha\alpha}/\partial \Omega_s \rangle_{\text{incoh}}$, for the same values of the angle of incidence used in obtaining Fig. 6.10 (González-Alcalde et al., 2016). There is a good quantitative agreement between the predicted angular positions of the Yoneda peaks presented in Fig. 6.10 and the experimental positions presented in Fig. 6.11. The experimental distributions $\langle \partial R_{\alpha\alpha}/\partial \Omega_s \rangle_{\text{incoh}}$, however, are broader than their computed counterparts, and the ratios of the amplitudes of the two co-polarized experimental intensity distributions are not consistently reproduced in the numerical simulation results. The several reasons for these differences between the experimental and numerical results which are primarily experimental in nature, are discussed in detail in González-Alcalde et al. (2016), and we refer the interested reader to that paper for these explanations.

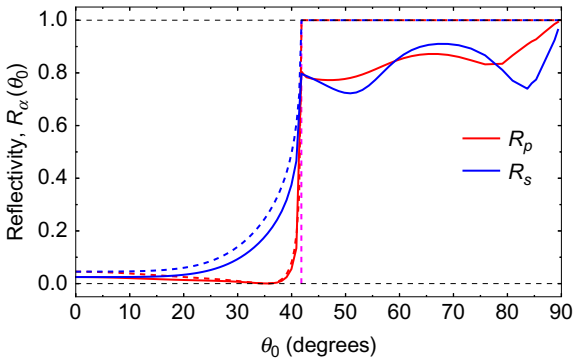


FIG. 6.12

The reflectivity $\mathcal{R}_\alpha(\theta_0)$ of the scattering system studied in this section. The dashed curves represent the Fresnel reflection coefficients, that is, the reflectivities of the corresponding films in the absence of the interface roughness.

The reflectivity of the rough surface has also been calculated for p- and s-polarized incident light, and the results are presented in Fig. 6.12 (González-Alcalde et al., 2016). Also plotted is the Fresnel reflectivity for light of each polarization. The effect of total internal reflection is clearly seen in these results. In the angular interval $\theta_c < \theta_0 < 90$ degrees the reflectivity in each polarization is decreased by the surface roughness by approximately 20% from the corresponding Fresnel reflectivity in much of this interval. This is a significant decrease for the degree of roughness possessed by this surface.

6.6 ANALYTICAL METHODS FOR THE SCATTERING FROM A 3D FILM WITH RANDOMLY ROUGH SURFACES

Theoretical and numerical approaches for wave scattering from rough structures have received wide interest. We can mention the SPM (Johnson, 1999; Rice, 1951; Nieto-Vesperinas, 1982; Tsang and Kong, 2001; Berginc, 2007), the Kirchhoff (or tangent plane) approximation method (Beckmann and Spizzichino, 1963; Ogilvy, 1991; Bourlier et al., 2001) and the previous sections give an overview of numerical methods. However, some restrictions limit the domain of their applicability: the perturbation method is only valid for surfaces with small roughness, and the Kirchhoff approximation is applicable to surfaces with a long correlation length. Many new approaches have been suggested, such as the full-wave method (Bahar, 1981), the surface-field phase-perturbation technique (Shen and Maradudin, 1980; Winebrenner and Ishimaru, 1985) and the quasislope approximation (Tatarskii, 1993). *V*oronovich (1985, 1994a,b, 1996a,b) proposed a new method called the SSA, which is valid for arbitrary roughness provided that the slopes of the surface are smaller than the angles of incidence and scattering, irrespective of the wavelength

of the incident radiation. The SSA makes a bridge between the Kirchhoff approximation and the SPM.

In this section, we will focus on the SSA method and the SPM with a view to studying different 3D rough structures like slabs or films, considering the effects of higher orders in a perturbative expansion.

The problem of scattering by randomly rough surfaces up to the order 3 is treated in Soubret et al. (2001a), Gilbert and Johnson (2003). Gilbert and Johnson (2003), Berginc (2002) consider the second order of the SSA. Gilbert and Johnson (2003) proposed simplified forms for the first three SSA terms in the case of penetrable surfaces under the assumption of a Gaussian random process with an isotropic Gaussian correlation function. Berginc (2002) gives results up to the third SSA term for incoherent scattering from dielectric and metallic surfaces with Gaussian and non-Gaussian correlation functions.

Since the higher order SSA corrections involve components of the SPM in the calculations, results of previous works (Soubret et al., 2001a; Berginc, 2007) developed under the Rayleigh hypothesis have been used in this section. We numerically develop two cases of the light scattering by a 2D randomly rough surface and a case of light scattering from a random film with randomly rough boundaries. The scattered intensities from a randomly rough surface or a random film can be decomposed into coherent and incoherent components. Coherent components contribute only in the specular reflected or transmitted directions, whereas incoherent components contribute in all directions. In this section, we focus on the incoherent components.

6.6.1 DEFINITION OF THE SCATTERING MATRIX

The main structure we consider in this section is shown in Fig. 6.13, where the two rough surfaces separate three media. The different media are characterized by isotropic, homogeneous, dielectric constants ε_0, ε_1, and ε_2, respectively. The two rough surfaces are located at the heights $z = h_1(\boldsymbol{x})$, $z = -H + h_2(\boldsymbol{x})$, where $\boldsymbol{x} = (x, y, 0)$. We assume that the randomly rough surfaces $h_1(\boldsymbol{x})$ and $h_2(\boldsymbol{x})$ are stationary, isotropic, uncorrelated Gaussian random processes defined by their moments:

$$< h_i(\boldsymbol{x}) >= 0, \tag{6.95}$$

$$< h_i(\boldsymbol{x}) h_i(\boldsymbol{x}') > W_i(\boldsymbol{x} - \boldsymbol{x}'), \tag{6.96}$$

$$< h_1(\boldsymbol{x}) h_2(\boldsymbol{x}') >= 0, \tag{6.97}$$

where $i = 1, 2$, and the angle brackets denote an average over the ensembles of realizations of the functions $h_1(\boldsymbol{x})$ and $h_2(\boldsymbol{x})$. A Gaussian form is used for the surface-height correlation functions $W_1(\boldsymbol{x})$ and $W_2(\boldsymbol{x})$:

$$W_i(\boldsymbol{x}) = \sigma_i^2 \exp\left(\frac{-\boldsymbol{x}^2}{l_i^2}\right), \tag{6.98}$$

where σ_i is the rms height of the surface $h_i(x)$, and l_i is the correlation length.

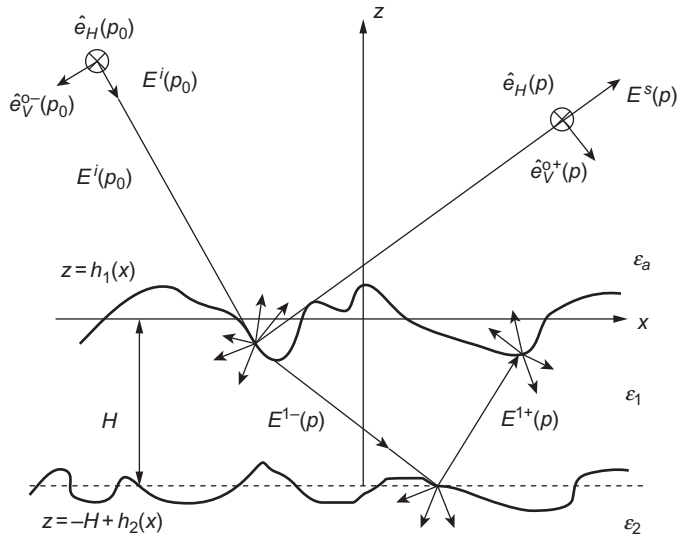


FIG. 6.13

Incident wave from medium 0 scattered by a slab with two rough surfaces.

We consider that the different electromagnetic waves propagate with a frequency ω, and the time dependence is assumed to be $\exp(-i\omega t)$. The electric fields $\boldsymbol{E}^i$ satisfy in the different media a Helmholtz equation.

In the medium 0, $\boldsymbol{E}^0$ can be written as a superposition of an incident and a scattered field:

$$\boldsymbol{E}^0(\boldsymbol{x}, z) = \boldsymbol{E}^i(\boldsymbol{p}_0)\exp(\mathrm{i}\boldsymbol{p}_0 \cdot \boldsymbol{x} - i\alpha_0(\boldsymbol{p}_0)z) + \int \frac{\mathrm{d}^2\boldsymbol{p}}{(2\pi)^2}\boldsymbol{E}^s(\boldsymbol{p})\exp(\mathrm{i}\boldsymbol{p} \cdot \boldsymbol{x} + \mathrm{i}\alpha_0(\boldsymbol{p})z), \tag{6.99}$$

where we define (see Fig. 6.14)

$$\alpha_0(\boldsymbol{p}) = \left(\varepsilon_0 K_0^2 - \boldsymbol{p}^2\right)^{\frac{1}{2}} \tag{6.100}$$

$$K_0 = \omega/c, \tag{6.101}$$

$$\boldsymbol{E}^i(\boldsymbol{p}_0) = E_V^i(\boldsymbol{p}_0)\hat{\boldsymbol{e}}_V^{0-}(\boldsymbol{p}_0) + \boldsymbol{E}_H^i(p_0)\hat{e}_H(p_0), \tag{6.102}$$

$$\boldsymbol{E}^s(\boldsymbol{p}) = \boldsymbol{E}_V^s(p)\hat{\boldsymbol{e}}_V^{0+}(p) + \boldsymbol{E}_H^s(\boldsymbol{p})\hat{\boldsymbol{e}}_H(\boldsymbol{p}). \tag{6.103}$$

The subscript H refers to the horizontal polarization (TE), and V to the vertical polarization (TM). They are defined by the following two vectors:

$$\hat{\boldsymbol{e}}_H(p) = \hat{\boldsymbol{e}}_z \times \hat{\boldsymbol{p}}, \tag{6.104}$$

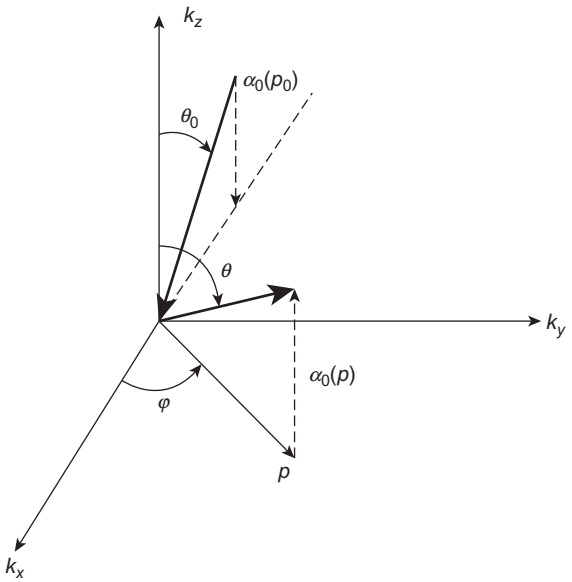


FIG. 6.14

Definition of the scattering vectors.

$$\hat{\boldsymbol{e}}_V^{0\pm}(\boldsymbol{p}) = \pm\frac{\alpha_0(\boldsymbol{p})}{\sqrt{\varepsilon_0 K_0}}\hat{\boldsymbol{p}} - \frac{\|\boldsymbol{p}\|}{\sqrt{\varepsilon_0 K_0}}\hat{\boldsymbol{e}}_z, \tag{6.105}$$

where the minus sign corresponds to the incident wave and the plus sign to the scattered wave.

It is important to note that the vectors $\boldsymbol{E}^s(\boldsymbol{p})$ and $\boldsymbol{E}^i(\boldsymbol{p}_0)$ are expressed in a different basis due the fact that $\hat{\boldsymbol{e}}_V^{0\pm}(\boldsymbol{p})$ and $\hat{e}_V^{1\pm}(\boldsymbol{p})$ depend on $\boldsymbol{p}$. In medium 1, we have a similar expression, viz.:

$$E^1(r) = \int\frac{\mathrm{d}^2 p}{(2\pi)^2}E^{1-}(p)\exp(\mathrm{i}p)\cdot x - \mathrm{i}\alpha_1(p)z) + \int\frac{d^2 p}{(2\pi)^2}E^{1+}(p)\exp(\mathrm{i}p)\cdot x - \mathrm{i}\alpha_1(p)z), \tag{6.106}$$

where

$$\alpha_1(\boldsymbol{p}) \equiv \left(\varepsilon_1 K_0^2 - \boldsymbol{p}^2\right)^{\frac{1}{2}}. \tag{6.107}$$

The field $\boldsymbol{E}^{1-}$ is decomposed on the basis of $\left(\hat{\boldsymbol{e}}_V^{1-}(\boldsymbol{p}), \hat{\boldsymbol{e}}_H(\boldsymbol{p})\right)$ and $\boldsymbol{E}^{1+}$ $\left(\hat{\boldsymbol{e}}_V^{1+}(\boldsymbol{p}), \hat{\boldsymbol{e}}_H(\boldsymbol{p})\right)$ with

$$\hat{\boldsymbol{e}}_H(\boldsymbol{p}) = \hat{\boldsymbol{e}}_z \times \hat{\boldsymbol{p}}, \tag{6.108}$$

$$\hat{\boldsymbol{e}}_V^1(\boldsymbol{p}) = \pm\frac{\alpha_1(\boldsymbol{p})}{\sqrt{\varepsilon_1 K_0}}\hat{\boldsymbol{p}} - \frac{\|\boldsymbol{p}\|}{\sqrt{\varepsilon_1 K_0}}\hat{\boldsymbol{e}}_z. \tag{6.109}$$

We can now define the scattering matrix connecting the incident field to the scattered field by the following expression:

$$\boldsymbol{E}^s(\boldsymbol{p}) \equiv \overline{\boldsymbol{R}}(\boldsymbol{p}|\,\boldsymbol{p}_0)\cdot\boldsymbol{E}^i(\boldsymbol{p}_0), \tag{6.110}$$

where $\overline{\boldsymbol{R}}(\boldsymbol{p}|\,\boldsymbol{p}_0)$ is a 2D matrix where the components depend on the polarizations V and H

$$\overline{\boldsymbol{R}}(\boldsymbol{p}|\,\boldsymbol{p}_0) = \begin{pmatrix} \boldsymbol{R}_{VV}(\boldsymbol{p}|\,\boldsymbol{p}_0)\boldsymbol{R}_{VH}(\boldsymbol{p}|\,\boldsymbol{p}_0) \\ \boldsymbol{R}_{HV}(\boldsymbol{p}|\,\boldsymbol{p}_0)\boldsymbol{R}_{HH}(\boldsymbol{p}|\,\boldsymbol{p}_0) \end{pmatrix}.$$

We will consider a perturbative development of $\overline{\boldsymbol{R}}$ in powers of the height h of the following form which is given by the SPM,

$$\overline{\boldsymbol{R}}(\boldsymbol{p}|\,\boldsymbol{p}_0) = \overline{\boldsymbol{R}}^{(0)}(\boldsymbol{p}|\,\boldsymbol{p}_0) + \overline{\boldsymbol{R}}^{(1)}(\boldsymbol{p}|\,\boldsymbol{p}_0) + \overline{\boldsymbol{R}}^{(2)}(\boldsymbol{p}|\,\boldsymbol{p}_0) + \overline{\boldsymbol{R}}^{(3)}(\boldsymbol{p}|\,\boldsymbol{p}_0) + \cdots. \tag{6.111}$$

The expression for the scattered field represents the general solution of the Maxwell equations that satisfies the radiation condition. For instance, in medium 0, the scattered field reads

$$\boldsymbol{E}^s(\boldsymbol{r}) = \int \frac{\mathrm{d}^2\boldsymbol{p}}{(2\pi)^2}\overline{\boldsymbol{R}}(\boldsymbol{p}|\,\boldsymbol{p}_0)\cdot\boldsymbol{E}^i(\boldsymbol{p}_0)\exp\left(\mathrm{i}\boldsymbol{k}_p^{0+}\cdot\boldsymbol{r}\right). \tag{6.112}$$

where $\boldsymbol{k}_p^{0+} \equiv \boldsymbol{p} \pm \alpha_0(\boldsymbol{p})\hat{e}_z$.

In order to determine the scattering matrix we have to take into account the boundary conditions on the rough surfaces by writing the continuity of the tangential components of the electric and magnetic fields.

6.6.2 THE SSA AND THE SPM FOR A 2D ROUGH SURFACE

6.6.2.1 Formulation

In this section, we will study the expression of the SSA and the SPM for the scattering of light from a 2D randomly rough surface. The expressions obtained in this case will be generalized for the case of a slab. We summarize the procedure to obtain the formulation which can be applied to the scattering from a 2D randomly rough surface. In the first step Voronovich (1994b) noted that the unitary of the scattering matrix implies a reciprocity theorem leading to the following properties:

$$\overline{\boldsymbol{R}}(\boldsymbol{p}|\,\boldsymbol{p}_0) = \overline{\boldsymbol{R}}(\boldsymbol{p}_0|\,-\boldsymbol{p}); \tag{6.113}$$

for a horizontal translation of the rough boundary $h(\boldsymbol{r}) \to h(\boldsymbol{r}-\boldsymbol{a})$

$$\overline{\boldsymbol{R}}(\boldsymbol{p}|\,\boldsymbol{p}_0) \to \overline{\boldsymbol{R}}(\boldsymbol{p}|\,\boldsymbol{p}_0)\exp\left[-i(\boldsymbol{p}-\boldsymbol{p}_0)\cdot\boldsymbol{a}\right]; \tag{6.114}$$

and for a vertical translation $h(\mathbf{r}) \to h(\mathbf{r}) + H$

$$\overline{\boldsymbol{R}}(\boldsymbol{p}|\,\boldsymbol{p}_0) \to \overline{\boldsymbol{R}}(\boldsymbol{p}|\,\boldsymbol{p}_0)\exp\left[-i(\alpha(\boldsymbol{p}) + \alpha(\boldsymbol{p}_0))\boldsymbol{H}\right]. \tag{6.115}$$

Using these results Voronovich (Furutsu, 1991) proposes the following expression for the scattering matrix

$$\overline{\boldsymbol{R}}(\boldsymbol{p}|\,\boldsymbol{p}_0)=\int\frac{\mathrm{d}^2\boldsymbol{r}}{(2\pi)^2}\exp\left[-i(\boldsymbol{p}-\boldsymbol{p}_0)\cdot\boldsymbol{r}-i(\alpha(\boldsymbol{p})+\alpha(\boldsymbol{p}_0))h(\boldsymbol{r})\right]\overline{\boldsymbol{\Phi}}[\boldsymbol{p}|\,\boldsymbol{p}_0;[h]], \tag{6.116}$$

in the case of a rough surface located between media 0 and 1. The functional $\overline{\boldsymbol{\Phi}}$ which depends on h has to be determined. The translation conditions Eqs. (6.114), (6.115) lead to some properties of $\overline{\boldsymbol{\Phi}}$. It can be noted that it is more convenient to work with the Fourier transform $\overline{\boldsymbol{\Phi}}[\boldsymbol{p},\boldsymbol{p}_0,\boldsymbol{r};[h]]$ with respect to the variable $\boldsymbol{r}$.

The first condition Eq. (6.114) reads:

$$\overline{\boldsymbol{R}}(\boldsymbol{p}|\,\boldsymbol{p}_0)=\int\frac{\mathrm{d}^{2\xi}}{(2\pi)^2}\boldsymbol{d}^2re^{-\mathrm{i}(\boldsymbol{p}-\boldsymbol{p}_0-\boldsymbol{\xi})\cdot\boldsymbol{r}-i(\alpha_0(\boldsymbol{p})+\alpha_0(\boldsymbol{p}_0))h(r)}\overline{\boldsymbol{\Phi}}(\boldsymbol{p},\boldsymbol{p}_0,\boldsymbol{\xi}), \tag{6.117}$$

and the second condition Eq. (6.115)

$$\overline{\boldsymbol{\Phi}}_{\boldsymbol{x}\to h(\boldsymbol{x}-\boldsymbol{\alpha})}(\boldsymbol{p},\boldsymbol{p}_0,\boldsymbol{\xi})=e^{\mathrm{i}\xi\cdot\boldsymbol{\alpha}}\overline{\boldsymbol{\Phi}}_{\boldsymbol{x}\to h(x)}(\boldsymbol{p},\boldsymbol{p}_0,\boldsymbol{\xi}), \tag{6.118}$$

for all vectors $\boldsymbol{a}$. In the framework of a perturbative development, $\overline{\Phi}$ is expanded as an integral-power series of h, viz.:

$$\begin{aligned}\overline{\boldsymbol{\Phi}}(\boldsymbol{p},\boldsymbol{p}_0,\boldsymbol{\xi})&=\delta(\boldsymbol{\xi})\widetilde{\boldsymbol{\Phi}}^0(\boldsymbol{p},\boldsymbol{p}_0)+\int\frac{\mathrm{d}^2\boldsymbol{\xi}_1}{(2\pi)^2}\delta(\boldsymbol{\xi}-\boldsymbol{\xi}_1)\widetilde{\boldsymbol{\Phi}}^{(1)}(\boldsymbol{p},\boldsymbol{p}_0,\boldsymbol{\xi}_1)h(\boldsymbol{\xi}_1)\\&+\int\int\frac{\mathrm{d}^2\boldsymbol{\xi}_1}{(2\pi)^2}\frac{\mathrm{d}^2\boldsymbol{\xi}_2}{(2\pi)^2}\delta(\boldsymbol{\xi}-\boldsymbol{\xi}-\boldsymbol{\xi}_2)\widetilde{\boldsymbol{\Phi}}^{(2)}(\boldsymbol{p},\boldsymbol{p}_0,\boldsymbol{\xi}_1,\boldsymbol{\xi}_2)h(\boldsymbol{\xi}_1)h(\boldsymbol{\xi}_2)+\ldots\end{aligned} \tag{6.119}$$

The condition Eq. (6.115) imposes:

$$\overline{\boldsymbol{\Phi}}_{\boldsymbol{x}\to h(\boldsymbol{x})+H}(p,\boldsymbol{p}_0,\boldsymbol{\xi})=\overline{\boldsymbol{\Phi}}_{\boldsymbol{x}\to h(\boldsymbol{x})}(\boldsymbol{p},\boldsymbol{p}_0,\boldsymbol{\xi}). \tag{6.120}$$

We have

$$\widetilde{\boldsymbol{\Phi}}^{(n)}(\boldsymbol{p},\boldsymbol{p}_0,\boldsymbol{\xi}_1,\ldots,\boldsymbol{\xi}_k=0,\ldots,\boldsymbol{\xi}_n)=0\forall k\in[1,n]. \tag{6.121}$$

Using a finite expansion with respect to the variables ξ_1, …, ξ_n it follows that

$$\widetilde{\boldsymbol{\Phi}}^{(n)}(\boldsymbol{p},\boldsymbol{p}_0,\boldsymbol{\xi}_1,\ldots,\boldsymbol{\xi}_n)=\sum_{\alpha_1,\ldots,\alpha_n=\boldsymbol{x},y}\boldsymbol{\xi}_{1\alpha1}\ldots\boldsymbol{\xi}_{n\alpha_n}\widetilde{\boldsymbol{\Phi}}^{(n)\alpha_1\ldots n}(\boldsymbol{p},\boldsymbol{p}_0,\boldsymbol{\xi}_1,\ldots,\boldsymbol{\xi}_n), \tag{6.122}$$

where $\boldsymbol{\xi}_i=(\boldsymbol{\xi}_{ix},\boldsymbol{\xi}_{iy},0)$. This expansion justifies the name of SSA when the effects due to the frontiers are neglected in the integration

$$\mathrm{i}\boldsymbol{\xi}_\alpha h(\boldsymbol{\xi})=\int\mathrm{d}^2x\frac{\partial h(\boldsymbol{x})}{\partial x_{\boldsymbol{\alpha}}}e^{-\mathrm{i}\boldsymbol{\xi}\cdot\boldsymbol{x}}. \tag{6.123}$$

Voronovich (Lam and Ishimaru, 1994) showed that $\overline{\boldsymbol{\Phi}}^{(n)}$ scan be expanded as

$$\widetilde{\boldsymbol{\Phi}}^{(n)}=\widetilde{\boldsymbol{\Phi}}^{(n)}\Big|_{\boldsymbol{\xi}_n=\boldsymbol{p}-\boldsymbol{p}_0-\boldsymbol{\xi}_1-\cdots-\boldsymbol{\xi}_{n-1}}+\left[\widetilde{\boldsymbol{\Phi}}^{(n)}-\widetilde{\boldsymbol{\Phi}}^{(n)}\Big|_{\boldsymbol{\xi}_n=\boldsymbol{p}-\boldsymbol{p}_0-\boldsymbol{\xi}_1-\cdots-\boldsymbol{\xi}_{n-1}}\right]. \tag{6.124}$$

The first term of the right side can be transformed into a term of order $n-1$ that is analogous to $\overline{\boldsymbol{\Phi}}^{(n-1)}$ and the term between brackets is transformed into a term of order $n+1$. This important relation will simplify the formulas in the following.

Taking as an example the first terms in the expansion Eq. (6.119), and using Eq. (6.124), the computation of the term $\widetilde{\boldsymbol{\Phi}}^{(0)}$ should involve $\widetilde{\boldsymbol{\Phi}}^{(1)}$ and its coefficient can be related to $\widetilde{\boldsymbol{\Phi}}^{(0)}$ and $\widetilde{\boldsymbol{\Phi}}^{(0)}$ and then replaced; we thus obtain the formula

$$\overline{\boldsymbol{R}}(\boldsymbol{p}|\,\boldsymbol{p}_0)=\int d^2r e^{-i(\boldsymbol{p}-\boldsymbol{p}_0).r-i(\alpha_0(\boldsymbol{p})+\alpha_0(\boldsymbol{p}_0))h(r)}\;\widetilde{\boldsymbol{\Phi}}^{(0)}(\boldsymbol{p},\boldsymbol{p}_0)$$
$$+\int\frac{d^2\boldsymbol{\xi}}{(2\pi)^2}d^2r e^{-i(\boldsymbol{p}-\boldsymbol{p}_0).r-i(\alpha_0(\boldsymbol{p})+\alpha_0(\boldsymbol{p}_0))h(r)}(2\pi)^2\delta(\boldsymbol{\xi}-\boldsymbol{\xi}_1-\boldsymbol{\xi}_2)\widetilde{\boldsymbol{\Phi}}^{(2)}(\boldsymbol{p},\boldsymbol{p}_0,\boldsymbol{\xi}_1,\boldsymbol{\xi}_2)h(\boldsymbol{\xi}_1)h(\boldsymbol{\xi}_2). \tag{6.125}$$

In this expression, if we take the term of order 1 in h, we obtain

$$\overline{\boldsymbol{R}}(\boldsymbol{p}|\,\boldsymbol{p}_0)=\widetilde{\boldsymbol{\Phi}}^{(0)}(\boldsymbol{p},\boldsymbol{p}_0)\Big[(2\pi)^2\delta(\boldsymbol{p}-\boldsymbol{p}_0)-i(\alpha_0(\boldsymbol{p})+\alpha_0(\boldsymbol{p}_0))h(\boldsymbol{p}-\boldsymbol{p}_0)\Big]. \tag{6.126}$$

Voronovich (1994a,b) proposed to identify the expression Eq. (6.125) with the SPM (see (Soubret et al., 2001a) Eq. (6.53)). It follows that

$$\begin{aligned}\overline{R}^{10}(\boldsymbol{p}|\,\boldsymbol{p}_0)&=(2\pi)^2\delta(\boldsymbol{p}-\boldsymbol{p}_0)\overline{X}_S^{(0)}(\boldsymbol{p}_0)+\alpha_0(\boldsymbol{p}_0)\overline{X}_S^{(1)}(\boldsymbol{p}|\,\boldsymbol{p}_0)h(\boldsymbol{p}-\boldsymbol{p}_0)\\&+\alpha_0(\boldsymbol{p}_0)\int\frac{\mathrm{d}^2\boldsymbol{p}_1}{(2\pi)^2}\overline{X}_S^{(2)}(\boldsymbol{p}|\,\boldsymbol{p}_1|\,\boldsymbol{p}_0)h(\boldsymbol{p}-\boldsymbol{p}_1)h(\boldsymbol{p}_1-\boldsymbol{p}_0).\end{aligned} \tag{6.127}$$

The upper indices 10 in Eq. (6.127) must be read from right to left, indicating the order of the successive media. The same notation will be used in the following, and we obtain the identities:

$$\widetilde{\boldsymbol{\Phi}}^{(0)}(\boldsymbol{p}_0,\boldsymbol{p}_0)=\boldsymbol{X}_s^{(0)}(\boldsymbol{p}|\,\boldsymbol{p}_0), \tag{6.128}$$

$$-i(\alpha_0(\boldsymbol{p})+\alpha_0(\boldsymbol{p}_0))\widetilde{\boldsymbol{\Phi}}^{(0)}(\boldsymbol{p},\boldsymbol{p}_0)=\alpha_0(\boldsymbol{p}_0)\overline{\boldsymbol{X}}_S^{(1)}(\boldsymbol{p}|\,\boldsymbol{p}_0), \tag{6.129}$$

or

$$\widetilde{\boldsymbol{\Phi}}^{(0)}(\boldsymbol{p}_0,\boldsymbol{p}_0)=\frac{\alpha_0(\boldsymbol{p}_0)}{-\mathrm{i}(\alpha_0(\boldsymbol{p})+\alpha_0(\boldsymbol{p}_0))}\overline{\boldsymbol{X}}_S^{(1)}(\boldsymbol{p}_0|\,\boldsymbol{p}_0), \tag{6.130}$$

$$-2i\overline{\boldsymbol{X}}^{(0)}(\boldsymbol{p}_0)=\overline{\boldsymbol{X}}_S^{(1)}(\boldsymbol{p}_0|\,\boldsymbol{p}_0). \tag{6.131}$$

The first equation gives the coefficient $\widetilde{\boldsymbol{\Phi}}^{(0)}(\boldsymbol{p}_0,\boldsymbol{p}_0)$, where the corresponding scattering matrix becomes

$$\overline{\boldsymbol{R}}^{10}(p|\,p_0)=\frac{i\alpha_0(p_0)}{(\alpha_0(p)+\alpha_0(p_0))}\overline{\boldsymbol{X}}_s^{(1)}(\boldsymbol{P}|\,\boldsymbol{P}_0)\int d^2r\,e^{-i(p-p_0).r-i(\alpha_0(p)+\alpha_0(p_0))h(r),} \tag{6.132}$$

where $\overline{\boldsymbol{X}}_s^{(1)}(\boldsymbol{p}|\,p_0)$ is given by Eq. (A.2) of Appendix A.1. Following the same procedure, the order 2 approximation $\overline{\boldsymbol{\Phi}}^{(2)}$ can be written in terms of orders 1 and 3, leading to the expression:

$$\begin{aligned}\overline{\boldsymbol{R}}^{10}(p|\,p_0) = &\frac{\alpha_0(p_0)}{-i(\alpha_0(p)+\alpha_0(p_0))}\int\frac{d\xi}{(2\pi)^2}d^2r\,e^{-i(p-p_0).r-i(\alpha_0(p)+\alpha_0(p_0))h(r),}\\ &\times\{(2\pi)^2\delta(\xi)\overline{\boldsymbol{X}}^{(1)}(p|\,p_0)\\ &+\frac{1}{2}[\overline{\boldsymbol{X}}^{(2)}(p|\,p-\xi|\,p_0)+\overline{\boldsymbol{X}}_s{}^{(2)}(p|\,\boldsymbol{P}+\xi|\,p_0)+i(\alpha_0(p_0)+(\alpha_0(p_0))\overline{\boldsymbol{X}}_s{}^{(1)}(p|p_0]h(\xi)\}\end{aligned} \tag{6.133}$$

where $\overline{\boldsymbol{X}}_s^{(2)}$ is given by Eq. (A.3). We immediately deduce.

$$\begin{aligned}\overline{\boldsymbol{\Phi}}^{(1)}(p|\,p_0,\xi) = &\frac{i\alpha_0(p_0)}{(\alpha_0(p)+\alpha_0(p_0)}\frac{1}{2}[\overline{\boldsymbol{X}}_s{}^{(2)}(p|\,p-\xi|\,p_0)+\overline{\boldsymbol{X}}_s{}^{(2)}(p|\,p_0+\xi|\,p_0)\\ &+i\Big(\alpha_0(p)+(\alpha_0(p_0))\overline{\boldsymbol{X}}_s{}^{(1)}(p|\,p_0)\Big].\end{aligned} \tag{6.134}$$

The SSA method contains, following the construction procedure, a perturbative term of order 1: Eq. (6.132), and of order 2: Eq. (6.134). It also contains a phase factor coming from the tangent plane approximation. In addition, Voronovich has shown in the scalar case with Dirichlet boundary conditions that the Kirchhoff tangent plane approximation is included in the SSM for order 2 (Eq. (6.134)).

6.6.2.2 Computation of the cross section and the Mueller matrices

In this section, we give the definition of the Mueller matrix. With this derivation, we can now calculate the cross section of the rough surface. The scattered field is related to the incident field by

$$\boldsymbol{E}^s(x,z) = \frac{\exp(ik_0\|r\|)}{\|\boldsymbol{r}\|}\bar{\boldsymbol{f}}(\boldsymbol{p}|\,\boldsymbol{p}_0).\boldsymbol{E}^i(\boldsymbol{p}_0), \tag{6.135}$$

with

$$\bar{\boldsymbol{f}}(\boldsymbol{p}|\,\boldsymbol{p}_0) \equiv \frac{K_0\cos\theta}{2\pi i}\overline{\boldsymbol{R}}(\boldsymbol{p}|\,\boldsymbol{p}_0), \tag{6.136}$$

$$\boldsymbol{p} = \boldsymbol{K}_0\frac{\boldsymbol{x}}{\|\boldsymbol{r}\|}, \tag{6.137}$$

where θ is the angle between $\hat{e}_z$ and the scattering direction. Introducing the Mueller matrix $\overline{\boldsymbol{M}}(\boldsymbol{p}|\,\boldsymbol{p}_0)$ in the relations, the bistatic matrix is defined by the relations:

$$\bar{\gamma}(\boldsymbol{p}|\,\boldsymbol{p}_0) \equiv \frac{1}{A\,\cos(\theta_0)}\overline{\boldsymbol{M}}(\boldsymbol{p}|\,\boldsymbol{p}_0), \tag{6.138}$$

$$= \frac{1}{A\,\cos(\theta_0)}\bar{\boldsymbol{f}}(\boldsymbol{p}|\,\boldsymbol{p}_0)\odot\bar{\boldsymbol{f}}(\boldsymbol{p}|\,\boldsymbol{p}_0), \tag{6.139}$$

$$= \frac{\boldsymbol{K}_0^2 \cos^2(\theta)}{(2\pi)^2 A \cos(\theta_0)} \overline{\boldsymbol{R}}(\boldsymbol{p}|\boldsymbol{p}_0) \odot \overline{\boldsymbol{R}}(\boldsymbol{p}|\boldsymbol{p}_0), \tag{6.140}$$

where the product $\odot$ of two matrices $\overline{f}$ and $\overline{g}$ is defined by.

$$\overline{f} \odot \overline{g} \equiv \begin{pmatrix} f_{VV} & f_{VH} \\ f_{HV} & f_{HH} \end{pmatrix} \odot \begin{pmatrix} g_{VV} & g_{VH} \\ g_{HV} & g_{HH} \end{pmatrix}$$

$$= \begin{pmatrix} f_{VV}\, g_{VV}^* & f_{VH}\, g_{VH}^* & \boldsymbol{R}\mathrm{e}(f_{VV}\, g_{VH}^*) & -\mathrm{Im}(f_{VV}\, g_{VH}^*) \\ f_{HV}\, g_{VV}^* & f_{HH}\, g_{HH}^* & \boldsymbol{R}\mathrm{e}(f_{HV}\, g_{HH}^*) & -\mathrm{Im}(f_{HV}\, g_{VH}^*) \\ 2\boldsymbol{R}\mathrm{e}(f_{VV}\, g_{VH}^*) & 2\boldsymbol{R}\mathrm{e}(f_{VH}\, g_{HH}^*) & \boldsymbol{R}\mathrm{e}(f_{VV}\, g_{VH}^* + f_{HV} g_{VH}^*) & -\mathrm{Im}(f_{VV}\, g_{HH}^* - f_{VH} g_{VH}^*) \\ 2\mathrm{Im}(f_{VV}\, g_{VV}^*) & 2\mathrm{Im}(f_{VH}\, g_{HH}^*) & \mathrm{Im}(f_{VV}\, g_{VV}^* + f_{HV} g_{VH}^*) & \boldsymbol{R}\mathrm{e}(f_{VV}\, g_{HH}^* - f_{VH} g_{VH}^*) \end{pmatrix}. \tag{6.141}$$

The scattering from a randomly rough surface is a stochastic process, so the computations of the laser cross section for the coherent and incoherent parts involve an average over the realizations of the surfaces. The definition of the coherent bistatic matrix reads.

$$\begin{aligned} \overline{\gamma}^{\mathrm{coh}} &\equiv \frac{1}{A\cos\,\theta_0} < \overline{f}(\boldsymbol{p}|\boldsymbol{p}_0) \odot \overline{f}(\boldsymbol{p}|\boldsymbol{p}_0) > \\ &= \frac{\boldsymbol{K}\frac{2}{0}\cos^2(\theta)}{A(2\pi)^2\cos(\theta_0)} < \overline{\boldsymbol{R}}(\boldsymbol{p}|\boldsymbol{p}_0) > \odot < \overline{\boldsymbol{R}}(\boldsymbol{p}|\boldsymbol{p}_0) >, \end{aligned} \tag{6.142}$$

and the definition of the incoherent bistatic matrix is.

$$\begin{aligned} \overline{\gamma}^{incoh}(\boldsymbol{p}|\boldsymbol{p}_0) &\equiv \frac{1}{A\cos\,\theta_0} < \overline{f}(\boldsymbol{p}|\boldsymbol{p}_0) \odot \overline{f}(\boldsymbol{p}|\boldsymbol{p}_0) > < \overline{f}(\boldsymbol{p}|\boldsymbol{p}_0) > \odot < \overline{\boldsymbol{f}}(\boldsymbol{p}|\boldsymbol{p}_0) >], \\ &= \frac{\boldsymbol{K}\frac{2}{0}\cos^2(\theta)}{A(2\pi)^2\cos(\theta_0)} < \overline{\boldsymbol{R}}(\boldsymbol{p}|\boldsymbol{p}_0) > \odot < \overline{\boldsymbol{R}}(\boldsymbol{p}|\boldsymbol{p}_0) > \\ &\quad - < \overline{\boldsymbol{R}}(\boldsymbol{p}|\boldsymbol{p}_0) > \odot < \overline{\boldsymbol{R}}(\boldsymbol{p}|\boldsymbol{p}_0) >]. \end{aligned} \tag{6.143}$$

These formulas are particularly important because they contain all the information about the scattering process. If we consider the case of a single rough surface, Eq. (6.133), where we have

$$\begin{aligned} \overline{\sum}_s^0(\boldsymbol{p}|\boldsymbol{p}_0|\boldsymbol{\xi}) &= \overline{X}_s^{(2)}(\boldsymbol{p}|\boldsymbol{p}-\boldsymbol{\xi}|\boldsymbol{p}_0) + \overline{X}_s^{(2)}(\boldsymbol{p}|\boldsymbol{p}_0+\boldsymbol{\xi}|\boldsymbol{p}_0) \\ &\quad + \mathrm{i}(\alpha_0(\boldsymbol{p}) + \alpha_0(\boldsymbol{p}_0))\overline{X}_s^{(1)}(\boldsymbol{p}|\boldsymbol{p}|\boldsymbol{p}_0), \end{aligned} \tag{6.144}$$

we must emphasize an important point: this matrix does not comply with the reciprocity condition, so we will define a reciprocal matrix by the relation:

$$\overline{\sum}_s(\boldsymbol{p}|\boldsymbol{p}_0|\boldsymbol{\xi}) = \frac{1}{2}\left[\overline{\sum}_s^0(\boldsymbol{p}|\boldsymbol{p}_0|\boldsymbol{\xi}) + \overline{\sum}_s^0(-\boldsymbol{p}_0|-\boldsymbol{p}|-\boldsymbol{\xi})^{aT}\right], \tag{6.145}$$

where aT means the antitranspose of a matrix, with the definition:

$$\begin{pmatrix} a & b \\ c & d \end{pmatrix}^{aT} = \begin{pmatrix} a & -c \\ -b & d \end{pmatrix}. \tag{6.146}$$

Taking the statistical average of the matrix $\boldsymbol{R}^{10}(\boldsymbol{p}\,|\boldsymbol{p}_0)$ one obtains for the coherent part:

$$\begin{aligned} <\boldsymbol{R}^{10}(\boldsymbol{p}|\,\boldsymbol{p}_0)> \equiv & \frac{i\alpha_0(\boldsymbol{p}_0)}{(\alpha_0(\boldsymbol{p})+\alpha_0(\boldsymbol{p}_0))} e^{-(\alpha_0(\boldsymbol{p})+\alpha_0(\boldsymbol{p}_0))^2\sigma^2/2.} \\ & \int \mathrm{d}^2 r e^{-(\boldsymbol{p}-\boldsymbol{p}_0)\cdot\boldsymbol{r}} \left\{ \overline{\boldsymbol{X}}_s^1(\boldsymbol{p}\,|\,\boldsymbol{p}_0) + \frac{(\alpha_0(\boldsymbol{p})+\alpha_0(\boldsymbol{p}_0))}{2} \int \frac{\mathrm{d}^2\boldsymbol{\xi}}{(2\pi)^2} W(\boldsymbol{\xi}) \overline{\sum}_s(\boldsymbol{p}|\boldsymbol{p}_0|\boldsymbol{\xi}) \right\}, \end{aligned} \tag{6.147}$$

and for the incoherent part the expression:

$$\begin{aligned} \overline{\gamma}^{incho}(p|\,p_0) \equiv & \frac{K_0^2\cos^2\theta}{A(2\pi)^2\cos\theta_0} [< R^{10}(p|\,p_0)\odot R^{10}(p|\,p_0) > \\ & - < R(p|\,p_0) > \odot < R^{10}(p|\,p_0) >], \end{aligned} \tag{6.148}$$

where

$$\begin{aligned} <R^{10}(p|\,p_0)\odot R^{10}(p|\,p_0)> = & \frac{\alpha_0(p_0)\alpha_0(p)}{-(\alpha_0(p)+\alpha(p_0))^2} e^{-(\alpha_0(p)+\alpha_0(p_0))^2\sigma^2/2}. \\ & \int \mathrm{d}^2 r \int \mathrm{d}^2 r' e^{(\alpha_0(p)+\alpha_0(p))^2 W(r-r')} e^{-i(p-p_0)\cdot(r-r').} \\ & \left\{ \left[\overline{X}_s^{(1)}(p,p_0) - \frac{\mathrm{i}(\alpha_0(p)+\alpha(p_0))}{2} \int \frac{\mathrm{d}^2\xi}{(2\pi)^2} W(\xi) \left(e^{i\xi\cdot(r-r')} - 1 \right) \right. \right. \\ & \left. \overline{\sum}_s(p|p_0|\xi) \right] \odot \left[\overline{X}_s^{(1)}(p,p_0) - \frac{\mathrm{i}(\alpha_0(p)+\alpha(p_0))}{2} \right. \\ & \left. \int \frac{\mathrm{d}^2\xi}{(2\pi)^2} W(\xi) \left(e^{i\xi\cdot(r-r')} - 1 \right) \right. \\ & \left. \left. \overline{\sum}_s(p|p_0|\xi) \right] + \frac{1}{4} \int \frac{\mathrm{d}^2\xi}{(2\pi)^2} W(\xi) \overline{\sum}_s(p|p_0|\xi) \odot \overline{\sum}_s(p|p_0|\xi) \right\}. \end{aligned} \tag{6.149}$$

6.6.2.3 A randomly rough surface between two semiinfinite media

In this section, we apply the above derivation to the case of a rough surface between two semiinfinite media. We consider a rough surface made of aluminum with relative permittivity $\varepsilon_1 = -40 - i1.1$. The rough surface is supposed to be homogeneous and isotropic with an rms height ($\sigma = 0.3/K_0$) of Gaussian nature, and with a correlation length ($l = 3/K_0$). The incident wavelength is $\lambda = 632.2\,\mathrm{nm}$, the angle of incidence $\theta_i = 20$ degrees, and the azimuthal plane of incidence $\varphi_i = 0$. The incoherent components $\gamma^{\mathrm{incoh}}(\theta_d)$ are plotted in Figs. 6.15 and 6.16 as functions of the scattering angle θ_d, calculated up to the second order in the SSA.

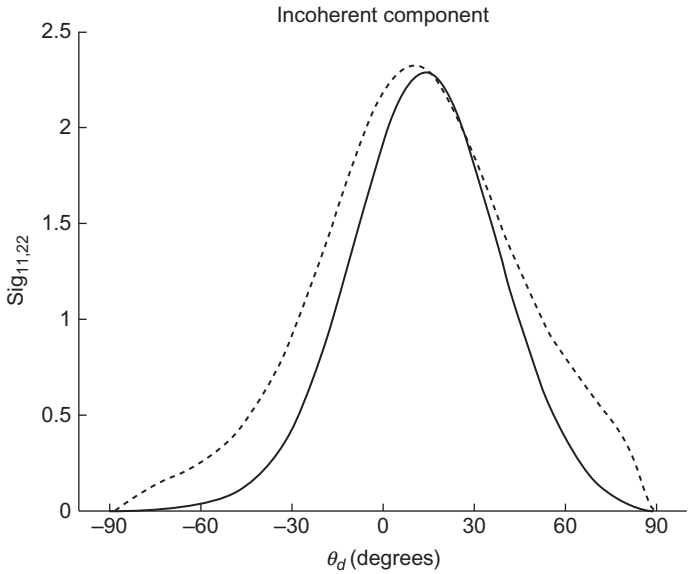


FIG. 6.15

Incoherent components $\gamma^{\text{incoh}}(\theta_d)$ as functions of the scattering angle θ_d. *VV (dashed line)*, *HH (solid line)*. Incident wavelength $\lambda = 632.8\,\text{nm}$, height $\sigma = 0.3/K_0$, correlation length $l = 3/K_0$. Angles: $\theta_i = 20\,\text{degrees}$, $\varphi_i = 0\,\text{degrees}$, permittivity: $\varepsilon_0 = 1$, $\varepsilon_1 = -40 - i1.1$.

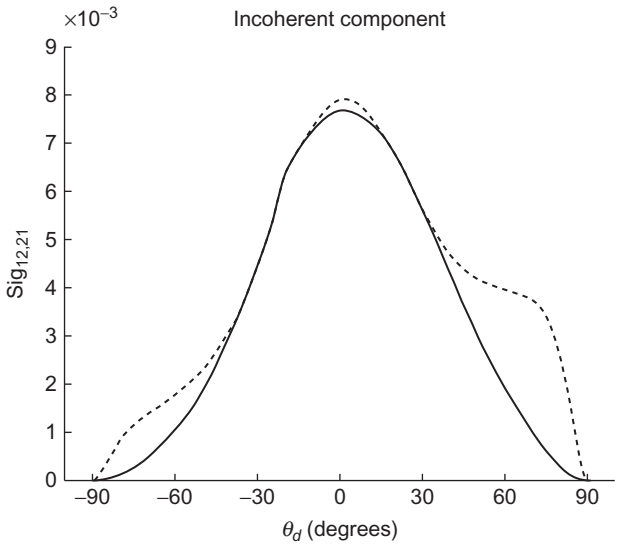


FIG. 6.16

Same characteristics as for Fig. 6.15 Components *VH (dashed line)*, and *HV (solid line)*.

6.6.3 THE SSA AND THE SPM FOR SLABS WITH RANDOMLY ROUGH BOUNDARIES

6.6.3.1 Formulation

In this section, we give some elements of the theory of the SSA and the SPM for the scattering of light from a 3D slab bounded by two randomly rough surfaces. The configuration is shown in Fig. 6.13, where the three regions are characterized by different homogenous and isotropic permittivities, ε_0, ε_1, and ε_2. The slab is delimited by two rough surfaces located at $z = h_1(\boldsymbol{x})$ and $z = -H + h_2(\boldsymbol{x})$, $\boldsymbol{x} = (x, y, 0)$.

The SSA method involves the knowledge of the scattering matrices calculated in the SPM. We summarize the results already obtained in Soubret et al. (2001b) and needed in the following. For a system with two rough surfaces the perturbative development of the scattering matrix $\overline{R}$ can be expanded as.

$$R = \overline{R}^{(00)} + \overline{R}^{(10)} + \overline{R}^{(01)} + \overline{R}^{(11)} + \overline{R}^{(20)} + \overline{R}^{(21)} + \overline{R}^{(22)} + \overline{R}^{(30)} + \overline{R}^{(03)} + \ldots \tag{6.150}$$

where the terms associated with the products of the heights of the two surfaces $h_1^n h_2^m$ are labeled $\overline{\boldsymbol{R}}^{(nm)}$.

Concerning the bistatic incoherent cross sections, we decompose their expressions into three terms corresponding to the contributions of the upper and lower surfaces alone plus a contribution due to the interferences between the two rough surfaces,

$$\overline{\gamma}^{incoh}(p|\,p_0) = \overline{\gamma}_u^{incoh}(p|\,p_0) + \overline{\gamma}_d^{incoh}(p|\,p_0) + \overline{\gamma}_{ud}^{incoh}(p|\,p_0), \tag{6.151}$$

where

$$\overline{\gamma}_u^{incoh}(p|\,p_0) = \frac{K_0^2 \cos^2\theta}{A(2\pi)^2 \cos\theta_0}\left[< \overline{R}^{(10)} \odot \overline{R}^{(10)} > + < \overline{R}^{(20)} \odot \overline{R}^{(20)} > + < \overline{R}^{(30)} \odot \overline{R}^{(10)} > \right] \tag{6.152}$$

corresponds to the contribution of the upper surface ($h_1(\boldsymbol{x}) = 0$), where the perturbative expansion is limited to the order 3 as a function of the mean height σ_1. In a similar way, the contribution due to the lower surface can be written by permuting the upper indices. The interference term $\overline{\gamma}_{ud}^{incoh}$, contains the contributions of the field interacting with the two rough surfaces, and the dominant parts are given by.

$$\begin{aligned}\overline{\gamma}_{ud}^{incoh}(\boldsymbol{p}|\,\boldsymbol{p}_0) = \frac{K_0^2 \cos^2\theta}{A(2\pi)^2 \cos\theta_0}\Big[& < \overline{\boldsymbol{R}}^{(10)} \odot \overline{\boldsymbol{R}}^{(12)} > + < \overline{\boldsymbol{R}}^{(12)} \odot \overline{\boldsymbol{R}}^{(10)} \\ & = < \overline{\boldsymbol{R}}^{(01)} \odot \overline{\boldsymbol{R}}^{(21)} > + < \overline{\boldsymbol{R}}^{(21)} \odot \overline{\boldsymbol{R}}^{(01)} > = \overline{\boldsymbol{R}}^{(11)} \odot \overline{\boldsymbol{R}}^{(11)} > + \ldots]\end{aligned} \tag{6.153}$$

These contributions contain all the terms with the elements $\sigma_1^i \sigma_2^j (1 \le i+j \le 4)$. If the values σ_1 and σ_2 are close, their contributions will be equivalent to fourth-order terms in Eqs. (6.152), (6.153). So we have supposed in Eq. (6.153) that the terms corresponding to $\sigma_1^4\sigma_1^2$, $\sigma_1^2\sigma_2^4$, $\sigma_1^4\sigma_1^4$ are negligible compared with the terms kept in Eq. (6.153).

In the case of the SSA method, we will study a perturbative development of the scattered field which depends on the slopes of the surfaces h_1, h_2. The scattering

matrix we have used in previous sections must be generalized to the case with two randomly rough surfaces. We propose the following generalization with an "Ansatz" similar to the functional form proposed by *V*oronovich:

$$\begin{aligned}\overline{\boldsymbol{R}}(\boldsymbol{p},\boldsymbol{p}_0) = \int d^2\boldsymbol{r}d^2r' \exp\left[-i(\boldsymbol{p}-\boldsymbol{p}_0).(\boldsymbol{r}+\boldsymbol{r}') - i(\alpha(\boldsymbol{p})+\alpha(\boldsymbol{p}_0))(h_1(\boldsymbol{r})+h_2(\boldsymbol{r}'))\right] \\ \times \overline{\boldsymbol{\Phi}}[\boldsymbol{p},\boldsymbol{p}_0;\boldsymbol{r};\boldsymbol{r}';[h_1(r)];[h_2(r')]].\end{aligned} \tag{6.154}$$

A natural extension of the scattering amplitude involving two rough surfaces reads in Fourier space:

$$\begin{aligned}\overline{\boldsymbol{R}}(\boldsymbol{p},\boldsymbol{p}_0) = \int d^2\boldsymbol{r}d^2\boldsymbol{r}' \frac{d^2\boldsymbol{\xi}}{(2\pi)^2}\frac{d^2\boldsymbol{\xi}'}{(2\pi)^2} \\ \times \exp\left[-i(\boldsymbol{p}-\boldsymbol{p}_0-\boldsymbol{\xi})\cdot\boldsymbol{r} - i(\boldsymbol{p}-\boldsymbol{p}_0-\boldsymbol{\xi}').r' - (\alpha(\boldsymbol{p})+\alpha(\boldsymbol{p}_0))(h_1(r)+h_2(r'))\right] \\ \times \widetilde{\Phi}[\boldsymbol{p},\boldsymbol{p}_0;\boldsymbol{\xi};\boldsymbol{\xi}';[h_1(\boldsymbol{\xi})];[h_2(\boldsymbol{\xi}')]],\end{aligned} \tag{6.155}$$

where, $h_1(\boldsymbol{\xi})$ and $h_2(\boldsymbol{\xi}')$ are the Fourier transforms of the roughnesses of the different surfaces. Following the method proposed by Voronovich, we expand the functional $\widetilde{\boldsymbol{\Phi}}$ in the form of a Taylor series:

$$\widetilde{\boldsymbol{\Phi}}(\boldsymbol{p},\boldsymbol{p}_0,\boldsymbol{\xi},\boldsymbol{\xi}') = \sum_{mm,i_1\cdots i_p}\int d^2\boldsymbol{\xi}_1\ldots d^2\boldsymbol{\xi}_p\,\delta(\boldsymbol{\xi}-\boldsymbol{\xi}_1-\ldots\boldsymbol{\xi}_p)\,\widetilde{\Phi}^{(nm)i_1\ldots i_p}(\boldsymbol{\xi}_1\ldots\boldsymbol{\xi}_p)h_1(\boldsymbol{\xi}_1)\ldots h_2(\boldsymbol{\xi}_p), \tag{6.156}$$

where we have truncated the series at the fourth order. $\widetilde{\Phi}^{(nm)i1..i_p}(\boldsymbol{\xi}_1\ldots\boldsymbol{\xi}_p)$ represents the 14 unknown kernel functions we have to determine for this structure. From gauge transformations we can derive an important relation between the orders $n-1$; n; and $n+1$, viz.:

$$\widetilde{\boldsymbol{\Phi}}^{(\boldsymbol{nm})} = \left[\widetilde{\boldsymbol{\Phi}}^{(\boldsymbol{nm})} - \widetilde{\boldsymbol{\Phi}}^{(\boldsymbol{nm})}\Big|_{\boldsymbol{\xi}_n=\boldsymbol{p}-\boldsymbol{p}_0-\boldsymbol{\xi}_1-\cdots-\boldsymbol{\xi}_{n-1}}\right] + \widetilde{\boldsymbol{\Phi}}^{(\boldsymbol{nm})}\Big|_{\boldsymbol{\xi}_n=\boldsymbol{p}-\boldsymbol{p}_0-\boldsymbol{\xi}_1-\cdots-\boldsymbol{\xi}_{n-1}}. \tag{6.157}$$

As an example of the expression of order 2 in the above series, we obtain the complex expression:

$$\begin{aligned}&\int\frac{d^2\boldsymbol{p}_1}{(2\pi)^2}\left[-\frac{(\alpha_0(\boldsymbol{p})+\alpha_0(\boldsymbol{p}_0))^2}{2}\left(\widetilde{\boldsymbol{\Phi}}_u^{(0)}(\boldsymbol{p},\boldsymbol{p}_0)+\widetilde{\boldsymbol{\Phi}}_{\mathbf{d}}^{(\mathbf{0})}(\boldsymbol{p},\boldsymbol{p}_0)\right)+\widetilde{\boldsymbol{\Phi}}^{(\mathbf{11})12}(\boldsymbol{p},\boldsymbol{p}_0,\boldsymbol{p}-\boldsymbol{p}_1,\boldsymbol{p}_1-\boldsymbol{p}_0)\right]h_1(\boldsymbol{p}-\boldsymbol{p}_1)h_2(\boldsymbol{p}=\boldsymbol{p}_0) \\ &+\int\frac{d^2\boldsymbol{p}_1}{(2\pi)^2}\left[-\frac{(\alpha_0(\boldsymbol{p})+\alpha_0(\boldsymbol{p}_0))^2}{2}\left(\widetilde{\boldsymbol{\Phi}}_u^{(0)}(\boldsymbol{p},\boldsymbol{p}_0)+\widetilde{\boldsymbol{\Phi}}_d^{(0)}(\boldsymbol{p},\boldsymbol{p}_0)\right)+\widetilde{\boldsymbol{\Phi}}^{(11)21}(\boldsymbol{p},\boldsymbol{p}_0-\boldsymbol{p}_1,\boldsymbol{p}_1-\boldsymbol{p}_0)\right]h_2(\boldsymbol{p}-\boldsymbol{p}_1)h_2(\boldsymbol{p}_1-\boldsymbol{p}_0) \\ &+\int\frac{d^2\boldsymbol{p}_1}{(2\pi)^2}\left[-\frac{(\alpha_0(\boldsymbol{p})+\alpha_0(\boldsymbol{p}_0))^2}{2}\widetilde{\boldsymbol{\Phi}}_u^{(0)}(\boldsymbol{p},\boldsymbol{p}_0)+\widetilde{\boldsymbol{\Phi}}^{(20)}(\boldsymbol{p},\boldsymbol{p}_0,\,-\boldsymbol{p}-\boldsymbol{p}_1,\boldsymbol{p}_1-\boldsymbol{p}_0)\right]h_1(\boldsymbol{p}-\boldsymbol{p}_1)h_1(\boldsymbol{p}-\boldsymbol{p}_0) \\ &+\int\frac{d^2\boldsymbol{p}_1}{(2\pi)^2}\left[-\frac{(\alpha_0(\boldsymbol{p})+\alpha_0(\boldsymbol{p}_0))^2}{2}\widetilde{\boldsymbol{\Phi}}_d^{(0)}(\boldsymbol{p},\boldsymbol{p}_0)+\widetilde{\boldsymbol{\Phi}}^{(02)}(\boldsymbol{p},\boldsymbol{p}_0,\boldsymbol{p}-\boldsymbol{p}_1,\boldsymbol{p}_1-\boldsymbol{p}_0)\right]h_2(\boldsymbol{p}-\boldsymbol{p}_1)h_1(\boldsymbol{p}_1-\boldsymbol{p}_0).\end{aligned} \tag{6.158}$$

We can find the expressions for the different orders in Berginc and Bourrely (2007). The kernel functions can be computed. For each order of the SSA the functions $\widetilde{\boldsymbol{\Phi}}^{(nm)}$

are identified with $\overline{X}^{(nm)}$ obtained from the small-amplitude perturbation method described in Berginc (2007).

For instance, $\widetilde{\boldsymbol{\Phi}}^{(12)221}$ describes the interaction of the electromagnetic field once with the upper surface and twice with the lower surface in the order 2-2-1 (see Berginc and Bourrely, 2007 for the expressions for the different contributions).

We have

$$\begin{aligned}\widetilde{\boldsymbol{\Phi}}^{(12)221}(\boldsymbol{p},\boldsymbol{p}_0,\boldsymbol{\xi}_1,\boldsymbol{\xi}_2,\boldsymbol{\xi}_3)=&\frac{i\alpha_0(\boldsymbol{p}_0)}{\alpha_0(\boldsymbol{p})+\alpha_0(\boldsymbol{p}_0)}\\&\left\{\frac{1}{5}\left[\overline{\boldsymbol{X}}^{(22)1221}+\overline{\boldsymbol{X}}^{(22)2121}+\overline{\boldsymbol{X}}^{(22)2211}+\overline{\boldsymbol{X}}^{(13)2221}+\overline{\boldsymbol{X}}^{(13)2221}\right]\right.\\&+i\frac{1}{240}(\alpha_0(\boldsymbol{p})+\alpha_0(\boldsymbol{p}_0))\,[72\overline{\boldsymbol{X}}^{(21)211}+90\overline{\boldsymbol{X}}^{(21)121}+18\overline{\boldsymbol{X}}^{(21)112}+138\overline{\boldsymbol{X}}^{(12)212}\\&+66\overline{\boldsymbol{X}}^{(12)211}+216\overline{\boldsymbol{X}}^{(12)221}+24\overline{\boldsymbol{X}}^{(30)}+120\overline{\boldsymbol{X}}^{(03)}]\\&-\frac{1}{240}(\alpha_0(\boldsymbol{p})+\alpha_0(\boldsymbol{p}_0))^2\left[312\overline{\boldsymbol{X}}^{(11)12}+516\overline{X}^{(11)21}+749\overline{\boldsymbol{X}}^{(02)}+389\overline{\boldsymbol{X}}^{(20)}\right]\\&\left.-i\frac{1}{480}(\alpha_0(\boldsymbol{p})+\alpha_0(\boldsymbol{p}_0))^3\left(1445\overline{\boldsymbol{X}}_u^{(\mathbf{1})}+1837\overline{\boldsymbol{X}}_d^{(\mathbf{1})}\right)\right\}.\end{aligned}\tag{6.159}$$

When the expressions $\widetilde{\boldsymbol{\Phi}}^{(nm)}$ are calculated we can deduce the scattering matrices $\overline{\boldsymbol{R}}^{(nm)}$. With the definition of the following integration operator

$$\begin{aligned}J^{(n)}=&\int d^2r d^2r'\frac{d^2\boldsymbol{\xi}}{(2\pi)^2}\frac{d^2\boldsymbol{\xi}'}{(2\pi)^2}\frac{d^2\boldsymbol{\xi}_1}{(2\pi)^2}\cdots\frac{d^2\boldsymbol{\xi}_n}{(2\pi)^2}\\&\times\exp\,[-i(\boldsymbol{p}-\boldsymbol{p}_0-\boldsymbol{\xi})\cdot r-i(\boldsymbol{p}-\boldsymbol{p}_0-\boldsymbol{\xi}')\cdot r'\\&-i(\alpha(p)+\alpha(p_0))(h_1(r)+h_2(r'))],\end{aligned}\tag{6.160}$$

we obtain the expressions:

$$\begin{aligned}\overline{\boldsymbol{R}}^{(10)}(p|\,p_0)=&J^{(1)}\widetilde{\boldsymbol{\Phi}}^{(10)}(p,p_0,\boldsymbol{\xi}_1)h_1(\boldsymbol{\xi}_1)\\\overline{\boldsymbol{R}}^{(01)}(p|\,p_0)=&J^{(1)}\widetilde{\boldsymbol{\Phi}}^{(01)}(p,p_0,\boldsymbol{\xi}_1)h_2(\boldsymbol{\xi}_1)\\\overline{\boldsymbol{R}}^{(11)}(p|\,p_0)=&J^{(2)}\left[\widetilde{\boldsymbol{\Phi}}^{(11)12}(p,p_0,\boldsymbol{\xi}_1,\boldsymbol{\xi}_2)h_1(\boldsymbol{\xi}_1)h_2(\boldsymbol{\xi}_2)\right.\\&\left.+\widetilde{\boldsymbol{\Phi}}^{(11)21}(p,p_0,\boldsymbol{\xi}_1,\boldsymbol{\xi}_2)h_2(\boldsymbol{\xi}_2)h_1(\boldsymbol{\xi}_1)\right]\\\overline{\boldsymbol{R}}^{(20)}(p|\,p_0)=&J^{(2)}\widetilde{\boldsymbol{\Phi}}^{(20)}(p,p_0,\boldsymbol{\xi}_1,\boldsymbol{\xi}_2\boldsymbol{\xi})h_1(\boldsymbol{\xi}_1)h_2(\boldsymbol{\xi}_2)\\\overline{\boldsymbol{R}}^{(02)}(p|\,p_0)=&J^{(2)}\widetilde{\boldsymbol{\Phi}}^{(02)}(p,p_0,\boldsymbol{\xi},\boldsymbol{\xi}_1\boldsymbol{\xi}_2)h_2(\boldsymbol{\xi}_1)h_2(\boldsymbol{\xi}_2)\\\overline{\boldsymbol{R}}^{(21)}(p|\,p_0)=&J^{(3)}\left[\widetilde{\boldsymbol{\Phi}}^{(21)112}(p,p_0,\boldsymbol{\xi}_1,\boldsymbol{\xi}_2\boldsymbol{\xi}_3)h_1(\boldsymbol{\xi}_1)h_1(\boldsymbol{\xi}_2)h_2(\boldsymbol{\xi}_3)\right.\\&+\widetilde{\boldsymbol{\Phi}}^{(21)121}(p,p_0,\boldsymbol{\xi}_1,\boldsymbol{\xi}_2\boldsymbol{\xi}_3)h_1(\boldsymbol{\xi}_1)h_2(\boldsymbol{\xi}_3)h_2(\boldsymbol{\xi}_2)\\&\left.+\widetilde{\boldsymbol{\Phi}}^{(21)211}(p,p_0,\boldsymbol{\xi}_1,\boldsymbol{\xi}_2\boldsymbol{\xi}_3)h_2(\boldsymbol{\xi}_3)h_1(\boldsymbol{\xi}_1)h_1(\boldsymbol{\xi}_2)\right]\\\overline{\boldsymbol{R}}^{(12)}(p|\,p_0)=&J^{(3)}\left[\widetilde{\boldsymbol{\Phi}}^{(12)221}(p,p_0,\boldsymbol{\xi}_1,\boldsymbol{\xi}_2\boldsymbol{\xi}_3)h_2(\boldsymbol{\xi}_1)h_2(\boldsymbol{\xi}_2)h_1(\boldsymbol{\xi}_3)\right.\\&+\widetilde{\boldsymbol{\Phi}}^{(12)212}(p,p_0,\boldsymbol{\xi}_1,\boldsymbol{\xi}_2\boldsymbol{\xi}_3)h_2(\boldsymbol{\xi}_1)h_1(\boldsymbol{\xi}_3)h_2(\boldsymbol{\xi}_2)\\&\left.+\widetilde{\boldsymbol{\Phi}}^{(12)122}(p,p_0,\boldsymbol{\xi}_1,\boldsymbol{\xi}_2\boldsymbol{\xi}_3)h_1(\boldsymbol{\xi}_3)h_2(\boldsymbol{\xi}_1)h_2(\boldsymbol{\xi}_2)\right]\\\overline{\boldsymbol{R}}^{(30)}(p|\,p_0)=&J^{(3)}\widetilde{\boldsymbol{\Phi}}^{(30)}(p,p_0,\boldsymbol{\xi}_1,\boldsymbol{\xi}_2\boldsymbol{\xi}_3)h_1(\boldsymbol{\xi}_1)h_1(\boldsymbol{\xi}_2)h_1(\boldsymbol{\xi}_3)\\\overline{\boldsymbol{R}}^{(03)}(p|\,p_0)=&J^{(3)}\widetilde{\boldsymbol{\Phi}}^{(03)}(p,p_0,\boldsymbol{\xi}_1,\boldsymbol{\xi}_2\boldsymbol{\xi}_3)h_2(\boldsymbol{\xi}_1)h_2(\boldsymbol{\xi}_2)h_2(\boldsymbol{\xi}_3).\end{aligned}\tag{6.161}$$

To calculate the bistatic cross section, we take the expansion of $\overline{\boldsymbol{R}}$ in terms of the (mn) scattering matrices given by $\overline{R}^{(nm)}$. The incoherent bistatic cross section is given by

$$\overline{\gamma}_{ij}^{incoh}(p|\,p_0) = \frac{K_0^2\cos^2\theta}{A(2\pi)^2\cos\theta_0}\left[<\overline{\boldsymbol{R}}(\boldsymbol{p}|\,\boldsymbol{p}_0)\odot\overline{\boldsymbol{R}}(\boldsymbol{p}|\,\boldsymbol{p}_0)> - <\overline{\boldsymbol{R}}(\boldsymbol{p}|\,\boldsymbol{p}_0)>\odot<\overline{\boldsymbol{R}}(\boldsymbol{p}|\,\boldsymbol{p}_0)>\right], \tag{6.162}$$

where the angle brackets denote an average over the ensembles of realizations of the functions $h_{i(}r)$, and ij are the polarization components.

An example of a contribution coming from $4h_2$ heights reads (Berginc and Bourrely, 2007):

$$\begin{aligned}
&<\overline{\boldsymbol{R}}^{(03)}(\boldsymbol{p}|\,\boldsymbol{p}_0)\odot\overline{\boldsymbol{R}}^{(01)}(\boldsymbol{p}|\,\boldsymbol{p_0})\geq \exp\left[-(\alpha_0(\boldsymbol{p})+\alpha_0(\boldsymbol{p}_0))^2/2W_{22}(0)\right]\\
&\times\int d^2\boldsymbol{x}_1 d^2\boldsymbol{x}_2\exp\left[-i(\boldsymbol{p}-\boldsymbol{p}_0)(\boldsymbol{x_1}-\boldsymbol{x}_2)\right]\exp\left[(\alpha_0(\boldsymbol{p})+\alpha_0(\boldsymbol{p}_0))^2W_{22}(\boldsymbol{x}_1-\boldsymbol{x}_2)\right]\\
&\times\int\frac{d^2\boldsymbol{\xi}}{(2\pi)^2}\exp[i\boldsymbol{\xi}(\boldsymbol{x}_1-\boldsymbol{x}_2)]W_{22}(\boldsymbol{\xi})\int\frac{\mathrm{d}^2\boldsymbol{\xi}_2}{(2\pi)^2}W_{22}(\boldsymbol{\xi}_2)\left[\widetilde{\boldsymbol{\Phi}}^{(03)}(\boldsymbol{p},\boldsymbol{p}_0,\boldsymbol{\xi},\boldsymbol{\xi}_2,-\boldsymbol{\xi}_2)\odot\widetilde{\boldsymbol{\Phi}}^{(01)*}(\boldsymbol{p},\boldsymbol{p}_0,\boldsymbol{\xi})\right.\\
&+\widetilde{\boldsymbol{\Phi}}^{(03)}(\boldsymbol{p},\boldsymbol{p}_{0,}\boldsymbol{\xi}_2,\boldsymbol{\xi},-\boldsymbol{\xi}_2)\odot\widetilde{\boldsymbol{\Phi}}^{(01)*}(\boldsymbol{p},\boldsymbol{p}_0,\boldsymbol{\xi})\\
&\left.+\widetilde{\boldsymbol{\Phi}}^{(03)}(\boldsymbol{p},\boldsymbol{p}_{0,}\boldsymbol{\xi}_2,-\boldsymbol{\xi}_2,\boldsymbol{\xi})\odot\widetilde{\boldsymbol{\Phi}}^{(01)*}(\boldsymbol{p},\boldsymbol{p}_0,\boldsymbol{\xi})\right],
\end{aligned} \tag{6.163}$$

where we have assumed a Gaussian expression for the heights in our applications, and W_{ij} are the correlation functions associated with the surfaces.

6.6.3.2 Applications of the SSA method

In this section, we give some examples of films with 2D randomly rough surfaces. In the following, the complex pattern of the cross section is related to the randomly rough surfaces. For the first example, we take as the incident medium a vacuum followed by a dielectric medium ($\varepsilon_1 = 1.62 + i0.001$), the boundary being a rough surface with an rms height $\sigma = 0.223\,\mu$m, a correlation length $l = 1.42\,\mu$m, the incident wavelength $\lambda = 632.8$ nm, the angle of incidence $\theta_i = 20$ degrees and the azimuthal angle $\varphi_i = 0$ degrees. We introduce a slab of thickness $H = 500$ nm with a perfectly conducting lower planar surface. The results are presented in Figs. 6.17 and 6.18. We observe the same maximum around the backscattering direction for the polarizations VV and HH but an increase of the scattered intensity by a factor of 100. We note for the polarizations HV and VH the presence of small oscillations for $\theta_d > 60$ degrees due to the numerical integration method.

We take as another example a slab of thickness $H = 500$ nm, with an upper rough surface $\sigma = 15$ nm, $l = 100$ nm, and a lower planar surface made of a perfect conductor. The successive media are defined with the following permittivities: $\varepsilon_0 = 1$, $\varepsilon_1 = 2.6896 + i0.0075$. The wavelength is $\lambda = 632.8$ nm and the angle of incidence is $\theta_i = 20$ degrees. The results are shown in Figs. 6.19 and 6.20. The intensities are concentrated in the backscattering region for the polarizations VV and HH, while for the VH and VH polarizations the intensities reach maxima in a region opposite the incident scattering angle.

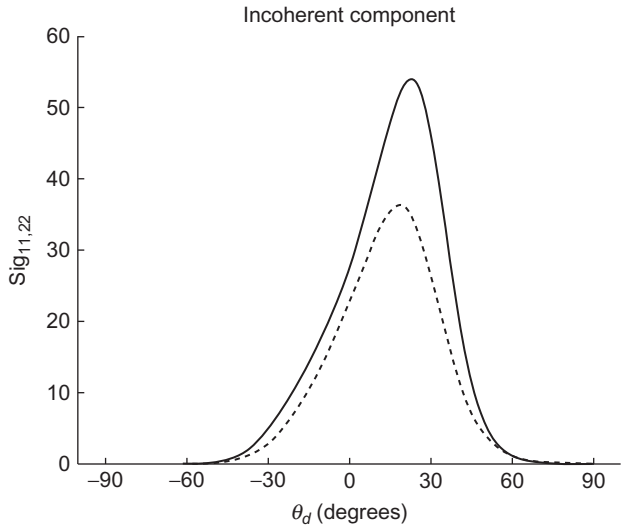


FIG. 6.17

Incoherent components $\gamma^{\text{incoh}}(\theta_d)$ to the order 2. *VV* (dashed curve), *HH* (solid curve), Surface height $\sigma = 0.223\,\mu\text{m}$, correlation length $l = 1.42\,\mu\text{m}$, slab thickness 500 nm. Permittivities $\varepsilon_0 = 1$, $\varepsilon_1 = 1.62 + i0.0001$, and $\varepsilon_2 = +\,\text{i}\,\infty$. Incident angles: $\theta_i = 20°$, $\varphi_i = 0°$, and wavelength $\lambda = 632.8\,\text{nm}$.

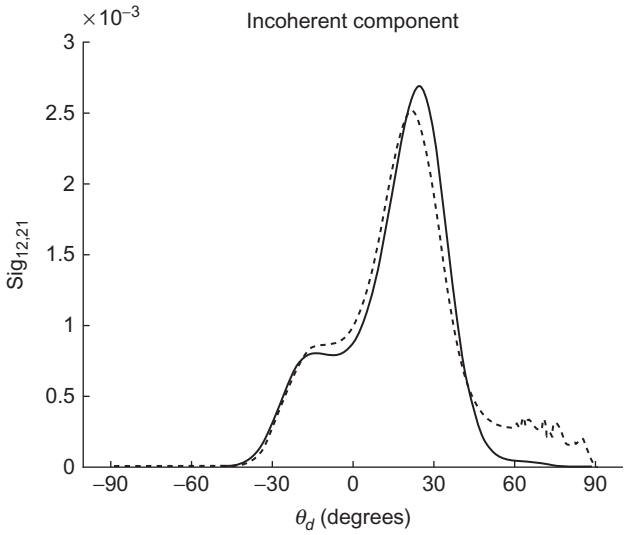


FIG. 6.18

Same characteristics as for Fig. 6.17. Incoherent components *VH* (dashed line) and *HV* (solid line).

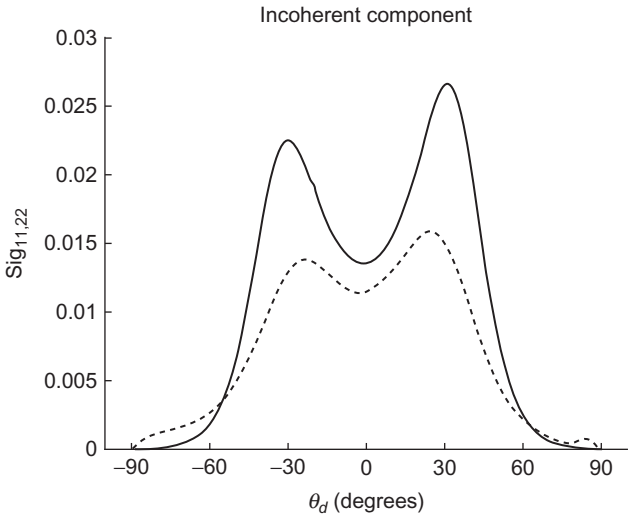


FIG. 6.19

Incoherent components $\gamma^{\text{incoh}}(\theta_d)$ to the order 2, *VV (dashed line)*, *HH (solid line)*, surface height $\sigma = 15\,\text{nm}$, correlation length $l = 100\,\text{nm}$, slab thickness 500 nm. Permittivities $\varepsilon_0 = 1$, $\varepsilon_1 = 2.6896 + i\,0.0075$, and $\varepsilon_2 = +i\infty$. Incident angles: $\theta_i = 20$ degrees, $\varphi_i = 0$ degrees, and wavelength $\lambda = 632.8\,\text{nm}$.

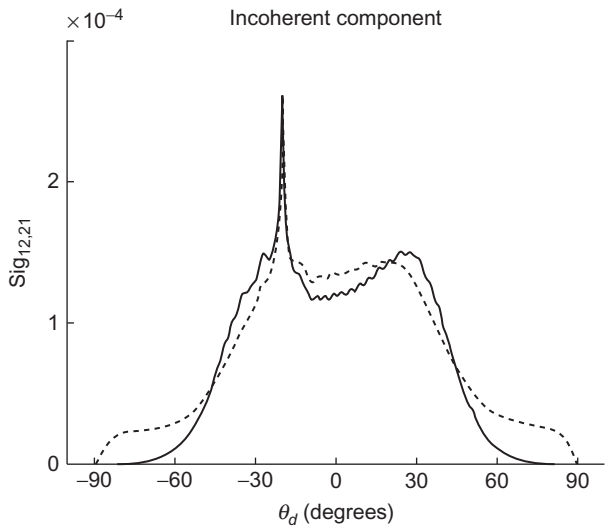


FIG. 6.20

Same characteristics as for Fig. 6.19. Incoherent components *VH (dashed line)* and *HV (solid line)*.

For the last example we take a slab of thickness $H = 500\,\text{nm}$, with an upper rough surface characterized by the parameters: rms height $\sigma_1 = 15\,\text{nm}$, correlation length $l_1 = 100\,\text{nm}$ and a lower rough surface: $\sigma_2 = 5\,\text{nm}$ and $l_2 = 100\,\text{nm}$. The permittivities of the successive media are: $\varepsilon_0 = 1$, $\varepsilon_1 = 2.6896 + i0.0075$, and $\varepsilon_2 = -18.3 + i0.55$. The incident angles are $\theta_i = 0\,\text{degrees}$ and $\varphi i = 0\,\text{degrees}$ and the wavelength is $\lambda = 632.8\,\text{nm}$. The results to the order 1 are plotted in Fig. 6.21.

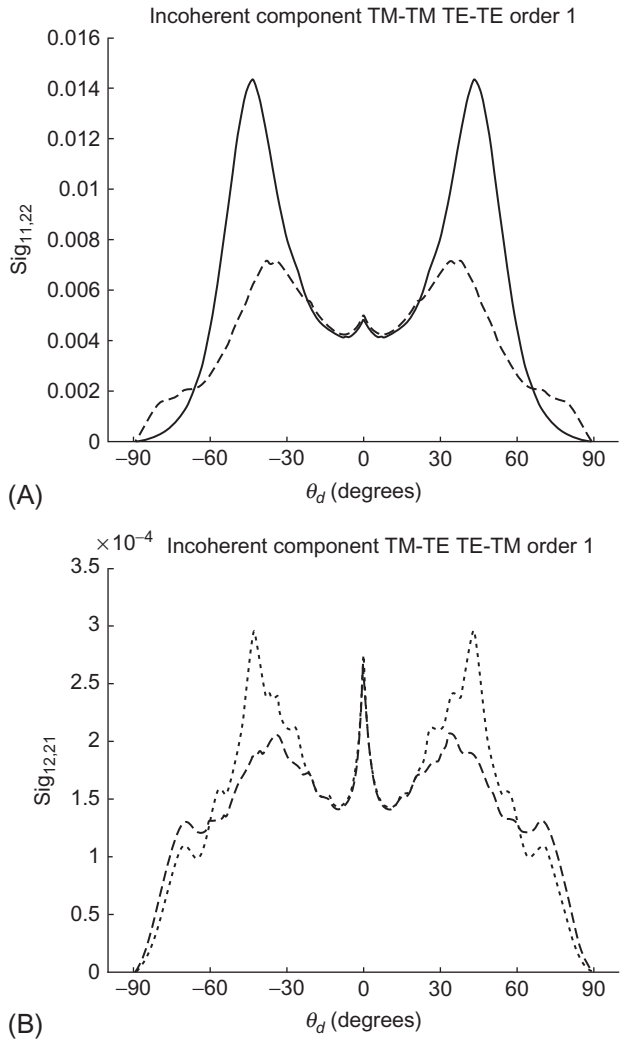


FIG. 6.21

Incoherent components $\gamma^{\text{incoh}}(\theta_d)$: *VV (dashed-dotted line)*, *HH (solid line)*, *HV (dashed line)*, and *VH (dotted line)*.

6.6.4 CONCLUSIONS

In this section, we have presented numerical results for the scattering of light from random rough films with the SSA and the SPM. We have shown the development of the SSA series with the third-order SPM kernel. These formulations generalize the SSA to a layer bounded with two randomly rough surfaces. The new terms introduced in the SSA development estimate the coupling between the two rough surfaces. We have given the complete expressions of the scattering matrices and the expressions of the cross sections needed for the different polarization states by introducing the Mueller matrices. With this formulation of the SSA, we have observed the backscattering enhancement for a rough layer. The calculation of the scattering amplitudes involves a knowledge of the SPM scattering matrices. We have used those obtained in Soubret et al. (2001a,b). This type of simulation computation can give some experimental conditions and specifications to realize integrated optical devices that use metallic or metallo-dielectric nanoscale structures.

6.7 THEORETICAL METHODS FOR THE SCATTERING OF POLARIZED LIGHT FROM RANDOMLY ROUGH INTERFACES AND RANDOM MEDIA

Random volume and surface scattering is a topic that has been studied in many domains such as optical wave propagation in turbulent media, plasmonics, and surface optics. Random media have attracted much attention, not only in electromagnetic wave propagation, but also in solid-state physics. On the other hand, randomly rough boundary scattering has been investigated to predict the angular distribution of the scattered waves. Useful phenomena in the optical range can be produced by random media with randomly rough surfaces. Designing disordered slabs with rough surfaces can produce new optical components, which can transmit or scatter optical fields with specified angular, spatial, or spectral properties. The equations for field moments in random media are known as: the Dyson equation for the first moment, the mean value of the field or the coherent part of the interaction with the random medium; and the Bethe-Salpeter equation for the second moment, the mean value of the intensity, or the incoherent part of the interaction with the random medium. They have been widely discussed in the literature (Tsang and Kong, 2001; Tsang et al., 1985; Apresyan and Kravtsov, 1996; Sheng, 1995; Frisch, 1968). As a rule, the complexity of the calculation of the statistical moments increases with their order. In this section, we consider a 3D disordered medium with randomly rough interfaces. We gave in an explicit way (Soubret and Berginc, 2003a,b) the theoretical formulas, which describe the intensity of a wave scattered from a disordered medium with rough surfaces. The governing equation can be written in the form of a Bethe-Salpeter equation. The problem is then reduced to finding a good approximation to the solution of this equation. For a 3D system composed of a random medium bounded by two randomly rough surfaces, the Bethe-Salpeter equation is constructed

in order that the medium and the boundaries are treated on the same footing. This unified Bethe-Salpeter equation enables us to obtain a general expression, whatever be the choice of the scattering operators used at the boundaries. We present a theory of transport based on the Bethe-Salpeter equation. We confine our considerations to the necessary background, and quote the final results.

6.7.1 SPECIFIC INTENSITY AND CROSS SECTION

The main characteristic we must study is the specific intensity $\boldsymbol{I}(\boldsymbol{R}, \boldsymbol{k})$. If we take into account the polarization of the wave, the specific intensity is defined as a Stokes vector or a tensor which gives the intensity at the point $\boldsymbol{R}$ in the direction $\hat{k}$. If particles are inside a slab with a permittivity different from that of the outside medium, boundary conditions must be added to the radiative transfer equation in order to calculate the specific intensity. For rough surfaces, these boundary conditions are expressed in terms of scattering operators, where several approximate analytical expressions exist depending on the roughness of the surface, for example the SPM or the SSA. It can be shown that the specific intensity can be deduced from the Wigner function of the electric field. After having determined the relation between the electromagnetic field and the specific intensity, we can derive the radiative transfer equation from the Maxwell equations. The procedure is to write the Maxwell equations in an integral form with the help of Green's function and to apply the Wigner transform to the equation obtained. The main advantage to start from wave equations is that we are able to take into account new contributions to the scattered intensity such as the enhanced backscattering and the correlations between the scatterers that cannot be obtained from phenomenological radiometric considerations. Our objective in this section is to derive the radiative transfer equations from the wave equations, taking into account rough boundaries. Several works have investigated this topic (Furutsu, 1991, 1983; Lam and Ishimaru, 1994; Pak et al., 1993; Mudaliar, 1999, 2001, 1994). In our approach, we use scattering operators, which are a unified way to describe how the electromagnetic waves interact with the boundaries. To use these operators, we have introduced two kinds of Green functions (Soubret and Berginc, 2003a). The first one $\overline{\boldsymbol{G}}_{SV}$ describes the field scattered by the volume (V), which contains the scatterers, and by the rough surfaces (S). The second type of Green function is $\overline{\boldsymbol{G}}_{S}$, which gives the field scattered by a slab with rough boundaries where the scatterers have been replaced by a homogeneous medium described by an effective permittivity. With these Green functions, we can separate the contributions of the surfaces and the volume. The main advantage of our approach is that the equations obtained are similar to the equations generally used to describe the wave scattered by an infinite random medium. The geometry of the problem and the notations are described in Section 6.6.1. We give the definitions of the incident and scattered wave vectors we use in Figs. 6.22 and 6.23. We consider harmonic waves with $e^{-i\omega t}$ time dependence. In order to characterize the intensity of a field scattered by an object, we usually introduce the bistatic cross section, which is the power scattered per solid angle normalized by the incident power. In this section, we will use a generalization of this

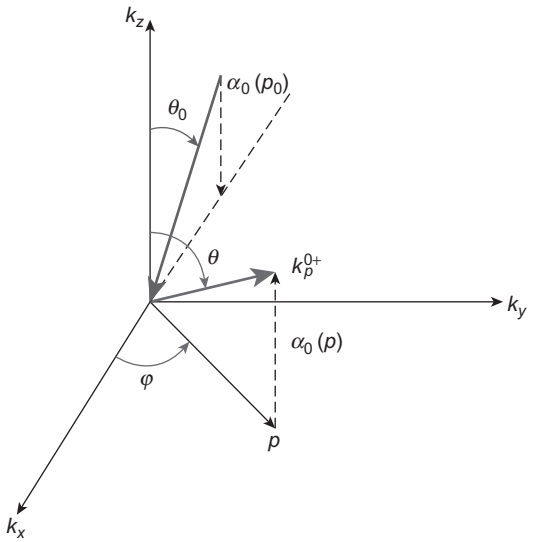


FIG. 6.22

Decomposition of the wave vectors with θ, $\theta_0 \in [-\pi/2, \pi/2]$ and $\varphi,\varphi_o \in [0,\pi]\theta_0$ is the incidence angle, θ is the scattering angle.

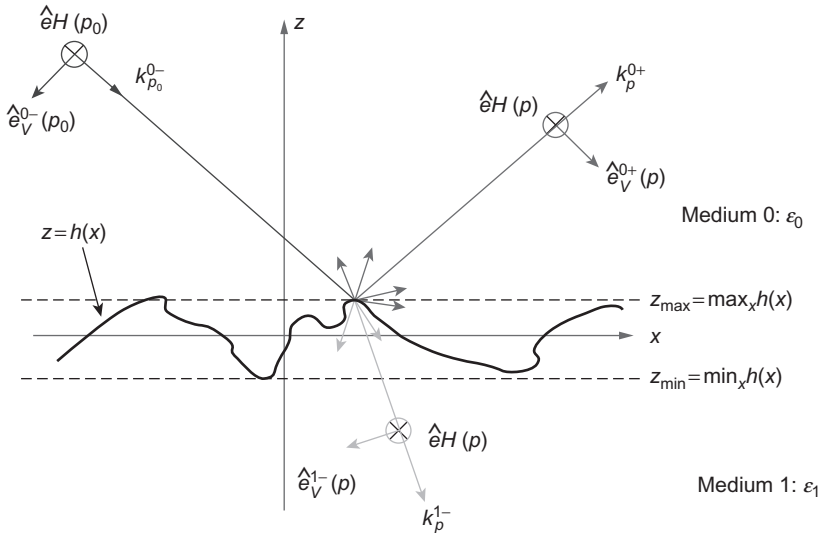


FIG. 6.23

Scattering of an incident plane wave with a wave vector $\boldsymbol{k}_{\boldsymbol{p}_0}^{0-}$, reflected wave vector $\boldsymbol{k}_{\boldsymbol{p}}^{0+}$, transmitted wave vector $\boldsymbol{k}_{\boldsymbol{p}}^{1-}$. The polarization bases TE and TM are given for each wave.

concept called Mueller bistatic cross section, which enables us to account for every polarization state of the incident and scattered wave. First, we define the different geometrical components. We have

$$K_0^2 = \varepsilon_0 \left(\frac{\omega}{c_{vac}}\right)^2, K_1^2 = \varepsilon_1 \left(\frac{\omega}{c_{vac}}\right)^2. \tag{6.164}$$

We define the wave vectors $\boldsymbol{k}_p^{0\pm}$ and $\boldsymbol{k}_p^{1\pm}$ by

$$\boldsymbol{k}_{\boldsymbol{p}}^{0\pm} \equiv \boldsymbol{p} \pm \alpha_0(\boldsymbol{p})\hat{\boldsymbol{e}}_z \tag{6.165}$$

$$\boldsymbol{k}_{\boldsymbol{p}}^{1\pm} \equiv \boldsymbol{p} \pm \alpha_1(\boldsymbol{p})\hat{\boldsymbol{e}}_z \tag{6.166}$$

where

$$\alpha_0(\boldsymbol{p}) = \sqrt{K_0^2 - \boldsymbol{p}^2}, \alpha_1(\boldsymbol{p}) = \sqrt{K_1^2 - \boldsymbol{p}^2}. \tag{6.167}$$

We now define the field $\boldsymbol{E}_S^{0s}(r)$ scattered by the interfaces without any interaction with the scatterers, and the field $\boldsymbol{E}_S^{0t}(r)$ transmitted into the layer before an interaction with the scatterers. Their expressions are given by

$$\boldsymbol{E}_S^{0s}(r) = \int \frac{d^2\boldsymbol{p}}{(2\pi)^2} e^{i\boldsymbol{p}\cdot\boldsymbol{x} + i\alpha_0(\boldsymbol{p})z} \overline{\boldsymbol{S}}^{0+,0-}(\boldsymbol{p}|\boldsymbol{p}_0) \cdot \boldsymbol{E}^{0i}(\boldsymbol{p}_0), \tag{6.168}$$

$$\boldsymbol{E}_S^{1t}(\boldsymbol{x}, z) = \int \frac{d^2\boldsymbol{p}}{(2\pi)^2} e^{i\boldsymbol{p}\cdot\boldsymbol{x}} \left[e^{i\alpha_1(\boldsymbol{p})z} \overline{\boldsymbol{S}}^{1+,0-}(\boldsymbol{p}|\boldsymbol{p}_0) + e^{-i\alpha_1(\boldsymbol{p})z} \overline{\boldsymbol{S}}^{1-,0-}(\boldsymbol{p}|\boldsymbol{p}_0) \right] . \boldsymbol{E}^{0i}(\boldsymbol{p}_0), \tag{6.169}$$

where $\boldsymbol{E}^{0i}(\boldsymbol{r})$ represents the incident field. We define an upgoing wave if the wave vector is directed along $z > 0$ ($a = +$), and a downgoing wave if the wave vector is directed along $z < 0$ ($a = -$). For the matrices and the operators, we introduce the following notations.

For example, $\overline{\boldsymbol{S}}^{1+0-}(p|\, p_0)$ describes the scattering operator of an incident downgoing wave from medium 0 which is scattered into an upgoing wave in medium 1, that is, the source in medium 0 generates in medium 1 a transmitted downgoing wave, which after a reflection on the second rough surface generates an upgoing wave. In Fig. 6.24, we give the representations of different scattering operators. We note that we have replaced the permittivity of the medium by an effective permittivity which will be defined in Section 6.7.3. With this effective permittivity we can consider the medium as homogeneous.

First of all, as an intermediate calculation, we have to introduce the scattering operators describing the field scattered by the rough surfaces and the random media. The slab is described in Fig. 6.25. We are going to study a 3D system (see Fig. 6.25), which is composed of an incident medium of permittivity ε_0, a first randomly rough boundary at $z = 0$, a random medium defined by a permittivity ε_1 which contains scatterers, a second randomly rough boundary at $z = -H$ and a semiinfinite homogeneous medium with a permittivity ε_2.

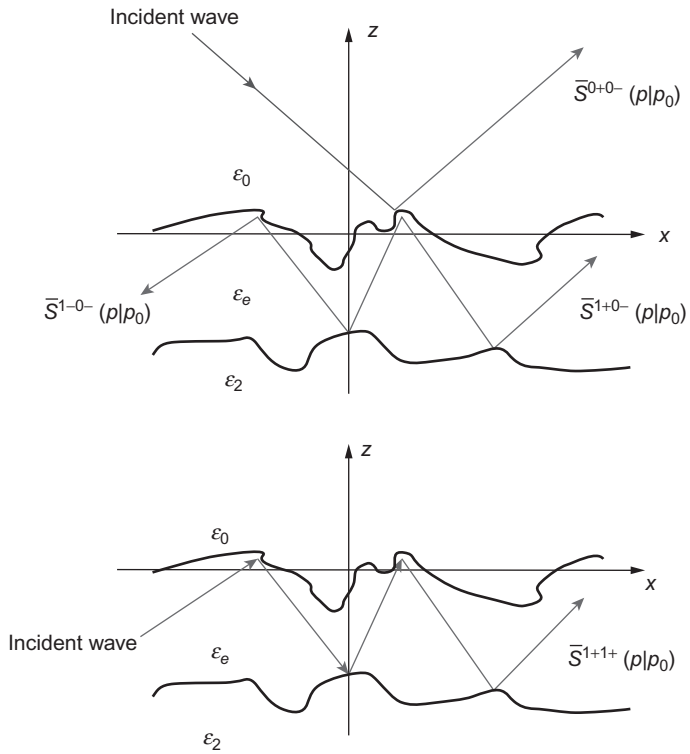


FIG. 6.24

Definition of the scattering operators.

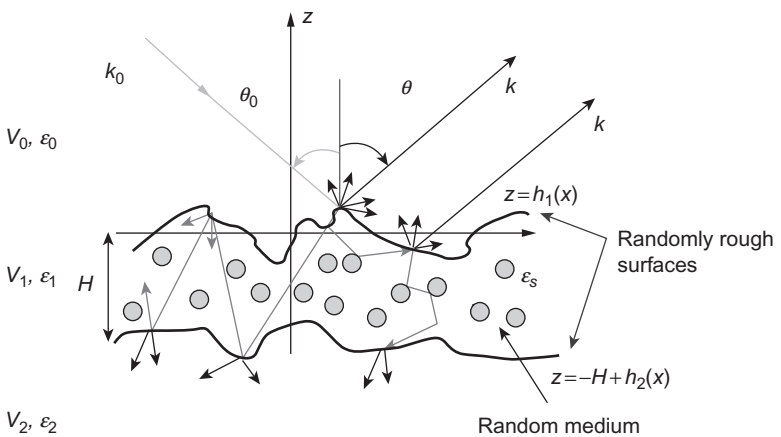


FIG. 6.25

Random volume with rough boundaries.

The field scattered by the random medium and the rough boundaries is

$$\boldsymbol{E}_{SV}^{0s}(\boldsymbol{r}) = \int \frac{d^2\boldsymbol{p}}{(2\pi)^2} e^{i\boldsymbol{p}\cdot\boldsymbol{x} + i\alpha_0(\boldsymbol{p})z} \overline{\boldsymbol{R}}_{SV}(\boldsymbol{p}|\,\boldsymbol{p}_0)\cdot\boldsymbol{E}^{0i}(\boldsymbol{p}_0). \tag{6.170}$$

We can write the scattering operators on the bases defined in Fig. 6.23 with a dyadic notation as follows:

$$\begin{aligned}\overline{\boldsymbol{R}}_{SV}(\boldsymbol{p}|\,\boldsymbol{p}_0) =& \boldsymbol{R}_{SV}(\boldsymbol{p}|\,\boldsymbol{p}_0)_{VV}\hat{\boldsymbol{e}}_V^{0+}(\boldsymbol{p})\hat{e}_V^{0-}(\boldsymbol{p}_0) + \boldsymbol{R}_{SV}(\boldsymbol{p}|\,\boldsymbol{p}_0)_{HV}\hat{\boldsymbol{e}}_H(\boldsymbol{p})\hat{e}_V^{0-}(\boldsymbol{p}_0)\\ &+ R_{SV}(\boldsymbol{p}|\,\boldsymbol{p}_0)_{VH}\hat{e}_V^{0+}(\boldsymbol{p})\hat{e}_H(\boldsymbol{p}_0) + R_{SV}R_{SV}(\boldsymbol{p}|\,\boldsymbol{p}_0)_{HH}\hat{\boldsymbol{e}}_H(\boldsymbol{p})\hat{e}_H(\boldsymbol{p}_0)\end{aligned} \tag{6.171}$$

or with a matrix notation,

$$\left[\overline{\boldsymbol{R}}_{SV}(\boldsymbol{p}|\,\boldsymbol{p}_0)\right] = \begin{pmatrix} R_{SV}(\boldsymbol{p}|\,\boldsymbol{p}_0)_{VV} & \boldsymbol{R}_{SV}(\boldsymbol{p}|\,\boldsymbol{p}_0)_{VH} \\ R_{SV}(\boldsymbol{p}|\,\boldsymbol{p}_0)_{VV} & \boldsymbol{R}_{SV}(\boldsymbol{p}|\,\boldsymbol{p}_0)_{HH} \end{pmatrix}. \tag{6.172}$$

As mentioned in the introduction, the fundamental quantity in the radiative transfer equation is the specific intensity. We define $\boldsymbol{I}(\boldsymbol{R},\boldsymbol{k})$ as the Wigner transform of the incoherent intensity of the light scattered by the random medium and the surfaces in the medium 0,

$$\begin{aligned}\boldsymbol{I}^{incoh}(\boldsymbol{R},\boldsymbol{k}) = e_0\int v_0 d^3\boldsymbol{r}\exp(-i\boldsymbol{k}\cdot\boldsymbol{r})\Big[&\ll\boldsymbol{E}_{SV}^{0s}\left(\boldsymbol{R}+\frac{\boldsymbol{r}}{2}\right)\otimes\boldsymbol{E}_{SV}^{0s*}\left(\boldsymbol{R}-\frac{\boldsymbol{r}}{2}\right)\gg_{SV}\\ &-\ll\boldsymbol{E}_{SV}^{0s}\left(\boldsymbol{R}+\frac{\boldsymbol{r}}{2}\right)\gg_{SV}\otimes\ll\boldsymbol{E}_{SV}^{0s*}\left(\boldsymbol{R}-\frac{\boldsymbol{r}}{2}\right)\gg_{SV}\Big]\end{aligned} \tag{6.173}$$

with $e_0 = \varepsilon_{\text{vacuum}}\, c_{\text{vacuum}}\, n_{0/2}$ $\otimes$ defines the tensorial product of two vectors, and the symbol $\ll..\gg_{SV}$ is the average over the surface and the volume disorder. We assume that the properties of the rough surfaces and the random medium are statistically independent. With the quasiuniform field approximation (Kuz'min and Romanov, 1996), we obtain the relation between the cross section $\overline{\sigma}^{incoh}\left(\hat{\boldsymbol{k}}|\,\hat{\boldsymbol{k}}_0\right)$ and the specific intensity:

$$4\pi\cos\theta\boldsymbol{I}^{incoh}\left(\boldsymbol{R},\hat{\boldsymbol{k}}\right) = \overline{\boldsymbol{\sigma}}^{incoh}\left(\hat{\boldsymbol{k}}|\,\hat{\boldsymbol{k}}_0\right):\boldsymbol{J}^{0i}\left(\hat{\boldsymbol{k}}_0\right), \tag{6.174}$$

where

$$\boldsymbol{J}^{0i}\left(\hat{\boldsymbol{k}}_0\right) = e_0\boldsymbol{E}^{0i}\left(\hat{\boldsymbol{k}}_0\right)\otimes\boldsymbol{E}^{0i*}\left(\hat{\boldsymbol{k}}_0\right). \tag{6.175}$$

The tensor $\boldsymbol{I}(\boldsymbol{R},\boldsymbol{k})$ is not exactly the specific intensity used in the radiometry theory since it is not homogeneous to an energy per unit time and solid angle. The specific intensity $\boldsymbol{I}^{incoh}\left(\boldsymbol{R},\hat{\boldsymbol{k}}\right)$ is related to the intensity $\boldsymbol{I}(\boldsymbol{R},\boldsymbol{k})$ by a Dirac distribution, which ensures that the wave propagation direction $\hat{\boldsymbol{k}}$ has a fixed norm given by k_0. The relation between the specific intensity and the cross section is given by a product of two tensors defined by the symbol ":" (see the definition in Appendix A.2). We have assumed that the medium 0 is nonabsorbing and the intensity does not depend on R as can be seen in Eq. (6.174). From Eq. (6.174), we can determine the bistatic cross section in calculating the specific incoherent intensity defined by the Wigner transform Eq. (6.173).

6.7.2 SPECIFIC INTENSITY AND BETHE-SALPETER EQUATIONS

To obtain the bistatic cross section, we are now going to calculate the specific intensity by using the Green functions of this problem. Hence, by having the Green functions of this problem, $\overline{G}_S^{00}, \overline{G}_S^{01}, \overline{G}_S^{11}$, we can derive Dyson and Bethe-Salpeter equations for a slab of a random medium with randomly rough surfaces. We obtain the Lippman-Schwinger equation for the source and the receiver in the medium,

$$\overline{G}_{SV}^{11} = \overline{G}_S^{11} + \overline{G}_S^{11} \cdot \overline{V}^{11} \cdot \overline{G}_{SV}^{11}, \tag{6.176}$$

where $\overline{V}^{11}$ is called the impurity potential operator. The superscripts i, j are, respectively, the receiver location and the source location (0, 1, 2 for the media 0, 1, or 2). We define the transition operator by

$$\overline{G}_{SV}^{11} = \overline{G}_S^{11} + \overline{G}_S^{11} \cdot \overline{T}_{SV}^{11} \cdot \overline{G}_S^{11}. \tag{6.177}$$

The operator $\overline{V}^{11}$ is related to the transition operator $\overline{T}_{SV}^{11}$ by

$$\overline{T}_{SV}^{11} = \overline{V}^{11} + \overline{V}^{11} \cdot \overline{G}_S^{11} \cdot \overline{T}_{SV}^{11}. \tag{6.178}$$

$\overline{T}_{SV}^{11}$ satisfies the coherent potential approximation $<\overline{T}_{SV}^{11}>_V = 0$. All the scattering processes in the random medium are contained in the transition operator. If we evaluate this operator, then we calculate the different fields in the different media. For example, we can evaluate the field in the medium scattered by the slab from a source in the medium 0. In a compact form, we have

$$\overline{G}_{SV}^{00} = \overline{G}_S^{00} + \overline{G}_S^{01} \cdot \overline{T}_{SV}^{11} \cdot \overline{G}_S^{10}. \tag{6.179}$$

To evaluate the scattered intensity in the medium, we define the tensor

$$\overline{I}_S^{11} = <\overline{T}_{SV}^{11} \otimes \overline{T}_{SV}^{11*}>_V. \tag{6.180}$$

We express the average tensorial product of the Green functions which is given by

$$\begin{aligned} \ll \overline{G}_{SV}^{11} \otimes \overline{G}_{SV}^{11*} \gg_{SV} &= <\overline{G}_S^{11} \otimes \overline{G}_S^{11*}>_S \\ &+ <\overline{G}_S^{11} \otimes \overline{G}_S^{11*}>_S : \overline{P}^{11} : \ll \overline{G}_{SV}^{11} \otimes \overline{G}_{SV}^{11*} \gg_{SV}. \end{aligned} \tag{6.181}$$

Here $<..>_S$ denotes the average over the ensemble of realizations of the random surfaces. In Eq. (6.181), we have introduced the intensity operator $\overline{P}^{11}$, which is defined by

$$<\overline{I}_S^{11}>_S = \overline{P}^{11} + \overline{P}^{11} : \ll \overline{G}_{SV}^{11} \otimes \overline{G}_{SV}^{11*} \gg_{SV} : \overline{P}^{11}. \tag{6.182}$$

In the next section, we will give an approximate expression for the intensity operator that will not depend on the rough surface profiles but only on the properties of the scatterers. It will appear that the tensor $\overline{P}^{11}$ describes the intensity of the light scattered by a particle taking into account the correlation with other particles. To simplify the notations, we introduce two new tensors:

$$\overline{\mathcal{G}}_{\ll SV \gg}^{-11} = \ll \overline{G}_{SV}^{11} \otimes \overline{G}_{SV}^{11*} \gg_{SV}, \tag{6.183}$$

$$\overline{\mathcal{G}}^{-11}_{\infty<S>} = <\overline{\boldsymbol{G}}^{11}_{S} \otimes \overline{\boldsymbol{G}}^{11*}_{S}>_{S}. \tag{6.184}$$

The Bethe-Salpeter equation can be written as follows:

$$\overline{\mathcal{G}}^{11}_{\ll SV\gg} = \overline{\boldsymbol{G}}^{11}_{\infty<S>} + \overline{\boldsymbol{G}}^{11}_{\infty<S>} : \overline{\boldsymbol{P}}^{11} : \overline{\boldsymbol{G}}^{11}_{\ll SV\gg}, \tag{6.185}$$

where we have introduced the symbol ∞ to emphasize that the propagator $\overline{\mathcal{G}}^{11}_{\infty<S>}$ between two scattering events by the particles describes either a wave propagating directly between the two scatterers or a wave reflected by the boundaries. We can express the intensity in the medium 0 produced by a source in the medium 0. This intensity is described by the tensor $\overline{\mathcal{G}}^{11}_{\ll SV\gg}$. We use the expression for the Green function $\overline{\mathcal{G}}^{11}_{\ll SV\gg}$,

$$\begin{aligned}\overline{\mathcal{G}}^{00}_{\ll SV\gg} = \overline{\mathcal{G}}^{00}_{\infty<S>} + \overline{\mathcal{G}}^{01}_{<S>} : \overline{\boldsymbol{P}}^{11} : \overline{\mathcal{G}}^{01}_{<S>} \\ + \overline{\mathcal{G}}^{01}_{<S>} : \overline{\boldsymbol{P}}^{11} : \overline{\mathcal{G}}^{11}_{\ll SV\gg} : \overline{\boldsymbol{P}}^{11} : \overline{\mathcal{G}}^{01}_{<S>},\end{aligned} \tag{6.186}$$

where

$$\overline{\mathcal{G}}^{00}_{\ll SV\gg} = \ll \overline{\boldsymbol{G}}^{00}_{SV} \otimes \overline{\boldsymbol{G}}^{00*}_{SV} \gg_{SV}, \tag{6.187}$$

$$\overline{\mathcal{G}}^{00}_{\infty<S>} = <\overline{\boldsymbol{G}}^{00}_{S} \otimes \overline{\boldsymbol{G}}^{00*}_{S}>_{S}, \tag{6.188}$$

$$\overline{\mathcal{G}}^{01}_{<S>} = <\overline{\boldsymbol{G}}^{01}_{S} \otimes \overline{\boldsymbol{G}}^{01*}_{S}>_{S}, \tag{6.189}$$

$$\overline{\mathcal{G}}^{10}_{<S>} = <\overline{\boldsymbol{G}}^{10}_{S} \otimes \overline{\boldsymbol{G}}^{10*}_{S}>_{S}. \tag{6.190}$$

As the intensity operator $\overline{\boldsymbol{P}}^{11}$ represents the intensity due to scattering by one particle, Eq. (6.186) decomposes the scattering process into three terms: the first one where no scattering in the volume occurs (medium 1 is modeled by an effective permittivity), the second one is the single-scattering term, and the third term contains higher scattering contributions by particles. We can now calculate $\boldsymbol{I}(\boldsymbol{R}, \boldsymbol{k})$ in Eq. (6.173). The intensity of the scattered light $\boldsymbol{E}^{0s}_{SV}$ is related to the Green function $\overline{\mathcal{G}}^{00}_{SV}$, and we can develop the tensorial product of the Wigner transform of the specific intensity by using Eq. (6.186). We obtain the four following contributions for the specific intensity defined by Eq. (6.173):

$$\overline{\boldsymbol{I}}^{incoh} = \overline{\boldsymbol{I}}^{incoh}_{L=0} + \overline{\boldsymbol{I}}^{incoh}_{L=1} + \overline{\boldsymbol{I}}^{incoh}_{\text{Ladder}} + \overline{\boldsymbol{I}}^{incoh}_{\text{Crossed}}, \tag{6.191}$$

where the contributions are given by

$$\begin{aligned}\overline{\boldsymbol{I}}^{incoh}_{L=0}(\boldsymbol{R}, \boldsymbol{k}) = e_0 \int_{V_0} \mathrm{d}^3\boldsymbol{r} \exp(-i\boldsymbol{k}\cdot\boldsymbol{r}) \Big[<\boldsymbol{E}^{0s}_{S}\left(\boldsymbol{R} + \frac{\boldsymbol{r}}{2}\right) \otimes \boldsymbol{E}^{0s*}_{S}\left(\boldsymbol{R} - \frac{\boldsymbol{r}}{2}\right) > s \\ - <\boldsymbol{E}^{0s}_{S}\left(\boldsymbol{R} + \frac{\boldsymbol{s}}{2}\right) > s \otimes <\boldsymbol{E}^{0s*}_{S}\left(\boldsymbol{R} - \frac{\boldsymbol{r}}{2}\right) > s \Big],\end{aligned} \tag{6.192}$$

$$\begin{aligned}\overline{\boldsymbol{I}}^{incoh}_{L=1}(\boldsymbol{R}, \boldsymbol{k}) = \; e_0 \int_{V_0} d^3\boldsymbol{r} \exp(-i\boldsymbol{k}\cdot\boldsymbol{r}) \overline{\mathcal{G}}^{01}_{<S>} : \overline{\boldsymbol{P}}^{11} \\ : <\boldsymbol{E}^{1t} \otimes \boldsymbol{E}^{1t*}>_{s} \left(\boldsymbol{R} + \frac{\boldsymbol{r}}{2}, \boldsymbol{R} - \frac{\boldsymbol{r}}{2}\right),\end{aligned} \tag{6.193}$$

$$\begin{aligned}\overline{\boldsymbol{I}}^{incoh}_{\text{Ladder}}(\boldsymbol{R},\boldsymbol{k}) = \; & e_0\int_{V_0} d^3\boldsymbol{r}\exp(-i\boldsymbol{k}\cdot\boldsymbol{r})\overline{\mathcal{G}}^{01}_{<S>}:\overline{\boldsymbol{P}}^{11}:\overline{\mathcal{G}}^{11}_{\ll SV\gg} \\ & :\overline{\boldsymbol{P}}^{\boldsymbol{II}}:<\boldsymbol{E}^{1t}\otimes\boldsymbol{E}^{1t*}>_s\left(\boldsymbol{R}+\frac{\boldsymbol{r}}{2},\boldsymbol{R}-\frac{\boldsymbol{r}}{2}\right),\end{aligned} \tag{6.194}$$

$$\begin{aligned}\overline{\boldsymbol{I}}^{incoh}_{\text{Crossed}}(\boldsymbol{R},\boldsymbol{k}) = \; & e_0\int_{V_0} d^3\boldsymbol{r}\exp|(-i\boldsymbol{k}\cdot\boldsymbol{r})\left[\overline{\mathcal{G}}^{01}_{<S>}:\overline{\boldsymbol{P}}^{11}:\overline{\mathcal{G}}^{11}_{\ll SV\gg}\right. \\ & \left.:\overline{\boldsymbol{P}}^{\boldsymbol{II}}:<\boldsymbol{E}^{1t}\otimes\boldsymbol{E}^{1t*}>_s\right]^{T_R}\left(\boldsymbol{R}+\frac{\boldsymbol{r}}{2},\boldsymbol{R}-\frac{\boldsymbol{r}}{2}\right).\end{aligned} \tag{6.195}$$

T_R defines the right transpose of a tensor. The superscripts for the operators and the Green functions correspond, respectively, to the receiver location and the source location (0 for medium 0, 1 for medium 1, and 2 for medium 2). In the previous formulas we can follow, from right to left, how the scattering process is defined by the combination of the different operators. The introduction of tensor products of matrices is related to the fact that we calculate a cross section, which depends on the squared modulus of a scattering amplitude. The first term $\boldsymbol{I}^{incoh}_{L=0}$ corresponds to the scattering by the slab with rough boundaries and defined by an effective permittivity ε_e we will study in the next subsection. The second term $\boldsymbol{I}^{incoh}_{L=1}$ corresponds to the first approximation where only one process of scattering by a particle is taken into account. We will examine the expression for the tensor $\overline{\boldsymbol{P}}^{11}$. The two last terms $\boldsymbol{I}^{incoh}_{\text{Ladder}}$ and $\boldsymbol{I}^{incoh}_{\text{Crossed}}$ correspond to the higher-order particle scattering contributions. $\overline{\mathcal{G}}^{11}_{\ll SV\gg}$ is the Green tensor, which contains the interaction between the scatterers and the surfaces. The lower index $\ll SV\gg$ represents the average over the randomly rough surfaces and the disordered medium. We will study the expression for $\overline{\mathcal{G}}^{11}_{\ll SV\gg}$ in the next subsections.

6.7.3 EFFECTIVE PERMITTIVITY

To determine the effective permittivity ε_e, we use the fact that when the effective medium is not spatially dispersive, it can be shown, using a diagrammatic technique, that the coherent part of the field $<\boldsymbol{E}>_V$ which propagates inside an infinite random medium behaves as a wave in an homogeneous medium with a renormalized effective permittivity. We introduce the Coherent Potential Approximation (CPA), which postulates that

$$<\overline{\boldsymbol{G}}^{11}_{SV}>_V = \overline{\boldsymbol{G}}^{11}_{S}\,. \tag{6.196}$$

We also use another approximation, which is the quasicrystalline approximation (QCA). This approximation is strictly valid when the particles have fixed positions, as in a crystal. The QCA is equivalent to neglecting the fluctuation of the effective field on a particle located at r_j, due to a deviation of a particle located at r_i from its average position. Under the quasicrystalline coherent potential approximation

(QC-CPA) for Rayleigh scatterers, an approximate formula for ε_e can generalize the usual Maxwell-Garnett formula. We can also obtain an approximate formula for the effective permittivity, which contains the Maxwell-Garnett formula and the Keller approximation (Soubret and Berginc, 2003c).

The equation for ε_e is given by the following expression:

$$\varepsilon_e = \varepsilon_1 + \frac{3(\varepsilon_d - \varepsilon_1)\varepsilon_e f_{vol}}{(\varepsilon_d - \varepsilon_1)\left(1 - f_{vol} - \frac{2i}{3}(K_{vac} r_d)^3 \varepsilon_e^{3/2} w\right)} + 3\varepsilon_e, \tag{6.197}$$

where ε_1 is the permittivity of the slab, ε_d the permittivity of the scatterers, f_{vol} the volume fraction of the scatterers, and r_d the radius of the scatterers. The function w is the Percus-Yevick distribution

$$w = \frac{(1 - f_{vol})^4}{(1 + 2f_{vol})^2}. \tag{6.198}$$

With a development at the first order of Eq. (6.197) we obtain

$$\begin{aligned} \varepsilon_e = \varepsilon_1 &+ \frac{\varepsilon_1(\varepsilon_d - \varepsilon_1)(1 - f_{vol}) + 3\varepsilon_1\varepsilon_e + 3(\varepsilon_d - \varepsilon_1)\varepsilon_e - f_{vol}}{(\varepsilon_d - \varepsilon_1)(1 - f_{vol}) + 3\varepsilon_e} \\ &+ 2i\frac{(K_{vac} r_d)^3 (\varepsilon_d - \varepsilon_1)^2 w f_{vol} \varepsilon_e^{5/2}}{\left[(\varepsilon_d - \varepsilon_1)(1 - f_{vol}) + 3\varepsilon_e\right]^2}. \end{aligned} \tag{6.199}$$

If the real part of ε_e is larger than the imaginary part, we obtain an approximate solution of Eq. (6.199):

$$\begin{aligned} \mathrm{Re}(\varepsilon_e) &= \frac{1}{6}\left[-\{(\varepsilon_d - \varepsilon_1)(1 - f_{vol}) - 3\varepsilon_1 - 3(\varepsilon_d - \varepsilon_1) f_{vol}\} + \sqrt{\Delta}\right], \\ \mathrm{Im}(\varepsilon_e) &= 2\frac{(K_{vac} r_d)^3 (\varepsilon_d - \varepsilon_1)^2 w f_{vol} Re(\varepsilon_e)^{5/2}}{\left[(\varepsilon_d - \varepsilon_1)(1 - f_{vol}) + 3Re(\varepsilon_e)\right]^2}, \end{aligned} \tag{6.200}$$

where

$$\Delta = \left[(\varepsilon_d - \varepsilon_1)(1 - f_{vol}) - 3\varepsilon_1 + 3(\varepsilon_d - \varepsilon_1) f_{vol}\right]^2 + 12\varepsilon_1(\varepsilon_d - \varepsilon_1)(1 - f_{vol}).$$

6.7.4 EXPRESSION OF THE INTENSITY OPERATOR $\overline{\boldsymbol{P}}^{11}$

In the preceding subsection, we introduced the intensity operator $\overline{\boldsymbol{P}}^{11}$ to write the Bethe-Salpeter equation. This intensity operator can be determined by using the energy conservation principle. With the Dyson equation and the Bethe-Salpeter Eq. (6.182) in the energy conservation equation, we obtain a Ward identity which defines a relation between the intensity operator $\overline{\boldsymbol{P}}^{11}$ and the mass operator $\overline{\boldsymbol{M}}^{11}$ which is a function of the effective permittivity ε_e (Barabanenkov et al., 1997). Under the QC-CPA, the scalar ε_e satisfies a nonlinear system of equations. In using these equations in the Ward identity, we obtain an expression, called the modified ladder approximation, for the intensity operator $\overline{\boldsymbol{P}}^{11}$, which satisfies energy conservation (Tsang and Kong, 2001). We do not reproduce here the derivation of the Ward identity since the demonstration is formally identical to the infinite random medium case

and is well documented (Tsang and Kong, 2001; Tsang et al., 1985). The expression for $\overline{\boldsymbol{P}}^{11}$ is given by

$$\begin{aligned}\overline{\boldsymbol{P}}^{11}(\boldsymbol{R},\boldsymbol{k}|\,\boldsymbol{R}_0,\boldsymbol{k}_0) = nw(\boldsymbol{k}-\boldsymbol{k}_0)\int\frac{d^3K}{(2\pi)^3}\exp\left(i\boldsymbol{K}\cdot(\boldsymbol{R}-\boldsymbol{R}_0)\right)\\ \times\overline{\boldsymbol{C}}^{11}_{(e)o}\left(\frac{\boldsymbol{K}}{2}+\boldsymbol{k}|\,\frac{\boldsymbol{K}}{2}+\boldsymbol{k}_0\right)\otimes\overline{\boldsymbol{C}}^{11*}_{(e)o}\left(-\frac{\boldsymbol{K}}{2}+\boldsymbol{k}|\,\frac{\boldsymbol{K}}{2}+\boldsymbol{k}_0\right),\end{aligned} \tag{6.201}$$

where $w(\boldsymbol{k}-\boldsymbol{k}_0)$ is the structure factor of the medium, identical to the one defined in the scattering of X-rays, and n is the density of the scatterers. $\overline{\boldsymbol{C}}^{11}_{(e)o}$ is the transition operator, which should be expressed as

$$\overline{\boldsymbol{C}}^{11}_{(e)o}(\boldsymbol{k}|\,\boldsymbol{k}_0) = \boldsymbol{t}^{-11}_{(e)o}(\boldsymbol{k}|\,\boldsymbol{k}_0) + \boldsymbol{n}\int\frac{d^3k_1}{(2\pi)^3}\boldsymbol{h}(\boldsymbol{k}-\boldsymbol{k}_1)\boldsymbol{t}^{-11}_{(e)o}(\boldsymbol{k}|\,\boldsymbol{k}_0)\cdot\overline{\boldsymbol{G}}^{\infty}_{e}(\boldsymbol{k}_1)\cdot\overline{\boldsymbol{C}}^{11}_{(e)o}(\boldsymbol{k}|\,\boldsymbol{k}_0), \tag{6.202}$$

with

$$h(\boldsymbol{k}-\boldsymbol{k}_1) = \int d^3\boldsymbol{r}\exp\left(-(\boldsymbol{k}-\boldsymbol{k}_1)\cdot\boldsymbol{r}\right)[g(\boldsymbol{r})-1]. \tag{6.203}$$

$g(\boldsymbol{r})$ is the correlation function between two scatterers, and

$$\begin{aligned}\overline{\boldsymbol{G}}^{\infty}_{e}(\boldsymbol{r},\boldsymbol{r}_0) = \frac{i}{2}\int\frac{d^2p_0}{(2\pi)^2}\exp\left(i\boldsymbol{p}_0\cdot(\boldsymbol{x}-\boldsymbol{x}_0)+i\alpha_{\boldsymbol{e}}(\boldsymbol{p}_0)(z-z_0)\right)\left(\bar{\boldsymbol{I}}-\hat{\boldsymbol{k}}^{1+}_{p_0}\hat{\boldsymbol{k}}^{1+}_{p_0}\right)\frac{1}{\alpha_e(p_0)}, for\ z<z_0,\\ \overline{\boldsymbol{G}}^{\infty}_{e}(\boldsymbol{r},\boldsymbol{r}_0) = \frac{i}{2}\int\frac{d^2p_0}{(2\pi)^2}\exp\left(i\boldsymbol{p}_0\cdot(\boldsymbol{x}-\boldsymbol{x}_0)-i\alpha_{\boldsymbol{e}}(\boldsymbol{p}_0)(z-z_0)\right)\left(\bar{\boldsymbol{I}}-\hat{\boldsymbol{k}}^{1-}_{p_0}\hat{\boldsymbol{k}}^{1-}_{p_0}\right)\frac{1}{\alpha_e(p_0)}, for\ z<z_0,\end{aligned} \tag{6.204}$$

with $\boldsymbol{k}^{1\pm}_{p_0} = \boldsymbol{p}_0 - \alpha_{\boldsymbol{e}}(\boldsymbol{p}_0)\hat{\boldsymbol{e}}$ and $\hat{\boldsymbol{k}}^{1\pm}_{p_0} = \boldsymbol{k}^{1\pm}_{p_0}/\|\boldsymbol{k}^{1\pm}_{p_0}\|$. Eq. (6.201) is given by a Wigner transform. The expression for $\overline{\boldsymbol{P}}^{11}$ is complex because the operator is nonlocal. The operator $\boldsymbol{t}^{-11}_{(\boldsymbol{e})\boldsymbol{o}}$ may be expressed with $\boldsymbol{t}^{-11}_{\boldsymbol{o}}$, for a particle located at the origin, which does not take into account the correlations with the other scatterers, by replacing the permittivity ε_d of the scatterer by the permittivity $\widetilde{\varepsilon}_{\boldsymbol{d}} \equiv \varepsilon_{\boldsymbol{d}} - \varepsilon_1 + \varepsilon_{\boldsymbol{e}}$, and replacing the permittivity ε_1 of the medium by the effective medium ε_e (see Fig. 6.26). With the CPA, we can express the transition operators $\boldsymbol{t}^{-11}_{(\boldsymbol{e})\boldsymbol{o}}$ with effective medium. The transition operator $\boldsymbol{t}^{-11}_{(\boldsymbol{e})\boldsymbol{o}}$ can be written in the Fourier space as

$$\bar{\boldsymbol{t}}^{11}_{(e)o}(\boldsymbol{k}|\,\boldsymbol{k}_0) = \iint\frac{\mathrm{d}^2\boldsymbol{r}\mathrm{d}^2|\boldsymbol{r}_0}{(2\pi)^3(2\pi)^3}\exp\left(-\mathrm{i}\boldsymbol{k}\cdot\boldsymbol{r}+\mathrm{i}\boldsymbol{k}_0\cdot\boldsymbol{r}_0\right)\bar{\boldsymbol{t}}^{11}_{(e)o}(\boldsymbol{r}|\,\boldsymbol{r}_0). \tag{6.205}$$

$$= \boldsymbol{t}^{1}_{(e)}(\omega)\delta(\boldsymbol{k}-\boldsymbol{k}_0)\,\bar{\boldsymbol{I}}. \tag{6.206}$$

For Rayleigh scatterers, we obtain

$$t^{1}_{(e)}(\omega) = K^2_{vac}\,\alpha^{1}_{(e)ray}, \tag{6.207}$$

$$\alpha^{1}_{(e)\,ray} \equiv \frac{\alpha^{1}_{(e)\,pol}}{1-K^2_{vac}\,\alpha^{1}_{(e)\,pol}\dfrac{iKe}{6\pi}}, \tag{6.208}$$

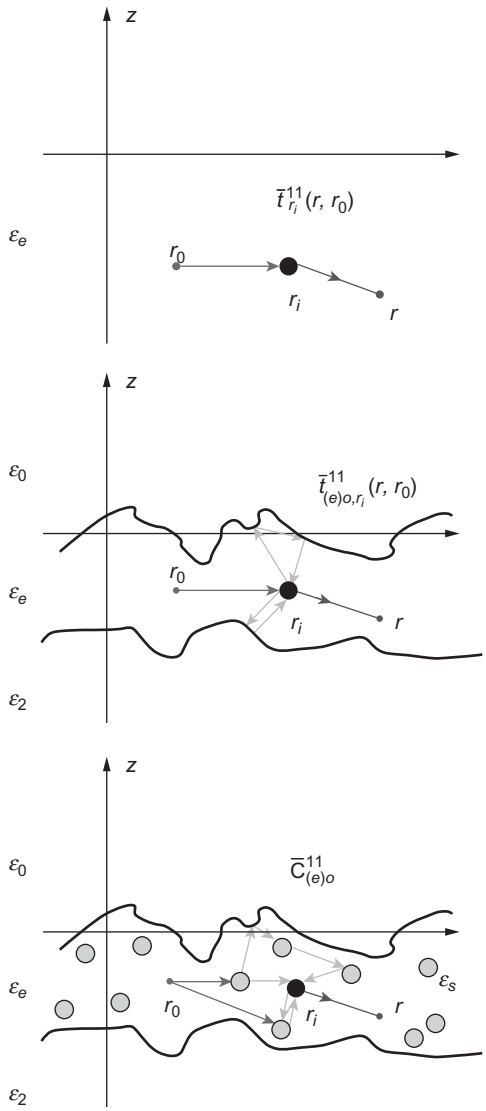


FIG. 6.26

The operator $\bar{\boldsymbol{t}}^{11}_{\boldsymbol{r_i}}$ represents the scattering from one particle in an infinite medium, the operator $\bar{\boldsymbol{t}}^{11}_{(e)o,r_i}$ gives the scattering by one particle in a finite volume, and $\bar{\boldsymbol{C}}^{11}_{(e)o}$ is the field scattered by a particle, taking into account the effects of the other particles and the boundaries.

$$\alpha^1_{(e)\,pol} = 3\,\varepsilon_e \mathrm{V}_d \frac{\widetilde{\varepsilon}_\mathrm{d} - \varepsilon_e}{\widetilde{\varepsilon}_d + 2\varepsilon_e}, \tag{6.209}$$

where $\widetilde{\varepsilon}_{\boldsymbol{d}} \equiv \varepsilon_{\boldsymbol{d}} - \varepsilon_1 + \varepsilon_e$ and V_d is the volume of a scatterer. By substituting Eq. (6.207) into Eq. (6.202), we obtain

$$\overline{\boldsymbol{C}}^{11}_{(e)o}(k|\,k_0) = \left[\bar{I} - \boldsymbol{n}\boldsymbol{t}^1_{(e)}(\omega)\int \frac{\mathrm{d}^3 k_1}{(2\pi)^3} h(k_1 - k_0)\overline{G}^\infty_e(k_1)\right]^{-1} \boldsymbol{t}^1_{(e)}(\omega)\bar{\boldsymbol{I}}. \tag{6.210}$$

By using the expression for $\overline{\boldsymbol{G}}^\infty_{\boldsymbol{e}}(\boldsymbol{k}_1)$ and the fact that the correlation function of small scatterers has an effect at small range, we have

$$h(\boldsymbol{r}_j - \boldsymbol{r}_l) \approx \delta(\boldsymbol{r}_j - \boldsymbol{r}_l)\int d^3\boldsymbol{r}\boldsymbol{h}(\boldsymbol{r}). \tag{6.211}$$

We obtain from Eq. (6.211) the expression for $\overline{\boldsymbol{C}}^{11}_{(\boldsymbol{e})\boldsymbol{o}}$. The expression for $h(0)$ comes from the singularity of the Green function $\overline{\boldsymbol{G}}^\infty_{\boldsymbol{e}}(\boldsymbol{r}, \boldsymbol{r}_0)$;

$$\overline{\boldsymbol{C}}^{11}_{(e)o}(\boldsymbol{k}|\,\boldsymbol{k}_0) = \frac{\boldsymbol{t}^1_{(e)}(\omega)\delta(k - k_0)\bar{\boldsymbol{I}}}{1 - n\left(\dfrac{h(0)}{3\boldsymbol{K}^2_e} + \dfrac{\mathrm{i}Ke}{6\pi}\displaystyle\int \mathrm{d}^3\boldsymbol{r}h(\boldsymbol{r})\right)\boldsymbol{t}^1_{(e)}(\omega)}, \tag{6.212}$$

where the integral expression $h(r)$ is obtained from the relation

$$w \equiv 1 + n\int \mathrm{d}^3\boldsymbol{r}h(\boldsymbol{r}) = 1 + n\int \mathrm{d}^3\boldsymbol{r}[g(r) - 1], \tag{6.213}$$

and w is the Percus-Yevick correlation function Eq. (6.198). We can finally write

$$\overline{\boldsymbol{C}}^{11}_{(e)o}(\boldsymbol{k}|\,\boldsymbol{k}_0) = \frac{\boldsymbol{t}^1_{(e)}(\omega)\delta(k - \boldsymbol{k}_0)\bar{I}}{1 + \left(\dfrac{n}{\boldsymbol{k}^2_e} + \dfrac{\mathrm{i}ke}{6\pi}(w-1)t^1_{(e)}(\omega)\right)}. \tag{6.214}$$

With these approximations, the intensity operator for one particle may be expressed as

$$\overline{\boldsymbol{P}}^{11}(\boldsymbol{k}|\,\boldsymbol{k}_0) = nw(\boldsymbol{k} - \boldsymbol{k}_0)\overline{\boldsymbol{C}}^{11}_{(e)o}(\boldsymbol{k}|\,\boldsymbol{k}_0)\otimes\overline{\boldsymbol{C}}^{11*}_{(e)o}(\boldsymbol{k}|\,\boldsymbol{k}_0). \tag{6.215}$$

We note that, with the several approximations, the intensity operator $\overline{\boldsymbol{P}}^{11}$ becomes localized at $\boldsymbol{R} = \boldsymbol{R}_0$.

6.7.5 EXPRESSION FOR THE INCOHERENT INTENSITY AND THE GREEN TENSORS $\overline{\boldsymbol{P}}^{11}$

As we have seen, the incoherent intensity is given by

$$\bar{\boldsymbol{I}}^{incoh} = \bar{\boldsymbol{I}}^{incoh}_{L=0} + \bar{\boldsymbol{I}}^{incoh}_{L=1} + \bar{\boldsymbol{I}}^{incoh}_{\mathrm{Ladder}} + \bar{\boldsymbol{I}}^{incoh}_{\mathrm{Crossed}}. \tag{6.216}$$

From Eq. (6.192), we note that the term $\bar{\boldsymbol{I}}^{incoh}_{L=0}$ is determined by the scattering matrix $\overline{\boldsymbol{S}}^{0+,0-}$ because we can write the field $\boldsymbol{E}^{0\mathrm{s}}_{\mathrm{S}}$ scattered by the effective medium bounded by the randomly rough surfaces as

$$\boldsymbol{E}_S^{0s}(r)=\int\frac{\mathrm{d}^2\boldsymbol{p}}{(2\pi)^2}e^{\mathrm{i}\boldsymbol{p}\cdot\boldsymbol{x}+\mathrm{i}\alpha_0(p)z}\overline{\boldsymbol{S}}^{0+,0-}(p|\,\boldsymbol{p}_0).\boldsymbol{E}^{0i}(\boldsymbol{p}_0). \tag{6.217}$$

The term $\overline{\boldsymbol{I}}_{L=1}^{incoh}$ is evaluated relative to the tensor $\overline{\boldsymbol{P}}^{11}$ and the scattering operators $\overline{\boldsymbol{S}}^{0+,1-}$,$\overline{\boldsymbol{S}}^{0+,1+}$,$\overline{\boldsymbol{S}}^{0+,0-}$ and $\overline{\boldsymbol{S}}^{0-,0-}$ because the transmitted field is given by

$$\boldsymbol{E}_S^{1t}(\boldsymbol{x},\ z)=\int\frac{\mathrm{d}^2\boldsymbol{p}}{(2\pi)^2}e^{\mathrm{i}\boldsymbol{p}\cdot\boldsymbol{x}}\left[e^{\mathrm{i}\alpha_1(p)z}\overline{\boldsymbol{S}}^{1+,0-}(\boldsymbol{p}|\,\boldsymbol{p}_0)+e^{\mathrm{i}\alpha_1(p)z}\overline{\boldsymbol{S}}^{1-,0-}(\boldsymbol{p}|\,\boldsymbol{p}_0)\right].\boldsymbol{E}^{0i}(\boldsymbol{p}_0), \tag{6.218}$$

and the Green function $\overline{\boldsymbol{G}}_S^{01}$ may be decomposed as

$$\overline{\boldsymbol{G}}_S^{01}=\overline{\boldsymbol{G}}_S^{0+1}+\overline{\boldsymbol{G}}_S^{0+1-}. \tag{6.219}$$

The symbol "−" describes a downgoing wave, the symbol "+" an upgoing wave relative to the direction Oz. These two Green functions may be evaluated as integral functions containing the two scattering operators $\overline{\boldsymbol{S}}^{0+,0-}$,$\overline{\boldsymbol{S}}^{0+,1+}$.

For the two terms $\overline{\boldsymbol{I}}_{\text{Ladder}}^{incoh}$ and $\overline{\boldsymbol{I}}_{\text{Crossed}}^{incoh}$, we need to evaluate the Green tensor $\overline{\mathcal{G}}_{\ll SV\gg}^{11}$, which satisfies a Bethe-Salpeter Eq. (6.185). It is convenient to write the Bethe-Salpeter Eq. (6.185), satisfied by $\overline{\mathcal{G}}_{\ll SV\gg}^{11}$, by introducing the Wigner transform of a tensor. Eq. (6.185) may be written as an integral,

$$\begin{aligned}\overline{\mathcal{G}}_{\ll SV\gg}^{11}(\boldsymbol{R},\boldsymbol{k}|\,\boldsymbol{R}_0,\boldsymbol{k}_0)=\overline{\mathcal{G}}_{\infty<S>}^{11}(\boldsymbol{R},\boldsymbol{k}|\,\boldsymbol{R}_0,\boldsymbol{k}_0)+\int_{V1}\mathrm{d}^3\boldsymbol{R}_1\mathrm{d}^3\boldsymbol{R}_2\int\frac{\mathrm{d}^3\boldsymbol{k}_1}{(2\pi)^3}\frac{\mathrm{d}^3\boldsymbol{k}_2}{(2\pi)^3}\\ \times\overline{\mathcal{G}}_{\infty<SV>}^{11}(\boldsymbol{R},\boldsymbol{k}|\,\boldsymbol{R}_1,\boldsymbol{k}_1):\overline{P}^{11}(\boldsymbol{R}_1,\boldsymbol{k}_1|\,\mathbf{R}_2,\boldsymbol{k}_2):\overline{\mathcal{G}}_{\ll SV\gg}^{11}(\boldsymbol{R}_2,\boldsymbol{k}_2|\,\boldsymbol{R}_0,\boldsymbol{k}_0).\end{aligned} \tag{6.220}$$

Between two scattering processes on the rough surfaces, the wave interacts with the particles, and accordingly, it is reasonable to assume that the scattering events on the rough surfaces are uncorrelated. The propagator $\overline{\mathcal{G}}_{\infty<S>}^{11}=<G_S^{11}\otimes\overline{G}_S^{11*}>s$ in Eq. (6.221) may be approximated by

$$\begin{aligned}\overline{\boldsymbol{G}}_S^{11}\otimes\overline{\boldsymbol{G}}_S^{11*}>_S=\overline{\boldsymbol{G}}_1^{\infty}\otimes\overline{\boldsymbol{G}}_1^{\infty*}+<\overline{\boldsymbol{G}}_S^{1+1+}\otimes\overline{\boldsymbol{G}}_S^{1+1+*}>_S+<\overline{\boldsymbol{G}}_S^{1-1+}\otimes\overline{\boldsymbol{G}}_S^{1-1+*}>_S\\ +<\overline{\boldsymbol{G}}_S^{1+1-}\otimes\overline{\boldsymbol{G}}_S^{1+1-*}>_S+<\overline{\boldsymbol{G}}_S^{1-1-}\otimes\overline{\boldsymbol{G}}_S^{1-1-*}>_S,\end{aligned} \tag{6.221}$$

which represents the scattering process of a wave propagating directly between two scatterers (the first term of the expansion) or a wave reflected by the randomly rough surfaces (the four following terms). We used the expansion of the Green function $\overline{\boldsymbol{G}}_S^{11}$. With a condensed notation Eq. (6.222) may be written as

$$\overline{\mathcal{G}}_{\infty<S>}^{11}=\overline{\mathcal{G}}_{\infty}^{11}+\sum_{a,a_0=\pm}\overline{\mathcal{G}}_{<S>}^{1a1a_0}, \tag{6.222}$$

with

$$\overline{\mathcal{G}}_{\infty}^{11}=\overline{\boldsymbol{G}}_1^{\infty}\otimes\overline{\boldsymbol{G}}_1^{\infty*}, \tag{6.223}$$

$$\overline{\mathcal{G}}_{<S>}^{1a1a_0}=\overline{\boldsymbol{G}}_S^{1a1a_0}\otimes\overline{\boldsymbol{G}}_S^{1a1a_0*}>_S, \tag{6.224}$$

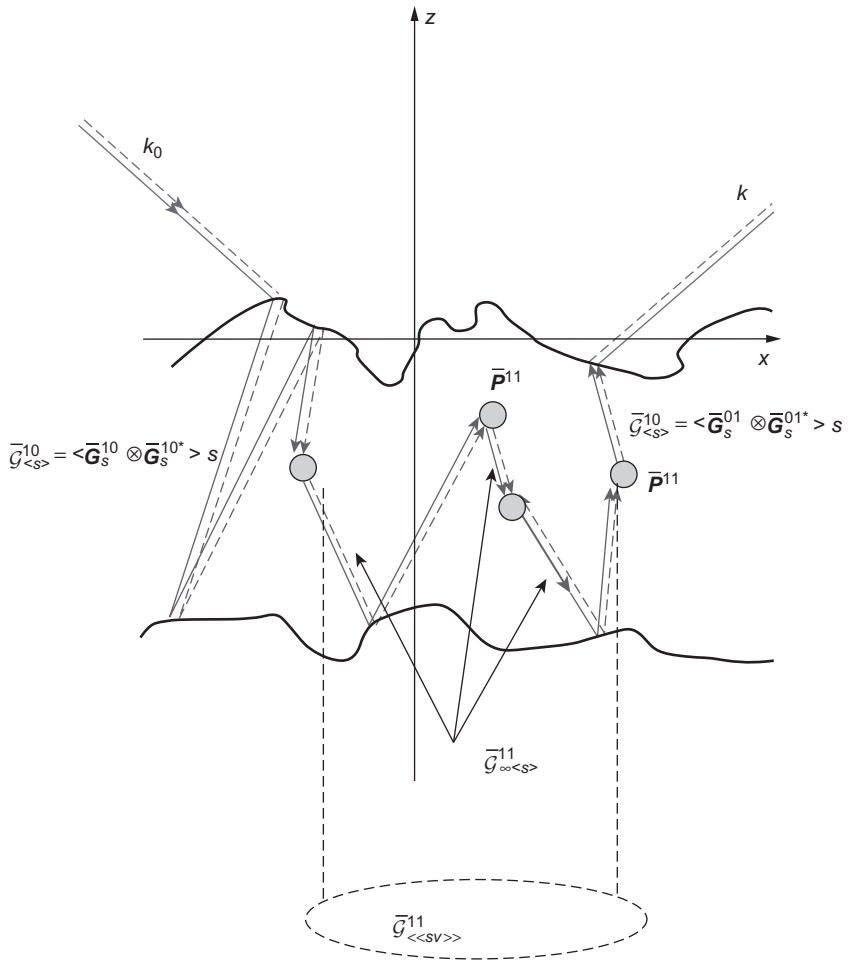


FIG. 6.27

Scattering processes for the ladder approximation. The solid and dashed lines represent, respectively, the propagating waves on the right and left sides of the tensorial products $\overline{\mathcal{G}}^{11}_{\ll SV\gg} = \ll \overline{\boldsymbol{G}}^{11}_{SV} \otimes \overline{\boldsymbol{G}}^{11*}_{SV} \gg_{SV}$.

where a, a_0 are the signs + or −. The Green functions $\overline{\boldsymbol{G}}^{1a1a_0}_{S}$ are defined with the scattering operators $\overline{\boldsymbol{S}}^{1a1a_0}$ (Soubret and Berginc, 2003a). Then, the hypothesis of noncorrelated diffusion on the rough surfaces must also be applied to each term of the operators $\overline{\boldsymbol{S}}^{1a1a_0}$. The Green function $\overline{\boldsymbol{G}}^{\infty}_{1}$ is given by Eqs. (6.204), (6.205), the permittivity in the expressions is the effective permittivity we have defined in the preceding section. Under these approximations, the Bethe-Salpeter Eq. (6.221) describes the scattering processes depicted in Fig. 6.27, where the waves on the left and right sides of the tensorial products follow the same path.

We can use Feynman diagrams (Barabanenkov et al., 1997) to represent the different terms of $\overline{\boldsymbol{G}}^{11}_{\ll SV\gg}$ in the ladder approximation obtained by iteration of the Bethe-Salpeter equation:

$$\begin{aligned}\overline{\mathcal{G}}^{11}_{\ll SV\gg} = \overline{\mathcal{G}}^{11}_{\infty<S>} + \overline{\mathcal{G}}^{11}_{\infty<S>} : \overline{\boldsymbol{P}}^{11} : \overline{\mathcal{G}}^{11}_{\infty<S>} \\ + \overline{\mathcal{G}}^{11}_{\infty<S>} : \overline{\boldsymbol{P}}^{11} : \overline{\mathcal{G}}^{11}_{\infty<S>} : \overline{\boldsymbol{P}}^{11} : \overline{\mathcal{G}}^{11}_{\infty<S>} + \dots \ .\end{aligned} \tag{6.225}$$

We have restricted ourselves to an approximate form of the Bethe-Salpeter equation: the ladder approximation. As we can see, the ladder approximation allows a microscopic derivation of the radiative transfer equation. For the transport of energy we must consider the intensity. We have to multiply the Green function by its complex conjugate. In other words, we multiply the retarded Green function by the advanced one before averaging over the disorder. This leads to the classical picture of propagation of intensity from one scatterer to another as depicted in Fig. 6.27. The term "ladder" comes from the pattern of the Feynman diagrams. As the Bethe-Salpeter equation sums up the interaction many times, the resulting Feynman graph has the form of a ladder.

By taking into account the fact that the random layer is infinite in the two directions x and y and that the medium and the rough surfaces are statistically homogeneous and independent, the tensors $\overline{\boldsymbol{G}}(R, k|\, R_0, k_0)$ depend on Z and Z_0 and the following difference $\boldsymbol{X} - \boldsymbol{X}_0 = (X - X_0,\ Y - Y_0)$. These functions are given in terms of a Fourier transform along the X, Y axes,

$$\overline{\mathcal{G}}(Z, \boldsymbol{k}|\, Z_0, \boldsymbol{k}_0; \boldsymbol{P}) = \int d^2(\boldsymbol{X} - \boldsymbol{X}_0)\, e^{-i(\boldsymbol{X}-\boldsymbol{X}_0).\boldsymbol{P}} \overline{\varsigma}(\boldsymbol{R}, \boldsymbol{k}|\, \boldsymbol{R}_0, \boldsymbol{k}_0), \tag{6.226}$$

with

$$R = X\hat{\boldsymbol{e}}_x + Y\hat{\boldsymbol{e}}_y + Z\hat{\boldsymbol{e}}_z = X + Z\hat{\boldsymbol{e}}_z,$$

$$\boldsymbol{R}_0 = \boldsymbol{X}_0\hat{\boldsymbol{e}}_x + Y_0\hat{\boldsymbol{e}}_y + Z_0\hat{\boldsymbol{e}}_z = \boldsymbol{X}_0 + Z_0\hat{\boldsymbol{e}}_z.$$

This transformation may be also applied to the operators $\overline{\mathcal{G}}^{1a1a_0}_{<S>}$ and $\overline{\mathcal{G}}^{11}_{\infty}$. We obtain for the terms $\overline{\mathcal{G}}^{11}_{\infty<S>}$ s in Eq. (6.221):

$$\overline{\mathcal{G}}^{11}_{\infty<S>}(Z, \boldsymbol{k}|\, Z_0, \boldsymbol{k}_0; \boldsymbol{P}) = \overline{\mathcal{G}}^{11}_{\infty}(Z, \boldsymbol{k}|\, Z_0, \boldsymbol{k}_0; \boldsymbol{P}) + \sum_{a, a_0 = \pm} \overline{\mathcal{G}}^{1a1a_0}_{<S>}(Z, \boldsymbol{k}|\, Z_0, \boldsymbol{k}_0; \boldsymbol{P}), \tag{6.227}$$

where a, a_0 are related to the propagation directions of the waves. With this expression, we can demonstrate that the Bethe-Salpeter Eq. (6.221) can be expressed as

$$\begin{aligned}\overline{\mathcal{G}}^{1a1a_0}_{\ll SV\gg}\left(Z, \hat{\boldsymbol{k}}|\, Z_0, \hat{\boldsymbol{k}}_0; \boldsymbol{P}\right) : \overline{\mathcal{G}}^{1a1a_0}_{<S>}(Z, \boldsymbol{p}|\, Z_0, \boldsymbol{p}_0; \boldsymbol{p}) + \sum_{a_1, a_2} \int \frac{\mathrm{d}^2\boldsymbol{p}_1}{(2\pi)^2} \frac{\mathrm{d}^2\boldsymbol{p}_2}{(2\pi)^2} \int_{-H}^{0} \mathrm{d}Z_{21} \\ \times \overline{\mathcal{G}}^{1a1a_2}_{\infty<S>}(Z, \boldsymbol{p}|\, Z_{21}, \boldsymbol{p}_2; \boldsymbol{P}) : \overline{\boldsymbol{P}}^{1a_2 1a_1}(\boldsymbol{p}_2|\, \boldsymbol{p}_1; \boldsymbol{p}) : \overline{\mathcal{G}}^{1a1a_0}_{\ll SV\gg}(Z_{21}, \boldsymbol{p}_1|\, Z_0, \boldsymbol{p}_0; \boldsymbol{P}),\end{aligned} \tag{6.228}$$

with

$$\overline{\mathcal{G}}^{1a1a_0}_{\infty<S>}(Z, \boldsymbol{p}|\, Z_0, \boldsymbol{p}_0; \boldsymbol{P}) = \overline{\mathcal{G}}^{1a1a_0}_{\infty}(Z, \boldsymbol{p}|\, Z_0, \boldsymbol{p}_0; \boldsymbol{P}), + \overline{\mathcal{G}}^{1a1a_0}_{<S>}(Z, \boldsymbol{p}|\, Z_0, \boldsymbol{p}_0; \boldsymbol{P}). \tag{6.229}$$

The propagator $\overline{\boldsymbol{P}}^{1a_2 1a_1}$ can be written as (Soubret and Berginc, 2003b)

$$\overline{\boldsymbol{P}}^{1a_2 1a_1}(\boldsymbol{p}_2|\boldsymbol{p}_1;\boldsymbol{P}) = nw\left(\hat{\boldsymbol{k}}_{\boldsymbol{p}_2}^{1a_2} - \hat{\boldsymbol{k}}_{\boldsymbol{p}_1}^{1a_1}\right)\overline{\boldsymbol{C}}_o^{11}\left(\hat{\boldsymbol{k}}_{\boldsymbol{p}_2^+}^{1a_2}|\hat{\boldsymbol{k}}_{\boldsymbol{p}_1^+}^{1a_1}\right)\otimes\overline{\boldsymbol{C}}_o^{11*}\left(\hat{\boldsymbol{k}}_{\boldsymbol{p}_{\bar{2}}}^{1a_2}|\hat{\boldsymbol{k}}_{\boldsymbol{p}_{\bar{1}}}^{1a_1}\right), \tag{6.230}$$

$$\boldsymbol{p}_1^{\pm} = \boldsymbol{p}_1 \pm \frac{\boldsymbol{p}}{2},\ \boldsymbol{p}_2^{\pm} = \boldsymbol{p}_2 \pm \frac{\boldsymbol{p}}{2}, \hat{\boldsymbol{k}}_{\boldsymbol{p}}^{1a} = \boldsymbol{p} + a\alpha_e^{'}(\boldsymbol{p})\hat{\boldsymbol{e}}_z, \tag{6.231}$$

where $\alpha'_e(\boldsymbol{p})$ is real part of α_e Eq. (6.229) can give us an iterative development of $\overline{\boldsymbol{G}}_{\ll SV\gg}^{1a1a_0}$. For example, introducing in Eq. (6.221) the first term of the iteration Eq. (6.226) is

$$\overline{\mathcal{G}}_{\ll SV\gg}^{1a1a_0}(Z,\boldsymbol{p}|Z_0,\boldsymbol{p}_0;\boldsymbol{P}) = \overline{\mathcal{G}}_{\infty}^{1a1a_0}(Z,\boldsymbol{p}|Z_0,\boldsymbol{p}_0;\boldsymbol{P}), + \overline{\varsigma}_{<S>}^{1a1a_0}(Z,\boldsymbol{p}|Z_0,\boldsymbol{p}_0;\boldsymbol{P}),$$

we obtain the contributions of the double scattering processes. $\overline{\boldsymbol{G}}_{\infty}^{1a1a_0}$ describes the direct propagation of the electromagnetic wave between two scatterers, and $\overline{G}_{<S>}^{1a1a_0}$ describes the interaction with the layer boundaries between a double scattering process by the particles. We give the following approximation which consists of retaining the two first terms of the expansion Eq. (6.226):

$$\begin{aligned}\overline{\mathcal{G}}_{\ll SV\gg}^{1a1a_0}(Z,\boldsymbol{p}|Z_0,\boldsymbol{p}_0;\boldsymbol{P}) &= \overline{\mathcal{G}}_{\infty<S>}^{1a1a_0}(Z,\boldsymbol{p}|Z_0,\boldsymbol{p}_0;\boldsymbol{P}) + \sum_{a_1,a_2}\int\frac{\mathrm{d}^2\boldsymbol{p}_1}{(2\pi)^2}\frac{\mathrm{d}^2\boldsymbol{p}_2}{(2\pi)^2}\int_{-H}^{0}\mathrm{d}Z_{21} \\ &\times\overline{\mathcal{G}}_{\infty<S>}^{1a1a_2}(Z,\boldsymbol{p}|Z_{21},\boldsymbol{p}_2;\boldsymbol{P}):\overline{\boldsymbol{P}}^{1a_2 1a_1}(\boldsymbol{p}_2|\boldsymbol{p}_1;\boldsymbol{P}):\overline{\mathcal{G}}_{\ll SV\gg}^{1a1a_0}(Z_{21},\boldsymbol{p}_1|Z_0,\boldsymbol{p}_0;\boldsymbol{P}).\end{aligned} \tag{6.232}$$

If we introduce the expression Eq. (6.230) for $\overline{G}_{\infty<S>}^{1a1a_0}$ we can write Eq. (6.233) as

$$\begin{aligned}\overline{\mathcal{G}}_{\ll SV\gg}^{1a1a_0}(Z,\boldsymbol{p}|Z_0,\boldsymbol{p}_0;\boldsymbol{P}) &= \left[\overline{\mathcal{G}}_{\infty}^{1a1a_0} + \overline{\mathcal{G}}_{<S>}^{1a1a_0}\right](Z,\boldsymbol{p}|Z_0,\boldsymbol{p}_0;\boldsymbol{P}) + \sum_{a_1,a_2}\int\frac{\mathrm{d}^2\boldsymbol{p}_1}{(2\pi)^2}\frac{\mathrm{d}^2\boldsymbol{p}_2}{(2\pi)^2}\int_{-H}^{0}\mathrm{d}Z_{21} \\ &\times\left[\overline{\mathcal{G}}_{\infty}^{1a1a_2} + \overline{\mathcal{G}}_{<S>}^{1a1a_2}\right](Z,\boldsymbol{p}|Z_{21},\boldsymbol{p}_2;\boldsymbol{P}):\overline{\boldsymbol{P}}^{1a_2 1a_1}(\boldsymbol{p}_2|\boldsymbol{P}_1;\boldsymbol{P}) \\ &:\left[\overline{\mathcal{G}}_{\infty}^{1a_1a_0} + \overline{\mathcal{G}}_{<S>}^{1a_1a_0}\right](Z_{21},\boldsymbol{p}_1|Z_0,\boldsymbol{p}_0;\boldsymbol{P}).\end{aligned} \tag{6.233}$$

The numerical solution of the integral equations is a difficult task. Owing to the large difference in the orders of magnitude of the computed quantities, special attention must be paid to the precision in the calculation of multiple integrals. The numerical calculation of the incoherent cross section requires multidimensional integration over 2D wave vectors. We adopt the following procedures: the integration domain is decomposed into subdomains whose size is adapted to the behavior of the functions to be integrated. In each subdomain a Gauss-Legendre method with N points is used, the number of points varies with the precision required. The integral equation is well suited if we want to obtain an iterative solution of Eq. (6.221) as we have seen. We define the Green tensor $\overline{\mathcal{G}}_{\ll SV\gg}$ describing the interactions between the surfaces and the medium with a perturbative development up to the second order. This development contains six terms, the physical meaning of which will now be explained. We omit the superscripts of the expressions of the different tensors.

For the first order, the term $\overline{\mathcal{G}}_{\infty}$ describes an incident wave penetrating into the layer, scattered by a first particle, propagating directly toward a second particle, scattered by this particle, and transmitted back into the incident medium. The term $\overline{\mathcal{G}}_{<S>}$ describes an incident wave penetrating into the layer, scattered by a first particle, interacting with the boundaries, reaching a second particle, scattered by this particle, and transmitted back into the incident medium.

For the second order, the term $\overline{\mathcal{G}}_{\infty} : \overline{P} : \overline{\mathcal{G}}_{\infty}$ describes a wave penetrating into the layer, scattered by a first particle, propagating directly toward a second particle, scattered by this particle, propagating directly toward a third particle, scattered by this particle, and transmitted into the incident medium. The term $\overline{\mathcal{G}}_{<S>} : \overline{P} : \overline{\mathcal{G}}_{<S>}$ describes a wave penetrating into the layer, scattered by a first particle, interacting with the boundaries, reaching a second particle, scattered by this particle, and interacting with the boundaries, reaching a third particle, scattered by this particle, and transmitted into the incident medium. The term $\overline{\mathcal{G}}_{\infty} : \overline{P} : \overline{\mathcal{G}}_{<S>}$ describes a wave penetrating into the layer, scattered by a first particle, interacting with the boundaries, reaching a second particle, scattered by this particle, propagating directly toward a third particle, scattered by this particle, and transmitted into the incident medium. The term $\overline{\mathcal{G}}_{<s>} : \overline{P} : \overline{\mathcal{G}}_{\infty}$ describes a wave penetrating into the layer, scattered by a first particle, propagating directly toward a second particle, scattered by this particle, interacting with the boundaries, reaching a third particle, scattered by this particle, and transmitted into the incident medium.

In Figs. 6.28 and 6.29 we can see the different contributions for a scattering sequence with two particles (second-order scattering) or for a scattering sequence with three particles (third-order scattering).

We now examine the term $\overline{\boldsymbol{I}}^{incoh}_{\text{Crossed}}$. Barabanenkov (e.g., Barabanenkov et al., 1997; Barabanenkov and Ozrin, 1988; Barabanenkov et al., 1991) observed a new class of Feynman diagrams (the maximally crossed diagrams), which contributes to the scattering with the ladder diagrams in the vicinity of the source direction. Far from the source direction, their contributions become negligible. The coherent backscattering enhancement is an interference effect which manifests itself at the level of the averaged mean intensity, it is also known as the weak localization effect. During the two last decades, several studies have been concerned with the enhanced backscattering (Kuz'min and Romanov, 1996; van Rossum and Nieuwenhuizen, 1999; Tsang and Ishimaru, 1984, 1985; Gorodnichev et al., 1987, 1989; van Tiggelen and Maynard, 1997; van der Mark et al., 1988; Stephen and Cwilich, 1986; Akkermans et al., 1988; van Tiggelen, 1999). This phenomenon produces a peak in the backscattering direction $\hat{\boldsymbol{k}} = -\hat{\boldsymbol{k}}_0$ due to the interference of waves following the same path but in opposite directions in a scattering medium composed of fixed, randomly placed spherical scatterers as shown in the schematic illustration in Fig. 6.30.

The most elegant way to introduce the enhanced backscattering in the theory is to use the reciprocity principle (van Tiggelen, 1999). Heuristically, it means that when we exchange the source and the detector positions (respectively given by $\boldsymbol{r}_0$ and $\boldsymbol{r}$ and their polarization), the field measured is the same. This physical property may be

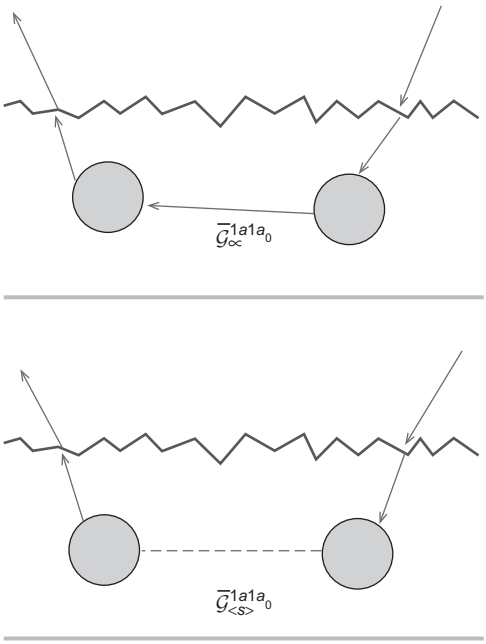


FIG. 6.28

Contributions of the Green tensor to the first order.

expressed with a mathematical operator the right transpose T_R of a tensor, whose definition is given in Appendix A.2. Therefore, we can write $\hat{\boldsymbol{I}}^{incoh}_{\text{Crossed}}(\boldsymbol{R},\boldsymbol{k})$ as a function of $\hat{\boldsymbol{I}}^{incoh}_{\text{Ladder}}(\boldsymbol{R},\boldsymbol{k})$. The demonstration is given in Soubret and Berginc (2003b). The maximally crossed terms are added to the expression for the specific intensity to satisfy the reciprocity principle. They correspond to the maximally crossed Feynman diagrams which describe the leading interference terms.

We have presented above a general formalism based on rigorous Dyson and Bethe-Salpeter equations which takes into account the scattering by the surface and the volume, the polarization components, the correlation between the scatterers and the expression for the coherent backscattering.

6.7.6 COHERENT BACKSCATTERING

In this section, we study the coherent backscattering and the pattern of the cross section from slabs illuminated by plane waves. We apply the transport theory based on the Bethe-Salpeter equation and its solution by moments discussed in the previous sections. We have obtained numerically the solutions for the cross section involving laser light reflection from disordered samples in which coherent backscattering may be directly observed. With these examples, we give direct demonstrations of the effect.

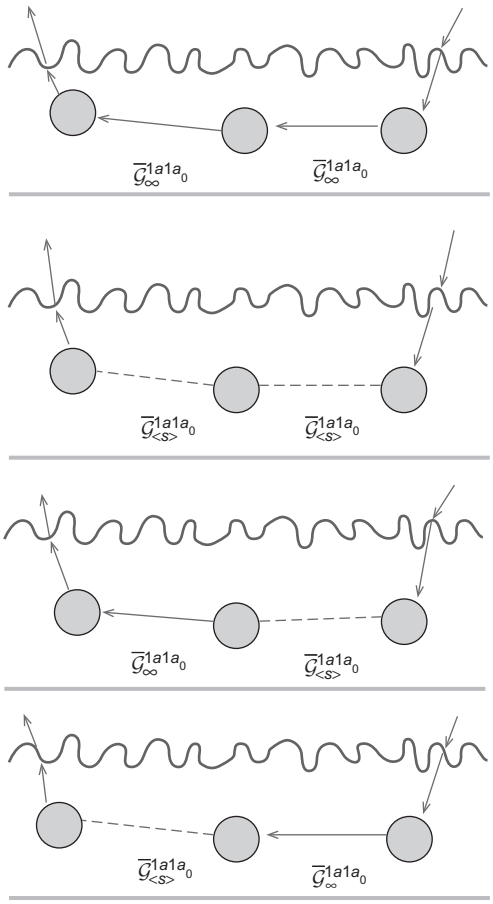


FIG. 6.29

Contributions of the Green tensor to the second order.

6.7.6.1 Semi-infinite medium

For the first example, we take a semiinfinite 3D medium with a planar interface. This example is interesting because the mean intensity, that is, the second moment of the Green function, contains only the contribution of the disordered medium. The permittivity of the medium containing the incident source is $\varepsilon_0 = 1$, and we can assume that $H/\lambda \gg 1$. With this configuration, we can consider layers with large depth. The permittivity of the medium is $\varepsilon_1 = 2 + i0.03$. We consider spherical scatterers with a radius given by $r_d = 0.035\lambda$, permittivity of $\varepsilon_d = 5$, and a volume fraction of $f_{vol} = 10\%$. The scatterers are located randomly in the medium. In Fig. 6.31, we have plotted the incoherent cross section of the polarization components $TM - TM$, $TE - TE$, $TE - TM$ and $TM - TE$ for an angle of incidence $\theta_0 = -20$ degrees. The bistatic coefficients are computed in the plane of incidence ($\varphi = \varphi_0 = 0$ degrees). The total volume contribution is given by the black solid curve, the first-order

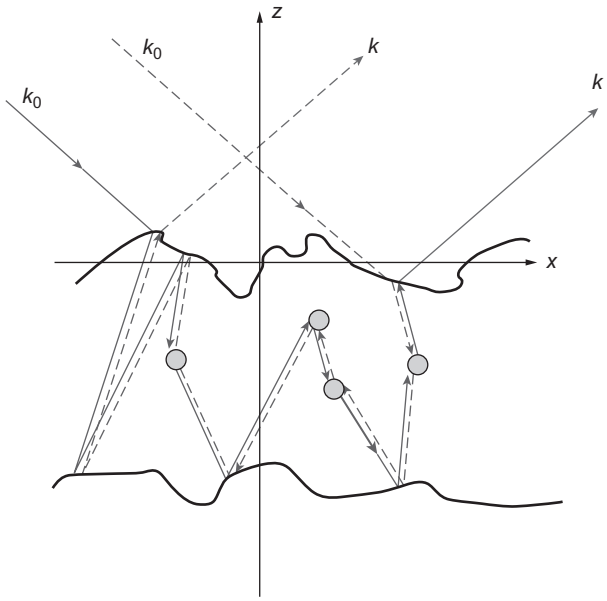


FIG. 6.30

Process of the backscattering enhancement.

contribution is given by the blue dashed curve, and the higher-order contribution (ladder and maximally crossed cross section) by the solid red curve. The theoretical profile demonstrates the presence of a backscattering enhancement due to the higher-order contributions. Only the "ladder + most-crossed" contributions give a depolarized effect ($TE-TM$ and $TM-TE$ curves). The fact that the peak value of the backscattering enhancement seems to be low is due to the dielectric scatterers for which the permittivity contrast between the medium and the scatterers is not high. As the contrast becomes lower, the higher-order contributions are cut-off from the effect. Another phenomenon can eliminate the higher-order contributions given by the perturbative development of the Bethe-Salpeter equation, viz. absorption in the medium. Limitation through absorption is a probabilistic process, whereas limitation through sample size is deterministic. We are in a configuration where the coherent backscattering peak is observable in the total scattered intensity, that is, it becomes measurable (Kuga and Ishimaru, 1984; van Albada and Lagendijk, 1985; Wolf and Maret, 1985; Etemad et al., 1986).

6.7.6.2 Random medium with two planar interfaces

In this section, we consider a dielectric slab with two planar interfaces. The depth of the layer is $H=5\lambda$. The permittivity of the medium of the layer is $\varepsilon_1=1.2$, this layer contains scatterers that are located randomly in the slab. The permittivity of the scatterers is $\varepsilon_d=2$, and they are considered to be spherical particles of radius $r_d=0.035\lambda$. The fractional volume of the scatterers is $f_{vol}=0.01\%$. The layer is deposited on a

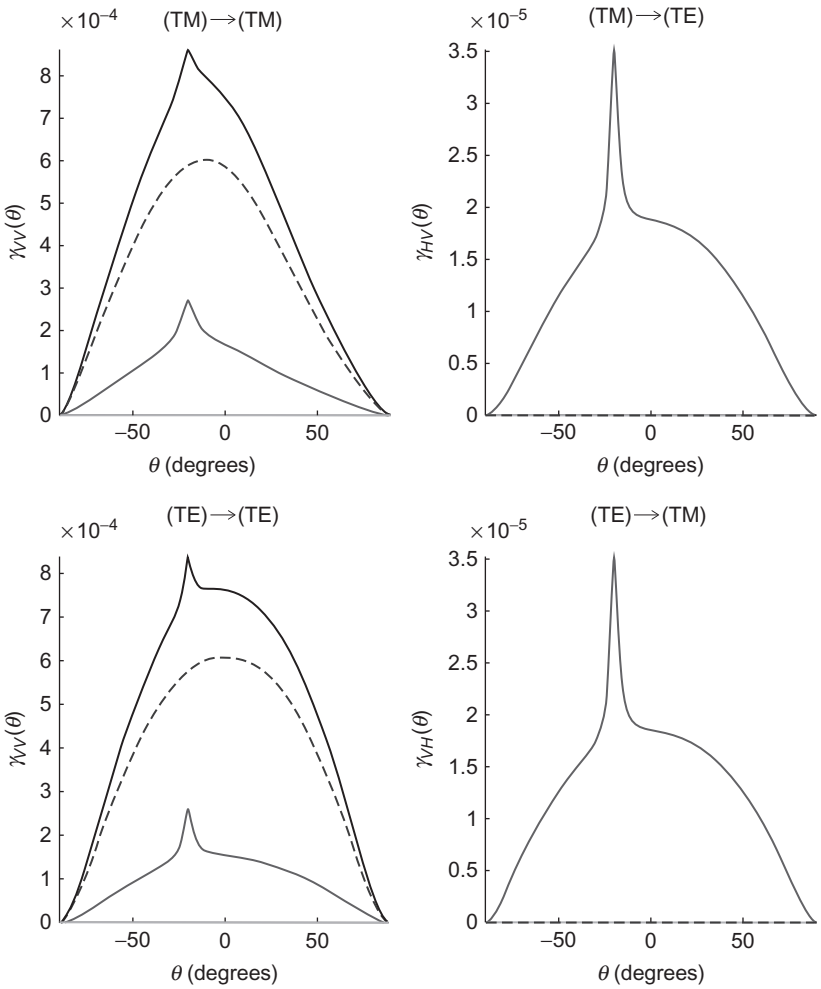


FIG. 6.31

Incoherent bistatic cross section for the co-polarized and the cross-polarized scattering in the plane of incidence ($\varphi = \varphi_0 = 0$ degrees). The parameters of the medium are $\varepsilon_1 = 2 + i0.03$, $\varepsilon_d = 5$, $r_d = 0.035\lambda$, $H/\lambda \gg 1$, and $f_{vol} = 10\%$. Total contribution *(solid line)*; order 1 contribution *(dashed line)*, the third curve (TE–TE and TM–TM components) represents higher-order contributions. We observe that the backscattering enhancement is given by the latter contributions. For the cross-polarized scattering only the higher-order contributions contribute to the total cross section.

semiinfinite medium of permittivity $\varepsilon_2 = 16$. We plot in Fig. 6.32 the polarized cross section as a function of the scattering angle in the plane of incidence, the angle of incidence in $\theta_i = -20$ degrees. For the four polarization components *TM–TM*, *TE–TE*, *TE–TM*, and *TM–TE*, we observe a backscattering enhancement and a reflective enhancement, although the magnitude of the cross section is small. In Fig. 6.33,

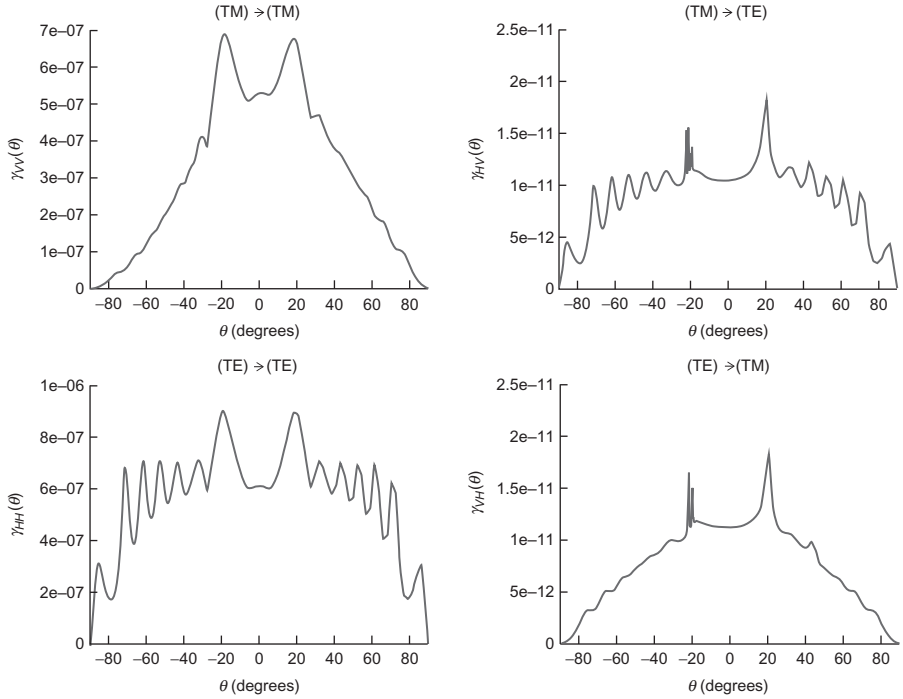


FIG. 6.32

Total incoherent cross section of a layer with dielectric scatterers bounded by two plane interfaces. Incident angle $\theta_i = -20$ degrees.

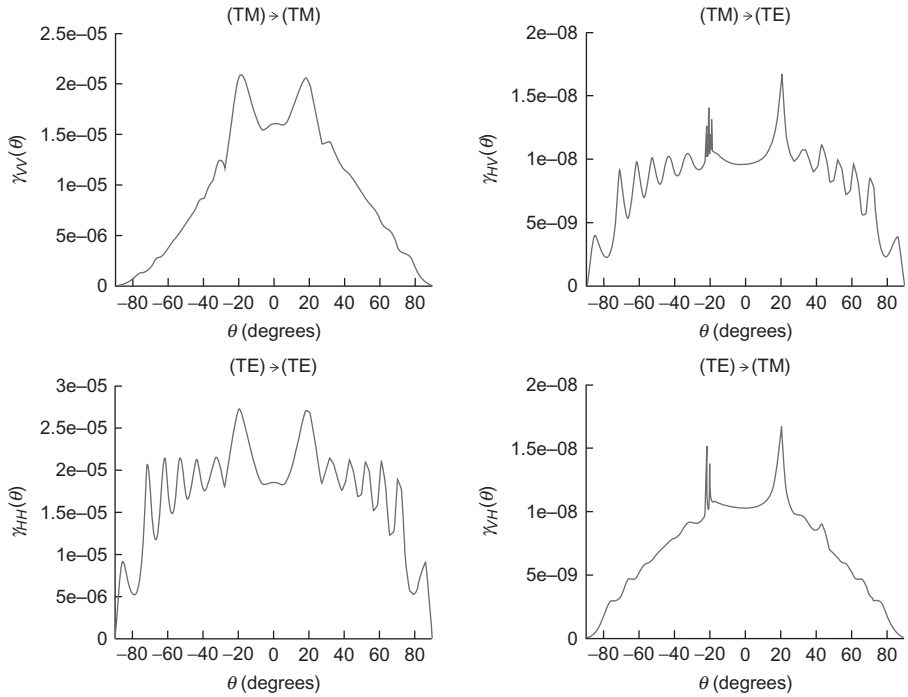


FIG. 6.33

Total incoherent cross section of a layer with metallic scatterers bounded by two planar interfaces. Incident angle $\theta_i = -20$ degrees.

we have the same parameters as Fig. 6.32 except that the scatterers are now metallic. The bistatic cross section is larger (almost 15 dB). The theoretical profile of the coherent scattering is the same as in Fig. 6.32. We observe an order of magnitude enhancement of the incoherent cross section in the specular and antispecular directions. We will now study the 3D profile of the coherent backscattering. We have the same parameters as before. The scatterers are dielectric but the depth of the layer is 15λ. In Fig. 6.34, we plot the 3D TM–TM scattering coefficient. The axis represent

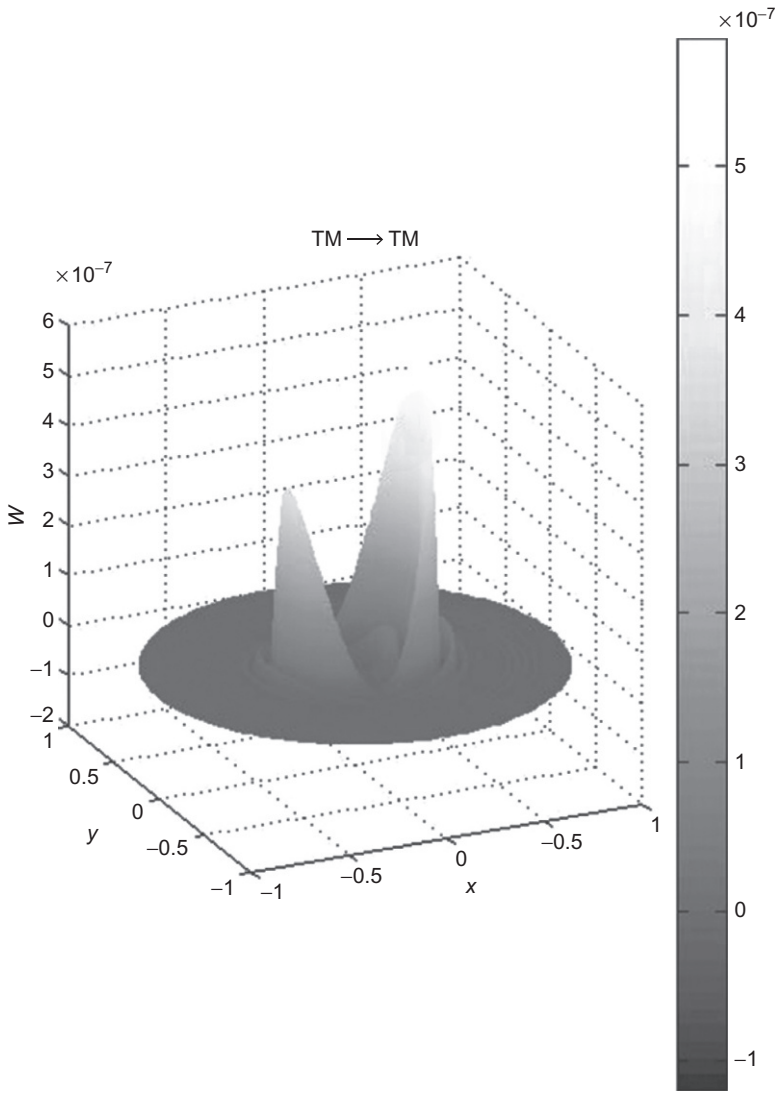


FIG. 6.34

3D profile of the TM-TM scattering coefficient. Same parameters as for Fig. 6.33, thickness of the slab is $H = 15\lambda$.

$x = \sin \vartheta_d . \cos \varphi_d$, $y = \sin \vartheta_d . \sin \varphi_d$. Comparison of the results in the two figures indicates that a larger thickness gives a sharper backscattering peak. An important point to be noted is that the 3D profile of the coherent backscattering has a cylindrical pattern.

6.7.6.3 Random medium with random rough interfaces

In this section, we consider a 3D layer with randomly located spherical scatterers, that is, bounded with a randomly rough upper surface and a planar lower interface. The upper surface is a Gaussian randomly rough surface, whose parameters are $\sigma/\lambda = 0.005$ and $l/\lambda = 0.25$. The contribution of the randomly rough surface is computed (Fig. 6.35) with the small-perturbation approximation presented in Section 6.6, and higher orders in the perturbative development must be used. The thickness of the layer is $H = 5\lambda$, its permittivity is $\varepsilon_1 = 1.2$, The scatterers are spherical with a radius $r_d = 0.035\lambda$ and their permittivity is $\varepsilon_d = 2$. The layer is deposited on a semiinfinite medium of permittivity $\varepsilon_2 = 16$. The volume fraction of the scatterers is 0.15%. The wavelength is $\lambda = 1.54\,\mu m$. The backscattering in the retroreflection direction is smaller than in the case of two planar interfaces, due to the contribution from the randomly rough surface.

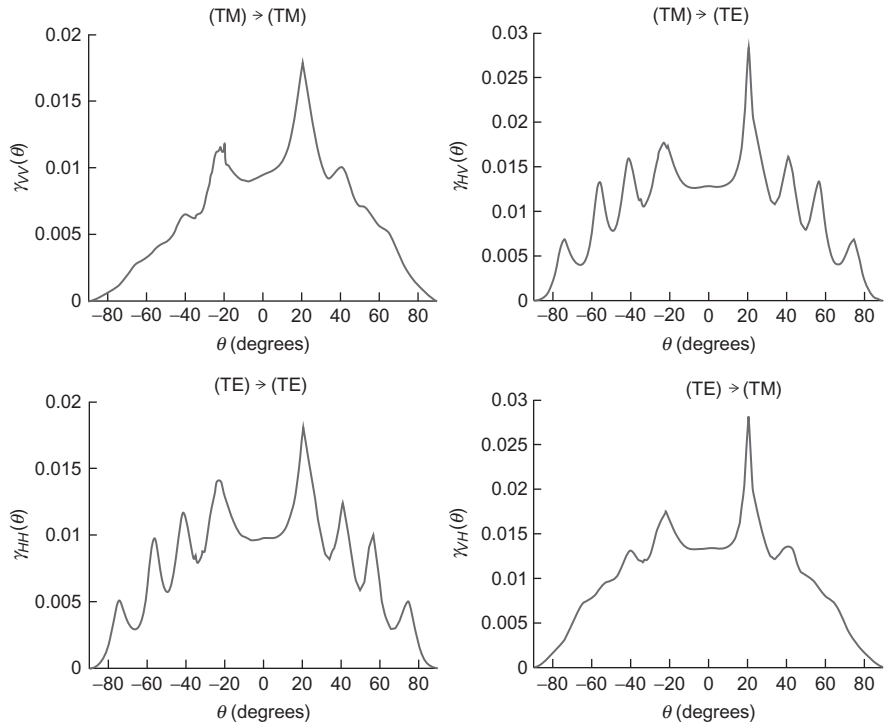


FIG. 6.35

Incoherent cross sections for a random slab with an upper rough surface and a plane lower interface in the plane of incidence ($\varphi = \varphi_0 = 0$ degrees). Angle of incidence $\theta_i = -20$ degrees.

We consider another example with a larger volume fraction of spherical nanoparticles. We compute the incoherent cross section in the plane of incidence for a slab that is defined as follows. The medium of incidence in vacuum ($\varepsilon_0 = 1$). The layer depth is $H = 5\lambda$, its permittivity is $\varepsilon_1 = 2$. The upper layer boundary is defined as a slightly randomly rough surface defined by the rms height of the surface $\sigma/\lambda = 0.01$ and the correlation length is given by $l/\lambda = 0.3$. The lower boundary is a planar interface that separates the layer from a semiinfinite medium of permittivity $\varepsilon_2 = 16$. The wavelength is $\lambda = 1.5\,\mu$m. The medium contains two types of spherical metallic particles defined as Rayleigh spherical scatterers. The radius of the first type of particles is $r_1 = \lambda/20$. The volume fraction of these particles is $f_{vol1} = 0.0125$. For the second type of particles, the radius is $r_2 = \lambda/200$, the volume fraction is $f_{vol2} = 0.0375$. The total volume fraction is 5%. We obtain (Fig. 6.36) the total incoherent cross section for an incident angle $\theta = 0$ degrees, for the co- and cross-polarized components and the circular polarization components (right to right and right to left). The backscattering enhancement is due to the most-crossed diagram contributions. We note that the second-order contribution in the expansion of the Green tensor is about 5% of the first-order contribution.

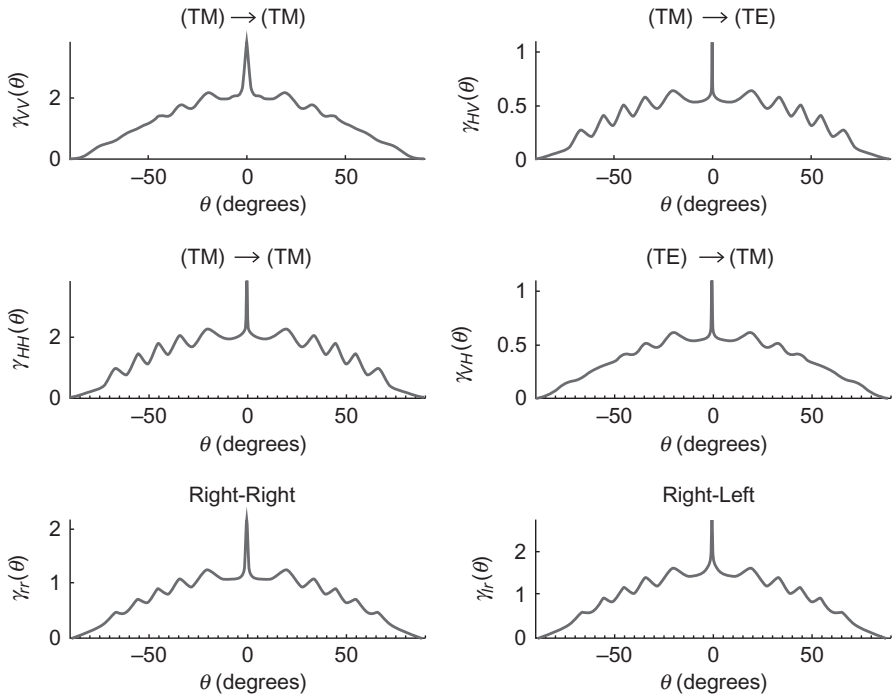


FIG. 6.36

Cross section of a slab with an effective permittivity $\varepsilon_e = 2.37 + i\,1.747 \times 10^{-2}$. The disordered medium contains nanoscale metallic particles, the upper surface of the slab is a randomly rough surface, the angle of incidence is $\theta_0 = 0$ degrees, the wavelength is $\lambda = 1.5\,\mu$m.

6.7.7 CONCLUSION

This section was devoted to a theory of transport based on a Bethe-Salpeter equation. We presented a multiple-scattering theory (up to third order) for a random slab with discrete scatterers and bounded with randomly rough surfaces. There is a smooth transition from the coherent regime, where a random medium appears locally homogeneous to the propagating electromagnetic wave, to the multiple-scattered behavior. Our approach is to treat this transition better by evaluating the Bethe-Salpeter equation. A new expansion of the Green tensor up to second order was developed, and calculations of the incoherent cross sections were performed taking into account polarization components with the Mueller matrix. With two or three scatterings, we can observe that a fraction of the wave energy becomes incoherent, but there is still a finite fraction of the energy that remains coherent. We treat the behavior of the transport equation as a superposition of coherent and diffusive components. With the computations realized in this section, we explored the effects of the different parameters that characterize the random medium and the rough surfaces. We observed interference effects, backscattering enhancement peaks for the different examples in the case of the maximally crossed contributions. But it remains an open question as to how many scatterings are required before a complete diffusive transport will be established. What we have demonstrated is that with a few scatterings, and despite the contributions of the rough boundaries, a weak localization of the polarized electromagnetic wave is well established.

6.8 APPLICATIONS

In this chapter, we dealt with light that has been scattered many times. As we have shown, this is typically the case when light penetrates a medium with many randomly placed scatterers. In this case, the light intensity diffuses through the medium. The mean free path gives the length scale defining when a wave is converted into diffuse light. For example, the mean free path exceeds the sample thickness in the ballistic regime and the mean free path is shorter than the sample thickness in the diffuse regime. There are medical applications that use diffusely scattered light, for example to locate and identify cancer cells by reconstructing 3D images. There is another vast range of application of diffuse light scattering: passive or active remote sensing. We can extract information from observation satellite data to investigate, for example, the diffuse reflection from ice in the polar regions. The reflection of laser light in the case of active remote sensing can be used to study the composition of air or to construct laser images of the observed scene. Below, we will give examples of these applications and show that extracting information from the scattered light is a mathematically complex problem.

To illuminate the different applications and examples linked to the computation of rough surface and random volume scattering, we will focus on the problem of active remote sensing. The problem of active remote sensing is governed by the

knowledge of the magnitude of the reflectance of the surfaces which compose the objects to be identified. To specify the equipment, it is necessary to compute the scattered intensity from the objects and the scene illuminated by the laser source. The nonconventional imaging systems explore the advantages of laser imagery to form hyperspectral polarimetric 2D or 3D images of the scene. There is considerable interest in the development of these new optical imaging systems that are able to give new information linked to the spectral reflectance of the surfaces of the objects. Potential applications range across the field of defense and security for the recognition of targets. For example, surveillance in land borders implies observation over wide areas and harsh environments like forests. The aim of such systems is to detect, locate, track, and recognize persons and vehicles entering territory. This makes it very difficult for common systems like radar or cameras to detect hidden objects. Hyperspectral imagers can provide area surveillance with high resolution and improved capability to detect and identify targets, and their traces in a complex background through the detailed analysis of target reflection properties. For these systems, technical challenges include development of software data processing for automatic target detection enabling both fast information and extraction from a large hyperspectral data stream. Polarimetric analysis can enhance the capabilities of the extracted information to better distinguish man-made objects from a natural background.

The technique of laser imagery is based on the illumination of the scene by a laser and the subsequent collection of the backscattered intensity by a focal plane array to form an intensity image. For laser imaging systems, laser pulse illumination can be used in all lighting conditions, combined with range-gating technology in order to see through vegetation, camouflage, and windows. Laser imaging can be applied to detection of persons and vehicles, but because of its high resolution, the technique is particularly suited for eliminating false alarms and for giving information of the target type (person, type of vehicle, etc.). The 1.54-μm laser band is attractive for 2D laser imagery applications where eye-safety is of concern. This band poses little chance for damage to retinal tissue at nominal power levels. Detector technology is critical to enabling 2D laser imagery. Competing focal plane areas in the 1.54 μm band or short wave infrared (SWIR) band are constructed from III to V materials such as InGaAs. Silicon is used for shorter wavelength laser systems that operate in the visible and near-infrared band. The technological challenges include better knowledge of natural background clutter and its dependence on environmental conditions, better knowledge of the intensity scattered by the objects and the surfaces, that is, a better analysis of light scattering by random media and rough surfaces. Owing to the wavelength of the laser, the surface of the considered objects must be considered as randomly rough surfaces. Broadband lasers allow detailed analysis of the reflection properties of a target and improve recognition capability. Technological challenges include further development of new active imaging concepts like multiaperture systems, photon counting imaging, reflective tomographic imaging, and range profiling for target identification.

High-resolution 3D imagery is one of the best candidates to identify objects hidden behind porous occluders like dense canopy. Laser radar (Ladar) technology has enjoyed significant advances over the past decade. Novel focal plane areas, compact laser illuminators, and advanced signal processing have enabled the construction of low power 3D laser imagery systems. Synthetic images of 3D objects are based on extraction of laser backscattered signals; the principle of 3D laser radar is based on the use of movable light sources and detectors to collect information on laser scattering, and to reconstruct the 3D object. A 3D reconstruction algorithm is a major component in these optical systems for identification of camouflaged objects. The ladar cameras can be used for measuring absolute distance by the time-of-flight technique. It is based on calculating the travel time of a light pulse to obtain the direct measures of distance. This technique offers outstanding qualities such as the ability to perform 3D measurements at distances from 1 to 10 km. The precision of the measurement is around a few centimeters. This 3D ladar system requires a short pulse of laser energy of the order of 1 ns to separate targets from overlaid camouflage or forest canopy. Resolving closely spaced returns requires a high-bandwidth detector ($>$1 GHz) and specific readout electronics. A substantial advantage over similar techniques, such as stereovision, is that the measurement process yields the distance value directly. Also, the devices can work in noisy environments such as dense vegetation spaces, generating 3D images from the measurement of many points forming dense point clouds with a good spatial resolution.

Another alternative approach is based on a reflective tomography concept that takes advantage of the properties of the scattered intensity. This technique uses a set of 2D laser images at different angles of view. These sets contain the data collected by the pixels of the detectors. These data are related to the intensity backscattered by the scene illuminated by a laser pulse. This 3D reconstruction requires a laser system of lower complexity than in the case of the 3D time-of-flight concept because we use an ordinary active imagery system. The scattered intensity contains the information for the 3D reconstruction. The robustness of identification of 3D reconstructed images is directly related to the inversion and completion algorithms used in the process of identification. A notable limitation of numerous methods is that inversion algorithms produce blurred and noisy images and incomplete 3D reconstruction regardless of the technology used (3D time-of-flight Laser Radar or Ladar reflective tomography).

We have seen that it is very important to have reliable numerical models and simulations for light scattering cross sections from random surfaces and media to specify the different 2D and 3D laser systems described above. The physics-based model must be designed to provide accurate results but also to include all the electromagnetic interaction mechanisms with the different elements of the scene. The numerical simulation includes the physical structure of the environment, the transfer of radiation through the environment and the interaction of the laser wave with the structure of the different elements of the scene. These models incorporate a detailed understanding of the interaction of the laser electromagnetic wave, which is calculated

by the SSA. The surface of the different vehicles or hard targets is considered as a randomly rough surface, and we compute the laser signature (Laser Cross Section) of the vehicles.

The total electrical field scattered by a randomly rough surface or a random volume $\boldsymbol{E}^s$ may be written as

$$\boldsymbol{E}^s = \boldsymbol{E}^{sc} + E^{si} \tag{6.234}$$

where $\boldsymbol{E}_{sc}$ and $\boldsymbol{E}^{si}$ are, respectively, the coherent and incoherent scattered components of the field defined by

$$\boldsymbol{E}^{sc} = <\boldsymbol{E}^s> \tag{6.235}$$

with $<\boldsymbol{E}^{si}> = 0$.

The coherent component $\boldsymbol{E}^{sc}$ is a deterministic component and the incoherent or diffuse component $\boldsymbol{E}^{si}$ is a stochastic component with a null mean value. The mean value of the intensity of the incoherent scattered field is given by the following relation:

$$<\left|\boldsymbol{E}^{si}\right|^2> = <|\boldsymbol{E}^s - <\boldsymbol{E}^s>|^2> = <|\boldsymbol{E}^s|^2> - |<\boldsymbol{E}^{sc}>|^2 \tag{6.236}$$

The scattering cross section for a randomly rough surface or a random volume, which is a random variable depending on the stochastic process of the representation of the target surface and the target paint, is given by the first and second moments of the field. With this representation of the field, we can calculate the intensity of the field scattered by the object. All the scattering coefficients (coherent and incoherent components of the electromagnetic field) are functions of the azimuth angles. We define, in this case, the Mueller matrix, which gives all the combinations of the polarization states of the scattered electromagnetic waves as demonstrated in the preceding sections. The randomly rough surfaces of the complex object are characterized by electromagnetic parameters (permittivity) and roughness parameters (standard deviation of rough surface height and autocorrelation function). We take into account an effective permittivity for the paints. Effective medium theory or a homogenization approach is a powerful way to handle the scattering properties of composite materials such as porous media and microstructured materials. We have demonstrated in Section 6.7 that the light scattered from a rough slab with rough boundaries can be decomposed into four terms whose first component corresponds to an effective permittivity modeling the random medium with discrete scatterers. For metamaterials, the other terms can bring interesting contributions in the global laser cross section in the backscattering direction. For example, small particles made of weakly dissipating materials may exhibit the so-called anomalous scattering (AS) without changes in the frequency of the incident light. AS has very little in common with Rayleigh scattering and results in giant optical resonances. We give examples (Figs. 6.37 and 6.38) of 2D laser images for vehicles. We define a CAD model with facets for the different objects. Each facet contains the electromagnetic and roughness parameters. The second step of the numerical computation contains the



(A)



(B)

FIG. 6.37

(A) Visible image of the vehicle. (B) Computation of a 2D laser image of the vehicle; the wavelength of the He-Ne laser is 632 nm. The laser wave is nonpolarized. The shades are related to the magnitude of the backscattered intensity. Our model also addresses transparent structures.

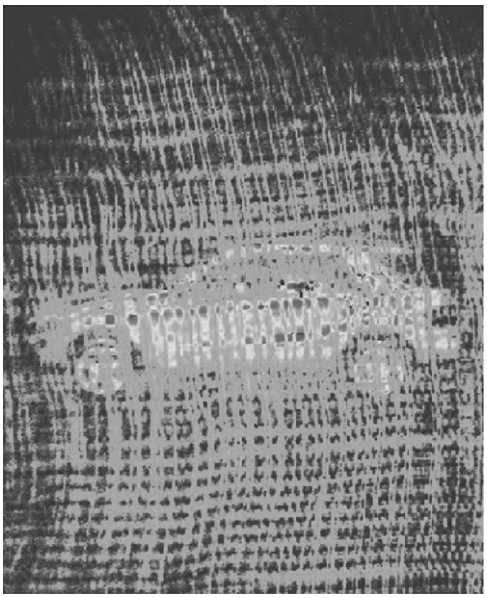


FIG. 6.38

Computation of a nonpolarized 2D laser image of a vehicle hidden behind a camouflage net. Laser wavelength 543 nm. The scattered intensity of the net is computed with measured reflectance data.

simulation of the receiver, the transmitter, and the optics system. The third step is the modeling of the electromagnetic scattering from the different objects of the scene. The fourth step contains the absorption and scattering of the laser wave by the components of the atmosphere, and the simulation of the atmospheric turbulence effects: speckles, scintillation, beam spreading, and beam wandering.

We can observe that the simulation results for the 2D laser imaging are highly accurate. The computation of the laser scattering with the SSA is applied to each facet. The Laser Cross Section of the object may be expressed as a 2×2 matrix in the polarization component basis related to the considered object.

We add now to the computing simulation a last step, which contains the development of a 3D reconstruction algorithm to obtain a high-resolved 3D image. This kind of computer model can help to predict 3D Ladar performance, and it is used to develop a 3D reconstruction algorithm. We shall focus on reflective tomography algorithms for reconstructing optical 3D scenes (Berginc and Jouffroy, 2010, 2011; Berechet and Berginc, 2011). We develop a cone-beam algorithm, related to the Feldkamp algorithm which is a convolution-backprojection algorithm deduced from the Radon transform (Feldkamp et al., 1984). It uses a set of 2D projections. In the case of laser images, these sets contain the data collected by the pixels of the planar detectors or focal plane areas. This backprojection algorithm allows the reconstruction of a 3D scene from a series of images parameterized by an angle of axial rotation. Reflective characteristics of target surfaces can be described by the combination of diffuse and coherent or specular reflection models. This combination is directly linked to the surface roughness and the structure of the volume bounded by the randomly rough surface. In Fig. 6.39, we give a full 3D reconstruction of a vehicle for an air-to-ground scenario. The reconstruction of the object is made of isodensity voxel (volumic pixel). The laser wavelength is 1.54 μm. The range between the scene and the sensor is 500 m. Fig. 6.40 describes the scenario used for the 3D reconstruction of concealed vehicles and represents the CAD model of the air-to-ground scenario. Most of the incident laser energy is reflected, scattered, or absorbed by the foliage; a small amount can reach the target and this energy is backscattered by the target toward the focal plane area of the sensor. The sensor collects 2D intensity images and our convolution-backprojection algorithm gives a 3D reconstruction of the vehicle under trees. Trees are modeled by polarized reflectance applied to the different facets generated by the CAD model.

Sparse data availability is due to the structures of the vehicle occluded by the canopy for the different angles of view. In Feldkamp et al. (1984), we describe an algorithmic process to complete sparse 3D images at satisfactory levels for reliable identification of concealed objects. We have demonstrated that the reflected light contains sufficient information to recover the 3D objects of the hidden scene. Therefore, computational scattering models for random volumes and surfaces are of considerable importance in numerical simulation of active remote sensing in the visible or infrared band. They must be sufficiently accurate to allow the complete analysis of the reflected information.

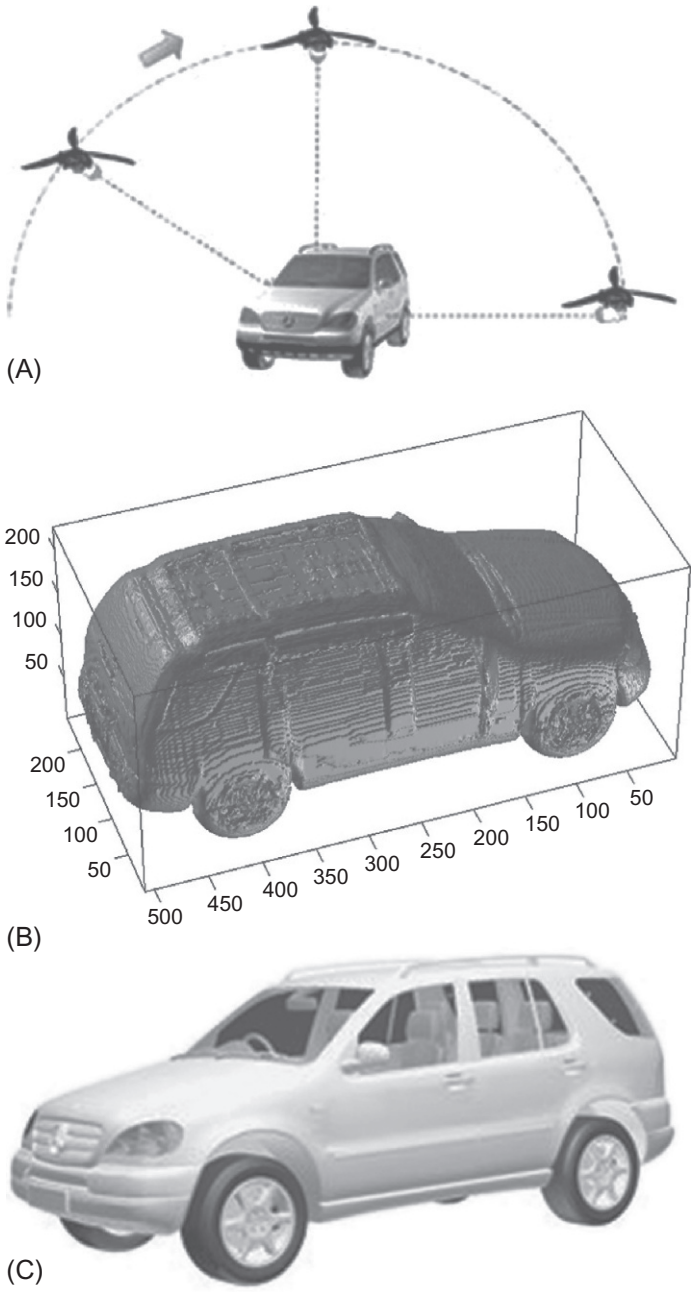


FIG. 6.39

(A) Description of the air-to-ground scenario; wavelength 1.54 μm, range 500 m. (B) Full 3D reconstruction with isodensity voxel (volume pixel), resolution $500 \times 200 \times 200$.
(C) Comparison with CAD model.

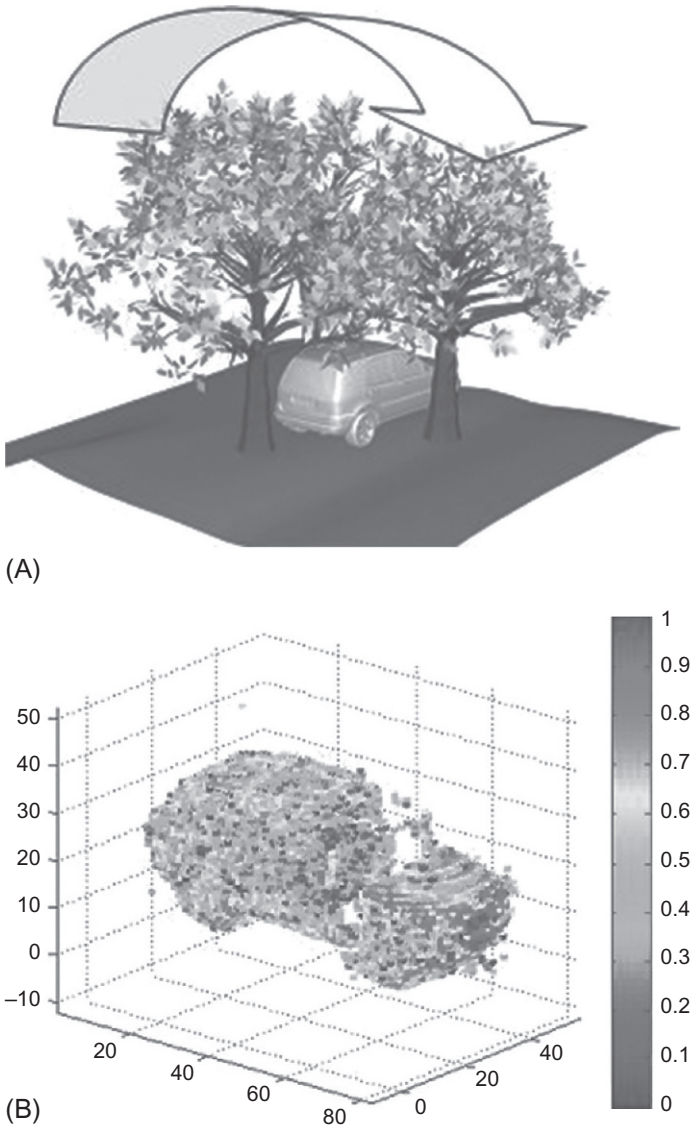


FIG. 6.40

(A) Description of the air-to-ground scenario; wavelength 1.54 μm, range 500 m, the arrow describes the trajectory of the sensor. (B) Full 3D reconstruction with intensity voxel, the intensity is related to the laser intensity scattered by the different parts of the vehicle for the different angles of view, resolution $50 \times 80 \times 50$.

6.9 CONCLUSION

This chapter contains a number of original concepts and new formulations for the scattering of light from random structures. The purposes of this chapter are to delineate a coherent outline of the theory and application of scattering from random structures and to make accessible the relevant theoretical methods of calculation by presenting both the physics and the mathematical framework. The complexity of the random structures considered increases along the different sections. With numerical nonperturbative solutions of reduced Rayleigh equations, we can now analyze extensively coherent phenomena due to multiple scattering for 2D structures or 3D films with one 2D randomly rough surface. The study of the presence of satellite peaks for this kind of structure could be very interesting for the specification of optical films and the analysis of wave energy redistribution, for example, the transfer of trapped electromagnetic radiation. The development of the SSA for 3D rough films can provide new insight into electromagnetic scattering from rougher films. Formulation for rough films with discrete scatterers can give rise to the development of new devices based on metallic nanoparticles embedded in dielectric or insulating media by studying the optical behavior of these layers containing nanostructures and the evaluation of the potential use of these structures for optical applications. These computational tools can specify the exploitation of features of such assemblies as high local scattered intensity enhancement, and resonant behavior inducing absorption in the visible and near-infrared spectral ranges. A last important point is the study of singularities in speckle patterns. With these formulations that take into account multiple scattering, we can study statistical properties in the scattering of an electromagnetic wave from rough random structures. For example, the calculation of the fourth moment of the field gives the intensity-intensity correlation function, and contains information about phase interference effects or speckle patterns.

APPENDIX

A.1 DEFINITIONS OF THE SCATTERING MATRICES FOR A SINGLE ROUGH SURFACE

We give here a summary of the formulas derived in Soubret et al. (2001a) in the case of the SPM.

$$\overline{\boldsymbol{X}}^{(0)}_{s\varepsilon_0\varepsilon_1}(\boldsymbol{p}_0) = \overline{\boldsymbol{D}}_{10} - (\boldsymbol{p}_0).\left[\overline{\boldsymbol{D}}_{10}{}^{+}(\boldsymbol{p}_0)\right]^{-1} \tag{A.1}$$

$$\overline{\boldsymbol{X}}^{(1)}_{s\varepsilon_0\varepsilon_1}(\boldsymbol{u}|\boldsymbol{p}_0) = 2i\overline{Q}^{+}(\boldsymbol{u}|\boldsymbol{p}_0), \tag{A.2}$$

$$\overline{\boldsymbol{X}}^{(2)}_{s\varepsilon_0\varepsilon_1}(\boldsymbol{u}|\boldsymbol{p}_1|\boldsymbol{p}_0) = \alpha_1(\boldsymbol{u})\overline{Q}^{+}(\boldsymbol{u}|\boldsymbol{p}_0) + \alpha_0(\boldsymbol{p}_0)\overline{Q}^{-}(\boldsymbol{u}|\boldsymbol{p}_0) - 2\overline{\boldsymbol{P}}(\boldsymbol{u}|\boldsymbol{p}_1).\overline{Q}^{+}(\boldsymbol{p}_1|\boldsymbol{p}_0), \tag{A.3}$$

where

$$\overline{Q}^{\pm}(\boldsymbol{u}|\boldsymbol{p}_0)\equiv\frac{\alpha_1(\boldsymbol{u})-\alpha_0(\boldsymbol{u})}{2\alpha_0(\boldsymbol{p}_0)}\left[\overline{M}^{1+,0+}(\boldsymbol{u}|\,\boldsymbol{u})\right]^{-1}.\left[\overline{M}^{1+,0-}(\boldsymbol{u}|\,\boldsymbol{p}_0)\pm\overline{M}^{1+,0+}(\boldsymbol{u}|\,\boldsymbol{p}_0).\overline{X}^{(0)}(\boldsymbol{p}_0)\right], \tag{A.4}$$

or explicitly.

$$\overline{Q}^{+}(\boldsymbol{u}|\boldsymbol{p}_0)=(\varepsilon_1-\varepsilon_0)\left[\overline{\boldsymbol{D}}^{+}_{10}(\boldsymbol{u})\right]+1.\begin{pmatrix}\varepsilon_1\|\boldsymbol{u}\|\|\boldsymbol{p}_0\|-\varepsilon_1\alpha_1(\boldsymbol{u})\alpha_1(\boldsymbol{p}_0)\hat{\boldsymbol{u}}.\hat{\boldsymbol{p}}_0 & -\varepsilon_0^{\frac{1}{2}}k_0\alpha_1(\boldsymbol{u})(\hat{\boldsymbol{u}}\times\hat{\boldsymbol{p}}_0)_z\\ -\varepsilon_0^{\frac{1}{2}}k_0\alpha_1(\boldsymbol{p}_0)(\hat{\boldsymbol{u}}\times\hat{\boldsymbol{p}}_0)_z & -\varepsilon_0{k_0}^2\hat{\boldsymbol{u}}.\hat{\boldsymbol{p}}_0\end{pmatrix}$$
$$\left[\overline{\boldsymbol{D}}^{+}_{10}(\boldsymbol{p}_0)\right]^{-1}, \tag{A.5}$$

$$\overline{Q}^{-}(\boldsymbol{u}|\boldsymbol{p}_0)=\frac{(\varepsilon_1-\varepsilon_0)}{\alpha_0(\boldsymbol{p}_0)}\left[\overline{\boldsymbol{D}}_{10}-(\boldsymbol{u})\right]-1$$
$$\begin{pmatrix}\varepsilon_0\alpha_1(\boldsymbol{p}_0)\|\boldsymbol{u}\|\|\boldsymbol{p}_0\|-\varepsilon_1\alpha_1(\boldsymbol{u})\alpha_0^2(\boldsymbol{p}_0)\hat{\boldsymbol{u}}.\widehat{\boldsymbol{p}}_0 & -\varepsilon_0^{\frac{1}{2}}k_0\alpha_1(\boldsymbol{u})\alpha_1(\boldsymbol{p}_0)(\hat{\boldsymbol{u}}\times\hat{\boldsymbol{p}}_0)_z\\ -\varepsilon_0^{\frac{1}{2}}k_0\varepsilon_1\alpha_0^2(\boldsymbol{p}_0)(\hat{\boldsymbol{u}}\times\hat{\boldsymbol{p}}_0)_z & \varepsilon_0{k_0}^2\alpha_1(\boldsymbol{p}_0)\hat{\boldsymbol{u}}.\hat{\boldsymbol{p}}_0\end{pmatrix} \tag{A.6}$$
$$.\left[\overline{\boldsymbol{D}}^{+}_{10}(\boldsymbol{p}_0)\right]^{-1},$$

$$\overline{\boldsymbol{p}}(\boldsymbol{u}|\boldsymbol{p}_1)\equiv(\alpha_1(\boldsymbol{u})-\alpha_0(\boldsymbol{u}))\left[\overline{M}^{1+,0+}(\boldsymbol{u}|\,\boldsymbol{u})\right]^{-1}\overline{M}^{1+,0+}(\boldsymbol{u}|\,\boldsymbol{p}_1) \tag{A.7}$$

$$=(\varepsilon_1-\varepsilon_0)\left[\overline{\boldsymbol{D}}^{+}_{10}(\boldsymbol{u})\right]^{-1}.\begin{pmatrix}\|\boldsymbol{u}\|\|\boldsymbol{p}\|+\alpha_1(\boldsymbol{u})\alpha_0(\boldsymbol{p})\hat{\boldsymbol{u}}.\widehat{\boldsymbol{p}}_1 & -\varepsilon_0^{\frac{1}{2}}k_0\alpha_1(\boldsymbol{u})\,(\hat{\boldsymbol{u}}\times\hat{\boldsymbol{p}}_1)_z\\ \varepsilon_0^{\frac{1}{2}}k_0\,\alpha_0(\boldsymbol{p})\,(\hat{\boldsymbol{u}}\times\hat{\boldsymbol{p}}_1)_z & k_0^2\,\hat{\boldsymbol{u}}.\hat{\boldsymbol{p}}_1\end{pmatrix} \tag{A.8}$$

where

$$\overline{\boldsymbol{D}}^{\pm}_{10}(\boldsymbol{p}_0)\equiv\left(\varepsilon_1\alpha_0(\boldsymbol{p}_0)\overset{\pm}{0}\varepsilon_0\alpha_1(\boldsymbol{p}_0)\;\;\alpha_0(\boldsymbol{p}_0)\overset{0}{\pm}\alpha_1(\boldsymbol{p}_0)\right). \tag{A.9}$$

A.2 MUELLER MATRIX AND TENSOR

A.2.1 Tensor product of two matrices

The dimensions of $\overline{\boldsymbol{A}}\{i,\,j\}$, $\overline{\boldsymbol{B}}\{i,\,j\}$ are 2×2, the resulting dimensions are $2\times2\times2\times2$.

$$\overline{\boldsymbol{A}}\otimes\overline{\boldsymbol{B}}=\sum_{i,j,i',j'=1}^{2}\overline{\boldsymbol{A}}\{i,j\}\overline{\boldsymbol{B}}^{*}\{i',j'\}, \tag{A.10}$$

where the asterisk * denotes the complex conjugation of the components.

A.2.2 Product of two tensors defined by the symbol ":"

We define the two tensors $\overline{\boldsymbol{T}}_1\{i,\ j,\ i',\ j'\}$, $\overline{\boldsymbol{T}}_2\{i,\ j,\ i',\ j'\}$.

The product is given by

$$\overline{\boldsymbol{T}}_3\{i,j,i',j'\}=\sum_{i_1,i'_1}\overline{\boldsymbol{T}}_1\{i,i',i_1,i'_1\}\overline{\boldsymbol{T}}^*{}_2\{i_1,i'_1,j,i'\}. \tag{A.11}$$

A.2.3 Mueller matrix

This matrix gives the intensity of the scattered wave as a function of two scattering matrices.

$$\overline{\boldsymbol{M}}(\boldsymbol{p}|\boldsymbol{p}_0)=\bar{f}(\boldsymbol{p}|\boldsymbol{p}_0)\odot\bar{f}(\boldsymbol{p}|\boldsymbol{p}_0), \tag{A.12}$$

$$\bar{f}\odot\bar{g}\equiv\begin{pmatrix}f_{VV} & f_{VH}\\ f_{HV} & f_{HH}\end{pmatrix}\odot\begin{pmatrix}g_{VV} & g_{VH}\\ g_{HV} & g_{HH}\end{pmatrix}=$$

$$\begin{pmatrix}
f_{VV}g^*{}_{VH} & f_{VH}g^*{}_{VH} & \mathrm{Re}(f_{VV}g^*{}_{VH}) & -\mathrm{Im}(f_{VV}g^*{}_{VH})\\
f_{HV}g^*{}_{HV} & f_{HH}g^*{}_{HH} & \mathrm{Re}(f_{HV}g^*{}_{HH}) & -\mathrm{Im}(f_{HV}g^*{}_{HH})\\
2\mathrm{Re}(f_{VV}g^{*VH}) & 2\mathrm{Re}(f_{VH}g^*{}_{HH}) & 2\mathrm{Re}(f_{VH}g^*{}_{HH}+f_{VH}g^*{}_{HV}) & -\mathrm{Im}(f_{VV}g^*{}_{HH}-f_{VH}g^*{}_{HV})\\
2\mathrm{Im}(f_{VV}g^{*VH}) & 2\mathrm{Im}(f_{VH}g^*{}_{HH}) & 2\mathrm{Im}(f_{VH}g^*{}_{HH}+f_{VH}g^*{}_{HV}) & \mathrm{Re}(f_{VV}g^*{}_{HH}-f_{VH}g^*{}_{HV})
\end{pmatrix} \tag{A.13}$$

A.2.4 Transformation Tr™

This operator transforms a tensor into a Mueller matrix:

$$Tr^{\otimes\to\odot}\overline{\boldsymbol{A}}^1\otimes\overline{\boldsymbol{A}}^{2*}=\overline{\boldsymbol{A}}^1\odot\overline{\boldsymbol{A}}^2, \tag{A.14}$$

where $\overline{A}^1$ and $\overline{A}^2$ are dyadic operators.

A.2.5 Right transpose of a tensor (the demonstration can be found in Akkermans et al. (1988), Eq. D)

$$\left[\overline{\boldsymbol{M}}(\boldsymbol{p}|\boldsymbol{p}_0)\right]^{T_R}=\sum_{\beta,\beta',\beta_0,\beta'_0,=H,V}\boldsymbol{M}^{TR}{}_{\beta,\beta';\beta_0,\beta'_0}\left(\hat{\boldsymbol{e}}_\beta{}^{0+}(p)\otimes\hat{\boldsymbol{e}}_\beta{}^{0+}(p)\right)\left(\hat{\boldsymbol{e}}_\beta{}^{0+}(p)\otimes\hat{\boldsymbol{e}}_\beta{}^{0+}(p_0)\right), \tag{A.15}$$

with

$$M^{T_R}{}_{\beta\beta';\beta_0\beta'_0}=M_{\beta\beta'_0;\beta\beta'}\quad\text{if}\quad\beta'=\beta'_0, \tag{A.16}$$

$$M^{TR}{}_{\beta,\beta';\beta_0,\beta'_0}=-M_{\beta\beta'_0;\beta\beta'}\quad\text{if}\quad\beta'\neq\beta \tag{A.17}$$

for β, β', β_0, $\beta'_0=H$, V.

ACKNOWLEDGMENTS

The authors would like to thank Dr. Elena I. Chaikina for preparing Figs. 6.1, 6.3, and 6.5; Professor Ingve Simonsen for providing Fig. 6.4; Professor Ingve Simonsen and Messers. Paul Anton Letnes and Tor Nordam for providing Figs. 6.8 and 6.9; Dr. Claude Bourrely for the numerical calculations necessary for many of the figures of Section 6.7 and Dr. Michel Jouffroy for providing figures for Section 6.8.

The research of A.A. Maradudin was supported in part by Air Force Research Laboratory contract FA 9453–08-C-0230.

REFERENCES

Akkermans, E., Wolf, P.E., Maret, G., 1988. Theoretical study of the coherent backscattering of light by disordered media. J. Phys. France. 49, 77–98.

Apresyan, L.A., Kravtsov, Y.A., 1996. Radiation Transfer: Statistical and Wave Aspects. Gordon and Breach, Amsterdam.

Avrutsky, I., Zhao, Y., Kochergin, V., 2000. Surface-plasmon-assisted resonant tunneling of light through periodically corrugated thin metal film. Opt. Lett. 25, 595–597.

Bahar, E., 1981. Full wave solutions for the depolarization of the scattered radiation fields by rough surfaces of arbitrary slopes. IEEE Trans. Antennas Propag. 29, 443–454.

Barabanenkov, Y.N., Ozrin, V.D., 1988. Coherent enhancement of backscattered radiation in a randomly inhomogeneous medium: the diffusion approximation. Sov. Phys. JETP. 67, 1117–1121.

Barabanenkov, Y.N., Kravtsov, Y.A., Ozrin, V.D., Saichev, A.I., 1991. Enhanced backscattering in optics. Prog. Opt. 29, 65–197.

Barabanenkov, Y.N., Zurk, L.M., Barabanenkov, M.Y., 1997. Single scattering and diffusion approximations for modified radiative transfer theory of wave multiple scattering in dense media near resonance. Prog. Electromagn. Res. 15, 27–61.

Baumeier, B., Leskova, T.A., Maradudin, A.A., 2006. Transmission of light through a thin metal film with periodically and randomly corrugated surfaces. *J. Opt.* A 8, S191S207.

Beckmann, A., Spizzichino, A., 1963. The Scattering of Electromagnetic Waves from Rough Surfaces. Pergamon, Oxford.

Berechet, I., Berginc, G., 2011. Advanced algorithms for identifying targets from a three-dimensional reconstruction of sparse 3D Ladar data. Proc. SPIE 8172, 81720Z.

Berginc, G., 2002. Small-slope approximation method: a further study of vector wave scattering from two-dimensional surfaces and comparison with experimental data. PIER 37, 251–287.

Berginc, G., 2007. Small-amplitude perturbation theory for two-dimensional surfaces. In: Maradudin, A.A. (Ed.), Light Scattering and Nanoscale Surface Roughness. Springer, Berlin.

Berginc, G., Bourrely, C., 2007. The small-slope approximation method applied to a three-dimensional slab with rough boundaries. PIER 73, 131–211.

Berginc, G., Jouffroy, M., 2010. Simulation of 3D laser imaging. PIERS Online 6 (5), 415–419.

Berginc, G., Jouffroy, M., 2011. 3D laser imaging. PIERS Online 7 (5), 411–415.

Berginc, G., Maradudin, A.A., 2013. Reduced Rayleigh equations for the scattering of p- and s-polarized light from and its transmission through a film with two 1D rough surfaces. In: Piegari, A., Flory, F. (Eds.), Optical Thin Films and Coatings, first ed. Woodhead Publishing, Oxford, pp. 177–289.

Bourlier, C., Berginc, G., Saillard, J., 2001. Theoretical study of the Kirchhoff integral from a two-dimensional randomly rough surface with shadowing effect: application to the backscattering coefficient for a perfectly-conducting surface. Waves Random Media 11, 91–118.

Brown, G.C., Celli, V., Haller, M., Marvin, A., 1984. Vector theory of light scattering from a rough surface: Unitary and reciprocal expansions. Surf. Sci. 136, 381–387.

Engheta, N., Murphy, W.D., Rokhlin, V., Vassilou, M.S., 1992. The fast multipole method (FMM) for electromagnetic scattering problems. IEEE Trans. Antenna Propag. 40, 634–641.

Etemad, S., Thompson, R., Andrejco, M.J., 1986. Weak localization of photons: universal fluctuations and ensemble averaging. Phys. Rev. Lett. 57, 575–578.

Feldkamp, L.A., Davis, L.C., Kress, J.W., 1984. Practical cone-beam algorithm. *J. Opt. Soc. Am.* A 6, 612–619.

Fitzgerald, R.M., Leskova, T.A., Maradudin, A.A., 2005. Transmission of light through a metal film with two corrugated surfaces. Proc. SPIE 5878 (58780Z), 1–14.

Freilikher, V., Pustilnik, M., Yurkevich, I., 1994. Wave scattering from a bounded medium with disorder. *Phys. Lett.* A 193, 467–470.

Frisch, U., 1968. Wave propagation in random medium. In: Bharucha-Reid, A. (Ed.), Probabilistic Methods in Applied Mathematics. In: vol. 1. Academic Press, New York.

Furutsu, K., 1983. Random Media and Boundaries – Unified Theory, Two-Scale Method, and Applications. Springer-Verlag, Berlin.

Furutsu, K., 1991. Random-volume scattering: Boundary effects, and enhanced backscattering. Phys. Rev. A 43, 2741–2762.

Gilbert, M.S., Johnson, J.T., 2003. A study of the higher-order small-slope approximation for scattering from a Gaussian rough surface. Waves Random Media 13, 137–149.

González-Alcalde, A.K., Banon, J.P., Hetland, Ø.S., Maradudin, A.A., Méndez, E.R., Nordam, T., Simonsen, I., 2016. Experimental and numerical studies of the scattering of light from a two-dimensional randomly rough interface in the presence of total internal reflection: optical Yoneda peaks. Opt. Express 24 (23), 25995–26005.

Gorodnichev, E.E., Dudarev, S.L., Rogozkin, D.B., Ryazanov, M.I., 1987. Coherent effects in backscattering of waves from a medium with random inhomogeneities. Sov. Phys. JETP. 66, 938–944.

Gorodnichev, E.E., Dudarev, S.L., Rogozkin, D.B., 1989. Coherent backscattering enhancement under conditions of weak wave localization in disordered 3D and 2D systems. Sov. Phys. JETP. 69, 481–490.

Greffet, J.J., 1988. Scattering of electromagnetic waves by rough dielectric surfaces. Phys. Ther. Rev. 37, 6436–6441.

Jandhyala, V., Shanker, B., Michielssen, E., Chew, W.C., 1998. Fast algorithm for the analysis of scattering by dielectric rough surfaces. *J. Opt. Soc. Am.* A 15, 1877–1885.

Johnson, J.T., 1999. Third order small perturbation method for scattering from dielectric rough surfaces. *J. Opt. Soc. Am.* A 16, 2720–2736.

Johnson, J.T., Tsang, L., Shin, R.T., Pak, K., Chan, C.H., Ishimaru, A., Kuga, Y., 1996. Backscattering enhancement of electromagnetic waves from two-dimensional perfectly conducting random rough surfaces: a comparison of Monte Carlo simulations with experimental data. IEEE Trans. Antenna Propag. 44, 748–756.

Johnson, P.B., Christy, R.W., 1972. Optical constants of the noble metals. *Phys. Rev.* B 6, 4370–4379.

Kawanishi, T., Ogura, H., Wang, Z.L., 1997a. Scattering of an electromagnetic wave from a planar waveguide structure with a slightly 2D random surface. Waves Random Media. 7, 35–64.

Kawanishi, T., Ogura, H., Wang, Z.L., 1997b. Scattering of an electromagnetic wave from a slightly random dielectric surface: Yoneda peak and Brewster angle in incoherent scattering. Waves Random Media 7, 351–384.

Kuga, Y., Ishimaru, A., 1984. Retroreflectance from a dense distribution of spherical particles. *J. Opt. Soc. Am.* A 1, 831–835.

Kuz'min, V.L., Romanov, V.P., 1996. Coherent phenomena in light scattering from disordered systems. Physics Uspekhi 39, 231–260.

Lam, C.M., Ishimaru, A., 1994. Mueller matrix calculation for a slab of random medium with both random rough surfaces and discrete particles. IEEE Trans. Antenna Propag. 44, 145–156.

Leskova, T.A., Maradudin, A.A., 1997. X-ray scattering from a randomly rough surface. Waves Random Media 7, 395–434.

Leskova, T.A., Maradudin, A.A., 2008. Reduced Rayleigh equations in the scattering of s-polarized light from, and its transmission through, a film with two one-dimensional rough surfaces. Proc. SPIE 7065 (706505), 1–12.

Leskova, T.A., Maradudin, A.A., Zierau, W., 2005. Surface plasmon polariton propagation near an index step. Opt. Commun. 249, 23–35.

Leskova, T.A., Letnes, P.A., Maradudin, A.A., Nordam, T., Simonsen, I., 2011. The scattering of light from two-dimensional randomly rough surfaces. *Proc* SPIE 8172 (817209), 1–20.

Madrazo, A., Maradudin, A.A., 1997. Numerical solutions of the reduced Rayleigh equation for the scattering of electromagnetic waves from rough dielectric films on perfectly conducting substrates. Opt. Commun. 134, 251–268.

Maradudin, A.A., Méndez, E., Michel, T., 1989. Backscattering effects in the elastic scattering of p-polarized light from a large amplitude random metallic grating. Opt. Lett. 14, 151–153.

Maradudin, A.A., Michel, T., McGurn, A.R., Méndez, E.R., 1990. Enhanced backscattering of light from a random grating. Ann.Phys. (N.Y.) 203, 255–307 Appendix A.

Maradudin, A.A., McGurn, A.R., Méndez, E.R., 1995. Surface plasmon polariton mechanism for enhanced backscattering of light from one-dimensional randomly rough metal surfaces. *J. Opt. Soc. Am.* A 12, 2500–2506.

McGurn, A.R., Maradudin, A.A., 1989. An analogue of enhanced backscattering in the transmission of light through a thin film with a randomly rough surface. Opt. Commun. 72, 279–285.

McGurn, A.R., Maradudin, A.A., 1996. Perturbation theory results for the diffuse scattering of light from two-dimensional randomly rough surfaces. Waves Random Media 6, 251–267.

McGurn, A.R., Maradudin, A.A., Celli, V., 1985. Localization effects in the scattering of light from a randomly rough grating. Phys. Rev. B 31, 4866–4871.

Mudaliar, S., 1994. Electromagnetic wave scattering from a random medium layer with a random interface. Waves Random Media 4, 167–176.

Mudaliar, S., 1999. Scattering from a rough layer of a random medium. Waves Random Media 9, 521–536.

Mudaliar, S., 2001. Diffuse waves in a random medium layer with rough boundaries. Waves Random Media 11, 45–60.

Nieto-Vesperinas, M., 1982. Depolarisation of electromagnetic waves scattered from slightly rough random surfaces: a study by means of the extinction theorem. J. Opt. Soc. Am. A 72, 539–547.

Nordam, T., Letnes, P.A., Maradudin, A.A., Simonsen, I., 2012. Satellite peaks in the scattering of light from the two-dimensional surface of a dielectric film on a planar metal surface. Opt. Express 20, 11336–11350.

Nordam, T., Letnes, P. A., Simonsen, I., n.d. Unpublished work.
Ogilvy, J.A., 1991. Theory of Wave Scattering from Random Rough Surfaces. Adam Hilger, Bristol.
Pak, K., Tsang, L., Li, L., Chan, C., 1993. Combined random rough surface and volume scattering based on Monte-Carlo solutions of Maxwell's equation. Radio Sci. 28, 331–338.
Pak, K., Tsang, L., Chan, C.H., Johnson, J.T., 1995. Backscattering enhancement of the electromagnetic waves from two-dimensional perfectly conducting random rough surfaces based on Monte Carlo simulations. *J. Opt. Soc. Am.* A 12, 2491–2499.
Pak, K., Tsang, L., Johnson, J.T., 1997. Numerical simulations and backscattering enhancement of electromagnetic waves from two-dimensional dielectric random rough surfaces with the sparse-matrix canonical grid method. *J. Opt. Soc. Am.* A 14, 1515–1529.
Porto, J.A., Garcia-Vidal, F.T., Pendry, J.B., 1999. Transmission resonances on metallic gratings with very narrow slits. Phys. Rev. Lett. 83, 2845–2848.
Press, W.H., Teukolsky, S.A., Vetterling, W.T., Flannery, B.P., 1992a. Numerical Recipes, third ed. Cambridge University Press, New York, p. 160.
Press, W.H., Teukolsky, S.A., Vetterling, W.T., Flannery, B.P., 1992b. Numerical Recipes, third ed. Cambridge University Press, New York, p. 605.
Press, W.H., Teukolsky, S.A., Vetterling, W.T., Flannery, B.P., 2007a. Numerical Recipes, third ed. Cambridge University Press, New York, p. 605.
Press, W.H., Teukolsky, S.A., Vetterling, W.T., Flannery, B.P., 2007b. Numerical Recipes, third ed. Cambridge University Press, New York, p. 161.
Rice, S.O., 1951. Reflection of electromagnetic waves from slightly rough surfaces. Commun. Pure Appl. Math. 4, 351–378.
Sánchez-Gil, J.A., Maradudin, A.A., Jun, Q.L., Freilikher, V.D., Pustilnik, M., Yurkevich, I., 1994a. Scattering of electromagnetic waves from a bounded medium with a random surface. *Phys. Rev.* B 50, 15353–15368.
Sánchez-Gil, J.A., Maradudin, A.A., Lu, J.Q., Freilikher, V.D., 1994b. New features in the transmission of light through thin metal films with randomly rough surfaces. In: Stein, I.I. (Ed.), IGARSS/IEEE 94 Digest. IEEE Publications, Piscataway, NJ, pp. 273–276.
Sánchez-Gil, J.A., Maradudin, A.A., Lu, J.Q., Freilikher, V.D., 1995. Transmission of electromagnetic waves through thin metal films with randomly rough surfaces. *Phys. Rev.* B 51, 17100–17115.
Sánchez-Gil, J.A., Maradudin, A.A., Jun, Q.L., Freilikher, V.D., Pustilnik, M., Yurkevich, I., 1996. Satellite peaks in the scattering of p-polarized light from a randomly rough film on a perfectly conducting substrate. J. Mod. Opt. 43, 435–452.
Shchegrov, A.V., Maradudin, A.A., Mendez, E.R., 2004. Multiple scattering of light from randomly rough surfaces. In: Wolf, E. (Ed.), Progress in Optics. In: vol. 46. Elsevier, 1 (Chapter 2).
Shen, J., Maradudin, A.A., 1980. Multiple scattering of waves from random rough surfaces. Phys. Rev. B 22, 4234–4240.
Sheng, P., 1995. Introduction to Wave Scattering, Localization, and Mesoscopic Phenomena. Academic Press, New York.
Simonsen, I., Maradudin, A.A., 1999. Numerical simulation of electromagnetic wave scattering from planar dielectric films deposited on rough perfectly conducting substrates. Opt. Commun. 162, 99–111.
Simonsen, I., Maradudin, A.A., Leskova, T.A., 2010a. Scattering of electromagnetic waves from two-dimensional randomly rough perfectly conducting surfaces: the full angular intensity distribution. *Phys. Rev.* A 81 (013806), 1–13.

Simonsen, I., Maradudin, A.A., Leskova, T.A., 2010b. Scattering of electromagnetic waves from two-dimensional randomly rough penetrable surfaces. Phys. Rev. Lett. 223904 (1–4), 104.

Simonsen, I., Kryvi, J.B., Maradudin, A.A., Leskova, T.A., 2011. Light scattering from anisotropic, randomly rough, perfectly conducting surfaces. Comput. Phys. Commun. 182, 1904–1908.

Sinha, S.K., Sirota, E.B., Garoff, S., Stanley, H.B., 1988. X-ray and neutron scattering from rough surfaces. Phys. Rev. B 38, 2297–2311.

Soriano, G., Saillard, M., 2001. Scattering of electromagnetic waves from two-dimensional rough surfaces with an impedance approximation. *J. Opt. Soc. Am.* A 18, 124–133.

Soubret, A., Berginc, G., 2003a. Electromagnetic wave scattering from a random layer with rough interfaces I: coherent field. arXiv physics/**0312133**.

Soubret, A., Berginc, G., 2003b. Electromagnetic wave scattering from a random layer with rough interfaces II: diffusive intensity. arXiv:physics/**0312136**.

Soubret, A., Berginc, G., 2003c. Effective dielectric constant for random medium, arXiv: physics/0312117.

Soubret, A., Berginc, G., Bourrely, C., 2001a. Application of reduced Rayleigh equations to electromagnetic wave scattering by two-dimensional rough surfaces. *Phys. Rev.* B 63 (245411), 1–20.

Soubret, A., Berginc, G., Bourrely, C., 2001b. Backscattering enhancement of an electromagnetic wave scattered by two-dimensional rough layers. *J. Opt. Soc. Am.* A 18, 2778–2788.

Soubret, A., Berginc, A., Bourrely, C., 2003. Application of reduced Rayleigh equations to electromagnetic wave scattering by two-dimensional randomly rough surfaces. *Phys. Rev.* B 53 (245411), 1–20.

Stephen, M.J., Cwilich, G., 1986. Rayleigh scattering and weak localization: effects of polarization. *Phys. Rev.* B 34, 7564–7572.

Tatarskii, V.I., 1993. The expansion of the solution of the rough-surface scattering problem in powers of quasi-slopes. Waves Random Media 3, 127–146.

Toigo, F., Marvin, A., Celli, V., Hill, N.R., 1977. Optical properties of rough surfaces: General theory and the small roughness limit. *Phys. Rev.* B 15, 5618–5626.

Torrungrueng, D., Chou, H.-T., Johnson, J.T., 2000. A novel acceleration algorithm for the computation of scattering from two-dimensional large-scale perfectly conducting random rough surfaces with the forward-backward method. IEEE Trans. Geosci. Remote Sensing. 38, 1656–1668.

Tran, P., Maradudin, A.A., 1994. Scattering of electromagnetic waves from a randomly rough 2D metallic surface. Opt. Commun. 110, 269–273.

Tran, P., Celli, V., Maradudin, A.A., 1994. Electromagnetic scattering from a two-dimensional, randomly rough, perfectly conducting surface: iterative methods. *J. Opt. Soc.Am.*A 11, 1685–1689.

Tsang, L., Ishimaru, A., 1984. Backscattering enhancement of random discrete scatterers. *J. Opt. Soc. Am.* A 1, 836–839.

Tsang, L., Ishimaru, A., 1985. Theory of backscattering enhancement of random discrete isotropic scatterers based on the summation of all ladder and cyclical terms. *J. Opt. Soc. Am.* A 2, 1331–1338.

Tsang, L., Kong, J.A., 2001. Scattering of Electromagnetic Waves, Advanced Topics. Wiley-Interscience, New York.

Tsang, L., Kong, J.A., Shin, R., 1985. Theory of Microwave Remote Sensing. Wiley-Interscience, New York.

Tsang, L., Chan, C.H., Pak, K., 1994. Backscattering enhancement of a two-dimensional random rough surface (three-dimensional scattering) based on Monte Carlo simulations. *J. Opt. Soc. Am.* A 11, 711–715.
van Albada, M.P., Lagendijk, A., 1985. Observation of weak localization of light in a random medium. Phys. Rev. Lett. 55, 2692–2695.
van der Mark, M.B., van Albada, M.P., Lagendijk, A., 1988. Light scattering in strongly scattering media: multiple scattering and weak localization. *Phys. Rev.* B 37, 3575–3592.
van Rossum, M.C.W., Nieuwenhuizen, T.M., 1999. Multiple scattering of classical waves: Microscopy, mesoscopy and diffusion. Rev. Mod. Phys. 71, 313–371.
van Tiggelen, B.A., 1999. Localisation of waves. In: Fouque, J. (Ed.), Diffuse Waves in Complex Media. Kluwer, Amsterdam, pp. 1–60.
van Tiggelen, B.A., Maynard, R., 1997. Reciprocity and coherent backscattering of light. In: -Papanicolaou, G. (Ed.), Wave Propagation in Complex Media. Springer-Verlag, Berlin, pp. 247–271.
Vineyard, G.H., 1982. Grazing-incidence diffraction and the distorted-wave approximation for the study of surfaces. Phys. Rev. B 26, 4146–4159.
Voronovich, A.G., 1985. Small-slope approximation in wave scattering by rough surfaces. Sov. Phys. JETP. 62, 65–70.
Voronovich, A.G., 1994a. Small-slope approximation for electromagnetic wave scattering at a rough interface of two dielectric half-space. Waves Random Media 4, 337–367.
Voronovich, A.G., 1994b. Wave Scattering from Rough Surfaces. Springer, Berlin.
Voronovich, A.G., 1996a. A two-scale model from the point of view of small-slope approximation. Waves Random Media 6, 73–83.
Voronovich, A.G., 1996b. Non-local small-slope approximation for wave scattering from rough surfaces. Waves Random Media 6, 151–167.
Wagner, R.L., Song, J., Chew, W.C., 1997. Monte Carlo simulation of electromagnetic scattering from two-dimensional randomly rough surfaces. IEEE Trans. Antenna Propag. 45, 235–245.
Wang, Z.L., Ogura, H., Takahashi, N., 1995. Enhanced scattering from a planar waveguide with a slightly rough boundary. *Phys. Rev.* B 52, 6027–6041.
West, C.S., O'Donnell, K.A., 1995. Observation of backscattering enhancement from polaritons on a rough metal surface. J. Opt. Soc. Am. A 12, 390–397.
Winebrenner, D.P., Ishimaru, A., 1985. Investigation of a surface-field phase-perturbation technique for scattering from rough surfaces. Radio Sci. 20, 161–170.
Wolf, P.E., Maret, G., 1985. Weak localization and coherent backscattering of photons in disordered media. Phys. Rev. Lett. 55, 2696–2699.
Yoneda, Y., 1963. Anomalous surface reflection of x-rays. Phys. Ther. Rev. 131, 2010–2013.

FURTHER READING

Fuks, I.M., Voronovich, A.G., 2000. Wave diffraction by rough interfaces in an arbitrary plane-layered medium. Waves Random Media 10, 253–272.
Lagendijk, A., van Tiggelen, B.A., 1996. Resonant multiple scattering of light. Phys. Rep. 270, 143–216.

This page intentionally left blank

CHAPTER

Optical properties of thin film materials at short wavelengths

7

Juan I. Larruquert
Institute of Optics-Spanish National Research Council, Madrid, Spain

7.1 INTRODUCTION

Electromagnetic waves are governed by equations that are common to the whole spectrum. This property displays the power and the beauty of the involved physics. However, materials behave very differently over the spectrum, which breaks to some extent this uniformity. The differences on material behavior are remarkable when one moves from the visible to shorter wavelengths, where dielectric materials start absorbing light somewhere in the ultraviolet (UV) until no material in nature is found to be transparent any more. When one moves to even shorter wavelengths, this lossy range is left behind and now materials start to interact less and less with radiation: we have reached the X-rays and gamma rays. This chapter is devoted to the description of these two regimes of material behavior at short wavelengths. The optical properties of a material are characterized at each wavelength by the refractive index n and the extinction coefficient k, usually named together as the optical constants. n is involved in the refraction introduced by the material, whereas k governs radiation absorption. Regarding the two distinctive regimes mentioned above, the first regime encountered at short wavelengths is characterized by a large value of k, whereas the second regime at even shorter wavelengths shows a continuous trend for a decreasing k, along with n approaching unity.

7.2 MATERIAL BEHAVIOR OVER THE SPECTRUM

The short-wavelength part of the spectrum can be divided into various ranges. Names for these ranges are not universal; the definitions used here are based on some natural thresholds and some simple wavelength numbers. At wavelengths shorter than the visible range, a first strong threshold on material behavior is found at $\approx$200 nm, where normal air (more properly, its oxygen component) starts to absorb radiation. This feature involves important technological implications, since radiation requires vacuum to propagate. For this reason, we call the range below 200 nm as the vacuum

Optical Thin Films and Coatings. https://doi.org/10.1016/B978-0-08-102073-9.00007-2
Copyright © 2018 Elsevier Ltd. All rights reserved.

ultraviolet. However, the range where air absorbs is wide and it is convenient to split it up into several subranges. The first subrange below 200 nm will be called the far ultraviolet (FUV), as the next in the series of near UV (NUV) and mid-UV. In spite of the strong absorption of air and most materials, a few of them are still transparent in the FUV, until a new threshold is reached: at ≈ 100 nm the last transparent material in nature, lithium fluoride (LiF), starts to absorb radiation. We are in front of a strong threshold for optics below 100 nm: the lack of windows and of the possibility to harness light through refraction, along with the difficulty to device efficient multilayer coatings. This threshold marks the entrance to the extreme ultraviolet (EUV), which will refer here to wavelengths shorter than 100 nm. The strong absorption of materials in the long EUV is due to the radiation excitation of outer-shell electrons; the energy levels of these less-bound electrons are strongly affected by the chemical bonds of atoms. At short wavelengths, photons are often referred to for their energy in electron volts:

$$E\ (\text{eV}) = \frac{hc}{\lambda} = \frac{1239.8}{\lambda\ (\text{nm})} \tag{7.1}$$

The strong EUV absorption of materials starts to decrease below ≈ 50 nm, that is, above ≈ 25 eV, although the specific wavelength depends on the material. When radiation wavelength keeps decreasing, and hence photon energy increases, the photon energy becomes large enough as to eject an electron from the second outermost shell of the atom; contrary to outer-shell electrons, the energy levels of more tightly bound electrons are much less affected by atom chemical bonds. We can call X-rays as the range at which tightly bound electrons are excited. The threshold for tightly bound electron excitation (electrons originating in a shell between the second outer one and the innermost one) varies with the material and hence the edge between EUV and X-rays is somewhat arbitrary; we will use here 10 nm (124 eV), even though for many materials the excitation of inner electrons starts at somewhat longer wavelengths. The penetration capacity of X-rays through matter increases with photon energy; X-rays are divided into the less penetrating ones, soft X-rays (SXR), and the more penetrating ones, hard X-rays (HXR). The edge between SXR and HXR can be placed at 0.1 nm (12.4 keV), which is in the order of the atom diameter. We have seen that absorption of materials starts to decrease below ≈ 50 nm; the wavelength below which we could say that transparent materials are again available can be placed at ≈ 1 nm (1.24 keV), where a mostly transparent, several-micron-thick Be window can hold vacuum over square-centimeter areas (Attwood, 1999). The absorption of air starts to be low enough as to enable optical systems operating in normal air (for a path of one decimeter) at wavelengths below ≈ 0.2 nm ($E > 6.2$ keV), at the short-wavelength part of SXR. Hence the wavelength range that requires vacuum to propagate spans over the ≈ 0.2–200 nm (6.2 eV to 6.2 keV) range, which involves SXR, EUV, and FUV.

The next edge for radiation interaction with materials is gamma rays, with wavelengths shorter than ≈ 0.01 nm ($E > 124$ keV), which is a markedly subatomic size.

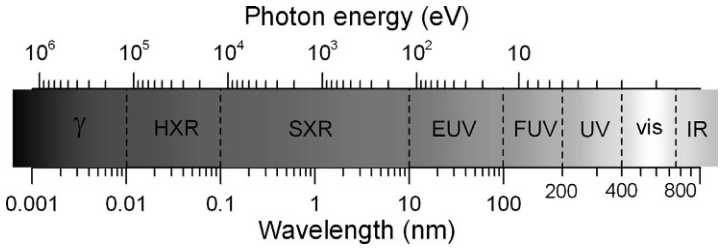


FIG. 7.1

Names and limits of ranges in the electromagnetic spectrum as used in the chapter.

The edge between HXR and gamma rays is not abrupt either and there is some common wavelength range where radiation will be called X-rays when they are emitted by electrons, and gamma rays when they are emitted by the nucleus. SXR, HXR, and gamma are ranges of decreasing absorption and refraction so that optical elements, and particularly coatings, become less and less efficient to manipulate radiation. Fig. 7.1 depicts the short-wavelength ranges over the spectrum.

In addition to what was said on absorption, materials show some other specific features at short wavelengths which differ from those exhibited in the visible:

- Reduced refraction in the SXR and shortwards, with the refractive index approaching unity. This makes light manipulation inefficient.
- Relaxed diffraction limit, which reduces with wavelength. This enables imaging with better resolution, useful for fields like microscopy or optical projection lithography.
- Increased scattering, which depends on the average roughness height normalized to wavelength.
- Total reflection at grazing incidence due to a refractive index slightly lower than unity in the SXR-HXR and the short EUV.
- Distinctive information obtained from materials compared to the visible; useful for spectroscopy in applications such as astrophysics, hot plasma diagnostics, and also X-ray photoelectron spectroscopy.
- High-energy photons. This results in a large penetration in the HXR and gamma, useful in medicine through radiography and scintigraphy. It also enables short-time pulses, such as attosecond pulses, which require photon energy at least in the short EUV because pulses must spread in a wide energy band.
- Ionizing radiation, which includes EUV, SXR, HXR, and gamma. This results in a health hazard, mainly with the latter two because they can propagate in air.

Fig. 7.2 displays $\delta = 1 - n$ and k for SiC in a broad spectrum, where the high absorption in the ultraviolet and the decrease of absorption and refraction at short wavelengths can be observed; δ is used for convenience when n is lower than unity.

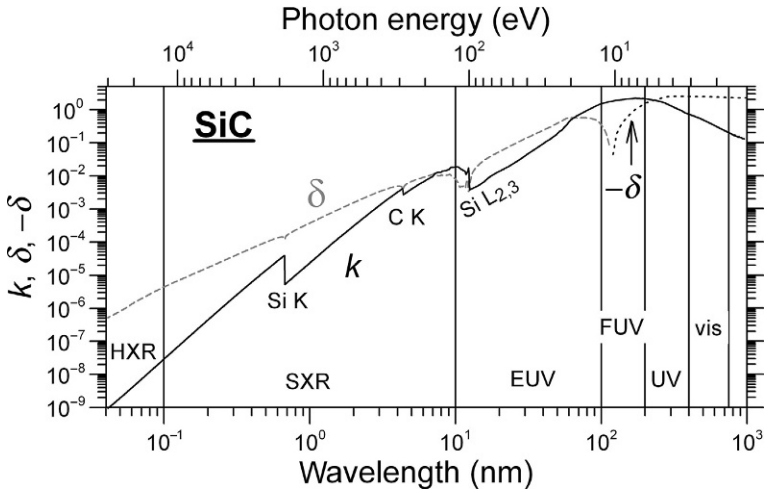


FIG. 7.2

k and $\delta = 1 - n$ of SiC in a broad spectral range (Larruquert et al., 2011a). At long wavelengths $-\delta = n - 1$ is plotted.

7.3 REFLECTION AND TRANSMISSION IN ABSORBENT MATERIALS

The absorption degree of a material is included in the refractive index as an imaginary part, turning the refractive index into a complex number:

$$N = n + ik \tag{7.2}$$

where the imaginary part k is called the extinction coefficient. In Eq. (7.2), k is always positive. It is also possible to work with a negative k in Eq. (7.2); both are correct if used properly and the specific sign depends on the choice of the temporal wave term $\exp(\pm i\omega t)$ (Holm, 1998). The complex index N is also usually called the refractive index, like its real part. To avoid confusion, we will use here the upper case for the complex number and the lower case for its real part. The transmission of light through an absorbent medium with thickness x, assuming reflectance is negligible, is given by the Beer-Lambert law:

$$I = I_0 e^{-\mu x} \tag{7.3}$$

where I_0 and I are the radiation irradiance (often called intensity) that enters and exits the medium, respectively. μ (also α is often used) stands for the absorption coefficient, which is related to k through

$$\mu = \frac{4\pi k}{\lambda} \tag{7.4}$$

where λ is the radiation wavelength in vacuum.

Let us review the formulae for the reflection and transmission at a boundary. Let a plane wave impinge from a nonabsorbent medium with refractive index n_0 onto an absorbent medium with refractive index $N_1 = n_1 + ik_1$. Let the incoming wave vector $\mathbf{k}$ (bold face, to avoid confusion with the extinction coefficient) form an angle θ_0 with the normal to the interface, which will be called the incidence angle. Then Snell's law of refraction can be extended to interfaces with absorbent materials through

$$n_0 \sin \Theta_0 = N_1 \ \sin \Theta_1 \tag{7.5}$$

This is a convenient expression although it must be understood correctly. Since N_1 is complex, so must be Θ_1. This does not mean that the light propagates with a complex angle; Eq. (7.5) and Θ_1 are just convenient tools to calculate radiation propagation through absorbent materials. The fact that Θ_1 is complex arises in that radiation in the absorbent medium propagates as an inhomogeneous wave, that is, the planes of constant amplitude are not coincident with the planes of constant phase, except at normal incidence (where Θ_1 turns real). The planes of constant amplitude are parallel to the interface, regardless of the incidence angle; the planes of constant phase form a real angle θ_1 (this is the lower case Greek letter versus the upper case complex Θ_1 in Eq. (7.5)) with the normal to the interface and it is given by

$$tg\,\theta_1 = \frac{n_0 \sin \theta_0}{Re(N_1 \cos \Theta_1)} \tag{7.6}$$

where *Re* stands for the real part of the complex number. If the material is transparent and hence N_1 is real, then complex Θ_1 of Eq. (7.6) simplifies to real θ_1. The optical response of materials can be also described with other parameters related with the refractive index, such as the dielectric constant ε (i.e., the permittivity of the material normalized to the vacuum permittivity ε_0), the optical conductivity σ (the electrical conductivity in the presence of an electromagnetic wave), and the susceptibility χ (the polarization in response to an electromagnetic wave):

$$\varepsilon = \varepsilon_1 + i\varepsilon_2 = 1 + \frac{i\sigma(\omega)}{\omega e_0} = 1 + x = N^2 = (n + ik)^2 \tag{7.7}$$

In the above equation, SI units are assumed. All $\varepsilon, \sigma, \chi$, and N are complex for absorbent materials, which means that the specific electrical function will get phase shifted at an interface with an absorbent material with respect to the incoming wave.

Let a plane wave impinge on a plane boundary from medium N_1 to N_2, both absorbent in general. The electric field of the incident wave at the boundary can be decomposed into two components: one in the incidence plane, which is called *p* polarization or TM (transversal magnetic), and the other in the perpendicular plane, which is referred to as *s* polarization or TE (transversal electric). The electric field in the reflected and transmitted waves (both normalized to the incident one) are given by Fresnel coefficients (Hecht, 2002):

$$
\begin{aligned}
r_s &= \frac{N_1 \cos \Theta_1 - N_2 \cos \Theta_2}{N_1 \cos \Theta_1 - N_2 \cos \Theta_2}, \\
t_s &= \frac{2N_1 \cos \Theta_1}{N_1 \cos \Theta_1 + N_2 \cos \Theta_2}, \\
r_p &= \frac{N_2 \cos \Theta_1 - N_1 \cos \Theta_2}{N_2 \cos \Theta_1 + N_1 \cos \Theta_2}, \\
t_p &= \frac{2N_1 \cos \Theta_1}{N_2 \cos \Theta_1 + N_1 \cos \Theta_2},
\end{aligned}
\tag{7.8}
$$

where r_s, r_p, t_s, and t_p are called the reflection and transmission coefficients for the electric fields. When absorbent materials are involved, all these coefficients are complex numbers, which means that at reflection and at transmission, both an amplitude change and also a phase shift are produced, which are given by the coefficient modulus and phase, respectively, of Fresnel coefficients. Depending on the sign convention for the electric field, r_p can be defined with opposite sign (Holm, 1998).

When we go from one interface to the various interfaces of a multilayer, the accumulated value of the electric field due to interferences among radiation reflected at all interfaces, as with transparent materials, is calculated iteratively starting with the innermost interface (Parratt, 1954), or equivalently with a matrix procedure (Abelès, 1948) which gives a total reflected/transmitted electric field (normalized to the incident one). The calculation procedure when layers absorb radiation is formally identical to the case of transparent layers.

In the most usual case of nonabsorbent entrance and exit media, the reflected/transmitted irradiances (intensities) of a multilayer, normalized to the incident one, are given by

$$
\begin{aligned}
R_{s,p} &= \left| r_{s,p} \right|^2 \\
T_{s,p} &= \frac{n_{\text{out}} \cos \theta_{\text{out}}}{n_{\text{in}} \cos \theta_{\text{in}}} \left| t_{s,p} \right|^2
\end{aligned}
\tag{7.9}
$$

where r and t stand for the accumulated value of the reflected or transmitted electric field of the whole multilayer system. Lower case r, t and upper case R, T are used for reflected/transmitted electric field and irradiance ratio, respectively. (Unfortunately, the previous rule to distinguish real/complex refractive indices with lower/upper case is reversed for reflected and transmitted ratios to follow typical notation.) In the following text, the irradiance ratios will simply be named as reflectance and transmittance unless otherwise specified. With absorbent materials, a fraction of the irradiation is lost by absorption A, so that

$$
A + R + T = 1 \tag{7.10}
$$

7.3.1 ROUGHNESS AND SCATTERING

When a wave front interacts with an interface, the presence of roughness distorts the wave front, giving rise to diffusely scattered waves in all directions and to modified (mostly reduced) specular reflectance and direct transmittance

(Kretschmann and Kröger, 1975). Roughness-induced effects are a function of interface roughness normalized to wavelength. When wavelength is long enough, it is technologically feasible to minimize roughness effects, but the shorter the wavelength, the more difficult this minimization, since surface irregularities that are negligible at long wavelengths may be destructive at short ones.

In addition to scattering, the interaction of light with roughness in metals generates absorbent modes called surface plasmons; these modes have a resonant frequency ω_{sp} called the surface plasmon frequency, which for free electron metals is:

$$\omega_{sp} = \frac{\omega_p}{\sqrt{2}} \tag{7.11}$$

where ω_p is the plasma frequency of the metal that will be defined in Section 7.4.3. In Eq. (7.11) light is assumed to impinge on the metal from vacuum. For a metal, the generation of surface plasmons results in a reflectance dip around ω_{sp}. A reflectance dip due to surface plasmon excitation is shown in Fig. 7.3. Surface plasmons are generated by the interaction of radiation with microirregularities with a width narrower than λ, whereas microirregularities wider than λ are responsible for scattered light away from the specular reflection or from the direct transmission.

The exact calculation of roughness effect on optical performance is rather complicated, and usually simple approaches are used. For high-quality optical surfaces, the deviation of the real surface from the theoretical one in the propagation direction

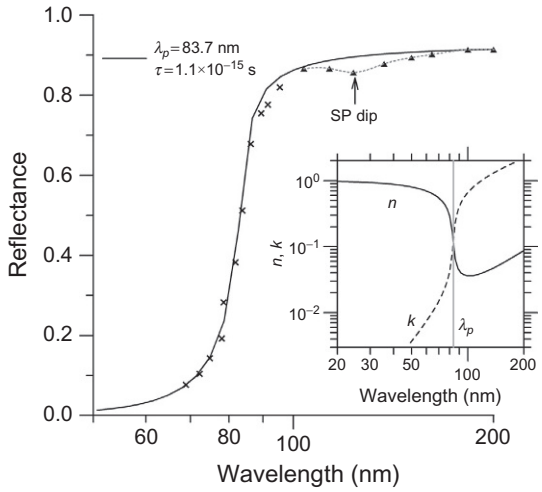


FIG. 7.3

Normal incidence reflectance of Al close to its plasma wavelength. Lines: reflectance calculated with a Drude model with $\lambda_p = 83.7$ nm and $\tau = 1.1 \times 10^{-15}$ s, as reported by Hunter (1964b). These parameters were calculated using the data of La Villa and Mendlowitz (1962) (crosses), Madden et al. (1963) (triangles), and Hunter (1964b). SP stands for surface plasmon. Inset: *n*, *k* calculated using the same Drude model.

can often be considered to be a small fraction of wavelength. This is usually the case in optics, so that perturbation models can be used.

A theory that gives second-order roughness correction for the reflectance and the transmittance at an interface was obtained by Croce (1977, 1978), with no further restriction other than the height of irregularities being small; Kretschmann and Kröger (1975) also developed a second-order theory that is limited to the case of normal incidence. These theories incorporate surface roughness by means of its 2-dimensional power spectral density, which is obtained through the square modulus of the Fourier transform of the roughness height distribution. Computing the effect of roughness on reflectance and transmittance with the Croce model requires some involved calculations. Therefore, more simple models are usually preferred.

The most common simple roughness-induced scattering model is the one based on the work of Debye (1913) and Waller (1923). In this approach roughness irregularities are assumed to have a width much larger than radiation wavelength; even though this requirement is often not satisfied, the model is used anyway for its simplicity. The model does not describe the generation of surface plasmons; it describes roughness through a single parameter, σ, which stands for the root-mean-square (RMS) height of irregularities with respect to an average plane. In this limit, the Fresnel coefficients of Eq. (7.8) can be modified to include surface/interface roughness (Croce, 1977):

$$\begin{aligned} r &= r_0 \exp\left(-\frac{8\pi^2\sigma^2 N_1^2 \cos\Theta_1^2}{\lambda^2}\right) \\ t &= t_0 \exp\left[-\frac{2\pi^2\sigma^2 (N_1\cos\Theta_1 - N_2\cos\Theta_2)^2}{\lambda^2}\right] \end{aligned} \tag{7.12}$$

where r_0 and t_0 stand for the reflection and transmission Fresnel coefficients of an identical interface that is perfectly smooth. N_1 and N_2 stand for the refractive index of the incident and transmission media, respectively. N_1, N_2, Θ_1, and Θ_2 can be complex numbers in general, as described in Section 7.3. A similar result is obtained if the rough interface is approximated by a refractive index continuously progressing from N_1 to N_2 following a certain distribution, such as Gaussian, of width σ (Stearns, 1989 and 1994). At grazing incidence and below the critical angle of total reflection (see Section 7.4.4), Nevot and Croce (1980) found that reflectance measurements fit better with the following equation:

$$r = r_0 \exp\left(-\frac{8\pi^2\sigma N_1 \cos\Theta_1 N_2 \cos\Theta_2}{\lambda^2}\right) \tag{7.13}$$

Additional information on optical effects of roughness can be found in Bennett and Porteus (1961), Kretschmann and Kröger (1975), Croce (1977), Croce (1978), Nevot and Croce (1980), Sinha et al. (1988), Stearns (1992) and Spiller (1994). Windt (1998) developed useful software that addresses all relevant calculations on multilayers with absorbent materials, including the effect of rough interfaces.

7.4 THE OPTICAL CONSTANTS OF MATERIALS AT SHORT WAVELENGTHS

This section gives a simple description of the material-radiation interaction at short wavelengths. More detailed information can be found in the literature (James, 1962; Stern, 1963; Henke et al., 1982; Henke et al., 1993; Spiller, 1994; Chantler et al., 1995; Attwood, 1999; Gullikson, 2000; Kittel, 2005). Other volumes centered on techniques that involve UV radiation also provide valuable information (Samson, 1967b; Samson and Ederer, 2000).

7.4.1 INTERACTION MECHANISMS BETWEEN PHOTONS AND MATTER

Absorption at short wavelengths is mostly due to the interaction of an incoming photon with an electron in an atom. The response of atoms (heavier than electrons) to an electric field results in resonance frequencies much smaller than those of electrons; hence the vibrations of atoms are in the IR, whereas those of electrons lie in the visible and shorter wavelengths. Absorption occurs when the incoming photon energy equals the difference between an occupied and a vacant electron energy level of the material; when the photon energy exceeds the binding energy of the electron, the latter is ejected and the atom or molecule is momentarily ionized. When the material is in a condensed state, the outer electron levels extend through a continuum of energies called bands. The excited or ionized atom or molecule will tend to relax by one or more electron transitions from a higher to a lower level, with the emission of one or more photons and sometimes also an electron. The emitted photon or electron brings important information about the atom or molecule energy levels, which is the basis for various spectroscopy techniques, such as fluorescence spectroscopy and X-ray photoelectron spectroscopy (XPS).

Photons in the visible, NUV, FUV, and long EUV have energies able to excite less-bound electrons, as those in the valence or conduction bands of a crystalline solid; these electrons carry information of the molecular bonds. When photon energy is large enough as to create a vacancy of a tightly bound electron, such as with HXR, SXR, and short EUV, the emitted photon or electron provides information mostly of the energy levels or states of the individual atom involved. Other than the photon-electron interaction, the absorption of high-energy gamma rays may involve interaction with the nucleus.

This simple approach to understanding the optical properties of materials in the FUV and shorter wavelengths will look at which electrons are involved in the absorption.

(a) In a dielectric (or semiconductor), there is no essential absorption while the photon energy is smaller than the material band gap. The band gap energy marks the edge between the transparent and the absorbent range of the material; this is addressed in Section 7.4.2. The largest band gaps (and hence the shortest

wavelength edge between the transparent and the absorbent range) of materials in nature are in the FUV.

(b) In a metal, the less-bound (conduction) electrons can be considered as free and their behavior governs the optical properties of the material, that is, high reflectivity and strong absorption. This is addressed in Section 7.4.3.

(c) In both metal or dielectric, when the photon energy is large enough to excite the inner electron levels of the atom (HXR, SXR, and short EUV) then the difference between metals and dielectrics mostly becomes blurred for optics. This is addressed in Section 7.4.4. An example of this blurring of the difference between metals and dielectrics is displayed in Fig. 7.4, which compares k of metal Sc and dielectric SiO: both show similar trends in the EUV and at shorter wavelengths (except for the specific material absorption edges), and they deviate from each other in the UV and longer wavelengths, where they show their metal or dielectric behavior.

7.4.2 TRANSPARENCY CUTOFF OF DIELECTRICS

In the visible range we are familiar with dielectrics, that is, materials transparent to radiation, which makes them essential in optics, and particularly in optical coatings. In crystalline dielectrics, their transparency arises in that their less-bound electrons fill what is called the valence band, and the next higher allowed level, called the conduction band, is empty; both valence and conduction bands are collective bands

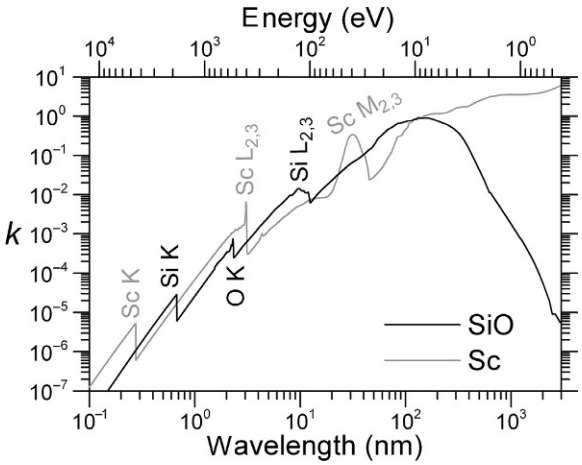


FIG. 7.4

k from the infrared to the SXR for metal Sc (Source: Data taken from Fernández-Perea et al., 2006; Henke et al., 1993; CXRO, n.d.) and dielectric SiO (Source: Data taken from Fernández-Perea et al., 2009; Henke et al., 1993; CXRO, n.d.). Atom absorption edges are indicated.

of the solid. The less-bound electrons of atoms or molecules do not absorb radiation unless the photon energy equals or exceeds the energy difference between the valence and the conduction band, called the band gap. The material is transparent at wavelengths longer than the corresponding band gap wavelength, which we will refer to as the cutoff, whereas it strongly absorbs at wavelengths shorter than the cutoff. It has been observed that crystals having small ions with strong bonding have a wide spectral range of transparency, such as alkali fluorides and alkaline earth fluorides (Li, 1980), as well as lanthanide trifluorides (Lingg, 1990). The materials that keep transparency to the shortest wavelengths include some oxides, such as SiO_2 and Al_2O_3, and finally some fluorides, such as BaF_2 and SrF_2, along with the two materials with the shortest cutoffs in nature: MgF_2 and LiF, which are transparent down to $\approx$115 and 105 nm, respectively. Among lanthanide fluorides, shortest cutoffs stand for LaF_3, GdF_3, and LuF_3, because of their empty, half-filled, and completely filled f shell of the lanthanide atom, respectively. This is due to the lack of atomic transitions that are present on the other lanthanide fluorides, which occur right around or superimposed on the absorption edge (Lingg, 1990). For a material, the cutoff wavelength increases somewhat with temperature due to the thermal broadening of the exciton band and, conversely, the cutoff can be shifted to slightly shorter wavelengths by cooling the material (Laufer et al., 1965; Hunter and Malo, 1969); by cooling a pure crystal of LiF, its cutoff can be moved down to $\approx$100 nm, the absolute shortest wavelength of bulk transmission in nature (the window opens again in the HXR and gamma, as mentioned in Section 7.2). Fig. 7.5 (left) displays the cutoff shift with temperature for a selection of useful materials (Hunter and Malo, 1969).

Coatings deposited on substrates at moderate temperatures are more often either amorphous or nanocrystalline, and hence the energy of the outer electrons does not perfectly follow the bands that are present in single crystals. The presence of defects or impurities in fluorides or oxides results in some blurring of the abrupt cutoffs and in the presence of enhanced absorption compared to the crystalline material in the transparent range, such as for a thin film of MgF_2 versus the MgF_2 crystal in Fig. 7.5 (right).

7.4.3 FREE ELECTRON METALS

For metals there is no gap between valence and conduction bands; the less-bound electrons, which are called conduction (also valence) electrons, are shared by all atoms. For photon energies smaller than the threshold for tightly bound electron excitation, the optical properties of many metals can be reasonably approximated by the simple, free-electron Drude model (Drude, 1900a,b), which assumes that the metal conduction electrons behave like a gas. The derivation of the model is presented in many books (e.g., Ashcroft and Mermin, 1976; Stenzel, 2005). When free conduction electrons sense a harmonic electric field, they give rise to oscillating dipoles, which determine the metal optical constants. In Drude's assumption, this oscillation is damped due to collisions of electrons with the mostly static positive ions of the solid. The Drude model results in the following dielectric constant:

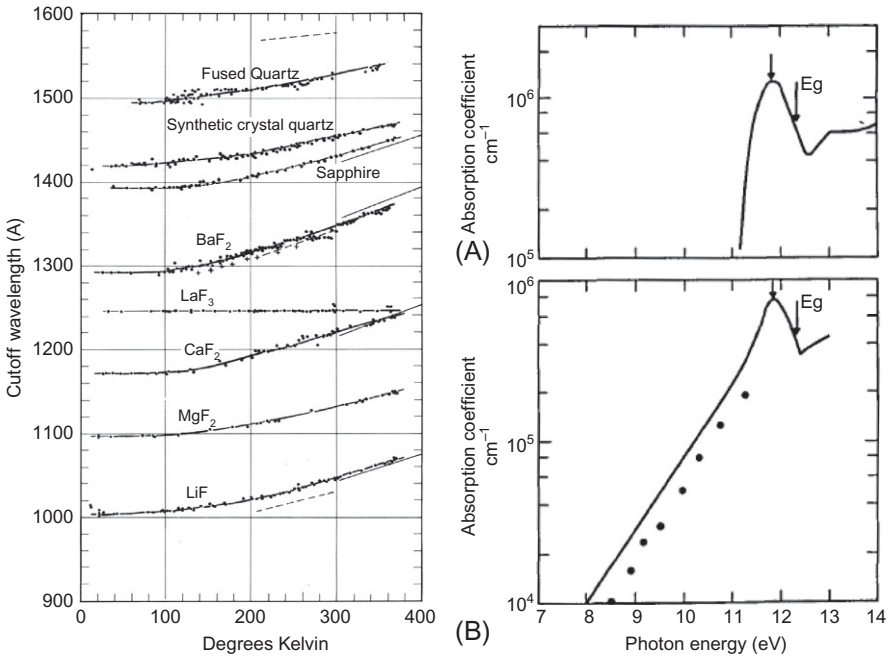


FIG. 7.5

Left: Temperature dependence of the transmittance cutoff of various fluorides and oxides. Chemically, quartz is SiO_2 and sapphire is Al_2O_3. Right: Absorption coefficient at the cutoff of (A) single crystal MgF_2 plate from Williams et al. (1967), (B) thin MgF_2 films deposited onto room temperature substrates from Wood et al. (1984); the solid line represents data by Fabre et al. (1964); the band gap energy, Eg, is 11.8eV.

Source: Left: *Reprinted from Hunter, W.R., Malo, S.A., 1969. The temperature dependence of the short wavelength transmittance limit of vacuum ultraviolet window materials—I. Experiment. J. Phys. Chem. Solids 30, 2739–2745, with permission from Elsevier.* Right: *With permission from the Optical Society of America.*

$$\varepsilon = (n+ik)^2 = 1 - \frac{\omega_p^2}{\omega^2 + i\omega/\tau} \tag{7.14}$$

where $\omega_p = (N_{\mathrm{el}}e^2/m\varepsilon_0)^{1/2}$ (in SI units) is called the plasma frequency, N_{el} is the free electron density, e and m are the electron charge and mass, and ε_0 is the vacuum permittivity. τ stands for an electronic relaxation time, and it is related with the dipole oscillation damping. Wave frequency and photon energy are related through

$$E = \hbar\omega \tag{7.15}$$

where $\hbar$ is the reduced Planck's constant. At low enough frequencies, free electrons can oscillate following the electric field, which results in a large reflection and absorption, a property that we intuitively attribute to metals. ω_p marks a frequency above which electrons cannot follow the electric field any more, which results in a

reduced interaction of light with the metal, with both ε and n evolving towards unity and with a relatively low absorption; hence above ω_p and away from absorption edges, a metal behaves in a way similar to a dielectric. ω_p is the frequency turning point between reflective ($\omega < \omega_p$) and relatively transparent ($\omega > \omega_p$) behavior. In spite of the simplicity of the free-electron model, it provides a good qualitative and sometimes even quantitative approach to provide the optical and electrical properties of metals away from resonances. Above some frequency/photon energy, tightly bound electrons start to be excited, and the free-electron model cannot explain this situation any more.

Aluminium is a good example of a metal following a Drude model in the EUV with a plasma wavelength $\lambda_p = 2\pi c/\omega_p \approx 83.5\,\text{nm}$. Al reflects efficiently at wavelengths longer than λ_p and has a relatively low absorption below λ_p down to the Al $L_{2,3}$ edge at $\approx 17.2\,\text{nm}$, so that it can be used both as a mirror and as a transmittance filter, depending on the range. Fig. 7.3 displays Al experimental reflectance from various sources and their fit to a Drude model in the range close to λ_p. The data of Madden et al. (1963) display a modest surface-plasmon reflectance dip (which reveals the presence of short-range roughness of small amplitude), which according to Eq. (7.11) (when expressed in terms of wavelength), is peaked at, or a little longer than, $\lambda_{sp} = \lambda_p\sqrt{2} = 120$ nm.

Alkali metals have their λ_p in the FUV to NUV, which makes them attractive materials for their relatively high FUV transmittance below λ_p, where most metal and nonmetal materials strongly absorb radiation. However, alkali metals are very reactive, and, furthermore, they have a low melting point; this may result in unstable coatings, which complicates their use in practical applications. Transmission filters based on the high FUV-to-visible transmittance of alkali metals are often called Wood filters (Wood, 1933). Table 7.1 displays λ_p for alkali metals. Wood filters based on Na and Li have been used occasionally (Clarke et al., 1999).

7.4.4 TIGHTLY BOUND ELECTRONS: ATOMIC SCATTERING FACTORS

In the short EUV ($\lambda < 40\,\text{nm}$) and shortwards, photon energy is large compared to the energies of the solid state bands, so that most of the radiation interaction occurs with tightly bound electrons, which are little affected by atom interplay with the surrounding atoms (except at photon energies close to the absorption edges). This is so

Table 7.1 Plasma wavelength of alkali metals (Srivastava, 1982)

Alkali metal	Plasma energy (eV)	Plasma wavelength (nm)	Melting point (°C)
Li	7.99	155.1	180.5
Na	5.92	209.4	97.7
K	4.27	290.4	63
Rb	3.86	321.2	39

because the wave functions corresponding to tightly bound electrons overlap those of neighboring atoms only to a small extent, contrarily to the larger orbital dimensions of outer-shell electrons, which results in a large overlap (Tombulian, 1957). Due to the small role played by atom bonds at short wavelengths, the optical properties of a material can be obtained to a good approximation by summing the responses of the electrons of all atoms (Gullikson, 2000).

In the classical picture, each bound electron in the atom has a specific resonant frequency; we obtain the interaction of the electromagnetic wave with a multi-electron atom by summing the interaction over all electron resonant frequencies. In a second step, the sum is also extended to all atoms. As a result of this, matter can be described with its refractive index given by (Attwood, 1999)

$$N(\omega) \approx 1 - \frac{N_{\text{at}} r_e \lambda^2}{2\pi} \sum_s \frac{g_s \omega^2}{\omega^2 - \omega_s^2 + i\gamma\omega} = 1 - \frac{N_{\text{at}} r_e \lambda^2}{2\pi} \left[f_1^0(\omega) - i f_2^0(\omega) \right] \tag{7.16}$$

where g_s stands for the oscillator strength associated with the resonant frequency ω_s of sth electron, and the sum of g_s over all resonant frequencies results in the total number of electrons Z, the atomic number:

$$\sum_s g_s = Z \tag{7.17}$$

in what is known the Thomas-Reiche-Kuhn sum rule. The sum is extended to all atoms through N_{at}, the atom density. In Eq. (7.16), $r_e = e^2/4\pi\varepsilon_0 m_e c^2 = 2.82 \times 10^{-15}$ m, the classical electron radius. The term in brackets in Eq. (7.16) is called the forward atomic scattering factor, which involves the sum of all the resonant terms, and hence the atomic scattering factors contain the information on the frequency-dependent light interaction with the specific atomic element. The above atomic scattering factors represent the electric field amplitude of the wave scattered by an individual atom in the forward direction relative to that scattered by a free electron (Attwood, 1999); Eq. (7.16) connects the atomic forward scattering with a collective parameter of the material as it is the refractive index. The approximate, instead of equal sign in Eq. (7.16), is there because the original expression is obtained for ε and an approximate square root (valid for a refractive index not far from unity) is performed.

The dispersive term connected with the refractive index is contained in f_1^0; it represents the amplitude scattered by one atom in the forward direction relative to that of a single free electron, so that for a high enough energy (above all the absorption edges of the atom), f_1^0 approaches Z (the atomic number), that is, at high enough energies the atom scatters radiation as if all electrons were free. In fact Z must be slightly modified to account for a relativistic correction (after the data of Kissel and Pratt, 1990 fitted by Henke et al., 1993):

$$Z^* = Z - \left(\frac{Z}{82.5} \right)^{2.37} \tag{7.18}$$

The imaginary part f_2^0 accounts for radiation absorption. Eq. (7.16) can be expressed as

$$N(\omega) = 1 - \delta + i\beta \tag{7.19}$$

where

$$\begin{aligned} \delta &= \frac{N_{\text{at}} r_e \lambda^2 f_1^0(\omega)}{2\pi}, \\ \beta &= \frac{N_{\text{at}} r_e \lambda^2 f_1^0(\omega)}{2\pi}. \end{aligned} \tag{7.20}$$

$\delta = 1 - n$ is called the refractive index decrement and β is identical to the extinction coefficient k, but the former notation is often used when data are obtained from the scattering factors. In the short EUV ($\lambda < \approx 40\,\text{nm}$) and shortwards, δ and β are small compared to unity; they are also positive, except for δ close to some atom absorption edges; this means $n < 1$ mostly at short wavelengths. Far from absorption edges, δ decreases with λ^2 since f_1^0 is relatively independent of λ. β also decreases with λ and it does faster than δ; its decay rate varies somewhat among materials, and it usually decreases with λ^p, with p of the order of 3; as a comparison, p equals 3 in the high-frequency asymptotic behavior of the free electron model given by Eq. (7.14).

The phase velocity of a wave in a medium of uniform atomic density is given by

$$v_\psi = \frac{c}{n} \tag{7.21}$$

At short wavelengths, it is larger than the speed of light since $n < 1$; it has to be noted that what cannot exceed c is the group velocity of the wave, which is involved in energy flow, and not the phase velocity.

A refractive index n smaller than unity results in that total reflection can be obtained when radiation impinges on the optics from the vacuum side at a grazing enough angle of incidence (Compton, 1923). Total reflection is a very useful property since it enables making efficient coatings at short wavelengths when they are not possible at normal incidence. There is a critical grazing angle θ_c (i.e., measured from grazing incidence) below which there is total reflection. When $\beta \ll \delta$, which is usually satisfied in the SXR and shortwards (away from absorption edges), there is a sharp transition in the reflectance-versus-grazing angle at θ_c, which is given by

$$\theta_c = \sqrt{2\delta} = \sqrt{\frac{N_{at} r_e \lambda^2}{\pi} f_1^0(\lambda)} \propto \lambda\sqrt{Z} \tag{7.22}$$

where Z is the atomic number of the material. θ_c is desired to be as large as possible to increase the optics aperture. Eq. (7.22) indicates that θ_c grows with wavelength and, for a fixed wavelength, a larger θ_c is obtained with the use of high-Z materials; proportionality with $Z^{1/2}$ in Eq. (7.22) is valid for energies above all electron resonances. Fig. 7.6 plots the critical angle versus wavelength for Si and W as calculated with Eq. (7.22).

Since atomic scattering factors and also δ and β are calculated by summing the responses of the individual atoms, the optical constants of compounds can be

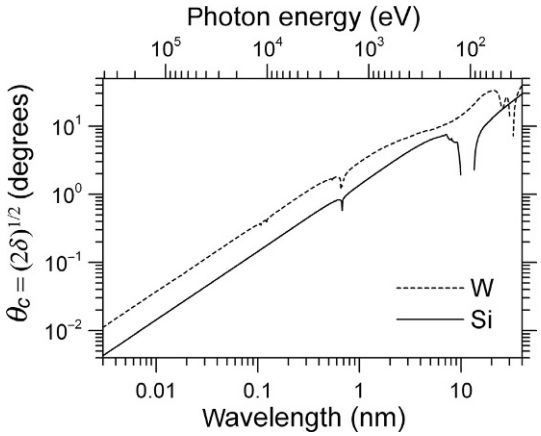


FIG. 7.6

The total reflection critical angle θ_c for Si and W calculated with Eq. (7.22) using δ from Henke et al. (1993) (downloaded from CXRO Web) and the atomic factor f_1^0 from Chantler et al. (1995) (downloaded from NIST-FFAST Web). $\beta \ll \delta \ll 1$ is assumed.

calculated by a further addition over all individual elements weighted with their respective atom density, which is a useful simplification. For a material with various possible densities, such as coal and diamond, the same atomic factors are valid to obtain the optical constants, but the specific atom density must be used. Thus, it is convenient to normalize the optical constants to the material density; when the absorption coefficient is tabulated as μ/ρ, with ρ being the density of the material, it is called the mass attenuation coefficient.

The atomic scattering factors f_1^0 and f_2^0, along with δ and β, have been calculated and compiled by Henke et al. (1982, 1993) for all elements from hydrogen to uranium (Z from 1 to 92) and for energies between 30 and 3×10^4 eV (41–0.041 nm); the data can be conveniently downloaded at CXRO Web.

7.4.5 ABSORPTION EDGES

In the short EUV ($\lambda < \approx 40$ nm) down to HXR, absorption, δ, and the atomic scattering factors steadily decrease with wavelength except for various abrupt absorption increases that are met, which are called absorption edges; an absorption edge occurs when the photon energy reaches the necessary value to eject a tightly bound electron from a specific inner shell. Related to this, a minimum absorption is found at a wavelength slightly longwards of each absorption edge of the atom, that is, minimum absorption is present when the photon energy is slightly insufficient to excite an electron from the next inner shell; this property is used to select the least absorbent material as a spacer in a multilayer coating, which will be addressed in Section 7.7.2. Absorption edges are referred to as K, L, M, etc., in alphabetical order according to the shell from which the electron creates a vacancy, starting with the most tightly

bound shell. A shell subscript, such as L_1, L_2, L_3, refers to the specific electron within the shell according to the electron configuration: $K = 1s$, $L_1 = 2s$, $L_2 = 2p_{1/2}$, $L_3 = 2p_{3/2}$, and so on. When the spin-orbit interaction is unresolved one may combine two edges, for example, $L_{2,3}$ for a state with a $2p$ vacancy (Inczédy et al., 1998). Figs. 7.2, 7.4, and 7.7 display data of k and/or δ of various materials in which absorption edges can be observed. The energy of absorption edges of the elements can be found in reference publications (Bearden and Burr, 1967) and in various Web sites (Schoonjans et al., 2011; NIST-FFAST Web, n.d.). Complementarily, when an atom is in an excited state, it can relax through an electron jumping from an upper level down to an inner incomplete shell; this will result in the emission of a photon with a specific energy corresponding to the level difference. Emission lines, named as $K_\alpha, K_\beta, \ldots$, are also characteristic of the atoms and have values close to the absorption edges.

In Sections 7.4.2 and 7.4.3 it was said that the interaction in a solid largely affects the energy states of the less-bound electrons of individual atoms or molecules in dielectrics and semiconductors. In Section 7.4.4 it was seen that the optical properties of solids in the SXR can be reasonably calculated as the sum of the radiation interaction with the individual atoms. However, the interaction with the other atoms cannot be neglected at photon energies close to the atom absorption edges; an example of the deviation of calculations with atomic scattering factors compared to experimental data close to an absorption edge is plotted in Fig. 7.7. Solid-state effects have been estimated to result in high-energy optical-constant corrections (compared to data calculated with the independent atom approach) of the order of 10%–20%, and they are largest near absorption edges (Rehr and Ankudinov, 2004). Unfortunately, most useful materials to make multilayer coatings are selected with an absorption edge at a

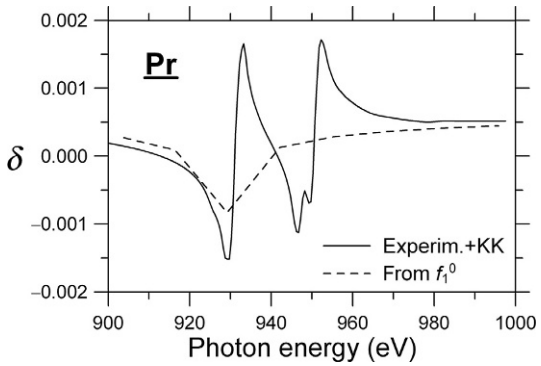


FIG. 7.7

$\delta = 1 - n$ of Pr obtained from experimental k data using the Kramers-Kronig analysis (Source: Data taken from Fernández-Perea et al., 2008) compared to data calculated with the tabulated atomic scattering factor f_1^0 from Henke et al. (1993) (downloaded from CXRO Web). The figure displays an important deviation close to $M_{4,5}$ absorption edge between experimental data and data obtained from the atomic scattering factor.

slightly smaller energy than the one of interest, so that optical-constant calculation with the independent atom approach is less accurate in the most interesting range.

An absorption edge not only displays a sudden absorption increase, but a careful analysis can provide valuable information on the atom surroundings. Hence absorption edges are fingerprints of the material. A consequence of this is that spectroscopy techniques such as X-ray photoelectron spectroscopy (XPS) and X-ray absorption spectroscopy (XAS) can give information of the chemical bonds of the atoms. When the photoelectron ejected by the X-ray photon leaves the atom, its wave is backscattered by the neighboring atoms. The constructive and destructive interference between the outgoing photoelectron wave and the backscattered wave gives rise to maxima and minima above the edge in what is called X-ray absorption fine structure (XAFS) (Newville, 2004). To analyse XAFS, a tunable source of X-rays is required, and the availability of synchrotron sources has permitted the important development of XAFS.

The X-ray absorption spectrum at the energy of an absorption edge and above can be divided into two regimes: (1) the structure found right around the absorption edge and up to some $\approx 50\,\text{eV}$ above it, which is called X-ray absorption near-edge spectroscopy (XANES); (2) the structure found at immediately higher energies than XANES up to $\approx 1000\,\text{eV}$ above the edge, which is called extended X-ray absorption fine structure spectroscopy (EXAFS). XANES is sensitive to the coordination (such as octahedral and tetrahedral) and to the oxidation state of the atom, whereas EXAFS gives information on the number of near neighbors and their identity along with the interatomic distances. As an example, Fig. 7.8 displays the XANES range and part of the EXAFS range of a Ti K-edge XAS spectrum of $PbTiO_3$ (Ravel, 2005).

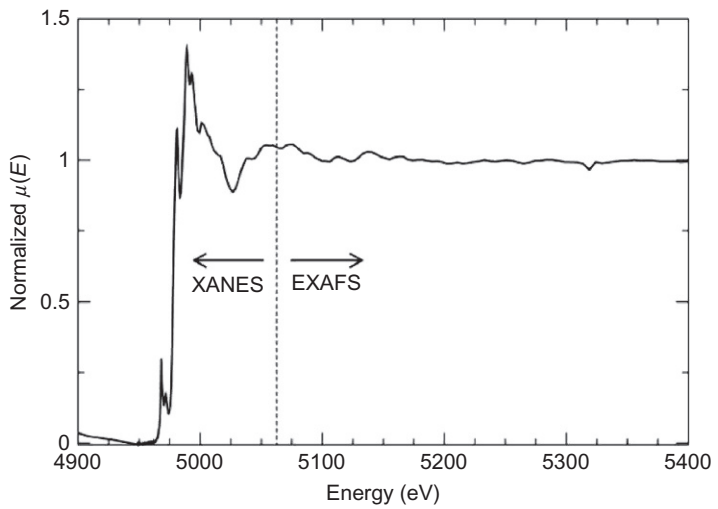


FIG. 7.8

The XANES and EXAFS regions of a Ti K-edge XAS spectrum of $PbTiO_3$.

Source: Reprinted from Ravel, B., 2005. A practical introduction to multiple scattering theory. J. Alloys Comp. 401, 118–126, with permission from Elsevier.

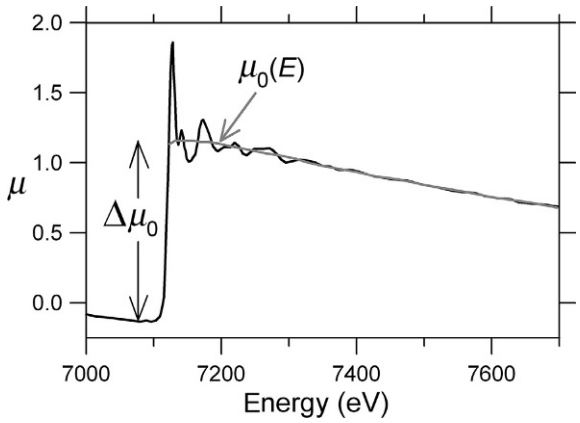


FIG. 7.9

Absorption coefficient μ at the Fe K-edge of FeO showing the XAFS spectrum (Newville, 2004). The spectrum oscillates around a smooth background $\mu_0(E)$ and it shows the edge-step $\Delta\mu_0$, which is the absorption jump at the threshold energy E_0.

Source: Reprinted with permission from Matt Newville.

These spectroscopy techniques have experienced a large development in recent decades and they are now in a mature state with an advanced theoretical description of experimental data (Rehr and Albers, 2000; Newville, 2004; Rehr and Ankudinov, 2004; Ravel, 2005). Useful Web sites with XAFS data have been made available (Materlik et al., 1994; UWXAFS Project, n.d.).

Fig. 7.9 displays the XAFS spectrum at the Fe K-edge of FeO (Newville, 2004) as an example of how to refer the oscillations to a smooth background function $\mu_0(E)$ representing the absorption of an isolated atom. $\Delta\mu_0$ is the measured absorption jump at the threshold energy E_0; it is used as a normalization parameter of the difference $\mu(E)-\mu_0(E)$ to define the EXAFS fine structure function $\chi(E)=([\mu(E)-\mu_0(E)]/\Delta\mu_0)$; the dependence of χ on $k \propto (E-E_0)^{1/2}$, where k is the wave number of the photoelectron, can give us information such as the number of neighboring atoms, the distance to the neighboring atom, and the disorder in the neighbor distance (Newville, 2004). Fig. 7.10 displays the Fe K-edge XANES spectrum of Fe metal and several Fe compounds (Newville, 2004). In the figure, the edge position and shape are sensitive to formal valence state, ligand type, and coordination environment. This figure suggests the potential of these spectroscopy techniques.

7.4.6 OPTICAL PROPERTIES AT HIGHER ENERGIES

At wavelengths short enough as to be comparable with the atom dimension, radiation senses the periodical distribution of electronic clouds in a crystal, which results in characteristic diffraction directions (satisfying Bragg's law). Let us see the situation at wavelengths even shorter than the atom dimension. Atomic

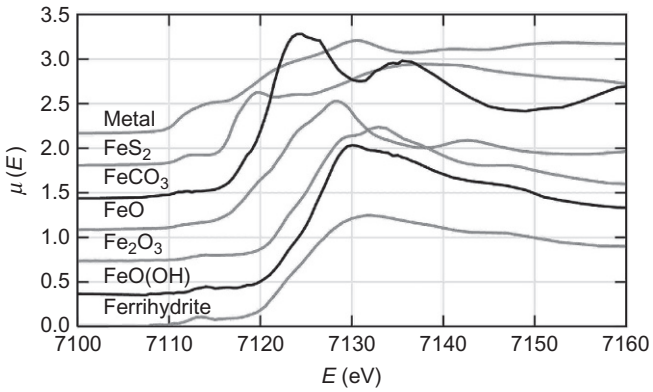


FIG. 7.10

Fe K-edge XANES spectrum of Fe metal and several Fe compounds (Newville, 2004).

Source: Reprinted with permission from Matt Newville.

scattering factors are given by Eq. (7.16) on the assumption that all electrons in an atom see approximately the same phase and collectively scatter light in phase (Attwood, 1999). This is valid as long as the wavelength is larger than the atom diameter. When radiation wavelength is smaller than the atom diameter (HXR and gamma), the above assumption is still valid for scattering in the forward direction, that is, in the propagation direction of the wave in the material; that is why Eq. (7.16) involved forward scattering factors, which remain valid at these larger energies. In fact, it is the interaction of the forward-scattered waves with the incident wave that is responsible for the wave propagation characteristics in the medium that is modified (compared to vacuum) in consistency with what is meant by a refractive index; among these modified characteristics are the phase velocity and the amplitude decay (Attwood, 1999). For wavelengths longer than the atom diameter, the atomic scattering factors are independent of the direction in which the atom scatters and hence the macroscopic interaction of an electromagnetic wave with a uniform medium is fully described with the refractive index. For wavelengths shorter than the atom diameter, the amplitude scattered by an atom decreases when one moves angularly away from the forward direction (Stanglmeier et al., 1992) due to out-of-phase interferences among the scattered waves at electrons that are separated within the atom at distances comparable to or larger than the wavelength; therefore, scattering away from the forward direction at wavelengths shorter than the atom diameter is not completely described with a macroscopic parameter such as the refractive index. For wavelengths shorter than the spatial distribution of electron density across an atom, radiation–matter interaction turns into a scattering process, which is expressed in terms of a cross section.

Interesting reviews of the behavior of matter at X-rays or gamma were written by Gålnander (2001) and von Ballmoos (2005). At these high energies, scattering is generated by various interaction mechanisms, which are summarized in Table 7.2 (Davisson, 1965). The most important are:

Table 7.2 Gamma-ray interaction processes

Process	Kind of interaction	Other name	Approximate energy range of maximum importance	Approximate variation with Z
Photoelectric effect	With bound atomic e^-		Dominates at low E (1–500 keV). Decreases as E increases	Z^5
Scattering from electrons: coherent	With bound atomic e^-	Rayleigh scattering electron resonance scattering	<1 MeV and greatest at small scattering angles	Z^2 (small angles), Z^3 (large angles)
	With free e^-	Thomson scattering	Independent of energy	Z
Scattering from electrons: incoherent	With bound atomic e^-		<1 MeV, least at small scattering angles	Z
	With free e^-	Compton effect	Dominates in region of 1 MeV. Decreases as energy increases	Z
Photonuclear absorption	With nucleus as a whole emits γ or particles	(γ, γ), (γ, n), (γ, p), etc., processes, particle production	Above threshold has broad maximum in range of 10–30 MeV	
Nuclear photoeffect		Nuclear photodisintegration Mössbauer effect		
Nuclear scattering: coherent	With material as a whole dependent on nuclear energy levels	Nuclear resonance scattering	Important only in very narrow range	
	With nucleus as a whole dependent on nuclear energy levels	Nuclear resonance scattering	Narrow resonance maxima at low energies. Broad maximum in range of 10–30 MeV	Z^2/A^2

Continued

Table 7.2 Gamma-ray interaction processes —cont'd

Process	Kind of interaction	Other name	Approximate energy range of maximum importance	Approximate variation with Z
	With nucleus as a whole dependent on nuclear energy levels	Nuclear Thomson scattering	$\lambda \gg$ nuclear radius. Independent of energy	Z^4/A^2
Nuclear scattering: incoherent	With individual nucleons	Nuclear Compton scattering	$\lambda \leq$ nuclear radius, i.e., >100 MeV	
Interaction with a Coulomb field: pair production	In Coulomb field of nucleus	Elastic pair production	Threshold ≈ 1 MeV. Dominates at high E (i.e., >5 or 10 MeV)	Z^2
	In Coulomb field of electron	Triplet production, inelastic pair production	Increases as E increases, threshold at 2 MeV, increases as E increases	Z
Interaction with a Coulomb field: Delbruck scattering	In coulomb field of nucleus	Nuclear potential scattering	Real part > imaginary below 3 MeV, < imaginary above 15 MeV, real and imaginary both increase as E increases	Z^4

Note: *Numbers 2, 3, 4, 5 mean powers of Z, the atomic number.*
Source: Reprinted from Davisson, C.M., 1965. Interaction of γ radiation with matter. In: Siegbahn, K. (Ed.), Chapter II in Alpha-, Beta-, and Gamma-Ray Spectroscopy. North-Holland, Amsterdam, pp. 38–39.

- Photoelectric absorption: photon energy is used in ejecting an electron from an atom and in providing the electron with kinetic energy; dominant below ≈ 100 keV for light atoms and up to 0.8 MeV for atoms with large Z.
- Compton (or incoherent) scattering: part of the photon energy ejects an electron and a smaller energy photon with the remaining energy is scattered; dominant in ≈ 100 keV to ≈ 10 MeV. For atoms with large Z the dominance energy range of Compton scattering is narrowed on both the lower and the upper energy limits.
- Pair production: photon energy is large enough (at least twice the electron rest mass, that totals 1.02 MeV) to generate an electron-positron pair mainly in an interaction in the presence of a nucleus; dominant at energies above ≈ 10 MeV for light atoms, but as low as 4 MeV for atoms with large Z. The positron later

annihilates with an electron, which results in the formation of two gamma-ray photons.

The transfer of dominance for the three main HXR/gamma-atom interactions as a function of energy and the atomic number Z was investigated by Evans (1955).

The connection between absorption coefficient and cross section σ is given by

$$\sigma = \frac{\mu}{N_{\text{at}}} \tag{7.23}$$

where N_{at} and μ stand for the atom density and the absorption coefficient, respectively. σ has the units of a surface, and it is measured in barns per atom; 1 barn (b) $= 10^{-24}$ cm^2. As an example, Fig. 7.11 displays the main cross-section components for carbon (C) (Hubbell et al., 1980). The total absorption coefficient is obtained by summing all the cross-section components for the different interactions.

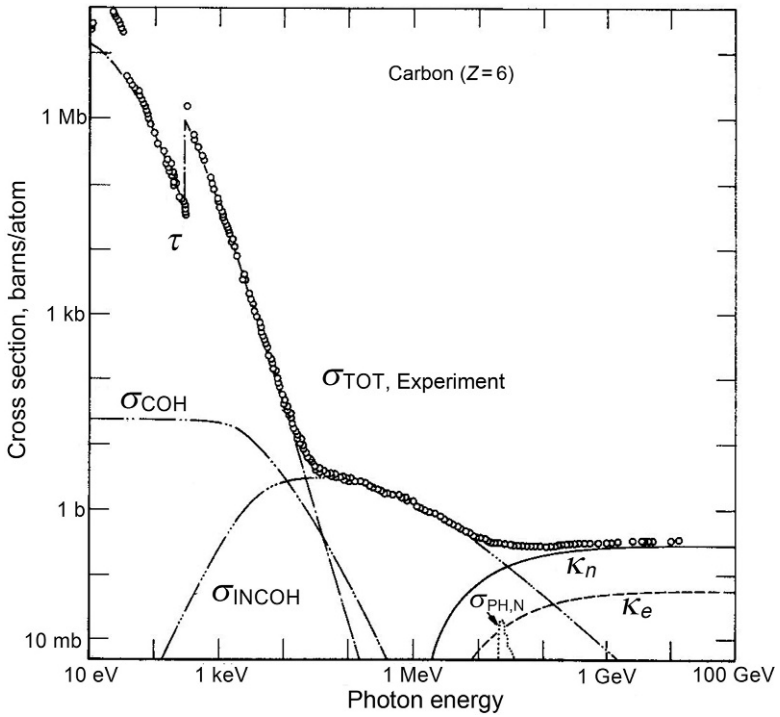


FIG. 7.11

Contributions to the total measured cross section σ_{TOT} (circles) in carbon over the photon energy range 10 eV to 100 GeV of atomic photoelectric effect, τ; coherent (Rayleigh) scattering, σ_{COH}; incoherent (Compton) scattering, σ_{INCOH}; nuclear-field pair production κ_n; electron-field pair production κ_e; nuclear photoabsorption, $\sigma_{\text{PH.N}}$.

Source: Reprinted with permission from Hubbell, J.H., Gimm, H.A., Øverbø, I., 1980. Pair, triplet, and total atomic cross sections (and mass attenuation coefficients) for 1 MeV–100 GeV photons in elements Z = 1 to 100. J. Phys. Chem. Ref. Data 9, 1023–1147. Copyright 1980, American Institute of Physics.

The different cross sections in HXR and gamma have mostly been obtained by calculations that make use of the relativistic quantum mechanics, in which each of the involved interactions requires a specific approach. There is a long literature of calculations of the atomic cross sections of most elements of the periodic table at wide energy ranges (Cromer and Mann, 1968; Scofield, 1973; Hubbell et al., 1980; Chantler et al., 1995). The National Institute for Standards and Technology (NIST) has gathered handy compilations of the mass attenuation coefficient and atomic factors of the elements of the periodic table which cover a large energy range: photon cross sections database (XCOM) (1 keV to 100 GeV) (Berger et al., 2010) and X-ray attenuation and absorption for materials of dosimetric interest database (XAAMDI) (1 keV to 100 MeV) (Hubbell and Seltzer, 1995), which were developed for radiological physics and dosimetry, and X-ray form factor, attenuation and scattering tables database (FFAST) (NIST-FFAST Web, Chantler, 2000) (1 eV to 433 keV), which was produced for X-ray diffraction, interferometry, and crystallography, among other areas. A comparison between XCOM and FFAST is also available (XCOM-FFAST Comparison Web, n.d.).

7.5 LINK BETWEEN *n* AND *k*: KRAMERS-KRONIG ANALYSIS

The real and imaginary parts of the refractive index $N = n + ik$ are linked as a result of basic principles: linearity and causality; the latter implies that a polarization cannot be induced on a material by an electric field before the field is applied. The links between n and k are referred to as the Kramers-Kronig dispersion relations, which are expressed as

$$\begin{aligned} n(E) - 1 &= \frac{2}{\pi} p \int_0^\infty \frac{E' k(E')}{E'^2 - E^2} dE' \\ k(E) &= -\frac{2E}{\pi} p \int_0^\infty \frac{n(E') - 1}{E'^2 - E^2} dE' \end{aligned} \tag{7.24}$$

P stands for the Cauchy principal value, which is an integration variant necessary to deal with the zero in the denominator at $E' = E$. Eq. (7.24) enables the calculation of one optical constant if the other is known over the whole spectrum. The latter is never fully possible and interpolations and extrapolations are always required to carry out the integration. Nevertheless, the range close to the energy at which the calculation is performed has a higher weight in the integration, which reduces the inaccuracy originating in the use of extrapolations at distant energies. Since it is frequently easier to obtain k from experimental measurements, the first integral is used more often, and thus n is obtained through Kramers-Kronig integration. Similar equations link the real and imaginary parts of the dielectric constant.

The modulus $R^{1/2}$ and phase ϕ of complex reflectance $r = R^{1/2}\exp(i\phi)$ are linked with analogous dispersion relations:

$$\varphi(E) = -\frac{E}{\pi} p \int_0^\infty \frac{\ln[R(E')/R(E)]}{E'^2 - E^2} dE' \tag{7.25}$$

This is called the Jahoda (1957) dispersion relation in the subtractive form (Shiles et al., 1980) and it is a useful relation to calculate the optical constants from reflectance measurements (Section 7.6). There is another formal equation that provides R when ϕ is known over the whole spectrum; however, R and not ϕ is what can usually be measured.

The use of the Kramers-Kronig or Jahoda-Velický dispersion relations is presented here because they are particularly useful in the determination of the optical constants of materials at short wavelengths, which is addressed in Section 7.6.

Useful sum-rules are available, which enable the evaluation of optical-constant consistency integrated over the full spectrum. The most common rules for n and k (in SI units) are

$$\frac{4\varepsilon_0 m}{\pi N_{at} e^2 \hbar^2}\int_0^\infty E' k(E')dE' = Z \tag{7.26}$$

$$\int_0^\infty [n(E)-1]dE = 0 \tag{7.27}$$

where N_{at} is the atom density, e and m are the electron charge and mass, ε_0 is the permittivity of vacuum, and $\hbar$ is the reduced Planck's constant. The first sum-rule expresses that the integral of k in the whole spectrum, conveniently normalized, equals the total number of electrons of the atom (a straightforward extension can be obtained for compounds by replacing N_{at} and Z with the compound equivalent parameters); it is another version of the Thomas-Reiche-Kuhn sum-rule given as Eq. (7.17). The second sum-rule, usually called the inertial sum-rule, expresses that the average of n through the spectrum is unity. The latter means for instance that the refractive index of a dielectric, which is larger than unity in the visible, must be compensated with a refractive index lower than unity in other parts of the spectrum, which occurs in most of the EUV and shortwards. Sum-rules have also been developed for the Jahoda-Velický reflectance dispersion relations (King, 1979). A procedure to check the optical-constant consistency in a narrow band of the spectrum has been developed with sum rules with window functions (Rodríguez-de Marcos et al., 2016a).

7.6 EXPERIMENTAL DETERMINATION OF OPTICAL CONSTANTS

We summarize below various techniques that are used for the characterization of the optical constants of materials at short wavelengths. An excellent review on techniques for optical constant determination was published in Palik (1998a,b). Large compilations of experimental optical constants of materials in broad spectral ranges including short wavelengths have been published: Hagemann et al. (1974), Haelbich

et al. (1977), Weaver et al. (1981), and Palik (1998a,b,c). In the following section the most common techniques are mentioned:

- Reflectance measured at various angles of incidence. Both n and k can be calculated using Fresnel formulae (Eq. 7.8). This technique has been described more extensively by Scott (1998) and Hunter (1998). At short wavelengths, microroughness plays an important role in reflectance and it has to be accounted for. Some examples of the use of the reflectance-versus-angle method are given in Windt et al. (1988), Larruquert et al. (1995), Soufli and Gullikson (1997), Windt et al. (2004a), and Monaco et al. (2006).
- Reflectance measured over a large spectrum at near-normal incidence (in a more general case it can be measured at a constant incidence angle, not necessarily near the normal), complemented with the use of the dispersion relations described in Section 7.5. The measured reflectance in a wide spectral range is used to calculate the complex reflection coefficient r with the Jahoda-Velický dispersion relation given by Eq. (7.25). From the Fresnel reflectance coefficient at normal incidence

$$r = \frac{1-N}{1+N} \tag{7.28}$$

we immediately obtain $N = n + ik$ as

$$N = \frac{1-r}{1+r} \tag{7.29}$$

Examples of the use of this method are in Philipp and Ehrenreich (1963) and Shiles et al. (1980).

- Transmittance over a large spectrum for various layers of the investigated material with film thicknesses x_i. k at each wavelength is obtained using the Beer-Lambert law:

$$T_i = T_0 \exp\left(-\frac{4\pi k x_i}{\lambda}\right) \tag{7.30}$$

where k is given by the linear fit of the logarithm of the normalized transmittance versus film thickness. Eq. (7.30) is immediately obtained from Eqs. (7.3) and (7.4) where T_0 and T_i stand for the transmittance of the bare substrate and of the substrate with the x_i film, respectively; Eq. (7.30) neglects reflectance. Once k is known, n is obtained with the Kramers-Kronig dispersion relations using Eq. (7.24) as described in Section 7.5; this requires knowing k in the whole spectrum. An advantage of this technique over those involving reflectance measurements is that the effect of any possible contamination can be minimized if it is common to all films regardless of their thicknesses. The dependence on roughness is much smaller for transmittance than for reflectance, as can be seen in Eq. (7.12); this is an important advantage at short wavelengths. Furthermore, transmittance is easier to measure than

reflectance. In the EUV and SXR there is a lack of transparent materials, which impedes the use of massive substrates onto which the target material is deposited; this can be solved by using self-supported thin films that operate as substrates to support the material to be investigated (Hunter, 1973). A variant of this technique has been developed in which the target film is directly deposited on the detector (Uspenski et al., 2005). A large amount of materials has been characterized with this method. In the pioneering work by Hagemann et al. (1974) several materials were characterized, mostly metals. Optical constant characterization at large energy ranges has been performed for various materials (Soufli and Gullikson, 1998; Soufli et al., 1999). A full characterization of Sc and lanthanides, except for radioactive Pm, has been performed with this method (Kjornrattanawanich et al., 2010; Fernández-Perea et al., 2011 and references therein).

- Ellipsometry. It is based on the determination of the complex ratio r_p/r_s with the use of linear polarizers and phase retarders. It provides both n and k of the material. There are few available ellipsometers at short wavelengths because of the shortage of efficient wideband polarizers and retarders. Barth et al. (1998) and Hilfiker (2005) discussed the use of ellipsometry to cover the EUV down to 12.8 nm and the FUV, respectively. Some synchrotron beamlines are getting available to perform ellipsometry at least in narrow ranges of the EUV (Tsuru and Yamamoto, 2008; Soltwisch et al., 2015). Section 7.7.3 addresses the properties of polarizers and phase retarders at short wavelengths.
- Interferometry. The introduction of a layer of the material into one arm of an interferometer produces an optical path difference from which n can be directly measured; it can be combined with transmittance measurements to obtain k (Svatos et al., 1993; Tatchyn, 1998; Joyeux et al., 1999; Chang et al., 2002). Yet few interferometers are available at short wavelengths. One reason is that beam splitters are difficult to make in the EUV and SXR since no massive substrates are possible. There is also a lack of wideband mirrors. Another difficulty is that this technique requires equaling optical paths to a fraction of a small wavelength.
- Critical angle. When $0<\delta\,(=1-n)<1$ and $\beta\,(\equiv k)\ll\delta$, such as in most of the SXR and HXR, δ can be obtained from the determination of the critical angle (see Section 7.4.4). The presence of a small amount of absorption is circumvented by determining the angle at which the slope of the reflectance versus angle of incidence curve has a maximum (Hunter, 1964a, 1998). The method provides δ.
- Refraction. When wavelength decreases towards the HXR, $\beta\,(\equiv k)$ decreases faster than $\delta\,(=1-n)$ does, so that it becomes possible to obtain n through refraction on a prism of the material at grazing incidence (Compton, 1923; Fontaine et al., 1985; Warburton and Ludwig, 1986; Jark et al., 2011), and even k can be obtained with supplementary transmittance measurements (Jark et al., 2011). Measurements at gamma energies up to 2 MeV have been reported (Habs et al., 2012).

- Electron energy loss spectroscopy (EELS). Optical methods to measure the refractive index involve the difficulty to cover a wide range of wavelengths, which needs a variety of sources, gratings, detectors, and other elements. In contrast, electron sources which can provide monoenergetic beams over a wide spectral range are more easily available. This results in the use of EELS in optical-constant evaluation. In transmission EELS, a beam of high-energy electrons crosses a self-supported thin film, and the electron beam undergoes inelastic scattering. EELS involves measurement of the energy distribution of the electrons that have lost energy in the interaction. Spectra with the number of electrons as a function of energy loss can be used to calculate the film optical constants up to energies mostly in the EUV. Electron mean free paths are small and an electron may undergo more than one scattering event, so that optical-constant calculation requires correcting for multiple scattering events. The method is described by Pflüger and Fink (1998). Reflection EELS has also been used to calculate optical constants (Tougaard and Chorkendorff, 1987; Werner, 2006).
- Total electron yield. The method is based on the generation of electrons within a film being proportional to radiation absorption, so that electron generation and optical properties are connected. The method is explained in Birken et al. (1998) and it is based on the work of Pepper (1970), Gesell and Arakawa (1971), and Arakawa et al. (1973). Both n and k can be calculated. The method is applicable at photon energies above the photoemission threshold, so that it is suitable for short wavelengths.

7.7 SPECIFICS OF OPTICAL COATINGS AT SHORT WAVELENGTHS

In the development of efficient multilayer (ML) coatings for short wavelengths, specific difficulties are encountered, such as (1) absorption of materials in the FUV to SXR, (2) very thin films required at short wavelengths, (3) roughness effect on scattering strongly grows at short wavelengths, and (4) small n contrast over materials, which requires an increase of the number of layers in the ML. Here we summarize the main aspects that are specific for short-wavelength MLs. The limited space will allow a short description of three varieties of coatings: transmission filters, high-reflectance coatings, and polarizers and retarders. Various optical devices other than coatings that are used at short wavelengths, such as zone plates, flat and bent crystals, polycapillaries, and compound refractive lenses, are out of the scope of this chapter.

7.7.1 TRANSMISSION FILTERS

Pass band filters are more efficient at rejecting the out-of-band when they work by transmission compared to reflection. In the FUV, the shortage of transparent materials is an obstacle for these filters. A few transparent materials below

200 nm, mostly fluorides, are still somewhat absorbent, which limits the maximum number of layers in the ML and hence the efficiency of all-dielectric transmission filters. Instead, metal-dielectric transmission filters are in common use in the FUV with a shortest peak wavelength of ≈120 nm. They consist of a ML alternating a fluoride film, such as MgF_2, with a metal film, usually Al (Malherbe and Guillard, 1970; Fairchild, 1973; Malherbe, 1974a, Rodríguez-de Marcos et al., 2014). Below ≈120 nm, interference transmission filters are not available. The situation is even worse in the EUV, since no transparent substrate material with a thickness of the order of ≈1 mm can be found below 105 nm; this limit can be shifted to ≈100 nm by cooling the substrate material with shortest cutoff wavelength in nature (LiF).

Let us look at filtering with natural bands of materials. In the FUV, few narrowband filters working by natural absorption have been prepared (Carruthers, 1971). The cutoff of various fluorides and oxides, mentioned in Section 7.4.2, provides good edge filters that reject the short wavelengths. However, the rejection of the long FUV wavelengths and still longer wavelengths remains a difficult task. Within this general lack of filtering materials, a natural transmission peak was found at 176 nm with Ce^{3+}-doped LaF_3 (Elias et al., 1973); peak bandwidth can be tuned by varying temperature and also the concentration of the Ce^{3+} ions. The authors predicted some tunability of the peak position by changing the host crystal.

An exception of the lack of natural FUV filters are alkali metals, with a high FUV-to-long wavelength transmittance ratio; in spite of this, their chemical reactivity and low melting point strongly limit their applicability and they are only occasionally used for FUV transmittance filters. They are called Wood filters, and they are referred to in Section 7.4.3.

Regarding the EUV, the natural low-absorption bands of materials can be used for filtering purposes; these bands are peaked immediately longwards of the material absorption edges. This provides a series of possible bands which are obviously limited by nature (Hunter et al., 1965; Rustgi, 1965; Samson, 1967a; Powell et al., 1990, 1994). Sometimes two or more materials are used in a two- or multilayer coating filter to provide a narrower combined passband (Powell et al., 1994). Since no transmitting bulk substrate is available in the EUV, the layers of the filtering materials must be deposited onto a self-supported thin film (the support film can at the same time be a filtering material) (Hunter, 1973). This results in fragile optical elements. In spite of this limitation, EUV filters based on natural low-absorption bands of materials have been largely used particularly in space instruments for astronomy or solar physics. Figs. 7.12 and 7.13 summarize the transmission properties of various common materials. Transmittance sharply decreases on the short-wavelength side of each absorption edge.

As for filter robustness involving two materials, each with its natural band, it has been found that its mechanical strength can be significantly increased if, instead of using a single layer of each material, the total thickness is fractioned in several thinner layers to make a multilayer of the two materials (Bibishkin et al., 2008; Chkhalo et al., 2011, 2016).

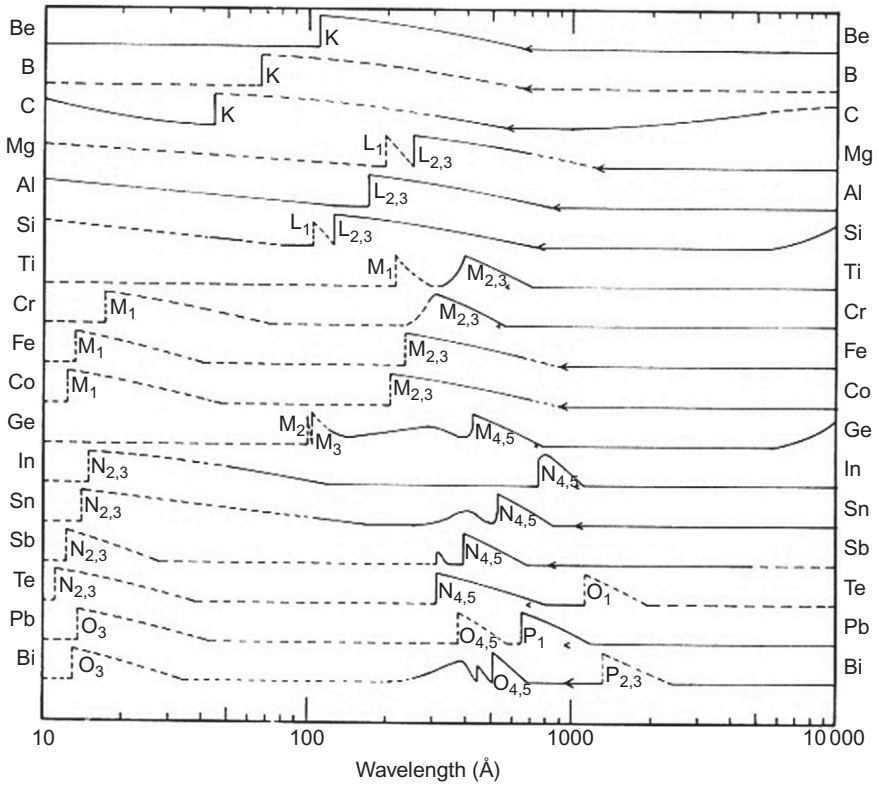


FIG. 7.12

A summary diagram of the transmission properties of several materials, most of which can be prepared as thin films. Absorption edges are shown as steps (Hunter et al., 1965). Dotted lines suggest probable trends which had not been verified experimentally. The positions of the various X-ray edges are indicated: those observed in absorption by solid lines and those calculated by broken lines.

Source: With permission from the Optical Society of America.

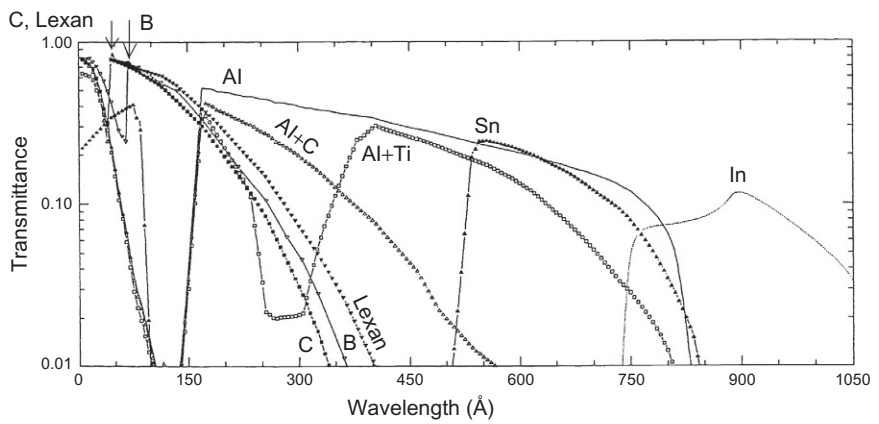


FIG. 7.13

Transmittance expected for commonly used filter materials (Powell et al., 1994).

Source: With permission from V. Drake and from SPIE.

The usefulness of all the above options in this section is limited. That is why in some cases one has to resort to the absorption of gases to use them for filtering purposes. For instance, a fortunate transmittance band of oxygen at the important hydrogen Lyman α line (121.6 nm) has been used to isolate it (Carrière and Heer, 1972). Flowing-gas elements are sometimes used as filters for instance in synchrotron beamlines (Cavasso Filho et al., 2007). They are based in that gases start absorbing photons with energies above their first ionization potential.

7.7.2 HIGH-REFLECTANCE COATINGS

The presence of relatively transparent materials in the FUV with $\lambda > 120$ nm enables the preparation of high-reflectance (HR) coatings as an extension of the experience in the visible and near UV, although with the efficiency decreasing at short wavelengths. Plenty of dielectric materials are transparent in the visible, which can be used to make MLs with virtually any spectral, angular, or polarizing profile. These materials turn absorbent at some wavelength shorter than the visible. Among the materials to turn absorbent at the shortest possible wavelength, we have some oxides and fluorides, as mentioned in Section 7.4.2. Regarding fluorides, it was mentioned that some alkaline and alkaline-earth fluorides (LiF, MgF_2, and CaF_2) keep their transparency down to almost the short-wavelength edge of the FUV. Another group of fluorides with usable transparency close to that same edge are some lanthanide fluorides, particularly LaF_3, GdF_3, and LuF_3 (Lingg, 1990). Self-consistent optical constants of MgF_2, LaF_3, and CeF_3 have been reported for the design of multilayers (Rodríguez-de Marcos et al., 2017).

MLs down to the short FUV are made mostly using the two mentioned fluoride groups. Narrowband, all-dielectric multilayers have been demonstrated in the FUV, typically alternating a low-refractive index material like MgF_2 with a high-refractive index material among the lanthanide fluorides (Malherbe, 1974b; Zukic and Torr, 1992; Park et al., 1996; Gatto et al., 2002; Rodríguez-de Marcos et al., 2015) down to a peak wavelength of ≈ 120 nm. Fig. 7.14 displays the reflectance of an all-fluoride ML peaked at 121.6 nm.

FUV narrowband MLs have also been prepared with the combination of Al and MgF_2 layers (Wang et al., 2015). A narrowband reflective coating peaked at a wavelength as short as ~ 100 nm has been developed based on Al, LiF, and SiC (Rodríguez-de Marcos et al., 2016b). A review with more information on FUV coatings was written by Thielsch (2003).

HR coatings in the EUV and shortwards are reviewed in the following, which summarizes the fast development of normal-incidence MLs for both mirrors and diffraction gratings that started around the 1980s. This development has been essential for the progress of fields such as projection lithography, astrophysics, and solar physics, among others.

In the EUV at $\lambda < 50$ nm, the reflectance of any single material at normal incidence is very low. To make an efficient mirror, we require the constructive interference of contributions coming from many interfaces, that is, a ML. The significant

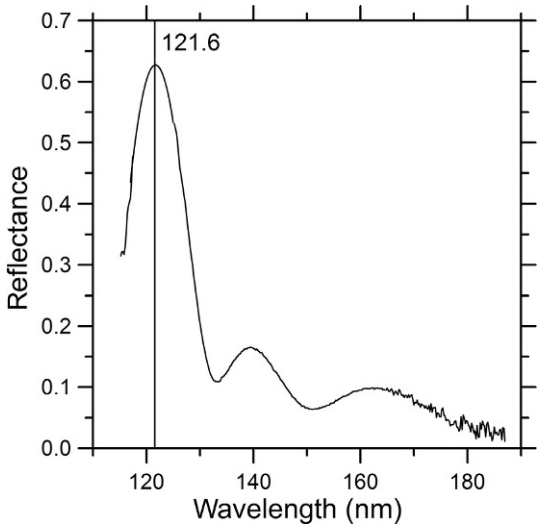


FIG. 7.14

Reflectance of a MgF_2/LaF_3 ML peaked at 121.6 nm **(**Rodríguez-de Marcos et al., 2015**).**

absorption of materials in the EUV, and to a lower extent in the SXR, strongly limits the performance of coatings. Reflective ML coatings in the EUV and SXR are based on the selection of at least one material with minimum absorption at the desired wavelength range; this material is called the spacer of the ML. As a reminder, the minimum absorption of a material occurs slightly longwards of an absorption edge. The second ML component is selected from those with largest n contrast with the spacer material and, if the contrast in n is large enough, with the smallest possible k; this material is sometimes called the scattering material. A good summary list of useful material pairs for EUV-SXR MLs can be found in Spiller (1994) and Windt et al. (2004b); a summary of some of the most commonly used material pairs with high reflectance at each range is plotted in Fig. 7.15. Among the plotted ML coatings, the Mo/Si pair at $\approx$13.5 nm, slightly above the Si $L_{2,3}$ edge, provides the largest normal reflectance achieved at any wavelength in the EUV or SXR, $\approx$70%; its application for the future EUV lithography (EUVL) has resulted in a very thoroughly investigated ML structure. An excellent review on Mo/Si and on other ML coatings for EUVL has been published (Soufli and Bajt, 2009).

The reflectance predicted by calculations may be strongly reduced in practice by roughness-induced scattering; the decrease of reflectance with roughness can be calculated in a simple approach given by Eqs. (7.12) and (7.13). For a given RMS roughness σ, the decrease of reflectance at some long wavelength λ may be negligible, but it may turn deleterious at some shorter one. In the above approach, reflectance decrease depends on $(\sigma/\lambda)^2$, which makes the turning point sharp. Spiller (1994) marks the largest acceptable interface roughness as about 1/10 of the ML period, hence typically $\lambda/20$. If σ may be technically difficult to reduce below $\approx$0.1 nm, then the shortest wavelength limit for which efficient normal-incidence MLs can be

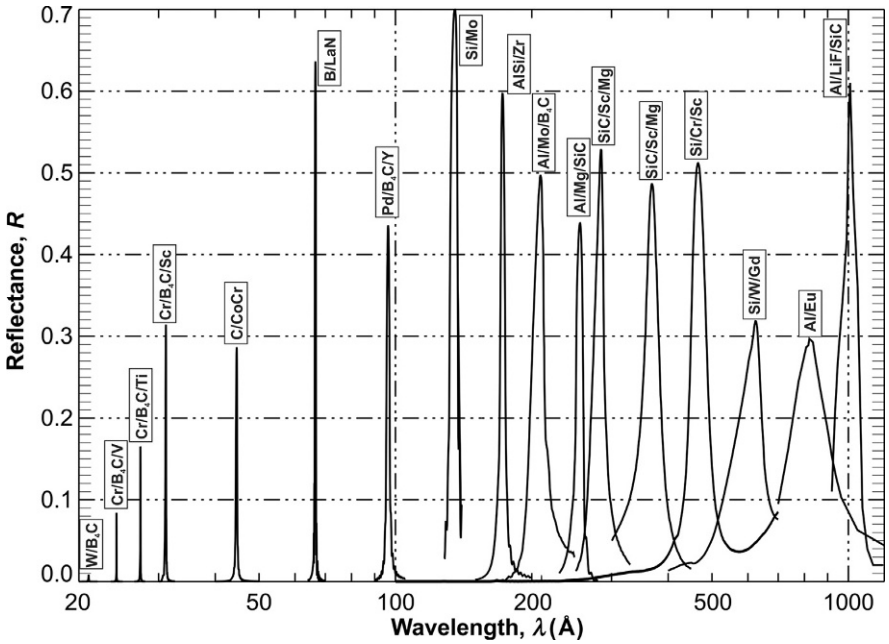


FIG. 7.15

HR coatings spanning the EUV to SXR.

Source: The figure was kindly prepared by David Windt. Data sources: W/B_4C from Windt et al. (2002); Cr/B_4C/V, Cr/B_4C/Ti, and Cr/B_4C/Sc from Gullikson et al. (2006); C/CoCr from Marshall et al. (2014); B/LaN from Kuznetsov et al. (2015); Pd/B4C/Y from Windt and Gullikson (2015); Si/Mo from Bajt et al. (2002); AlSi/Zr from Windt (2015); Al/Mo/B4C from Meltchakov et al. (2011); Al/Mg/SiC from Windt (2015); SiC/Sc/Mg from Aquila et al. (2008); Si/Cr/Sc from Yulin et al. (2004); Si/W/Gd from Windt (unpublished data); Al/Eu from Larruquert et al. (2011a); Al/LiF/SiC from Rodríguez-de Marcos et al. (2016b).

prepared is roughly 2 nm. A way to overcome this short-wavelength limit is by working away from normal incidence, taking advantage of the inclination factor mentioned in Eqs. (7.12) and (7.13). There is a cost for working away from normal incidence, since it results in an optical system with reduced aperture and effective area as well as increased aberrations compared to a normal-incidence system. It was said in Section 7.4.4 that total reflection is obtained with a single material working just more grazing than its critical angle θ_c. Compared to a single material at the critical angle, a ML may be designed to have high reflectance at a much less grazing incidence, which increases the aperture and helps minimize aberrations. ML coatings working at grazing incidence for energies as high as 200 keV have been developed (Windt et al., 2003; Ogasaka et al., 2007), and MLs for an energy as large as 384 keV have been demonstrated (Fernández-Perea et al., 2013a). The physics describing the latter ML extension has been presented (Fernández-Perea et al., 2013b).

The reactivity of some materials impedes their use in MLs in spite of their favorable optical constants. In Section 7.4.4, it was shown that the optical constants of compounds at short wavelengths are obtained as a weighted combination of the

compound elements. Therefore, if one focuses only on optical constants, the most useful materials for short-wavelength MLs are always single elements and not compounds, since for instance there will always be a constituent element within a compound with smaller k than the compound, which is important for MLs limited by absorption. But often low-absorption single elements are reactive, and they may give rise to unstable MLs. As an example, reactive Sr has a low-absorption range below its M_5 edge at 133 eV, which makes it attractive as a ML spacer; however, it results in unstable MLs with Mo (Sae-Lao and Montcalm, 2001). To improve ML stability, an element can be replaced with a compound of which it is a constituent, and a reasonable compromise between stability gain and reflectance loss may be found; an example is the replacement of Mo in Mo/Si MLs with Mo_2C to get stable MLs at high temperatures (Feigl et al., 2001).

A useful method to passivate an otherwise unstable interface between two materials is the use of barrier layers. Barrier layers are thin films of a third material that separate layers of the main components to minimize the reactivity or interdiffusion between the basic components of the ML. Typical optical layer thickness in MLs is roughly $\lambda/4$; such thickness is very small for MLs operating in the SXR and short EUV. Therefore, barrier layers must be extremely thin not to degrade significantly ML reflectance. For instance, barrier layers of C, B_4C, or SiC with thicknesses of $\approx$0.5 nm and even thinner have been used in Mo/Si MLs to get sharp interfaces and to stabilize them when MLs have to survive at high temperatures (Bajt et al., 2002; Braun et al., 2002; Hecquet et al., 2007). ML reflectance can be optimized with the use of specific barrier layer materials at each of the two interfaces (Larruquert, 2004). Likewise, reactivity of the outermost layer in contact with air can be avoided or at least minimized with the use of a protective capping layer (Bajt et al., 2002; Yulin et al., 2008).

The period for MLs with maximum reflectance at a desired λ and angle of incidence is given by Bragg's law:

$$2d\overline{n}\cos\theta = m\lambda \tag{7.31}$$

where d is the period thickness, θ is the angle referred to the normal, $\overline{n}$ represents an average refractive index through the period, and m stands for the reflection order (or Bragg peak order); in most cases m is set to 1. Bragg's law was formulated to describe X-ray diffraction patterns, but it also governs the optimization of MLs by replacing diffraction planes with layers. For $m = 1$ and transparent materials, the period thickness is shared by the two materials (more than two materials are also possible, as it will be shown below), so that the optimum optical layer thickness (physical thickness times the refractive index times the inclination term $\cos\theta$) of each material is $\lambda/4$; such layers are called quarterwave.

The presence of absorption influences the optimum film thicknesses in a ML. For MLs with absorbent materials, a reflectance increase is obtained by reducing the thickness of the scattering material below a quarterwave, to increase the wave penetration through the ML (Spiller, 1972a); this thickness reduction is supplemented on the spacer material so that a period consisting of two layers, one of each material,

totals an optical thickness of approximately $\lambda/2$. Let us see the film thicknesses that maximize the ML reflectance. Let Γ be the ratio of scattering-to-period layer thicknesses, then

$$\Gamma = \frac{x_H}{x_L + x_H} \tag{7.32}$$

where x_H and x_L are the layer thicknesses of the high (scattering) and the low (spacer) absorption material, respectively; strictly speaking, x_H and x_L should refer to optical thickness (the refractive index times the thickness) although often they can be approached by physical thickness, since n approaches 1 in the short EUV and shortwards. With absorbent materials, the optimum Γ that maximizes reflectance (Γ_{opt}) is smaller than 0.5. Vinogradov and Zeldovich (1977) found a transcendental equation to calculate Γ_{opt} that maximizes reflectance at a given λ for a ML with a large number of periods:

$$\tan\left(\pi\Gamma_{\text{opt}}\right) = \left(\pi\Gamma_{\text{opt}} + \rho\right) \tag{7.33}$$

with $\rho = n_L k_L/(n_H k_H - n_L k_L)$ a function of the optical constants of the materials.

When $k_L \ll k_H$, Eq. (7.33) can be approximately solved:

$$\Gamma_{\text{opt}}^{(0)} = \frac{1}{\pi}(3\pi\rho)^{1/3} \tag{7.34}$$

The latter approximate solution is correct for small values of Γ_{opt}, but starts deviating from the correct solution when Γ_{opt} is larger than ≈ 0.16 ($\rho > 0.013$). An approximate solution of Eq. (7.33) that is valid in a wider range has been derived:

$$\Gamma_{\text{opt}}^{(1)} = \gamma + \frac{1}{2}\left[\sqrt{(\gamma+\rho)^2 - \frac{4}{\pi^2}\left(1 - \frac{\gamma+\rho}{\tan\pi\gamma}\right)} - (\gamma+\rho)\right] \tag{7.35}$$

with

$$\gamma = \Gamma_{\text{opt}}^{(0)}\left[1 - \frac{2}{15}\frac{\left(2\pi\Gamma_{\text{opt}}^{(0)}\right)^2}{1 + \frac{2}{3\left(\pi\Gamma_{\text{opt}}^{(0)}\right)^2}}\right] \tag{7.36}$$

which is valid in the range $0 < \Gamma_{\text{opt}} < 0.42$ ($0 < \rho < 2.6$). For even larger values of ρ we can use

$$\Gamma_{\text{opt}} = \frac{1}{4} + \frac{1}{2}\left(\sqrt{(\rho + 1/2)^2 - 4/\pi^2} - \rho\right) \tag{7.37}$$

which is valid in the range $0.40 < \Gamma_{\text{opt}} < 0.50$ ($\rho > 1.8$).

When material absorption is large, and the maximum number of ML periods contributing to reflectance is limited by absorption, reflectance can be optimized with the use of aperiodic better than periodic MLs. Here Γ is no longer constant through the ML and it decreases from the innermost to the outermost layer to enhance radiation penetration; to design the ML with the largest reflectance, every film thickness

must be optimized. MLs with maximum reflectance at a given λ are easy to design step by step: the addition of a new period on top of an already optimized ML does not require the reoptimization of the thickness of the inner periods (actually the outermost layer of the ML with one fewer period must also be recalculated) (Carniglia and Apfel, 1980). In fact it was found that layer thickness optimization can be done even more easily, in a layer-by-layer process (Yamamoto and Namioka, 1992; Larruquert, 2002b).

The standard ML design results in coatings with a bandwidth that amounts approximately (normal incidence) to

$$\frac{\Delta\lambda}{\lambda} \geq 1/\mathrm{mN}, \tag{7.38}$$

where N is the number of periods in the ML and m is the reflection order. Absorption decreases with wavelength, which enhances the penetration and hence it enables the increase of N (which is also necessary due to the decreased reflectance at each interface); as a result, the relative bandwidth ($\Delta\lambda/\lambda$) of the ML decreases with wavelength. There are cases in which modified values of $\Delta\lambda/\lambda$ are required. When a reduced $\Delta\lambda/\lambda$ is needed, one degree of freedom is the reduction of Γ: if we use a Γ lower than the aforementioned optimum value, this enables a larger penetration through the multilayer (with a cost in reflectance), so that more periods contribute to the ML reflectance and this results in a narrower band, according to Eq. (7.38). Fig. 7.16A displays the reflectance of Mo/Si MLs optimized at 13.5 nm calculated with decreasing Γ, which results in a decrease of the bandwidth; the thinnest feasible layer thickness limits the lower possible value of Γ. A means of strongly decreasing

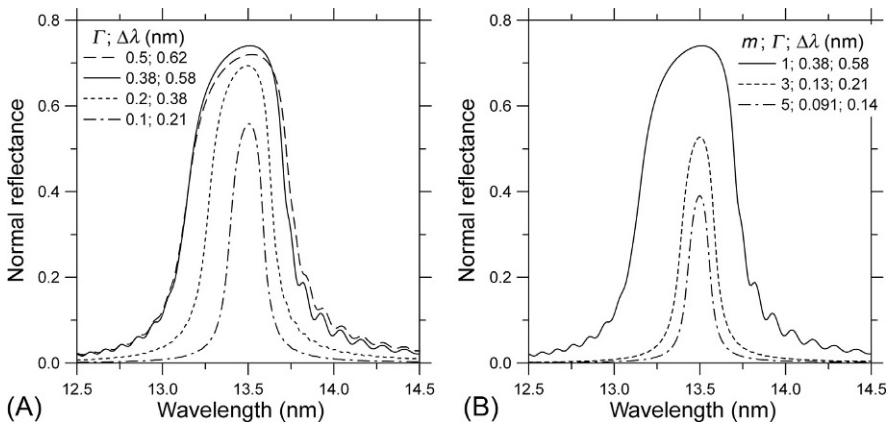


FIG. 7.16

Calculated reflectance as a function of wavelength of Mo/Si MLs optimized at 13.5 nm for various values of (A) Γ and (B) Γ and the reflection order m. The bandwidth, as FWHM, is also plotted. The optical constants of Mo (Soufli and Gullikson, 1998) and Si (Soufli and Gullikson, 1997), which were downloaded at CXRO Web, were used in the calculations.

the ML bandwidth is to increase the reflection order as per Eq. (7.38) (Feigl et al., 2005). This results in an important increase of layer thicknesses according to Bragg Eq. (7.31); for absorbent materials, this thickness increase has a cost on peak reflectance due to the larger absorption per reflectance contribution at each interface; to minimize the absorption increase of using higher reflection orders, the thickness increase may be performed only at the spacer material (Wu et al., 2011). Fig. 7.16B displays the reduced bandwidth calculated for Mo/Si MLs optimized at 13.5 nm designed with the first odd reflection orders (the even orders are also possible), which also results in a decrease of the reflectance peak.

For the opposite requirement of an extended bandwidth, a simple option is the superposition of various MLs, each designed to reflect a specific bandwidth (or angle range); such device is called a supermirror (Christensen et al., 1992). Supermirrors were originally developed for neutron optics (Mezei, 1976). The basics for supermirrors is that a small enough absorption permits penetration through more layers than are required to produce a good mirror for a single wavelength, and the extra layers can contribute to reflect at additional wavelengths (Spiller, 1994). A supermirror is feasible for very low absorption materials, that is, at very short wavelengths such as in the HXR, so that radiation penetrates through many layers. Since the penetration is larger for shorter wavelengths, the ML can be made graded in depth in a way that the period decreases from top to bottom. In practice, an extended bandwidth can be obtained with the optimization of every single layer in a ML. The extended bandwidth always results in some peak-reflectance decrease compared to the ML optimized at a single λ, although the integrated reflectance, either in wavelength, in incidence angle, or in both, can be enhanced significantly. MLs with extended bandwidth have been developed by different authors (Joensen et al., 1992; Yamashita et al., 1998; Morawe et al., 2002; Kozhevnikov et al., 2001; Feigl et al., 2005; Aquila et al., 2006; Maury et al., 2010, Windt and Gullikson, 2015). There are some cases in which, besides an extended bandwidth, a coating is required to reflect more than one individual wavelength and/or to reject secondary wavelengths with a very low reflectance, such as for the simultaneous imaging of various spectral lines while at the same time masking more intense parasitic lines, in applications for astronomical or solar telescopes (Edelstein, 1989; Larruquert and Keski-Kuha, 2001; Hecquet et al., 2009).

At wavelengths in the long EUV ($50\,\text{nm} < \lambda < 105\,\text{nm}$), the absorption of all materials in nature is too large. This complicates the development of efficient ML coatings because there is too small a penetration in the ML to get the benefit of constructive interferences.

In the spectral range of wavelengths longer than 50 nm, the reflectance of a single layer may be moderately large. Hence reflective coatings in the long EUV and longwards are often based on single layers, sometimes overcoated with a protective layer. Fig. 7.17 displays the reflectance of various materials used for single layer mirrors in the long EUV and short FUV. CVD SiC provides a relatively large reflectance at any wavelength above ~60 nm. CVD is a technique that requires deposition on a substrate at a very high temperature and the coating requires a demanding polishing

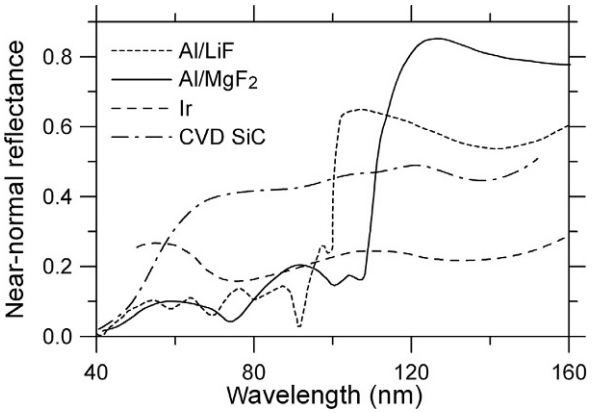


FIG. 7.17

Reflectance of materials used for single-layer mirrors in the long EUV: Ir (Hass et al., 1967), chemical-vapor-deposited SiC (Keski-Kuha et al., 1988), and Al protected with either LiF or MgF2 (Hunter et al., 1971).

Source: With permission from the Optical Society of America.

process; to avoid these difficulties, SiC or B_4C coatings deposited by sputtering are often preferred even though they present a more modest reflectance.

Bare Al films have a remarkably high reflectance in a wide range, which extends down to ≈83 nm; however, its high reflectance is lost shortwards of ≈200 nm because a thin film of natural aluminum oxide grows on Al in contact with the atmosphere. To avoid this, a protective overcoating layer of MgF_2 on Al can keep high reflectance down to ≈115 nm, which can be extended down to almost 100 nm when MgF_2 is replaced with LiF. Al protected with MgF_2 is a very popular coating which was developed over 50 years ago (Hass and Tousey, 1959); it is stable over time, whereas LiF in Al/LiF mirrors is more reactive in the presence of water vapor and hence it is only used when high reflectance is strictly required below ≈120 nm. Best fluoride-protected Al films are deposited with the evaporation technique.

A significant reflectance increase has been recently obtained on these popular coatings by Quijada et al. (2012, 2014). It consists in depositing the MgF_2 or LiF protective overcoating on a hot, Al-coated substrate, so that the fluoride grows more transparent than at the standard room temperature. First, the Al film is deposited on a room temperature substrate, since Al would grow rougher if deposited on a hot substrate, and a small fraction of the fluoride film is promptly deposited to avoid Al oxidation. The mirror is then immediately heated in vacuum to complete deposition of the fluoride protective film on a hot Al film. Fig. 7.18 displays the reflectance increase with this technique.

Another approach to Al mirrors is under research. Atomic layer deposition (ALD) technique has the property of growing a film monolayer by monolayer. This property

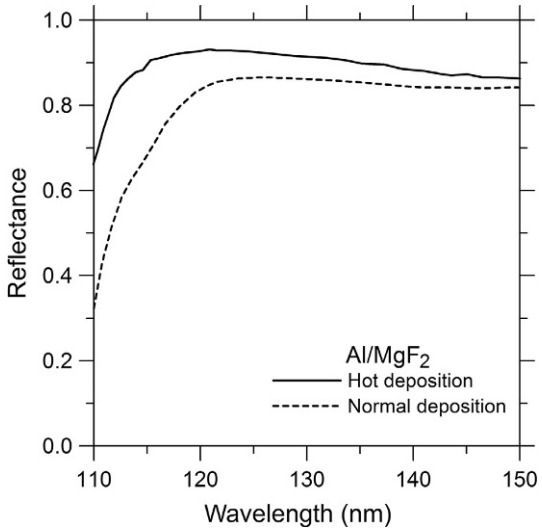


FIG. 7.18

FUV reflectance of an Al + MgF_2 mirror coating. Al and an overcoat of 4 – 5 nm layer of MgF_2 deposited at room temperature, later heated to 493 K to complete the MgF_2 film thickness. For comparison, measurements on coatings at room temperature are also displayed (Quijada et al., 2014).

With permission from M.A. Quijada and from SPIE.

suggests that, ideally, an Al film could be protected with just an ultrathin film of one or few monolayers of a fluoride such as MgF_2 or AlF_3. It assumes that the ultrathin ALD-deposited fluoride will grow with no voids to avoid any oxygen or water vapor molecules to reach the Al film. The ultrathin protective coating would ideally enable Al to keep its high reflectance down to its plasma wavelength at ~83 nm. No demonstration has been reported so far on the Al protection with such an ultrathin film. Nevertheless, a remarkable development has been obtained with introducing ALD-protective layers on Al, although still more progress is required. Best results have been obtained so far on Al deposited by evaporation and later protected with a film of AlF_3 deposited by ALD with a thickness to obtain interferential maxima in the short FUV; even with nonprotected Al layers that were exposed to the air before transferred to the ALD reactor to deposit the protective AlF_3 overcoating, and hence that must be significantly oxidized, a FUV reflectance was reported by Hennessy et al. (2016) that is not far from the reflectance of coatings all deposited by evaporation.

Other than single layers, and in spite of the strong absorption in the 50–105 nm range, some relatively narrow MLs of moderate efficiency have been developed; they are based on the comparatively low absorption of lanthanides like Tb (Windt et al., 2005; Kjornrattanawanich et al., 2006), Gd (Kjornrattanawanich et al., 2008), Yb (Vidal-Dasilva et al., 2009), and Eu (Larruquert et al., 2011b); in fact,

these MLs have few periods: only one and a half for those based in Yb and Eu. An exception to this is a 10-period, narrowband AlMg/SiC ML with a large reflectance peaked at 75 nm (Soufli et al., 2012).

A procedure to make MLs with strongly absorbent materials that are more efficient than single layer coatings has been devised in what has been called subquarterwave MLs (SQWMs) (Larruquert, 2001a,b). SQWMs use layers of up to three or more materials with reduced thickness to increase the number of interfaces close to the outermost one; this adds extra reflected components close to the outermost interface where radiation has not yet been fully absorbed. For SQWMs, materials must be selected in the correct sequence for the extra reflected components to result in an incremental contribution. The procedure starts by plotting in the complex plane the optical constants (n, k) of many materials at the desired target λ. The materials with the most extreme optical constants are the most promising for SQWMs. If all considerations about film thickness and interface stability are obviated, a mere reflectance calculation predicts that maximum ML reflectance is obtained if all the materials with the most extreme optical constants are successively deposited in the SQWM. The condition for the extra reflected components to result in constructive interferences is that the material sequence in the ML is given by counterclockwise rotation in the $n - k$ plot (in the direction from the innermost to the outermost layer). Calculated reflectance increases with the number of materials. Fig. 7.19 plots n and k of a selection of materials with extreme optical constants at 91.2 nm; arrows indicate the counter-clockwise deposition sequence from the innermost to the outermost layer

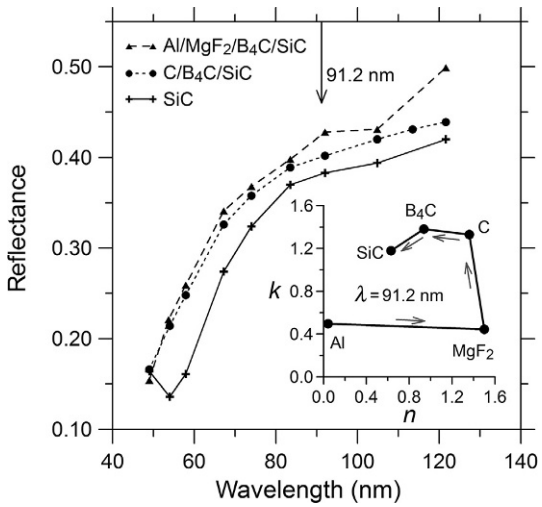


FIG. 7.19

Measured reflectance at near-normal incidence of SQWM with 1–4 layers of as many materials optimized at 91.2 nm. Inset: n, k plot of materials with extreme optical constants at 91.2 nm; arrows indicate the deposition sequence from the innermost to the outermost layer.

(Larruquert and Keski-Kuha, 2002). Fig. 7.17 also displays the reflectance increase measured for SQWM when increasing from 1 to 4 materials, one layer per material. The reflectance increase, although modest, extends to a wide range.

SQWMs can be also applied to regions where absorption is not so strong so that there is enough penetration to make standard MLs that alternate layers of two materials. In this case, SQWMs provide a reflectance increase over standard MLs when increasing the number of materials from two to three or more (Larruquert, 2002a). Fig. 7.20 displays the optical constants n, k of many materials at 30.4 nm; the outer polygon connects the materials with the most extreme optical constants, which are the most promising candidates for SQWMs from the optical constants point of view. The figure also gives the calculated reflectance at 30.4 nm for SQWM with 25 periods when the number of materials is increased from two to ten. A significant reflectance increase is calculated when the number of materials is increased above the standard of two, particularly with three materials; the reflectance increase tends to saturation with the number of materials so that the insignificant increase with the addition of the last several materials would be neither worth the complication nor realistic in practice. Fig. 7.21 displays the measured reflectance enhancement for a ML optimized at 37 nm when the number of materials is increased from two (Mg/SiC) to three (Mg/Sc/SiC) (Aquila et al., 2009). Various successful attempts to obtain a reflectance

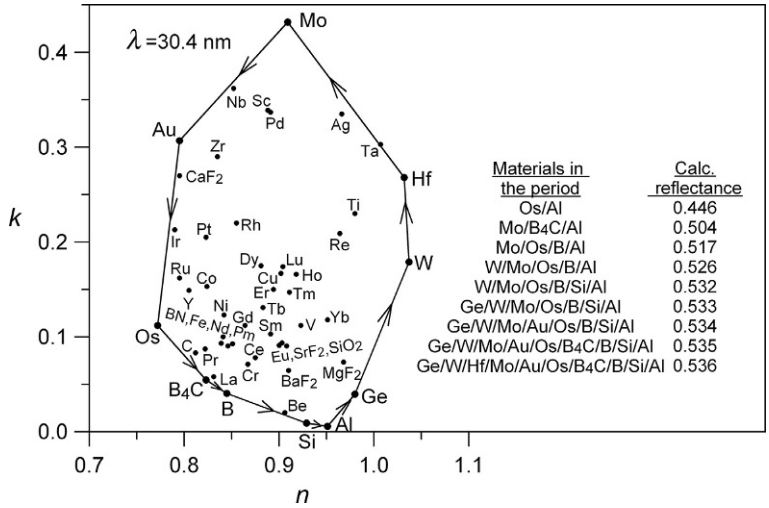


FIG. 7.20

Optical constants of many materials at 30.4 nm. The outer polygon connects the materials with the most extreme optical constants; arrows indicate the deposition sequence from the innermost to the outermost layer. Inset table: calculated normal reflectance at 30.4 nm of 25-period MLs with increasing number of materials optimized for the largest reflectance at near-normal incidence. For each number of materials, the maximum achievable reflectance among all possible material combinations is given.

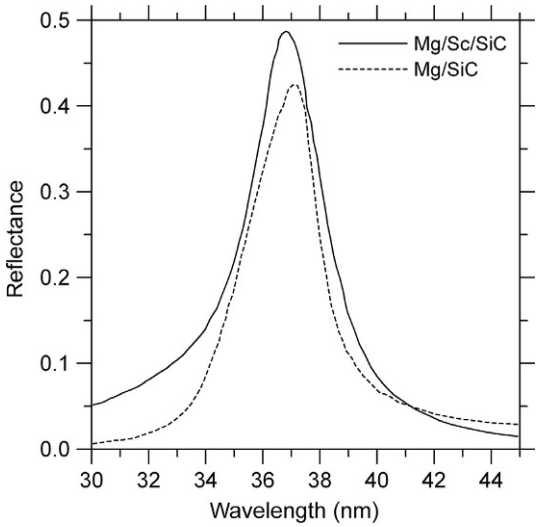


FIG. 7.21

Reflectance enhancement measured for MLs when the number of materials is increased from two (Mg/SiC) to three (Mg/Sc/SiC) (Aquila et al., 2009).

Source: With permission from the Optical Society of America.

enhancement through multilayers with more than two materials have been reported (Boher et al., 1990; Larruquert and Keski-Kuha, 1999; Gautier et al., 2005; Zhu et al., 2008; Meltchakov et al., 2010; He et al., 2011; Le Guen et al., 2011). A fast SQWM design algorithm that optimizes each layer thickness in the ML has been reported (Larruquert, 2002b).

SQWMs are useful only if reflectance is limited by absorption. If one material existed with negligible absorption, a theoretical reflectance of 100% could be calculated with MLs alternating such material with any secondary absorbent material (Spiller, 1994) so that an SQWM would be unnecessary. Hence the benefit of SQWM is intrinsic to absorption.

7.7.3 LINEAR POLARIZERS AND PHASE RETARDERS

Linear polarizers and phase retarders, the basic elements for polarimetry, are required for an increasing number of applications at short wavelengths, including ellipsometry, imaging instrumentation for solar physics and astrophysics, synchrotron radiation, lasers, solid state physics, atomic and molecular physics, particle-matter interaction, magnetic and chiral material analysis, circular dichroism spectroscopy, spin-polarized photoelectron spectroscopy, and magnetic Compton scattering. The polarization state of radiation can be described in terms of the four Stokes parameters S_0, S_1, S_2, and S_3, which represent the total intensity (S_0), the linearly polarized intensity (S_1, S_2), and the circularly polarized intensity (S_3).

To make a complete polarization analysis of light, two elements are required: a phase retarder (referred to here simply as retarder), which ideally provides 90° phase retardation between two perpendicular components of the electric field, and a linear polarizer (referred to here simply as polarizer), which provides linearly polarized light. To make a polarization measurement we need to have independent rotations of the polarizer and the retarder around the optical axis. Stokes parameters, and hence the polarizing properties of the beam, are obtained from a fit of the recorded intensity upon rotations of the two elements (Schäfers et al., 1999).

Polarizers and retarders for wavelengths shorter than the LiF cutoff are based on the different reflectance/transmittance modulus or phase for parallel and perpendicular polarization at angles other than normal or grazing incidence.

For polarizers and retarders operating by reflection, the ratio

$$\rho = \frac{r_s}{r_p} = \left|\frac{R_s}{R_p}\right|^{1/2} e^{j(\phi_s - \phi_p)} \tag{7.39}$$

contains the information for polarimetry purposes, where p (TM) and s (TE) stand for the electric vector parallel and perpendicular, respectively, to the plane of incidence. A polarizer is required to provide a modulus of ρ as large as possible; a retarder is required to provide a large phase difference between the s and p components, ideally 90°, with the modulus of ρ as close to 1 as possible. For elements working by transmission, reflectance is replaced with transmittance in Eq. (7.39) and the roles of p and s are usually inverted.

In the visible range, it is often preferred that polarizers and retarders operate by transmittance, because the optical beam can pass essentially undeviated. This same concept can be extended to short wavelengths, as long as bulk transparent materials are available, that is, down to the LiF cutoff wavelength of $\approx 105\,\text{nm}$; below this wavelength, a thin-film, self-supported substrate can be used. In the transparent range of $\lambda > 105\,\text{nm}$, two main mechanisms are used to introduce linear polarization and retardation: birefringence and operation at Brewster angle. Birefringence, that is, the dependence of the refractive index on the direction of the electric field in the medium, which is present for instance in noncubic crystals, is a useful property to make polarizers and retarders. Rochon prisms are an example of linear polarizers based on birefringence that have been used in the FUV; Rochon prisms deviate the extraordinary ray and keep the ordinary ray undeviated. Birefringence can also provide a phase shift between two waves with perpendicular planes of polarization, which is the basis for retarders. LiF is a cubic crystal and hence it is not a candidate to make retarders; however, its shortest cutoff in nature has made it attractive for inducing piezo-birefringence by compressing the crystal of LiF in one direction (Metcalf and Baird, 1966), which results in a retarder operating at a wavelength as short as 105 nm at room temperature. Other than birefringence, polarization using transparent materials can be produced through the reflection at the Brewster angle, at which the reflectance for p polarization turns zero. The Brewster angle θ_B is connected with the refractive index of the material n by

$$\tan \Theta_B = n \tag{7.40}$$

This formula is obtained using the r_p expression of Eq. (7.8) and Snell's law (7.5). Hence to linearly polarize light by reflection, it is necessary that the material be transparent. A polarizer working by reflection at θ_B results in an undesired deviation of the optical beam (by $2\theta_B$). We can capitalize the existence of the Brewster angle also operating by transmittance: we take advantage of the increased T_p/T_s ratio at Brewster angle of the beam transmitted through a plate. Since a single plate at θ_B provides a modest transmittance polarization ratio, a pile of plates in series at the Brewster angle can be used to increase this ratio (Walker, 1964).

A third mechanism, originally developed for long wavelengths, is reaching the FUV: wire grid polarizers. These polarizers consist in an arrangement of microscopic wires on a transparent substrate so that a high extinction ratio is obtained by transmission of the p to s component. They can also operate by reflection by interchanging s and p components. Extending to the FUV involves the difficulty to fabricate denser grid lines and to find materials with the right optical properties. Coatings are involved within a complicated process that is required to make a thin enough period and a high aspect ratio. Polarizers operating at a wavelength as small as 193 nm have been prepared based on tungsten wires (Weber et al., 2012).

A review of the developments based on all sorts of transparent bulk structures working by transmittance or reflectance and operating in the FUV was written by Hunter (2000) and will not be included here. An older review was reported by Samson (1967c). In the following, only polarizers and retarders based on coatings will be addressed. Interesting reviews on coatings for polarimetry in the EUV and SXR have been reported by Schäfers (2007) and Watanabe et al. (2008). Some further reference to polarizers and retarders was made in Section 7.6 under the subject of ellipsometry.

7.7.3.1 Polarizers

Let us start with linear polarizers. In contrast to what was said on the Brewster angle for transparent materials, when at least one material at the interface is absorbent, as for every material below the LiF cutoff wavelength, there is no angle at which R_p reaches zero. In spite of this, there is still an angle at which $R_p(\theta)$ reaches a minimum; this angle is often called the pseudo-Brewster angle. The ratio R_s/R_p takes the largest value at an angle in the vicinity of the pseudo-Brewster angle. This property enables polarizers to be made using coatings even when only absorbent materials are available. Fig. 7.22 displays the calculated s and p reflectance versus the incidence angle for a Au layer at two wavelengths; the minimum of R_p versus angle and the enhanced R_s/R_p ratio can be observed. For short enough wavelengths in which the complex refractive index $N = 1 - \delta + i\beta$ satisfies $\delta, \beta \ll 1$, the pseudo-Brewster angle can be approximated by (Attwood, 1999)

$$\theta_{p-B} \approx \frac{\pi}{4} - \frac{\delta}{2} \tag{7.41}$$

Thus at short wavelengths, where δ is mostly positive, the minimum R_p is obtained at an angle slightly smaller than 45° (slightly closer to normal incidence). In the

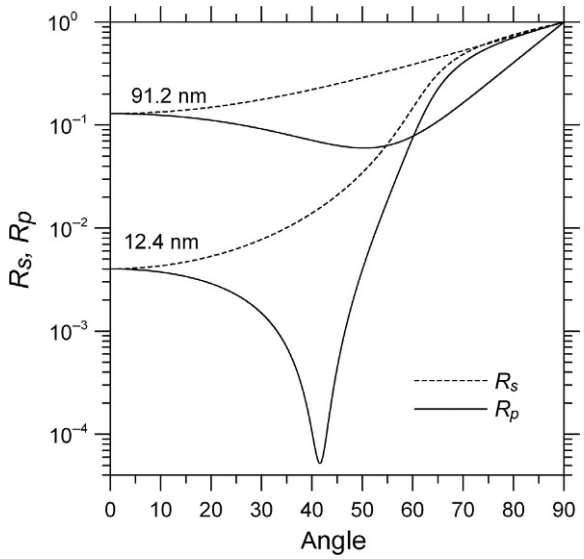


FIG. 7.22

The reflectance (log scale) of Au calculated for parallel (R_p) and perpendicular (R_s) polarization versus the angle of incidence (from the normal) at the indicated wavelengths. Data were calculated with optical constants of Canfield et al. (1964) (91.2 nm) and also downloaded from CXRO Web (12.4 nm).

examples of Fig. 7.22, the angle given by Eq. (7.41) is accurate at 12.4 nm and less precise at 91.2 nm (where δ is negative), since in the latter the above condition for β is not met. Yet if we do not restrict ourselves to materials satisfying Eq. (7.41), for any wavelength and optical constants and for a single interface it is satisfied that $R_p = R_s^2$ at 45° (Rabinovitch et al., 1965), which results in an enhanced $R_s/R_p = 1/R_s$ ratio at this angle when R_s becomes small; unfortunately a good polarization ratio with a single interface is only obtained with a low R_s.

Hence the angle range around 45° is a natural choice to develop reflection polarizers. Unfortunately, at short wavelengths R_s at θ_{p-B} for a single interface, even though larger than R_p, is still small. Since the angle for minimum R_p is close to 45° and this is relatively insensitive to the specific optical constants of the materials at the interface, a multilayer can be optimized for high R_s at angles $\theta \approx 45°$ while keeping a large R_s/R_p ratio (Spiller, 1972b; Gluskin et al., 1986; Dhez, 1987; Kortright, 1993; Bruch et al., 1999; Imazono et al., 2009). Mertins et al. (1998) prepared this sort of polarizer for the water window. Schäfers et al. (1999) prepared reflective polarizers based on various material pairs for several spectral ranges up to ≈570 eV. Fig. 7.23 displays R_s and R_s/R_p data calculated at 45° for prospective ML polarizers based on various material pairs covering the range of 50–900 eV, after Schäfers et al. (1999). The increasing absorption at long EUV wavelengths causes a decrease in the R_s/R_p ratio (Hunter, 1965).

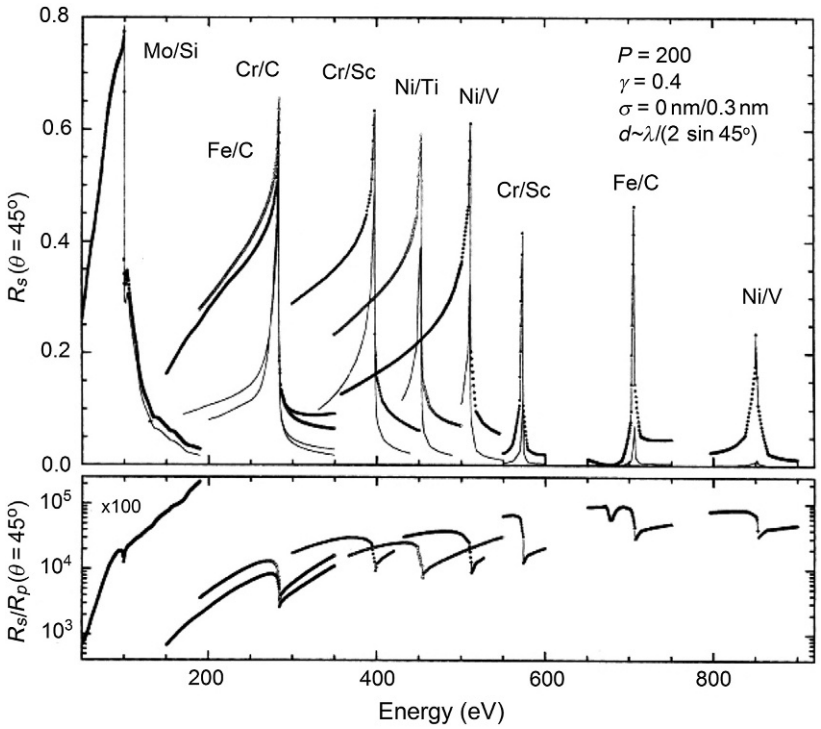


FIG. 7.23

R_s and R_s/R_p calculated at 45° for prospective ML polarizers based on various material pairs covering the range of 50–900 eV (Schäfers et al., 1999).

Source: With permission from the Optical Society of America.

Coating polarizers can also be prepared in the FUV (in addition to those based on bulk properties of transparent materials mentioned at the beginning of this section). One possible combination is Al/MgF_2 MLs (Bridou et al., 2011; Larruquert et al., 2014), and such coatings are sometimes preferred over bulk devices when a large R_s is required.

When the coating consists of a ML with many layers, the simple and common approach is the use of a periodic ML. One limitation of a polarizer made using this approach is that it is efficient in a narrow spectral and angular band. By varying the angle of incidence, the band of a ML can be spectrally shifted, which enables covering a larger spectral range with a single ML (Maehara et al., 1991; Yanagihara et al., 1992; Yamamoto, 1993); however, the variation of the angle of incidence results in a deviation of the reflected beam, which complicates the design of a polarimeter. Wideband polarizers have also been developed based on the displacement of a laterally graded multilayer (Kortright et al., 1995). To avoid rotation or travel, wideband polarizers and/or polarizers effective in an enhanced angular range can

be designed by optimizing each layer thickness in the ML following a desired figure of merit; experimental demonstration of aperiodic ML polarizers with an increased EUV or SXR spectral band (Wang et al., 2006a,b, 2007b; Tan et al., 2011) and with a wide angular band at 13 nm (Wang et al., 2006c) have been reported.

One disadvantage of reflective polarizers is that they divert the optical beam; this can be avoided by using various mirrors in series. The minimum number of mirrors to avoid beam rotation and shift is three, with the two extreme reflections at a common angle and a central reflection at double the grazing angle of the extreme reflections. If additionally all reflections are desired at a common angle, a minimum of four reflections is required. Fig. 7.24 displays the two configurations. The multiple reflections can provide an increased reduction of R_p (Hamm et al., 1965; Rosenbaum et al., 1968; Horton et al., 1969; Hunter, 1978, 2000). These configurations, particularly the three-mirror one, have been extensively used in the long EUV (and even in the FUV) and they may result in polarizers with a relatively wide band (Horton et al., 1969;

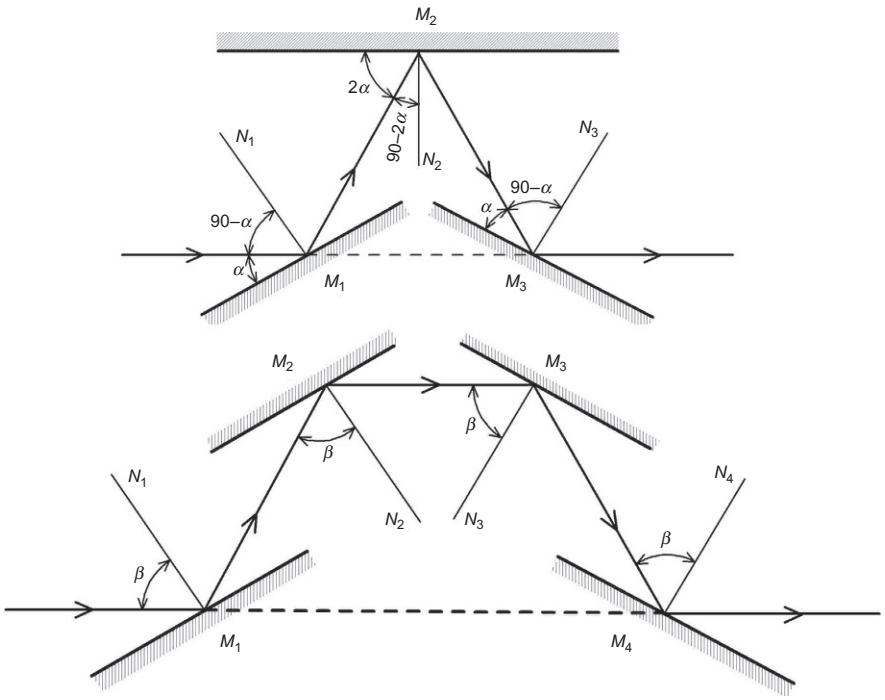


FIG. 7.24

3-mirror (top) and 4-mirror (bottom) polarizer configurations to avoid the deviation of the optical beam. The planes of incidence of all mirrors are coincident and they are on the plane of the sheet. The component of the electric field that is reduced is the one in the plane of incidence.

Naik and Lodha, 2006). The use of a specific coating for each of the mirrors may provide a polarizer that is operative in a wider band (Hass and Hunter, 1978), with the additional gain of suppressing higher diffraction orders (Yang et al., 2007).

Transmittance polarizers have also been developed with the benefit that they do not deviate the beam. A transmittance polarizer was proposed by Hu et al. (1996); it consists of a free-standing (self-supported) transmission multilayer for which a high R_s at an incident angle close to the Bragg angle of the multilayer (angle at which the ML satisfies Eq. 7.31) results in a reduced T_s; hence T_p/T_s in a transmission polarizer is enhanced versus R_s/R_p for the reflection polarizer. One property of transmission polarizers is that when the layer number increases, the throughput of transmitted light T_p always decreases but the polarization ratio increases (Tan et al., 2009). Transmission polarizers were developed by Haga et al. (1998, 1999). Polarization by transmission through a ML was developed by Kjornrattanawanich et al. (2004) in which the coating was deposited on the detector. FUV transmissive polarizers based on Al/MgF_2 MLs have also been prepared (Larruquert et al., 2014).

For high energies above $\approx$1 keV, polarizers based on perfect crystals operating close to a Bragg angle can be used and are preferred over MLs (Marx et al., 2011; Wang et al., 2012). Some polarizers are based on the anomalous transmission of X-rays or Borrmann effect (Batterman and Cole, 1964; Hart, 1978; Batterman, 1992).

7.7.3.2 Retarders

Let us now address phase retarders. They introduce a relative phase change between the *s* and *p* components in either the reflected or the transmitted beam. As with linear polarizers, bulk retarders based on the transparency of materials in the FUV are not reviewed here and the reader is again referred to Hunter (2000). Very useful retarders are those that introduce a phase shift of 90°, called quarter-wave retarders (not to be confused with a quarterwave layer referred to in Section 7.3.3: the latter refers to the optical thickness of a layer, whereas the former refers to phase retardation between the *s* and *p* components), which, in combination with a linear polarizer, enable a complete polarimetric analysis of the incoming beam. As mentioned above, retarders also require that the throughput for *s* and *p* polarization be very similar.

Phase retarders have been developed based on both reflection and transmission. Wideband retarders based on reflection have been fabricated or at least designed with single (Westerveld et al., 1985; Saito et al., 1990) and multiple (Johnson and Smith, 1983; Höchst et al., 1994; Naik and Lodha, 2006) Au-coated mirrors. Multiple reflectors can provide 90° total phase retardation through the addition of the individual phase shifts produced by each single mirror; the configuration for retarders based on multiple mirrors is the same as the one displayed in Fig. 7.24. Höchst et al. (1995) could turn linear polarization into circular polarization, that is, could provide 90° phase retardation, by adjusting the common incidence angle of the 4 mirrors and by rotating the quadruple reflector with respect to an axis coincident with the incident beam. Smith and Howells (1994) replaced each of the 4 flat mirrors with a whispering gallery, that is, a cylindrical mirror in which the beam is reflected not once but

several times on each mirror, all of them at a more grazing incidence (and hence more efficiently) than when plane mirrors are used. Kim et al. (1992) designed 3-layer MgF_2-Al reflection retarders tuned at 121.6 nm. Imazono et al. (2009) prepared reflection Mo/Si ML retarders (and also polarizers) tuned at 13.5 nm.

Similar to polarizers, reflection retarders have the disadvantage that they cause the deviation of the beam (except for the 3- and 4-element configuration), and hence transmission retarders are often preferred. Kortright and Underwood (1990) calculated that an efficient quarter-wave retarder could be made by transmission through an optimized multilayer. The benefit of such a retarder compared to those working by reflection is that the beam is not essentially deviated; a drawback is that it must be self-supported to avoid full absorption from the substrate, which makes the retarder fragile. Kortright and Underwood (1990) observed how the *s* component of the electric field is subject to larger interference effects than the *p* component, which results in a phase shift between the two components; they found a useful incidence angle range for retardation purposes between the Bragg angle and the critical angle of total reflection.

Fig. 7.25 displays the transmission phase retardation, the transmittance ratio, and the transmittance for the *p* component calculated for Mo/Si MLs with various numbers of periods at 13.5 nm as a function of the angle of incidence. It can be seen that retardation increases with the number of periods, which is an intuitive result for a transmission coating, although obviously both T_p and T_s decrease with this same number. The request of $T_p \approx T_s$ is satisfied at ≈50–52°. In this example, the ML with 32.5 periods at an angle of ≈50° is calculated to have a phase retardation of 90° with equal transmittance for the *p* and *s* components of 0.18.

Various quarter-wave retarders working by transmission have been developed for the spectral range around 13 nm (Kortright et al., 1992; Nomura et al., 1992; Yamamoto, 1993; Haga et al., 1998, 1999; the latter developed a polarimeter with no deviation based on a transmissive polarizer and retarder), at the water window (Kimura et al., 2005; Chkhalo et al., 2011) and at energies up to ≈1.5 keV (Wang et al., 2012). At high energies it becomes difficult to achieve large retardation values. The trend of the refractive index towards unity at increasing energies makes it difficult to reach a phase shift as large as 90°. Even though a retardation of 90° is the ideal value to analyze elliptical polarization, a phase-shift angle of a few tens of degrees (Di Fonzo et al., 1994) or even a few degrees at $E > 600$ eV (MacDonald et al., 2008) has been demonstrated to be sufficient to obtain the characterization of a beam. Schäfers et al. (1999) used Si_3N_4 membranes for retarder substrates to improve robustness; they prepared transmission retarders based on various material pairs to cover several spectral ranges up to ≈570 eV.

Similarly to linear polarizers, transmissive retarders based on periodic MLs are often efficient only in a narrow spectral band. As with polarizers, aperiodic-ML transmission retarders that are effective in a wider spectral range can be designed with the optimization of all layer thicknesses in the ML according to a specific figure of merit (Wang et al., 2007a,b); in the latter pieces of research, Si_3N_4 membranes were used as substrates to improve robustness.

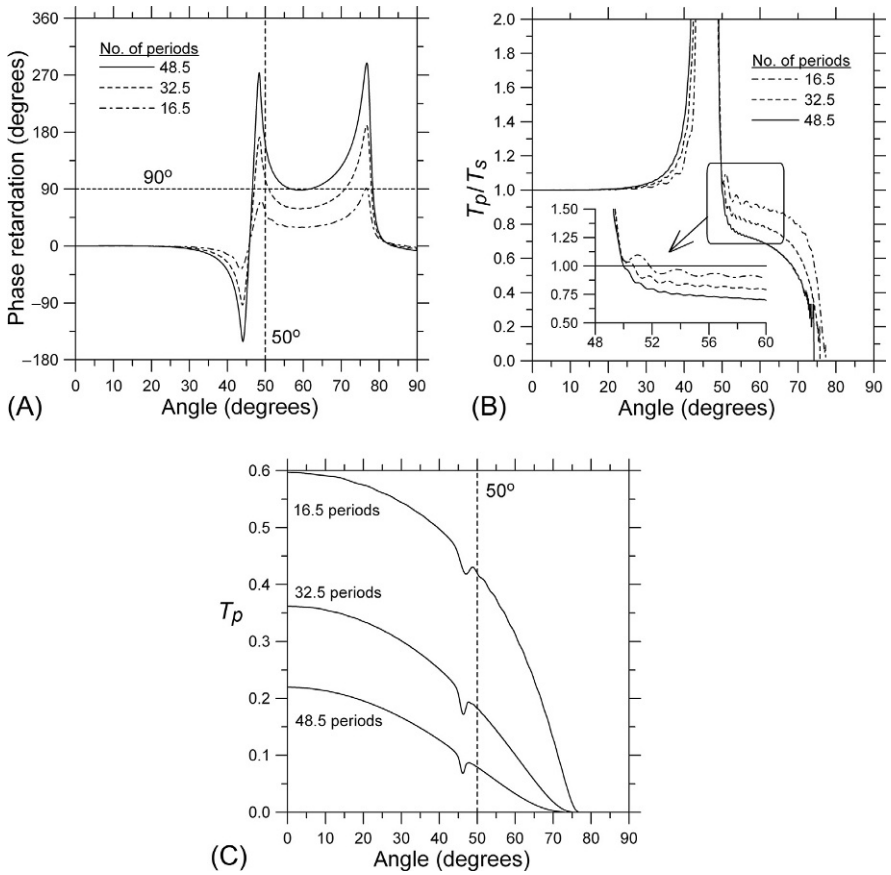


FIG. 7.25

The phase retardation on transmission (A), the T_p/T_s (B), and T_p (C) calculated for Mo/Si MLs with various numbers of periods versus the angle of incidence referred to the normal. MLs are designed to satisfy the Bragg condition at 13.5 nm at 45°. The optical constants of Mo (Soufli and Gullikson, 1998) and Si (Soufli and Gullikson, 1997), which were downloaded from CXRO Web, were used in the calculations.

At increasing X-ray energies, MLs become increasingly less efficient for making retarders; in this case, perfect crystals can be used instead. When a plane-polarized X-ray beam enters a crystal, the electric field can be separated into a parallel and a perpendicular component with respect to the diffraction planes. The two components propagate with different phase velocities through the crystal, as a sort of birefringence. On recombination at the exit, a phase difference proportional to the optical path length is generated. Two geometries are possible: the diffraction planes are perpendicular (Laue) or parallel (Bragg) to the plate surface, and each of them can operate in transmission or reflection (Hirano et al., 1995; Malgrange et al., 1999).

The phase difference is tunable by changing an angle offset away from the Bragg condition (Bouchenoire et al., 2012). A 90° phase retardation can be introduced by a single thin crystal operating in transmission mode (Lang and Srajer, 1995; Giles et al., 1995; Hirano et al., 1995); quarter-wave crystal plates based on multiple reflections have also been developed (Batterman, 1992). Such crystal plates have been used for energies from a few keV to the HXR (Venkataraman et al., 1998).

To finish Section 7.7, a brief reference to a subject that has received important attention in the last years: the use of ML mirrors to compress ultrashort pulses to the attosecond (as) regime; also transmittance filters have been used to compress filters, such as Gustafsson et al. (2007). Ultrashort pulses open the possibility to obtain snapshots of ultrafast electron dynamics in matter with unprecedented time resolution, of great interest to various scientific areas such as atomic, molecular, and solid state physics. Attosecond pulses must be in the EUV or even higher photon-energy domain since the Fourier transform of a 100 as pulse has a bandwidth of $\sim$18 eV, which only fits in a large-energy spectral range. To compress pulses to the as regime, an aperiodic ML is designed to reflect such a broad spectral band and to obtain a specific spectral dependence of the reflectivity phase which results in the time compression of the pulses. This subject will not be covered here and the reader is addressed to the literature, which includes a large development of mirrors for the spectral range below $\sim$105 eV, mostly based on Mo/Si MLs (Morlens et al., 2006; Suman et al., 2007; Bourassin-Bouchet et al., 2012), and in the last years also above 100 eV heading to the water window (Hofstetter et al., 2011; Guggenmos et al., 2013). A parallel progress has experienced the metrology of these optics, which additionally requires the characterization of the reflectance phase (Aquila et al., 2008; Loch et al., 2011; Schultze et al., 2011).

This concludes the present section, which has focused on the state of the art of MLs at short wavelengths for three main sorts of elements: filters, reflective mirrors, and polarizers and retarders. A short reference has been given to coatings for attosecond pulses. Various reviews on MLs for EUV and SXR that may provide supplementary information can be found in the literature (Dhez, 1990; Spiller, 1994; Yulin, 2003).

7.8 CONCLUSION

The optical properties of materials at short wavelengths are different from those in more familiar ranges, such as the visible, and these differences often make this spectral range difficult to handle in an efficient way. On the other hand, materials can also provide valuable information at short wavelengths that supplements what is obtained in more common ranges. And coatings at short wavelengths are considered as enabling challenging applications that are becoming possible now that the difficulties inherent in dealing with this radiation are gradually being harnessed. The dramatic development of optics at short wavelengths in recent decades promises a near future full of progress and success.

ACKNOWLEDGEMENTS

I am indebted to José Antonio Méndez and Mónica Fernández for reading the draft and giving me many valuable suggestions, and for constant discussions, which were extremely helpful to clarify many points. I gratefully acknowledge David Windt for making Fig. 7.15 for this chapter; he kindly updated older versions with recently developed multilayers. I acknowledge financial support from the National Programme for Space Research, Subdirección General de Proyectos de Investigación, Ministerio de Ciencia y Tecnología, Project Nos. AYA2013-42590-P and ESP2016-76591-P.

REFERENCES

Abelès, F., 1948. Sur la propagation des ondes électromagnétiques dans les milieux stratifiés. Ann. Phys. (Paris) 3, 504–520.

Aquila, A.L., Salmassi, F., Dollar, F., Liu, Y., Gullikson, E.M., 2006. Developments in realistic design for aperiodic Mo/Si multilayer mirrors. Opt. Express 14, 10073–10078.

Aquila, A., Salmassi, F., Gullikson, E., 2008. Metrologies for the phase characterization of attosecond extreme ultraviolet optics. Opt. Lett. 33, 455–457.

Aquila, A., Salmassi, F., Liu, Y., Gullikson, E.M., 2009. Tri-material multilayer coatings with high reflectivity and wide bandwidth for 25 to 50 nm extreme ultraviolet light. Opt. Express 17, 22102–22107.

Arakawa, E.T., Hamm, R.N., Williams, M.W., 1973. Optical properties and electron-attenuation lengths from photoelectric yield measurements. J. Opt. Soc. Am. 63, 1131.

Ashcroft, N.W., Mermin, N.D., 1976. Solid State Physics. Saunders College Publishing, Philadelphia.

Attwood, D., 1999. Soft X-rays and Extreme Ultraviolet Radiation: Principles and Applications. Cambridge University Press, Cambridge.

Bajt, S., Alameda, J.B., Barbee Jr., T.W., Folta, J.A., Kaufmann, B., Spiller, E.A., Clift, W.M., 2002. Improved reflectance and stability of Mo-Si multilayers. Opt. Eng. 41, 1797–1804.

Barth, J., Johnson, R.L., Cardona, M., 1998. Spectroscopic ellipsometry in the 6–35 eV region. In: Palik, E.D. (Ed.), Handbook of Optical Constants of Solids II. Academic Press, San Diego.

Batterman, B.W., 1992. X-ray phase plate. Phys. Rev. B 45, 12677–12681.

Batterman, B.W., Cole, H., 1964. Dynamical diffraction of x rays by perfect crystals. Rev. Mod. Phys. 36, 681–717.

Bearden, J.A., Burr, A.F., 1967. Reevaluation of X-ray atomic energy levels. Rev. Mod. Phys. 39, 125–142.

Bennett, H.E., Porteus, J.O., 1961. Relation between surface roughness and specular reflectance at normal incidence. J. Opt. Soc. Am. 51, 123–129.

Berger, M.J., Hubbell, J.H., Seltzer, S.M., Chang, J., Coursey, J.S., Sukumar, R., Zucker, D.S., Olsen, K., 2010. XCOM: Photon Cross Section Database, Version 1.5. Available from: http://physics.nist.gov/PhysRefData/Xcom/html/xcom1.html (Online, Wednesday, 20 June 2012 03:27:19 EDT). National Institute of Standards and Technology, Gaithersburg, MD

Bibishkin, M.S., Chkhalo, N.I., Gusev, S.A., Kluenkov, E.B., Lopatin, A.Y., Luchin, V.I., Pestov, A.E., Salashchenko, N.N., Shmaenok, L.A., Tsybin, N.N., Zuev, S.Y., 2008. Multilayer Zr/Si filters for EUV lithography and for radiation source metrology. Proc SPIE 7025, 702502.

Birken, H.-G., Blessing, C., Kunz, C., 1998. Determination of optical constants from angular-dependent, photoelectric-yield measurements. In: Palik, E.D. (Ed.), Handbook of Optical Constants of Solids II. Academic Press, San Diego.

Boher, P., Hennet, L., Houdy, P., 1990. Three materials soft X-ray mirrors: theory and application. Proc. SPIE 1345, 198–212.

Bouchenoire, L., Morris, R.J.H., Hase, T.P.A., 2012. A silicon <111> phase retarder for producing circularly polarized X-rays in the 2.1–3 keV energy range. Appl. Phys. Lett. 101, 064107.

Bourassin-Bouchet, C., de Rossi, S., Wang, J., Meltchakov, E., Giglia, A., Mahne, N., Nannarone, S., Delmotte, F., 2012. Shaping of single-cycle sub-50-attosecond pulses with multilayer mirrors. New J. Phys. 14, 023040.

Braun, S., Mai, H., Moss, M., Scholz, R., Leson, A., 2002. Mo/Si multilayers with different barrier layers for applications as extreme ultraviolet mirrors. Jpn. J. Appl. Phys. 41, 4074–4081.

Bridou, F., Cuniot-Ponsard, M., Desvignes, J.-M., Gottwald, A., Kroth, U., Richter, M., 2011. Polarizing and non-polarizing mirrors for the hydrogen Lyman-α radiation at 121.6 nm. Appl. Phys. A 102, 641–649.

Bruch, R., Merabet, H., Bailey, M., Siems, A., 1999. Characterization of a compact multilayer mirror (MLM) polarimeter for measurements of the degree of linear polarization in the 256 A to 584 A wavelength EUV range. Proc. SPIE 3764, 28–39.

Canfield, L.R., Hass, G., Hunter, W.R., 1964. The optical properties of evaporated gold in the vacuum ultraviolet from 300 Å to 2 000 Å. J. Phys. 25, 124–129.

Carniglia, C.K., Apfel, J.H., 1980. Maximum reflectance of multilayer dielectric mirrors in the presence of slight absorption. J. Opt. Soc. Am. 70, 523–534.

Carrière, J.D., Heer, J.F., 1972. Transmission properties of a LiF-O_2 filter for radiation resulting from electron impact on H_2: cross sections for Lyman-α radiation. J. Chem. Phys. 56, 2993–2996.

Carruthers, G.R., 1971. Narrow-band filter for the Lyman-β wavelength region. Appl. Opt. 10, 1461–1463.

Cavasso Filho, R.L., Homen, M.G.P., Fonseca, P.T., Naves de Brito, A., 2007. A synchrotron beamline for delivering high purity vacuum ultraviolet photons. Rev. Sci. Instrum. 78, 115104.

Chang, C., Anderson, E., Naulleau, P., Gullikson, E., Goldberg, K., Attwood, D., 2002. Direct measurement of index of refraction in the extreme-ultraviolet wavelength region with a novel interferometer. Opt. Lett. 27, 1028–1030.

Chantler, C.T., 2000. Detailed tabulation of atomic form factors, photoelectric absorption and scattering cross section, and mass attenuation coefficients in the vicinity of absorption edges in the soft X-ray (Z = 30–36, Z = 60–89, E = 0.1 keV–10 keV), addressing convergence issues of earlier work. J. Phys. Chem. Ref. Data 29, 597–1048.

Chantler, C.T., Olsen, K., Dragoset, R.A., Chang, J., Kishore, A.R., Kotochigova, S.A., Zucker, D.S., 1995. Theoretical form factor, attenuation and scattering tabulation for Z = 1–92 from E = 1–10 eV to E = 0.4–1.0 MeV. J. Phys. Chem. Ref. Data 24, 71–643.

Chkhalo, N.I., Drozdov, M.N., Gusev, S.A., Kluenkov, E.B., Lopatin, A.Y., Luchin, V.I., Salashchenko, N.N., Shmaenok, L.A., Tsybin, N.N., Volodin, B.A., 2011. Freestanding multilayer films for application as phase retarders and spectral purity filters in the soft X-ray and EUV ranges. Proc. SPIE 8076, 807600.

Chkhalo, N.I., Drozdov, M.N., Kluenkov, E.B., Kuzin, S.V., Lopatin, A.Y., Luchin, V.I., Salashchenko, N.N., Tsybin, N.N., Zuev, S.Y., 2016. Thin film multilayer filters for solar EUV telescopes. Appl. Opt. 55, 4683–4690.

Christensen, F.E., Hornstrup, A., Westergaard, N.J., Schnopper, H.W., 1992. A graded d-spacing multilayer telescope for high energy X-ray astronomy. Proc. SPIE 1546, 160–167.

Clarke, J.T., Skinner, W.R., Vincent, M.B., Irgang, T., Suratkal, V., Grassl, H., Trauger, J.T., 1999. Laboratory studies of alkali metal filter deposition, ultraviolet transmission, and visible blocking. Appl. Opt. 38, 1803–1813.

Compton, A.H., 1923. The total reflexion of X-rays. Philos. Mag. 45, 1121–1131.

Croce, P., 1977. Sur l'effet des couches très minces et des rugosités sur la réflexion, la transmission et la diffusion de la lumière par un dioptre. J. Opt. 8, 127–139.

Croce, P., 1978. Complément à l'étude de l'effet des couches minces sur la réflexion, la transmission et la diffusion de la lumière. J. Opt. 9, 61–63.

Cromer, D.T., Mann, J.B., 1968. X-ray scattering factors computed from numerical Hartree-Fock wave functions. Acta Crystallogr. A 24, 321–324.

CXRO, http://www-cxro.lbl.gov/optical_constants/.

Davisson, C.M., 1965. Interaction of γ radiation with matter. In: Siegbahn, K. (Ed.), Alpha-, Beta-, and Gamma-Ray Spectroscopy. Elsevier, North-Holland, Amsterdam.

Debye, P., 1913. Über der Intensitätetsverteilung in den mit Röntgenstrahlung erzeugten Interferenzbildern. Verh. Dtsch. Phys. Ges. 15, 738.

Dhez, P., 1987. Polarizers and polarimeters in the X-UV range. Nucl. Instrum. Meth. A 261, 66–71.

Dhez, P., 1990. X and X-UV multilayered optics: principles, fabrication methods, tests and applications. Ann. Phys. Fr. 15, 493–527.

Di Fonzo, S., Jark, W., Schafers, F., Petersen, H., Gaupp, A., Underwood, J.H., 1994. Phase-retardation and full-polarization analysis of soft-X-ray synchrotron radiation close to the carbon K edge by use of a multilayer transmission filter. Appl. Opt. 33, 2624–2632.

Drude, P., 1900a. Zur Elektronentheorie der metalle. Ann. Phys. 306, 566–613.

Drude, P., 1900b. Zur Elektronentheorie der Metalle; II. Teil. Galvanomagnetische und thermomagnetische Effecte. Ann. Phys. 308, 369–402.

Edelstein, J., 1989. Reflection/suppression coatings for the 900–1200 Å radiation. Proc. SPIE 1160, 19–25.

Elias, L.R., Flach, R., Yen, W.M., 1973. Variable bandwidth transmission filter for the vacuum ultraviolet: $La_{1-x}Ce_xF_3$. Appl. Opt. 12, 138–139.

Evans, R.D., 1955. The Atomic Nucleus. McGraw-Hill, New York.

Fabre, D., Romand, J., Vodar, B., 1964. Constants optiques et pouvoir réflecteur de couches minces de fluorures dans l'ultraviolet lointain. J. Phys. 25, 55–59.

Fairchild, E.T., 1973. Interference filters for the VUV (1200–1900 Å). Appl. Opt. 12, 2240–2241.

Feigl, T., Lauth, H., Yulin, S., Kaiser, N., 2001. Heat resistance of EUV multilayer mirrors for long-time applications. Microelectron. Eng. 57–58, 3–8.

Feigl, T., Yulin, S., Benoit, N., Kaiser, N., 2005. Multilayer optics for the EUV and soft X-rays. Opt. Precis. Eng. 13, 421–429.

Fernández-Perea, M., Larruquert, J.I., Aznárez, J.A., Méndez, J.A., Poletto, L., Malvezzi, A.M., Giglia, A., Nannarone, S., 2006. Determination of optical constants of scandium films in the 20–1000 eV range. J. Opt. Soc. Am. A 23, 2880–2887.

Fernández-Perea, M., Vidal-Dasilva, M., Aznárez, J.A., Larruquert, J.I., Méndez, J.A., Poletto, L., Garoli, D., Malvezzi, A.M., Giglia, A., Nannarone, S., 2008. Transmittance and optical constants of Pr films in the 4–1,600-eV spectral range. J. Appl. Phys. 103, 113515.

Fernández-Perea, M., Vidal-Dasilva, M., Larruquert, J.I., Aznárez, J.A., Méndez, J.A., Gullikson, E., Aquila, A., Soufli, R., 2009. Optical constants of evaporation-deposited silicon monoxide films in the 7.1–800 eV photon energy range. J. Appl. Phys. 105, 113505.

Fernández-Perea, M., Larruquert, J.I., Aznárez, J.A., Méndez, J.A., Poletto, L., Frassetto, F., Malvezzi, A.M., Bajoni, D., Giglia, A., Mahne, N., Nannarone, S., 2011. Transmittance and optical constants of Ho films in the 3–1,340 eV spectral range. J. Appl. Phys. 109083525.

Fernández-Perea, M., Pivovaroff, M.J., Soufli, R., Alameda, J., Mirkarimi, P., Descalle, M.-A., Baker, S.L., McCarville, T., Ziock, K., Hornback, D., Romaine, S., Bruni, R., Zhong, Z., Honkimäki, V., Ziegler, E., Christensen, F.E., Jakobsen, A.C., 2013a. Ultra-short-period WC/SiC multilayer coatings for X-ray applications. Nucl. Instrum. Meth. A 710, 114–119.

Fernández-Perea, M., Descalle, M.-A., Soufli, R., Ziock, K., Alameda, J., Baker, S.L., McCarville, T., Honkimäki, V., Ziegler, E., Jakobsen, A.C., Christensen, F.E., Pivovaroff, M.J., 2013b. Physics of reflective optics for the soft gamma-ray photon energy. Phys. Rev. Let. 111, 027404.

Fontaine, A., Warburton, W.K., Ludwig Jr., K.F., 1985. Determination of anomalous scattering factors in GaAs using X-ray refraction through a prism. Phys. Rev. B 31, 3599–3605.

Gålnander, B., 2001. Thin films and deposition processes studied by soft X-ray spectroscopy, (Thesis), Uppsala, Sweden.

Gatto, A., Thielsch, R., Heber, J., Kaiser, N., Ristau, D., Günster, S., Kohlhaas, J., Marsi, M., Trovò, M., Walker, R., Garzella, D., Couprie, M.E., Torchio, P., Alvisi, M., Amra, C., 2002. High-performance deep-ultraviolet optics for free-electron lasers. Appl. Opt. 41, 3236–3241.

Gautier, J., Delmotte, F., Roulliay, M., Bridou, F., Ravet, M.-F., Jérome, A., 2005. Study of normal incidence of three-component multilayer mirrors in the range 20–40 nm. Appl. Opt. 44, 384–390.

Gesell, T.F., Arakawa, E.T., 1971. Attenuation length for photoelectrons excited in aluminum by 21.2-eV photons. Phys. Rev. Lett. 26, 377–380.

Giles, C., Vettier, C., de Bergevin, F., Malgrange, C., Grübel, G., Grossi, F., 1995. X-ray polarimetry with phase plates. Rev. Sci. Instrum. 88, 1518–1521.

Gluskin, E.S., Gaponov, S.V., Dhez, P., Ilyinsky, P.P., Salashchenko, N.N., Shatunov Yu, M., Trakhtenberg, E.M., 1986. A polarimeter for soft X-ray and VUV radiation. Nucl. Instrum. Meth. A 246, 394–396.

Guggenmos, A., Rauhut, R., Hofstetter, M., Hertrich, S., Nickel, B., Schmidt, J., Gullikson, E.M., Seibald, M., Schnick, W., Kleineberg, U., 2013. Aperiodic CrSc multilayer mirrors for attosecond water window pulses. Opt. Express 21, 21728–21740.

Gullikson, E.M., 2000. Optical properties of materials. In: Samson, J.A., Ederer, D.L. (Eds.), Vacuum Ultraviolet Spectroscopy I. Academic Press, San Diego, CA.

Gullikson, E., Salmassi, F., Aquila, A., Dollar, F., 2006. Progress in short period multilayer coatings for water window applications.PXRMS Conference, Sapporo, Japan.

Gustafsson, E., Ruchon, T., Swoboda, M., Remetter, T., Pourtal, E., López-Martens, R., Balcou, Ph., L'Huillier, A., 2007. Broadband attosecond pulse shaping. Opt. Lett. 32, 1353–1355.

Habs, D., Günther, M.M., Jentschel, M., Urban, W., 2012. Refractive index of silicon at γ ray energies. Phys. Rev. Lett. 108, 184802.

Haelbich, R.-P., Iwan, M., Koch, E.E., 1977. Optical properties of some insulators in the vacuum ultraviolet region. In: Physik Daten Collection. vols. **8-1** and **18-2**. Zentralstelle für Atomkernenergie-Dokumentation, Eggenstein-Leopoldshafen, Germany.

Haga, T., Utsumi, Y., Itabashi, S., 1998. Soft X-ray ellipsometer using transmissive multilayer polarizers. Proc. SPIE 3443, 117–127.

Haga, T., Tinene, M.C.K., Ozawa, A., Utsumi, Y., Itabashi, S., Ohkubo, T., Shimada, M., 1999. Fabrication of semitransparent multilayer polarizer and its application to soft X-ray ellipsometer. Proc. SPIE 3764, 13–27.

Hagemann, H.-J., Gudat, W., Kunz, C., 1974. Optical constants from the far infrared to the X-ray region: Mg, Al, Cu, Ag, Au, Bi, C, and Al_2O_3. In: DESY report SR-74/7. Deutsches Elektron-Synchrotron, Hamburg.

Hamm, R.N., MacRae, R.A., Arakawa, E.T., 1965. Polarization studies in the vacuum ultraviolet. J. Opt. Soc. Am. 55, 1460–1463.

Hart, M., 1978. X-ray polarization phenomena. Philos. Mag. B 38, 41–56.

Hass, G., Hunter, W.R., 1978. Reflection polarizers for the vacuum ultraviolet using Al + MgF_2 mirrors and an MgF_2 plate. Appl. Opt. 17, 76–82.

Hass, G., Tousey, R., 1959. Reflecting coatings for the extreme ultraviolet. J. Opt. Soc. Am. 49, 593–602.

Hass, G., Jacobus, G.F., Hunter, W.R., 1967. Optical properties of evaporated iridium in the vacuum ultraviolet from 500 A to 2000 Å. J. Opt. Soc. Am. 57, 758–762.

He, S., Liu, Y., Zhu, J., Li, H., Huang, Q., Zhou, H., Huo, T., Wang, Z., Fu, S., 2011. SiC/W/Ir multilayer-coated grating for enhanced efficiency in 50–100 nm wavelength range in Seya–Namioka mount. Opt. Lett. 36, 163–165.

Hecht, E., 2002. Optics. Addison-Wesley, San Francisco.

Hecquet, C., Ravet-Krill, M.-F., Delmotte, F., Jérôme, A., Hardouin, A., Bridou, F., Varnière, F., Roulliay, M., 2007. Design, conception, and metrology of EUV mirrors for aggressive environments. Proc. SPIE 6586, 65860X.

Hecquet, C., Delmotte, F., Ravet-Krill, M.F., de Rossi, S., Jérome, A., Bridou, F., Varnière, F., Meltchakov, E., Auchère, F., Giglia, A., Mahne, N., Nanaronne, S., 2009. Design and performance of two-channel EUV multilayer mirrors with enhanced spectral selectivity. Appl. Phys. A 95, 401–408.

Henke, B.L., Lee, P., Tanaka, T.J., Shimabukuro, R.L., Fujikawa, B.K., 1982. At. Data Nucl. Data Tables 1, 27.

Henke, B.L., Gullikson, E.M., Davis, J.C., 1993. X-ray interactions: photoabsorption, scattering, transmission, and reflection at $E = 50$–$30{,}000\,\text{eV}$, $Z = 1$–92. At. Data Nucl. Data Tables 54, 181.

Hennessy, J., Balasubramanian, K., Moore, C.S., Jewell, A.D., Nikzad, S., France, K., Quijada, M., 2016. Performance and prospects of far ultraviolet aluminum mirrors protected by atomic layer deposition. J. Astron. Telesc. Instrum. Syst. 2, 041206.

Hilfiker, J.N., 2005. VUV ellipsometry. In: Tompkins, H.G., Irene, E.A. (Eds.), Handbook of Ellipsometry. William Andrew, New York.

Hirano, K., Ishikawa, T., Kikuta, S., 1995. Development and application of X-ray phase retarders. Rev. Sci. Instrum. 66, 1604–1609.

Höchst, H., Patel, R., Middleton, F., 1994. Multiple-reflection $\lambda/4$ phase shifter: a viable alternative to generate circular-polarized synchrotron radiation. Nucl. Instrum. Meth. A 347, 107–114.

Höchst, H., Bulicke, P., Nelson, T., Middleton, F., 1995. Performance evaluation of a soft Xrayquadruple reflection circular polarizer. Rev. Sci. Instrum. 66, 1598–1600.

Hofstetter, M., Schultze, M., Fieß, M., Dennhardt, B., Guggenmos, A., Gagnon, J., Yakovlev, V.S., Goulielmakis, E., Kienberger, R., Gullikson, E.M., Krausz, F., Kleineberg, U., 2011. Attosecond dispersion control by extreme ultraviolet multilayer mirrors. Opt. Express 19, 1767–1776.

Holm, R.T., 1998. Convention confusions. In: Palik, E.D. (Ed.), Handbook of Optical Constants of Solids II. Academic Press, San Diego.

Horton, V.G., Arakawa, E.T., Hamm, R.N., Williams, M.W., 1969. A triple reflection polarizer for use in the vacuum ultraviolet. Appl. Opt. 8, 667–670.

Hu, W., Yamamoto, M., Watanabe, M., 1996. Development of EUV free-standing multilayer polarizers. Proc. SPIE 2873, 74–77.

Hubbell, J.H., Seltzer, S.M., 1995. 'X-ray attenuation and absorption for materials of dosimetric interest'. Tables of X-ray mass attenuation coefficients and mass energy-absorption coefficients from 1 keV to 20 MeV for elements Z = 1 to 92 and 48 additional substances of dosimetric interest. NIST Physical Reference Data. Report NISTIR 5632. http://www.nist.gov/pml/data/xraycoef/index.cfm.

Hubbell, J.H., Gimm, H.A., Øverbø, I., 1980. Pair, triplet, and total atomic cross sections (and mass attenuation coefficients) for 1 MeV–100 GeV photons in elements Z = 1 to 100. J. Phys. Chem. Ref. Data 9, 1023–1147.

Hunter, W.R., 1964a. Optical constants of metals in the extreme ultraviolet. I. A modified critical-angle technique for measuring the index of refraction of metals in the extreme ultraviolet. J. Opt. Soc. Am. 54, 15–19.

Hunter, W.R., 1964b. On the optical constants of metals at wavelengths shorter that their critical wavelengths. J. Phys. 25, 154–160. https://doi.org/10.1051/jphys:01964002501-2015400.

Hunter, W.R., 1965. Polarizers for the extreme ultraviolet. Jpn. J. Appl. Phys. 4 (1), 520–526.

Hunter, W.R., 1973. The preparation and use of unbacked metal films as filters in the extreme ultraviolet. Phys. Thin Films 7, 43–114.

Hunter, W.R., 1978. Design criteria for reflection polarizers and analyzers in the vacuum ultraviolet. Appl. Opt. 17, 1259–1270.

Hunter, W.R., 1998. Measurement of optical constants in the vacuum ultraviolet spectral region. In: Palik, E.D. (Ed.), Handbook of Optical Constants of Solids. Academic Press, San Diego.

Hunter, W.R., 2000. Polarization. In: Samson, J.A., Ederer, D.L. (Eds.), Vacuum Ultraviolet Spectroscopy I. Academic Press, San Diego, CA.

Hunter, W.R., Malo, S.A., 1969. The temperature dependence of the short wavelength transmittance limit of vacuum ultraviolet window materials-I. Experiment. J. Phys. Chem. Solids 30, 2739–2745.

Hunter, W.R., Angel, D.W., Tousey, R., 1965. Thin films and their uses for the extreme ultraviolet. Appl. Opt. 4, 891–898.

Hunter, W.R., Osantowski, J.F., Hass, G., 1971. Reflectance of aluminum overcoated with MgF_2, and LiF in the wavelength, region from 1600 Å to 300 Å at various angles of incidence. Appl. Opt. 10, 540–544.

Imazono, T., Sano, K., Suzuki, Y., Kawachi, T., Koike, M., 2009. Development and performance test of a soft X-ray polarimeter and ellipsometer for complete polarization analysis. Rev. Sci. Instrum. 80, 085109.

Inczédy, J., Lengyel, T., Ure, A.M., 1998. Compendium of analytical nomenclature: definitive rules 1997. International Union of Pure and Applied Chemistry/Blackwell Science, Osney Mead, Oxford/Malden, MA (Chapter 10, Section 3.4.8). http://old.iupac.org/publications/analytical_compendium/Cha10sec348.pdf.

Jahoda, F.C., 1957. Fundamental absorption of barium oxide from its reflectivity spectrum. Phys. Rev. 107, 1261–1265.

James, R.W., 1962. The Optical Principles of the Diffraction of X-rays. G. Bell and Sons Ltd., London.

Jark, W., Rigon, L., Oliver, K., 2011. Simultaneous determination of the X-ray refractive index and the attenuation length from a single digitally registered radiograph of rectangular prisms. Opt. Commun. 284, 4525–4528.

Joensen, K.D., Christensen, F.E., Schnopper, H.W., Gorenstein, P., Susini, J., Høghøj, P., Hustache, R., Wood, J., Parker, K., 1992. Medium-sized grazing incidence high-energy X-ray telescopes employing continuously graded multilayers. Proc. SPIE 1736, 239–248.

Johnson, P.D., Smith, N.V., 1983. Production of circularly polarized light from synchrotron radiation in the vacuum ultraviolet region. Nucl. Instrum. Meth. 214, 505–508.

Joyeux, D., Polack, F., Phalippou, D., 1999. An interferometric determination of the refractive part of optical constants for carbon and silver across soft X-ray absorption edges. Rev. Sci. Instrum. 70, 2921–2926.

Keski-Kuha, R.A.M., Osantowski, J.F., Herzig, H., Gum, J.S., Toft, A.R., 1988. Normal incidence reflectance of ion beam deposited SiC films in the EUV. Appl. Opt. 27, 2815–2816.

Kim, J., Zukic, M., Torr, D.G., Wilson, M.W., 1992. Multilayer thin film design as far ultraviolet quarterwave retarders. Proc. SPIE 1742, 403–412.

Kimura, H., Hirono, T., Tamenori, Y., Saitoh, Y., Salashchenko, N.N., Ishikawa, T., 2005. Transmission type Sc/Cr multilayer as a quarter-wave plate for near 400 eV. J. Electron Spectrosc. Relat. Phenom. 144–147, 1079–1081.

King, F.W., 1979. Dispersion relations and sum rules for the normal reflectance of conductors and insulators. J. Chem. Phys. 71, 4726–4733.

Kissel, L., Pratt, R.H., 1990. Corrections to tabulated anomalous-scattering factors. Acta Crystallogr., Sect. A: Cryst. Phys. Diffr. Theor. Gen. Crystallogr. 46, 170–175 (A fit to the data of Kissel and Pratt was made by Henke et al. (1993)).

Kittel, C., 2005. Introduction to Solid State Physics, eighth ed. John Wiley & Sons, New York.

Kjornrattanawanich, B., Bajt, S., Seely, J.F., 2004. Mo/B4C/Si multilayer-coated photodiode with polarization sensitivity at an extreme-ultraviolet wavelength of 13.5 nm. Appl. Opt. 43, 1082–1090.

Kjornrattanawanich, B., Windt, D.L., Seely, J.F., Uspenskii Yu, A., 2006. SiC/Tb and Si/Tb multilayer coatings for extreme ultraviolet solar imaging. Appl. Opt. 45, 1765–1772.

Kjornrattanawanich, B., Windt, D.L., Seely, J.F., 2008. Normal incidence silicon-gadolinium multilayers for imaging at 63 nm wavelength. Opt. Lett. 33, 965–967.

Kjornrattanawanich, B., Windt, D.L., Seely, J.F., 2010. Optical constants determination of samarium, holmium, and erbium in the 1.5–850 eV spectral range using a transmittance method. Appl. Opt. 49, 6006–6013.

Kortright, J.B., 1993. Polarization properties of multilayers in the EUV and soft X-ray. Proc. SPIE 2010, 160–167.

Kortright, J.B., Underwood, J.H., 1990. Multilayer optical elements for generation and analysis of circularly polarized X-rays. Nucl. Instrum. Meth. A 291, 272–277.

Kortright, J.B., Kimura, H., Nikitin, V., Mayama, K., Yamamoto, M., Yanagihara, M., 1992. Soft X-ray (97-eV) phase retardation using transmission multilayers. Appl. Phys. Lett. 60, 2963–2965.

Kortright, J.B., Rice, M., Franck, K.D., 1995. Tunable multilayer EUV/soft X-ray polarimeter. Rev. Sci. Instrum. 66, 1567–1569.

Kozhevnikov, I.V., Bukreeva, I.N., Ziegler, E., 2001. Design of X-ray supermirrors. Nucl. Instrum. Meth. A 460, 424–443.
Kretschmann, E., Kröger, E., 1975. Reflection and transmission of light by a rough surface, including results for surface plasmon effects. J. Opt. Soc. Am. 65, 150–154.
Kuznetsov, D.S., Yakshin, A.E., Sturm, J.M., Van De Kruijs, R.W.E., Louis, E., Bijkerk, F., 2015. High-reflectance La/B-based multilayer mirror for 6.x nm wavelength. Opt. Lett. 40, 3778–3781.
La Villa, R., Mendlowitz, H., 1962. Optical constants of aluminum in vacuum ultraviolet. Phys. Rev. Lett. 9, 149–150.
Lang, J.C., Srajer, G., 1995. Bragg transmission phase plates for the production of circularly polarized x rays. Rev. Sci. Instrum. 66, 1540–1542.
Larruquert, J.I., 2001a. Reflectance enhancement with sub-quarterwave multilayers of highly absorbing materials. J. Opt. Soc. Am. A 18, 1406–1414.
Larruquert, J.I., 2001b. General theory of sub-quarterwave multilayers with highly absorbing materials. J. Opt. Soc. Am. A 18, 2617–2627.
Larruquert, J.I., 2002a. Reflectance enhancement in the extreme ultraviolet and soft X-rays by means of multilayers with more than two materials. J. Opt. Soc. Am. A 19, 391–397.
Larruquert, J.I., 2002b. New layer-by-layer multilayer design method. J. Opt. Soc. Am. A 19, 385–390.
Larruquert, J.I., 2004. Layer-by-layer design method for multilayers with barrier layers: application to Si/Mo multilayers for EUV lithography. J. Opt. Soc. Am. A 21, 1750–1760.
Larruquert, J.I., Keski-Kuha, R.A.M., 1999. Multilayer coatings with high reflectance in the EUV spectral region from 50 to 121.6 nm. Appl. Opt. 38, 1231–1236.
Larruquert, J.I., Keski-Kuha, R.A.M., 2001. Multilayer coatings for narrow-band imaging in the extreme ultraviolet. Appl. Opt. 40, 1126–1131.
Larruquert, J.I., Keski-Kuha, R.A.M., 2002. Sub-quarter-wave multilayer coatings with high reflectance in the extreme ultraviolet. Appl. Opt. 41, 5398–5404.
Larruquert, J.I., Méndez, J.A., Aznárez, J.A., 1995. Far UV reflectance measurements and optical constants of unoxidized aluminum films. Appl. Opt. 34, 4892–4899.
Larruquert, J.I., Pérez-Marín, A.P., García-Cortés, S., Rodríguez-de Marcos, L., Aznárez, J.A., Méndez, J.A., 2011a. Selfconsistent optical constants of SiC thin films. J. Opt. Soc. Am. A 28, 2340–2345.
Larruquert, J.I., Vidal-Dasilva, M., García-Cortés, S., Rodríguez-de Marcos, L., Fernández-Perea, M., Aznárez, J.A., Méndez, J.A., 2011b. Multilayer coatings for the far and extreme ultraviolet. Proc. SPIE 8076, 80760D.
Larruquert, J.I., Aznárez, J.A., Rodríguez-de Marcos, L., Méndez, J.A., Miotti, P., Frassetto, F., Massone, G., Nannarone, S., Crescenzio, G., Capobianco, G., Fineschi, S., 2014. Reflective and transmissive coating polarizers in a spectral range centered at 121.6 nm. J. Opt. 16, 125713.
Laufer, A.H., Pirog, J.A., Mcnesby, J.R., 1965. Effect of temperature on the vacuum ultraviolet transmittance of lithium fluoride, calcium fluoride, barium fluoride, and sapphire. J. Opt. Soc. Am. 55, 64–66.
Le Guen, K., Hu, M.-H., André, J.-M., Jonnard, P., Zhou, S.K., Li, H.C., Zhu, J.T., Wang, Z.S., Mahne, N., Giglia, A., Nannarone, S., 2011. Introduction of Zr in nanometric periodic Mg/Co multilayers. Appl. Phys. A Mater. Sci. Process. 102, 69–77.
Li, H.H., 1980. Refractive index of alkaline earth halides and its wavelength and temperature derivatives. J. Phys. Chem. Ref. Data 9, 161–289.

Lingg, L.J., 1990. 'Lanthanide trifluoride thin films: Structure, composition, and optical properties', Thesis, U. Arizona, USA.

Loch, R.A., Dubrouil, A., Sobierajski, R., Descamps, D., Fabre, B., Lidon, P., van de Kruijs, R.W.E., Boekhout, F., Gullikson, E., Gaudin, J., Louis, E., Bijkerk, F., Mével, E., Petit, S., Constant, E., Mairesse, Y., 2011. Phase characterization of the reflection on an extreme UV multilayer: comparison between attosecond metrology and standing wave measurements. Opt. Lett. 36, 3386–3388.

MacDonald, M.A., Schaefers, F., Pohl, R., Poole, I.B., Gaupp, A., Quinn, F.M., 2008. A W: B4C multilayer phase retarder for broadband polarization analysis of soft X-ray radiation. Rev. Sci. Instrum. 79, 025108.

Madden, R.P., Canfield, L.R., Hass, G., 1963. On the vacuum-ultraviolet reflectance of evaporated aluminum before and during oxidation. J. Opt. Soc. Am. 53, 620–625.

Maehara, T., Kimura, H., Nomura, H., Yanagihara, M., Namioka, T., 1991. Performance of a wideband soft X-ray polarizer. Appl. Opt. 30, 5018–5020.

Malgrange, C., Varga, L., Giles, C., Rogalev, A., Goulon, J., 1999. Phase plates for X-ray optics. Proc. SPIE 3773, 326–339.

Malherbe, A., 1974a. Interference filters for the far ultraviolet. Appl. Opt. 13, 1275–1276.

Malherbe, A., 1974b. Multidielectric components for the far ultraviolet. Appl. Opt. 13, 1276.

Malherbe, A., Guillard, M., 1970. Réalisation industrielle de filtres interférentiels pour l'ultraviolet lointain. Nouv. Rev. Opt. Appl. 1, 401–404.

Marshall, H.L., Schulz, N.S., Windt, D.L., Gullikson, E.M., Blake, E., Getty, D., McInturff, Z., 2014. The use of laterally-graded multilayer mirrors for soft X-ray polarimetry. Proc. SPIE 9144, 91441K.

Marx, B., Uschmann, I., Höfer, S., Lötzsch, R., Wehrhan, O., Förster, E., Kaluza, M., Stöhlker, T., Gies, H., Detlefs, C., Roth, T., Härtwig, J., Paulus, G.G., 2011. Determination of high-purity polarization state of X-rays. Opt. Commun. 284, 915–918.

Materlik, G., Sparks, C.J., Fischer, K., 1994. Resonant anomalous X-ray scattering: theory and applications. North-Holland, Amsterdam, pp. 389–420. http://cars9.uchicago.edu/dafs/.

Maury, H., Bridou, F., Troussel, P., Meltchakov, E., Delmotte, F., 2010. Design and fabrication of supermirrors for (2–10 keV) high resolution X-ray plasmas diagnostic imaging. Nucl. Instrum. Meth. A 621, 242–246.

Meltchakov, E., Hecquet, C., Roulliay, M., De Rossi, S., Menesguen, Y., Jérome, A., Bridou, F., Varniere, F., Ravet-Krill, M.-F., Delmotte, F., 2010. Development of Al-based multilayer optics for EUV. Appl. Phys. A 98, 111–117.

Meltchakov, E., Ziani, A., Auchère, F., Zhang, X., Roulliay, M., De Rossi, S., Bourassin-Bouchet, C., Jérome, A., Bridou, F., Varniere, F., Delmotte, F., 2011. EUV reflectivity and stability of tri-component Al-based multilayers. Proc. SPIE 8168, 816819.

Mertins, H.-C., Schäfers, F., Grimmer, H., Clemens, D., Böni, P., Horisberger, M., 1998. W/C, W/Ti, Ni/Ti, and Ni/V multilayers for the soft-X-ray range: experimental investigation with synchrotron radiation. Appl. Opt. 37, 1873–1882.

Metcalf, H., Baird, J.C., 1966. Circular polarization of vacuum ultraviolet light by piezobirefringence. Appl. Opt. 5, 1407–1410.

Mezei, F., 1976. Novel polarized neutron devices: supermirror and spin component amplifier. Commun. Phys. 1, 81–85.

Monaco, G., Garoli, D., Frison, R., Mattarello, V., Nicolosi, P., Pelizzo, M.G., Rigato, V., Armelao, L., Giglia, A., Nannarone, S., 2006. Optical constants in the EUV Soft X-ray (5 ÷ 152 nm) spectral range of B4C thin films deposited by different deposition techniques. Proc. SPIE 6317, 631712.

Morawe, C., Ziegler, E., Peffen, J.-C., Kozhevnikov, I.V., 2002. Design and fabrication of depth-graded X-ray multilayers. Nucl. Instrum. Meth. A 493, 189–198.

Morlens, A.-S., López-Martens, R., Boyko, O., Zeitoun, P., Balcou, P., Varjú, K., Gustafsson, E., Remetter, T., L'Huillier, A., Kazamias, S., Gautier, J., Delmotte, F., Ravet, M.-F., 2006. Design and characterization of extreme-ultraviolet broadband mirrors for attosecond science. Opt. Lett. 31, 1558–1560.

Naik, S.R., Lodha, G.S., 2006. The effect of misalignment errors in optical elements of VUV polarimeter. Nucl. Instrum. Meth. A 560, 211–218.

Nevot, L., Croce, P., 1980. Caractérisation des surface par réflexion rasante de rayons X. Application a l'étude du polissage de quelques verres silicates. Rev. Phys. Appl. 15, 761–779.

Newville, M., 2004. Fundamentals of XAFS. In: Consortium for Advanced Radiation Sources. University of Chicago, Chicago, IL.

NIST-FFAST Web, http://physics.nist.gov/PhysRefData/FFast/html/form.html.

Nomura, H., Mayama, K., Sasaki, T., Yamamoto, M., Yanagihara, M., 1992. Design, fabrication, and polarization of soft-X-ray transmission multilayers. Proc. SPIE 1720, 395–401.

Ogasaka, Y., Iwahara, T., Miyazawa, T., Fukaya, Y., Sasaki, N., Tamura, K., Kanou, Y., Kunieda, H., Yamashita, K., 2007. Characterization of Pt/C multilayer at 200 keV soft gamma-ray. Proc. SPIE 6688, 66880S.

Palik, E.D., 1998a. Handbook of Optical Constants of Solids. Academic Press, San Diego.

Palik, E.D., 1998b. Handbook of Optical Constants of Solids II. Academic Press, San Diego.

Palik, E.D., 1998c. Handbook of Optical Constants of Solids III. Academic Press, San Diego.

Park, J.H., Zukic, M., Wilson, M., Keffer, C.E., Torr, D.G., Hoover, R.B., 1996. Design and fabrication of multilayer reflective filters for a Ritchey-Chretien Lyman-α telescope. Opt. Eng. 35, 1479–1482.

Parratt, L.G., 1954. Surface studies of solids by total reflection of X-rays. Phys. Rev. 95, 359–369.

Pepper, S.V., 1970. Optical analysis of photoemission. J. Opt. Soc. Am. 60, 805–812.

Pflüger, J., Fink, J., 1998. Determination of optical constants by high-energy, electron-energy-loss spectroscopy (EELS). In: Palik, E.D. (Ed.), Handbook of Optical Constants of Solids II. Academic Press, San Diego.

Philipp, H.R., Ehrenreich, H., 1963. Optical properties of semiconductors. Phys. Rev. 129, 1550–1560.

Powell, F.R., Lindblom, J.F., Powell, S.F., Vedder, P.W., 1990. Thin film filter performance for extreme ultraviolet and X-ray applications. Opt. Eng. 29, 614–624.

Powell, F.R., Drake, V.A., Sandel, B.R., Mitchell, D.G., 1994. The selection of materials for soft X-ray (SXR) and extreme ultraviolet (EUV) filters for space astronomy and other applications. Proc. SPIE 2209, 480–490.

Quijada, M., Rice, S., Mentzell, E., 2012. Enhanced MgF_2 and LiF over-coated Al mirrors for FUV space astronomy. Proc. SPIE 84502, 84502H.

Quijada, M.A., del Hoyo, J., Rice, S., 2014. Enhanced far-ultraviolet reflectance of MgF_2 and LiF over-coated Al mirrors. Proc. SPIE 9144, 91444G.

Rabinovitch, K., Canfield, L.R., Madden, R.P., 1965. A method for measuring polarization in the vacuum ultraviolet. Appl. Opt. 4, 1005–1010.

Ravel, B., 2005. A practical introduction to multiple scattering theory. J. Alloys Compd. 401, 118–126.

Rehr, J.J., Albers, R.C., 2000. Theoretical approaches to X-ray absorption fine structure. Rev. Mod. Phys. 72, 621–654.

Rehr, J.J., Ankudinov, A.L., 2004. Solid state effects on X-ray absorption, emission and scattering processes. Radiat. Phys. Chem. 70, 453–463.

Rodríguez-de Marcos, L., Larruquert, J.I., Méndez, J.A., Aznárez, J.A., Vidal-Dasilva, M., Fu, L., 2014. Narrowband filters for the FUV range. Proc. SPIE 9144, 914437.

Rodríguez-de Marcos, L., Larruquert, J.I., Méndez, J.A., Aznárez, J.A., 2015. Multilayers and optical constants of various fluorides in the far UV. Proc. SPIE 9627, 96270B.

Rodríguez-de Marcos, L.V., Méndez, J.A., Larruquert, J.I., 2016a. Tuning sum rules with window functions for optical constant evaluation. J. Opt. 18, 075606.

Rodríguez-de Marcos, L., Aznárez, J.A., Méndez, J.A., Larruquert, J.I., Vidal-Dasilva, M., Malvezzi, A.M., Giglia, A., Capobianco, G., Massone, G., Fineschi, S., Nannarone, S., 2016b. Advances in far-ultraviolet reflective and transmissive coatings for space applications. Proc. SPIE 9912, 99122E.

Rodríguez-de Marcos, L., Larruquert, J.I., Méndez, J.A., Aznárez, J.A., 2017. Self-consistent optical constants of MgF_2, LaF_3, and CeF_3 films. Opt. Mater. Express 6, 3622–3637.

Rosenbaum, G., Feuerbacher, B., Godwin, R.P., Skibowski, M., 1968. Measurement of the polarization of extreme ultraviolet synchrotron radiation with a reflecting polarimeter. Appl. Opt. 7, 1917–1919.

Rustgi, O.P., 1965. Transmittance of thin metallic films in the vacuum-ultraviolet region below 1000 Å. J. Opt. Soc. Am. 55, 630–634.

Sae-Lao, B., Montcalm, C., 2001. Molybdenum–strontium multilayer mirrors for the 8–12-nm extreme-ultraviolet wavelength region. Opt. Lett. 26, 468–470.

Saito, T., Ejiri, A., Onuki, H., 1990. Polarization properties of an evaporated aluminum mirror in the VUV region. Appl. Opt. 29, 4538–4540.

Samson, J.A.R., 1967a. Filter and window materials. In: Chapter 6 of Techniques of Vacuum Ultraviolet Spectroscopy. John Wiley and Sons Inc., New York.

Samson, J.A.R., 1967b. Techniques of Vacuum Ultraviolet Spectroscopy. John Wiley and Sons Inc., New York.

Samson, J.A.R., 1967c. Polarization'. In: Chapter 9 of Techniques of Vacuum Ultraviolet Spectroscopy. John Wiley and Sons Inc., New York.

Samson, J.A., Ederer, D.L., 2000. Vacuum Ultraviolet Spectroscopy I. Academic Press, San Diego, CA.

Schäfers, F., 2007. Multilayer-based soft X-ray polarimetry. Opt. Precis. Eng. 15, 1850–1861.

Schäfers, F., Mertins, H.-C., Gaupp, A., Gudat, W., Mertin, M., Packe, I., Schmolla, F., Di Fonzo, S., Soullié, G., Jark, W., Walker, R., Le Cann, X., Nyholm, R., Eriksson, M., 1999. Soft-X-ray polarimeter with multilayer optics: complete analysis of the polarization state of light. Appl. Opt. 38, 4074–4088.

Schoonjans, T., Brunetti, A., Golosio, B., Sanchez del Rio, M., Solé, V.A., Ferrero, C., Vincze, L., 2011. The xraylib library for X-ray-matter interactions. Recent developments. Spectrochim. Acta B 66, 776–784. Web of Biomolecular Structure Center at the University of Washington School of Medicine:http://ftp.esrf.eu/pub/scisoft/xraylib/readme.html.

Schultze, M., Wirth, A., Grguras, I., Uiberacker, M., Uphues, T., Verhoef, A.J., Gagnon, J., Hofstetter, M., Kleineberg, U., Goulielmakis, E., Krausz, F., 2011. State-of-the-art attosecond metrology. J. Electron. Spect. Relat. Phenom. 184, 68–77.

Scofield, J.H., 1973. Theoretical photoionization cross sections from 1 to 1500 keV. In: Lawrence Livermore Laboratory, Report UCRL-51326.

Scott, M.L., 1998. Measurement of n and k in the XUV by the angle-of-incidence, total-external-reflectance method. In: Palik, E.D. (Ed.), Handbook of Optical Constants of Solids II. Academic Press, San Diego.

Shiles, E., Sasaki, T., Inokuti, M., Smith, D.Y., 1980. Self-consistency and sum-rule tests in the Kramers-Kronig analysis of optical data: applications to aluminium. Phys. Rev. B 22, 1612–1628.
Sinha, S.K., Sirota, E.B., Garoff, S., Stanley, H.B., 1988. X-ray and neutron scattering from rough surfaces. Phys. Rev. B 38, 2297–2311.
Smith, N.V., Howells, M.R., 1994. Whispering galleries for the production of circularly polarized synchrotron radiation in the XUV region. Nucl. Instrum. Meth. A 347, 115–118.
Soltwisch, V., Fischer, A., Laubis, C., Stadelhoff, C., Scholze, F., Ullrich, A., 2015. Polarization resolved measurements with the new EUV Ellipsometer of PTB. Proc. SPIE 9422, 942213.
Soufli, R., Bajt, S., 2009. Multilayer coatings for EUVL. In: Bakshi, V. (Ed.), EUV Lithography. SPIE, Bellingham and John Wiley & Sons, Inc., Hoboken.
Soufli, R., Gullikson, E.M., 1997. Reflectance measurements on clean surfaces for the determination of optical constants of silicon in the extreme ultraviolet–soft-X-ray region. Appl. Opt. 36, 5499–5507.
Soufli, R., Gullikson, E.M., 1998. Absolute photoabsorption measurements of molybdenum in the range 60–930 eV for optical constant determination. Appl. Opt. 37, 1713–1719.
Soufli, R., Bajt, S., Gullikson, E.M., 1999. Optical constants of beryllium from photoabsorption measurements for X-ray optics applications. Proc. SPIE 3767, 251–258.
Soufli, R., Fernández-Perea, M., Baker, S.L., Robinson, J.C., Alameda, J., Walton, C.C., 2012. Spontaneously intermixed Al-Mg barriers enable corrosion-resistant Mg/SiC multilayer coatings. Appl. Phys. Lett. 101, 043111.
Spiller, E., 1972a. Low-loss reflection coatings using absorbing materials. Appl. Phys. Lett. 20, 365–367.
Spiller, E., 1972b. In: Multilayer interference coatings for the vacuum ultraviolet.Space Optics, Proc. ICO—IX Santa Monica, 1972, pp. 581–597.
Spiller, E., 1994. Soft X-ray Optics. SPIE Optical Engineering Press, Bellingham, Washington.
Srivastava, K., 1982. Plasmon approach to the band gap of alkali halides. Phys. Stat. Sol. (b) 114 (2), 667–671. https://doi.org/10.1002/pssb.2221140245.
Stanglmeier, F., Lengeler, B., Weber, W., Göbel, H., Schuster, M., 1992. Determination of the dispersive correction f'(E) to the atomic form factor from X-ray reflection. Acta Crystallogr. A 48, 626–639.
Stearns, D.G., 1989. The scattering of x rays from nonideal multilayer structures. J. Appl. Phys. 65, 491–506.
Stearns, D.G., 1992. X-ray scattering from interfacial roughness in multilayer structures. J. Appl. Phys. 71, 4286–4298.
Stenzel, O., 2005. The physics of thin film optical spectra. In: Springer Series in Surface Sciences, vol. 44. Springer-Verlag, Berlin.
Stern, F., 1963. Elementary theory of the optical properties of solids. In: Seitz, F., Turnbull, D. (Eds.), Solid State Physic. Advances in Research and Applications. In: vol. 15. Academic Press, New York.
Suman, M., Frassetto, F., Nicolosi, P., Pelizzo, M.-G., 2007. Design of aperiodic multilayer structures for attosecond pulses in the extreme ultraviolet. Appl. Opt. 46, 8159–8169.
Svatos, J., Joyeux, D., Phalippou, D., Polack, F., 1993. Soft-X-ray interferometer for measuring the refractive index of materials. Opt. Lett. 18, 1367–1369.
Tan, M.Y., Zhu, J.T., Wang, H.C., Wang, Z.S., Chen, R., Watanabe, M., 2009. Design of transmission multilayer polarizer for soft X-ray using a merit function. Opt. Express 17, 2586–2599.

Tan, M.Y., Zhu, J.T., Chen, L.Y., Wang, Z.S., Le Guen, K., Jonnard, P., Giglia, A., Mahne, N., Nannarone, S., 2011. Molybdenum–silicon aperiodic multilayer broadband polarizer for 13–30 nm wavelength range. Nucl. Instrum. Meth. A 654, 588–591.

Tatchyn, R., 1998. Methods based on multiple-slit Fourier transform interferometry for determining thin-film optical constants in the VUV/soft X-ray range. In: Palik, E.D. (Ed.), Handbook of Optical Constants of Solids II. Academic Press, San Diego.

Thielsch, R., 2003. Optical coatings for the DUV/VUV. In: Kaiser, N., Pulker, H.K. (Eds.), Optical Interference Coatings. Springer Series in Optical Sciences, Springer-Verlag, Berlin, Heidelberg, pp. 255–279.

Tombulian, D.H., 1957. The experimental methods of soft X-ray spectroscopy and the valence band spectra of the light elements. In: Flügge, S. (Ed.), Röntgenstrahlen/X-Rays. Handbuch der Physik/Encyclopedia of Physics, vol. 6. Springer-Verlag, Berlin, Germany.

Tougaard, S., Chorkendorff, I., 1987. Differential inelastic electron scattering cross sections from experimental reflection electron-energy-loss spectra: application to background removal in electron spectroscopy. Phys. Rev. B 35, 6570–6577.

Tsuru, T., Yamamoto, M., 2008. Precise determination of layer structure with EUV ellipsometry data obtained by multilayer polarizing elements. Phys. Status Solidi C 5, 1129–1132.

Uspenski, Y., Seely, J., Popov, N., Artioukov, I., Vinogradov, A., Windt, D., Kjornrattanawanich, B., 2005. Extreme UV optical constants of rare-earth metals free from effects of air contamination. Proc. SPIE 5919, 59190S.

UWXAFS Project, It Involves the Development and Distribution of High Quality Analysis Software for XAFS. http://depts.washington.edu/uwxafs/.

Venkataraman, C.T., Lang, J.C., Nelson, C.S., Srajer, G., Haeffner, D.R., Shastri, S.D., 1998. A high energy phase retarder for the simultaneous production of right- and left-handed circularly polarized X rays. Rev. Sci. Instrum. 69, 1970–1973.

Vidal-Dasilva, M., Fernández-Perea, M., Méndez, J.A., Aznárez, J.A., Larruquert, J.I., 2009. Narrowband multilayer coatings for the extreme ultraviolet range of 50–92 nm. Opt. Express 17, 22773–22784.

Vinogradov, A.V., Zeldovich, B.Y., 1977. X-ray and far UV multilayer mirrors: principles and possibilities. Appl. Opt. 16, 89–93.

von Ballmoos, P., 2005. Instruments for nuclear astrophysics. In: Kahn, S.M., von Ballmoos, P., Sunyaev, R.A. (Eds.), High-Energy Spectroscopy Astrophysics.In: Saas-Fee Advanced Courses, vol. 30, pp. 82–197.

Walker, W.C., 1964. Pile-of-plates polarizer for the vacuum ultraviolet. Appl. Opt. 3, 1457–1459.

Waller, I., 1923. Zur Frage der Einwirkung der Wärmebewegung auf die Interferenz von Röntgenstrahlen. Z. Phys. 17, 398–408.

Wang, Z., Wang, H., Zhu, J., Xu, Y., Zhang, S., Li, C., Wang, F., Zhang, Z., Wu, Y., Cheng, X., Chen, L., Michette, A.G., Pfauntsch, S.J., Powell, A.K., Schäfers, F., Gaupp, A., MacDonald, M., 2006a. Extreme ultraviolet broadband Mo/Y multilayer analyzers. Appl. Phys. Lett. 89, 241120.

Wang, Z., Wang, H., Zhu, J., Wang, F., Gu, Z., Chen, L., Michette, A.G., Powell, A.K., Pfauntsch, S.J., Schäfers, F., 2006b. Broadband multilayer polarizers for the extreme ultraviolet. J. Appl. Phys. 99, 056108.

Wang, Z.S., Wang, H.C., Zhu, J.T., Wang, F.L., Gu, Z.X., Chen, L.Y., Michette, A.G., Powell, A.K., Pfauntsch, S.J., Schäfers, F., 2006c. Broad angular multilayer analyzer for soft X-rays. Opt. Express 14, 2533–2538.

Wang, Z., Wang, H., Zhu, J., Zhang, Z., Xu, Y., Zhang, S., Wu, W., Wang, F., Wang, B., Liu, L., Chen, L., Michette, A.G., Pfauntsch, S.J., Powell, A.K., Schäfers, F., Gaupp, A., MacDonald, M., 2007a. Broadband Mo/Si multilayer transmission phase retarders for the extreme ultraviolet. Appl. Phys. Lett. 90, 031901.

Wang, Z., Wang, H., Zhu, J., Zhang, Z., Wang, F., Xu, Y., Zhang, S., Wu, W., Chen, L., Michette, A.G., Pfauntsch, S.J., Powell, A.K., Schäfers, F., Gaupp, A., Cui, M., Sun, L., MacDonald, M., 2007b. Complete polarization analysis of extreme ultraviolet radiation with a broadband phase retarder and analyzer. Appl. Phys. Lett. 90, 081910.

Wang, H., Dhesi, S.S., Maccherozzi, F., Sawhney, K.J.S., 2012. Complete polarization analysis of high energy soft X-rays by combining a multilayer phase retarder with crystal analyzer. J. Appl. Phys. 111, 123117.

Wang, X.-D., Chen, B., Wang, H.-F., He, F., Zheng, X., He, L.-P., Chen, B., Liu, S.-J., Cui, Z.-X., Yang, X.-H., Li, Y.-P., 2015. Design and fabrication of far ultraviolet filters based on π-multilayer technology in high-k materials. Sci. Rep. 5, 8503.

Warburton, W.K., Ludwig Jr., K.F., 1986. Absorption effects in the determination of anomalous scattering factors using X-ray refraction through a prism. Phys. Rev. B 33, 8424–8432.

Watanabe, M., Hatano, T., Saito, K., Hu, W., Ejima, T., Tsuru, T., Takahashi, M., Kimura, H., Hirono, T., Wang, Z., Cui, M., Yamamoto, M., Yanagihara, M., 2008. Multilayer polarization elements and their applications to polarimetric studies in vacuum ultraviolet and soft X-ray regions. Nucl. Sci. Tech. 19, 193–203.

Weaver, J.H., Krafka, C., Lynch, D.W., Koch, E.E., 1981. Optical properties of metals. In: Physik Daten Collection. vols. 18-1 and 18-2. Fachinformationszentrum Energie-Physik-Mathematik, GmbH, Karlsruhe, Germany.

Weber, T., Käsebier, T., Helgert, M., Kley, E.-B., Tünnermann, A., 2012. Tungsten wire grid polarizer for applications in the DUV spectral range. Appl. Opt. 51, 3224–3227.

Werner, W.S.M., 2006. Optical constants of Cu measured with reflection electron energy loss spectroscopy (REELS). Surf. Sci. 600, L250–L254.

Westerveld, W.B., Becker, K., Zetner, P.W., Corr, J.J., McConkey, J.W., 1985. Production and measurement of circular polarization in the VUV. Appl. Opt. 24, 2256–2262.

Williams, M.W., MacRae, R.A., Arakawa, E.T., 1967. Optical properties of magnesium fluoride in the vacuum ultraviolet. J. Appl. Phys. 38, 1701–1705.

Windt, D.L., 1998. IMD—software for modeling the optical properties of multilayer films. Comput. Phys. 12, 360–370.

Windt, D.L., 2015. EUV multilayer coatings for solar imaging and spectroscopy. Proc. SPIE 9604. 96040P.

Windt, D.L., Gullikson, E.M., 2015. Pd/B4C/Y multilayer coatings for extreme ultraviolet applications near 10 nm wavelength. Appl. Opt. 54, 5850–5860.

Windt, D.L., Cash Jr., W.C., Scott, M., Arendt, P., Newnam, B., Fisher, R.F., Swartzlander, A.B., 1988. Optical constants for thin films of Ti, Zr, Nb, Mo, Ru, Rh, Pd, Ag, Hf, Ta, W, Re, Ir, Os, Pt, and Au from 24 Å to 1216 Å. Appl. Opt. 27, 246–278.

Windt, D.L., Gullikson, E.M., Walton, C.C., 2002. Normal-incidence reflectance of optimized W/B4C multilayers in the range 1.4 nm $< \lambda <$ 2.4 nm. Opt. Lett. 27, 2212–2214.

Windt, D.L., Donguy, S., Hailey, C.J., Koglin, J., Honkimaki, V., Ziegler, E., Christensen, F.E., Chen, H., Harrison, F.A., Craig, W.W., 2003. W/SiC X-ray multilayers optimized for use above 100 keV. Appl. Opt. 42, 2415–2421.

Windt, D.L., Donguy, S., Hailey, C.J., Koglin, J., Honkimaki, V., Ziegler, E., Christensen, F.E., Harrison, F.A., 2004a. Optical constants for hard X-ray multilayers over the energy range E = 35 – 180 keV. Proc. SPIE 5168, 35–40.

Windt, D.L., Donguy, S., Seely, J.F., Kjornrattanawanich, B., Gullikson, E.M., Walton, C.C., Golub, L., DeLuca, E., 2004b. EUV multilayers for solar physics. Proc. SPIE 5168, 1–11.

Windt, D.L., Seely, J.F., Kjornrattanawanich, B., Uspenskii, Y.A., 2005. Terbium-based extreme ultraviolet multilayers. Opt. Lett. 30, 3186–3188.

Wood, R.W., 1933. Remarkable optical properties of the álcali metals. Phys. Rev. 14, 353–360.

Wood II, O.R., Craighead, H.G., Sweeney, J.E., Maloney, P.J., 1984. Vacuum ultraviolet loss in magnesium fluoride films. Appl. Opt. 23, 3644–3649.

Wu, W.-J., Wang, Z.-S., Zhu, J.-T., Zhang, Z., Wang, F.-L., Chen, L.-Y., Zhou, H.-J., Huo, T.-L., 2011. Spectral resolution improvement of Mo/Si multilayers. Chin. Opt. Lett. 28, 086801.

XCOM-FFAST Comparison Web, http://physics.nist.gov/PhysRefData/XrayNoteB.html.

Yamamoto, M., 1993. Polarimetry with use of soft X-ray multilayers. Proc. SPIE 2010, 152–159.

Yamamoto, M., Namioka, T., 1992. Layer-by-layer design method for soft-X-ray multilayers. Appl. Opt. 31, 1622–1630.

Yamashita, K., Akiyama, K., Haga, K., Kunieda, H., Lodha, G.S., Nakajo, N., Nakamura, N., Okajima, T., Tamura, K., Tawara, Y., 1998. Fabrication and characterization of multilayer supermirrors for hard X-ray optics. J. Synchrotron Radiat. 5, 711–713.

Yanagihara, M., Maehara, T., Nomura, H., Yamamoto, M., Namioka, T., 1992. Performance of a wideband multilayer polarizer for soft x rays. Rev. Sci. Instrum. 63, 1516–1518.

Yang, M., Cobet, C., Esser, N., 2007. Tunable thin film polarizer for the vacuum ultraviolet and soft X-ray spectral regions. J. Appl. Phys. 10, 1053114.

Yulin, S., 2003. Multilayer coatings for EUV/soft X-ray mirrors. In: Kaiser, N., Pulker, H.K. (Eds.), Optical Interference Coatings. Springer Series in Optical Sciences, Springer-Verlag, pp. 281–308.

Yulin, S., Schäfers, F., Feigl, T., Kaiser, N., 2004. Enhanced reflectivity and stability of Sc/Si multilayers. Proc. SPIE 5193, 155–163.

Yulin, S., Benoit, N., Feigl, T., Kaiser, N., Fang, M., Chandhok, M., 2008. Mo/Si multilayers with enhanced TiO_2- and RuO_2-capping layers. Proc. SPIE 6921, 692118.

Zhu, J., Wang, Z., Zhang, Z., Wang, F., Wang, H., Wu, W., Zhang, S., Xu, D., Chen, L., Zhou, H., Huo, T., Cui, M., Zhao, Y., 2008. High reflectivity multilayer for He-II radiation at 30.4 nm. Appl. Opt. 47, C310–C314.

Zukic, M., Torr, D.G., 1992. Multiple reflectors as narrow-band and broadband vacuum ultraviolet filters. Appl. Opt. 31, 1588–1596.

CHAPTER

Controlling thermal radiation from surfaces☆

8

Carl G. Ribbing
Uppsala University, Uppsala, Sweden

8.1 INTRODUCTION

This chapter discusses why and how the heat radiation from solid surfaces can be controlled. Like the other chapters in this book, it is mainly application oriented. However, the first section will present some basic equations that are required for the ensuing description of applications.

The applications will include cases in which either the temperature of the solid, or the thermal radiation emitted by the solid, is to be controlled. In the most general perspective, the purpose may be to heat an object radiatively, to avoid heating it, to avoid cooling it, to cool it, or to reduce the infrared radiation from the object.

Initially, an elementary comment is given about measuring the heat radiation upon or from a body. The "spectrophotometer version" of the law of conservation of energy for an impinging light beam is

$$R + A + T = 1 \tag{8.1}$$

that is, a sum of fractions of light intensity. Light is either reflected, R, absorbed, A, or transmitted, T. This sum is equal to unity. However, when properties in the infrared are studied, care must be taken when measurements are made. If the thermal emission from the sample is registered by the spectrophotometer, *as if it were reflected or transmitted*, errors are introduced. There is a well-known solution to this problem. The instrument light beam should be chopped in the right place such that only true signals, phase locked to the frequency are amplified and registered. The sketch in Fig. 8.1 illustrates the problem and the standard solution.

If the light chopper is placed directly in front of the light source, that is, position a, then the light from the light source will be modulated and amplified by the phase-locked detection system. In position b, the thermal emission from the sample and the surrounding compartment *will also be chopped* and therefore amplified to a

☆This chapter is a reprint of the chapter originally published in the first edition of Optical Thin Films and Coatings: From Materials to Applications

Optical Thin Films and Coatings. https://doi.org/10.1016/B978-0-08-102073-9.00008-4
Copyright © 2013 Woodhead Publishing Limited. All rights reserved.

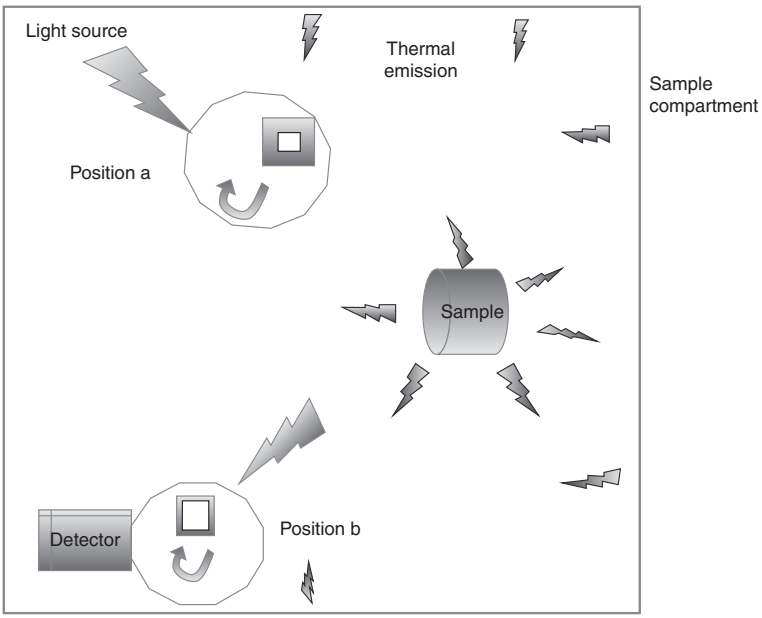


FIG. 8.1

Sketch illustrating the importance of correct light chopping in a spectrophotometer. The chopper positions a and b are critically different—see text.

signal violating Eq. (8.1). Modern IR spectrophotometers are type a, but there are cases of early publications of IR reflectance spectra that suffer from an error of type b. It should be noted that also in modern instruments, small contributions by thermal emission from the chopper to the surroundings may be registered.

Section 8.2 will present some formalism for thermal emission. The upper limit is that of a *blackbody*, which is the thermodynamic limiting case. The actual thermal emission from a solid is modified by the emissivity function, $\varepsilon(\lambda, T) \leq 1$. The emissivity as a function of wavelength and temperature will be the subject of Section 8.3 which briefly surveys the formalism and measurement methods for spectral emissivity. In some of the literature on thermal properties and processes, the emissivity is treated as a constant, that is, the material is assumed to be *gray*. In this chapter the ambition is to go beyond that. The fact that emissivity may exhibit variation with wavelength opens possibilities for applications based on spectral selectivity. This will be discussed in Section 8.4.

Section 8.4 describes four different applications of thermal control coatings or surfaces. The first two: thermal solar collectors and, even more so, low-emissivity coatings for energy-conserving windows have been on the market for a long time. Different techniques for large-scale manufacturing have been developed and there is an extensive literature discussing these two areas. For this reason, the description

and discussion will be limited. It is hoped the references given will compensate for the omissions.

The final three cases are coatings used to increase or prevent radiative cooling. In terms of optical performance the requirements are related. However, they involve different materials being used, which will lead to quite different solutions. None of these potential applications is presently exploited in large-scale applications—or at least they are not generally known to be. The scientific literature is not as extensive as for the first two cases. The principles will be explained and some laboratory-scale results will be quoted.

8.2 BLACKBODY RADIATION

Blackbody radiation is the upper limit on the thermal emission intensity from a solid surface (Wolfe, 1989; Zalewski, 1995). It is based on Planck's law for oscillators, which in turn is derived by using the Bose–Einstein distribution for vibrations in a box (a "holeraum") of macroscopic dimension. The spectral radiance emitted from a small hole in this "box" in one unit of space angle is

$$L_{bb}(\nu, T) = \frac{2h}{nc^2} \frac{\nu^3}{\exp(h\nu/kT) - 1} \tag{8.2}$$

where ν is the frequency, c the vacuum velocity for light, h is the Planck constant, k the Boltzmann constant, and T is the absolute temperature. In most cases, the refractive index of the medium, $n = 1$. The SI dimension of spectral radiance is W/m^2, Hz, sr. The radiance from a blackbody is Lambertian, so the total emission into the half-sphere is given by multiplication with 2π.

In Fig. 8.2, we plot this spectral radiance for a few temperatures chosen to show the characteristic behavior in the infrared where the unit W/m^2, THz, sr is appropriate.

We notice that the curves never intersect, that is, a curve for a higher temperature is always above one for a lower temperature. In Fig. 8.2, *frequency* is the independent variable, which is directly linked to the Planck theory. In optics, the corresponding expression as a function of wavelength is often used. The coordinate transformation, $\lambda = c/\nu$, is nonlinear which has consequences for the Planck function. The wavelength version is

$$L_{bb}(\lambda, T) = \frac{2hc^2}{nc^2\lambda^5} \frac{1}{\exp(h\nu/kT) - 1} \tag{8.3}$$

with dimension W/m^3, sr. In Fig. 8.3, radiance as a function of wavelength for the same temperatures is plotted per μm wavelength as the relevant unit in the infrared.

In this case, we also use the diagram to illustrate the well-known Wien's displacement law. The thick dash-dotted curve joins the maxima λ_m of the spectral curves. It is given by the expression

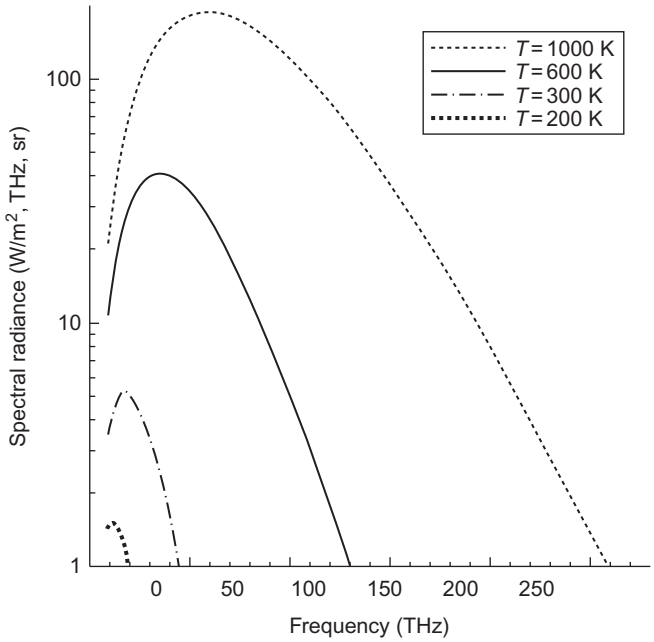


FIG. 8.2

The spectral radiance from a blackbody as a function of frequency in THz at the four temperatures indicated. Note that the diagram is lin-log.

$$\lambda_m = \frac{b_\lambda}{T} \tag{8.4}$$

where the constant $b_\lambda = 2.8978 \times 10^{-3}\,\text{mK}$.

It shows that the maxima of the blackbody curves move to a shorter wavelength when the temperature increases. The corresponding expression for the frequency version of Eq. (8.2) is

$$\nu_m = b_\nu T \tag{8.5}$$

with the constant $b_\nu = 5.8786 \times 10^{10}\,(\text{sK})^{-1}$.

As expected, the maxima move to higher frequencies when the temperature increases. A comparison of Figs. 8.2 and 8.3, shows, however, that *the positions of the maxima are not conserved in the coordinate transformation*. The maximum of the 1000 K curve in Fig. 8.3 is $\approx$ 2.9 μm. If this wavelength is converted to frequency $\nu = c/\lambda$, we get 103 THz. Looking at Fig. 8.2 the maximum position of the 1000 K curve is considerably lower at $\approx$59 THz. The reason for this shift is the nonlinear $\nu \Leftrightarrow \lambda$ coordinate transformation. Physically, it is a consequence of the Planck function being a distribution and having a dimension *per frequency* or *per wavelength unit*. It gives the power density in each infinitesimal frequency

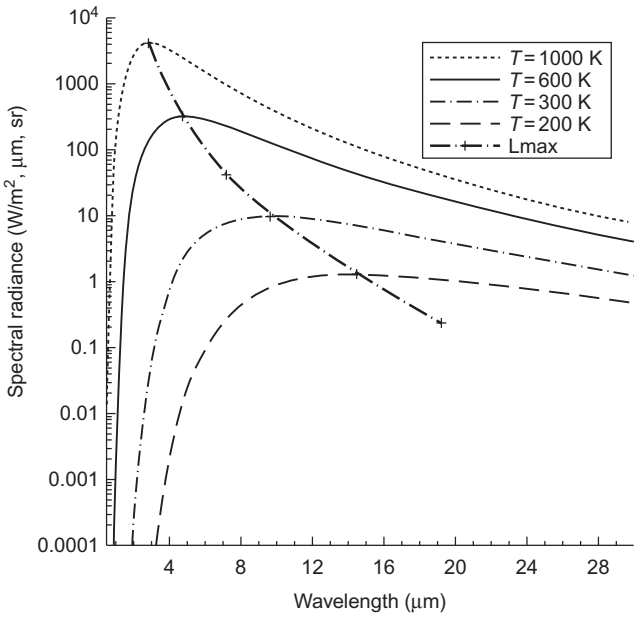


FIG. 8.3

The spectral radiance from a blackbody as a function of wavelength in μm at the same temperatures as in the previous figure. As in Fig. 8.2 the *y*-axis is logarithmic. The peaks of the spectral curves for different temperatures are joined by the *fat dash-dotted curve* which illustrates Wien's displacement law.

or wavelength interval. The nonlinear transformation makes the corresponding infinitesimal steps unequal, which influences the shape of the curve. Comparing the diagrams above, we notice that the widths of the peaks increase with temperature in Fig. 8.2, while they decrease in Fig. 8.3.

As an example we choose the solar spectrum, which is on the short wavelength side of Fig. 8.3. It agrees roughly with that for a blackbody at 5800 K. The maximum is at $\lambda = 0.50\,\mu\text{m}$ (cf. Eq. 8.4). This wavelength almost agrees with the peak of the sensitivity of the human eye—but this agreement is only in the wavelength version. Eq. (8.5) gives the corresponding maximum on the frequency axis at 341 THz, which corresponds to 0.88 μm, that is, well beyond 0.50 and actually outside the visible range. The eye sensitivity curve is dimensionless and not affected by the transformation. Consequently, in the wavelength representation the peak of solar radiation is in the middle of the sensitivity of the human eye, but in frequency space the maximum is outside our range of vision. This and a few more consequences of the nonlinear transformation of the Planck distribution function have been described in more detail by Soffer and Lynch (1999). Heald (2003) has also discussed the issue of the "Wien peak" position.

Expressions (8.2) and (8.3) tend to 0 in both directions, that is, whether ny or $\lambda \Rightarrow 0$ or ∞. Analyzing the integral of the expression it turns out that they are both finite as long as the temperature is finite (Zalewski, 1995). This was a strong argument in favor of quantum mechanics when Planck made his derivation, because earlier classical attempts had indicated the opposite. The integral is required to calculate the **total radiance** M from the surface of a blackbody, that is, the Stefan–Boltzmann equation summing the contributions for all wavelengths into the solid angle 2π:

$$M(T) = \sigma T^4 \tag{8.6}$$

with the Stefan–Boltzmann constant $\sigma = 5.6693 \times 10^{-8}$ W/m^2/K^4. Eq. (8.6) is obtained, whether the variable is ν or λ.

This signals that we should recheck are the differences in curve shapes noted above. The area under each curve, that is, the total radiance, should be independent of variables. A formal verification requires integration of the two versions (8.2) and (8.3). The following comment is only a hint: the peak *heights* in the wavelength version increase as T^5, which is easily shown by inserting Eq. (8.4) into Eq. (8.3) (Ribbing, 1999). In contrast, the peaks of the frequency curves only grow as T^3, which is found by inserting Eq. (8.5) into Eq. (8.2). This is compensated for by the changes in peak *widths* noted above. In both versions therefore the Stefan–Boltzmann integrals grow as T^4.

Emission from a small hole through a large enclosure is virtually noncoherent. This may be the reason for the widespread notion that thermal radiation in general is noncoherent. It is often a reasonable first assumption that radiation from thermal sources has a very short coherence length. Nevertheless, microscopic features on a thermally emitting surface cause spectral and directional interference variations (Carter and Wolf, 1975; Wolf and Carter, 1975). In particular, it was proved that the Lambertian emission requires a source with some degree of periodicity.

8.3 EMISSIVITY

The previous section considered the special case of thermal emission from a blackbody. This is the theoretical maximum, which a real surface never reaches for all wavelengths. The real emission is obtained by multiplication with the *emissivity* function $\varepsilon(\lambda)$ which is dimensionless and $0 \leq \varepsilon(\lambda) \leq 1$. The emissivity expresses to what extent a real body is a blackbody and modifies Eq. (8.3). A simple illustration is given in Fig. 8.4.

A simple consideration may help to understand the relation between emissivity and other optical properties. The blackbody radiation from the inside of a real body is partly reflected by the interface toward the outside. This interface cannot store energy. Thus, the fraction that is not reflected is emitted as thermal radiation. The arrow to the left in the diagram gives the result $\varepsilon = 1 - R$, which will be obtained under better defined circumstances as (8.10) given below.

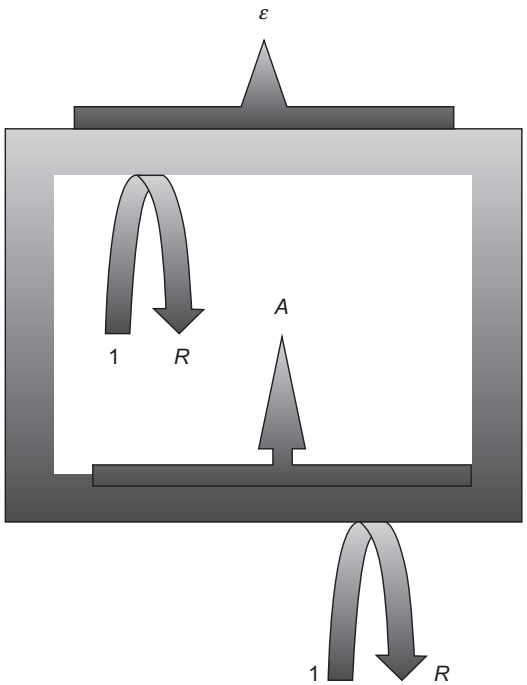


FIG. 8.4

Simplistic illustration of the relationship between thermal emission from a real body and that from a blackbody. Expressed in the dimensionless fractions for the *left arrow* in the diagram the obvious result $\varepsilon = 1 - R$ is obtained. The *right arrow* gives a similar argument for Kirchhoff's law.

The spectral, thermal emission from a general body is

$$L(\lambda, T) = \varepsilon(\lambda) L_{bb}(\lambda, T) \tag{8.7}$$

While the Planck function is an expression from statistical thermodynamics and only a function of temperature, $\varepsilon(\lambda)$ expresses the limits set by *material properties*. We need, for example, the optical functions $n(\lambda)$ and $k(\lambda)$ to obtain the emittance, $\varepsilon(\lambda)$. If the optical constants are temperature dependent this will also make the emissivity temperature dependent. Generally, we should therefore write $\varepsilon(\lambda,T)$. This temperature dependence may be important at phase changes. However, in general, the temperature dependence in Eq. (8.7) is dominated by that of the Planck function, $L_{bb.}$

There is a general thermodynamic relation concerning emissivity. According to Kirchhoff's law, the emissivity is equal to the optical absorptivity, A, the fraction of the total intensity that is absorbed by the solid. This is understood from a thought experiment. If a body is placed inside the enclosure, it must eventually reach the

same temperature as the inner walls of the enclosure. At equilibrium, the radiation intensity emitted by the body is equal to that absorbed, that is,

$$\varepsilon(\lambda) = A(\lambda) \tag{8.8}$$

for all wavelengths and temperatures. Kirchhoff's law has some caveats when we leave the isotropic environment of the *holeraum*. The exceptions are connected to cases when angular dependence and polarization of the radiation have to be considered. In more general cases, the impinging radiation may have an angle of incidence different from that where most of the outgoing thermal radiance is leaving. Similarly, the thermal radiation may be more or less polarized depending on the material properties. For the details of these exceptions, we refer the reader to more complete sources (Siegel and Howell, 1981; Palmer, 1995).

The intensive research work with photonic crystals during the 1990s evolved around the concept of *photonic bandgaps,* within which electromagnetic waves cannot be transmitted (John, 1984; Yablonovitch, 1987). An incident wave in such a gap is totally reflected and the corresponding thermal emission is suppressed as illustrated in Fig. 8.4. The possibility of controlling, or at least changing part of the thermal emission from a surface with a one-dimensional photonic crystal on the surface of a bulk solid was investigated with model calculations by Cornelius and Dowling (1999). A "one-dimensional photonic crystal" is equivalent to an optical multilayer which is a major component in optical technology. These relatively recent works therefore formulate findings from traditional optical filter technology in a new terminology.

If we combine Kirchhoff's law (8.8) with (8.1) and assume that polarization and angular effects are negligible, we can express the emissivity in quantities that are measurable in a conventional spectrophotometer. The R- and T-measurements should be made with an integrating sphere if the sample is not highly specular:

$$\varepsilon(\lambda) = 1 - R(\lambda) - T(\lambda) \tag{8.9}$$

Adding the condition that the sample is opaque we arrive at the relation which was hinted to in Fig. 8.4:

$$\varepsilon(\lambda) = 1 - R(\lambda) \tag{8.10}$$

This points to the simplest method for determining the spectral emissivity, that is, measuring the bulk reflectance of an opaque sample. Provided that the incoming beam is already chopped, as in modern spectrophotometers, this method avoids the problem with eigen-emission mentioned in Section 8.1.

An alternative method is to use a dual-beam spectrophotometer in emission mode, as illustrated in Fig. 8.5.

In emission mode, the instrument does not use the built-in light source, but instead normalizes the spectral intensity from the heated sample to that from the sample in the reference channel. This reference should either be an approximate blackbody or a calibrated emissivity standard. The difficulty in this case is to measure at temperatures different from room temperature. Attempts to heat the sample in a

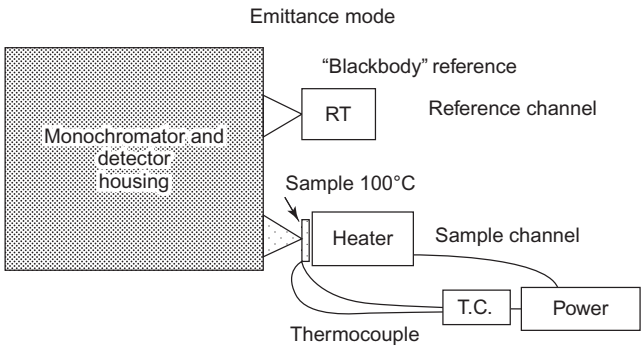


FIG. 8.5

Schematic showing the use of a conventional infrared spectrophotometer in emittance mode. The spectral intensity of thermal emission from the heated sample is normalized to that from the reference. The reference sample should either be an approximate blackbody or a calibrated emissivity standard.

From Chibuye, T., Ribbing, C.G., Wäckelgård, E., 1994. Reststrahlen band studies of polycrystalline beryllium oxide. Appl. Opt. 33, 5975–81.

double-beam spectrophotometer often cause thermal movements of the sample or the sample holder that shift the beam on the detector, which increases the measurement error.

As a third option for emissivity measurement we show an example of a radiometer, or heat-camera, measurement in Fig. 8.6. Such instruments do not have a light source and a monochromator, but often have one or several filters that transmit over a

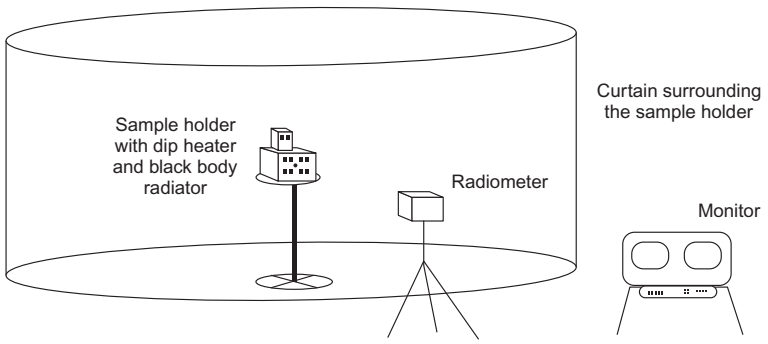


FIG. 8.6

Illustration of radiometric determination of band emittance for the sample in the warm-water tank with samples mounted over holes, and an inside spherical shell as a blackbody reference.

From Ribbing, C.G., Staaf, Ö., Andersson, S.K., 1995. Selective supression of thermal emission from radomes and materials selection therefore. Opt. Eng. 34 (11), 3314–22.

limited wavelength range $\{a,b\}$. The emissivity to be determined is then an average over $\{a,b\}$:

$$\overline{\varepsilon}(T) = \frac{\int_a^b \varepsilon(\lambda) L_{bb}(\lambda, T\mathrm{d}\lambda)}{\int_a^b L_{bb}(\lambda, T)\mathrm{d}\lambda} \tag{8.11}$$

where the nominator is the total thermal emission from the sample. $\overline{\varepsilon}(T)$ may be named *a,b-band-emittance*. T is the sample temperature, which has to be different from that of the ambient, T_a. The radiometer reads the intensity of the thermal emission from the sample plus the thermal emission from the surroundings that is reflected by the sample. This total intensity of the two added components is not sufficient to obtain sample emissivity. The standard procedure to obtain sample emissivity is illustrated in Fig. 8.6 and summarized in a few equations. Complete descriptions have been published by, for example, McCluney (1994) and Zhang et al. (1986).

Given that the sample is opaque we can use Eq. (8.10) and obtain an expression for the radiance reflected by the sample from the surroundings at the ambient temperature, T_a:

$$\begin{aligned} L_r(T_a) &= \int_a^b (1-\varepsilon(\lambda)) L_{bb}(\lambda, T_a)\mathrm{d}\lambda \\ &= (1-\overline{\varepsilon}(T_a)) \int_a^b L_{bb}(\lambda, T_a)\mathrm{d}\lambda \end{aligned} \tag{8.12}$$

In this expression, it is assumed that the surroundings radiate as a blackbody. This is an approximation which is satisfactory if the surrounding surfaces are sufficiently distant or almost black in $\{a,b\}$. In the arrangement shown in Fig. 8.6, the cylindrical object is a black curtain several meter s from the sample. The intensity reading, L_A from the sample can then be written as

$$L_A(T, T_A) = \overline{\varepsilon}(T) \int_a^b L_{bb}(\lambda, T)\mathrm{d}\lambda + (1-\overline{\varepsilon}(T_a)) \int_a^b L_{bb}(\lambda, T_a)\mathrm{d}\lambda \tag{8.13}$$

This sample reading is complemented with two more: L_B, which is from a blackbody spot at temperature T, that is, the opening of an empty sphere mounted in the water container as in Fig. 8.6; and L_C, the measured intensity from a representative spot of the surroundings at temperature T_a. The two quantities are given by the expressions

$$= L_B(T) = \int_a^b L_{bb}(\lambda, T_a)\mathrm{d}\lambda \tag{8.14}$$

and

$$L_C(T_a) = \int_a^b L_{bb}(\lambda, T_a)\mathrm{d}\lambda \tag{8.15}$$

using Eqs. (8.13)–(8.15) we obtain a relationship between the three measured intensities:

$$L_A(T, T_a) = \overline{\varepsilon}(T)L_B(T) + (1 - \overline{\varepsilon}(T_a))L_C(T_a) \tag{8.16}$$

which, just as expected, shows that the reading A is a sum of two radiances B and C.

If we make the approximation $\overline{\varepsilon}(T) = \overline{\varepsilon}(T_a) = \langle\overline{\varepsilon}(T)\rangle$, then Eq. (8.16) gives

$$\langle\varepsilon(T)\rangle = \frac{L_A - L_B}{L_B - L_C} \tag{8.17}$$

This is a standard expression and under favorable conditions it gives an acceptably accurate approximation of $\overline{\varepsilon}(T)$. In particular, one notices that if the emittance is gray, that is, independent of wavelength $= \varepsilon'$ in the a,b interval, then Eq. (8.11) gives $\overline{\varepsilon}(T) = \varepsilon'$ and Eq. (8.17) is exact. Since this is not always the case we keep the distinction between $\langle\varepsilon(T)\rangle$ and $\overline{\varepsilon}(T)$. In the opposite case, that is, if $\varepsilon(\lambda)$ has strong variation within $\{a,b\}$, then $\langle\varepsilon(T)\rangle$ requires corrections to obtain an approximate value for $\overline{\varepsilon}(T)$ (Staaf et al., 1996).

8.4 OPTICALLY SELECTIVE COATINGS

In this section, we review two areas of applications of coatings and surfaces that have been established for several decades. Extensive research has been carried out in the two fields and the scientific literature is vast. Existing products are based on the principles of solar selectivity in the two fields: *Solar thermal absorbers* and *energy efficient window coatings*. The label "solar selective" refers to the spectral separation between the incoming solar radiation and the thermal emission of moderately hot objects. This separation makes it possible for a surface to have different, or even opposite, optical properties in the two spectral regions. Section 8.4.2 on window coatings will to some extent overlap with Chapter 20. We hope that some duplications will add depth, rather than cause irritation among readers.

8.4.1 COATINGS FOR THERMAL SOLAR COLLECTORS

In this case, the purpose is to heat a medium using solar radiation. The medium, water or air, is in good thermal contact with an absorbing surface. Primarily this surface should be a perfect absorber of the incoming solar radiation. This will raise the surface temperature, which causes thermal losses to the surroundings. Conduction and convective losses can be insulated against, but the radiative losses from the front surface cannot be shielded. To reduce radiative losses, the surface should exhibit low emittance in the thermal range of the absorber, for a flat plate of typically

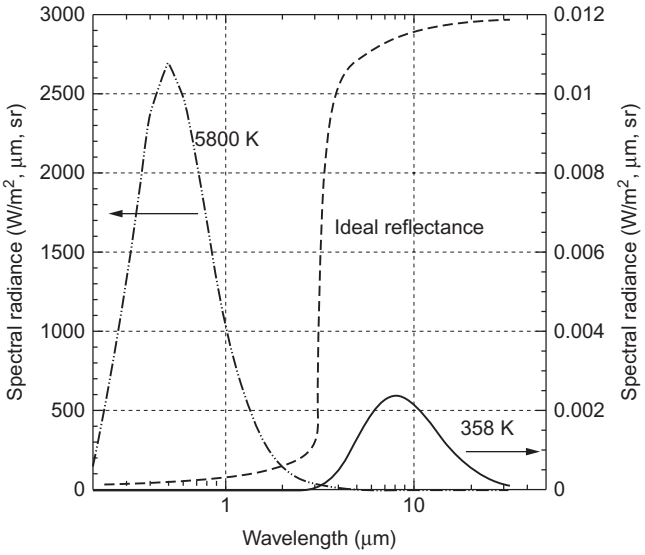


FIG. 8.7

Two blackbody radiance curves on log-lin axes. In principle as Fig. 8.3 but the two different temperatures, display the wavelength gap between the curves. Note the large difference in radiance values on the *y*-axis. The high-temperature curve 5520°C is a reasonable approximation for the incoming solar radiation, while the 75°C blackbody radiation represents potential losses from a solar collector that is "black" also in the infrared. The sketched idealized reflectance profile between 0 and 1 on a dimensionless scale illustrates thermal solar selectivity.

50–120°C. The high solar absorbance is only required in the wavelength range where the solar radiation is significant (cf. Section 8.2). The situation is illustrated with two blackbody curves at temperatures 358 K (85°C) and 5800 K (5527°C) in Fig. 8.7.

The diagram verifies that a high solar absorption, that is, blackbody behavior, is only essential in the range 0.4–2 μm, while low emittance is needed in the range 3–30 μm. Using Eqs. (8.8) and (8.10), we realize that the required optical behavior is a reflectance that is very low for 0.4–2 μm and as high as possible for 3–30 μm. This ideal reflectance spectrum is sketched in Fig. 8.7. This ideal behavior is unphysical, but it represents a target for developing solar thermal absorbers and *solar selectivity* is a common label for this property. This concept is old and the pioneering work of Tabor (1955) is often cited as a start for systematic material development. The results of this development have been documented in several monographs (Meinel and Meinel, 1976; Seraphin, 1979; Agnihotri and Gupta, 1981; Duffie and Beckman, 1991; Granqvist, 1991) and review articles on particular aspects, for example, by Craighead et al. (1979). An annotated bibliographic listing commenting publications for the period 1955–81 has been published (Niklasson and Granqvist, 1983). To keep within the framework of this book we shall focus on solar selectivity obtained with

optical thin films. The references cited immediately above include other examples like paints and electrochemical treatments.

A natural starting point is a metal substrate. Metals in general have high reflectance that increases with wavelength toward the infrared according to the Hagen–Rubens relation. This corresponds to low thermal emittance, that is, the second requirement for solar selectivity. Most metals exhibit high reflectance in the visible range, this will impair the first requirement—it will not be effectively heated. If we choose copper, it represents a small step in the right direction. Thanks to interband transitions, copper absorbs some green and blue light, and has low thermal emittance. However, a clean surface of copper does not get hot enough in sunshine to be of any technical use. To summarize a long history of research on single metals as well as compounds, it has been concluded that no single material will provide sufficient and stable solar selectivity for viable heat production. A historical account, including many high stability metal compounds, can be found in Seraphin (1979). The failure in the search for a single material has led to attempts with double layers. Based on the low thermal emissivity of metals a first choice has been to try oxidized metals. Many metal oxides are black or exhibit a color which indicates absorption bands in the visible range. As an example we again choose copper. It has two oxides, CuO is black and Cu_2O is red, which to some extent grow spontaneously in air depending on the temperature. As early as the 1960s, a chemical oxidizing agent "Ebanol" was already on the market for the production of selective solar absorbers. Roos et al. (1983) studied the difference between thermal and chemical copper oxide mixtures and concluded that the higher selectivity in the chemical case was due to the roughness of the interface between the growing oxide and the metal.

In a wider perspective we can categorize these tandem absorbers into two different types *the dark mirror* or the *heat mirror* illustrated by Fig. 8.8.

As explained in the caption, the difference between the two cases is the layer in which the main absorption of solar radiation and reflection of heat radiation occurs, respectively. In both cases, the top layers must have low reflectance for the impinging solar radiation which is a definite loss. This is the reason for sometimes adding a second optical film, that is, a third material, for antireflection of the upper layer.

With this background we can understand and distinguish the role of optical thin film technology for research, development, and production of thermal solar collectors. The transmission required through the top layer indicates that it should be a thin film. The requirements on the base suggest a metal substrate, which would also effectively conduct the collected heat to a transfer medium. In the case of Fig. 8.8A, a dark mirror, one option would be a metal base with a metal oxide coating that "antireflects" the metal in the visible and near-infrared (NIR) ranges and also increases the absorption in the metal. This interference approach is the subject of a classical paper by Haas et al. (1956) intended for applications in IR instruments. The paper demonstrates the difficulty in making this with high reflectance metals. Apart from the general problem of antireflection over a wide enough wavelength range, the paper identifies the condition to antireflect high metallic reflectance in

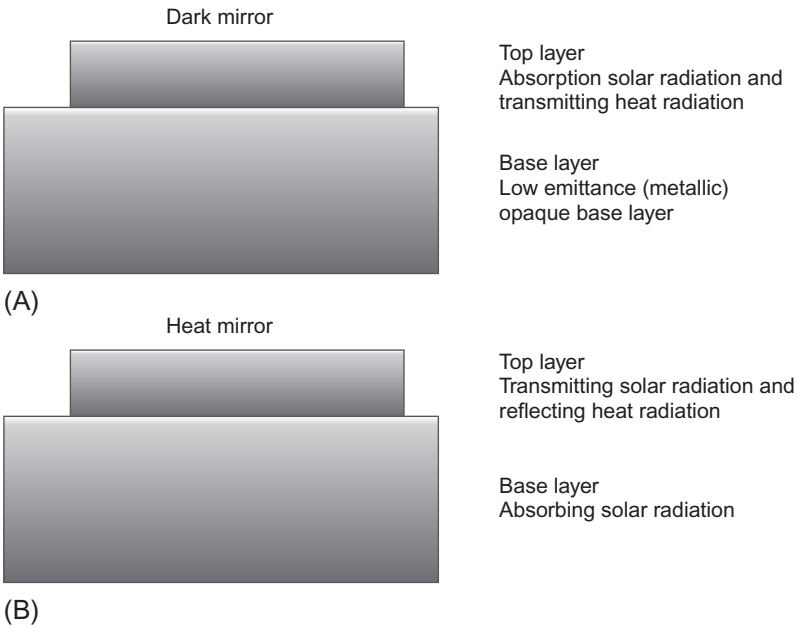


FIG. 8.8

(A) The dark mirror primarily absorbs short wave radiation in the top layer which transmits heat radiation. The tandem exhibits low thermal emittance thanks to the substrate. (B) The heat mirror reflects heat radiation from the top layer, which transmits the solar radiation to the absorbing substrate.

an expression for the optical constants. If the dielectric coating has refractive index n_1 and the metal substrate $N = n + ik$, the condition for a zero reflectance minimum is

$$n_1 = \left[n + \frac{k^2}{n-1} \right]^{1/2} \tag{8.18}$$

For high reflectance metals $n < 1$. This gives $n_1 < 1$, which is impossible for a dielectric film. The authors also tested evaporated titanium oxide on an aluminum substrate. In evaporation at normal temperatures, a substochiometric oxide is grown. This oxide is yellowish and has some visible absorption, that is, $k_1 > 0$. In this case low reflectance over most of the visible range can be obtained.

There are limits on the selectivity that can be obtained with a simple tandem concept. The reliance on interference also limits the width on the minimum that can be obtained with just one dielectric film. In this case a low minimum over the entire range 0.3–2.5 μm is not realistic. An additional problem is that interference will also create a *maximum* at some shorter wavelength.

In Fig. 8.9, we cite the example of black chrome tandem reflectance. This coating had already been extensively studied in the early 1970s and marketed for solar thermal collector systems.

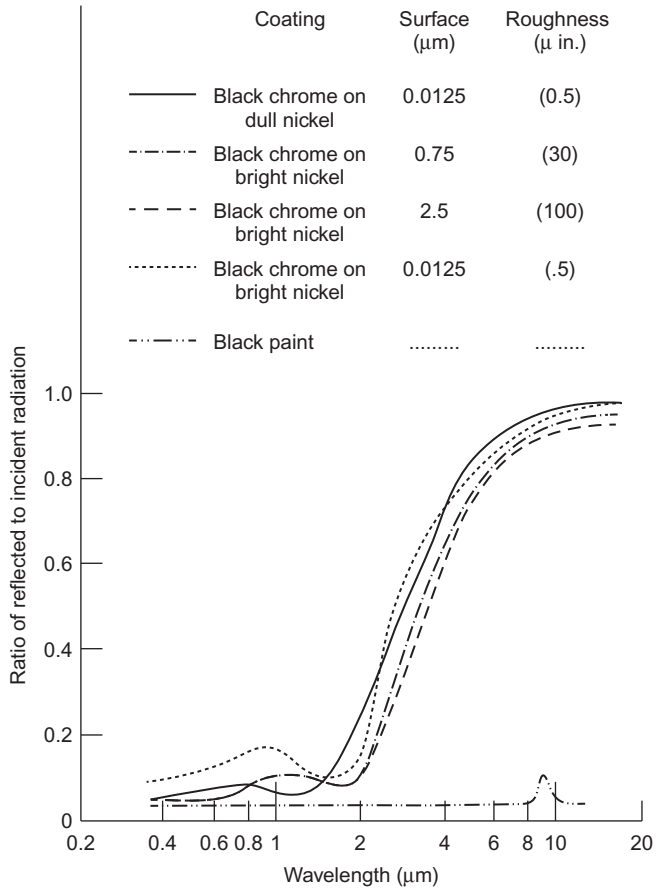


FIG. 8.9

Reflectance spectra for four different samples of black chrome on dull and bright nickel and one for ordinary black paint.

From McDonald, G.E., 1974. Refinement in black chrome for use as a solar selective coating, NASA Report TM X-3136, Lewis Res. Ctr. Cleveland, OH.

Black chrome is applied in a two-step electrochemical process on a nickel or copper base. This application technique does not result in optically smooth interfaces (Lampert and Washburn, 1979) and agreement with straightforward interference behavior should not be expected. Nevertheless, the different cases in Fig. 8.9 show some interference structure in the region below 2.0 μm. Obviously, the maxima cause losses in collection efficiency. For comparison, the spectrum for ordinary black paint is also given. It has significant IR-absorption and will therefore cause thermal losses.

Black chrome is an early example of a more advanced concept of *inhomogeneous* surface coatings for solar heat collection. Typically, a metal surface is coated with a

cermet, that is, a dielectric matrix containing a significant density of small metal particles. Sievers (1979) reviewed the optical properties of small metal particles in which the mean-free path of the conduction electrons is limited by the particle size. The optical properties of particles+matrix have been modeled with scattering and effective media theories, to determine one dielectric function for the composite medium (Niklasson, 1991).

As already mentioned, it is possible to use a top layer for antireflection in the visible spectral range (VIS)-NIR-region and thereby increasing the solar heat collection. An attractive version of this method is to prepare this top layer with a graded index, such that $n(z) \rightarrow 1$ when z approaches the front surface. The literature cited discusses a wide variety of these latter two methods. The advantages gained, however, must balance increased cost for a more complicated production process, and possibly an increased sensitivity for thermal and chemical damage. Fig. 8.10 shows high solar selectivity for a graded Ni/Al_2O_3 cermet film on silver. In this case (Craighead and Buhrman, 1978), the concentration gradient was achieved by evaporating from two sources that were separately controlled.

Section 8.4.3 treats the deposition techniques used for large-scale fabrication of thermal solar collectors. The Tabor patent mentions the electrochemical treatments of a smooth nickel surface. Painting is mentioned and there are special low-emissive black paints containing aluminum flakes which have lower emittance than the example shown in Fig. 8.9. As mentioned above, these kinds of coatings have been analyzed and modeled, but they are not typical products of "optical technology". It may be painful for experts in optical technology to find that "optical perfection" often reduces solar selectivity. Evaporation of films normally results in a higher degree

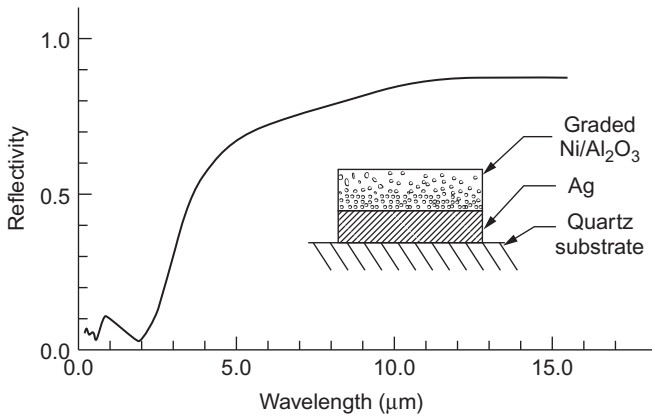


FIG. 8.10

Reflectance spectrum for a coevaporated graded Ni/Al_2O_3 cermet coating on a silver backing. The solar absorption $\alpha = 0.94$ and thermal emissivity $\varepsilon \approx 0.1$ reported.

From Craighead, H.G., Buhrman, R.A., 1978. Optical properties of selectively absorbing metal/insulator composite films. J. Vac. Sci. Technol. 15(2), 269–71.

of structural perfection and smooth interfaces that fulfill the requirements for interference calculations. Laboratory-scale deposition of evaporated solar absorber coatings has been a valuable method to test new materials and check the extent to which interference calculations modified for inhomogeneous composition and/or roughness agree with measurements. However, evaporation is not suited for economic production of m^2 size solar collectors. It has thus been quite important that lab-scale development of *magnetron-sputtered* coatings has also been successful, and in a few cases, transferred to full-scale production.

A particular advantage with sputtering is that it can be adapted to deposit on curved surfaces. This was required for making tube-shaped collectors for mounting in a moderately concentrating system: a cylindrical solar mirror with the absorber tube along the center. In Fig. 8.11 we cite an early design of a cylindrical sputter unit made by Harding et al. (1976).

The particular carbide coating tested in this work was solar selective, but not sufficiently so compared with alternatives that have appeared. Through a number of intermediate steps this has been developed to a commercially successful production of solar collectors in China. The coating is a mixed AlN and stainless steel cermet that is created by successive deposition of the two materials in very thin layers. This is obtained by a rotation as fast as 6 rpm of the batch of tubes. The two materials interdiffuse to a semihomogeneous, high-temperature stable cermet. The substrate is a metallic heat reflector as in Fig 8.8A. The resulting collector tubes

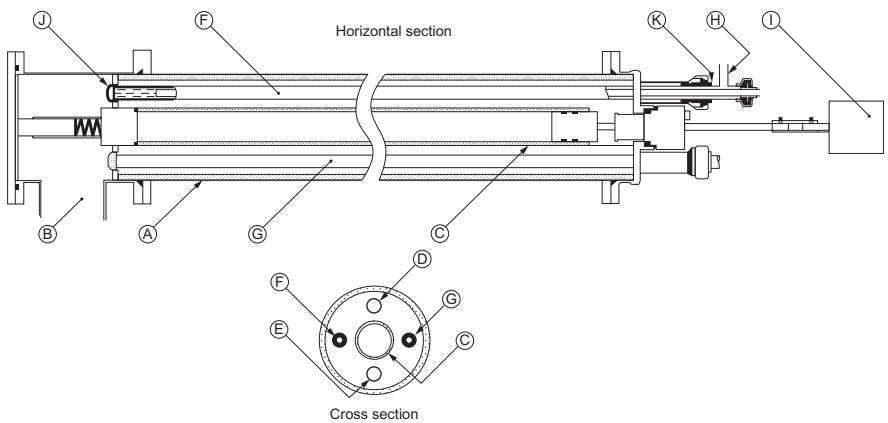


FIG. 8.11

Schematic diagram showing the design of a DC magnetron sputtering unit for deposition of a cermet coating on the exterior of tubes for concentrating solar collectors. (A) glass envelope, (B) pumping port, (C) tubular glass substrate, (D) gas inlet tube, (E) gas outlet tube, (F) stainless steel cathode, (G), copper cathode, (H) cooling water inlet, (I) motor, (J) glass insulator, and (K) Teflon insulator and seal.

From Harding, G.L., McKenzie, D.R., Window, B., 1976. The dc sputter coating of solar selective surfaces onto tubes. J. Vac. Sci. Technol. 13(5), 1073–75.

are reported to have solar absorption as high as 0.95 and the thermal emittance is only 0.05 (Zhang et al., 1998).

A corresponding development has taken place for the production of flat solar collectors. The collector comprises 20 cm wide, double aluminum fins that embed a flat copper tube. After the coating process, the tube was reshaped using pressurized air. In the application, it is used for circulating the water to be heated. Originally, the coating was made electrochemically in large containers with aggressive chemicals. Today, the corresponding product has similar aluminum fins that are DC sputter-coated with an antireflected Ni–NiO cermet. The sputtering unit is a roll coater that is charged with up to 1000 m of the rolled fin, which is fed through the deposition zone at a speed that gives the suitable deposition time. The performance is solar absorption 0.96 and thermal emission 0.10 at 100°C (Wäckelgård and Hultmark, 1998).

8.4.2 ENERGY-EFFICIENT WINDOW COATINGS

Energy-conserving window coatings have been a commercially successful application of advanced and large-scale optical coating technology for several decades. The requirements on visual perfection, in transmission as well as reflectance, are very stringent with regard to windows. It is remarkable that they can be satisfied for large areas in different coating processes. The window coatings belong to a larger group named *architectural coatings* (cf. Chapter 20), which are generally used to improve exterior visual impression. Energy saving, which is the focus of this treatment, is obtained differently depending on the local climate. In warm climate zones the coating should reflect invisible solar heat radiation to save electric power otherwise needed for air conditioning or for improved comfort. It should be noted that >40% of the total solar energy appears beyond visible wavelengths, cf. Fig. 8.7. These coatings are sometimes named *solar screens*. In cold climates, the coating should reduce thermal emission. They are named *low emissive* or *LE coatings*. In Fig. 8.12, we show the idealized reflectance and transmittance spectra for the two types of coatings.

As shown, the difference between a solar screen and LE coating is in the wavelength position of the step between transmittance and reflectance. Beyond 4 μm the transmission of the window glass is zero, but the absorption heats the glass, that is, an increase of the heat load to the inside. The high reflectance in the infrared thus reduces this heating as well as the emission losses in the LE case as given by Eq. (8.10). As in the case of the seemingly very different applications of solar thermal absorbers, the threshold between absorption/transmission and reflectance should ideally be in the 2–3 μm interval.

Integrated parameters can be used for evaluating performance. T_{SOLAR} is the measured transmittance weighted by the solar spectrum and integrated over the visible and near-infrared ranges. R_{IR} is the measured IR-reflectance weighted by the blackbody function for room temperature integrated over the IR. An LE-window should have both T_{SOLAR} and R_{IR} as close as possible to 100%. In Fig. 8.13, we show

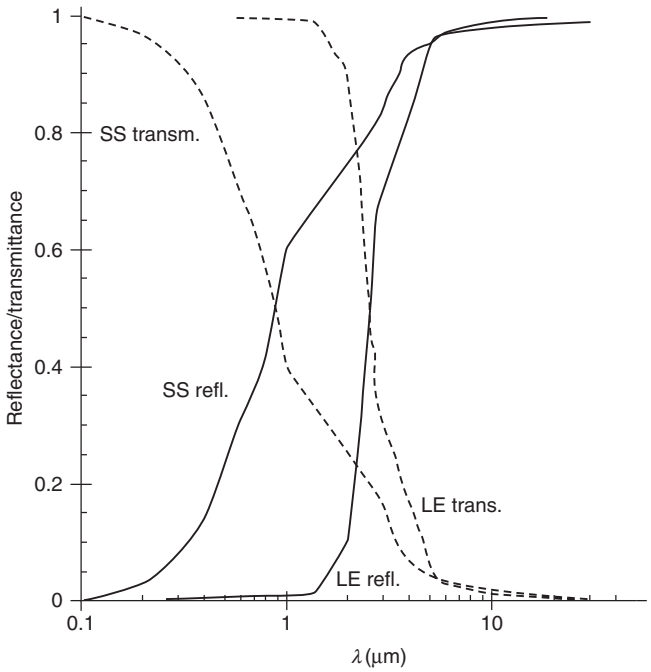


FIG. 8.12

Idealized reflectance and transmittance spectra for the two types of window coatings mentioned in the text.

examples of the two parameters for thin metal films on a glass substrate. A third parameter, T_{EYE} is an alternative to T_{SOLAR} when solar screen coatings are evaluated. In this case, the sensitivity of the human eye is used as a weight function in the integration.

In this subsection, we shall first list and comment on the various *coating materials* and combinations thereof that are used to achieve optical selectivity. Much more extensive treatment of the subject is given in the monographs and reviews by Gläser (2000), Hollands et al. (2001), Jelle et al. (2012), and Pulker (1984).

The dominant type of window coating is the *metal-based multilayer*. In typical cases, this is a 10–40-nm thick noble metal film sandwiched between two nonabsorbing, somewhat thicker metal oxide films. Noble metals, and actually a wider group of free-electron- or Drude-like films, have a small selectivity by themselves. In other words, thin free-electron-like (FE-) films exhibit visual transmission that gradually shifts to high infrared reflectance with longer wavelengths. This follows from the Drude model and the relation between a typical relaxation time for the conduction electrons and the period of the EM field in the visible and infrared regions. In Fig. 8.13, we show the parameter values of T_{SOLAR} and R_{IR} for seven different sets of thin metal films.

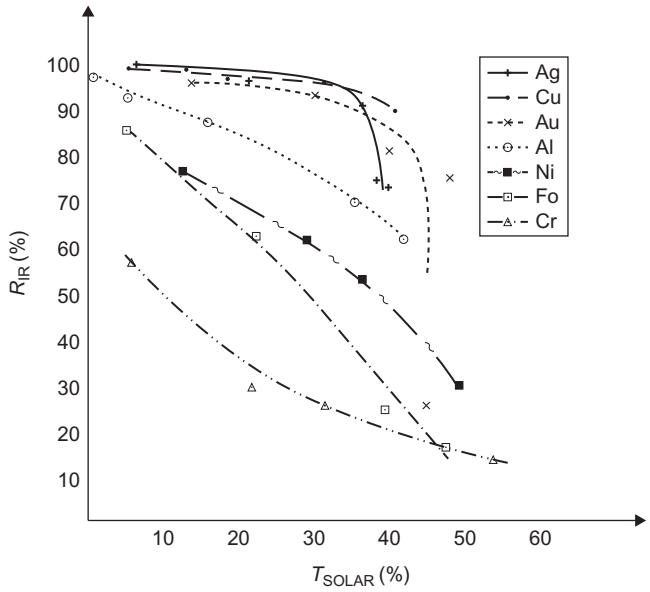


FIG. 8.13

The respective R_{IR} and T_{SOLAR} values as described in the text, for different metal films as indicated. Note that the noble and Fe–metals are closer to the upper-right corner than the transition metals.

From Karlsson, B., Valkonen, E., Karlsson, T., Ribbing, C-G., 1981. Materials for solar-transmitting heat-reflecting coatings. Thin Solid Films 86, 91–8.

Moving from left to right in the diagram, we obtain values for successively thinner single films on a glass substrate. We notice that a noble metal film alone can give values like $R_{IR} \approx 90\%$ and $T_{SOLAR} \approx 40\%$.

In practice, a single metal film is not used as an LE-coating for at least two reasons: the parameter values are too low, and the long-term stability is poor if the coating is exposed to variations of temperature, humidity, and acidity in a normal ambient atmosphere. It is fortunate that there are thin film materials that can solve both problems. Typically, these materials are stable metal oxides with optical constants in the visible range suited to antireflect the metal film, and thus increase the T_{SOLAR} value. Typical oxides used are TiO_2, In_2O_3, and SnO_2. In some cases, 3–7 layers are used to even further improve the optical performance. The long-term stability is still an issue, in particular when a noble metal film is used. The noble metals have the best optical properties, but are easily damaged by humid or acidic atmospheres. The solution is to use sealed double glazings with the coating facing the sealed space. With this arrangement, lifetimes of up to 10, or even 20, years have been guaranteed.

A higher stability alternative to noble metals, group IVB transition metal nitrides (TiN, ZrN, and HfN), have been suggested by Karlsson and Ribbing (1982). These

nitrides are well-known hard coatings with high thermal, mechanical, and chemical stability. In particular, opaque coatings of TiN are used for the protection of tools as well as replacement for gold on exposed surfaces. The color of gold and TiN originates in both cases from a threshold in the interband optical transitions, but the reasons for the optically FE-like behavior below this threshold is subtly different (Karlsson, 1981; Karlsson et al., 1983; Delin et al., 1996). To date, the thin nitride films have not been introduced in commercial LE coatings although thicker, TiN films have been used in solar coatings. Lab-scale investigations have indicated that TiN-base multilayers are optically not quite as effective as silver-based ones, but they might be stable enough to also be used in unsealed windows (Georgson et al., 1991).

The second material group in LE coatings is doped wide-bandgap semiconductors. The bandgaps in SnO_2, In_2O_3, and ZnO are large enough for films to be transparent over the visible range, that is, >3 eV. Such a large bandgap ensures that even a 1-μm thick coating is transparent. Equally important is that the transmission is only weakly thickness dependent, in contrast to the metal multilayer case. This makes large area production easier to control. However, the larger physical thickness of the semiconductor film causes interference variations that impair the visual impression. The main advantage with semiconductor coatings is their higher robustness, such that a sealed atmosphere is not required.

The low emissivity, that is, high IR reflectance, is obtained by a strong doping of the semiconductor. This doping creates an FE-like gas in the conduction band (or a "hole gas" in the valence band) that has lower density, but higher mobility, than the conduction electrons in metals.

Finally, a few words about the production methods for large-area window coatings: Today, direct magnetron sputtering of the metal layer and reactivity of the oxides dominate in the deposition of the metal-based multilayers, whether the production is online or in batches. The tight control of the sputtering process results in a high degree of visual perfection. Also, the group IVB nitrides mentioned above can be reactively magnetron sputtered (Valkonen et al., 1986). Historically, evaporation has been used and is still used for coating of smaller areas.

The doped semiconductor coatings, SnO_2 and In_2O_3 can be obtained by pyrolytic spraying at atmospheric pressure (Jarzebski and Marton, 1976). A solution of $SnCl_4$ in alcohol is sprayed as an aerosol against a hot (400°C) glass surface. The chloride decomposes into an SnO_2 layer on the glass, and HCl is vented off.

8.4.3 COATINGS FOR CONTROL OF RADIATIVE EXCHANGE WITH THE ATMOSPHERE

In this last subsection, we shall consider a few more potential applications of selectivity in the infrared that is based on the nongray behavior of the atmosphere. These applications have not found large-scale applications or markets as thermal solar absorbers and energy-saving window coatings. The nongray property of the atmosphere is manifested by the *atmospheric windows*. In Fig. 8.14, we cite a MODTRAN

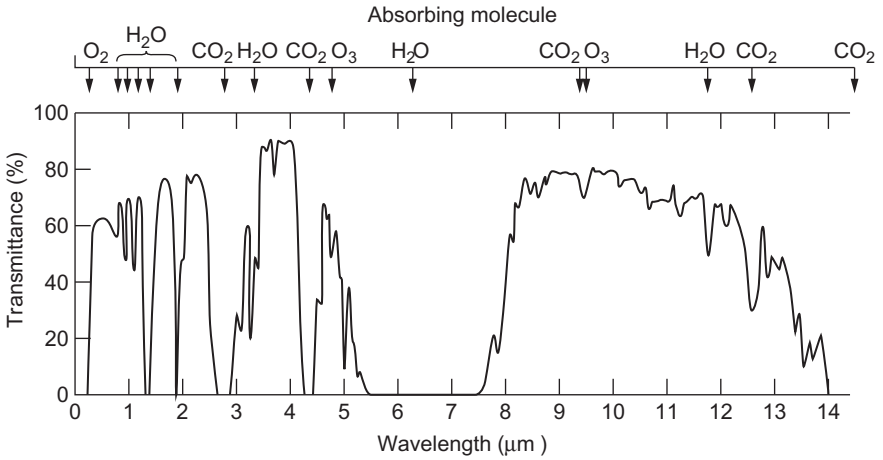


FIG. 8.14

Atmospheric transmittance over the distance 1.8 km through a rural, dry mid-latitude atmosphere with 23 km visibility at an altitude of 1000 m.

From Bass, M., Handbook of Optics, 1978.

calculated transmittance spectrum over a distance of 1.8 km for a dry, rural atmosphere at an altitude of 1000 m.

We notice that the overall transmittance of the atmosphere is not as high as the transmission of visible radiation 0.36–0.78 μm might lead us to take for granted. Besides this transparent interval, one conventionally, talks about the NIR: 0.8–2.5 μm, the medium wave (MW): 3–5 μm and long-wave (LW): 8–13 μm windows. However, in the 8–13 μm window, transmission is sensitive to the water content. It is reduced by rain or high humidity in tropical climates.

Comparing these wavelengths with the blackbody peaks in Fig. 8.3 it is obvious that for "normal" temperatures, 300 K, it is the LW window that is of interest. Through this window room temperature objects on ground can interact radiatively with much cooler parts of the atmosphere at high altitudes. In thermodynamic jargon, the "closed system of object + surroundings" is not even approximately limited to the nearby air—it must be extended to these higher layers of the atmosphere. As a consequence of this, an object on the ground can cool radiatively to temperatures well below that of the surrounding air. This explains why water puddles in the desert may freeze during nights, even if the ground temperature is not below zero. Three further factors help to explain this: water has high emittance ≈ 0.8; the desert sky is indeed dry; and often the wind is very weak, that is, the convective contribution to the heat transport is negligible.

This takes us to the subject of radiative cooling. If we want the highest possible radiative cooling power of a hot object—it should simply be as black as possible at the temperature it has. In a more sophisticated application we might wish for the lowest possible equilibrium temperature (during nighttime). This suggests a different

kind of optical selectivity: high emittance in the LW window, and low at other wavelengths. This possibility has a long history in the scientific literature (Arago, 1858; Heads, 1960; Trombe, 1967). In more recent publications, advanced material combinations by sputtering of mixed films, as well as serial combination of coolers, have been considered (Hamberg et al., 1987). Fig. 8.15 shows the reason for optical selectivity in this case and illustrates the potential for radiative cooling.

The three curves are the computed spectral radiance functions using the mid-latitude winter model in Fig. 8.14. The topmost curve is the Earth's blackbody curve at 272 K, that is, −1°C. The other full line curve is the *outward* radiation seen from the top of the atmosphere. We notice that in the LW window it comes close to the blackbody representation of Earth's surface. In other intervals the emission originates from cooler upper layers and is thus reduced intensity. The dashed curve represents the *downward* radiation from the atmosphere. It is weak in the LW window since it originates from the cold outer space, while it is close to a −1°C blackbody in the 5–8 μm interval, where the humidity in the atmosphere is important. When the outward radiance is above the downward one, the interval represents a potential for cooling. When the dashed curve is above the full line, the interval represents possible radiative heating. The spectral emissivity, or reflectance, of the object to be cooled, determines to what extent the radiative cooling or heating actually occurs. Here, high emittance in the LW-range favors cooling. Depending on their spectral properties, it is feasible for two outdoor objects to show different

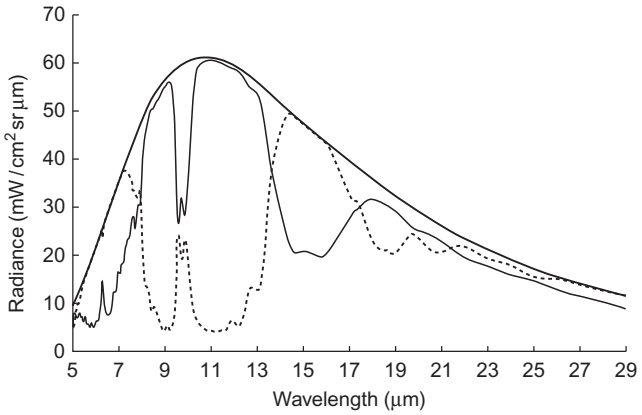


FIG. 8.15

Radiance functions computed according to the mid-latitude winter model. The top curve is a blackbody curve for −1°C, the assumed temperature of the Earth's surface. The *lower full line curve* is the *outward* radiation. The *dashed curve* is the *downward* radiation from the atmosphere. The interval, with sign, between the two latter curves represents the potential power of radiative cooling.

From Driscoll, W.G., Vaughan, W., 1978. Optical Properties of the Atmosphere. In OSA (Ed.) McGraw-Hill, New York (Chapter. 14, Fig. 30).

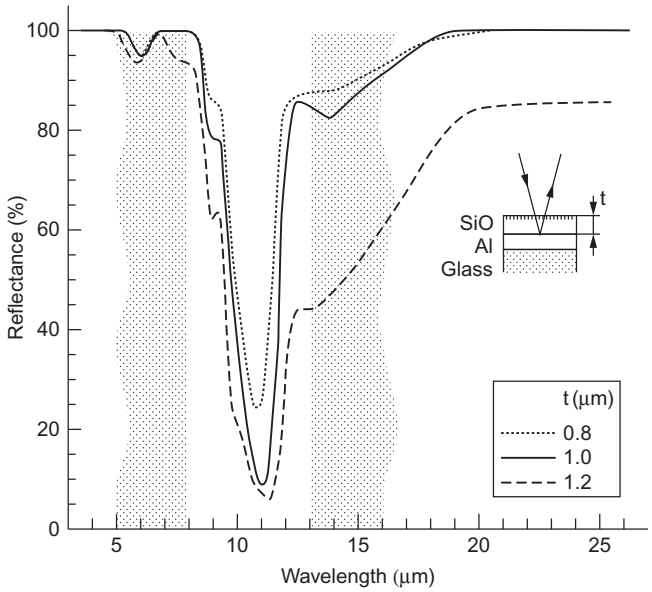


FIG. 8.16

Reflectance spectra for evaporated SiO films on an Al substrate with thicknesses as indicated. In all cases, this reflectance behavior will result in high outgoing thermal emission through the LW-window, but high reflectance for the incoming thermal radiation from the atmosphere.
From Granqvist, C G., Hjortsberg, A., 1981. Radiative cooling to low temperatures: general considerations and application to selectively emitting SiO films, J. Appl. Phys. 52(6), 4205–20.

thermal behaviors. One cools below the temperature of the surrounding air, T_{air}, while the other does not. These considerations of *selective emittance* have taken us to a deeper understanding than the treatment in Section 8.3. Again, the possibility is strongly dependent on dry air, a clear sky, and almost zero wind speed. Even a modest wind could otherwise make convective heat transport take over.

In Fig. 8.16, the reflectance spectra for evaporated SiO films on an Al substrate are cited from Granqvist and Hjortsberg (1981). SiO has an absorption band at 10 μm, that is, in the middle of the LW window. This will cause strong emission in that interval, while the high transmission for surrounding wavelengths will let the low emittance of the Al substrate dominate (Heads, 1960).

The three recorded spectra in the diagram all show a pronounced reflectance minimum in the LW range, but otherwise high reflectance, that is, the selectivity required for radiative cooling. The reduced reflectance in the interval 13–20 μm for the 1.2 μm film impairs the cooling capacity and therefore the authors conclude that the 1-μm thick film represents an optimum for radiative cooling.

We shall conclude with some specific applications that require the opposite to radiative cooling, that is, to reduce radiative emission in the LW window. It is

interesting to note that the conditions introduced by the applications make the solutions different, although they share this one optical feature.

The first two cases concern frost prevention during clear, windless spring or autumn evenings and nights. The frost will preferentially deposit on surfaces that are colder than the surrounding air. In a cold climate one frequently observes car windows facing the sky to be coated with frost in the morning after such nights. A coating on a car window must be visibly transmitting. A low-emissive metallic coating is therefore excluded. Otherwise, it would most probably be efficient as proven by the observation that this kind of frost coating is rarely seen on blank metallic surfaces. It is not surprising that the two Scandinavian car producers SAAB (Adamson, 1976) and Volvo (Hamberg et al., 1987) have made efforts to prevent frost deposition on windscreens using a doped wide-bandgap semiconductor coating. As for LE windows, pyrolytic, doped SnO_2 coatings have been used. Volvo actually marketed cars with such a coating for frost prevention, but problems with the wiper-cleaning halted this.

A second case of frost prevention by selective emission was for high-voltage China insulators. These insulators stick out of the power station at an angle, which exposes the upper surface toward the sky. The insulator is made of China, and as with most silicates (and glass windows), it has high emittance in the LW window. It may therefore become frost coated like the sky-facing car windows described above. When the frost melts in the morning the water will create a conducting surface layer that may short-circuit the insulator with serious consequences. A doped SnO_2 film cannot be used for this case of frost prevention—the electrical conductivity is too high. The requirement in this case is good *electrical insulation*. In summary, we need an electrically insulating material with high average reflectance in the LW window. In principle, there is a dielectric multilayer solution to these requirements—a difficult and probably costly solution for such long and curved objects.

An alternative solution to the materials problem is a compound with ionic bonding. It will be absorbing somewhere in the infrared. Typically, oxides classified as "dielectrics": SiO_2, TiO_2, Al_2O_3, MgO, etc., have at least one strong absorption band in the infrared. The absorption band is caused by lattice excitation of the ionic components and, in that range, the refractive index has strong dispersion combined with high k-values. The textbook cases of this phenomenon are the ionic crystals. Their resonances occur in the wavelength interval of 50–200 μm, that is, far beyond the LW interval. A characteristic feature called the *reststrahlen* band (Eng: residual rays) occurs at wavelengths just below such an absorption band. A group of harder compounds than the ionic crystals: oxides, nitrides, carbides, etc., also feature an ionic contribution to their bonding and exhibit reststrahlen bands at shorter wavelengths (Dobrowolski, 1978; Ribbing and Wäckelgård, 1991).

Instead of a multilayer solution, one could therefore hope to identify a compound whose bulk reflectance exhibits a reststrahlen band in the LW window and thereby reduce the thermal emittance through this window. In such a search BeO (Ribbing, 1990) and SiO_2 (Högström et al., 2005) have been identified as solving at least part of the problem. Fig. 8.17 shows the reststrahlen bands of these two compounds and the transmission spectrum for a dry atmosphere with the MW and LW windows.

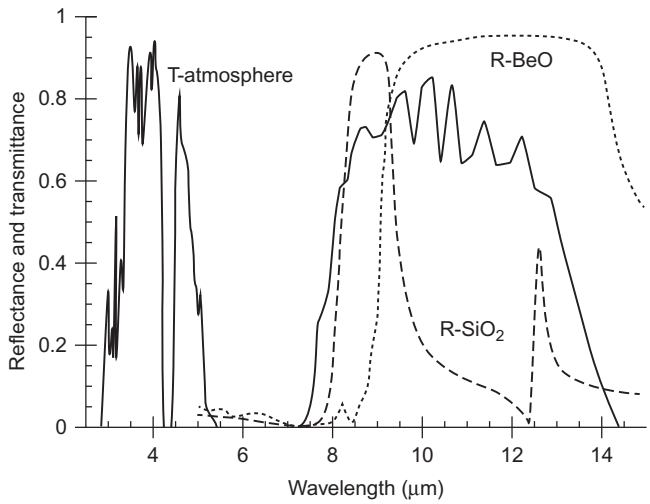


FIG. 8.17

Spectra showing the reststrahlen bands of BeO *(dotted)* and SiO_2 *(dashed)* as well as the transmittance spectrum for 1 km of MODTRAN atmosphere *(full line)* showing the MW- and LW-windows.

From Högström, H., Forssell, G., Ribbing, C.G., 2005. Realization of selective low emittance in both thermal atmospheric windows. Opt. Eng. 44 (2), 026001–1–7.

Except for the interval 8–9.5 μm, BeO covers the LW-window reasonably well, while the SiO_2 band only reduces the emittance in that short wavelength part of the window. BeO at 50°C was estimated to have the average emittance $e_{LW} \approx 0.5$ in the LW-window. This is considerably lower than standard silicate ceramics and sufficiently low to avoid growth of frost in most weather situations and environments. Unfortunately, BeO has hygiene problems. Well-controlled green forming is an accepted process (National Beryllia Div. of General Ceramics Inc., Haskell, NJ), but coating deposition is difficult and not suited for large scale production.

It has been demonstrated in laboratory-scale that the LW emittance of BeO can be further reduced by a dielectric coating with suitable refractive index. Again, it should be remembered that BeO is not dielectric at these wavelengths, but the behavior close to resonance absorption can be modified with a thin coating. Interference calculations for a double layer of Si(d)/BeO indicated that maximum average reflectance, that is, minimum thermal emittance in the LW-window, should occur for $d = 0.83$ μm. Fig. 8.18 shows a comparison between the calculated reflectance spectrum and the corresponding near-normal measured curve for a BeO substrate with a 0.83-μm magnetron-sputtered Si-film. The optical constants for BeO were obtained by fitting of the Lorentz oscillator model to the bulk, near-normal reflectance spectrum measured on the polycrystalline BeO used as substrate. Optical constants for Si were taken from the literature, although they may be somewhat different from those of the sputtered films.

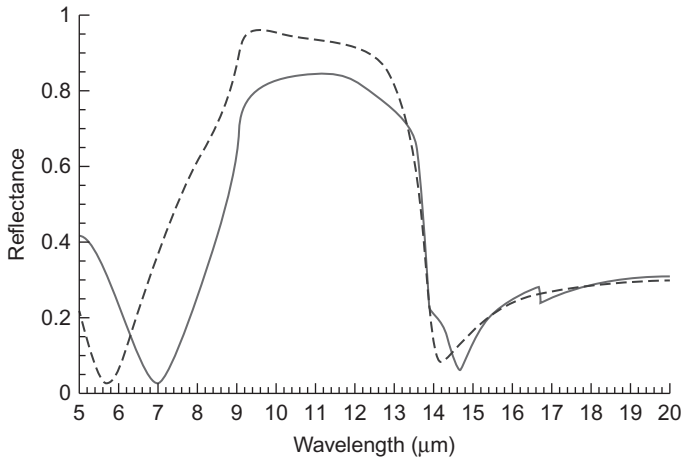


FIG. 8.18

Measured *(line)* and calculated *(dashed)* reflectance spectra for Si(0.83 μm)/BeO illustrating that the Si coating modifies the short wavelength edge of the BeO restsrahlen band to further increase the reflectance within the LW-window.

From Ribbing, C.G., Staaf, Ö., Andersson, S.K., 1995. Selective supression of thermal emission from radomes and materials selection therefore. Opt. Eng. 34 (11), 3314–22.

Radiometer measurements gave an average emittance for the coated sample $e_{LW} \approx 0.29$ in the LW-window. Chemical vapor deposition (CVD) of the Si film would probably improve the agreement with literature values and further reduce the LW emittance.

This final part concerns another application of selectively low thermal emittance. In this case, the aim is to reduce the radiance in both LW-and MW-atmospheric windows. This is relevant for thermal camouflage of objects that are either just above room temperature or as high as 300°C. In the latter case, the blackbody curve has maximum intensity at around 4 μm, that is, in the MW-window. The IR seekers can only discover distant objects using detectors that are filtered for one of the atmospheric windows, and even then, only through a dry atmosphere with few clouds. Under such circumstances, it is militarily relevant to suppress thermal radiation to minimize the chance for detection. An advantage with narrowing the low emittance to the window intervals alone is that the heated object can then still cool radiatively at other wavelengths. In Fig. 8.19, the result of such an attempt is cited. It proved possible to use the dielectric behaviors in the MW-window, as well as a combination of the reststrahlen band of SiO_2 and Si in the LW-window for a double layer on an Si substrate.

Obviously, the narrow SiO_2 band is not sufficient to cover the long wavelength part of the LW-window. In this case, both layers were deposited using a high-temperature CVD process that is thoroughly documented and used on a large scale in the electronics industry. One notices that the agreement between the calculated and the measured spectrum is excellent.

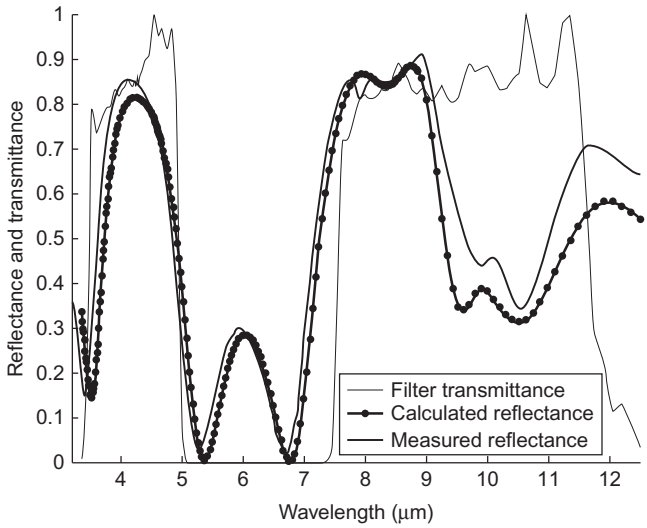


FIG. 8.19

Calculated *(dotted line)* and measured *(thick line)* near-normal reflectance spectra for the double-layer Si(0.9 μm)/SiO_2(2.45 μm) on an Si wafer. The *thin*, *full lines* are the transmittance spectra for the IR filters used in the radiometer.

From Högström, H., Forssell, G., Ribbing, C.G., 2005. Realization of selective low emittance in both thermal atmospheric windows. Opt. Eng. 44 (2), 026001–1–7.

8.5 CONCLUSION

This chapter has treated various options to control either the temperature of a material or the thermal emission from a surface, using optical materials with a variety of spectral properties. Seemingly very different applications may benefit from a surprisingly simple surface treatment or deposition of a thin film.

The applications considered were thermal solar collector, energy-efficient windows, frost-preventing coatings, and thermal camouflage coatings, all of which have a particular optical selectivity designed for their purposes.

We conclude with a repeated reminder that radiation is only one mechanism out of three that control the equilibrium temperature. Convection from wind has already been mentioned as a threat for effective radiative cooling applications. Conduction should also be considered and arrangements aimed at this are detailed in some of the references. In the case of frost prevention using BeO, the unusually high thermal conductance of this insulator appears to be beneficial. If the dynamics of the mechanism of frost growth are considered (Chibuye et al., 1994), BeO and metals conduct the stored heat to the surface more efficiently than in cases of coated glass. The high thermal conductivity might partly explain why metal surfaces are rarely frost coated.

REFERENCES

Adamson, B.L. (1976), Fordonsruta av Glas Swedish Patent No. 7609870–7, Patentoch registreringsverket, Stockholm.

Agnihotri, O.P., Gupta, B.K., 1981. Solar Selective Surfaces. J. Wiley & Sons, New York.

Arago, F., 1858. In: Barral, M.J.-A. (Ed.), Oevres Complètes de François Arago. vol. 8. Gide, Paris.

Carter, W.H., Wolf, E., 1975. Coherence properties of lambertian and non-lambertian sources. J. Opt. Soc. Am. 65 (9), 1067–1071.

Chibuye, T., Ribbing, C.G., Wäckelgård, E., 1994. Reststrahlen band studies of polycrystalline beryllium oxide. Appl. Optics 33, 5975–5981.

Cornelius, C.M., Dowling, J.P., 1999. Modification of Planck blackbody radiation by photonic band-gap structures. Phys. Rev. A 59 (6), 4736–4746.

Craighead, H.G., Buhrman, R.A., 1978. Optical properties of selectively absorbing metal/insulator composite films. J. Vac. Sci. Technol. A 15 (2), 269–271.

Craighead, H.G., Bartynski, R., Buhrman, R.A., Wojcik, L., Sievers, A.J., 1979. Metal/insulator composite selective absorbers. Sol. Energy Mat. 1, 105–124.

Delin, I., Eriksson, O., Ahuja, R., Johansson, B., Brooks, M., Gasche, T., Auluck, S., Will, J.M., 1996. Optical properties of the group IVB refractory metal compounds. Phys. Rev. B 54, 1673.

Dobrowolski, J., 1978. Reststrahlen filters. In: Driscoll, W., Vaughan (Eds.), Handbook of Optics. OSA-McGraw-Hill, New York (Chapter 8, Sec. 99).

Duffie, J.A., Beckman, W.A., 1991. Solar Engineering of Thermal Processes, second ed. J. Wiley & Sons, New York.

Georgson, M., Roos, A., Ribbing, C.-G., 1991. Titanium nitride based low emissive coatings—a stability comparison. Glastech. Ber. 64, 147–154.

Gläser, H.J., 2000. Large Area Glass Coatings. von Ardenne Anlagentachnik GMBH, Dresden.

Granqvist, C.G. (Ed.), 1991. Materials Science for Solar Energy Conversion Systems. SPIE, Pergamon Press, Oxford.

Granqvist, C.G., Hjortsberg, A., 1981. Radiative cooling to low temperatures: general considerations and application to selectively emitting SiO films. J. Appl. Phys. 52 (6), 4205–4220.

Hamberg, I., Svensson, J.S.E.M., Eriksson, T.S., Granqvist, C.G., Arrenius, P., Norin, F., 1987. Radiative cooling and frost formation on surfaces with different thermal emittance: theoretical analysis and practical experience. Appl. Optics 26, 2131–2136.

Harding, G.L., McKenzie, D.R., Window, B., 1976. The dc sputter coating of solar selective surfaces onto tubes. J. Vac. Sci. Technol. A 13 (5), 1073–1075.

Hass, G., Schroeder, H.H., Turner, A.F., 1956. Mirror coatings for low visible and high infrared reflectance. J. Opt. Soc. Am. 40 (1), 31–35.

Heads, A.K. (Ed.), 1960. Methods and Means for Producing Refrigeration by Selective Radiation. Gov. of the Commonweath, Canberra.

Heald, 2003. Where is the 'Wien Peak'. Am. J. Physiol. 71 (12), 1322–1323.

Högström, H., Forssell, G., Ribbing, C.G., 2005. Realization of selective low emittance in both thermal atmospheric windows. Opt. Eng. 44 (2). 026001–1–7.

Hollands, K.G.T., Wrigth, J.L., Granqvist, C.G., 2001. Glazing and coatings. In: Gordon, J. (Ed.), Solar Energy: The State of the Art ISES Position Papers. James & James, London, pp. 29–107.

Jarzebski, Z.M., Marton, J.P., 1976. Physical properties of SnO_2 materials. J. Electrochem. Soc. 123, 1–3.
Jelle, B.P., Hynd, A., Gustavsen, A., Arasteh, D., Goudey, H., Hart, R., 2012. Fenestration of today and tomorrow: a state-of-the-art review and future research opportunities. Sol. Energy Mat. Solar Cells 96, 1–28.
John, S., 1984. Electromagnetic absorption in a disordered medium near a photon mobility edge. Phys. Rev. Lett. 53, 2169–2173.
Karlsson, B., 1981. Optical Properties of Solids for Solar Energy Conversion (Thesis). 620Acta Universitatis Upsaliensis, Uppsala.
Karlsson, B., Ribbing, C.-G., 1982. Optical properties of transparent heat mirrors based on thin films of TiN, ZrN and HfN. Proc. Soc. Photo-Opt. Instrum. Eng. 324, 52.
Karlsson, B., Shimshock, R.P., Seraphin, B.O., Haygarth, J.C., 1983. Optical properties of CVD-coated TiN, ZrN and HfN. Sol. Energy Mater. 7, 401.
Lampert, C.M., Washburn, J., 1979. Microstructure of a black chrome solar selective absorber. Sol. Energy Mat. 1, 81–92.
McCluney, R., 1994. Introduction to Radiometry and Photometry. Artech House Publishers, Boston-London.
Meinel, A.B., Meinel, M.P., 1976. Applied Solar Energy: An Introduction. Addison-Wesley, Michigan.
Niklasson, G.A., 1991. Optical properties of of inhomogenous two-component materials. Mater. Sci. Solar Energy Convers. Syst., 7–43.
Niklasson, G.A., Granqvist, C.G., 1983. Surfaces for selective absorption of solar energy: an annotated bibliography 1955–1981. J. Mater. Sci. 18, 3475–3534.
Palmer, J.H., 1995. The measurement of transmission, absorption, emission and reflection. In: -Bass, M. (Ed.), Handbook of Optics II. McGrawHill Inc., pp. 25.1–25.25. OSA. (Chapter 25).
Pulker, H.K., 1984. Coatings on glass. In: Thin Films Sc. and Techn. 6, Elsevier, Amsterdam.
Ribbing, C.G., 1990. Beryllium oxide: a frost preventing insulator. Opt. Lett. 15, 882–884; Swedish Patent 8901422-9 (April 1989).
Ribbing, C.G., 1999. Getting the sunshine right. In: Lampert, C.M. (Ed.), Solar Optical Materials XVI Denver, 22 July, 84–90. Proc. SPIE, vol. 3789.
Ribbing, C.G., Wäckelgård, E., 1991. Reststrahlen bands as property indicator for dielectric coatings. Thin Solid Films 206, 312–317.
Roos, A., Chibuye, T., Karlsson, B., 1983. Properties of oxidized copper surfaces for solar applications I & II. Sol. En. Mat. 7, 453–465. Roos, and Karlsson, B. (1983) *ibid* II, 467–80.
Seraphin, B.O. (Ed.), 1979. Solar Energy Conversion Solid-State Physics Aspects. Topics in Applied Phyisca, vol. 31. Springer-Verlag, Berlin, Heidelberg.
Siegel, R., Howell, J.R., 1981. Thermal Radiation Heat Transfer, second ed. McGrawHill. Sections 2.4.4–2.4.10.
Sievers, A.J., 1979. Spectral selectivity of composite materials. In: Seraphin, B.O. (Ed.), Solar Energy Conversion Solid-State Physics Aspects. In: Topics in Applied Physica, vol. 31. Springer-Verlag, Berlin, Heidelberg, pp. 56–114.
Soffer, B.H., Lynch, D.K., 1999. The spectral optimization of human vision: some paradoxes, errors and resolutions. Am. J. Physiol. 67 (11), 946–953.
Staaf, Ö., Ribbing, C.G., Andersson, S., 1996. Temperature dependence of the band emittance for nongray bodies. Appl. Optics 35 (31), 6120–6125.
Tabor, H., 1955. Solar energy collector design. Bull. Res. Counc. Isr. Sect. C. J. 5C(1).

Trombe, F., 1967. Perspectives sur l'utilization des Rayonnements Solaires et Terrestres dans Certaines Régiones du Monde. Rev. Gen. Therm. 6, 1285.
Valkonen, E., Ribbing, C.G., Sundgren, J.-E., 1986. Optical constants of thin TiN films: thickness and preparation effects. Appl. Optics 25 (20), 3624–3630.
Wäckelgård, E., Hultmark, G., 1998. Industrially sputtered solar absorber surface. Solar Energy Mat. Solar Cells 54, 165–170.
Wolf, E., Carter, W.H., 1975. Angular distribution of radiant intensity from sources of different degrees of spatial coherence. Opt. Commun. 13 (3), 205–209.
Wolfe, W.L., 1989. Radiation theory. In: Wolfe, W.L., Zissis, G.J. (Eds.), The Infrared Handbook. Environmental Research Institute of Michigan, Ann Arbor, Ch 1, 1–38.
Yablonovitch, E., 1987. Inhibited spontaneous emission in solid state physics and electronics. Phys. Rev. Lett. 58, 2059–2062.
Zalewski, E.F., 1995. Radiometry and photometry. In: Bass, M. (Ed.), Handbook of Optics II. McGraw-Hill Inc., New York, pp. 1–49 (Chapter 24).
Zhang, Y.-W., Zhang, C.-G., Klemas, V., 1986. Quantitative measurements of ambient radiation, emissivity and truth temperture of a greybody: measurements and experimental results. Appl. Optics 25, 3683–3689.
Zhang, Q.-C., Zhao, K., Zhang, B.-C., Wang, L.-F., Shen, Z.-L., Lu, D.-Q., Xie, D.-L., Zhou, Z.-J., Li, B.-F., 1998. A cylindrical magnetron sputtering system for depositing metal-aluminium nitride cermet solar coatings onto batches of tubes. J. Vac. Sci. Technol. A 16 (2), 628–632.

FURTHER READING

Bass, M., 1995. In: OSA, (Ed.), Handbook of Optics I. McGraw-Hill, Inc., New York (Chapter 44, Fig. 1).
Driscoll, W.G., Vaughan, W., 1978. In: OSA, (Ed.), Optical Properties of the Atmosphere. McGraw-Hill, New York (Chapter 14, Fig. 30).
Karlsson, B., Valkonen, E., Karlsson, T., Ribbing, C.-G., 1981. Materials for solar-transmitting heat-reflecting coatings. Thin Solid Films 86, 91–98.
McDonald, G.E., 1974. Refinement in Black Chrome for Use as a Solar Selective Coating. NASA Report TM X-3136, Lewis Res. Ctr., Cleveland, OH.
Ribbing, C.G., Staaf, Ö., Andersson, S.K., 1995. Selective supression of thermal emission from radomes and materials selection therefore. Opt. Eng. 34 (11), 3314–3322.

This page intentionally left blank

CHAPTER

Color in optical coatings

9

Claudio Oleari
University of Parma, Parma, Italy

9.1 INTRODUCTION

The color of nonluminous objects in nature is due mainly to absorption, diffusion, refraction, and diffraction of light. Traditionally, the colors are called *chemical colors* if caused by pigment absorption and *structural colors* if produced by other fundamental optical processes such as reflection, refraction, interference, diffraction, and scattering (Kinoshita et al., 2008). In particular, colors are called *prismatic colors* if caused by refraction of white light through a prism and *interference color* if caused by interference effects.

Interference color effects are produced when a material is scored with fine parallel lines formed of one or more parallel thin layers, or otherwise composed of microstructures on the scale of the color wavelength. In nature, structural colors are those of the feathers of many birds, of certain butterfly wings, and of beetle shells. These colors depend on the viewing angle and often give rise to an iridescent effect, as in peacock feathers, soap bubbles, films of oil, and mother of pearl. The color of the optical coatings is an interference color and belongs to the *gonio-apparent* or *special-effect* colors. Since 1942, electron microscopy has been used to see the structure of materials and to understand structural colors.

Generally, industrial colorimetry does not deal with interference color and the usual colorimetric instruments are inadequate for measuring it. Only recently, with the new mica-pigment coatings, has colorimetry been considered in the measurement of interference color and new multiangle spectrophotometers been produced, mainly for the metallic and micapigment finishes applied to automobiles.

Section 9.2 is dedicated to a short historical review of interference color science. Section 9.3 is a general introduction to basic colorimetry, whose standardization is made by Commission Internationale de l'Éclairage (CIE), subdivided into three parts: *psychophysical colorimetry*, *psychometrical colorimetry*, and *instrumental color measurement*. Section 9.4 deals with colorimetry of interference colors and generally gonio-apparent colors. For a complete and detailed optical characterization

Optical Thin Films and Coatings. https://doi.org/10.1016/B978-0-08-102073-9.00009-6
Copyright © 2018 Claudio Oleari. Published by Elsevier Ltd. All rights reserved.

of interference color, the measurement of *bidirectional transmittance* and *reflectance* is needed.

9.2 THE DEVELOPMENT OF THE UNDERSTANDING OF INTERFERENCE COLOR

Interference-color science and color-vision science have parallel, though very different, histories. The understanding of interference colors relates to a physical knowledge, whereas the understanding of human color vision relates to the connection between optical radiations and visual sensations and involves many disciplines: optics, physiology, and psychology. Both histories started with Isaac Newton (1642–1727). This section considers, in a very concise way, the history of the color of thin films of transparent materials. Before Newton, we had only an intriguing description of the phenomenon, mainly due to Boyle and Hooke:

1. Boyle (1627–91) seems to have first observed that thin bubbles of the essential oils, spirit of wine, turpentine, and soap and water exhibited beautiful colors and he then succeeded in blowing glass so thin as to show the same hues.
2. Hooke (1635–1703) obtained equally thin films that exhibited the same brilliant color over their whole surface.
3. Brereton (1631–79) observed the colors of the thin films which the action of the weather produces upon glass (*weathering* phenomenon).

9.2.1 ISAAC NEWTON (1642–1727)

Newton (1704) dedicated the second book of his *Opticks, or a Treatise of the Reflections, refractions, Inflections & Colours of Light*, to the *Observations Concerning the Reflections, Refractions, and Colours of Thin Transparent Bodies*. He made very accurate measurements of the thickness of layers of air, water, and glass in relation to the reflected and transmitted colors, and, between these color pairs, he described the *complementary color* correspondence. His "Fig. 3" is famous, regarding the well-known Newton rings, where the sequence of the transmitted and reflected colors are given up to the third order in graphical relation to the air thickness between two glass bodies (Fig. 9.1).

Although Newton described these phenomena well and measured them accurately, he was unable to give a complete explanation and suggested the definition of a new quantity, the "fits." Let us recall his definition and the subsequent proposition XIII from the *Opticks* book (Newton, 1704, p. 256):

> DEFINITION
> *The returns of the disposition of any Ray to be reflected I will call its* **Fits of easy Reflexion**, *and those of its disposition to be transmitted its* **Fits of easy Transmission**, *and the space it passes between every return and the next return, the* **Interval of its Fits**.

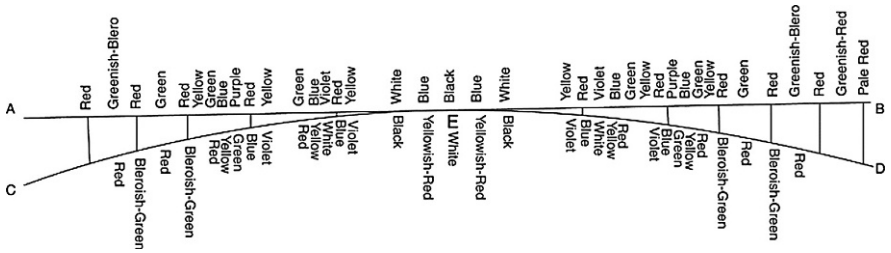


FIG. 9.1

Newton's representation of the colors of the reflected and transmitted lights when a convex lens (C–D) is pressed against a glass plate (A–B) with a contact point (E). The illuminating light is constituted by parallel rays of white light coming down from the top. Transmitted colors and reflected colors constitute complementary color pairs. These colors, ordered according to this sequence, are known as "Newton's color series." (N.B. This name is not referring to the seven colors of the solar spectrum produced by Newton through prism dispersion.)

PROP. XIII

The reason why the Surfaces of all thick transparent Bodies reflect part of the Light incident on them, and refract the rest, is, that some Rays at their Incidence are in Fits of easy Reflexion, and others in Fits of easy Transmission.

Although Newton saw a relationship between colors and thicknesses that to us today appears very accurate and so clear as to lead us to the correct interpretation of these phenomena, he gave only a very hypothetical origin of the fits, as a hidden internal degree of freedom of the light (Newton, 1704, p. 257):

> *… And hence Light is in Fits of easy Reflexion and easy Transmission, before its Incidence on transparent Bodies. And probably it is put into such Fits at its first emission from luminous Bodies, and continues in them during all its progress. ….*

A very important item in the Newton analysis is the description of the goniodependence of these phenomena. Newton let himself imagine the origin of all the colors of natural bodies, as produced by the same mechanisms present in the thin transparent plates. In Part III of the second book of his *Opticks*, he wrote *Of the Permanent Colours of Natural Bodies and the Analogy Between Them and the Colours of Thin Transparent Plates*, and considered *How the Phaenomena of Thin Transparent Plates Stand Related to Those of All Other Natural Bodies*. In proposition III (Newton, 1704, p. 223), he described a possible microscopic structure of matter:

> *Between the parts of opake and colour'd Bodies are many Spaces, either empty or replenish'd, with Mediums of other Densities; as Water between the tinging Corpuscles wherewith any Liquor is impregnated, Air between the aqueous Globules that constitute Clouds or Mists; and for the most part Spaces void of both Air and Water, but yet perhaps not wholly void of all Substance between the parts of hard Bodies.*

In proposition IV (Newton, 1704, p. 225):

> *The parts of Bodies and their Interstices must not be less than of some definite bigness, to render them opake arid colour'd.*

and in proposition V (Newton, 1704, p. 226):

> *The transparent parts of Bodies according to their several Sizes reflect Rays of one Colour, and transmit those of another, on the same grounds that thin Plates or Bubbles do reflect or transmit those Rays. And this I take to be the ground of all their Colours.*

The implausibility of this Newtonian imagination was shown by Thomas Young one century later.

9.2.2 THOMAS YOUNG (1773–1829)

A new vision of light was necessary to understand the color phenomena and Young's contribution to color science (physiological hypothesis of three kinds of receptors in the human retina that Young called "fibers"), and to optics in general (hypothesis of a wave nature of the light), was very great, similar to that of Newton.

Let us recall the hypotheses and the most interesting propositions of the wave theory of light given by Young in his Bakerian Lecture on the "Theory of Light and Colors" read November 12, 1801 (Young, 1802a):

HYPOTHESIS I
A luminiferous ether pervades the universe, rare and elastic in a high degree.
HYPOTHESIS II
Undulations are excited in this ether whenever a body becomes luminous.
HYPOTHESIS III
The sensation of different colors depends on the different frequency of vibrations excited by light in the retina.
HYPOTHESIS IV
All material bodies have an attraction for the ethereal medium, by means of which it is accumulated within their substance, and for a small distance around them, in a state of greater density but not of greater elasticity.
PROPOSITION I
All impulses are propagated in a homogeneous elastic medium with an equable velocity.
PROPOSITION II
An undulation conceived to originate from the vibration of a single particle must expand through a homogeneous medium in a spherical form, but with different quantities of motion in different parts.

PROPOSITION III

A portion of a spherical undulation, admitted through an aperture into a quiescent medium, will proceed to be further propagated rectilinearly in concentric superficies, terminated laterally by weak and irregular portions of newly diverging undulations.

PROPOSITION IV

When an undulation arrives at a surface which is the limit of mediums of different densities, a partial reflection takes place proportionate in force to the difference of the densities.

PROPOSITION VIII

When two undulations, from different origins, coincide either perfectly or very nearly in direction, their joint effect is a combination of the motions belonging to each.

Young's interpretation of the colors of thin bodies was based on a wave description of light. These colors are produced by interference of two light waves, one reflected at the first surface and the second reflected at the second surface, and such an interference is constructive or destructive, exactly as happens for the waves on the surface of the water. The very new concept of *optical path* is given. Let us recall the *universal law* written by Young (1802b, s. 376, p.112):

> *When two portions of the same light arrive at the eye by different routes, either exactly or very nearly in the same direction, the appearance or disappearance of various colours is determined by the greater or less difference in the lengths of the paths: the same colour recurring, when the intervals are multiples of a length, which, in the same medium, is constant, but in different mediums, varies directly as the sine of refraction.*

For Young, the waves were longitudinal. The complete understanding of the nature of light was possible only with Maxwell's electromagnetism theory and Einstein's photon hypothesis. Finally, all the mistakes were corrected: light waves are transversal and today the hidden "Fits" are considered only as a working hypothesis (N.B. the hidden variables are also considered today in work hypotheses for describing unexplained aspects of quantum mechanics).

Optical interference has been investigated deeply and widely during the entire 19th century. The detailed history is too long for a section of a chapter on optical coating colorimetry. However, the contribution of some other scientists merits recognition.

9.2.3 LEOPOLDO NOBILI (1784–1835)

A large part of Nobili's work is related to the color of optical coatings and, in particular, he discovered the *electrochemical appearances* and began a new art form called *Metallocromia* and presented it at the French Institute in 1828 (Nobili, 1830).

The Nobili work describes the production of optical coatings on metals by an electrochemical method and the visual classification of the colors in relation to the thickness of the coatings. He produced a scale, or gamut, of 44 colors of coatings on steel with increasing thickness, carefully controlled by electrochemical deposition with constant current and increasing time. Of course, Nobili had to compare his color scale, shown here in Fig. 9.2, with that given by Newton (Fig. 9.1). Some discrepancies exist, of which Nobili was aware but gave no reason (he had to consider the superposition of the waves of spectral lights, following the Young hypotheses).

Since these colors are dependent on the incidence angle, Nobili called these colors *iridescent* (in Italian "cangiante"). These phenomena induced him to enlarge the investigation to the interference colors in insects and the feathers of birds. For Nobili, the polarization of colored light was decisive for the classification of the different mechanisms producing colored light. The analysis of the polarization was made through a birefringence layer of Iceland spar (Nobili, 1830).

Metallocromia is an art and Nobili dedicated some effort into the production of pieces of this art. One piece is reproduced here (Plate 9.1, see color section between pages 404 and 405).

9.2.4 DAVID BREWSTER (1781–1868)

A review of all the efforts made toward understanding the nature of light by Grimaldi, Newton, Young, and Fresnel was given by Brewster (1853) in his *Treatise on Optics*. Chapter XIII of this book was dedicated to the *Colours of Thin Plates*. In Fig. 62 (Brewster, 1853, p. 125), Brewster summarized in a diagram the relationship between colors and thin plate thicknesses (Fig. 9.3). The interference fringes are drawn on a disk at a distance from the center proportional to the corresponding plate thickness and, by choosing a circle on the disk (represented by a dashed line in Fig. 9.3), it is possible to evaluate the contribution of the different spectral lights to the resulting color for a thickness equal to the radius of the chosen circle. Moreover, the sectors of these wheels are proportional to the amounts of spectral light constituting the white light and the fringes drawn on the wheel have the same spectral color, and therefore, "*if we now suppose all these coloured sectors to revolve rapidly round C as a centre, the effect of them all thus mixed should be the production of the coloured rings as seen by white light*".

9.2.5 AUGUSTE MICHEL-LÉVY (1844–1911)

Pleochroism is the term used to describe the color variation for destructive interference with the polarization direction of the light, which depends on the orientation of the material in the light path and is a characteristic of anisotropic materials only. The view in a microscope of transparent or translucent materials in plane-polarized light is similar to the view in natural light until the specimen is rotated around the microscope optical axis. With the rotation, the brightness and/or color of the specimen under examination change. This effect, termed the *pleochroic effect*, is useful for

44	Pinkish-lacquer
43	Yellow-green
42	Green
41	Violetish-green
40	Violetish-carmine
39	Pinkish-carmine
38	Pinkish-orange
37	Greenish-orange
36	Orange-green
35	Yellow-green
34	Yellowish-green
33	Green
32	Greenish-purple
31	Purplish-carmine
30	Carmine with a hint of turquoise
29	Purplish-carmine
28	Vivid carmine
27	Carmine
26	Orange-carmine
25	Orange-red
24	Red-orange
23	Reddish-orange
22	Orange
21	Orange-yellow
20	Vivid yellow
19	Yellow
18	Very light yellow
17	Sky blue with a hint of yellow
16	Sky blue
15	Light blue
14	Blue
13	Intense blue
12	Indigo
11	Violet
10	Violetish-red
9	Violetish-ochre
8	Ochre
7	Copper red
6	Vivid fulvous
5	Fulvous
4	Vivid blond
3	Gold blond
2	Blond
1	Silver blond

FIG. 9.2

Nobili's metallocromia color gamut (termed in Italian "Scala cromatica") of the lights reflected from 44 coatings on steel with increasing thickness, subdivided into four orders (Nobili, 1830). The illuminating light is constituted by parallel rays of white light almost orthogonal to the coatings and seen almost orthogonally.



PLATE 9.1

Nobili's metallocromia piece of art, preserved in the Physics Department of the University of Parma.

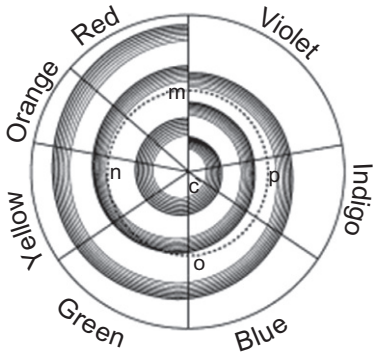


FIG. 9.3

Brewster's diagram with the correspondence of the color fringes to the plate thicknesses, and rotating wheel for producing a visual simulation of the color fringes (Brewster, 1853).

the identification of a wide variety of materials. An example of a material showing this effect is crocidolite, commonly known as blue asbestos.

Michel-Lévy and Lacroix first gave the *Interference Color Chart* in a book entitled "*Les Mineraux des Roches*" (Lévy and Lacroix, 1888). Today, after more than a century, the *Michel-Lévy Interference Color Chart* (Plate 9.2, see color section between pages 404 and 405), also known as the *Michel-Lévy Table of Birefringence*, remains in use by analytical microscopists and the most important manufacturers of microscopes also supply this interference color chart.

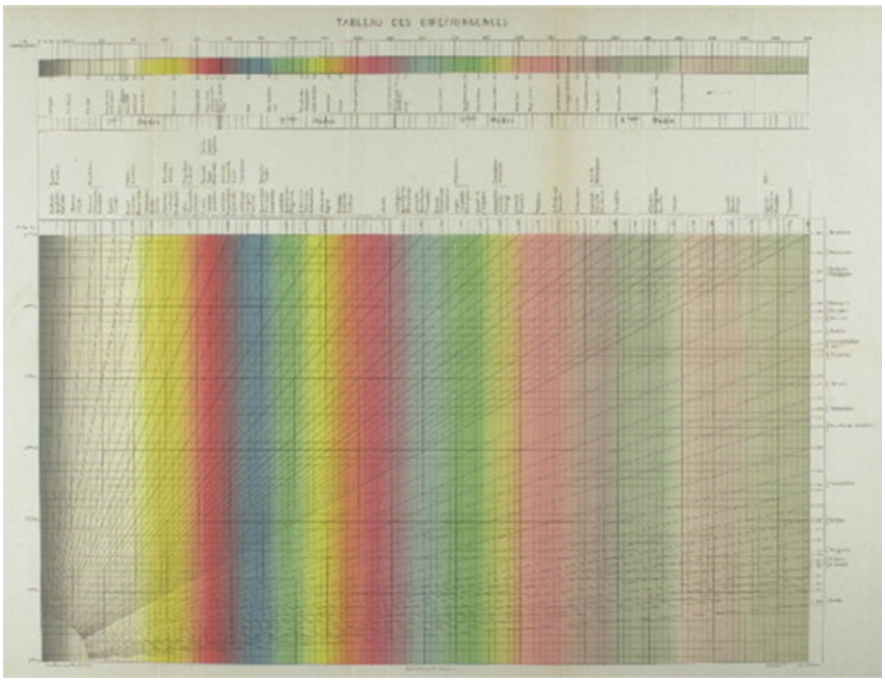


PLATE 9.2

The different interference color orders are shown in increasing order in the abscissa, while the thickness of the specimen is given in the ordinate. The straight lines radiating from the origin of the coordinates are in correspondence to the birefringence refractive index difference ($n_1 - n_2$), written on the right and upper sides of the diagram.

Reproduction of the original Michel-Lévy Interference Color Chart Michel-Lévy, A., Lacroix, A., 1888. Les Minéraux des Roches, Paris, Librairie Politechnique Baudry et C. Editeurs.

Polarization colors result from the interference of the two components of light split by the anisotropic specimen and may be regarded as white light minus those colors that are interfering destructively. Interference colors vary in hue with the retardation according to the sequence known as Newton's series (Fig. 9.1). Since the Michel-Lévy chart shows the interrelationships between thickness, birefringence, and interference color, the microscopists can determine any one from the chart if they know the other two (Plate 9.2, see color section). The early applications of the Michel-Lévy Interference Color Chart were in the fields of mineralogy and petrology, for the identification of minerals. Today, the chart is used as an aid, not only for the identification of minerals, but also for synthetic textile fibers, chemicals, food ingredients, biological agents, drugs, catalysts, ores, fertilizers, explosives, etc.

9.2.6 J.F. GABRIEL LIPPMANN (1845–1921)

Lippmann was the inventor of *interference color photography* (Connes, 1987) and for this reason was awarded the Nobel Prize in Physics in 1908. He was able to record colors as standing light waves in an emulsion. This technique is very interesting from a scientific point of view, but was not very effective for color photography since the technique for practical use was complicated and the exposure times were too long. Moreover, difficulties were encountered in viewing and copying the photographs. He produced four color photographs which, after one century, remain very well preserved.

To understand Lippmann photography, let us consider a monochromatic optical image on a photosensitive emulsion layer that is put on a mirror of mercury. A constructive interference is obtained by the light back-reflected by the mirror and the light reflected by the other side of the emulsion. The standing wave of the interfering light produces a very fine fringe pattern throughout the emulsion with a periodic spacing of $\lambda/(2n)$ that has to be recorded (λ is the wavelength of light in air and n is the refractive index of the emulsion). The color information is stored locally in this way. The larger the separation between the fringes, the longer the wavelength of the recorded part of the image information will be. A polychrome recording is more complex, and was first treated mathematically by Lippmann. The developed photograph lit by white light shows different colors in different parts of the recorded image. The light reflected from the recorded fringes creates different colors corresponding to the original ones that produced the recorded interference fringes. The illumination and the view must have normal incidence and if the angle changes, the colors of the image change (iridescence phenomenon).

9.2.7 SOAP BUBBLES

With regard to soap bubbles, history is rich with mathematical attempts to describe their shape. In particular, this problem was called the *Plateau problem*, taken from the name of the mathematician Antoine Ferdinand Plateau, who published two volumes on this topic (Plateau, 1873).

9.2.8 LENS OPTICAL COATINGS

The evolution of lenses for photographic use, and not only, in the past half century, obtained by means of optical coatings is so important in practical terms that it can be considered a historical step in optics. A simple computation of the light reflected in an objective lens and in any complex refractive optical system, made according to Fresnel's laws, shows that the stray light increases significantly with the number of lenses. This was a very important practical problem and was solved by optical coatings conceived to minimize light reflection on the surfaces of the lenses. A single-layer antireflection coating on the air-glass surfaces of a modern objective

made of high refractive index glasses, centered at $\lambda = 520$ nm (magenta coating), reduces the average reflection loss to $<10\%$, which is acceptable in many practical situations. However, the magenta coloration is distracting and three or more coating layers are necessary for an acceptable achromatization. These problems in antireflection coatings are solved only by a proper application of colorimetry (Dobrowolski and Mandler, 1979).

The colorimetric computation of interference colors is particularly complex and only in the 1950s do we find computations in the literature related to simple coatings, monolayer, bilayers and tri-layers. These historic works are considered in Section 9.4.

9.2.9 THIN FILM ANTICOUNTERFEITING COATINGS

The last historical application of interference colors that we will consider is in the anticounterfeiting of documents and valuable papers, and this was so successful that today we see interference-color figures on banknotes, credit cards, trademarks, and many valuable documents. Interference colors are effective against color copying by printers, copiers or cameras, and lithographic reproduction. These kinds of color copying are unable to reproduce optical effects, which include raised intaglio printed line patterns that reveal special designs or messages when viewed obliquely; special geometric patterns on documents printed at different screen frequencies that become apparent only when combined with the raster of reproduction machines; scrambled printed messages that become intelligible only when a prismatic reader is placed in contact with the document; and holographic devices that present different or changing images when viewed from different angles (Dobrowolski et al., 1989). Colorimetric properties of thin film security devices are very important, because they are easily recognized and reproduced with difficulty. The main constraints in the production of these thin film security devices are imposed by the color detection capability of the human visual system, and are a compromise between the luminance factor and spectral purity: any purity increment decreases the luminance detection (Dobrowolski et al., 1973, 1989).

9.3 OVERVIEW OF BASIC COLORIMETRY

Many textbooks, written by outstanding authors, treat color vision and colorimetry from different points of view: Kaiser and Boynton (1996), Valberg (2005), OSA Committee (1963), Le Grand (1968), Wyszeky and Stiles (1982), Wyszeky and Judd (1975), MacAdam (1993, 1985), McDonald (1987), Sève (1996), Kuehni (1997, 2003), Hunt and Pointer (2011), Berns (2000), Shevell (2003), Schanda (2007), Kuehni and Schwarz (2008), Malacara (2002), CIE (2004a), Oleari (2016).

Any colorimetric treatment of optical coating colorimetry needs a short introduction to standard basic colorimetry. For practical reasons, this introduction does not follow the historical line and is limited to color vision, called *photopic vision*.

Table 9.1 Different colorimetries with reference to the vision zones, visual fields and CIE standard systems

		Psychophysical system First visual zone: transduction Basic phenomena: color matching	Psychometric system Second visual zone: illuminant adaptation Basic phenomena: color difference/color scales
Visual field	Macular vision (visual field <4 degrees) Extra-macular vision (10 degrees visual field)	Standard observer CIE 1931 (X, Y, Z) Supplementary standard observer CIE 1964 (X_{10}, Y_{10}, Z_{10})	CIELUV system (L^*,u^*,v^*) CIELAB system (L^*,a^*,b^*) CIELUV system ($L^*_{10},u^*_{10},v^*_{10}$) CIELAB system ($L^*_{10},a^*_{10},b^*_{10}$)

Note: *Apex "10" is referred to as the 10 degrees visual field.*

Color is a visual sensation, which is a purely subjective and incommunicable entity. Moreover, the human visual system has an adaptation to the visual situation with the consequence that any color judgment is relative to the visual situation itself. We should consider the human visual system to understand this phenomenon. Standard colorimetry proceeds along two different paths that can be termed *psychophysical* and *psychometric*.

Physiology explains that psychophysical colorimetry is based only on the activation of the three kinds of photosensitive cones, that is, the first step in visual processing, while psychometric colorimetry also involves subsequent stages that are not yet completely understood. Moreover, the retina is a nonhomogeneous tissue in the central region, termed *macula lutea*, that has a yellow inert pigment filtering the light before activating the cones. Therefore, two different kinds of colors exist: one for the macular region (visual field of 2 degrees, and always lower than 4 degrees), and one for the extra macular region (visual field of 10 degrees). By combining these distinctions, four standard colorimetries exist, as shown in Table 9.1.

9.3.1 PSYCHOPHYSICAL COLORIMETRY OF COLOR STIMULI

Psychophysical colorimetry is based on the phenomenon, termed *color matching*, according to which different visible electromagnetic radiation (lights, *color stimuli*) produce the same color sensation. Physiology explains that any color sensation is producible by mixing in a proper ratio three independent lights, and three lights are independent if none of these lights is matched by a mixture of the other two lights. *Trichromacy* means that three is the highest number of independent colors. Color matching is independent of the visual situation, but not the color sensation. The classical visual situation in the laboratory is in *aperture mode*, that is, the pair of colors to

be matched is viewed in a bipartite field through a hole in a dark room. The color specification in psychophysical colorimetry is given by three numbers that represent the amounts of the three lights entering the mixture. Grassmann's laws state that these sets of three numbers, termed *tristimulus values*, are the elements of a three-dimensional linear vector space, termed *tristimulus space*. Many different reference frames are possible and therefore many different color specifications with different meanings. Typical specifications are outlined below:

- (L, M, S)

  Here L, M, and S, termed *cone activations*, are proportional to the (positive) numbers of photons absorbed in the unit of time by the three kinds of photosensitive cells (cones) in the retina; L, M, and S refer to Long, Medium, and Short wavelength-sensitive cones, respectively. This reference frame is related to the physiology and is used mainly by physiologists.

  Light is measured outside the eye and the visible range of wavelength is 360–760 nm. The light entering the eye is named *color stimulus* and is physically represented by a spectral radiance $L_{e,\lambda}$ [W/(sr m^2 nm)]. Cone activation is based on *Rushton's univariance principle*, which says that the visual effect of a radiation depends only on the number of absorbed photons and is independent of the photon energy, that is, a photon, once absorbed by the pigment of a cone, triggers a photochemical process, which is independent of the photon energy. Photons with different energy have their own probability of being absorbed and consequently produce different visual effects. In a defined visual situation, the cone activation is in one-to-one correspondence with the color sensation, and therefore the cone activations (L, M, S) specify the color sensation.

  The *tristimulus values* (L, M, S) are defined by three integrals

$$L = \int_{380}^{780} L_{e,\lambda}\bar{l}(\lambda)\mathrm{d}\lambda \quad \text{for L cones}, M = \int_{380}^{780} L_{e,\lambda}\bar{m}(\lambda)\mathrm{d}\lambda \quad \text{for M cones},$$

$$S = \int_{380}^{780} L_{e,\lambda}\bar{s}(\lambda)\mathrm{d}\lambda \quad \text{for S cones} \tag{9.1}$$

where the functions $\bar{l}(\lambda)$, $\bar{m}(\lambda)$, and $\bar{s}(\lambda)$ (Fig. 9.4), named *color-matching functions* (CMFs), are the spectral sensitivities of the cones L, M, and S, respectively, and also take into account the light absorption of the lens of the eye and of the macula lutea. The CMFs are normalized to give $S = M = L = 1$ for the *equal-energy radiance* $L_{e,\lambda} = 1$, therefore representing the monochromatic components of the equal-energy stimulus $\left(\bar{l}(\lambda),\ \bar{m}(\lambda),\ \bar{s}(\lambda)\right)$ in the tristimulus space (Figs. 9.4 and 9.5), that is, at any given wavelength λ, the CMFs represent the cone activations produced by a monochromatic radiation at equal wavelength and with unitary radiance.

The addition of color stimuli is represented in the tristimulus space by the addition of the corresponding vectors.

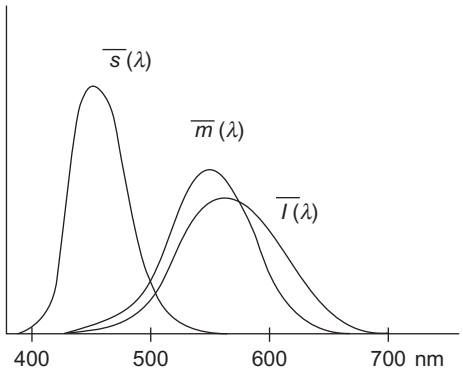


FIG. 9.4

Color-matching functions in the fundamental reference frame for macular vision and the CIE 1931 observer.

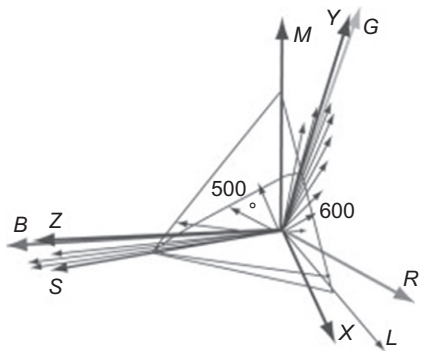


FIG. 9.5

Perspective view of the tristimulus space in the fundamental reference frame with tristimulus vectors related to monochromatic color stimuli with unitary radiance, with the plane of the chromaticity diagram, the spectrum locus, as well as the *RGB* and *XYZ* axes of the other reference frames.

Expression (9.1) that define the (L, M, S) vectors say that the correspondence between color stimuli and tristimulus vectors is many to one, that is, different radiances can produce equal color sensation. This phenomenon is named *metamerism*.

The length of the vectors is related to the intensity of the color stimuli and the direction is related to chromatic sensation. Since the vector directions are in one-to-one correspondence with the intersection points between the tristimulus vectors and a plane, these points constitute a diagram (Fig. 9.5), termed a *chromaticity diagram*, representing the chromaticity, the practical role of which is very important. The chromaticities of the monochromatic lights are points of a line named the

spectrum locus and the segment between short wavelength and long wavelength regions relates to the *purple hues*.

- (R, G, B)

  Here R, G, and B are the intensities of three lights, one red, one green and one blue; very saturated colors require that one of these numbers is negative; this specification is typical for monitors, computers, scanners, photocameras, and so on; many different RGB reference frames exist, which must not be confused.

  Fig. 9.5 shows the tristimulus space in the fundamental reference frame and the vectors **X**, **Y**, **Z** and **R**, **G**, **B** representing the axes of the XYZ and RGB reference frames, respectively. The RGB reference frame is defined by three lights, one red, one green, and one blue, and is termed the *instrumental reference frame* because these three lights are used as reference and this choice is proper for the laboratory. The passage between the LMS reference frame and, for example, RGB is made by the matrix that renders mutually orthogonal the **R**, **G**, **B** vectors with the constraint that $\boldsymbol{R}=\boldsymbol{G}=\boldsymbol{B}=1$ for the *equal-energy radiance* $L_{e,\lambda}=1$. (In some cases, where the white light has a meaningful role, as in the television standards, the same constraint regards the radiance of the chosen white light.) The same linear transformation is made on the CMFs and $\left(\overline{l}(\lambda),\ \overline{m}(\lambda),\ \overline{s}(\lambda)\right)$ are transformed into $\left(\overline{r}(\lambda),\ \overline{g}(\lambda),\ \overline{b}(\lambda)\right)$. The tristimulus values are defined by the integrals

$$R=\int_{380}^{780} L_{e,\lambda}\overline{r}(\lambda)\mathrm{d}\lambda, G=\int_{380}^{780} L_{e,\lambda}\overline{g}(\lambda)\mathrm{d}\lambda, B=\int_{380}^{780} L_{e,\lambda}\overline{b}(\lambda)\mathrm{d}\lambda \tag{9.2}$$

and the chromaticity coordinates are represented by *baricentric coordinates* (r, g, b)

$$r=\frac{R}{R+G+B}, g=\frac{G}{R+G+B}, b=\frac{B}{R+G+B}=1-r-g \tag{9.3}$$

Historically, the CMFs have been measured in an RGB reference frame by a color-matching technique, because in this kind of reference frame it is possible to match a unitary spectral light by a mixture of three reference spectral lights, one red, one green, and one blue. The CMFs were first measured by J.C. Maxwell in 1860. Two sets of standard CMFs exist related to the *2 degrees visual field CIE 1931 standard observer* and denoted by $\left(\overline{r}(\lambda),\ \overline{g}(\lambda),\ \overline{b}(\lambda)\right)$, and to the *10 degrees visual field CIE 1964 standard observer* and denoted by $\left(\overline{r}_{10}(\lambda),\ \overline{g}_{10}(\lambda),\ \overline{b}_{10}(\lambda)\right)$, respectively (CIE, 2004a). All the quantities related to the standard observer CIE 1931 have no denoting apex while those related to the standard observer CIE 1964 have the apex 10.

A linear transformation exists between the tristimulus values (L, M, S) and (R, G, B).

- (X, Y, Z)

  Here X, Y, and Z are the tristimulus values (always positive) related to three standard "imaginary" reference vectors **X**, **Y**, **Z**, properly defined by CIE in 1931, where **Y** represents the *luminance*.

  The CIE 1931 colorimetric system was realized by embedding photometry in colorimetry. The *photometry* relates the luminosity sensation of a light defining the *luminance*, the quantity that would represent the brightness associated with the radiance $L_{e,\lambda}$,

$$L_v = k_m \int_{380}^{780} L_{e,\lambda} V(\lambda) \mathrm{d}\lambda \, \mathrm{cd/m^2} \tag{9.4}$$

with

- $V(\lambda)$ = *relative photopic luminous efficiency function* that defines the *standard photometric observer CIE 24* (Fig. 9.5)
- $K_m = 683$ lm/W

Abney's law states that the luminance of a color stimulus obtained as a sum of many stimuli is equal to the sum of the corresponding luminances. This law induced scientists to represent luminance as a linear weighted sum of the tristimulus values:

$$L_v = L_L L + L_M M + L_S S = L_R R + L_G G + L_B B \tag{9.5}$$

This equation is known as Schrödinger's "Helligkeit" equation (Schrödinger, 1926), where the weights L_L, L_M, L_S, L_R, L_G, and L_B are known as Exner's coefficients. Consequently, this led scientists to search for a reference frame XYZ such that

- the Y component of the stimulus is proportional to the luminance L_v, that is,

$$L_v = K_m Y \, \mathrm{cd/m^2} \quad \text{and} \quad \bar{y}(\lambda) = V(\lambda) \tag{9.6}$$

where $\bar{y}(\lambda)$ is the second color-matching function of the XYZ system,

- the X, Y, and Z axes are mutually orthogonal,
- the X and Z axes belong to the zero luminance plane $Y = 0$,
- the tristimulus vectors with physical meaning have all positive components,
- the planes $X = 0$ and $Z = 0$ are tangent to the spectrum locus in the short and in the long wavelength region, respectively.

This reference frame is possible and is obtained from the *RGB* one by a linear transformation. This reference frame is the *XYZ* of the *CIE 1931 standard colorimetric observer* (Figs. 9.6 and 9.7). The tristimulus values are

$$X = \int_{380}^{780} L_{e,\lambda} \bar{x}(\lambda) \mathrm{d}\lambda, Y = \int_{380}^{780} L_{e,\lambda} \bar{y}(\lambda) \mathrm{d}\lambda = \int_{380}^{780} L_{e,\lambda} V(\lambda) \mathrm{d}\lambda = \frac{L_v}{K_m}, Z = \int_{380}^{780} L_{e,\lambda} \bar{Z}(\lambda) \mathrm{d}\lambda \tag{9.7}$$

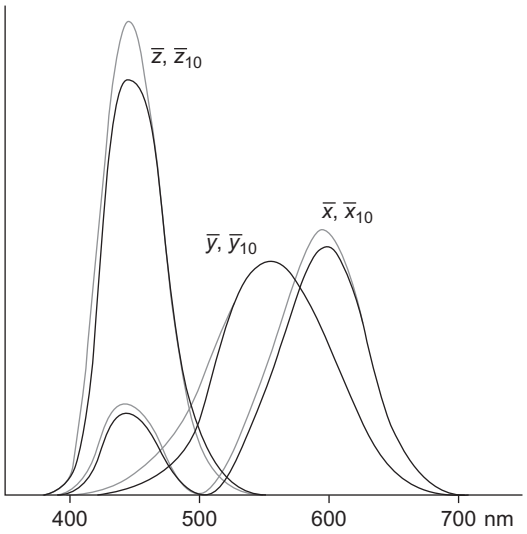


FIG. 9.6

CIE 1931 *(black line)* and CIE 1964 *(gray line)* color-matching functions. The relative photopic luminous efficiency function of the standard photometric observer CIE 1924 is represented by $V(\lambda) = \overline{y}(\lambda)$.

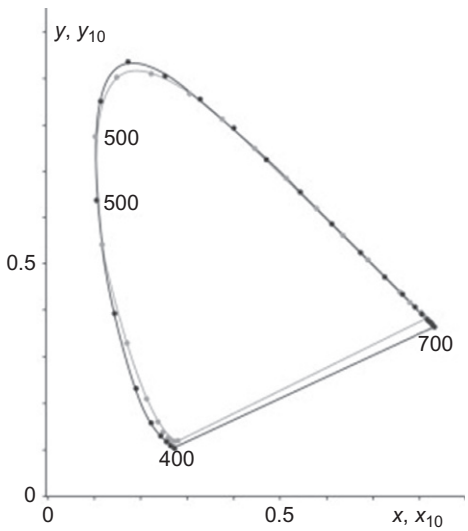


FIG. 9.7

CIE 1931 *(black line)* and CIE 1964 *(gray line)* chromaticity diagrams.

and the chromaticity

$$x=\frac{X}{X+Y+Z},y=\frac{Y}{X+Y+Z},z=\frac{X}{X+Y+Z}=1-x-y \tag{9.8}$$

The usual chromaticity diagram is obtained from the diagram on the plane $X+Y+Z=1$ by a projection from infinity on the plane $Z=0$ (Fig. 9.7).

All the quantities related to the standard observer CIE 1931 have no denoting apex while those related to the standard observer CIE 1964 have the apex 10: as such, the CMFs are $(\bar{x}(\lambda),\ \bar{y}(\lambda),\ \bar{z}(\lambda))$ and $(\bar{x}_{10}(\lambda),\ \bar{y}_{10}(\lambda),\ \bar{z}_{10}(\lambda))$, the tristimulus values (X, Y, Z) and (X_{10}, Y_{10}, Z_{10}), and the chromaticities (x, y, z) and (x_{10}, y_{10}, z_{10}), respectively. Comparisons of the CMFs and of the chromaticity diagrams of these two standard observers are shown in Figs. 9.6 and 9.7.

9.3.2 PSYCHOPHYSICAL COLORIMETRY OF LIGHT SOURCES AND NONSELF-LUMINOUS SURFACES

The psychophysical color specification defined in Section 9.3.1 considers the radiance $L_{e,\lambda}$ entering the eye. Conventionally, the color specification of light sources and of nonself-luminous surfaces is made with a normalization: the quantity Y, termed *percentage luminance factor*, is defined on a percentage scale and $Y=100$ is associated with the radiance reflected by the *perfect reflecting diffuser*, which is nonabsorbing and nontransmitting, but it is an isotropic diffuser such that the reflected radiance is the same in all directions and is independent of the irradiation geometry and of the wavelength (the isotropic reflection is called *Lambertian*). This color specification is independent of the exitance value of the light source and of the illuminance value of the specimens. The reflected radiance is proportional to the *relative spectral power distribution* of the illuminant $S(\lambda)$ and to the *spectral reflectance factor* $R(\lambda)$, that is, $L_{e,\lambda} \propto S(\lambda)R(\lambda)$ (McCamy, 1966):

$$\begin{aligned} &X=K\int_{380}^{780}S(\lambda)R(\lambda)\bar{x}(\lambda)\mathrm{d}\lambda,\ Y=K\int_{380}^{780}S(\lambda)R(\lambda)\bar{y}(\lambda)\mathrm{d}\lambda,\\ &Z=K\int_{380}^{780}S(\lambda)R(\lambda)\bar{z}(\lambda)\mathrm{d}\lambda,\ \text{ with }\ K=100/\int_{380}^{780}S(\lambda)\bar{y}(\lambda)d\lambda \end{aligned} \tag{9.9}$$

where the spectral reflectance factor of the perfect reflecting diffuser is $R(\lambda)=1$. Here the XYZ reference frame is considered, but any other is possible by a linear transformation.

The tristimulus values and the chromaticities related to the standard observer CIE 1931 have no denoting apex while those related to the standard observer CIE 1964 have the apex 10.

The color also depends on the illuminating light. CIE has standardized and specified *illuminants*, that is, files representing the *relative spectral power*

distributions $S(\lambda)$ of light sources. The most important CIE illuminants are (CIE, 2004a):

- the *illuminant* A, associated with a tungsten lamp with the radiant exitance of the black body at the temperature of $\approx$2856 K;
- the *daylight-type* illuminants, associated with conventional daylights denoted by D50, D55, D65, D75, …, corresponding to a temperature of 5000, 5500, 6500, 7500 K, …, respectively;
- *fluorescent lamps*: F2 coolwhite, F7 daylight fluorescent, and F11 white fluorescent.
- *new set of fluorescent lamps*: Standard Halo, DeLuxe, three bands, multibands, and the JIS Z 8716:1991 designed by the American National Standard Institute (ANSI) to simulate the D65 illuminant.

In recent years, new sources of light, termed light-emitting diode (LED), came into production. These sources have not yet been classified by CIE and have reopened the old problem of the evaluation of a color rendering index (CRI) (CIE, 1965, 1974, 1995). The sources and illuminants considered by CIE are now destined to become important objects from the historical point of view. Unfortunately, the difficulty of the problem and rapid technological developments have not yet allowed a colorimetric and spectral practical classification of LED sources and illuminants. The definition of a new color rendering index is necessary but very difficult, as shown by the Illuminating Engineering Society of North America (IES) (IES, 2015).

Spectral reflectance factor is the ratio of the spectral flux reflected by a specimen to the spectral flux reflected by the perfect diffuse reflector under the same geometric and spectral conditions (McCamy, 1966). Since the perfect diffuse reflector does not exist, this is replaced by a physical tile whose spectral reflectance factor is certified by a reference metrological laboratory. The geometries for the reflectance-factor measurement recommended by CIE are (CIE, 2004a):

1. *forty-five degree/normal geometry*, denoted by (45°/0°): the color sample is lit by a parallel light beam with an incidence angle of 45° and the light emerging from the sample with an angle of 0° is analyzed by a spectrometer;
2. *forty-five degree annular/normal geometry*, denoted by (45°a/0°): the color sample is irradiated by light beams uniformly distributed from all directions between two right circular cones with their axes on the normal and with an incidence angle of 45°. The light emerging from the sample with an angle of 0° is analyzed by a spectrometer;
3. *diffuse/eight-degree geometry, specular component excluded*, denoted by (de/8°): the color sample is lit by a diffuse light obtained by integration sphere with specular component excluded and the light emerging from the sample with an angle of 8° is analyzed by a spectrometer;

4. *diffuse/eight-degree geometry, specular component included*, denoted by (di/8°): the color sample is lit by a diffuse light obtained by integration sphere with specular component included and the light emerging from the sample with an angle of 8° is analyzed by a spectrometer.

In the case of a transmitting specimen, the *spectral transmittance factor* $T(\lambda)$ is considered instead of the spectral reflectance factor $R(\lambda)$. $T(\lambda)$ is defined as the *ratio of the spectral flux transmitted by a specimen to the spectral flux through the same optical system with the specimen removed* and the measurement geometries recommended by CIE (all the following geometries relate to the definition of *transmittance* measurement except the situations with the regular component excluded, which relate to *transmittance factor* measurement) (McCamy, 1966; CIE, 2004a):

1. *normal/normal geometry*, denoted by (0°/0°);
2. *diffuse/normal geometry, regular component included*, denoted by (di/0°);
3. *diffuse/normal geometry, regular component excluded*, denoted by (de/0°);
4. *normal/diffuse geometry, regular component included*, denoted by (0°/di);
5. *normal/diffuse geometry, regular component excluded*, denoted by (0°/de);
6. *diffuse/diffuse geometry*, denoted by (d/d).

For transmission measurements, there is a reference plane for the incident light and a second reference plane, displaced by the sample thickness, for the transmitted light. The measurements are based on the assumption of negligible thickness.

The *spectral reflectance* (*transmittance*) *factors* depend on temperature and consequently the color is temperature dependent, too. Therefore, any color specification must be given with the measurement geometry and the temperature; in the case of hygroscopic material, the relative humidity also has to be measured. These standard geometries are meaningful in the vast majority of cases with nearly diffuse reflection or nearly regular transmission.

CIE recommends no particular geometry for optical coatings seen in reflection or in transmission. The gonio-dependence of the reflected and transmitted light requires the definition of a new quantity, which is given in Section 9.4.1.

The passage between different reference frames is made by a linear transformation, represented by a 3×3 matrix. The choice of the reference frame is for practical purposes only.

9.3.3 PSYCHOMETRIC COLORIMETRY

Psychometric colorimetry is based on the visual ordering of color samples seen in a defined visual situation (defined illuminant, geometry of illumination, point of view, defined size of color samples, and defined background on which the color samples are viewed), and the ordering relates to the perceived color attributes of *lightness*, *hue*, and *chroma*. The attributes under consideration are not merely three, but, these are sufficient for our objective. Different and contradictory phenomena exist in relation to the adaptation to a visual situation:

- on the one hand is the *color constancy* phenomenon, according to which the perceived color of lit objects seems unchanging with changing illumination;
- on the other hand is the mutability of perceived color related to the proximal field, background, surroundings, and illumination level.

These phenomena should be considered in psychometric colorimetry.

In practical terms, psychometric colorimetry is represented by color atlases (not considered here).

The practice of instrumental colorimetry has always used a psychometric system of CIE. In 1976, CIE defined two psychometric systems, termed CIELAB and CIELUV, which are based on the psychophysical color specification (X, Y, Z) of the color sample and of the illuminant (X_n, Y_n, Z_n), for the CIE 1931 standard observer, and on (X_{10}, Y_{10}, Z_{10}) and $(X_{10,n}, Y_{10,n}, Z_{10,n})$, for the CIE 1964 standard observer (CIE, 2004a). CIELAB is the most widely used system in industry. CIELUV was conceived for monitors, television, etc., but in practice has become obsolete. Here only the widely used CIELAB is considered.

The CIELAB colorimetric system is spanned by the coordinates (L^*, a^*, b^*), which are derived by nonlinear transformations from the CIE 1931 or the CIE 1964 tristimulus space (in this second case, the coordinates must be denoted by the subscript "10," that is, $L^*_{10}, a^*_{10}, b^*_{10}$). The motivations and the purposes that form the basis of this system are ambitious and not completely satisfied, and the success of this system is due to no more advantageous alternatives existing.

Once an illuminant is chosen, whose specification $(X_n, Y_n = 100, Z_n)$ is obtained from the spectral measurement of the light reflected by the perfect reflecting diffuser, a color stimulus (X, Y, Z) is specified in the CIELAB system by the coordinates (L^*, a^*, b^*):

1. L^* is the CIE 1976 psychometric lightness
2. a^* and b^* are coordinates recalling the opponent unique hues, according to Hering's hypothesis that synthetically says that color sensation is perceptually organized in two *chromatic opponent processes*, *red-green* and *yellow-blue*, and one *dark-light process*.

Lightness is defined as the brightness of an area judged relative to the brightness of a similarly illuminated area that appears to be white. In 1976, CIE proposed the following definition of *psychometric lightness* with the range 0–100

$$L^* = \begin{cases} 119(Y/Y_n)^{1/3} - 16 & \text{for } (Y/Y_n) > 0.008856 \\ 903.3(Y/Y_n) & \text{for } (Y/Y_n) \leq 0.008856 \end{cases} \tag{9.10}$$

that is a function of the ratio of the percentage-luminance factor Y of the surface color (X, Y, Z) being considered over Y_n of the color of the perfect diffuser $(X_n, Y_n = 100, Z_n)$ illuminated by the chosen illuminant; Eq. (9.10) describes the perceived quantity L^* as a function of the relative luminance Y/Y_n stimulating the visual system, according to *Stevens' power law* (in this case, the power is 1/3).

The coordinates a^* and b^*, which should describe the red-green and blue-yellow opponent processes, are defined by differences of suitable quantities:

$$\begin{cases} a^* = 500[f(X/X_n) - f(Y/Y_n)] \\ b^* = 200[f(Y/Y_n) - f(Z/Z_n)] \end{cases} \tag{9.11}$$

where

$$\begin{cases} f(X/X_n) = (X/X_n)^{1/3} \quad \text{for} \quad (X/X_n) > 0.008856 \\ f(X/X_n) = 7.7867(X/X_n) + 16/116 \quad \text{for} \quad (X/X_n) \le 0.008856 \end{cases}$$

and likewise for (Y/Y_n) and (Z/Z_n).

Often, cylindrical coordinates are used (L^*, h_{ab}, C^*_{ab}) with

$$\begin{cases} h_{ab} = \arctan(b^*/a^*) \quad \text{hue angle measured in degrees} \\ C^*_{ab} = \sqrt{a^{*2} + b^{*2}} \quad \text{chroma} \end{cases} \tag{9.12}$$

All the standard color-difference formulae for industrial practice are defined on the CIELAB system: the original Euclidean formula, the CMC formula, the CIE94, and CIEDE2000.

There is also *Color-Appearance Colorimetry*, which takes into account an almost complete visual adaptation. Over time, CIE proposed two models, CIECAM97s and CIECAM02 (Fairchild, 2004). This chapter considers none of the color appearance models because optical coating color does not need such a sophisticated color specification.

9.4 OPTICAL COATING COLORIMETRY

In the sections above, with the definitions of the measurement geometries for spectral reflectance factor and spectral transmittance factor, we have considered nonself-luminous objects, whose appearance has little modification with the directions of illumination and viewing. However, it is also common for the appearance of colored samples to vary with the directions of illumination and viewing. A popular example is the often colored, metallic finish applied to many automobiles (McCamy, 1996, 1998; CIE, 2006). In this case, the pigment of the finish is constituted of micrometric aluminum mirrors and the effect is due to a non-Lambertian diffusion of light. Another popular example is the mica-pigment finish, again applied to automobiles. In this case, the pigment is constituted of micrometric chips of mica coated with a very thin layer of oxide, such as SiO_2. This coating layer, when illuminated, produces iridescent colored effects. The appearance of this finish changes according to the angles of illumination and viewing. Their color is the so-called *gonio-apparent color* or, more generally, *special-effect color*. The colors of the bodies with optical dishomogeneities constituted of layers with different refractive index and with thicknesses of the same order as the wavelength of the illuminating radiation are produced by interference and are named *interference colors*. Also, colors of optical coatings of glasses and lenses are of this kind. In nature, we see interference color in

butterfly wings, insects, bird feathers, and soap bubbles. Since this kind of color is strongly dependent on the illuminating and viewing geometries, it cannot be adequately measured by using the limited conditions of the CIE measuring geometries described above and the color, for a complete characterization, should be measured at more than one illumination/viewing angle combination.

9.4.1 GONIO-APPARENT COLOR MEASUREMENT

For a detailed color specification, both the bidirectional transmittance and reflectance have to be measured and *spectro-goniometric measurements* are needed. Here the term "directional" refers to an infinitesimally small solid angle in a specified direction from the point considered for the measurement, and in this case the rays are very close to being parallel. Let us consider an element of incident spectral irradiance $dE_i(\vartheta_i, \varphi_i, \lambda)$ approaching from the direction (ϑ_i, φ_i) of incidence within the solid angle element $d\omega_i$ (Fig. 9.8). In the case of reflected light, Nicodemus et al. (1977) defined the *bidirectional reflectance distribution function* (BRDF):

$$f_r(\theta_i, \varphi_i; \theta_r, \varphi_r; \lambda) = \frac{dL_r(\vartheta_i, \varphi_i; \theta_r, \varphi_r; \lambda; E_i)}{dE_i(\theta_i, \varphi_i; \lambda)} \left(\mathrm{sr}^{-1}\right) \tag{9.13}$$

which is the ratio of the spectral radiance $dL_r(\vartheta_i, \varphi_i; \vartheta_r, \varphi_r; \lambda)$ exiting the specimen in the direction ϑ_i, φ_r internal to the solid angle $d\omega$ and the spectral irradiance $dE_i(\vartheta_i, \varphi_i, \lambda)$ irradiating the specimen at the same point. Analogously, the *bidirectional transmittance distribution function* (BTDF) is defined.

The instrument for this measurement is the *gonio-spectrophotometer*, which enables the sample to be illuminated from any angle and viewed over a wide range of angles, often by scanning a range from ±80 degrees to the normal to the surface. Instruments of this kind are commercially available, but today their use is exceptional due to the high cost and the current lack of a standard procedure for making multiangle measurements (Fig. 9.9).

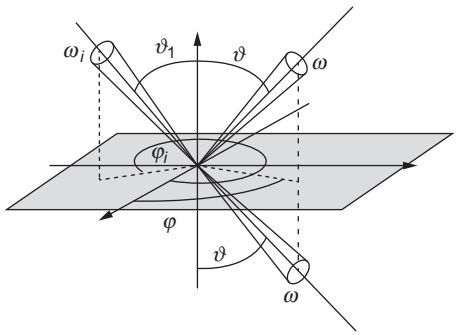


FIG. 9.8

Geometry for the definition of bidirectional transmittance and reflectance spectral distribution function (BTDF, BRDF).

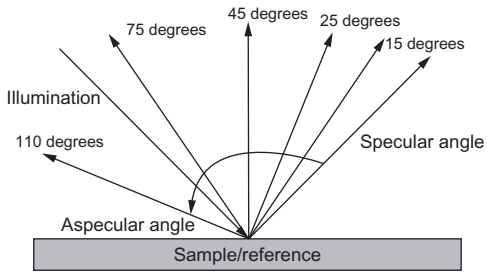


FIG. 9.9

Multiangle spectrophotometry: viewing angles are shown measured with respect to the specular angle.

This limitation is partly overcome by the introduction of so-called *multiangle spectrophotometers*, which typically measure at four or five angles of reflection. As shown in Fig. 9.9, the illumination angle in these instruments is 45 degrees to the normal to the surface and the measurement angles are designated with respect to the specular angle by introducing the concept of *aspecular angle* (Baba, 1990; Rodrigues, 1990; Rössler, 1990; Carroll, 1997). DIN and ASTM International have published standard defining methods for color measurement using four aspecular angles: 25, 45, 75, and 110 degrees corresponding to 45 degrees illumination (DIN, 2001; Mikula et al., 2003; Nadal and Earley, 2004; ASTM, 2014). The ASTM International (ASTM, 2014) has also introduced three lines of interference associated with three angles of incidence of 25, 45, and 75 degrees. For each of these angles of incidence are considered two directions of observation shifted by ± 15 degrees with respect to the angle of specular reflection (155 ± 15 degrees, 135 ± 15 degrees, 105 ± 15 degrees). The two viewing directions are called *cis* and *trans* at -15 degrees and +15 degrees, respectively. On the market there are also other multiangle geometries, wherein the illumination is circumferential by Xenon Flash according to different angles of incidence (25, 45, 75 degrees) and the vision is orthogonal.

However, for many surfaces, notably some of the pearlescent and interference pigments that are now being used for product finishes, the limitation to four angles is probably insufficient and the use of a gonio-spectrophotometer becomes necessary. This comment also holds true for optical coatings.

The resulting color specification, made in *XYZ* or CIELAB systems, must be given combined with the geometry of measurement and the temperature. Moreover, since the interference colors are generally seen in macular vision, the preferable observer is CIE 1931.

The CIE technical Commettee TC 2-53 (Terms of Reference: To write a technical report giving recommendations for the color measurement and evaluation of colorimetric properties of gonioapparent materials.), chaired by Gerhard Rösler (†), is still stopped at Draft No. 3a dated 2006.06.10, (Title: Multigeometry color measurement of gonioapparent materials and metrics for evaluation).

9.4.2 OPTICAL COATING COLOR

The colorimetric evaluation of interference color in reflection and transmission of a simple system constituted of three media is considered here from the theoretical point of view. This analysis is based on a few classical papers (Kubota, 1950, 1966; Murray, 1956; Berning, 1963; Heavens, 1964, 1965; MacLeod, 1986).

The interference produced by optical coatings constituted by a set of thin parallel layers of different dielectrics can be described by solutions of Maxwell's equations combined with initial conditions and boundary conditions. In the simplest case of only two isotropic nonabsorbing media, the reflection and transmission at the interface is well described by Snell's laws, with regard to the geometry of the phenomenon, and by Fresnel's laws with regard to the polarization and power fluxes, and no interference effect appears (Berning, 1963; Heavens, 1964). The role of the critical and Brewster's angles is important.

If the media are more than two and the thickness of a medium is comparable to the wavelength of the illuminating radiation, interference appears and color changes strongly with the illumination direction, polarization, viewing direction, and thickness of the layer (Berning, 1963; Heavens, 1964, 1965; Kubota, 1966; MacLeod, 1986).

Let n_0, n_1, and n_2 be the refractive indices of the three media, respectively, and d the thickness of the intermediate layer (Fig. 9.10). The spectral reflectance and transmittance, computed as a superposition of only two waves ignoring multiple reflections within the layer, are

$$\rho(\lambda)=\frac{r_1^2+2r_1r_2\cos(2\delta_1)+r_2^2}{1+2r_1r_2\cos(2\delta_1)+r_1^2r_2^2},\quad \tau(\lambda)=\frac{n_2}{n_0}\frac{t_1^2t_2^2}{1+2r_1r_2\cos(2\delta_1)+r_1^2r_2^2} \tag{9.14}$$

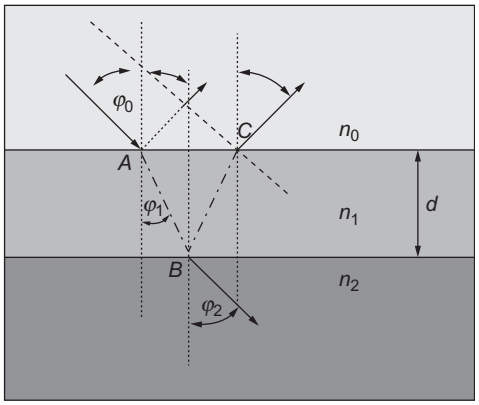


FIG. 9.10

Representation on the incidence plane of a system of three media, with the intermediate layer of thickness d comparable to the wavelength.

where δ_1 is the *phase thickness* of the layer

$$\delta_1 = 2\pi(n_1 d/\lambda)\cos\phi_1 \tag{9.15}$$

and r_1, r_2, t_1, and t_2 are Fresnel's coefficients, which depend on the polarization and on the refractive indices:

- *p-component* for polarization parallel to the incidence plane

$$\begin{aligned} r_{1p} &= \frac{n_0\cos\phi_1 - n_1\cos\phi_0}{n_0\cos\phi_1 + n_1\cos\phi_0},\ r_{2p} = \frac{n_1\cos\phi_2 - n_2\cos\phi_1}{n_1\cos\phi_2 + n_2\cos\phi_1}, \\ t_{1p} &= \frac{2n_0\cos\phi_0}{n_0\cos\phi_1 + n_1\cos\phi_0},\ t_{2p} = \frac{2n_1\cos\phi_1}{n_1\cos\phi_2 + n_2\cos\phi_1} \end{aligned} \tag{9.16}$$

- *s-component* for polarization orthogonal to the incidence plane

$$\begin{aligned} t_{1s} &= \frac{n_0\cos\phi_0 - n_1\cos\phi_1}{n_0\cos\phi_0 + n_1\cos\phi_0},\ r_{2s} = \frac{n_1\cos\phi_1 - n_2\cos\phi_2}{n_1\cos\phi_1 + n_2\cos\phi_2}, \\ t_{1s} &= \frac{2n_0\cos\phi_0}{n_0\cos\phi_0 + n_1\cos\phi_1},\ t_{2s} = \frac{2n_1\cos\phi_1}{n_1\cos\phi_1 + n_2\cos\phi_2} \end{aligned} \tag{9.17}$$

where the angles φ_j are defined by Snell's laws.

Two colorimetric computations are made by applying these formulae with varying layer thickness and varying incidence angle, respectively.

The first computation relates to a coating of an optical glass, like a lens, chosen to obtain the lowest reflection (Kubota, 1950; Murray, 1956). In this case, the normal incidence with $\varphi_0 = \varphi_1 = \varphi_2 = 0$ is close to the practical situation and the coating is achieved satisfying the condition of nonreflection, that is, with the refractive index $n_1 = \sqrt{n_0 n_2}$. The *p* and *s* components of Fresnel's coefficients become equal and are

$$r_1 = \frac{n_0 - n_1}{n_0 + n_1},\ r_2 = \frac{n_1 - n_2}{n_1 + n_2},\ t_1 = \frac{2n_0}{n_0 + n_1},\ t_2 = \frac{2n_1}{n_1 + n_2} \tag{9.18}$$

The reflectances computed for $n_0 = 1$, $n_2 = 1.6$, and $n_1 = 1.2649$ and for a coating thickness d between 0 and 200 nm are represented in Fig. 9.11. The reflectance is always lower than or equal to Fresnel's reflectance $\rho_{\text{FRESNELL}} = 0.0533$ of the uncoated substrate. The spectral reflectance has a minimum equal to 0 moving toward a longer wavelength in correspondence to increasing thickness. This minimum, for a thickness equal to 115 nm, is close to the wavelength 555 nm, where the spectral luminous sensitivity function $V(\lambda)$ has the maximum value. This situation is very important in practice, in order to minimize the reflected light, which is disturbing.

The chromatic specification of the reflected light is represented in Fig. 9.12 for the CIE 1931 observer and equal-energy illuminant, where it is shown that the

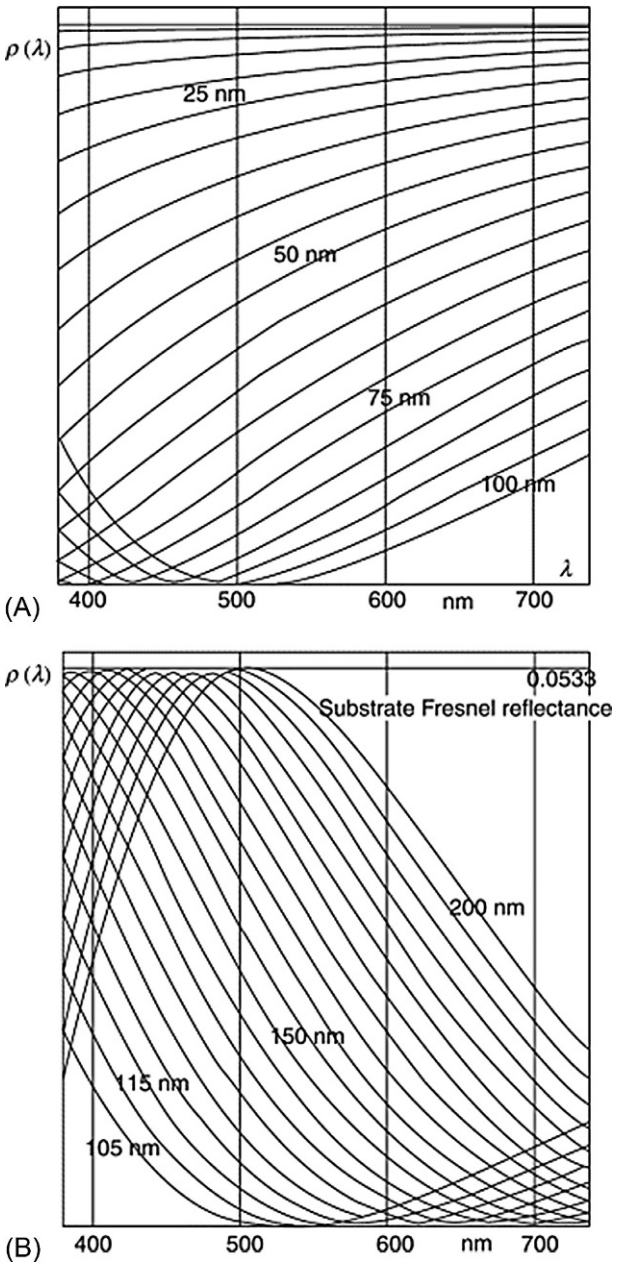


FIG. 9.11

Spectral reflectances computed by Eq. (9.14) for a glass with refractive index $n_2 = 1.6$ in air coated by a layer with $n_1 = 1.2649$ in a condition of nonreflection and for different values of thickness ranging between 0 and 200 nm (A: 0–100 nm, B: 105–200 nm). The maximum value of the reflectance is equal to Fresnel's reflectance of the glass and is 0.0533.

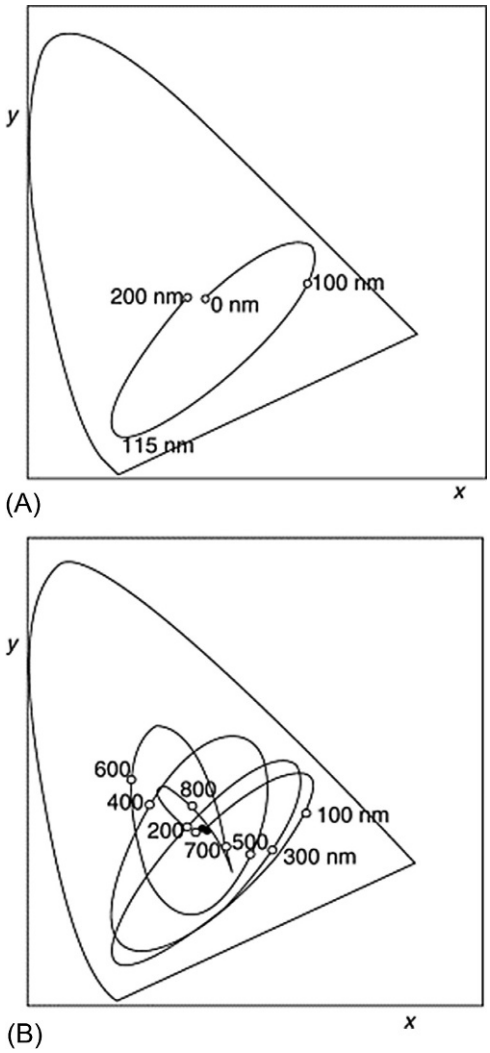


FIG. 9.12

CIE 31 chromaticity coordinates produced by the equal-energy illuminant combined (A) with the reflectances represented in Fig. 9.11 and (B) as obtained with higher thickness values. Around a thickness of 115 nm, the reflectance is equal to zero at 555 nm wavelength in correspondence to the maximum of the luminous efficiency $V(\lambda)$ of the visual system. This property of the optical coating is useful for reducing the stray light in the objective lenses. A very small residual reflectance in the short and long wavelength regions generates the typical *magenta color* of the objective lenses.

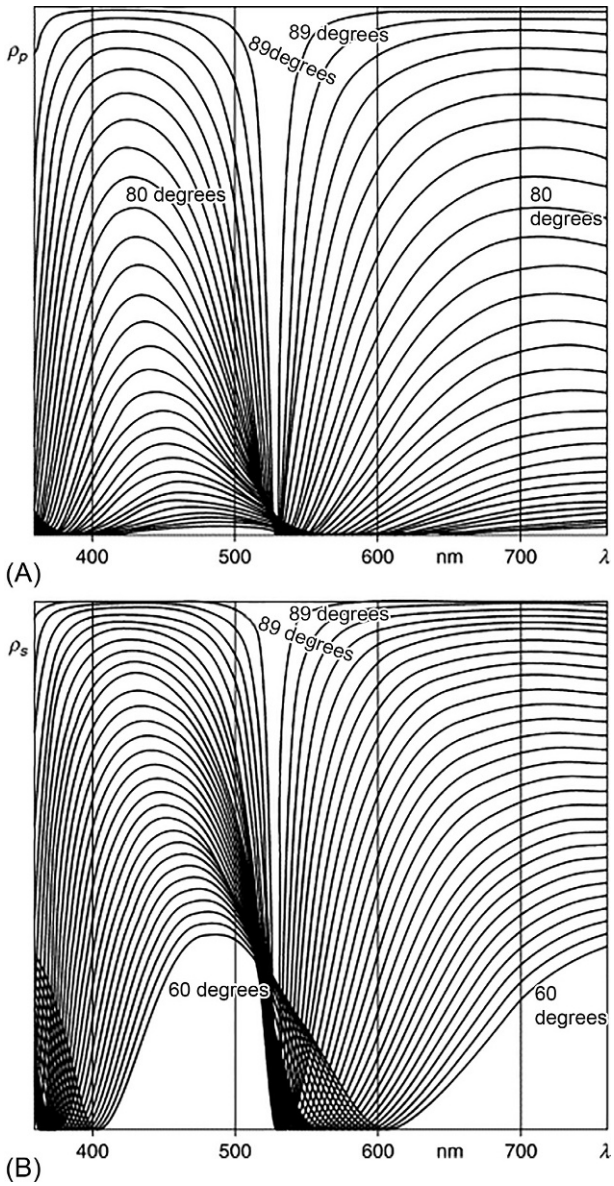


FIG. 9.13

Spectral reflectances related to the polarization *p* (A) and *s* (B), respectively, of a 600 nm layer of water in air for the incidence angle ranging from 60 to 89 degrees. It is remarkable that the reflectance in the visible range approaches the value one with increasing incidence angle, excluding the wavelengths close to 527 nm, where it is almost equal to zero.

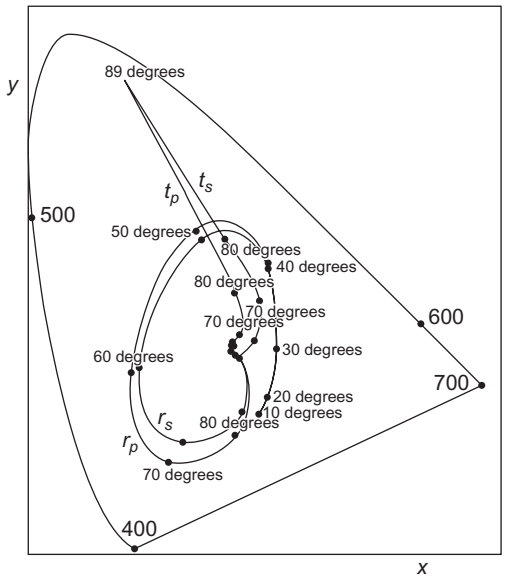


FIG. 9.14

CIE 1931 chromaticity diagram with the chromaticities of the lights with *p*-and *s*-polarization and with different incidence angles, reflected and transmitted by a 600-mm water layer in air (r_p for reflectance with *p*-polarization; r_s for reflectance with *s*-polarization; t_p for transmittance with *p*-polarization; t_s for transmittance with *s*-polarization). The corresponding reflectances for incidence angles in the range 60–89 degrees are represented in Fig. 9.13. The color specification is made for the equal-energy illuminant.

reflected light for a thickness of 115 nm assumes the typical color magenta due to the very small reflectance in the short and long wavelength regions.

The second computation relates to a 600-nm water layer in air with light incident at a varying angle. In this case, the polarization has an evident role. Fig. 9.13 represents the reflectances for *p*- and *s*-polarization for incidence angles ranging from 60 to 89 degrees. The reflectances below 60 degrees are low and the transmitted lights are almost achromatic (Fig. 9.14). It is remarkable that the reflectance in the visible range approaches the value one with increasing incidence angle, excluding wavelengths close to 527 nm, where it is almost equal to zero. In this geometrical situation, the layer is very selective in wavelength. The selected wavelength depends on the layer thickness. The chromaticities for all incidence angles, between 0 and 89 degrees, are represented in Fig. 9.14 where the wavelength selectivity is well represented by the chromaticity of the transmitted light, which approaches the spectrum locus with increasing incidence angle. The color specification is made for the CIE 1931 observer and the equal-energy illuminant.

9.5 CONCLUSION

Colorimetry of the interference color is not yet specifically considered by CIE, although some technical committees have given extensive attention to Color Appearance and technical committee TC2-53 "Multigeometry color measurement of effect materials" is working in a field close to colorimetry of optical coatings. Today, multiangle spectrophotometry is a practical proposal for the measurement of the gonioapparent colors and the colorimetry of the optical coating is not yet standardized.

ACKNOWLEDGMENTS

The author is very grateful to Pietro Polato, for the introduction to optical coating colorimetry, and to Angela Piegari for the dialog and discussion on this paper.

REFERENCES

ASTM, 2014. E2539-14. Standard Practice for Multi-Angle Color Measurement of Interference Pigments. ASTM International, West Conshohocken, PA.https://www.astm.org/Standards/E2539.htm.

Baba, G., 1990. Gonio-spectrophotometric analysis of pearl-mica paint. Die Farbe 37, 99–110.

Berning, P.H., 1963. Theory and calculations of optical thin films. In: Hass, G. (Ed.), Physics of Thin Films, Advances in Research and Development. In: vol. 1. Academic Press, Riverport Ln, pp. 69–121.

Berns, R.S., 2000. Billmeyer and Saltzman's Principles of Color Technology, third ed. John Wiley & Sons, New York.

Brewster, D., 1853. Treatise on Optics. Printed for Longman Brown, Green & Longmans, Paternoster Row, London.

Carroll, J., 1997. Measuring pearlescent color. Modern Paint Coat. 87, 30–34.

CIE, 1965. Publication 13. Method of Measuring and Specifying Colour Rendering Properties of Light Sources. CIE Central Bureau, Wien.

CIE, 1974. Publication 13.2. Method of Measuring and Specifying Colour Rendering Properties of Light Sources, second ed. CIE Central Bureau, Wien.

CIE, 1995. Publication 13.3. Method of Measuring and Specifying Colour Rendering Properties of Light Sources, third ed. CIE Central Bureau, Wien.

CIE, 2004a. Publication 15:2004. Colorimetry, third ed. CIE Central Bureau, Wien.

CIE, 2006. Publication 175:2006. Technical Report, 2005. A Framework for the Measurement of Visual Appearance. CIE Central Bureau, Wien.

Connes, P., 1987. Silver salts and standing waves: the history of interference colour photography. Aust. J. Optom. 18 (4), 147–166.

DIN, 2001. Standard 6175–2. Colour Tolerances for Automobile Lacquer Finishes, Part 2: Effect Lacquer Finishes. http://www.din.de/cmd?level=tpl-home&contextid=din&languageid=en.

Dobrowolski, J.A., Mandler, W., 1979. Color correcting coatings for photographic objectives. Appl. Optics 18, 1879–1880.

Dobrowolski, J.A., Baird, K.M., Carman, P.D., Waldorf, A., 1973. Optical interference coatings for inhibiting of counterfeiting. Opt. Acta 20, 925–937.
Dobrowolski, J.A., Ho, F.C., Waldorf, A., 1989. Research on thin film anticounterfeiting coatings at the National Research Council of Canada. Appl. Optics 28, 2702–2717.
Fairchild, M.D., 2004. Color Appearance Models, second ed. Wiley-IS&T series/John Wiley & Sons Ltd, West Sussex.
Heavens, O.S., 1964. Measurement of optical constants of thin films. In: Hass, G., Thun, R.E. (Eds.), Physics of Thin Films, Advances in Research and Development. In: vol. 2. Academic Press, Riverport, LN, pp. 193–238.
Hevans, O.S., 1965. Optical Properties of Thin Solid Films. Dover Publications, New York, pp. 56–59.
Hunt, R.W.G., Pointer, M.R., 2011. Measuring Color, fourth ed. Wiley-IS&T series/John Wiley & Sons Ltd, West Sussex.
IES, 2015. IES_TM-30. IES Method for Evaluating Light Source Color Rendition, Technical Memorandum. Color-Metrics Task Group of Illuminating Engineering Society of North America, Washington, DC. 202-586-5000, ISBN # 978-0-87995-312-6, http://ies.org/ http://energy.gov/.
Kaiser, P.K., Boynton, R.M., 1996. Human Color Vision. Optical Society of America, Washington, DC.
Kinoshita, S., Yoshioka, S., Miyazaki, J., 2008. Physics of structural colors. Rep. Prog. Phys. 71, 1–30.
Kubota, H., 1950. On the interference color of thin layers on glass surface. J. Opt. Soc. Am. 40, 146–149.
Kubota, H., 1966. Interference color. In: Kubota, H., Wolf, E. (Eds.), Progress in Optics. In: vol. I. Amsterdam, North Holland, Pub. C., Cap VI, pp. 213–251.
Kuehni, R.G., 1997. Color, An Introduction to Practice and Principles. John Wiley & Sons, New York.
Kuehni, R.G., 2003. Color Space, and Its Division. John Wiley & Sons, Inc., New York.
Kuehni, R.G., Schwarz, A., 2008. Color Ordered, A Survey of Color Order Systems from Antiquity to the Present. Oxford University Press, New York.
Le Grand, Y., 1968. Light, Colour and Vision, second ed. Chapman and Hall, London.
MacAdam, D.L., 1985. Color Measurement. Springer-Verlag, Berlin.
MacAdam, D.L. (Ed.), 1993. Colorimetry-Fundamentals. In: SPIE MS, vol. 77. SPIE—The International Society for Optical Engineering, Washington, DC.
MacLeod, H.A., 1986. Thin Film Optical Filters. MacMillan Publishing Company, New York, pp. 40–43.
Malacara, D., 2002. Color Vision and Colorimetry, Theory and Applications. SPIE Press, Bellingham, WA.
Maxwell, J.C., 1860. On the theory of compounds colours, and the relations of the colours of the spectrum. Philos. Trans. R. Soc. Lond. A 150, 57–84.
McCamy, C.S., 1966. Concepts, terminology, and notation for optical modulation. Photogr. Sci. Eng. 10, 314–325.
McCamy, C.S., 1996. Observation and measurement of the appearance of metallic materials. I. Macro appearance. Color. Res. Appl. 21, 292–304.
McCamy, C.S., 1998. Observation and measurement of the appearance of metallic materials. II. Micro appearance. Color. Res. Appl. 23, 362–373.
McDonald, R. (Ed.), 1987. Colour Physics for Industry. Society of Dyers and Colourist, Bradford.

Michel-Lévy, A., Lacroix, A., 1888. Les Minéraux des Roches. Librairie Politechnique Baudry et C. Editeurs, Paris.
Mikula, M., Čeppan, M., Vaško, K., 2003. Gloss and goniocolorimetry of printed materials. Color. Res. Appl. 28, 335–342.
Murray, A.E., 1956. Effect of antireflection films on color in optical instruments. J. Opt. Soc. Am. 46, 790–796.
Nadal, M., Earley, E.A., 2004. Color measurements for pearlescent coatings. Color. Res. Appl. 29, 38–42.
Newton, I., 1704. Opticks, or a Treatise of the Reflections, Refractions, Inflections & Colours of Light. Reprinted, Dover, New York, p. 1952.
Nicodemus, F.E., Richmond, J.C., Hsia, J.J., Ginsberg, I.W., 1977. Geometrical Considerations on Nomenclature for Reflectance. National Bureau of Standards, Washington.
Nobili, L. (1830). Sui colori in generale ed in particolare sopra una nuova scala cromatica dedotta dalla metallocromia ad uso delle sienze e delle arti. ANTOLOGIA, September, tomo trigesimonono, N° 117. Firenze: Tipografia di Luigi Pezzati, pp. 1–39.
Oleari, C., 2016. Standard Colorimetry, Definitions, Algorithms and Software. JohnWiley & Sons, Ltd, Chichester-West Sussex.
OSA Committee on Colorimetry, 1963. The Science of Color. OSA—The Optical Society of America, Washington.
Plateau, A.F., 1873. Statique expérimentelle et théorique des liquides aux seules forces moléculaires. Gauthier-Villars, Paris.
Rodrigues, A.B.J., 1990. Measurement of metallic and pearlescent colors. Die Farbe 37, 65–78.
Rössler, G., 1990. Multigeometry color measurement of effect surfaces. Die Farbe 37, 111–121.
Schanda, J., 2007. Colorimetry: Understanding the CIE System. John Wiley & Sons, New York.
Schrödinger, E. (1926). Über das Verhältnis der Vierfarben- zur Dreifarbentheorie. SbAkad Wien, 134, abt. 2a, pp. 471–490.
Sève, R., 1996. Physique de la couleur. Masson, Paris.
Shevell, S., 2003. The Science of Color, second ed. OSA-Elsevier, Amsterdam.
Thomas, Y., 1802a. A Syllabus of a Course of Lectures on Natural and Experimental Philosophy. From the Press of the Royal Institution, W. Savage, Printer, London.
Thomas, Y., 1802b. On the theory of light and colors. Bakerian lecture read November 12, 1801. Philos. Trans. R. Soc. Lond. A 92, 12–48.
Valberg, A., 2005. Light Vision Color. JohnWiley & Sons, Ltd, Chichester-West Sussex.
Wyszecky, G., Judd, D.B., 1975. Color in Business, Science and Industry. John Wiley & Sons, New York.
Wyszecky, G., Stiles, W.S., 1982. Color Science. John Wiley & Sons, New York.

FURTHER READING

CIE, 2004b. Publication 159:2004. A Colour Appearance Model for Colour Management Systems: CIECAM02. CIE Central Bureau, Wien.
Ohta, N., Robertson, A.R., 2005. Colorimetry—Fundamentals and Applications. John Wiley & Sons, New York.

This page intentionally left blank

PART

III

Novel materials for optical thin films and coatings

This page intentionally left blank

CHAPTER

Organic optical coatings 10

Thomas Neubert, Michael Vergöhl
Fraunhofer Institute for Surface Engineering and Thin Films—IST, Braunschweig, Germany

10.1 INTRODUCTION

Stacks or single layers of transparent thin films are commonly used to modify the optical behavior of surfaces and to integrate new functions such as scratch resistance or antifingerprint. Examples, therefore, are antireflective coatings for display glass or optical instruments, high reflective mirrors for laser applications, and optical filters with practically any kind of spectral characteristic. Very often, dense layers without any spectral shift due to environmental changes (humidity) are required. Therefore, such optical layers are usually made of ceramic materials with a low and high refractive index. A wide number of metal oxides such as silicon oxide (SiO_2), tantalum oxide (Ta_2O_5), and titanium oxide (TiO_2) are used for applications from near ultraviolet to the mid-infrared spectra range. These materials are often deposited by vacuum deposition processes like (ion assisted) evaporation, magnetron or ion beam sputtering, or plasma-enhanced chemical vapor deposition (PECVD). Besides the excellent optical properties (low absorption, well-defined refraction index, low optical haze), high hardness close to the bulk values and low mechanical flexibility are typical for these layers whenever plasma technology is applied. However, for many applications of optical coatings, high hardness and low mechanical flexibility, which are normally connected close to each other, are not suited. Hard and thus nonflexible layer systems on polymer substrates (like foils or plates) will break and produce stray light and delamination, especially under thermal and mechanical load or after deformation. On the other hand, organic materials have a significantly higher mechanical flexibility. Furthermore some organic materials may offer additional functions such as hydrophobicity (Gürsoy and Karaman, 2016), hydrophilicity (Kuzminova et al., 2014), fluorescence (Zhao et al., 2015), permittivity (Lin et al., 2008; Zenasni et al., 2003), and chemical activity (Jung et al., 2006). Last but not least, they have a low price. This makes organic materials interesting for optical coatings. However, the mechanical stability of organic layers is too low for many applications. The goal in current research, therefore, is not only to work on deposition processes for pure optical organic layers but also to improve the

Optical Thin Films and Coatings. https://doi.org/10.1016/B978-0-08-102073-9.00010-2
Copyright © 2018 Elsevier Ltd. All rights reserved.

mechanical stability of these layers by the use of composites. Therefore, organic layers are also of interest as an additional part of a ceramic layer system.

Organic materials are of practical interest not only for optical interference coatings but also for other applications. Examples of other important applications are organic light emitting diodes (OLEDs) and organic photovoltaic (OPV) cells.

10.2 SPECIFIC PROPERTIES OF ORGANIC LAYERS

In organic materials like polymers, the binding energies of the molecules are lower and the structures of the molecules are often more complex than in most metal oxide materials. In vacuum- and plasma-based deposition processes it is often a difficult task to keep the same polymeric structure in a thin organic layer as in polymer "bulk" materials. This may be one of the reasons that, depending on the organic material, a large variety of deposition techniques have been tried out and some of them have been established in recent years. In this chapter an overview of different vacuum deposition processes is given and some properties of organic materials performed at the Fraunhofer Institute for Surface Engineering and Thin Films (IST) in Braunschweig, Germany, and elsewhere are shown.

Organic materials show some special properties compared to ceramic materials. As already mentioned, the mechanical flexibility of organic layers is much higher. The mechanical flexibility or elasticity of films can be determined by measuring the so-called crack onset strain (COS) value. To measure this COS value a coated film on a flexible substrate like polycarbonate (PC) of specific thickness can be bent in a well-defined way while the film is observed by a microscope. If cracks appear the crack onset strain ε can be calculated from the bending radius R and the substrate thickness d by Eq. (10.1). Fig. 10.1 shows the principle.

$$\varepsilon = \frac{\Delta L}{L} = \frac{\Delta R}{R} = \frac{d}{2 \cdot R} \tag{10.1}$$

As shown in Fig. 10.2 the crack onset strain value of many organic layer materials is above 12% (this was the maximum value of the experimental setup). Ceramic layer materials typically show values of about 1% or less.

For the application in optical interference layer systems a broad range of refraction indices in combination with low absorption and also low haze value is necessary. The refractive indices of organic materials vary from 1.4 (at 550 nm) for RF sputtered fluorocarbon layers to 1.8 for materials like evaporated melamine (Fig. 10.3). This variation is broad enough for simple optical designs like antireflective coatings. Haze values and absorptions of organic thin films are often not as low as in metal oxides used for optical applications. This has to be considered for more complex optical designs.

It is well known that fluorine-containing organic materials (such as parylene AF-4, PTFE, etc.) show a high water contact angle up to 120° and a low surface

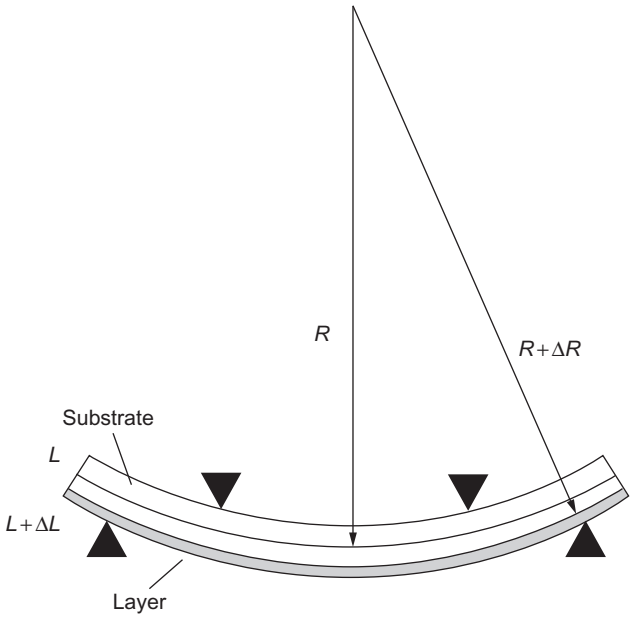


FIG. 10.1

Setup for the determination of the crack onset strain.

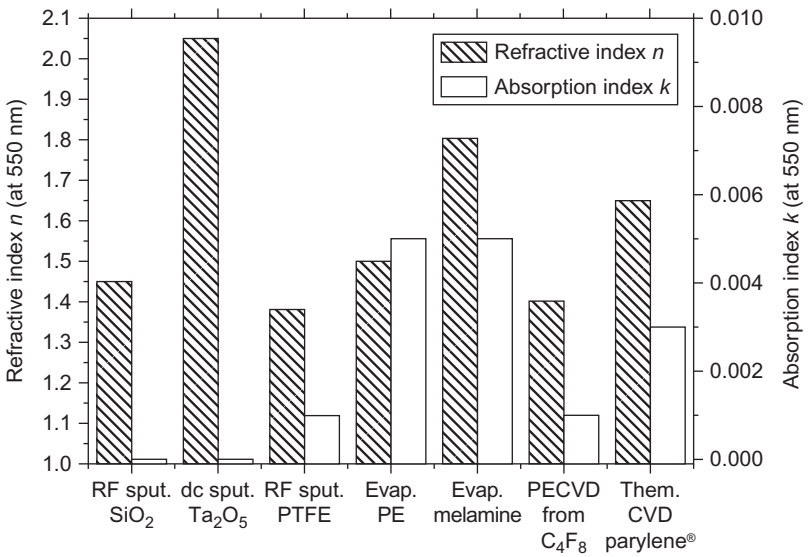


FIG. 10.3

Refractive and absorption indices of various deposited layer materials (Neubert et al., 2011a).

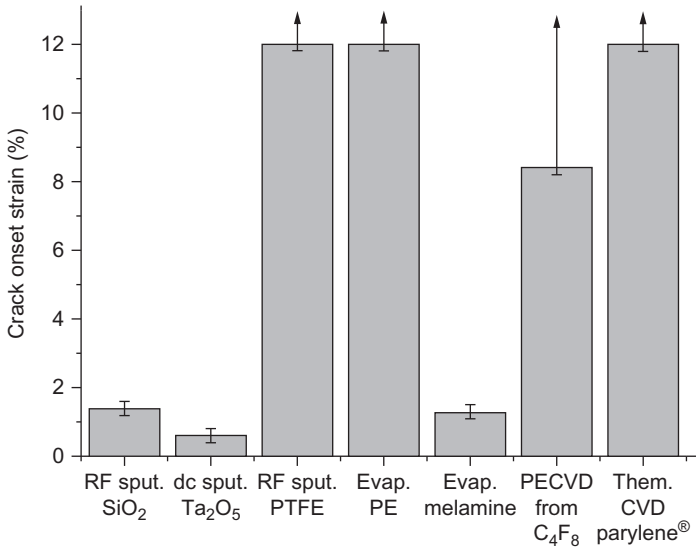


FIG. 10.2

Crack onset strain of various layer materials on polycarbonate substrates (Neubert et al., 2011a).

energy (Li et al., 2011a,b). By the use of sputtered PTFE, for example, release layers or easy to clean surfaces of optical systems can be produced. However, care must be taken to avoid delamination of the layers on top of such fluorocarbon layers, since it also reduces the adhesion of subsequent layers. This will be described in more detail in Section 10.4.5.

Organic materials are generally not as stable against heat, radiation, and energetic particle bombardment as most oxide materials. This fact limits the tolerable process conditions in the preparation and operation of these layers. On the other hand, it offers a possibility to modify these layers, for example, by plasma treatment for better adhesion of following layers, for better cross-linking, or to gain special surface structures. A good example, therefore, is poly(methyl methacrylate) (PMMA). Deposition on PMMA substrates by sputtering or other plasma-involved techniques often damages the molecular structure on the surface of the substrate, causing typically weak adhesion of the sputtered layers (Munzert et al., 2003). However, under special conditions, improved adhesion on PMMA was also observed (Schulz et al., 2001; Bandorf et al., 2016). On the other hand, plasma etching of PMMA surfaces can be used to generate fractal moth eye-like surface structures to lower reflectivity of these surfaces (Kaless et al., 2005).

In electronic devices such as OLEDs on polymer substrates and OPV cells, both transparency and excellent diffusion barriers against water and oxygen are required. The permeability of organic materials for water, oxygen, and other gases is often higher than in most oxides. However, the high crack onset strain of organic layers and some deposition processes which have the tendency to level out the surface

roughness like the parylene deposition process provide useful layers for diffusion barriers, especially in combination with ceramic layers as multilayer systems (Chiang et al., 2006). Creation of diffusion barriers by the use of multilayers and composite materials is a widely studied topic of materials and process research.

10.3 OPTICAL COATINGS WITH ORGANIC LAYERS

Because of their special properties different applications for organic layers in optical layer systems are possible. Since there is a relatively broad variation of refractive indices from 1.4 to 1.8, pure organic optical interference filters are theoretically possible. Weber showed that these kinds of optical interference layer systems are possible to make with an extruding technique of polymer foils (Weber, 2012). However, pure organic optical interference filters made with vacuum deposition techniques from low and high refractive index materials are hard to find in the literature. Better realizable are combinations of organic layer materials and oxide or metal thin films. Affinito et al. showed this for vacuum flash evaporated and radiation cross-linked monomers (hexanediol diacrylate) in combination with sputtered silver for Fabry-Perot filters (Affinito et al., 1995). Such polymer-containing layers are suitable for web coating and coatings for thermoformable substrates.

Due to its low surface energy in combination with sufficient optical properties (low refraction and absorption indices) of fluorocarbon layers these layers are suited as top coating for optical layer systems with antisticking or easy to clean properties (Jaszewski et al., 1999).

An interesting further application is the use of stacks of organic materials and metal oxides as transparent bendable diffusion barriers. These types of barriers are interesting as corrosion protection or diffusion barriers for OLEDs and organic photovoltaic (OPV) systems that react very sensitively to water and oxygen (Singh et al., 2007).

Well-defined thin films of organic materials like stearic acid or fluorescent dyes can be used for measurements of photocatalytic surfaces (Neumann and Cerezuela Barreto, 2004; Neubert et al., 2007, 2008). The photocatalytic decomposition processes oxidize the organic layers which can be measured and analyzed by optical measuring methods like fluorescence or haze measurements.

Composites of organic materials with metal oxides can be used to combine different properties of the materials. A good example for this is evaporated color pigments in metal oxides for decorative applications. The composites combine sufficient wear resistance with the intense color of organic dyes (Jäger, 1997).

10.4 DEPOSITION TECHNIQUES

Organic layers can be deposited by various techniques, such as lacquering, sol-gel, and atmospheric plasma deposition processes. Here, the focus is on vacuum deposition methods, which are often used to obtain dense layers with good uniformity, homogeneity, and material properties. Thus, for all processes discussed in this

chapter, vacuum chambers with suitable pumps (turbo molecular pumps or oil diffusion pumps) were used. Chambers with these pumps typically reach pressures in the range of 10^{-6} mbar.

Using organic materials as deposition materials, some factors have to be considered. Organic materials often have lower evaporation temperatures than many inorganic materials. Thus the effort for process equipment can be lower than for the evaporation of metals or oxides. The organic molecules in the gas phase are also often more complex and can act like a precursor in a chemical vapor deposition (CVD) process if a gas discharge is involved in the deposition process. That is why fragments of these molecules can coat pressure gauges or other sensitive parts of the reactor. Organic molecules are also more sensitive against overheating, plasma UV radiation, high energetic particles, or chemical active species such as oxygen radicals. Chemical reactions caused by these processes can generate unwanted species in the deposition process and can be harmful. Therefore, the development of processes suitable for organic coatings has to consider these aspects. In the next section, an overview is given on different processes which were used at the author's facility to deposit organic layers.

10.4.1 THERMAL EVAPORATION

Probably the easiest way to deposit organic matter is by thermal evaporation. Many organic materials can be deposited in a classical evaporation setup with thermal boat evaporators. Because of its lower evaporation temperature (often below 500 °C), organic materials can also be evaporated with simple setups, such as using a crucible in a heating cartridge (Figs. 10.4 and 10.5). Typical for these types of processes the deposition rate is very sensitive to the heating power. To gain constant deposition rates and defined thicknesses quartz controlling of the deposition process is recommended.

The choice of evaporable organic materials is mainly limited by thermal degradation processes. In particular, polymers and other large molecules with low vapor pressure will be thermally cracked before being evaporated. Organic materials that can be evaporated are polyethylene (PE) (Bekiarov et al., 1988), polyamide (PA) (Meurisch et al., 2012), polyimide (PI) (Spassova et al., 1996), melamine (Schulz et al., 2011), various color pigments (e.g., Cu-phthalocyanine (Jäger, 1997), and stearic acid (Neubert et al., 2007), for example. Emission layers in OLEDs like tris-(8-hydroxyquinolinolato) aluminum (Alq3) are also known to be deposited with evaporation processes (Lee et al., 2004; Eritt et al., 2010). Evaporated organic materials like Tinuvin 360 (a commercial UV pigment by BASF) and *N*,*N*′-di (1-naphthyl)-*N*,*N*′-diphenyl-1,1′-diphenyl-1,4′-diamine (NPD) (a material that can also be used as organic hole transport layer in OLEDs (Iwama et al., 2006)) have been found to be useful as UV protective layers on polymer substrates like polycarbonate (PC) (Präfke et al., 2012). There are also commercial water and oil repellent materials like Patinal WR5 from Merck, for example, to improve the easy to clean,

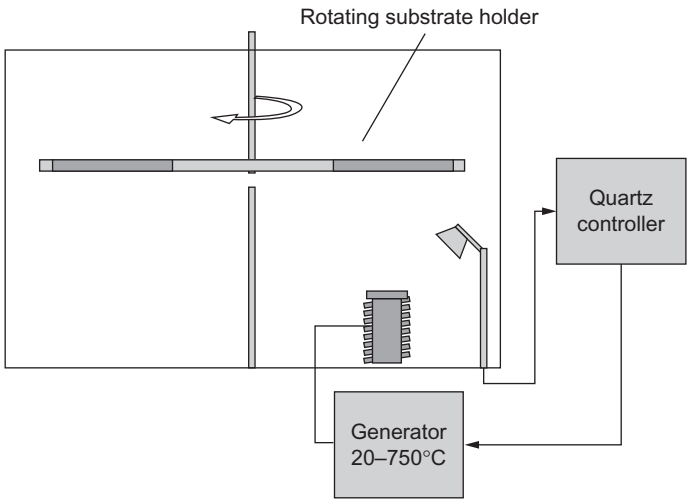


FIG. 10.4

Evaporation setup with substrate holder, quartz deposition controller, and evaporation source.

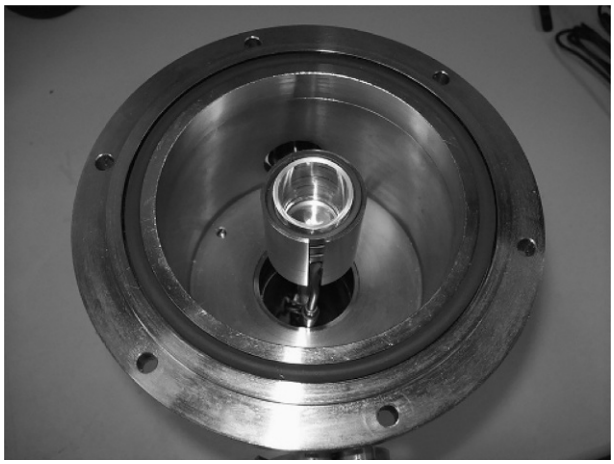


FIG. 10.5

Heating cartridge with quartz crucible as evaporation source for organic material.

antifingerprint properties and the haptic properties of touch screen surfaces. These materials are typically coated using evaporation, too.

Some materials like polyethylene form a highly viscous melt during the evaporation process. Boiling of a melt like this may cause spitting of droplets that condense on the growing layers with sizes of some 100 µm. This effect is highly undesirable

and can be suppressed by higher source-to-substrate distances and heated covers on the crucible.

The addition of energy to the forming layers—by UV radiation or particle bombardment—can induce chemical reactions. Cross-linking of the molecules and the mechanical stability of the layers can be improved by this process (Choukourov et al., 2006). The particle bombardment can be performed with an ion source or by a radio frequency (RF) gas discharge with the substrate as cathode.

Matrix-assisted pulsed laser evaporation (MAPLE) is a very special type of evaporation process for organic materials. For this kind of process a pulsed laser beam hits a frozen target (100 – 200 K) of organic matter in a solvent matrix (Piqué et al., 1999). The laser pulse evaporates the frozen solvent and the solved organic material is released to the gas phase. The solvent concentration has to be high enough that the dissolved molecules are more or less separated from each other. By this technique it is possible to deposit materials with large molecular weights such as polymer chains like PMMA (Sellinger et al., 2008), polyethylene glycol (PEG) (Paun et al., 2011), or even sugars (Piqué et al., 1999), without damaging the molecules. Although this technique is very promising it seems difficult to scale this deposition process up for large surfaces.

10.4.2 SPUTTER DEPOSITION

Most organic materials cannot be deposited by direct current (DC) magnetron sputtering. On the one hand, their electrical conductivity is often too low to keep the electric discharge running. On the other hand, the ion bombardment in the sputtering process influences the molecular structure. Normally molecular chains are broken, leading to layers with an amorphous, undefined structure on the substrate. However, there are some reports of sputtered polymer layers like polytetrafluoroethylene (PTFE) (Pratt and Lausman, 1972; Morrison and Robertson, 1973; Biederman et al., 1977; Li et al., 2011a,b), polyimide (PI), poly(methyl methacrylate) (PMMA) (Bodas and Gangal, 2005; Biederman et al., 2003), polypropylene (PP) (Stelmashuk et al., 2004), and polyethylene (PE) (Kholodkov et al., 2003; Kousal et al., 2005). The deposited layers are structurally not identical to the polymer source materials but they basically consist of shorter fragments of the original material with strong cross-linking (Li et al., 2011a,b). Nevertheless, some optical, chemical, and mechanical properties make these films interesting.

RF sputtering of PTFE has been known since the 1970s. The sputtered fluorocarbon layers typically show a low absorption index ($k \approx 0.001$) (Neubert et al., 2011a), low refractive index ($n = 1.35$–1.48, Biederman et al., 1977), and high hydrophobicity (water contact angle of about 120° and greater) (Kylián et al., 2011). For the deposition a magnetron sputter deposition chamber with a PTFE plate as sputter target can be used (Fig. 10.6). An RF power supply is needed since PTFE is electrically nonconducting. To avoid chemical reactions, a pure argon atmosphere in the range of 10^{-2} to 10^{-3} mbar should be used. Adding oxygen to the process gas causes a decreasing deposition rate and an increasing optical absorption of the layers

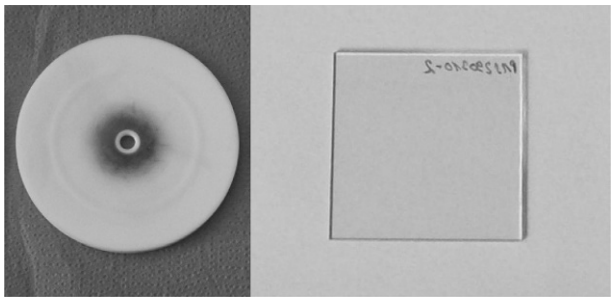


FIG. 10.6

Pictures of a PTFE sputter target and a sputtered fluorocarbon layer on a glass substrate.

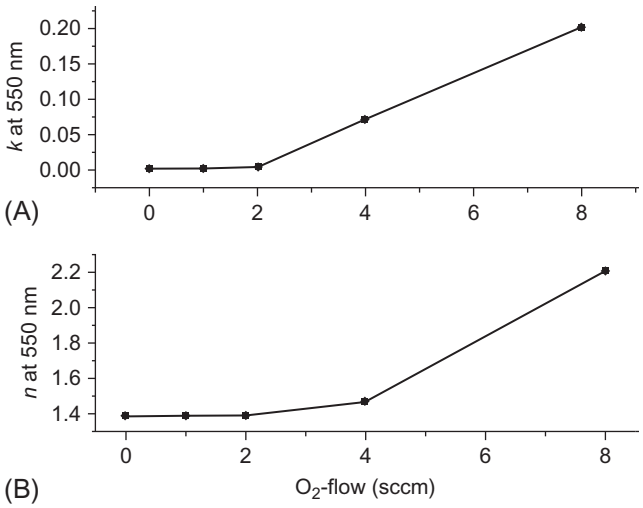


FIG. 10.7

Influence of oxygen on (A) refractive and (A) absorption index of RF-sputtered fluorocarbon layers (Neubert et al., 2010).

(Fig. 10.7). It can be shown that the deposition rate of sputtered PTFE is not constant during the deposition process compared with "standard" sputtering processes for metal or metal oxide films (Fig. 10.8). Obviously heating of the PTFE target causes an increasing emission of fluorocarbon fragments. For exact thickness and rate control an optical or quartz crystal monitoring controlling device can be used.

Pressure and the target-to-substrate distance have an influence on the surface energy and water contact angle of the sputtered fluorocarbon layers. For layers made at relatively high sputter pressures (50 Pa) and with large target-to-substrate distances (25 cm) values of over 170° have been reported (Kylián et al., 2011). The intrinsic hydrophobic effect of the fluorocarbon is amplified by a very porous and

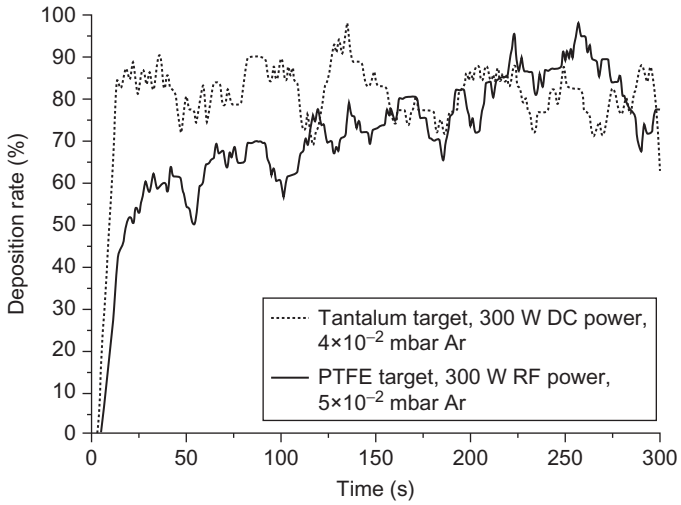


FIG. 10.8

Deposition rate of sputtered PTFE and sputtered tantalum in argon atmosphere as a function of deposition time measured with a quartz monitor.

rough structure of the layers caused by the lower energy input to the growing layer (Kylián et al., 2011).

Ion beam sputtering for the deposition of PTFE/oxide composites has been investigated by Gauch et al. (2014). As sputter targets, both a composite target of PTFE with 25% glass fibers and a zone target consisting of silicon and PTFE were used. It was found, that in the case of a zone target, films only grew without additional oxygen in the plasma. For the composite target sputtering, films consisting of carbon, fluorine, and oxygen but without silicon in the films result, indicating that the silicon remained in the target. In the work of Gauch, it was found out that nanoparticles could be produced promisingly by that method.

Pihosh et al. (2006) deposited composite SiO_x/hydrocarbon plasma polymer films by RF *co*-magnetron sputtering from silica and polyethylene (PE) or polypropylene (PP) targets. Depending on the power ratio between the two targets, static contact angles of water between 75° and 25° for PE and 80° and 33° for PP have been observed. The hardness of the composite films varied from 2400 to 3400 N/mm^2 (PE) and from 1600 to 2000 N/mm^2 (PP), respectively.

10.4.3 PLASMA-ENHANCED CHEMICAL VAPOR DEPOSITION (PECVD)

All chemical vapor deposition processes have in common that gases, vapors, or aerosols are delivered to a substrate where they condense to solid layers during controlled process conditions such as energy, temperature, and pressure. Plasma-enhanced

chemical vapor deposition (PECVD) is a widely used technique for the production of coatings. The main advantage of PECVD is that the temperature can be reduced from a range of 400–2000°C down even to room temperature so that temperature-sensitive substrates such as polymers can be coated. The plasma can be generated in different ways: electric fields are commonly used, ranging from low frequency (kHz region) to high frequency (MHz) to microwaves in the GHz range. To generate the plasma in a practical way, a large variety of process variations have been developed. Plasma sources can be powered from low frequency to microwave and may have a circular or linear shape. Also double linear sources are available. Hollow cathodes or even sputter magnetrons can be used as plasma sources. Often the plasma density is increased by the use of magnetic fields.

To form plasma polymers, an electrical gas discharge is used to crack bonds in organic gaseous precursor molecules to create reactive species that react on surfaces next to the discharge plasma. The gas discharge can be provided by a special ion or plasma source or by a simple glowing cathode. A separate electrode or the substrate itself can be used as cathodes. Since electrical nonconducting layers are often produced, the power supply is often by RF, pulsed DC, or microwave. Typical working pressures are in the range of 0.01–10 Torr (c. 10^{-2}–10 mbar) (Kinzig and Smardzewski, 1981). However, there are also processes at higher pressures like atmospheric pressure CVD using special dielectric barrier discharge sources. A sketch of a low pressure PECVD setup using parallel plates is shown in Fig. 10.9. The same setup can be used for the deposition of ceramic and organic films

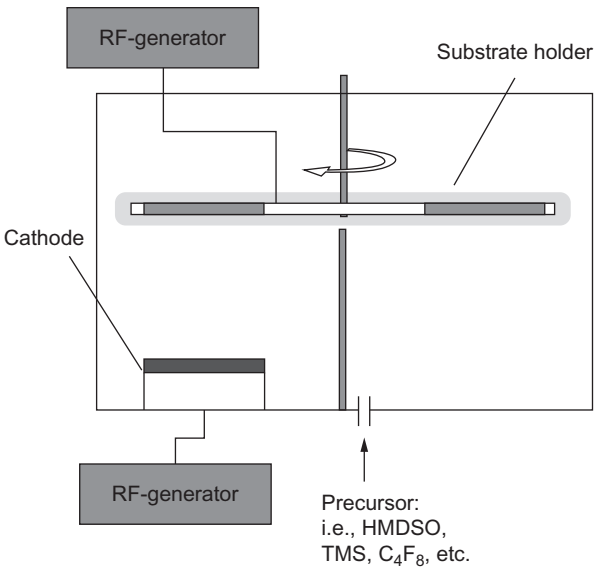


FIG. 10.9

Sketch of a PECVD coating setup.

by PECVD. The type of films is determined by the type of process gases and the deposition conditions.

Well-known precursors for organic coatings are, for example, silanes like hexamethyldisiloxane (HMDSO) (Schwarz et al., 1998) or tetramethylsilane (TMS) (Noborisaka et al., 2012). While oxygen is present, silicon dioxide-like films can be produced with these compounds. In the absence of oxygen the films gain more organic properties such as higher flexibility and lower hardness (Fig. 10.10). Carbon bindings do not get oxidized by the oxygen and the films get more mechanically flexible. These layers are reported to be transparent in the visible range with a refractive index n between 1.45 and 1.58 and absorption index k below 2.6×10^{-3} (Martin-Palma et al., 2006). Typical applications of these layers are wear resistant coatings to protect sensitive substrates like polymer foils. Nonsticking layers with high water contact angle are also known (SICON) (Corbella et al., 2008).

Methyl methacrylate (MMA) as a precursor can be used to prepare plasma-polymerized poly(methyl methacrylate) (pPMMA) thin films (Kinzig and Smardzewski, 1981; Lim and Shin, 2007; Li et al. 2014). These layers have been found to be useful, for example, as buffer layers in OLEDs.

Also different fluorinated precursors such as tetrafluoromethane (CF_4) and octafluorocyclobutane (C_4F_8) can be used (Takahashi et al., 2000). Films prepared with these precursors show very similar properties to RF sputtered thin films from PTFE targets. They are highly transparent. They have high water contact angles of 110° (Matsumoto and Ishida, 2000) and a low refraction index of $n = 1.40$ (Fig. 10.11), and the infrared absorption spectra (Fig. 10.12) are almost identical

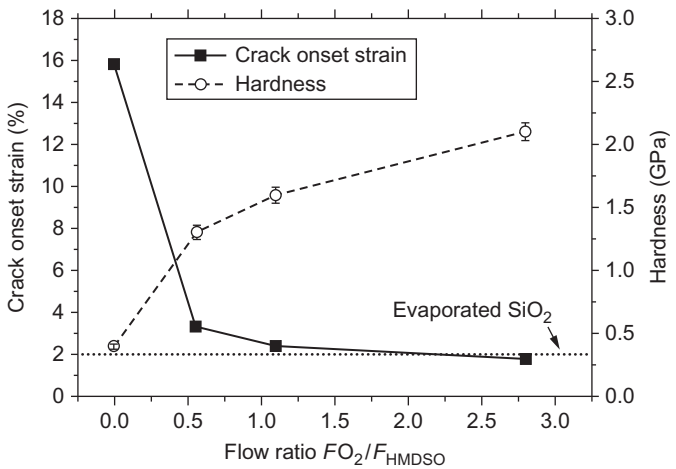


FIG. 10.10

Crack onset strain and hardness as a function of the ratio of oxygen to HMDSO for PECVD made thin films.

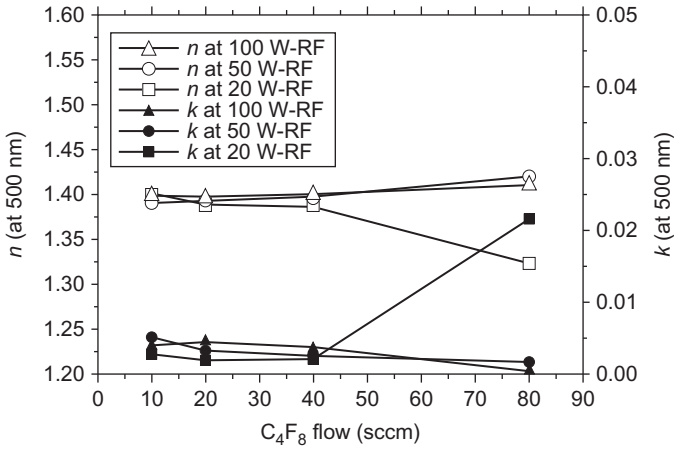


FIG. 10.11

Refraction and absorption indices at 500 nm for different plasma powers as a function of C_4F_8 precursor flow.

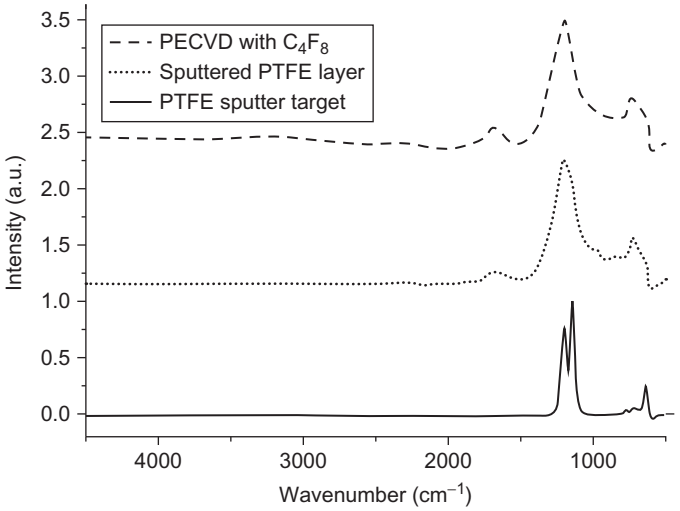


FIG. 10.12

Infrared attenuated total reflectance (IR-ATR) spectra for PECVD made layers with C_4F_8 as precursor, for RF sputtered fluorocarbon layers and for the used PTFE sputter target.

(Neubert et al., 2011a). The deposition rate for these processes depends on the electrical power and the amount of available precursor molecules (Fig. 10.13). Thus, there is an optimal working point: If there are not enough precursor molecules the deposition itself is limited. On the other hand, if there are too many precursor

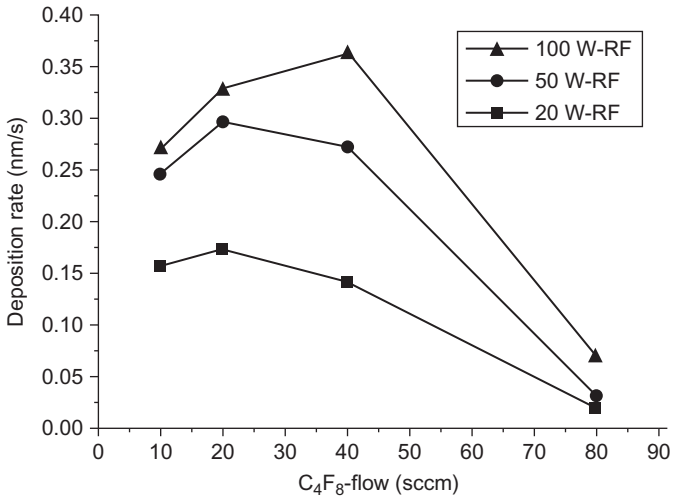


FIG. 10.13

Deposition rate for different plasma powers as a function of C_4F_8 precursor flow.

molecules only a part of them can be activated, which limits the deposition process as well. It is reported that a further increase of the deposition rate can be achieved for instance by the addition of methane (CH_4) to the process (Matsumoto and Ishida, 2000).

10.4.4 NONPLASMA-ACTIVATED CHEMICAL VAPOR DEPOSITION

Vacuum deposition processes that use gas discharge plasmas, such as assisted evaporation, sputtering, and PECVD are not suited to obtain organic layers with well-defined chemical structure like polymers. The high energies of particles in gas discharges of up to some 10 eV (some 100 eV for reflected ions) (Frey, 1995) and UV radiation damage the organic material in the gas phase and in the growing layers. For the preparation of layers with a typical polymer molecular structure (long chains of monomer molecules) using CVD processes, other ways for activating the polymerization reactions have to be used. Possibilities, therefore, are activations by thermal or chemical processes. Activation by UV light is also known (Ruiz et al., 2010).

A good example for a CVD process with thermal excitation of the precursor is the deposition of poly-para-xylylene (parylene). For different applications various derivatives of this material are available. Parylene N is the nonmodified poly-para-xylylene. Parylene types C and D are modified with chlorine atoms to gain a more dense coating for applications like diffusion barriers, while parylene type AF-4 is modified

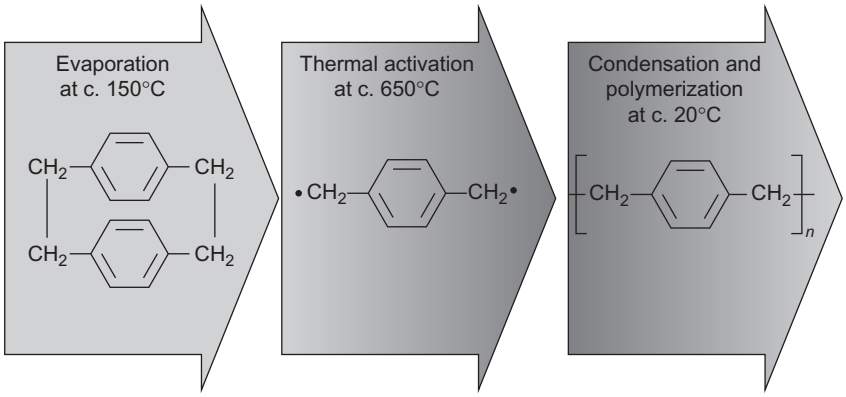


FIG. 10.14

Scheme of the polymerization process of poly-para-xylylene (Neubert et al., 2011a).

with fluorine and generates hydrophobic surfaces. Typical applications for parylene layers are diffusion barriers (Ke et al., 2004), biocompatible layers in the medical field (Li et al., 2011b), and corrosion protective layers for electrical devices (Cieslik et al., 2011).

For the parylene deposition process the dimer molecules (di-paraxylylene) are evaporated in vacuum at temperatures of about 150°C. The vapor is then heated further (up to 650°C) to create radicals. The condensation of these radicals on surfaces at room temperature and low pressures leads to a polymerization process (Fig. 10.14).

Important aspects of these types of deposition process are that the layers are very uniform and dense (Fortin and Lu, 2004). The deposition process takes place in the whole deposition chamber. Thus the backsides and cavities of the substrates and all nonheated parts of the chamber (like vacuum pumps, other deposition sources, or pressure gauges) are being coated. The deposition rate strongly correlates with the process pressure and the substrate temperature (Fortin and Lu, 2002). The pressure is a measure for the amount of molecules in the gas phase. Thus a higher pressure causes more monomer molecules to hit the substrate. Substrate temperature influences the sticking coefficient of the monomers. Higher substrate temperatures reduce the resident time of the monomer molecules and lower their possibility to polymerize. It is also known that there are threshold temperatures above which no deposition takes place.

A possible deposition setup is sketched in Fig. 10.15. Turbomolecular pumps have water-cooled surfaces inside that are being coated by this type of deposition process. This will damage these kinds of pumps. Better suited are oil diffusion pumps in combination with nitrogen-cooled cooling traps. Similar to evaporation processes the deposition rate can be controlled by a quartz deposition controller.

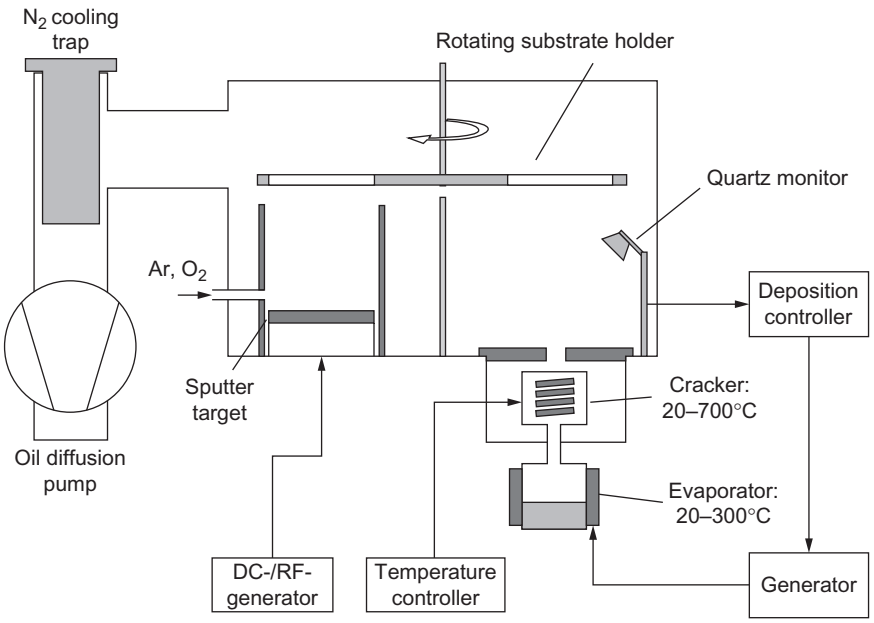


FIG. 10.15

Deposition setup for poly-para-xylylene (Neubert et al., 2011b).

The refractive index depends slightly on the type of parylene. For the nonmodified poly-para-xylylene values in the range from 1.65 to 1.67 (Fortin and Lu, 2004; Neubert et al., 2011b) are known. Absorption index with $k = 0.001$ and haze values smaller than 1% can be reached for deposition pressures below 10^{-2} mbar (Neubert et al., 2011b).

Another special type of CVD process for the deposition of polymer thin films is the so-called initiated CVD (iCVD), for example, for PMMA (Chan and Gleason, 2005; Chen and Anthamatten, 2008) or poly(glycidyl methacrylate) (PGMA) (Spee et al., 2011) thin films. For this process monomer molecules (i.e., methyl methacrylate (MMA) or glycidyl methacrylate (GMA)) and initiator molecules (i.e., organic peroxides like t-butyl peroxide (TBPO)) are used. At low pressures of a few millibars, the initiator molecules are cracked into radicals at temperatures of about 220°C at a hot zone of the reactor (i.e., a heated tube that the precursor mixtures are conducted through). At low substrate temperatures of about −15°C the gas mixture condenses and the radicals start a polymerization process. The layers are reported to be very similar to PMMA bulk material. iCVD in combination with ceramic films also turned out to be suitable for barrier layers. It is well known that polymer layers can cover defects which are present in ceramic layers. In addition the spreading of cracks in the ceramic films can be stopped by the organic interlayers. On the other hand, ceramic layers have an intrinsically good barrier property; therefore,

the use of multilayers can be very effective for the realization of ultra-barriers with low water vapor transmission rates.

10.4.5 ADHESION IMPROVEMENT BY PLASMA TREATMENT

Adhesion in vacuum deposition processes depends on the substrate material and its surface structure. On organic substrates and surfaces the adhesion can often be improved by special treatments to remove pollutants, to roughen the surface, or to create functional groups on the surface. Therefore, a plasma treatment in different gas atmospheres (argon, oxygen, nitrogen, etc.) can be used. These treatments can be performed under low pressure conditions by ion sources or under atmospheric conditions by dielectric barrier discharge setups (Zhang et al., 2016).

Good examples of adhesion improvement by plasma treatment are fluorocarbon surfaces or PTFE substrates. Due to their low surface energy, adhesion of thin films on these surfaces is mostly very poor. A plasma treatment of the surfaces in a hydrogen-containing atmosphere (i.e., argon with 5% hydrogen or ammonia) at low pressures of about 5×10^{-2} mbar can lead to a substitution of fluorine atoms by hydrogen (Badey et al., 1996; Neubert et al., 2012). This effect changes the surface energy and water contact angle of the surfaces and causes better adhesion. This can be used for good adhesion of metal or metal oxide thin films on PTFE substrates as well as for RF-sputtered fluorocarbon layers in optical layer stacks.

10.5 COMPOSITES

Composite materials offer ways to combine the properties of different materials. The combination of high refractive index oxides with mechanically flexible polymer layers, for example, generates layers with higher refractive index than the original polymer which remain flexible (Figs. 10.16 and 10.17). Combinations of evaporated color dyes with hard metal oxides generate decorative layers with higher wear resistance than the dye layers (Jäger, 1997).

A good way to prepare thin film composites is by parallel deposition from two sputter or evaporation deposition sources. The substrate can oscillate between the two sources, or the two sources can be focused on one substrate position. Problems occur when the deposition processes influence each other. Activated oxygen and UV radiation from a sputtering process of a metal oxide can chemically attack organic molecules. Gaseous organic substances can be decomposed by the gas discharge of a sputter target and poison the target surface. A good separation of the sources by housing and suitable gas flows can solve problems like this (Fig. 10.18).

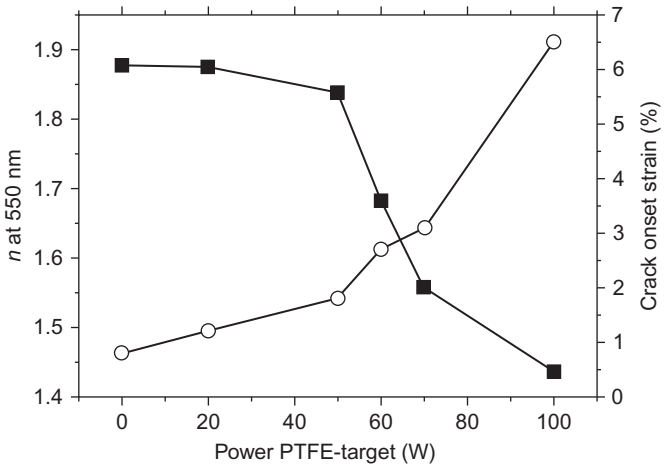


FIG. 10.16

Refractive index and crack onset strain for co-sputtered Ta_2O_5-PTFE-composite thin films (Neubert et al., 2010).

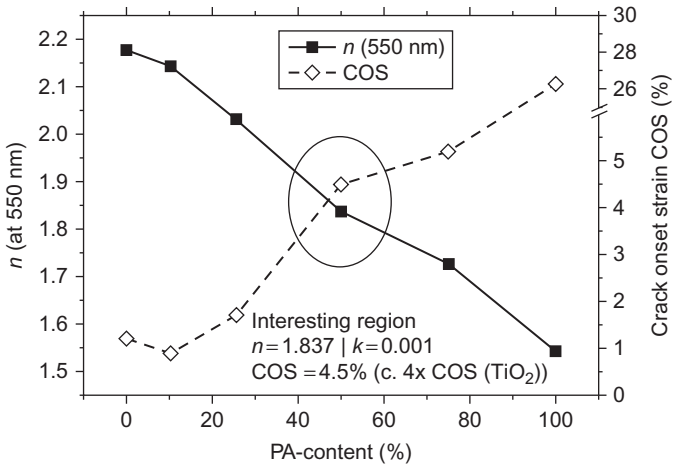


FIG. 10.17

Refractive index and crack onset strain for *co*-evaporated TiO_2-polyamide-composite thin films.

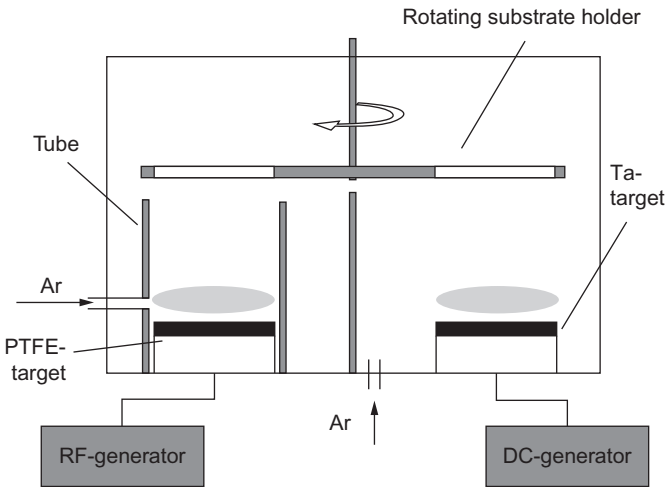


FIG. 10.18

Sketch of a sputtering setup for organic-inorganic composites (Neubert et al., 2010). *Ta-target*, Tantalum sputter target.

10.6 CONCLUSION

The vacuum deposition of organic thin films is often a difficult task. In particular the complex molecular structure can be influenced by the deposition process. Thus, depending on the coating material, the desired layer properties, the layer applications, and the substrate material, different deposition techniques are possible. We presented in this chapter an overview of various vacuum deposition techniques for organic thin films with examples for evaporation, sputter deposition, PECVD, and other CVD processes. Nevertheless the organic layer materials offer a broad spectrum of new optical, mechanical, chemical, and other properties that make them interesting to extend the usability of ceramic (oxide) layer systems or even to replace them. Besides the deposition of single organic layers, problems like adhesion and the preparation of composites were mentioned too.

Many questions within this topic remain unanswered. An interesting field for further research would be, for example, better ultra-barriers for OLED and OPV applications on flexible substrates, flexible optical thin films for tunable optical filters, switchable wettability, and the upscaling of some organic deposition processes for larger substrates.

REFERENCES

Affinito, J., Martin, P., Gross, M., Coronado, C., Greenwell, E., 1995. Vacuum deposited polymer/metal multilayer films for optical application. Thin Solid Films 270, 43–48.

Badey, J.P., Espuchet, E., Sage, D., Chabert, B., Jugnet, Y., Batier, C., Duc, T.M., 1996. Comparative study of the effects of ammonia and hydrogen plasma downstream treatment on the surface modification of polytetrafluoroethylene. Polymer 37, 1377–1386.

Bandorf, R., Waschke, S., Carreri, F.C., Vergöhl, M., Grundmeier, G., Bräuer, G., 2016. Direct metallization of PMMA with aluminum films using HIPIMS. Surf. Coat. Technol. 290, 77–81.

Bekiarov, D., Pashmakov, B., Vateva, A., 1988. A study of the adhesion of vacuum evaporated polyethylene films on aluminium. Thin Solid Films 157, 43–48.

Biederman, H., Ojha, S.M., Holland, L., 1977. The properties of fluorocarbon films prepared by r. f. sputtering and plasma polymerization in inert and active gas. Thin Solid Films 41, 329–339.

Biederman, H., Stelmashuk, V., Kholodkov, I., Choukourov, A., Slavinska, D., 2003. RF sputtering of hydrocarbon polymers and their derivatives. Surf. Coat. Technol. 174–175, 27–32.

Bodas, D.S., Gangal, S.A., 2005. Structural characterization of sputtered PMMA in argon plasma. Mater. Lett. 59, 2903–2907.

Chan, K., Gleason, K., 2005. Initiated CVD of poly(methyl methacrylate) thin films. Chem. Vap. Depos. 11, 437–443.

Chen, X., Anthamatten, M., 2008. Multicomponent vapor deposition polymerization of poly(methyl methacrylate) in an axisymmetric vacuum reactor. Polymer 49, 1823–1830.

Chiang, C.C., Wuu, D.S., Lin, H.B., Chen, Y.P., Chen, T.N., Lin, Y.C., Wu, C.C., Chen, W.C., Jaw, T.H., Horng, R.H., 2006. Deposition and permeation properties of SiN_x/parylene multilayers on polymeric substrates. Surf. Coat. Technol. 200, 5843–5848.

Choukourov, A., Hanus, J., Kousal, J., Grinevich, A., Pihosh, Y., Slavinska, D., Biederman, H., 2006. Thin polymer films from polyimide vacuum thermal degradation with and without a glow discharge. Vacuum 80, 923–929.

Cieslik, M., Engvall, K., Pan, J., Kotarba, A., 2011. Silane–parylene coating for improving corrosion resistance of stainless steel 316L implant material. Corros. Sci. 53, 296–301.

Corbella, C., Bialuch, I., Kleinschmidt, M., Bewilogua, K., 2008. Modified DLC coatings prepared in a large-scale reactor by dual microwave/pulsed-DC plasma-activated chemical vapour deposition. Thin Solid Films 517, 1125–1130.

Eritt, M., May, C., Leo, K., Toerker, M., Radehaus, C., 2010. OLED manufacturing for large area lighting applications. Thin Solid Films 518, 3042–3045.

Fortin, J.B., Lu, T.-M., 2002. A model for the chemical vapor deposition of poly(para-xylylene) (parylene) thin films. Chem. Mater. 14, 1945–1949.

Fortin, J.B., Lu, T.-M., 2004. Chemical Vapor Deposition—The Growth and Properties of Parylene Thin Films. Kluwer Academic Publishers, Dordrecht.

Frey, H., 1995. Vakuumbeschichtung 1 Plasmaphysik—Plasmadiagnostik—Analytik. VDI Verlag, Düsselforf.

Gauch, M., Ehlers, H., Ristau, D., 2014. Mixing of PTFE and oxides by sputtering techniques: a comparison of different approaches. Proc. Technol. 15, 540–548.

Gürsoy, M., Karaman, M., 2016. Hydrophobic coating of expanded perlite particles by plasma polymerization. Chem. Eng. J. 284, 343–350.

Iwama, Y., Itoh, T., Mori, T., Mizutani, T., 2006. Electroluminescent properties of organic light-emitting diodes using BAlq and Alq3 co-evaporation layer. Thin Solid Films 499, 364–368.

Jäger, S., 1997. Investigation on the optical and mechanical properties of organic dye-metal oxide composite films. Surf. Coat. Technol. 93, 58–63.

Jung, D., Yeo, S., Kim, J., Kim, B., Jin, B., Ryu, D.-Y., 2006. Formation of amine groups by plasma enhanced chemical vapor deposition and its application to DNA array technology. Surf. Coat. Technol. 200, 2886–2891.

Jaszewski, R.W., Schift, H., Schnyder, B., Schneuwly, A., Gröning, P., 1999. The deposition of anti-adhesive ultra-thin teflon-like films and their interaction with polymers during hot embossing. Appl. Surf. Sci. 143, 301–308.

Kaless, A., Schulz, U., Munzert, P., Kaiser, N., 2005. NANO-motheye antireflection pattern by plasma treatment of polymers. Surf. Coat. Technol. 200, 58–61.

Ke, L., Kumar, R.S., Zhang, K., Chua, S.-J., Weeb, A.T.S., 2004. Effect of parylene layer on the performance of OLED. Microelectron. J. 35, 325–328.

Kholodkov, I., Biederman, H., Slavinska, D., Choukourov, A., Trchova, M., 2003. Plasma polymers prepared by RF sputtering of polyethylene. Vacuum 70, 505–509.

Kinzig, B.J., Smardzewski, R.R., 1981. Plasma polymerized thin coatings from methylmethacrylate, styrene and tetrafluoroethylene. Surf. Technol. 14, 3–16.

Kousal, J., Hanus, J., Choukourov, A., Hlídek, P., Biederman, H., Slavínská, D., Zemek, J., 2005. RF magnetron sputtering and evaporation of polyisobutylene and low density polyethylene. Surf. Coat. Technol. 200, 472–475.

Kuzminova, A., Shelemin, A., Kylian, O., Petr, M., Kratochvíl, J., Solar, P., Biederman, H., 2014. From super-hydrophilic to super-hydrophobic surfaces using plasma polymerization combined with gas aggregation source of nanoparticles. Vacuum 110, 58–61.

Kylián, O., Drábik, M., Polonskyi, O., Čechvala, J., Artemenko, A., Gordeev, I., Choukourov, A., Matolínová, I., Slavínská, D., Biederman, H., 2011. Deposition of nanostructured fluorocarbon plasma polymer films by RF magnetron sputtering of polytetrafluoroethylene. Thin Solid Films 519, 6426–6431.

Lee, C.B., Uddin, A., Hu, X., Andersson, T.G., 2004. Study of Alq3 thermal evaporation rate effects on the OLED. Mater. Sci. Eng. B 112, 14–18.

Li, C., Hsieh, J.H., Hu, W.W., Lin, Y.H., 2014. Fabrication and characterization of polymethylmethacrylate (PMMA) thin film by plasma polymerization used for cell culture. Surf. Coat. Technol. 259, 20–26.

Li, L., Jones, P.M., Hisa, Y.-T., 2011a. Characterization of a nanometer-thick sputtered polytetrafluoroethylene film. Appl. Surf. Sci. 257, 4478–4485.

Li, W., Rodger, D.C., Pinto, A., Meng, E., Weiland, J.D., Humayun, M.S., Tai, Y.-C., 2011b. Parylene-based integrated wireless single-channel neurostimulator. Sensors Actuators A 166, 193–200.

Lim, J.-S., Shin, P.-K., 2007. Improved performance of organic light-emitting devices with plasma treated ITO surface and plasma polymerized methyl methacrylate buffer layer. Appl. Surf. Sci. 253, 3828–3833.

Lin, Y., Xiang, Y., Tsui, T.Y., Vlassak, J.J., 2008. PECVD low-permittivity organosilicate glass coatings: adhesion, fracture and mechanical properties. Acta Mater. 56, 4932–4943.

Martin-Palma, R.J., Gago, R., Torres-Costa, V., Fernández-Hidalgo, P., Kreissig, U., Martinez Duart, J.M., 2006. Optical and compositional analysis of functional SiOxCy:H coatings on polymers. Thin Solid Films 515, 2493–2496.

Matsumoto, Y., Ishida, M., 2000. The property of plasma-polymerized fluorocarbon film in relation to CH_4/C_4F_8 ratio and substrate temperature. Sensors Actuators 83, 179–185.

Meurisch, K., Gojdka, B., Strunskus, T., Zaporojtchenko, V., Faupel, F., 2012. Vapour phase deposition of highly crystalline self-poled piezoelectric nylon-11. J. Phys. D: Appl. Phys. 45, 055304 (+6 pp.).

Morrison, D.T., Robertson, T., 1973. RF sputtering of plastics. Thin Solid Films 15, 87–101.
Munzert, P., Schulz, U., Kaiser, N., 2003. Transparent thermoplastic polymers in plasma-assisted coating processes. Surf. Coat. Technol. 174–175, 1048–1052.
Neubert, T., Sun, W., Neumann, F., Vergöhl, M., 2007. In: Characterization of photocatalytic activity of TiO_2 thin films for optical applications.Conference Optical Interference Coatings. ThA10.
Neubert, T., Neumann, F., Vergöhl, M. Method for quantifying the photocatalytic activity of surfaces and use thereof. Patent WO 2008/046588 A1, 2008.
Neubert, T., Drost, S., Nagel, K., Vergöhl, M., 2010. In: Polymer metal oxide composite layers for optical functional coatings.Conference Proceedings Society of Vacuum Coaters, April 17–22, 2010, Orlando, USA, pp. 308–312.
Neubert, T., Gaida, A., Huwer, W., Vergöhl, M., 2011a. In: Organic materials for the use in optical layer systems.Conference Proceedings Optical Systems Design, September 5–8, 2011, Marseille, France.
Neubert, T., Gaida, A., Huwer, W., Nagel, K., Vergöhl, M., 2011b. In: Deposition of optical coatings on plastics using poly-para-xylylene.Conference Proceedings Society of Vacuum Coaters, April 16–21, Chicago, USApp. 265–269.
Neubert, T., Vergöhl, M., Strunskus, T., Faupel, F., 2012. In: Investigations on adhesion of sputtered layers on polytetrafluorethylene surfaces.Conference Proceedings Society of Vacuum Coaters, April 28–May 3, 2012, Santa Clara, USA.
F. Neumann, M. Cerezuela Barreto, 'Verfahren zum Nachweis des photokatalytischen Abbau-sorganischer Farbstoffe mittels Fluoreszenzanalyse. Patent DE102004027118B4 (2004).
Noborisaka, M., Kodama, H., Nagashima, S., Shirakura, A., Horiuchi, T., Suzuki, T., 2012. Synthesis of transparent and hard SiOC(–H) thin films on polycarbonate substrates by PECVD method. Surf. Coat. Technol. 206, 2581–2584.
Paun, I.A., Ion, V., Moldovan, A., Dinescu, M., 2011. Thin films of polymer blends deposited by matrix-assisted pulsed laser evaporation: effects of blending ratios. Appl. Surf. Sci. 257, 5259–5264.
Pihosh, Y., Biederman, H., Slavinska, D., Kousal, J., Choukourov, A., Trchova, M., Mackova, A., Boldyryeva, A., 2006. Composite SiOx/fluorocarbon plasma polymer films prepared by rf magnetron sputtering of SiO_2 and PTFE. Vacuum 81 (1), 38–44.
Piqué, A., McGill, R.A., Chrisey, D.B., Leonhardt, D., Mslna, T.E., Spargo, B.J., Callahan, J.H., Vachet, R.W., Chung, R., Bucaro, M.A., 1999. Growth of organic thin films by the matrix assisted pulsed laser evaporation (MAPLE) technique. Thin Solid Films 355–356, 536–541.
Pratt, I.H., Lausman, T.C., 1972. Some characteristics of sputtered polytetrafluoroethylene films. Thin Solid Films 10, 151–154.
Präfke, C., Schulz, U., Kaiser, N., 2012. Preparation and characterization of organic layers for UV protection of polycarbonate. Thin Solid Films 520, 4180–4183.
Ruiz, J.-C., Girard-Lauriault, P.-L., Truica-Marasescu, F., Wertheimer, M.R., 2010. Plasma and vacuum-ultraviolet (VUV) photo-polymerisation of N- and O-rich thin films. Radiat. Phys. Chem. 79, 310–314.
Schulz, U., Munzert, P., Kaiser, N., 2001. Surface modification of PMMA by DC glow discharge and microwave plasma treatment for the improvement of coating adhesion. Surf. Coat. Technol. 142–144, 507–511.

Schulz, U., Präfke, C., Munzert, P., Gödeker, C., Kaiser, N., 2011. Formation of antireflective nanostructures on melamine and *N*,*N*′-di (1-naphthyl)-*N*,*N*′-diphenyl benzidine (NPB). Opt. Mater. Exp. (1), 101–107.

Schwarz, J., Schmidt, M., Ohl, A., 1998. Synthesis of plasma-polymerized hexamethyldisiloxane (HMDSO) films by microwave discharge. Surf. Coat. Technol. 98, 859–864.

Sellinger, A.T., Martin, A.H., Fitz-Gerald, J.M., 2008. Effect of substrate temperature on poly(methyl methacrylate) nanocomposite thin films deposited by matrix assisted pulsed laser evaporation. Thin Solid Films 516, 6033–6040.

Singh, B., Bouchet, J., Rochat, G., Leterrier, Y., Månson, J.-A.E., Fayet, P., 2007. Ultra-thin hybrid organic/inorganic gas barrier coatings on polymers. Surf. Coat. Technol. 201, 7107–7114.

Spassova, E., Jivkov, I., Danev, G., Dimitrova, T., Koprinarova, J., Paskaleva, A., 1996. Low-permittivity evaporated polymer-polyimide. Vacuum 47, 1345–1346.

Spee, D.A., Bakker, R., van der Werf, C.H.M., van Steenbergen, M.J., Rath, J.K., Schropp, R.E.I., 2011. Polymer layers by initiated chemical vapor deposition for thin film gas barrier encapsulation. Thin Solid Films 519, 4479–4482.

Stelmashuk, V., Biederman, H., Slavinska, D., Trchova, M., Hlidek, P., 2004. Rf magnetron sputtering of polypropylene. Vacuum 75, 207–215.

Takahashi, K., Itoh, A., Nakamura, T., Tachibana, K., 2000. Radical kinetics for polymer film deposition in fluorocarbon (C_4F_8, C_3F_6 and C_5F_8) plasmas. Thin Solid Films 374, 303–310.

Weber, M.F., 2012. Recent advances in multilayer polymeric interference reflectors.Conference Proceedings Society of Vacuum Coaters.

Zhang, H., Li, H., Fang, M., Wang, Z., Sang, L., Yang, L., Chen, Q., 2016. Roll-to-roll DBD plasma pretreated polyethylene web for enhancement of al coating adhesion and barrier property. Appl. Surf. Sci. 388, 539–545.

Zhao, F., Zhu, L., Liu, Y., Wang, Y., Ma, D., 2015. Doping-free hybrid white organic light-emitting diodes with fluorescent blue, phosphorescent green and red emission layers. Org. Electron. 27, 207–211.

Zenasni, A., Raynaud, P., Sahli, S., Rebiai, S., Segui, Y., 2003. Investigation on the origin of dielectric constant evolution in films deposited from organosilicon molecules in microwave DECR plasma reactor. Surf. Coat. Technol. 174–175, 162–165.

This page intentionally left blank

CHAPTER

11 Surface multiplasmonics with periodically nonhomogeneous thin films

Muhammad Faryad[a], **Akhlesh Lakhtakia**

Department of Engineering Science and Mechanics, The Pennsylvania State University, University Park, PA, United States

11.1 INTRODUCTION

The emerging area of *surface multiplasmonics* deals with the excitation and the propagation of multiple surface plasmon-polariton (SPP) waves—all of the same frequency, but different phase speeds, attenuation rates, and spatial profiles of fields—guided by the planar interface of a metal and a periodically nonhomogeneous dielectric material (Lakhtakia, 2011).

This chapter contains an overview of boundary-value problems relevant to the propagation and excitation of multiple SPP waves guided by the interface of a metal and a periodically nonhomogeneous dielectric material that is either a rugate filter or a sculptured nematic thin film (SNTF). Rugate filters are isotropic, but SNTFs are anisotropic. A brief history of surface multiplasmonics is presented in Section 11.2. In Section 11.3, the fabrication techniques and the permittivity profiles of rugate filters and SNTFs are presented. The theoretical formulation of a general canonical boundary-value problem of SPP-wave propagation guided by the planar interface of (i) a semiinfinite, periodically nonhomogeneous, anisotropic, dielectric material and (ii) a semiinfinite metal is presented in Section 11.4.1. Representative numerical results are presented in Sections 11.4.2 and 11.4.3, respectively, for the metal/rugate-filter interface and the metal/SNTF interface. Illustrative numerical results showing the excitation of multiple SPP waves in the grating-coupled configuration and a prism-coupled configuration called the Turbadar-Kretschmann-Raether (TKR) configuration. are discussed, respectively, in Sections 11.5 and 11.6 for both the metal/rugate-filter and the metal/SNTF interfaces. The numerical results presented here are a representative subset of those presented in journal publications. Significant conclusions drawn from the numerical results are provided in

[a]Department of Physics, Lahore University of Management Sciences, Lahore, Pakistan

Optical Thin Films and Coatings. https://doi.org/10.1016/B978-0-08-102073-9.00011-4
Copyright © 2018 Elsevier Ltd. All rights reserved.

Section 11.7. Finally, a few suggestions and resources for future work are presented in Sections 11.8 and 11.9, respectively.

An $\exp(-i\omega t)$ time-dependence is implicit, with ω denoting the angular frequency, t as time, and $i = \sqrt{-1}$. Explicit dependencies of various quantities on ω are suppressed throughout the chapter. The free-space wavenumber, the free-space wavelength, and the intrinsic impedance of free space are denoted by $k_0 = \omega\sqrt{\epsilon_0\mu_0}$, $\lambda_0 = 2\pi/k_0$, and $\eta_0 = \sqrt{\mu_0/\epsilon_0}$, respectively, with μ_0 and ϵ_0 being the permeability and permittivity of free space. For all the numerical results reported in this chapter, $\lambda_0 = 633$ nm was fixed. Vectors are in boldface, dyadics are underlined twice, column 4-vectors are in boldface and enclosed within square brackets, and 4×4 matrixes are underlined twice and enclosed within square brackets. The 4×4 identity matrix is denoted by $[\underline{\underline{I}}]$. Cartesian unit vectors are identified as $\hat{\mathbf{u}}_x$, $\hat{\mathbf{u}}_y$, and $\hat{\mathbf{u}}_z$.

11.2 HISTORICAL DEVELOPMENT

Until 2008—barring a few scattered reports on the evidence of *s*-polarized SPP waves (Gaspar-Armenta and Villa, 2003; Salamon et al., 1997; Salamon and Tollin, 2001)—it was conventional wisdom that, at a specific frequency, only one SPP wave, that too of the *p*-polarization state, can be guided by an interface of a metal and a dielectric material. This belief was held because the solution of a canonical boundary-value problem (Maier, 2007; Dragoman and Dragoman, 2008) shows that only one SPP wave can propagate guided by the interface if the partnering dielectric material is isotropic and homogeneous. The same conclusion holds true even if that material is anisotropic (Borstel and Falge, 1982; Wallis, 1982; Elston and Sambles, 1990; Wang, 1995; Yan et al., 2007; Abdulhalim, 2009). However, SPP waves guided by the interface of a metal and a periodically nonhomogeneous dielectric material exhibit remarkable characteristics (Polo and Lakhtakia, 2011).

In 2008, it was predicted theoretically (Motyka and Lakhtakia, 2008, 2009) that more than one SPP waves—with different phase speeds, attenuation rates, and field distributions, but all of the same frequency—can propagate in a specific direction, guided by the interface of a metal and a periodically nonhomogeneous SNTF. An SNTF is a dielectric material that is anisotropic and periodically nonhomogeneous in the thickness direction (which is normal to the waveguiding interface) (Lakhtakia and Messier, 2005). This theoretical prediction was later verified experimentally (Lakhtakia et al., 2009). Shortly afterward, it was also found, both theoretically (Lakhtakia, 2007; Polo and Lakhtakia, 2010a,b) and experimentally (Devender et al., 2009; Gilani et al., 2010; Erten, 2011), that multiple SPP waves can also be guided in a specific direction by an interface of a metal and a chiral sculptured thin film (STF). A chiral STF is also a dielectric material that is anisotropic and periodically nonhomogeneous in the thickness direction (Lakhtakia and Messier, 2005).

In all of these studies, the partnering dielectric materials were anisotropic in addition to being periodically nonhomogeneous in the direction normal to the waveguiding interface. However, it has been shown by the solution of the canonical boundary-value problem that multiple SPP waves can still be guided if the partnering (periodically nonhomogenous) dielectric material is isotropic (Faryad and Lakhtakia, 2010b).

Furthermore, multiple SPP waves can be excited in the TKR (Turbadar, 1959; Otto, 1968; Kretschmann and Raether, 1968) and the grating-coupled configurations with the partnering periodically nonhomogeneous dielectric material being either isotropic (Faryad and Lakhtakia, 2011e,c) or anisotropic (Faryad and Lakhtakia, 2011d). Moreover, the coupling of two interfaces of a metal and a periodically nonhomogeneous dielectric material—the Sarid configuration (Sarid, 1981)—has also been shown to increase the number of SPP waves (Jen et al., 2009; Jen and Yu, 2011; Faryad and Lakhtakia, 2010a,c; Faryad, 2012). Parenthetically, let us note that not all the SPP waves predicted by the theoretical investigations on the canonical boundary-value problem can be excited with a finitely thick partnering dielectric material (Polo et al., 2011); the thickness of the partnering dielectric material could be impractically large for some SPP waves to be excited.

SPP waves are widely used for sensing chemicals and biochemicals (Homola, 2006; Abdulhalim et al., 2008). Furthermore, SPP imaging systems are used for high-throughput analysis of biomolecular interactions—for proteomics, drug discovery, and pathway elucidation (Abdulhalim et al., 2007; Usui-Aoki et al., 2005). SPP-based imaging technology has been successfully applied to the screening of bioaffinity interactions with DNA, carbohydrates, peptides, phage display libraries, and proteins (Kanda et al., 2005). SPP-based imaging techniques are also going to be useful for lithography (Maier, 2007; Kik et al., 2002). Finally, as SPP waves can be excited in the terahertz and optical regimes, they may be useful for high-speed communication of information on computer chips (Maier et al., 2001). Whereas conventional wires are very attenuative at frequencies beyond a few tens of gigahertz, ohmic losses are minimal for plasmonic transmission (Dragoman and Dragoman, 2008), which enables long-range communications (Berini, 2009). Recently, SPP waves have been found to be useful for light-harvesting applications in thin-film solar cells due to the coupling of a part of the incident light with the SPP waves (Ferry et al., 2008).

That multiple SPP waves can be launched provide exciting prospects for enhancing the scope of the applications of SPP waves. For sensing applications, the use of more than one distinct SPP waves would increase confidence in a reported measurement; also, more than one analyte could be sensed at the same time, thereby increasing the capabilities of multianalyte sensors (Mackay and Lakhtakia, 2010b, 2012). For imaging applications, the simultaneous creation of two images may become possible. For plasmonic communications, the availability of multiple channels would make information transmission more reliable as well as enhance capacity. Moreover,

light absorption can be enhanced further in thin-film solar cells by the use of multiple SPP waves (Faryad and Lakhtakia, 2011b).

11.3 PERIODICALLY NONHOMOGENEOUS DIELECTRIC MATERIALS

Multiple SPP waves have been found to be guided by an interface of a metal and a dielectric material that is periodically nonhomogeneous normal to the SPP-wave-guiding interface (Faryad, 2012). One type of each of such isotropic and anisotropic dielectric materials is described in brief in the following sections.

11.3.1 RUGATE FILTERS

Rugate filters are isotropic dielectric thin films that have continuously varying and periodic refractive index along the thickness direction (Bovard, 1993). A multilayered structure with a large number of sufficiently thin layers made of isotropic dielectric materials of different refractive indexes may also be classified as a rugate filter (Bovard, 1993). Rugate filters find applications as optical filters (Baumeister, 2004) and light-trapping layers in thin-film solar cells (Fahr et al., 2008).

Rugate filters can be fabricated with various physical- and chemical-deposition techniques. Physical-deposition techniques include cluster-beam deposition (Overend et al., 1992), magnetron sputtering (Zhang et al., 2011), and ion-beam sputtering (Lee et al., 2006), whereas chemical-deposition techniques include molecular assembly (Nolte et al., 2004) and electrolysis (Lorenzo et al., 2005). Rugate-filter technology is very sophisticated nowadays in suppressing sidebands and reducing the impact of impedance mismatch on either pupil of a rugate filter (Lorenzo et al., 2005; Perilloux, 2002), but these issues are not of direct relevance in this chapter.

The relative permittivity of a rugate filter with sinusoidally changing permittivity along the z axis—designated as parallel to the thickness direction—is given by

$$\epsilon_{\text{rug}}(z) = \left[\left(\frac{n_\text{b} + n_\text{a}}{2} \right) + \left(\frac{n_\text{b} - n_\text{a}}{2} \right) \sin\left(\pi \frac{z}{\Omega} \right) \right]^2, \tag{11.1}$$

where n_a and n_b are the lowest and the highest indexes of refraction, respectively, and 2Ω is the period. For the numerical results presented in this chapter, the minimum and maximum indexes of refraction of the rugate filter were fixed as follows (Baumeister, 2004): $n_\text{a} = 1.45$ and $n_\text{b} = 2.32$.

11.3.2 SCULPTURED NEMATIC THIN FILMS

An STF is an assembly of parallel columns of nanoscale cross-sectional diameter, all columns being of the same shape. Shortly after the conceptualization of helicoidal bianisotropic mediums in 1993 (Lakhtakia and Weiglhofer, 1993), the basis of

realizing these materials using thin-film technology was enunciated (Lakhtakia and Messier, 1994). The general concept of STFs was presented in August 1995 by Lakhtakia and Messier to a group of thin-film researchers assembled at Penn State (Lakhtakia et al., 1996). The topic has enjoyed considerable growth in the ensuing years, chiefly in theory initially, but now in experiments and applications as well (Lakhtakia and Messier, 2005; Lakhtakia and Geddes, 2010).

STFs are commonly grown using physical vapor deposition (PVD), where a directional vapor flux is incident on a substrate, which could be fixed, rotating and/or rocking. Under the right temperature and pressure, a film grows with columns whose shape is determined by the motion of the substrate. PVD methods adapted to grow STFs include thermal evaporation (Young and Kowal, 1959; Robbie et al., 1995), electron-beam evaporation (Messier et al., 1997), sputtering (Sit et al., 1999; Messier et al., 2000), pulsed laser deposition (Vick et al., 1999), and physico-chemical vapor deposition (Pursel et al., 2005; Wei et al., 2010). The interested reader is referred to Martín-Palma and Lakhtakia (2010) for a crash course on PVD techniques and to Martin (2010) for detailed treatments.

Macroscopically, for optical purposes, an STF is a material continuum that is periodically nonhomogeneous in a fixed direction. STFs of three types have been considered thus far in the literature on surface multiplasmonics:

(i) columnar thin film (CTF), in which all columns are parallel to a straight line;
(ii) SNTF, in which the shape of each column is described by the same two-dimensional curve in space; and
(iii) chiral STF, in which each column is described by the same helix.

For the illustrative numerical results presented in this chapter, only periodically nonhomogeneous SNTFs were considered.

While an SNTF is grown, the substrate is only rocked about a tangential axis (Messier et al., 1997). The nature of the rocking defines the shape of the columns of the film and hence its macroscopic electromagnetic properties. The plane in which the columnar shape lies is the morphologically significant plane of the SNTF.

As the z axis is parallel to the thickness direction, a periodically nonhomogeneous SNTF's permittivity dyadic is of the form (Lakhtakia et al., 2009; Motyka and Lakhtakia, 2008, 2009)

$$\underline{\underline{\epsilon}}_{\text{SNTF}}(z) = \epsilon_0 \, \underline{\underline{S}}_y(z) \cdot \underline{\underline{\epsilon}}^{\circ}_{\text{ref}}(z) \cdot \underline{\underline{S}}_y^{-1}(z), \tag{11.2}$$

where the dyadics

$$\left.\begin{aligned} \underline{\underline{S}}_y(z) &= (\hat{\mathbf{u}}_x\hat{\mathbf{u}}_x + \hat{\mathbf{u}}_z\hat{\mathbf{u}}_z)\cos[\chi(z)] + (\hat{\mathbf{u}}_z\hat{\mathbf{u}}_x - \hat{\mathbf{u}}_x\hat{\mathbf{u}}_z)\sin[\chi(z)] + \hat{\mathbf{u}}_y\hat{\mathbf{u}}_y \\ \underline{\underline{\epsilon}}^{\circ}_{\text{ref}}(z) &= \epsilon_{\text{a}}(z)\,\hat{\mathbf{u}}_z\hat{\mathbf{u}}_z + \epsilon_{\text{b}}(z)\,\hat{\mathbf{u}}_x\hat{\mathbf{u}}_x + \epsilon_{\text{c}}(z)\,\hat{\mathbf{u}}_y\hat{\mathbf{u}}_y \end{aligned}\right\} \tag{11.3}$$

depend on the vapor flux angle $\chi_v(z) = \chi_v(z \pm 2\Omega)$ with respect to the substrate (xy) plane, and 2Ω is the period. In this chapter, $\chi_v(z) = \widetilde{\chi}_v + \delta_v \sin(\pi z/\Omega)$ varies sinusoidally about the mean value $\widetilde{\chi}_v$ with period 2Ω. The dyadic $\underline{\underline{S}}_y(z)$ is a rotation dyadic that describes the tilt of the columns of the SNTF at a given value of z. The tilt angle

$\chi(z)$ with respect to the substrate plane depends upon the vapor flux angle $\chi_v(z)$. The quantities $\epsilon_a(z')$, $\epsilon_b(z')$, and $\epsilon_c(z')$ are the eigenvalues of $\underline{\underline{\epsilon}}^{\circ}_{ref}(z')$—and hence of $\underline{\underline{\epsilon}}_{SNTF}(z')$—and should be interpreted as the principal relative permittivity scalars in the plane $z = z'$ (Mackay and Lakhtakia, 2010a). These three quantities and $\chi(z')$ depend on $\chi_v(z')$, the conditions for the fabrication of the SNTF, and the material (s) evaporated to fabricate the SNTF—and therefore need to be found experimentally.

For all the numerical results presented in this chapter, an SNTF made of titanium oxide was considered. The parameters of a CTF of titanium oxide were found experimentally by Hodgkinson et al. (1998), but the same have been used for an SNTF in surface multiplasmonics in the absence of more realistic data. These parameters for $\lambda_0 = 633$ nm are (Motyka and Lakhtakia, 2008)

$$\left.\begin{array}{l} \epsilon_a(z) = [1.0443 + 2.7394v(z) - 1.3697v^2(z)]^2 \\ \epsilon_b(z) = [1.6765 + 1.5649v(z) - 0.7825v^2(z)]^2 \\ \epsilon_c(z) = [1.3586 + 2.1109v(z) - 1.0554v^2(z)]^2 \\ \chi(z) = \tan^{-1}[2.8818\tan\chi_v(z)] \end{array}\right\}, \tag{11.4}$$

where $v(z) = 2\chi_v(z)/\pi$. Recent evidence indicates that the relationships are likely to be more complicated for SNTFs (Swiontek et al., 2013), but the ones used so far should suffice for illustration.

11.4 CANONICAL BOUNDARY-VALUE PROBLEM

The canonical boundary-value problem when both partnering materials are isotropic is straightforward because field representations on both sides of the planar interface are of the textbook kind (Uller, 1903; Zenneck, 1907; Simon et al., 1975). Field representation is not simple in a periodically nonhomogeneous half-space (Lakhtakia, 2010). A matrix procedure devised by Martorell et al. (2006) for a periodically piecewise homogeneous half-space was adapted by Lakhtakia and Polo (2007) to formulate the canonical problem, first, for surface waves called Dyakonov-Tamm waves and, then, for surface multiplasmonics (Polo and Lakhtakia, 2009b; Faryad et al., 2010; Faryad and Lakhtakia, 2010b).

11.4.1 THEORETICAL FORMULATION

Suppose the half-space $z < 0$ is occupied by a homogeneous metal of relative permittivity ϵ_{met}, while the half-space $z > 0$ is occupied by a linear anisotropic dielectric material (Weiglhofer and Lakhtakia, 2003; Mackay and Lakhtakia, 2008) that is periodically nonhomogeneous along the z axis. The frequency-domain constitutive relations of the periodically nonhomogeneous partnering material are written in vector-dyadic notation as

$$\mathbf{D}(\mathbf{r}) = \underline{\underline{\epsilon}}(z) \cdot \mathbf{E}(\mathbf{r}) \tag{11.5}$$

and

$$\mathbf{B}(\mathbf{r}) = \mu_0 \mathbf{H}(\mathbf{r}), \tag{11.6}$$

where

$$\underline{\underline{\epsilon}}(z \pm 2\Omega) = \underline{\underline{\epsilon}}(z) \tag{11.7}$$

and 2Ω is the period.

Let the SPP wave propagate in the xy plane along the direction which makes an angle $\psi \in [0, 2\pi)$ with respect to the x axis, and attenuate as $z \to \pm\infty$. The electromagnetic field phasors in the metal may be written as

$$\mathbf{E}(\mathbf{r}) = \left[a_p \left(\frac{\alpha_{\text{met}}}{k_0} \, \hat{\mathbf{u}}_1 + \frac{\kappa}{k_0} \, \hat{\mathbf{u}}_z \right) + a_s \, \hat{\mathbf{u}}_2 \right] \exp\left(i \mathbf{k}_{\text{met}} \cdot \mathbf{r} \right), \quad z \leq 0, \tag{11.8}$$

and

$$\mathbf{H}(\mathbf{r}) = \eta_0^{-1} \left[-a_p \, \epsilon_{\text{met}} \, \hat{\mathbf{u}}_2 + a_s \left(\frac{\alpha_{\text{met}}}{k_0} \, \hat{\mathbf{u}}_1 + \frac{\kappa}{k_0} \, \hat{\mathbf{u}}_z \right) \right] \exp\left(i \mathbf{k}_{\text{met}} \cdot \mathbf{r} \right), \quad z \leq 0, \tag{11.9}$$

where

$$\mathbf{k}_{\text{met}} = \kappa \, \hat{\mathbf{u}}_1 - \alpha_{\text{met}} \, \hat{\mathbf{u}}_z, \tag{11.10}$$

$$\kappa^2 + \alpha_{\text{met}}^2 = k_0^2 \, \epsilon_{\text{met}}, \tag{11.11}$$

$$\hat{\mathbf{u}}_1 = \hat{\mathbf{u}}_x \cos\psi + \hat{\mathbf{u}}_y \sin\psi, \tag{11.12}$$

$$\hat{\mathbf{u}}_2 = -\hat{\mathbf{u}}_x \sin\psi + \hat{\mathbf{u}}_y \cos\psi, \tag{11.13}$$

κ is a complex-valued scalar such that $\omega/\text{Re}(\kappa)$ is the phase speed, and $\text{Im}(\alpha_{\text{met}}) > 0$ for attenuation as $z \to -\infty$. Furthermore, a_p and a_s are unknown scalars with the subscripts p and s, respectively, denoting the parallel and perpendicular polarization states with respect to the plane formed by $\hat{\mathbf{u}}_1$ and $\hat{\mathbf{u}}_z$. The field representation (Eqs. 11.8–11.13) is of the textbook kind.

The field representation in the half-space $z \geq 0$ is more complicated. For all $z \in (-\infty, \infty)$, let us define the fields $\mathbf{e}(z)$ and $\mathbf{h}(z)$ via

$$\left. \begin{aligned} \mathbf{E}(\mathbf{r}) &= \mathbf{e}(z) \, \exp\left[i\kappa (x\cos\psi + y\sin\psi) \right] \\ \mathbf{H}(\mathbf{r}) &= \mathbf{h}(z) \, \exp\left[i\kappa (x\cos\psi + y\sin\psi) \right] \end{aligned} \right\}. \tag{11.14}$$

Substitution of this representation in the frequency-domain Faraday and Ampère-Maxwell equations and the subsequent use of the constitutive relations (11.5), (11.6) yields two algebraic and four differential equations. The algebraic equations allow the components $e_z(z)$ and $h_z(z)$ to be expressed in terms of the column 4-vector

$$[\mathbf{f}(z)] = [\, e_x(z) \;\; e_y(z) \;\; h_x(z) \;\; h_y(z) \,]^T \tag{11.15}$$

which satisfies the matrix ordinary differential equation

$$\frac{d}{dz}[\mathbf{f}(z)] = i \left[\underline{\underline{P}}(z) \right] \cdot [\mathbf{f}(z)], \quad z > 0, \tag{11.16}$$

where the 4×4 matrix $\left[\underline{\underline{P}}(z) \right]$ is a periodic function of z such that

$$\left[\underline{\underline{P}}(z\pm 2\Omega)\right]=\left[\underline{\underline{P}}(z)\right]. \tag{11.17}$$

By virtue of the Floquet-Lyapunov theorem (Yakubovich and Starzhinskii, 1975), the solution of the matrix ordinary differential equation (11.16) has to be of the form

$$[\mathbf{f}(z)]=\left[\underline{\underline{F}}(z)\right]\cdot\exp\left\{iz\left[\underline{\underline{\widetilde{Q}}}\right]\right\}\cdot[\mathbf{f}(0+)], \tag{11.18}$$

where

$$\left[\underline{\underline{F}}(z\pm 2\Omega)\right]=\left[\underline{\underline{F}}(z)\right] \tag{11.19}$$

is a periodic 4×4 matrix with $\left[\underline{\underline{F}}(0)\right]=\left[\underline{\underline{I}}\right]$, and $\left[\underline{\underline{\widetilde{Q}}}\right]$ is a 4×4 matrix independent of z.

Without resorting to the Floquet-Lyapunov theorem, the solution of Eq. (11.16) must lead to the relation

$$[\mathbf{f}(2\Omega)]=\left[\underline{\underline{Q}}\right]\cdot[\mathbf{f}(0+)], \tag{11.20}$$

where the 4×4 matrix $\left[\underline{\underline{Q}}\right]$ can be computed by the piecewise-uniform-approximation method (Lakhtakia and Messier, 2005) as follows. After choosing a sufficiently large number N, the following quantities are defined:

$$\left.\begin{aligned} z_n &= 2\Omega\frac{n}{N}\\ \left[\underline{\underline{W}}_n\right] &= \exp\left\{i\frac{2\Omega}{N}\left[\underline{\underline{P}}\left(\frac{z_{n-1}+z_n}{2}\right)\right]\right\}\end{aligned}\right\},\quad n\in[1,\infty). \tag{11.21}$$

Then, the approximation

$$\left[\underline{\underline{Q}}\right]\cong\left[\underline{\underline{W}}_N\right]\cdot\left[\underline{\underline{W}}_{N-1}\right]\cdot\cdots\cdot\left[\underline{\underline{W}}_2\right]\cdot\left[\underline{\underline{W}}_1\right] \tag{11.22}$$

should be adequate, provided that the thickness $2\Omega/N$ is sufficiently small.

Comparison of Eqs. (11.18), (11.20) yields the identity

$$\left[\underline{\underline{Q}}\right]=\exp\left\{i2\Omega\left[\underline{\underline{\widetilde{Q}}}\right]\right\}. \tag{11.23}$$

Both $\left[\underline{\underline{Q}}\right]$ and $\left[\underline{\underline{\widetilde{Q}}}\right]$ share the same eigenvectors, and their eigenvalues are also related as follows. Let $\left[\mathbf{t}^{(m)}\right]$, $m\in[1,4]$, be the eigenvector corresponding to the mth eigenvalue σ_m of $\left[\underline{\underline{Q}}\right]$; then, the corresponding eigenvalue α_m of $\left[\underline{\underline{\widetilde{Q}}}\right]$ is given by

$$\alpha_m=-i\frac{\ln(\sigma_m)}{2\Omega},\quad m\in[1,4]. \tag{11.24}$$

The admissible values of κ for SPP-wave propagation are such that all four eigenvalues of $\left[\underline{\underline{\widetilde{Q}}}\right]$ have nonzero imaginary parts. These four eigenvalues are labeled such that $\mathrm{Im}[\alpha_1]>0$, $\mathrm{Im}[\alpha_2]>0$, $\mathrm{Im}[\alpha_3]<0$, and $\mathrm{Im}[\alpha_4]<0$. As the third and the fourth eigenvalues of $\left[\underline{\underline{\widetilde{Q}}}\right]$ describe fields that amplify as $z\to\infty$, it follows that

$$[\mathbf{f}(0+)] = \sum_{m=1}^{2} \tau_m \left[\mathbf{t}^{(m)}\right], \tag{11.25}$$

with τ_1 and τ_2 as unknown scalars (Lakhtakia, 2010).

Satisfaction of the usual boundary conditions across the interface $z = 0$ demands that

$$[\mathbf{f}(0+)] = [\mathbf{f}(0-)], \tag{11.26}$$

where the boundary values $[\mathbf{f}(0\pm)]$ can be obtained using Eqs. (11.8), (11.9), (11.14). Eq. (11.26) may be rearranged as

$$\left[\underline{\underline{M}}(\kappa)\right] \cdot \begin{bmatrix} \tau_1 \\ \tau_2 \\ a_s \\ a_p \end{bmatrix} = \begin{bmatrix} 0 \\ 0 \\ 0 \\ 0 \end{bmatrix}. \tag{11.27}$$

The dispersion equation for SPP-wave propagation is then as follows:

$$\det\left[\underline{\underline{M}}(\kappa)\right] = 0. \tag{11.28}$$

The solution of the dispersion equation (11.28) is independent of the value of ψ when the partnering dielectric material is isotropic.

11.4.2 METAL/RUGATE-FILTER INTERFACES

For illustrative numerical results, let us begin with the simpler of the two cases chosen for the dielectric partnering material, that is, a rugate filter with relative permittivity given by Eq. (11.1). Then the 4×4 matrix $[\underline{\underline{P}}(z)]$ of Eq. (11.16) is

$$[\underline{\underline{P}}(z)] = \omega \begin{bmatrix} 0 & 0 & 0 & \mu_0 \\ 0 & 0 & -\mu_0 & 0 \\ 0 & -\epsilon_0\,\epsilon_{\rm rug}(z) & 0 & 0 \\ \epsilon_0\,\epsilon_{\rm rug}(z) & 0 & 0 & 0 \end{bmatrix} + \frac{\kappa^2}{\omega\epsilon_0\epsilon_{\rm rug}(z)\mu_0} \begin{bmatrix} 0 & 0 & 0 & -\mu_0 \\ 0 & 0 & 0 & 0 \\ 0 & \epsilon_0\epsilon_{\rm rug}(z) & 0 & 0 \\ 0 & 0 & 0 & 0 \end{bmatrix}. \tag{11.29}$$

Faryad and Lakhtakia (2010b) fixed $\epsilon_{\rm met} = -56 + 21i$ (bulk aluminum) and $\underline{\underline{\epsilon}}(z) = \epsilon_{\rm rug}(z)\underline{\underline{I}}$, but kept Ω variable. The solutions of the dispersion equation, computed using the Newton-Raphson method (Jaluria, 1996) for $0.005 \leq \Omega/\lambda_0 \leq 2$ and $\kappa/k_0 > 1.0$, are shown in Fig. 11.1. These solutions are organized in 16 branches: eight branches labeled as $s1$–$s8$ represent SPP waves of the s-polarization state and eight branches labeled as $p1$–$p8$ represent SPP waves of the p-polarization state. The gaps in branches $p7$, $s4$, and $s8$ are not numerical artifacts, each gap being accompanied by a discontinuity in $\text{Im}(\kappa/k_0)$.

Clearly from Fig. 11.1, more than one SPP wave can propagate in a specific direction in the xy plane for $\Omega \geq 0.145\lambda_0$. These SPP waves have different phase speeds $\omega/\text{Re}(\kappa)$ and attenuation rates $1/\text{Im}(\kappa)$. As both partnering materials are isotropic, this multiplicity is due to the periodic nonhomogeneity of the dielectric partnering

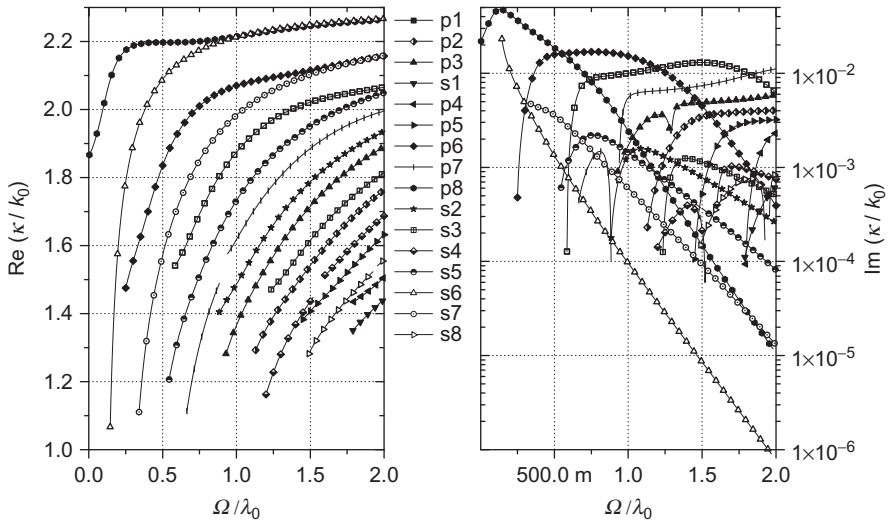


FIG. 11.1

Real (*left*) and imaginary (*right*) parts of κ/k_0 as functions of Ω/λ_0 for SPP-wave propagation guided by the planar interface of bulk aluminum and a rugate filter in the canonical boundary-value problem. The rugate filter is described by Eq. (11.1) with $n_a = 1.45$ and $n_b = 2.32$. Most but not all solutions have been captured in this figure (after Faryad and Lakhtakia, 2010b).

material (i.e., the rugate filter). Although the observability of two SPP waves—one of either linear polarization state—when the partnering dielectric material is periodically nonhomogeneous in a piecewise uniform fashion has recently been established numerically for the Sarid and TKR configurations (Jen et al., 2009), the solution of the canonical boundary-value problem not only provides necessary mathematical rigor but also shows that the number of simultaneously excitable SPP waves can exceed two. Moreover, the possibility of solutions of the dispersion equation with $\text{Re}(\kappa/k_0) \in [1, n_a)$ shows that the SPP waves with high phase speed can also be guided by the metal/rugate-filter interface. Very recently, even solutions with $\text{Re}(\kappa/k_0) < 1$ have been found, but their fields are very weakly localized in the rugate filter to the interface (Atalla et al., 2012).

Representative plots of the Cartesian components of the time-averaged Poynting vector

$$\mathbf{P}(x,z) = \frac{1}{2}\,\text{Re}\left[\mathbf{E}(x,z) \times \mathbf{H}^{*}(x,z)\right] \tag{11.30}$$

along the line $\{x = 0, y = 0\}$ are given in Fig. 11.2 as functions of z for one solution on the branch $s2$: $\Omega = \lambda_0$. The data were computed by setting $a_s = 1$ V/m. The plots show quite strong localization of the SPP wave to the interface. Moreover, the SPP wave is carrying energy along the x axis because the y- and z-components of

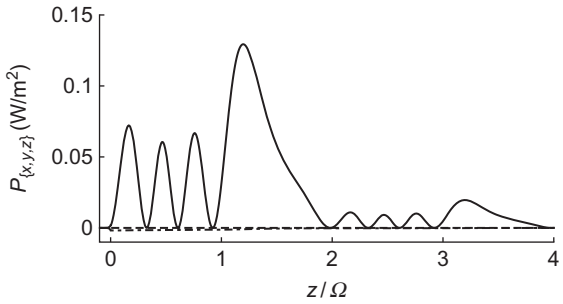


FIG. 11.2

Variations with z of the Cartesian components of $\mathbf{P}(x, z)$ along the line $\{x = 0, y = 0\}$ for an s-polarized SPP wave guided by the planar interface of aluminum and the rugate filter in the canonical boundary-value problem, when $\Omega/\lambda_0 = 1$ and $\kappa/k_0 = 1.4864 + 0.0013203i$. The components parallel to $\hat{\mathbf{u}}_x$, $\hat{\mathbf{u}}_y$, and $\hat{\mathbf{u}}_z$ are represented by *solid*, *dashed*, and *chain-dashed lines*, respectively. The data were computed by setting $a_s = 1$ V/m, with a_p, τ_1, and τ_2 then obtained using Eq. (11.27) (Faryad and Lakhtakia, 2010b).

P are negligible as compared with its x component. The power density resides in the rugate filter almost wholly within a distance equal to the period 2Ω for the case shown; however, Faryad and Lakhtakia (2010b) have shown that different SPP waves have different deg of localization to the interface.

As the period 2Ω of the rugate filter increases in relation to λ_0, the branches in Fig. 11.1 come closer to each other. At some very high value of Ω/λ_0, only one solution—indicating a p-polarized SPP wave—should survive, because the rugate filter would be virtually homogeneous over the region of width $\sim 1.5\lambda_0$ next to the interface. Although this possibility could be tested by setting a very large value of Ω/λ_0, the correct identification of $\alpha_{1,2}$ became problematic for $\Omega/\lambda_0 > 2$, owing to numerical errors in computing $[\underline{\underline{Q}}]$.

In order to overcome this difficulty, Faryad and Lakhtakia (2010b) modified the relative permittivity of the rugate filter from Eq. (11.1) to

$$\epsilon_{\text{rug}}^{\text{mod}}(z) = \left[\left(\frac{n_\text{b} + n_\text{a}}{2}\right) + \Gamma\left(\frac{n_\text{b} - n_\text{a}}{2}\right)\sin\left(\pi\frac{z}{\Omega}\right)\right]^2, \quad \Gamma \in [0,1], \tag{11.31}$$

fixed $\Omega = 2\lambda_0$, and decreased the parameter Γ from 1 to 0.001. Close to the interface, a decrease in Γ tantamounts to an increase in Ω. It was then shown that all the solution branches in Fig. 11.1 die out when the value of Γ decreases from unity because the imaginary part of κ decreases to zero, except one branch representing p-polarized SPP waves. This branch extends to $\Gamma = 0.001$. As Γ decreases even further, the branch approaches the solution for a metal/dielectric interface with the relative permittivity of the dielectric partnering material uniform at $(1/4)(n_\text{a} + n_\text{b})^2$. For instance, at $\Gamma = 0.001$, the solution of the dispersion equation gives a p-polarized SPP wave with wavenumber $\kappa = (1.9395 + 0.02140i)k_0$, while the p-polarized wave

guided by the interface of aluminum and a homogeneous isotropic dielectric material with relative permittivity $(1/4)(n_a + n_b)^2 = 3.5532$ has wavenumber $\kappa = (1.9394 + 0.02141i)k_0$ (Homola, 2006; Abdulhalim et al., 2008).

The spatial profiles (such as given in Fig. 11.2) can act as a guide if one wishes to design an experiment to test the foregoing theoretical results. In the conventional TKR configuration, SPP waves are excited at the interface of a metallic thin film and a dielectric thin film. Faryad and Lakhtakia (2010b) have shown that most of the SPP waves guided by the interface of the rugate filter and aluminum are confined within three structural periods of the rugate filter when the real part of κ exceeds k_0. So a four-period-thick rugate filter deposited upon a metallic thin film, which is thicker than the penetration depth of the metal, can be used in the TKR configuration to excite SPP waves.

11.4.3 METAL/SNTF INTERFACE

Let the partnering dielectric material now be an SNTF. The 4×4 matrix $[\underline{\underline{P}}(z)]$ for this case is

$$
\begin{aligned}
[\underline{\underline{P}}(z)] = \omega & \begin{bmatrix} 0 & 0 & 0 & \mu_0 \\ 0 & 0 & -\mu_0 & 0 \\ 0 & -\epsilon_0\,\epsilon_c(z) & 0 & 0 \\ \epsilon_0\,\epsilon_d(z) & 0 & 0 & 0 \end{bmatrix} \\
& + \frac{\kappa^2}{\omega\epsilon_0}\,\frac{\epsilon_d(z)}{\epsilon_a(z)\,\epsilon_b(z)} \begin{bmatrix} 0 & 0 & \cos\psi\,\sin\psi & -\cos^2\psi \\ 0 & 0 & \sin^2\psi & -\cos\psi\,\sin\psi \\ 0 & 0 & 0 & 0 \\ 0 & 0 & 0 & 0 \end{bmatrix} \\
& + \kappa \frac{\epsilon_d(z)\,[\epsilon_a(z) - \epsilon_b(z)]}{\epsilon_a(z)\,\epsilon_b(z)}\,\sin[\chi(z)]\,\cos[\chi(z)] \begin{bmatrix} \cos\psi & 0 & 0 & 0 \\ \sin\psi & 0 & 0 & 0 \\ 0 & 0 & 0 & 0 \\ 0 & 0 & -\sin\psi & \cos\psi \end{bmatrix} \\
& + \frac{\kappa^2}{\omega\mu_0} \begin{bmatrix} 0 & 0 & 0 & 0 \\ 0 & 0 & 0 & 0 \\ -\cos\psi\,\sin\psi & \cos^2\psi & 0 & 0 \\ -\sin^2\psi & \cos\psi\,\sin\psi & 0 & 0 \end{bmatrix},
\end{aligned}
\tag{11.32}
$$

where

$$
\epsilon_d(z) = \frac{\epsilon_a(z)\,\epsilon_b(z)}{\epsilon_a(z)\,\cos^2[\chi(z)] + \epsilon_b(z)\,\sin^2[\chi(z)]}. \tag{11.33}
$$

Faryad et al. (2010) fixed $\epsilon_{met} = -56 + 21i$ (bulk aluminum) and $\underline{\underline{\epsilon}}(z) = \underline{\underline{\epsilon}}_{SNTF}(z)$. The SNTF was chosen to be made of titanium oxide, and the angles $\widetilde{\chi}_v$ and δ_v were taken to be 45 and 30 deg, respectively, and $\Omega = 200$ nm for the results presented in this section.

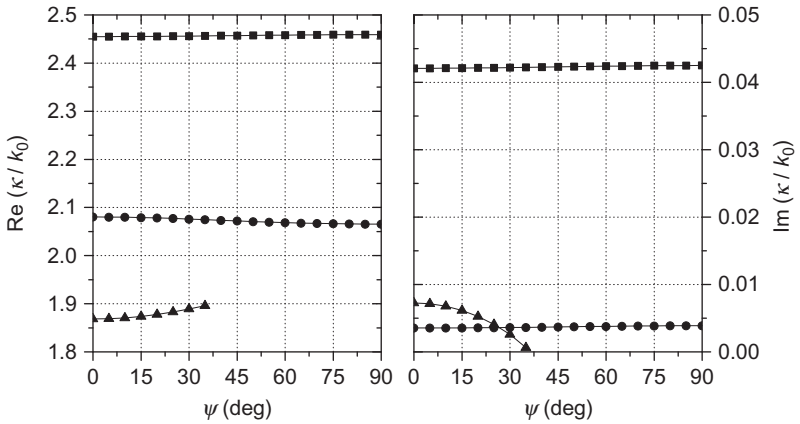


FIG. 11.3

Real (*left*) and imaginary (*right*) parts of κ as functions of ψ, for SPP-wave propagation guided by the planar interface of bulk aluminum and a periodically nonhomogeneous SNTF in the canonical boundary-value problem. See Section 11.3.2 for the constitutive parameters of the SNTF. Either two or three modes are possible, depending on ψ (Faryad et al., 2010).

Computed values of the real and imaginary parts of κ for the canonical problem are shown in Fig. 11.3. These solutions are organized into three branches. For $0 \text{ deg} \leq \psi \lesssim 36 \text{ deg}$, three values of κ satisfy Eq. (11.28) and therefore represent SPP waves. For $36 \text{ deg} \lesssim \psi \leq 90 \text{ deg}$, two values of κ satisfy Eq. (11.28). The different solutions of Eq. (11.28) for any specific value of ψ indicate that the SPP waves have different phase speeds $\omega/\text{Re}(\kappa)$ and different e-folding distances $1/\text{Im}(\kappa)$ along the direction of propagation. These results are consistent with theoretical (Motyka and Lakhtakia, 2008, 2009) and experimental (Lakhtakia et al., 2009) results obtained for the TKR configuration.

Specifically, for $\psi = 0$ deg the values of κ which satisfy Eq. (11.28) are $\kappa_1 = (2.455 + 0.04208i)k_0$, $\kappa_2 = (2.080 + 0.003538i)k_0$, and $\kappa_3 = (1.868 + 0.007267i)k_0$. These solutions represent SPP waves with wave vectors lying wholly in the morphologically significant plane of the SNTF. Faryad et al. (2010) have shown that the SPP waves with the wavenumbers κ_1 and κ_3 are p-polarized, and the SPP wave with κ_2 is s-polarized. The localization of these SPP waves around the interface $z = 0$ is evident from the spatial profiles provided by Faryad et al. (2010). Moreover, the examination of the spatial profiles provided by Faryad et al. (2010) shows that, after spatial averaging over an appropriate z-range, the component of the time-averaged Poynting vector along the direction of propagation is higher in magnitude in the SNTF than in the metal, regardless of the polarization state of the SPP wave. This means that the energy of the SPP wave primarily resides in the SNTF.

Only two values of κ were found to satisfy Eq. (11.28) for $\psi = 75$ deg: $\kappa_1 = (2.459 + 0.04247i)k_0$ and $\kappa_2 = (2.066 + 0.003861i)k_0$. The phase speed of the SPP wave with

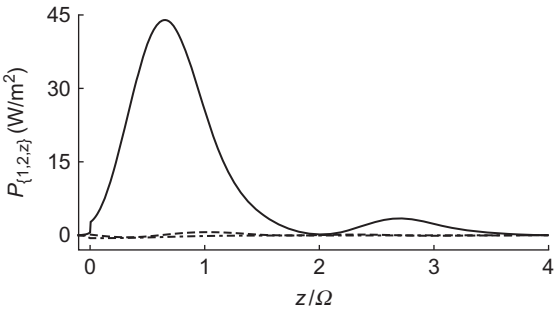


FIG. 11.4

Variations of components of $\mathbf{P}(x, z)$ with z along the line $\{x = 0, y = 0\}$ for the SPP waves guided by a planar interface of bulk aluminum and the SNTF in the canonical boundary-value problem, for $\kappa = (2.066 + 0.003861\,i)k_0$ and $\psi = 75$ deg. The components parallel to $\hat{\mathbf{u}}_1$, $\hat{\mathbf{u}}_2$, and $\hat{\mathbf{u}}_z$ are represented by *solid*, *dashed*, and *chain-dashed lines*, respectively. The data were computed by setting $a_p = 1$ V/m, with a_s, τ_1, and τ_2 then obtained using Eq. (11.27) (Faryad et al., 2010).

$\kappa = \kappa_2$ exceeds the phase speed of the other SPP wave ($\kappa = \kappa_1$), and the former SPP wave will propagate a longer distance along the interface than the latter SPP wave. The variations of the Cartesian components of $\mathbf{P}$ along the z axis are shown in Fig. 11.4 for κ_2. This SPP wave cannot be rigorously classified as either p or s polarized. However, the electric field of this SPP wave is predominantly oriented parallel to $\hat{\mathbf{u}}_2$ (Faryad et al., 2010), thereby suggesting that the SPP wave for κ_2 could be classified as quasi-s polarized on both sides of the interface. By contrast, the electric field in the spatial plots for κ_1 is predominantly oriented in the plane formed by $\hat{\mathbf{u}}_1$ and $\hat{\mathbf{u}}_z$, which implies that the SPP wave for κ_1 is quasi-p polarized on both sides of the interface.

11.5 GRATING-COUPLED CONFIGURATION

Solutions of the canonical boundary-value problem discussed in Section 11.4 provide information about several characteristics of possible SPP waves, such as their number, wavenumbers, and e-folding distance along the direction of propagation and into the partnering materials. However, the canonical boundary-value problem cannot be implemented in a laboratory because it involves semiinfinite expanses of both partnering materials. Therefore, the grating-coupled configuration in this section, and the TKR configuration in Section 11.6, with finitely thick partnering materials is discussed for the practical excitation of multiple SPP waves.

11.5.1 METAL/RUGATE-FILTER INTERFACE

Let us consider the boundary-value problem shown schematically in Fig. 11.5 for the grating-coupled configuration. The regions $z < 0$ and $z > d_3$ are vacuous, the region $0 \leq z \leq d_1$ is occupied by the dielectric partnering material with relative

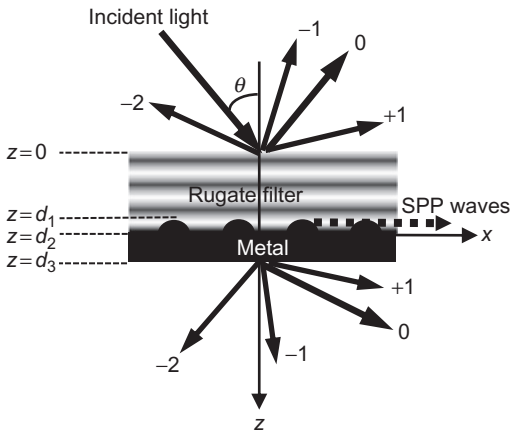


FIG. 11.5

Schematic of the grating-coupled configuration used for the excitation of multiple SPP waves by an incident plane wave. Specular reflection and transmission are denoted by order $n = 0$, whereas nonspecular modes are denoted by orders $n \neq 0$. The SPP waves are guided by the periodically corrugated metal/rugate-filter interface. The rugate filter has to be replaced by a periodically nonhomogeneous SNTF for the problem addressed in Section 11.5.2.

permittivity $\epsilon_{\rm rug}(z)$, and the region $d_2 \le z \le d_3$ is occupied by the metallic partnering material with spatially uniform relative permittivity $\epsilon_{\rm met}$. The region $d_1 < z < d_2$ contains a surface-relief grating of period L along the x axis. The relative permittivity $\epsilon_g(x, z) = \epsilon_g(x \pm L, z)$ in this region is specified as

$$\epsilon_g(x,z) = \begin{cases} \epsilon_{\rm met} - [\epsilon_{\rm met} - \epsilon_{\rm rug}(d_2 - z)]\mathcal{U}[d_2 - z - g(x)], & x \in (0, L_1), \\ \epsilon_{\rm rug}(d_2 - z), & x \in (L_1, L), \end{cases} \tag{11.34}$$

for $z \in (d_1, d_2)$, with

$$g(x) = (d_2 - d_1)\sin\left(\frac{\pi x}{L_1}\right), \quad L_1 \in (0, L), \tag{11.35}$$

and

$$\mathcal{U}(\zeta) = \begin{cases} 1, & \zeta \ge 0, \\ 0, & \zeta < 0. \end{cases} \tag{11.36}$$

The depth of the surface-relief grating defined by Eq. (11.35) is $L_{\rm g} = d_2 - d_1$.

In the vacuous half-space $z \le 0$, let a plane wave propagating in the xz plane at an angle θ to the z axis, be incident on the structure. Hence, the incident, reflected, and transmitted electric field phasors may be written in terms of Floquet harmonics as

$$\mathbf{E}_{\rm inc}(\mathbf{r}) = \sum_{n=-N_t}^{n=N_t} \left(a_s^{(n)} \mathbf{s}_n + a_p^{(n)} \mathbf{p}_n^+ \right) \exp\left[i \left(k_x^{(n)} x + k_z^{(n)} z \right) \right], \quad z \le 0, \tag{11.37}$$

$$\mathbf{E}_{\rm refl}(\mathbf{r}) = \sum_{n=-N_t}^{n=N_t} \left(r_s^{(n)} \mathbf{s}_n + r_p^{(n)} \mathbf{p}_n^- \right) \exp\left[i \left(k_x^{(n)} x - k_z^{(n)} z \right) \right], \quad z \le 0, \tag{11.38}$$

and

$$\mathbf{E}_{\rm tr}(\mathbf{r}) = \sum_{n=-N_t}^{n=N_t} \left(t_s^{(n)} \mathbf{s}_n + t_p^{(n)} \mathbf{p}_n^+ \right) \exp\left\{ i \left[k_x^{(n)} x + k_z^{(n)} (z - d_3) \right] \right\}, \quad z \geq d_3, \tag{11.39}$$

where $k_x^{(n)} = k_0 \sin\theta + n\kappa_x$, $\kappa_x = 2\pi/L$, and

$$k_z^{(n)} = \begin{cases} +\sqrt{k_0^2 - \left(k_x^{(n)}\right)^2}, & k_0^2 > \left(k_x^{(n)}\right)^2 \\ +i\sqrt{\left(k_x^{(n)}\right)^2 - k_0^2}, & k_0^2 < \left(k_x^{(n)}\right)^2 \end{cases}. \tag{11.40}$$

The s- and p-polarization states are represented, respectively, by

$$\mathbf{s}_n = \hat{\mathbf{u}}_y \tag{11.41}$$

and

$$\mathbf{p}_n^{\pm} = \mp \frac{k_z^{(n)}}{k_0} \hat{\mathbf{u}}_x + \frac{k_x^{(n)}}{k_0} \hat{\mathbf{u}}_z. \tag{11.42}$$

The boundary-value problem was formulated using the rigorous coupled-wave approach (RCWA) (Moharam and Gaylord, 1982; Li, 1993) and was implemented using a stable algorithm (Moharam et al., 1995; Wang et al., 2004; Chateau and Hugonin, 1994). The accuracy of the solution using RCWA depends on the value of N_t, the number of terms of Floquet harmonics in the representation of field phasors being $2N_t + 1$. The formulation of the boundary-value problem and the numerical algorithm have been explained elsewhere in detail (Faryad and Lakhtakia, 2011c,d) and we skip both to go directly to present some representative numerical results.

The planewave absorptance was computed as

$$A = 1 - \sum_{n=-N_t}^{N_t} \frac{|r_s^{(n)}|^2 + |r_p^{(n)}|^2 + |t_s^{(n)}|^2 + |t_p^{(n)}|^2}{|a_s^{(0)}|^2 + |a_p^{(0)}|^2} \mathrm{Re}\left(\frac{k_z^{(n)}}{k_z^{(0)}} \right). \tag{11.43}$$

The absorptance for p-polarized incidence is denoted by $A_p = A\left(a_s^{(0)} = 0, a_p^{(0)} \neq 0\right)$, and that for s-polarized incidence by $A_s = A\left(a_s^{(0)} \neq 0, a_p^{(0)} = 0\right)$. Let us note that $r_s^{(n)} = 0$ and $t_s^{(n)} = 0 \;\; \forall n \in \mathbb{Z}$ for p-polarized incident planewaves, and vice versa for the s-polarized case, when the dielectric partnering material is isotropic.

For all calculations reported in the remainder of this section, $\epsilon_{\rm met} = -56 + 21i$ (bulk aluminum) and $\Omega = \lambda_0$. The surface-relief grating is defined by Eq. (11.35) with $L_1 = 0.5L$. The grating depth $L_{\rm g} = 50$ nm and the thickness of the metal layer $d_3 - d_2 = 30$ nm were also fixed, as their variations would not qualitatively affect the excitation of multiple SPP waves. The rugate filter ($0 < z < d_1$) and the grating region ($d_1 < z < d_2$) were divided into 2-nm- and 1-nm-thick slices, respectively, to use the piecewise-uniform-approximation method. Both A_p and A_s were calculated as functions of θ for $d_1 \in \{4\Omega, 5\Omega, 6\Omega\}$. Absorptances calculated for $N_t = 8$ lay within $\pm$ 1% of the absorptances calculated with $N_t = 9$.

Table 11.1 Relative wavenumbers κ/k_0 of possible SPP waves obtained by the solution of the canonical boundary-value problem involving bulk aluminum and a rugate filter (Section 11.4.2) for $\Omega = \lambda_0$

p-pol	1.36479 + 0.00169*i*	1.61782 + 0.00548*i*	1.87437 + 0.00998*i*
	2.06995 + 0.01526*i*	2.21456 + 0.00246*i*	
s-pol	1.48639 + 0.00132*i*	1.7324 + 0.0014*i*	1.9836 + 0.0006*i*
	2.2128 + 9.6 × 10^{-5}*i*		

Notes: *If* κ *represents an SPP wave propagating in the* $\hat{\mathbf{u}}_x$ *direction,* $-\kappa$ *represents an SPP wave propagating in the* $-\hat{\mathbf{u}}_x$ *direction.*

The solution of the corresponding canonical boundary-value problem formulated in Section 11.4.1 (when both the rugate filter and the metal are semi-infinite in thickness and their interface is planar) results in five *p*-polarized and four *s*-polarized SPP waves, the relative wavenmbers κ/k_0 being provided in Table 11.1.

For all three values of d_1, a peak is present at $\theta = 37.7$ deg in the plots of A_p vs. θ in Fig. 11.6A. The relative wavenumbers $k_x^{(n)}/k_0$ of several Floquet harmonics at this incidence angle are given in Table 11.2. At $\theta = 37.7$ deg, $k_x^{(1)}/k_0 = 1.6115$ is close to $\text{Re}(\kappa/k_0) = 1.61782$, where κ/k_0 is the relative wavenumber of a *p*-polarized SPP wave in the canonical boundary-value problem as provided in Table 11.1. Thus, this A_p-peak represents the excitation of a *p*-polarized SPP wave as a Floquet harmonic of order $n = 1$. This conclusion is also confirmed from an examination of the spatial profile of $P_x(0.75L, z)$ provided by Faryad and Lakhtakia (2011c) for $\theta = 37.7$ deg. Indeed, P_x decays quickly away from the plane $z = d_1$ in the region containing metal, and it also decays periodically (Yakubovich and Starzhinskii, 1975) inside the rugate filter away from the same interface.

For the A_p-peak at $\theta \simeq 21$ deg, the angular location changes slightly with the change in the value of d_1. However, this peak also represents the excitation of a *p*-polarized SPP wave because (i) $k_x^{(1)}/k_0 = 1.3584$ (Table 11.2) is close to $\text{Re}(\kappa/k_0) = 1.36479$ (Table 11.1), and (ii) the spatial profile of $P_x(0.75L, z)$ provided by Faryad and Lakhtakia (2011c) is also indicative of a surface wave guided by the metal/rugate-filter interface. The reason for the change in the θ-value of the A_p-peak is the weak localization of this SPP wave in the region $z < d_1$. However, for a sufficiently large value of d_1, the peak should be independent of the value of d_1.

Three A_s-peaks are present at $\theta \simeq 16.3$, 28.4, and 31.6 deg in the plots of A_s vs. θ, for all three values of d_1 in Fig. 11.6B. The relative wavenumbers of the Floquet harmonics at these values of the incidence angle are also provided in Table 11.2. At $\theta = 16.3$ deg, an *s*-polarized SPP wave is excited as a Floquet harmonic of order $n = -2$ because $k_x^{(-2)}/k_0 = -1.7210$ (Table 11.2) is close to $\text{Re}(\kappa/k_0) = -1.7324$ (Table 11.1). The spatial profile of $P_x(0.75L, z)$ given in Fig. 11.7 for $\theta = 16.3$ deg also confirms this conclusion. The *s*-polarized SPP wave is propagating in the $-\hat{\mathbf{u}}_x$ direction because it is excited as a Floquet harmonic of a negative order.

The A_s-peak at $\theta = 28.4$ deg represents the excitation of an *s*-polarized SPP wave, as a Floquet harmonic of order $n = 1$, because (i) $k_x^{(1)}/k_0 = 1.4756$ (Table 11.2) is

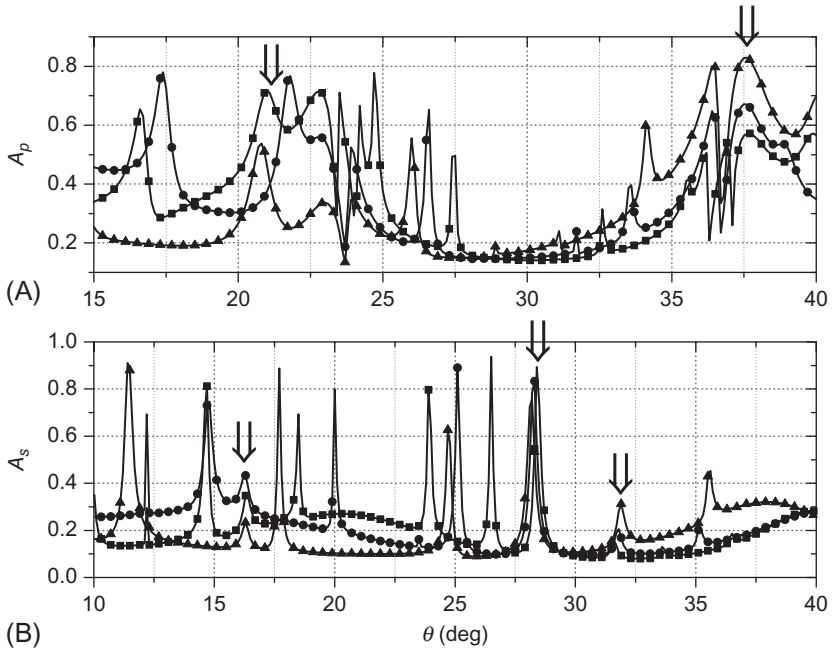


FIG. 11.6

Absorptances (A) A_p and (B) A_s as functions of the incidence angle θ in the grating-coupled configuration. The surface-relief grating formed by bulk aluminum and a rugate filter defined by Eq. (11.35) with $L_1 = 0.5L$, $\lambda_0 = 633$ nm, $\Omega = \lambda_0$, and $L = \lambda_0$. *Squares* are for $d_1 = 6\Omega$, *circles* for $d_1 = 5\Omega$, and *triangles* for $d_1 = 4\Omega$. The grating depth ($d_2 - d_1 = 50$ nm) and the thickness of the metallic layer ($d_3 - d_2 = 30$ nm) are the same for all plots. Each *vertical arrow* identifies an SPP wave (Faryad and Lakhtakia, 2011c).

Table 11.2 Relative wavenumbers $k_x^{(n)}/k_0$ of Floquet harmonics at the θ-values of the peaks identified in Fig. 11.6 by vertical arrows when the half-period Ω of the rugate filter is λ_0 and the period L of the surface relief-grating is λ_0

θ (deg)	$n = -2$	$n = -1$	$n = 0$	$n = 1$	$n = 2$
16.3	**−1.7210**	− 0.7210	0.2790	1.2790	2.2790
21.0	− 1.6416	− 0.6416	0.3584	**1.3584**	2.3584
28.4	− 1.5244	− 0.5244	0.4756	**1.4756**	2.4756
31.6	**−1.4760**	− 0.4760	0.5240	1.5240	2.5240
37.7	− 1.3885	− 0.3885	0.6115	**1.6115**	2.6115

Note: *Boldface entries signify SPP waves.*

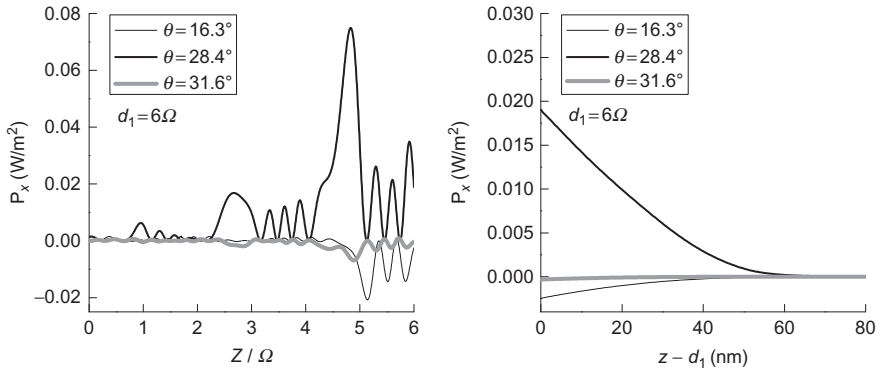


FIG. 11.7

Variation of the x-component of the time-averaged Poynting vector $\mathbf{P}(x, z)$ in the grating-coupled configuration along the z axis in the regions (*left*) $0 < z < d_1$ and (*right*) $d_1 < z < d_3$ at $x = 0.75L$, when the surface-relief grating is defined by Eq. (11.35) and the partnering dielectric material is a rugate filter. The grating period $L = \lambda_0$ and the incident plane wave is s polarized (after Faryad and Lakhtakia, 2011c).

close to $\text{Re}(\kappa/k_0) = 1.48639$ (Table 11.1), and (ii) the spatial profile of $P_x(0.75L, z)$ provided in Fig. 11.7 shows that an s-polarized SPP wave is guided by the interface $z = d_1$ in the $+\hat{\mathbf{u}}_x$ direction. Coincidently, the A_s-peak at $\theta = 31.6$ deg represents the excitation of the same s-polarized SPP wave but as a Floquet harmonic of order $n = -2$ because $k_x^{(-2)}/k_0 = -1.4760$ (Table 11.2) is close to $\text{Re}(\kappa/k_0) = -1.48639$ (Table 11.1). This is also evident from the comparison of the spatial profiles given in Fig. 11.7 for $\theta = 28.4$ deg and $\theta = 31.6$ deg. Although the two spatial profiles are mirror images of each other, the excitation of the s-polarized SPP wave at $\theta = 31.6$ deg is not very efficient because it is excited as a Floquet harmonic of a higher order ($|n| = 2$).

Since not all possible SPP waves (predicted from the solution of the canonical boundary-value problem) can be excited with period $L = \lambda_0$ of the surface-relief grating, the grating period needs to be changed in order to excite the remaining SPP waves (Faryad, 2012). Moreover, a comparison of A_p- and A_s-peaks in Fig. 11.6A and B shows that A_s-peaks are generally narrower than A_p-peaks.

11.5.2 METAL/SNTF INTERFACE

Let us now consider the same boundary-value problem as in the foregoing section with the rugate filter in the region $0 \leq z \leq d_1$ replaced by a periodically nonhomogeneous SNTF with the permittivity dyadic (Lakhtakia et al., 2009; Motyka and Lakhtakia, 2008, 2009)

$$\underline{\underline{\epsilon}}_{\text{SNTF}}^{\text{rot}}(z) = \underline{\underline{S}}_z(\gamma) \cdot \underline{\underline{\epsilon}}_{\text{SNTF}}(z) \cdot \underline{\underline{S}}_z^{-1}(\gamma), \tag{11.44}$$

where

$$\underline{\underline{S}}_z(\gamma) = (\hat{\mathbf{u}}_x\hat{\mathbf{u}}_x + \hat{\mathbf{u}}_y\hat{\mathbf{u}}_y)\cos\gamma + (\hat{\mathbf{u}}_y\hat{\mathbf{u}}_x - \hat{\mathbf{u}}_x\hat{\mathbf{u}}_y)\sin\gamma + \hat{\mathbf{u}}_z\hat{\mathbf{u}}_z. \tag{11.45}$$

Here, $\underline{\underline{\epsilon}}^{\,\mathrm{rot}}_{\mathrm{SNTF}}(z)$ is a rotated version of $\underline{\underline{\epsilon}}_{\mathrm{SNTF}}(z)$ so that the plane formed by the unit vectors $\hat{\mathbf{u}}_z$ and $\hat{\mathbf{u}}_x\cos\gamma + \hat{\mathbf{u}}_y\sin\gamma$ is the morphologically significant plane of the SNTF.

The relative permittivity dyadic $\underline{\underline{\epsilon}}_g(x,z) = \underline{\underline{\epsilon}}_g(x \pm L, z)$ in the region $d_1 < z < d_2$ is taken to be as

$$\underline{\underline{\epsilon}}_g(x,z) = \begin{cases} \epsilon_{\mathrm{met}}\underline{\underline{I}} - \left[\epsilon_{\mathrm{met}}\underline{\underline{I}} + \underline{\underline{\epsilon}}^{\,\mathrm{rot}}_{\mathrm{SNTF}}(d_2 - z)\right] \mathcal{U}[d_2 - z - g(x)], & x \in (0, L_1), \\ \underline{\underline{\epsilon}}^{\,\mathrm{rot}}_{\mathrm{SNTF}}(d_2 - z), & x \in (L_1, L), \end{cases} \tag{11.46}$$

for $z \in (d_1, d_2)$, with $\underline{\underline{I}} = \hat{\mathbf{u}}_x\hat{\mathbf{u}}_x + \hat{\mathbf{u}}_y\hat{\mathbf{u}}_y + \hat{\mathbf{u}}_z\hat{\mathbf{u}}_z$. Let us note that the permittivity dyadic defined by Eq. (11.46) is a simplistic description of the region $d_1 < z < d_2$ and the actual morphology of the region is very hard to model for the fabricated device (Fiumara et al., 2006).

Faryad and Lakhtakia (2011d) have provided the formulation of this problem in detail where the incidence plane, the grating plane, and the morphologically significant plane of the SNTF can be rotated with respect to each other. Both *p*- and *s*-polarized SPP waves are excited by *p*- and *s*-polarized incident planewaves, respectively, when the morphologically significant plane, the grating plane, and the incidence plane are the same, that is, $\gamma = 0$ deg.

Let us discuss the special case of $\gamma = 75$ deg, i.e., when the morphologically significant plane makes an angle of 75 deg with the *xz* plane—the incidence plane and the grating plane. Relative wavenumbers κ/k_0, obtained from the solution of the canonical boundary-value problem for SPP waves propagating at an angle of 75 deg with respect to the morphologically significant plane, are $\kappa/k_0 = 2.0664 + 0.0039i$ and $\kappa/k_0 = 2.4588 + 0.0425i$. As was discussed in Section 11.4.3, both of these SPP waves are neither purely *p* nor *s* polarized because of the anisotropy of the SNTF.

The absorptances A_p and A_s for $L = 286$ nm and $\gamma = 75$ deg are presented in Fig. 11.8 as functions of the angle of incidence θ. Independent of the value of d_1 and the polarization state of the incident plane wave, an absorptance peak is present at $\theta \simeq 9.2$ deg. This peak represents the excitation of an SPP wave as a Floquet harmonic of order $n = -1$ because $k_x^{(-1)}/k_0 = -2.0534$ is very close to $\mathrm{Re}(-2.0664 - 0.0039i)$.

The spatial profiles of the *x*- and *y*-components of $\mathbf{P}(0.75L, z)$, given in Fig. 11.9, for $\theta = 9.2$ deg indicate that the SPP wave is localized to the metal/SNTF interface. As the magnitude of P_y is approximately ten times smaller than that of P_x, the SPP wave transports energy mainly along the $-\hat{\mathbf{u}}_x$ direction. This is reasonable because the SPP wave is excited in the grating-coupled configuration as a Floquet harmonic of negative order. The notable characteristic of this SPP wave is that it can be excited by a plane wave of either polarization state; however, the excitation is more efficient

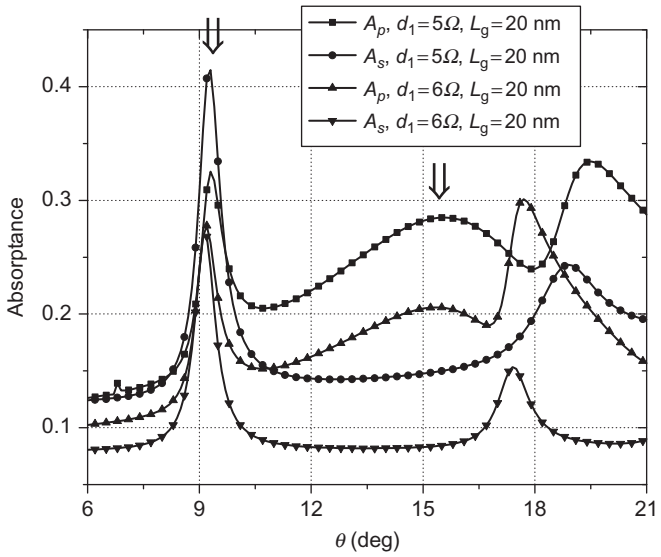


FIG. 11.8

Absorptances A_p and A_s versus θ in the grating-coupled configuration when $L = 286$ nm, $\psi = 0$ deg, $\gamma = 75$ deg, and $d_3 - d_2 = 30$ nm. The metal is bulk aluminum and the partnering dielectric material is a periodically nonhomogeneous SNTF with relative permittivity defined by Eq. (11.2). The *vertical arrows* identify the peaks that represent the excitation of SPP waves (Faryad and Lakhtakia, 2011d).

if the incident plane wave is *s* polarized. This is due to the fact that this SPP wave is quasi-*s* polarized, as discussed in Section 11.4.3.

At $\theta \simeq 15.5$ deg in Fig. 11.8, a peak is present independent of the value of d_1 in the plots of A_p but not of A_s. This A_p-peak represents the excitation of an SPP wave as a Floquet harmonic of order $n = 1$ because $k_x^{(1)}/k_0 = 2.4805$ is very close to $\text{Re}(2.4588 + 0.0425i)$. Contrary to the SPP wave excited at $\theta = 9.2$ deg, the absence of the peak in the curves of A_s shows that this SPP wave is excited only by a *p*-polarized incident plane wave. The spatial profile of $\mathbf{P}(0.75L, z)$ at $\theta = 15.5$ deg for *s*- and *p*-polarized incident plane waves, provided by Faryad and Lakhtakia (2011d), also support this conclusion; furthermore, the SPP wave is strongly localized in the SNTF to the plane $z = d_1$.

The A_p- and A_s-peaks at $\theta = 9.2$ deg are narrower than the A_p-peak at $\theta = 15.5$ deg, thereby supporting the conclusion that the absorptance peak representing the excitation of an SPP wave with smaller phase speed is broader. The spatial profiles in the SNTF ($0 < z < d_1$) of the SPP wave presented in Fig. 11.9 are similar to the profile for the corresponding SPP waves guided by the planar metal/SNTF interface in the canonical boundary-value problem (Fig. 11.4).

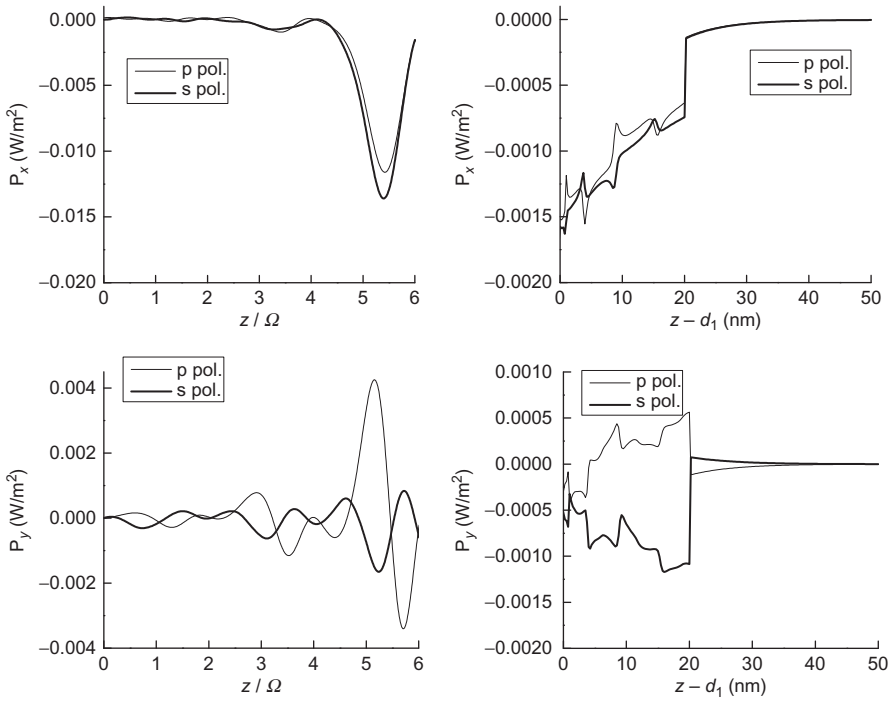


FIG. 11.9

Variation of the *x*- and *y*-components of the time-averaged Poynting vector $\mathbf{P}(0.75L, z)$ in the grating-coupled configuration (metal/SNTF interface) along the *z* axis in the regions (*left*) $0 < z < d_1$ and (*right*) $d_1 < z < d_3$ for *p*- and *s*-polarized incident plane waves when $\theta = 9.2$ deg, $L = 286$ nm, $\gamma = 75$ deg, $d_1 = 6\Omega$, $L_g = 20$ nm, and $d_3 - d_2 = 30$ nm (after Faryad and Lakhtakia, 2011d).

To analyze the effect of the direction of the electric field of the incident linearly polarized plane wave on the efficiency of the excitation of SPP waves when $\gamma = 75$ deg, Faryad and Lakhtakia (2011d) also calculated the absorptance A for an incident plane wave with electric field phasor

$$\mathbf{E}_{\text{inc}}(\mathbf{r}) = \left(\cos\alpha\,\mathbf{s}_0 + \sin\alpha\,\mathbf{p}_0^+\right)\exp\left[i\left(k_x^{(0)}x + k_z^{(0)}z\right)\right], \quad z \le 0, \tag{11.47}$$

where $\alpha \in [0\text{ deg}, 360\text{ deg})$. This plane wave is *s* polarized when $\alpha \in \{0\text{ deg}, 180\text{ deg}\}$ and *p* polarized when $\alpha \in \{90\text{ deg}, 270\text{ deg}\}$. Efficient excitation of an SPP wave was found to depend not only on the direction of the incident electric field but also on the thickness of the SNTF. This is because A depends on α, and more generally, on the vibration ellipse of the incident plane wave. In addition, as depolarization affects the absorptance and depolarization must depend on d_1, the absorptance must also depend on the thickness of the SNTF. The higher the absorptance at the peak representing the excitation of an SPP wave, the more efficient is the excitation of the SPP wave.

11.6 TURBADAR–KRETSCHMANN–RAETHER CONFIGURATION

The TKR configuration is an alternative to the grating-coupled configuration for exciting SPP waves, and is widely used for optical-sensing applications (Abdulhalim et al., 2007, 2008; Homola, 2006). This configuration is now briefly discussed for both the metal/rugate-filter and the metal/SNTF interfaces. This configuration is often called the Kretschmann configuration, and sometimes the Kretschmann-Raether configuration after the authors of a 1968 paper (Kretschmann and Raether, 1968). But, Turbadar (1959) had anticipated that paper by a decade, although he had not used the word "plasmon." Propriety demands that Turbadar's contribution be adequately acknowledged.

11.6.1 METAL/RUGATE-FILTER INTERFACE

The boundary-value problem of the TKR configuration is shown schematically in Fig. 11.10. Let the half-spaces $z < 0$ and $z > L$ be occupied by a dielectric material with relative permittivity $\epsilon_\ell = n_\ell^2$, the region $0 < z < L_m$ by a metal with relative permittivity ϵ_{met}, and the region $L_m < z < L_m + L_d = L_\Sigma$ by a rugate filter with relative permittivity $\epsilon_{\text{rug}}(z - L_m)$. The rugate filter was chosen to have integral number of periods: $L_d = 2\Omega N_p$, $N_p \in \{1, 2, 3, \ldots\}$; furthermore, $n_\ell > n_{\text{b}}$ is required for the TKR configuration. The half-space $z < 0$ represents a prism.

Let a linearly polarized plane wave, propagating in the half-space $z \leq 0$ and with its wave vector making an angle θ with the z axis, be incident on the metal-capped rugate filter. The incident, reflected and transmitted electric field phasors may be represented as (Motyka and Lakhtakia, 2008)

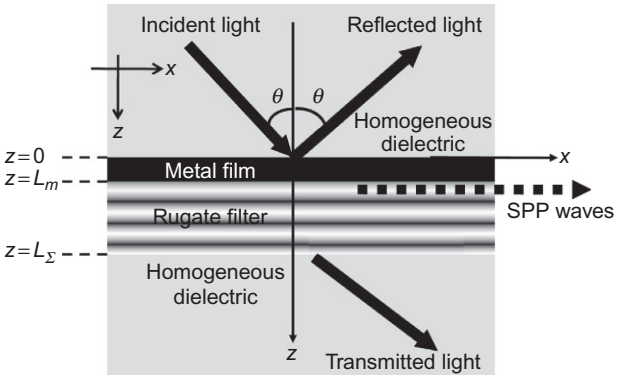


FIG. 11.10

Schematic of the TKR configuration. Incident light inside an optically dense material excites a metal-capped rugate filter. The SPP waves are guided by the metal/rugate-filter interface. The rugate filter has to be replaced by a periodically nonhomogeneous SNTF for the problem addressed in Section 11.6.2.

$$\mathbf{E}_{\rm inc}(\mathbf{r}) = \left(a_s\mathbf{s} + a_p\mathbf{p}^+\right)\exp\left(ik_x x + ik_0 n_\ell z\cos\theta\right), \quad z \leq 0, \tag{11.48}$$

$$\mathbf{E}_{\rm refl}(\mathbf{r}) = \left(r_s\mathbf{s} + r_p\mathbf{p}^-\right)\exp\left(ik_x x - ik_0 n_\ell z\cos\theta\right), \quad z \leq 0, \tag{11.49}$$

and

$$\mathbf{E}_{\rm tr}(\mathbf{r}) = \left(t_s\mathbf{s} + t_p\mathbf{p}^+\right)\exp\left[ik_x x + ik_0 n_\ell (z - L_\Sigma)\cos\theta\right], \quad z \geq L_\Sigma, \tag{11.50}$$

where the unit vectors $\mathbf{s} = \hat{\mathbf{u}}_y$ and $\mathbf{p}_\pm = \mp\hat{\mathbf{u}}_x\cos\theta + \hat{\mathbf{u}}_z\sin\theta$ represent s- and p-polarization states, respectively, and $k_x = k_0 n_\ell \sin\theta \in \mathbb{R}$.

The reflection amplitudes $r_{p,\,s}$ and the transmission amplitudes $t_{p,\,s}$ have to be determined in terms of known amplitudes $a_{p,\,s}$ of the incident plane wave. The numerical method of finding unknown transmission and reflection amplitudes r_p, r_s, t_p, t_s in terms of a_p and a_s is provided in detail by Faryad and Lakhtakia (2011e). For the numerical solution, the region $L_m < z < L_\Sigma$ has to be divided into N_d slices, each a couple of nanometers in thickness.

For all the calculations reported in the remainder of this section, the half-spaces $z < 0$ and $z > L_\Sigma$ are occupied by zinc selenide ($n_\ell = 2.58$), and the metal film is thin-film aluminum for which $\epsilon_{\rm met} = (0.75 + 3.9i)^2$ (Lakhtakia et al., 2009). The half-period of the rugate filter is $\Omega = 1.5\lambda_0$ so that the interface of a semiinfinite metal and rugate filter can guide multiple p- and multiple s-polarized SPP waves according to Section 11.4.2. No depolarization can occur because the partnering dielectric material is isotropic, and absorptances for p- and s-polarization states can be defined as

$$A_p = 1 - \frac{|r_p|^2 + |t_p|^2}{|a_p|^2}, \quad A_s = 1 - \frac{|r_s|^2 + |t_s|^2}{|a_s|^2}. \tag{11.51}$$

The variation of absorptance A_p versus the angle of incidence θ is given in Fig. 11.11 for $N_p \in \{3,4\}$ and $L_m = 30$ nm. The absorptances were calculated for two values of N_p in order to identify and eliminate waveguide modes (Marcuse, 1991; Kapany and Burke, 1972), which must depend on L_d (Motyka and Lakhtakia, 2008; Otto and Sohler, 1971). At seven values of the incidence angle θ, given in Table 11.3, a peak is present independent of the value of N_p. The relative wavenumbers k_x/k_0 at these values of θ are also given in Table 11.3. The seven A_p-peaks in Fig. 11.11 represent the excitation of p-polarized SPP waves because of the independence of their θ-value from the value of N_p. Furthermore, any peak identified in Table 11.3 represents either an SPP wave guided by the metal/rugate-filter interface or a coupled SPP wave guided by the metal film (Faryad and Lakhtakia, 2011e).

Further evidence in support of the conclusion that the peaks identified in Table 11.3 represent the excitation of p-polarized SPP waves was provided by the solution of the canonical boundary-value problem formulated in Section 11.4. The solutions of the dispersion equation (11.28) for the chosen metal and the rugate filter are given in Table 11.4. All solutions of the canonical boundary-value problem represent SPP waves. A comparison of Tables 11.3 and 11.4 shows that $\mathrm{Re}(\kappa/k_0)$ of

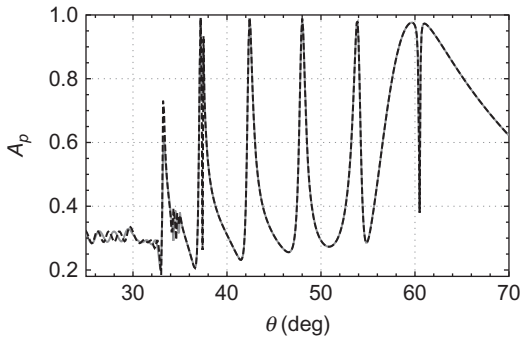


FIG. 11.11

Absorptance A_p as function of the incidence angle θ in the TKR configuration, when $\epsilon_{\text{met}} = (0.75 + 3.9i)^2$, $n_\ell = 2.58$, $L_m = 30$ nm, and the partnering dielectric material is a rugate filter with $\Omega = 1.5\lambda_0$. *Solid gray line* is for $N_p = 3$ and *dashed black line* is for $N_p = 4$ (Faryad and Lakhtakia, 2011e).

Table 11.3 Values of the incidence angle θ and the relative wavenumber k_x/k_0, where a peak is present in Fig. 11.11 independent of the value of N_p in the TKR configuration

θ (deg)	$k_x/k_0 = n_\ell \sin\theta$
33.23	1.4138
37.20	1.5599
42.41	1.7400
48.01	1.9176
53.86	2.0836
59.66	2.2266
61.01	2.2567

Note: *Each peak represents a* p*-polarized SPP wave, not a waveguide mode.*

each item in Table 11.4 for p-polarized SPP waves is close to the relative wavenumber k_x/k_0 at one of the A_p-peaks, showing that the seven peaks identified in Table 11.3 represent the excitation of p-polarized SPP waves.

The absorptance A_s for an s-polarized incident plane wave is given in Fig. 11.12 as a function of the incidence angle θ for the TKR configuration with a 30-nm-thick metal film for $N_p \in \{3, 4\}$. For five values of the incidence angle θ, an absorptance peak is present, independent of the value of N_p. The θ-values of these peaks along with the relative wavenumbers $k_x/k_0 = n_\ell \sin\theta$ are given in Table 11.5. All of the A_s-peaks represent the excitation of s-polarized SPP waves because (i) the peaks are independent of the value of N_p and (ii) the value of $\text{Re}(\kappa/k_0)$ of each item in Table 11.4 for s-polarized SPP waves is close to the relative wavenumber k_x/k_0 at

Table 11.4 Relative wavenumbers κ/k_0 of SPP waves guided by the interface between semiinfinite metal and semiinfinite rugate filter, when $\Omega = 1.5\lambda_0$ and the metal is thin-film aluminum

p-pol	1.4109 + 0.0019*i*	1.5579 + 0.0053*i*	1.7374 + 0.0072*i*
	1.9163 + 0.0077*i*	2.0856 + 0.0081*i*	2.2060 + 0.0987*i*
	2.2447 + 0.0022*i*		
s-pol	1.6205 + 0.0018*i*	1.7910 + 0.0012*i*	1.9528 + 0.0006*i*
	2.1037 + 0.0001*i*	2.2490 + 1.1021 × 10^{-5}*i*	

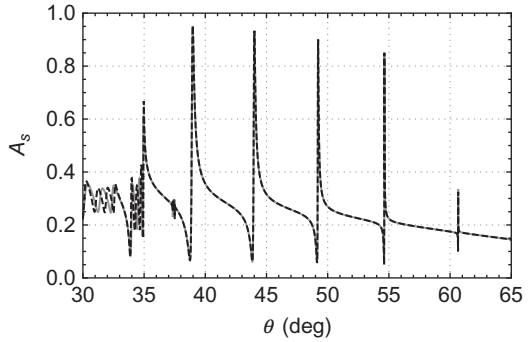


FIG. 11.12

Same as Fig. 11.11 except that A_s is plotted instead of A_p (Faryad and Lakhtakia, 2011e).

Table 11.5 Values of the incidence angles θ, and the relative wavenumbers k_x/k_0, where a peak is present in Fig. 11.12 independent of the value of N_p

θ (deg)	$k_x/k_0 = n_\ell \sin\theta$
38.97	1.6226
44.01	1.7925
49.22	1.9536
54.63	2.1038
60.66	2.2491

one of the A_s-peaks given in Table 11.5. The peak at $\theta \simeq 35$ deg does not represent the excitation of an *s*-polarized SPP wave (Faryad and Lakhtakia, 2011e).

In Fig. 11.12, the value of A_s at all the peaks, which represent the excitation of *s*-polarized SPP waves, is greater than 0.8 except for the peak at $\theta = 60.66$ deg. So the excitation of the *s*-polarized SPP wave at $\theta = 60.66$ deg is not that efficient as those of the rest of the *s*-polarized SPP waves. Moreover, a comparison of Figs. 11.11 and 11.12 shows that the peaks representing the excitation of

s-polarized SPP waves are narrower than those representing the excitation of p-polarized SPP waves.

Faryad and Lakhtakia (2011e) have shown that the efficiency of excitation of all p-polarized SPP waves in the TKR configuration is maximum when L_m is close to the penetration depth $\Delta_{\text{met}} = \left[\text{Im}\left(k_0\sqrt{\epsilon_{\text{met}}}\right)\right]^{-1} = 24.91$ nm of the aluminum thin film at the chosen wavelength. The same holds true for all s-polarized SPP waves except for the SPP wave excited at $\theta = 60.66$ deg. The excitation of the s-polarized SPP wave at $\theta = 60.66$ deg is most efficient when $L_m \simeq 12$ nm. Therefore, to excite maximum number of s-polarized SPP waves efficiently, a value of L_m close to Δ_{met} should be used.

Representative plots of the variations of the Cartesian components of time-averaged Poynting vector $\mathbf{P}(x, z)$ are presented in Fig. 11.13—when the incident plane wave is p polarized and $\theta \in \{33.21 \text{ deg}, 42.41 \text{ deg}, 59.66 \text{ deg}\}$—along a line normal to the plane $z = L_m$; $\mathbf{P}(x, z) \equiv \mathbf{P}(z)$ as $k_x \in \mathbb{R}$. The figure shows that P_z decays in the metal film as $z \to L_m$ and is negligible in the rugate filter ($z > L_m$). This should

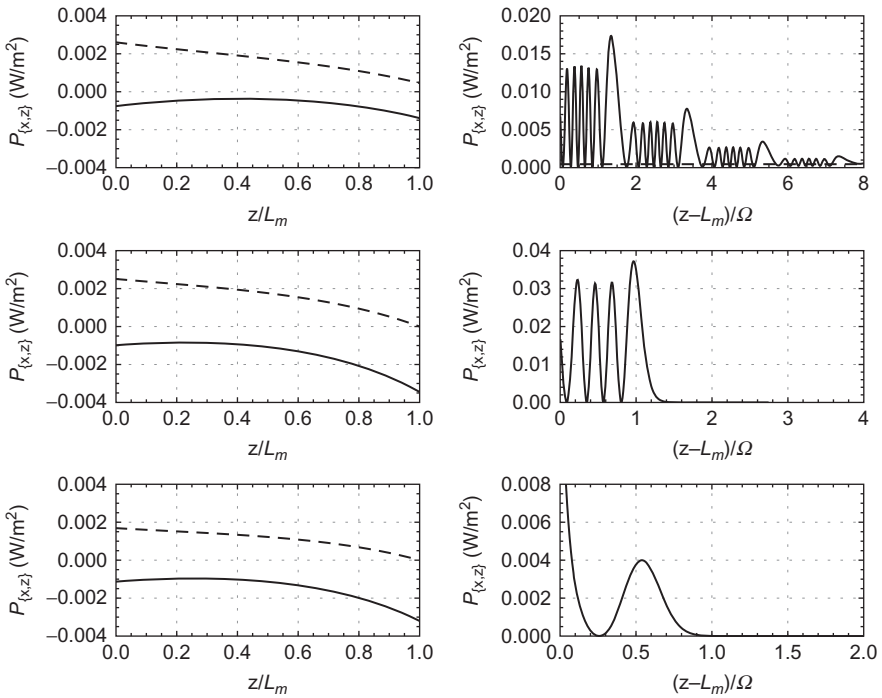


FIG. 11.13

Variations of the x- and z-components of the time-averaged Poynting vector $\mathbf{P}(z)$ in the TKR configuration in (*left*) the metal film and (*right*) the rugate filter when $L_m = 30$ nm and the incident plane wave is p polarized ($a_p = 1$ V/m, $a_s = 0$). (*Top*) $\theta = 33.23$ deg, (*middle*) $\theta = 42.41$ deg, and (*bottom*) $\theta = 59.66$ deg. *Solid lines* represent P_x and *dashed lines* represent P_z, while P_y is identically zero (Faryad and Lakhtakia, 2011e).

be expected because a metal is dissipative. However, P_x is localized to the metal/rugate-filter interface and decays away from that interface on both sides. The localization of the P_x to the interface plane $z = L_m$ is a clear indication of an SPP wave. While the variation of P_x is similar in the metal for the three SPP waves, the spatial profiles of P_x in the rugate filter are different for all three, indicating the different degree of localization of the SPP wave excited with a different value of θ.

In all the plots in Fig. 11.13, $P_x(z = 0) \neq 0$, whereas $P_x(z = L_\Sigma) \simeq 0$. Because the thickness of the metal film is almost equal to the penetration depth of the metal, P_x does not decay to zero in the thin metal film. If the metal film is sufficiently thick, the energy may reside completely in the rugate filter and the metal film; however, no SPP waves may be excited in the TKR configuration if the metal film is made too thick. Faryad and Lakhtakia (2011e) noted the same behavior of P_x and P_z for all SPP waves excited by p- and s-polarized incident plane waves.

Faryad and Lakhtakia (2011e) have also shown that the SPP waves excited in the TKR configuration may be coupled to both zinc-selenide/metal and metal/rugate-filter interfaces because of the thin metal film; however, the coupling does not result in new SPP waves. Moreover, the coupling is stronger for p-polarized SPP waves than s-polarized SPP waves.

11.6.2 METAL/SNTF INTERFACE

The excitation of multiple SPP waves guided by a planar metal/SNTF interface in the TKR configuration is briefly discussed now. In this configuration, a plane wave propagating in a half space occupied by a homogeneous dielectric material of real refractive index n_ℓ is taken to be incident on a metal-capped SNTF at an angle θ with respect to the thickness direction of the SNTF. The SNTF is of finite but sufficiently large thickness and is terminated by a half space that is occupied by a homogeneous material, whereas the metal film is very thin.

Faryad and Lakhtakia (2011d) implemented the formulation provided by Motyka and Lakhtakia (2008), when the morphologically significant plane of the SNTF and the incidence plane are the same, with $n_\ell = 2.58$ (zinc selenide), $\epsilon_{\text{met}} = -56 + 21i$ (bulk aluminum), and the same SNTF as described in Section 11.3.2, and determined the θ-values of the absorptance peaks that are independent of the thickness of the SNTF and the relative wavenumbers $k_x/k_0 = n_\ell \sin\theta$ at these values of θ. The θ-values for p-polarized incident plane waves are 46.3 and 53.0 deg, and the corresponding values of k_x/k_0 are 1.8653 and 2.0605. For s-polarized incidence, $\theta = 75.0$ deg and $k_x/k_0 = 2.4921$. These values are in excellent agreement with the solutions provided in Fig. 11.3 for the canonical boundary-value problem and the grating-coupled configuration (Faryad and Lakhtakia, 2011d), indicating the excitation of two p- and one s-polarized SPP waves.

Similarly, the relative wavenumbers $k_x/k_0 = n_\ell \sin\theta$ at the θ-values of the absorptance peaks independent of the thickness of the SNTF were determined when the morphologically significant plane of the SNTF makes an angle of 75 deg with the incidence plane (Motyka and Lakhtakia, 2009). These relative wavenumbers (2.0796 and 2.4782) were found to be in agreement with the solutions of the

canonical boundary-value problem provided in Fig. 11.3 for $\psi = 75$ deg, and with the grating-coupled configuration described in Section 11.5.2.

11.7 GENERAL REMARKS

The solution of the canonical boundary-value problem showed that multiple SPP waves of both *p*- and *s*-polarization states can be guided by the planar interface of a metal and a periodically nonhomogeneous, isotropic dielectric material. The partnering dielectric material must be nonhomogeneous in the direction normal to the waveguiding interface. Furthermore, some SPP waves that are neither *p*- nor *s*-polarized can be guided when the partnering dielectric material is anisotropic, although other SPP waves may be linearly polarized. The solution of the canonical boundary-value problem unequivocally proved the existence of multiple SPP waves because the possibility of waveguide modes is not present in a canonical boundary-value problem as is the case with the TKR and the grating-coupled configurations. The possibility of guiding multiple SPP waves by the metal/rugate-filter interface showed that it is the periodic nonhomogeneity—and not the anisotropy—of the partnering dielectric material that is responsible for the multiplicity of SPP waves, provided that the period lies within a certain range.

The excitation of multiple SPP waves by a surface-relief grating formed by a metal and a dielectric material, both of finite thickness, was studied theoretically using the rigorous coupled-wave approach (RCWA) for a practically implementable setup. The presence of an SPP wave is inferred by a peak in the plot of absorptance versus the angle of incidence θ, provided that the θ-location of the peak is independent of the thickness of the dielectric partnering material. If that material is homogeneous, only one SPP wave, that too of *p*-polarization state, is excited. When the partnering dielectric material is anisotropic, the efficient excitation of SPP waves does not only depend on the direction of the electric field of the incident linearly polarized plane wave but also on the thickness of the SNTF. So, optimization of the grating profile and the thickness of the dielectric partnering material may be necessary for efficient simultaneous excitation of many SPP waves as well as for broadband performance. The excitation of different SPP waves in the grating-coupled configuration sometimes requires different periods of the surface-relief grating. Therefore, the simultaneous excitation of all possible SPP waves may be achieved by using a quasiperiodic grating (Dolev et al., 2011).

In the TKR configuration, a plane wave of either *p*- or *s*-polarization state, propagating in an optically denser dielectric material, was taken to be incident on a metal-capped rugate filter or a metal-capped SNTF. The absorptances were calculated using a stable numerical algorithm as functions of the incidence angle. The excitation of SPP waves was inferred from the presence of those peaks in the absorptance plot that were independent of the thickness of the rugate filter. The results of the canonical boundary-value problem, the grating-coupled configuration, and the TKR configuration were successfully correlated with each other. Besides the agreement of

relative wavenumbers of SPP waves in the grating-coupled and the TKR configurations, it turns out that the higher the phase speed of an SPP wave, the narrower is the absorptance peak representing the excitation of that SPP wave. Furthermore, the spatial profiles of SPP waves are similar in both configurations.

In general, the absorptance peak is narrower for an *s*-polarized SPP wave than for of a *p*-polarized SPP wave, and the absorptance peak is narrower for an SPP wave of higher phase speed in both the grating-coupled and the TKR configurations. The fact that only *p*-polarized SPP waves can be excited when the partnering dielectric material is homogeneous indicates the difficulty of exciting *s*-polarized SPP waves—which is reflected both in the narrower peaks for A_s than for A_p in the results for the grating-coupled and the TKR configurations, as well as in the greater number of solutions of a relevant canonical boundary-value problem for *p*- than for *s*-polarized SPP waves. Underlying all of these observations are the great mismatch in optical admittance (Jen et al., 2009) across metal/dielectric interfaces that usually prevails for *s*-polarized fields (Salamon and Tollin, 2001).

The choice of using the TKR or the grating-coupled configuration comes with several trade-offs. On one hand, the TKR configuration is popular because all interfaces involved are planar and, therefore, easy to fabricate. It is also advantageous because the absorptances' peaks associated with the excitation of SPP waves are easy to identify because only one SPP wave can be excited only at one value of incidence angle with a prism of a specific shape and made of a specific material. On the other hand, the grating-coupled configuration does not require a prism, and therefore does not require an index-matching oil between the prism and the substrate on which the metal film and the partnering dielectric material are deposited. Consequently, the grating-coupled configuration offers greater flexibility in the selection of materials for the periodically nonhomogeneous dielectric partner (Rosenblatt et al., 1997). However, these advantages of the grating-coupled configuration come with the requirement of fabricating a periodically undulating interface. Even though it is not as straightforward as fabricating a planar interface, the fabrication of a periodically undulating surface with features on the scale of a few hundreds of nanometers is nowadays a routine matter (Gates et al., 2005).

Whereas the TKR configuration is popular for sensing applications (Homola, 2006), the grating-coupled configuration is becoming popular in enhancing the efficiency of thin-film solar cells (Xiao et al., 2012; Green and Pillai, 2012). Furthermore, the grating-coupled configuration allows the reverse process: the efficient coupling of SPP waves, which are otherwise nonradiative, with light (Moreland et al., 1982; Worthing and Barnes, 2001). This is an important advantage over the TKR configuration because it allows for better incorporation of chemical sensors based on SPP waves (Barnes et al., 2003) in integrated optical circuits (Lambeck, 2006).

The numerical results discussed in this chapter were all computed for one value of λ_0; however, multiple SPP waves for other values of λ_0 must also be expected. The numbers of *p*- and *s*-polarized SPP waves and their wavenumbers in any related

canonical boundary-value problem must depend on λ_0. This is because all constitutive parameters of causal materials are frequency-dependent, not to mention that the effects of the spatial dimensions of the materials require interpretation in terms of λ_0. Experimental verification has recently been made (Hall et al., 2013; Liu et al., 2014).

Let us also note that the periodic nonhomogeneity of a partnering dielectric material leads to the multiplicity of Fano waves (Faryad et al., 2011). The same attribute is responsible for engendering surface waves recently named as Tamm waves (Maab et al., 2011) although known for quite a while (Martorell et al., 2006; Robertson and May, 1999; Yeh et al., 1977), as well as the recently predicted Dyakonov-Tamm waves (Faryad, 2012; Agarwal et al., 2009; Gao et al., 2009a,b,c, 2010; Faryad and Lakhtakia, 2011a,f). Moreover, the coupling of two interfaces have also been found to increase the number of surface waves (both SPP and Dyakonov-Tamm waves) when the homogeneous material separating the two interfaces is thinner than twice the e-folding distance of the surface wave into that homogeneous material (Faryad and Lakhtakia, 2010a,c, 2011f; Faryad, 2012), besides the periodic nonhomogeneity of the partnering dielectric materials.

11.8 SUGGESTIONS FOR FUTURE WORK

The field of *surface multiplasmonics* is still in its infancy, and there is considerable room available to work both theoretically and experimentally to gain understanding of the phenomenon and its exploitation for practical devices. A few suggestions for theoretical work are follows.

11.8.1 EXCITATION OF MULTIPLE SPP WAVES WITH FINITE SOURCES

The study of excitation of multiple surface waves with a finite source, such as a line source, in either the TKR or the grating-coupled configuration will not only increase the scope of applications of SPP waves can but also provide a route toward exciting multiple SPP waves without the inconvenience of changing the angle of incidence. This can lead to the possibility of exciting multiple surface waves in nanodevices with embedded light sources. This problem can be analyzed easily by expressing the electromagnetic field of the finite source as a spectrum of plane waves (Chew, 1990, Section 2.2).

11.8.2 COMPOUND SURFACE-RELIEF GRATINGS

As discussed in Section 11.5, the excitation of all possible SPP waves requires that the period of the surface-relief grating be changed. In a practical situation, this amounts to the fabrication of many different gratings. This problem can be overcome by having a new surface-relief grating such that each period of the new surface-relief grating contains, say, two or three periods of two (or as many as one likes) different surface-relief gratings. This new structure may allow the simultaneous excitation of

all possible SPP waves. Theoretical analysis then requires a new grating shape-function $g(x)$ in the formulations provided by Faryad and Lakhtakia (2011c,d), but the number of terms in the Fourier expansion of the grating shape-function $g(x)$ is much higher. Research in this direction has recently commenced (Faryad and Lakhtakia, 2012).

11.8.3 EFFECTS OF MULTIPLE SPP WAVES ON THE EFFICIENCY OF THIN-FILM SOLAR CELLS

Faryad and Lakhtakia (2011b) have shown that the light absorption can be enhanced if the partnering dielectric material in the grating-coupled configuration is taken to be a periodically nonhomogeneous semiconductor. However, the boundary-value problem in their paper cannot be used for actual solar cells because it does not have any *p-n* junctions and no antireflection coatings or transparent-conducting-oxide layers for electrical connection. Moreover, the problem solved in that paper was limited only to the enhancement of light absorption and not the output electrical power. We believe that a complete problem, which includes the geometry of actual solar cell with the aim to optimize the output power, is worth investigating. For this purpose, the formulation provided by Faryad and Lakhtakia (2011c) has recently been modified by Faryad et al. (2012) in order to incorporate the layered structure of the solar cell.

11.9 RESOURCES

As has been stated in the foregoing section, surface multiplasmonics is an emerging area of research; therefore, not many resources are available for (potential) entrants to this area. To this date, three theses (Motyka, 2009; Erten, 2011; Faryad, 2012) and a review article (Polo and Lakhtakia, 2011) are available for consultation. A recent book also provides necessary information (Polo et al., 2013). In addition, anyone interested in finding the latest articles on this field should keep an eye on the journals published by Society of Photo-Optical Instrumentation Engineers (SPIE), Optical Society of America (OSA), American Physical Society (APS), and Institute of Physics (United Kingdom).

REFERENCES

Abdulhalim, I., 2009. Surface plasmon TE and TM waves at the anisotropic film-metal interface. J. Opt. A Pure Appl. Opt. 11, 015002.

Abdulhalim, I., Zourob, M., Lakhtakia, A., 2007. Overview of optical biosensing techniques. In: Marks, R., Cullen, D., Karube, I., Lowe, C.R., Weetall, H.H. (Eds.), Handbook of Biosensors and Biochips. Wiley, Chichester, pp. 413–446.

Abdulhalim, I., Zourob, M., Lakhtakia, A., 2008. Surface plasmon resonance for biosensing: a mini-review. Electromagnetics 28, 214–242.

Agarwal, K., Polo Jr., J.A., Lakhtakia, A., 2009. Theory of Dyakonov-Tamm waves at the planar interface of a sculptured nematic thin film and an isotropic dielectric material. J. Opt. A Pure Appl. Opt. 11, 074003.

Atalla, M.R.M., Faryad, M., Lakhtakia, A., 2012. On surface plasmon-polariton waves guided by the interface of a metal and a rugate filter with a sinusoidal refractive-index profile. Part ii: high-phase-speed solutions. J. Opt. Soc. Am. A 29, 3078–3086.

Barnes, W.L., Dereux, A., Ebbesen, T.W., 2003. Surface plasmon subwavelength optics. Nature 424, 824–830.

Baumeister, P.W., 2004. Optical Coating Technology. SPIE Press, Bellingham, WA.

Berini, P., 2009. Long-range surface plasmon polaritons. Adv. Opt. Photon. 1, 484–588.

Borstel, G., Falge, H.J., 1982. Surface phonon-polaritons. In: Boardman, A.D. (Ed.), Electromagnetic Surface Modes. Wiley, New York, NY.

Bovard, B.G., 1993. Rugate filter theory: an overview. Appl. Opt. 32, 5427–5442.

Chateau, N., Hugonin, J.P., 1994. Algorithm for the rigorous coupled-wave analysis of grating diffraction. J. Opt. Soc. Am. A 11, 1321–1331.

Chew, W.C., 1990. Waves and Fields in Inhomogeneous Media. IEEE Press, Piscataway, NJ.

Devender, Pulsifer, D.P., Lakhtakia, A., 2009. Multiple surface plasmon polariton waves. Electron. Lett. 45, 1137–1138.

Dolev, I., Volodarsky, M., Porat, G., Arie, A., 2011. Multiple coupling of surface plasmons in quasiperiodic gratings. Opt. Lett. 36, 1584–1586.

Dragoman, M., Dragoman, D., 2008. Plasmonics: applications to nanoscale terahertz and optical devices. Prog. Quantum Electron. 32, 1–41.

Elston, S.J., Sambles, J.R., 1990. Surface plasmon-polaritons on an anisotropic substrate. J. Mod. Opt. 37, 1895–1902.

Erten, S., 2011. Excitation of multiple surface-plasmon-polariton waves at metal/chiral-sculptured-thin-film interfaces. M.S. thesis (Engineering Science), Pennsylvania State University.

Fahr, S., Ulbrich, C., Kirchartz, T., Rau, U., Rockstuhl, C., Lederer, F., 2008. Rugate filter for light-trapping in solar cells. Opt. Express 16, 9332–9343.

Faryad, M., 2012. Propagation and excitation of multiple surface waves. Ph.D. dissertation (Engineering Science and Mechanics), Pennsylvania State University.

Faryad, M., Lakhtakia, A., 2010a. Multiple surface-plasmon-polariton waves localized to a metallic defect layer in a sculptured nematic thin film. Phys. Status Solidi RRL 4, 265–267.

Faryad, M., Lakhtakia, A., 2010b. On surface plasmon-polariton waves guided by the interface of a metal and a rugate filter with sinusoidal refractive-index profile. J. Opt. Soc. Am. B 27, 2218–2223.

Faryad, M., Lakhtakia, A., 2010c. Surface plasmon-polariton wave propagation guided by a metal slab in a sculptured nematic thin film. J. Opt. (United Kingdom) 12, 085102.

Faryad, M., Lakhtakia, A., 2011a. Dyakonov-Tamm waves guided by a phase-twist combination defect in a sculptured nematic thin film. Opt. Commun. 284, 160–168.

Faryad, M., Lakhtakia, A., 2011b. Enhanced absorption of light due to multiple surface-plasmon-polariton waves. Proc. SPIE 8110, 81100F.

Faryad, M., Lakhtakia, A., 2011c. Grating-coupled excitation of multiple surface-plasmon-polariton waves. Phys. Rev. A 84, 033852.

Faryad, M., Lakhtakia, A., 2011d. Multiple trains of same-color surface plasmon-polaritons guided by the planar interface of a metal and a sculptured nematic thin film. Part V: grating-coupled excitation. J. Nanophoton. 5, 053527.

Faryad, M., Lakhtakia, A., 2011e. On multiple surface-plasmon-polariton waves guided by the interface of a metal film and a rugate filter in the Kretschmann configuration. Opt. Commun. 284, 5678–5687.

Faryad, M., Lakhtakia, A., 2011f. Propagation of surface waves and waveguide modes guided by a dielectric slab inserted in a sculptured nematic thin film. Phys. Rev. A. 83, 013814.

Faryad, M., Lakhtakia, A., 2012. Excitation of multiple surface-plasmon-polariton waves using a compound surface-relief grating. J. Nanophoton. 6, 061701.

Faryad, M., Polo Jr., J.A., Lakhtakia, A., 2010. Multiple trains of same-color surface plasmon-polaritons guided by the planar interface of a metal and a sculptured nematic thin film. Part IV: canonical problem. J. Nanophoton. 4, 043505.

Faryad, M., Maab, H., Lakhtakia, A., 2011. Rugate-filter-guided propagation of multiple Fano waves. J. Opt. (United Kingdom) 13, 075101.

Faryad, M., Hall, A.S., Barber, G.D., Mallouk, T.E., Lakhtakia, A., 2012. Excitation of multiple surface-plasmon-polariton waves guided by the periodically corrugated interface of a metal and a periodic multilayered isotropic dielectric material. J. Opt. Soc. Am. B 29, 704–713.

Ferry, V.E., Sweatlock, A., Pacifici, D., Atwater, H.A., 2008. Plasmonic nanostructure design for efficient light coupling into solar cells. Nano Lett. 8, 4391–4397.

Fiumara, V., Chiadini, F., Scaglione, A., Lakhtakia, A., 2006. Theory of thin-film, narrow-band, linear-polarization rejection filters with superlattice structure. Opt. Commun. 268, 182–188.

Gao, J., Lakhtakia, A., Lei, M., 2009a. On Dyakonov-Tamm waves localized to a central twist defect in a structurally chiral material. J. Opt. Soc. Am. B 26, B74–B82.

Gao, J., Lakhtakia, A., Polo Jr., J.A., Lei, M., 2009b. Dyakonov-Tamm waves guided by a twist defect in a structurally chiral material. J. Opt. Soc. Am. A 26, 1615–1621.

Gao, J., Lakhtakia, A., Polo Jr., J.A., Lei, M., 2009c. Dyakonov-Tamm waves guided by a twist defect in a structurally chiral material: erratum. J. Opt. Soc. Am. A 26, 2399.

Gao, J., Lakhtakia, A., Lei, M., 2010. Dyakonov-Tamm waves guided by the interface between two structurally chiral materials that differ only in handedness. Phys. Rev. A 81, 013801.

Gaspar-Armenta, J.A., Villa, F., 2003. Photonic surface-wave excitation: photonic crystal-metal interface. J. Opt. Soc. Am. B 20, 2349–2354.

Gates, B.D., Xu, Q., Stewart, M., Ryan, D., Wilson, C.G., Whitesides, G.M., 2005. New approaches to nanofabrication: molding, printing and other techniques. Chem. Rev. 105, 1171–1196.

Gilani, T.H., Dushkina, N., Freeman, W.L., Numan, M.Z., Talwar, D.N., Pulsifer, D.P., 2010. Surface plasmon resonance due to the interface of a metal and a chiral sculptured thin film. Opt. Eng. 49, 120503.

Green, M.A., Pillai, S., 2012. Harnessing plasmonics for solar cells. Nature Photon. 6, 130–132.

Hall, A.S., Faryad, M., Barber, G.D., Liu, L., Erten, S., Mayer, T.S., Lakhtakia, A., Mallouk, T.E., 2013. Broadband light absorption with multiple surface plasmon polariton waves excited at the interface of a metallic grating and photonic crystal. ACS Nano. 7, 4995–5007.

Hodgkinson, I.J., Wu, Q.h., Hazel, J., 1998. Empirical equations for the principal refractive indices and column angle of obliquely deposited films of tantalum oxide, titanium oxide, and zirconium oxide. Appl. Opt. 37, 2653–2659.

Homola, J., (Ed.) 2006. Surface Plasmon Resonance Based Sensors. Springer, Heidelberg, Germany.

Jaluria, Y., 1996. Computer Methods for Engineering. Taylor & Francis, Washington, DC.

Jen, Y.J., Yu, C.W., 2011. Optical configuration for unpolarized ultra-long-range surface-plasmon-polariton waves. Appl. Opt. 50, C154–C158.

Jen, Y.J., Lakhtakia, A., Yu, C.W., Chan, T.Y., 2009. Multilayered structures for *p*- and *s*-polarized long-range surface-plasmon-polariton propagation. J. Opt. Soc. Am. A 26, 2600–2606.

Kanda, V., Kitov, P., Budle, D.R., McDermott, M.T., 2005. Surface plasmon resonance imaging measurements of the inhibition of Shiga-like toxin by synthetic multivalent inhibitors. Anal. Chem. 77, 7497–7504.

Kapany, N.S., Burke, J.J., 1972. Optical Waveguides. Academic Press, New York, NY.

Kik, P.G., Maier, S.A., Atwater, H.A., 2002. Plasmon printing—a new approach to near-field lithography. MRS Symp. Proc. 705, Y3.6.

Kretschmann, E., Raether, H., 1968. Radiative decay of non radiative surface plasmons excited by light. Z. Naturforsch. A 23, 2135–2136.

Lakhtakia, A., 2007. Surface-plasmon wave at the planar interface of a metal film and a structurally chiral medium. Opt. Commun. 279, 291–297.

Lakhtakia, A., 2010. Reflection of an obliquely incident plane wave by a half space filled by a helicoidal bianisotropic medium. Phys. Lett. A 374, 3887–3894.

Lakhtakia, A., 2011. Surface multiplasmonics. Proc. SPIE 8104, 810403.

Lakhtakia, A., Geddes III, J.B., 2010. Thin-film metamaterials called sculptured thin films. In: Aldea, A., Bârsan, V. (Eds.), Trends in Nanophysics. Springer, Heidelberg, Germany, pp. 59–71.

Lakhtakia, A., Messier, R., 1994. The key to a thin film HBM: the Motohiro-Taga interface. In: Mariotte, F., Parneix, J.P. (Eds.), Proceedings of Chiral 94 (Périgueux, France, May 18-20). French Atomic Energy Commission, Le Barp, France, pp. 125–130.

Lakhtakia, A., Messier, R., 2005. Sculptured Thin Films: Nanoengineered Morphology and Optics. SPIE Press, Bellingham, WA.

Lakhtakia, A., Polo Jr., J.A., 2007. Dyakonov-Tamm wave at the planar interface of a chiral sculptured thin film and an isotropic dielectric material. J. Eur. Opt. Soc. Rapid Pubs. 2, 07021.

Lakhtakia, A., Weiglhofer, W.S., 1993. Axial propagation in general helicoidal bianisotropic media. Microw. Opt. Technol. Lett. 6, 804–806.

Lakhtakia, A., Messier, R., Brett, M.J., Robbie, K., 1996. Sculptured thin films (STFs) for optical, chemical and biological applications. Innov. Mater. Res. 1, 165–176.

Lakhtakia, A., Jen, Y.J., Lin, C.F., 2009. Multiple trains of same-color surface plasmon-polaritons guided by the planar interface of a metal and a sculptured nematic thin film. Part III: experimental evidence. J. Nanophoton. 3, 033506.

Lambeck, P.V., 2006. Integrated optical sensors for the chemical domain. Meas. Sci. Technol. 17, R93–R116.

Lee, C.C., Tang, C.J., Wu, J.Y., 2006. Rugate filter made with composite thin films by ion-beam sputtering. Appl. Opt. 45, 1333–1337.

Li, L., 1993. Multilayer modal method for diffraction gratings of arbitrary profile, depth, and permittivity. J. Opt. Soc. Am. A 12, 2581–2591.

Liu, L., Faryad, M., Hall, A.S., Barber, G.D., Erten, S., Mallouk, T.E., Lakhtakia, A., Mayer, T.S., 2014. Experimental excitation of multiple surface-plasmon-polariton waves and waveguide modes in a one-dimensional photonic crystal atop a two-dimensional metal grating. J. Nanophoton. 9, 093593.

Lorenzo, E., Oton, C.J., Capuj, N.E., Ghulinyan, M., Navarro-Urrios, D., Gaburro, Z., Pavesi, L., 2005. Fabrication and optimization of rugate filters based on porous silicon. Phys. Status Solidi C 2, 3227–3231.

Maab, H., Faryad, M., Lakhtakia, A., 2011. Surface electromagnetic waves supported by the interface of two semi-infinite rugate filters with sinusoidal refractive index profiles. J. Opt. Soc. Am. A 28, 1204–1212.

Mackay, T.G., Lakhtakia, A., 2008. Electromagnetic fields in linear bianisotropic mediums. Prog. Opt. 51, 121–209.

Mackay, T.G., Lakhtakia, A., 2010a. Electromagnetic Anisotropy and Bianisotropy: A Field Guide. World Scientific, Singapore.

Mackay, T.G., Lakhtakia, A., 2010b. Modeling columnar thin films as platforms for surface-plasmonic-polaritonic optical sensing. Photon. Nanostruct. Fund. Appl. 8, 140–149.

Mackay, T.G., Lakhtakia, A., 2012. Modeling chiral sculptured thin films as platforms for surface-plasmonic-polaritonic optical sensing. IEEE Sens. J. 12, 273–280.

Maier, S.A., 2007. Plasmonics: Fundamentals and Applications. Springer, New York, NY.

Maier, S.A., Brongersma, M.L., Kik, P.G., Meltzer, S., Requicha, A.A.G., Atwater, H.A., 2001. Plasmonics—a route to nanoscale optical devices. Adv. Mater. 13, 1501–1505.

Marcuse, D., 1991. Theory of Dielectric Optical Waveguides. Academic Press, San Diego, CA.

Martin, P.M., (Ed.) 2010. Handbook of Deposition Technologies for Films and Coatings: Science, Applications and Technology, third ed. Elsevier, Oxford.

Martín-Palma, R.J., Lakhtakia, A., 2010. Nanotechnology: A Crash Course. SPIE Press, Bellingham, WA.

Martorell, J., Sprung, D.W.L., Morozov, G.V., 2006. Surface TE waves on 1D photonic crystals. J. Opt. A Pure Appl. Opt. 8, 630–638.

Messier, R., Gehrke, T., Frankel, C., Venugopal, V.C., Otaño, W., Lakhtakia, A., 1997. Engineered sculptured nematic thin films. J. Vac. Sci. Technol. A 15, 2148–2152.

Messier, R., Venugopal, V.C., Sunal, P.D., 2000. Origin and evolution of sculptured thin films. J. Vac. Sci. Technol. A 18, 1538–1545.

Moharam, M.G., Gaylord, T.K., 1982. Diffraction analysis of dielectric surface-relief gratings. J. Opt. Soc. Am. 72, 1385–1392.

Moharam, M.G., Grann, E.B., Pommet, D.A., 1995. Formulation for stable and efficient implementation of the rigorous coupled-wave analysis of binary gratings. J. Opt. Soc. Am. A 12, 1068–1076.

Moreland, J., Adams, A., Hansma, P.K., 1982. Efficiency of light emission from surface plasmons. Phys. Rev. B 25, 2297–2300.

Motyka, M.A., 2009. Multiple trains of same-color surface plasmon-polaritons guided by the planar interface of a metal film and a sculptured nematic thin film. M.S. thesis (Engineering Science), Pennsylvania State University.

Motyka, M.A., Lakhtakia, A., 2008. Multiple trains of same-color surface plasmon-polaritons guided by the planar interface of a metal and a sculptured nematic thin film. J. Nanophoton. 2, 021910.

Motyka, M.A., Lakhtakia, A., 2009. Multiple trains of same-color surface plasmon-polaritons guided by the planar interface of a metal and a sculptured nematic thin film. Part II: arbitrary incidence. J. Nanophoton. 3, 033502.

Nolte, A.J., Rubner, M.F., Cohen, R.E., 2004. Creative effective refractive index gradients within polyelectrolyte multilayer films: molecularly assembled rugate filters. Langmuir 20, 3304–3310.

Otto, A., 1968. Excitation of nonradiative surface plasma waves in silver by the method of frustrated total reflection. Z. Phys. 216, 398–410.

Otto, A., Sohler, W., 1971. Modification of the total reflection modes in a dielectric film by one metal boundary. Opt. Commun. 3, 254–258.

Overend, R., Gibson, D.R., Marshall, R., Lewis, K., 1992. Rugate filter fabrication using neutral cluster beam deposition. Vacuum 43, 51–54.

Perilloux, B.E., 2002. Thin-Film Design: Modulated Thickness and Other Stopband Design Methods. SPIE Press, Bellingham, WA.

Polo Jr., J.A., Lakhtakia, A., 2009a. Energy flux in a surface-plasmon-polariton wave bound to the planar interface of a metal and a structurally chiral material. J. Opt. Soc. Am. A 26, 1696–1703.

Polo Jr., J.A., Lakhtakia, A., 2009b. On the surface plasmon polariton wave at the planar interface of a metal and a chiral sculptured thin film. Proc. R. Soc. Lond. A 465, 87–107.

Polo Jr., J.A., Lakhtakia, A., 2011. Surface electromagnetic waves: a review. Laser Photon. Rev. 5, 234–246.

Polo Jr., J.A., Mackay, T.G., Lakhtakia, A., 2011. Mapping multiple surface-plasmon-polariton-wave modes at the interface of a metal and a chiral sculptured thin film. J. Opt. Soc. Am. B 28, 2656–2666.

Polo Jr., J.A., Mackay, T.G., Lakhtakia, A., 2013. Electromagnetic Surface Waves: A Modern Perspective. Elsevier, Waltham, MA.

Pursel, S., Horn, M.W., Demirel, M.C., Lakhtakia, A., 2005. Growth of sculptured polymer submicronwire assemblies by vapor deposition. Polymer 46, 9544–9548.

Robbie, K., Brett, M.J., Lakhtakia, A., 1995. First thin film realization of a helicoidal bianisotropic medium. J. Vac. Sci. Technol. A 13, 2991–2993.

Robertson, W.M., May, M.S., 1999. Surface electromagnetic wave excitation on one-dimensional photonic band-gap arrays. Appl. Phys. Lett. 74, 1800–1802.

Rosenblatt, D., Sharon, A., Friesem, A.A., 1997. Resonant grating waveguide structures. IEEE J. Quantum Electron. 33, 2038–2059.

Salamon, Z., Tollin, G., 2001. Optical anisotropy in lipid bilayer membrane: coupled plasmon-waveguide resonance measurements of molecular orientation, polarizability, and shape. Biophys. J. 80, 1557–1567.

Salamon, Z., Macleod, H.A., Tollin, G., 1997. Coupled plasmon-waveguide resonators: a new spectroscopic tool for probing proteolipid film structure and properties. Biophys. J. 73, 2791–2797.

Sarid, D., 1981. Long-range surface-plasma waves on very thin metal films. Phys. Rev. Lett. 47, 1927–1930.

Simon, H.J., Mitchell, D.E., Watson, J.G., 1975. Surface plasmons in silver films—a novel undergraduate experiment. Am. J. Phys. 43, 630–636.

Sit, J.C., Vick, D., Robbie, K., Brett, M.J., 1999. Thin film microstructure control using glancing angle deposition by sputtering. J. Mater. Res. 14, 1197–1199.

Swiontek, S.E., Pulsifer, D.P., Xu, J., Lakhtakia, A., 2013. Suppression of circular Bragg phenomenon in chiral sculptured thin films produced with simultaneous rocking and rotation of substrate during serial bideposition. J. Nanophoton. 7, 073599.

Turbadar, T., 1959. Complete absorption of light by thin metal films. Proc. Phys. Soc. 73, 40–44.
Uller, K., 1903. Beiträge zur Theorie der Elektromagnetischen Strahlung. Ph.D. dissertation, Universität Rostock.
Usui-Aoki, K., Shimada, K., Nagano, M., Kawai, M., Koga, H., 2005. A novel approach to protein expression profiling using antibody microarrays combined with surface plasmon resonance technology. Proteomics 5, 2396–2401.
Vick, D., Tsui, Y.Y., Brett, M.J., Fedosejevs, R., 1999. Production of porous carbon thin films by pulsed laser deposition. Thin Solid Films 350, 49–52.
Wallis, R.F., 1982. Surface magnetoplasmons on semiconductors. In: Boardman, A.D. (Ed.), Electromagnetic Surface Modes. Wiley, New York, NY.
Wang, H., 1995. Excitation of surface plasmon oscillations at an interface between anisotropic dielectric and metallic media. Opt. Mater. 4, 651–656.
Wang, F., Horn, M.W., Lakhtakia, A., 2004. Rigorous electromagnetic modeling of near-field phase-shifting contact lithography. Microelectron. Eng. 71, 34–53.
Wei, L., Lakhtakia, A., Roopnariane, A.P., Ritty, T.M., 2010. Human fibroblast attachment on fibrous parylene-C thin-film substrates. Mater. Sci. Eng. C 30, 1252–1259.
Weiglhofer, W.S., Lakhtakia, A., 2003. Introduction to Complex Mediums for Optics and Electromagnetics. SPIE Press, Bellingham, WA.
Worthing, P.T., Barnes, W.L., (Ed.) 2001. Efficient coupling of surface plasmon polaritons to radiation using a bi-grating. Appl. Phys. Lett. 79, 3035–3037.
Xiao, S., Stassen, E., Mortensen, N.A., 2012. Ultrathin silicon solar cells with enhanced photocurrents assisted by plasmonic nanostructures. J. Nanophoton. 6, 061503.
Yakubovich, V.A., Starzhinskii, V.M., 1975. Linear Differential Equations With Periodic Coefficients. Wiley, New York, NY.
Yan, W., Shen, L., Ran, L., Kong, J.A., 2007. Surface modes at the interfaces between isotropic media and indefinite media. J. Opt. Soc. Am. A 24, 530–535.
Yeh, P., Yariv, A., Hong, C.S., 1977. Electromagnetic propagation in periodic stratified media. I. General theory. J. Opt. Soc. Am. 67, 423–438.
Young, N.O., Kowal, J., 1959. Optically active fluorite films. Nature 183, 104–105.
Zenneck, J., 1907. Über die Fortpflanzung ebener elektromagnetischer Wellen längs einer ebenen Lieterfläche und ihre Beziehung zur drahtlosen Telegraphie. Ann. Phys. Lpz. 23, 846–866.
Zhang, J.C., Fang, M., Shao, Y.C., Jin, Y.X., He, H.B., 2011. Rugate filters prepared by rapidly alternating deposition. Chin. Phys. B 20, 094212.

CHAPTER

Optical thin films containing quantum dots 12

François Flory*, Yu-Jen Chen†, Hung-Ju Lin†
*Ecole Centrale Marseille, Marseille, France** National Central University, Taoyuan, Taiwan†*

12.1 INTRODUCTION AND OVERVIEW

Photodetectors including solar cells, environment sensors, and wide spectra-wide aperture antireflection coatings are important applications in photonics. In all of them, the incoming radiation energy should not be lost.

Nanostructured materials are extensively studied to reduce the loss of energy from reflection, inefficient absorption, or nonuseful wavelengths. Photonic crystals are studied to increase the lifetime of the light in the active material, structured antireflection coatings to increase the transmission of light through the surface, nanovelour structure like black silicon to increase useful light absorption, reticulated materials for organic solar cells, semiconductor nanoparticles, metallic nanoparticles to benefit from plasmonic effect, and Grätzel cells, carbon nanotubes, and silicon nanowires.

It is mandatory to understand carrier generation, carrier behavior, and more generally the interaction of light with such nanostructures to develop new applications. Most of the models used to study the optical properties of nanophotonic components are based on the electromagnetic theory. They all need the value of the complex refractive index or permittivity as an input. However, the bulk value of the refractive index is not fitted when the materials are structured in very small dimensions. It is then necessary to take into account the packing density of the material, the crystalline state, or to consider the homogenization theory and to use an effective index.

Moreover, when the critical dimension becomes in the order of a few nanometers, the model needs to be revisited further as quantum phenomena must be considered. A quantum dot (QD) is made of a semiconductor nanocrystal of a size smaller than the de Broglie wavelength, in the order of a few nanometers in the three spatial dimensions, surrounded by a material of a larger bandgap. QDs were discovered at the beginning of the 1980s by Ekimov et al. (1985) in a glass matrix and by Brus (1984) in colloidal solutions. The term "quantum dot" was coined by Reed et al. (1988). In these nanoparticles, the carriers, electrons, and holes are confined and they can have only discrete energy levels (Fig. 12.1), which depend on the

Optical Thin Films and Coatings. https://doi.org/10.1016/B978-0-08-102073-9.00012-6
Copyright © 2018 Elsevier Ltd. All rights reserved.

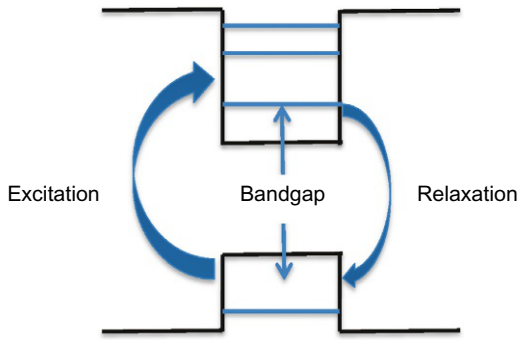


FIG. 12.1

Discrete energy levels, excitation, and relaxation processes.

QD size. Owing of their very attractive properties they have been studied by many research laboratories since several years. The atom-like behavior of the QDs gives absorption and luminescent spectra, which depend both on the properties of the semiconductor used and on the size of the QDs. In photonic structures, QDs can be embedded in another material or deposited as a QDs layer or coupled to some other structures. The complex refractive index of these materials, generally in thin film form, must be known to model the propagation of optical electromagnetic fields. We will try to bring here some elements of a response.

When the confinement takes place in only one dimension, similar to the semiconductor films of a few nanometers thickness we speak about quantum wells (QWs). We will present a simple model to describe the electron and hole distributions in not coupled and coupled QWs and in single QDs. This model gives results, which will be discussed in particular for coupled QWs. The limits of these models are also addressed and the extension of the effective mass model taking into account nonparabolicity of energy bands to QDs is presented. This theoretical part concludes with some elements for calculating the optical properties of QDs. In a third part, we will present the realization technique used to make PMMA layers containing different concentrations of core/shell CdSe/ZnS and TiO_2 QDs. The reflection, transmission, and absorption of these layers are presented and discussed. Ellipsometry and m-lines are used to measure the effective index of the layers. We will then discuss application of QDs layers for solar cells, for lighting and displays, and in optical interference coatings for extra high reflection and transmission coefficients. A conclusion and some perspectives are also given.

12.2 MODELING

Numerous techniques are available to calculate energy levels in quantum nanostructures. The most simple ones based on the particle in-a-box (PIB) model (Kittel, 2005), which is based on the effective mass approximation (EMA) (Sham and

Nakayama, 1979) like the quantum transfer matrix methods (Jonsson and Eng, 1990) are fast and give the general deviation from the bulk theory. They are suitable to study structures ranging from tenth of nanometers to several micrometers. Actual band-structures show that the approximation by a parabolic shape is only valid upon a small energetic domain near the band edges. This is the main limit of the effective mass approximation and the main source of errors. It limits the resolution of the high-energy levels that are increasingly inaccurate the further away they are from the band edge. This is due to the fact that the radius of curvature of the approximate shape is not constant but increases with the energy. More precise approaches based on multi-band methods such as tight-binding (Goringe et al., 1999) or k-p methods (Voon and Willatzen, 2009) allow a more precise evaluation of the electronic properties in the range of a few Angstroms to hundreds of nanometers. It should be noted that the EMA is a one-band k-p method. Atomistic and ab initio calculations such as pseudopotential methods (Andrae et al., 1990) and density functional theories (DFT) (Geerlings et al., 2003) are exacts but they are limited to the study of a few thousands of atoms due to hardware and time limitations. The band nonparabolicity can be taken into account in the EMA by an effective mass that increases accordingly with the energy. Accurate and fast methods can then be implemented (Thierry et al., 2015).

12.3 ELECTRONIC PROPERTIES OF QUANTUM WELLS AND THE EFFECTIVE MASS MODEL

Because of quantum confinement, the electronic levels are discretized in structures of a few nanometers, smaller than the Bohr radius. The simplest case to model is the electronic behavior in QWs.

In the approximation of the effective mass, the allowed energies of electrons are the eigenvalues of the stationary Schrödinger equation (Cohen-Tannoudji et al., 1997):

$$\frac{-\left(\frac{h^2}{4\pi^2}\right)}{2m}\left[\nabla^2 + V(r)\right]\psi(r) = E\psi(r) \tag{12.1}$$

For the 2D problem of QWs, the equation giving the energy levels is very similar to that used for planar waveguides, the electron wave function ψ taking place of the electric field. For QWs in the x direction, the wavefunction can be written as.

$$\psi(x) = Ae^{i\chi x} + Ae^{-i\chi x} \quad \text{for} \quad E > V \tag{12.2}$$

and

$$\psi(x) = Ae^{\rho x} + Ae^{-\rho x} \quad \text{for} \quad E < V \tag{12.3}$$

with

$$\chi^2 = \frac{2m}{\hbar^2}(E - V) \tag{12.4}$$

and

$$\rho^2 = \frac{2m}{\hbar^2}(V - E) \tag{12.5}$$

and m the effective mass of electron. Depending on the material, the effective mass of the electron can take different values.

As for multilayer planar waveguides, this formalism can be extended to multiple QWs (Flory et al., 2011). Thanks to the continuity of $\frac{1}{m}\psi$ and its derivative with the direction x perpendicular to the well boundaries, a recurrent relation can be found for the function $Q = \frac{\frac{1}{m}\frac{d\psi}{dx}}{\psi}$, which is similar to the recurrent relation obtained for the optical admittance in multilayer waveguides:

$$Q_j = k_j \frac{Q_{j-1} - k_j \tan(k_j a_j)}{Q_{j-1} \tan(k_j a_j) + k_j} \tag{12.6}$$

with j referring to a well boundary in the structure. Therefore, the value of Q on one limit of a structure can be obtained as a function of Q on its other limit.

If the electron is confined in a structure, ψ is evanescent in the surrounding media like the electric field is evanescent in the media surrounding a waveguide. The values of Q is then known on both sides of the structure. The equation describing the possible discrete energy levels is then derived from these considerations. The wavefunction and its square giving the electron density probability distribution can then be calculated in the whole structure:

$$\Psi_j = C_j^+ \left[e^{ik_j x} + \frac{ik_j - Q_{j-1}}{Q_{j-1} + ik_j} e^{ik_j(2x_{j-1} - x)} \right] \tag{12.7}$$

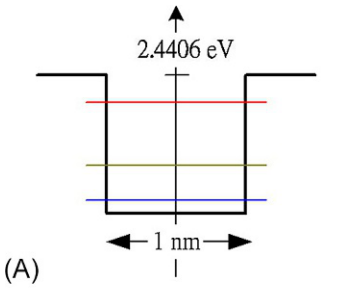
Let us now consider some examples of numerical results.

For a single QW, analytic values can be obtained (Eisberg and Resnick, 1985). The results obtained from the presented formalism are in good agreement with them. An example of a comparison between the analytical values and the values obtained with our calculation is given in Fig. 12.2, together with the wavefunctions.

An example of agreement between the bandgap calculated with this model and the measured bandgap is shown for 6-nm ZnO QDS dispersed in a liquid (Flory et al., 2011).

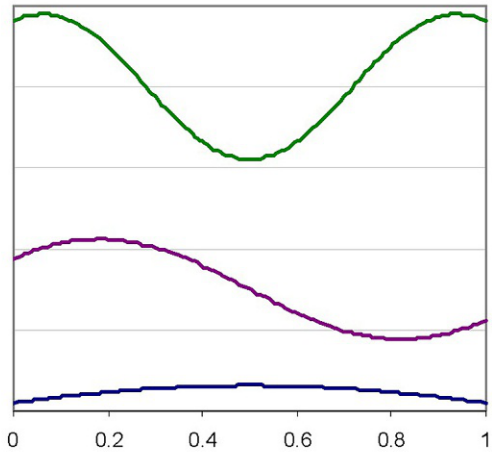
When N identical QWs are coupled, each energy level is split in N sublevels. Fig. 12.3 gives an example of the energy levels of electrons for 3 coupled identical wells of 1 nm width and 1 nm spacing with a depth of 3.2 eV. In a molecule, the electron energies of an atom are split into sublevels when the atom is coupled to others because of vibrational and rotational modes. Coupled QWs behave in a similar way.

Fig. 12.4 shows how the highest energy level of the electrons in a single well is split when considering 2, 3, 4, and 5 identical coupled wells. Each well has a depth of 2.9 eV, a width of 1 nm, and the distance between the wells is also 1 nm. When the number of coupled wells increases, the different sublevels fill a band.



1 nm, 2.4406 eV		
	Reference	Program
E1	0.239178	0.239237
E2	0.934749	0.934067
E3	1.972003	1.971731

(B)



(C)

FIG. 12.2

(A) Single-well structure, (B) numerical results from analytical formula and from our program, and (C) wave functions for the three energies levels (Flory et al., 2011).

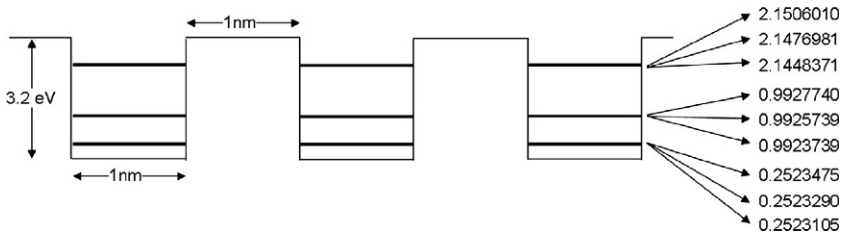


FIG. 12.3

Energy levels of electrons for 3 coupled identical quantum wells of 1 nm width, 1 nm spacing, and of 3.2 eV depth (Flory et al., 2011).

The Krönig-Penney model applies when the structure is periodic and infinite (Carpena et al., 1999). The different energy bands found with this model are in agreement with the solutions obtained with the previous formalism for a periodic structure. Therefore, for a large number of identical coupled QWs, each energy level of a single well is split into a large number of sublevels filling an energy band. It is a homogeneous band broadening. When the coupling is strong, the different bands are widened and can join to make a continuous band, and the material behaves like bulk. The coupling distance must not be larger than a few nanometers.

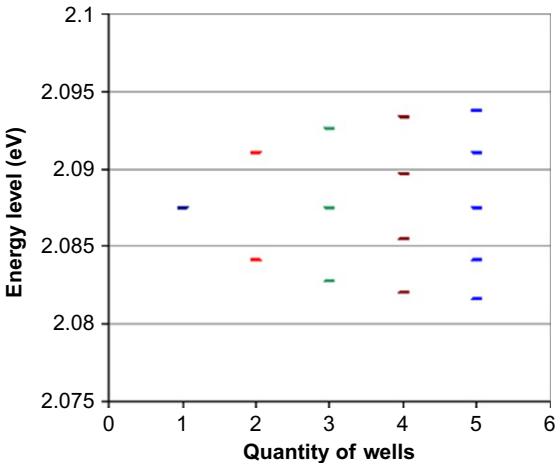


FIG. 12.4

Highest energy level of the electrons in a single well is split when considering 2, 3, 4, and 5 identical coupled wells (Flory et al., 2011).

Fig. 12.5 gives the electron probability density of the lowest energy in the structure composed of 9 identical wells of 2.9 eV depth, of 1 nm width, and the distance between the wells is 1 nm. As can be seen, the electrons are delocalized in the whole structure.

When the coupled wells are not identical the electron density of probability can be confined into one well or distributed into several wells depending on the

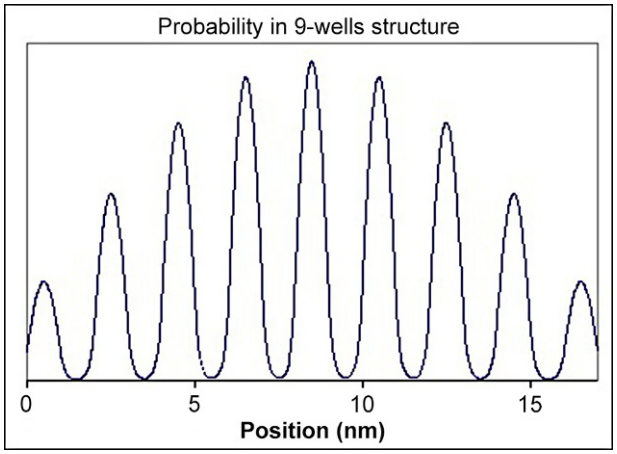


FIG. 12.5

Electron probability density of the lowest energy in the structure composed of 9 identical wells of 2.9 eV depth, of 1 nm width, and the distance between the wells is 1 nm (Flory et al., 2011).

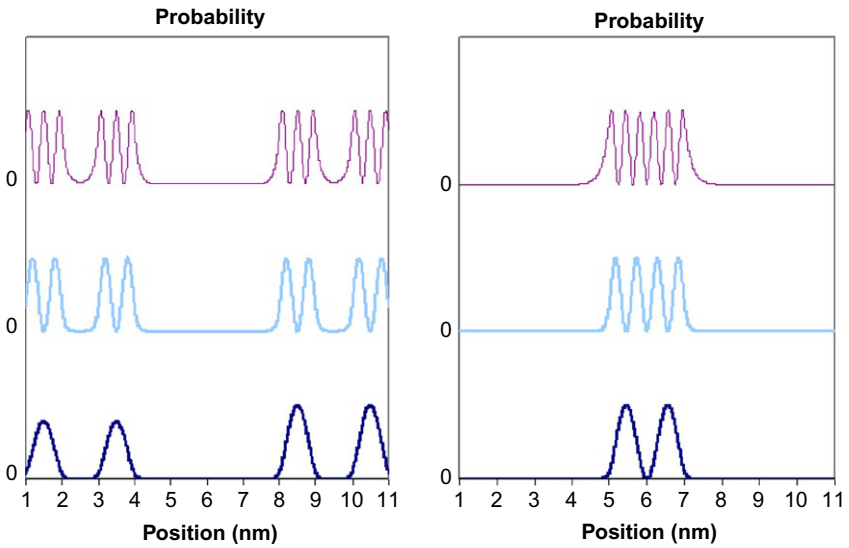


FIG. 12.6

Density of probability of electrons in a nonperiodic structure composed of 5 coupled wells of depth 2.9 eV, of width 1, 1, 2, 1, 1 nm, respectively. The distance between each well is 1 nm (Flory et al., 2011).

considered structure and the considered energy level. The electron density of probability is presented in Fig. 12.6 for a nonperiodic structure composed of 5 coupled wells, the well in the center of the structure being of 2 nm width, twice larger than the others.

The electrons can be localized in the largest well or delocalized in the other wells depending on the energy level considered. The electrons behave in a similar manner than in molecules for which the electrons can be linked to a particular atom or delocalized in the whole molecule.

Electron energy and wavefunction can be calculated also in deformed potential wells with the matrix formalism by approximating each deformed potential with a step function (Chen et al., 2014). This can be used to study electron behavior in QWs deformed by electrical fields.

12.4 ELECTRONIC PROPERTIES OF QUANTUM DOTS

Very simple approximate formula can be given in the effective mass approximation from the particle in the box consideration. According to Brus (1984) the band energy E_g of a QD of radius R is given by

$$E_g = E_{bulk} + \frac{h^2}{8R^2}\left(\frac{1}{m_e^*} + \frac{1}{m_h^*}\right) - \frac{1.786e^2}{4\pi\varepsilon_0\varepsilon_r R^2}$$

where E_{bulk} = bandgap energy of bulk semiconductor;
m_e^* = effective mass of electron;
m_h^* = effective mass of hole;
h = Planck's constant.

The equation is expected to fail when the dimension of the QDs is small because the wavefunction overlaps with the crystal boundaries. An energy-dependent effective mass can then be defined to have a better approximation. Following Harrison (2005) one can take into account the nonparabolicity of the energy band by using the corrected effective mass:

$$m^*_{corr}(r) = m^*(r)\left[1 + \left(1 - \frac{m^*(r)}{m_0}\right)^2 \frac{E_n - V(r)}{E_g(r)}\right]$$

where E_n is the energy of the considered level n; m_0 is the electron mass.

It should be noted that $E_g(r)$ is size dependent. The bulk values can be used to calculate the first-level energies in the conduction and valence bands as they present the smallest deviations induced by nonparabolicity. The calculated value of the gap obtained from these energy levels are then used to apply the nonparabolicity correction upon higher levels. The ballistic method has been used to calculate the energy bandgaps of different materials for different QD sizes (Thierry et al., 2015).

Fig. 12.7 shows a comparison for CdSe QDs between calculations performed with different methods including the corrected mass approximation method and measured values.

The absorption spectra of QDs layers exhibit strong modulations with maxima corresponding to excitonic states. In practice, in a set of QDs there is some size dispersion.

The size dispersion induces a band broadening, which is an inhomogeneous band broadening. QD coupling induces homogenous band broadening.

There could be other band-broadening phenomena like natural broadening link to the excited state lifetimes or the temperature, which can induce coupling to phonons or trap states. Hence, it is very difficult to model all these effects.

12.4.1 OPTICAL PROPERTIES

The complex refractive index of a material corresponds to its response to an optical wave. This response is linked to the local oscillators in the material. There are different oscillators in the material such as the atoms or the molecules. In bulk these oscillators are incoherent. In quantum structures, the electrons have coherent response corresponding to discrete values of their energy, each one corresponding to a different resonant frequency. The effective refractive indices of such quantum structures are then different from that of bulk. To model the effective refractive index, it is necessary to calculate the oscillator strengths associated with the intraband and interband excitonic states, coupling between the oscillators and possible coupling with phonons resonances. The oscillator strengths depend on the

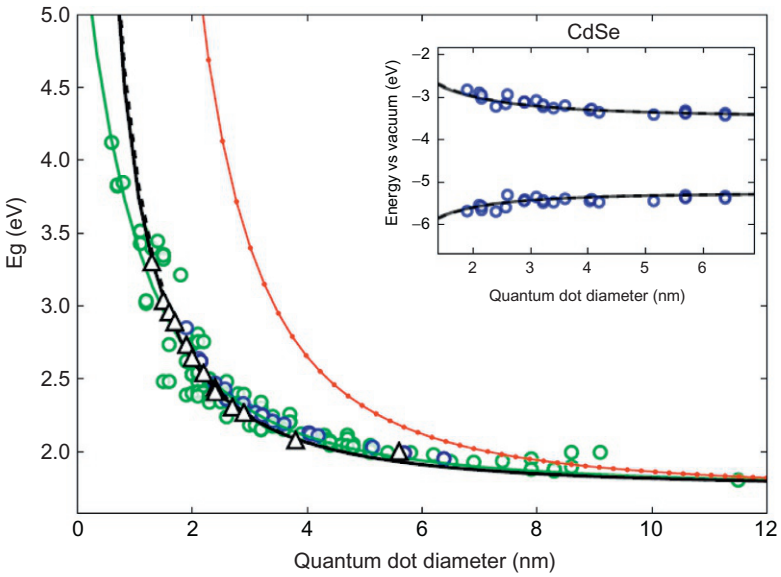


FIG. 12.7

Calculation of the bandgap of CdSe nanospheres with *(solid line)* and without *(dashed line)* the nonparabolicity correction. Comparison with semiempirical pseudo-potential calculations *(triangles)* and experimental data *(circles)* from the literature. The results with Brus equation *(red-dotted line)* and the sizing curve *(green line)* are also drawn. The inset shows the results in comparison with conduction and valence band edges measured by cyclic voltammetry (Thierry et al., 2015).

overlapping integral of the wave functions. Different band-broadening phenomena, coulomb interactions, and space charge distribution make a full modeling of the complex refractive index more complex. The refractive index must then be obtained from measurements. A review of theory is given by Woggon (1997).

It has also been shown by FDTD calculation that enhanced field confinement can be obtained with QDs, like plasmonic effect with metallic nanoparticles (Lin et al., 2013).

12.5 PROPERTIES OF THIN FILMS CONTAINING QUANTUM DOTS

12.5.1 REALIZATION

Silicium QDs can be obtained in a silica film when the silica film is substoichiometric (Conibeer et al., 2012). After annealing, Si nanocrystals appear in the silica matrix. But generally thin films containing QDs are made by spin coating.

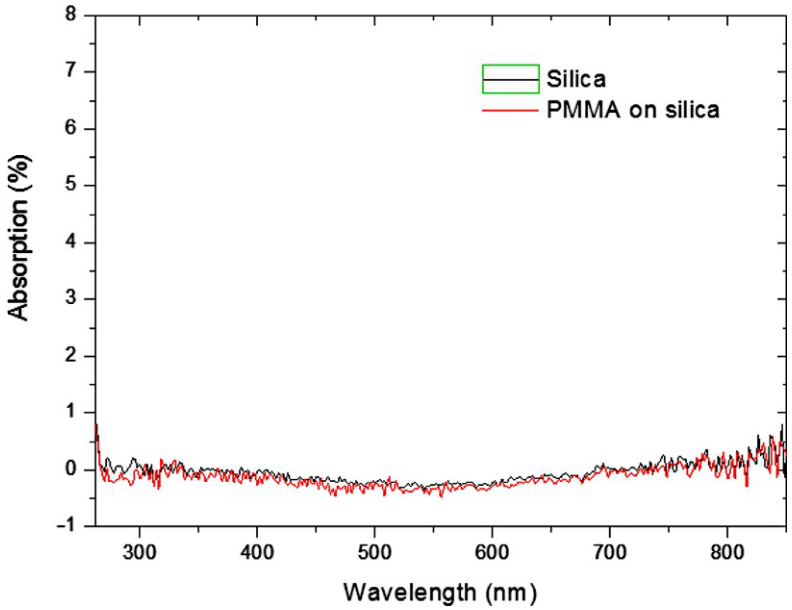


FIG. 12.8

Measured absorption spectra of a pure silica glass and a silica glass coated with a PMMA layer.

In particular, it is interesting to use PMMA as a host material because it is easy to spin coat thin films and it is a highly transparent material in the visible, with a wavelength bandgap below 260 nm (Fig. 12.8).

PMMA is soluble in Chloroform. Therefore, by choosing hydrophobic QDs that are also soluble in chloroform, one can use solutions with different concentrations of QDs to add to the PMMA solution before depositing the layer by spin coating. As an important part of the atoms are on the surface of nanocrystals of a few nanometers, a shell is required to have a good charge confinement and large photoluminescence efficiency. For example, roughly 15% of the atoms in a 5-nm CdS QDs are at the surface (Wang and Herron, 1991).

CdSe/ZnS QDs of ~3 nm have been bought to the company PlasmaChem GmbH.

The TiO_2 nanocrystals were prepared through hydrothermal method, described in greater detail by Reyes-Coronado et al. (2008). Amorphous Titania was prepared by drop-wise addition of a solution of 1.14 mL of water in 105 mL of two-propanol to a solution of 5 mL of titanium (IV) isopropoxide (Aldrich 97%) in 105 mL of two-propanol. The solution was stirred for 24 h at room temperature, and filtered to yield a white paste of amorphous Titania. Then, the amorphous Titania paste was diluted to 0.3 M in aqueous solutions of acetic acid and subjected to hydrothermal treatment at 200°C during 2 h. The as-obtained samples were characterized by X-ray diffraction (XRD) and transmission electron microscopy (TEM). The XRD patterns of the

as-synthesized samples present diffraction peaks that could be indexed as the TiO_2 anatase phase. TEM images show that the as-obtained samples were composed of nanoparticles of around 5 nm.

12.5.1.1 Realization process of PMMA layers including different QDs concentrations

The samples were all prepared on silica substrate. The substrates were cleaned at first in an ultrasonic bath of deionized (DI) water. They were then immersed in DI water three more times and in acetone also three times before being kept in an oven at 200°C for 20 min.

Two types of QDs have been considered: core/shell CdSe/ZnS of ~2.7 nm and TiO_2 of ~5 nm. Different QDs concentrations have been used.

These QDs are hydrophobic and then can be well dispersed in chloroform. QDs of 2.5, 5, and 10 mg corresponding to weight ratio of approximately 4.2%, 8.3%, and 16.6%, respectively, have been separately dispersed in 0.4 mL of chloroform. Each QD solution has been mixed to a solution of 60 mg of PMMA in 0.6 mL so as to obtain 1 mL of mixture. An ultrasonic bath was used for 15 min after several hours with mechanical stirring for the mixed solutions. These solutions have then been spin coated on fused silica substrates at 2000 rpm in a glove box in a neutral atmosphere and baked at 80°C for a few minutes for evaporating the rest of the chloroform. The layers have a thickness close to 2 μm.

12.5.2 CHARACTERIZATION

TEM can be used to measure the QD size and spectroscopy to measure reflection, transmission, and absorption of PMMA thin films containing QDs. Photoluminescence also brings information related to quantum confinement. Ellipsometry and guided wave techniques can be used together to study the refractive index of QDs and of thin films containing QDs.

12.5.2.1 Transmission electronic microscopy

CdSe/ZnS QDs has been examined by transmission electronic microscopy (TEM) in order to study their size distribution, as shown in Fig. 12.9. We can see that the QDs are well dispersed. The crystallized QDs appear to be approximately 3 nm with weak size dispersion, as expected.

Due to the structure of core-shell CdSe/ZnS QDs, the electrons are well confined in the structure. Therefore, the layers including this type of QD exhibit strong excitonic absorption peaks.

12.5.2.2 Reflection, transmission, and absorption

The transmittance spectra of the different samples measured with an integrating sphere spectrometer are shown in Fig. 12.10. It can be seen that the transmittance is decreasing when the QD weight ratio percentage is increasing. However, the transmittance spectrum of the layer with 16.6 wt% QDs revealed interference ripples in

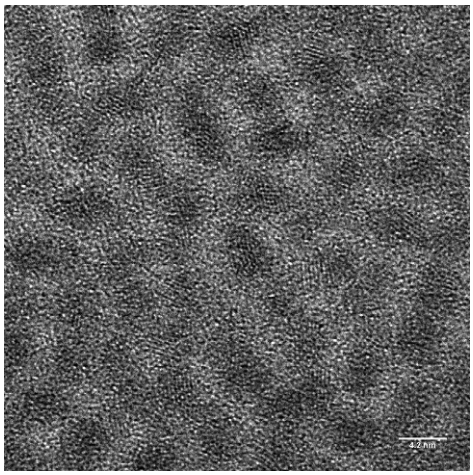


FIG. 12.9

TEM images of CdSe/ZnS QDs.

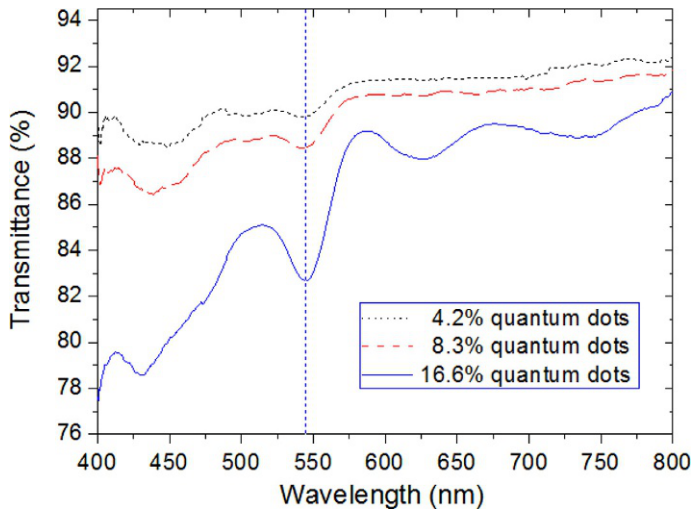


FIG. 12.10

Transmittance spectrum of CdSe/ZnS QDs with weight ratio percentage of 4.2%, 8.3%, and 16.6%.

the range of 575–800 nm more pronounced than for the two other samples. This is due to an increase of effective refractive index leading to stronger interference effects in the film thickness, in its transparency range. After measuring the transmittance and reflectance spectrum, the absorption could be determined, as shown in Fig. 12.11.

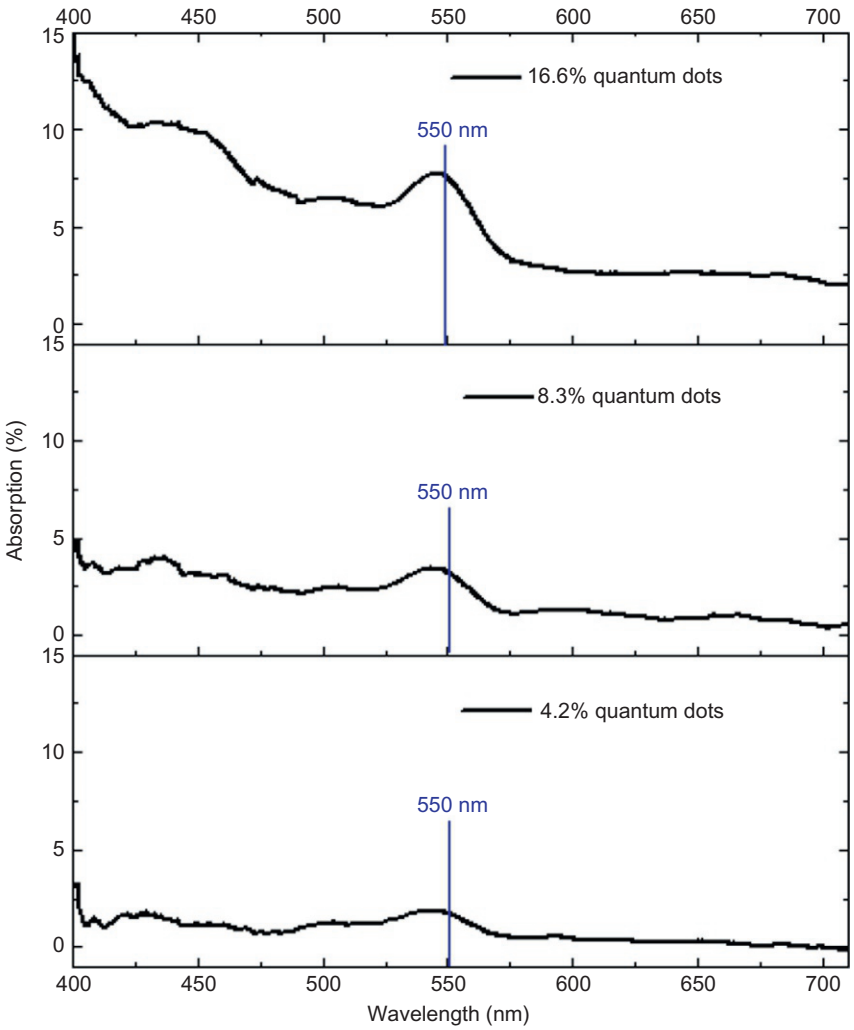


FIG. 12.11

Absorption spectrum of PMMA layers including CdSe/ZnS QDs with a weight ratio of 4.2%, 8.3%, and 16.6%.

All samples exhibit the same absorption shape with an absorption peak close to 550 nm. As expected, the absorption increases while the weight ratio increases. Other absorption peaks at 500 and 450 nm clearly appear when increasing the percentage of QDs. They should be induced by transitions between other discrete energy levels in the QDs. As PMMA material has wide bandgap at around 4.9 eV, it does not affect the absorption in the near UV and visible spectral range. This allows us to attribute the optical absorption in the spectral range of 400–560 nm to the QDs.

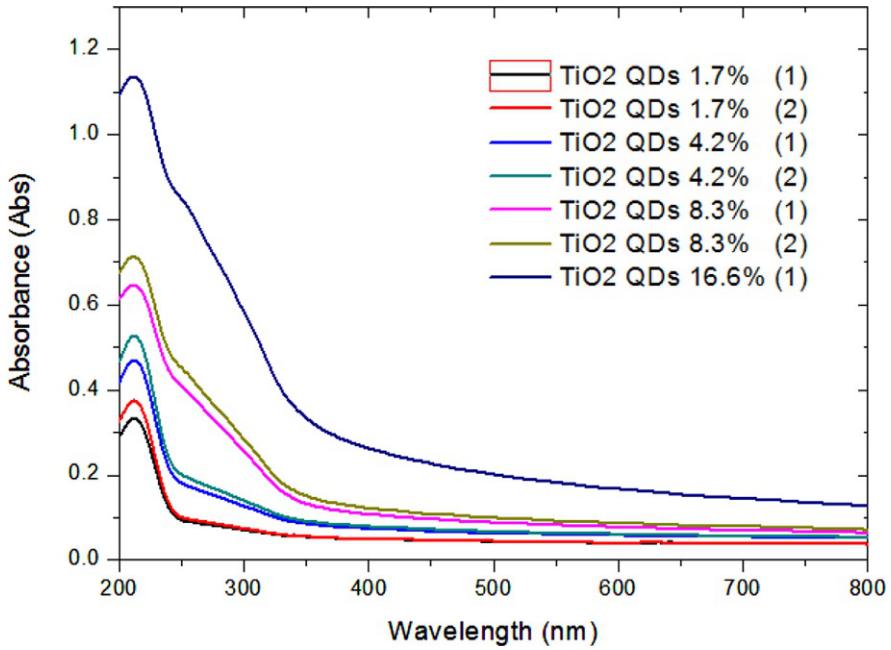


FIG. 12.12

Absorbances of PMMA layers including TiO_2 anatase nanocrystal on pure silica (1) and on BK7 glass (2) with different weight ratios.

PMMA layers including TiO_2 nanoparticles are also interesting to consider. Absorbances of such layers including TiO_2 anatase nanocrystals with different weight ratios are shown in Fig. 12.12. The absorbance is increasing with the weight ratio and their wavelength bandgap is nearly the same than bulk anatase, that is, 387 nm, for all the samples. Therefore, no bandgap shift is observed. No evidence of quantum confinement is shown. The absorption also increases with the concentration in the visible range. This is certainly due to a lack of oxygen and clustering effects.

12.5.2.3 Luminescence

In QDs radiative decays occur between the lowest energy level in the conduction band and the highest level in the valence band. A 1 s electron is then recombined with a 1 s hole.

The PMMA layers including CdSe/ZnS QDs considered before exhibit strong luminescence around 560 nm, as expected from the QDs size. The luminescence is strong because of the ZnS core, which reduces electron trapping on the core surface or electron coupling in the surrounding medium. It is also interesting to notice that the luminescent spectrum fits well with that provided by the company, which is

obtained for QDs in a solution. Therefore, the luminescent spectrum appears not to depend on the host PMMA medium.

The luminescence of these layers has been measured with a continuous Ar laser excitation at the wavelength of 514 nm. As can been seen in Fig. 12.13, the luminescence increases with the QDs concentration. The luminescent bands can be well fitted with Gaussian curves indicating an inhomogeneous band broadening. The band broadening is certainly induced by the QDs size dispersion. Luminescence measurement performed with a pump line at 488 nm shows the same spectrum.

The evolution of the average value of the luminescence as a function of pumping time at 514 nm with a 0.3-μW pump power is shown in Fig. 12.14. It can be seen that under several minutes of illumination a strong increase appears, with a saturation behavior.

Similar results have been obtained by Korsunska et al. (2005) showing an increase but also a possible decrease in luminescence depending on the pump power density for the same CdSe/ZnS QDs of ~3 nm, diluted with phosphate buffer (PBS) in a 1:50 volume ratio (Fig. 12.15). The reversible and nonreversible parts of the effects are also described. The increase of the photoluminescence intensity is mainly attributed to an increase in the potential barrier around the QDs because of charge trapping, inducing an increase in the recombination rate of the carriers. The increase of the potential barrier could be due to charge trapping in the QDs surface or in the ZnS shell.

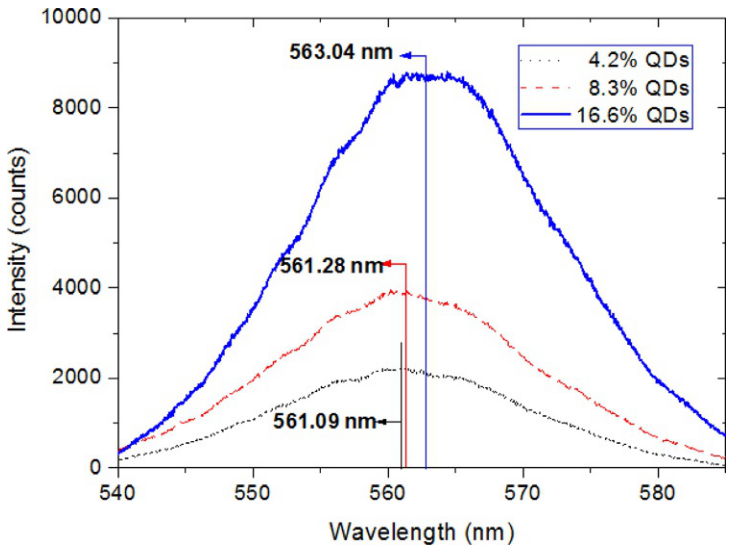


FIG. 12.13

Luminescence spectra of PMMA layers containing different QDs concentrations.

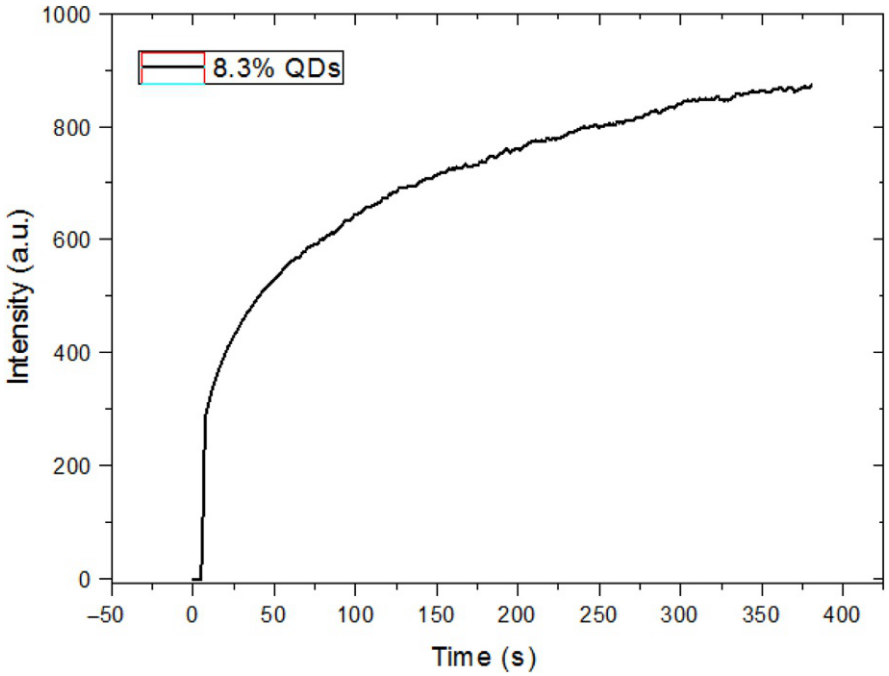


FIG. 12.14

Evolution of the average value of the luminescence in function of the time with a pump power of 0.3 μW at 514 nm.

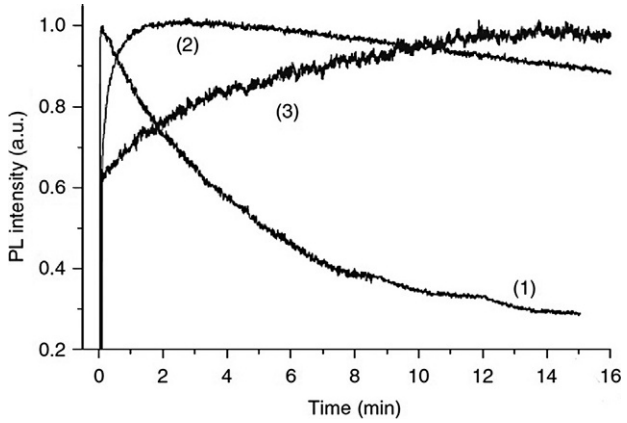


FIG. 12.15

Photoluminescence intensity variations of the 550-nm luminescence band at room temperature and different laser power density ($W cm^{-2}$): (1), 500; (2), 20; (3), 0.2. The photoluminescence intensity is normalized using a multiplication factor of 25 in curve (2), 2500 in curve (3) (Korsunska et al., 2005).

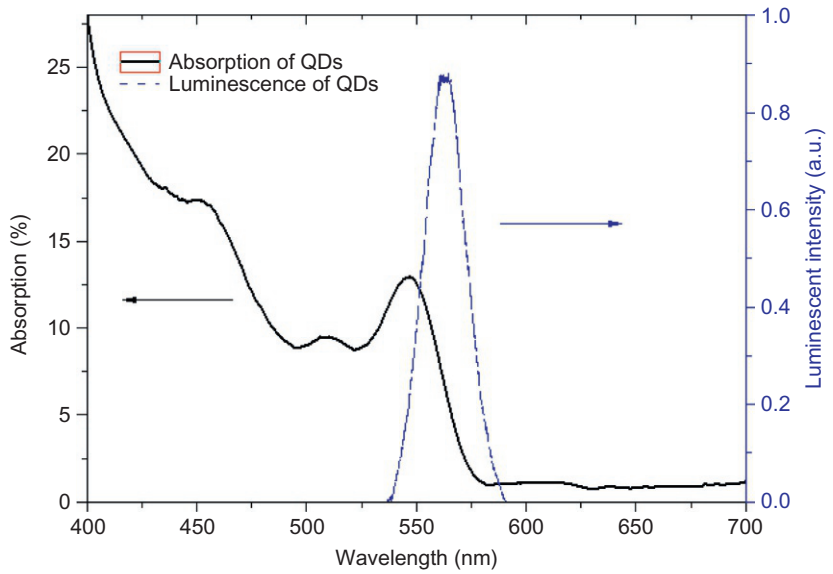


FIG. 12.16

Absorption and luminescent spectra of a PMMA layer with a weight ratio of 16.6% of CdSe/ZnS QDs.

The photoluminescence wavelength band is centered at a larger wavelength than the maximum of the absorbed wavelength band (Fig. 12.16). So it is a down-conversion process.

The frequency down-conversion could be induced by phonon coupling or could involve some forbidden transition sometime called "dark exciton" (Demchenko and Wang, 2009).

This down-conversion effect can be used to collect the UV of the solar spectrum and to change it in visible, which is more efficiently converted into charges in the solar cells. An evidence of an effective down-conversion process is shown in Fig. 12.16. The external quantum efficiency (EQE) of Si solar cell has been measured with a substrate coated with a pure PMMA layer put in front and with a substrate coated with a PMMA including 5.4 wt% of CdSe/ZnS QDs of 3 nm size (Fig. 12.17). As expected, it can be seen that the response is reduced in the absorption band of the layer with QDs and increased in the region of its luminescence.

An interesting perspective is to consider including both QDs and metallic nanoparticles in order to enhance the luminescence by plasmon resonance (Song et al., 2005).

12.5.2.4 Refractive index of layers containing QDs and of QDs alone

As mentioned in the introduction, the knowledge of the refractive index is necessary to design photonics components by using Maxwell equations. We then need to determine the refractive index of QDs to study different structures including QDs.

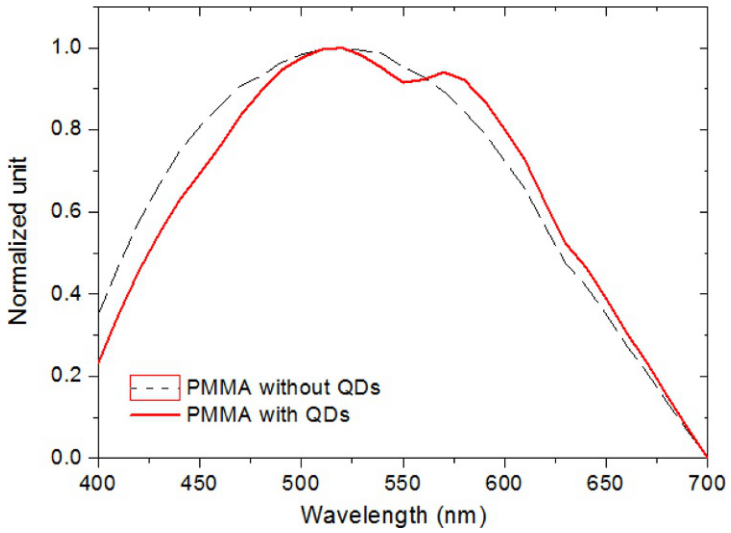


FIG. 12.17

Normalized EQE for a Si solar cell with a silica substrate coated with a pure PMMA layer and the same solar cell with a silica coated with a PMMA layer including CdSe/ZnS QDs.

With dimension very small in front of the wavelength of light, the quantum confinement that governs the electrons and holes behavior changes the optical properties drastically. As seen in part 12.4 it is impossible up to now to model the properties of a set of QDs, in particular band-widening phenomena, oscillator strengths, QDs coupling, phonon coupling, heavy and light electron and hole behavior. Therefore, it is necessary to find the complex refractive index from measurement. The absorption spectrum of QDs in solution or in a thin film can be easily measured on a large wavelength range. As proposed by Moreels et al. (2010), and implemented by him in 2012 for different PbS QDs concentrations below 2‰, the extinction coefficient dispersion with wavelength of a thin film can be obtained from the absorption spectrum. The dispersion with wavelength of the real part of the refractive index can then be deduced from the Kramers-Krönig relations.

$$n(E)-1=\frac{2}{\pi}P\int_0^{\infty}\frac{E'k(E')}{E'^2-E^2}dE'$$

and

$$k(E)=-\frac{2E}{\pi}P\int_0^{\infty}\frac{n(E')-1}{E'^2-E^2}dE'$$

Knowing the refractive index of the host material one can determine a value for the refractive index of QDs alone from an inverse effective index medium theory like Maxwell-Garnett or the homogenization theory.

The refractive index of the films can also be obtained with conventional methods like ellipsometry or m-lines technique (Flory, 1995). As examples we can consider again the samples whose absorption spectra are given in Fig. 12.18. Tables 12.1–12.3 gives, for different wavelengths, the refractive index of these PMMA films including 4.2, 8.3, and 16.6 wt% of CdSe/ZnS QDs of 3-nm size deposited of silica substrates.

These results are obtained from guided mode measurements with the m-lines technique at 633, 594, 543, and 532 nm. The thicknesses of the films are 1964, 1969, and 1268 nm (uncertainty 2 nm), respectively. The refractive index is modulated in the wavelength range close to 550 nm where a resonant electronic transition occurs (uncertainty 1.10^{-3}).

12.6 APPLICATIONS

12.6.1 HYBRID ORGANIC/QUANTUM DOT SOLAR CELLS

Solar cell efficiency is given by the ratio between the generated electrical power and the received optical power. The number of charges collected per incident photon is the EQE. For a homojunction solar cell diode the EQE can be expressed as

$$\mathrm{EQE} = \eta_{abs}\eta_{quan}\eta_{diff}\eta_{diss}\eta_{trans}\eta_{coll}$$

where η_{abs} is the absorption rate, η_{quan} the rate of exciton generated by absorbed photon, η_{diff} the exciton diffusion length, η_{diss} the rate of exciton dissociation in free charges in the depleting zone, η_{trans} is the transfer rate to the electrodes, and η_{coll} the collection rate of the electrodes.

η_{abs}, characteristic to the light absorption in the active material, depends on the wavelength. The absorbed wavelength range depends on the bandgap of the active material. Thermodynamic considerations (Shockley and Queisser, 1961) give the limit of efficiency, which can be achieved with a p-n junction solar cell. This limit of 36.7% is achieved for a semiconductor bandgap of 1.35 eV. Organic materials donors such as P3HT (poly(3-hexylthiophène)) or PCDTBT (poly[*N*-9′-heptadecanyl-2,7-carbazole-alt-5,5-(4,7-di-thienyl-2′,1′,3′-benzothiadiazole]) with a bandgap of ∼2 and ∼1.9 eV, respectively, have been used in association with PC60BM ([6,6]-phenyl-C60-methyl butanoate) as acceptor to make organic solar cells (OSC). The limitation in efficiency of OSC is mainly due to the small diffusion length of the excitons and to a low hole transport. The inclusion of inorganic QDs in OSC is under study to enlarge the absorption band and to enhance the charge transport. Different considerations have to be taken into account in order to optimize such hybrid solar cells. The QDs can be inserted in an acceptor material, a donor material, or a mixture of both. In any case, the choice of the materials must be made by considering band alignment so that, after the dissociation of the excitons, electrons and hole can easily be transferred from one material to the other. The advantage of using QDs is that the energy levels can be tuned to a certain extent by changing their size. The charge transfer from QDs to the surrounding material depends on the QDs

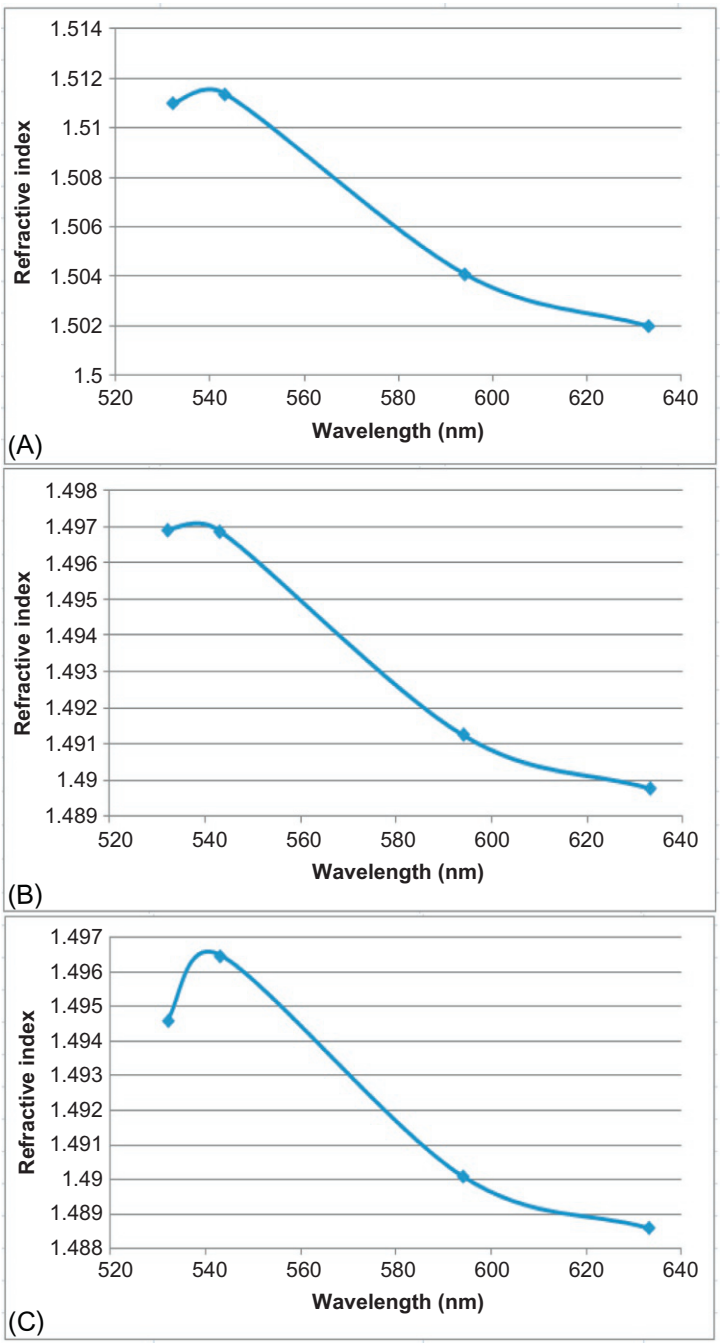


FIG. 12.18

Refractive index dispersion of PMMA layers including QDs with (A) 16.6wt%, (B) 8.3wt%, and (C) 4.2wt%. Uncertainty 1.10–3.

Table 12.1 Refractive index measured by m-line technique for different wavelengths of a PMMA layer with 4.2 wt% of CdSe/ZnS QDs

Wavelength (nm)	Refractive index
16.6 wt% QDs	
532	1.5110
543	1.5114
594	1.5041
633	1.5020

Table 12.2 Refractive index measured by m-line technique for different wavelengths of a PMMA layer with 8.3 wt% of CdSe/ZnS QDs

Wavelength (nm)	Refractive index
8.3 wt% QDs	
532	1.49692
543	1.49635
594	1.49126
633	1.48979

Table 12.3 Refractive index measured by m-line technique for different wavelengths of a PMMA layer with 16.6 wt% of CdSe/ZnS QDs

Wavelength (nm)	Refractive index
4.2 wt% QDs	
532	1.4946
543	1.4965
594	1.4901
633	1.4886

surface states. Only short ligands must be used and surface charge traps must be minimized. Once separated, electrons and holes have to find a path to go to the electrodes. This depends on the material microstructure, in particular on the QDs density. A review of recent results on hybrid solar cells is given in (Wright and Uddin, 2012). QDs can also be used in QD sensitized solar cells (Sogabe et al., 2016).

12.6.2 LIGHTING AND DISPLAYS

Most of white LEDs are made of blue LEDs on which yellow phosphorous is deposited. The white is obtained by tuning the blue and the yellow parts, changing the proportion of phosphorous. White can also be obtained from blue LED by using QDs

(Lim et al., 2012). Part of the blue energy is down converted into green and red in composite resins in which QDs of different sizes are dispersed. In a color display, each pixel contains red, green, and blue subpixels. These colors are combined in varying intensities to produce millions of colors. Thanks to their narrow luminescence band, QDs allows to produce a larger range of high-purity colors. The QDs are dispersed in clear and thermal-resistant resin-like polystyrene to make passive devices used in back light units of conventional liquid crystal displays. They can be arranged in red emissive and green emissive QD layers (Steckel et al., 2016). A scattering layer is used to disperse the light. Oxygen and water blocking layer can also be added to enhance the lifetime of the unit. Blue LED provides the pumping energy for the QDs layers. A part of the blue light is not absorbed by the QDs layers so that a large colorimetric range can be achieved. Added to the high stability and the large quantum efficiency of LCD displays, QD backlighting units appear to be very promising. They are already commercialized by some companies.

The electroluminescent properties of QDs layers are now also under study to make QD LEDs and QD displays (Lim et al., 2012). They need to be associated with hole transporting and electron injecting layers. Electron blocking layer may also be used.

It is also necessary to consider the use of nonhazardous chemical compounds as QDs. Cd and Se are toxic materials but other alloys made of III–V materials, like InP, could be nontoxic good candidates.

12.7 OPTICAL INTERFERENCE COATINGS CONTAINING QUANTUM DOTS

Thin films containing QDs exhibits gain in their luminescent band when excited with wavelength shorter than the wavelength bandgap. Such gain layers can be part of multilayer coatings. This field has drawn only little attention up to now but can have great interest to compensate for losses or to design filters with extraordinary optical properties. As an example, QDs layers can be part of multilayer mirrors made of quarter-wave layers. Mirrors with a reflection coefficient larger than one can be obtained in such a way (Chen et al., 2013). Fig. 12.19 shows the reflectance spectra, which can be achieved with a mirror centered at 390 nm made of eight pairs of high and low index quater-wave layers, respectively H and L. A QDs layer L′ is added on the stack. The CdSe/ZnS QDs of this layer are assumed to have a diameter of 2.5 nm in corresponding to a luminescence centered at 390 nm. When adding a supplementary H layer, when pumped at 325 nm, the He-Cd emission wavelength, the reflectance increases to more than 1.01 at 390 nm. Therefore, extra high-reflective coatings with reflection coefficient larger than the unity can be made. In a similar way, transmission larger than the unity can be obtained with Fabry-Pérot multilayers, the cavity layer being a QDs layer but this has not been investigated in detail yet.

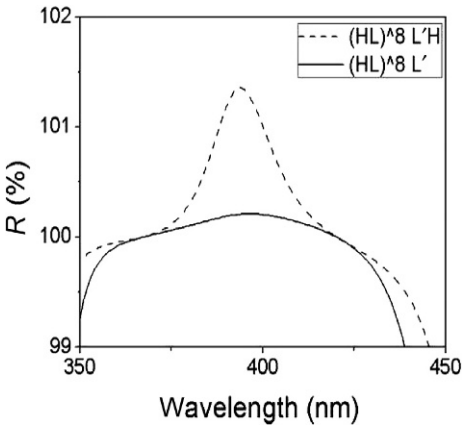


FIG. 12.19

Reflectance spectra of a mirror centered at 390 nm made of eight pairs of high- and low-index quater-wave layers, respectively, H and L. A CdSe/ZnS QDs layer L′ is added on the stack. The QDs are assumed to have a diameter of 2.5 nm corresponding to a luminescence centered at 390 nm.

12.8 CONCLUSION

In QDs, the energy and wave function of electrons and holes can be controlled by the QDs size and coupling. As the optical properties strongly depend on the electronic properties it appears possible to tune the dielectric function by controlling the QDs geometry. The dispersion of QDs in thin films gives materials with new properties. The complex refractive index is modified and photoluminescence is observed. Thanks to simple models and experiments, the optical properties of thin films including QDs are beginning to be understood but there still remains considerable work to be undertaken. Models for 1D and 0D structures, charge transfer, band broadening, phonon coupling, forbidden states, oscillator strength, lifetime of excited states, charges trapping … are all subjects under investigations. Thin film is part of nanophotonics and, when they include QDs, the knowledge of their basic properties such as their complex refractive index paves the way to complex nanophotonics components like multilayers, diffracting structures, photonics crystals, and waveguides with both a control of charge properties, spectral and spatial responses to optical waves, spectral and spatial light emission, and materials with optical gain. The application potential is very large. In thin film solar cells, the use of QDs is a way to enhance their efficiency by frequency conversion, hot electron collection, or multiple electron generation. QDs made of different materials can certainly be associated and adjusting their energy band diagram can allow better exciton generation, and better charge transport. Plasmonic effect and field enhancement obtained with metallic

nanoparticles are used to enhance light trapping by an increase of the local field around the particles and by extending the path of light because of scattering (Duche et al., 2009). The association of metallic nanoparticles and QDs is also worthy to be studied (Pillai et al., 2011).

Applications of QDs layers for displays and lightening are already implemented. QD LED and QD backlighting units for displays have superior color properties.

Thin films containing QDs can also be part of multilayer structures to design absorbing or luminescent coatings, in particular coatings with optical gain.

ACKNOWLEDGMENTS

We thank the French Institute in Taipei and National Central University in Taiwan for their support. We also thank Alexandre Merlen and Claude Alfonso from the Institut Matériaux, Microélectronique et Nanosciences de Provence for the photoluminescence measurement and TEM measurement, respectively.

REFERENCES

Andrae, D., Huermann, U., Dolg, M., Stoll, H., Preu, H., 1990. Energy-adjusted ab initio pseudopotentials for the second and third row transition elements. Theor. Chim. Acta 77 (2), 123–141.

Brus, L.E., 1984. Electron-electron and electron-hole interactions in small semiconductor crystallites: the size dependence of the lowest excited electronic state. J. Chem. Phys. 80, 4403–4409.

Carpena, P., Gasparian, V., Ortuño, M., 1999. Number of bound states of a Krönig-Penney finite-periodic superlattice. Eur. Phys. J. B. 8, 635–641.

Chen, Y.J., Lee, C.C., Chen, S.H., Flory, F., 2013. Extra high reflection coating with negative extinction coefficient. Opt. Lett. 38 (17), 3377–3379.

Chen, Y.J., Lee, C.C., Flory, F., 2014. Experimental and theoretical study of localization of electrons by deformed potential well in quantum dots. J. Nanophot. 8, 083090.

Cohen-Tannoudji, C., Diu, B., Laloë, F., 1997. Mécanique Quantique. vol. 1. Hermann, Paris.

Conibeer, G., Perez-Wurfl, I., Hao, X., Di, D., Lin, D., 2012. Si solid state quantum dot based materials for tandem solar cells. Nanoscale Res. Lett. 7, 193. https://doi.org/10.1186/1556-276X-7-193.

Demchenko, D.O., Wang, L.W., 2009. Optical Transitions and Nature of Stokes Shift in Spherical CdS Quantum Dots. Lawrence Berkeley National Laboratory. Retrieved from: http://escholarship.org/uc/item/20v0s9td.

Duche, D., Torchio, P., Escoubas, L., Monestier, F., Simon, J.J., Flory, F., Mathian, G., 2009. Improving light absorption in organic solar cells by plasmonic contribution. Sol. Energy Mater. Sol. Cells 93, 1377–1382.

Eisberg, R., Resnick, R., 1985. Quantum Physics of Atoms, Molecules, Solids, Nuclei and Particles, second ed. John Wiley and Sons, Hoboken, Appendix H.

Ekimov, A.I., Efros, A.L., Onushchenko, A.A., 1985. Quantum size effect in semiconductor microcrystals. Solid State Commun. 56, 921–924.

Flory, F., 1995. Characterization: guided wave techniques. In: Flory, F. (Ed.), Thin Films for Optical Systems. In: Optical Engineering Series, vol. 49. Marcel Dekker Inc.

Flory, F., Chen, Y.-J., Lee, C.-C., Escoubas, L., Simon, J.-J., Torchio, P., Le-Rouzo, J., Vedraine, S., Derbal-Habak, H., Shupyk, I., Didane, Y., Ackermann, J., 2011. Optical properties of dielectric thin films including quantum dots. Appl. Optics 50 (9), 129–134.

Geerlings, P., De Proft, F., Langenaeker, W., 2003. Conceptual density functional theory. Chem. Rev. 103 (5), 1793–1873.

Goringe, C.M., Bowler, D.R., Hernndez, E., 1999. Tight-binding modelling of materials. Rep. Prog. Phys. 60 (12), 1447–1512.

Harrison, P., 2005. Quantum Wells, Wires and Dots: Theoretical and Computational Physics of Semiconductor Nanostructures. Wiley, Hoboken.

Jonsson, B., Eng, S.T., 1990. Solving the schrödinger equation in arbitrary quantum-well potential profiles using the transfer matrix method. IEEE J. Quant. Electron. 26 (11), 2025–2035.

Kittel, C., 2005. Physique de l'état solide: cours et problèmes. Sciences sup, Dunod.

Korsunska, N.E., Dybiec, M., Zhukov, L., Ostapenko, S., Zhukov, T., 2005. Reversible and non-reversible photo-enhanced luminescence in CdSe/ZnS quantum dots. Semicond. Sci. Technol. 20, 876–881.

Lim, J., Bae, W.K., Kwak, J., Lee, S., Lee, C., Char, K., 2012. Perspective on synthesis, device structures, and printing processes for quantum dot displays. Opt. Mat. Express 2 (5), 594–628.

Lin, H.J., Vedraine, S., Le-Rouzo, J., Chen, S.H., Flory, F., Lee, C.C., 2013. Optical properties of quantum dots layers: Application to photovoltaic solar cells. Sol. Energy Mater. Sol. Cells 117, 652–656.

Moreels, I., Allan, G., De Geyter, B., Wirtz, L., Delerue, C., Hens, Z., 2010. Dielectric function of colloidal lead chalcogenide quantum dots obtained by a Kramers-Kronig analysis of the absorbance spectrum. Phys. Rev. B 81 (23), 235319–235325.

Pillai, S., Perez-Wurfl, I., Conibeer, G.J., Green, M.A., 2011. Surface plasmons for improving the performance of quantum dot structures for third generation solar cell applications. Phys. Status Solid. C 8 (1), 181–184.

Reed, M.A., Randall, J.N., Aggarwal, R.J., Matyi, R.J., Moore, T.M., Wetsel, A.E., 1988. Observation of, discrete electronic states in a zero-dimensional semiconductor nanostructure. *Phys. Rev. Lett.* 60, 535–537.

Reyes-Coronado, D., Rodriguez-Gattorno, G., Espinosa-Pesqueira, M.E., Cab, C., de Coss, R., Oskam, G., 2008. Phase-pure TiO_2 nanoparticles: anatase, brookite and rutile. Nanotechnology 19, 45605–145604.

Sham, L.J., Nakayama, M., 1979. Effective-mass approximation in the presence of an interface. Phys. Rev. B 20 (2), 734–747.

Shockley, W., Queisser, H.J.J., 1961. Efficiency loss mechanisms: theory and characterization. Appl. Phys. 32, 510–519.

Sogabe, T., Shen, Q., Yamaguchi, K., 2016. Recent progress on quantum dot solar cells: a review. J. Photon. Energy 6 (4), 040901.

Song, J.H., Atay, T., Shi, S., Urabe, H., Nurmikko, A.V., 2005. Large enhancement of fluorescence efficiency from CdSe/ZnS quantum dots induced by resonant coupling to spatially controlled surface Plasmons. Nano Lett. 5 (8), 1557–1561.

Steckel, J., Sajjad K., Drolet, J.J. 2016, Display Light Sources with Quantum Dots, United States Patent Application, n°20160218252, July 28.

Thierry, F., Le Rouzo, J., Flory, F., Berginc, G., Escoubas, L., 2015. Fast and reliable approach to calculate energy levels in semiconductor nanostructures. J. Nanophot. 9 (1), 093080.
Voon, L., Willatzen, M., 2009. The k-p Method: Electronic Properties of Semiconductors. Springer, Berlin.
Wang, Y., Herron, N., 1991. Nanometer-sized semiconductor clusters–materials synthesis, quantum size effects, and photophysical properties. J. Phys. Chem. 95, 525–532.
Woggon, U., 1997. Optical Properties of Semiconductor Quantum Dots. In: Springer Tracts in Modern Physics. vol. 136. Springer Verlag, Berlin, https://doi.org/10.1007/BFb0119351.
Wright, M., Uddin, A., 2012. Organic-inorganic hybrid solar cells: a comparative review. Sol. Energy Mater. Sol. Cells 107, 87–111.

FURTHER READING

Bera, D., Qian, L., Tseng, T.-K., Holloway, P.H., 2010. Quantum dots and their multimodal applications: a review. Dent. Mater. 3, 2260–2345.
Chen, Z.-H., Hellstrom, S., Ning, Z.-J., Yu, Z.-Y., Fu, Y., 2011. Exciton Polariton contribution to the stokes shift in colloidal quantum dots. J. Phys. Chem. C 115 (13), 5286–5293.
Ellingson, R.J., Beard, M.C., Johnson, J.C., Yu, P., Micic, O.I., Nozik, A.J., Shabaev, A., Efros, A.L., 2005. Highly efficient multiple exciton generation in colloidal PbSe and PbS quantum dots. Nano Lett. 5 (5), 865–871.
Fattal, D., Diamanti, E., Inoue, K., Yamamoto, Y., 2004. Quantum teleportation with a quantum dot single-photon source. Phys. Rev. Lett. 92, 037904.
Gaponenko, S.V., 1998. Optical Properties of Semiconductor Nanocrystals. Cambridge University Press, Cambridge.
Günesa, S., Fritzb, K.P., Neugebauera, H., Sariciftci, N.S., Kumarb, S., Scholes, G.D., 2007. Hybrid solar cells using PbS nanoparticles. Sol. Energy Mater. Sol. Cells 91 (5), 420–423.
Huynh, W.U., Dittmer, J.J., Alivisatos, A.P., 2002. Hybrid nanorod-polymer solar cells. Science 295 (5564), 2425–2427.
Jang, J.W., Ryun, S.H., Lee, S.H., Lee, I.C., Jeong, W.G., Stevenson, R., 2004. Room temperature operation InGaAs/InGaAsP/InP quantum dots laser. Appl. Phys. Lett. 85, 3674.
Jiu, T., Reiss, P., Guillerez, S., de Bettignies, R., Bailly, S., Chandezon, 2010. F hybrid solar cells based on blends of CdSe nanorods and poly(3-alkylthiophene) nanofibers. IEEE J. Sel. Top. Quant. Electron. 16 (6), 1619–1626.
Kamat, P.V., 2008. Quantum dot solar cells. Semiconductor nanocrystals as light harvesters. J. Phys. Chem. C 112, 18737–18753.
Kim, T.H., Cho, K.S., Lee, E.K., Lee, S.J., Chae, J., Kim, J.W., Kim, D.H., Kwon, J.Y., Amaratunga, G., Lee, S.Y., Choi, B.L., Kuk, Y., Kim, J.M., Kim, K., 2011. Full-colour quantum dot displays fabricated by transfer printing. Nat. Photon. 5, 176–182.
Kongkanand, A., Tvrdy, K., Takechi, K., Kuno, M., Kamat, P.V., 2008. Quantum dot solar cells. Tuning photoresponse through size and shape control of CdSe-TiO_2 architecture. J. Am. Chem. Soc. 130, 4007–4015.
Larson, D.R., Zipfel, W.R., Williams, R.M., Clark, S.W., Bruchez, M.P., Wise, F.W., 2003. Water-soluble quantum dots for multiphoton fluorescence imaging in vivo. Science 300 (5624), 1434–1436.
Moreels, I., Kruschke, D., Glas, P., Tomm, J.W., 2012. The dielectric function of PbS quantum dots in a glass matrix. Opt. Mater. 2 (5), 496–500.

Nozik, A.J., 2002. Quantum dot solar cells. Physica E: Low-dimensional Syst. Nanostruct. 14 (1–2), 115–120.

Nozik, A.J., 2008. Multiple exciton generation in semiconductor quantum dots. Chem. Phys. Lett. 457 (1–3), 3–11.

Pagan, J.G., Stokes, E.B., Patel, K., Burkhart, C.C., Ahrens, M.T., Barletta, P.T., O'Steen, M., 2006. Colloidal quantum dot active layers for light emitting diodes. Solid State Electron. 50 (7–8), 1461–1465.

Reiss, P., Bleuse, J., Pron, A., 2002. Highly luminescent CdSe/ZnSe core/shell nanocrystals of low size dispersion. Nano Lett. 2, 781–784.

Robel, I., Subramanian, V., Kuno, M., Kamat, P.V., 2006. Quantum dot solar cells. Harvesting light energy with CdSe nanocrystals molecularly linked to mesoscopic TiO_2 films. J. Am. Chem. Soc. 128, 2385–2393.

Rossetti, R., Nakahara, S., Brus, L.E., 1983. A simple model for the ionization potential, electron affinity, and aqueous redox potentials of small semiconductor crystallite. J. Chem. Phys. 79, 5566–5571.

Studenikin, S.A., Golego, N., Cocivera, M., 1998. Fabrication of green and orange photoluminescent, undoped ZnO films using spray pyrolysis. J. Appl. Phys. 84 (4), 2287–2294.

This page intentionally left blank

PART

Applications of optical thin films and coatings

IV

This page intentionally left blank

CHAPTER

Optical coatings on plastic for antireflection purposes 13

Ulrike Schulz*, Robert W. Schaffer†
*Fraunhofer Institute of Applied Optics and Precision Engineering IOF, Jena, Germany**
Evaporated Coatings Inc., Willow Grove, PA, United States†

13.1 INTRODUCTION

Plastic materials are replacing glass optics whenever advantageous physical properties or cost reduction can be achieved. Plastic materials benefit from properties like low weight and low breakage. They can be shaped into cost-effective mass production by injection molding or embossing. The requirement for optical coating has to be considered in a very early stage of development. Antireflection (AR) is the most important optical function. The requirements to achieve AR properties are increasing continuously. AR coatings have been tried and tested on lacquered eyeglasses for about 50 years. AR coatings on precision plastic optics have been in existence for about 40 years. However, AR coatings for camera lenses and display covers consisting of thermoplastic polymers like acrylic [poly(methyl methacrylate) (PMMA)] or polycarbonate (PC) are still challenging. New applications create increasingly stringent environmental requirements. The basic problems involved with vacuum coating of plastics are illustrated in Fig. 13.1. The effort to achieve coatings with high adhesion and extended environmental stability is different for each type of polymer and in some cases it is difficult or impossible to obtain good results. Complex chemical reactions may occur, especially in the common plasma-assisted deposition processes. The following sections may help to understand the special behavior of polymer materials for coating, especially in vacuum coating processes. The state-of-the-art processes for vacuum coating, as well as new results of research and development in the fields of wet-chemical coatings and antireflective structures, will be introduced and discussed.

13.2 TRANSPARENT POLYMER MATERIALS FOR OPTICS

Plastic optics include spherical and aspherical lenses, prisms, free form, diffractive, Fresnel, and mirror surfaces. There are many different materials available for

Optical Thin Films and Coatings. https://doi.org/10.1016/B978-0-08-102073-9.00013-8
Copyright © 2018 Elsevier Ltd. All rights reserved.

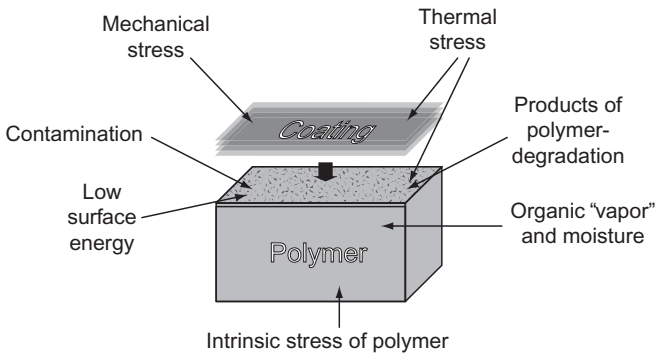


FIG. 13.1

Basic problems for vacuum coating of plastics.

producing plastic optics, each one having different benefits and limitations. Injection molding is the most common process for forming the optics and can also be used for assembly components. It is even possible to mold two or more optical functions into one integrated molded part. At the prototyping stage single-point diamond turning manufacturing processes are commonly used.

The progress in material grades is continuing; for example, advances in PC and polycycloolefine materials have resulted in higher heat resistance, improved stability and lower birefringence properties. The optical properties of the polymers and also properties such as specific gravity, as well as chemical and environmental stability must be considered in developing applications (Bäumer, 2010). Table 13.1 shows an extract of materials and their most important properties to be taken into account for coating.

Plastics are mainly used for eyeglasses and numerous precision optical lens systems used in cameras, medical devices, projectors, displays, fiber optics, and automotive devices, to name a few. Eyeglasses are special because thermosetting materials are used rather than the thermoforming materials listed in Table 13.1. Developments for eyeglasses include especially high index polymers based on thiourethanes and lightweight materials with high impact resistance, such as, Trivex and Tribrid (PPG Optical Products, 2012). Some of the eyeglass materials would also be attractive for other optical parts. But shaping to lenses can only be carried out by casting the monomer and during polymerizations a considerable shrinkage occurs which makes the technology impractical for precision optics. Substrates for optical coating nowadays also include biobased and biodegradable materials (Narayan, 2008). During the last few years, some new thermoplastic materials have been entered the market for optics. Examples are Iupizeta EP PC resins. They combine properties like high-temperature stability with low birefringence and high refractive indices (MGC, 2016).

Table 13.1 Properties of important thermoplastics for optics

Polymer name	Brand name	n_D (587.6 nm)	Abbe number	Transmittance 3 mm (%)	Density (g/cm^3)	Water absorption (%) ISO 62	Tensile modulus (MPa)	Pencil hardness	Deflect temperature ISO75-2 (°C)	Coating adhesion[a]
Poly(methyl methacrylate)	Plexiglas 7 N	1.491	58	92	1.19	2.2	3200	3H	85	+
Methyl methacrylate copolymer	Plexiglas HW55	1.51	49	90	1.19	2.2	3600	3H	106	++
Poly(*n*-methyl methacryl imide)	Pleximid TT70	1.54	43	91	1.21	6	4000	4H	158	++
Polycarbonate	Makrolon LQ2647	1.585	30	89	1.2	0.4	2400	B	120	++
Polycarbonate copolymer	Apec HT9351	1.572	30	88	1.15	0.3	2400	B	159	+
Cycloolefin copolymer	Topas 5013	1.533	58	92	1.02	<0.01	3100	H	123	+++
Cycloolefin polymer	Zeonex E48R	1.53	56	92	1.01	<0.01	2500	H	122	+++
Cycloolefin polymer	Zeonex 480R	1.525	56	92	1.01	<0.01	2200	H	123	+++
Cycloolefin polymer	Zeonor 1020R	1.53	56	92	1.01	<0.01	2100	HB	101	+++
Cycloolefin polymer	Zeonex 330R	1.509	56	92	0.95	<0.01	1770	2H	110	+
Polyether sulfone	Ultrason E2010	1.65	20	83	1.37	2.2	2700	H	212	+++
Polyamide	Trogamid CX7323	1.516	45	89	1.02	3.5	1400	B	122	+++
Polyester	OKP-4	1.607	27	88	1.22	0.15	2000	2H	105	+++

[a]*Own experiences, AR coatings deposited by plasma-ion-assisted deposition; +++, very good; ++, good with some limitations; +, good only by applying special conditions.*

13.3 PLASTICS IN VACUUM COATING PROCESSES

Vacuum evaporation and sputtering processes are commonly used for depositing AR coatings. Therefore, the unique behavior of polymer materials in vacuum processes will be discussed here.

13.3.1 INTERACTION WITH EMISSIONS FROM PLASMA

Polymers differ from each other in regard to their chemical composition. In contrast to optical glass, a variety of different surface compositions and surface states are characteristic for the polymers used in optics. The surface regions can additionally be affected by the shaping process and the environmental conditions. Boat-evaporated oxide layers deposited without the influence of plasma emissions exhibit excellent layer adhesion on most plastic substrates. However, such cold deposited coatings may suffer from the low energy level. The films are porous and cannot pass all environmental tests. A common method to deposit coatings on temperature-sensitive substrates is plasma-ion-assisted deposition (PIAD) (Pongratz and Zöller, 1992). However, special magnetron sputtering methods have also been described for coating plastics, among them are closed field magnetron sputtering (Gibson et al., 2004) and reactive pulse magnetron sputtering in an unipolar mode (Lau et al., 2009). In these modern vacuum coating processes plasma, and therefore short wavelength radiation, is produced by electron beam evaporators, ion source, glow-discharge cathodes, and other enhancements.

For most plastic materials, their special interaction with plasma emissions is the essential factor for good or bad coating adhesion. Plasma treatments typically produce polar groups on polymer surfaces. Wettability is therefore always increased. Improvement in adhesion by plasma treatments has been variously attributed to this improved wettability or to surface cross-linking (Liston et al., 1993; Fozza et al., 1997; Sarto et al., 1999; Rank et al., 2005). However, ions emitted by ion sources and short wavelength radiation often break chemical bonds in polymers and thereby chemical modifications are initiated. Normally a weakly bonded coating can be removed from the substrate using a tape. It is important to identify the locus of failure by investigating both the tape with the removed coating and the substrate. If the break has occurred cohesively inside the substrate, parts of the destroyed polymer are detectable by X-ray photoelectron spectroscopy (XPS) or Fourier transform infrared spectroscopy (FTIR) on the removed tape and efforts should be directed to avoid the formation of a weak boundary layer. Taking into account the very short treatment times sufficient for the activation of most polymer surfaces and the danger of forming weakly bonded layers, all plasma or ion treatments should be as short as possible. Fig. 13.2 shows the increase of the polar component of surface energy dependent on the plasma treatment time for different polymers. In particular, polycycloolefines like Zeonex can be activated within seconds.

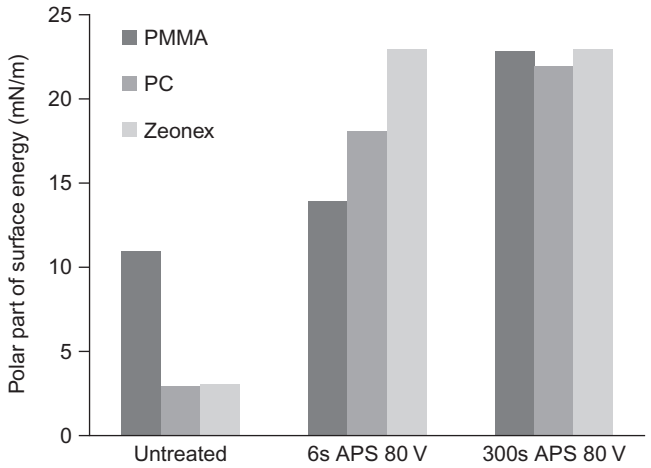


FIG. 13.2

Polar component of surface energy of PMMA, Makrolon and Zeonex depending on the treatment time (ion source APS (Leybold), 80 V Bias, Ar, 2×10^{-4} mbar).

In the case of acrylic, the adhesion is typically decreased after contact with plasma (Lian et al., 1995; Licciardello et al., 1996). To switch on the e-beam evaporator for a short time can always be critical. It is proven that the inadequate adhesion is caused by the formation of weak boundary layers of degradation products (Hook et al., 1987). For PMMA we suggest as a first step to deposit a protection layer without the use of plasma. The layer has to effect blocking ultraviolet (UV) radiation at wavelengths shorter than about 350 nm. After that, optical interference coatings can be deposited on this base layer by applying plasma assistance and taking into account some limitations for the coating design (Munzert et al., 2007).

As shown in Table 13.1, electron-beam-evaporated oxide layers deposited with plasma-ion assistance show best adhesion on certain types of polycycloolefines, PCs, polyamides and polyether sulfones (Munzert et al., 2004). However, poly-bisphenol-A-carbonate (Makrolon, Lexan), not only provides adhesion problems caused by plasma but also by UV radiation at a later time. Some plasma conditions are described to assist in improving the adhesion properties (Vallon et al., 1996; Hofrichter et al., 2002; Muir et al., 2006). But unfavorable results are also possible if longer or more intensive treatments are applied. UV-protective coatings are necessary for outdoor uses of PC to prevent coating ablation later (Schulz et al., 2008). This is a special challenge for optical coatings because the absorption characteristics of the typical evaporation materials are not sufficient to block the critical wavelength range between 350 and 400 nm by absorption (Rivaton, 1995). An antireflective coating with improved sunlight resistance was achieved with a high reflecting band as part of a nonabsorbing interference multilayer (Fig. 13.3).

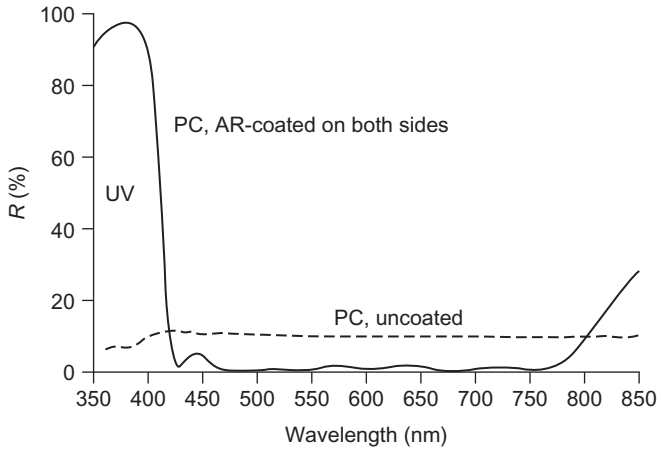


FIG. 13.3

Antireflection coating (17 layers, 1.5 μm total thickness) providing ultraviolet-protection to the polycarbonate substrate.

13.3.2 THERMAL AND STRESS-RELATED EFFECTS

Further material-specific properties with more or less influence on vacuum processes are thermal characteristics and degassing behavior. Stress can adversely affect the interface between coating and polymer and initiate cracking or ablation of thin films. The mechanical stress of coatings mainly depends on the deposition parameters, especially on ion bombardment energy and deposition rate (Doerner and Nix, 1988). If deposited cold and without ion assistance, most high index coating materials would exhibit tensile stress. With the application of ion bombardment at a low level the growth stress of nearly all materials can be shifted in the compressive range. However, on polymers, a thermal stress component must always be considered if the substrate temperature is slowly increasing during layer deposition. This is caused by the typically high thermal expansion coefficient of plastic substrates. Therefore, thermal stress during film deposition may cause tensile stress cracking despite the compressive growth stress of the film. The residual stress of TiO_2-coatings deposited by PIAD on silicon and a plastic substrate are compared in Fig. 13.4 (Schulz and Kaiser, 2003). The growth stress of the layers is increasing with higher ion assistance energy because of the higher densification. In addition, the substrate temperature rises if higher ion energy is applied. Because of the higher thermal expansion the plastic sample will receive much higher compressive stress than the silicon substrate. One possibility for avoiding tensile stress during film deposition is to heat the substrates carefully to a value below their heat distortion temperature. The coating design and temperature management during film deposition are essential factors to avoid cracking. The deposition rate and ion energy in ion-assisted processes have to be carefully optimized for the respective coating material and coating thickness.

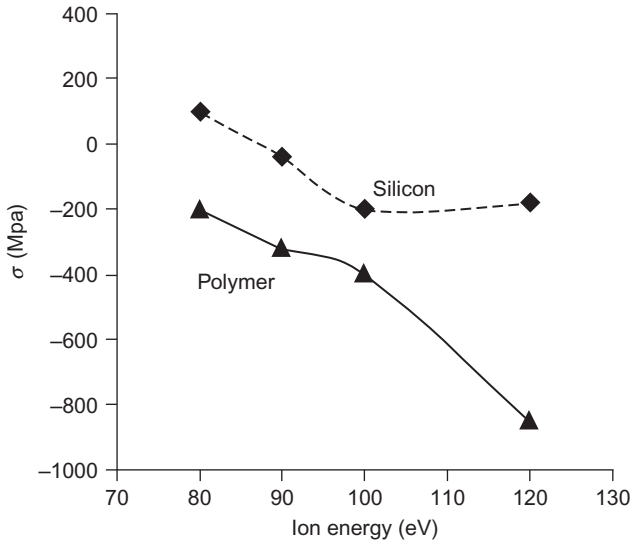


FIG. 13.4

Residual stress of TiO_2-coatings on silicon and plastic depending on the ion assistance energy applied during PIAD-process. Higher ion energy yields to increased layer densification but also to an increased substrate temperature. The stronger increase of compressive stress on plastic compared to silicon is caused by the thermal stress.

In choosing the optimal deposition parameters, the later application conditions (temperature range, outdoor, or indoor conditions) have been taken into account. From our experience the best results on polymers can be achieved if all deposited layers have a moderate compressive stress in a range of −150 to −250 MPa (Schulz and Kaiser, 2003). Fig. 13.5 shows typical pictures of tensile stress cracking and of a "buckling" defect caused by high compressive stress in combination with insufficient adhesion.

13.3.3 WATER ABSORPTION AND DESORPTION

Most polymers absorb water and exhibit a certain water content dependent on the environment. Some examples are shown in Fig. 13.6. Contrary to popular opinion, there is no obvious relationship between the coating ability of a material and its water content. Certainly a high outgassing may increase the time to achieve a good vacuum. A warming of the substrate during deposition can increase the rate of desorption and these gases can react with the arriving atoms affecting both the refractive index and the condensation rate of the arriving film. Storage at moderate temperature before coating may help. However, an intense reduction to a water content below the equilibrium value would trigger stronger water diffusion through the deposited coating and promote cracking and delamination. If the materials have higher water

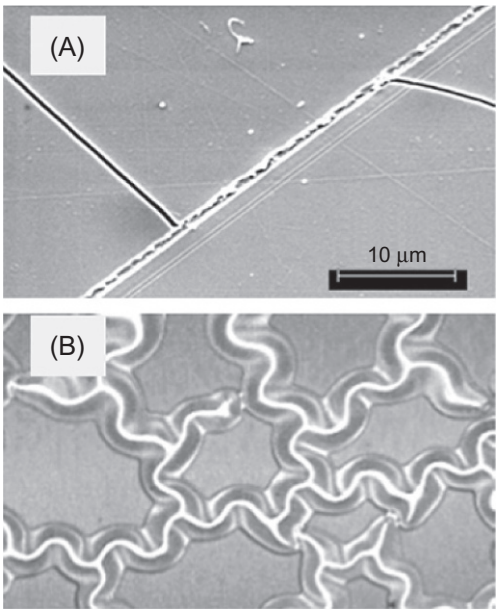


FIG. 13.5

Typical defects in coatings on plastic: (A) tensile stress cracking and (B) "buckling" caused by high compressive stress in combination with insufficient adhesion.

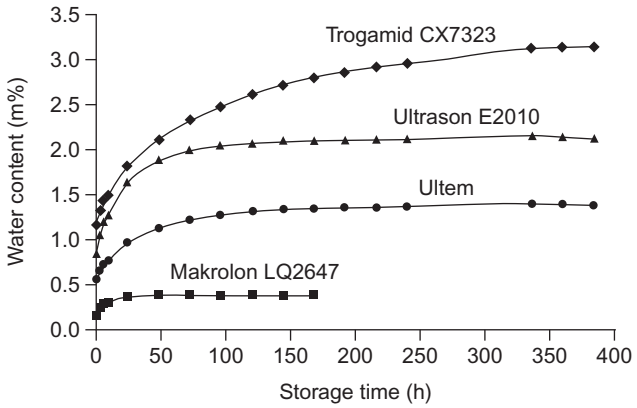


FIG. 13.6

Water content of polymers depending on storage time at 25°C, 95% humidity.

content than about 0.2 wt% the barrier properties of the thin film material have to be taken into account. Fig. 13.7, shows the water absorption of PC samples without coating and when covered with 1-µm thick silica layers. The ion assistance energy was varied obtaining layers with different density and barrier effect. In principle, the deposition parameters (deposition rate, temperature, ion energy) have to be adjusted so that water vapor is able to penetrate through the coating. Otherwise crinkling and

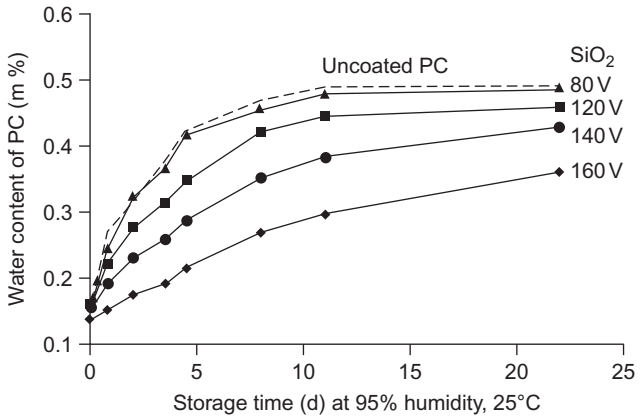


FIG. 13.7

Water absorption of polycarbonate (PC) without coating *(dashed line)* and coated with 1-μm silica applying PIAD with APS ion source. Different levels of ion assistance energy (corresponding to the Bias Voltage value) cause the different barrier behavior.

delamination can occur. For the same reason, metallic layers, which always inhibit the penetration of water, should not be applied on polymers with higher water content.

13.3.4 GENERAL CONSIDERATIONS FOR PLASMA-ASSISTED VACUUM COATING PROCESSES

Concluding from the section above, some rules can be derived for vacuum deposition of interference coatings on plastics:

- The materials and thicknesses of the layers have to be adjusted taking into consideration the stress of the thin film materials. Fluorides are in any case less favorable than oxides.
- The total amount of heat dissipated in the film during the deposition process has to be taken into account. The composition of coatings may be displaced in favor of the low-index ratio because the evaporation of silica occurs at a lower temperature than of higher index oxides.
- Evaporation and plasma-assist parameters have to be chosen carefully to reduce the danger of damage to the polymer. Effects in the bulk (yellowing) and interface (delamination) may occur immediately. But they can also begin to appear after a longer period of time.
- High-index materials have to be considered in order to achieve protection of the interfaces or the bulk polymer from UV radiation, depending on the type of polymer substrate.
- Outgassing of some polymers can affect the condensation rate and the refractive index of arriving materials and must be taken into account in the calculation of the design.

- In some cases interfacial zones with changed optical properties due to plasma treatment have to be taken into account in the calculation of the design.
- Designs have to be tolerant to changes of the optical constants because the layer materials cannot be densified completely.

13.4 ANTIREFLECTION METHODS

Due to the physical properties of polymers, special techniques and requirements must be applied. This section will discuss unique techniques to achieve good AR results and other physical enhancements. Vacuum deposited coatings which are the most common method used, as well as AR structures and wet-chemical processes, will be covered.

13.4.1 VACUUM DEPOSITED ANTIREFLECTIVE COATINGS

The most frequently used broadband AR coatings for the visible spectral range are adapted from the "quarter-half-quarter" design, where the first quarter-wave layer, of medium refractive index, is replaced by parts of high-index and low-index layers followed by a half-wave high-index layer and a low-index quarter-wave layer (Angus Macleod, 2001). The commonly used low-index material for coating plastics is silica ($n = 1.5$) because magnesium fluoride is hard to densify without heating the substrate and would exhibit unfavorable tensile stress. The higher index materials can be selected from a variety of oxide materials with refractive indices in the range between 1.67 (alumina) and 2.4 (titanium dioxide). The selection of the material is important for coating plastics because of effects such as heat emission during evaporation and the absorption of UV light as mentioned before.

Modern software tools allow the generation of specific antireflective designs. An increased total coating thickness is sometimes desirable because of the hardening effect obtained together with the optical effect. By applying the design called "AR-hard" developed for plastics it is possible to adjust the total thickness on the AR stack by introducing a large amount of low-index material (Schulz et al., 2002). The basic construction scheme of AR-hard is shown in Fig. 13.8. For example, a 3-μm thick AR-hard coating on Zeonex shown in Fig. 13.9 is withstanding an abrasion test with steel wool. The much softer PC surfaces would require a coating thickness of about 5 μm to achieve similar results.

AR-hard design was developed for thermoplastic optics where lacquering is unfavorable or cost intensive. On eyeglasses, combinations of a hard-coating lacquer (i.e., a wet-chemical applied polysiloxane compound) with an interference antireflective layer on top are commonly used (Blacker et al., 2000). Sony has developed a broadband three-layer antireflective coating on plastic film. The structure is plastic film/SiOx/TiN/SiO_2. This AR coating has a high wear resistance and high AR quality. The residual reflectance is about 0.2% and the bandwidth is 1.65 (Ishikawa et al., 1999).

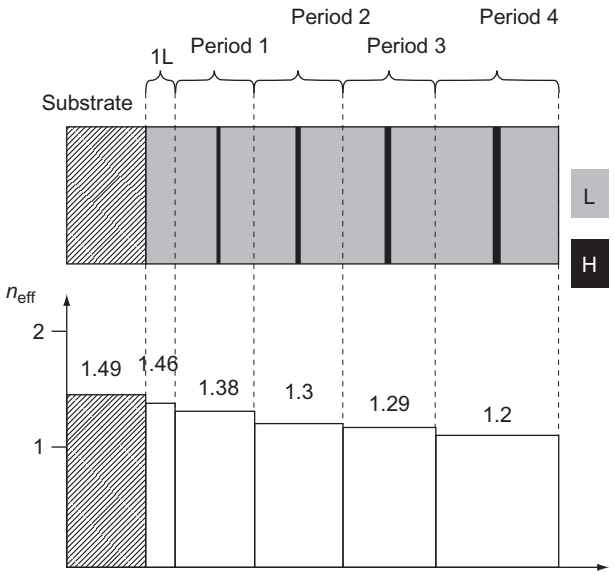


FIG. 13.8

Principle of design AR-hard: equivalent layers with low effective refractive index n_{eff} are formed by periods of conventional low (L) and high (H)-index layers.

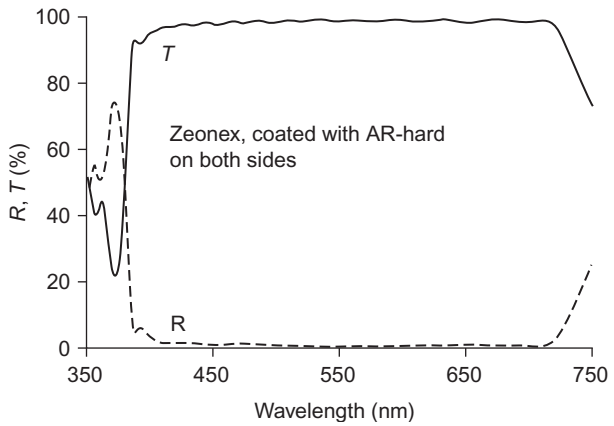


FIG. 13.9

Reflection (R) and transmission (T) of scratch resistant AR-hard layer (thickness 3 μm) on Zeonex E48R (coating on both sides).

13.4.2 ANTIREFLECTIVE STRUCTURES

Investigations of antireflective structures (ARS) have been pursued for almost four decades since they were discovered and explained on the eye of a night-active moth (Clapham and Hutley, 1973). The periodically structured moth eye acts as an effective antireflective medium featuring a decreasing refractive index from the substrate side to the surrounding air. Subwavelength surface structures are typically less sensitive to the angle of incidence of light than homogeneous multilayer stacks (Minot, 1977; Dobrowolski et al., 2002). Most theoretical analysis of reflection characteristics is done by using a rigorous coupled-wave analysis (Gaylord and Moharam, 1985) or effective medium theory (Raguin and Morris, 1993).

A number of bottom-up (coating) and top-down (etching, embossing) techniques have been developed in order to create ARS. In the case of plastics, top-down procedures are preferred because of the removal of material as well as the deformation by thermal embossing being much easier than on glass and other inorganic substrates. The first technical implementation of ARS into a polymer was achieved using a holographic superposition of a light-exposed photoresist (Gombert et al., 1999). Currently, master structures with a pitch of 250 nm and an average depth of 200 nm are commercially available (Temicon, 2018). Another method for producing a master tool for embossing into plastics is the use of anodic oxidation of aluminum (Yanagishita et al., 2008). The structure is generated directly on the tool for hot embossing by depositing the metal layer followed by the wet-chemical oxidation procedure. Modern development of embossing comprises the use of nano-imprint lithography (NIL) (Chen et al., 2009). To overcome deformation problems, the structures are introduced into an acrylic resist material that is typically cross-linked by UV radiation before the deforming step. Embossing processes are mostly restricted to flat or slightly curved substrates. Embossing of ARS with an aspect ratio (depth-to-period ratio) higher than about one seems to be difficult to achieve because of deforming problems. Burghoorn prepared moth eye-structured Ormocomp coatings on flat sheets of PMMA and PC, using a wafer-by-wafer step-and-flash NIL process (Burghoorn et al., 2013).

ARS can also be achieved directly from the top-down by applying plasma etching on polymers (Kaless et al., 2005). Optimized plasma-etched structures on poly(methyl methacrylate) (PMMA) and in Zeonex are shown in Fig. 13.10. For the PMMA structure the aspect ratio is about 2 and the residual reflectance is below 0.5% from 420 to 750 nm and incidence angles from 0 to 45 degrees. The "sponge"-like structure of Zeonex exhibits lower gradient characteristics. Reflectance and transmission for both samples are shown in Fig. 13.11. However, the Zeonex surface structure shown in Fig. 13.10 can be preserved during cleaning and handling because the surface holes were closed almost completely by a protective silica top-layer (Schulz et al., 2007; Wendling et al., 2009). The optical advantages of plasma etched ARS can be revealed especially with sharp curved plastic lenses and Fresnel lenses. Such lenses are protected from mechanical damage if they are mounted inside of an objective.

During recent years a number of additional single layers with a nanoporous structure have been described. In particular, the aqueous-based layer-by-layer assembly process is harmless to plastics (Hiller et al., 2002). A basic procedure is based on the sequential

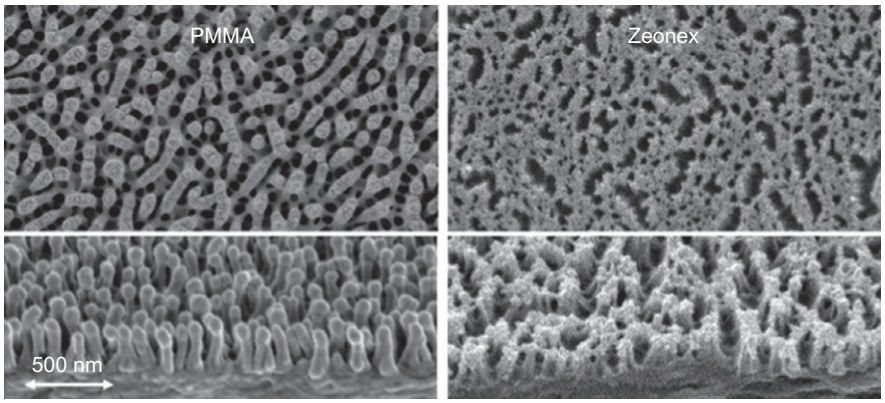


FIG. 13.10

Scanning electron micrographs showing PMMA and Zeonex surfaces with optimized antireflective nanostructures (top view and 45 degrees inclined view below).

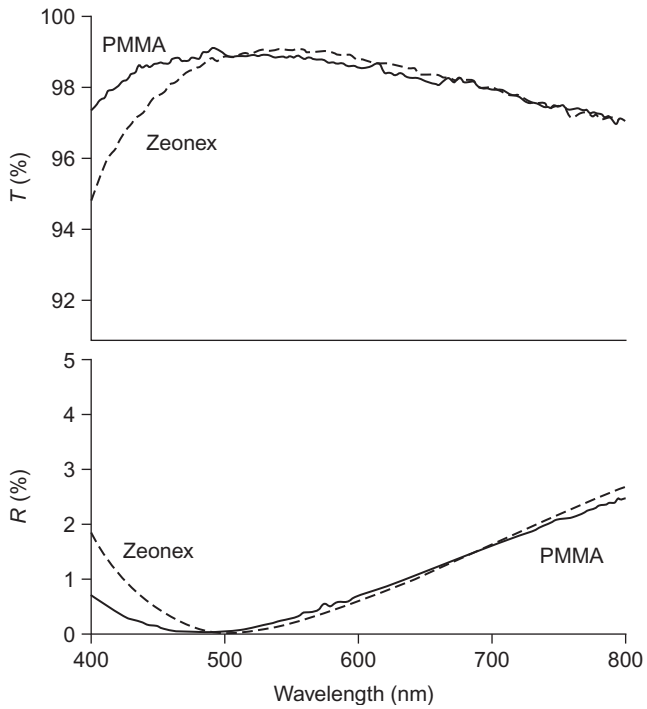


FIG. 13.11

Reflectance and transmission spectra of plasma-etched plastic sheets (both sides) caused by the nanostructures shown in Fig. 13.10.

adsorption of poly(acrylic acid) and poly(allylamine) (Mendelsohn et al., 2000). Porous acrylic (PMMA) films were produced by spin-coating of a polystyrene (PS)/PMMA-blend followed by selectively etching the PS phase (Walheim et al., 1999), by selectively solving the PS phase (Zhao et al., 2005, Dai et al., 2014) or by spin-coating and microphase separation between two PMMA blocks (Park et al., 2005). Another spin-casted PMMA/PS latex with antireflective properties was synthesized by emulsion polymerization (Jiang et al., 2011). The PMMA nanoparticles were used to form a porous skeleton structure, while the PS particles were used to control the porosity. Al_2O_3 gel films (flower-like Al_2O_3) were prepared on PMMA substrates through immersion of the films in hot water. The reflectance of PMMA substrates coated with the flower-like Al_2O_3 was $<0.8\%$ in the visible light region and exhibited very small incident-angle dependence in transmittance up to 60 degrees (Tadanaga et al., 2008).

A special property of ARS is the opportunity to manage the wettability over a wide range. In combination with a hydrophobic layer, nanostructured surfaces can exhibit the Lotus effect whereas a hydrophilic surface chemistry may cause antifogging properties (Cebeci et al., 2006).

Wavelength ranges exceeding the visible spectral range or for a broader range of light incidence angles are still challenging. Wideband AR coatings are especially useful for sharply curved plastic lenses. The residual reflectance achievable with AR interference stacks depends on the refractive index of the last layer and is limited therefore if classical materials like silica or MgF_2 are used. Etched nanostructured surfaces can provide a broadband and wide-angle AR performance if a sufficient structure depth in a range of at least 200 nm can be realized. Stacks consisting of two nanostructured layers were prepared by etching a first structure directly into the polymer and adding a second structure by depositing an organic layer and a subsequent second etching step. The optical properties achieved and the SEM image of such a double-structure on Zeonex is shown in Fig. 13.12 (Schulz et al., 2014).

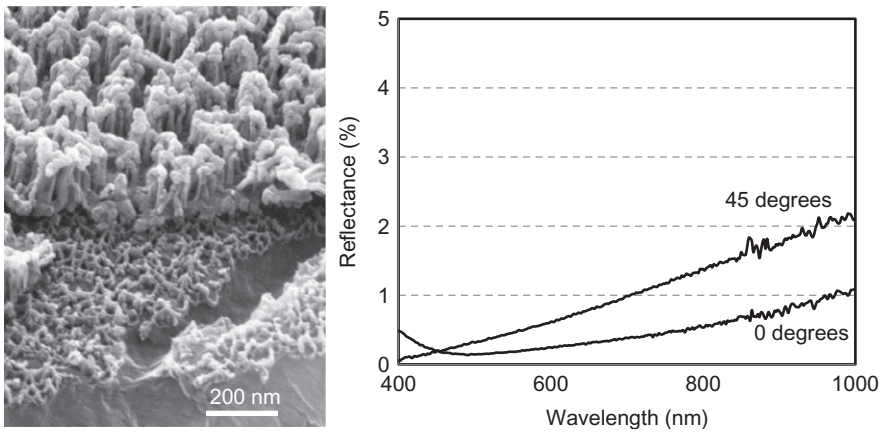


FIG. 13.12

SEM micrograph of Zeonex with plasma-etched AR nanostructure exhibiting low reflectance in the visible and near infrared range at light incidence angles of 0 and 45 degrees.

SEM micrograph of Zeonex with plasma-etched AR nanostructure exhibiting low reflectance in the visible and near-infrared range at light incidence angles of 0 and 45 degrees.

The weak mechanical strength caused by porosity of the surfaces is the main disadvantage of AR structures. To the knowledge of the authors not a single one of the AR structured surfaces described in the literature is able to pass the mechanical tests defined by ISO standards. Most of the surfaces may not be touched; some can be touched and cleaned carefully.

13.4.3 WET-CHEMICAL AR COATINGS ON PLASTICS

Wet-chemical coatings for antireflective applications on glass have been commercially produced since the 1960s. The Sol-gel process classically involves the use of inorganic salts or metal alkoxides as precursors. Typically an elevated temperature up to 400°C is needed for hydrolysis and polycondensation to accomplish an inorganic oxide network (Dislich, 1983). An alternative way was opened by the use of organic-inorganic composite materials. Typical examples are organically modified silanes (Chen, 2001). The final polymerization can either be performed photochemically or thermally, or by a combination of both. The principles of varying the composition and the properties of hybrid sol-gel derived materials are reviewed by Schottner et al. (2003). Scratch-resistant coatings are often modified with cross-linking agents and colloidal silica. On PC substrates the pencil hardness was increased from grade 2B to 5H by adjusting the composition and the total layer thickness (Wu et al., 2008). Wet-chemical coatings are usually deposited by dip coating or spin coating on flat or slightly curved substrates. Injection-molded parts with complicated shapes are not suitable for this deposition method. Moreover, the preparation of multilayers is complex because the depositing and hardening steps have to be repeated several times.

Wet-chemical antireflective coatings may exhibit some advantages compared to vacuum deposited coatings. The mechanical properties of the coatings can be easily adapted to suit plastic substrates and the stability during temperature change should therefore be better. In addition, the variety of materials allows formulations with defined middle refractive indices for two-layer AR coatings or to match the index of a protective layer index perfectly to that of the substrate.

Antireflective coatings for plastics comprise mainly single-layer and two-layer systems. An early described porous single-layer coating for PMMA was produced from a reliquefied gel containing long polymer chains and exhibited low-index layers ($n = 1.22$) (Ashley and Reed, 1990). Many of the single composite layers contain fluorine, among them is an organic fluoropolymer for curing at 120°C (Sakai et al., 2001), a fluorine-containing binder-aided colloidal silica (Floch and Belleville, 1994) and UV-curable fluorine containing polymers (Araki et al., 2003). Patented systems especially for eyeglasses typically start with a hard coating formulation followed by a high-index and a low-index layer. A thermal hardening sol-gel coating made from metal alkoxides for eyeglasses was developed by Vision Ease Lens Inc. (Moravec et al., 2004). The formulations for the interference layers

can be filled with nanoparticles and are mostly cured by UV-radiation (Yoshikawa and Yamaya, 2004). The high index nanoparticles may comprise TiO_2 but also indium tin oxide to achieve antistatic properties (Nishida et al., 2002). Another two-layer coating on a protective acrylate layer consists of metal oxide sol with $n = 1.6$ followed by a cured fluorinated organic-group bearing silicone (Yamaya and Sato, 2003). Seiko has developed a similar system for eyeglasses consisting of a high-index layer filled with TiO_2-nanoparticles followed by an organo-silicone layer containing silica fine particles with index 1.16–1.39 (Naito et al., 2006). This first organic AR layer for eyeglasses was introduced to the market by Seiko (2007). Wet-chemical antireflective coatings are nowadays on the market especially for acrylic or PC sheets for display application (Eyesaver International, 2012). Other commercially available formulations contain nanoparticles immobilized into binders depending on the substrate material (i.e., PC, CR39 and triacetyl cellulose) (Oxford Advanced Surfaces, 2012). The products are not recommended for outdoor use. The optical performance of all wet-chemical compositions do not seem to accomplish the quality of high-performance vapor deposited AR-coatings. However, the number of single layer solutions has been steadily increasing during the recent years, especially in achieving good layers on glass for solar applications. It is apparent that coatings on plastics will follow this trend, especially for achieving AR properties on larger and slightly curved screens.

13.5 CONCLUSION

Optics increasingly appear in all aspects of our everyday lives. We see plastic optics used in eyeglasses, scanners, CD players, cameras for phones, automobiles, security, ink jet printers, image scanners, laparoscopic devices, diagnostic medical devices, fiber optics, identification and tracking systems, laser guided systems, displays, lighting systems, and more.

New applications are being developed daily, particularly in medical and bio-photonic devices, smart phones and displays of all types. Precision plastic optics are at the forefront of these applications because of cost, ease of manufacture and the ability to make complex and multifunctional configurations in one part. Without the benefits of plastic optics many of these applications would not be feasible. As new ideas and applications expand, so do the demands for increased durability, environmental stability, and stringent spectral output. The farther we stretch these physical limits, the more new innovative products will become feasible.

The challenge for AR coatings is to improve physical characteristics and achieve uniformity on complex surfaces ranging from micro to large parts with minimal angular effects. This needs to be accomplished with minimum cost and handling. Vacuum deposited coatings with appropriate plasma treatment have been successful in producing efficient, high-quality AR coatings on plastics. At present it is the most widely used and practical method in the industry. The type of polymer selected has an impact on the adherence and environmental stability of the

films and is an integral part of the finished result. Work continues in the development of organic coatings and nanostructures, both of which offer their own unique benefits depending on the application. An optimum solution for AR coatings may come from integrating multiple technologies combined in a unique way. Research has been directed in this area and continues with the goal to push the state of the art to the next level.

13.6 SOURCES OF FURTHER INFORMATION AND ADVICE

More information about plastic optics in general is available from the book "Handbook of Plastic Optics" including one chapter about coatings (Bäumer, 2010). An online database for plastic materials is available which includes >55,000 data sheets (Kipp, 2010). Important review articles (Liston et al., 1993; Gerenser, 2002; Weikart and Yasuda, 2000) and books (Agostino, 1990; Sabatini and Zambonin, 1993) deal with the surface chemistry of plasma-treated polymers. The special problems connected with vacuum coating of plastics are already covered in early review articles by Schaffer (1988) and Günther (1988). Other review articles are focused especially on plasma-enhanced chemical vapor deposition (PECVD) processes (Martinu and Klemberg-Sapieha, 2003) and on AR coatings (Schulz, 2006). Recently published review articles describe the state-of-the-art of ARS including several substrate materials (Chattopadhyay et al., 2010; Askar et al., 2013), and give guidelines for the design of one-dimensional periodic surface microstructures for antireflective polymer lenses (Søndergaard et al., 2010).

REFERENCES

Agostino, R., 1990. Plasma Deposition, Treatment, and Etching of Polymers. Academic Press Inc, Burlington.

Angus Macleod, H., 2001. Thin-Film Optical Filters, third ed. CRC Press.

Araki, T., Ohashi, M., Tanaka, Y. and Shimizu, T. (2003) Curable fluoropolymer, curable resin composition containing the same, and antireflection film. EP 1347001 A1, Daikin Industries, Ltd., 24 September 2003.

Ashley, C. S. and Reed, S. T. (1990) Sol-gel antireflective coating on plastics. US patent 4,966,812, US Department of Energy, 30 October 1990.

Askar, K., Phillips, B.M., Fang, Y., Choi, B., Gozubenli, N., Jiang, P., Jiang, B., 2013. Self-assembled self-cleaning broadband anti-reflection coatings. Coll. Surf. A Physicochem. Eng. Aspects 439, 84–100.

Bäumer, S., 2010. Handbook of Plastic Optics. Wiley-VCH, Berlin.

Blacker, R., Bohling, D., Coda, M., Kolosey, M., Marechal, N., 2000. In: Development of intrinsically conductive antireflection coatings for the ophthalmic industry.Society of vacuum coaters: 43rd annual technical conference proceedings, pp. 212–216.

Burghoorn, M., Roosen-Melsen, D., Riet, J., Sabik, S., Vroon, Z., Yakimets, I., Buskens, P., 2013. Single layer broadband anti-reflective coatings for plastic substrates produced by

full wafer and roll-to-roll step-and-flash nano-imprint lithography. Materials (Basel) 6 (9), 3710–3726. https://doi.org/10.3390/ma6093710.

Cebeci, F., Wu, Z., Zhai, L., Cohen, R.E., Rubner, M.F., 2006. Nanoporosity-driven superhydrophilicity. In: A Means to Create Multifunctional Antifogging Coatings.22, pp. 2856–2862.

Chattopadhyay, S., Huang, Y.F., Jen, Y.J., Ganguly, A., Chen, K.H., Chen, L.C., 2010. Anti-reflecting and photonic nanostructures. Mater. Sci. Eng. Rep. 69, 1–35.

Chen, D., 2001. Anti-reflection (AR) coatings made by sol-gel processes: A review. Sol. Energy Mater. Sol. Cells 68, 313–336.

Chen, Q., Hubbard, G., Shields, P.A., Liu, C., Allsopp, D.W.L., Wang, W.N., Abbott, S., 2009. Broadband moth-eye antireflection coatings fabricated by low-cost nanoimprinting. Appl. Phys. Lett. 94, 263118.

Clapham, P.B., Hutley, M.C., 1973. Reduction of lens reflexion by the "moth eye" principle. Nature 244, 281–282.

Dai, M., Wang, Y., Pan, M., Lina, S., Rempel, G.L., Pan, Q., 2014. Synthesis and characterization of nanostructured poly(methylmethacrylate) for antireflection coating. Appl. Surf. Sci. 289, 209–217.

Dislich, H., 1983. Glassy and crystalline systems from gels: Chemical basis and technical application. J. Non Cryst. Solids 57, 371–388.

Dobrowolski, J.A., Poitras, D., Ma, P., Vakil, H., Acree, M., 2002. Toward perfect antireflection coatings: numerical investigation. Appl. Optics 41 (16), 3075–3083.

Doerner, M.F., Nix, W.D., 1988. Stresses and deformation processes in thin films on substrates. CRC Crit. Rev. Solid State Mater. Sci. 14, 225–268.

Eyesaver International, 2012. Viewmax' Premium Reflection and Glare Protection. Eyesaver International, Hanover, MA. Available from: http://www.eyesaver-international.com/viewmax_anti_glare.htm. Accessed 20 February 2012.

Floch, H.G., Belleville, P.F., 1994. A scratch-resistant single-layer antireflective coating by a low temperature sol-gel route. J. Sol-Gel Sci. Technol. 1, 293–304.

Fozza, A.C., Roch, J., Klemberg-Sapieha, J.E., Kruse, A., Holländer, A., Wertheimer, M.R., 1997. Oxidation and ablation of polymers by vacuum-UV radiation from low pressure plasmas. Nucl. Instrum. Methods Phys. Res., Sect. B 131, 205–210.

Gaylord, T.K., Moharam, M.G., 1985. Analysis and applications of optic diffraction by gratings. Proc. IEEE 73, 894–937.

Gerenser, L.J., 2002. Surface chemistry for plasma-treated polymers. In: Glocker, D., Ismat Shah, S. (Eds.), Handbook of Thin Film Process Technology. In: vol. 2. Taylor Francis. Sec E.3.1.

Gibson, D.R., Walls, J.M., Brinkley, I., Teer, D.G., Teer, P., Hampshire, J., 2004. In: Flexible and high throughput deposition of multilayer optical coatings using closed field magnetron sputtering.Society of vacuum coaters: 47th annual technical conference proceedings, pp. 1–6.

Gombert, A., Glaubitt, W., Rose, K., Dreibholz, J., Blasi, B., Heinzel, A., Sporn, D., Doll, W., Wittwer, V., 1999. Subwavelength-structured antireflective surfaces on glass. Thin Solid Films 351, 73–78.

Günther, K.H., 1988. Coating of plastics—coatings on plastic. Proc. SPIE 896, 134–139.

Hiller, J., Mendelsohn, J.D., Rubner, M.F., 2002. Reversibly erasable nanoporous antireflection coatings from polyelectrolyte multilayers. Nat. Mater. 1, 59–63.

Hofrichter, A., Bulkin, P., Drévillon, B., 2002. Plasma treatment of polycarbonate for improved adhesion. J. Vac. Sci. Technol. A 20, 245–250.

Hook, T.J., Gardella, J.A., Salvati, L., 1987. Multitechnique surface spectroscopic studies of plasma-modified polymers I: H_2O/AR plasma-modified polymethylmethacrylates. J. Mater. Res. 2, 117–131.

Ishikawa, H., Honjo, Y., Watanabe, K., 1999. Three-layer broad-band antireflective coating on web. Thin Solid Films 351, 212–215.

Jiang, H., Zhao, W., Li, C., Wang, Y.C., 2011. Polymer nanoparticle-based porous antireflective coating on flexible plastic substrate. Polymer 52, 778–785.

Kaless, A., Schulz, U., Munzert, P., Kaiser, N., 2005. NANO moth eye antireflection pattern by plasma treatment of polymers. Surf. Coat. Technol. 200, 58–61.

Kipp, D.O., 2010. Plastic Material Data Sheets. MatWeb—Division of automation creation, Inc. Available from: http://www.knovel.com/web/portal/browse/display?_EXT_KNOVEL_DISPLAY_bookid=1023&VerticalID=0. Accessed 4 March 2012.

Lau, K., Weber, J., Bartzsch, H., Frach, P., 2009. Reactive pulse magnetron sputtered SiO_xN_y coatings on polymers. Thin Solid Films 517, 3110–3114.

Lian, Y.M., Leu, K.W., Liau, S.L., Tsai, W.H., 1995. Effects of surface treatments and deposition conditions on the adhesion of silicon dioxide thin film on polymethylmethacrylate. Surf. Coat. Technol. 71, 142–150.

Licciardello, A., Fragala, M.E., Foti, G., Compagnini, G., Puglisi, O., 1996. Ion beam effects on the surface and on the bulk of thin films of polymethylmethacrylate. Nucl. Instrum. Methods Phys. Res., Sect. B 116, 168–172.

Liston, E.M., Martinu, L., Wertheimer, M.R., 1993. Plasma surface modification of polymers for improved adhesion: a critical view. J. Adhes. Sci. Technol. 7 (10), 1091–1127.

Martinu, L., Klemberg-Sapieha, E.J., 2003. Optical Coatings on Plastics. In: Coatings, N.K., Pulker, H. (Eds.), Optical Interference. Springer-Verlag, Berlin/Heidelberg.

Mendelsohn, J.D., Barrett, C.J., Chan, V.V., Pal, A.J.A., Mayes, M., Rubner, M.F., 2000. Fabrication of microporous thin films from polyelectrolyte multilayers. Langmuir 16, 5017–5023.

MGC, 2016. Mitsubishi Gas Chemical: Iupizeta (The special polycarbonate resin). Available from: http://www.mgc.co.jp/eng/products/fghi/09.html. Accessed 27 December 2016.

Minot, M., 1977. The angular reflectance of single-layer gradient refractive-index films. J. Opt. Soc. Am. 67, 1046–1050.

Moravec, T. J., Hage, M. L. and Boulineau, M. S. (2004) Rapid, thermally cured, back side mar resistant and antireflective coating for ophthalmic lenses, WO/2004/056495, Vision-Ease Lens, Inc., 08 July 2004.

Muir, B.W., Thissen, H., Simon, G.P., Murphy, P.J., Griesser, H.J., 2006. Factors affecting the adhesion of microwave plasma deposited siloxane films on polycarbonate. Thin Solid Films 500, 34–40.

Munzert, P., Schulz, U., Kaiser, N., 2004. Transparent thermoplastic polymers in plasma-assisted coating processes. Surf. Coat. Technol. 173–174, 1048–1052.

Munzert, P., Schulz, U., Kaiser, N., 2007. Method for the vacuum deposition of optical coatings on polymethyl methacrylate. Plasma Processes Polym. 4, 1036–1040.

Naito, S., Kinoshita, J. Kutsukake, Y., Mizuno, H. and Tanaka, H. (2006) Plastic lens and method for producing plastic lens. WO/2006/095469, Seiko Epson Corporation, 14 September 2006.

Narayan, R., 2008. In: Tutorial on biobased and biodegradable plastic films—new substrates for vacuum coating and related technologies.Society of vacuum coaters: 51st annual technical conference proceedings, pp. 229–234.

Nishida, M., Ohno, S., Yoshikawa, M. and Kato, N. (2002) Antireflection film. US patent 2002/0127408 A1, Bridgestone Corporation, 12 September 2002.

Oxford Advanced Surfaces, 2012. VISARC™ Anti-Reflective Coatings, Oxford Advanced Surfaces. Available from: http://www.oxfordsurfaces.com/content/visarc/visarc.asp. Accessed 5 March 2012.

Park, M.S., Lee, Y., Kim, J.K., 2005. One-step preparation of antireflection film by spin-coating of polymer/solvent/nonsolvent ternary system. Chem. Mater. 17, 3944–3950.

Pongratz, S., Zöller, A., 1992. Plasma ion-assisted deposition: a promising technique for optical coatings. J. Vac. Sci. Technol. A 10, 1897–1904.

PPG Optical Products, 2012. Trivex® Lens Material. Available from: http://www.ppg.com/optical/opticalproducts/opticalmaterials/Pages/Trivex.aspx. Accessed 5 March 2012.

Raguin, D.H., Morris, G.M., 1993. Analysis of antireflection-structured surfaces with continuous one-dimensional surface profiles. Appl. Optics 32, 2582–2598.

Rank, R., Wuensche, T., Fahland, M., Charton, C., Schiller, N., 2005. Adhesion promotion techniques for coating of polymer films. SVC Winter News Bull. 34–42.

Rivaton, A., 1995. Recent advances in bisphenol-a polycarbonate photodegradation. Polym. Degrad. Stab. 49 (1), 163–179.

Sabatini, L., Zambonin, P.G., 1993. Surface Characterization of Advanced Polymers. VCH Publishers, Cambridge.

Sakai, Y., Norimatsu, H., Saito, Y., Inomata, H., Misuno, T., 2001. Silica coating on plastics by liquid phase deposition (LPD) method. Thin Solid Films 392, 294–298.

Sarto, F., Alvisi, M., Melissano, E., Rizzo, A., Scaglione, S., Vasanelli, L., 1999. Adhesion enhancement of optical coatings on plastic substrate via ion treatment. Thin Solid Films 346, 196–201.

Schaffer, R.W., 1988. Problems and solutions for coating plastic optics. Proc. SPIE 896, 140–144.

Schottner, G., Rose, K., Posset, U., 2003. Scratch and abrasion resistant coatings on plastic lenses—state of the art, current developments and perspectives. J. Sol-Gel Sci. Technol. 27, 71–79.

Schulz, U., 2006. Review of modern techniques to generate antireflective properties on thermoplastic polymers. Appl. Optics 45, 1608–1618.

Schulz, U., Kaiser, N., 2003. In: Thermal stress in antireflective coatings on polymer substrates. Society of vacuum coaters: 46th annual technical conference proceedings, pp. 419–424.

Schulz, U., Schallenberg, U.B., Kaiser, N., 2002. Antireflection coating design for plastic optics. Appl. Optics 41 (16), 3107–3110.

Schulz, U., Munzert, P., Leitel, R., Wendling, I., Kaiser, N., Tünnermann, A., 2007. Antireflection of transparent polymers by advanced plasma etching procedures. Opt. Express 15, 13108–13113.

Schulz, U., Lau, K., Kaiser, N., 2008. Antireflection coating with UV-protective properties for polycarbonate. Appl. Optics 47, C83–C87.

Schulz, U., Munzert, P., Rickelt, F., Kaiser, N., 2014. Breakthroughs in photonics 2013: organic nanostructures for antireflection. IEEE Photon. J. 6(2), https://doi.org/10.1109/JPHOT.2014.2311432.

Seiko Optical Europe GmbH, 2007. Orgatech-Press Release. Seiko Optical Europe GmbH, Willich. Available from: http://www.seikooptical.com/fileadmin/media/de_sonstiges/startseite/SEIKO_Orgatech_pressrelease_consumer.pdf. Accessed 7 February 2012.

Søndergaard, T., Gadegaard, J., Kristensen, P.K., Jensen, T.K., Pedersen, P.K., Pedersen, K., 2010. Guidelines for 1D-periodic surface microstructures for antireflective lenses. Opt. Express 18, 26245–26258.

Tadanaga, K., Yamaguchi, N., Uraoka, Y., Matsuda, A., Minami, T., Tatsumisago, M., 2008. Anti-reflective properties of nano-structured alumina thin films on poly(methyl methacrylate) substrates by the sol-gel process with hot water treatment. Thin Solid Films 516, 4526–4529.

Temicon, 2018. https://www.temicon.com/en/products/our-brands/holotools (Accessed 27 February 2018).

Vallon, S., Hofrichter, A., Drévillon, B., Klemberg-Sapieha, J., Martinu, L., Poncin-Epaillard, F., Schalchli, A., Benattar, J., 1996. In: Adhesion improvement of silica layers on polypropylene and polycarbonate induced by plasma treatments.23rd international conference on metallurgical coatings and thin films, pp. 325–330.

Walheim, S., Schäffer, E., Mlynek, J., Steiner, U., 1999. Nanophase-separated polymer films as high-performance antireflection coatings. Science 283, 520–522.

Weikart, C.M., Yasuda, H.K., 2000. Modification, degradation, and stability of polymeric surfaces treated with reactive plasmas. J. Polym. Sci. A Chem. 38, 3028–3042.

Wendling, I., Munzert, P., Schulz, U., Kaiser, N., Tünnermann, A., 2009. Creating antireflective nanostructures on polymers by initial layer deposition before plasma etching. Plasma Processes Polym. 6, 716–721.

Wu, L.Y.L., Chwa, E., Chen, Z., Zeng, X.T., 2008. A study towards improving mechanical properties of sol-gel coatings for polycarbonate. Thin Solid Films 516, 1056–1062.

Yamaya, M. and Sato, K. (2003) Antireflective, mar-resistant multilayer laminate. US patent 2003/0087102 A1, Shin-Etsu Chemical Co., Ltd, 8 May 2003.

Yanagishita, T., Kondo, T., Nishio, K., Masuda, H., 2008. Optimization of antireflection structures of polymer based on nanoimprinting using anodic porous alumina. J. Vac. Sci. Technol. B 26, 1856–1860.

Yoshikawa, Y. and Yamaya, M. (2004) Antireflection films and their manufacture. EP 1403665 A2, Shin-Etsu Chemical Co., Ltd., 31 March 2004.

Zhao, M., Yang, Z., Zhu, D., Huang, D., 2005. Influence of the fabrication technique on the porous size of the polymer nanoporous antireflection coatings. J. Opt. Soc. Am. B 22, 1330–1334.

FURTHER READING

Schulz, U., 2010. Coating on Plastics. In: Bäumer, S. (Ed.), Handbook of Plastic Optics, second ed. Wiley-VCH, Berlin, pp. 161–195.

This page intentionally left blank

CHAPTER

Protective coatings for durability enhancement of optical surfaces

14

Tjhay W. Boentoro*, Bernd Szyszka†, Ludvik Martinu‡

*Fraunhofer Institute for Surface Engineering and Thin Films—IST, Braunschweig, Germany**

TU Berlin, Institute for High Frequency and Semiconductor System Technologies, Berlin, Germany†

Department of Engineering Physics, Polytechnique Montréal, Montreal, QC, Canada‡

14.1 INTRODUCTION

The continuous growth of thin film and coating technologies is driven by industrial needs, specifically aiming at new coating functionalities, improvement of coating quality, production cost-efficiency, environmental aspects, and coating system durability. Technological development of thin films and coatings allows these useful functions to be applied in an elegant way on the optical surfaces as illustrated in Figs. 14.1 and 14.2 (Szyszka et al., 2012; Bewilogua et al., 2009).

A particular example of functional film systems is their application as protective coatings on polycarbonate (PC) substrates. PC is an excellent alternative material to replace glass (Staudigl et al., 2000). It is transparent, but it is also lighter, more impact resistant, and can be produced in complex shapes. However, PC can be easily scratched and degraded by UV radiation. By applying functional coatings a few micrometers thick (Katsamberis et al., 1998), the mechanical and chemical properties of PC can be significantly improved. The most common protective coating on PC coating is made of thermally cured, wet chemically deposited lacquers (Schmauder et al., 2006). The UV protection is provided by the organic UV-blocking molecules, which are dissolved in a wet chemical lacquer. This coating offers a very good adhesion, but its hardness is relatively low for protecting the underneath coatings and substrate. Furthermore, UV stability of the UV-blocking molecules is rather limited (Sargent and Pickett, 2006).

In order to improve the mechanical and tribological performance of optical systems and their durability, there has been a significant progress regarding the vapor-based film deposition techniques (Section 14.2), as well as coating system optimization by using appropriate functional testing methods (Section 14.3). In what follows, we give a brief overview of the advances in plasma- and ion-assisted technologies, and we describe specific examples when functional coatings with different

Optical Thin Films and Coatings. https://doi.org/10.1016/B978-0-08-102073-9.00014-X
Copyright © 2018 Elsevier Ltd. All rights reserved.



FIG. 14.1

Thin film applications in architectural glazing can provide different functions such as low-emissivity, sun control, antireflection, hydrophobicity, and hydrophilicity. Switchable optical properties can also be achieved, for example, by electrochromic coatings (left dark state, right transparent state).

architectures were applied to PC and to related substrates (Section 14.4), mostly in conjunction with their potential use in the automotive sector (Section 14.5).

14.2 PLASMA- AND ION-BASED DEPOSITION OF FUNCTIONAL COATINGS

Both issues mentioned above, namely, the mechanical properties and the UV stability, can be improved by dry, vacuum-based coating technologies (Schmauder et al., 2006; Suchentrunk et al., 1999) that have been intensively studied and developed for precision optics and for ophthalmic applications (Beckmann et al., 2002). In fact, fabrication of optical and protective coatings on PC using plasma-based deposition techniques has been a major theme over the past 20 years. In general, coating

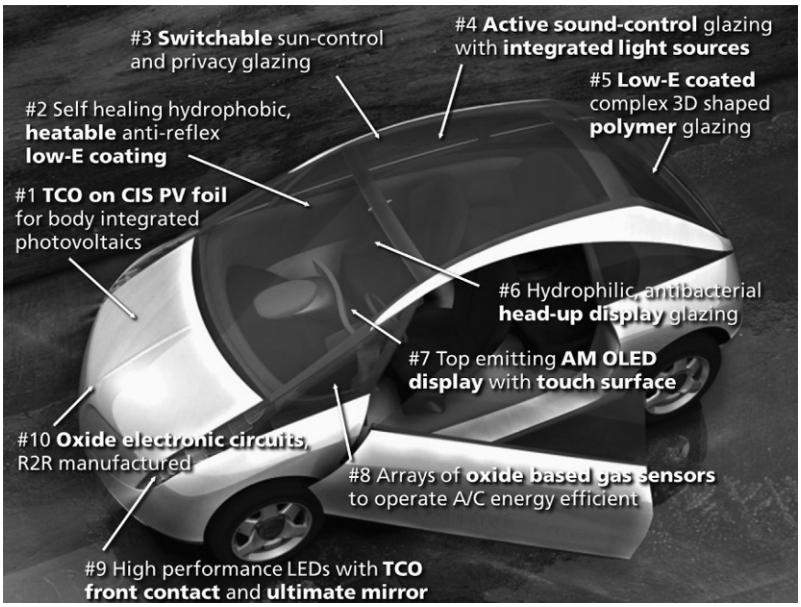


FIG. 14.2

Potential applications of functional thin films and coatings in the automotive sector (Szyszka et al., 2012; Bewilogua et al., 2009). CIS PV means a copper, indium, and selenium-based photovoltaic module.

methods such as Physical Vapor Deposition (PVD) have to cope with the plasma and thermal load during deposition that may lead to micro-cracking and adhesion problems. In comparison, the technology of plasma Ion Assisted Deposition (plasma IAD) offers a process at lower substrate temperature (Schulz et al., 1996). Therefore, plasma IAD is well suited for coating plastics, and it has, in fact, originally been developed for coating injection-molded precision lenses under vacuum.

Plasma Enhanced Chemical Vapor Deposition (PECVD) technology has been extensively studied for optical coating applications (for a review, see Martinu and Poitras, 2000; Martinu et al., 2010), and it offers a possibility of depositing coating on a larger geometry (Schmauder et al., 2006). Several variants of this technique can be distinguished: (a) PECVD with RF-excited plasma polymerization was used in the early 1990s for applying the first hard coating system on CR39 plastic substrates. Primarily, this approach was aimed at competing with the already developed lacquer process technique (Wohlrab and Hofer, 1995). (b) Plasma impulse chemical vapor deposition (PICVD) where plasma excitation is gained by coupling microwave power in a pulsed process. This technology is suitable for optical lenses; however, it is not scalable and, therefore, applicable for automotive glass coating (Kuhr et al., 2003). (c) Radiofrequency (RF), microwave (MW), and the dual-mode MW/RF deposition technology that allows one to tailor the film growth under energetic

ion bombardment while selectively adjusting the ion energy and ion flux for an appropriate microstructural control (Martinu and Poitras, 2000; Martinu et al., 2010).

The subject of optical coatings on plastics has attracted considerable attention (for a review, see Martinu and Klemberg-Sapieha, 2004). Specifically, coatings on plastics applied by PECVD show good adhesion and scratch resistance, but the deposition rate is relatively low and must be improved. In this respect, further development has shown that employing MW power can increase the deposition rate (Beckmann et al., 2001). Moreover, the coating composition can be adjusted by regulating the reactive gas and precursors during the deposition process. Such adjustment of the chemical composition is necessary to achieve soft, substrate-like mechanical properties near the substrate, and hard, glass-like properties near the surface. This concept of gradient layers is crucial in order to achieve highly adherent and scratch resistant systems (Beckmann et al., 2001).

The importance of the gradient optical systems and coatings deposited by PECVD has been taken one step further by assessing the interface between an inorganic layer and a plastic substrate, and by designing and fabricating inhomogeneous (rugate) filters, both initially applied to PC (Bergeron et al., 1998; Poitras, 2000; Poitras and Martinu, 2000). Specifically, it has been shown that the interfacial region ("interphase") between PC (or other plastic) and the mineral film's low index (SiO_2) or high index (e.g., $SiN_{1.3}$) is physically thick (tens of nanometers), over which the hardness and the Young's modulus vary by one to two orders of magnitude (Bergeron et al., 1998). This leads to a uniform distribution of stress, giving rise to a generally better adhesion of PECVD films compared to their PVD counterparts. This concept has further been included in the design of film systems such as antireflective (AR) layers, allowing one to decrease the reflection (e.g., by additional about 0.5% for the $SiO_2/SiN_{1.3}$ stacks on PC) (Poitras, 2000). In addition, well adhering, stress-compensated multiband rugate filters have been successfully designed and fabricated on PC (Martinu et al., 2010; Poitras and Martinu, 2000).

In mineral glass-based architectural and automotive glazings (windshield, side window, quarter glass, sunroof, rear window, etc.), the use of surface coatings has increased significantly (Gläser, 2007). The glazing can be transformed into a multifunctional device by means of coating technology. For example, tailoring the optical properties such as spectral selectivity allows one to obtain low-emissivity (low-E) coatings which minimize the infrared (IR) transmission, thus reducing heat loss and leading to energy saving (Arbab and Finley, 2010). The same concept can also be used for near infrared (NIR) light blocking to achieve sun protection. In general, such low-E or sun-control layers consist of complex insulator–metal–insulator stacks which must be encapsulated to hinder environmental degradation.

The deposition of more durable coatings on the outer or inner surfaces of the glazing allows for adding further functionalities: for example, transparent conductive oxide (TCO) layers can be used as heatable electrodes and even as low-E coatings on the outer pane of the window to minimize thermal losses. The ice-free window (Szyszka et al., 2012) takes advantage of such low-E coating on the outer surface.

Coating technologies can provide additional functions; this includes hydrophobicity (Gunji, 2001) or hydrophilicity (Takagi et al., 2001). Hydrophobic coatings

serve as non-stick and thus as easy-to-clean surfaces. Such surfaces can be produced either by wet chemical deposition (Gunji, 2001) or by low pressure plasma processes including sputtering (Taga, 1999) and PECVD (Takai et al., 1997). Hydrophobic layers on automotive windshields may possibly substitute the use of wipers.

Hydrophilic layers, on the other hand, increase the surface energy of the glass and give rise to the formation of a homogeneous layer of the liquid. As a consequence, the formation of stray light and unwanted reflections due to water droplets is suppressed (Nakamura et al., 2006). Such hydrophilicity can be achieved, for example, by short wavelength illumination of photocatalytic materials (e.g., TiO_2), where the photocatalyst is also used for the decomposition of organic contaminations (Mills et al., 2003) (e.g., fingerprints).

Another advantage of coating technology is the increase in the materials' life span. For example, corundum (α-Al_2O_3) coating, which is harder than quartz, was studied to increase the abrasion resistance of windshields. A 100-nm thick coating was deposited by the sol–gel technique in combination with high-temperature annealing (1200°C) to obtain optimal corundum properties with 10 nm grains (Hauk et al., 1999).

In this context, hard transparent optical coatings with bulk-like density have been obtained by high power impulse magnetron sputtering (HiPIMS) (Hála et al., 2014a; Hála et al., 2014b; Kohout et al., 2016; Kohout et al., 2017). During the HiPIMS process, the applied power is concentrated within short pulses (typically tens to hundreds of microseconds; i.e., very low duty cycle) leading to a high plasma density (Gudmundsson et al., 2012). This gives rise to a high ionization rate, allowing one to deposit dense films under energetic conditions characterized by very high ion fluxes. In this context, over-dense high index materials have been obtained (e.g., Ta_2O_5) (Hála et al., 2014a), complete HiPIMS-deposited environmentally stable optical filters with low stress and enhanced scratch resistance have been demonstrated (Hála et al., 2014b), and hard transparent protective layers on glass have been shown (Al_2O_3 and AlN with hardness values of 14 and 23 GPa, respectively, compared to a hardness of 10 GPa for fused silica) (Kohout et al., 2016; Kohout et al., 2017).

The next interesting development in surface coating is adapted from aeronautical application. Deicing of aircraft windows by transparent and conductive layers serving as ohmic resistors has been applied since the 1940s (Greenall, 2003) while using fluorine-doped tin oxide (SnO_2:F, FTO) deposited by spray pyrolysis on large area glass. Furthermore, low-E coating on the outside of the windowpane also allows for an ice-free window even without heating (Laffay et al., 1978). In the 1980s, researchers at the University of Uppsala and at Volvo applied these airplane window coatings to automotive winds—FTO coating which was deposited by pyrolysis, had reconfirmed the ice-free characteristics. They showed that part of the coated windshield stayed ice-free while the uncoated part was fully covered with ice (Hamberg et al., 1987). However, the pyrolysis technology resulted in the formation of rough layers which caused substantial wear of the windshield when mechanical loading was applied. Therefore, the coating could not fulfill the automotive glazing standard requirements (Horstmann et al., 2009). Following the initial work by Laffay

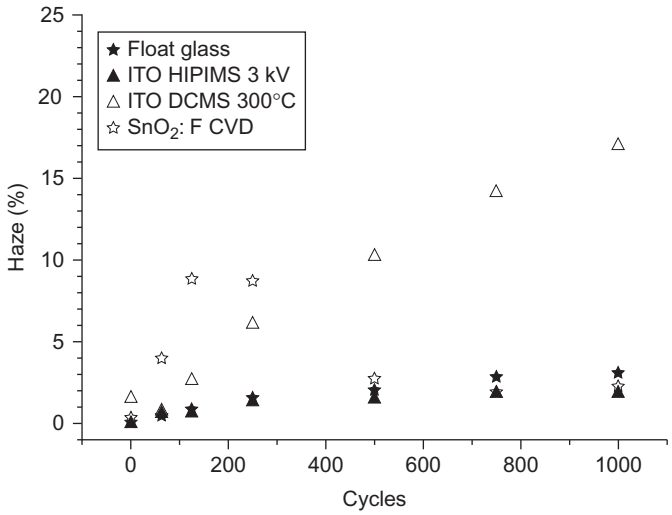


FIG. 14.3

Abrasive performance of float glass, and of HiPIMS-deposited ITO, DC magnetron sputtered ITO, and SnO_2:F coatings (Horstmann et al., 2009).

(Laffay et al., 1978) and Hamberg (Hamberg et al., 1987), the subject of FTO coatings for windshields has been discontinued, while another TCO material suitable for durable low-E coatings became popular, namely tin-doped indium oxide (In_2O_3:Sn) (indium tin oxide, ITO). It has been an important subject of many studies since it also allows application on bendable glass and provides improved scratch resistance compared to uncoated glass (see Fig. 14.3).

For use in optics such as ophthalmic and camera lenses, watches, etc., thin films play an essential active role (such as reduction of reflection), but they have to maintain high mechanical and environmental stability. In general, most of the aforementioned coating applications consider external environmental effects such as erosion and abrasion processes induced by dust or sand particles, UV-radiation, and chemical attack. In automotive applications, the coatings also face additional mechanical solicitations due to car washing, wipers movement, ice scraping, etc. The application of protective coatings thus requires careful selection of materials and of fabrication and characterization techniques which can provide high toughness, as well as high chemical and UV resistance, in order to assure the required functions as well as long-term stability.

14.3 TESTING METHODS

The mechanical behavior of films and coatings is generally well described by their elastoplastic properties, namely, hardness, H, and Young's modulus, E. The H and E values for optical films and coatings are best determined from depth sensing

indentation by analyzing the load–displacement curve using the Oliver and Pharr method frequently obtained using the Berkovich pyramidal diamond tip (Oliver and Pharr, 1992; Yang and Li, 2008). In addition, this technique also allows one to determine the elastic rebound (*ER*) which is related to the elastic response of the coating and thus a capability to elastically dissipate the applied mechanical energy from the load. In order to obtain reliable *H*, *E*, and *ER* data, that is, in order to avoid the effect of the substrate and of the surface imperfections (such as roughness), the load–displacement curves should be obtained at different indentation depths and statistically from different locations. Typically, the minimum film thickness should be between 300 and 500 nm, also depending on the film/substrate combination.

From the practical point of view, the coatings and optical surfaces are exposed to different types of tribomechanical solicitation depending on the working environment. For example, owing to the exposure to abrasive processes at the outside of the windowpane, coatings require particularly high mechanical stability. Therefore, the evaluation of coating practical durability is essential. There are diverse methods and coating property measurements for quantifying coating mechanical durability, and some of the tests have been standardized according to the field of application (for a review, see Pulker, 1999). The methods for evaluating the coating quality in automotive glazings are covered in the international regulation for vehicle glazing, ECE R43 (UN Economic Commission for Europe, ECE R43, 2003), and the test methods in architectural glazings mostly referred to are DIN ISO 9211–3 (Deutsches Institut für Normung, DIN ISO 9211–3, 2010) and DIN ISO 9211–4 (Deutsches Institut für Normung, DIN ISO 9211–4, 2006), which can be combined with test methods from automotive applications. Some of the principal test methods as well as some new characterization techniques are described in this section.

14.3.1 TABER ABRASER TEST OF ABRASION RESISTANCE

To evaluate the mechanical stability of coatings, various abrasion tests have been developed, for example, Taber abraser test, falling sand test, oscillating sand abrasion test (Bayer Test), steel wool abrasion test, eraser rub test, cheesecloth test, etc. The Taber abraser test is one of the commonly used methods for evaluating the coating resistance against wear, which corresponds to the DIN 52347 standard (British Standards Institution, DIN 52347, 1987). In this test, planar samples with upside surface coating are placed against a pair of abrading wheels, while each wheel has a weight of 500 g. The sample rotates and, consequently, the abrading wheels rotate in the opposite direction. Fig. 14.4 shows a schematic of the Taber abraser test setup. The abrasion resistance of the sample can be quantitatively evaluated by measuring the increase in haze (see Section 14.3.8) before and after the test in the four positions of the abraded area. As a baseline, the abraded area of an uncoated glass exhibits a haze increase of about 2% after 1000 cycles. Functional coating on a glass substrate should have at least a comparable abrasion resistance with respect to the uncoated glass or possibly better.

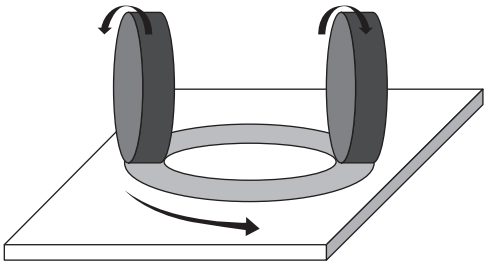


FIG. 14.4

Schematic illustration of the Taber abraser test.

14.3.2 SAND TRICKLING TEST

The sand trickling test (similar to the sand falling test) is used for characterizing the coating abrasion due to particle impact. According to the DIN 52348 standard (British Standards Institution, DIN 52348, 1985), 3 kg of sand with a defined grain size is dropped perpendicularly over the rotating coated sample from a height of 1.5 m. The surface damage can be quantified by comparing the haze before and after the sand trickling test (see Section 14.3.8).

14.3.3 SCRATCH TEST

The scratch test is a very popular method for evaluating the coating adhesion and scratch resistance. The scratch is produced by moving a hemispherical diamond tip (e.g., Rockwell C) or other specified tip along the coated surface with an increasing load, loading rate, specific velocity, and length as schematically illustrated in Fig. 14.5. During the test, sliding, indentation, and plowing occur simultaneously (Holmberg et al., 2003), and different failure modes can be observed; this includes coating detachment, through-thickness cracking and plastic deformation, or cracking within the coating or the substrate (Bull and Berasategui, 2006). The mechanical behavior can then be qualitatively judged from the failure mode, or each failure mode can be semi-quantitatively associated with a specific critical load at its onset. Such critical loads can then be used as the coating performance criterion.

A new in situ real-time approach to perform and analyze scratch tests in transparent coating/substrate systems has recently been introduced (Poirié et al., 2017a). This method allows one to observe, in real time, the contact region during the scratching process (see Fig. 14.6). As an example, thin TiO_2 layers exhibiting stress levels ranging from tensile to compressive were prepared by IAD onto plastic (CR39) substrates. Failure processes obtained using an increasing and a (novel) decreasing load scratch sequence were linked to the internal stress in the coatings allowing one to derive a stress management diagram and to evaluate the yield stress of the layers. Such an approach helped to enhance understanding of the coating failure mechanisms, but it also outlined a new pathway to increase scratch measurement reproducibility.

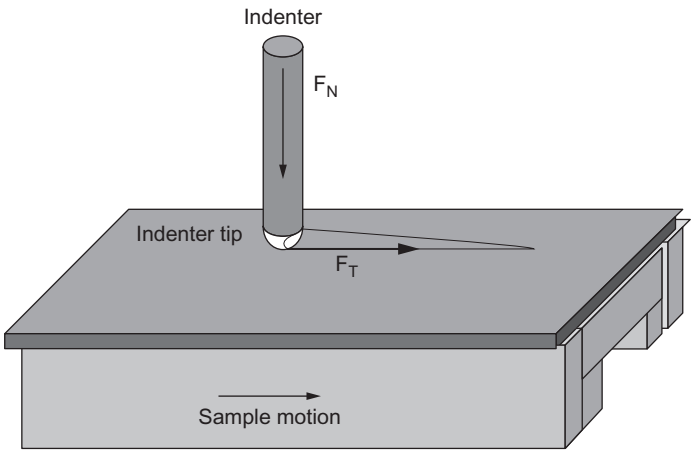


FIG. 14.5

Schematic illustration of the scratch test.

14.3.4 CRACK ONSET STRAIN

PC substrate is softer and much more elastic in comparison to glass. The coating applied on such a surface requires sufficient toughness in order to compensate for the flexibility of the substrate. One method to observe the coating toughness is the Crack Onset Strain (COS) technique (Leterrier et al., 2004). This approach is essentially based on a four-point bending loading system; specifically, the coated substrate (PC) is stretched and bent with the help of a micrometric screw. By using a binocular loupe, first crack occurrence can be observed. Then, on the basis of the measured displacement at the first cracks, the maximum strain at failure can be obtained (see Fig. 14.7).

14.3.5 ADHESION TESTS

Coating adhesion to PC is known to be critical and many studies have been carried out to improve it (Martinu and Klemberg-Sapieha, 2004; Vallon et al., 1996; Leterrier, 2003; Muir et al., 2006). Therefore, the methods for evaluating adhesion have been expanded as well. In the optical industry, crosshatch and peel tests are common methods for evaluating the coating adhesion (Chalker et al., 1991; Awaja et al., 2009). The cutter contains multiple and equally spaced blades. When it is applied carefully with steady pressure, the blades will generate parallel cuts. The second cut performed at a 90° angle to the first cut will form a square pattern (Fig. 14.8). Primary adhesion can thus be observed. On the basis of the amount of delamination in the square area, the coating adhesion can be visually classified from 0 to 5. The value 0 refers to no delamination and an increased detachment area of the crosscut of less than 5% (grade 1), 5%–15% (grade 2), 15%–35% (grade 3), and 35%–65% (grade 4), and a value of 5 corresponds to larger delamination than grade 4 in the observed crosscut field. Afterward, an adhesive tape test is carried out over

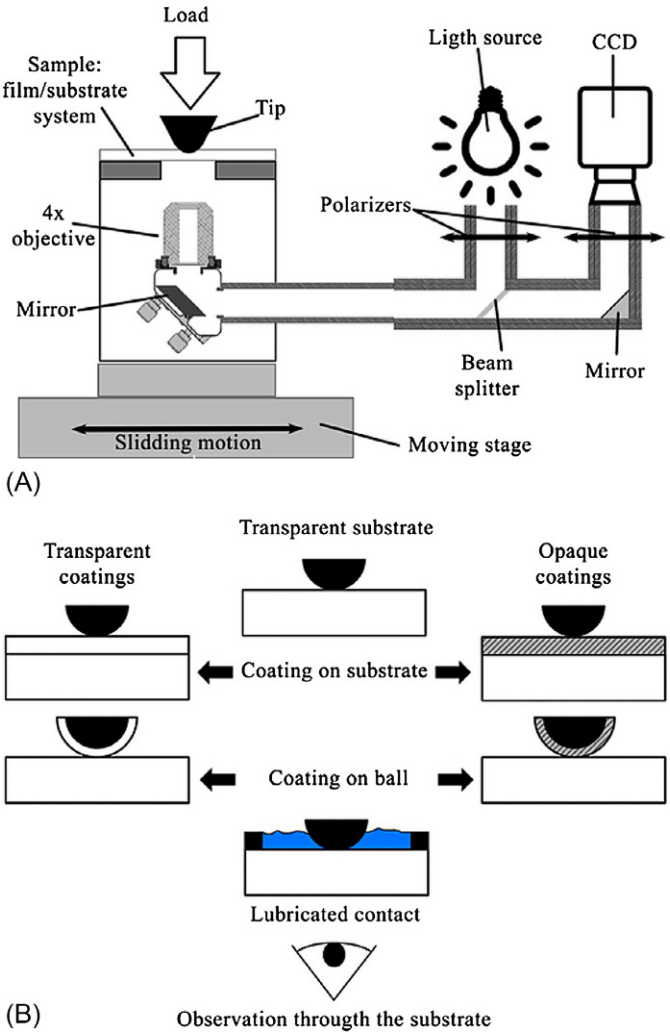


FIG. 14.6

In situ real-time scratch tester (TribTik): (A) schematic representation, (B) Illustrations of the possible configurations for different scratch experiments (from Poirié et al., 2017a).

this pattern. The type of adhesive tape and its removal, as well as the detailed grading of the detached crosscut area, are described in the DIN EN ISO 2409 standard (Deutsches Institut für Normung, DIN EN ISO 2409, 2010).

Coatings with excellent adhesion can be further evaluated at the intensified test level. This evaluation involves the crosshatch test, tape test, and additionally the boiling test. The boiling test simulates the temperature and humidity load to the coating, which is critical for mineral coatings on plastics due to the major difference between

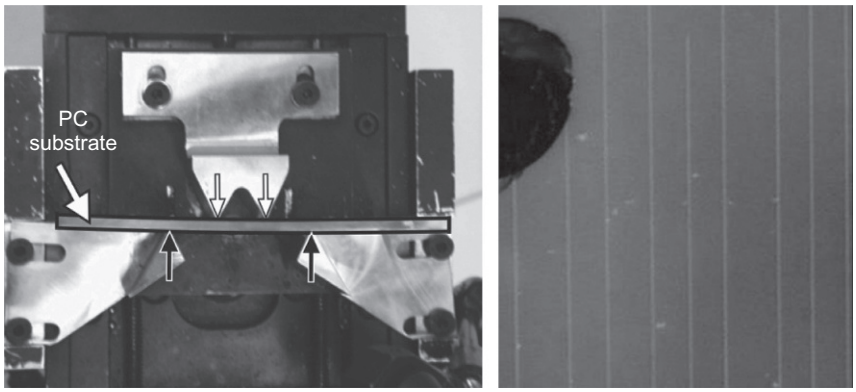


FIG. 14.7

Four point bending test for measuring the Crack Onset Strain (COS) where the coated sample will be stretched and bent (A). The occurrence of the first cracks in the deflection of the substrate is observed with a binocular microscope (B). On the basis of the substrate deflection at failure, the maximum strain can be calculated.

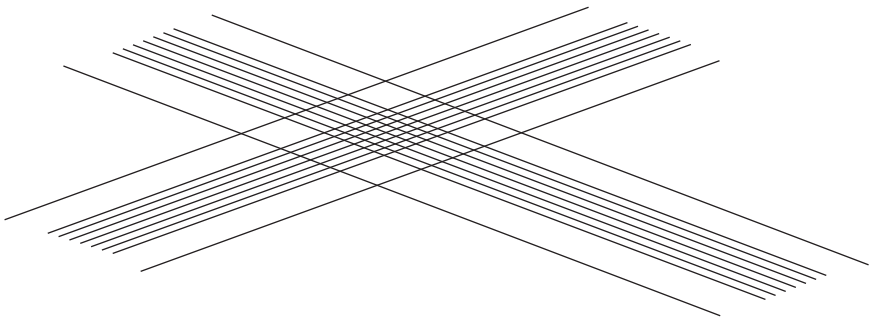


FIG. 14.8

Surface damage by the crosshatch cutter for evaluating the coating adhesion on a plastic substrate.

the coefficient of thermal expansion (CTE) of PC (70×10^{-6}/K), which is much larger compared to that of the SiO_2-like coating (0.56×10^{-6}/K). This difference may induce a significant stress at the interface. The boiling test at the early test phase can be combined with switching from boiling deionized water to room temperature for a specific duration; at the next level, it can be extended periodically.

14.3.6 WEATHERING TEST

The weatherability of coatings on optical surfaces is dependent upon complex interactions of environmental effects that may act in synergy; this mainly includes solar

radiation, temperature, and humidity at a proportion related to the geographical area (Wypyck, 2003). For outdoor uses, these aspects negatively influence the service life of PC because, when exposed to UV-radiation, photolysis reactions can occur and induce degradation such as discoloration and loss of mechanical properties (Diepens, 2009). Similar behavior is also observed in siloxane-based hardcoats on PC where the coating becomes brittle during outdoor exposure. Moreover, during the service life in automotive applications, damage may occur due to car washing or due to dusty environments. Coating degradation caused by mechanical loading may result in damage on a micrometer scale (mar) or even in a larger damage such as scratches that can be further enhanced by additional outdoor exposure. As a result, catastrophic cracking of PC may be induced and followed by delamination of the hardcoats (Nichols and Peters, 2002; Schulz et al., 2001). Therefore, PC requires not only an appropriate scratch resistant coating, but also a UV absorbing layer. To evaluate the lifetime of the coating system, critical weathering environments need to be simulated as illustrated by the following example:

- South Florida: high intensity and duration of solar radiation, high average temperature, high humidity, and rainfall.
- Arizona desert or Kalahari, South Africa: high intensity and long duration of solar radiation, high annual average temperature, low humidity, and almost no rainfall.

For accelerated weathering characterizations, there are specific industrial climatic tests (Pickett et al., 2009) that simulate climates such as Florida or Arizona, and can be combined with varying temperature, humidity, etc. For example, coatings on PC need to provide sufficient mechanical and chemical stability for at least 3000 h of an accelerated Florida weathering test (Schmauder et al., 2006) which is equivalent to 3 years of outdoor exposure.

14.3.7 CHARACTERIZATION OF THE OPTICAL PROPERTIES

Spectrophotometry is generally applied for characterizing the optical properties of the coating systems such as reflectance and transmittance in a specific wavelength range depending on the field of application. For PC, optical properties from the UV to visible regions are essential; for example, coatings with a UV-protection function should have an absorption edge in the 380–400 nm range (Lau, 2006).

The use of glazing for energy control and saving requires optical characterization in a broader spectral range including near and far infrared regions. For example, low-E coating for a hot climate exhibits high transmittance in the visible range, but it reflects heat in the NIR region to reduce the cooling costs. On the other hand, low-E coating for a cold climate is able to transmit light in the visible and NIR regions, which is important to allow the visible light and the near infrared energy from the sun to enter the room, while the black body radiation, which has its maximum in the far infrared region, can be reflected back into the room (Arbab and Finley, 2010). This opens attractive opportunities for the use of TCOs in which one can achieve an appropriate balance between transmission and reflection. Specifically,

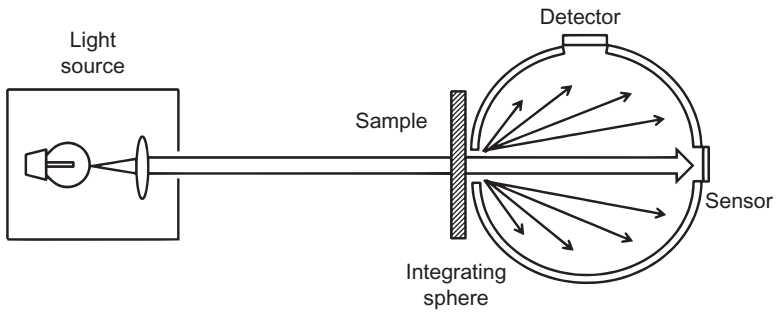


FIG. 14.9

Schematic of the haze measurement principle: Incidence of light is directed through the sample, and the detector captures the difference of the diffused and transmitted light.

the electrical conductivity of the coating is related to the emissivity, while emissivity can, in a simplified way, be expressed as $(1 - R)$ (Szczyrbowski et al., 1999). Therefore, the amount of heat transfer by radiation can be estimated in relation to the electrical conductivity and to its spectral reflection (R) in the far infrared (see the European Standard EN 673; Deutsches Institut für Normung, DIN EN 673, 2003). By controlling spectral selectivity, the coatings can be optimized for reducing the energy used to heat or to cool buildings.

14.3.8 HAZE

The mechanical wear (especially abrasion) of a coating results in surface defects, which become critical in the visible wavelength range. To evaluate the performance of the coatings, the defects can not only be inspected visually, but also it can be determined quantitatively by the measurement of haze (ASTM D1003) (American Society for Testing and Materials, ASTM D1003, 2000). Haze is defined as the percentage of transmitted light that is diffusely scattered due to surface defects, compared with the total transmitted light; it is evaluated using a spectrometer equipped with an integrating sphere (Fig. 14.9).

14.4 COATING CONCEPTS

In order to achieve optimum coating performance, it is necessary to consider the material selection, the coating process, and their influence on the production costs. Additionally, computer-based modeling or simulation enables the observation of coating behavior, for example, due to mechanical and thermal loading, which may help to improve the coating system functionality.

14.4.1 COATING SYSTEMS ON GLASS SUBSTRATE

The magnetron sputtering technique is an industrially viable cost-effective process for ITO coatings allowing one to coat large areas while assuring good mechanical stability. As an example from the large area flat panel displays (Betz et al., 2006), ITO with an average thickness of 100 nm and a substrate area of about 0.6 m^2 has fulfilled the necessary properties for flat panel display performance, with a specific electrical resistivity of about 150 μΩ-cm and a transmittance above 92% at 550 nm. These properties were achieved for polycrystalline ITO films prepared at an elevated substrate temperature (200°C) during deposition. However, heating the substrate during the coating step is less economically effective for industrial applications. As an alternative, post annealing is mostly preferred to attain polycrystalline coatings with excellent properties.

Further improvement of the performance of ITO coatings has been achieved by using the HiPIMS process. In comparison to architectural glazing and flat panel displays, the form of windshields is typically curved according to their design and styling. For this demand, coatings for windshields challenge the deposition techniques because the homogeneity of magnetron sputtering onto three-dimensional substrates is generally insufficient. Therefore, annealing and bending should be carried out after ITO deposition, which is economically more attractive. In this respect, it has been shown that HiPIMS-deposited coatings are fully compatible with the glass annealing and bending steps, especially when using a top encapsulating layer to protect ITO from oxidation (Horstmann et al., 2009). Compared to the previous study of SnO_2:F films, which exhibit premature wear in the abrasive test due to high surface roughness, the complete stack of encapsulated ITO has a smoother surface and hence a higher abrasion resistance.

14.4.2 COATING SYSTEM ON POLYCARBONATE SUBSTRATE

The beneficial properties of PC may be exploited for replacing mineral glass if its mechanical stability through coating techniques is improved. Hard coating material on soft PC is expected to protect the substrate (Schmauder et al., 2006). However, a coating with high hardness applied on soft PC will induce the so-called ‘eggshell’ effect. When an impact load is applied, the soft substrate is plastically deformed underneath the harder coating, and the hard coating induces a high stress difference at the interface. This condition may lead to an abrupt delamination. Therefore, the coating system on PC requires an appropriate gradual adjustment of the mechanical properties to improve the coating adhesion between the substrate (very low hardness, low elasticity) and the hard coating (higher hardness, higher elasticity), in addition to integrating the UV protective coating (Fig. 14.10).

Gradient coatings can be obtained by varying the coating properties (from organic to inorganic), the coating composition (hydrocarbons to oxides), or the coating microstructure (columnar to amorphous). PECVD allows one to deposit gradient

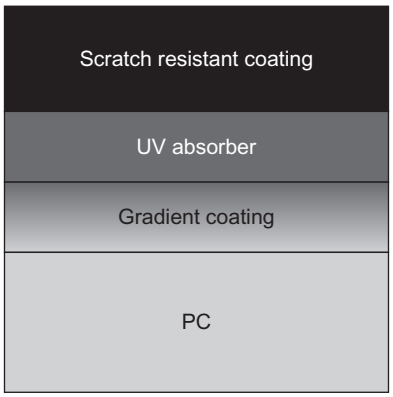


FIG. 14.10

Schematic design of a coating stack with a graded coating varying its properties from soft to hard to bridge the UV absorber and the scratch resistant coating.

coatings that involve silicon-containing monomers such as tetramethylsilane (TMS), hexamethyl-disiloxane (HMDSO), etc. The material properties of the resulting coatings can be controlled by varying the process parameters such as plasma power, activation frequency, and oxygen flow.

14.4.3 NUMERICAL SIMULATION

To optimize the performance of the coating stacks, it is important to study the mechanical behavior of the coating under loading conditions by using numerical methods. The finite element method serves as an effective tool to analyze and optimize the mechanical and thermal behavior of various coating systems. As an example, Fig. 14.11 illustrates the development of numerical simulations based on experimental results. The material characteristics can be extracted from the experiments, such as the E or the COS values, and implemented in the simulation in order to determine guidelines toward appropriate solutions (Fig. 14.12).

As an example, simulation of the cooling down of the PC/SiO_x system indicated that the main compressive stress is located between the glass-like coating and the substrate. By modeling the graded layer between the coating and the substrate, the stress could be uniformly distributed across the graded layers, and the stress mismatch at the interface could be reduced (Fig. 14.13). Such an approach will be helpful in decreasing the experimental efforts, in de-emphasizing the coating material selection, and help to optimize the production costs.

14.4.4 MULTIFUNCTIONAL COATINGS

It is a very attractive proposition to combine PC with coatings possessing functions such as UV protection, scratch resistance, photocatalysis, and antireflection.

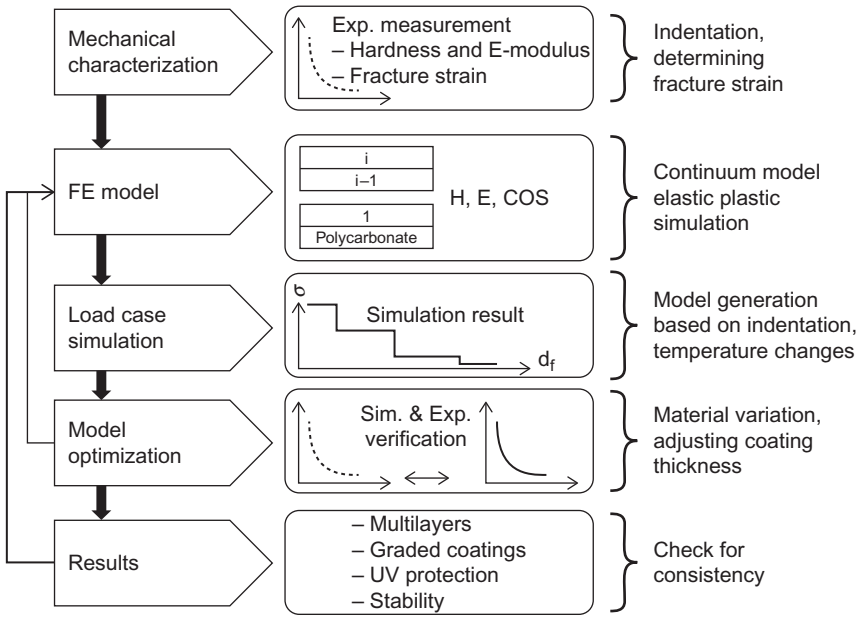


FIG. 14.11

Overview of the simulation and experimental results for understanding the critical condition under diverse loading conditions for optimizing the coating system.

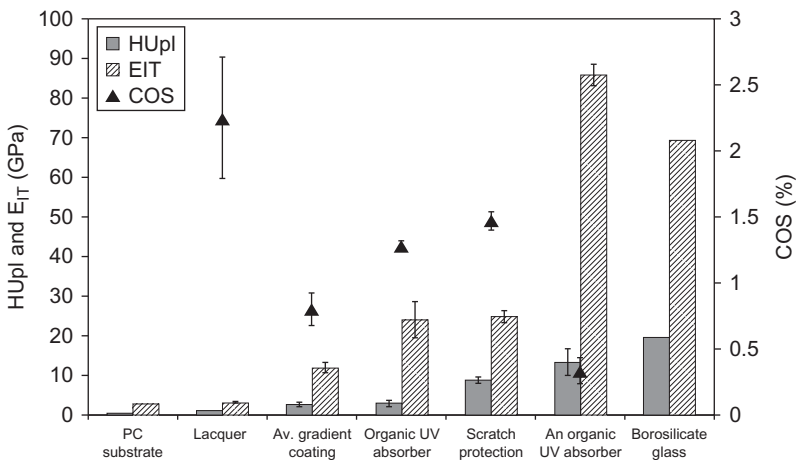


FIG. 14.12

Experimental results from the indentation and bending tests from different coatings in comparison with polycarbonate and a glass substrate. HUpl means plastic hardness.

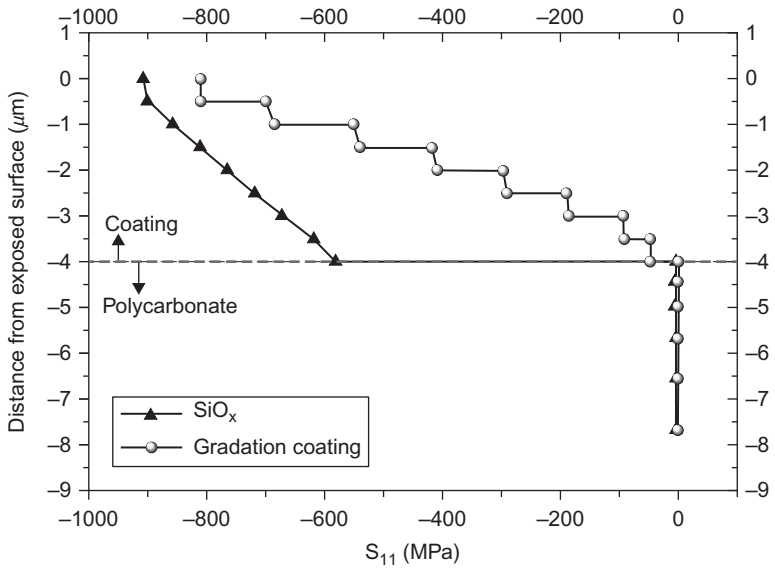


FIG. 14.13

Simulated stress distribution in two coating systems after 100°C cooling: one with and one without a gradient. High stress accumulation at the substrate/coating interface is minimized by applying an initial coating which has properties close to those of the substrate.

However, an important obstacle is frequently the coating adhesion on PC, generally caused by the large difference in the CTE values between the coating and the PC, leading to a necessity to optimize the PC/coating interface.

An interesting approach to control adhesion is to tailor the phenomena involving energetic photons, ions, and reactive species that allow one to obtain a structured interphase over which the mechanical stress can be more uniformly distributed (Martinu and Klemberg-Sapieha, 2004). Such an interphase consists of a cross-linked layer followed by a transition layer formed by intermixing the growing film with the substrate material, and possibly by voids. In the case of $SiN_{1.3}$ considered in the context of optical or gas permeation barrier applications, the refractive index increases from 1.59 for PC to 1.80, while H increases by two orders of magnitude from 0.2 GPa for bulk PC to $\sim$2 GPa for the cross-linked surface layer, and up to 18 GPa for $SiN_{1.3}$. This inhomogeneity generally leads to enhanced adhesion, tribological properties, flexibility, and stretchability, and other functional characteristics suitable for coated plastics, and it can be tuned by using appropriate working gases and plasma conditions (Martinu and Klemberg-Sapieha, 2004).

A suitable approach to improving adhesion at the interface is to apply a coating which can follow the deformation of PC in the case of loading. In fact, this can be achieved by depositing a coating which has similar mechanical properties to PC. In this context, and in order to assure better compatibility between a plastic substrate

and the coating, hybrid films have recently been proposed and explored (Zabeida et al., 2013; Caron et al., 2017; Poirié et al., 2017b), fabricated by ion beam assisted chemical vapor deposition (IBA-CVD), in which an organic precursor is introduced into the path of an ion beam. Such hybrid films have been found to possess optical properties suitable for optical interference filter applications, while providing mechanical performance enhancement due to high mechanical flexibility, high hardness/modulus ratio, and high durability of the plastic optical components leading, for example, to decreased "crazing" (visible fracture patterns). In addition, such hybrid films are substantially less prone to water vapor sorption compared to their inorganic counterparts. This effect has important consequences on the stress contribution in a humid environment.

Along the same line of thought, to combine the functional coatings with PC, several micrometers thick films can be inserted to adjust the material properties. An appropriate coating technique that allows one to deposit films with controlled hardness and elasticity, such as the ones mentioned above, can be applied. Specifically, depositing a PC-like coating next to the substrate, followed by coatings with gradually increased hardness and stiffness, can help to provide higher durability and long-term stability.

14.5 EXAMPLES OF PROTECTIVE COATING APPLICATIONS

Protective coatings for outdoor applications need to withstand the sometimes harsh environmental conditions. As an example, TCOs can be applied in low-E coating systems to prevent moisture accumulation on the outer glass surface. For the emerging field of PC glazing, scratch resistant films are necessary to achieve durability comparable to glass.

14.5.1 LOW-E COATINGS ON WINDSHIELD

By adapting the HiPIMS technique, ITO coatings have been developed for windshield applications with no need of substrate heating (Horstmann et al., 2009). The ITO film on a glass substrate has a thickness of about 140 nm, and it is overcoated with a 40-nm silicon oxy-nitride (SiO_xN_y) film to avoid further oxidation during annealing. The ITO coating, which is prepared at optimized process conditions and subsequently annealed, has a transmittance of more than 80% and a resistivity lower than 300 μΩ-cm. The coating obtained without heating is polycrystalline, and this structure remains unaffected after annealing. The optimized process conditions include a target voltage of 3 kV, an important aspect that also contributes to a better performance of the ITO films in terms of mechanical stability in comparison with the SnO_2:F and with the DC-magnetron sputtered (DCMS) ITO coatings, as well as uncoated glass.

Following the Taber abraser test, the conventional DCMS ITO coating with 300°C substrate heating showed an increased haze of 17% after 1000 cycles. For

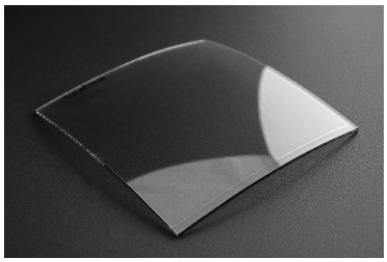


FIG. 14.14

ITO coating on glass after annealing and bending.

comparison, the uncoated glass reached about 2% haze after 1000 abrasive cycles, while the pyrolysis-deposited SnO_2:F coating showed a haze of 10% only after 200 Taber rotations following which the haze decreased to that of uncoated glass. The HIPIMS-deposited ITO exhibited a haze that was lower than for uncoated glass. The root-mean-squared (rms) roughness value of the HiPIMS ITO coating was about 2 nm, that is, much lower than the rms roughness of 18 nm of SnO_2:F coating (Szyszka, 1999).

The sand trickling test confirmed the results of the abrasion test. After 3 kg of sand fell over the coating, the haze of the HiPIMS ITO coating was only about 0.6%, compared to 0.8% for bare float glass and 1% for DCMS ITO. Similarly, the scratch test using a Rockwell C indenter with a linearly increasing load from 1 to 30 N and a velocity of 5 mm/min has shown that the optimized HiPIMS (3 kV) ITO film possessed a higher average critical load (14 N) than the uncoated glass (8–13 N) and other variants of HiPIMS (2 kV) ITO films (12.5 N). Fig. 14.14 shows an example of annealed and bent glass panes exhibiting a high coating stability, while in Fig. 14.15 the thin ITO layer on glass demonstrates its function as a surface resistant to ice accumulation.

14.5.2 POLYCARBONATE IN AUTOMOTIVE GLAZING

PC offers very attractive opportunities in the automotive industry, especially for weight reduction leading to increased fuel efficiency. The replacement of traditional glass with PC is mainly witnessed for the panoramic roof, lighting systems, and side-car windows. These applications demand a high environmental stability since the exposed surfaces are subject to weathering, UV-radiation, and mechanical wear that all represent a considerable challenge (Sargent and Pickett, 2006).

Protection of PC can be well provided by SiO_2 coatings. Using PECVD, such coatings have been shown to fulfill the automotive criteria, but the corresponding deposition rates were still low. Improved rates and similar coating quality were achieved by using hollow cathode activated deposition (HAD) (Katsamberis et al., 1998). However, for industrial implementation, the HAD technology met some difficulties in depositing the UV-protective coating. As an alternative, a promising



FIG. 14.15

Two glass panes placed side by side under the same weathering conditions for comparison: uncoated glass (left) is ice-coated; ITO coating on the glass pane (right) remains ice-free (Szyszka et al., 2012).

concept combining the available UV-protective coating from a lacquer process and the scratch resistant coating from the PECVD technique has been evaluated. A major constraint of this approach is the two-step process (i.e., coating of a primer and UV protection, followed by vacuum coating), which significantly increases the cost. Since PECVD appears to be very promising for depositing the SiO_2 coating with good adhesion and high scratch resistance, Schmauder et al. (2006) have applied microwave power excitation during the PECVD process, and have shown that this approach can be economically competitive with the lacquer technique. However, the demanding criteria of high UV-stability have also to be fulfilled.

Coated PC systems for exterior applications need to be protected against radiation in the wavelength range from 350 to 400 nm. In such a case, classical materials such as titanium oxide and zinc oxide are potential candidates as UV-protective coating. They can be deposited by using a specific sputtering technique, namely, gas flow sputtering (GFS). Examples of the ZnO coatings and their performance are illustrated in Figs. 14.16 and 14.17 from the work by Lübke (2009). Although the ZnO coatings appear acceptable, they failed the boiling test, mainly due to the large difference in the CTE between PC (65×10^{-6}/K) and ZnO (4×10^{-6}/K) (Prasada Rao et al., 2009).

In response to the above-described problem, a graded transition coating has been proposed to bridge the soft PC and the harder ZnO coating. While no ZnO film withstood the boiling test when deposited directly on PC (Lübke, 2009), the graded

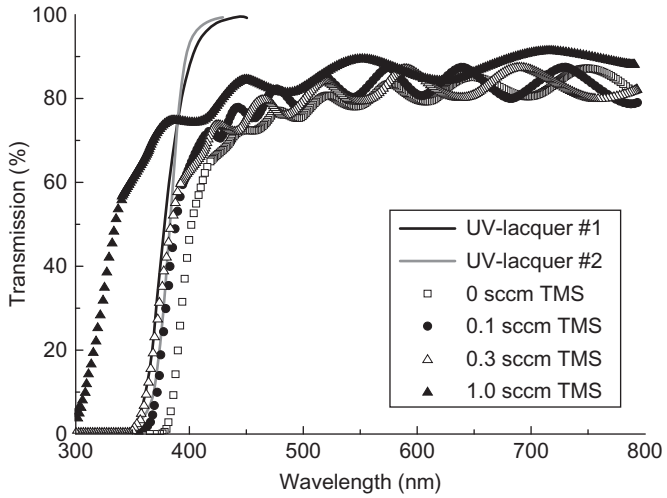


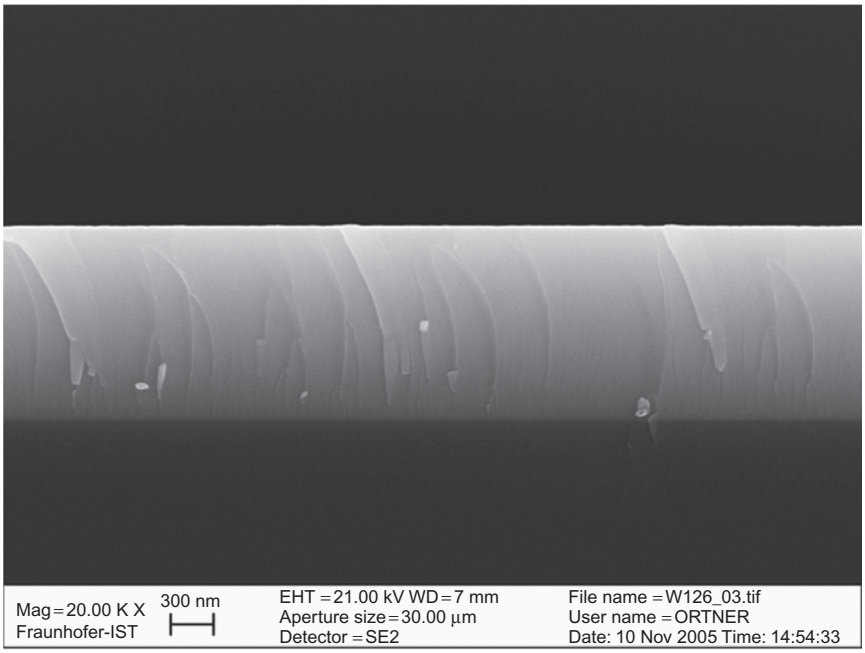
FIG. 14.16

UV absorption edge of two different lacquers, and of the ZnO coatings prepared with different amounts of TMS (Lübke, 2009).

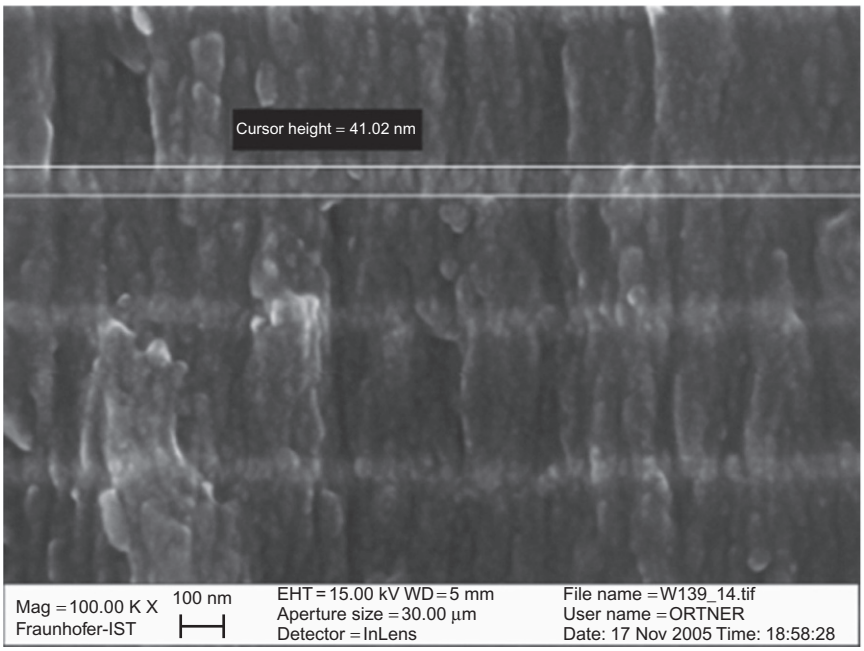
interlayer system has shown much better adhesion in the boiling test. In the latter case, the stress due to thermal loading of the boiling water is more uniformly distributed, thus reducing the stress concentration at the PC/ZnO interface.

14.6 CONCLUSION

Continuous development of coating materials, process techniques, and characterization approaches enables the expansion of high-performance coatings to numerous applications, thanks to new functionalities. In the case of vapor- and vacuum-based deposition technologies, coatings can be fabricated by tailoring the film growth conditions in processes such as HiPIMS. In the area of automobile applications, particularly for the windshields, ITO coatings deposited by HiPIMS using high peak voltage during individual pulses (3 kV) have shown excellent optical transmittance, low electrical resistivity, and high durability during post-deposition treatment including annealing and bending. In mechanical tests, this coating provides better scratch resistance in comparison to uncoated glass, and it prevents the windshield from freezing and offers high stability with respect to weathering conditions. This creates a great potential for applications in other areas, for example, as part of energy saving glazing for buildings, where ITO coatings can improve the insulation by hampering condensation on the outside of the glass panes. In addition, the coating can also be used as a heat conductor. Similarly, in chemical process engineering, reactor vessels can be equipped with a transparent heating system.



(A)



(B)

FIG. 14.17

SEM Cross sections of the TMS-doped ZnO samples: (A) dense single layer coating on silicon wafer; (B) multilayer coating of alternating ZnO and ZnO:TMS films (Lübke, 2009).

Vacuum- and plasma-based technologies have shown considerable advances with respect to the fabrication of coatings possessing functionalities such as scratch-, wear-, abrasion-, and UV-resistance compatible with plastic substrates such as polycarbonate. With the assistance of advanced characterization methods and numerical simulations, the critical conditions of the coating performance can be studied and optimized. Specifically, the concept and control of the structured interfacial region, as well as application of mechanically graded films and of novel hybrid (organic–inorganic) coatings can lead to enhanced adhesion and durability of the coated systems. In addition, recent progress in optimizing PECVD process parameters (e.g., using microwave activation) resulted in an improved deposition rate, rendering such technologies compatible with large area requirements and economic viability. Finally, the development of realistic multi-scale models bridging the gap between the materials properties, layer designs, and coating processes appears as a very powerful approach to fulfill these urgent demands on cost-effective deposition of high-performance coatings.

REFERENCES

American Society for Testing and Materials, ASTM D1003, 2000. Standard test method for haze and luminous transmittance of transparent plastics. Philadelphia.

Arbab, M., Finley, J.J., 2010. Glass in architecture. Int. J. Appl. Glas. Sci. 1, 118–129.

Awaja, F., Gilbert, M., Kelly, G., Fox, B., Pigram, P.J., 2009. Adhesion of polymers. Prog. Polym. Sci. 34, 948–968.

Beckmann, R., Nauenburg, K.-D., Naumann, T., Patz, U., Ickes, G., Hagedorn, H., Snyder, J., 2001. A new high-rate deposition process for scratch- and wipe-resistant coatings for optical and decorative plastic parts. In: Society of Vacuum Coaters.44th Annual Technical Conference Proceedings-Philadelphia, 21–26 April 2001, pp. 288–294.

Beckmann, R., Deppisch, G., Hagedorn, H., Hermann, H.-U., Naumann, T., Pistner, J., 2002. Beschichten transparenter Kunststoffe mit Kratzschutz und AR in einer kombinierten InLine-Anlage. Vakuum in Forschung und Praxis (1), 9–15.

Bergeron, A., Klemberg-Sapieha, J.E., Martinu, L., 1998. Structure of the interfacial region between polycarbonate and plasma-deposited $SiN_{1.3}$ and SiO_2 optical coatings studied by ellipsometry. J. Vac. Sci. Technol. A 16, 3227–3234.

Betz, U., Kharrazi Olsson, M., Marthy, J., Escolá, M.F., Atamny, F., 2006. Thin films engineering of indium tin oxide: Large area flat panel displays application. Surf. Coat. Technol. 200, 5751–5759.

Bewilogua, K., Bräuer, G., Dietz, A., Gäbler, J., Goch, G., Karpuschewski, B., Szyszka, B., 2009. Surface technology for automotive engineering. In: CIRP Annals—Manufacturing Technology.58, pp. 608–627.

British Standards Institution, DIN 52347, 1987. Testing of Glass and Plastics, Abrasion Test; Method Using Abrasion Wheels and Scattered Light Measurement. Technical Help to Exporters, Milton Keynes.

British Standards Institution, DIN 52348, 1985. Testing of Glass and Plastics: abrasion Test; Sand Trickling Method. Technical Help to Exporters, Milton Keynes.

Bull, S.J., Berasategui, E.G., 2006. An overview of the potential of quantitative coating adhesion measurement by scratch testing. Tribol. Int. 39, 99–114.

Caron, M., Zabeida, O., Klemberg-Sapieha, J.E., Martinu, L., 2017. Stability and performance of organic-inorganic thin films on polymer substrates. Surf. Coat. Technol. 314, 131–138.

Chalker, P.R., Bull, S.J., Rickerby, D.S., 1991. A review of the methods for the evaluation of coating—substrate adhesion. Mater. Sci. Eng. A140, 583–592.

Deutsches Institut für Normung, DIN EN 673, 2003. Glass in Building—Determination of Thermal Transmittance (U Value)—Calculation Method. Beuth, Berlin.

Deutsches Institut für Normung, DIN EN ISO 2409, 2010. Paints and Varnishes—Cross-Cut Test. Beuth, Berlin.

Deutsches Institut für Normung, DIN ISO 9211–3, 2010. Optics and Photonics—Optical Coatings—Part 3: Environmental Durability. Beuth, Berlin.

Deutsches Institut für Normung, DIN ISO 9211–4, 2006. Optics and Optical Instruments—Optical Coatings—Part 4: Specific Test Methods. Beuth, Berlin.

Diepens, M., 2009. Photodegradation and stability of bisphenol A polycarbonate in weathering conditions. PhD thesis. Eindhoven University of Technology.

Gläser, H.J., 2007. The European history of coatings on architectural glazing. glassfiles.com. Article from March 22, 2007.

Greenall, M.R., 2003. Heated glazing for vehicles.Proceedings Glass Processing Days, Tampere, 15–18 June 2003, pp. 519–524.

Gudmundsson, J.T., Brenning, N., Lundin, D., Helmersson, U., 2012. High power impulse magnetron sputtering discharge. J. Vac. Sci. Technol. A. 30. 030801.

Gunji, F., 2001. Present status and future trends of coatings on glass for automobiles.Proceedings Glass Processing Days, Tampere, 15–18 June 2001, pp. 502–504.

Hála, M., Vernhes, R., Zabeida, O., Bousser, E., Klemberg-Sapieha, J.E., Sargent, R., Martinu, L., 2014a. Growth and properties of high index Ta_2O_5 optical coatings prepared by HiPIMS and other methods. Surf. Coat. Technol. 241, 33–37.

Hála, M., Vernhes, R., Zabeida, O., Klemberg-Sapieha, J.E., Martinu, L., 2014b. Reactive HiPIMS deposition of SiO_2/Ta_2O_5 optical interference filters. J. Appl. Phys. 116. 213302.

Hamberg, I., Svensson, J.S.E.M., Eriksson, T.S., Granqvist, C.G., Arrenius, P., Norin, F., 1987. Radiative cooling and frost formation on surfaces with different thermal emittance: theoretical analysis and practical experience. Appl. Opt. 26 (11), 2131–2136.

Hauk, R., Frischat, G.H., Ruppert, K., 1999. Sol-gel preparation of scratch-resistant Al_2O_3 coatings on float glass. Glastech. Ber Glas. Sci. Technol. 12, 386–392.

Holmberg, K., Laukkanen, A., Ronkaien, H., Wallin, K., Varjus, S., 2003. A model for stresses, crack generation and fracture toughness calculation in scratched TiN-coated steel surfaces. Wear 254, 278–291.

Horstmann, F., Sittinger, V., Szyszka, B., 2009. Heat treatable indium tin oxide films deposited with high power pulse magnetron sputtering. Thin Solid Films 517, 3178–3182.

Katsamberis, D., Browall, K., Iacovangelo, C., Neumann, M., Morgner, H., 1998. Highly durable coatings for automotive polycarbonate glazing. Prog. Org. Coat. 34, 130–134.

Kohout, J., Bousser, E., Schmitt, T., Vernhes, R., Zabeida, O., Klemberg-Sapieha, J.E., Martinu, L., 2016. Stable reactive deposition of amorphous Al_2O_3 films with low residual stress and enhanced toughness using pulsed dc magnetron sputtering with very low duty cycle. Vacuum 124, 96–100.

Kohout, J., Qian, J., Schmitt, T., Vernhes, R., Zabeida, O., Klemberg-Sapieha, J.E., Martinu, L., 2017. Hard AlN films prepared by low duty cycle magnetron sputtering and by other deposition techniques. J. Vac. Sci. Technol. A. 35. 061505.

Kuhr, M., Bauer, S., Rothhaar, U., Wolff, D., 2003. Coatings on plastics with the PICVD technology. Thin Solid Films 442, 107–116.

Laffay, G., Fadeuilhe, G., Schambourg, F., and Keita, K. (1978), Patent DE2833234C2, filed 28 June 1978.

Lau, K., 2006. Plasmagestützte Aufdampfprozesse für die Herstellung haftfester optischer Beschichtungen auf Bisphenol-A Polycarbonat. PhD thesis, Fraunhofer IOF.

Leterrier, Y., 2003. Durability of nanosized oxygen-barrier coatings on polymers. Prog. Mater. Sci. 48, 1–55.

Leterrier, Y., Medico, L., Demarco, F., Manson, J.-A.E., Betz, U., Escola, M.F., Kharrazi Olsson, M., Atamny, F., 2004. Mechanical integrity of transparent conductive oxide films for flexible polymer-based displays. Thin Solid Films 460, 156–166.

Lübke, M., 2009. Abscheidung einer PVD-PECVD Hybridschicht als UV-Schutz auf Polycarbonat. Master's thesis in Fraunhofer IST and IOT TU Braunschweig, Germany.

Martinu, L., Klemberg-Sapieha, J.E., 2004. Optical Coatings on Plastics. In: Kaiser, N., Pulker, H. (Eds.), Optical Interference Filters. Springer, Berlin, pp. 460–489.

Martinu, L., Poitras, D., 2000. Plasma deposition of optical films and coatings: a review. J. Vac. Sci. Technol. A 18, 2619–2645.

Martinu, L., Zabeida, O., and Klemberg-Sapieha, J.E. (2010), 'Plasma-enhanced chemical vapor deposition of functional coatings', Chapter 9 in the "Handbook of Thin Film Deposition Technologies", P.M. Martin, ed., Elsevier, Amsterdam, pp. 394–467.

Mills, A., Lepre, A., Elliott, N., Bhopal, S., Parkin, I.P., O'Neill, S.A., 2003. Characterisation of the photocatalyst Pilkington Activ™: a reference film photocatalyst? J. Photochem. Photobiol. A Chem. 160, 213–224.

Muir, B.W., Thissen, H., Simon, G.P., Murphy, P.J., Griesser, H.J., 2006. Factors affecting the adhesion of microwave plasma deposited siloxane films on polycarbonate. Thin Solid Films 500, 34–40.

Nakamura, M., Kobayashi, M., Kuzuya, N., Komatsu, T., Mochizuka, T., 2006. Hydrophilic property of SiO_2/TiO_2 double layer films. Thin Solid Films 502, 121–124.

Nichols, M.E., Peters, C.A., 2002. The effect of weathering on the fracture energy of hardcoats over polycarbonate. Polym. Degrad. Stab. 75, 439–446.

Oliver, W.C., Pharr, G.M., 1992. Improved technique for determining hardness and elastic modulus using load and displacement sensing indentation experiments. J. Mater. Res. 7, 1564–1583 also see: International Organization for Standardization; metallic materials—Instrumented indentation test for hardness and materials parameters—Part 4: Test method for metallic and non-metallic coatings. In: ISO 14577-4, Geneva, Switzerland: International Organization for Standardization; 2007.

Pickett, J.E., Sargent, J.R., Blaydes, H.A., Babbie, N., 2009. Effects of temperature on the weathering lifetime of coated polycarbonate. Polym. Degrad. Stab. 94, 1085–1091.

Poirié, T., Schmitt, T., Bousser, E., Martinu, L., Klemberg-Sapieha, J.E., 2017a. Influence of internal stress in optical thin films on their failure modes assessed by in situ real-time scratch analysis. Tribol. Int. 109, 355–366.

Poirié, T., Schmitt, T., Bousser, E., Vernhes, R., Martinu, L., Klemberg-Sapieha, J.E., 2017b. Hybrid organic/inorganic nanolaminate structures with enhanced tribo-mechanical properties for optical applications. Surf. Coat. Technol. 315, 399–407.

Poitras, D., 2000. Investigation of Plasma-Deposited Inhomogeneous Optical Thin Films (Ph.D. thesis). Ecole Polytechnique de Montreal.

Poitras, D., Martinu, L., 2000. Interphase in plasma-deposited films on plastics: Effect on the spectral properties of optical filters. Appl. Opt. 39, 1168.

Prasada Rao, T., Santosh Kumar, M.C., Anbumozhi Angayarkanni, S., Ashok, M., 2009. Effect of stress on optical band gap of ZnO thin films with substrate temperature by spray pyrolysis. J. Alloys Compd. 485 (1–2), 413–417.

Pulker, H.K., 1999. Coatings on Glass, second ed. Elsevier Science.

Sargent, J.R., Pickett, J.E., 2006. Accelerated Weathering Using Xenon Arc with Boro/Boro Filters, Important Factors for Testing and Translation to Standard 5° FL Outdoor Test Protocols.Proceedings ICCG, Dresden, 18–22 June 2006pp. 215–219.

Schmauder, T., Nauenburg, K.-D., Kruse, K., Ickes, G., 2006. Hard coatings by plasma CVD on polycarbonate for automotive and optical applications. Thin Solid Films 502, 270–274.

Schulz, U., Jakobs, S., Kaiser, N., 1996. SiO_2 protective coatings on plastic optics deposited with plasma-IAD. In SPIE 2776, 169–174.

Schulz, U., Wachtendorf, V., Klimmasch, T., Alers, P., 2001. The influence of weathering on scratches and on scratch and mar resistance of automotive coatings. Prog. Org. Coat. 42, 38–48.

Staudigl, G., Benien, H., Suchentrunk, R., 2000. Transparente Kratzschutzbeschichtungen für Kunststoff. Mat.-wiss. u. Werkstofftech 31, 360–364.

Suchentrunk, R., Fuesser, H.J., Staudigl, G., Jonke, D., Meyer, M., 1999. Plasma surface engineering—innovative processes and coating systems for high-quality products. Surf. Coat. Technol. 112, 351–357.

Szczyrbowski, J., Bräuer, G., Ruske, M., Schilling, H., Zmelty, A., 1999. New low emissivity coating based on TwinMag sputtered TiO_2 and Si_3N_4 layers. Thin Solid Films 351, 254–259.

Szyszka, B., 1999. Reaktives Magnetronsputtern von transparenten und leitfähigen Oxidschichten. PhD thesis, Fraunhofer IST, Braunschweig, Germany.

Szyszka, B., Dewald, W., Gurram, S.K., Pflug, A., Schulz, C., Siemers, M., Sittinger, V., Ulrich, S., 2012. Recent developments in the field of transparent conductive oxide films for spectral selective coatings, electronics and photovoltaics. Curr. Appl. Phys. 12, S2–S11.

Taga, Y., 1999. Review of plasma thin-film technology in automobile industry. Surf. Coat. Technol. 112, 339–346.

Takagi, K., Makimoto, T., Hiraiwa, H., Negishi, T., 2001. Photocatalytic, antifogging mirror. J. Vac. Sci. Technol. 19 (6), 2931.

Takai, O., Hozumi, A., Sugimoto, N., 1997. Coating of transparent water-repellent thin films by plasma-enhanced CVD. J. Non-Cryst. Solids 218, 280–285.

UN Economic Commission for Europe, ECE R43, 2003. Uniform provisions concerning the approval of safety glazing materials and their installation on vehicles. Rev. 2.

Vallon, S., Hofrichter, A., Guyot, L., Drevillon, B., Klemberg-Saphieha, J.E., Martinu, L., Poncin-Epaillard, F., 1996. Adhesion mechanisms of silica layers on plasma-treated polymers. Part I. Polycarbonate. J. Adhes. Sci. Technol. 10, 1287–1311.

Wohlrab, C., Hofer, M., 1995. Application of plasma polymerization on ophthalmic lenses: Equipment and processes. Opt. Eng. 34, 2712–2718.

Wypyck, G., 2003. Handbook of Material Weathering, third ed. ChemTec Publishing, Canada.

Yang, F., Li, J.C.M., 2008. Micro and Nano Mechanical Testing of Material and Devices. 49, Spring, New York.

Zabeida, O., Schmitt, T., Marushka, V., Poirié, T., Vernhes, R., Klemberg-Sapieha, J.E., Martinu, L., 2013. In: Hybrid organic-inorganic optical films deposited by ion beam assisted CVD. OSA Optical Interference Coatings 2013 Topical Conference. Whistler, BC, Canada.

CHAPTER

Optical coatings for displays and lighting☆

15

Cheng-Chung Lee, Chien-Cheng Kuo
National Central University, Taoyuan City, Taiwan

15.1 INTRODUCTION

The invention of the liquid crystal display (Brody et al., 1973) opened the way to a thin and light flat panel display (FPD) (Tannas, 1989), which could take the place of the cathode ray tube (CRT). The FPD then became generally used in notebooks (Mentley, 2002), cell phones (Allen, 2005), video games (Tannas, 1994), personal digital assistants (Kimmel et al., 2002), and many other displays used in daily life, even extending to global positioning systems (GPS), etc. There are several types of FPDs such as plasma display panel (PDP), field emission display (FED), electroluminescence display (ELD), vacuum fluorescent display (VFD), and thin film transistor liquid crystal display (TFT LCD). The front surfaces of all these FPDs need antireflection (AR) coatings and/or antiglare coatings. A different type of display popularly used in conference rooms, public places, and home theaters is projection television (PTV) (Epstein and Maloff, 1945). It needs not only AR coating, but also other kinds of optical coatings, such as cold light high reflection (HR) coating, UV–IR cut coating, color separation coating, polarization splitting coating, etc. Thanks to the optical coatings, the PTV can be made very small so that it can be installed easily while having a large display area. Therefore, nowadays most meeting rooms and classrooms are equipped with different types of PTV. Furthermore, technologies such as microelectro mechanical system (MEMS) (Van Kessel et al., 1998), liquid crystal on silicon (LCoS) (Shimizu, 2001), digital light processing (DLP) (Hornbeck, 1997), digital micromirror device (DMD) (Hornbeck, 1993), and so on, help us make the FPD and PTV still more compact with larger display screens and higher image resolution.

At the same time, energy saving, lifetime, and environmental benefit requirements have encouraged a new type of light source—the light-emitting diode (LED) (Ponce and Bour, 1997). This is a possible replacement for halogen lamps

☆This chapter is a reprint of the chapter originally published in the first edition of Optical Thin Films and Coatings: From Materials to Applications

Optical Thin Films and Coatings. https://doi.org/10.1016/B978-0-08-102073-9.00015-1
Copyright © 2018 Elsevier Ltd. All rights reserved.

or fluorescent tubes in lighting applications (Arik et al., 2002). Some types of FPDs and PTVs already use LED light sources (Harbers and Hoelen, 2001). Nowadays, there are many types of FPDs, PTVs, and LEDs, but all of them need different kinds of coatings. These assure their function but also improve their quality, make them visually comfortable to the eyes and increase their output efficiency.

15.2 OPTICAL COATINGS FOR FLAT PANEL DISPLAY (FPD)

To avoid blurred images and to eliminate unwanted reflected light, the screen surface of an FPD must carry an AR coating. To reduce the annoying disturbance from external sources like bright ambient lights, and to enhance the contrast of the images, an antiglare (AG) coating is necessary. In some cases, the coating can combine the AR and AG attributes. In addition, a hydrophobic coating to keep the screen surface free of contamination from fingerprints and dirt, as well as making the surface easier to clean with a soft cloth or tissue, is a general requirement for a daily used FPD.

The AR coating must make the FPD screen surface present low reflectance throughout the visible range within certain view angles. If the screen is constructed from glass, nonabsorbing oxides are usually the coating materials of choice for AR coatings. The high-index material is usually chosen from TiO_2, Nb_2O_5, Ta_2O_5, and ZrO_2, while SiO_2 is the general choice for low-index material, although MgF_2 can occasionally be employed. For an intermediate index Al_2O_3 is a good material. Coatings of up to five layers are normally good enough to meet the specification for general purpose AR coatings (Macleod, 2001). However, very high pixelated cameras embedded in cell phones require coatings of up to eight layers.

Since glare is caused by the reflection of bright, ambient light from the surface of the screen, antiglare quality and contrast enhancement can be achieved with a matte finish. Alternatively adding microparticles to the screen or attaching a thin sheet embedded with microparticles will increase the diffusive properties so that unwanted light is scattered. However, a disadvantage of those methods is possible reduction in the clarity and resolution of the image. To retain good clarity, coatings depending on optical interference are better. Then, one may use absorbing material as one of the coating layers to provide an AG property, although it will certainly decrease the transmittance by a few percent (Al-Dahoudi et al., 2001). In fact, the coating can combine both AR and antiglare properties if the correct materials are used. For example, Cr/CrO_x, Fe/FO_x, ITO/SiO_2, $TiNO_x/SiO_2$ (Zheng et al., 1997), and TiN_xW_y/SiO_2 (Ishikawa and Lippey, 1996) have been tried as AR and AG coating materials. Recently, a new type of FPD has been developed using ambient light instead of backlight as a light source; in this case AR and AG coatings with better performance are required.

Since the screen of an FPD is exposed to the outside world, it will normally accumulate contamination by dirt and fingerprints, unpopular with customers. To help keep it free from such contamination, as well as making the surface easier to clean with a soft cloth or tissue, a hydrophobic coating can be added. The key technology

of a hydrophobic coating is the addition of a coating of low surface energy over the final layer of the existing coating. Usually, the water contact angle should be >110° (McHale et al., 2004). Although physical vapor deposition is usually more convenient for multilayer coatings, a silica sol–gel dip coating has been found to be good for large FPDs that has hydrophobic and AR properties coupled with high scratch resistance. Sol–gel coatings produced by dipping or spinning processes are also suitable for plastic substrates, such as polymer molded optics (including eye glasses and camera lenses), of materials such as polycarbonate, acrylic, poly(methyl methacrylate) (PMMA), Zeonex, polyethylene terephthalate (PET), polyethylene naphthalate (PEN), polyimide (PI), etc. (Chen et al., 2000) Alternatively, perfluoropolyether polymers modified with organofunctional silanes have been developed to present a hydrophobic surface (Mascia and Tang, 1998). In all circumstances, keeping surfaces dry and clean is very important for good coatings no matter whether by vacuum processes or by non-vacuum sol–gel techniques. Ion sources also improve adhesion for coatings on plastic substrates in vacuum coating. For glass substrates, the use of an ion source in assisted ion deposition can reduce the need for substrate heating and thus reduce the coating process time.

Color filters used in FPDs are absorption filters in most cases. A red color filter absorbs green and blue light, green absorbs red and blue, and blue absorbs green and red. This absorption costs us at least two-thirds of the available light. Although mosaics with coated blue, green, and red high transmission color filters, based on interference rather than absorption, have been proposed, commercial FPDs do not use them for economic reasons. However, with a new lithographic technology and a new design of using mosaics with coated blue, green, and red high transmission color filters, based on interference rather than absorption, have been proposed again. Then the reflected complementary colors can be reused through the process of bounces back and forth. The light will be fully used, since no light is wasted. For instance, when white light is incident on the blue filter, blue light is transmitted, while its complementary color, yellow, containing green and red light will be reflected and bounced back and then transmit to the green and red filters, respectively. Similarly, when the white light is incident on the green or red filter, their complementary colors will be reflected and reused.

Another important coating for FPDs is a transparent conductive coating. It is used as an electrode for TFT LCDs (Katayama, 1999), touch panels (Exarhos Gregory and Zhou, 2007), *E*-paper (Rogers et al., 2001), low emissivity glass (Szczyrbowski et al., 1989), electrochromic windows (Rauh, 1999), LEDs (Hosono et al., 2002), etc. Nowadays, most transparent conductive coatings are oxides because of their chemical stability, and the term used to describe them is transparent conductive oxide (TCO). TCO was pioneered in the early 20th century by Streintz (Streintz, 1902). Later, magnetron sputtering brought fabrication to lower temperatures (Minami, 1999). Then indium tin oxide (ITO) became the main TCO for most applications (Zhang et al., 2000). Several types of doped TCO, such as F:SnO_2, Al:ZnO, Ga:ZnO, Nb:TiO_2, Sb:SnO_2, etc., are under development with the objective of taking over from ITO, since indium is a rare material in short supply (Manifacier et al., 1979;

Tominaga et al., 1998; Bhosle et al., 2006; Dabney et al., 2008; He et al., 1993; Li et al., 2011; Liao et al., 2011). All TCO films are required to have high transmittance, higher than 85%, and low sheet resistance ranging from a few tens to several hundreds of Ω/□, according to the application.

The traditional backlight used in FPDs is either the cold-cathode fluorescent lamp (CCFL), the external electrode fluorescent lamp (EEFL), the hot cathode fluorescent lamp (HCFL), or the flat fluorescent lamp (FFL). Nowadays these lamps are gradually being replaced by LEDs because of energy saving and lifetime issues and because of environmental factors. Thin film coatings are necessary in backlighting units so that full use can be made of the light source. Besides AR coatings, high reflectance behind the light source is required. The reflector is coated with a silver thin film (about 100 nm) and a protective film, like thin nickel or nickel–chromium nitride (a few nanometers) or with dielectric films (SiO_2/TiO_2) to achieve a reflectance >98%.

15.3 OPTICAL COATINGS FOR PROJECTORS

As well as the AR coatings on each surface of its optical components, projectors need several other types of coatings, such as cold mirrors, UV–IR cut filters, three primary color filters (dichroic filters), beam splitters, polarizers, and so on, as indicated in Figs. 15.1 and 15.2. Fig. 15.1 is a transmission-type projector with liquid crystal

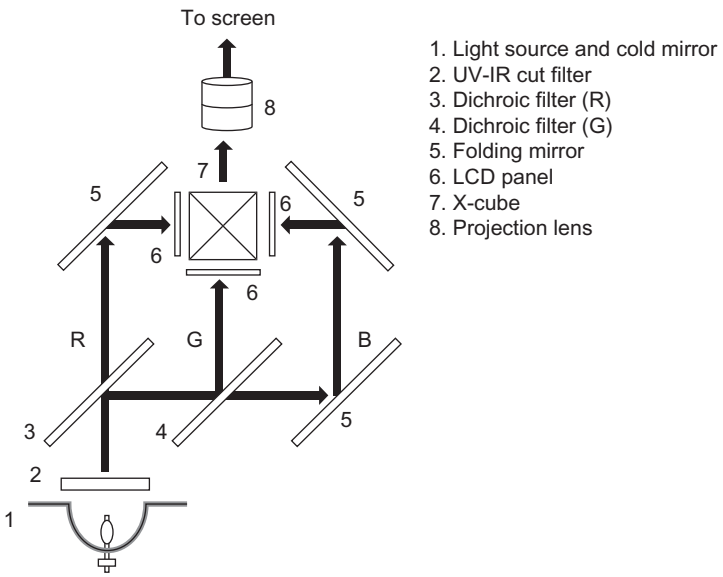


FIG. 15.1

Transmission-type projector with liquid crystal panel. R, G, and B stand for red, green, and blue light, respectively.

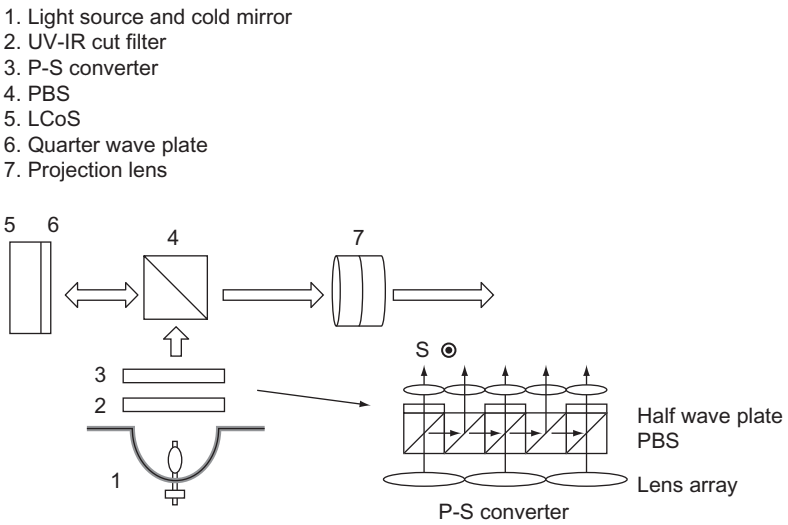


FIG. 15.2

Reflection-type projector using LCoS.

display, where the three primary colors are separated spatially by red (R) and green (G) dichroic filters and folding mirrors (Takeda and Miyatake, 1992). The X-cube prism is constructed from crossed dichroic filters. These recombine the light that has passed through the three LCD light valves, located at the three faces of the cube (Shikama et al., 1993). After their combination the images are projected onto the screen by the projection lens.

Light generated by an ultrahigh-pressure (UHP) mercury lamp or halogen lamp is collected by an elliptical reflector carrying a cold mirror. The cold mirror reflects only the visible light letting the UV and IR radiation be transmitted. The reflection cup is a very deep elliptical reflector and the coating, based on quarter-wave stacks, on such a deep cup must be very uniform, so that the reflectance can be high enough to achieve flux >8000 lx from a 120-W halogen lamp. A UV–IR cut filter is also placed in front to filter direct light from the source. UV and IR radiation are eliminated to prevent damage to the liquid crystal, the optical components, and charge-coupled device (CCD)/complementary metal–oxide–semiconductor (CMOS) and to keep the right color temperature. Fig. 15.3 shows the spectrum of UV–IR cut filter coated with a multilayer of TiO_2 and SiO_2, based on the design: Sub/(0.6 L 1.2H.6 L) ^10 (0.5LH.5 L) ^10/air, with central wavelength at 780 nm, where Sub indicates the substrate, and H and L are quarter wave layers of high (TiO_2) and low (SiO_2) refractive index, respectively.

Fig. 15.2 shows a reflection-type projector using Liquid Crystal on Silicon (Jepsen, 2003) technology. In an LCoS device, the CMOS transistors and pixel mirrors, designed to modulate the light with the image data, are built on a silicon chip by semiconductor techniques. The liquid crystal filled a gap between the silicon chip

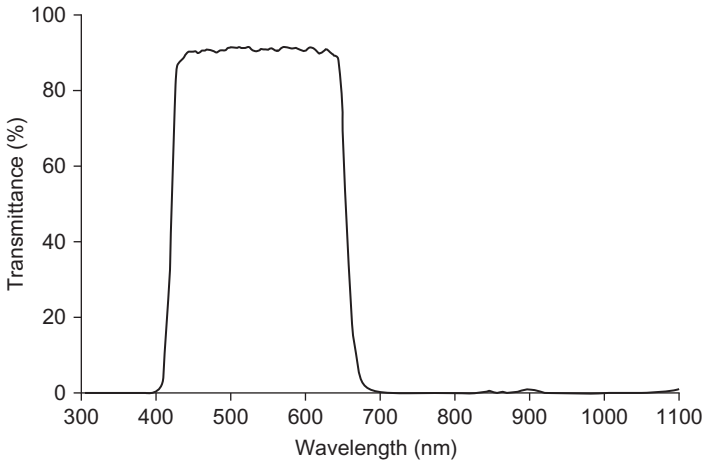


FIG. 15.3

Spectrum of UV–IR cut filter.

and an overlaid glass plate. The p–s converter in front of the lamp converts all the output light to pure s-polarized. A schematic of a p–s converter is included at the foot of Fig. 15.2 on the right. It is a combination of an array of lenses and polarization beam splitters (PBSs). There are half wave plates on the output surfaces of the odd numbered PBSs to convert p-polarized light to s-polarized light. The s-polarized light is then reflected by a PBS (#4) and modulated by an LCoS light valve. The phase retarder in front of the LCoS is a quarter wave plate that acts as an s–p converter. The modulated light (that is light impressed with the image data) then passes through the PBS and the projection lens and then to the screen.

For high throughput we use three LCoS light valves as shown in Fig. 15.4. Here we need two dichroic beam splitters to extract three primary colors, modulated by three LCoS light valves. The dichroic beam splitters must be insensitive to polarization.

Reflection-type projectors using LCoS technology need a high extinction ratio (ER) of PBS. The coating for such a PBS is based on the principle of the Brewster angle to have high transmission for p-polarized and HR for s-polarized light. The ER should be >1000 and the transmittance of p-polarized light higher than 80% for wavelengths from 440 to 650 nm within incident angles of $45° \pm 14°$. Two stacks and three coating materials coated on a high-index substrate will usually meet this requirement. The design can be based on Sub/0.7(MHML) ^7 0.95(MHML) ^7/Sub, where typically, the substrate can be Schott glass SF57HHT having refractive index 1.847 at 550 nm, and H, L, and M quarter wave layers with refractive indices 2.3 (TiO_2), 1.46 (SiO_2), and 1.9 (Mixed Ta_2O_5 with Al_2O_3), respectively. Fig. 15.5 shows the spectra and ERs of the PBSs at 31° and 45° based on the above design (Fig. 15.6).

An alternative way to separate the three primary colors is to use a multisegment color wheel composed of three primary color filters. Here the different colors pass through the color wheel in sequence, as shown in Fig. 15.6. Such a projector system is known by the term digital light processing (DLP). The light is collected by an

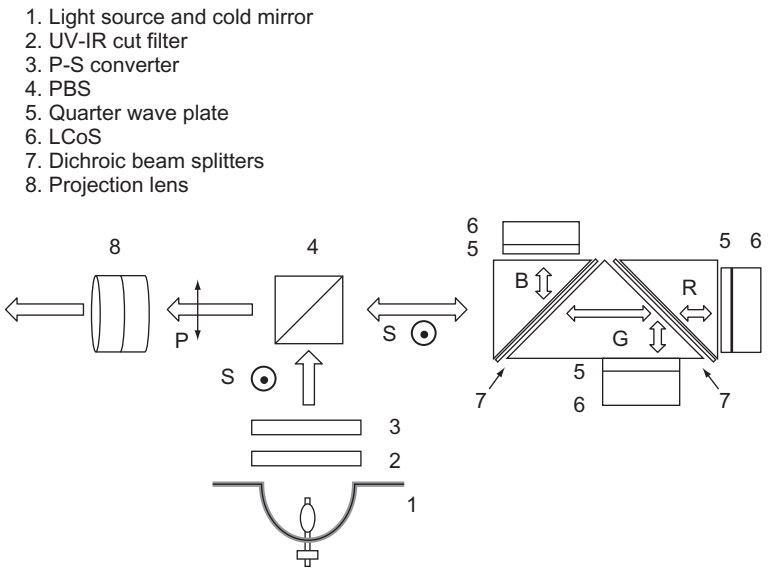


FIG. 15.4

Reflection-type projector using three LCoSs.

elliptical reflector and focused on an end face of a mixing rod, a type of light integrator. After the light passes through the light integrator and relay lens, the collimated colored light is then reflected by a digital micromirror device (DMD) chip. The DMD chip is an optical semiconductor that is at the core of DLP projection technology. It was invented by Dr. Larry Hornbeck and Dr. William E. 'Ed' Nelson of Texas Instruments (TI) in 1987. With a DMD, the image can be digitally processed. The light integrator is a rectangular tunnel with a highly reflecting internal surface. It is usually silver coated with a protective overcoat or carries a broadband quarter-wave stack. The average reflectance must be >98% for 70° incident angle from 420 to 680 nm.

Separation of the three primary colors using a multisegment color wheel can also be applied to the LCoS projector, as shown in Fig. 15.7. In which case we need only one LCoS panel, but we do also need a broadband p–s converter.

To achieve high throughput in a DLP projection system (Fig. 15.6) we can use three DMDs for the three primary colors, blue (B), green (G), and red (R) as shown in Fig. 15.8, where #6 and #7 indicate blue and red reflective coatings, respectively.

15.4 OPTICAL COATINGS FOR PROJECTORS USING LIGHT-EMITTING DIODE (LED) LIGHT SOURCE

The increase in efficiency of blue LEDs makes white light LEDs possible and could be a new lighting source, particularly when the energy saving, lifetime of the light source and environmental benefits are considered. Therefore, traditional

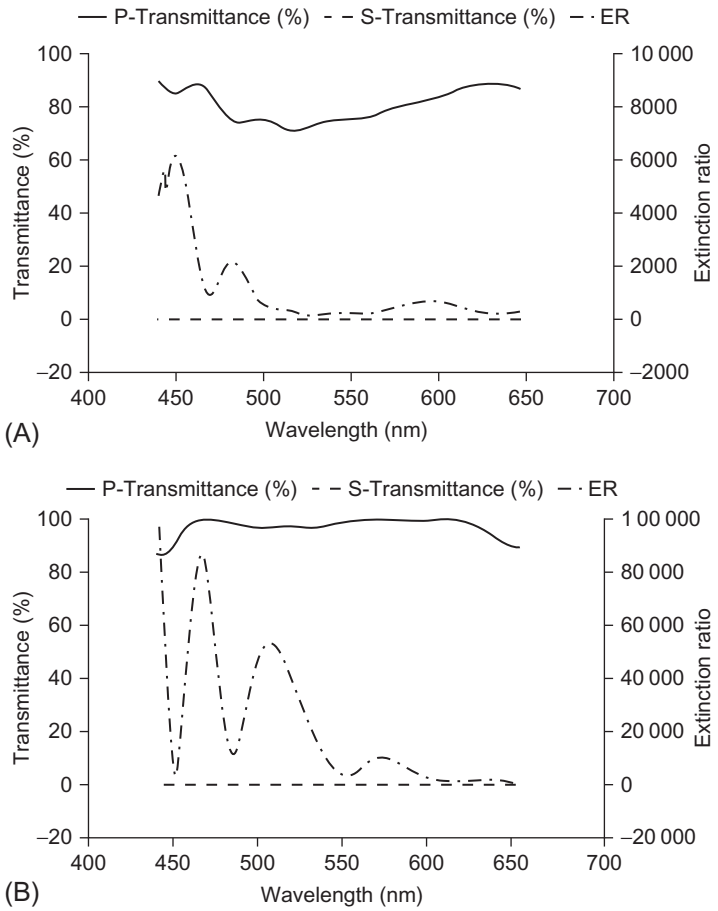


FIG. 15.5

Spectrum and ER of PBS at (A) 31° and (B) 45°.

high-pressure halogen lamps could be replaced by LEDs and laser diodes (LDs) (Yu et al., 2007) as the light source of projectors. Careful choice of LEDs with the correct three primary colors could make PTVs with a better color gamut.

The color gamut can also be increased by adding a red LD with wavelength 635 nm combined with a long wavepass filter (LPF), in a regular DLP as shown in Fig. 15.9. The long wave pass filter passes red and reflects most of the white light coming from the ultrahigh-pressure (UHP) halogen lamp. The elliptical reflector collects the white light and focuses it on the end face of the light integrator. We can further increase the color gamut by replacing the long wave pass filter with a band pass filter, as shown in Fig. 15.10. This is a three-cavity narrowband pass filter (BPF) using TiO_2 and SiO_2, combed with a long wave pass filter. The half maximum

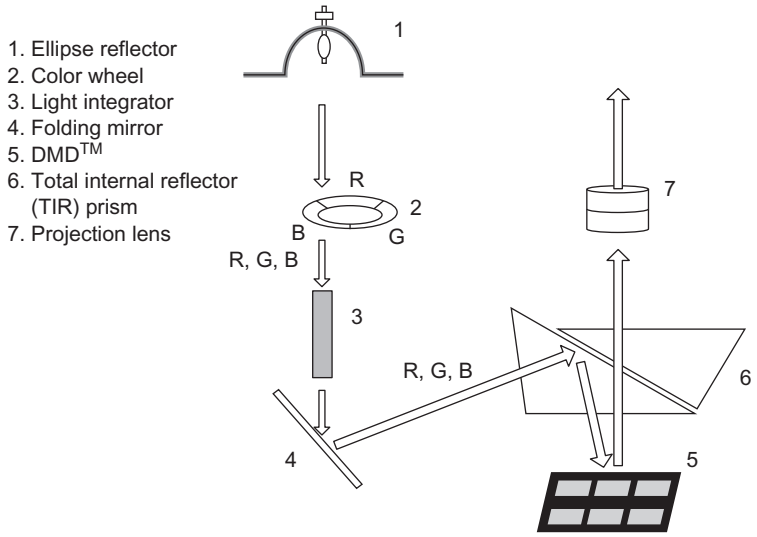


FIG. 15.6

Schematic drawing of DLP project system.

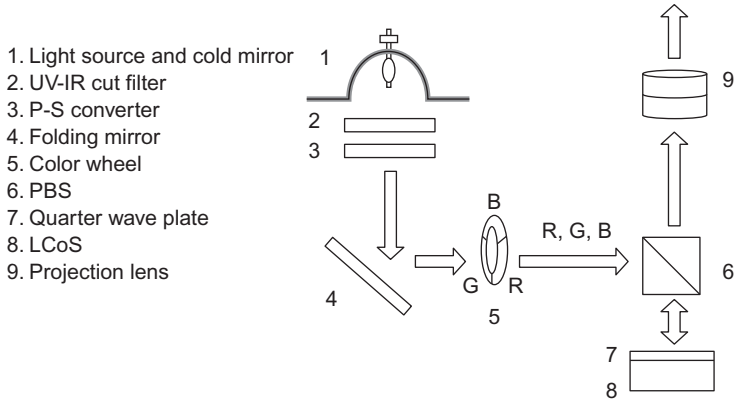


FIG. 15.7

Schematic drawing of LCoS projector using color wheel.

bandwidth is 8 nm and there is no influence on the transmission at 639 nm within $\pm 8°$ such that light intensity is increased by 9% resulting in a better color gamut. The increase of color gamut is shown by the CIE (Commission Internationale de L'Eclairage or International Commission on Illumination) 1931 chromaticity diagram in Fig. 15.11.

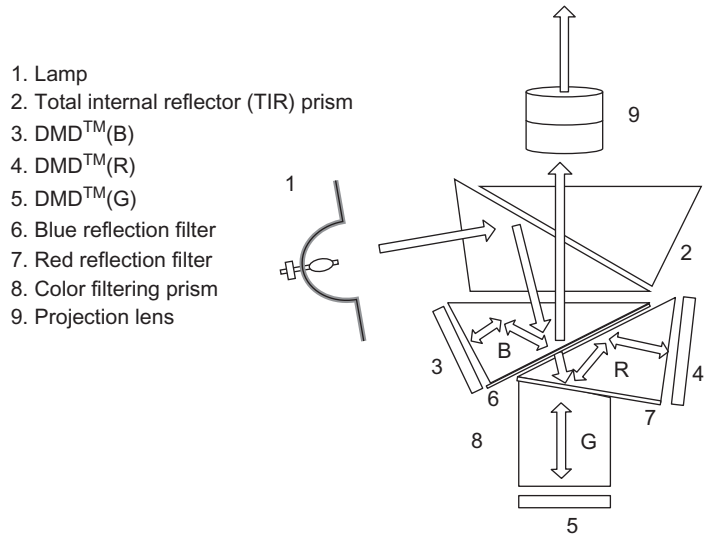


FIG. 15.8

Schematic drawing of DLP project system with three DMDs.

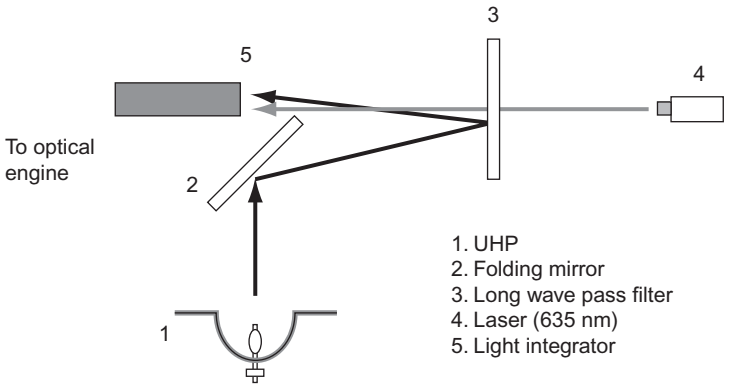


FIG. 15.9

Increasing the color gamut by adding a red LD in a regular DLP.

Using LEDs, we can save energy still further by using a phosphor color wheel, as shown in Fig. 15.12. The green phosphor is excited by a blue LED to emit green light. The angular selection filter (ASF) (Wei et al., 2010) allows only light with an incident angle $<35°$ to pass through. Light with an incident angle larger than 40° is reflected and reused to excite the phosphor, as shown in Fig. 15.13. The design principle of this ASF is as follows.

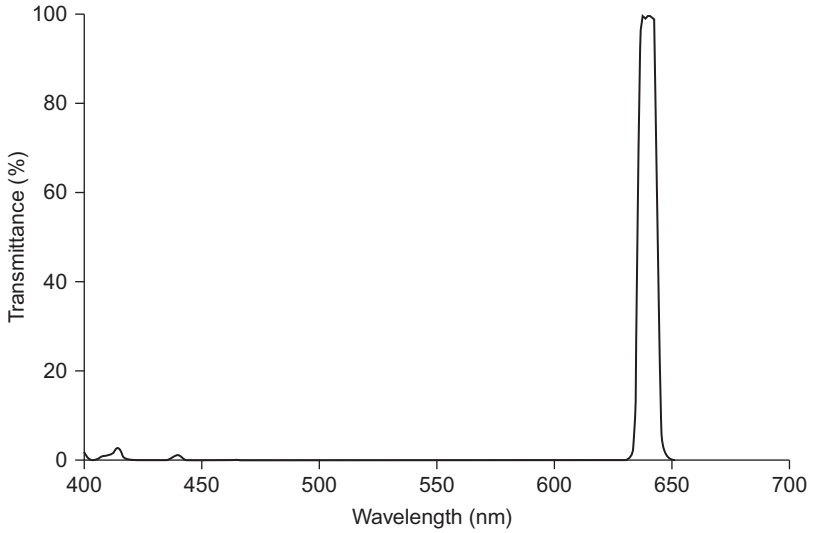


FIG. 15.10

Spectrum of a band pass filter used in color gamut-enhanced DLP.

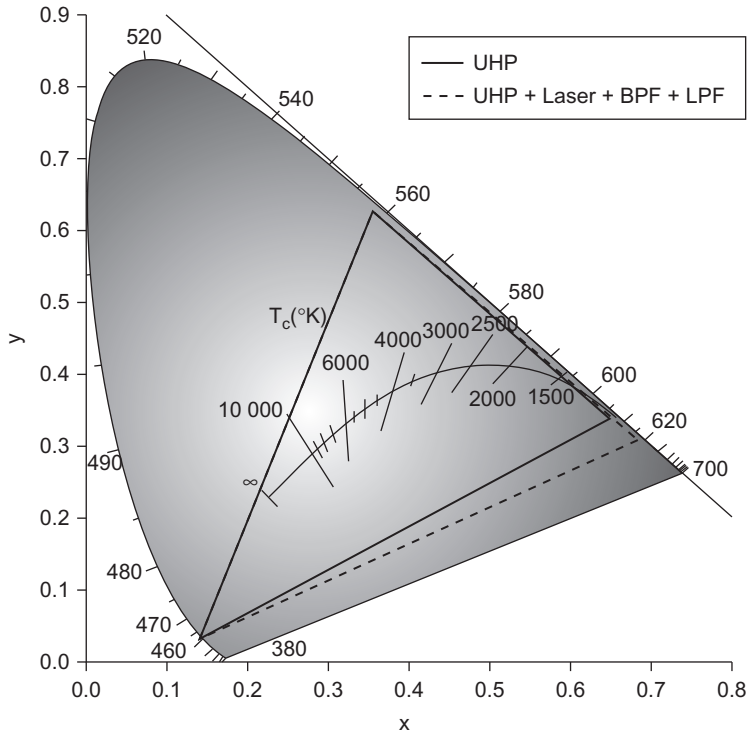


FIG. 15.11

The CIE 1931 chromaticity diagram shows the increase of color gamut when LD is added to the UHP light source.

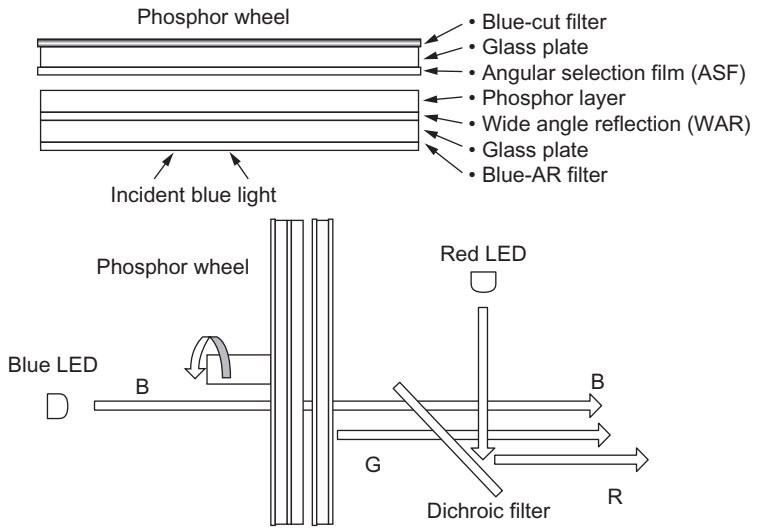


FIG. 15.12

Phosphor color wheel and red LED to produce red, green, and blue colors.

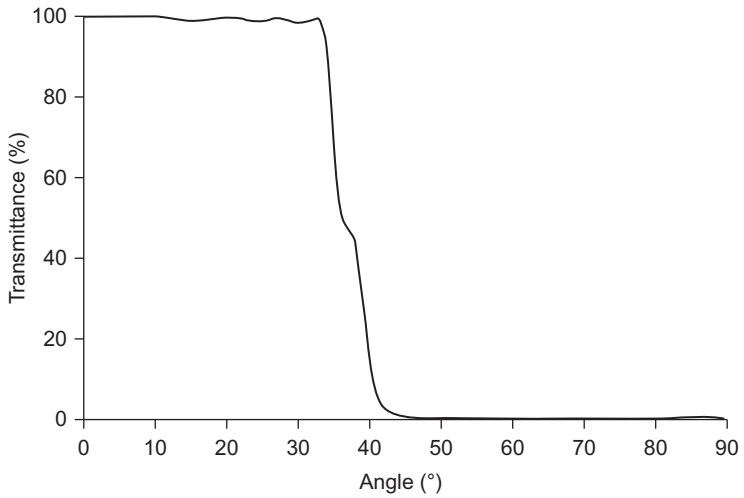


FIG. 15.13

Transmittance of green light 525 nm by ASF at different incident angles—a design.

An ASF is a kind of edge filter in which the main property is a rapid change between the regions of rejection and transmission. Its basic design is a symmetrical stack or a quarter-wave stack from two or more alternating dielectric thin films with a large contrast of refractive indices (Macleod, 2001). Most of the thin-film

interference filters are angle-sensitive, which means that the pass band and cut-off region shifts toward shorter wavelengths with the increase of incident angle from normal incidence to a higher angle. In addition, the polarizing effect of optical filters at oblique angles of incidence makes the s- and p-polarized lights shift differently. ASFs can control the amount of spectrum shift at the oblique incidence. Therefore, the ASF design can be used to control emission direction and feed back the large-angle light for recycling of light. Previous investigations (Mailloux, 1976; Fink et al., 1998; Hsueh et al., 2010) have led to the development of dielectric layer filters with angle-selective properties.

Let the design of angular selection filter be as follows:

$$\text{Substrate}|(aHbL)^p aH|\text{Air} \tag{15.1}$$

where H and L represent the quarter-wave optical thickness of the high and low refractive indices layer, respectively, p is the number of periods, and a and b are the ratio of thickness of the corresponding high and low refractive index layers. The width of the high reflectance zone can be derived from the characteristic matrix of thin film (Macleod, 2001),

$$[M] = [m]^p,\ [m] = \begin{bmatrix} m_{11} & m_{12} \\ m_{21} & m_{22} \end{bmatrix} \tag{15.2}$$

where $[m]$ is the matrix of fundamental period. Then, the high reflectivity is dependent on the condition whether.

$$\left|\frac{m_{11}+m_{22}}{2}\right| \geq 1 \tag{15.3}$$

The reflectance increases steadily with increasing periodic number. A high reflectance zone should exist and obtain the full width at half maximum (FWHM) of the stop band. This boundary is expressed by (Epstein, 1955)

$$\left|\frac{m_{11}+m_{22}}{2} = 1\right| \tag{15.4}$$

The quarter-wave stack consists of a number of two-layer periods with one extra high-index layer. Each period has a characteristic matrix given by.

$$[m] = \begin{bmatrix} \cos\delta_H \cos\delta_L - \dfrac{n_L}{n_H}\sin\delta_H \sin\delta_L & i\left(\dfrac{1}{n_L}\cos\delta_H \sin\delta_L + \dfrac{1}{n_H}\sin\delta_H \cos\delta_L\right) \\ i(n_H \sin\delta_H \cos\delta_L + n_L \cos\delta_H \sin\delta_L) & \cos\delta_H \cos\delta_L - \dfrac{n_L}{n_H}\sin\delta_H \sin\delta_L \end{bmatrix} \tag{15.5}$$

so that

$$\left|\frac{m_{11}+m_{22}}{2}\right| = \left|\cos\delta_H \cos\delta_L - \frac{1}{2}\left(\frac{n_L}{n_H}+\frac{n_H}{n_L}\right)\sin\delta_H \sin\delta_L\right| \tag{15.6}$$

The right-hand side cannot be greater than +1, therefore the boundary of the high reflectance zone can be set as follows:

$$\cos\delta_H \cos\delta_L - \frac{1}{2}\left(\frac{n_L}{n_H}+\frac{n_H}{n_L}\right)\sin\delta_H \sin\delta_L = -1 \tag{15.7}$$

Since the phase thickness of high and low indices layer are the same, that is $\delta_H = \delta_L$, which can be set equal to δ_e such that.

$$\cos\delta_e = \left(\frac{n_H - n_L}{n_H + n_L}\right)^2 \tag{15.8}$$

Let the edge of the high reflectance zone be $g = 1 \pm \Delta g$, then.

$$\delta_e = \frac{\pi}{2} g = \frac{\pi}{2}(1 \pm \Delta g) \tag{15.9}$$

where $g = \lambda_0/\lambda$, the relative wave number, and λ_0 is the central wavelength for which the layers have quarter-wave optical thickness.

The FWHM of the high reflectance zone is $2\Delta g$. With some rearrangement, we can write this as.

$$2\Delta g = \frac{4}{\pi}\sin^{-1}\left(\frac{n_H - n_L}{n_H + n_L}\right) \tag{15.10}$$

The spectrum shift at oblique incidence Δg_θ is given by the expression.

$$\Delta g_\theta = \Delta g_{\theta i} - \Delta g_{\theta=0} \tag{15.11}$$

where $\Delta g_{\theta i}$ is half of FWHM at angle θ_i. In this case, δ_H is not equal to δ_L. This is a complex expression, and we need a computer to do the calculation to understand the spectrum shift at oblique incidence. We choose the periodic number of 12, and the high and low refractive index materials are Ta_2O_5 and SiO_2, respectively, in the ASF design. Fig. 15.14 shows the spectrum shift at different ratios of a to b as a function of incident angle. This shows the interesting result that the spectrum shift with incident angle can be controlled by adjusting the ratio of a to b. The spectrum shift is larger

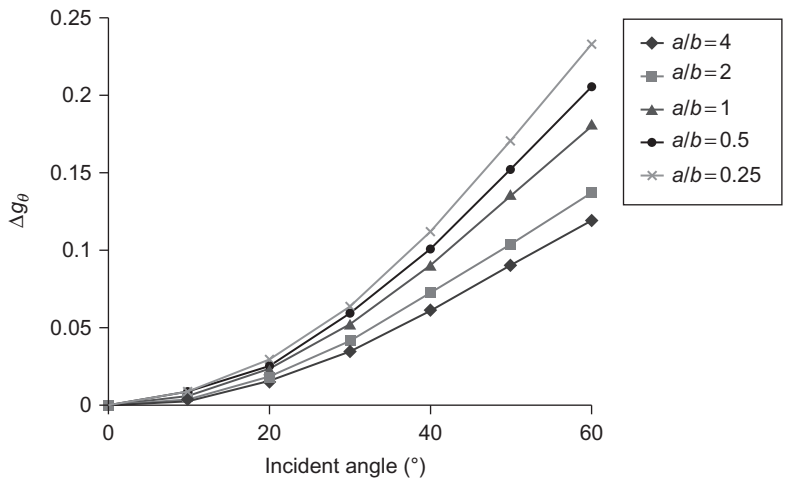


FIG. 15.14

Simulation of spectrum shift at incident angle from 0° to 60°.

than quarter-wave stacks when *a*/*b* is less than one, and smaller when *a*/*b* is greater than one. Nevertheless, the FWHM becomes narrower as *a*/*b* tends away from one as shown in Fig. 15.15. Therefore, a good ASF should choose a correct value of *a*/*b* so that the ASF can have a suitable spectrum shift while keeping a larger FWHM.

Figs. 15.16 and 15.17 show the simulation and experiment spectrum shift and the FWHM vs. incident angle. The experimental result is similar to the simulation. The

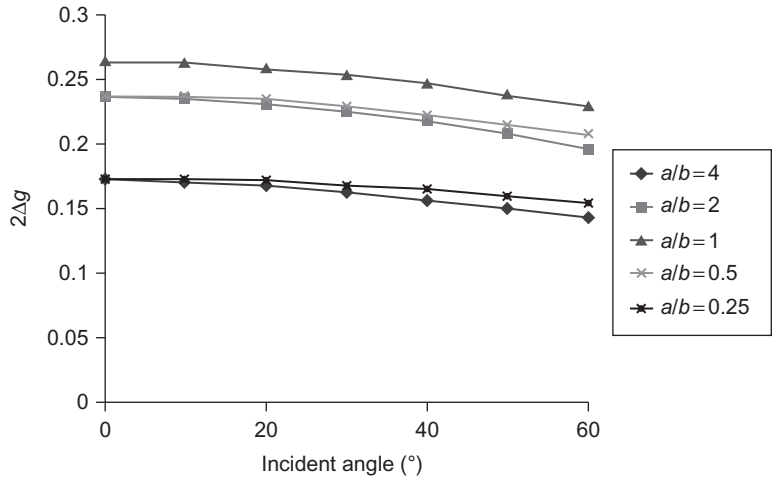


FIG. 15.15

Simulation of FWHM at incident angle from 0° to 60°.

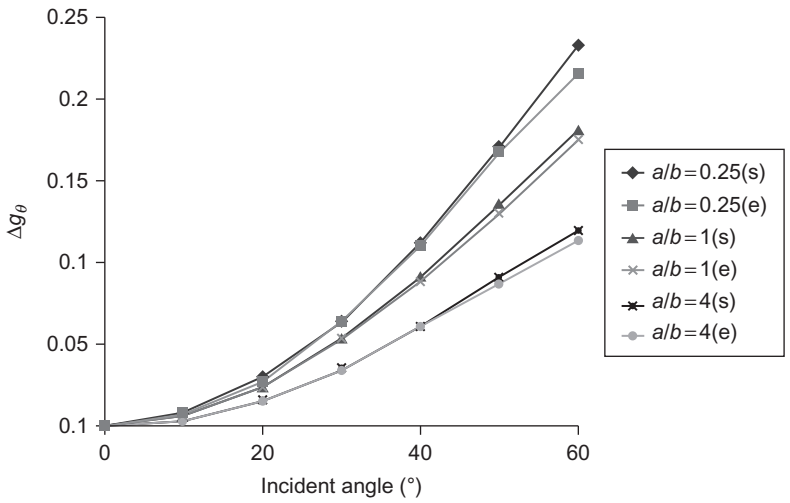


FIG. 15.16

Simulation(s) and experiment (e) of the spectrum shift at incident angle from 0° to 60°.

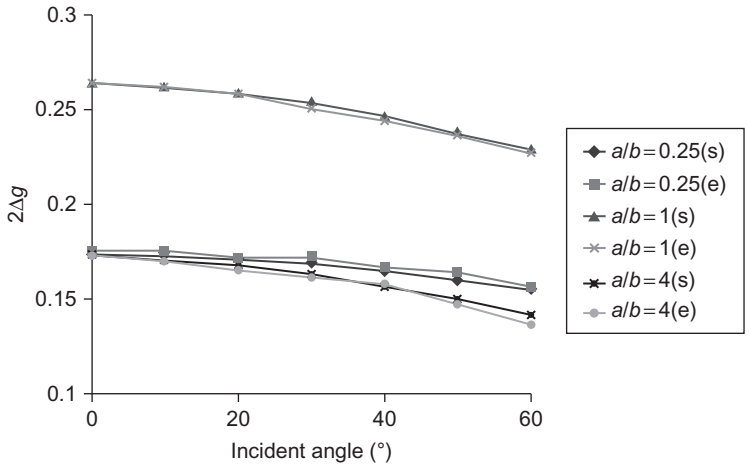


FIG. 15.17

Simulation(s) and experiment (e) of FWHM at incident angle from 0° to 60°.

ASF is a 61-layer coating with $a/b = 0.25$ using Ta_2O_5/SiO_2, based on the design Sub/(0.5H2L)^15 0.525H 2.2L (0.55H2.2L)^14 0.55H/Air, with central wavelength at 500 nm. The simulated and experimental spectra of the ASF at different incident angles are shown in Figs. 15.18 and 15.19. The wavelength shift from 0° to 30° is 40 nm, and from 0° to 60° is near 100 nm. As we expected, the wavelength shift to angle of the new design is more sensitive than the conventional design.

Without the ASF, the green LED chip output light angle is from 0° to 70°. The output light angle is limited to 40° when an ASF is applied on the green LED chip, as

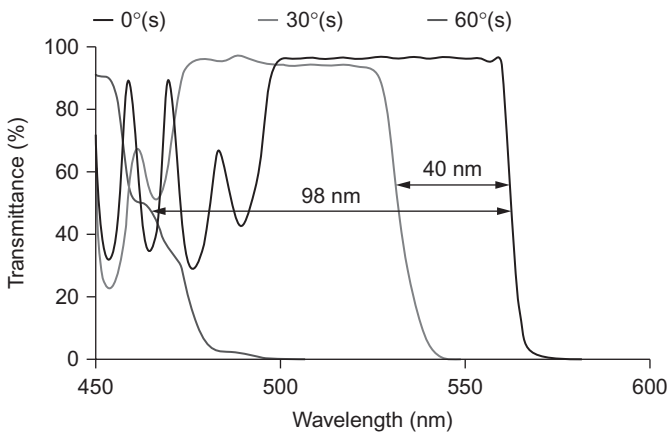


FIG. 15.18

Simulated spectrum of ASF at different incident angles.

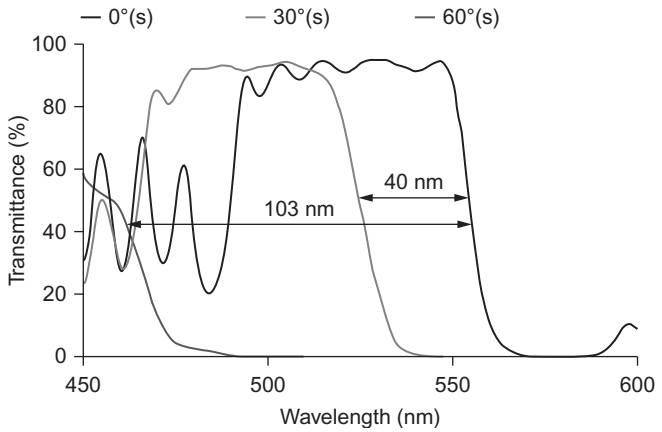


FIG. 15.19

Experimental spectrum of ASF at different incident angles.

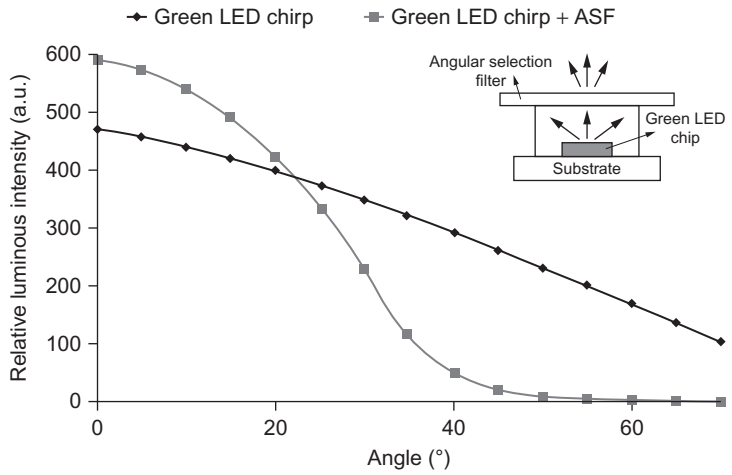


FIG. 15.20

Luminance with and without ASF measured at different output angles. The inset shows green LED with angular selection filter.

shown in Fig. 15.20. The ASF recycles the light at the output light from 40° to 70° and increases the output light from 0° to 30° of green LED light source system.

To keep the purity of green color and increase the output, a blue-cut filter was installed after the ASF. The blue-cut filter reflects the blue light to excite the green phosphor again. In the phosphor color wheel, there is a section not coated with phosphor but with an AR for blue light.

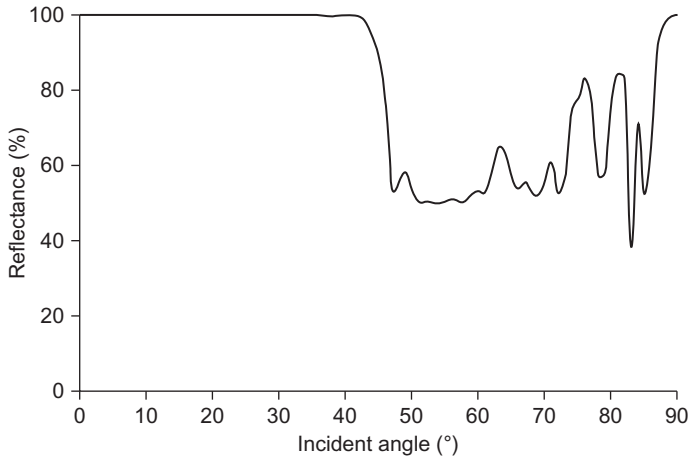


FIG. 15.21

Reflectance of green light 525 nm by WAR filter at different incident angles.

Therefore, that section allows blue light to pass through, so that we have blue, green, and red colors, as shown in Fig. 15.12. The wide-angle reflection filter (WAR) shown in Fig. 15.21, reflects all the green light from 0° to 45° to recycle it. The WAR filter is a 43-layer coating made from Ta_2O_5/SiO_2, based on the design Sub/(1.2H1.2L) ^10 (HL) ^12H/Air, with central wavelength 550 nm.

A phosphor color wheel can be coated with a green phosphor on one part and with red phosphor on another. In that case we employ only a blue LED or LD, as shown in Fig. 15.22.

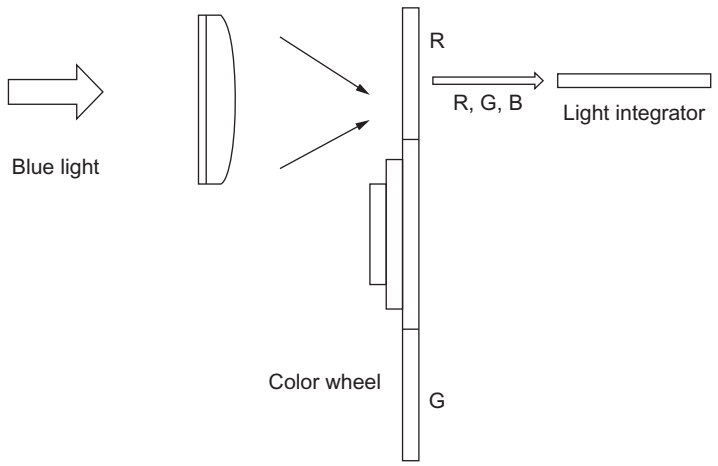


FIG. 15.22

Phosphor color wheel to produce red, green, and blue colors.

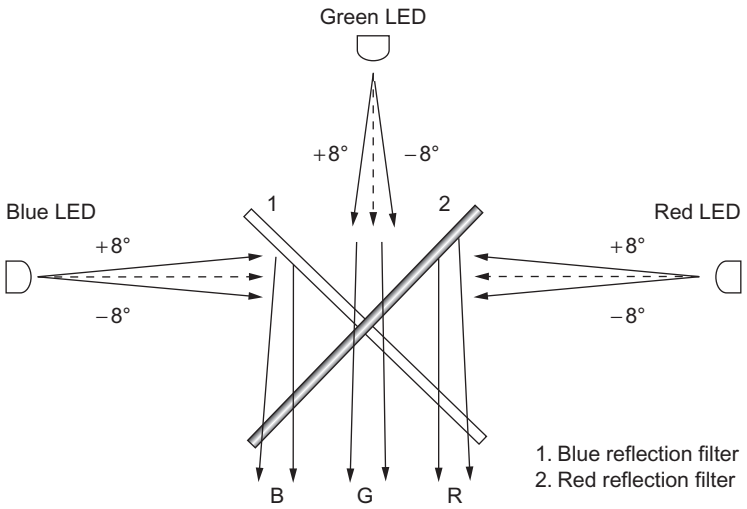


FIG. 15.23

LEDs and X-plate used in a projector.

By utilizing LEDs and a specially designed X-plate, we can also increase the color gamut. Fig. 15.23 shows three LEDs (red, green, and blue) combined with an X-plate in a projector to increase the color gamut. Since the divergence angle of the LEDs is confined to $\pm 8°$ to maintain high brightness, the coatings on the X-plate must have properties insensitive to angle. The spectra of typical coatings for an X-plate (Chen et al., 2006), the blue and red reflection filters shown in Fig. 15.24, indicate a shift of <15 nm in their spectrum with incidence in the range $45° \pm 8°$. The blue and red reflection filters are angle insensitive filters with $a/b = 4$ having coatings with 40 layers (based on the design Sub/(2H 0.5L) ^20/Air, central wavelength at 550 nm) and 47 layers (based on the design Sub/(3H 0.5L) ^17 (1.07L 2.14H 1.07L) ^6/Air, central wavelength at 390 nm) of TiO_2/SiO_2, respectively.

15.5 OPTICAL COATING FOR AUTOMOBILES HEAD UP DISPLAY (HUD)

A head up display (HUD) is a display that allows the user to see displayed data without looking away from the outside world. It was initially developed for military aircraft pilots but now has many other applications. In this chapter, we will talk only about the displays for automobiles. The displayed data can be the speed of the car, navigational information, warning signals, and so forth.

Normally, the projected image from a HUD is fuzzy because of the double reflection from the two surfaces of the thick windshield of the car. This is known as a double image or ghost image. A possible solution for automotive head-up displays is the attachment of a dark film over the windshield to decrease the reflective lightness of

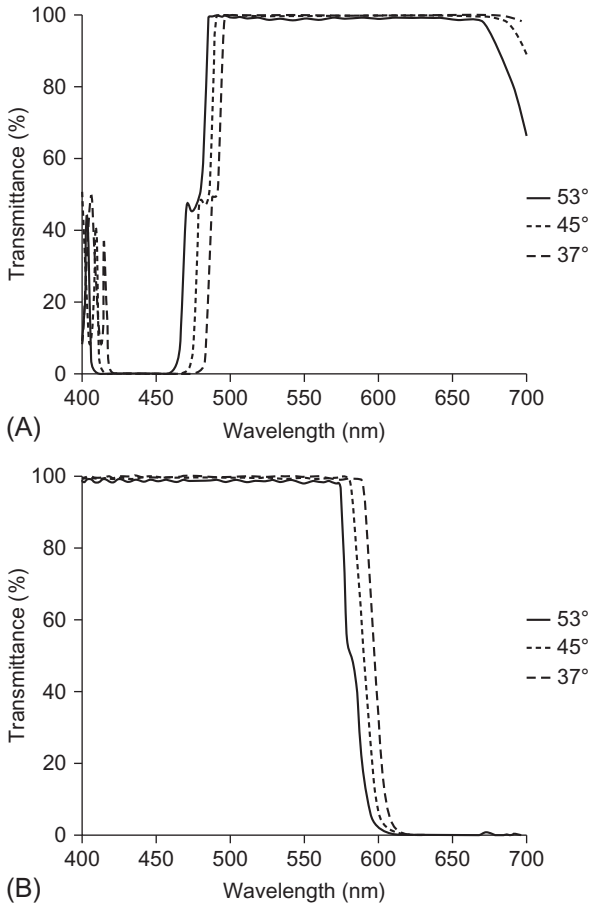


FIG. 15.24

Spectra of (A) blue reflection filter and (B) red reflection filter of X-plate at 45° ± 8°.

the second image. However, although improving the contrast of the image, this might decrease the transparency of the windshield. Another popular solution is using wedge or doublet glasses to separate the second reflection image sufficiently far from the first one or to superimpose the two images (Peng et al., 2009; Sauer and Stolberg, 2005). However, there are two main disadvantages of wedge or doublet glasses. They need very precise design and their manufacture would be very expensive.

The other way of combining the outside view with the data is to use a beam splitter using optical thin film technology (Caudell and Mizell, 1992). This approach has many advantages such as multicolor reflectance, decreasing the influence of double images, and achieving a transmittance of 70% or more.

In general, an automotive HUD system includes four parts, an LED array, a thin film transistor (TFT) projection display, a lens system, and the beam splitter.

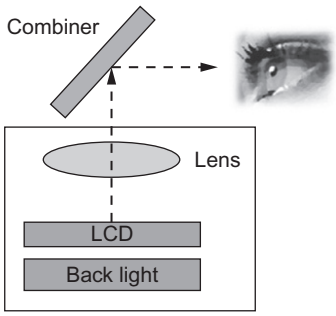


FIG. 15.25

Schematic architecture of HUD system.

Fig. 15.25 shows the schematic architecture of such an HUD system. The light source of the HUD is a white LED. An aspheric lens is positioned in front of the LCD panel to magnify the image to the desired display size, correcting aberration introduced by optical system and placing the virtual image at a desired viewing distance in front of the driver. This HUD unit also has an ambient light sensor, so that the brightness of the display can be controlled with feedback from the sensor. In this way, the power consumption can be reduced according to the brightness of surroundings, and this also helps to improve the visual comfort of the driver.

The optical design of a beam splitter consisting of a coated multilayer on a polyethylene propylene (PEP) substrate is shown in Fig. 15.26. The angle between windshield and dashboard is $70° \pm 5°$. We can eliminate double images by increasing the contrast ratio of the first reflection (R_1) to the second one (R_2). Typically, the viewing distance from the windshield is 50 cm, and the eye box on the viewer side is about 135 mm (W) $\times$ 50 mm (H), which is the spatial range

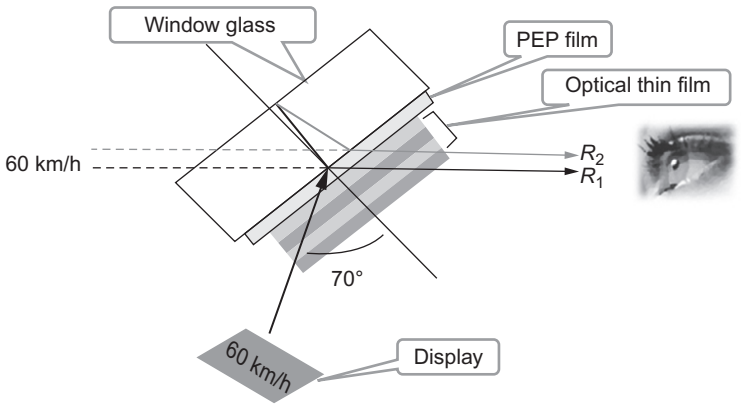


FIG. 15.26

The optical design of a beam splitter for HUD.

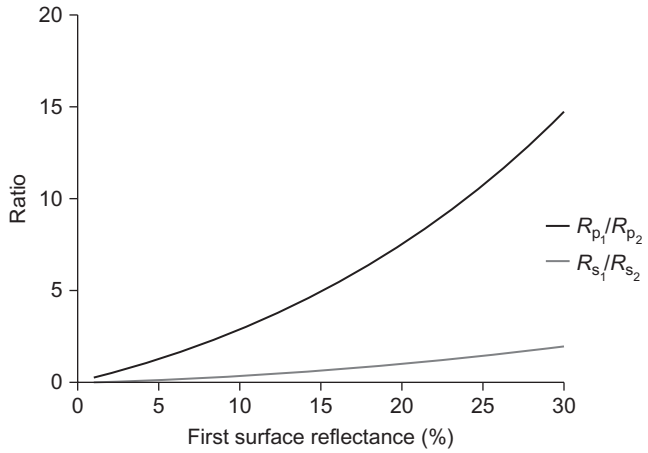


FIG. 15.27

R_1/R_2 for s- and p-polarization in $R_1 < 30\%$ region.

within which the entire HUD image can be seen without vignetting (Lee et al., 2011). The eye box size determines the required aperture of the optical system and consequently the required space for mounting the HUD in a vehicle.

The light includes both s- and p-polarizations. Let the reflectance of the first surface of the PEP substrate be R_1 and of the second surface R'. Let R_2 be the reflectance for light passing through the first surface, reflecting off the second surface then finally emerging from the first surface. R_2 is equal to $(1-R_1)\times R'\times(1-R_1)$. The contrast ratio R_1/R_2 for p-polarization is better than that for s-polarization, as shown in Fig. 15.27. For that reason, p-polarized light was chosen for the optical film design in this study.

In order to see both the outside scene and the projected information clearly, it is necessary to arrange a high transmittance beam splitter. Fig. 15.27 demonstrates that it is only where R_1 is $<30\%$ that we need to enhance total reflecting contrast. Transmittance of the simulated coating together with that of an actual fabricated one are shown in Fig. 15.28. The average transmittance is 74.5% and the contrast R_1/R_2 is 6.6.

The color in CIE 1931 x–y chromaticity coordinates was calculated from the transmittance spectra of the sample beam splitter and clearly it is located almost at the white point, implying that the color of the beam splitter is almost neutral. Precise calculation shows that the color of the beam splitter is sited near the chromatic discrimination ellipse of white light, as shown in Fig. 15.29.

15.6 OPTICAL COATINGS FOR LEDS

Energy saving, lifetime and environmental considerations make the light-emitting diode (LED) an attractive new light source that could possibly replace halogen lamps or fluorescent tubes for lighting applications (Muthu and Gaines, 2003). To increase

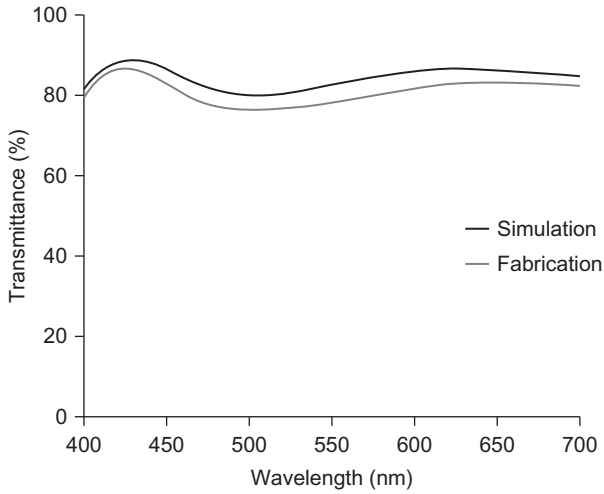


FIG. 15.28

Transmittance spectra with different wavelengths for simulation and fabricated films.

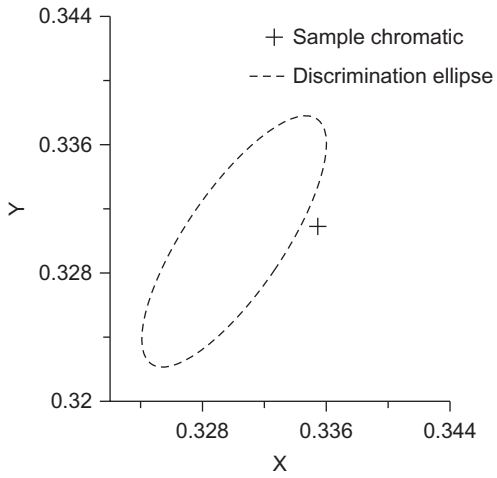


FIG. 15.29

The relationship between the chromatic discrimination ellipse of white light and beam splitter.

light extraction, an AR coating on the output side of an LED chip and a HR coating on the rear side are necessary (Gessmann et al., 2003; Kim et al., 2006a; Kim et al., 2006b; Gessmann et al., 2004; Huang et al., 2007). The HR coating can be a multilayer quarter-wave stack, sometimes called a diffraction Bragg reflector (DBR) or it can be a single layer of high reflectance silver, or aluminum with enhancing dielectric layers, or a so-called omnidirectional reflecting coating (ODR). Fig. 15.30 shows

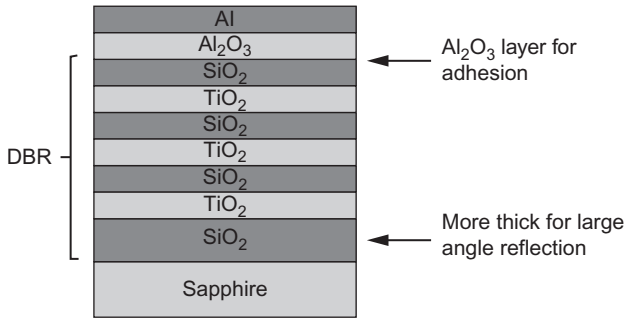


FIG. 15.30

Structure of an ODR coating, where the thickness of the first SiO_2 layer is larger than 500 nm to give high reflectance at large angles.

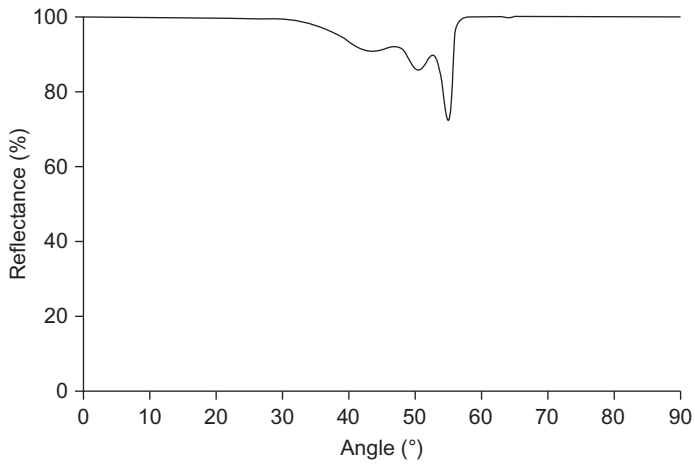


FIG. 15.31

Reflectance at 460 nm vs. angle of ODR reflector.

the structure of an example ODR where the first SiO_2 layer must be >500 nm to give high reflectance at large angles, as shown in Fig. 15.31. A structural photonic crystal ODR has also been proposed (Dong et al., 2003). The AR can be achieved by texturing the outside surface of the LED (Cho et al., 2011), adding a multilayer coating, or a coating with graded refractive-index layer.

In general, LEDs cannot be true white light sources similar to sunlight or, say, the D_{65} illuminant. Such a deficiency can be overcome by using a gain modified filter (GMF), the so-called daylight simulation coating (Lo et al., 2011; Lee et al., 2009). Fig. 15.32 shows a spectrum of white light from a combination of six LEDs, as well as the spectra of the GMF and the D_{65} illuminant. The addition of the GMF gives us a spectrum equivalent to the D_{65}. The GMF shown in Fig. 15.32 is a 19-layer TiO_2/SiO_2 multilayer coating. Based on the same principle we can enhance the color

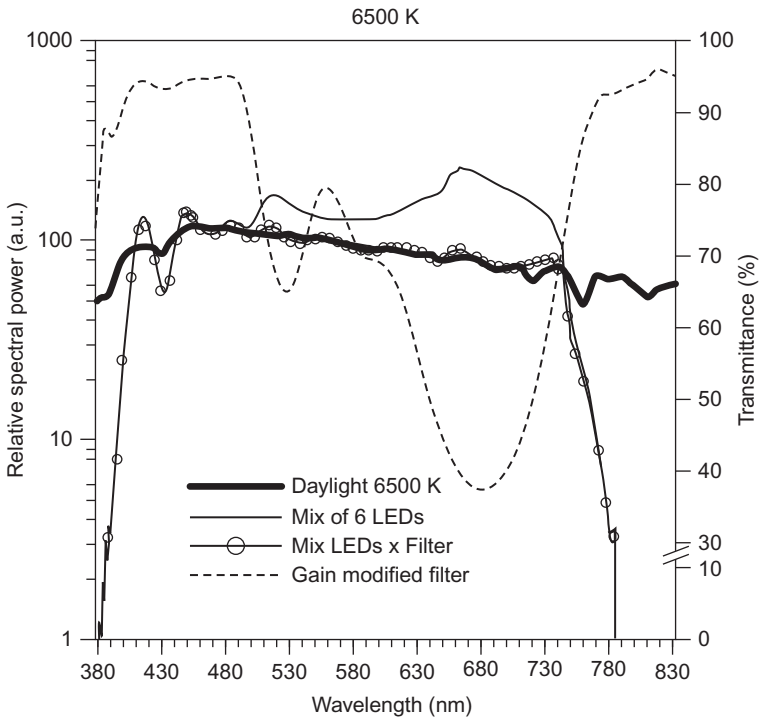


FIG. 15.32

Daylight simulation coating of LEDs by adding GDF.

gamut by adding a GMF to LEDs of any color when they are used as the light source in projectors or for other applications.

15.7 CONCLUSION

Display and LED lighting have been developed to the stage where they play an important part in our daily life. Most people, however, would not accept them without their optical coatings. Several types of optical coatings are required. These include antireflective coatings, antiglare coatings, high reflectance coatings, color selection coatings (band pass filters, long wave pass filters, short pass filters), polarizers, polarization insensitive coatings, angle insensitive coatings, angular selection filter, wide angle reflection filter, view angle limited coatings (for privacy), and even hydrophobic repelling (repelling water, dirt, dust, fingerprints, stains) coatings, and hard coating. These make displays and LEDs function properly, improve their quality and make them visually comfortable to the human eye, increase their output efficiency, and improve their durability with consequently long life. Some of the coatings are quite simple and others are very challenging. Examples are coatings

for high incident angle in short throw PTV (Jorke et al., 2009) and multi-band pass filters (MBPF) for 3D projectors (http://www.ob-optics.com).

For 3D cinema applications, optical coatings are simpler with better color saturation and brightness compared with other methods. 3D cinema usually employs a polarization methodology. To have a solution that does not involve polarization, an MBPF is utilized. Fig. 15.33 shows the spectra of two three-primary-color filters for glasses of the right eye (A) and the left eye (B), which also are the two halves of

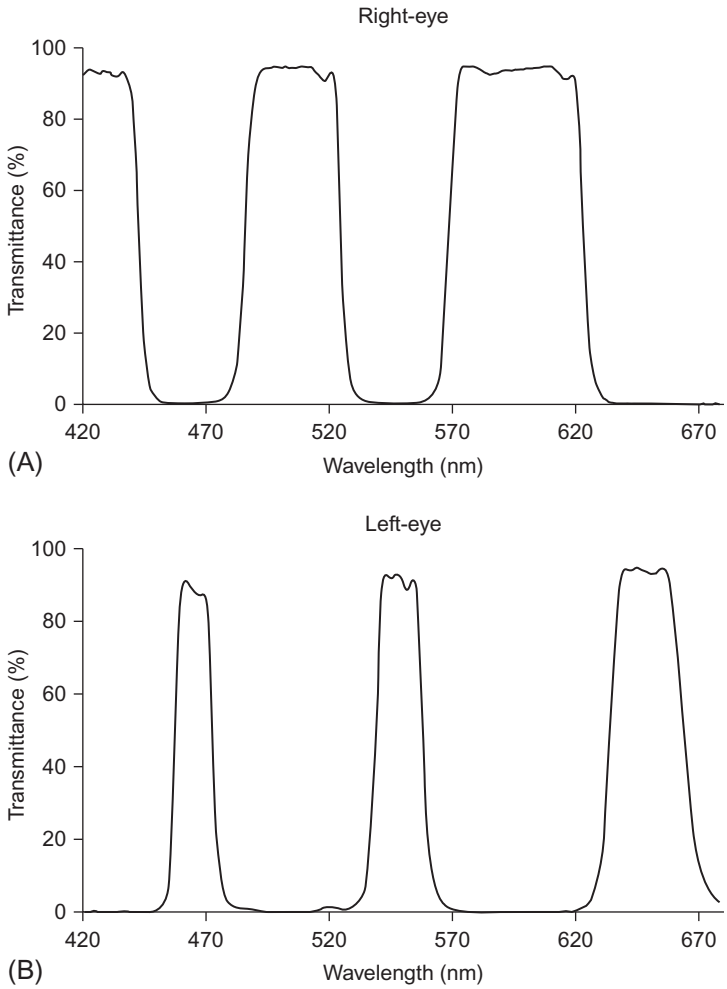


FIG. 15.33

High-resolution multiband coating technology without cross-talk of the R/L signal, (A) R signal, (B) L signal.

Courtesy of Orange Bright Optics: http://www.ob-optics.com.

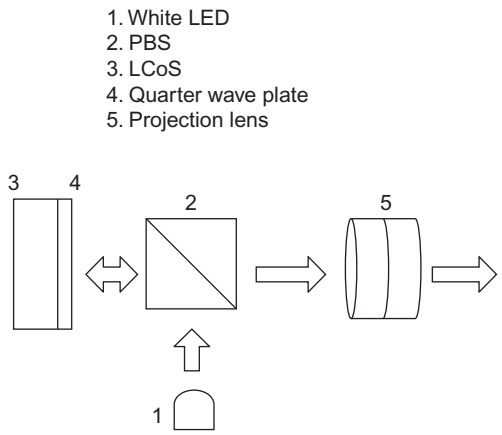


FIG. 15.34

Schematic drawing of a microprojector.

the color wheel. That means there are six colors composed in the color wheel. With a high color wheel rotation rate, the right eye and left eye receive three different primary colors sequentially and thus see the 3D images.

A handy projector with minimal size is a dream of many people. This has been realized by utilizing a micro-LCoS technique. Fig. 15.34 shows the schematic drawing of a microprojector. Its size is small enough to put in the palm of the hand or carry in a pocket or be installed in a cell phone. However, the output flux is still not high enough to make it widely popular.

ACKNOWLEDGMENTS

The authors would like to thank Prof. Angus H. Macleod and Prof. Francois Flory for their valuable suggestions.

REFERENCES

Al-Dahoudi, N., Bisht, H., Gobbert, C., Krajewski, T., Aegerter, A.M., 2001. Transparent conducting, anti-static and anti-static–anti-glare coatings on plastic substrates. Thin Solid Films 392, 299–304.

Allen, K.J., 2005. Reel to real: Prospects for flexible displays. Proc. IEEE 93, 1394–1399.

Arik, M., Petroski, J., Weaver, S., 2002. Thermal challenges in the future generation solid state lighting applications: light emitting diode. ITHERM 2002, 113–120.

Bhosle, V., Tiwari, A., Narayan, J., 2006. Electrical properties of transparent and conducting Ga doped ZnO. J. Appl. Phys. 100, 033713–033718.

Brody, T.P., Asars, J.A., Dixon, G.D., 1973. A 6 × 6 inch 20 lines-per-inch liquid-crystal display panel. IEEE Trans. Electron Devices 20 (11), 995–1001.

Caudell, T.P., Mizell, D.W., 1992. Augmented reality: an application of heads-up display technology to manual manufacturing processes. Proc. Hawaii International Conf. Syst. Sci. 2, 659–669.

Chen, D., Yan, Y., Westenberg, E., Niebauer, D., Sakaitani, N., Chaudhuri, S.R., 2000. Development of anti-reflection (AR) coating on plastic panels for display applications. J. Sol-Gel Sci. Tech. 19, 77–82.

Chen, H.C., Lee, C.C., Huang, J.J., 2006. Improving the illumination efficiency and color temperature for a projection system by depositing thin-film coatings on an x-cube prism. Opt. Eng. 45, 113801–113805.

Cho, J.Y., Byeon, K.J., Lee, H., 2011. Forming the graded-refractive-index antireflection layers on light-emitting diodes to enhance the light extraction. Opt. Lett. 36, 3203–3205.

Dabney, M.S., van Hest, M.F.A.M., Teplin, C.W., Arenkiel, S.P., Perkins, J.D., Ginley, D.S., 2008. Pulsed laser deposited Nb doped TiO_2 as a transparent conducting oxide. Thin Solid Films 516, 4133–4138.

Dong, J.W., Han, P., Wang, H.Z., 2003. Broad omnidirectional reflection band forming using the combination of Fibonacci quasiperiodic and periodic one-dimensional photonic crystals. Chin. Phys. Lett. 20, 1963–1965.

Epstein, L.I., 1955. Low loss multilayer dielectric mirrors. J. Opt. Soc. Am. 45, 360–362.

Epstein, D.W., Maloff, I.G., 1945. Projection television. SMPTE Mot Imag. J. 44, 443–455.

Exarhos Gregory, J., Zhou, X.D., 2007. Discovery-based design of transparent conducting oxide films. Thin Solid Films 515, 7025–7052.

Fink, Y., Winn, J., Fan, S., Chen, C., Michel, J., Joannopoulos, J.D., Thomas, E.L., 1998. A dielectric omnidirectional reflector. Science 282, 1679–1682.

Gessmann, T., Schubert, E.F., Graff, J.W., Streubel, K., Karnutsch, C., 2003. Omnidirectional reflective contacts for light-emitting diodes. Electron Dev. Lett. 24, 683–685.

Gessmann, T., Luo, H., Xi, J.-Q., Streubel, K.P., Schubert, E.F., 2004. Light-emitting diodes with integrated omnidirectionally reflective contacts. Proc. SPIE 5366, 53–61.

Harbers, G., Hoelen, C., 2001. High performance LCD backlight using high intensity red, green and blue light emitting diodes. SID Tech. Dig. 32, 702–705.

He, Y.S., Campbell, J.C., Murphy, R.C., 1993. Electrical and optical characterization of Sb: SnO_2. J. Mater. Res. 8, 3131–3134.

Hornbeck, L.J., 1993. Current status of the digital micromirror device (DMD) for projection television applications. IEDM 93, 381–384.

Hornbeck, L.J., 1997. Digital light processing for high-brightness, high-resolution applications. Proc. SPIE Vol. 3013, 27–40.

Hosono, H., Ohta, H., Orita, M., Ueda, K., Hirano, M., 2002. Frontier of transparent conductive oxide thin films. Vacuum 66, 419–425.

Hsueh, W.J., Wun, S.J., Yu, T.H., 2010. Characterization of omnidirectional bandgaps in multiple frequency ranges of one-dimensional photonic crystals. J. Opt. Soc. Am. B 27, 1092–1098.

Huang, H.W., Kuo, H.C., Lai, C.F., Lee, C.E., Chiu, C.W., Lu, T.C., Wang, S.C., Lin, C.H., Leung, K.M., 2007. High-performance GaN-based vertical-injection light-emitting diodes with TiO_2–SiO_2 omnidirectional reflector and n-GaN roughness. Photon. Tech. Lett. 19, 565–567.

Ishikawa, H., Lippey, B., 1996. in: Two layer broad band AR coating.Proceedings of Tenth International Conference on Vacuum Web Coating; 12 November. pp. 221–233.

Jepsen, M.L., 2003. Rear projection TV: Single panel LCOS lumen throughput. SID Symp Digest 34, 112–125.

Jorke, H., Simon, A., Fritz, M., 2009. Advanced stereo projection using interference filters. J. Soc. Inf. Disp. 17, 407–410.
Katayama, M., 1999. TFT-LCD technology. Thin Solid Films 341, 140–147.
Kim, J.K., Gessmann, T., Schubert, E.F., Xi, J.Q., Hong, L., Cho, J., Sone, C., Park, Y., 2006a. GaInN light-emitting diode with conductive omnidirectional reflector having a low-refractive-index indium-tin oxide layer. Appl. Phys. Lett. 88, 013501–013503.
Kim, J.K., Luo, H., Xi, Y., Shah, J.M., Gessmann, T., Schubert, E.F., 2006b. Light extraction in GaInN light-emitting diodes using diffuse omnidirectional reflectors. J. Electrochem. Soc. 153, G105–G107.
Kimmel, J., Hautanen, J., Levola, T., 2002. Display technologies for portable communications devices. Proc. IEEE 90, 581–590.
Lee, C.C., Yang, T.H., Liao, S.F., Chang, K., 2009. LED-spectrum shaping by optical filter achieves tunable daylight simulator. SPIE Newsroom. (17 June).
Lee, C.C., Tsai, S.H., Kuo, C.C., Chen, C.H., Teng, L.M., Luo, K.T., 2011. Free ghost image and high transmittance optical thin film beam splitter for head-up display. SID Symp. Digest 42, 1451–1453.
Li, M.C., Kuo, C.C., Peng, S.H., Chen, S.H., Lee, C.C., 2011. Influence of hydrogen on the properties of Al and Ga-doped ZnO films at room temperature. Appl. Opt. 50, C197–C200.
Liao, B.H., Kuo, C.C., Chen, P.J., Lee, C.C., 2011. Fluorine-doped tin oxide films grown by pulsed direct current magnetron sputtering with an Sn target. Appl. Opt. 50, C106–C110.
Lo, M.L., Yang, T.H., Lee, C.C., 2011. Fabrication of a tunable daylight simulator. Appl. Opt. 50, C95–C99.
Macleod, H.A., 2001. Thin-Film Optical Filters, third ed. Institute of Physics Publishing, Bristol, Philadelphia.
Mailloux, R.J., 1976. Synthesis of spatial filters with Chebyshev characteristics. IEEE Trans. Antennas Propagat. 24, 79–85.
Manifacier, J.C., Szepessy, L., Bresse, J.F., Perotin, M., Stuck, R., 1979. In_2O_3: (Sn) and SnO_2 : (F) films—application to solar energy conversion part II—Electrical and optical properties. Mater. Res. Bull. 14, 163–175.
Mascia, L., Tang, T., 1998. Polyperfluoroether-silica hybrids. Polymer 39, 3045–3057.
McHale, G., Shirtcliffe, N.J., Newton, M.I., 2004. Contact-angle hysteresis on super-hydrophobic surfaces. Langmuir 20, 10146–10149.
Mentley, D.E., 2002. State of flat-panel display technology and future trends. Proc. IEEE 90, 453–459.
Minami, T., 1999. Transparent and conductive multicomponent oxide films prepared by magnetron sputtering. J. Vac. Sci. Technol. A 17, 1765–1772.
Muthu, S., Gaines, J., 2003. Red, green and blue LED-based white light source: implementation challenges and control design. Proc. IEEE IAS Annu. Meeting 1, 515–522.
Peng, G., Rapids, C., Steffensmeier, M.J., Rapids, C., 2009. Head up display having a combiner with wedge lenses. United States Patent, Patent No. US 7,570,430 Bl.
Ponce, F.A., Bour, D.P., 1997. Nitride-based semiconductors for blue and green light-emitting devices. Nature 386, 351–359.
Rauh, R.D., 1999. Electrochromic windows: an overview. Electrochim. Acta 44, 3165–3176.
Rogers, J.A., Bao, Z., Baldwin, K., Dodabalapur, A., Crone, B., Raju, V.R., Kuck, V., Katz, H., Amundson, K., Ewing, J., Drzaic, P., 2001. Paper-like electronic displays: Large-area rubber-stamped plastic sheets of electronics and microencapsulated electrophoretic inks. Proc. Natl. Acad. Sci. U. S. A. 98, 4835–4840.

Sauer, G., Stolberg, 2005. Laminated glass windscreen intended to be used at the same time as a HUD system reflector. United States Patent, Patent No.: US 6,866,918 B2.
Shikama, S., Kida, H., Daijogo, A., Maemura, Y., Kondo, M., 1993. A compact LCD rear projector using a new bent-lens optical system. SID Symp. Digest 24, 295–298.
Shimizu, J.A., 2001. Scrolling color LCOS for HDTV rear projection. SID Symposium Digest 32, 1072–1075.
Streintz, F., 1902. On the electrical conductivity of pressed powders. Ann. Phys. (Leipzig) 9, 854.
Szczyrbowski, J., Dietrich, A., Hartig, K., 1989. Bendable silver-based low emissivity coating on glass. Solar Energy Mater. 19, 43–53.
Takeda, M., Miyatake, Y., 1992. Three-LCD projector having specified scanning directions. US Patent 5122870.
Tannas, L.E., 1989. Flat-panel displays displace large, heavy, power-hungry CRTs. Spectrum, IEEE 26, 34–35.
Tannas, L.E., 1994. Evolution of flat-panel displays. Proc. IEEE 82, 499–509.
Tominaga, K., Umezu, N., Mori, I., Ushiro, T., Morifa, T., Nakabaayashi, I., 1998. Transparent conductive ZnO film preparation by alternating sputtering of ZnO:Al and Zn or Al targets. Thin Solid Films 334, 35–39.
Van Kessel, P.F., Hornbeck, L.J., Meier, R.E., Douglass, M.R., 1998. A MEMS-based projection display. Proc. IEEE 86, 1687–1704.
Wei, Z.C., Kuo, C.C., Huang, J.J., Lee, C.C., 2010. Research on angle-selective filters of phosphors color wheel for LED projector. Proc. SPIE. Vol. 7786. 778604.
Yu, X.J., Ho, Y.L., Tan, L., Huang, H.C., Kwok, H.S., 2007. LED based projection systems. J. Disp. Technol. 3, 295–303.
Zhang, K., Zhu, F., Huan, C.H.A., Wee, A.T.S., 2000. Indium tin oxide films prepared by radio frequency magnetron sputtering method at a low processing temperature. Thin Solid Films 376, 255–263.
Zheng, Y., Kikuchi, K., Yamasaki, M., Sonoi, K., Uehara, K., 1997. Two-layer wideband antireflection coatings with an absorbing layer. Appl. Opt. 36, 6335–6338.

FURTHER READING

Born, M., Wolf, E., 1965. Principles of Optics, third ed. Pergamon Press Ltd. 66.

CHAPTER

Innovative approaches in thin-film photovoltaic cells 16

Nicolas Barreau*, David Duche†, Carmen M. Ruiz†, Ludovic Escoubas†, Jean-Jacques Simon†, Judikael Le Rouzo†, Veronica Bermudez‡

*Nantes University, CNRS, Institut des Matériaux Jean Rouxel (IMN), UMR6502, Nantes, France** *Aix-Marseille University, University Toulon, CNRS, IM2NP, Marseille, France† Nexcis, Rousset, France‡*

16.1 INTRODUCTION

The production of a considerable amount of CO_2 is the consequence of the generation of the largest part of the energy requirements that come from fossil fuel. In our society, sustainable development is a priority and we must develop renewable energies allowing innovative solutions to the problem of greenhouse gas emission. In 2016, <20% of energy production worldwide corresponded to renewable energy. Thus, huge efforts have gone into harvesting renewable energy, such as solar, hydroelectric, wind, and hydrothermal energy.

As regards solar energy, and more precisely photovoltaic energy conversion, the market is widely dominated by solar modules based on the use of bulk silicon wafers. Si-wafer-based technology accounted for about 94% of the total production in 2016; the share of multicrystalline technology is now about 70% of total production. Total installed photovoltaic power represents 300 GWp in 2017, and should reach 1 TWp in 2021 (GMO, 2017).

In the photovoltaic market, thin-film photovoltaic modules show great promise for producing sustainable, low-cost, clean electricity from sunlight (Topič, 2011): the global marketshare of inorganic thin-film photovoltaic materials in 2016 was around 6% (6 GWp of 100 GWp). The two main advantages, among others, of thin-film solar cells are:

1. lower consumption of materials and energy during their fabrication processes and
2. low-cost production because processes are applicable to large areas in either batch or roll-to-roll production lines.

But solar-cell thin-film technologies also face some drawbacks:

- lower module conversion efficiencies and
- in some cases, light-induced degradation of the materials.

Optical Thin Films and Coatings. https://doi.org/10.1016/B978-0-08-102073-9.00016-3
Copyright © 2018 Elsevier Ltd. All rights reserved.

However, inorganic thin-film solar cells and modules are competitive with crystalline silicon solar cells, regarding total cost and state-of-the-art performance (Jäger-Waldau, 2011).

Two main classes of thin-film solar cells have been developed at an industrial level: one based on silicon in amorphous, nanocrystalline, and polycrystalline phases and the other on polycrystalline chalcogenide semiconductor compounds (CdTe, CI(G)S). A third class, based on organic materials coming from chemical synthesis, has developed very quickly over recent years thanks to the efforts of companies such as Mitsubishi, Sumitomo Chemical, Heliatek, Konarka, Solarmer, and Philips 66.

Even if thin-film solar cells share a common device structure—typically consisting of a front contact, a p-n junction comprising an absorber layer and a back contact—various fabrication processes depending on thin-film materials need to be used to reach the best conversion efficiency (Yan, 2011). Indeed, thin-film silicon-based solar cells include hydrogenized amorphous, nanocrystalline, or microcrystalline silicon (a-Si:H, nc-Si:H, μc-Si:H). To achieve high efficiencies, Si thin-film solar cells require hydrogen (H) passivation. The record efficiency of an a-Si:H solar cell, from AIST in 2016, is 14% (for a single junction it is 10.2% (Green et al., 2017)) (Table 16.1).

As regards solar devices based on chalcogenide materials, the two main representatives are $Cu(In,Ga)(Se,S)_2$ (CIGSSe) and cadmium telluride (CdTe). Both these materials, CIGSSe and CdTe, as polycrystalline thin films show a very efficient absorption of solar spectrum as they exhibit higher absorption coefficients than crystalline silicon (c-Si).

The use of various rigid or flexible substrates such as glass, plastic, or metal foils is possible as thin layers of the materials may be deposited at low temperatures (e.g., 200–500°C for a-Si:H) or even at room temperature.

When considering the efficiency performances of thin-film solar cells, to date, the record conversion efficiencies for CIGSSe- and CdTe-based solar cells have reached 22.9% and 22.1%, respectively (Table 16.1). These thin-film absorber materials share the same basic structural feature—diamond based.

Defects, including point defects, extended defects, and interfaces, make a major contribution to the performance of thin-film solar cells. A good review of defects physics in thin-film solar cell materials including Si, CdTe, copper indium selenium (CIS), and CIGS by the combination of the transmission electron microscopy (TEM) technique and density functional theory (DFT) is given by Yan (2011). It is shown that some defects, such as stacking faults and special twins, have similar electronic properties in these thin-film materials but some other defects, such as grain boundaries and interfaces, exhibit very different electronic properties. As an example, whereas grain boundaries produce deep levels in CdTe, it is generally not the case in CIGSSe with alkali (Na, K, Rb, Cs) in diffusion treatments.

With the exception of silicon thin-film solar cells, CdTe and CIGSSe absorbing materials have dominated the research in thin-film solar cells in the past decade. But, one important issue concerns the environmental impact of cadmium and a second is linked to the limited availability of indium. Indeed, viable solar cells should be made

Table 16.1 Record conversion efficiency of thin-film solar cells (end of 2017)

Technology	a-Si:H	CIGSSe	CdTe	CZTSSe	DSSC	Organic	Organic tandem	Quantum dot	Perovskite
Conversion efficiency	12.5%	22.9%	22.1%	12.6%	11.9%	12.1%	10.7%	5.1% (PbS dots)	22.7%
Laboratory or company	United Solar	Solar Frontier	First Solar	IBM	SHARP	Philips 66	Heliatek	Univ Toronto	KRICT

from cheap and simple materials for the terawatt scale production of energy. Abundance of the elements comprising the solar cell is a prerequisite. And it is very important to consider materials exhibiting extraction costs that are lower than for silicon as well as electricity production potential which is greater than silicon. Thus, new substitute light absorbers made from earth-abundant, environmentally benign materials, and showing good stability and long life are highly desirable. Unconventional solar cell candidates including FeS_2, CuO, and Zn_3P_2 have been proposed by Wadia et al. (2009). But Cu_2ZnSnS_4 (CZTS) semiconductor material has emerged a promising candidate for this application and has attracted interest recently (Liu et al., 2016). All the constituent elements in CZTS are earth abundant and environmentally benign. It is found that the abundance of Zn and Sn in the Earth's crust is 1500 times and 45 times greater than that of In, respectively, and the price of In is almost two orders of magnitude higher than those of Zn and Sn. The record conversion efficiency for a CZTS solar cell has been pushed up to 12.6% by IBM (Table 16.1) using wet chemical methods (Wang et al., 2014).

A third class of emerging technologies is based on organometallic dyes and polymers. Organic (or plastic) solar cell (OPV) and dye-sensitized solar cells (DSSC) are promising emerging PV technologies based on organic semiconductor materials. Organic solar cells consist of conductive organic polymers (deposited from spin-coated solutions of molecules in solvents) or small organic molecules (evaporated under vacuum) for light absorption, charge separation, and transport. Such active organic materials are sandwiched between the contact layers: a transparent conductive oxide layer such as indium tin oxide (ITO) is used as the front contact and usually aluminum as the back contact. Confirmed record power conversion efficiencies (PCE) for OPV single junction, OPV multijunction solar cells, and DSSC have reached 12.1%, 10.7%, and 11.9%, respectively (Table 16.1).

In the past few years, a new material has emerged in the thin-film photovoltaic community. Organometallic perovskite materials, which were initially used as dyes in DSSC, were transferred to a planar stack of layers structure and soon afterwards they disrupted the photovoltaic materials status quo. In less than 2 years, performances achieved the 20% barrier and nowadays the record is at 22.7%, right next to CIGS and CdTe solar cells, showing an enormous potential as a photovoltaic technology.

In the following sections, we will present a few innovative approaches in thin-film solar cells. We begin with the use of nanostructures, such as nanowires or quantum dots, to improve the performances of thin-film solar cells. Indeed, a thin-film solar cell can be considered as a multilayer interference optical coating to calculate the solar optical field distribution. Furthermore, photonic crystals, nanoplasmonics, and other light-trapping strategies concern nanostructured thin films. A state-of-the-art review of organic solar cells is then presented along with light-trapping strategies, which are also a major concern for organic solar cells. However, material and electrical considerations also have to be taken into account. The next part of this chapter is devoted to CIGSSe coatings, and finally, organometallic perovskite-based solar cells are described.

16.2 INORGANIC NANOSTRUCTURES FOR PHOTOVOLTAIC SOLAR CELLS

As mentioned in the introduction of this chapter, the costs of photovoltaic energy are still too large in comparison with those of conventional energies. Cost reduction can be obtained by an increase of cell performance. Luque (2011), in one of his last articles, asked whether it is possible to achieve solar cell efficiencies above 50% and thus overcome the current record, obtained by a multijunction solar cell under concentrated sunlight (Green et al., 2011). To do this, the photovoltaic research and industry must answer two fundamental questions. Firstly, how to succeed in lowering the expenses of manufacture? And secondly, how to enhance the efficiency of solar cells? One route of investigation is the development of nanostructures in thin film layers.

As described previously, the use of thin films for solar cells is one of the keys of success for photovoltaics. Direct bandgap materials like CIGS, CdTe, or GaAs can directly address this issue. And if we go further, some thin-film solar cells, including nanostructures, have both improved light trapping and photo-carrier collection thus improving the efficiency of solar cells.

16.2.1 NEW CONCEPTS OF SOLAR CELLS

The fast development of nanotechnology allows the realization of objects with very small dimensions such as nanowires (Lu and Lieber, 2006) or quantum dots (see Chapter 12). Two nanostructures will be detailed in this part. These nanostructures have the distinction of having different physical properties from those of macroscopic structures. Of these, one can notice changes in the bandgap, the refractive index, the rate of recombination of carriers, and a large surface-to-volume ratio. For example, because of quantum confinement effects, alteration of their physical and electronic properties is observed when the size of these structures is as small as or smaller than the Bohr exciton radius of the material providing some new concepts of solar cells. Quantum structures can reach the Shockley-Queisser limit of 32% for Si-based solar cells (Shockley and Queisser, 1961).

Different materials and solar cell structures based on nanostructures have been studied. Both new photovoltaic mechanisms and new concepts for solar cells are thus expected such as multijunction solar cells (Kandala et al., 2008), hot carrier solar cells (Tisdale et al., 2010), intermediate band solar cells (Luque et al., 2012), hybrid solar cells (Skompska, 2010), frequency conversion (Meijer et al., 2010), and multiple-exciton generation (Nozik, 2008), which belongs to a new generation of photovoltaic technology (Brown and Wu, 2009). These cells are very interesting in terms of theoretical research and very promising for the future of photovoltaic devices and more generally for optoelectronics. More than that, different photonic structures can be studied to enhance either the absorption or the antireflective effect in these solar cells such as photonic crystals or plasmonics, two innovative concepts

widely studied nowadays (El Daif et al., 2010; Pillai et al., 2011). Although most of these technologies are still under research, the many advances made in recent years make it possible to foresee a rapid evolution of these cells toward their commercial manufacture (Lunt et al., 2011).

16.2.2 LIGHT TRAPPING AND PHOTO-CARRIER COLLECTION

Now that we know the current possibilities of "nanostructured solar cells," we will enter into more detail on the benefits of these thin films including nanostructures. As previously written, in order to enhance the performance of solar cells, we need to improve both the light trapping and the photo-carrier collection. Indeed, in a 'classical' silicon solar cell, because of its indirect bandgap, we need a sufficiently thick layer to optimize the absorption of sunlight. This large thickness results in a decrease of the collection of photogenerated carriers, due to a higher probability of recombination. Similarly, in thin-film solar cells, the collection of carriers is increased at the expense of the absorption of photons, even in high-absorbing materials.

The use of different mechanisms of light trapping in solar cells is a prerequisite in order to improve the absorption. Several nanostructures, such as nanowires, nanopillars, or nanocones, have already shown their ability to absorb light very efficiently. For example, a strong increase in path length enhancement factor with nanowire length has been demonstrated in silicon nanowire solar cells (Garnett and Yang, 2010). The path length enhancement factor is defined as the apparent optical thickness of the structure divided by its actual thickness. The best nanowire arrays showed path length enhancement factors of up to 73, exceeding the randomized scattering limit ($2n^2 \approx 25$ because there was no back reflector) (Yablonovitch and Cody, 1982). Zhu et al. (2009) have also shown that for a-Si:H nanocone arrays, >90% of light is absorbed at angles of incidence up to 60 degrees, which is better than thin films (45%). A highly efficient antireflective coating for photovoltaic solar cells can also be developed thanks to silicon nanowires. These structures, known as "Black Silicon," exhibit an average reflection value around 2% in the wavelength range of 300–1000 nm (Jung et al., 2010). The optical properties (reflection, transmission, absorption, scattering) of InP and GaP nanowires (Muskens et al., 2008), Ge nanowires (Cao et al., 2009), and CdS nanopillars (Fan et al., 2009) have also been studied showing a great interest in these materials for photovoltaic applications. Instead of structuring direct semiconductors at the nanoscale, Yu et al. (2011) have developed a simple and inexpensive method to fabricate Al nanospike (NSP) arrays on which they deposit thin-film photovoltaic materials, such as a-Si or CdTe to form 3D conformal coating. With these kinds of structures, they achieve up to 94% day-integrated sunlight, in the 300–900 nm wavelength range.

In order to optimize the ratio of collected and photogenerated carriers, the nanostructures must be well defined. It means that the diffusion length of the minority carriers must fit with the dimensions of the structure. As we need a p-n junction to collect carriers, one solution consists of making a nano-structure that offers a p-n junction orthogonal to the absorption of light. In this configuration, the decoupling

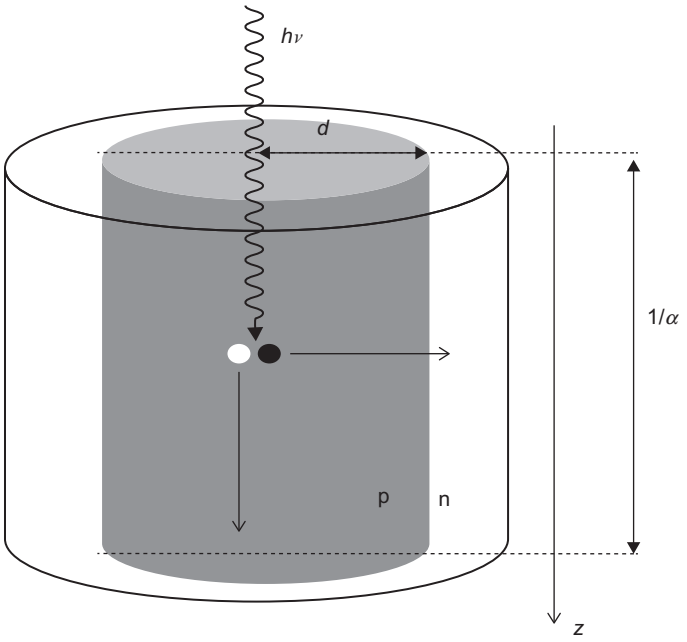


FIG. 16.1

Design of a radial p-n junction in a nanorod. The decoupling of light absorption and carrier extraction is clearly shown.

of light absorption and carrier extraction might provide a way to improve carrier-collection efficiency (Kayes et al., 2005; Spurgeon et al., 2008), which is clearly identified in Fig. 16.1. Indeed, the absorption of photons occurs along the nanowire measuring a few micrometers, while the depletion region of the p-n junction is in the radial direction with dimensions of few nanometers.

16.2.3 QUANTUM DOTS AND NANOWIRES INCLUDED IN THIN-FILM SOLAR CELLS

Among all the nanostructures used in photovoltaic solar cells, we are particularly interested in nanowires and quantum dots, which are the most studied and most promising for solar cells for all the reasons described previously. We thus present some examples of new architectures of photovoltaic solar cells including these nanostructures, which exhibit many advantages to increase solar cell efficiencies.

First, quantum dots and nanowires can be inserted into multijunction solar cells and particularly in tandem solar cells. This architecture allows considerable increases in the absorption of light over a larger spectral range than a conventional solar cell made with a single junction. To go into further detail regarding this device, we take silicon material as an example. The principle is as follows: the upper cell is a

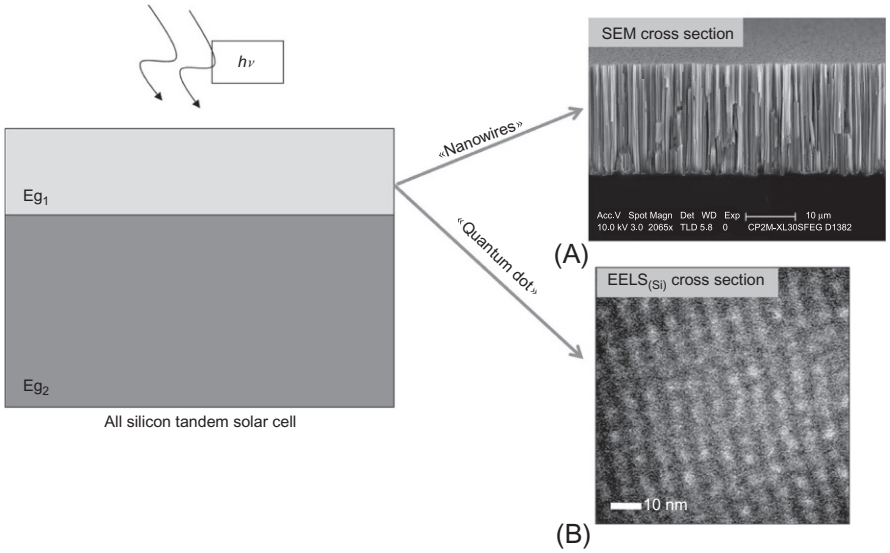


FIG. 16.2

An all-silicon tandem solar cell. The upper cell is a nanostructured layer in silicon of bulk silicon (Eg_1) and the cell below is made of bulk silicon (Eg_2). The first cell is made by either: (A) an array of nanowires (SEM cross-section, Le Rouzo et al., 2009), or (B) an array of quantum dots (EELS cross section, Rezgui et al., 2010).

nanostructured layer in silicon and the cell below is made of bulk silicon. The first solar cell presents a gap (Eg_1) higher than the second one (Eg_2) in order to avoid losses in absorption. This difference in the bandgap of the two layers is obtained thanks to quantum confinement. Indeed, Fig. 16.2 presents a tandem silicon solar cell (two junctions) with the first layer, which can be either an array of nanowires or a layer comprising quantum dots. De Vos (1980) proposed a model to calculate the limit efficiency of a tandem solar cell, taking into account the fact that a particular cell is not only illuminated by part of the solar irradiance but also by the electroluminescence of other cells of the set. He showed that a maximum of 42.3% occurs for $Eg_1 = 1.9\,eV$ and $Eg_2 = 1.0\,eV$ (above the Shockley-Queisser limit for a single junction). If the value $Eg_2 = 1.12\,eV$ is taken for bulk silicon, several bandgaps Eg_1, between 1.6 and 2.2 eV, are available to reach an efficiency around 40% as shown in Fig. 16.3. A higher bandgap for silicon (e.g., 1.7 eV) can be obtained by reducing the size until a few nanometers (<3 nm for nanowires and quantum dots) (Takagi et al., 1990). These experimental constraints are an impediment to the development of inorganic tandem solar cells using nanostructures. However, we can note that multijunction solar cells using inorganic materials are manufactured and work well providing the record photovoltaic efficiency of 42.3% with GaInp/GaInAs/Ge two-terminal, triple-junction cells (Green et al., 2011).

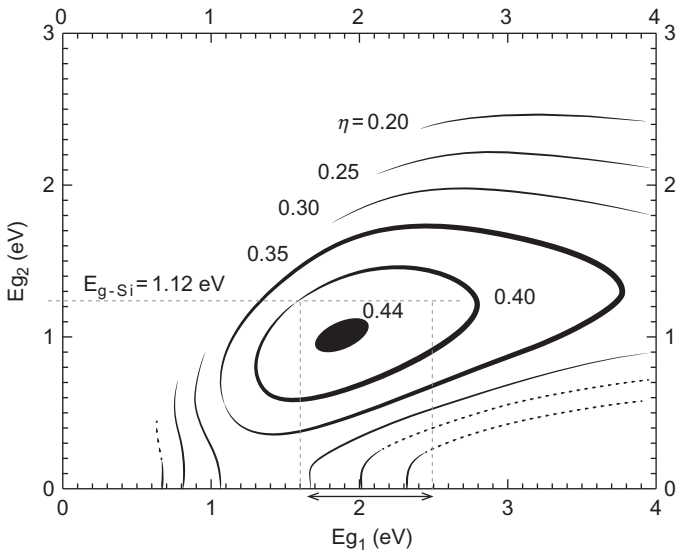


FIG. 16.3

Theoretical calculation of the conversion efficiency of a tandem solar cell. The silicon material has been taken as an example for the cell.

Reproduced from De Vos, A., 1980. Detailed balance limit of the efficiency of tandem solar cells. J. Phys. D: Appl. Phys. 13, 839, with the permission of IOPP Publications (in progress).

Several teams have recently obtained promising results on nanowire solar cells combining low cost and high efficiency. The most recent study is proposed by Huang et al. (2012). Nanowire arrays were synthesized by using the wet electroless etching technique. This study proposes a low cost, silicon nanowire (SiNW) array fabrication process using a new solution as the doping source, with a screen-printing method to coat electrodes to create SiNW array-based solar cells. This latter exhibits a conversion efficiency of 10.15% with a short-circuit current J_{sc} of 30.65 mA cm^{-2} and an open circuit voltage V_{oc} of 520 mV. This is very promising for the low-cost fabrication of solar cells with high efficiency.

Another research method for increasing solar cell efficiency with nanostructures is the modulation of the solar spectrum. The two main losses in a single-junction solar cell are, firstly, the inability of the bulk semiconductor to absorb photons of lower energy than their energy bandgap and, secondly, the thermalization of photogenerated carriers. The idea is to change the whole solar spectrum to accommodate the absorption of the solar cell (directly connected to the gap); it requires some frequency conversion. This can be done by the up- and downconverter structures placed, respectively, in the back and in the front side of a solar cell (Conibeer, 2007). Recently, Huang et al. (2010) have demonstrated that a hybrid colloidal ZnS nanoparticle/Si nanotip p-n active layer in crystalline silicon-based solar cells presents an enhancement of 20% in the short-circuit current and approximately 10%

in power conversion efficiency compared to its counterpart without integrating ZnS nanoparticles. ZnS nanoparticles not only act as frequency downconversion centers in the ultraviolet region but also serve as antireflective coating for light trapping in the measured spectral regime.

Multiple exciton generation (MEG) is another mechanism that will increase the photocurrent. The energetic hot carriers (with energy higher than the bandgap of the material) must produce two or more electron-hole pairs through impact ionization (Conibeer, 2007). Semonin et al. (2011) reported on photocurrent enhancement arising from MEG in lead selenide (PbSe) QD-based solar cells, as manifested by an external quantum efficiency (the spectrally resolved ratio of collected charge carriers to incident photons) that peaked at $114 \pm 1\%$ in the best device measured. The associated internal quantum efficiency (corrected for reflection and absorption losses) was 130%.

To conclude for these new concepts of solar cells, we will finish with hybrid nanostructure solar cells that combine both organic and inorganic semiconductors (Skompska, 2010). Different inorganic semiconductor materials are used like either quantum dots or nanowires. Ren et al. (2011) demonstrated quantum dot-based hybrid solar cells. The CdS quantum dots were bound onto crystalline poly(3-hexylthiophene) (P3HT) nanowires through solvent-assisted grafting and ligand exchange, leading to controlled organic-inorganic phase separation and an improved maximum power conversion efficiency of 4.1% under AM 1.5 solar illumination.

Organic solar cells will be described in more detail in the following part of this chapter.

16.3 ORGANIC THIN-FILM SOLAR CELLS

Organic solar cells (OSC) have received increasing attention over the past few years. Indeed, the materials used in the photovoltaic polymer domain offer many practical advantages over conventional photovoltaic materials such as silicon thanks to the solution processing techniques used to fabricate the cells (low-cost, flexible, and large-scale applications). Moreover, OSC performance has significantly increased in the past few years through the design and synthesis of novel donor and acceptor organic semiconducting molecules to be used as active materials (Boudreault et al., 2011; Zhang and Wang, 2012; Zhao et al., 2017), modified interfacial layers (Motiei et al., 2010; Yip and Alex Jen, 2012), optimized film morphologies (Ma et al., 2005; Peet et al., 2009; Ben Dkhil et al., 2014), and engineered device architectures (Sun et al., 2011; Zhang et al., 2011; Gaceur et al., 2016). The power conversion efficiency of polymer-based solar cells has been significantly increased from 1% in 1986 (Tang, 1986) to 5% in 2005 (Xue et al., 2005) and, more recently, a confirmed efficiency of 12.1% has been reached in 2016 by Philips 66 (2016) (Green et al., 2017). With such efficiencies, OSC could become a competitive alternative to inorganic solar cells in the near future. The revolutionary development in OSC came in the mid-1990s with the introduction of bulk heterojunction (BHJ) devices (Yu and Heeger, 1995), where

the donor and acceptor material are blended together. In such a nanoscale-interpenetrated network, each exciton created could reach a dissociating site (interface D/A) within a distance smaller than the exciton diffusion length. Nowadays, the bulk heterojunction is still the most promising concept for all-organic PV cells. While various combinations of donor and acceptor materials have been studied, the most reported material system in BHJs, from 2002 to 2010, is the mixture of regioregular poly(3-hexylthiophene) (RR-P3HT) as donor and 6,6-phenyl C61-butyric acid methyl ester (PCBM) as acceptor (Dang et al., 2011). In the past decade, hundreds of new donor polymers have been developed and tremendous efforts concerned the development of low-bandgap push-pull copolymers composed of donor (D) and acceptor (A) alternating units. Impressive high-performance low bandgap copolymers are those designed by Liang et al. (2009), which are composed of thieno[3,4-*b*]-thiophene (TT) and benzodithiophene (BDT) alternating units. Donor systems based on TT-BDT derivatives were capable of reaching a power conversion efficiency (PCE) higher than 10% (Wan et al., 2016). A new push-pull donor copolymer based on 5,6-difluorobenzothiadiazole (FBT) as the acceptor unit and quarter-thiophene (Th4) as the donor unit has been synthetized by Chen in 2014. This polymer is one of the most promising donor polymers since certified PCE up to 11.7% were obtained by Zhao in 2016. For a long time, researchers have essentially developed new donor polymers and small molecules for improving the OSC PCE while the acceptor organic materials were dominated by fullerene derivatives. Due to their spherical geometries, fullerene derivatives present quasiisotropic charge transport. Nevertheless, they absorb very weakly on the solar spectrum and thus limit the device currents. Furthermore, due to their low tunability in energy levels, fullerene derivatives would induce quite high-energy losses during the separation of excitons into free charges resulting in limited device voltages (Li et al., 2017). Nowadays, the development of new nonfullerene acceptors is a promising route in order to improve both the device currents and voltages and thus the OSC performances. The most promising nonfullerene acceptors are small molecules composed of donor (D) and acceptor (A) units (A-D-A) such as those synthesized by Lin in 2015 with 1,1-dicyanomethylene-3-indanone (IC) as the acceptor unit. Nonfullerene acceptors composed of indacenodithieno[3,2-*b*]thiophene (IDTT) as donor unit and a fluorinated IC (ITIC-Th1) as acceptor unit allowed reaching PCE up to 12.1% (Zhao et al., 2017).

Generally, the different organic solar cells are distinguished by the production technique (roll-to-roll or vacuum deposition techniques), by the photoactive materials used (polymer or small molecules), and by the device architecture (single or tandem, bilayer heterojunction or bulk heterojunction, normal or inverted structure).

16.3.1 WORKING PRINCIPLES OF AN ORGANIC SOLAR CELL

Today, two main device geometries exist: the traditional and the inverted structure schematically represented in Fig. 16.4.

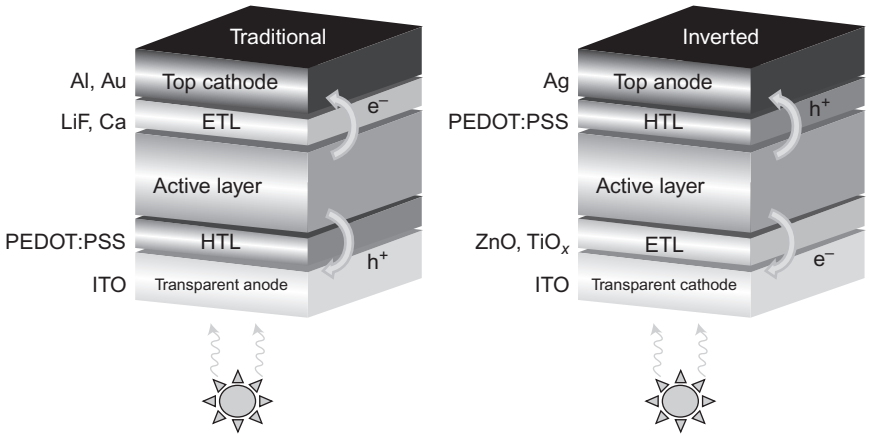


FIG. 16.4

The traditional structure (left) and the inverted structure (right) of an organic solar cell. *ETL*, electron transport layer; *HTL*, hole transport layer.

As observed, the cells are illuminated through a transparent substrate. A conductive and semitransparent electrode (usually indium tin oxide, ITO) is deposited on the substrate and usually five layers are then deposited on top of this electrode. In the normal geometry, the first layer stack is an interfacial hole transport layer (HTL) of poly(3,4-ethylenedioxythiophene):poly(styrene sulfonate) (PEDOT:PSS), followed by the active layer, an electron transport layer (ETL, LiF, or Ca) and a low work function metal thick top layer (Al or Au). In the inverted type geometry, the order of the layers is reversed with the high work function top metal electrode now being the hole-collecting anode (Ag). The PEDOT:PSS usually remains as the HTL while the ETL can be made of ZnO or TiO_x. The main advantage of the inverted structure is the improvement of the device stability, which can be related to the chemical properties of the interfaces (Norrman et al., 2012). The organic materials composing the photoactive layers are generally split into two groups: small molecules and conjugated polymers. These two classes of materials are rather different in terms of their synthesis, purification, and device-fabrication processes. Small molecules, which have a well-defined molecular weight, are usually deposited by low- or high-pressure vapor methods. To create interpenetrating donor-acceptor networks, co-evaporation techniques can be applied. We should notice that the group of Heeger has reported a power conversion efficiency of 6.7% for a BHJ OSC based on solution-processed small donor molecules (Sun et al., 2011). Recent works also proved that solution-processed techniques assisted by solvent vapor annealing (SVA) allow a fine control of the morphology of BHJs based on dithienopyrrole-based A-D-A oligothiophene (dithieno[3,2-*b*:2′,3′-d]pyrrole) blended with [6,6]-phenyl-C71-butyric acid methyl ester (PC71BM). In this study, it was claimed that additional SVA results in a bilayer exhibiting highly intermixed phases and leading

to an optimal blend morphology (Ben Dkhil et al., 2017). Polymers are usually processed from solution in organic solvents [spin coating and doctor blading in laboratories, screen-printing or roll-to-roll techniques in companies (Søndergaard et al., 2012)].

There is a fundamental difference between solar cells based on inorganic or on organic semiconductors. In solar cells made from inorganic semiconductors, photons are directly converted at room temperature into free charge carriers. In OSCs, a photon absorption leads to the creation of a bound electron-hole pair called an exciton, for which binding energies range from 50 meV up to >1 eV (Gregg, 2003). Excitons then have to diffuse to be dissociated into free charges. This additional stage of exciton diffusion completely changes the scale of the physical phenomenon involved in OSCs. Indeed in organic materials, both the exciton diffusion length and the charge carrier diffusion lengths are in the submicronic range (10–20 nm for excitons and 100–200 nm for charge carriers). The most visible consequence of such low values is the design of the organic photovoltaic devices where the active layer thicknesses do not exceed 200 nm. In addition, the control of the morphology of each layer at the nanometer scale strongly impacts the performance of OSCs.

Before going into more detail, we recall here the four steps of the photovoltaic conversion process in OSCs.

16.3.1.1 Photon absorption

Upon absorption of a photon having an energy larger than the gap, an electron is promoted from the HOMO band (highest occupied molecular orbital) to the LUMO band (lowest unoccupied molecular orbital) of the donor material. The majority of organic materials have bandgaps higher than 2 eV, which limits to <30% of the possible harvesting of solar photons. One way to overcome such limitation consists in integrating multiple materials with complementary absorption in a tandem architecture or using ternary BHJs. Indeed, although conventional single-junction OSCs comprise binary bulk heterojunctions based on acceptor small molecules and donor polymers, very promising results have been obtained using ternary bulk heterojunctions allowing broadening the active layer absorption spectrum (Lu et al., 2015). On the other hand, due to low charge carrier mobility, the active layer thickness should be restricted to around 150 nm to avoid series resistances. Fortunately, absorption coefficients are high in organic donor materials (exceeding $10^5\,cm^{-1}$) and make absorbing the main part of the incident light possible, even with thicknesses of around 100 nm. Recent works also showed that nonfullerene acceptors are capable to reach absorption coefficients close to $10^5\,cm^{-1}$ (Bin et al., 2016). Thus, thicknesses of the films are not the bottleneck.

16.3.1.2 Exciton diffusion

The strong local electrical field at a donor-acceptor material interface will be used to dissociate excitons. For efficient dissociation of excitons, the distance between the photon absorption and the first interface should be lower than the exciton diffusion length (between 10 and 30 nm).

16.3.1.3 Exciton dissociation or charge separation

When an exciton reaches the interface between donor and acceptor materials, the charge separation takes place in an ultrafast timescale of about 45 fs (Brabec et al., 2001). However, a necessary condition for the efficient dissociation of the created excitons is that the difference between the LUMO of the donor and the acceptor is higher than the exciton binding energy. If this is the case, electrons are transferred to the acceptor. Up to now, in conjugated polymer-based organic solar cells the most efficient electron acceptors found are C_{60}-based fullerenes. As mentioned previously, nowadays, tremendous efforts concern the development of nonfullerene acceptors with optimized HOMO and LUMO energy levels in order to reduce energy losses during the charge separations.

16.3.1.4 Charge transport

The separated charges then need to diffuse to the respective device electrodes, holes to the anode and electrons to the cathode, to provide voltage. In conjugated polymers, the transport of charge carriers is done by successive jumps (hopping) from a localized state to another. Mobility in organic materials is low and could also be reduced by traps. Values are typically in the 10^{-4} to 10^{-2} cm^2 V^{-1} s^{-1} range.

16.3.2 LIGHT TRAPPING STRATEGIES FOR ORGANIC SOLAR CELLS (OSCs)

The basic idea developed in this section is to increase the part of the incident light which is absorbed in the photoactive layer. If we consider the spectral redistribution of the incoming light in the traditional structure of Fig. 16.4, most of the incoming light is absorbed in the blend in the 400–700 nm range, average reflection is about 10%, ITO absorption is about 15%, while PEDOT absorbs mainly in the blue range (4%). The first approach to improving the performance of the cell is to increase the thickness of the absorbing layer. However, this thickness is generally restricted (<150 nm) by the limited charge carrier mobility in conjugated polymers (highly efficient devices with thickness around 200–250 nm have been demonstrated (Irwin et al., 2008)). Thus, to overcome this problem, and from the optical point of view, the following solutions can be considered:

- optimization of the electromagnetic field distribution inside an organic solar cell;
- implementation of periodic structures (such as gratings or photonic crystals) in the thin-layer stacking;
- investigation of plasmon effects for increasing absorption in OSCs.

16.3.2.1 Optimization of the electromagnetic field distribution

An organic solar cell is modeled as stacked thin films surrounded by a semiinfinite substrate and a semiinfinite transparent medium. Each layer "i" is defined by its thickness d_i, its refracive index n_i, and its extinction coefficient k_i as a function of wavelength, λ. This model assumes layers to be smooth and homogeneous, interfaces

to be parallel, and does not take scattering into account. To go further into detail and to link the optical properties to the electrical properties in OSCs, the key equation is:

$$Q_i(z,\lambda) = \frac{1}{2}\sqrt{\frac{\varepsilon_0}{\mu_0}} n_i \alpha_i |E(z)|^2 = \frac{n_i}{n_0} \alpha_i I_{\text{solarlight}} \left| \frac{E_{(z)}}{E_0} \right|^2 \tag{16.1}$$

where $|E|^2$ is the squared modulus of the electromagnetic field, Q_i is the local energy dissipated in the material, ε_0 is the permittivity of vacuum, μ_0 is the permeability of vacuum, α_i is the absorption coefficient, n_0 is the real part of the complex refractive index of the glass substrate, and $I_{\text{solarlight}}$ is the polychromatic incoming light with standard AM 1.5 spectrum. Indeed, the generation rate of excitons and then the short circuit current density J_{sc} can be computed from Eq. (16.1) and used to predict the organic solar cell efficiency (Pettersson et al., 1999). It has also been shown that for organic solar cells based on blended heterojunctions the dependence of the short circuit current density (J_{sc}) on the active layer thickness follows a rather complicated behavior (Hoppe et al., 2003; Monestier et al., 2007a,b). More generally, to optimize an OSC, interference effects should be taken into account inside the multilayer thin-film structure. The optimal thicknesses of each layer are determined to maximize the square modulus of the normalized electromagnetic field in the photoactive layer and, as a consequence, the short-circuit current of the solar cells. To achieve such multilayer optimization by varying all layer thicknesses independently of each other, a numerical software package, based on a simple optimization matrix method, can be used (Monestier et al., 2007a,b).

Such a control of optical interferences inside the OSCs can be employed to play with their apparent colors. The development of new organic materials with optimized energy levels and absorbing in the visible range of the solar spectrum provides very interesting color properties to the OSCs. In combination with their extraordinary mechanical properties of flexibility and stretchability (Lipomi et al., 2011; Hsieh et al., 2018), OSCs would involve the emergence of new markets aiming a better integration of the solar cells in new applications such as power-generating bags, laptops, mobile phones and for fashion and architectural applications. It has been recently proposed to optimize both the efficiency and the color of OSCs by adjusting the layer thicknesses in their stack and by adding an optical spacer in ZnO allowing the control of the optical interferences. The authors experimentally fabricated green, yellow, and blue OSCs exhibiting PCEs of 6.73%, 7.10%, and 7.59%, respectively. It has to be noticed that, for all these colored OSCs, the active layers were based on poly [[4,8-bis[(2-ethylhexyl)oxy]benzo[1,2-*b*:4,5-*b*0]dithiophene-2,6-diyl][3-fluoro-2-[(2-ethylhexyl)carbonyl]thieno[3,4-*b*]thiophenediyl]] (PTB7) blended with [6,6]-phenyl-C71-butyric acid methyl ester (PC71BM) and, thus, had the same composition (Gaceur et al., 2016).

16.3.2.2 Implementation of periodic structures in the multilayer stack

The challenge in OSCs is to implement periodic structures inside the multilayer stack to confine the incident light in the active layer. Although there were some difficulties in correlating computations and initial experimental results, the potential of

diffractive optical structures for OSCs has been evaluated for the first time by Niggemann et al. (2004) with the simulation and realization of diffraction gratings and buried nano-electrodes. In 2006, nanometric periodic patterning in OSCs was reported by Cocoyer et al. (2006). More recently, the concept of 2D and 3D photonic crystals in OSCs has been investigated in order to improve light trapping. For example, Duché et al. (2008) are the first to theoretically demonstrate that an improved absorption, close to the band edge of the material ($\lambda > 600\,\text{nm}$), can be obtained in nanostructured P3HT/PCBM thin films by coupling slow Bloch modes with very low group velocities in the photonic crystal (Fig. 16.5). Effective indices n_{eff} higher than 10, which prove the coupling of very low group velocity Bloch modes, have been estimated through optical modeling for OSCs integrating photonic crystals. Finally, by adjusting both the photonic crystal geometries and the optical interferences inside the stack to vertically confine the slow Bloch modes in the thickness of the active layer, an absorption gain up to 15.67% has been estimated for photonic crystal OSCs made of poly(3-(2-methyl-2-hexylcarboxylate) thiophene-*co*-thiophene: PCBM (Duché et al., 2015). This concept was experimentally demonstrated in 2011 by the group of Richard Friend, who realized a double nanoimprinting process that allows the formation of nanostructured polymer:PCBM heterojunctions of composition and morphology that can be selected independently (He et al., 2011).

16.3.2.3 Plasmons for increasing absorption in OSCs

An optically generated oscillation of free electrons that takes place along a metal/dielectric interface is a surface plasmon. By tuning the excitation light, a resonance occurs when the incident photon frequencies match the collective oscillations of the conduction electrons of the metallic particles. In photonics, this field of interest is

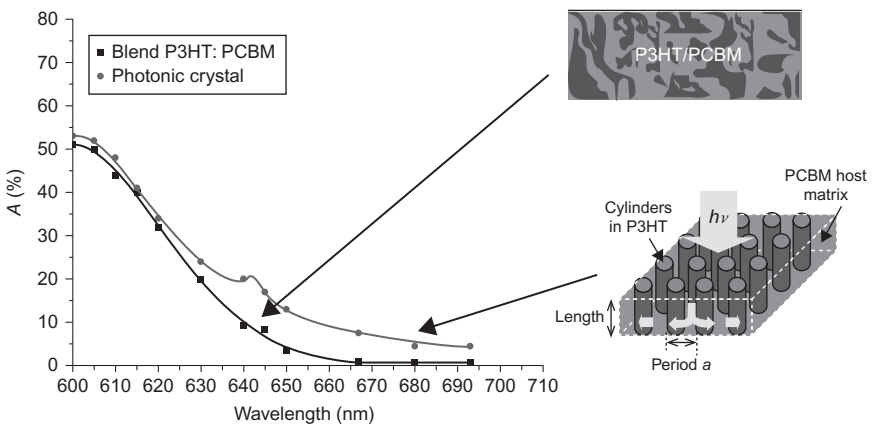


FIG. 16.5

Absorption of a P3HT/PCBM blend active layer ↔ compared to P3HT/PCBM photonic crystal-ordered heterostructure absorption. The thickness of the two layers is the same: 150 nm.

known as plasmonics. Among a wide range of applications, these surface plasmon properties can be used in the organic photovoltaic domain in order to improve performances of solar cells. Noble metal particles such as gold or silver allow enhancing light absorption in the visible range when they are incorporated inside an OSC.

In the systems ITO/metal-clusters/CuPc/In, it was shown by Stenzel et al. (1995) that the incorporation of copper or gold increases the photocurrent by a factor of more than two. This work was also performed with ITO/silver-clusters/ZnPc/Ag components by Westphalen et al. (2000). More recently, Morfa et al. (2008) at the National Renewable Energy Laboratory (Golden, Colorado) included plasmon-active silver nanoparticle layers in solution-processed bulk heterojunction solar cells, as shown in Fig. 16.6. A strong increase in EQE (external quantum efficiency) is observed for all samples with silver nanoparticles. The optimized thickness of the silver layer is 1 nm and the resulting solar energy conversion efficiency for a bulk heterojunction photovoltaic device of P3HT:PCBM was found to increase from 1.3% to 2.2% for devices employing thin-plasmon active layers.

16.4 CHALCOGENIDE MATERIALS IN THIN-FILM SOLAR CELLS

In the past decade, all of the thin-film photovoltaic technologies have demonstrated impressive increase of record efficiencies owing to improved basic understanding of the materials, interfaces, and their processing. This progress led to further industrial developments focused in high efficiency thin-film-based devices. Among the numerous companies existing before 2015, only a few could survive the worldwide competitiveness driven by crystalline silicon-modules mass production and thereby confirm their dominant position in the TF-PV market [e.g., First Solar

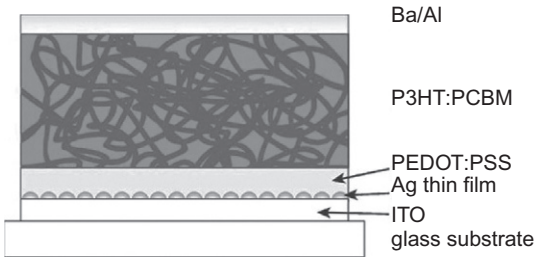


FIG. 16.6

Device fabricated with a thin silver film deposited onto ITO on a glass substrate. PEDOT:PSS was spun onto the silver layer followed by P3HT:PCBM and a barium/aluminum back electrode.

Reproduced from Morfa, A.J., Rowlen, K.L., Reilly, T.H., Romero, M.J., Van De Lagemaat, J., 2008. Plasmon-enhanced solar energy conversion in organic bulk heterojunction photovoltaics. Appl. Phys. Lett. 92, 013504, with permission from the American Institute of Physics (in progress).

(United States), Solar Frontier (JAP), Miasolé (United States), Solibro (EU), and AvanCIS (EU)].

Today, the number of chalcogenide thin-film solar cell technologies being mature enough to widely penetrate the market does not exceed three: CdTe, CIGSSe, and CZTS. The most intriguing and probably complex material is the chalcopyrite copper indium gallium di-sulfo-selenide ($CuIn_{1-x}Ga_xSe_{2-2y}S_{2y}$), which has great potential to make new applications cost-effective and viable. CIGSSe technologies are differentiated from competing thin-film materials by a combination of several factors. Firstly, the chalcopyrite structure tolerates large deviations to stoichiometry and offers a large scope for PV applications thanks to its electro-optical properties. Secondly, it already demonstrated efficiency surpassing multicrystalline silicon while using much less material; the champion device performance is 22.9% at the cell level ($1\,cm^2$), 19.2% at the submodule level ($900\,cm^2$) and 17.5% for commercial modules ($119 \times 79\,cm^2$) (Green et al., 2018).

However, despite the low-energy payback time, wide scope of applications, low material consumption, and high efficiency, scaling polycrystalline CIGSSe technology to large-volume production remains highly challenging. In particular, besides the efforts made in technology transfer, a big gap between previously cited efficiencies and medium commercial modules (15% efficiency) still exists, mainly related to the specific characteristics of CIGSSe material and thin-film-based PV modules (Klenk, 2001; Karg, 2001; Kato, 2017).

CIGSSe is a direct bandgap semiconductor with a high absorption coefficient; moreover, its bandgap energy is rather well matched to the solar spectrum. It belongs to the multinary Cu-chalcopyrite system, where the bandgap can be modified by varying the group III cations among In, Ga, and Al and the anions between Se and S (Dimmler et al., 1987; Theodoropoulou et al., 2009; Kato, 2017). This p-type semiconductor material has excellent long-term stability and has been called a 'smart' or a "self-healing" material because of its copper-related properties. A wide range of bandgap can be obtained by mixing Ga/In and/or S/Se, varying the absorption threshold from 1.0 eV (pure $CuInSe_2$) to 2.5 eV (pure $CuGaS_2$). Up until now, the bandgap range yielding the best efficiency for this technology remains between 1.1 and 1.3 eV (Shafarman et al., 1996; Contreras et al., 2012). In the following are detailed the materials and the structure of the typical CIGSSe solar cells.

16.4.1 THE SUBSTRATES

CIGSSe devices are usually grown in what is known as substrate configuration, which means that the substrate remains the first step in the fabrication process, but the back layer to illumination. The preferred substrate for CIGSSe devices is soda-lime glass as it is cheap and used all over the world in architecture; moreover, it has a well-adapted thermal expansion coefficient to the layers constituting the devices and allows for Na doping of the CIGSSe absorber during growth.

Other substrates, such as stainless steel foils, modified aluminum foils, or polyimides, have been chosen because significant competitive advantages are possible

compared with other thin-film technologies and processes. The foil is relatively lightweight and flexible, valuable characteristics for emerging building integrated photovoltaic (BIPV) applications. At present, polyimide-based CIGSSe devices provide the largest efficiency in terms of flexible CIGSSe cells, while commercial modules on stainless steel or aluminum-based foils can be found in industry with efficiencies of about 14%.

16.4.2 THE DEVICE STACK FOR CELLS

The layers stack constituting a standard CIGSSe solar cell is rather simple (Fig. 16.7) but the complexity stands in the way of preparation of PV-grade layers and interfaces.

16.4.2.1 Back contact electrode

The fabrication of the devices starts with the deposition of the back electrode on the chosen substrate. The back electrode material is generally deposited by DC sputtering. The preferred metal is molybdenum, due to its insignificant diffusion into the absorber during cell processing and the optimal interface it forms with the CIGSSe polycrystalline layer (Granath et al., 1995; Yoon et al., 2010). The thickness and density of the Mo layer has to be optimized for adhesion, sheet resistance, morphology, permeability to substrate alkali species, and maximum performance and minimal costs for long-term device operation. Similar to what is reported in the literature (Thornton and Hoffman, 1989), the characteristics of the Mo back electrode, and particularly its permeability to sodium-based compounds, are highly influenced by the growth parameters, such as working gas flow rate, the power density applied to the

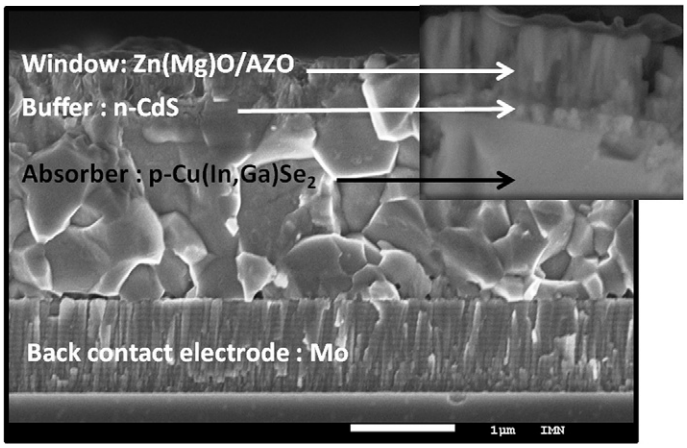


FIG. 16.7

Scanning electron microscope (SEM) image of a typical CIGSSe solar cell cross-section. The inset shows a higher magnification of the close-to-junction area.

target, and the substrate temperature. Generally, the Mo back electrode consists of at least two stacked layers: the first one deposited at a rather high working gas pressure (or low DC power), thus rather porous and ensuring the good adhesion to the substrate, and a toping one deposited at lower pressure and/or higher DC power providing a low sheet resistance of the electrode. This combination is also valuable for laser patterning in the case of monolithic interconnected cells for module application (Karg, 2001; Kato, 2017).

16.4.2.2 Absorber layer deposition

Two strategies can be followed to synthesize CIGSSe thin films for photovoltaic application. A first one consists in forming the chalcopyrite polycrystalline thin film during the deposition onto the heated substrate. This approach, used for pure selenide absorber, offers the opportunity of managing group III element ratio throughout the growing layer either by varying their deposition fluxes, or by varying the sequence of Cu delivery as in the case of the so-called three-stage process (Contreras et al., 1996). The deposition techniques allowing this fine growth tuning are exclusively based on vacuum processes, as element co-evaporation or reactive sputtering. A second strategy consists in firstly deposit the elements constituting the absorber onto the substrate, then in providing enough energy to the system to form the chalcopyrite crystal. For this two-step synthesis, metal stacks are usually grown by sputtering (or electro-deposition), then selenized and/or sulfurized with H_2Se and/or H_2S. A variation of this method avoiding the use of highly toxic H_2Se during the selenization is the rapid thermal process of stacked elemental layers including the chalcogens (Se and/or S). This two-step approach allows a controlled partial substitution of Se atoms by S close to the absorber surface.

An interesting property of the $CuIn_{1-x}Ga_x(S_{1-y}Se_y)_2$ compound system is the possibility of designing graded bandgap structures that optimize the electronic properties of the final device. Fig. 16.8 illustrates how the composition depth profile modifies the bandgap profile of the absorber and thus the optoelectronic properties of the device. The art of designing optimal bandgap grading is to push back charge carriers from critical regions, that is, regions with high recombination probability within the device. Such critical regions are: (1) interfaces between back contacts and absorber layers; and (2) the heterojunction, including the p-absorber/n-buffer interface. We can imagine an optimal band diagram of a so-called V-shaped graded structure fulfilling requirements for minimizing recombination losses (Chirilă et al., 2011). This band diagram is very similar to those expected in the recent record efficiency devices.

In addition to these optimized band diagram configurations, the efficiency boost observed since the middle of 2010s is associated with the introduction of a so-called heavy-alkali-fluoride postdeposition treatment (namely KF-, RbF-, or CsF-PDT), which, when combined with Na doping, drastically minimizes output voltage deficits and improves the collection of photo-generated carriers (Chirilă et al., 2013; Jackson et al., 2016).

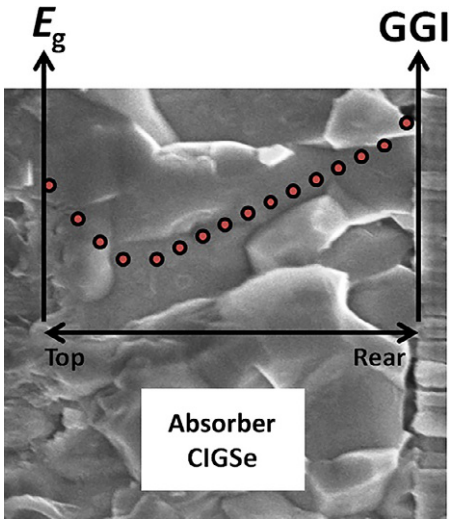


FIG. 16.8

Illustration of a V-shape graded bandgap CIGSe absorber. GGI represents the gallium content relative to group III element contents.

As suggested in this section, the presence of sodium within the absorber is needed in order to achieve the optimal performance of devices. In particular, the presence of sodium increases the effective hole density in the absorber layer, thus the output voltage of about 100 mV. Advanced optoelectronic investigations have shown that the increased carrier density is not due to direct CIGSSe extrinsic doping as in the case of c-Si, but inherent to the decrease of compensating defect density (Rau et al., 1996; Keyes et al., 1997; Kronik et al., 1998). Therefore, growth on substrates with no Na content, or with Na-species diffusion barrier between the glass substrate and the Mo back electrode, requires the addition of a controlled amount of Na-containing compound (usually NaF) either before the CIGSSe film growth on the Mo back electrode, or as a postdeposition treatment (NaF-PDT, Rudmann et al., 2003) after the absorber layer is completed. The latter alkali-fluoride treatments have been extensively studied and are undoubtedly a key parameter to achieve the best performance (Pianezzi et al., 2014).

16.4.2.3 n-Type junction partner: the buffer layer

A cadmium sulfide (CdS) layer is then applied. This layer acts as the "n" part of the p-n junction that forms the solar cell, and is usually deposited in a wet chemical bath, although vacuum methods such as thermal evaporation or sputtering are also starting to be used (as in the case of the manufacturer MiaSolé). CdS and the deposition method used have diverse beneficial properties and are important factors in the manufacturing of a robust photovoltaic material. The targeted CdS thickness is approximately 50 nm. If the CdS coating thickness is less than optimal, the open

circuit voltage (V_{oc}) and field factor (FF) are reduced; in much the same way, if the CdS thickness exceeds the optimal value, the short circuit current density (J_{sc}) is decreased because of increased absorption of light within the CdS coating.

Alternative Cd-free buffer layers been developed due to the concerns over the toxicity of Cd. Indium sulfide and zinc sulfide derivatives are of the most promising candidates for high-efficiency Cd-free CIGS solar cells (Naghavi et al., 2010; Barreau, 2009). Solar Frontier (with >1 GWp of capacity production) is already using CIGSSe modules with a ZnS(O,OH) buffer layer (Kato, 2017) in mass exploitation and AvanCIS is using evaporated InS:Na.

16.4.2.4 Window layer

To finish the photovoltaic cell, a transparent conducting oxide is deposited on the buffer layer. Transparent conducting oxides (TCOs) are major components of all nonwafer-based solar cells using thin-film compound semiconductors, thin-film silicon, dye-sensitized titanium dioxide, and organic absorbers to generate electricity from light. The main requirements for TCOs for use as contacts in a solar cell are: (i) a high enough conductivity to minimize resistive losses and (ii) minimal optical absorption over the wavelength range in which the solar cell absorber is responsive. Typically, as the conductivity of a TCO is increased, the NIR wavelength range transparency is reduced as a result of enhanced free charge carrier absorption. Thus, in the design of TCO materials, a trade-off is sought between these two properties. However, the conductivity also depends on the carrier mobility, which has no influence on the TCO transparency. Therefore, high carrier mobility is a prerequisite for developing transparent conducting materials with coexisting high electrical conductivity and high transparency over the wavelength range from 300 to at least 1200 nm.

In particular in CIGSSe technology, a bilayer consisting of resistive zinc oxide (undoped ZnO or $Zn_{1-x}Mg_xO$) and conducting ZnO (typically ZnO:Al, aluminum-doped zinc oxide AZO) is deposited by sputtering. These layers can also be deposited by chemical-vapor deposition processes. Alternatively, indium tin oxide and ZnO:Ga are also used. The TCO layer acts as the front electrode for the device, allowing electrical contact with the device and the current collection layer, and protecting the semiconductor layer below. The TCO is an n^+-degenerated semiconductor that complements the underlying CdS n-type buffer coat. Highly conductive AZO films can exhibit significant nonhomogeneity in the spatial distribution of resistivity and transparency values. The origin of this spatial distribution is usually related to the use of ceramic targets instead of metallic ones.

TCO films useful for most applications must have a wide bandgap ($E_g > 3.0$ eV, to assure a high number of photons being absorbed by the CIGSSe layer), which requires a degenerate carrier density $\geq 10^{20}\,cm^{-3}$ and ideally a resistivity of $\rho < 10^{-3}\,\Omega$ cm; so the corresponding Hall mobility should be $\mu \geq 62.5\,cm^2\,V^{-1}\,s^{-1}$ (Coutts et al., 2000). As already mentioned, resistivity values of the films are mainly affected by carrier concentration (N) and mobility. Though the NIR optical losses may be further reduced by reducing carrier concentration, doing so indiscriminately can decrease the conductivity and/or the optical bandgap of the TCO layer and

adversely affect the electrical properties and transparency in the visible wavelength region. Therefore, TCO materials with sufficiently high N ($\geq 10^{20}\,\mathrm{cm}^{-3}$) while maintaining a high mobility and transparency are desirable. High-mobility TCO materials have been prepared in the past but the resistivity has been $>10^{-3}\,\Omega\,\mathrm{cm}$ because of a relatively low $N < 10^{19}\,\mathrm{cm}^{-3}$ (Nozik, 1972; Tsukazaki et al., 2006). Such low carrier-density levels would require a Hall mobility in excess of $400\,\mathrm{cm}^2\,\mathrm{V}^{-1}\,\mathrm{s}^{-1}$ to achieve $\rho < 10^{-4}\,\Omega\,\mathrm{cm}$.

The conduction mechanism for TCOs can be classified into two large categories: (i) occurrence of an intrinsic carrier by oxygen vacancies and (ii) introduction of an extrinsic carrier by impurity doping.

Jeong et al. (2006) showed that impurity doping is a determinant for the occurrence of the carrier caused by the development of resistivity. In this work, they perform different experiments with metallic and ceramic targets to identify the possible influence on target nature in the resistivity of the AZO film. In this case, films deposited by the undoped target did not show a great increase in resistivity as they do in the case of an Al target.

16.4.3 STATE-OF-THE-ART TECHNOLOGIES AT INDUSTRY LEVEL

At present, Solar Frontier is leading the market with its CIGSSe modules and a >1 GWp production capacity. Solar Frontier produces modules using thin-film synthesis by selenization/sulfurization of metal precursors and chemical bath deposited ZnS as an alternative buffer layer.

Solibro GmbH, MiaSolé Hi-Tech Corp., and AvanCIS GmbH, among others, are prominent manufacturers of CIGSSe thin-film modules employing different technologies. As mentioned above, during 2011 and early 2012 many of the leading companies including Solyndra, Q-cells, Soltecture and Odersun filed for bankruptcy; this exemplifies the challenges this technology is affording in their competition with costs, time, and Si module producers.

16.4.4 NOVEL CHALCOGENIDE ABSORBERS

The thin-film PV technology offers in principle the opportunity to lower the cost of materials and processing compared to its crystalline silicon counterpart. The most efficient compound demonstrated today is based on the chalcopyrite system $Cu(In,Ga)(Se,S)_2$. To develop a lasting and credible photovoltaic technology capable of playing an important role in the energy production of tomorrow, it is however crucial to base it on inexpensive and abundant materials. Therefore, in the long run, the increasing price and accelerating rarity of indium and to a lesser extent gallium imposes a necessity to find alternative earth-abundant and nontoxic materials. Indium scarcity is considered an economical and geo-economical political issue in the mass expansion of CIGSSe technologies. To comply with this objective, a new $Cu_2ZnSn(S,Se)_4$ (CZTS) Këserite compound, where In and Ga are replaced by Sn and Zn, has been put forward and extensively studied in recent years. The first

reported high efficiency for Këesterite cells was 12.6% (Wang et al., 2014) obtained from cells fabricated using liquid approaches based on the toxic hydrazine solution. Whatever the implemented process, whether it is vacuum- or liquid-based, a strong output-voltage deficit is at the origin of the lower performance achieved. Several routes are currently explored to improve the interface between the p-CZTS and the n-CdS (Liu et al., 2016).

16.4.5 VACUUM-FREE DEPOSITION

In spite of the considerable promise of CIGSSe photovoltaic technology, commercialization is progressing slowly, in large part due to the high cost and complexity of the processes used to deposit photovoltaic thin films. Photovoltaic thin films, typically deposited by using co-evaporation or sputtering methods, capture only a portion of the materials cost savings inherent in thin-film concepts. The complexity of the process and cost of the capital equipment needed for vacuum-based deposition further complicate high yield manufacturing and limit the overall cost savings.

Most of the proposed low-cost methods for the deposition of chalcogenide-based solar cells were already developed many years ago. However, the efficiencies achieved have remained rather low largely due to a lack of knowledge and understanding of the layer and interface formation. As a result, the development of these methods was substantially diminished. Over the past few years, much progress was made on this fundamental understanding by groups working on vacuum-based chalcogenide deposition. With this improved knowledge, low-cost deposition processes were revisited and allowed for the development of decent efficiency and cost-effective chalcogenide solar cells (Heather et al., 2012). However, the outstanding level of performance achieved by vacuum-based absorber deposition processes makes such devices hardly competitive on the PV market.

16.5 ORGANOMETALLIC PEROVSKITE-BASED SOLAR CELLS

In recent years, dye-sensitized solar cell (DSSC) technology has attracted a lot of attention. A DSCC solar cell is not based on the classical p-n configuration; in fact, its behavior mimics photosynthesis. A monolayer of a dye is deposited over a mesoporous oxide, which also works as a photoelectrode (Maçaira et al., 2013). A photon that arrives at the dye is absorbed, resulting in the excitation of an electron from HOMO to LUMO. The electrons are collected via the TCO. To regenerate the oxidized dye, an electrolyte solution containing a redox couple is used. The efficiency of the best research cells is close to 12%, and some companies have started producing modules with reported efficiencies of 10.7% (Green et al., 2018). Through successive modifications, the liquid electrolyte has been replaced by a solid-state hole transporter, normally an organic semiconductor, with no significant impact on efficiency (Maçaira et al., 2013; Snaith 2013).

In order to reduce the thickness of the whole DSSC cell, inorganic materials with high absorption coefficients started being used instead of organic dyes (Maçaira et al., 2013). Although the performances were interesting (Sb_2S_3, 5%), this approach was not really a breakthrough until the application of organometallic halide perovskites, such as $CH_3NH_3PbI_3$ perovskite; DSSCs with perovskite nanocrystals exhibited 9.7% efficiency in 2012 (Maçaira et al., 2013; Snaith, 2013; Park, 2013). Soon after, the substitution of conducting TiO_2 by insulating Al_2O_3 in the mesoporous layer led to efficiencies of 10.9% (Snaith, 2013), with a significant open-circuit voltage increment and no reduction of the short-circuit current. This result provided evidence for the specific nature of these materials and suggested the possibility of using them in configurations other than DSSCs (Liu et al., 2013; Laban and Etgar, 2013).

Solar cells based on organometal halide perovskites have achieved PCEs as high as 22.7% within a research time of merely 5 years (Green et al., 2018). Studies have shown that devices can be fabricated in a planar configuration (no mesoporous layer used) (Fu et al., 2016) or without a hole-transport layer (Chen et al., 2015), with efficiencies being high enough to consider this material as the next step in photovoltaic technologies. Efficient perovskite-based solar cells have been prepared in a variety of device structures such as SSCs, hybrid organic or standard planar heterojunctions that all exhibit efficiencies reported to be over 10%, summarized in Fig. 16.9.

Perovskites are a large family of materials that share a generic chemical formula ABX_3 and a crystallographic system with the natural occurrent mineral $CaTiO_3$. Among the different perovskites, halide-based perovskites present semiconducting properties and have shown an impressive potential both in photovoltaics and in light-emitting devices. In this case, the X anion place is an halogen, normally I^-, but also Cl^- or Br^-, the M-site cation is for a metal such as Pb^{2+} or Sn^{2+} and, finally, the A position is generally occupied by a short organic chain such as methylammonium (MA) $CH_3NH_3^+$ and formamidinium (FA) $CH_3(NH_2)_2^+$), but single atoms such as Cs^+ can be also used. These perovskites are composed by earth-abundant elements and the fabrication process is also low cost and low temperature, making of this material a potential candidate for large-scale manufacture (Ball and Petrozza, 2016).

Different bandgaps are achievable by modifying the X-site composition (e.g., alloying iodine with bromine). Indeed, it is possible to change the bandgap of the semiconductor from 1.57 eV up to 2.3 eV covering the visible spectrum up to the near-infrared, as can be observed in Fig 16.10 (Sutter-Fella et al., 2016). One can take advantage of this to design tandem solar cells that would allow a broader absorption of the light and higher efficiencies (Eperon et al., 2016; Albrech et al., 2016; Fu et al., 2015) and to adapt the transparency of the devices to selective ranges of the solar spectrum. In particular, it has already been reported that it is possible to fabricate semitransparent solar cells based on perovskite materials with efficiencies as high as 14% with an average transmittance of 30% in the visible range (Roldán-Carmona et al., 2014; Eperon et al., 2014a,b). In addition, halide-based perovskites present a high absorption coefficient in the visible region, in the order of 10^4–$10^5\,cm^{-1}$ (De Wolf et al., 2014), which allows the absorption of most of the desired light within a 300–500-nm-thick layer with reflective back contacts (Ball et al., 2015).

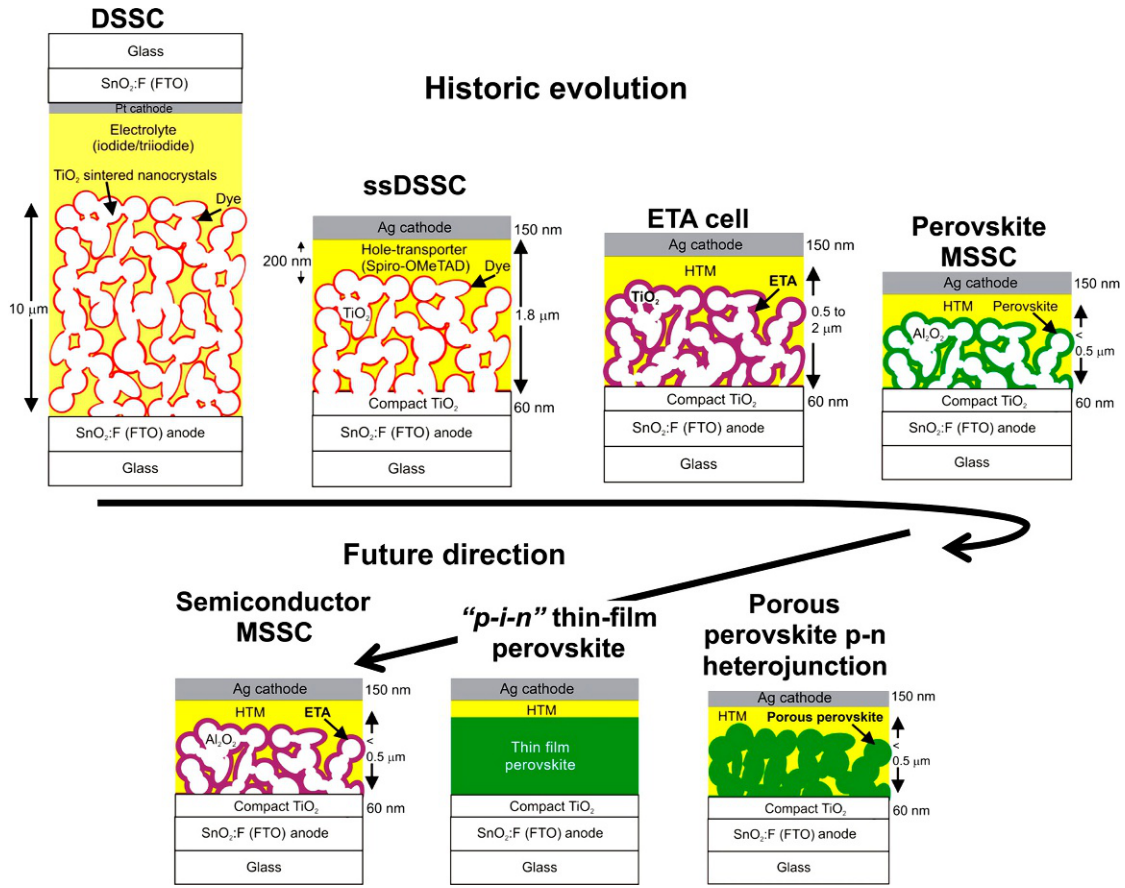


FIG. 16.9

Evolution of the structure of perovskite solar cells.

From Snaith, H.J., 2013. Perovskites: the emergence of a new era for low-cost, high efficiency solar cells. J. Phys. Chem. Lett. 4, 3623.

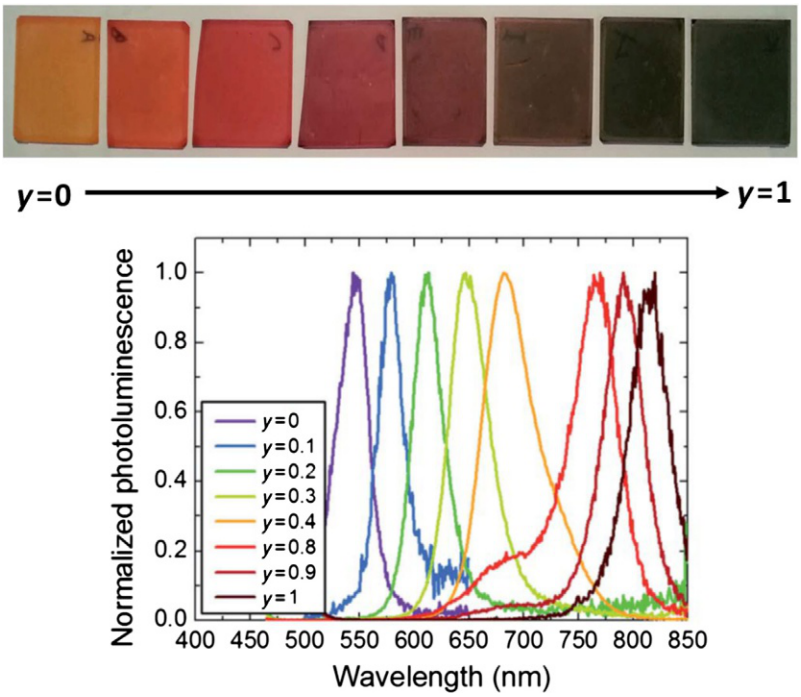


FIG. 16.10

Perovskite layers with different bandgaps (top) and photoluminescence of perovskite samples with different bandgaps controlled by the I/Br ratio.

From Eperon, G.E., Stranks, S.D., Menelaou, C., Johnston, M.B., Herz, L.M., Snaith H.J., 2014. Formamidinium lead trihalide: a broadly tunable perovskite for efficient planar heterojunction solar cells. Energy Environ. Sci. 7, 982.

Despite these amazing results, there is still a lot to learn about the behavior of perovskites in order to obtain maximum potential from these materials. For instance, the fact that no mesoporous layer is needed shows that perovskites can actually work like traditional semiconductors (Snaith, 2013). Furthermore, the analysis of the electrical properties, such as carrier density and mobility, points to a behavior more consistent with inorganic semiconductors than organic ones (Manser et al., 2016), while the unusual high luminescence yield, seemingly controlled by excitonic transitions is more like the organic semiconductors (Sharma et al., 2016). Also, some particular features that limit device performances, such as ion migration under voltage bias, have yet to be fully understood (Li et al., 2015).

At this point, this material presents the best record sheet in photovoltaics efficiency, but the possibility of maturing into a profitable technology is still burdened by its low stability (Niu et al., 2015). Although some of the limitations are inherent to

the perovskite itself, other sources of instability are related to the use of different selective contacts. Exploratory works in this sense have increased the stability (You et al., 2016), but the lifetime of the cells is still well behind (around some thousand hours) the necessities of a well-established technology.

Perovskite-based solar cells are generally fabricated on superstrate configuration, where light passes through the substrate (normally glass) and a transparent conductive oxide (TCO) layer (generally ITO or FTO) that works as the front contact. Afterwards, a large band-gap electron selective layer is deposited. Then, the perovskite absorber is deposited, and over it a hole-selective layer to finish the semiconductor structure and a metallic back contact.

Perovskite layers are generally deposited by chemical wet methods. A precursor solution where a mixture of PbI_3 and a cation-based iodide salts are dissolved in organic solvents is deposited over a TiO_2 /TCO coated substrate. Then the layer is subjected to a mild annealing at temperatures around 100–150°C, where the ions crystallize and form the perovskite polycrystalline layer. Crystalline quality, size, layer rugosity, and other structural characteristics are very sensitive to growth factors such as solvent nature, precursor ratio, temperature, and atmosphere annealing (Petrus et al., 2017). While a certain amount of humidity seems to be beneficial to the device stability (Ko et al., 2015), in general perovskite formation is always performed under neutral atmosphere conditions, under a glove box, and requires the device to be finished under the same conditions.

Also, perovskite layers can be deposited by physical methods. Co-evaporation systems where lead iodide and anion sources are used for the formation of the perovskite layer lead to very smooth films, but device performances are still shorter than the solution-processed ones (Petrus et al., 2017; Frolova et al., 2017).

For the carrier-selective layers, materials such as oxides and organic polymers are used. The traditional structure uses a mesoporous TiO_2 layer as the electron-selective contact and spiroOMeTAD as the hole-selective contact (Petrus et al., 2017). Nevertheless, due to different studies (Niu et al., 2015) that pinpoint the origin of degradation on these layers, alternative materials have successfully been tested such as NiO, MoO_x PEDOT:PSS, bathocuproine (BCP), and PCBM (Schulz et al., 2016; Yin et al., 2016; Zhu et al., 2017) The requirements for both materials are to have a large gap that permits light to go through up to the absorber layer, good work functions, and the possibility of depositing them at low temperature by methods that do not involve water-based solvents, for being respectful with the perovskite layer.

The combination of high bandgaps, low-cost deposition methods, and simplicity of the device has prompted the design of novel tandem cell designs with perovskite cells as subcells on top of already established technologies (Bailie et al., 2015). Tandem devices based on perovskites and other materials such as silicon (Bush et al., 2017), CIGS (Fu et al., 2016) or even këesterites (Todorov et al., 2014) have been proposed and even fabricated. While modeling suggests an important increase of the performance in the tandem system, the fabrication has been hindered by the elaboration of the interface between the two cells in a two-terminal

configuration. Four terminal devices show an increased absorption of the solar spectrum (Fu et al., 2015).

16.6 CONCLUSION

The use of thin films in the design of solar cells is of high interest in decreasing the quantity of material required, which accounts for a large part of the cost of the devices. Yet, when using thin films, new strategies have to be developed to minimize or avoid difficulties lowering the efficiency of devices such as inefficient absorption of solar photons, low mobilities of charge carriers and poor electronic transport properties, high density of defects, resistivity of transparent conductive oxides, reliability of materials and devices and so on. Furthermore, thin-film nonpollutant deposition processes on large surfaces, with high throughput, and at low energy expense, such as roll-to-roll or batch processing, are highly in demand for solar-cell fabrication. Last but not least, cheap and simple materials are required for terawatt-scale production of energy via solar cells. It is thus mandatory to consider abundant elements in the Earth's crust and their associated extraction costs. The merit figure to be maximized corresponds to the efficiency/cost ratio aimed at decreasing the kW per hour electricity cost produced from the Sun.

This chapter summarizes new insights in the use of nanotechnologies and nanostructures, such as nanowires, quantum dots, and photonic crystals, to tune or optimize the physical properties of materials in terms of photon absorption and photon-to-electron conversion and charge transport. Organic solar cells, which present the main advantage to allow the fine-tuning of materials by chemical synthesis, are also described. Indeed, we have faced in the past few years a very sharp increase of organic solar cell efficiencies (about 1% per year). This efficiency increase was mainly due to the discovery of new polymer materials the properties of which (absorption band, electronic properties, etc.) are shaped by the chemists. Nowadays, the development of new nonfullerene acceptors is a promising route in order to further improve both the device currents and voltages and thus the OSC performances. The next part of this chapter is devoted to new efficient processes developed at the industrial level to produce solar cells from CIGSSe and from earth-abundant materials composing CZTS. Finally, the last part of this chapter presents the organometallic perovskite-based solar cells, which had recently made a disruption in the photovoltaic research field in terms of materials research and performances.

To conclude, studying and understanding physical phenomena at the nanoscale, in the laboratories, will open many research directions in the future to reach high-efficiency, low-cost, nonpollutant, and reliable solar cells. Furthermore, many challenges mainly related to closing the gap between cell efficiencies and commercial modules, assuring low cost through increasing efficiency and securing source materials need to be addressed. All these challenges (plus those related to quality, reliability, and energy production) will need strong implication of R&D and development actors to lead the emerging technologies toward market.

REFERENCES

Albrech, S., Saliba, M., Correa Baena, J.P., Lang, F., Kegelmann, L., Mews, M., Steier, L., Abate, A., Rappich, J., Korte, L., Schlatmann, R., Nazeeruddin, M.K., Hagfeldt, A., Grätzel, M., Rech, B., 2016. Monolithic perovskite/silicon-heterojunction tandem solar cells processed at low temperature. Energy Environ. Sci. 9, 81.

Bailie, C.D., Christoforo, M.G., Mailoa, J.P., Bowring, A.R., Unger, E.L., Nguyen, W.H., Burschka, J., Pellet, N., Lee, J.Z., Grätzel, M., Noufi, R., Buonassisi, T., Salleo, A., McGehee, M.D., 2015. Semi-transparent perovskite solar cells for tandems with silicon and CIGS. Energy Environ. Sci. 8, 956.

Ball, J.M., Petrozza, A., 2016. Defects in perovskite-halides and their effects in solar cells. Nat. Energy. 1. 16149.

Ball, J.M., Stranks, S.D., Hörantner, M.T., Hüttner, S., Zhang, W., Crossland, E.J.W., Ramirez, I., Riede, M., Johnston, M.B., Friend, R.H., Snaith, H.J., 2015. Optical properties and limiting photocurrent of thin-film perovskite solar cells. Energy Environ. Sci. 8, 602.

Barreau, N., 2009. Indium sulfide and relatives in the world of photovoltaics. Sol. Energy 83 (3), 363.

Ben Dkhil, S., Duché, D., Gaceur, M., Thakur, A.K., Aboura, F., Escoubas, L., Simon, J.-J., Guerrero, A., Bisquert, J., Garcia-Belmonte, G., Bao, Q., Fahlman, M., Videlot-Ackermann, C., Margeat, O., Ackermann, J., 2014. Interplay of optical, morphological, and electronic effects of ZnO optical spacers in highly efficient polymer solar cells. Adv. Energy Mater. 4(18).

Ben Dkhil, S., Pfannmöller, M., Ata, I., Duche, D., Gaceur, M., Koganezawa, T., Yoshimoto, N., Simon, J.-J., Escoubas, L., Videlot-Ackermann, C., Margeat, O., Bals, S., Baeuerle, P., Ackermann, J., 2017. Time evolution studies of dithieno[3,2-b:2′,3′-d]pyrrole-based A-D-A oligothiophene bulk heterojunctions during solvent vapor annealing towards optimization of photocurrent generation. J. Mater. Chem. A 5, 1005–1013.

Bin, H., Zhang, Z.-G., Gao, L., Chen, S., Zhong, L., Xue, L., Yang, C., Li, Y., 2016. Non-fullerene polymer solar cells based on alkylthio and fluorine substituted 2D-conjugated polymers reach 9.5% efficiency. J. Am. Chem. Soc. 138 (13), 4657–4664.

Boudreault, P.-L.T., Najari, A., Leclerc, M., 2011. Processable low-bandgap polymers for photovoltaic applications. Chem. Mater. 23 (3), 456–469.

Brabec, C.J., Zerza, G., Cerullo, G., De Silvestri, S., Luzzati, S., Hummelen, J.C., Sariciftci, N.S., 2001. Tracing photoinduced electron transfer process in conjugated polymer/fullerene bulk heterojunctions in real time. Chem. Phys. Lett. 340, 232.

Brown, G.F., Wu, J., 2009. Third generation photovoltaics. Laser Photon. Rev. 3, 394–405.

Bush, K.A., Palmstrom, A.F., Yu, Z.J., Boccard, M., Cheacharoen, R., Mailoa, J.P., McMeekin, D.P., Hoye, R.L.Z., Bailie, C.D., Leijtens, T., Peters, I.M., Minichetti, M.C., Rolston, N., Prasanna, R., Sofia, S., Harwood, D., Ma, W., Moghadam, F., Snaith, H.J., Buonassisi, T., Holman, Z.C., Bent, S.F., McGehee, M.D., 2017. 23.6%-efficient monolithic perovskite/silicon tandem solar cells with improved stability. Nat. Energy 2, 17009.

Cao, L., White, J.S., Park, J.-S., Schuller, J.A., Clemens, B.M., Brongersma, M.L., 2009. Engineering light absorption in semiconductor nanowire devices. Nat. Mater. 8, 643–647.

Chen, Z., Cai, P., Chen, J., Liu, X., Zhang, L., Lan, L., Peng, J., Ma, Y., Cao, Y., 2014. Low band-gap conjugated polymers with strong interchain aggregation and very high hole

mobility towards highly efficient thick-film polymer solar cells. Adv. Mater. 26, 2586–2591.
Chen, W., Wu, Y., Yue, Y., Liu, J., Zhang, W., Yang, X., Chen, H., Bi, E., Ashraful, I., Grätzel, M., Han, L., 2015. Efficient and stable large-area perovskite solar cells with inorganic charge extraction layers. Science 350, 944.
Chirilă, A., Buecheler, S., Pianezzi, F., Bloesch, P., Gretener, C., Uhl, A.R., Fella, C., Kranz, L., Perrenoud, J., Seyrling, S., Verma, R., Nishiwaki, S., Romanyuk, E., Bilger, G., Tiwari, A.N., 2011. Highly efficient Cu(In,Ga)Se_2 solar cells grown on flexible polymer films. Nat. Mater. 10 (11), 857–861.
Chirilă, A., Reinhard, P., Pianezzi, F., Bloesch, P., Uhl, A.R., Fella, C., Kranz, L., Keller, D., Gretener, C., Hagendorfer, H., Jaeger, D., Erni, R., Nishiwaki, S., Buecheler, S., Tiwari, A.N., 2013. Potassium-induced surface modification of Cu(In,Ga)Se_2 thin films for high efficiency solar cells. Nat. Mater. 12, 1107.
Cocoyer, C., Rocha, L., Sicot, L., Geffroy, B., de Bettignies, R., Sentein, C., Fiorini-Debuisschert, C., Raimond, P., 2006. Implementation of submicrometric periodic surface structures toward improvement of organic-solar-cell performances. Appl. Phys. Lett. 88, 133808/1–3.
Conibeer, G., 2007. Third-generation photovoltaics. Mater. Today 10 (11), 42–50.
Contreras, M.A., Tuttle, J., Gabor, A., Tennant, A., Ramanathan, K., Asher, S., Franz, A., Keane, J., Wang, L., Noufi, R., 1996. High efficiency graded bandgap thin-film polycrystalline Cu(In,Ga)Se_2-based solar cells. Sol. Energy Mater. Sol. Cells 41–42, 231–246.
Contreras, M.A., Mansfield, L.M., Egaas, B., Li, J., Romero, M., Noufi, R., Rudiger-Voigt, E., Mannstadt, W., 2012. Wide bandgap Cu(In,Ga)Se2 solar cells with improved energy conversion efficiency. Prog. Photovolt. Res. Appl. 20, 843 (acc. publication). https://doi.org/10.1002/pip.2244.
Coutts, T.J., Young, D.L., Li, X., 2000. Characterization of transparent conducting oxides. MRS Bull. 25, 58.
Dang, M.T., Hirsch, L., Wantz, G., 2011. P3HT:PCBM, best seller in polymer photovoltaic research. Adv. Mater. 23, 3597–3602.
De Vos, A., 1980. Detailed balance limit of the efficiency of tandem solar cells. J. Phys. D. Appl. Phys. 13, 839.
De Wolf, S., Holovsky, J., Moon, S.-J., Löper, P., Niesen, B., Ledinsky, M., Haug, F.-J., Yum, J.-H., Ballif, C., 2014. Organometallic halide perovskites: sharp optical absorption edge and its relation to photovoltaic performance. J. Phys. Chem. Lett. 5, 1035.
Dimmler, B., Dittrich, H., Menner, R., Schock, H.W., 1987. In: Performance and optimization of heterojunctions based on Cu(Ga,In)Se_2.19th IEEE Photovoltaic Specialists Conference, New Orleans, Louisiana, May 1987, pp. 1454–1460.
Duché, D., Escoubas, L., Simon, J.-J., Torchio, P., Vervisch, W., Flory, F., 2008. Slow Bloch modes for enhancing the absorption of light in thin films for photovoltaic cells. Appl. Phys. Lett. 92. 193310.
Duché, D., Masclaux, C., Le Rouzo, J., Gourgon, C., 2015. Photonic crystals for improving light absorption in organic solar cells. J. Appl. Phys. 117 (5), 053108.
El Daif, O., Drouard, E., Gomard, G., Kaminski, A., Fave, A., Lemiti, M., Ahn, S., Kim, S., Roca i Cabarrocas, P., Jeon, H., Seassal, C., 2010. Absorbing one-dimensional planar photonic crystal for amorphous silicon solar cell. Opt. Express 18 (S3), A293–A299.
Eperon, G.E., Burlakov, V.M., Goriely, A., Snaith, H.J., 2014a. Neutral color semitransparent microstructured perovskite solar cells. ACS Nano 8, 591.

Eperon, G.E., Stranks, S.D., Menelaou, C., Johnston, M.B., Herz, L.M., Snaith, H.J., 2014b. Formamidinium lead trihalide: a broadly tunable perovskite for efficient planar heterojunction solar cells. Energy Environ. Sci. 7, 982.

Eperon, G.E., Leijtens, T., Bush, K.A., Prasanna, R., Green, T., Wang, J.T.-W., McMeekin, D.P., Volonakis, G., Milot, R.L., May, R., Palmstrom, A., Slotcavage, D.J., Belisle, R.B., Patel, J.B., Parrott, E.S., Sutton, R.J., Ma, W., Moghadam, F., Conings, B., Babayigit, A., Boyen, H.-G., Bent, S., Giustino, F., Herz, L.M., Johnston, M.B., McGehee, M.D., Snaith, H.J., 2016. Perovskite-perovskite tandem photovoltaics with optimized bandgaps. Science 9717, 1.

Fan, Z., Razavi, H., Do, J.-W., Moriwaki, A., Ergen, O., Chueh, Y.-L., Leu, P.W., Ho, J.C., Takahashi, T., Reichertz, L.A., Neale, S., Yu, K., Wu, M., Ager, J.W., Javey, A., 2009. Three-dimensional nanopillar-array photovoltaics on low-cost and flexible substrates. Nat. Mater. 8, 648–653.

Frolova, L.A., Anokhin, D.V., Piryazev, A.A., Luchkin, S.Y., Dremova, N.N., Stevenson, K.J., P Troshincite, P.A., 2017. Highly efficient all-inorganic planar heterojunction perovskite solar, cells produced by thermal coevaporation of CsI and PbI_2. J. Phys. Chem. Lett. 8, 67.

Fu, F., Feurer, T., Jäger, T., Avancini, E., Bissig, B., Yoon, S., Buecheler, S., Tiwari, A.N., 2015. Low-temperature-processed efficient semi-transparent planar perovskite solar cells for bifacial and tandem applications. Nat. Commun. 6, 8932.

Fu, F., Feurer, T., Weiss, T.P., Pisoni, S., Avancini, E., Andres, C., Buecheler, S., Tiwari, A.N., 2016. High-efficiency inverted semi-transparent planar perovskite solar cells in substrate configuration. Nat. Energy 2, 16190.

Gaceur, M., Dkhil, S.B., Duché, D., Bencheikh, F., Simon, J.-J., Escoubas, L., Mansour, M., Guerrero, A., Garcia-Belmonte, G., Liu, X., Fahlman, M., Dachraoui, W., Diallo, A.K., Videlot-Ackermann, C., Margeat, O., Ackermann, J., 2016. Ligand-free synthesis of aluminum-doped zinc oxide nanocrystals and their use as optical spacers in color-tuned highly efficient organic solar cells. Adv. Funct. Mater. 26 (2), 243–253.

Garnett, E., Yang, P.D., 2010. Light trapping in silicon nanowire solar cells. Nano Lett. 10 (3), 1082–1087.

GMO, 2017. Global Market Outlook for Solar Power 2017–2021. Europe, Solar Power.

Granath, K., Rockett, A., Bodegard, M., Nender, C., Stolt, L., 1995. In: Mechanical issues of Mo back contacts for Cu(In,Ga)Se_2 devices.13th European Photovoltaic Solar Energy Conference, Nice, France, October 1995.

Green, M.A., Emery, K., Hishikawa, Y., Warta, W., 2011. Solar cell efficiency tables (version 37). Prog. Photovolt. Res. Appl. 19, 84.

Green, M.A., Emery, K., Hishikawa, Y., Warta, W., Dunlop, E.D., Levi, D.H., Hohl-Ebinger, J., Ho-Baillie, A.W.Y., 2017. Solar cell efficiency tables (version 50). Prog. Photovolt. Res. Appl. 25, 668.

Green, M., Hishikawa, Y., Dunlop, E.D., Levi, D.H., Hohl-Ebinger, J., Ho-Baillie, A.W.Y., 2018. Solar cell efficiency tables (version 51). Prog. Photovolt. Res. Appl. 26, 3.

Gregg, B.A., 2003. Excitonic solar cells. J. Phys. Chem. B 107 (20), 4688–4698.

He, X., Gao, F., Tu, G., Hasko, D.G., Hüttner, S., Greenham, N.C., Steiner, U., Friend, R.H., Huck, W.T.S., 2011. Formation of well-ordered heterojunctions in polymer:PCBM photovoltaic devices. Adv. Funct. Mater. 21, 139–146.

Heather, A.S., Platt, H.A.S., Li, Y., Nowak, J.P., Van Hest, M.F.A.M., 2012. Atmospheric deposition techniques for photovoltaics. Photovolt. Technol. 19, 121–127.

Hoppe, H., Arnold, N., Sariciftci, N.S., Meissner, D., 2003. Modeling the optical absorption within conjugated polymer/fullerene-based bulk-heterojunction organic solar cells. Sol. Energy Mater. Sol. Cells 80, 105–113.

Hsieh, Y.-T., Chen, J.-Y., Shih, C.-C., Chueh, C.-C., Chen, W.-C., 2018. Mechanically robust, stretchable organic solar cells via buckle-on-elastomer strategy. Org. Electron. 53, 339–345.

Huang, C.-Y., Wang, D.-Y., Wang, C.-H., Chen, Y.-T., Wang, Y.-T., Jiang, Y.-T., Yang, Y.-J., Chen, C.-C., Chen, Y.-F., 2010. Efficient light harvesting by photon downconversion and light trapping in hybrid ZnS nanoparticles/Si nanotips solar cells. ACS Nano 4 (10), 5849–5854.

Huang, B.-R., Yang, Y.-K., Lin, T.-C., Yang, W.-L., 2012. A simple and low-cost technique for silicon nanowire arrays based solar cells. Sol. Energy Mater. Sol. Cells 98, 357–362.

Irwin, M.D., Buchholz, D.B., Hains, A.W., Chang, R.P.H., Marks, T.J., 2008. P-type semiconducting nickel oxide as an efficiency-enhancing anode interfacial layer in polymer bulk-heterojunction solar cells. PNAS 105 (8), 2783–2787.

Jackson, P., Wuerz, R., Hariskos, D., Lotter, E., Paetel, S., Witte, W., Powalla, M., 2016. Effects of heavy alkali elements in Cu(In,Ga)Se_2 solar cells with efficiencies up to 22.6%. Phys. Status Solidi RRL 10 (8), 583.

Jäger-Waldau, A., 2011. PV Status Report 2011. Office for Official Publications of the European Union, Brussels, Luxembourg. Available from: http://re.jrc.ec.europa.eu/refsys/.

Jeong, W.J., Kim, S.K., Park, G.C., 2006. Preparation and characteristic of ZnO thin film with high and low resistivity for an application of solar cell. Thin Solid Films 506–507, 180–183.

Jung, J.-Y., Guo, Z., Jee, S.-W., Um, H.-D., Park, K.-T., Lee, J.-H., 2010. A strong antireflective solar cell prepared by tapering silicon nanowires. Opt. Express 18 (S3), A286–A292.

Kandala, A., Betti, T., Fontcuberta i Morral, A., 2008. General theoretical considerations on nanowire solar cell designs. Phys. Status Solidi A 206 (1), 1–6.

Karg, F.H., 2001. Development and manufacturing of CIS thin film solar modules. Sol. Energy Mater. Sol. Cells 66, 645.

Kato, T., 2017. Cu(In,Ga)($Se,S)_2$ solar cell research in solar frontier: progress and current status. Jpn. J. Appl. Phys. 56. 04CA02.

Kayes, B.M., Atwater, H.A., Lewis, N.S., 2005. Comparison of the device physics principles of planar and radial p-n junction nanorod solar cells. J. Appl. Phys. 97. 114302.

Keyes, B.M., Hasoon, F., Dippo, P., Balcioglu, A., Abulfotuh, F., 1997. In: Influence of Na on the electro-optical properties of Cu(In,Ga)Se_2.Proceedings of the 26th PVSC, Anaheim, CA, p. 479.

Klenk, R., 2001. Characterisation and modelling of chalcopyrite solar cells. Thin Solid Films 387, 135.

Ko, H.S., Lee, J.-W., Park, N.G., 2015. 15.76% efficiency perovskite solar cells prepared under high relative humidity: Importance of PbI_2 morphology in two-step deposition of $CH_3NH_3PbI_3$. J. Mater. Chem. A 3, 8808.

Kronik, L., Cahen, D., Schock, H.W., 1998. Effects of sodium on polycrystalline Cu(In,Ga) Se2 and its solar cell performance. Adv. Mater. 10, 31–36.

Laban, W.A., Etgar, L., 2013. Depleted hole conductor-free lead halide iodide heterojunction solar cells. Energy Environ. Sci. 6, 3249.

Le Rouzo, J., Maestre, D., Barakel, D., Palais, O., Escoubas, L., Alfonso, C., Charrin, L., Gailhanou, M., 2009. In: Growth and characterization of Si nanowires by an electroless etching process.EU PVSEC Proceedings, pp. 408–410.

Li, X., Wang, X., Zhang, W., Wu, Y., Gao, F., Fang, Y., 2015. The effect of external electric field on the performance of perovskite solar cells. Org. Electron. 18, 107.
Li, S., Liu, W., Li, C.-Z., Shi, M., Chen, H., 2017. Efficient organic solar cells with non-fullerene acceptors. Small 13 (37), 1701120.
Liang, Y.W., Yue, F.D., Tsai, S.-T., Son, H.-J., Li, G., Yu, L., 2009. Development of new semiconducting polymers for high performance solar cells. J. Am. Chem. Soc. 131 (1), 56–57.
Lipomi, D.J., Tee, B.C.-K., Vosgueritchian, M., Bao, Z., 2011. Stretchable organic solar cells. Adv. Mater. 23, 1771–1775.
Liu, M., Johnston, M.B., Snaith, H.J., 2013. Efficient planar heterojunction perovskite solar cells by vapour deposition. Nature 501, 395.
Liu, X., Feng, Y., Cui, H., Liu, F., Hao, X., Conibeer, G., Mitzi, D.B., Green, M., 2016. The current status and future prospects of kesterite solar cells: a brief review. Prog. Photovolt. Res. Appl. 24, 879.
Lu, W., Lieber, C.M., 2006. Semiconductor nanowires. J. Phys. D. Appl. Phys. 39, R387.
Lu, L., Chen, W., Xu, T., Yu, L., 2015. High-performance ternary blend polymer solar cells involving both energy transfer and hole relay processes. Nat. Commun. 6, 7327.
Lunt, R.R., Osedach, T.P., Brown, P.R., Rowehl, J.A., Bulovic, V., 2011. Practical roadmap and limits to nanostructured photovoltaics. Adv. Mater. 23, 5712–5727.
Luque, A., 2011. Will we exceed 50% efficiency in photovoltaics? J. Appl. Phys. 110. 031301.
Luque, A., Martí, A., Stanley, C., 2012. Understanding intermediate-band solar cells. Nat. Photonics 6, 146–152.
Ma, W., Yang, C., Gong, X., Lee, K., Heeger, A.J., 2005. Thermally stable, efficient polymer solar cells with nanoscale control of the interpenetrating network morphology. Adv. Funct. Mater. 15 (10), 1617–1622.
Maçaira, J., Andrade, L., Mendes, A., 2013. Review on nanostructured photoelectrodes for next generation dye-sensitized solar cells. Renew. Sustain. Energy Rev. 27, 334.
Manser, J.S., Christians, J.A., Kamat, P.V., 2016. Intriguing optoelectronic properties of metal halide perovskites. Chem. Rev. 116, 12956.
Meijer, J.-M., Aarts, L., Van der Ende, B.M., Vlugt, T.J.H., Meijerink, A., 2010. Downconversion for solar cells in YF3:Nd3+, Yb3+. Phys. Rev. B. 81. 035107.
Monestier, F., Simon, J.J., Torchio, P., Escoubas, L., Flory, F., Bailly, S., De Bettignies, R., Guillerez, S., Defranoux, C., 2007a. Modeling the short-circuit current density of polymer solar cells based on P3HT:PCBM blend. Sol. Energy Mater. Sol. Cells 91, 405–410.
Monestier, F., Torchio, P., Simon, J.J., Escoubas, L., Cathelinaud, M., 2007b. Software for automatic optimization of the electromagnetic field in organic solar cells. Nonlinear Opt. Quantum Opt. 37, 159–168.
Morfa, A.J., Rowlen, K.L., Reilly, T.H., Romero, M.J., Van De Lagemaat, J., 2008. Plasmon-enhanced solar energy conversion in organic bulk heterojunction photovoltaics. Appl. Phys. Lett. 92. 013504.
Motiei, L., Yao, Y., Choudhury, J., Marks, T.J., van der Boom, M.E., Facchetti, A., 2010. Self-propagating molecular assemblies as interlayers for efficient inverted bulk-heterojunction solar cells. J. Am. Chem. Soc. 132 (36), 12528–12530.
Muskens, O.L., Gómez Rivas, J., Algra, R.E., Bakkers, E.P.A.M., Lagendijk, A., 2008. Design of light scattering in nanowire materials for photovoltaic applications. Nano Lett. 8 (9), 2638.
Naghavi, N., Abou-Ras, D., Allsop, N., Barreau, N., Bücheler, S., Ennaoui, A., Fischer, C.-H., Guillen, C., Hariskos, D., Herrero, J., Klenk, R., Kushiya, K., Lincot, D., Menner, R., Nakada, T., Platzer-Björkman, C., Spiering, S., Tiwari, A.N., Törndahl, T., 2010. Buffer

layers and transparent conducting oxides for chalcopyrite Cu(In,Ga)(S,Se)$_2$ based thin film photovoltaics: present status and current developments. Prog. Photovolt. Res. Appl. 18, 411–433.

Niggemann, M., Glatthaar, M., Gombert, A., Hinsch, A., Wittwer, V., 2004. Diffraction gratings and buried nano-electrodes – architectures for organic solar cells. Thin Solid Films 451–452, 619–623.

Niu, G., Guo, X., Wang, L., 2015. Review of recent progress in chemical stability of perovskite solar cells. J. Mater. Chem. A: Mater. Energy Sustain. 3, 8970.

Norrman, K., Madsen, M.V., Gevorgyan, S.A., Krebs, F.C., 2012. Degradation patterns in water and oxygen of an inverted polymer solar cell. J. Am. Chem. Soc. 132, 16883–16892.

Nozik, A.J., 1972. Optical and electrical properties of Cd_2SnO_4: a defect semiconductor. Phys. Rev. B 6, 453.

Nozik, A.J., 2008. Multiple exciton generation in semiconductor quantum dots. Chem. Phys. Lett. 457 (1–3), 3–11.

Park, N.G., 2013. Organometal perovskite light absorbers toward a 20% efficiency low-cost solid-state mesoscopic solar cell. J. Phys. Chem. Lett. 4, 2423.

Peet, J., Heeger, A.J., Bazan, G.C., 2009. "Plastic" solar cells: Self-assembly of bulk heterojunction nanomaterials by spontaneous phase separation. Acc. Chem. Res. 42, 1700–1708.

Petrus, M.L., Schlipf, J., Li, C., Gujar, T.P., Giesbrecht, N., Müller-Buschbaum, P., Thelakkat, M., Bein, T., Hüttner, S., Docampo, P., 2017. Capturing the sun: a review of the challenges and perspectives of perovskite solar cells. Adv. Energy Mater. 7, 1700264.

Pettersson, L.A.A., Roman, L.S., Inganas, O., 1999. Modeling photocurrent action spectra of photovoltaic devices based on organic thin films. J. Appl. Phys. 86 (1), 487–496.

Philips 66, 2016. http://investor.phillips66.com.

Pianezzi, F., Reinhard, P., Chirilă, A., Bissig, B., Nishiwaki, S., Buecheler, S., Tiwari, A.N., 2014. Unveiling the effects of post-deposition treatment with different alkaline elements on the electronic properties of CIGS thin film solar cells. Phys. Chem. Chem. Phys. 16, 8843.

Pillai, S., Perez-Wurfl, I., Conibeer, G.J., Green, M.A., 2011. Surface plasmons for improving the performance of quantum dot structures for third generation solar cell applications. Phys. Status Solidi C 8 (1), 181–184.

Rau, U., Schmitt, M., Hilburger, D., Engelhardt, F., Seifert, O., Parisi, J., Riedl, W., Rimmasch, J., Karg, F., 1996. In: Influence of Na and S incorporation on the electronic transport properties of Cu(In,Ga)Se$_2$ solar cells. Proceedings of the 25th PVCS, Washington DC, p. 1005.

Ren, S., Chang, L.-Y., Lim, S.-K., Zhao, J., Smith, M., Zhao, N., Bulović, V., Bawendi, M., Gradečak, S., 2011. Inorganic–organic hybrid solar cell: bridging quantum dots to conjugated polymer nanowires. Nano Lett. 11 (9), 3998–4002.

Rezgui, B., Sibai, A., Nychyporuk, T., Lemiti, M., Bremond, G., Maestre, D., Palais, O., 2010. Effect of total pressure on the formation and size evolution of silicon quantum dots in silicon nitride films. Appl. Phys. Lett. 96 (18), 183105–183105-3.

Roldán-Carmona, C., Malinkiewicz, O., Betancur, R., Longo, G., Momblona, C., Jaramillo, F., Camacho, L., Bolink, H.J., 2014. High efficiency single-junction semitransparent perovskite solar cells. Energy Environ. Sci. 7 (9), 2968.

Rudmann, D., Bilger, G., Kaelin, M., Haug, F.J., Zogg, H., Tiwari, A.N., 2003. Effects of NaF coevaporation on structural properties of Cu(In,Ga)Se$_2$ thin films. Thin Solid Films 431–432, 37–40.

Schulz, P., Tiepelt, J.O., Christians, J.A., Levine, I., Edri, E., Sanehira, E.M., Hodes, G., Cahen, D., Kahn, A., 2016. High-work-function molybdenum oxide hole extraction contacts in hybrid organic-inorganic perovskite solar cells. ACS Appl. Mater. Interfaces 8, 31491.

Semonin, O.E., Luther, J.M., Choi, S., Chen, H.-Y., Gao, J., Nozik, A.J., Beard, M.C., 2011. Peak external photocurrent quantum efficiency exceeding 100% via MEG in a quantum dot solar cell. Science 334 (6062), 1530–1533.

Shafarman, W.N., Klenk, R., McCandless, B.E., 1996. Device and material characterization of $Cu(InGa)Se_2$ solar cells with increasing band gap. J. Appl. Phys. 79 (9), 7324.

Sharma, V., Aharon, S., Gdor, I., Yang, C., Etgara, L., Ruhman, S., 2016. New insights on exciton binding and relaxation from high time resolution ultrafast spectroscopy of $CH_3NH_3PbI_3$ and $CH_3NH_3PbBr_3$ films. J. Mater. Chem. A 4, 3546.

Shockley, W., Queisser, H.J.J., 1961. Efficiency loss mechanisms: theory and characterization. Appl. Phys. 32, 510–519.

Skompska, M., 2010. Hybrid conjugated polymer/semiconductor photovoltaic cells. Synth. Met. 160, 1–15.

Snaith, H.J., 2013. Perovskites: the emergence of a new era for low-cost, high efficiency solar cells. J. Phys. Chem. Lett. 4, 3623.

Søndergaard, R., Hösel, M., Angmo, D., Larsen-Olsen, T.T., Krebs, F.C., 2012. Roll-to-roll fabrication of polymer solar cells. Mater. Today 15 (1–2), 36–49.

Spurgeon, J.M., Atwater, H.A., Lewis, N.S., 2008. A comparison between the behavior of nanorod array and planar Cd(Se, Te) photoelectrodes. J. Phys. Chem. C 112, 6186–6193.

Stenzel, O., Stendhal, A., Voigtsberger, K., von Borczyskowski, C., 1995. Enhancement of the photovoltaïc conversion efficiency of copper phthalocyanine thin film devices by incorporation of metal clusters. Sol. Energy Mater. Sol. Cells 37, 337–348.

Sun, Y., Seo, J.H., Takacs, C.J., Seifter, J., Heeger, A.J., 2011. Inverted polymer solar cells integrated with a low-temperature-annealed sol-gel-derived ZnO film as an electron transport layer. Adv. Mater. 23, 1679–1683.

Sutter-Fella, C.M., Li, Y., Amani, M., Ager III, J.A., Toma, F.M., Yablonovitch, E., Sharp, I.D., Javey, A., 2016. High photoluminescence quantum yield in band gap tunable bromide containing mixed halide perovskites'. Nano Lett. 16, 800.

Takagi, H., Ogawa, H., Yamazaki, Y., Ishizaki, A., Nakagiri, T., 1990. Quantum size effects on photoluminescence in ultrafine Si particles. Appl. Phys. Lett. 56, 2379.

Tang, C.W., 1986. 2-Layer organic photovoltaic cell. Appl. Phys. Lett. 48, 183.

Theodoropoulou, S., Papadimitriou, D., Anestou, K., Cobet, C., Esser, N., 2009. Optical properties of $CuIn_{1-x}Ga_xSe_2$ quaternary alloys for solar-energy conversion. Semicond. Sci. Technol. 24. 015014.

Thornton, J.A., Hoffman, D.W., 1989. Stress-related effects in thin films. Thin Solid Films 171, 5.

Tisdale, W.A., Williams, K.J., Timp, B.A., Norris, D.J., Aydil, E.S., Zhu, X.-Y., 2010. Hot-electron transfer from semiconductor nanocrystals. Science 328, 1543.

Todorov, T., Gershon, T., Gunawan, O., Sturdevant, C., Guha, S., 2014. Perovskite-kesterite monolithic tandem solar cells with high open-circuit voltage perovskite-kesterite monolithic tandem solar cells with high open-circuit voltage. Appl. Phys. Lett. 105, 173902.

Topič, M., 2011. Contemporary inorganic thin film photovoltaic materials and technologies. Contemp. Mater. II-2, 94–102.

Tsukazaki, A., Ohtomo, A., Kawasaki, M., 2006. High-mobility electronic transport in ZnO thin films. Appl. Phys. Lett. 88, 152106:1.

Wadia, C., Alivisatos, P.A., Kammen, D.M., 2009. Materials availability expands the opportunity for large-scale photovoltaics deployment. Environ. Sci. Technol. 43 (6), 2072–2077. https://doi.org/10.1021/es8019534.

Wan, Q., Guo, X., Wang, Z., Li, W., Guo, B., Ma, W., Zhang, M., Li, Y., 2016. 10.8% efficiency polymer solar cells based on PTB7-Th, and PC 71 BM via binary solvent additives treatment. Adv. Funct. Mater. 26, 6635–6640.

Wang, W., Winkler, M.T.T., Gunawan, O., Gokmen, T., Todorov, T.K., Zhu, Y., Mitzi, D.B., 2014. Device characteristics of CZTSSe thin film solar cells with 12.6% efficiency. Adv. Energy Mater. 4. (7) 1301465.

Westphalen, W., Kreibig, U., Rostalski, J., Lüth, H., Meissner, D., 2000. Metal cluster enhanced organic solar cells. Sol. Energy Mater. Sol. Cells 61, 97–105.

Xue, J., Rand, B.P., Uchida, S., Forrest, S.R., 2005. Mixed donor-acceptor molecular heterojunctions for photovoltaic applications', II. Device performance. J. Appl. Phys. 98. 124903.

Yablonovitch, E., Cody, G.D., 1982. Intensity enhancement in textured optical sheets for solar cells. IEEE Trans. Electron Devices 29, 300–305.

Yan, Y., 2011. In: Understanding of defect physics in polycrystalline photovoltaic materials. Presented at the 37th IEEE Photovoltaic Specialists Conference (PVSC 37) Seattle, Washington June 19–24, 2011. Conference paper NREL/CP-5200–50650, Available from: http://www.nrel.gov/docs/fy11osti/50650.pdf.

Yin, X., Chen, P., Que, M., Xing, Y., Que, W., Niu, C., Shao, Y., 2016. Highly efficient flexible perovskite solar cells using solution-derived NiO_x hole contacts. ACS Nano 10, 3630.

Yip, H.-L., Alex Jen, K.-Y., 2012. Recent advances in solution-processed interfacial materials for efficient and stable polymer solar cells. Energy Environ. Sci. 5, 5994–6011.

Yoon, J.-H., Yoon, K.-H., Kim, J.-K., Kim, W.-M., Park, J.-K., Lee, T.S., Baik, Y.-J., Seong, T.-Y., Jeong, J.-H., 2010. Effect of the Mo back contact microstructure on the preferred orientation of CIGS thin films.35th IEEE Photovoltaic Specialists Conference, Hawaii Convention Center (USA), 20–25 June 2010, p. 2443.

You, J., Meng, L., Song, T.B., Guo, T.F., Yang, Y., Chang, W.-H., Hong, Z., Chen, H., Zhou, H., Chen, Q., Liu, Y., De Marco, N., Yang, Y., 2016. Improved air stability of perovskite solar cells via solution-processed metal oxide transport layers. Nat. Nanotechnol. 11, 75.

Yu, G., Heeger, A.J., 1995. Charge separation and photovoltaic conversion in polymer composites with internal donor/acceptor heterojunctions. J. Appl. Phys. 78, 4510.

Yu, R., Ching, K.-L., Lin, Q., Leung, S.-F., Arcrossito, D., Fan, Z., 2011. Strong light absorption of self-organized 3-D nanospike arrays for photovoltaic applications. ACS Nano 5 (11), 9291–9298.

Zhang, Z.-G., Wang, J., 2012. Structures and properties of conjugated donor–acceptor copolymers for solar cell applications. J. Mater. Chem. 22, 4178–4187.

Zhang, F., Xua, X., Tang, W., Zhang, J., Zhuoa, Z., Wang, J., Wang, J., Xu, Z., Wang, Y., 2011. Recent development of the inverted configuration organic solar cells. Sol. Energy Mater. Sol. Cells 95 (7), 1785–1799.

Zhao, J., Li, Y., Yang, G., Jiang, K., Lin, H., Ade, H., Ma, W., Yan, H., 2016. Efficient organic solar cells processed from hydrocarbon solvents. Nat. Energy. 1, 15027.

Zhao, F., Dai, S., Wu, Y., Zhang, Q., Wang, J., Jiang, L., Ling, Q., We, Z.i., Ma, W., You, W., Wang, C., Zhan, X., 2017. Single-junction binary-blend nonfullerene polymer solar cells with 12.1% efficiency. Adv. Mater. 1700144.

Zhu, J., Yu, Z., Burkhard, G.F., Hsu, C.-M., Connor, S.T., Xu, Y., Wang, Q., McGehee, M., Fan, S., Cui, Y., 2009. Optical absorption enhancement in amorphous silicon nanowire and nanocone arrays. Nano Lett. 9 (1), 279–282. https://doi.org/10.1021/nl802886y.

Zhu, Z., Zhao, D., Chueh, C.-C., Shi, X., Li, Z., Jen, A.K.-Y., 2017. Highly efficient and stable perovskite solar cells enabled by all-crosslinked charge-transporting layers. Joule 2, 1.

FURTHER READING

Green, M.A., 2007. Thin film solar cells: review of materials, technologies and commercial status. J. Mater. Sci. Mater. Electron. 18, S15–S19.

Hava, S., Auslender, M., 2000. Design and analysis of low-refection grating microstructures for a solar energy absorber. Sol. Energy Mater. Sol. Cells 61, 143–151.

Hüpkes, J., Rech, B., Kluth, O., Repmnn, T., Zwaygardt, B., Müller, J., Drese, R., Wuttig, M., 2006. Surface textured MF-sputtered ZnO films for microcrystalline silicon-based thin-film solar cells. Sol. Energy Mater. Sol. Cells 90, 3054–3060.

King, R.R., Law, D.C., Edmondson, K.M., Fetzer, C.M., Kinsey, G.S., Yoon, H., Sherif, R.A., Karam, N.H., 2007. 40% efficient metamorphic GaInP/GalnAs/Ge multijunction solar cells. Appl. Phys. Lett. 90 (18), 183516.

Lin, Y., Wang, J., Zhang, Z.-G., Bai, H., Li, Y., Zhu, D., Zhan, X., 2015. An electron acceptor challenging fullerenes for efficient polymer solar cells. Adv. Mater. 27, 1170.

Liu, W.F., Du, G.T., Sun, Y.F., Bian, J.M., Cheng, Y., Yang, T.P., Yang, Y.C., Xu, Y.B., 2007. Effects of hydrogen flux on the properties of Al-doped ZnO films sputtered in Ar + H_2 ambient at low temperature. Appl. Surf. Sci. 253 (6), 2999–3003.

Minami, T., Sonohara, H., Kakumu, T., Takata, S., 1995. Highly transparent and conductive $Zn_2In_2O_5$ thin films prepared by RF magnetron sputtering. Jpn. J. Appl. Phys. 34, L971–L974.

Oh, B.-Y., Jeong, M.-C., Kim, D.-S., Lee, W., Myoung, J.-M., 2005. Post-annealing of Al-doped ZnO films in hydrogen atmosphere. J. Cryst. Growth 281, 475–480.

Tarrant, D.E., 2006. CIS module process R&D. Final technical report to NREL, October 2005–June 2006.

Theyv, B., Sallet, V., Jomard, F., Lusson, A., Rommeluere, J.F., Teukam, Z., 1997. Effects of intentionally introduced hydrogen on the electrical properties of ZnO layers grown by metalorganic chemical vapor deposition. J. Appl. Phys. 91, 3922.

Yang, L.-G., Chen, L., Bai, R., Yang, F., Wang, M., Chen, H.-Z., 2007. Modelling of organic nanograting heterojunctions for photoelectric conversion. Sol. Energy Mater. Sol. Cells 91, 1110–1119.

Zank, J., Mehilin, M., Fritz, H.P., 1996. Electrochemical codeposition of indium and gallium for chalcopyrite solar cells. Thin Solid Films 286, 259.

Zhang, K., Zhu, F., Huan, C.H.A., Wee, A.T.S., 1999. Effect of hydrogen partial pressure on optoelectronic properties of indium tin oxide thin films deposited by radio frequency magnetron sputtering method. J. Appl. Phys. 86, 974.

Zhou, Z., Kato, K., Komaki, T., Yoshino, M., Yukawa, H., Morinaga, M., Morita, K., 2004. Effects of dopants and hydrogen on the electrical conductivity of ZnO. J. Eur. Ceram. Soc. 24, 139.

CHAPTER

17 Optical coatings for security and authentication devices

Bill Baloukas, Ludvik Martinu
Department of Engineering Physics, Polytechnique Montréal, Montreal, QC, Canada

17.1 INTRODUCTION

Counterfeiting is unfortunately here to stay. Besides the most frequently considered security documents such as passports and identity cards, as well as valuable documents such as banknotes and credit cards, counterfeiting also affects everyday consumer products from golf clubs to airplane parts. In fact, the Federal Aviation Administration (FAA) estimates that some 520,000 counterfeit parts are installed in planes each year (Wotherspoon and Cheng, 2009). Other than significant financial consequences—economic losses were estimated to be between 1.1 and 1.6 trillion dollars in 2015 (Frontier Economics, 2016)—it is the public's safety that is most at risk. Indeed, copied products made without any regulation and supervision rarely fulfill quality and safety requirements. A perfect example of this is counterfeit pharmaceutical products that, according to the World Health Organization (WHO), may represent up to 25% of the available medicine in developing countries (World Health Organization, 2005). It is therefore no surprise that governments and institutions have always wielded technology to their advantage to protect their documents and products.

Historically, currency has always benefited from the most advanced security devices. Before the advent of such devices, one of the most popular methods of anticounterfeiting was the death penalty (van Renesse, 2006). Although this may have been an effective means of discouragement it was abandoned as human right issues made headway. As a result, emphasis was put on printing bank notes with intricate and complex images, distinctive typefaces, exclusive colored inks, watermarks, microprinting, and unique serial numbers. These features were sufficient until the arrival of accurate color copiers and, more recently, scanners and high-resolution printers (so-called digifeiting). Incidentally, color was introduced on banknotes in part due to the appearance of black and white photography. To counteract these potentially serious threats, optically variable devices (OVDs) based on diffraction (diffractive optically variable image devices (DOVIDs): holograms, stereograms, kinegrams, etc.) and interference (interference-based security devices—ISDs) were

Optical Thin Films and Coatings. https://doi.org/10.1016/B978-0-08-102073-9.00017-5
Copyright © 2018 Elsevier Ltd. All rights reserved.

introduced; the iridescence presented by these devices inhibits the use of standard reprographic technologies. It is important to note that no device is infallible and for this reason modern banknotes benefit from the use of multiple features, each with its own specific purpose (Church, 2001).

Although all of these features have contributed in some way to the fight against counterfeiting, one must never forget that even the best features are rendered useless without the participation of the general public. It is now recognized that public awareness and understanding, provided through education, is crucial in increasing counterfeit detection (DiNunzio and Church, 2002). As a result, security features should always remain simple to use and the effects they present should be easy to remember. Indeed, despite the presence of multiple devices, studies have shown that, on average, the public remembers a fairly low number of them (1.7 currency features in The Netherlands in 1999, de Heij, 2002). In another remarkable example, it was shown that the awareness level in the United States for the black to green color shifting feature on American banknotes was only 17% in 2004 (Setlakwe and DiNunzio, 2004).

In 1968, the Bank of Canada approached the National Research Council (NRC) for ideas on novel security devices. The NRC, spearheaded by Dobrowolski, proposed optical interference coatings as potential candidates (Dobrowolski et al., 1973; Baird et al., 1975). Although a feature often considered as undesirable in the field of optical filters, the observed angular color change was judged not only as an excellent counterfeiting deterrent but also as an efficient and simple means of authentication for the general public. These structures also had the added advantage of being machine readable (Davies and Dobrowolski, 1996; Coombs et al., 2006).

In December 1987, the Bank of Thailand introduced a commemorative banknote protected with optically variable ink (OVI) produced by Optical Coating Laboratory, Inc. (OCLI). A few months later, in April 1988, British Columbia introduced driver's licenses displaying a transparent to red color shifting five-layer ISD (made by Identicard Ltd. and NRC). In December 1989, following extensive work at the NRC in collaboration with Vadeko International, an engineering firm, the Bank of Canada introduced its first 50-dollar bill with a gold to green color shifting ISD. Since then, ISDs have demonstrated excellent efficiency (Klein et al., 2004) and are highly appreciated by the general public (Setlakwe and DiNunzio, 2004); for example, more than 40 metric tons of optically variable pigments (OVPs) are produced yearly (Weinert, 2006) and OVI is used on the currencies of more than 100 countries (Despland et al., 2008).

17.2 BASIC PRINCIPLES AND STRUCTURES CURRENTLY APPLIED

Let us now consider the basic principles behind the use of optical coatings for security purposes. As previously mentioned, it is the intrinsic color shift observed as a function of the observation angle which is the key feature of ISDs. The color change

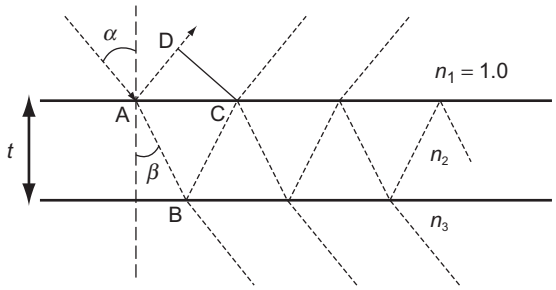


FIG. 17.1

Multiple reflections in a thin film of refractive index n_2 and thickness t. The incident medium is air and therefore $n_1 = 1$.

is due to a shift in the spectral characteristics of the filter towards shorter wavelengths at higher angles of incidence. This can be demonstrated by considering the case of a single thin film of refractive index n_2 and thickness t (see Fig. 17.1). The difference in optical paths Δ between the beam which travels inside the film (ABC) and the incident beam which was simply reflected at point A (AD) is given by (ABC)n_2 − (AD) n_1 (in the case where absorption is negligible). One can show following simple trigonometry that

$$\Delta = 2t\sqrt{n_2{}^2 - \sin\alpha^2} \quad \text{if } n_1 = 1 \tag{17.1}$$

where α is the angle of incidence of the beam. As α is increased, Δ is seen to decrease and therefore if one has constructive interference at λ_0 at normal incidence (i.e., Δ contains an integer number of wavelengths λ_0), this same constructive interference will occur at a $\lambda < \lambda_0$ at higher α values. Consequently, all interference-based devices will shift towards shorter wavelengths as a function of the observation angle. A device having a gold color at normal incidence will thus shift towards the green and eventually blue when observed at a more inclined angle.

Note that the final optical path difference also depends on the presence of soft (when going from a high to low refractive index) and/or hard (when going from a low to high refractive index) reflections at points A and B. In the case where the incident medium is air, point A will typically present a hard reflection and thus a $\lambda/2$ phase shift. For example, if the thickness of a film is equal to a quarter-wave ($t = \lambda/4n_2$) then Eq. (17.1) results in a path difference of $\lambda/2$ at normal incidence. Now, if the index of this quarter-wave film is higher than that of the substrate, a hard reflection will only be present at point A. The total path difference will thus be equal to zero and constructive interference will take place between both beams (increased reflectance).

On the contrary, if the refractive index of the film is lower than that of the substrate, hard reflections will be present at both points A and B. As a result, the final path difference will be $\lambda/2$, and destructive interference will ensue (decreased reflectance, i.e., antireflection). Correspondingly, the constructive and destructive

interference conditions will be inverted for a film of half-wave ($t = \lambda/2n_2$) thickness. Both these specific thicknesses are very often the basis of many classic filter designs. For example, one can construct a reflector by alternating high (H) and low (L) refractive index quarter-wave thick materials ($[HL]^xH$ where x is an integer) or fabricate a Fabry-Perot filter by separating two reflectors by a half-wave ($[HL]^xHH[LH]^x$).

It is worth mentioning that single dielectric layer structures (e.g., pearl luster or nacreous pigments) benefiting from interference effects have been used for their high luster and brilliance in many applications such as plastics, cosmetics, and paints (Pfaff, 2004); one such example is TiO_2-covered mica flakes. However, the fact that these pigments offer practically no color change as a function of the observation angle limits their use for security applications.

Two main categories of optical filters exist: those based on all-dielectric materials and those based on metallic and dielectric materials (metal-dielectric filters). Using dielectric materials with negligible absorption in the visible offers the possibility of a device which can be used both in reflection and in transmission (e.g., through the use of a window or when placed over printed information). On the other hand, a high number of layers is often required to obtain a sufficiently high color saturation which will inevitably increase fabrication costs. Addition of metallic layers offers the opportunity of rapidly increasing the reflectance and thus decreases the number of layers required as well as the total cost. On the other hand, the high absorption of metallic films drastically decreases the transmission as well as the maximum attainable reflection, and it can thus limit their use in particular applications. Although more expensive, it has also been shown that all-dielectric filters possess a much higher chemical and mechanical stability over time when compared to metallic layers which have a tendency to age in an unpredictable manner (Dobrowolski et al., 1989; Çetinörgü-Goldenberg et al., 2011). As a result, metal-dielectric structures must typically be laminated for protection. Note that lamination decreases the saturation of colors due to the added surface reflection and, considering Snell's refraction law, can also limit the maximum incidence angle and thus the color shift (Dobrowolski et al., 1989).

17.2.1 ALL-DIELECTRIC FILTERS

Over the years, there have been a multitude of proposed devices. In his paper published in 1973 (Dobrowolski et al., 1973), Dobrowolski proposed numerous all-dielectric filters with interesting properties, mainly, a red to blue color shifting filter, a broad-band reflector which would hide underlying information at normal incidence and become transparent at higher angles, and a transparent to red filter (a reflection peak in the near-infrared would shift into the visible). Note that the latter two effects are more difficult to obtain convincingly with metal-dielectric filters.

As previously mentioned, for physical reasons one typically observes color changes towards shorter wavelengths. In this regard, another interesting filter design exists, known for its reverse color shift from blue to red. This effect is obtained by carefully positioning two reflectance/transmittance bands, one in the

blue wavelength region and one in the near-infrared. Thus, when the filter is tilted, the blue band shifts into the ultraviolet (UV), whereas the band in the near-infrared falls into the visible (red).

One example of an all-dielectric filter applied for security is the gold to green color shifting filter present on the 1986 Birds of Canada banknote series. More precisely, this filter was based on five layers of SiO_2 and ZrO_2 (HL^3HL^3H at 585 nm) (Rolfe, 1990) (see Fig. 17.2 for simulated spectra of the gold to green color shift of this particular device). The filter was transferred from a polyethylene terephthalate (PET) substrate covered by a release layer of organic or synthetic wax (Glick et al., 1994) using a UV curable black adhesive developed by 3M (Dobrowolski et al., 1989). Indeed, when using all-dielectric filters, the background onto which the filter is apposed is very important. When using a white background, the light which is transmitted through the filter will be reflected back towards the observer, thus adding itself to the reflected beam and resulting in a decreased saturation (reflection and transmission are complementary in the absence of absorption). Obviously, the amount of light which is reflected back specularly will greatly depend on the surface roughness of the background. As a result, a black background is often used to eliminate the transmitted component of the light. Since optical filters reflect light specularly, it can be difficult to observe the color shift when using a single light source; artificially roughening the surface has been shown to help. This is not the

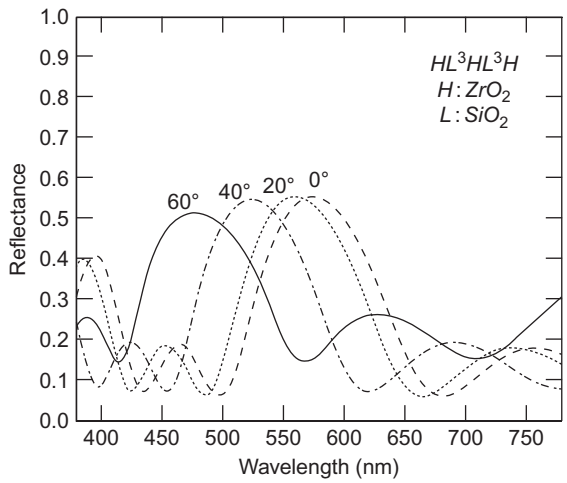


FIG. 17.2

Reflection spectra at various angles (for unpolarized light) of an all-dielectric interference filter simulating the five-layer optical security device initially developed for the Bank of Canada. The high refractive index material is ZrO_2 ($n_{550\ nm} = 1.88$—taken from the J.A. Woollam material library) and the low refractive index SiO_2 ($n_{550\ nm} = 1.46$) (Palik, 1985). The structure of the device is indicated in the upper right corner.

case for filters used in transmission, since authentication can simply be made by positioning the filter towards a light source and looking through it.

Placing a filter over sensitive information can also limit forgery while still allowing the information to be read. In fact, tamper evident filters have been developed which exhibit an irreversible color change when tampered with; for example, when an individual tries to remove a filter to transfer it onto another document. This effect can be obtained by modifying the adherence between two layers of a thin-film stack (Smits et al., 1989; Bishop, 2001; Phillips et al., 1988).

17.2.2 METAL-DIELECTRIC FILTERS

The most popular metal-dielectric structure currently in use is generally based on the following three-layer system: a metallic reflector, followed by a dielectric spacer, and completed by a thin, partially absorbing film. Often described as Fabry-Perot-like, this structure allows one to obtain a very high color saturation with a minimum of layers due to a combination of interference and of selective absorption (at specific wavelengths the electric field reaches a maximum at the absorber) (Phillips, 1994). This absorption also results in a lower brightness when compared with absorption-free all-dielectric filters.

The choice of material for each of the individual layers as well as their thickness is made to increase performance and obtain the desired color shifting properties. Modifying the thickness of the spacer allows one to adjust the position of the reflection peaks (see Fig. 17.3). In the example presented in Fig. 17.3A, the reflection of a Fabry-Perot-like structure based on $Al|MgF_2|Cr$ is shown for various thicknesses of MgF_2: two quarter-waves (QWs), four QWs, and six QWs at 575 nm (knowing that one QW $= \lambda/4n$ and two QWs is one half-wave). One can see how the width of the main peak decreases as the thickness is increased; this correspondingly increases the saturation in color (curve shown is farther away from the origin in the $L^*a^*b^*$ color space in Fig. 17.3A). Thicknesses are therefore typically chosen between 2 and 8 QWs. On the other hand, the use of too many QWs results in multiple peaks in the visible and can thus lead to desaturated colors (Phillips, 1990). One can also see, in the present example, that the color varies from gold to green and eventually to blue. To obtain a simplified two-color shift, considered more obvious for lay viewers (Lancaster and Mitchell, 2004), it has been shown that an overlying colored dye can filter colors at high angles of incidence (e.g., a yellow dye to block blue light) (Berning and Phillips, 1987).

As for the spacer material, it can be shown that choosing a low refractive index dielectric material increases the color variation (from Snell's law $n_1 \sin a = n_2 \sin \beta$; β will be larger for lower values of n_2) so that SiO_2 or MgF_2 is most often the material of choice. This is clearly demonstrated in Fig. 17.3B for three spacer materials of a thickness of 4QW: Al_2O_3 ($n_{550\ nm} = 1.77$), SiO_2 ($n_{550\ nm} = 1.49$), and MgF_2 ($n_{550\ nm} = 1.38$).

To increase the brightness of the filter, metals possessing a high reflectance and neutral color such as Ag and Al are typically chosen as the bottom reflector. Fig. 17.3C shows the effect of different metals when choosing from Ag, Al, and

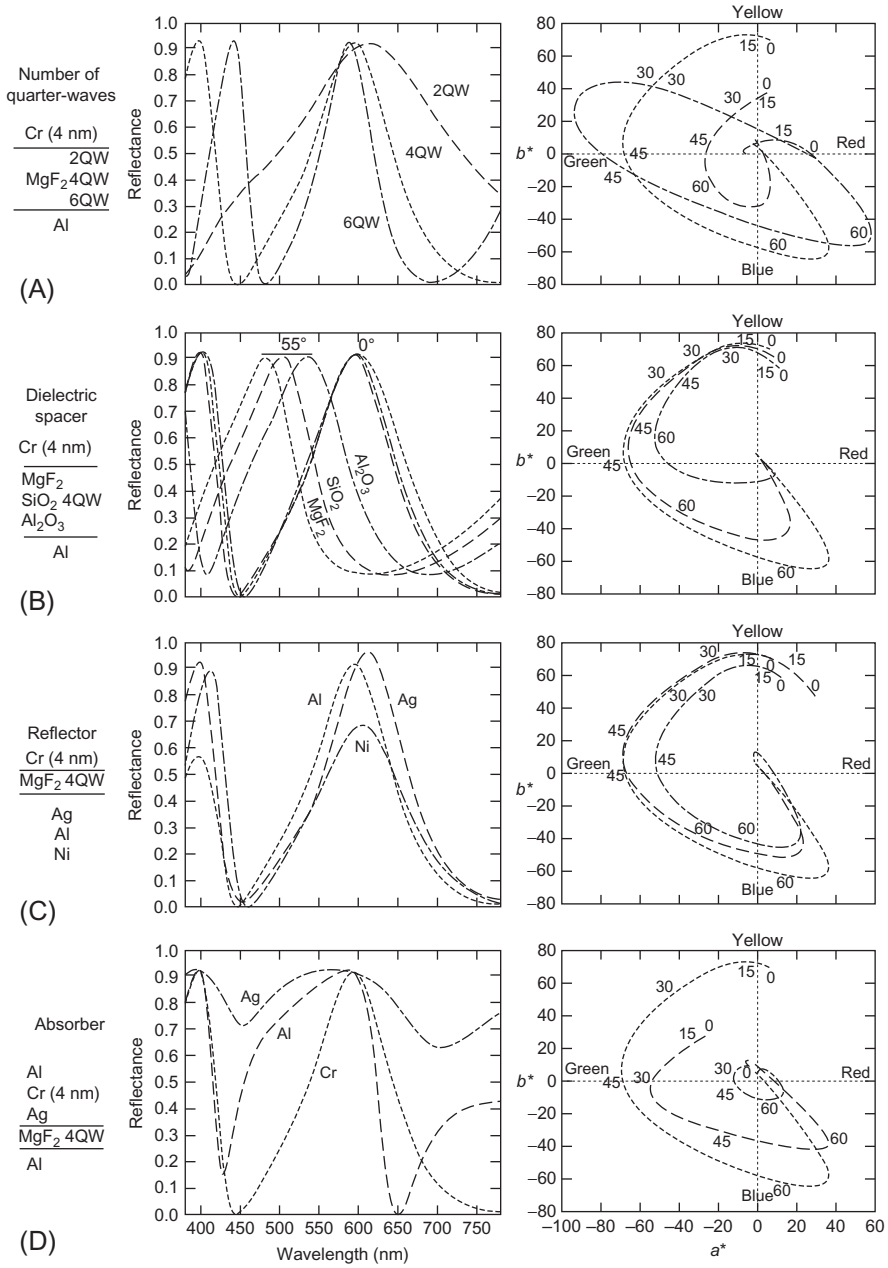


FIG. 17.3

Various configurations of Fabry-Perot-like metal-dielectric filters and their effect on the reflectance and the color variation performance in the $L^*a^*b^*$ color space (calculated under illuminant D65). From top to bottom, we present the effect of changing: (A) the thickness in quarter-waves of the dielectric spacer (at 575 nm), (B) the dielectric spacer material, (C) the metallic reflector material, and (D) the absorber material.

Ni ($R_{Ag}=96\%$, $R_{Al}=92\%$, and $R_{Ni}=61\%$ at 550 nm). As predicted, the only significant effect one notices is the decrease in the maximum amplitude of the reflectance peaks as the reflectance of the mirror decreases. In terms of color variation, Ag and Al offer a very similar performance; typically, Al is the material of choice due to its lower cost and higher chemical stability. Although most devices are reflection based, some transmission-based metal-dielectric structures have also been proposed (Phillips, 1994; Phillips and Coombs, 1994). A new, until now unexploited effect has been recently demonstrated when using a semi-transparent mirror: fabricating an asymmetric stack allows one to obtain a device whose color in reflection is dependent on the side of observation, as well as being semi-transparent (Baloukas et al., 2005). Fig. 17.4 shows an example of such a filter which presents a purple to black color shift in transmission, a red to greenish yellow shift in reflection, and a green to blue shift in reverse reflection.

It is also possible to design and fabricate a simpler version of the filter presented in Fig. 17.4 by implementing a typical Fabry-Perot-like filter. Indeed, as shown in Fig. 17.5, a $V|SiO_2|Al|SiO_2|V$ filter, where the Al is made thinner ($\sim$10 nm) to transmit light and the SiO_2 layers are of different thicknesses, results in a side-dependent reflectance. Interestingly, it has been shown that by using a single filter it is possible to create a feature displaying a positive/negative image on both of its sides (e.g., a yellow triangle on a purple background on side A and a purple triangle on a yellow background on side B), while in transmission, no image is visible (as the transmittance is side independent) (Baloukas and Martinu, 2016); this is also illustrated in Fig. 17.5.

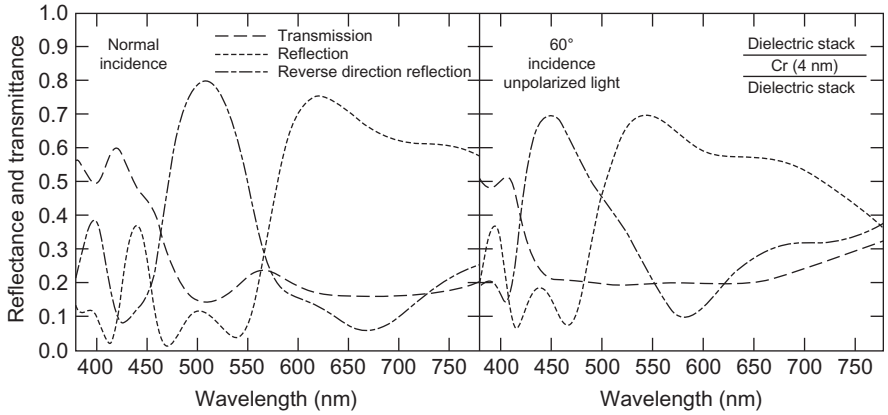


FIG. 17.4

Reflection and transmission spectra at normal incidence of a filter with three different color shifts, one in transmission (purple (RGB = 55, 42, 109) to black (52, 48, 61)) and two in reflection (forward direction from red (229, 32, 40) to greenish yellow (151, 169, 24) and reverse direction from green (0, 156, 68) to blue (20, 62, 169)—calculated under illuminant D65). Note that the structure of the filter is shown in the upper right corner.

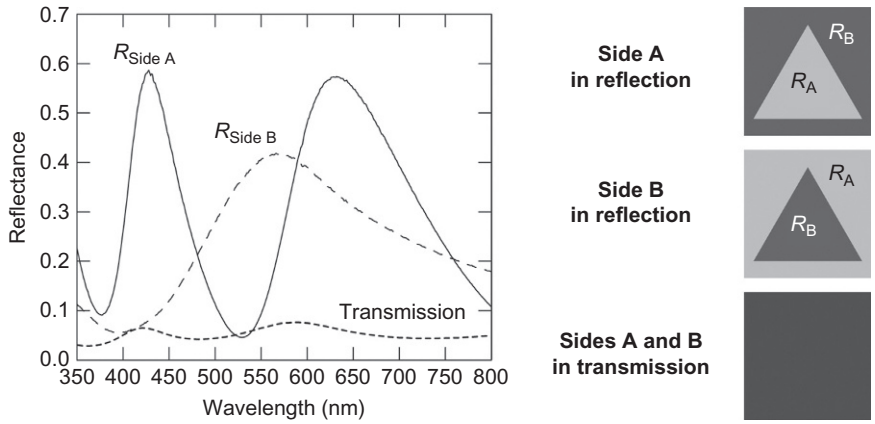


FIG. 17.5

Reflection at 25 degrees for sides A and B and transmission at normal incidence of a $V|SiO_2|Al|SiO_2|V$ filter showing side-dependent reflectance. The reflected color varies from purple to green on side A, from gold to bluish-green on side B, and dark purple to dark green in transmission. Using a single filter, it is then possible to generate an image such as the one shown on the right; sides A and B show positive/negative images of themselves while in transmission the image disappears.

Modified from Baloukas, B., Trottier-Lapointe, W., Martinu, L., 2014. Fabry-Perot-like interference security image structures: from passive to active. Thin Solid Films 559, 9–13.

Finally, it has also been demonstrated that the top semi-absorbing film must present a ratio of $n/k \sim 1$ (Phillips and Bleikolm, 1996). In Fig. 17.3D, we show three examples where the absorber is either Ag ($n/k = 0.04$), Al ($n/k = 0.14$ at 550 nm), or Cr ($n/k = 0.70$) all with a thickness of 4 nm; note that all these metals possess a fairly neutral color. Clearly, the closer the n/k ratio is to 1 (in this case Cr), the higher is the color saturation obtained at normal incidence and the higher the color travel. Despite this finding, simple structures based purely on the use of aluminum ($Al|Al_2O_3|Al$) have recently been proposed as potential candidates for security and decorative purposes (Lotz and Steiniger, 2007). Obviously, the thickness of the absorber must also be optimized.

The fact that metal-dielectric filters require fewer layers has made them the structure of choice to protect most banknotes. Indeed, the sheer number of banknotes which require protection, often reaching the billions, makes the cost of fabrication a critical parameter. For example, the Bank of Canada converted its five-layer all-dielectric filter to a three-layer metal-dielectric filter with a similar performance. Cost is also the reason why fabrication of OVDs is mostly done by roll-to-roll coating using e-beam evaporation, known for its high deposition rate. Systems must also be equipped with an optical monitoring system to control the thickness of the layers in situ and, consequently, the resulting color (Nofi and Matteucci, 1998). A precision as high as 1.5% on thickness is typical and can be required to maintain color consistency

(Rolfe, 1991). A very high uniformity is required to ensure a steadfast color across the whole web. Due to the porous nature of e-beam evaporated films, the design may need to be adjusted to account for the absorption of water once exposed to the ambient environment (Dobrowolski, 1998).

Although outside the scope of the present chapter, it is important to stress that subwavelength features relying on plasmonic resonance effects and others are of obvious interest for security applications (Smith and Skrabalak, 2017). Indeed, in one example, it has been proposed to replace the top semi-absorbing film with a metal film presenting nanoclusters (Brandsealing®) (Haglmüller et al., 2004; Bergsmann et al., 2003). By carefully controlling the size and shape of the clusters, the plasmon resonance excitation can be finely tuned and serve as an optical code which is machine readable (Bauer et al., 2003). Others have also integrated an anisotropically scattering layer over the dielectric spacer which is then coated with a semi-absorbing metal film (anisotropically scattering Fabry-Perot). Although these structures show a limited change in color when tilted, due to their highly diffuse character, they still retain good color saturation. Their anistropic nature also allows for the generation of rotation-dependent optical effects (Stalder and Seils, 2006).

In another recent example, plasma-etched 100 nm polystyrene nanospheres sputter-coated with gold or silver at high angles of incidence result in anisotropic features displaying angular- and polarization-dependent properties. Due to the fact that the resulting plasmonic resonance is the result of the unique ordering of the nanospheres, this also makes such features resistant to tampering (Alvine et al., 2015). Other polarization-dependent nanostructures such as silver nanowires displaying surface-enhanced Raman scattering have also been proposed for security labels (Cui et al., 2014). Interestingly, commercial implementation of plasmonic nanohole arrays which can be imprinted onto a variety of materials and made on an industrial scale are presently available on the market (Chuo et al., 2014).

All of the previous plasmonic-based examples employ subwavelength features to generate innovative optical signatures. This obviously brings up the subject of metamaterials for security applications. While still in its infancy, the use of "artificial" materials to generate what, a priori, seem to be physically impossible feats is bound to produce new and innovative features. For instance, many recent examples show promise for anticounterfeiting applications:

- Martínez et al. have proposed a metamaterial possessing strong negative magnetic activity in the visible spectrum (Martínez et al., 2009).
- James et al. have demonstrated full-color macroscopic images using plasmonic pixels based on aluminum nanostructures (James et al., 2016).
- Davidson II et al. have shown that gold Archimedean nanospirals displaying second-harmonic generation could easily be authenticated using a laser (Davidson et al., 2015).
- And, finally, as mentioned by Larouche et al. in their work on infrared phase holograms (Larouche et al., 2012), using 3D metamaterials will allow the creation of "new devices combining diffraction, scattering, and refraction."

The general implications of metamaterials and their possible uses are discussed further in Zheludev and Kivshar (2012) and Naruse et al. (2012).

17.2.3 OPTICALLY VARIABLE PIGMENTS

Patterning an interference filter into a specific shape is not a simple task. Although it has been done by using masking during deposition, laser etching (Dobrowolski and Waldorf, 1986), hot stamping, using soluble materials (Raksha et al., 2010), embossing (Phillips and Bie, 2009), etc., one method which allows highly complex images to be created is based on using optically variable pigments (OVPs). In this particular case, the desired filter is first deposited onto a release-coated web, it is then delaminated, milled into a powder, and incorporated into a printing vehicle, thus forming what is known as optically variable ink (OVI) (Phillips and Bleikolm, 1996; Phillips et al., 1992) (OVP is produced by Viavi Solutions Inc. (formerly Flex Products Inc.) as a base material for OVI by Société Industrielle et Commerciale de Produits Alimentaires (SICPA) (Phillips et al., 1991, 1994, 1995a). These pigments are based on Fabry-Perot-like structures, but consist of five layers (absorber|spacer|mirror|spacer|absorber) because they are symmetric around the opaque mirror. This symmetry is essential since, during the printing process, one cannot control on which side the pigment will fall. To ensure the pigments lie flat, the aspect ratio of the thickness versus size of the pigments is kept at approximately 10:1 (Phillips, 1990). Obviously, all the pigments do not lie perfectly flat (~10 degree angle on average); therefore, the diffuse reflection is increased (10% specular and 90% diffuse) giving rise to lower color saturation (average of colors from slightly different angles) (Rolfe, 1991; Phillips et al., 1995b).

Another advantage procured by the incorporation of OVPs into an ink is that the whole structure is essentially laminated and, as a result, oxidation and damaging of the sensitive metallic layers are no longer an issue. Additionally, OVI is more flexible when compared to a foil-type device where the mechanical properties can be limiting once apposed onto a flexible substrate (Phillips and Bleikolm, 1996).

Lately, in an effort to increase the covert security offered by OVPs, it has been demonstrated that the pigments can be made into various shapes (diamonds, squares, etc.) by using an embossed foil as the substrate during deposition (see Fig. 17.6) (Phillips and Argoitia, 2005). When viewed under a microscope, one can easily observe these shaped pigments and therefore rapidly validate the authenticity of the device. Furthermore, additional effects can also be generated by patterning one or more of the layers of the filter (laser ablation, flexographic printed oil which vaporizes during deposition (Phillips and Argoitia, 2005; Schmid, 2006), chemical etching, etc.).

Lastly, note that there are commercial products currently on the market which display iridescent effects (wrapping paper based on *co*-extruded polymer films, ChromaFlair by Viavi (Phillips and Nofi, 1999), etc.). Although the color shifts offered by such products may not be of the same quality as current security devices, their potential use for counterfeiting must be seriously considered.



FIG. 17.6

Example of a microstructured, square-shaped optically variable pigment displaying a Euro symbol.

Modified from Argoitia, A., Delst, K.-J., 2008. Micro structured taggants in security pigments and inks. In: van Renesse, R.L. (Ed.), Optical Document Security I. Reconnaissance International, pp. 1–16.

17.3 SPECIFIC OPTICAL EFFECTS SUITABLE FOR SECURITY DEVICES

Realizing that a simple color shift may not be sufficient to protect against future counterfeiters, most of the current research has focused on implementing additional features to the classic ISD. The main goal is to increase fabrication complexity while still maintaining or even simplifying the authenticity validation phase for the general public. In the following subsections, we give a survey of these augmented interference-based devices.

17.3.1 METAMERISM

Metamerism is a phenomenon where two objects with different reflection or transmission spectra appear to possess the same color under a specific light source. Juxtaposing two such elements therefore allows for the creation of a hidden image effect. For example, the 1985 Dutch 250 guilder banknote sported a metameric feature based on green metameric inks. Under normal lighting the feature was fairly uniform in color, but when observed through a red filter, a rabbit would appear. This effect was possible since the inks had almost identical spectra in the green-wavelength region, whereas they differed in the red (van Renesse, 2005). Hence, the use of a red filter accentuated these differences. In 1999, the polymer Romanian 2000 Lei went one step further by incorporating a magenta filter onto the banknote itself hence resulting in a self-authenticating banknote. In the previous examples, the metameric devices were based on classical noniridescent inks. However, there have

also been some examples of interference-based metameric features. To our knowledge, the first metameric feature to be proposed (Dobrowolski et al., 1973) consisted of two filters with identical colors, which when superposed would transmit no light. Perhaps due to its relative complexity and potential cost, this feature was never implemented but, nonetheless, it proposed an innovative concept.

About two decades later, metamerism was once again suggested after it was noticed that Fabry-Perot-like metal-dielectric filters with different spacer thicknesses resulted in similar colors (Phillips et al., 1995b). Fig. 17.7A presents the variation of color in the $L^*a^*b^*$ color space as a function of increasing MgF_2 thickness for a $Al|MgF_2|Cr$ structure (from 0 to 800 nm). As can be seen, there are multiple points where the color trajectories intersect. These points correspond to different MgF_2 thicknesses which generate identical a^* and b^* coordinates. Keep in mind that to ensure an adequate color match, one must also consider the luminance value L^* of both configurations (presented in Fig. 17.7B).

In Fig. 17.7B we present the difference in color $\Delta E^*_{ab,\ D65}$ between all possible thickness combinations of MgF_2 between 0 and 800 nm. We first notice that this figure is symmetric (line of symmetry $x = y$). We can also see that the lowest $\Delta E^*_{ab,\ D65}$ is obtained along the diagonal since this region corresponds to two samples with identical MgF_2 thicknesses. In total, there are 13 regions with a fairly low $\Delta E^*_{ab,\ D65}$. Let us now choose one of these intersections (see circle in Fig. 17.7A and hexagon in Fig. 17.7B); the lowest color difference in this particular case is obtained when comparing samples with MgF_2 thicknesses equal to 383 and 589 nm. The resulting reflection spectra of both these samples are shown in Fig. 17.7C. It is fairly straightforward to understand why these two samples are metameric. Indeed, the spectra match fairly well in the region of sensitivity of the human eye (between 400 and 700 nm; see Fig. 17.8B), whereas they differ in regions where the eye is less sensitive (near-UV and near-IR). The fact that both filters possess different spectra results in their having different color trajectories as a function of the observation angle (see Fig. 17.7D). Therefore, at normal incidence both samples are green and at an angle of 45 degrees the 383 nm MgF_2 filter displays a bluish tint, whereas the 589 nm MgF_2 filter is more purplish. As a result, printing both these filters side-by-side allows the creation of hidden images. In fact, a product was developed using this principle and adopted by the pharmaceutical industry (MetaSwitch) (Phillips and Argoitia, 2005; Phillips et al., 2000). In addition, a similar effect is also possible by replacing one of the variable inks with a non-iridescent material (NIM) (e.g., metallic inks).

In the example presented above, $\Delta E^*_{ab,\ D65} = 6.83$, a value which is fairly high and which may result in a slightly different color to appear even at normal incidence. When changing the illuminant to incandescent or fluorescent lighting, the color differences are even higher ($\Delta E^*_{ab,\ A} = 11.79$ and $\Delta E^*_{ab,\ F1} = 9.40$). As a result, the present device is highly sensitive to changes in light sources and, therefore, to changes in observer. Consequently, these metameric features are often optimized for specific lighting conditions (usually fluorescent lighting due to its popularity). Other variations of more complex metal-dielectric metameric structures have also

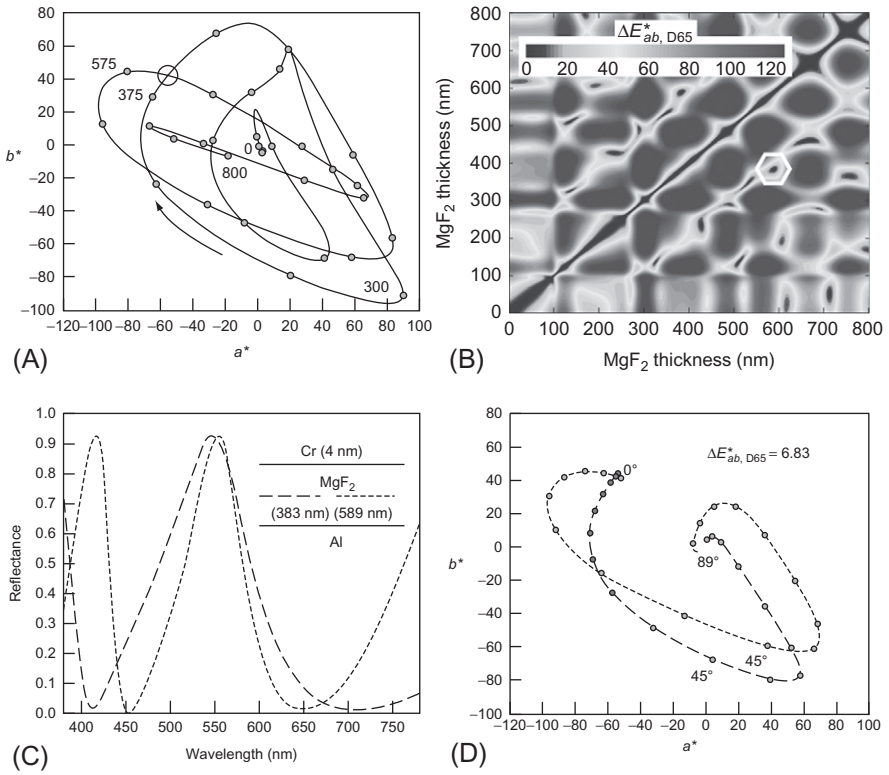


FIG. 17.7

Metameric pairs based on metal-dielectric Fabry-Perot-like filters. Part (A) shows the variation in color in the $L^*a^*b^*$ color space when the thickness of the MgF_2 layer is varied between 0 and 800 nm. Each dot represents a 25 nm increment in thickness. Interestingly, the outer boundary formed by the present curve represents the gamut of all possible colors attainable by the present structure. Part (B) presents the $\Delta E^*_{ab,\ D65}$ for all thickness combinations. This figure is symmetric (line of symmetry $x=y$) and shows that there are 13 combinations resulting in a low color difference. In part (C) we show the reflection spectra of the chosen metameric pair (circle in (A) and hexagon in (B)). Note that the structure of the simulated filters is also shown in the upper right corner. Finally, (D) shows the color variation of both filters as a function of the observation angle. Notice how at 0 degree the colors coincide (the color difference is also indicated). Each dot represents a 5 degrees increment in angle. Data generated using a combination of *OpenFilters* (Larouche and Martinu, 2008) and *Matlab*.

been proposed, such as a nine layer design (additional absorber|dielectric pairs) which allows fabrication of a filter that presents the same color at normal incidence as well as the same color shift as a typical five-layer OVP but with the absence of reflection peaks in the near-UV and near-infrared (Phillips and Bleikolm, 1996; Coombs and Phillips, 1993). As a result, this type of feature could only be identified via a machine.

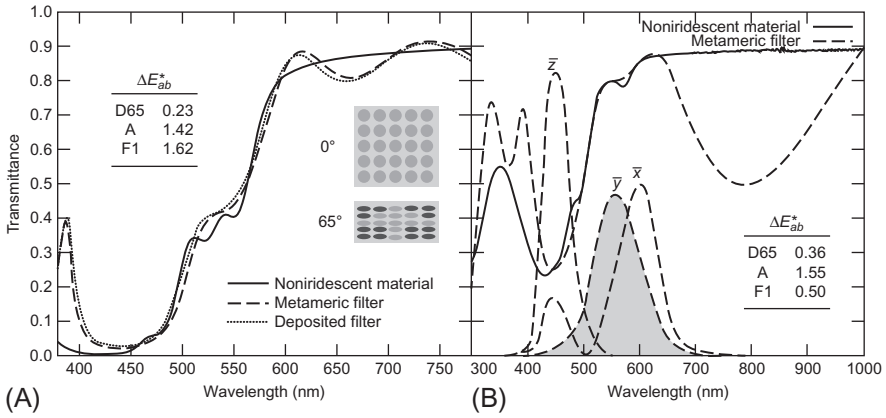


FIG. 17.8

Two examples of all-dielectric metameric filters designed to match the transmission spectra of transparent colored inks. In (A), one can see how the filter (13 layers) matches the whole visible transmission spectrum of the NIM. This automatically results in a low color difference ΔE^*_{ab} under all three illuminants. A hidden image effect is also possible by patterning both elements. In (B), the filter's (9 layers) spectrum is allowed to diverge in regions where the eye is less sensitive as a means to decrease the number of layers without compromising performance. The CIE 1931 color matching functions $\overline{xyz}$ are also shown as reference.

Recently, it has been shown that using a slightly higher number of layers allows one to surpass the previous shortcomings, that is, design and fabricate metameric pairs with a good performance (low ΔE^*_{ab}) and lower sensitivity to changes in light sources and observers (Baloukas et al., 2005, 2006; Baloukas and Martinu, 2008a, 2011). By using all-dielectric filters, these devices could also be used in a transmission mode. Fig. 17.8 shows two examples of filters which were designed to match the color of a transparent (noniridescent) colored ink. In Fig. 17.8A, one can clearly see that the designed filter (13 layers of SiO_2 and Ta_2O_5) matches the whole transmission spectrum of the NIM and, consequently, the color difference ΔE^*_{ab} remains low under all three illuminants (decreased metamerism leading towards isomerism). In this same example, the NIM and the filter were patterned to create a hidden image effect: an arrow appears at high angles of incidence due to the orange to light yellow color shift of the filter.

In an attempt to reduce the number of layers of the filters, a design methodology based on the use of the luminous efficiency curve of the human eye was developed. Fig. 17.8B shows the International Commission on Illumination (CIE) 1931 color matching functions used in color calculations, $\overline{xyz}, \overline{y}$ having the same distribution as the luminous efficiency curve of the human eye. By using transmission targets with tolerances which are inversely proportional to $\overline{y}$ (maximum weight in regions of highest sensitivity), the authors show that filters with a smaller number of layers can be designed without compromising their performance (Baloukas et al., 2011a;

Baloukas and Martinu, 2008b). An example of this is shown in Fig. 17.8B, where the designed filter is allowed to diverge from the NIM's spectrum in the low and high wavelength regions where the eye is less sensitive. Obviously, $\bar{y}$ is only one of the three components used in color calculations so that this design methodology cannot be used alone, but must be combined with color target coordinates under at least one illuminant. On the other hand, it does guide the optimization process in the right direction by reducing the amount of possible solutions; indeed, an infinity of metameric spectra exists resulting in color matches.

17.3.2 MAGNETIC FILMS

The presence of magnetic materials (Fe_2O_3, Fe_3O_4, barium or strontium ferrite, soft iron or nickel particles, etc.) in security has typically been used to include covert information in documents (Jagielinski and Chamberlain, 2002); obviously, a high coercivity (resistance to demagnetization) is necessary to ensure protection against erasure. They are also commonly used for antitheft security labels (Lienvens, 1995). It follows that by combining regular inks with magnetic inks of identical color one can encrypt information which is readable using various types of detectors and sensors (e.g., see the Canadian five-dollar bird series banknote from Jagielinski and Chamberlain, 2002).

More recently, optically variable pigments combining both interference effects and a magnetic signature have been demonstrated. Although mixing color shifting pigments with magnetic inks may seem the simplest solution, the colorless nature of the latter renders these mixtures unattractive. A better solution can be obtained by integrating the magnetic material into the structure of the interference filter. For example, one can replace the metallic reflector or absorber by a specific magnetic material (e.g., Co-Ni alloy reflector|MgF_2 spacer|Cr absorber, Coombs et al., 2002). Although a slightly more expensive solution, incorporating the magnetic film below the reflector allows one to preserve the optimized optical performance of the filter.

The presence of a magnetic material also offers another interesting possibility. When in the presence of a magnetic field, OVPs will align themselves with the field lines. As a result, when an ink comprising such pigments is cured in the presence of a magnet, specific optical effects can be created (see Fig. 17.9) (Coombs et al., 2004). In the present example, the reflection will be at its lowest in region 1 since light is essentially lost due to multiple reflections between pigments and absorbed by the substrate, whereas it will be at its highest in region 2. The pigments in region 3 having a fairly acute angle will also present a fairly low reflectivity. Finally, the magnetic field intensity decreases as a function of distance so pigments in region 4 will only be subjected to low magnetic forces and will naturally lay flat (as nonmagnetic pigments). For a complete survey of the optical effects which can be generated using this technology, consult the article by Raksha et al. (2008). Commercial applications of this concept have been proposed (Despland et al., 2008; Raksha et al., 2011a) and implemented in high-speed printing (Raksha et al., 2011b).

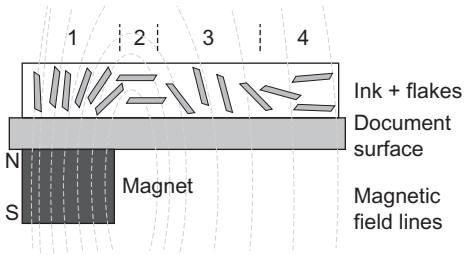


FIG. 17.9

Magnetic color shifting pigments exposed to the magnetic field of a cylindrical magnet. Notice how the pigments align with the magnetic field lines. This alignment allows for the creation of interesting optical effects.

Figure inspired by Coombs, P.G., Argoitia, A., Raksha, V.P., Phillips, R.W., 2004. Integration of contrasting technologies into advanced optical security devices. In Optical Security and Counterfeit Deterrence Techniques V, San Jose, California, USA, vol. 5310. SPIE, pp. 299–311.

17.3.3 COMBINING INTERFERENCE AND DIFFRACTION

Although DOVIDs are outside the scope of this chapter, it is important to note that there have been significant efforts to combine them with ISDs in the hopes of generating stronger features benefiting from the advantages of both technologies. Indeed, holograms do present interesting optical effects, but the security they procure has been questioned due to the relative ease with which they can be counterfeited (McGrew, 1990). Another key feature resides in the fact that interference-based devices can still be viewed under diffused lighting whereas diffractive devices perform best under direct lighting. Their combination therefore results in an increased versatility making authentication possible under various types of lighting situations (Coombs et al., 2004). For a complete review of diffraction-based devices, see van Renesse (2005).

It is well known that diffraction arises when light arrives upon a surface possessing a periodic structure whose period is near the wavelength of the incident light. Following the Huygens-Fresnel principle, each point on the diffractive grating becomes a secondary source of spherical light emission. These spherical waves then interfere constructively and destructively and result in each wavelength being diffracted at a specific angle. The following equation allows for the calculation of these angles:

$$m\lambda = d(\sin\alpha + \sin\beta), \tag{17.2}$$

where m is the diffraction order, λ is the wavelength, d is the distance between two grooves, and α and β are the incident and diffracted angles, respectively (relative to the normal of the surface) (Phillips and Argoitia, 2005). When light arrives at normal incidence ($m\lambda = d\sin\beta$), Eq. (17.2) dictates that higher wavelengths will be diffracted at higher angles (see Fig. 17.10A). Also note that, in the present case of a grating with 1400 lines/mm as presented in Fig. 17.10, only the first diffraction order is visible.

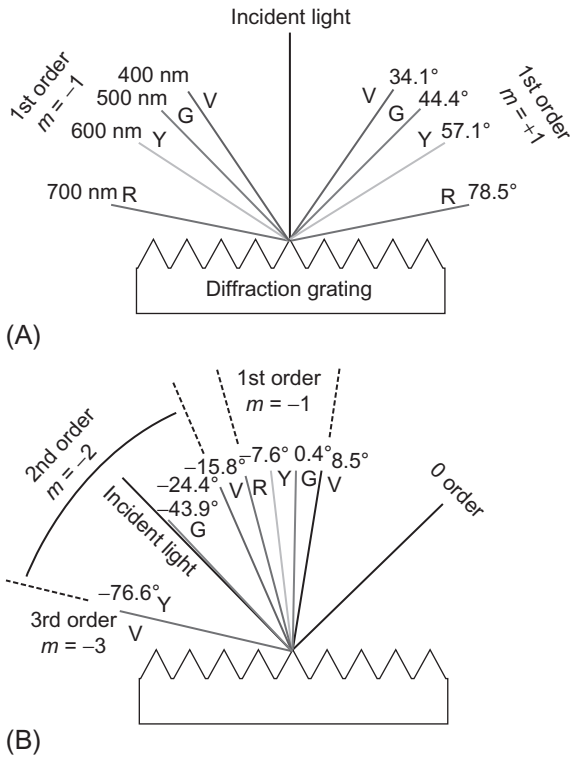


FIG. 17.10

Diffraction of light at (A) normal and (B) 45 degrees of incidence for four different wavelengths on a 1400 lines per mm grating. Letters indicating the color of the wavelength are indicated next to each beam of light (R = red, Y = yellow, G = green, and V = violet). Note that in (B), the 2nd order yellow coincides with the 3rd order violet which can result in a decrease in saturation.

Figure inspired by Phillips, R.W., Argoitia, A., 2005. Using vacuum roll coaters to produce anticounterfeiting devices. In: 48th Annual Technical Conference of the Society of Vacuum Coaters, Louisville, Kentucky, USA. Society of Vacuum Coaters, pp. 145–152.

When light arrives obliquely, for example at 45 degrees (see Fig. 17.10B), the zero order ($m = 0$) will be specularly reflected at the same opposite equivalent angle. We can also see that the -1 order has been rotated clockwise, so that contrary to ISDs the observed color change as a function of the observation angle is from shorter to longer wavelengths when observing a diffraction grating. Also note that higher orders are now also visible. Changing the shape (triangular, sinusoidal, etc.), depth, and orientation (blazed) of the grooves of a grating allows one to modify the relative intensities of the various orders (Argoitia and Whitzman, 2002). Interesting color effects can also be obtained by using combination gratings benefiting from the superposition of two diffractive grating profiles or more (Tompkin et al., 2004).

The concept of printable holograms through the use of diffractive pigments has also been demonstrated (Argoitia and Chu, 2004a, b). The fact that these pigments contain ferromagnetic materials allows for their alignment using electromagnetic fields and thus the creation of interesting three-dimensional (3D) effects, but also rotation-dependent color effects by printing flakes with a 90 degrees difference in orientation (Argoitia and Delst, 2008). Indeed, to observe diffraction the grooves must be perpendicular to the observation direction. Finally, metameric diffractive pigments have also been proposed (Orava et al., 2008; Argoitia et al., 2010).

Deposition of an interference filter on an embossed substrate results in a highly complex interaction of diffraction and interference (Phillips and Argoitia, 2005; Phillips, 2001; Kittler et al., 2010). Generally speaking, the effect of the interference filter is to block specific wavelengths so that the rainbow effect of diffraction is attenuated and only specific colors are enforced. Various configurations of these two effects are presented in Argoitia and Phillips (2006). Once again, using an all-dielectric filter allows for transmission-based devices to be created (Argoitia et al., 2004). The simplest configuration is the use of a high refractive index material (e.g., ZnS) on an embossed polymer substrate for see-through holograms (Ahmed and Whitnall, 2001). Another possibility is to simply laminate a hologram with an interference filter (Phillips and Bonkowski, 2000; Bonkowski et al., 2010).

From Eq. (17.2), it can be seen that when the grating spacing is equivalent to half the wavelength of light (200 nm for a 400 nm violet light, more than 5000 lines/mm), no order other than the zero order will be present ($2m - \sin\alpha = \sin\beta$); these structures are known as zero-order diffraction gratings (ZODs) (Tompkin et al., 2002). Note that for spacings between 200 and 400 nm, diffraction will occur, but at very high angles of incidence. Although ZODs do not present any diffraction, they do present a surprising in-plane color variation (rotation-induced color shift) if viewed parallel or perpendicular to the grooves, typically from red to green (Chen and Liu, 2011). For obvious reasons, ZODs are harder to replicate since they require very high embossing precision (van Renesse, 2005).

17.3.4 OTHER COLOR SHIFTING TECHNOLOGIES

There are other technologies displaying color shifting properties. This is the case of coextruded polymer films first developed by Dow Chemical in the late 1960s (Jonza and Dubner, 2004). Essentially used for decorative and packaging purposes, due to a fairly low color uniformity, the technology has matured, and coextruded polymer films have now made their way into the optical security field. Indeed, 3M has proposed filters based on PET and acrylic polymer layers (coPMMA) as well as polyethylene naphthalate (PEN) and coPEN. The low refractive index contrast (1.67 vs. 1.50 in the case of PET and PMMA, respectively) requires a very high number of layers. For example, an orange to yellow color shifting film consisting of 275 layers of PEN and coPEN has been demonstrated with a total thickness of 33 μm. Interestingly, due to the stretching which occurs during extrusion, both the PET and PEN layers display birefringence. This birefringence allows for the creation of interesting

polarization effects (in-plane rotation-dependent color shifts when viewed under polarized light parallel or perpendicular to the stretch direction) (Jonza and Dubner, 2004).

There are obviously other technologies which display angle-dependent color variations, which for reasons of conciseness have not been covered in the present chapter; these include liquid crystals (Moia, 2002, 2004; Jiang et al., 2002), Lippmann photography, volume-reflection holography, and even nanocrystalline cellulose (Zhang et al., 2012). For those interested, a detailed coverage of these technologies in the context of security is given in the book by van Renesse (2005).

17.4 ACTIVE DEVICES

Lately, it has become clear that an ongoing trend in security is the integration of active features in future anticounterfeiting devices (Trevor, 2008). For example, De La Rue, in one of its 2010 patents (Jeacock and Whiteman, 2010), clearly mentions that inks may contain "functional components that react to an external stimulus" such as "fluorescent, phosphorescent, infrared absorbing, thermochromic, photochromic, magnetic, electrochromic, conductive and piezochromic" materials. In this section we will describe structures which not only present an active optical change but also endeavor to preserve the passive optical change of ISDs.

17.4.1 APPLICATION OF ACTIVE MATERIALS

In the context of active materials, one particular example is a Fabry-Perot-like structure incorporating a luminescent material which offers an overt color shift as well as a covert feature—in this case the emission of light under the influence of an external stimulus (ultraviolet, visible or infrared radiation, electric (Dobrowolski et al., 1991) or magnetic fields, chemicals, or even pressure) (Coombs et al., 2003). Incorporating the luminescent material inside an interference filter also renders the light emission angle dependent; this feature can thus provide an added level of security (MacPherson et al., 2011; Rozumek and Müller, 2004). Others have replaced the dielectric spacer (see Section 17.2.2) by a piezoelectric material which, under the application of fairly high voltages (100–1000 V), sees its thickness change and, as a result, changes the color of the device (MacPherson, 2011). Such high voltages would obviously require extreme caution when authenticating the device and could potentially limit their applicability.

In another example, upconverting nanoparticles (UCNPs) which, when excited with near-IR light reemit in the visible, have been incorporated in a Fabry-Perot-like structure. UCNPs have in fact been considered for security applications, where by modifying their composition, they can also be made to emit differently in the visible and thus offer the opportunity of creating images (Kim et al., 2009). In the present case, 15 nm UCNPs of $NaGd_{0.78}F_4Er_{0.02}Yb_{0.2}$ (Baloukas et al., 2016) were spin coated onto an $Al|SiO_2$ (225 nm) sample. They were then overcoated with an additional 225 nm of SiO_2 and with a ~6 nm Cr absorbing film (thickness values were obtained through ellipsometric modeling). As can be seen in Fig. 17.11A, the

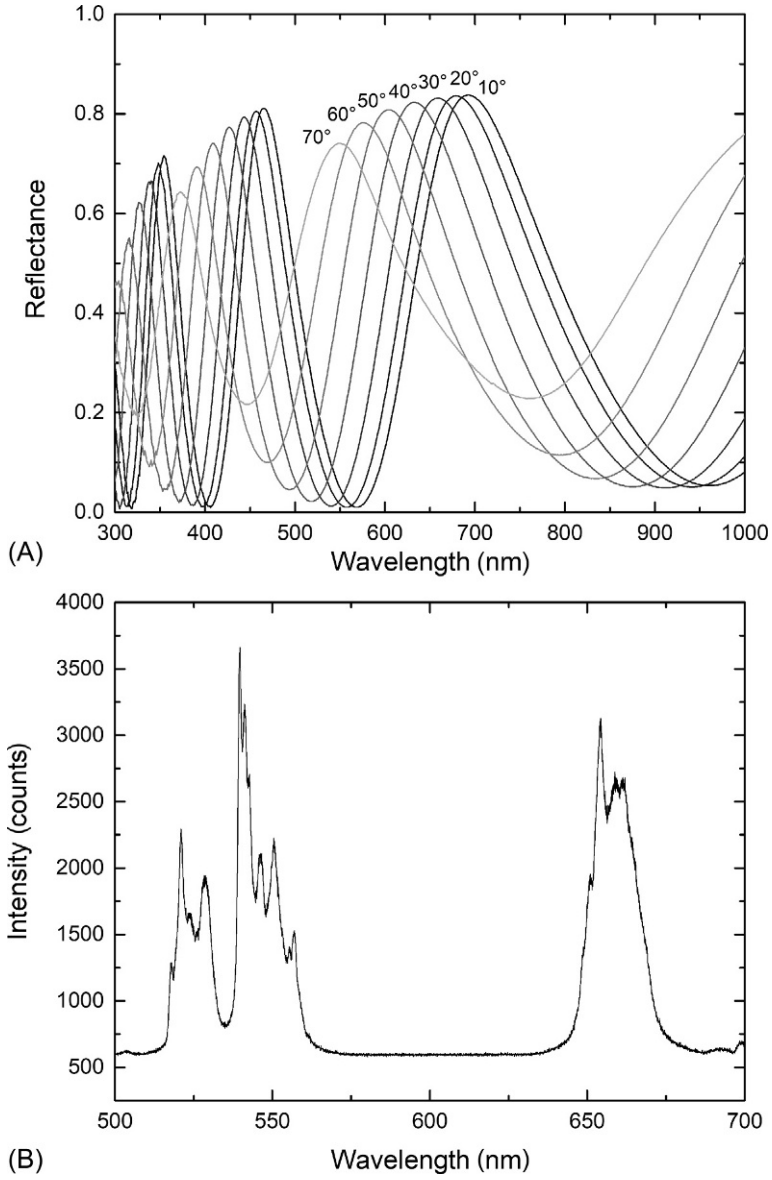


FIG. 17.11

Fabry-Perot-like filter incorporating UCNPs in its SiO_2 dielectric spacer. The top figure displays the angular reflectance between 10 degrees and 70 degrees every 10 degrees, whereas the bottom figure displays the emission spectrum of the UCNPs upon being illuminated by a 980 nm laser in an epifluorescence microscope.

expected angular variation of the reflectance from purple to yellow is confirmed. In addition, when a laser with a 980 nm wavelength is shined upon the sample, it is seen to reemit light in the red (~660 nm) and in the blue-green (520–560 nm) regions of the visible spectrum (see Fig. 17.11B). The resulting device thus displays two levels of authentication.

It is also expected that the position of the UCNPs inside the SiO_2 cavity will have an impact on the level of emission as the electric field intensity is known to vary significantly; thus by positioning them in a high intensity electric field region, we may expect a higher efficiency (Coombs et al., 2003). In addition, as the Fabry-Perot-like cavity also filters the visible spectrum by highly absorbing or reflecting specific wavelengths, we can also expect, as previously mentioned, that the emission will also be angular dependent.

Another recent proposition includes photonic crystals as possible innovative structures for optical security devices (Arsenault et al., 2008). By using colloidal self-assembly, low-cost 3D photonic crystals were fabricated. In this particular case, self-organized monodisperse silica microspheres were deposited onto a periodic lattice. The space in between the spheres was then filled with the desired material. The spheres were then dissolved resulting in what is typically called an inverse opal structure displaying an angle-dependent color variation. If the matrix material is elastomeric, devices which show a color change under an applied pressure are possible. This change in color due to compression results from a decrease in the distance between the spherical cavities and hence a lower total optical thickness. A similar effect has been demonstrated in Fabry-Perot-like structures using a pressure-deformable spacer layer (MacPherson and Hardwick, 2011). However, acceptance of the pressure-sensitive devices may be surpassed by their thermochromic counterparts that can mimic their characteristics since a finger not only applies pressure but also heat.

In addition to pressure actuated systems, using an electrically active matrix can result in a structure whose color changes by applying an electric field (Arsenault et al., 2007). Similarly, an electrochromic WO_3-based inversed opal structure has been proposed as a tunable photonic band gap (Kuai et al., 2005). Such a structure possessing iridescence as well as a change in color following the application of a voltage (to allow ion intercalation) could be of interest for security as a two-level authentication device.

17.4.2 ELECTROCHROMIC DEVICES

The rapid evolution of printed electronics has also led to various proposed optical security devices where the features are optically variable when a voltage is applied. Here too, electrochromic materials are very often the materials of choice due to the low potential required to switch them, as well as their memory effect (colored state is maintained once voltage is removed). For example, Hewlett-Packard suggested an electrochromic device for security tags (Champion and Betrabet, 2009). Another example based on electrochromics was suggested for security documents such as

passports and smart cards (NTERA, 2011). In this particular case, the electronic components of the passport (radio frequency identification (RFID) technology) could also be used to power the feature via a radio frequency (RF) signal. Based on a five to seven layer structure the total thickness was approximately 30 μm. Such a high thickness may limit their use for banknotes (a pile of 1000 banknotes would result in 3 cm of added thickness). This technology was based on an electrochromic viologen containing TiO_2 matrix apposed onto a white reflector (reflection-based device) (Corr et al., 2003). Others have developed strategies to reduce the total number of layers as well as the driving potentials to reduce cost and permit facile authentication (Danine et al., 2014; Rougier et al., 2015). It has also been suggested to use electrochromic paper as a potential candidate for vouchers, tokens, and banknotes (Monk et al., 2001). Although all of these examples offer an innovative means of authentication, they are mostly aimed as a second level authentication feature for experienced personnel and not for the general public.

To combine both the voltage-driven color shift of an electrochromic device (ECD) and the angle-dependent color shift of an ISD, Baloukas et al. have demonstrated a device linking both of these effects through metamerism (Baloukas et al., 2010, 2011a). More precisely, an all-dielectric metameric filter was designed and fabricated which matched an intermediate colored state of the ECD. Fig. 17.12 presents a schematic which outlines the basic concept of this system. One can see that at normal incidence, ISD B is visible, but upon application of a voltage, it disappears following the dark and opaque blue coloration of the ECD (disappearing image effect). The authors mention that a metameric filter could also be designed with the bleached state (ISD A in Fig. 17.12). On the other hand, long-term cycling of the ECD may affect the bleached state transmission and thus the color match; an

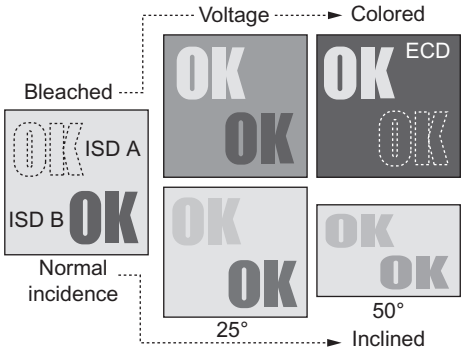


FIG. 17.12

Active metameric interference security image structure based on the combination of ISDs and an ECD. ISD A matches the bleached state transmission of the ECD, while ISD B matches an intermediate colored state. Such a device possesses two levels of authentication: an angular color shift and a voltage-driven color shift.

intermediate colored state would not suffer from this issue. Although the present concept is based on the use of an ECD, any other active technology could be used.

In an attempt to lower fabrication costs, the same authors have also shown that it is possible to combine both of the previously presented effects into a single structure. This was made possible by fabricating single-material electrochromic interference filters based on porous and dense WO_3 films (low and high refractive index, respectively) (Baloukas et al., 2011b). To increase the refractive index contrast, SiO_2-WO_3 composite films have also been used to replace the porous WO_3 (Baloukas and Martinu, 2012a, b). The resulting filters possessed an angular color shift as well as demonstrating electrochromic properties. However, there are still some issues to solve: for example, the creation of multiple interfaces impacts the coloration and bleaching dynamics of the filters. One proposed solution is to use simpler structures such as the one based on a Deb-type ECD which typically presents the following architecture (Baloukas et al., 2011a, 2014):

Substrate|Electrode (Al, Au, ITO, etc.)|WO_3|Electrolyte (SiO_2, MgF_2, etc.)|Electrode (Au, ITO, etc.).

Both electrodes are obviously required to apply the potential and activate the device. The bottom electrode will supply electrons to the WO_3 layer during coloration, while the electrolyte will supply neutralizing hydrogen ions (from electrolysis of the absorbed ambient water). By inverting the potential the electrons and ions are extracted and the device is bleached. One will notice that with the exception of the additional WO_3 film, this structure is very similar to OVI and therefore interesting from a fabrication point of view. Initial tests have indicated that such structures display an angular color shift in reflection, when using an aluminum mirror bottom electrode, as well as a voltage-driven color shift. While this solution works well in reflection, more layers are required when replacing the aluminum with ITO, to obtain an interesting color shift in transmission. Note that replacing the typical ITO electrode by a metal has been shown to be beneficial from a flexibility standpoint for potential devices on polymer substrates, for example, using thin silver electrodes (Li et al., 2015). Although more work is required to demonstrate the feasibility of such devices, if achieved, they will possess two levels of authentication.

17.5 FILM FUNCTIONALITY AND STRUCTURALLY CONTROLLED OPTICAL COATINGS

Besides the basic optical function of an ISD, other characteristics are also required for a device to be commercially viable (Glick et al., 1994; Phillips and Bleikolm, 1996) First and foremost, the system must offer good protection against counterfeiters (hard to duplicate, simulate, and originate). To increase the efficiency of use, the color shift must be easy to detect. This implies choosing the right color shift and a minimum device size to view it adequately ($\sim 1\,cm^2$). For example, choosing a red to green color shift might not be ideal considering that most colorblind individuals (between 7% and 10% of the male population) have difficulty distinguishing red

from green. The color of the filter must also be stable as a function of time when exposed to the everyday wear and tear of the protected product, but must also be stable from one production series to another to ensure color consistency (thickness control during deposition). Calculating the effect of deposition errors on the color of a filter is possible and color tolerances can be defined (Baloukas and Martinu, 2008a); however, the best method to tackle this issue is always to proceed with real-life testing. For obvious reasons, the materials used must also meet environmental, safety, and health regulations. In the particular case of banknotes, all OVDs must resist very stringent durability tests such as crumpling, abrasion, laundering in washing machines, and immersion in chemical solvents, so as not to shorten the lifetime of the banknote (Çetinörgü-Goldenberg et al., 2011; Rolfe, 1990). Finally, generally speaking, the fabrication costs must be kept low although some higher-end products, such as passports, may allow for more expenditure.

We have seen above that nanostructured optical coatings have made their headway to the field of optical security devices. One particular category is nanoporous materials whose application also illustrates progress and added coating functionalities in related fields, specifically in optical gas sensors (Shi et al., 2004). Such sensors are of particular interest since the use of light to probe the analytes and to carry the information offers numerous advantages, in particular, (i) the ability to operate in conductive or spark-sensitive environments without contact with the probed medium; (ii) the immunity to electromagnetic interference, cosmic rays or radioactivity; and (iii) the possibility to combine the sensors with optical fibers to create a sensor network and/or minimize invasion.

Porous films benefit from large surface areas in small volumes, hence considerably increasing the sensitivity of the devices. Several technologies for forming optical sensors based on multilayer interference filters have been considered:

- Formation of porous silicon by electrochemical etching (Volk et al., 2004; Kovacs et al., 2009). In general, this process is difficult to control and monitor and the chemical instability of porous silicon over time and its strong absorption in the visible spectrum are all important factors that restrict its use in high-quality optical filters.
- Optical films prepared by glancing-angle deposition (GLAD), for example, those based on porous TiO_2 rugate filters (Steele, 2007; Chang et al., 2008). This deposition technique depends on the complex rotation of the substrate relative to the vapor flux, an approach that may render scale-up rather complicated.
- Control of the porosity by adjusting the energy of the bombarding ions during the film growth as stipulated by the structure zone model (Messier et al., 1984). For example, Vernhes et al. have designed and fabricated an all-optical gas sensor based on multilayer porous/dense Si_3N_4 Fabry-Perot stacks (Vernhes et al., 2004, 2006, 2007) using plasma-enhanced chemical vapor deposition (Martinu et al., 1994; Vernhes et al., 2013). The effective refractive index variations caused by the gas (analyte) sorption inside the porous Si_3N_4 material give rise to a shift of the transmission spectrum of the optical filter,

which can be easily measured by using a laser diode and a photodetector. In fact, it was this approach which inspired the development of the porous/dense WO_3 and WO_3/SiO_2 ISD devices described in Section 17.4.2 (Baloukas et al., 2011b).

- In another recent example, by specially controlling the surface contact angle using superhydrophobic nanopillar arrays selectively overcoated with a hydrophilic layer, the authors were able to generate images which only appeared when exposed to high humidity levels, for instance, simply by breathing on the samples (Lee et al., 2014).

17.6 CONCLUSION

This chapter has covered the main concepts and trends in optical coating security devices and cited examples of recent innovations in this field. In addition, interested readers can learn further details in the excellent work by Dobrowolski (1998), the inventor of the first ISD, as well as in a complementary work by van Renesse (2005). For the latest developments, the biennial conference on Optical Document Security is highly recommended.

Although interference-based optical security devices have now been in circulation for more than 30 years, they are still going strong. We have seen in this chapter that to achieve such a long-term performance, these features have constantly been refined and additional levels of complexity have been added, mainly through the use of metamerism, magnetic materials, and hybrid interference/diffractive elements. It is also important to note that polymer banknotes as well as recent hybrid paper/polymer banknotes allow for the presence of windows which, therefore, open up an abundance of possibilities when it comes to transmission-based security features. Clearly, passive ISDs will play an important role in this context.

In an attempt to go even further, we have also shown that passive ISDs have been combined with active materials which can react to various energy sources such as heat, pressure, current, and light. Many of the designers of such features have gone to great lengths to incorporate these materials inside classic interference structures to preserve their well-known angle-dependent color shift. Thus, these devices offer two levels of authentication making them even harder to counterfeit. Some examples presented are already in use, while others still require further research and development. Nevertheless, these devices will provide original means of authentication which hopefully will capture public attention by their innovativeness and result in stronger and more efficient anticounterfeiting features.

Finally, we have seen throughout this chapter that much of the progress has been achieved by implementing new and novel, frequently nanostructured and active materials, and thin film structures. Although this has had a significant impact on the advancement of security devices themselves, it is important to note that similar advancements can also be noted in optical sensors, architectural and automobile glazing, and other areas of optical coating technology.

REFERENCES

Ahmed, N.A.G., Whitnall, M., 2001. Semi-transparent optical coating for security holograms. 44th Annual Technical Conference of the Society of Vacuum CoatersSociety of Vacuum Coaters, Philadelphia, Pennsylvania, USA, pp. 444–447.

Alvine, K.J., Suter, J.D., Bernacki, B.E., Bennett, W., 2015. Optically resonant subwavelength films for tamperindicating tags and seal. Sensors, and Command, Control, Communications, and Intelligence (C3I) Technologies for Homeland Security, Defense, and Law Enforcement XIV, vol. 9456. SPIE, pp. 94560C C1–C7.

Argoitia, A., Chu, S., 2004a. The concept of printable holograms through the alignment of diffractive pigments. Optical Security and Counterfeit Deterrence Techniques IV, vol. 5310. SPIE, San Jose, California, USA, pp. 275–288.

Argoitia, A., Chu, S., 2004b. The concept of printable holograms through the alignment of diffractive pigments. 47th Annual Technical Conference of the Society of Vacuum Coaters. Society of Vacuum Coaters, Dallas, Texas, USA, p. 677.

Argoitia, A., Delst, K.-J., 2008. Micro structured taggants in security pigments and inks. In: van Renesse, R.L. (Ed.), Optical Document Security I. Reconnaissance International, pp. 1–16.

Argoitia, A., Phillips, R.W., 2006. The security enhancement of diffractive optically variable image devices. Optical Security and Counterfeit Deterrence Techniques VI, vol. 6075. SPIE, San Jose, California, USA, pp. P1–P18.

Argoitia, A., Whitzman, M., 2002. Pigments exhibiting diffractive effects. 45th Annual Technical Conference of the Society of Vacuum Coaters. Society of Vacuum Coaters, Lake Buena Vista, Florida, USA, pp. 539–545.

Argoitia, A., Raksha, V.P., Kohlmann, P.T., 2004. All-dielectric optical diffractive pigments. U.S. Patent, no. US6815065.

Argoitia, A., Chu, D., Teitelbaum, N., 2010. Security device with metameric features using diffractive pigment flakes. U.S. Patent, no. US7729026.

Arsenault, A.C., Puzzo, D.P., Manners, I., Ozin, G.A., 2007. Photonic-crystal full-colour displays. Nat. Photonics 1, 468–472.

Arsenault, A.C., Kamp, U., Cheng, A., Ozin, G.A., 2008. Interactive elastic photonic crystals. In: van Renesse, R.L. (Ed.), Optical Document Security I. Reconnaissance International, San Francisco, California, USA, pp. 1–10.

Baird, K.M., Dobrowolski, J.A., Waldorf, A.J., Carman, P.D., 1975. Optical interference authenticating means. U.S. Patent, no. US3858977.

Baloukas, B., Martinu, L., 2008a. Metameric interference security image structures. Appl. Opt. 47 (10), 1585–1593.

Baloukas, B., Martinu, L., 2008b. Advances in metameric security image structures. Optical Document Security I Reconnaissance International, San Francisco, California, USA.

Baloukas, B., Martinu, L., 2011. Interference security image structure. U.S. Patent, no. US8064632.

Baloukas, B., Martinu, L., 2012a. Electrochromic interference filters based on WO_3 and composite SiO_2/WO_3 films. 55th Annual Technical Conference of the Society of Vacuum Coaters, Society of Vacuum Coaters, Santa Clara, California, USA.

Baloukas, B., Martinu, L., 2012b. WO_3/SiO_2 composite optical films for the fabrication of electrochromic interference filters. Appl. Opt. 51 (16), 3346–3356.

Baloukas, B., Martinu, L., 2016. Interference security image structure. U.S. Patent, no. US2016/0109629A1.

Baloukas, B., Larouche, S., Martinu, L., 2005. Playing with light – the quest for new optically variable devices. 48th Annual Technical Conference of the Society of Vacuum Coaters, Society of Vacuum Coaters, Denver, Colorado, USA, pp. 381–386.

Baloukas, B., Larouche, S., Martinu, L., 2006. Use of metameric filters for future interference security image structures. Optical Security and Counterfeit Deterrence Techniques VI, vol. 6075. SPIE, San Jose, California, USA, pp. T1–T9.

Baloukas, B., Lamarre, J.-M., Martinu, L., 2010. From passive to active: future optical security devices. Optical Interference Coatings, Optical Society of America, Tucson, Arizona, USA.

Baloukas, B., Lamarre, J.-M., Martinu, L., 2011a. Active metameric security devices using an electrochromic material. Appl. Opt. 50 (9), C41–C49.

Baloukas, B., Lamarre, J.-M., Martinu, L., 2011b. Electrochromic interference filters fabricated from dense and porous tungsten oxide films. Sol. Energy Mater. Sol. Cells 95 (9), 807–815.

Baloukas, B., Trottier-Lapointe, W., Martinu, L., 2014. Fabry-Perot-like interference security image structures: from passive to active. Thin Solid Films 559, 9–13.

Baloukas, B., Quintanilla, M., Venne, F., Benayas, A., Skripka, A., Santato, C., Vetrone, F., Martinu, L., 2016. Unpublished results.

Bauer, G., Hassmann, J., Walter, H., Haglmüller, J., Mayer, C., Schalkhammer, T., 2003. Resonant nanocluster technology – from optical coding and high quality security features to biochips. Nanotechnology 14 (12), 1289–1311.

Bergsmann, M., Kastner, F., Bauer, G., Domnick, R., Walter, H., 2003. Novel security feature made by thin film coating technique. 46th Annual Technical Conference of the Society of Vacuum Coaters, Society of Vacuum Coaters, San Francisco, California, USA, pp. 566–569.

Berning, P.H., Phillips, R.W., 1987. Thin film optically variable article and method having gold to green color shift for currency authentication. U.S. Patent, no. US4705300.

Bishop, C.A., 2001. The use of vacuum deposited coatings for security applications. 44th Annual Technical Conference of the Society of Vacuum Coaters, Society of Vacuum Coaters, Philadelphia, Pennsylvania, USA, pp. 425–430.

Bonkowski, R., Higgins, P.K., Markantes, C.T., Phillips, R.W., 2010. Methods for forming security articles having diffractive surfaces and color shifting backgrounds. U.S. Patent, no. US7754112.

Çetinörgü-Goldenberg, E., Baloukas, B., Zabeida, O., Klemberg-Sapieha, J., Martinu, L., 2011. Optical and tribomechanical stability of optically variable interference security devices prepared by dual ion beam sputtering. Appl. Opt. 50 (19), 3351–3359.

Champion, D.A., Betrabet, C.S., 2009. Security device. U.S. Patent, no. US7599109.

Chang, D.-H., Park, Y.J., Hwangbo, C.K., 2008. Optical humidity sensor using a narrow band-pass filter prepared by glancing angle deposition. J. Korean Phys. Soc. 53 (5), 2700–2704.

Chen, Y., Liu, W., 2011. Short period resonant dual-grating structures for applications to anisotropic color change securities. Opt. Eng. 50 (4), 048001.

Chuo, Y., Landrock, C.K., Omrane, B., Kaminska, B., 2014. Method for fabrication of nanostructures, World International Property Organization Patent, no. WO2014047740 A1.

Church, S.E., 2001. The technology and practice of currency printing. 38th Annual Technical Conference of the Society of Vacuum Coaters, Society of Vacuum Coaters, Chicago, Illinois, USA, pp. 425–430.

Coombs, P.G., Phillips, R.W., 1993. Optically variable interference device with peak suppression and method. U.S. Patent, no. US5214530.

Coombs, P.G., Raksha, V.P., Markantes, T., 2002. Overt and covert verification via magnetic optical security devices. Optical Security and Counterfeit Deterrence Techniques IV, vol. 4677. SPIE, San Jose, California, USA, pp. 182–193.

Coombs, P.G., Zieba, J., Bradley Jr., R.A., Lantman, C.W., Mayer, T., Phillips, R.W., Yamanaka, S.A., 2003. Luminescent pigments and foils with color-shifting properties.. U.S. Patent, no. US6572784.

Coombs, P.G., Argoitia, A., Raksha, V.P., Phillips, R.W., 2004. Integration of contrasting technologies into advanced optical security devices. Optical Security and Counterfeit Deterrence Techniques V, vol. 5310. SPIE, San Jose, California, USA, pp. 299–311.

Coombs, P.G., McCaffery, S.F., Markantes, T., 2006. Advanced verification methods for OVI® security ink. Optical Security and Counterfeit Deterrence Techniques VI, vol. 6075. SPIE, San Jose, California, USA, pp. I1–I8.

Corr, D., Bach, U., Fay, D., Kinsella, M., McAtamney, C., O'Reilly, F., Rao, S.N., Stobie, N., 2003. Coloured electrochromic 'paper-quality' displays based on modified mesoporous electrodes. Solid State Ionics 165, 315–321.

Cui, Y., Hegde, R.S., Phang, I.Y., Lee, H.K., Ling, X.Y., 2014. Encoding molecular information in plasmonic nanostructures for anti-counterfeiting applications. Nanoscale 6, 282–288.

Danine, A., Faure, C., Campet, G., Rougier, A., 2014. Electrochromic device comprising three or four layers. World International Property Organization Patent, no. WO2014135804.

Davidson II, R.B., Ziegler, J.I., Vargas, G., Avanesyan, S.M., Gong, Y., Hess, W., Haglund Jr., R.F., 2015. Efficient forward second-harmonic generation from planar Archimedean nanospirals. Nanophotonics 4 (1), 108–113.

Davies, M., Dobrowolski, J.A., 1996. Authenticating system. U.S. Patent, no. US5568251.

de Heij, H.A.M., 2002. A method for measuring the public's appreciation and knowledge of banknotes. Optical Security and Counterfeit Deterrence Techniques IV, vol. 4677. SPIE, San Jose, California, USA, pp. 15–55.

Despland, C.-A., Schmid, M., Degott, P., 2008. Creation of novel security features using optically variable magnetic inks. In: van Renesse, R.L. (Ed.), Optical Document Security I. Reconnaissance International, San Francisco, California, USA, pp. 1–10.

DiNunzio, L.A., Church, S.E., 2002. Evaluating public awareness of new currency design features. Optical Security and Counterfeit Deterrence Techniques IV, vol. 4677. SPIE, San Jose, California, USA, pp. 1–14.

Dobrowolski, J.A., 1998. Optical Thin-Film Security Devices, second ed. Artech House, Boston/London, pp. 289–328 (Chapter 13).

Dobrowolski, J.A., Waldorf, A.J., 1986. Method of manufacturing an optical interference authenticating device. U.S. Patent, no. US4626445.

Dobrowolski, J.A., Baird, K.M., Carman, P.D., Waldorf, A., 1973. Optical interference coatings for inhibiting of counterfeiting. Opt. Acta 20 (12), 925–937.

Dobrowolski, J.A., Ho, F.C., Waldorf, A., 1989. Research on thin film anticounterfeiting coatings at the National Research Council of Canada. Appl. Opt. 28 (14), 2702–2717.

Dobrowolski, J.A., Sullivan, B.T., Bajcar, R.C., 1991. Optical interference electroluminescent device having low reflectance. U.S. Patent, no. US5049780.

Frontier Economics, 2016. The Economic Impacts of Counterfeiting and Piracy – Report Prepared for BASCAP and INTA.

Glick, I., Grigg, D.F., Wilkinson, R.L., 1994. Manufacturing of optical security devices by sputtering techniques. 37th Annual Technical Conference of the Society of Vacuum Coaters, Society of Vacuum Coaters, Boston, Massachusetts, USA, pp. 85–96.

Haglmüller, J., Alguel, Y., Mayer, Ch., Matyushin, V., Bauer, G., Pittner, F., Leitner, A., Aussenegg, F., Schalkhammer, T., 2004. Cluster optical coding – from biochips to counterfeit security. Photon Processing in Microelectronics and Photonics III, vol. 5339. SPIE, pp. 652–663.

Jagielinski, T., Chamberlain, F., 2002. Magnetic imaging of currencies and secure documents. Optical Security and Counterfeit Deterrence Techniques IV, vol. 4677. SPIE, San Jose, California, USA, pp. 159–168.

James, T.D., Mulvaney, P., Roberts, A., 2016. The plasmonic pixel: large area, wide gamut color reproduction using aluminum nanostructures. Nano Lett. 16, 3817–3823.

Jeacock, A., Whiteman, R., 2010. Security device and method. U.S. Patent, no. US20100164219.

Jiang, Y., Wilson, B., Hochbaum, A., Carter, J., 2002. Novel pigment approaches in optically variable security inks including polarizing cholesteric liquid crystal (CLC) polymers. Optical Security and Counterfeit Deterrence Techniques IV, vol. 4677. SPIE, San Jose, California, USA, pp. 247–254.

Jonza, J.M., Dubner, A.D., 2004. Multilayer polymeric color-shifting polarizer films. Optical Security and Counterfeit Deterrence Techniques IV, vol. 5310. SPIE, San Jose, California, USA, pp. 256–263.

Kim, W.J., Nyk, M., Prasad, P.N., 2009. Color-coded multilayer photopatterned microstructures using lanthanide (III) ion co-doped $NaYF_4$ nanoparticles with upconversion luminescence for possible applications in security. Nanotechnology. 20, 185301.

Kittler Jr., W.C., Raksha, V.P., Phillips, R.W., Zambory, G., 2010. Patterned optical structures with enhanced security feature. U.S. Patent, no. US7880943.

Klein, R.M., Gadbois, S., Christie, J.J., 2004. Perception and detection of counterfeit currency in Canada: note quality, training and security features. Optical Security and Counterfeit Deterrence Techniques V, vol. 5310. SPIE, San Jose, California, USA, pp. 1–12.

Kovacs, A., Jonnalagadda, P., Meng, X.Y., Mescheder, U., 2009. Characterization of porous silicon based optical sensor system for biosensor applications. 2009. IEEE Sensors, Christchurch, pp. 21–26.

Kuai, S.-L., Bader, G., Ashrit, P.V., 2005. Tunable electrochromic photonic crystals. Appl. Phys. Lett. 86, 221110.

Lancaster, I.M., Mitchell, A., 2004. The growth of optically variable features on banknotes. Optical Security and Counterfeit Deterrence Techniques V, vol. 5310. SPIE, San Jose, California, USA, pp. 34–45.

Larouche, S., Martinu, L., 2008. OpenFilters: open-source software for the design, optimization, and synthesis of optical filters. Appl. Opt. 47 (13), C219–C230.

Larouche, S., Tsai, Y.-J., Tyler, T., Jokerst, N.M., Smith, D.R., 2012. Infrared metamaterial phase holograms. Nat. Mater. 11, 450–454.

Lee, K.G., Choi, B.G., Kim, B.I., Shyu, T., Oh, M.S., Im, S.G., Chang, S.-J., Lee, T.J., Kotov, N.A., Lee, S.J., 2014. Scalable nanopillar arrays with layer-by-layer patterned overt and covert images. Adv. Mater. 26 (35), 6119–6124.

Li, H., Lv, Y., Zhang, X., Wang, X., Liu, X., 2015. High-performance ITO-free electrochromic films based on bi-functional stacked WO_3/Ag/WO_3 structures. Sol. Energy Mater. Sol. Cells 136, 86–91.

Lienvens, H., 1995. Soft magnetic films for security devices. 38th Annual Technical Conference of the Society of Vacuum Coaters, Society of Vacuum Coaters, Chicago, Illinois, USA, pp. 147–151.

Lotz, H.G., Steiniger, G., 2007. Production of color shift layers with electron beam technology for identification and decorative applications. 50th Annual Technical Conference of the Society of Vacuum Coaters, Society of Vacuum Coaters, Louisville, Kentucky, USA, pp. 742–744.
MacPherson, C.D., 2011. Optically variable devices, their production and use. Patent, no. WO2011130843A1, World International Property Organization.
MacPherson, C.D., Hardwick, B.A., 2011. Optically variable devices, their production and use. U.S. Patent, no. US20130207374A1.
MacPherson, C.D., Vendette, D.G., Girouard, G., Stone, A.O., 2011. Security device. U.S. Patent, no. US8894098B2.
Martínez, A., García-Meca, C., Ortuño, R., Rodríguez-Fortuño, F.J., Martí, J., 2009. Metamaterials for optical security. Appl. Phys. Lett. 94, 251106.
Martinu, L., Klemberg-Sapieha, J.E., Küttel, O.M., Raveh, A., Wertheimer, M.R., 1994. Critical ion energy and ion flux in the growth of films by plasma-enhanced chemical vapor deposition. J. Vac. Sci. Technol. A 12 (4), 1360–1364.
McGrew, S.P., 1990. Hologram counterfeiting: problems and solutions. Optical Security and Anticounterfeiting Systems, vol. 1210. SPIE, Los Angeles, California, USA, pp. 66–76.
Messier, R., Giri, A.P., Roy, R.A., 1984. Revised structure zone model for thin film physical structure. J. Vac. Sci. Technol. A 2 (2), 500–503.
Moia, F., 2002. New coloured security elements using Rolic's LPP/LCP technology: devices for 1st to 3rd level inspection. Optical Security and Counterfeit Deterrence Techniques IV, vol. 4677. SPIE, San Jose, California, USA, pp. 194–202.
Moia, F., 2004. New colour shifting security devices. Optical Security and Counterfeit Deterrence Techniques IV, vol. 5310. SPIE, San Jose, California, USA, pp. 312–320.
Monk, P.M.S., Delage, F., Vieira, S.M.C., 2001. Electrochromic paper: Utility of electrochromes incorporated in paper. Electrochim. Acta 46, 2195–2202.
Naruse, M., Tate, N., Ohtsu, M., 2012. Optical security based on near-field processes at the nanoscale. J. Opt. 14 (9), 1–13.
Nofi, M., Matteucci, J., 1998. On-line evaluation of web coatings for color applications. 41st Annual Technical Conference of the Society of Vacuum Coaters, Society of Vacuum Coaters, Boston, Massachusetts, USA, pp. 392–396.
NTERA, 2011. Nanochromics printed security solutions. Adv. Microelectr. 38, 14–20.
Orava, J., Heikkila, N., Jaaskelainen, T., Parkkinen, J., 2008. Diffractive parameric colors. J. Opt. Soc. Am. A 25 (12), 2901–2907.
Palik, E.D., 1985. Handbook of Optical Constants of Solids. Academic Press Inc.
Pfaff, G., 2004. Optical coatings for special effect pigments. 47th Annual Technical Conference of the Society of Vacuum Coaters, Society of Vacuum Coaters, Dallas, Texas, USA, pp. 79–85.
Phillips, R.W., 1990. Optically variable films, pigments and inks. Optical Thin Films III: New Developments, vol. 1323. SPIE, San Diego, California, USA, pp. 98–109.
Phillips, R.W., 1994. Color effects from thin film designs. 8th International Conference on Vacuum Web Coating. pp. 270–284. Las Vegas, Nevada, USA.
Phillips, R.W., 2001. Graphic images in optical thin film stacks. 44th Annual Technical Conference of the Society of Vacuum Coaters. Society of Vacuum Coaters, Philadelphia, Pennsylvania, USA, pp. 93–98.
Phillips, R.W., Argoitia, A., 2005. Using vacuum roll coaters to produce anticounterfeiting devices. 48th Annual Technical Conference of the Society of Vacuum Coaters. Society of Vacuum Coaters, Louisville, Kentucky, USA, pp. 145–152.

Phillips, R.W., Bie, R., 2009. Covert security coating. U.S. Patent, no. US7630109.
Phillips, R.W., Bleikolm, A.F., 1996. Optical coatings for document security. Appl. Opt. 35 (28), 5529–5534.
Phillips, R.W., Bonkowski, R., 2000. Security enhancement of holograms with interference coatings. Optical Security and Counterfeit Deterrence Techniques III, vol. 3973. SPIE, San Jose, California, USA, pp. 304–315.
Phillips, R.W., Coombs, P.G., 1994. Transparent optically variable device. U.S. Patent, no. US5278590.
Phillips, R.W., Nofi, M., 1999. Colors by chemistry or by physics? 42nd Annual Technical Conference of the Society of Vacuum Coaters. Society of Vacuum Coaters, Chicago, Illinois, USA, pp. 494–499.
Phillips, R.W., Spellman, V.C., Gossett, W.L., Kamerling, M.A., 1988. Tamper evident optically variable device and article utilizing the same. U.S. Patent, no. US4721217.
Phillips, R.W., Mayer, T., Ash, G.S., 1991. Ink incorporating optically variable thin film flakes. U.S. Patent, no. US5059245.
Phillips, R.W., Mayer, T., Ash, G.S., 1992. Optically variable thin film flake and collection of the same. U.S. Patent, no. US5135812.
Phillips, R.W., Mayer, T., Ash, G.S., 1994. Optically variable printing inks. U.S. Patent, no. US5279657.
Phillips, R.W., Mayer, T., Ash, G.S., 1995a. Method of making optical thin flakes and inks incorporating the same. U.S. Patent, no. US5383995.
Phillips, R.W., Slusser, R., Holton, B., 1995b. Angle dependent metamerism in multilayer thin films. Proceedings of the 9th International Conference on Vacuum Web Coating. pp. 127–138.
Phillips, R.W., Markantes, C.T., Fisher, S.P., Slusser, R.G., Higgins, P.K., Bleikolm, A.F., 2000. Paired optically variable article with paired optical structures and ink, paint and foil incorporating the same and method. U.S. Patent, no. US6114018.
Raksha, V.P., Markantes, C.T., Coombs, P.G., Phillips, R.W., Nofi, M., Delst, K.-J., 2008. Printable appearance-changing graphical security devices. In: van Renesse, R.L. (Ed.), Optical Document Security I. Reconnaissance International, San Francisco, California, USA, pp. 1–15.
Raksha, V.P., Delst, C.J., Coombs, P.G., Markantes, C.T., Argoitia, A., 2010. Patterning of a spacer layer in an interference filter. U.S. Patent, no. US20100239753.
Raksha, V.P., Delst, C.J., Coombs, P.G., Markantes, C.T., Argoitia, A., 2011a. Printed magnetic ink overt security image. U.S. Patent, no. US8025952.
Raksha, V.P., Holman, J.M., Coombs, P.G., Markantes, C.T., Phillips, R.W., 2011b. Apparatus for orienting magnetic flakes. U.S. Patent, no. US7934451.
Rolfe, J., 1990. Optically variable devices for use on bank notes. Optical Security and Anticounterfeiting Systems, vol. 1210. SPIE, Los Angeles, California, USA, pp. 14–19.
Rolfe, J., 1991. Vacuum coatings for document security. 34th Annual Technical Conference of the Society of Vacuum Coaters. Society of Vacuum Coaters, Washington, DC, USA, pp. 20–25.
Rougier, A., Danine, A., Faure, C., Buffière, S., 2015. Electrochromism: from oxide thin films to devices. Oxide-based Materials and Devices VI, vol. 9364. SPIE, pp. 9364 1D 1–10.
Rozumek, O., Müller, E., 2004. Pigments having a viewing angle dependent shift of color, method of making, use and coating composition comprising of said pigments and detecting device. U.S. patent, no. US6695905B2.

Schmid, M., 2006. Optical security in ink: an industry standard that continues to evolve. Optical Security and Counterfeit Deterrence Techniques VI, vol. 6075. SPIE, San Jose, California, USA, pp. N1–N6.
Setlakwe, L., DiNunzio, L.A., 2004. Comparative analysis of public opinion research in the U.S. and Canada. Optical Security and Counterfeit Deterrence Techniques V, vol. 5310. SPIE, San Jose, California, USA, pp. 13–24.
Shi, J., Zhu, Y., Zhang, X., Baeyens, W.R.G., García-Campaña, M., 2004. Recent developments in nanomaterial optical sensors. TrAC Trends Anal. Chem. 23 (5), 351–360.
Smith, A.F., Skrabalak, S.E., 2017. Metal nanomaterials for optical anti-counterfeiting labels. J. Mater. Chem. C 5 (13), 3207–3215.
Smits, P., Rosenfeld, A.M., DeFerrari, H.F., 1989. Tamper-evident structures, U.S. Patent, no. US4837061.
Stalder, M., Seils, F., 2006. Novel optically variable color devices. Optical Security and Counterfeit Deterrence Techniques VI, vol. 6075. SPIE, San Jose, California, USA, pp. U1–U10.
Steele, J.J., 2007. Nanostructure engineering in porous columnar thin films: Recent advances. J. Mater. Sci. Mater. Electron. 18 (4), 367–379.
Tompkin, W.R., Schilling, A., Weiteneder, C., 2002. Zero-order gratings for optically variable devices. Optical Security and Counterfeit Deterrence Techniques IV, vol. 4677. SPIE, San Jose, California, USA, pp. 227–237.
Tompkin, W.R., Schilling, A., Staub, R., 2004. Color-shifting features for optically variable devices. Optical Security and Counterfeit Deterrence Techniques VI, vol. 5310. SPIE, San Jose, California, USA, pp. 244–255.
Trevor, D.J., 2008. A path to the next generation of U.S. banknotes. In: van Renesse, R.L. (Ed.), Optical Document Security I. Reconnaissance International, San Francisco, California, USA, pp. 1–8.
van Renesse, R.L., 2005. Optical Document Security, third ed. Artech House, Boston/London.
van Renesse, R.L., 2006. Protection of High Security Documents. Renesse Consulting.
Vernhes, R., Zabeida, O., Klemberg-Sapieha, J.E., Martinu, L., 2004. Single-material inhomogeneous optical filters based on microstructural gradients in plasma-deposited silicon nitride. Appl. Opt. 43 (1), 97–103.
Vernhes, R., Amassian, A., Klemberg-Sapieha, J.E., Martinu, L., 2006. Plasma treatment of porous SiN_x:H films for the fabrication of porous-dense multilayer optical filters with tailored interfaces. J. Appl. Phys.. 99 (11) 114315-1–114315-12.
Vernhes, R., Zabeida, O., Klemberg-Sapieha, J.E., Martinu, L., 2007. Properties, growth, and filter applications of a-SiN_x:H alloys prepared in pulsed radiofrequency plasma. OSA Topical Meeting on Optical Interference Filters. Tucson.
Vernhes, R., Klemberg-Sapieha, J.E., Martinu, L., 2013. Fabrication and testing of nanoporous Si_3N_4 optical filters for gas sensing applications. Sensors Actuators B Chem. 185, 504–511.
Volk, J., Balázs, J., Tóth, A.L., Bársony, I., 2004. Porous silicon multilayers for sensing by tuneable IR-transmission filtering. Sensors Actuators B 100 (1–2), 163–167.
Weinert, H.H., 2006. New developments for the continuous high rate production of physical vapor deposition (PVD) flake pigments without the use of consumable substrates. 49th Annual Technical Conference of the Society of Vacuum Coaters. Society of Vacuum Coaters, San Francisco, California, USA, pp. 642–647.

World Health Organization, 2005. Counterfeit Medicines: Some Frequently Asked Questions. World Health Organization. Available at:http://www.wpro.who.int/mediacentre/factsheets/fs_20050506/en/index.html (Online, Consulted on 3 March 2018).

Wotherspoon, D., Cheng, M., 2009. Web of deceit: the global impact of counterfeit products. Risk Manag. 56 (8), 32–36.

Zhang, Y.P., Chodavarapu, V.P., Kirk, A.G., Andrews, M.P., 2012. Nanocrystalline cellulose for covert optical encryption. Organic Photonic Materials and Devices XIV, vol. 8258. SPIE, p. 825 808–1.

Zheludev, N.I., Kivshar, Y.S., 2012. From metamaterials to metadevices. Nat. Mater. 11, 917–924.

CHAPTER

18 Optical coatings for high-intensity femtosecond lasers

Volodymyr Pervak
Ludwig-Maximilians-University, Munich, Germany

18.1 INTRODUCTION TO THE FIELD OF ULTRAFAST OPTICS

The goal of generating short laser pulses down to the limit set by a single wave cycle of light has been pursued ever since the invention of lasers. Laser pulses consisted of only a small number of wave cycles which allow more efficient exploitation of nonlinear optical effects (Brabec and Krausz, 2000) with implications as striking as the generation of single subfemtosecond light pulses (Hentschel et al., 2001). The controlled superposition of light frequencies extending over more than one octave together with carrier-envelope phase control (Jones et al., 2000; Apolonski et al., 2000; Baltuska et al., 2003) paves the way for shaping the subcycle evolution of light fields in laser pulses.

Here, we provide an overview of dispersive multilayer optics (Szipöcs et al., 1994) offering high reflectivity and controlled group delay dispersion (GDD) over some 1.5 octaves spanning ultraviolet to near infrared frequencies. Nowadays, we cannot imagine ultrashort pulses being obtained without dispersive multilayer optics. A dispersive mirror (DM) (Szipöcs et al., 1994) is a multilayer optical interference coating with the controllable phase upon reflection, usually designed by optimizing the initial multilayer design. A DM is characterized by a certain value of the group delay (GD) or GDD. GD is the first derivative of the phase shift with respect to the angular frequency:

$$\mathrm{GD} = \frac{d\varphi}{d\omega},$$

where φ is the phase shift obtained on reflection or transmission and ω is the angular frequency. GDD is the second derivative of the phase shift with respect to the angular frequency or is the first derivative of the GD:

$$\mathrm{GDD} = \frac{d(\mathrm{GD})}{d\omega} = \frac{d^2\varphi}{d\omega^2}.$$

The short pulse penetrating through dispersive medium becomes longer due to the introduced GD, as illustrated in Fig. 18.1. By introducing an inverse GD with a

Optical Thin Films and Coatings. https://doi.org/10.1016/B978-0-08-102073-9.00018-7
Copyright © 2018 Elsevier Ltd. All rights reserved.



FIG. 18.1

Basic scheme of pulse compression.

DM, the pulse can be compressed to its original pulse duration. In general, the GDD of mirror should compensate the dispersion of material (through which the initially short pulse passes) or the (nonlinear) chirp of the pulse. All mediums have dispersion of refractive index, that is, different wavelength components penetrate at different speeds. We can consider a short pulse as superposition of different frequencies matched in time. It is then obvious that the different frequencies, which penetrate through some dispersive medium, become mismatched in time and thus the pulse becomes longer. DM is supposed to match the different frequencies in time after the pulse penetrates trough some dispersive medium.

The DM (Szipöcs et al., 1994; Kärtner et al., 1997, 2001; Laude and Tournois, 1999; Matuschek et al., 1999, 2000; Sutter et al., 1999; Szipocs et al., 2000; Golubovic et al., 2000; Tempea et al., 2001; Yakovlev and Tempea, 2002; Schibli et al., 2003; Steinmeyer, 2003, 2006; Morlens et al., 2005; Dombi et al., 2005; Baum et al., 2006; Wonisch et al., 2006; Pervak et al., 2007a, b, 2008, 2009a,b,c, 2011, 2012; Nohadani et al., 2008; Chen et al., 2008, 2010; Trubetskov et al., 2008; Rivera et al., 2010; Trubetskov and Tikhonravov, 2010; Jinlong et al., 2011; Pervak, 2011; Hofstetter et al., 2011) is one of the key elements of most ultrafast (femtosecond) lasers. While being able to provide control of phase over unprecedented bandwidths and high efficiency, the DM technology suffers from unavoidable spectral oscillations of the phase. Reflection from the top layer of a multilayer structure introduces oscillations to the GDD curve due to interference between waves reflected from the top layer and waves which have penetrated and have been reflected from deeper. These oscillations may adversely affect the quality of the femtosecond laser pulses which are being controlled with DMs. Usually during design optimization the residual fluctuations drop down to a low level. The GDD oscillations can broaden the pulse and lead to energy transfer from the initial single pulse to satellites. The period of the ripples in the spectral domain determines the position of the satellite in the temporal domain, and the amplitude of these oscillations determines the amount of energy which is transferred to the satellites.

The manufacture of DMs can be as challenging as their design, as DMs are extremely sensitive to a discrepancy in layer thickness. In most cases, magnetron sputtering and ion-beam sputtering technologies provide sufficient precision of the layer thickness control. Modern sputtering technology can provide subnanometer precision in controlling the layer thickness. Some applications such as highly

dispersive mirrors (Pervak et al., 2008, 2009c, 2012) require angstrom precision. The extreme sensitivity of the DM can then be overcome by applying a special, robust design algorithm (Trubetskov and Tikhonravov, 2010; Pervak et al., 2011).

The result of the 25-year evolution of the design and fabrication of dispersive multilayers (Szipöcs et al., 1994; Kärtner et al., 1997, 2001; Laude and Tournois, 1999; Matuschek et al., 1999, 2000; Sutter et al., 1999; Szipocs et al., 2000; Golubovic et al., 2000; Tempea et al., 2001; Yakovlev and Tempea, 2002; Schibli et al., 2003; Steinmeyer, 2003, 2006; Morlens et al., 2005; Dombi et al., 2005; Baum et al., 2006; Wonisch et al., 2006; Pervak et al., 2007a,b, 2008, 2009a,b,c, 2011, 2012; Nohadani et al., 2008; Chen et al., 2008, 2010; Trubetskov et al., 2008; Rivera et al., 2010; Trubetskov and Tikhonravov, 2010; Jinlong et al., 2011; Pervak, 2011; Hofstetter et al., 2011) now allows the development of structures with low loss and high dispersion over a wide spectral range and permits compression down to the theoretical limit of the pulse duration.

18.2 MIRROR DESIGN APPROACHES

18.2.1 DISPERSIVE MIRRORS

The main problem of DM design concerns unavoidable phase oscillations which appear due to interface mismatch between the top layer of the multilayer structure and the external medium. The GDD oscillations lead to the destruction of the pulse shape. Several approaches have been devised for suppressing these undesirable oscillations: double-chirped mirrors (Kärtner et al., 1997; Matuschek et al., 1999), back-side-coated DMs (Matuschek et al., 2000), complementary pairs of DMs (Laude and Tournois, 1999; Kärtner et al., 2001; Schibli et al., 2003; Pervak et al., 2007a,b), tilted-front-interface DMs (Tempea et al., 2001), "Brewster-angle" DMs (Steinmeyer, 2003; Baum et al., 2006), and double-angled DMs (Pervak et al., 2009b). Recently, a time-domain approach based on the direct optimization of the parameters of the compressed optical pulse was also reported (Dombi et al., 2005; Trubetskov et al., 2008; Pervak et al., 2009a). Chirped mirrors (CMs) rely on a multilayer structure with a gradual change in the optical thickness across the structure, resulting in a wavelength-dependent penetration depth of the incident radiation (Szipöcs et al., 1994). A CM is characterized by a certain value of the GDD (see Fig. 18.2A). Alternatively, GD variation may be introduced by using resonant structures (or Gires-Tournois interferometer (GTI), Szipocs et al., 2000; Golubovic et al., 2000) employing a wavelength-dependent storage time of the incident radiation (see Fig. 18.2B). Both effects may coexist in a single multilayer structure (Pervak et al., 2008, 2009c, 2012) to improve the performance; in this case the multilayer mirrors should be called DMs.

Optimization software [such as Optilayer (Tikhonravov and Trubetskov, n.d.), TFCalc (TFcalc Software, n.d.), Essential Macleod (Macleod, n.d.)] can be used to design the DM. During design optimization, residual GDD oscillations can be

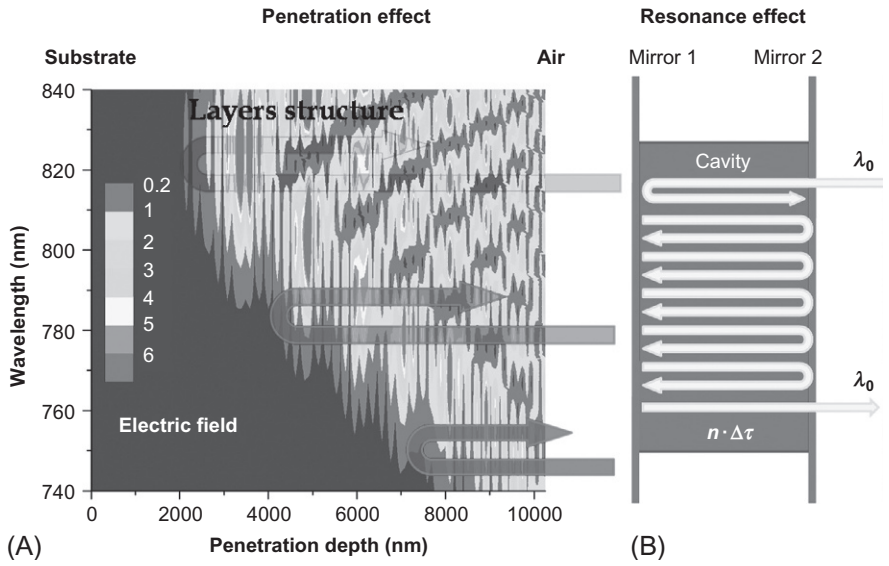


FIG. 18.2

(A) Schematic explanation of the penetration effect. The optical thickness between different coating layers in the dielectric chirped mirror structure changes gradually. This causes different wavelengths to penetrate to a different extent and hence exhibit a GD. In this example, the shorter wavelengths are reflected near the surface of the multilayer mirror while the longer wavelengths penetrate deeper. (B) Schematic explanation of the resonance effect: When the optical thickness of the layers is close to half of the wavelength, they act as a cavity of a Fabry-Pérot interferometer.

reduced to demonstrate advantages and disadvantages for pulse compression of different design approaches of DM which fulfill the following specifications: (i) reflectance $>99.9\%$ in bandwidth 600–1000 nm, (ii) GDD $= -50$ fs^2, the comparison of the compression performance of different approaches will be provided at the end of this section.

18.2.2 RESONANT STRUCTURE OR GIRES-TOURNOIS INTERFEROMETER MIRROR

Two interfaces separated by an optical distance corresponding to the half wavelength of the incident radiation resonantly enclose the impinging wave. Such nanoscale Fabry-Pérot interferometers embedded in the multilayer structure can introduce large GDs at selected wavelengths, as shown in Fig. 18.2B. The GTI approach is realized by optimizing the last few layers in the symmetrical quarter-wave layer stacks that make the reflecting mirrors (or Bragg structure). A standard quarter-wave stack or Bragg structure has zero GDD at the center of its stop band with little variation over the entire high-reflectivity range. This results in a design exhibiting greater tolerance

for manufacturing errors. The lower number of aperiodic layers means that this approach leads to a structure with smooth GDD that exhibits little sensitivity to deposition errors.

For a broader bandwidth, multi-GTI can be used (Szipocs et al., 2000). The only difference between multi- and single resonance effects being that a number of cavities are organized in a single multilayer structure. The multi-GTI mirror is characterized by a larger bandwidth and a large GDD value compared to a single GTI mirror. By using this approach, however, it would be difficult to design DM with a bandwidth of 600–1000 nm, because it will require tens of cavities. It would be hard to design and produce multilayer structures consisting of tens of cavities.

18.2.3 DOUBLE-CHIRPED MIRRORS

The multilayer Bragg structure can be decomposed into a series of symmetric index steps as shown in Fig. 18.3. The depicted structure with an antireflection (AR) coating on the top can provide a smooth GDD characteristic allowing the compression of the pulse down to a duration of 6.5 fs (Matuschek et al., 1999). AR makes it possible to match an interface mismatch between the top layer and the external medium, resulting in oscillation-free GDD characteristics.

Double CM has its limitations, as does any approach. The main limitation is a relatively narrow operating bandwidth. To overcome this bandwidth limitation and keep the GDD oscillations small, it is necessary to design broadband AR with a reflection below 0.1% over the entire bandwidth. The amount of light reflected by

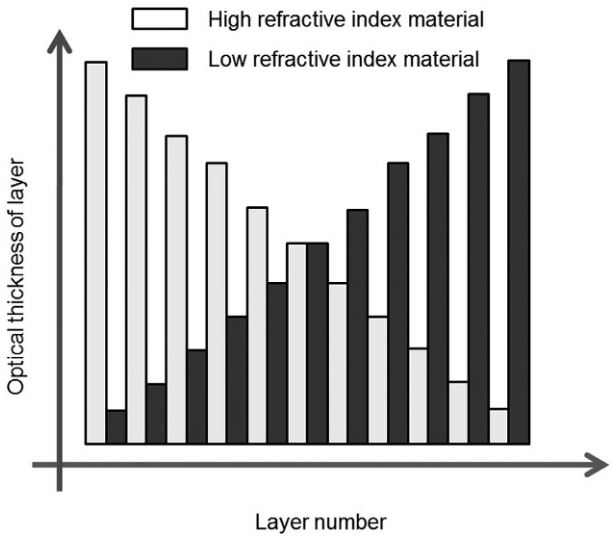


FIG. 18.3

The layer structure of the double CM is depicted.

the AR coating mainly depends on the bandwidth and the maximal contrast of available coating materials. The number of materials is limited. The largest contrast in refractive indexes can be obtained with TiO_2 and SiO_2 (2.4 and 1.45, respectively, at 800 nm). The maximal bandwidth of AR with a reflectivity <0.1% (Dobrowolski et al., 1996; Tikhonravov et al., 2008; Amotchkina, 2008) can be estimated to be ~300 nm. As a result, one individual double CM cannot be used for the full bandwidth wider than 300 nm.

18.2.4 BREWSTER-ANGLE CM

The elegant way of avoiding the cause of oscillations—due to interface mismatch—is to use p-polarized light at the Brewster angle (Steinmeyer, 2003). Placing a CM at the Brewster angle for the top layer ensures only a small amount of Fresnel-reflected light, resulting in oscillation-free GDD. Baum et al. (2006) report the compression of a broadband spectrum corresponding to a pulse duration of a few cycles. P-polarized light at large angles (e.g., the Brewster angle of fused silica is ~56 degrees) requires a significantly higher number of layers and greater total optical thickness. As a result, the manufacture of Brewster angle mirrors with a reflectivity >99% becomes a problem. In Fig. 18.4, we demonstrate designed Brewster angle mirror which has reflectance >99% and GDD = −50 fs^2 in bandwidth 600–1000 nm. This design consists of alternating 135 layers of Nb_2O_5/SiO_2. The total physical thickness is >14 μm. The design is characterized by smooth GDD and high sensitivity to angle

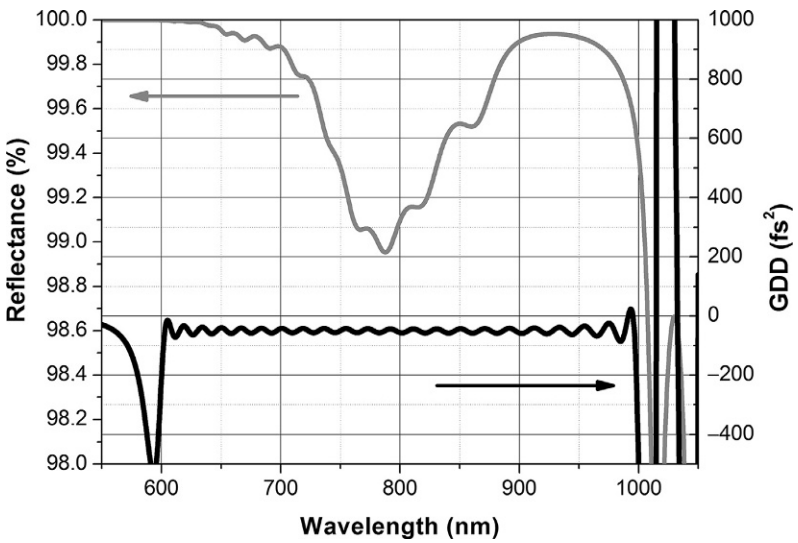


FIG. 18.4

Calculated reflectivity (gray) and GDD (black) of Brewster angle DM at angle of incidence of 55.6°.

of incidence. This mirror can be used in an extra-cavity application where angle of 55.6 degrees is easily realized. Contrariwise, the intracavity beam bounces at a small incidence angle, which makes it unrealistic to use the Brewster-angle CM as a laser oscillator mirror.

18.2.5 BACK-SIDE-COATED CM

In 2000, the back-side-coated CM was proposed by Matuschek et al. (2000). The authors suggest using a one-side-wedged substrate. The radiation penetrates through the wedged side of the substrate and interacts with a multilayer structure, as shown in Fig. 18.5. The wedge spatially splits the Fresnel reflection from the top layer and the main part of the irradiation reflected from the inner layers. Such a design can be used to obtain a smooth GDD characteristic.

Unfortunately, the substrate has to be a few millimeters thick to stay flat with a relatively thick dielectric multilayer on the top. The delay caused by reflection from the multilayer structure is neglected due to the delay caused by the beam twice passing through the substrate. Again, back-side-coated CM which covers 600–1000 nm, $R > 99\%$, and GDD $= -50$ fs^2 can be designed. Reflectance and GDD are shown in Fig. 18.6. This design consists of alternating 60 layers of Nb_2O_5/SiO_2. Total physical thickness is 6.7 μm. Back-side-coated CM has relative smooth GDD but it cannot be used for compression of a pulse due to the large path which the beam travels inside the substrate.

18.2.6 TILTED-FRONT-INTERFACE CM

The back-side-coated CM paved the way for the tilted-front-interface CM (Tempea et al., 2001). To avoid Fresnel reflection from the top layer, we now attach the wedge on the top layer (see Fig. 18.5). The tilted-front-interface CM requires an additional AR coating on top of the wedge to minimize losses. The requirements for AR of the coating on the top of the tilted-front-interface CM are not as strict as for double CM. The amount of Fresnel-reflected light brings only additional losses, but it has no influence on the GDD oscillation.

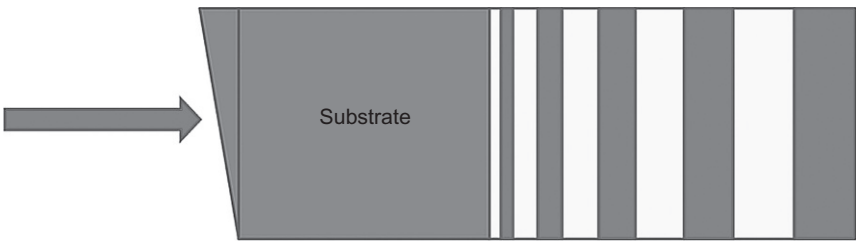


FIG. 18.5

Sketch of the main principal of back-side-coated CM.

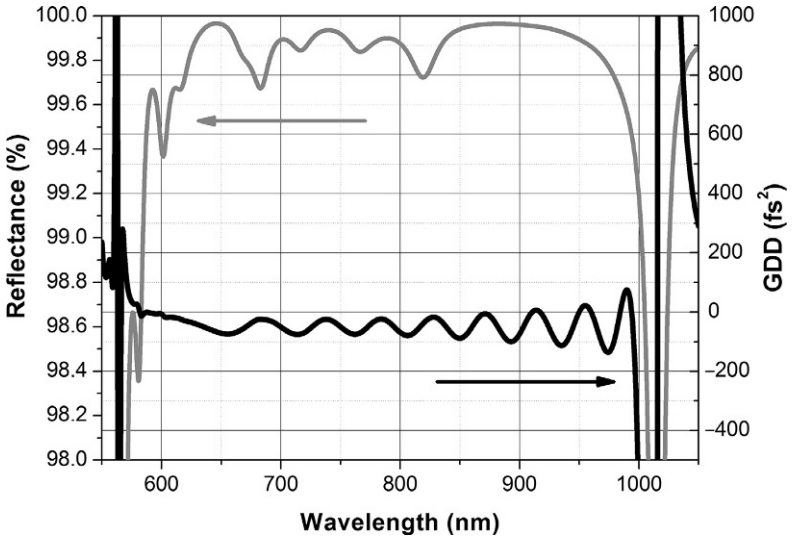


FIG. 18.6

Calculated reflectivity (gray) and GDD (black) of back-side-coated DM at angle of incidence of 5°.

The weakest point in the tilted-front-interface CM is the technology for applying a wedge onto the top of the multilayer stack. As far as we know, a tilted-front-interface CM with only a small diameter (half an inch) was fabricated using the tilted-front-interface approach. Nevertheless, the tilted-front-interface approach will be developed further as soon as the technology provides a process for applying a high-quality wedge on the top of the multilayer. The performance of design of tilted-front-interface CM looks identical to the back-side-coated CM as shown in Fig. 18.6.

18.2.7 COMPLEMENTARY PAIRS OF CMS

Complementary pair was first mentioned by Laude and Tournois (1999); later, Kärtner et al. (2001) used two different mirrors for which the GDD curves have the same oscillations and are shifted by only half a period, so that the average GDD curve has oscillations which are as low as possible (see Fig. 18.7). For a pair of CMs covering <1 octave, such a design can be realized easily.

In (Pervak et al., 2007b) the authors numerically and experimentally demonstrate a CM pair with controlled dispersion over 1.5 optical octaves. The complementary pair of such mirrors has average reflectivity >95% in a range between 400 and 1200 nm with a residual GDD oscillation <100 fs^2, as shown in Fig. 18.8. The mirror pair makes it possible to compensate a chirp of the corresponding spectrum (with a smooth phase), resulting in sub-3 fs pulses.

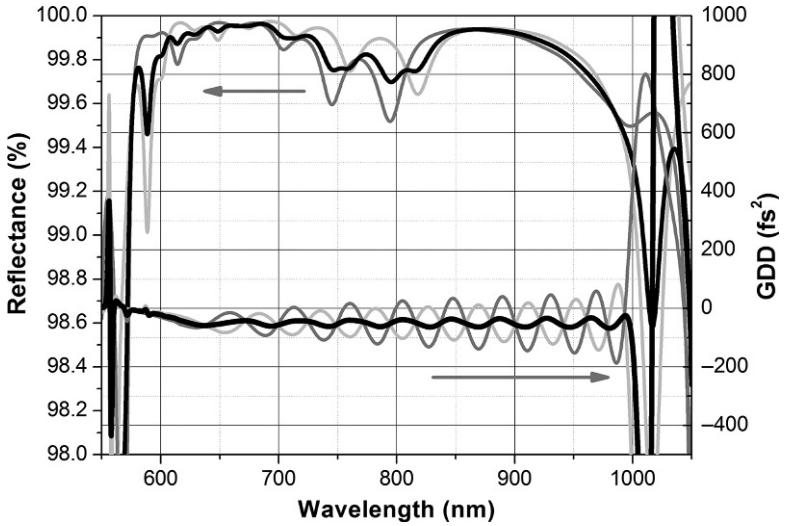


FIG. 18.7

Calculated reflectivity and GDD of a pair of complementary pair of DMs. The gray curves represent one single mirror, the light gray curves the other single mirror of the pair. The black curve is the average of the gray and light gray curves per bounce.

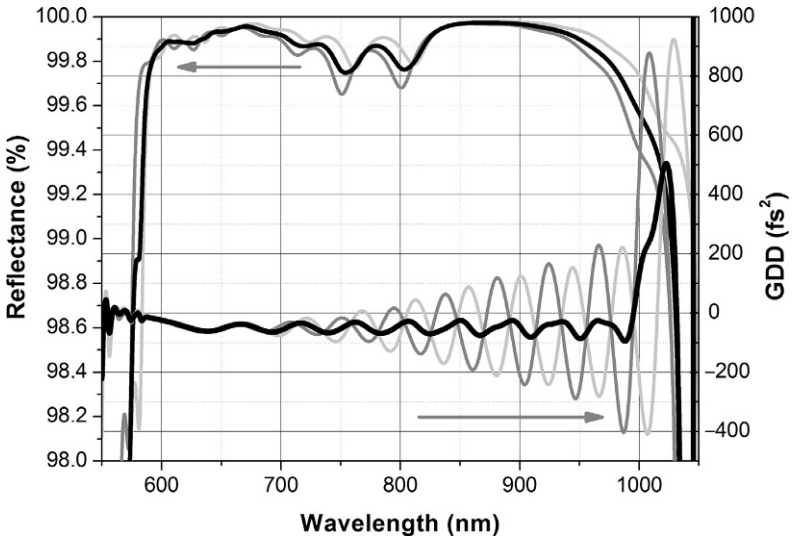


FIG. 18.8

Calculated reflectance and GDD of double-angle DM. Gray and light gray curves correspond to angles of incidence of 5 and 19 degrees, respectively. Black curves show the average calculated reflectance and GDD.

To design a complementary CM pair, the following merit function can be used (Pervak et al., 2007b):

$$F = \frac{1}{L}\sum_{j=1}^{L}\left(\frac{R_p(\lambda_j) - R^{(j)}}{\Delta R^{(j)}}\right)^2 + \left(\frac{\mathrm{GDD}_p(\lambda_j) - \mathrm{GDD}^{(j)}}{\Delta \mathrm{GDD}^{(j)}}\right)^2, \tag{18.1}$$

where $R_p(\lambda_j)$ and $\mathrm{GDD}_p(\lambda_j)$ are theoretical characteristics at wavelength λ_j, $R^{(j)}$ and $\mathrm{GDD}^{(j)}$ are target values, $\Delta R^{(j)}$ and $\Delta\mathrm{GDD}^{(j)}$ are corresponding tolerances, and L is the number of selected wavelength points.

The currently available pulse limit of 1.5 optical cycles (Pervak et al., 2007b) can be pushed to a suboptical cycle pulse by using broader DMs based on the complementary approach. To reduce GDD oscillations, one can use three, four, and even more independent mirrors.

Here, a complementary pair of DM which covers 600–1000 nm, $R > 99\%$, and $\mathrm{GDD} = -50\ \mathrm{fs}^2$ was designed. The reflectance and GDD are shown in Fig. 18.7. These designs consist of alternating 58 layers of Nb_2O_5/SiO_2. The total physical thicknesses of the design pair are 5.95 μm and 6.1 μm, respectively.

18.2.8 THE TIME-DOMAIN DM

A transform-limited short pulse, which can be calculated by the inverse Fourier transform of an arbitrary input spectrum, propagates in a dispersive medium or a set of dispersive materials (see Fig. 18.1). The pulse stretches in dispersive mediums due to the fact that the speed of light is different for different frequencies. A DM compressor can be employed to compensate this dispersion and thus compress the pulse. In femtosecond optics, the Fourier transform-limited pulse (FTLP) has the shortest possible pulse duration for a given spectrum with flat phase. Using ideal DMs for pulse compression will give us FTLP. In the conventional design approach, the ideal mirror dispersion has to be as close as possible to the dispersion of the laser elements but of the opposite sign. Usually DM has unavoidable GDD oscillations, which is the reason why pulse becomes longer, and cannot be compressed to its FTL. In the new time-domain design approach the algorithm needs structures which allow the best possible comparability of the pulse after passage through the dispersive medium and the DMs.

In publications (Dombi et al., 2005; Trubetskov et al., 2008; Pervak et al., 2009a), authors report the results of the realization, application, and comparison of the two design approaches for sub-5-fs pulse compression. By changing the optimization parameters (Trubetskov et al., 2008), the pulse duration can be traded off against the energy concentration. The time-domain approach allows us to control the pulse duration directly. There are two experimental requirements: (i) optimize the design so that the shortest pulse is generated and (ii) optimize the design so that the maximum energy is concentrated in the main pulse (in this case the pulse duration can be 10% longer). The time-domain approach has greater flexibility in controlling the pulse duration, and the pulse energy concentration, compared to conventional approaches which use phase, GD, or GDD as target for optimization.

18.2.9 DOUBLE-ANGLE DM

In their publication (Pervak et al., 2007a) the authors suggest a novel concept for suppressing GDD oscillations. It is based on identical DMs used at two different angles of incidence in combination (Fig. 18.8). The "double-angle" DMs offer (i) better manufacturing stability compared to the conventional complementary-pair approach (Laude and Tournois, 1999; Matuschek et al., 2000; Kärtner et al., 2001; Morlens et al., 2005; Dombi et al., 2005); (ii) reduced manufacturing costs compared to the complementary-pair approach which requires two perfectly matched coating runs. By proper selection of incidence angles and application of a specialized version of the needle-optimization technique (Tikhonravov et al., 1996, 2007) a double-angle DM has been designed, manufactured, and characterized with very low overall GDD oscillations. To demonstrate the utility of the double-angle approach, the mirrors were used for compressing pulses which had been spectrally broadened in a hollow fiber. Theoretical simulation shows that the pulse can be compressed to duration of 4.3 fs, which is very close to their Fourier limit of 4.2 fs.

This time double-angle DM approach has been used to design DM which covers a range of 600–1000 nm with $R > 99\%$ and GDD $= -50$ fs^2. Resulting reflectance and GDD curves are shown in Fig. 18.8, for 5 and 19 degrees as angles of incidence.

18.2.10 PULSE COMPRESSION AND ANALYSIS

In this section, we will compare the designed mirrors from the previous sections for the same virtual theoretical experiment. We have considered a hypothetical broadband dispersive delay line with compensating the GDD +500 fs^2. A Gaussian pulse carried at a wavelength of 780 nm with a Fourier transform duration of 5.86 fs (FWHM) was sent through its optical delay line and calculated the temporal intensity profile of the pulse exiting the system. The results are summarized in Table 18.1 and in Fig. 18.9. The uncompensated spectral oscillations in the mirror's GDD curve

Table 18.1 Summarized design parameters (number of layer and total physical thickness)

Design type	Pulse duration (fs)	Number of layers	Total physical thickness (nm)
Fourier transform limited pulse	5.86	–	–
Back-side-coated/tilt interface	6.09	60	6732
Brewster angle	5.94	135	14,738
Complementary pair	6.00	58	6109
		58	5947
Double angle	5.98	58	6126

Note: *Pulse durations obtained by using a certain mirror design approach in a virtual compression experiment after 10 bounces are shown.*

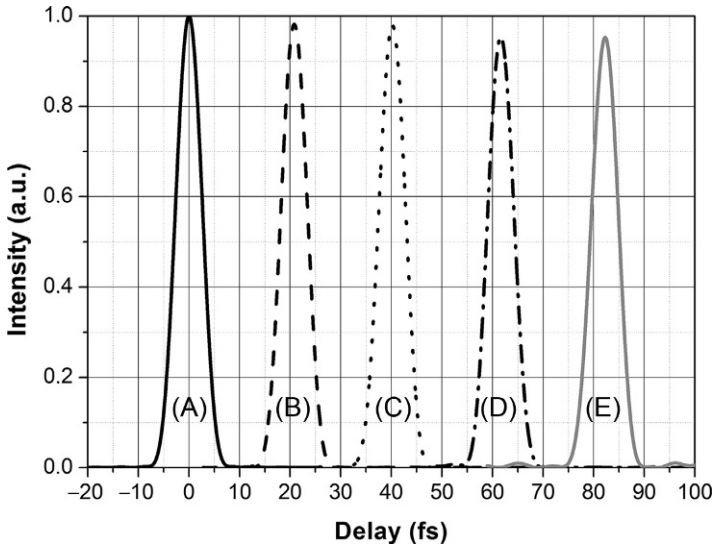


FIG. 18.9

(A) Temporal analysis of the reflection of an incident Gaussian-shaped free-chirp 5.86 fs pulse (*Black solid line*). Pulse compressed by different design approaches: (B) double angle design approach (*dashed line*), (C) complementary pair approach (*dotted line*), (D) Brewster angle approach (*dash dotted line*), (E) back-side coated or tilted-front-interface approaches (*gray solid line*).

leads to broadening of the pulse, accompanied by a decrease of the pulse energy. The results from the different approaches are similar, but still different. The shortest pulse has been obtained by using Brewster angle mirrors. The largest pulse intensity was obtained by using double-angle approach (see Fig. 18.9B). The difference in the results, obtained using the double-angle and complementary pair approaches is almost indistinguishable. The double angle design is robust and easier to produce. Usually, however, the complementary pair gives theoretically better results. All of the approaches have advantages and disadvantages. There is no universal solution; depending upon experimental requirements one of the approaches demonstrate better performance for a certain laser system. For a broadband mirror with bandwidth $>$300 nm, the best solution is double-angle and complementary pair approaches.

18.3 THE HIGHEST POSSIBLE VALUE OF GDD

During the last years, dispersive mirrors have resulted in a quantum leap in their performance (reflectance and amount of the GDD) and pave the way for a purely dispersive mirror compressors for different applications. Recently it has been revealed that the broader the spectrum for which the GDD must be controlled, the lower the

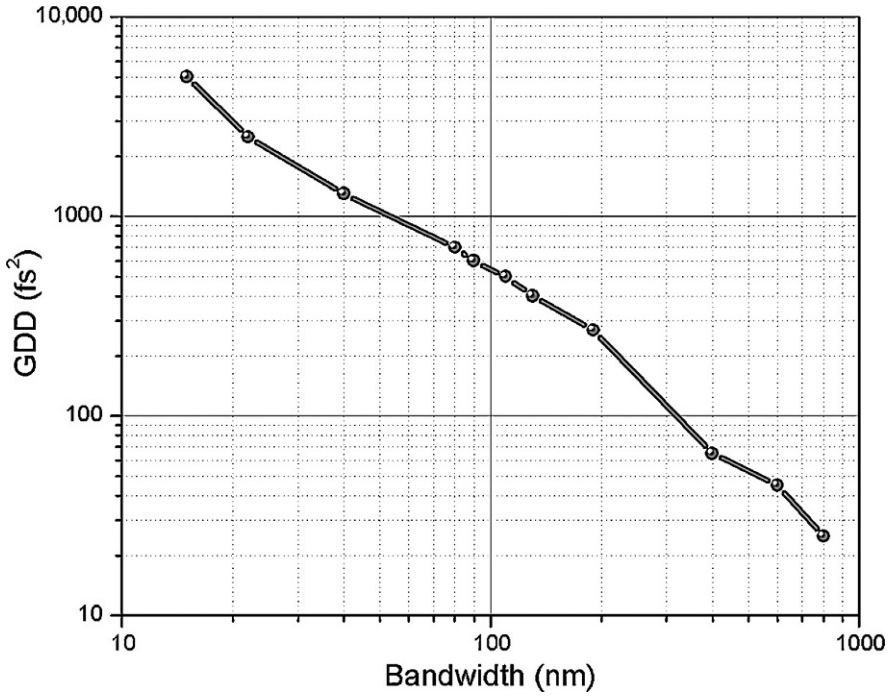


FIG. 18.10

The highest absolute value of GDD as a function of the relative bandwidth, obtained at center design wavelength of about 800 nm. The sign of GDD presented here is negative, it can be positive as well. The lines connecting the points serve as a guide to the eye.

nominal value of the GDD that can be achieved. In other words, relaxing the requirements on bandwidths allows higher values of the GDD. This finding has been inferred from the design and manufacturing of 11 different DMs, described in references Pervak et al. (2007a,b, 2008, 2009a,c, 2011, 2012), Pervak et al., 2009b and Pervak (2011), each of which represents the highest absolute value of the GDD obtained for a certain spectral width by using the same optimization technique (see Fig. 18.10). The actual values of the points along the GDD axis depend on the central frequency, layer materials, and total thickness.

18.4 PRODUCTION OF DM

To produce designed DM coatings, ion-beam sputtering (e.g., Navigator plant, Cutting Edge Coating GmbH) or magnetron sputtering (e.g., HELIOS plant, Leybold Optics) using time monitoring or broadband monitoring (Ristau et al., 2006) of layer thicknesses can be used. High quality dispersive mirrors with many dozens of layers

were successfully deposited (Pervak et al., 2008, 2009a,b,c, 2011, 2012; Trubetskov et al., 2008; Trubetskov and Tikhonravov, 2010; Jinlong et al., 2011; Pervak, 2011) and the monitoring accuracy is estimated to be 1–2 nm (Pervak et al., 2008, 2009b).

Helios deposition plant is equipped also with BBM system (Trubetskov et al., 2008). Depending on the designs of the coating, time control, broadband monitoring, or a combination of both can be used. The most frequently used high refractive index materials are Nb_2O_5, Ta_2O_5 (2.3 and 2.12 @ 800 nm, respectively), and SiO_2 low (1.47 @ 800 nm) refractive index, respectively. These materials offer optimum trade-off between low loss and high difference in the refractive indices for the wavelength range around 800 nm. The actual refractive indices of the coating materials should be determined just before the coating process is started to maximize the degree to which the designs can be produced in the manufacturing process. As an example DMs produced with the magnetron-sputtering Helios machine (Leybold Optics) are considered. Helios is equipped with two of proprietary TwinMags magnetrons and a plasma source for plasma/ion-assisted reactive middle-frequency dual-magnetron sputtering. The magnetrons were optimized for high sputtering rates and high optical layer performance. The system was pumped by turbo-molecular pumps to 1×10^{-6} mbar before deposition. Argon and oxygen were used for both magnetrons. In the magnetron cathodes, Nb, Ta, and Si targets were used. The electric power of the Si cathode was 4500 W and the power of the Nb cathode was 3500 W. The power applied to the Nb and Ta cathode was not constant because it operated in the oxygen control (or lambda control) mode, which guaranteed stable process and film properties. The gas pressure was 1×10^{-3} mbar during the sputtering process. Oxygen was fed near the targets to oxidize the sputtering films. The distance from the targets to the substrates was 100 mm. The purity of the Si target was 99.999% and that of the Nb and Ta target was 99.9%. By changing the electric power applied to the cathode, it was possible to increase or decrease the sputtering rate. It was found that the film quality degrades at high rates and good film quality was realized at a rate of around 0.5 nm/s for both materials. In the experiments usually BK7 and FS substrates were used.

18.5 PULSE COMPRESSION WITH DM

As an example for pulse compression of broadband spectrums, double-angle DMs can be considered. The design of double-angle DM consists of 80 alternating Nb_2O_5/SiO_2 layers, with a multilayer structure shown in Fig. 18.11. The thickness of both types of layers tends to decrease with increasing distance from the substrate, which resembles the design of "classical" chirped mirrors (Szipöcs et al., 1994). The physical thicknesses of the layers range from 13 to 210 nm. The successful fabrication of DMs can be as challenging as their design. The main problem is connected to the high sensitivity of GDD to even small errors in layer thicknesses. Therefore a high precision of the deposition process is mandatory for successful DM production. The GDD of the DMs was measured using a white light interferometer (Amotchkina

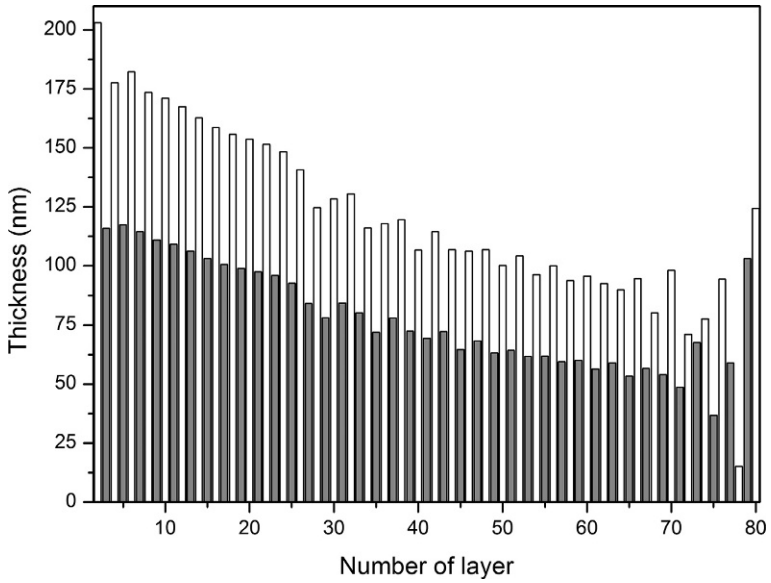


FIG. 18.11

Physical thicknesses of layers in our prototypical double-angle DM design. Layers are numbered starting from the substrate. Empty and full bars correspond to low and high refractive index materials, SiO_2 and Nb_2O_5, respectively.

et al., 2009). The result is summarized in Fig. 18.12. In the inset of Fig. 18.12, a comparison of measured and theoretical GDD of double-angle DM (Pervak et al., 2009b) for an angle of incidence of 5 degrees is shown. A good agreement has been observed between the calculated and measured reflectance as well as GDD values.

To check the implications of the residual oscillations of the effective GDD of the double-angle mirror, the propagation of an ideal transform-limited pulse having the frequency spectrum originating from a hollow-core fiber (see Fig. 18.13) was simulated through simple optical system following the fiber. The hollow-core fiber was used to stretch the existing spectrum. After proper compression of the stretched spectrum in a hollow-core fiber using DM, sub-5 fs pulses could be obtained. Four bounces on our double-angle DMs at each of the two selected angles of incidence used to compensate GVD of a 3-mm path through fused silica and a 5-m path through air. As revealed by the dashed line in Fig. 18.14, the Fourier limited input pulse with a duration of 4.2 fs measured as the full width at half maximum (FWHM), of the intensity profile (solid line in Fig. 18.14), suffers virtually no broadening; merely a small fraction ($\sim$5%) of its energy is scattered into the satellite pulses.

The double-angle DMs were tested in a hollow-core-fiber/dispersive mirror compressor seeded by millijoule scale, sub-25-fs pulses from a kilohertz-rate femtosecond Ti:sapphire laser. The hollow fiber with a length of $\sim$1 m and a core diameter of

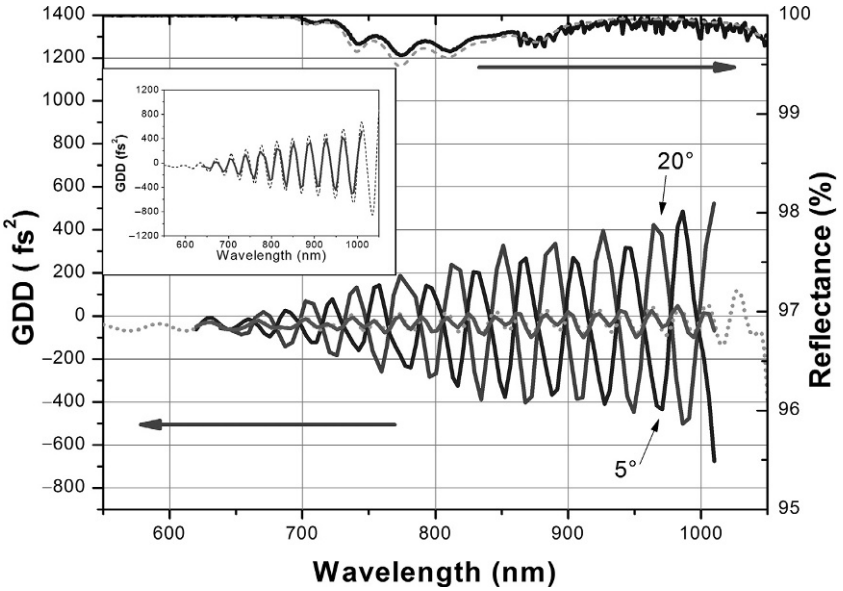


FIG. 18.12

Measured GDD and reflectance of our prototypical double-angle DM for an angle of incidence of 5 and 20 degrees (full lines). GDD and reflectance of the theoretical design are shown by dashed lines. Grey curves correspond to angles of incidence of 5 and 20 degrees. Black curves show the effective measured GDD and reflectance.

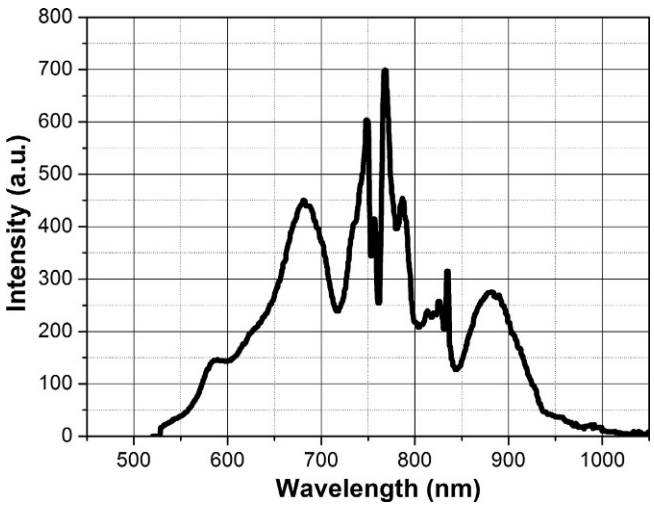


FIG. 18.13

Spectrum of femtosecond pulses originating from our gas-filled hollow fiber. With constant or linearly varying spectral phase, it allows the generation of 4.2-fs transform-limited pulses.

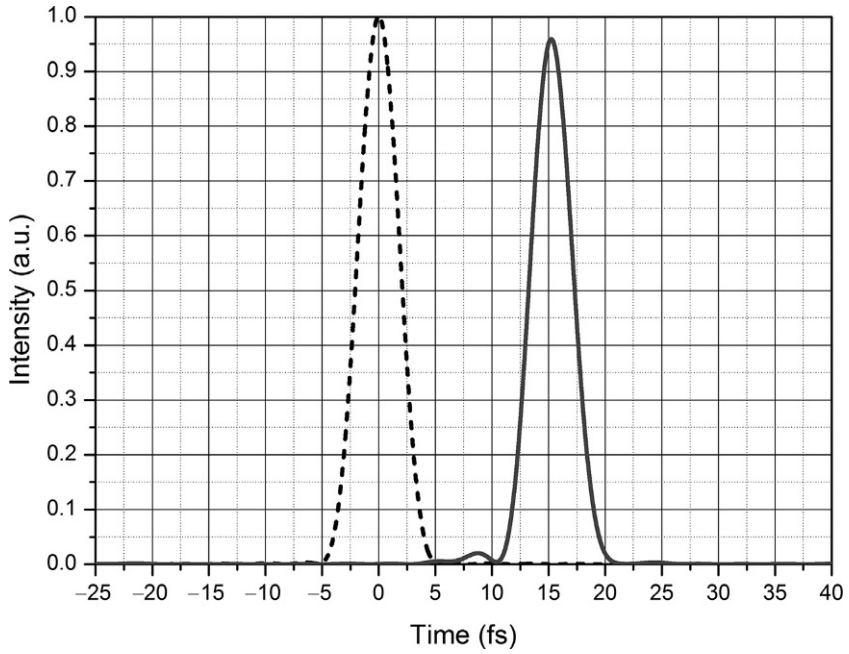


FIG. 18.14

4.2-fs Fourier-limited pulse before (dashed line) and after (full line) propagation through dispersive material and our double-angle DM compressor.

0.3 mm was filled with neon at a pressure of 2.2 bar and resulted in the output spectrum shown in Fig. 18.13. The pulses exiting the fiber traveled a distance of 1.7 m in air and 1.5 mm in fused silica and were passed through the double-angle DM compressor. The duration of the compressed pulse was measured by second-harmonic generation interferometric autocorrelation, utilizing a 5-μm thick, type-1 phase-matched BBO crystal. The measured autocorrelation function is shown in Fig. 18.15 (full line) along with the one calculated from the measured spectrum (Fig. 18.13) under the assumption of the absence of spectral phase modulation (dashed line).

Interferometric autocorrelation measurement yields a near-bandwidth-limited pulse duration of 4.3 fs after the double-angle DM compressor. The autocorrelation trace has some small oscillations over a delay range of several 10 fs, indicative of small pre-/postpulsing as a consequence of the residual GDD oscillations in the compressor and incomplete high-order dispersion compensation.

For purpose of further suppression of residual GDD oscillations or increasing bandwidth, while keeping the oscillations at the same level, the number of different angles of incidence can be increased, without compromising complexity and cost of manufacturing.

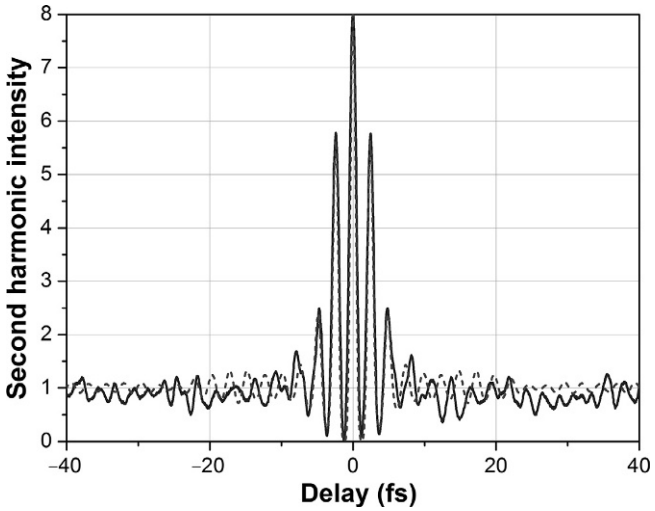


FIG. 18.15

Dashed line: theoretical interferometric autocorrelation of a pulse with the frequency spectrum shown in Fig. 18.13 in the absence of spectral phase modulation. This Fourier-limited pulse has a duration (FWHM) of 4.2 fs. Full line: measured interferometric autocorrelation function of the pulses compressed with double-angle DM compressor, indicating a pulse duration of $\sim$ 4.3 fs.

18.6 MEASUREMENT OF GROUP DELAY WITH WHITE LIGHT INTERFEROMETER

A number of dispersion measurement devices, including white light interferometers (WLIs), were reported (Knox et al., 1988; Knox, 1994; Beck and Walmsley, 1990; Gosteva et al., 2005; Naganuma et al., 1990; Daddams and Diels, 1996; Grupe, 2008; McFadden, 2011). WLI is a powerful tool for measuring the GD wavelength dependence of optical elements in a broad spectral range (Knox et al., 1988; Knox, 1994). Usually the WLI is a Michelson-type interferometer of the scanning arm type with a broadband light source (Knox et al., 1988; Knox, 1994; Gosteva et al., 2005; Naganuma et al., 1990; Daddams and Diels, 1996). That allows for group delay dispersion measurements from UV to the NIR range. The measurement scheme is shown in Fig. 18.16. More detailed description can be found in (Grupe, 2008; McFadden, 2011).

As is apparent from the figure, the obtained spectra result from the overlap of the beams from the reference arm and from the sample arm. There are a number of ways in which this setup can be used to measure the GD, but we need to consider the nature of the interference in the first place. Unlike interferometry with lasers, where coherence length is large (that it can often be practically taken for granted), the white light interferometry essentially requires small difference in the optical path length, of both

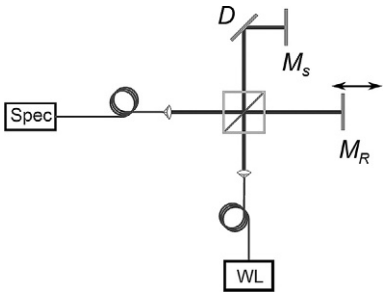


FIG. 18.16

Diagram of the set-up. A broadband while light source (WL) couples into an optical fiber. After exiting the fiber the beam is collimated and divided by a beam splitter. The reference arm is terminated by a mirror (M_r) mounted on a linear stage. A dispersive sample such as a dielectric multilayer mirror (D) is inserted into the other arm. The superposed beams are collimated into a fiber and analyzed by a spectrograph (Spec).

arms, which is within a few micrometers. The relative delay of the two beams is then low enough for the short coherence time of the white light source. Spatial coherence is already achieved by using an optical fiber to propagate the beam into the interferometer. If the optical path lengths of both arms are perfectly balanced, then the two waves that recombine at the beam splitter will have the same phase and will thus interfere constructively. If one mirror is moved slightly, then the optical path lengths are not equal and a phase difference between the two waves results. The detector registers an intensity which is given by the coherent interference.

In a dispersionless balanced interferometer all parts of the spectrum have the same optical path lengths. Therefore the maxima of all interferograms will coincide for a particular geometric reference arm length Δx (Fig. 18.17, top). Now, if a dispersive substance is put into the sample arm the optical path length becomes wavelength dependent. This shift in path length must be compensated by a corresponding shift of the reference mirror to regain maximum visibility. So the respective shift of a spectrally confined interferogram (read out from the changed reference arm length Δx at the center of an interferogram) reveals the respective group delay (bottom).

There are a number of different methods for retrieving the GD by using this set of measurement data: contour fringe shift interferometry (Knox et al., 1988; Bruning, 1978; Tateda et al., 1990), Fourier Transform Spectroscopy (Gosteva et al., 2005; Naganuma et al., 1990; Imran et al., 2004; Takeda et al., 1982; Nebel, 2005), phase-locked interferometry (Beck and Walmsley, 1990; Beck et al., 1991), utilizing wavelet analysis (Luo et al., 2011), and reconstruction of precise distance between each measurement of the interference pattern (Amotchkina et al., 2009). All these methods have advantages and disadvantages. Here, we will not discuss retrieving methods in details; interested reader can easily find all details in (Amotchkina et al., 2009; Knox et al., 1988; Knox, 1994; Beck and Walmsley, 1990; Gosteva et al., 2005; Naganuma et al., 1990; Daddams and Diels, 1996; Grupe, 2008;

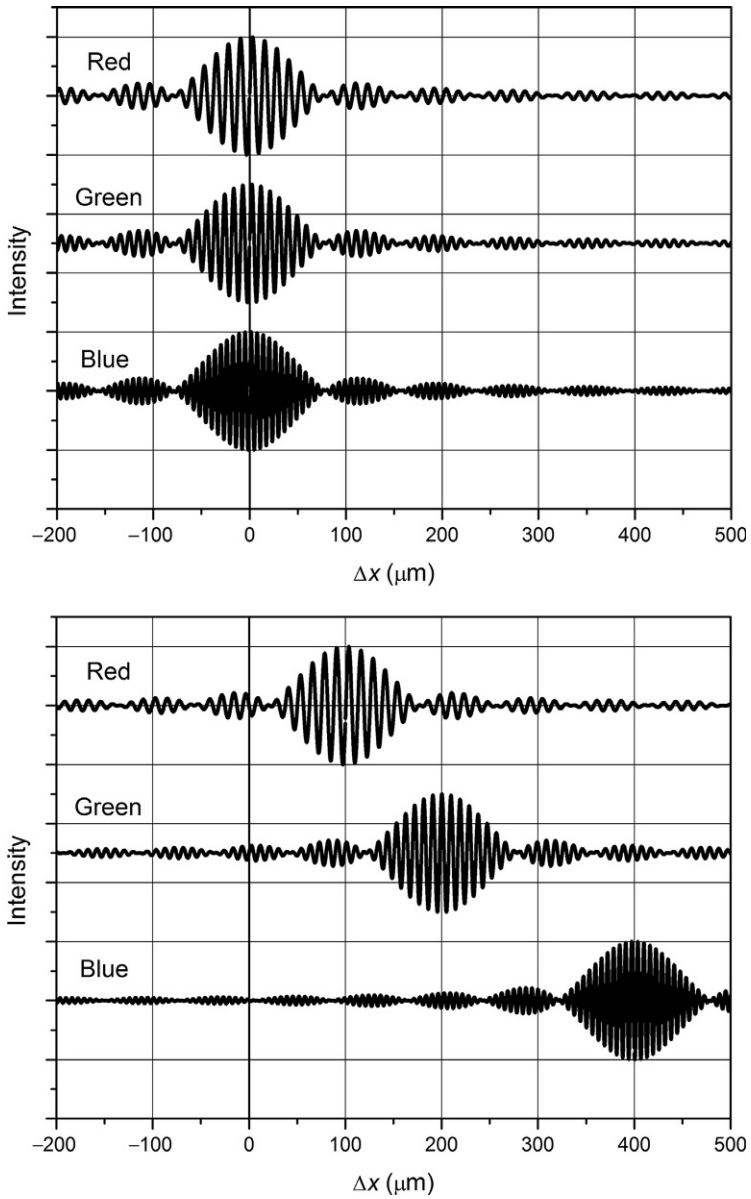


FIG. 18.17

Positions of the interferograms with a balanced interferometer (top) and a dispersive sample inserted (bottom).

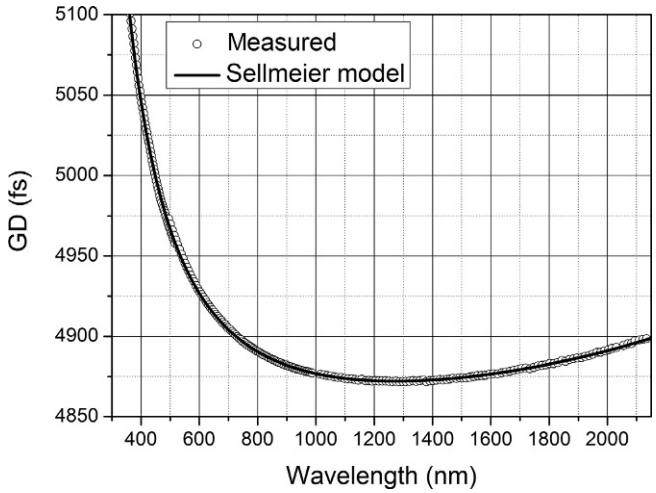


FIG. 18.18

Full-bandwidth measurement on fused-silica. The measurements' overlap at 1500 shows mismatch within the resolution limit (10 nm).

McFadden, 2011; Bruning, 1978; Tateda et al., 1990; Imran et al., 2004; Takeda et al., 1982; Nebel, 2005; Beck et al., 1991; Luo et al., 2011). It is important to note that currently Michelson interferometer setups allow GDD measurements of dispersive optics over the range 250–2150 nm comprising different independent evaluation methods mentioned above. As an example, in Fig. 18.18, the measurement of Fused Silica substrate on transmission is shown. The figure consists of four independent measurements. They replicate the theoretical curve calculated from the Sellmeier model of fused silica. One of the best results being achieved by a full-bandwidth applicable phase-tracking technique yielded a GD repeatability (standard deviation) of GD = 0.2 fs in a reference range 700–950 nm for a spectral resolution of 2.2 nm (Grupe, 2008).

The data acquisition does generally suffer from inaccuracies of various origins which provide space for further improvement. While setting up the interferometer, a trade-off had to be made between practicality and precision. A higher spectral resolution could be achieved by better resolving gratings and a spectrograph of longer focal length. However, this would necessarily mean smaller bandwidths of the single measurements and consequently a higher number of measurements to be performed.

18.7 APPLICATION OF DM IN THE HIGH-INTENSITY LASERS

At the moment there are a lot of ongoing research projects involving high intensity lasers. Such well-known projects are ELI (extreme light infrastructure) (ELI Delivery Consortium, n.d.), CALA (Centre for Advanced Laser Applications)

(ATTOWORLD, n.d.), APOLLON, GEMINI, Vulcan, and PFS (Petawatt Field Synthesizer) (Chambaret et al., 2010). All of these research activities will be based on an incremental development of the light sources to achieve unprecedented peak power performance, from tens of petawatt up to a fraction of exawatt (10^{18} W) (Chambaret et al., 2010).

The ELI project was selected in 2006 by the European Strategic Forum for Research Infrastructure (ESFRI) committee as one of the 37 major research infrastructure projects. ELI is now about to complete its preparatory phase (ELI-PP) funded by the EC, in which 13 EU countries and around 50 academic institutions have been involved (ELI Delivery Consortium, n.d.). The ELI will be the first facility in the world dedicated to laser-matter interaction in the ultrarelativistic regime ($>10^{24}$ W/cm^2), providing unprecedented intensity levels. It will be the gateway to new regimes in physics. At the same time, it will also promote new technologies such as relativistic microelectronics with the development of compact laser accelerators. The ELI will be built with a joint international effort and form an integrated infrastructure comprising at least three branches: Attosecond Science (in Szeged, Hungary) designed to make temporal investigation at the attosecond scale of electron dynamics in atoms, molecules, plasmas, and solids. High Field Science will be mainly focused on producing ultraintense and ultrashort sources of electrons, protons, and ions, and coherent and high energetic X rays (in Prague, Czech Republic) as well as laser-based nuclear physics (in Magurele, Romania) (ELI Delivery Consortium, n.d.).

The new Centre for Advanced Laser Applications (CALA) research facility expands laser science applications to biology and medicine. The unique spectrum of particle beam sources and ultrashort, intense light pulses will enable CALA to open up new fields of research in biochemistry, physics, medicine, and material sciences to the universities involved in this excellence initiative—Ludwig-Maximilians-Universität München (LMU) and Technische Universität München (TUM). CALA will produce light pulses with properties that are unique in the world. They last just a few femtoseconds (10^{-15} s) and yield an extremely high energy within this incredibly short length of time. When focused to very few thousandths of a millimeter, this unique concentration of light energy causes hitherto unattained forces to be exerted on charged particles. Electrons accelerated with this immense femtosecond light force can in turn produce extremely brilliant (i.e., intense and bunched) X-radiation as well as proton and ion beams. These can be enlisted to detect very fine structures, such as that of biomolecules, or to detect tumors in the earliest stage of growth and then eradicate them (Chambaret et al., 2010).

Most high intensity laser projects rely on the so-called chirped-pulse amplification (CPA) concept (Strickland and Mourou, 1985). CPA of ultrashort light pulses in solid-state lasers and parametric amplifiers has permitted the generation of optical pulses with multigigawatt to multiterawatt peak powers and holds promise for scaling high-power laser technology far beyond the petawatt frontier (Mourou et al., 2006; Perry and Mourou, 1994; Gerstner, 2007). CPA systems

constitute a pivotal research tool in nonlinear optics, ultrafast spectroscopy (Krausz and Ivanov, 2009; Brabec and Krausz, 2000), and high-field science (Mourou et al., 2006). Chirped-pulse amplifiers are seeded with low-energy ultrashort pulses temporally broadened in a dispersive pulse stretcher to permit for amplification without damaging the gain medium. The chirp of the amplified pulses is subsequently removed in a pulse compressor introducing a GDD of opposite sign. The pulse duration is thereby restored close to that of the input pulse. Conventional CPA systems rely on rather lossy, complex, and alignment-sensitive systems of gratings (Treacy, 1969; Pessot et al., 1987) and/or prisms (Cheng et al., 2002) for pulse stretching and recompression, which have compromised the production efficiency and the spatiotemporal quality of the amplified pulses. When diffraction gratings or prisms are used in stretchers/compressors, their angular dispersion introduces the desired wavelength-dependent delay. The alignment sensitivity of these components poses a serious challenge in the day-to-day operation of CPA systems. Minute deviations from optimum prism and grating orientations lead to angular chirp and pulse front tilt. The consequence is the deterioration of the pulse profile in focus, both spatially and temporally (Pretzler et al., 2000), which may be additionally impaired by thermal and nonlinear effects in these optical components. Moreover, their relatively large amount of uncompensated higher-order dispersion requires the use of additional dispersion management such as dispersive multilayer mirrors (Cheng et al., 2002; Cavalieri et al., 2007), or hybrid (prism-grating-material) stretcher-compressor systems (Tavella et al., 2007) for bandwidth-limited pulse generation in broadband (10-fs-scale) amplifiers. Recently, a novel implementation of CPA that overcomes these problems by using dominantly dispersive multilayer mirrors for chirp control was reported (Pervak et al., 2009c).

Dispersive mirrors offer the potential for eliminating these drawbacks owing to their capability of providing tailored dispersion over unprecedented bandwidths without spatial separation of spectral components. The wavelength-dependent delay originates from short propagation through virtually lossless, highly dispersive multilayered media. CPA implemented with dispersive mirrors is therefore intrinsically free from the angular chirp, pulse-front tilt, and nonlinear effects with the added benefit of higher-order dispersion control. They can be designed to provide GDD of either sign and hence compensate material dispersion both in the visible/near-infrared and the mid-infrared spectral range, where the dispersion of most materials changes its sign.

The exploitation of this potential calls for multilayer structures with high GDD and low loss (denoted by L) over a spectral range of several tens of THz. The figure of merit $\mathrm{FOM} = |\mathrm{GDD}|/\mathrm{L}$ determines the loss at the expense of which a certain amount of dispersion for a certain stretching factor can be realized. The first generation of chirped multilayer mirrors has typically exhibited a GDD of several tens of fs^2 with a loss of a fraction of a percent. Stretching the duration of sub-50-fs pulses by

a factor of ~1000 requires a GDD of the order of tens of thousands of fs^2. This demand would have called for a prohibitively large number of bounces leading to excessive overall losses with early-generation chirped multilayers.

Recent progress in the design and manufacture of multilayer high-dispersive mirrors (HDMs) (Pervak et al., 2009c, 2011; Trubetskov and Tikhonravov, 2010) has resulted in a quantum leap in enhancing the FOM and opened the door for an all dispersive mirror compressor for CPA.

All of the above mentioned projects rely on unique highly dispersive optics with high laser-induced damage threshold (LIDT). The generation of ultrashort pulses with large pulse energies is constrained by the LIDT of the dispersive optics. The LIDT of the dispersive optics is one of the bottlenecks in the development of high-power ultrafast systems. The optical breakdown thresholds of the single layer depositions are shown in Fig. 18.19. The damage threshold of the single layer dielectric coatings was found to be dependent on the band gap of the material used. Dispersive coatings had damage thresholds close to that of a single layer of the high index material used for the respective coating, see Fig. 18.20. The LIDT measurements of dispersive mirrors (Angelov et al., 2011; Von Conta, 2011) confirmed previously reported band gap dependence of the laser-induced damage for ultrashort pulses (Mero et al., 2005; Nguyen et al., 2008). The dispersive mirrors consist of Ta_2O_5 and Nb_2O_5 as high refractive index materials have damage of ~0.3 J/cm^2 (Angelov et al., 2011) for Ti:sapphire laser yielding 1 mJ, 30 fs pulses at 500 Hz repetition rate at 790 nm central wavelength. Increasing the current LIDT will make the femtosecond and attosecond applications to reach the higher intensity and energy levels (Pervak et al., 2014; Razskazovskaya et al., 2015, 2017).

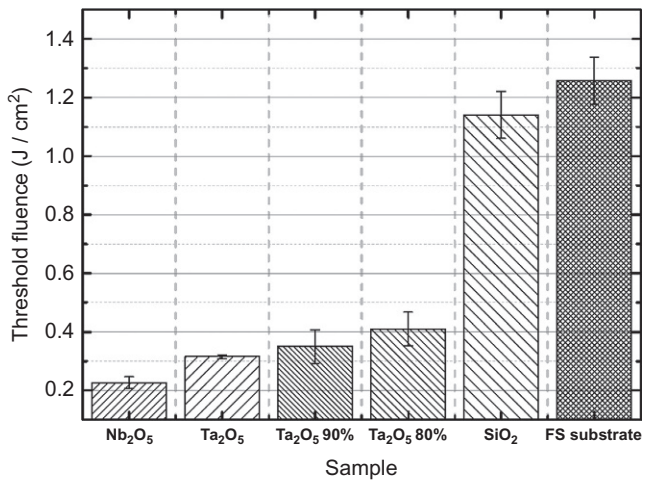


FIG. 18.19

Threshold fluencies of single layer deposition and fused silica substrate.

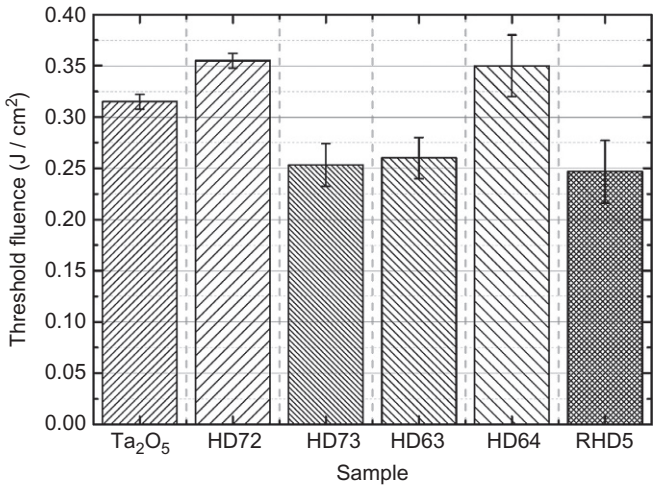


FIG. 18.20

Comparisons between a single layer of Ta_2O_5 and dispersive coatings employing Ta_2O_5 as high and SiO_2 as low index materials.

18.8 CONCLUSIONS

Existing approaches are still not at their limit. Mentioned designing approaches can be successfully used for a certain application. There is no universal approach. Another material combination with higher refractive index contrast and better accuracy of the deposition process together with further development of the mathematical designing approaches could push the now existing frontier toward shorter pulse durations, higher peak powers, and higher average powers. Another alternative for improving performance may be a combination of different approaches: for example, double-angle DM approach with the time-domain optimization or any other combinations. In the near future, dispersive multilayers will continue to play a critical role in the field of ultrafast physics.

REFERENCES

Amotchkina, T.V., 2008. Empirical expression for the minimum residual reflectance of normal and oblique-incidence antireflection coatings. Appl. Opt. 47, 3109–3113.

Amotchkina, T.V., Tikhonravov, A.V., Trubetskov, M.K., Grupe, D., Apolonski, A., Pervak, V., 2009. Measurement of group delay of dispersive mirrors with white-light interferometer. Appl. Opt. 48, 949–956.

Angelov, I.B., von Conta, A., Trushin, S.A., Major, Z., Karsch, S., Krausz, F., Pervak, V., 2011. Investigation of the laser-induced damage of dispersive coatings. In: Exarhos, G.J., Gruzdev, V.E., Menapace, J.A., Ristau, D., Soileau, M.J. (Eds.), Laser-Induced Damage in Optical Materials. vol. 8190. p. 81900B.

Apolonski, A., Poppe, A., Tempea, G., Spielmann, C., Udem, T., Holzwarth, R., Hänsch, T., Krausz, F., 2000. Observation of light-phase-sensitive photoemission from a metal. Phys. Rev. Lett. 85, 740.

ATTOWORLD, n.d., http://www.attoworld.de/Documents/pdf/CALA-Flyer_englisch.pdf.

Baltuska, A., Udem, T., Uiberacker, M., Hentschel, M., Goulielmakis, E., Gohle, C., Holzwarth, R., Yakovlev, V.S., Scrinzi, A., Hänsch, T.W., Krausz, F., 2003. Attosecond control of electronic processes by intense light fields. Nature 421, 611.

Baum, P., Breuer, M., Riedle, E., Steinmeyer, G., 2006. Brewster-angled chirped mirrors for broadband pulse compression without dispersion oscillations. Opt. Lett. 31, 2220–2222.

Beck, M., Walmsley, I.A., 1990. Measurement of group delay with high temporal and spectral resolution. Opt. Lett. 15, 492–494.

Beck, M., Walmsley, I.A., Kafka, J.D., 1991. Group delay measurement of optical components near 800 nm. IEEE J. Quantum Electron. 27, 2074–2081.

Brabec, T., Krausz, F., 2000. Intense few-cycle laser fields: frontiers of nonlinear optics. Rev. Mod. Phys. 72, 545.

Bruning, J.H., 1978. Fringe scanning interferometers. In: Malacara, D. (Ed.), Optical Shop Testing.pp. 409–437 New York.

Cavalieri, A.L., Goulielmakis, E., Horvath, B., Helml, W., Schultze, M., Fieß, M., Pervak, V., Veisz, L., Yakovlev, V.S., Uiberacker, M., Apolonski, A., Krausz, F., Kienberger, R., 2007. Intense 1.5-cycle near infrared laser waveforms and their use for the generation of ultra-broadband soft-x-ray harmonic continua. New J. Phys. 9, 242.

Chambaret, J., Chekhlov, O., Cheriaux, G., Collier, J., Dabu, R., Dombi, P., Dunne, A.M., Ertel, K., Georges, P., Hebling, J., Hein, J., Hernandez-Gomez, C., Hooker, C., Karsch, S., Korn, G., Krausz, F., Le Blanc, C., Zs, M., Mathieu, F., Metzger, T., Mourou, L., Nickles, P., Osvay, K., Rus, B., Sandner, W., Szabo, G., Ursescu, D., Varjú, K., 2010. Extreme light infrastructure: architecture and major challenges. In: SPIE Photonics Europe: High-Power Lasers, Brussels, Belgium, Proc SPIE. vol. 7721, p. 77211D.

Chen, R., Wang, F., Wang, Z., 2008. Design of chirped Mo/Si multilayer mirror in the extreme ultraviolet region. Chin. Opt. Lett. 6, 310–312.

Chen, L., Chang, G., Birge, J.R., Kärtner, F.X., 2010. Complementary chirped-mirror pair for broadband dispersion-free cavities. In: Optical Interference Coatings, OSA Technical Digest. Optical Society of America. paper FB5.

Cheng, Z., Krausz, F., Spielmann, C., 2002. Compression of 2 mJ kilohertz laser pulses to 17.5 fs by pairing double-prism compressor: analysis and performance. Opt. Commun. 201, 145–155.

Daddams, S., Diels, J.C., 1996. Dispersion measurements with white-light interferometry. J. Opt. Soc. Am. B 13, 1120–1129.

Dobrowolski, J.A., Tikhonravov, A.V., Trubetskov, M.K., Sullivan, B.T., Verly, P.G., 1996. Optimal single-band normal-incidence antireflection coatings. Appl. Opt. 35, 644–658.

Dombi, P., Yakovlev, V.S., O'Keeffe, K., Fuji, T., Lezius, M., Tempea, G., 2005. Pulse compression with time-domain optimized chirped mirrors. Opt. Express 13, 10888–10894.

ELI Delivery Consortium, n.d., https://www.eli-laser.eu.

Gerstner, E., 2007. Laser physics: extreme light. Nature 446, 16–18.

Golubovic, B., Austin, R.R., Steiner-Shepard, M.K., Reed, M.K., Diddams, S.A., Jones, D.J., Van Engen, A.G., 2000. Double Gires-Tournois interferometer negative-dispersion mirrors for use in tunable mode-locked lasers. Opt. Lett. 25, 275–277.

Gosteva, A., Haiml, M., Paschotta, R., Keller, U., 2005. Noiserelated resolution limit of dispersion measurements with white-light interferometers. J. Opt. Soc. Am. B 22, 1868–1874.
Grupe, D., 2008. Measuring Group Delay Dispersion in the UV-VIS-IR Range by White-Light Interferometry, Munich. (Master thesis).
Hentschel, M., Kienberger, R., Spielmann, C., Reider, G.A., Milosevic, N., Brabec, T., Corkum, P., Heinzmann, U., Drescher, M., Krausz, F., 2001. Attosecond metrology. Nature 414, 509.
Hofstetter, M., Schultze, M., Fieß, M., Dennhardt, B., Guggenmos, A., Gagnon, J., Yakovlev, V.S., Goulielmakis, E., Kienberger, R., Gullikson, E.M., Krausz, F., Kleineberg, U., 2011. Attosecond dispersion control by extreme ultraviolet multilayer mirrors. Opt. Express 19, 1767–1776.
Imran, T., Hong, K.H., Yu, T.J., Nam, C.H., 2004. Measurement of the group delay dispersion of femtosecond optics using white-light interferometry. Rev. Sci. Instrum. 75, 2266–2270.
Jinlong, Z., Xinbin, C., Zhanshan, W., Hongfei, J., Tao, D., 2011. HfO_2/SiO_2 chirped mirrors manufactured by electron beam evaporation. Appl. Opt. 50, C388–C391.
Jones, D.J., Diddams, S.A., Ranka, J.K., Stentz, A., Windeler, R.S., Hall, J.L., Cundiff, S.T., 2000. Carrier-envelope phase control of femtosecond Modelocked lasers and direct optical frequency synthesis. Science 288, 635.
Kärtner, F.X., Matuschek, N., Schibli, T., Keller, U., Haus, H.A., Heine, C., Morf, R., Scheuer, V., Tilsch, M., Tschudi, T., 1997. Design and fabrication of double-chirped mirrors. Opt. Lett. 22, 831–833.
Kärtner, F.X., Morgner, U., Ell, R., Schibli, T., Fujimoto, J.G., Ippen, E.P., Scheuer, V., Angelow, G., Tschudi, T., 2001. Ultrabroadband double-chirped mirror pairs for generation of octave spectra. J. Opt. Soc. Am. B 18, 882–885.
Knox, W.H., 1994. Dispersion measurements for femtosecond-pulse generation and applications. Appl. Phys. B Lasers Opt. 58, 225–235.
Knox, W.H., Pearson, N.M., Li, K.D., Hirlimann, C.A., 1988. Interferometric measurements of femtosecond group delay in optical components. Opt. Lett. 13, 574–576.
Krausz, F., Ivanov, M., 2009. Attosecond physics. Rev. Mod. Phys. 81, 163–234.
Laude, V., Tournois, P., 1999. Chirped mirror pairs for ultrabroadband dispersion control. In: Digest of Conference on Lasers and Electro-Optics (CLEO_US). Optical Society of America, pp. 187–188.
Luo, Z., Zhang, S., Shen, W., Xia, C., Ma, Q., Liu, X., Zhang, Y., 2011. Group delay dispersion measurement of a dispersive mirror by spectral interferometry: comparison of different signal processing algorithms. Appl. Opt. 50, C239–C245.
Macleod A, n.d., Essential Macleod, http://www.thinfilmcenter.com/.
Matuschek, N., Kärtner, F.X., Keller, U., 1999. Analytical design of double-chirped mirrors with custom-tailored dispersion characteristics. IEEE J. Quantum Electron. 35, 129–137.
Matuschek, N., Gallmann, L., Sutter, D.H., Steinmeyer, G., Keller, U., 2000. Back-side-coated chirped mirrors with ultrasmooth broadband dispersion characteristics. Appl. Phys. B Lasers Opt. 71, 509–522.
McFadden, D., 2011. Operating a White Light Interferometer for the Measurement of Group Delay in the Ultraviolet Range, Munich. (Bachelor thesis).
Mero, M., Clapp, B., Jasapara, J.C., Rudolph, W., Ristau, D., Starke, K., Krüger, J., Martin, S., Kautek, W., 2005. On the damage behavior of dielectric films when illuminated with multiple femtosecond laser pulses. Opt. Eng. 44 (5), 051107.

Morlens, A., Balcou, P., Zeitoun, P., Valentin, C., Laude, V., Kazamias, S., 2005. Compression of attosecond harmonic pulses by extreme-ultraviolet chirped mirrors. Opt. Lett. 30, 1554–1556.

Mourou, G., Tajima, T., Bulanov, S.V., 2006. Optics in the relativistic regime. Rev. Mod. Phys. 78, 309–371.

Naganuma, K., Mogi, K., Yamada, H., 1990. Group-delay measurement using the Fourier transform of an interferometric cross correlation generated by white light. Opt. Lett. 15, 393–395.

Nebel, T., 2005. Measuring the Group Delay Dispersion of Optical Elements. (Diploma thesis). Fakultaet Fuer Physik Der Ludwig-Maximilians-Universitaet, Munich.

Nguyen, D., Emmert, L.A., Cravetchi, I.V., Mero, M., Rudolph, W., Jupe, M., Lappschies, M., Starke, K., Ristau, D., 2008. TixSi1-xO_2 optical coatings with tunable index and their response to intense subpicosecond laser pulse irradiation. Appl. Phys. Lett. 93 (26), 261903.

Nohadani, O., Birge, J.R., Kärtner, F.X., Bertsimas, D.J., 2008. Robust chirped mirrors. Appl. Opt. 47, 2630–2636.

Perry, M.D., Mourou, G., 1994. Terawatt to Petawatt subpicosecond lasers. Science 264, 917–924.

Pervak, V., 2011. Recent development and new ideas in the field of dispersive multilayer optics. Appl. Opt. 50, C55.

Pervak, V., Krausz, F., Apolonski, A., 2007a. Dispersion control over the UV-VIS-NIR spectral range with HfO_2/SiO_2 chirped dielectric multilayers. Opt. Lett. 32, 1183–1185.

Pervak, V., Tikhonravov, A.V., Trubetskov, M.K., Naumov, S., Krausz, F., Apolonski, A., 2007b. 1.5-Octave chirped mirror for pulse compression down to sub-3 fs. Appl. Phys. B Lasers Opt. 87, 5–12.

Pervak, V., Teisset, C., Sugita, A., Naumov, S., Krausz, F., Apolonski, A., 2008. High-dispersive mirrors for femtosecond lasers. Opt. Express 16, 10220–10233.

Pervak, V., Ahmad, I., Fulop, J., Trubetskov, M.K., Tikhonravov, A.V., 2009a. Comparison of dispersive mirrors based on the time-domain and conventional approaches, for sub-5-fs pulses. Opt. Express 17, 2207–2217.

Pervak, V., Ahmad, I., Trubetskov, M.K., Tikhonravov, A.V., Krausz, F., 2009b. Double-angle multilayer mirrors with smooth dispersion characteristics. Opt. Express 17, 7943–7951.

Pervak, V., Ahmad, I., Trushin, S.A., Major, Z., Apolonski, A., Karsch, S., Krausz, F., 2009c. Chirped-pulse amplification of laser pulses with dispersive mirrors. Opt. Express 17, 19204–19212.

Pervak, V., Trubetskov, M.K., Tikhonravov, A.V., 2011. Robust synthesis of dispersive mirrors. Opt. Express 19, 2371.

Pervak, V., Pronin, O., Razskazovskaya, O., Brons, J., Angelov, I.B., Trubetskov, M.K., Tikhonravov, A.V., Krausz, F., 2012. High-dispersive mirrors for high power applications. Opt. Express 20, 4503–4508.

Pervak, V., Razskazovskaya, O., Angelov, I.B., Vodopyanov, K.L., Trubetskov, M., 2014. Dispersive mirror technology for ultrafast lasers in the range 220–4500 nm. Adv. Opt. Technol. 3, 55–63.

Pessot, M., Maine, P., Mourou, G., 1987. 1000 times expansion compression of optical pulses for chirped pulse amplification. Opt. Commun. 62, 419–421.

Pretzler, G., Kasper, A., Witte, K.J., 2000. Angular chirp and tilted light pulses in CPA lasers. Appl. Phys. B Lasers Opt. 70, 1–9.

Razskazovskaya, O., Luu, T.T., Trubetskov, M.K., Goulielmakis, E., Pervak, V., 2015. Nonlinear absorbance in dielectric multilayers. Optica 2, 803–811.
Razskazovskaya, O., Krausz, F., Pervak, V., 2017. Multilayer coatings for femto- and attosecond technology. Optica 4, 129–138.
Ristau, D., Ehlers, H., Gross, T., Lappschies, M., 2006. Optical broadband monitoring of conventional and ion processes. Appl. Opt. 45, 1495–1501.
Rivera, C.A., Bradforth, S.E., Tempea, G., 2010. Gires-Tournois interferometer type negative dispersion mirrors for deep ultraviolet pulse compression. Opt. Express 18, 18615–18624.
Schibli, T.R., Kuzucu, O., Kim, J.W., Ippen, E.P., Fujimoto, J.G., Kaertner, F.X., Scheuer, V., Angelow, G., 2003. Toward single-cycle laser systems. IEEE J. Sel. Top. Quantum Electron. 4, 990–1001.
Steinmeyer, G., 2003. Brewster-angled chirped mirrors for highfidelity dispersion compensation and bandwidths exceeding one optical octave. Opt. Express 11, 2385–2396.
Steinmeyer, G., 2006. Femtosecond dispersion compensation with multilayer coatings: toward the optical octave. Appl. Opt. 45, 1484–1490.
Strickland, D., Mourou, G., 1985. Compression of amplified chirped optical pulses. Opt. Commun. 56, 219–221.
Sutter, D.H., Steinmeyer, G., Gallmann, L., Matuschek, N., Morier-Genoud, F., Keller, U., Scheuer, V., Angelow, G., Tschudi, T., 1999. Semiconductor saturable-absorber mirror assisted Kerr-lens mode-locked Ti:sapphire laser producing pulses in the two-cycle regime. Opt. Lett. 24, 631–633.
Szipöcs, R., Ferencz, K., Spielmann, C., Krausz, F., 1994. Chirped multilayer coatings for broadband dispersion control in femtosecond lasers. Opt. Lett. 19, 201–203.
Szipocs, R., Koházi-Kis, A., Lako, S., Apai, P., Kovács, A.P., DeBell, G., Mott, L., Louderback, A.W., Tikhonravov, A.V., Trubetskov, M.K., 2000. Negative dispersion mirrors for dispersion control in femtosecond lasers: chirped dielectric mirrors and multicavity Gires-Tournois interferometers. Appl. Phys. B Lasers Opt. 70, S51–S57.
Takeda, M., Hideki, I., Kobayashi, S., 1982. Fourier-transform method of fringe pattern analysis for computer-based topography and interferometry. J. Opt. Soc. Am. 72, 156–160.
Tateda, M., Shibata, N., Seikai, S., 1990. Interferometric method for chromatic dispersion measurement in a single-mode optical fiber. IEEE J. Quantum Electron. QE-17, 404–407.
Tavella, F., Nomura, Y., Veisz, L., Pervak, V., Marcinkevičius, A., Krausz, F., 2007. Dispersion management for a sub-10-fs, 10 TW optical parametric chirped-pulse amplifier. Opt. Lett. 32, 2227–2229.
Tempea, G., Yakovlev, V., Bacovic, B., Krausz, F., Ferencz, K., 2001. Tilted-front-interface chirped mirrors. J. Opt. Soc. Am. B 18, 1747–1750.
TFcalc Software, n.d., http://www.sspectra.com.
Tikhonravov A V and Trubetskov MK, OptiLayer Thin Film Software, n.d., http://www.optilayer.com.
Tikhonravov, A.V., Trubetskov, M.K., DeBell, G.W., 1996. Application of the needle optimization technique to the design of optical coatings. Appl. Opt. 35, 5493–5508.
Tikhonravov, A.V., Trubetskov, M.K., DeBell, G.W., 2007. Optical coating design approaches based on the needle optimization technique. Appl. Opt. 46, 704–710.
Tikhonravov, A.V., Trubetskov, M.K., Amotchkina, T.V., Dobrowolski, J.A., 2008. Estimation of the average residual reflectance of broadband antireflection coatings. Appl. Opt. 47, 124–130.
Treacy, E.B., 1969. Optical pulse compression with diffraction gratings. IEEE J. Quantum Electron. QE-5, 454–458.

Trubetskov, M.K., Tikhonravov, A.V., 2010. Robust synthesis of multilayer coatings. In: Optical Interference Coatings, OSA Technical Digest. Optical Society of America. paper TuA4.

Trubetskov, M., Tikhonravov, A., Pervak, V., 2008. Time-domain approach for designing dispersive mirrors based on the needle optimization technique. Theory. Opt. Express 16, 20637–20647.

Von Conta, A., 2011. Characterization of the Laser Induced Damage Threshold of Mirrors in the Ultra Short Pulse Regime. (Bachelor thesis). Hochschule Muenchen, Muenchen.

Wonisch, A., Neuhäusler, U., Kabachnik, N.M., Uphues, T., Uiberacker, M., Yakovlev, V., Krausz, F., Drescher, M., Kleineberg, U., Heinzmann, U., 2006. Design, fabrication, and analysis of chirped multilayer mirrors for reflection of extreme-ultraviolet attosecond pulses. Appl. Opt. 45, 4147–4156.

Yakovlev, V., Tempea, G., 2002. Optimization of chirped mirrors. Appl. Opt. 41, 6514–6520.

CHAPTER

Optical coatings for large facilities

19

Catherine Grèzes-Besset*, Grégory Chauveau*, Laurent Pinard†
CILAS, Aubagne, France Lyon I University—CNRS-IN2P3, Lyon, France†*

19.1 INTRODUCTION

This chapter deals with the characteristics of the coatings that are required for large facilities. In fact, it is necessary to consider both the industrial environment and the hard environmental conditions and also the specific properties that are asked for these components.

Moreover, in such facilities, it is common to encounter optical components that present large dimensions, and it is first important to define what is considered as large optics. In the modern optical systems, progress in the last decades has led to dimensions in optics that now exceed 600 mm of diameter that can be considered as large optics.

For example, the mirrors in large telescopes have a common diameter > 1 m, and shown in Fig. 19.1.

19.2 DOMAINS OF APPLICATIONS AND MAJOR PROGRAMS

Optical coatings have their use in large dimension facilities, and the coating technology is pushed to its limits due to the increasing demand in performances.

The domains of applications of large optics may be split into different parts as the characteristics that are motivated are not the same. The domains focused are as follows:

- Scientific large instruments
- Laser
- Space
- Astronomy
- Solar

Optical Thin Films and Coatings. https://doi.org/10.1016/B978-0-08-102073-9.00019-9
Copyright © 2018 Elsevier Ltd. All rights reserved.

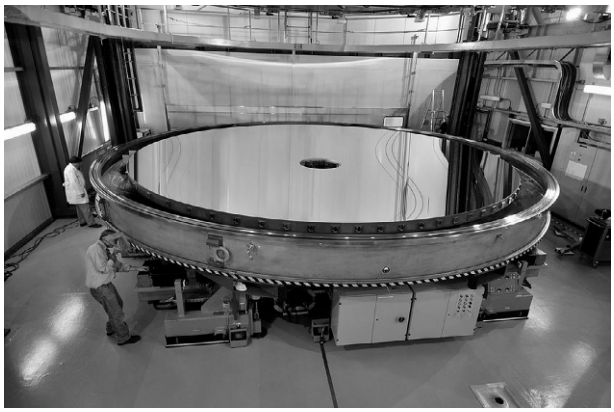


FIG. 19.1

The 8.2-m primary mirror of Yepun, Unit Telescope 4 of European Southern Observatory (ESO) Very Large Telescope, after its recoating in early March

Credit: ESO/G. Huedepohl.

19.2.1 SCIENTIFIC LARGE INSTRUMENTS

The first domain of applications is the very large research infrastructures (VLRIs) for which the cost of construction and use must be shared among several research organizations. Such VLRIs allow the scientific community to access sophisticated installations and innovative technologies that could not be supported by a lone laboratory. Major international collaborations between different countries are implemented to address fundamental experiments. Through such partnerships, it is thus possible to design, to develop, and to maintain the operation of ambitious projects that could not have emerged alone; that is the case for international projects such as Virgo, which will be presented in detail later.

A lot of facilities are implemented for many simultaneous users as it is in the case of ESRF (European Synchrotron Radiation Facility) synchrotron in Grenoble, France, for example, dedicated to electromagnetic research intended for elementary particles acceleration and that requires multilayer coatings for X-ray optical devices on substrates up to 100 cm long, or for the ILL, Institut Laue-Langevin, which is an international research center based in Grenoble, France, that operates one of the most intense neutron sources in the world and involves super mirrors based on several hundred layers of Ni/Ti coatings on large substrate surfaces.

On the other hand, user facilities are also implemented for a small number of simultaneous users, such as big optical telescopes, or forthcoming extremely large telescope of ESO and are also great prescribers of optical coatings. In this case, the sophisticated instruments installed in the telescopes demand for spectral performances as well as environmental conditions. As an example, the "Planet Finder" Instrument for the VLT, SPHERE (Spectro-Polarimetric High-contrast Exoplanet Research) involves a lot of coatings and filters working at cryogenic temperature (Beuzit et al., 2006; Krol et al., 2011).

19.2.2 LASER

The large-scale laser facilities that have been driven by laser fusion research are also a huge applicant of optical coatings; we can quote some examples of current laser projects such as the National Ignition Facility, NIF Project, or the Laser Megajoule, for which very high fluences are the key driver of the optical components requirements.

In about 50 years, a lot of developments have been made to reduce laser damage in optical coatings (Bloembergen, 1973; Porteus and Seitel, 1984; Kozlowski and Chow, 1994; Natoli et al., 2002; Neauport et al., 2004; Amra, 2005), involving the whole scientific community through the improvement of all the steps involved in the fabrication of coated components. Major works have been carried out from the improvement of coating technologies to the implementation of postprocessing steps by laser conditioning, where the optics are exposed to a progressive increasing fluence, allowing a high increase of the optic threshold of about a factor 2.

For these projects, a lot of additional coatings are required such as reflective coatings, beam splitters, and antireflection coatings on large substrate as well as small-size components. An example is that of the National Ignition Facility (NIF) that is equipped with 192 laser beams in operation from March 2009 and includes several thousands of large optics (1 m scale) mirrors, polarizers, and transport mirrors, whose size is compatible with the $40 \times 40\,\mathrm{cm}^2$ beams and also smaller optics (Stolz et al., 2001).

Ambitious laser projects are implemented around the world; hereafter, we give a quick overview of these projects for which large optics are required:

- Upgrading of existing laser facility up to 10 PW. Vulcan is a (1015 W) laser available in the United Kingdom and international research community. The Vulcan laser at the Rutherford Appleton Laboratory's Central Laser Facility in Oxfordshire, United Kingdom, is constituted of eight beams of 2.5 kJ each (~2 ns) pulse infrared neodymium glass laser. Vulcan is also capable of operating in double frequency mode, where it can deliver about 1 kJ to a target at 532 nm in 2 ns pulses. One of Vulcan's beams is also available as an ultrashort pulse (~700 J in ~700 fs) with an ultrahigh intensity beam using chirped pulse amplification called the "Vulcan petawatt."
- HiPER—New facility (High Power Laser Energy Research facility) will be a civilian facility whose main mission is to demonstrate that inertial fusion could be used as a future energy source.
- NIF—Largest and most powerful laser project based in the United States.
- LMJ—Laser facility on a similar scale is based in France.
- ELI—Collaborative laser project based over several sites with the first in Romania.
- ORION—New laser facility is based in AWE, UK.
- XFEL—European free-electron laser project is based in Germany.
- Others—Projects that are currently ongoing in China, Japan, Russia, and elsewhere.

Such complex projects require optical components of >900 mm diameter, 100 mm thick coated with high reflective mirrors that must withstand >10 J/cm^2 for 1053-nm pulse duration 1 ns. Requirements are also there for performance of wave front, and sophisticated components are included in the laser systems involving adaptive optics systems.

As an example, we show here after a monomorph deformable mirror developed by CILAS for high-intensity lasers (Fig. 19.2). In this case, the mirror is equipped with 63 actuators over an 85 mm useful aperture.

The ambitious collaborative European Project ELI (Extreme Light Infrastructure) is a good example of laser facilities challenges. Optical coatings are considered as one of the bottlenecks of the project, which involves nearly 40 research and academic institutions from 13 EU member countries, forming a pan-European laser facility that aims to host the most intense lasers worldwide. It will be required for the production of large-sized optics and mirrors of dimensions 250 × 350 mm and with high damage threshold better than 1 J/cm^2 for 15 fs pulses, such mirrors are required to present a 200 nm broadband of high reflectivity on the 700–900 nm spectral range.

Sophisticated coatings for gratings are also required, as it is the case for the under technological development Apollon laser (150 J/15 fs @1 shot/mn) from Institut de Lumière Extrême (ILE) in France, Saclay. This laser uses the world's largest (940 × 750 mm^2) gold gratings available at 800 nm wavelength for broadband spectrum from Livermore and that has been tested at a maximum fluence on gratings of 0.2 J/cm^2.

A challenging goal is to increase the laser-induced damage threshold to a value of 1 J/cm^2, as it would lead to the avoiding of one compressor and beam collimators in the laser. So research on coatings is in progress in order to meet this requirement; in particular, design and deposition processes are under development (Chambaret, 2010).

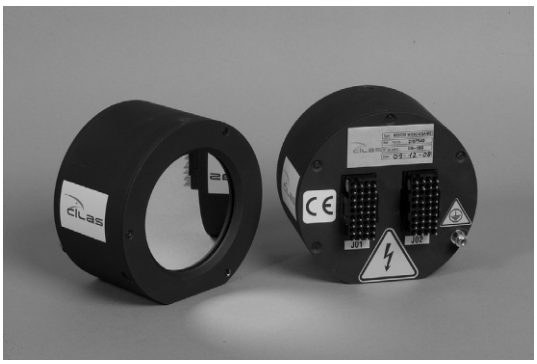


FIG. 19.2

Deformable mirror developed by CILAS for high-intensity lasers.

An accurate wave front control is also necessary, and the deformable mirror development is considered as a technological leap as ILE/ELI requires a useful aperture larger than 200 mm with hard dielectric coating for broadband femtosecond pulses.

19.2.3 SPACE

Space industry that has shown a tremendous growth of about 10% per year in the last 10 years is another domain that requires complicated coated optics with strong environmental performances.

In this field of applications, space-based observatory is considered as an attractive alternative solution to ground-based telescopes as it allows overcoming the atmosphere turbulence so that the limitation in angular resolution is only related to diffraction and also it permits to work in infrared and ultraviolet regions, which are strongly absorbed by the atmosphere. Moreover, due to the technological advances, in particular, in reducing the weight of mirrors, space telescopes are involving larger mirrors for several years.

With its 2.4 m aperture, the Hubble Telescope that was carried into orbit by a Space Shuttle in 1990 is one of the largest space telescopes.

The Herschel Space Observatory from European Space Agency with its 3.5-m diameter mirror is the largest infrared space telescope ever launched and is now in orbit since 2009. The protected mirror coating consisting in a 65-nm-thick Al layer protected with a 25-nm-thick MgF2 layer has been realized in one of the two coating facilities of the Calar Alto Observatory.

The James Webb Space Telescope developed by the NASA with the support of European Agency and Canadian Space Agency is intended to succeed Hubble space telescope for infrared observation. JWST will work at a low temperature of about 40 K in order to avoid the infrared emission from the telescope itself. It includes the following four instruments:

- NIRCam (Near-InfraRed Camera)—a wide field camera working in the near infrared (0.6–5 μm).
- NIRSpec (Near-InfraRed Spectrometer)—a multiobject spectrometer working in the near-infrared (1–5 μm).
- MIRI (Mid-InfraRed Instrument)—a set constituted with a camera and a spectrometer working in the mid-infrared (5–28 μm).
- FGS (Fine Guidance System)—an imager system working over the range (0.6–5 μm).

The main scientific goals of JWST are the first stars and galaxies in the universe just after the big bang. Planned to be launched in 2019, JWST will have a total mass of about 6200 kg.

The primary mirror is 6.5 m diameter and is constituted with 18 individual hexagonal-shaped beryllium segments. The coating of the segments is made with a thin layer of gold to be suited for infrared and is challenging and has been done with success (Childers et al., 2012).

As an example of an international Japanese-led Japan Aerospace Exploration Agency, JAXA-European Space Agency, ESA mission collaboration, including Canada, USA, and South Korea, the SPICA mission (Space Infrared Telescope for Cosmology and Astrophysics) is to be launched in 2022 for mid-infrared and far-infrared astronomy and is constituted with a cryogenically cooled telescope that involves a 3.5-m diameter primary mirror.

With the benefit of a large heritage from Herschel program, the SPICA mission gathers the European industry and scientific community whose respective contributions are effective.

19.2.4 ASTRONOMY

Generally, telescope mirrors are coated with a thin layer of highly reflecting material such as aluminum. It is common to install the coating plant next to the telescope for ease of refurbishing that usually occurs at intervals of some years due to the normal aging (oxidation and abrasion by airborne particles).

In the case of the Very Large Telescope (VLT), this coating plant has a diameter of 9.4 m and is equipped with eight cryo-pumps on the top of the vacuum chamber.

The Gemini Observatory that consists of two 8.1 m diameter is located at Cerro Pachon in Chile, it is to be noticed that it is the first large telescope to be coated with a silver protected coating constituted with four layers. An advantage of silver-based coating is that it leads to a reduction of the thermal infrared emission of the telescope by a factor of 2–3 compared to aluminum coatings. However, silver coating exhibits a lower reflectivity below 400 nm than aluminum coating but a higher reflectivity of wavelengths >450 nm.

Generally, as large components are the result of a long and expensive process of fabrication, including steps of molding, polishing, metrology before the step of coating, it is necessary to guarantee as much as possible a zero error coating process. However, it is also required to provide a means to remove the coating in the case of major nonconformance encountered during this step or aging effect due to environmental conditions. Processes involved for this operation are mainly based on immersion in chemical baths or under vacuum ion bombardment.

Very ambitious projects involving extremely large telescopes are in progress, and we can quote, for example, the Thirty-Meter Telescope, the Giant Magellan Telescope, or the *E*-ELT, for which the primary mirror consists of nearly a thousand of 1.4 m wide and 50-mm-thick hexagonal segments.

Adaptive mirrors are also incorporated into the optics of the telescope for the correction of the atmospheric turbulence that induces fuzziness in the stellar observation from earth.

19.2.5 SOLAR PLANTS

A solar furnace is a facility that gives out concentrated solar energy to produce very high temperatures. It is constituted by a complex optical and mechanical structure

with automatically controlled systems, involving parabolic mirrors or heliostats that concentrate light onto a focal point at which the temperature may reach a value of 3500°C. The energy at the focal point is mainly used to generate electricity or to irradiate various materials for studying different effects (thermal, photonic, etc.).

The largest solar furnace is 54 m high and 48 m wide and opened in 1970 at Odeillo in the Pyrenees-Orientales in France, as the site presents clear skies up to 300 days a year; it is composed of 63 heliostats, plane mirrors automatically rotated depending on the direction of the sun that concentrate the sun rays onto a larger parabolic mirror constituted with 9500 square mirrors 45 cm wide. Another solar furnace is located in Uzbekistan near Tashkent, with Odeillo they are the two largest solar furnaces in the world.

Coatings of the mirrors consist of enhanced metallic mirror so that the efficiency in the blue region is optimized.

Other facilities are also available as the high-flux solar furnace and xenon-high-flux solar simulator that are implemented at the German Aerospace Center's Solar Research in Cologne, where irradiances of up to 5 MW/m^2 and temperatures of above 2000°C are possible to achieve. The mirrors are made of float glass with a reflective layer of silver on their backside and coated on their frontside with titanium oxide to guarantee the reflection of the UV spectrum of the solar radiation. Such systems are used for exploration and testing new technologies with concentrated sunlight and artificial light.

In terms of concentrating solar power collectors, main challenges are increasing the lifetime of aluminum- or silver-based mirrors up to >10 years. Coating design and used technology have to allow for low manufacturing cost. Different approaches are used in order to protect the metallic reflective layer. We can find for example thin glass mirrors that use a 1-mm-thick glass as a protection against moisture, or adhesive polymer coated with a roll-to-roll technology using various techniques from sputtering to Sol–Gel.

19.3 REVIEW OF TECHNOLOGICAL SOLUTIONS

Among the range of physical vapor deposition techniques that are available, the techniques that are mostly used for optical coatings are based on techniques of evaporation and sputtering.

19.3.1 THERMAL AND ELECTRON GUN EVAPORATION

Thermal evaporation under vacuum for which the material is evaporated from crucibles heated with electrical current and electron gun deposition under vacuum are the easiest physical vapor deposition techniques to implement.

Such techniques allow the deposition of a large range of materials such as metals, semiconductors, or composite materials (Maissel and Glang, 1970; Bunshah, 1994; MacLeod, 2010; Baumeister, 2004). Generally, as the energy of the ions impinging

on the surface of the substrate is very low, it is necessary to heat the substrate to be coated at a high temperature of about 250 up to 350°C. As a consequence, the deposited layers generally present a microstructure that is widely far from the bulk material that has been evaporated.

Large coating of protected or enhanced mirrors is widely using electron beam gun evaporation as this technology is easy to implement and the deposition speed is quite high. However, the microstructure of the deposited layers is known to be porous and this is a strong limitation for use in climatic environment.

To overcome these difficulties, we generally use the help of assisted deposition by plasma or ion beams; in this case, as presented in Fig. 19.3, an ion beam gun is added inside the chamber, directed to the surface of the component to be coated, and it allows increasing the density of the layer under construction while working at room temperature (Martin et al., 1983).

19.3.2 SPUTTERING

Considering the environmental conditions of the coatings, it is necessary to use a coating technology that guarantees that layers density is close to bulk.

Ion-beam sputtering (IBS) that uses one ion beam gun for sputtering a target or dual-ion-beam sputtering (DIBS) that uses an second one for compacting the sputtered material (Fig. 19.4) are particularly suited as the growth of the material is very close to bulk. IBS technique has been widely studied by the French Laboratory

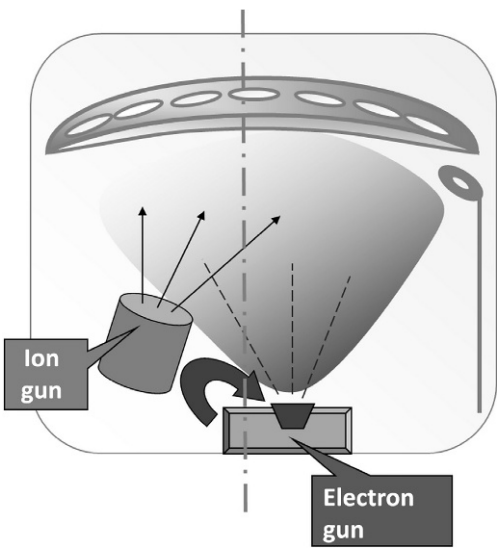


FIG. 19.3

Schematic of ion-assisted deposition technique.

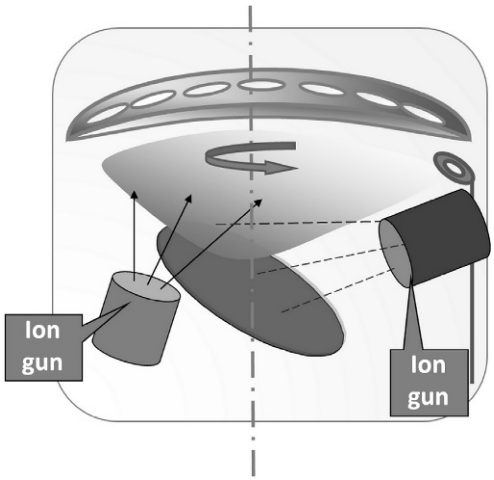


FIG. 19.4

Schematic representation of dual-ion-beam sputtering technique.

Laboratoire des Matériaux Avancés in Villeurbanne (LMA) for the production of low loss and low-scattering mirrors involved in the VIRGO project that will be presented later (see Section 19.6.2). DIBS technique is the best technology for having very dense layers and high-quality coatings. This technology is used intensively for manufacturing very narrow filters for the optical telecommunication market. The density of the deposited layer is very close to the bulk material and enables the optical functions to be nearly insensitive to environmental parameters. It enables very smooth interfaces too that lead to very low-scattering levels.

This is also a privileged technology for space applications as there is no measurable spectral shift between air and vacuum and versus temperature variations, and the coatings show very low aging effects.

The second assisting ion beam is also used for cleaning the substrate before coating and leads to very good adhesion.

The overall process is very stable and enables, together with optical monitoring system, excellent manufacturing yields.

Plasma sputtering technology is widely used since several years (Hermann and Bräuer, 1995; Pawlewicz et al., 1982) as it allows reaching high uniformity over large surfaces. A schematic of the magnetron sputtering technique is illustrated in Fig. 19.5. When the pressure inside the chamber is low enough (typically 5×10^{-3} mbar), the cathode is polarized at several hundred volts. This generates a plasma polarization—a mixture of ions, electrons, and atoms—in the vicinity of the cathode. The magnets placed behind the cathode produce magnetic field lines and confine the plasma to the vicinity of the cathode. Sputtering takes place when the material of the cathode is bombarded with ions from the plasma. A major advantage of sputtering is the high deposition rates it is possible to be obtained, particularly for metals.

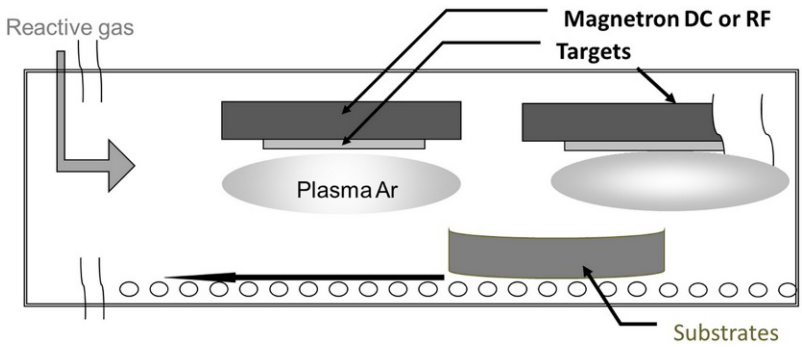


FIG. 19.5

Schematic of an in-line magnetron sputtering technique.

Another interesting advantage is the energy with which the material is sputtered on the surface. Atoms or molecules collapse the substrate with a kinetic energy at least 10 times greater than that of a conventional evaporation. This produces denser layers and improves the mechanical attachment to the substrate. In addition, in comparison with the conventional evaporation, sputtering is extremely stable that allows for the automation of deposition.

Fig. 19.5 illustrates the main elements of a magnetron sputtering source, in the case of an in-line configuration. Rotative configurations are also available and are generally used for smaller components.

In order to produce uniform coatings on large optical components, it is necessary to optimize sputtering parameters in order to obtain good level of uniformity, including the following main parameters that influence uniformity such as magnetic field that has to be adjusted regarding sputtered material, pumping speed uniformity, plasma power, target voltage, substrate potential, target-substrate distance, and gas inlet position, and so on.

For reactive processes (Sproul et al., 2005), such as pulsed DC (direct current), radio frequency (RF), or mid-frequency (MF), oxygen partial pressure is another important parameter that impacts the uniformity, both in terms of thickness and optical refractive index.

Other technologies of fabrication other than physical vapor deposition have to be mentioned as they are widely used in optical thin-film community such as chemical vapor deposition (CVD) or sol–gel, although we will not speak about them in this chapter. For example, sol–gel process allows producing thin-film multilayer stacks constituted by nanoparticles of metal oxides (SiO_2, ZrO_2, TiO_2, Ta_2O_5, etc.) and is applied on large components for high laser flux resistance applications (Belleville et al., 2002).

19.4 THIN-FILM UNIFORMITY: KEY PROBLEM

When large components are involved or sophisticated optical functions are required, uniformity of performances of reflectivity and transmittance is a key factor that has

to be mastered. And directly linked to the uniformity of performances over the whole surface of the components is the spatial distribution of thickness and refractive indices on the surface.

In fact, the effect of nonuniformity is directly connected to the complexity of the optical function to perform. If some percent of nonuniformity can be bearable in the case of standard antireflections, it will not be the same for more complicated functions like narrowband filters.

As the optical response is dependent on the optical thickness, the main parameters that must be mastered are uniformity of thickness and uniformity of refractive index for each material involved in the multilayer.

However, in the case of metallic mirrors, dielectric layers that are involved in the protection of the mirror or in the enhancement of the spectral response over a particular spectral range need to be precisely mastered.

In the case of ion-assisted deposition or sputtering, process parameters play a key role in the construction of the layers microstructure and a fine characterization of these parameters is necessary over the substrates holder to guarantee their stability.

Commonly, uniformity can be improved by the definition of a samples holder suited for components, and the implementation of sophisticated masks of uniformity in the chamber would be necessary (Abel-Tibérini et al., 2008; Sassolas et al., 2009). The problem may be very different depending on the dimensions of the substrate. Although sometimes problematical, planetary, or more complex movements can be implemented on smaller components as it may not be possible to apply some to larger components.

Masking techniques are based on the fact that identical thickness repartition should be reached over the whole surface of the substrate. For this, a mechanical shape positioned between the target and the substrates is implemented that aims to stop the material deposition on some parts of the substrate and allow it on the other ones. These techniques are commonly used in thin-film-coating industry, but some major drawbacks have to be managed; first, as the thickness repartition that will be reached will be close to the smallest thickness value deposited over the surface without mask, use of mask may have a great impact on the deposition rate, leading sometimes to a reduction greater than a factor 10. Second, as the mask is located between the target and the substrates, coating deposition is also done on the mask resulting in a nonperfectly condensed material and greater thickness deposited on the mask, leading to potential pollution on the substrates.

However, as presented in the following paragraph, some significant improvements can be made to compensate for the sophisticated shapes on large components (Fig. 19.6) or to increase remarkably the uniformity on flat substrates.

In the case of large substrates, complex movements are difficult to implement related to parameters such as mass, inertia, size of the component, and corrective masks could be a preferred solution. Improvement of deposition conditions has to be also implemented to achieve a uniformity curve as constant as possible, or at least characterization of this curve has to be done so that it can be taken into account in the design synthesis of the stacks and their impact be assessed.

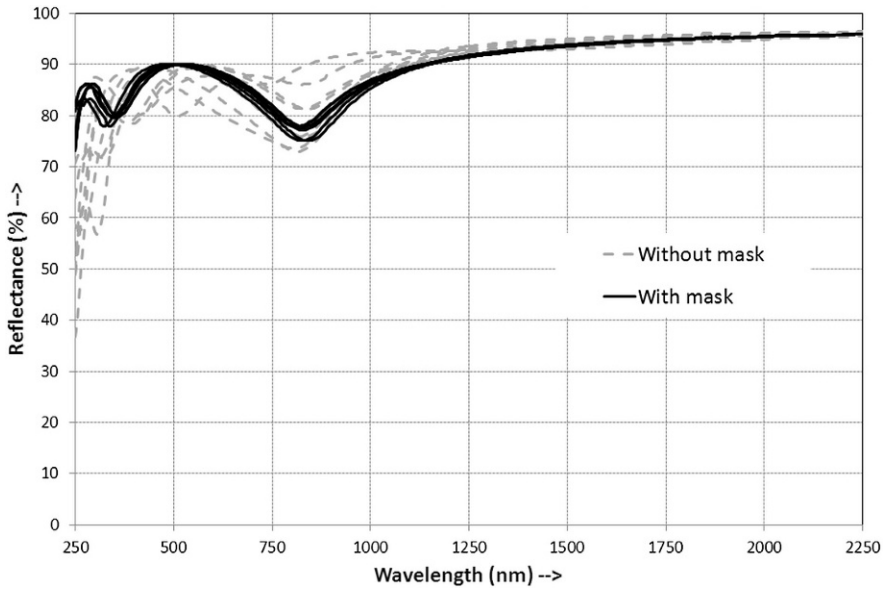


FIG. 19.6

Improvement of uniformity obtained by masking technique on large concave reflectors (500 mm diameter and 200 mm high). Measurement of reflectivity without mask and with mask is done on witnesses distributed over the reflectors.

From the production point of view, the key parameters that play a major role during the process are the deposition rate, the partial pressure of oxygen, the temperature of the component, and also the voltage and the current values of the ion beams and plasma that are responsible for the growth of the material on the surface of the component. However, and in most cases, it must be done a trade-off between the process parameters and the production yield, as process conditions may have a direct impact on the deposition rate and consequently on the duration of the process.

19.5 FOCUS ON LARGE MAGNETRON SPUTTERING FACILITY

Here, we are focusing on the large deposition magnetron sputtering machine called PACA2M (PulvérisAtion CAthodique de 2 Mètres), that CILAS has been implemented for coating large optics up to 2 m, within a dedicated consortium, with the financial support from the French Department of Industry and of the local administrations, and with the help and the expertise of the French OPTITEC optical cluster.

This innovative large size deposition machine (Fig. 19.7) has been developed to be able to coat large optical components, up to 2 m × 2 m, 40 cm thick, and with 1.5 ton weight. It has been equipped with seven large planar magnetrons measuring 2.5 m, and some of them can be polarized in DC or pulsed DC mode in order to coat



FIG. 19.7

Two-meter scale deposition sputtering chamber.

metallic layers from a few tenths of nanometers to hundreds of manometers. Other pairs of magnetron can be polarized in mid-frequency (MF) that allows the deposition of metals and also dielectric oxides under reactive atmosphere. An innovative 2.5-m-long planar magnetron has been developed that can be polarized in radio frequency (RF) mode in order to allow the deposition of dielectric oxides with or without reactive atmosphere. In particular, it allows the realization of dielectric oxides protective layer on silver.

An in situ analysis of the plasma emission is achieved with an optical device that monitors the gas flow rate and regulates the gas flow during reactive deposition.

Such large coating machine is an in-line coating system in which the components to be coated are moving under the targets of the various materials. It is equipped with an automatic load lock system including a five positions substrates-holder stacker and a 9-m^3 load lock chamber. It is possible to perform a glow discharge either under argon or oxygen to clean the components surface before coating, with the help of $2\,m \times 2\,m$ electrodes positioned in the load lock chamber. Pumping down to 1×10^{-5} mbar of the load lock chamber can be achieved in 30 min. The main 14 m^3 chamber is pumped down by 12 turbo pumps and a polycold® to reach a 10^{-7} mbar lower limit pressure.

With this sputtering system, it is then possible to produce optical coatings such as enhanced metallic mirrors, metal-dielectric absorbing coatings, or multidielectric coatings, deposited on different kinds of substrates. During the coating process, the substrate can be either polarized or at a floating potential.

Sputtering process optimization and characterization of plasma parameters can be implemented for different oxygen ratios, with the help of the ratio between optical

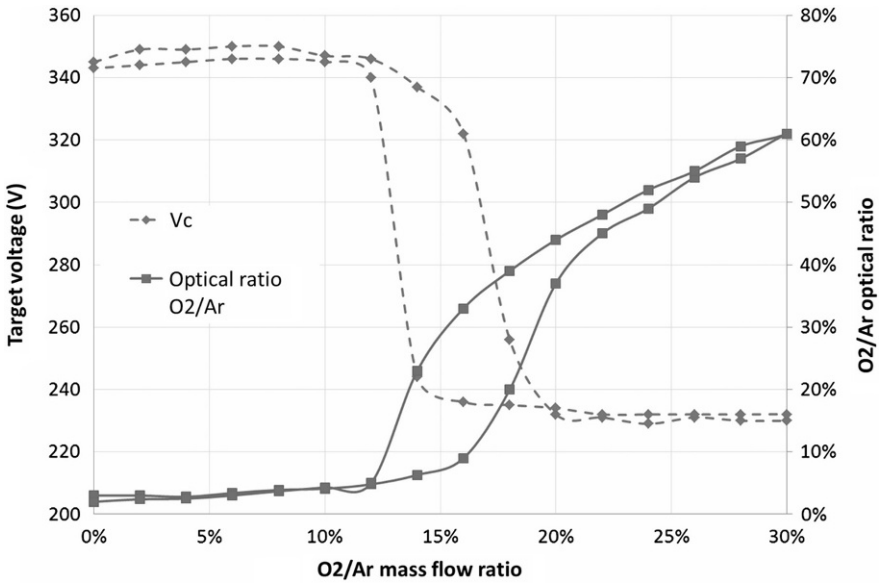


FIG. 19.8

Typical experimental hysteresis curve for SiO_2-reactive sputtering in pulsed DC.

amplitude of oxygen and argon rays emitted by the plasma, allowing the calibration of required quantity of oxygen with the help of using usual hysteresis curve (Fig. 19.8), which characterizes the two different operating modes of reactive magnetron sputtering (metallic mode and poisoned mode) (Chauveau et al., 2011).

With such inline configuration, nonuniformity is mainly parallel to the targets and can be optimized by tuning the sputtering parameters. In some cases, increasing the number of reactive gas inlets controlled with dedicated plasma optical monitoring system could be also a way of improvement of coating uniformity. In a direction perpendicular to the magnetron, uniformity can be influenced by the modifications in the local geometry of the chamber due to the substrate movement that induces local changes in pressure, oxygen partial pressure, or target potential.

It has been shown that a uniformity value better than 5% can be achieved for various metallic and dielectric materials over $2\,m \times 2\,m$ and that it is possible to reach a value around 3% for nonreactive pulsed DC and RF sputtering and 1.5% over 1.5 m.

Production of metallic mirrors by magnetron sputtering technology is particularly well suited to severe environments as protected silver coatings can be fabricated with successful space qualification, including humidity tests and thermal cycling under vacuum. Deposition on various types of substrates such as glass or silicon carbide is possible, and additional dielectric materials can be used to enhance reflectivity.

For space projects, a major advantage of such large coating chamber is that it allows producing in the same batch Flight Models sets and spare sets.

Moreover, this large coating machine has been equipped with an in situ broadband optical monitoring system that allows production of sophisticated spectral specifications on large optics, with a good agreement with theoretical design, such as multi dielectric broadband antireflection, or mirrors (Stojcevski et al., 2011).

Specific optical systems have been developed for light beam entrance and exit inside the coating chamber, gathering emission, and reception optics for transmission and reflection monitoring. Compatibility with industrial environment is completed by means of an all-fibered system equipped with 10-m long optical fibers. Its all-fibered characteristics and its digital driving devices allow a robust and fast processing over an extended spectral range from 280 to 2200 nm with a 10,000 high value signal-to-noise ratio that could be increased by increased averaging. However, with an in-line system, conventional continuous optical monitoring while the layer is growing is not achievable, and intermittent monitoring has been carried out where the layer to be deposited is split in several steps at the end of which optical measurement is done and monitoring of the next step is computed. With such monitoring system, high spectral performances can then be obtained, where production errors defined as the difference between in situ determined layer thickness and end-of-layer stop thickness set in the deposition strategy have a value $<1\%$ per layer. Moreover, accurate in situ refractive index characterizations and in situ thickness uniformity cartography on large surface coatings can be achieved due to its nine optical throughputs implemented at the top and the bottom of the large coating chamber.

At last, due to the high stability of sputtering technology, deposition of few nanometers-thick layers is reachable with a good accuracy and metal-dielectric absorbers can be achieved accurately.

19.6 HIGHLIGHTS ON TWO MAJOR PROGRAMS

19.6.1 FOCUS ON LMJ

The Laser Megajoule (LMJ) project led by the French nuclear agency is experimental inertial confinement fusion (ICF) system located on the site of CESTA (Centre d'Etudes Scientifiques et Techniques d'Aquitaine) near Bordeaux. The Laser Megajoule (LMJ) is 300 m long and will be one of the two most powerful lasers in the world. The system involves several thousand of high-quality optical components and has been dimensioned for 240 laser beams each producing an energy of 7500 J, which is focalized on a 2-mm diameter target. An assembly of functions such as mirrors, polarizers, transportation, or sealing is required and sophisticated coatings most of them working in the infrared are necessary to meet the requirements over a wide range of incidence (Daurios, 2009; Le Garrec, 2009; Chenais-Popovics and Vanderhaegen, 2005).

Each laser beam is constituted with 40 large optics with demanding performances in terms of reflection or transmission, roughness, wave front quality, cosmetics,

cleanliness, laser damage, etc. in order to guaranty the final performances of the laser and the lifetime of the components.

The laser chain is separated in several subsets whose functions are, respectively, amplification, transport, frequency conversion, and focus; at each stage, the requirements on the optics are different related in particular to beam dimensions and laser density (Lamaignère et al., 2011). Due to the square dimension of the beam, major part of the optics is in the $400 \times 400\,\text{mm}^2$ dimensions.

Typical optical performances required on these components are a reflectivity higher than 99% for the mirrors, or a transmittance in p-polarization is >98.5% and lower than 1% in s-polarization for the polarizers.

The role of laser chain amplifiers is to increase the efficiency of the optical pumping and they need high value of reflectivity. After the design phase, CILAS is in charge of the production of all the amplifiers, which are metallic reflective mirrors on large complex-shaped reflectors of about $1\,\text{m}^2$ dimensions, as presented in Fig. 19.9.

As mentioned earlier, coatings on large optics are mainly performed by evaporation techniques. As the magnetron sputtering technique leads to very dense layers close to bulk material, it is particularly well suited for applications that require environmental resistance, as it is the case for the Laser MegaJoule program. Moreover, other properties that are required for the coatings are hardness, uniformity, and also cleanability in an automatic washing system because the ultracleanliness of the LMJ hall of integration shall be preserved.

The PACA2M magnetron sputtering machine that has been presented above will produce the coating on $>4000\,\text{m}^2$ of stainless steel substrates; moreover, some of them are not completely flat (Fig. 19.9).

In the framework of LMJ program, such coating has been qualified on stainless steel and has been proven to resist thermal cycling (−25/+55°C).

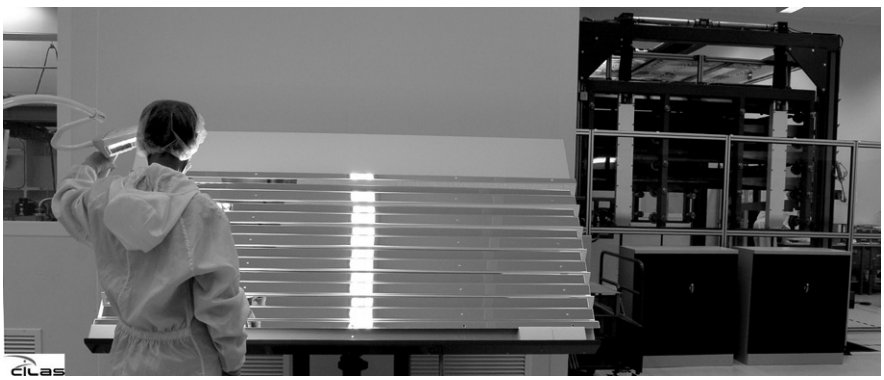


FIG. 19.9

Complex-shaped coated reflectors involved in the laser chain amplifier.

19.6.2 FOCUS ON VIRGO

Another ambitious facility that implements large sophisticated optical components is the Virgo project in the field of gravitational wave interferometric detectors (GWIDs) located on the site of the European Gravitational Observatory (EGO) in Italy (Beauville et al., 2004). An enhanced partnership is established involving the teams from Virgo and also the others from similar projects such as LIGO (Laser Interferometer Gravitational Wave Observatory) constructed by the California Institute of Technology and Massachusetts Institute of Technology in the United States and GEO in the United Kingdom and Germany.

This project is gathering a large amount of experts from the international scientific community in a large variety of domains from optics to quantum physics and has driven advanced developments in the field of high-reflectivity mirrors with very low losses, as it will be presented below.

The Virgo detector for gravitational waves consists in a Michelson laser interferometer that involves two orthogonal 3-km long arms and the optical length of each arm is stretched up to 120 km by means of multiple reflections between mirrors located at the ends of each arm.

Key optical components are the large mirrors (diameter, 35 cm; thickness, 10–20 cm) developed by the French Laboratory Laboratoire des Matériaux Avancés in Villeurbanne that require to be mastered in terms of optical shape imperfections, coating losses, mechanical losses, uniformity, and so on. Tremendous characteristics of very low scattering and absorption are required for these mirrors, and long-term developments at LMA have been held on IBS technology to succeed in the production of Ta_2O_5/SiO_2 multilayers. Such mirrors have been realized on ultrapure fused silica substrates (Suprasil from Heraeus) (Forest et al., 2006).

A specific optical coating facility that is presented in Fig. 19.10 has been built to produce these extremely high-quality mirrors that combine the highest reflectivity (over 99.999%) with nanometer surface control.

The cleanliness of the mirrors has also to be severely mastered because it can induce some losses that would be responsible for the decrease in Virgo sensitivity due to thermal lensing effect. All the operations are thus performed in clean rooms of laboratories with $>500\,m^2$ of clean rooms available at LMA, involving $150\,m^2$ in ISO3.

As optical properties must be identical all over the surface of the mirror, as well as for reflection in transmission, a very good uniformity of thickness is also required (Sassolas et al., 2009).

Innovative thin film materials developments have been held at LMA to reduce the mechanical dissipation in the coatings that appears to be responsible for a limitation in mechanical losses of mirrors (Forest et al., 2006; Granata et al., 2016). In particular, such mechanical losses have been demonstrated to occur mainly in the high index material, and specific research has been focused on tantala high-index material. New alternative materials such as titania-doped tantalum pentoxide have been synthesized at LMA (Flaminio et al., 2010; Granata et al., 2016) taking into account the optical absorption that has to be minimized in the coating.



FIG. 19.10

Large $2.40 \times 2.40 \times 2.20\,m^3$ IBS coater.

Courtesy of L. Pinard, Laboratoire des Matériaux Avancés—CNRS/IN2P3, France.

For the next generation of interferometers (Advanced Virgo), the symmetry between the two Fabry–Perot cavities becomes crucial and both mirrors have to be coated during the same coating run so that they could exhibit identical transmittance performances in both cavities. For this improvement, masking techniques combined with a planetary motion have been considered, and the development of two masks for each material involved in the multilayer has been done in order to control the coating thickness profiles on the rotating substrates.

A resulting uniformity value of 0.1% over 15 cm diameter was achieved on the high-reflective coating multilayer, leading to a very low difference below 0.01% in transmission over 15 cm diameter between the two Advanced Virgo mirrors (Pinard et al., 2017).

With such optimization of the high-index material and implementation of doping the Ta_2O_5 with Ti atoms, it has been shown a reduction of the extinction coefficient to a value of 4×10^{-8} at 1064 nm instead of 2×10^{-7} for nondoped Ta_2O_5 (Pinard et al., 2011). Characterization of absorption by photothermal deflection technique of low-transmission multilayer revealed an average value of 0.26 ± 0.05 ppm at 1064 nm over a diameter of 15 cm. This value has to be compared to 0.67 ppm with nondoped high-index material, Ta_2O_5 (Beauville et al., 2004; Pinard et al., 2017).

A perfect master of the shape of the mirrors is also needed as the imperfections may lead to additional losses in the cavities or reduction of contrast at interferometer output. It has been demonstrated that the substrate is a limitation as the multilayer coating replicates the initial surface, obviously if the coating uniformity is good. A corrective coating technique has thus been developed in order to lower the surface flatness by adding silica where it is needed and experimental results have been reported on an initial Virgo substrate down to <1 nm rms on 150 mm and <0.4 nm rms without astigmatism and residual curvature (Bonnand et al., 2012).

Thanks to all these technical developments, the second generation of mirrors for gravitational waves detectors (Advanced Virgo and Advanced LIGO) developed by LMA have reached exceptional performances: very low absorption of the high-reflective (HR) coating (0.2–0.3 ppm at 1064 nm), very low scattering (<5 ppm at 1064 nm), low RMS flatness of the HR coating (0.36 nm RMS on 15 cm diameter), and low residual reflectivity of the AR coatings (<50 ppm at 1064 nm). With these exceptional mirrors performances, on September 14, 2015, the two detectors of the Laser Interferometer Gravitational-wave Observatory (LIGO) simultaneously observed a transient gravitational-wave signal (LIGO Scientific Collaboration and Virgo Collaboration, 2016) produced by a merger of a pair of black holes. It was the first direct detection of gravitational waves on the earth.

19.7 CONCLUSION

As a conclusion of this chapter dedicated to optical coatings of large facilities, we have seen that sophisticated coatings are involved in many different domains such as laser, astronomy, and space applications.

Optical coatings for large facilities become more and more crucial for major national and international programs. Successfully coating large areas involves challenges and risks first connected with substrate, polishing, flatness, cleaning and control. Durability, hardness and stability under severe environmental conditions are requirements which have to be fulfilled in regard to the growing demand of performances.

Recent progress in large coating technologies permits the management and optimization of major process parameters. Moreover, with the help of sophisticated monitoring systems, it is now possible to produce large scale components mastering key factors such as thicknesses, real indices and extinction coefficients, uniformity and stress.

In some situations, a compromise must be found between compacity and uniformity of films. Surely complete control of uniformity in the future will open the door to mass production of extremely complex filters.

REFERENCES

Abel-Tibérini, L., Lemarquis, F., Lequime, M., 2008. Masking mechanisms applied to thin-film coatings for the manufacturing of linear variable filters for two-dimensional array detectors. Appl. Opt. 47, 5706–5714.

Amra, C., 2005. Endommagement laser dans les composants optiques interférentiels, Élaboration et caractérisation des cristaux massifs et en couches minces pour l'optique. EDP Sciences. 227 pp.

Baumeister, P.W., 2004. Optical Coating Technology. vol. PM137 SPIE Press Monograph.

F. Beauville, F. Beauville, D. Buskulic, R. Flaminio, F. Marion, A. Masserot, L. Massonnet, B. Mours, F. Moreau, J. Ramonet, E. Tournefier, D. Verkindt, O. Veziant, M. Yvert, R.

Barille, V. Dattilo, D. Enard, F. Frasconi, A. Gennai, P. LaPenna, M. Loupias, F. Paoletti, L. Bracci, G. Calamai, E. Campagna, G. Conforto, E. Cuoco, I. Fiori, G. Guidi, G. Losurdo, F. Martelli, M. Mazzoni, B. Perniola, R. Stanga, F. Vetrano, A. Vicere, D. Babusci, G. Giordano, J.-M. Mackowski, N. Morgado, L. Pinard, A. Remillieux, F. Acernese, F. Barone, E. Calloni, R. De Rosa, L. Di Fiore, A. Eleuteri, L. Milano, K. Qipiani, I. Ricciardi, G. Russo, S. Solimeno, M. Varvella, F. Bondu, A. Brillet, E. Chassande-Mottin, F. Cleva, T. Cokelaer, J.-P. Coulon, B. Dujardin, J.-D. Fournier, H. Heitmann, C. N. Man, F. Mornet, J. Pacheco, A. Pai, H. Trinquet, J.-Y. Vinet, N. Arnaud, M. Barsuglia, M. A. Bizouard, V. Brisson, F. Cavalier, M. Davier, P. Hello, P. Heusse, S. Kreckelberg, C. Boccara, V. Loriette, J. Moreau, V. Reita, P. Amico, L. Bosi, L. Gammaitoni, M. Punturo, F. Travasso, H. Vocca, L. Barsotti, S. Braccini, C. Bradaschia, G. Cella, C. Corda, A. Di Virgilio, I. Ferrante, F. Fidecaro, A. Giazotto, E. Majorana, L. Holloway, R. Passaquieti, D. Passuello, R. Poggiani, A. Toncelli, M. Tonelli, L. Brocco, S. Frasca, C. Palomba, P. Puppo, P. Rapagnani, and F. Ricci, Proc. SPIE vol. 5250, 483 (2004).

Belleville, P., Prené, P., Bonnin, C., Montouillout, Y., 2002. Use of sol-gel hybrids for laser optical thin films. Mat. Res. Soc. Symp. Proc. 726.

Beuzit, J.L., Feldt, M., Dohlen, K., Mouillet, D., Puget, P., Antichi, J., Baruffolo, A., Baudoz, P., Berton, A., Boccaletti, A., Carbillet, M., Charton, J., Claudi, R., Downing, M., Feautrier, P., Fedrigo, E., Fusco, T., Gratton, R., Hubin, N., Kasper, M., Langlois, M., Moutou, C., Mugnier, L., Pragt, J., Rabou, P., Saisse, M., Schmid, H.M., Stadler, E., Turrato, M., Udry, S., Waters, R., Wildi, F., 2006. SPHERE: a 'planet finder' instrument for the VLT. The Messenger 125, 29.

Bloembergen, N., 1973. Role of cracks, pores, and absorbing inclusions on laser induced damage threshold at surfaces of transparent dielectrics. Appl. Opt. 12 (4), 661–664.

Bonnand, R., Cochez, G., Degallaix, J., Flaminio, R., Giacobone, L., Lagrange, B., Marion, F., Michel, C., Mours, B., Mugnier, P., Pacaud, E., Pinard, L., 2012. In: Improving the substrate flatness: the corrective coating technique.Gravitational Waves Advanced Workshop, Hawaii.

Bunshah, R.F., 1994. Deposition Technologies for Films and Coatings: Developments and Applications, second ed. Noyes Publications, Park Ridge.

Chambaret, J.P., 2010. The "10 PW Ti-Sapphire Based" Lasers for the Romanian ELI NP Pillar. How far are we today from its availability? ELI Executive Committee, Bucarest.

Chauveau, G., Torricini, D., Grèzes-Besset, C., Stojcevski, D., Lequime, M., 2011. In: Dobisz, E.A., Eldada, L.A. (Eds.), PACA2M: magnetron sputtering for 2-meter optics. Proceedings of the SPIE, Advances in Optical Thin Films IV. vol. 8168, p. 81680P.

Chenais-Popovics, C., Vanderhaegen, D., 2005. In: Le Laser Mégajoule et la fusion inertielle. Laboratoire pour l'utilisation des lasers intenses, CNRS/Ecole polytechnique, CEA. Available from: http://www.cnrs.fr/publications/imagesdelaphysique.

Childers, C., Patriarca, D., Sadkhin, G., Stevenson, I., 2012. In: Gold coatings for the reflective optics on the JWST. Presentation given by I. Stevenson at Society of Vacuum Coaters (SVC). TechCon, Santa Clara, CA.

Daurios, J., 2009. In: Spécifications des grands composants lasers et métrologie optique associée.Journée du Polissage Optique pour les Grands Instruments de la Physique et de l'Astronomie, Bordeaux.

Flaminio, R., Franc, J., Michel, C., Morgado, N., Pinard, L., Sassolas, B., 2010. A study of coating mechanical and optical losses in view of reducing mirror thermal noise in gravitational wave detectors. Class. Quantum Grav. 27084030.

Forest, D., Ganau, P., Lagrange, B., Mackowski, J.M., Michel, C., Montorio, J.L., Morgado, N., Pignard, R., Pinard, L., Remillieux, A., 2006. Ion beam sputtering coatings on large substrates: towards an improvement of the mechanical and optical performances. Appl. Opt. 45 (7), 1436–1439.

Granata, M., Saracco, E., Morgado, N., Cajgfinger, A., Cagnoli, G., Degallaix, J., Dolique, V., Forest, D., Franc, J., Michel, C., Pinard, L., Flaminio, R., 2016. Mechanical loss in the state-of-the-art amorphous optical coatings. Phys. Rev. Lett. D. 93, 012007.

Hermann, R., Bräuer, G., 1995. DC and RF-magnetron sputtering. In: Hummel, R.E., Guenther, K.H. (Eds.), Handbook of Optical Properties: Thin Films for Optical Coatings. In: 1, CRC Press, Boca Raton, FL, pp. 135–187.

Kozlowski, M.R., Chow, R., 1994. In: Bennett, H.E., Chase, L.L., Guenther, A.H., Newnam, B.E., Soileau, M.J. (Eds.), Role of defects in laser damage of multilayer coatings.Proc. SPIE 2114, Laser-Induced Damage in Optical Materials: 1993, pp. 640–649.

Krol, H., Valette, N., Torricini, D., Grèzes-Besset, C., Dohlen, K., Le Mignant, D., Saïsse, M., Moreaux, G., Langlois, M., Moutou, C., Vigan, A., Lemarquis, F., 2011. In: Dobisz, E.A., Eldada, L.A. (Eds.), IRDIS filters: from design to qualification.Proceedings of the SPIE, Advances in Optical Thin Films IV. vol. 8168, p. 81680X.

L. Lamaignère, R. Courchinoux, J. C. Poncetta, H. Bercegol, "L'endommagement des optiques du LMJ: problématique, mécanismes et métrologie", UVX 2010 (2011) 99–105, EDP Sciences, 2011

Le Garrec, B., 2009. In: Lasers de puissance et composants optiques.Journée du Polissage Optique pour les Grands Instruments de la Physique et de l'Astronomie, Bordeaux.

LIGO Scientific Collaboration and Virgo Collaboration, 2016. Observation of gravitational waves from a binary black hole merger. Phys. Rev. Lett. 116061102.

MacLeod, H.A., 2010. Thin-Film Optical Filters, fourth ed. Taylor & Francis Group, CRC Press.

Maissel, L.I., Glang, R., 1970. Handbook of Thin Film Technology. McGraw-Hill, New-York.

Martin, P.J., Macleod, H.A., Netterfield, R.P., Pacey, C.G., Sainty, W.G., 1983. Ion-beam-assisted deposition of thin films. Appl. Opt. 22 (1), 178–184.

Natoli, J.Y., Gallais, L., Akhouayri, H., Amra, C., 2002. Laser-induced damage of materials in bulk, thin-film, and liquid forms. Appl. Opt. 41 (16), 3156–3166.

J. Neauport, D. Valla, J. Duchesne, P. Bouchut, L. Lamaignere, J. Bigarre, N. Daurios, "Building high-damage-threshold surfaces at 351 nm", R. Geyl, L. Wangs, Proc. SPIE 5252, Optical Fabrication, Testing, and Metrology, 131–139 (2004).

Pawlewicz, W.T., Martin, P.M., Hays, D.D., Mann, I.B., 1982. Recent developments in reactively sputtered optical thin films. Proc. Soc. Photo-Opt. Instrum. Eng. 325, 105–116.

Pinard, L., Sassolas, B., Flaminio, R., Forest, D., Lacoudre, A., et al., 2011. Toward a new generation of low-loss mirrors for the advanced gravitational waves interferometers. Opt. Lett. 36, 1407–1409.

Pinard, L., Michel, C., Sassolas, B., Balzarini, L., Degallaix, J., Dolique, V., Flaminio, R., Forest, D., Granata, M., Lagrange, B., Straniero, N., Teillon, J., Cagnoli, G., 2017. Mirrors used in the LIGO interferometers for first detection of gravitational waves. Appl. Opt. 56 (4), C11–C15.

Porteus, J.O., Seitel, S.C., 1984. Absolute onset of optical surface damage using distributed defect ensembles. Appl. Opt. 23 (21), 3796–3805.

Sassolas, B., Flaminio, R., Franc, J., Michel, C., Montorio, J.L., Morgado, N., Pinard, L., 2009. Masking technique for coating thickness control on large and strongly aspherical optics. Appl. Opt. 48 (19), 3760.

Sproul, W.D., Christie, D.J., Carter, D.C., 2005. Control of reactive sputtering processes. Thin Solid Films 491 (1–2), 1–17.

Stojcevski, D., Lequime, M., Chauveau, G., Torricini, D., Grèzes-Besset, C., 2011. Dobisz, E.A., Eldada, L.A. (Eds.), Broadband optical monitoring for a 2-meter optics magnetron sputtering deposition machine. Proceedings of the SPIE, Advances in Optical Thin Films IV. vol. 8168, p. 81681G.

Stolz C., Weinzapfel C., Rogowski G.T., Smith D., Rigatti A., Oliver J. and Taniguch J., Optical Interference Coating, Banff, Canada, 15 July 2001.

RELEVANT WEBSITES

http://www.clf.rl.ac.uk/Facilities.
http://www.ego-gw.it.
http://www.jwst.nasa.gov.
http://www.ligo.caltech.edu.
https://lasers.llnl.gov/about/nif/.
http://www-lmj.cea.fr/fr/lmj/index.htm.

FURTHER READING

Este, G., Westwood, W.D., 1988. A quasi-direct-current sputtering technique for the deposition of dielectrics at enhanced rates. J. Vac. Sci. Technol. A 6(3).

Rettich, T., Weidemuth, P., 1999. In: MF sputtering—a power-ful process tool for large area coating.42nd Annual Technical Conference Proceedings of the Society of Vacuum Coatersvol. 147.

Sassolas, B., Benoit, Q., Flaminio, R., Forest, D., Franc, J., et al., 2011. Twin mirrors for laser interferometric gravitational wave detectors. Appl. Opt. 50, 1894–1899.

CHAPTER

Optical coatings for automotive and building applications

20

Chris H. Stoessel

Southwall Technologies (a Subsidiary of Eastman Chemical Co.), Palo Alto, CA, United States

20.1 INTRODUCTION

Optical coatings provide important functionality in vehicles and architecture. They can be found in countless applications such as rain sensors, headlight lens systems, lighting reflectors, rear view mirrors, motion detectors, or camera systems (to name just a few) that have been adopted from other application specialties. However, optical coatings in automotive and architectural glazing are a distinct application with specific market characteristics. Thus, this chapter focuses on the use of optical coatings on windows for use in vehicles and buildings.

Energy efficiency has become a prominent goal in western industrialized societies, particularly since the first "oil crisis" in the 1970s, and is receiving renewed attention with the recognition of the role of energy consumption in the anthropogenic contribution to global warming. According to the United States Department of Energy (US Department of Energy, 2009), fenestration influences approximately one third of all energy used in the United States, highlighting the role of energy-efficient glazing in vehicles and buildings. The impact of windows on energy consumption is various and complex; consequently, many technical approaches have emerged for optical coatings to improve the performance of windows. Energy efficiency regulation increasingly shapes the requirements for architectural window coatings, while automotive window coating applications are largely restrained by safety considerations imposed either by industry standards or government regulation.

After a discussion of the various use requirements and corresponding coating types for automotive and architectural glazing applications, the reader should have a good overview of coating options available today. An outlook on general industry trends from the perspective of the author will end this chapter.

Optical Thin Films and Coatings. https://doi.org/10.1016/B978-0-08-102073-9.00020-5
Copyright © 2018 Elsevier Ltd. All rights reserved.

20.2 THE ROLE OF THERMAL CONTROL IN GLAZING

Windows provide a visual connection between the contained (internal) environment and the external environment while maintaining a separation from the elements such as wind or precipitation. The desirable visible transparency of common commercial plate glass comes with a rather "transparent" characteristic along a broader range of the electromagnetic spectrum, be it ultraviolet or infrared (IR) radiation. This transparency can result in a large energy transfer through windows that can result in undesirable heating of spaces from solar (daylight) radiation that require air-conditioning to remove the built-up heat, or in excessive heat loss through windows by means of long-wavelength blackbody radiation that increases the heat load of an enclosed space.

The mitigation of thermal radiation transmission (either leaving or entering an enclosed structure) is an important function of windows. Optical coatings are just one means to accomplish this—well before the advent of optical coating technology, architects were adept at incorporating overhangs, louvers, storm windows, careful site selection, internal or external shading systems, and other design elements to achieve a comfortable built environment—so it is important to recognize that optical coatings compete with other techniques, and thus a thorough understanding of their costs and merits in a competitive marketplace is required. An awning or carefully designed external louver system in a south-facing window in a hot climate will doubtlessly be a simpler (and lower up-front cost) solution than an advanced switchable electrochromic window until specific design constraints or a more comprehensive energy analysis justifies a coating-based solution. Fortunately, modern modeling tools (e.g., United States Department of Energy "EnergyPlus") allow a very detailed analysis of the impact of various design options, and are routinely used by developers and architects who are conscious of the significant influence of a building on the long-term energy-efficient use of the built environment. Recent energy efficiency programs such as LEED ("Leadership in Energy and Environmental Design," developed in 1998 by the US Green Build Council), Energy Star in the United States, or EnEV ("Energieeinsparverordnung") in Germany—to name just three of many national incentives and regulations—encourage the design of sustainable architecture, and recognize the role of energy use in the overall "cradle-to-grave" (life cycle) cost of a building, compared to the emphasis on low construction cost that tends to ignore opportunities to incorporate energy-efficient construction techniques that exceed basic construction code requirements.

Compared to architectural applications, thermal control in automotive glazing has historically been a niche market. This is largely due to the relatively small fraction of engine power required for cabin heating or cooling (and the fact that cabin heating is a convenient by-product of the classic internal combustion engine). Air-conditioning in cars, however, is an "optional" load, with a typical 400-W compressor load imposing added fuel consumption of at least 1 mile per gallon (mpg) (http://www.nrel.gov/docs/fy00osti/28960.pdf). However, since peak loads can be substantially higher and impose a much larger load on modern energy-efficient

vehicles, studies identify air-conditioning as the single most significant means to improve fuel economy (aside from the range of electric vehicles). Energy-efficient glazing employing thermal control coatings is an effective means to reduce both cabin soak temperatures and air-conditioning load.

20.2.1 BUILDING WINDOW ENERGY EFFICIENCY

For buildings in northern climate zones, thermal losses through poorly insulated windows are a significant source of wasted energy. Of the approximately 40% of the primary energy that was spent on buildings in the United States (http://buildingsdatabook.eren.doe.gov/TableView.aspx?table=1.1.1) in 2008, about a quarter (http://buildingsdatabook.eren.doe.gov/TableView.aspx?table=1.2.5) is spent on space heating. In view of the realistic prospect of "Zero-Energy" buildings that eliminate the need for any external energy supply—to a large extent by efficiently harvesting the solar energy received through windows in the "passive house" concept—adequate window coatings contribute significantly to energy conservation.

In the United States, the US Environmental Protection Agency (EPA) initiated the "Energy Star" program in 1992 to promote energy-efficient products in order to reduce greenhouse gas emissions. In 1996, the EPA partnered with the US Department of Energy (DOE) to focus on certain products, and today the DOE maintains several laboratories and Government initiatives dedicated to energy efficiency. The DOE collaborates with industry and academia on defining voluntary goals and performance targets for energy-efficient products for the building envelope, including energy conservation targets and strategies for windows (http://www.efficientwindows.org/). For windows, the US Lawrence Berkeley National Laboratory (LBNL) develops thermal simulation software and maintains a database of glazing products (WINDOW) (http://windows.lbl.gov/software/window/window.html) that allows modeling of the energy and visual characteristics of a wide range of window systems.

In Europe, the German "Energieeinsparverordung" (EnEV—law for the conservation of energy) is a leading example of energy efficiency legislation. In contrast to the promotional character of the United States "Energy Star" program, the EnEV mandates certain energy efficiency performance standards for windows (among many other products). EnEV regulates the total energy balance for buildings (with a targeted primary energy reduction by approximately 30% in 3-year intervals [http://www.bmu.de/fileadmin/bmu-import/files/pdfs/allgemein/application/pdf/klimapaket_aug2007.pdf, page 22 (in German)], and focuses on the energy transfer through the building envelope as a "system boundary," thus taking the energy efficiency of windows into consideration.

In regions with intense solar radiation, a significant amount of energy is consumed to remove accumulating heat from buildings, mostly through air-conditioning. Those regions are referred to as "cooling-dominated." In commercial buildings with a higher window-to-wall ratio (compared to residential buildings), the cooling-dominated region even extends into moderate climate zones. Simple plate

glass windows contribute heavily to the "greenhouse effect" of trapping thermal energy. Along with the high-energy transmission, glare is often a problem during sunny days in rooms with all but northern orientation, and shading is a common means to address these two issues. Well designed exterior shading fixtures such as awnings, louvers, or overhangs deliver excellent results (and are effective tools in the daylighting management toolbox of any architect), whereas interior shading fixtures (curtains, drapes, blinds) primarily address glare as they allow a significant amount of solar energy to enter the room without effective re-radiation of trapped heat.

Tinted glass is another common solution. However, most tinted glass is absorbing and becomes a significant source of radiant heat—for a simple single pane of absorbing glass, 50% of the absorbed energy radiates into the room, whereas the exterior surface may get cooled from wind. The spectral performance of the absorbing glass plays another role—if it is absorbing primarily in the visible spectrum with little blocking of the IR spectrum, the glare problem may be solved but the significant energy of solar IR radiation will still heat up the room. Therefore, energy-efficient windows for cooling-dominated applications employ coatings to optimize the thermal performance.

Partially reflective coatings offer an effective approach for this application. In theory, sufficiently thick silver, gold, or copper coatings can reflect almost all of the solar radiation, and shading or glare control for the inhabitants is achieved by reducing the visible transmission to between 10% and 50%.

However, aesthetic demands often limit this approach—the high external reflectivity is often not desired, and architects often demand window designs that balance reflection and absorption to achieve a tolerable compromise between energy efficiency and design constraints. Laminated glass or multipane glazing opens up a myriad of possibilities by combining different glass types and coatings to achieve the desired effect and still be energy-efficient. More details on design guidelines are given in Section 20.4.

Glare control typically is a "Comfort" function of glazing in the visible solar spectrum, but the choice of glare attenuation can also affect the IR portion of the spectrum, which often is an important consideration for the thermal performance of windows. Here, spectrally selective coating designs (explained in Section 20.3.2) allow decoupling of glare and IR transmission functions.

20.2.2 AUTOMOTIVE WINDOW ENERGY EFFICIENCY

As mentioned earlier, solar cabin heating of vehicles and the subsequent need for air-conditioning have become a focus for energy conservation efforts in the automotive industry. The fundamental problem is similar to that of buildings in cooling-dominated regions, but the design constraints favor coating-based solutions—awnings and interior blinds are rarely options—and regulations mandate a minimum of visible transmission for windshields and frontside windows in most countries. For example, in the United States, the minimum visible transmission of a windshield is 70%, and was only recently reduced from 72% in order to allow for more efficient dual-silver IR-reflecting coatings that reduce solar heating of the cabin.

Thus, effective energy-efficient automotive windows have only been possible since the advent of spectrally selective coatings that allow a combination of the high visible transmission with the desired IR reflection. For cars, there also is a noticeable difference in cabin heating when parked or while driving—the moving air during motion can help cool absorptive windows, but the heat radiation of absorbing (often dark tinted) window glass contributes greatly to the cabin heat buildup of a parked car, illustrating how the shading function of tinted absorbing glass does not really present an effective means of energy conservation, contrary to common consumer perception.

20.3 WINDOW COATING TYPES BY FUNCTIONALITY

In a window, energy travels primarily in three modes: conduction, convection, and radiation. Conduction is controlled by the conductivity of a glass pane, and is generally controlled by the thermal conductivity, k, of a bulk material. Since optical window coatings are very thin compared to a glass pane, the conductive impact of window coatings is usually negligible. The conductive impact, however, becomes important when radiation control (transmission, reflections, absorption) comes into play. Convection plays a significant role in the energy efficiency of insulated glazing units (IGUs) that have one or more gas-filled cavities and the movement of the gas affects the heat transfer. Another convective contribution is how air movement (e.g., from wind in a building or a moving vehicle) affects the steady-state temperature of absorptive glass. In general, however, the biggest energy efficiency contributions in glazing come from controlling the radiative properties (emissivity) and spectral transmission properties of windows.

20.3.1 LOW EMISSIVITY

While the control of transmission of electromagnetic radiation is important for windows, the role of thermal emissivity is a significant contributor to energy transfer as well. Any material surface will radiate energy at a given temperature, and the emissivity, ε, is defined as the ratio of energy emitted from a surface versus a blackbody (perfect emitter) at the same temperature. For energy efficiency purposes, one seeks the smallest possible emissivity for a surface that is designed to minimize heat loss.

As a rule of thumb, highly glossy (reflective) or highly conductive materials have lower emissivity. Silver, in particular, is a preferred coating material for low-emissivity window coatings. While clear float glass has an emissivity of about 0.95, silver has an emissivity of about 0.02. Conductive tin oxide (SnO_2), along with similar materials of the group of transparent conductive oxides (TCOs), with an emissivity of 0.15–0.2 is another attractive low-emissivity material for windows. In Chapter 8, Carl-Gustav Ribbing explains the physics of emissivity. The physics and design characteristics of TCO coatings are described in detail by Clark Bright in Chapter 21.

20.3.2 SPECTRAL SELECTIVITY (INFRARED REFLECTING, ULTRAVIOLET BLOCKING)

Spectral selectivity is another important concept in window coatings, as it allows customized transmission and rejection (either by reflection or absorption) of certain spectral ranges, such as in a band-pass filter. For windows, a common requirement is high transmission of the visible light (e.g., to allow occupants a clear view of the outside, or to enable daylighting of a room utilizing natural sunlight) while minimizing transmission of exterior solar heat or loss of long-range heat (IR) energy from a room. Thus, spectral selectivity applies to both heating- and cooling-dominated regions (Fig. 20.1).

Since the solar spectrum delivers 52% of its total energy primarily in the (non-visible) IR spectrum, blocking the IR portion of the solar spectrum (780–2300 nm) is an important function to suppress heat buildup in cooling-dominated regions. Ideally, this requires a very steep band-pass edge just past the visible spectrum.

Blocking longer-range IR radiation in the range of 2300 nm (the energy of a blackbody at ~21°C room temperature) is essential for conserving energy in a room in heating-dominated regions. Here, it is desirable to allow as much of the solar radiation to contribute to heating the building, while simultaneously suppressing the heat loss from room objects at room temperature by shifting the band-pass edge toward longer wavelengths.

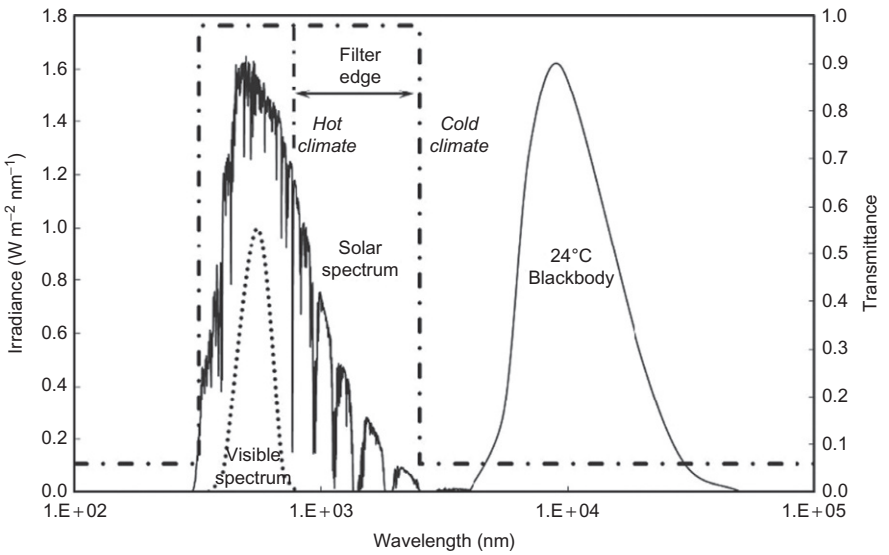


FIG. 20.1

Graph of solar + blackbody spectrum with short/long pass.

Based on McCluney, R., 1996. Sensitivity of fenestration solar gain to source spectrum. ASHRAE Trans. 10.

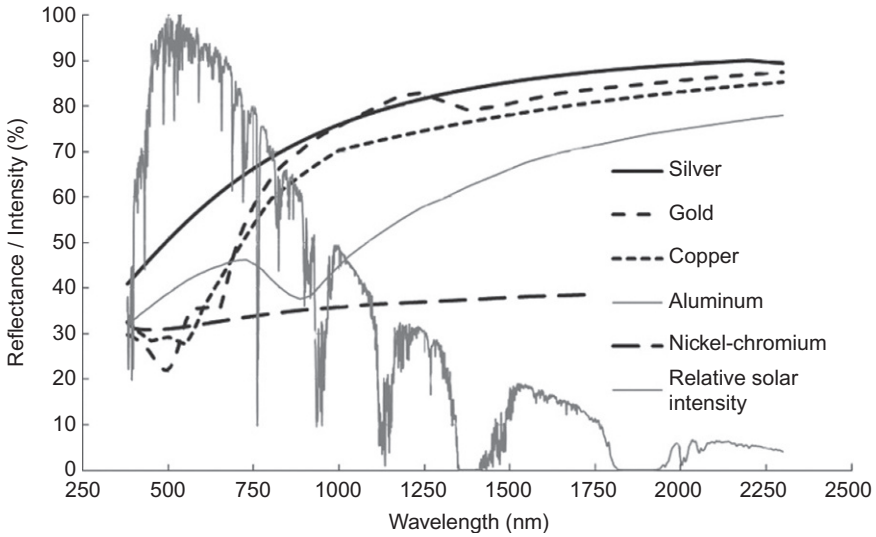


FIG. 20.2

Graph of reflectivity of different metals at 15 nm thickness.

In thin film form, most metals have a fairly uniform reflectivity across the solar spectrum, that is, they show no or moderate selectivity (Fig. 20.2). Copper and gold have the best selectivity (Valkonen et al., 1984) (especially compared to transition metals, which are essentially nonselective), and although not of optimum selectivity, in industrial practice silver is the preferred material as it combines practical selectivity with neutral reflected and transmitted color which is important for glazing aesthetics. The graph also shows the reflection properties of a nickel-chromium alloy, as an example for a material that is significantly more absorbing than noble metals.

The ratio of solar transmittance versus visible transmittance for a thin film of silver is 1.2, and can be enhanced through the use of multilayer stacks, where the silver layers are separated by adequate dielectric layers of a thickness that effectively antireflects the entire stack as efficiently as possible. Such a stack design is known as an "induced transmission filter." The dielectric layers in such a stack have the added benefit of protecting the sensitive metal layers. With this, the selectivity of a silver stack can be designed to approach the band-pass filter design indicated in Fig. 20.1, and with a much lower layer count than with a nonmetal (i.e., all-dielectric) high-/low-index Fabry-Perot filter, which might contain approximately 8–12 or more high-/low-index pairs, and which is much thicker and more expensive to produce. Fig. 20.3 shows the effect of single-, dual-, and triple-silver stacks (each silver layer approximately 9 nm thick and properly antireflection-coated for the visible spectral range). The resulting overall coating thickness (approximately 300 nm for a two-silver stack) is significantly lower than what could be accomplished with a similarly performing all-dielectric filter stack.

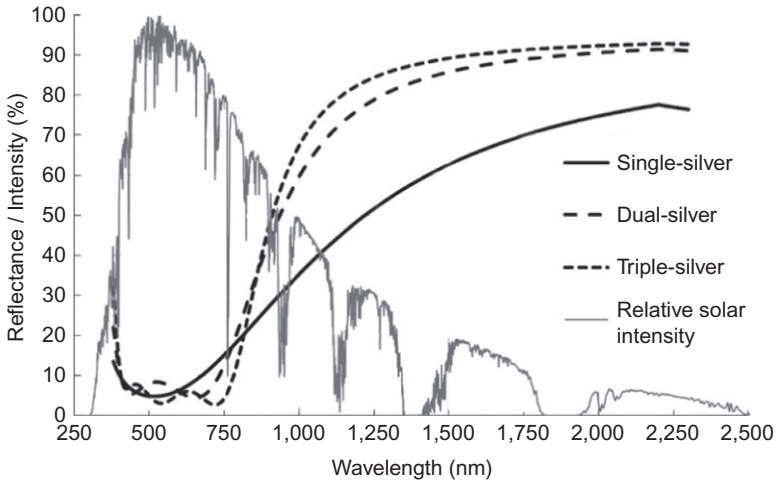


FIG. 20.3

Graph of 30-nm silver stack—1×30 nm, 2×15 nm, 3×10 nm, 4×7.25 nm.

20.3.3 ANTIGLARE

Avoiding the glare of bright sunlight is a common requirement in buildings and vehicles. The most common and cost-effective approach by far is the use of absorptive tinted glass. Glazing coatings can also be made absorptive, especially if suppression of excessive reflection in antiglare applications is desired (however, if the coating becomes too thick, it will become noticeably reflective, so this design approach has limits). Nickel-chrome (as shown in Fig. 20.2) is a typical example of this approach.

Absorptive glazing solutions are notorious for their challenging thermal management properties. The absorbed light is converted to thermal energy, which heats up the respective component, and can lead to problems with stress buildup due to mismatch in the coefficient of thermal expansion (CTE). A hot, absorptive window also influences the thermal properties of the adjacent airspaces, and may require special considerations in the location of energy-efficient coatings by placing any reflective coatings as close to the heat source to minimize the absorptive heat load. This can result in a "mirror glass" effect that building designers often try to avoid, preferring a more absorptive, antiglare look, so the balance between aesthetics and thermal performance can result in some intricate glazing design compromises.

20.4 GLAZING TYPES: MONOLITHIC, LAMINATED, AND MULTICAVITY GLAZING DESIGNS

A glazing designer has three general window constructions available: monolithic glass, laminated glass, and multicavity glazing.

Monolithic glass consists of just a single window pane, coated or uncoated. In addition to any potential thin film coatings, monolithic glass comes in a vast array

of clearness or absorptive tints (produced by adding minerals during the glass melt, and therefore distributed uniformly throughout the glass thickness), colors, transmissivity grades and glass types (e.g., borofloat glass, mid-, or low-iron glass), all of which have different thermal and spectral characteristics. These glazing types are typically the building blocks for more complex window structures, particularly laminated or IGUs.

Among the coated glass types, only the "hardcoat" (pyrolytic) versions (e.g., for low-e glazing) are suitable for stand-alone, single-pane applications. TCOs (e.g., tin oxide) are the prevalent candidates for such coatings. "Softcoat" (sputtered) versions, especially those containing silver as a low-emissivity or spectrally selective component, require protection of the coating from the elements, and are suitable for laminated or IGU glazing.

Laminated glazings expand the application horizon by using two glass panes (or a glass plus an applied window film). Lamination of two glass panes requires an adhesive, which is typically polyvinyl butyral (PVB), or sometimes ethylene vinyl acetate (EVA), which is more expensive.

Laminated glass is often required for structural or safety reasons such as hurricane-resistant windows, intrusion protection in buildings, or impact resistance in automotive windshields, for example. Another common nonoptical reason for laminated glass is sound attenuation. These requirements frequently dictate the thickness and type of PVB, but often allow integration of optical coatings, especially high-performing solar-selective coatings that may require protection from the elements (sputtered "softcoats," especially) at the laminate interface. It is important to recognize that low-emissivity coatings lose their low-emissivity function when immersed in an adhesive (the thermal conductivity of the composite will prevail), but retain their IR-reflective function, and thus spectrally selective filtering can be integrated very effectively through adequate coatings.

20.5 COATINGS ON GLASS SUBSTRATES

Most modern architectural glazing incorporates optical coatings for thermal and aesthetic functionality. Coating processes are often closely coupled to the glass float line (such as pyrolytic coatings), or in subsequent vacuum coating processes. They can provide the key functionalities of low emissivity (and spectral selectivity, with respective coating stacks) and glare reduction.

20.5.1 LOW-EMISSIVITY COATINGS

Low-emissivity coatings on glass are divided into two families: pyrolytic ("hardcoat") and "softcoat." In Chapter 8, Carl-Gustav Ribbing explains the physics of emissivity.

Pyrolytic coatings are produced from CVD processes, and are all-dielectric materials, typically with indium tin oxide (ITO) as the functional low-e material (see also Chapter 21). The deposition process requires high temperatures to dissociate

a gas-phase precursor for forming the coating, and is often implemented directly at a glass float line to take advantage of the thermal energy from the cooling glass. Pyrolytic coatings can also be tempered and subjected to glass bending after the deposition process; they are hard, resilient, and environmentally robust, and thus can be used on the glass exterior. This makes them an attractive option when a low-e surface is desired inside a room to boost energy efficiency of a multipane window, and the coating still tolerates user practices such as window cleaning. Modern pyrolytic coatings can also be combined with photocatalytic coatings (e.g., rutile titanium dioxide, TiO_2) to improve self-cleaning, or with hydrophobic window treatments that take advantage of rain to clean windows.

Softcoat low-e coatings have much lower emissivity in comparison to ITO-based coatings, due to the lower emissivity of silver that is part of the coating stack. Soft coatings are produced almost exclusively by magnetron sputtering, a vacuum-based physical vapor deposition (PVD) process that ensures optimum quality (thickness control, purity, and morphology) of the thin silver layers. The glass is usually coated in the form of large cut sheets in a semibatch process to obtain the necessary high vacuum atmosphere required for best silver quality. The silver must be protected from tarnishing and degradation, and thus soft coats are more fragile compared to hard coats. Postcoating bending, forming, or tempering has only recently become possible, but is generally more problematic than for hardcoats. Softcoats cannot be used in exposed applications, and thus are typically found on the interior surfaces of IGUs where the noble gas fill and desiccant ensures a safe environment. In certain applications, it is also necessary to "cut back" (grind off or edge-delete) the silver-containing coating stack at a glass edge to prevent deleterious environmental interactions with the softcoat stack at the edge of the glass.

20.5.2 ANTIGLARE

Antiglare coatings aim at reducing reflective or transmissive glare, and are therefore almost always designed as absorptive coatings. For thin film coatings, metals such as chromium, nickel, or suitable alloys (nickel-chrome or even stainless steel in varying compositions) are the most typical materials. By choosing an appropriate coating thickness, the transmissive attenuation can be achieved rather easily, however usually at the cost of increased reflectivity, which can create aesthetic problems, and therefore it is typical to combine the metallic coating with tinted glass (or, in laminates, tinted PVB lamination adhesives or polymer films). Modifying the growth morphology of the metallic coating by creating a rough or porous coating can somewhat mitigate that effect, but in practice it is not possible to achieve absorption that is lower than the resulting reflectivity (see the nickel-chrome profile in Fig. 20.2). Also, the aforementioned problem of absorptive heating and the responding thermal balance as well as stress buildup due to mismatch in CTEs need to be taken into account. It is noteworthy that, for example, applying an absorptive tinted plastic window film to an IGU typically voids the warranty given by the IGU manufacturer because such windows are not designed for the thermal imbalance and the resulting stresses in the glass can lead to glass breakage.

20.6 COATINGS ON POLYMER SUBSTRATES

Optical glazing coatings are very commonly applied to glass, but can also be deposited on thin, transparent, and flexible polymer films. The differences in coating substrates lead to differences in coating performance, applicable coating types, and coating process strategies for the two material groups.

The lower thermal budget of polymer films precludes them from use for hardcoat low-e coatings, and restricts them to vacuum thin film coated variants, especially magnetron sputtering, thermal evaporation, or low-temperature (e.g., plasma-assisted) variations of CVD, both in vacuum and atmospheric plasma. The lower tolerable coating temperatures also make it difficult to achieve the same coating quality as for glass (e.g., high-temperature deposited silver for improved nucleation and coating morphology, or posttempering for postoxidized ITO which is necessary to ensure optimum spectral and electrical/emissive functionality for this semiconductor material). The flexible substrate makes coatings more susceptible to stress effects such as curl. Proprietary additives in the polymer film may migrate and contaminate thin film coatings over time. Most polymer films have one side textured to prevent "blocking" (the melding of coating wraps during storage or transport), and the surface roughness may degrade the nucleation and growth of an optimal solar control stack. Surface plasmon effects have been observed (Kleinhempel et al., 2011) in high-performance low-e coatings, inducing absorption in the visible spectrum. High-index dielectric materials enhance the surface roughness effect, and leveling or smoothing layers or lower-index transition layers can mitigate the undesired effect.

Thin polymer substrates require special care and handling as they are prone to wrinkling, creases, can be difficult to clean, and can build up static charges, but they do provide a very cost-effective approach to delivering thin film coating stacks for glazing applications. Thicker substrates are more robust to handle in web winding and rewinding operations, and may be required for thicker coatings to control curl from the typically compressive sputter coating stack.

On the benefits side, coatings on thin polymer substrates have a significantly lower embodied energy when compared to glass, and enable reduced shipping, transportation, and installation costs. The capital investment required for a polymer film coating operation is much lower (at least half) when compared to a glass coating line of the same capacity, particularly for specialty applications as with the coating of curved substrates such as automotive windshield glass. The possibility of incorporating functionally coated thin plastic films into glazing products through lamination or suspension significantly expands the design space for glazing designers.

The most common plastic type for glazing applications is polyethylene terephthalate (PET), a very ubiquitous plastic material. PET films for glazing are usually of the high-value variety (as compared to packaging PET) due to their superior optical clarity, well-controlled physical properties, and environmental stability. All major global PET suppliers (e.g., DuPont, Teijin, ICI, Dow Chemical) sell

high-grade PET films suitable for glazing applications. PET films can be impregnated with ultraviolet-blocking (absorbing) agents without degrading their optical, mechanical, or thermal properties to resist long-term yellowing, and to help protect against UV radiation damage. With proper material selection and application design, PET-based window products can easily exceed 30 years' service life.

Another notable polymer substrate is ethylene tetrafluoroethylene (ETFE). Architects prefer this material for the design of clear tent structures due to its outstanding chemical robustness, radiation stability, and high temperature tolerance in combination with acceptable optical properties (clarity in the visible spectral range, neutral color) and acceptable cost. Recently, the use of this material in static or dynamic multilayer structures such as pneumatic cushions, which can be adjusted to meet changing seasonal or climatic thermal needs for a given structure, has received considerable interest (Poirazis et al., 2009) and the material is suitable for enhancement with the same types of low-e or spectrally selective coatings as have been proven for PET films to improve the energy efficiency of resulting buildings. Since a cushion structure allows silver-containing softcoats to be protected from direct environmental impacts that would otherwise destroy the silver rather quickly, new concepts for the control of optical and thermal characteristics are conceivable. However, only a very few such projects have been realized to date, and it remains to be seen how robust and reliable such coatings are over time.

20.6.1 FILMS FOR LAMINATES

PET films with optical coatings can be found in many laminated glazing applications, particularly in the automotive or commercial architectural market where lamination is required for safety or other considerations. For such applications, it is important that the PET film and coating are compatible with the adjacent encapsulation materials (typically PVB, sometimes EVA). This covers chemical stability, mechanical integrity, and optical properties. Chemical compatibility requires that no additives that can potentially leak from the PET penetrate the top dielectric coating to degrade the silver. Mechanical integrity requires that the coating can tolerate the shear loads and thermal expansion mismatch that the lamination process imposes.

Optical compatibility requires that residual film stress does not result in excessive film waviness or optical distortion of the finished laminate, and may include the compliance of the film/coating structure with compound curvatures often found in automotive applications. In laminates with soft-coated films, it is common to include a "cutback" where the film is recessed from the glass edge by a few millimeters in order to embed the film edge in a seal of surrounding encapsulant to prevent any environmental degradation of the silver coating over time. Often, the cutback is obscured by printed perimeter patterns or the windshield adhesive or other window frame structures so that it is typically not noticed by the end user.

20.6.2 FILMS FOR MULTICAVITY GLAZING APPLICATIONS

Optically coated films also find applications in multicavity/multipane windows. They increase the thermal insulation achieved by adding additional cavities filled with noble gas (argon or krypton). The gas cavities can be separated by glass panes, or by suspending plastic films to create additional cavities.(Lizardo and O'Shaughnessy, 1982) In such applications, one or more coated PET films are suspended in the space between the inner and outer glass panes, replacing what would typically be a glass pane for a triple- or quadruple-pane IGU. The benefit of using coated PET film is primarily a significant reduction in IGU weight (approximately 50% compared to an all-glass quadruple-pane IGU) as well as a thinner overall IGU thickness due to the thin film in comparison to the thicker glass, which helps accommodate multicavity glazing into traditional window frame dimensions. Silver-based low-e coatings perform very well in such applications as the noble gas environment and desiccant prevents long-term degradation (similar to soft-low-e coated glass panes), and the PET films usually preserve a more neutral color of the IGU as compared to the noticeable green tint imposed by additional soda-lime glass panes. The suspension systems for such PET films require special care to suppress distortion from wrinkles or other cosmetic blemishes.

20.6.3 APPLIED WINDOW FILM PRODUCTS FOR RETROFIT APPLICATIONS

Optically coated film products also enable retrofitting of existing windows for improved thermal efficiency by applying a flexible film to a window surface by use of adhesives. Aside from a few recent examples of low-e window films (which must expose the rather fragile softcoat to either the interior or exterior environment of a window in order to retain the low-emissivity functionality), the majority of these products aim at glare reduction (using absorptive/tinted films) and/or IR reflection from suitable solar-selective coating stacks. Since silver is a typical component of most high-performance solar control coatings, it must be protected from the environment, and is usually part of a laminate structure, resulting in a product that features an adhesive (for mounting on the glass surface, protected by a removable liner) and two PET films that encapsulate the silver-dielectric stack with the help of a suitable laminating adhesive. For added robustness, hardcoats, or antifouling coatings can be added to the exterior laminate surface, improving scratch resistance and cleaning. Depending on additional use requirements (antiglare, privacy), the laminate may include tinted absorptive PET or sputtered films.

20.7 SPECIAL CONSIDERATIONS FOR APPLICATIONS

While the fundamental functionalities of glass, polymer films, and coatings described earlier constitute the common building blocks for windows, glazing applications for vehicles and buildings have distinct use constraints that influence the implementation of coatings.

20.7.1 AUTOMOTIVE APPLICATIONS

In comparison to architectural applications (which are subject to rather broad energy conservation requirements), the coating considerations for automotive applications face more complex regulatory and applications-related constraints. Windshields must meet requirements for both impact resistance as well as visible transmission, which extend to any coatings that are involved. Windshields must sustain impacts without penetration from exterior objects (into the cabin) as well as passenger ejection resistance (such as a head impact during an accident) that are qualified with rigorous tests in the industry, and require any coatings to maintain the mechanical integrity of the windshield laminate. This is particularly critical for laminated PET films, as the additional interfaces may introduce additional failure points. Since the impact resistance is primarily delivered from the plastic deformation of the PVB laminating adhesive, it is critical that the embedded PET film and coating stack does not diminish the structural properties of the laminating adhesive.

Automotive windshields have strict requirements regarding the minimum visible transmission (T_{vis}). For example, Europe (Standard UN/ECE R-43, n.d.) requires a T_{vis} of at least 75% for windshields and at least 70% for sidelights and backlights, whereas the United States (US Federal Motor Vehicle Safety Standard 205 (49 C.F.R Part 571.205), n.d.) and Japan require a T_{vis} of at least 70% for automotive glazing. In practice, the 75% limit allows for just a single-silver IR-reflective coating, whereas the 70% limit can accommodate a more spectrally selective dual-silver coating.

20.7.1.1 Coating-based window heating applications

The permitted visible transmission limits have also allowed the introduction of resistive heating into windshields. While the most common technical approach is the use of microwires, sufficiently thick direct-coated ITO films have been used in the past as well (see also Chapter 21). The thickness of the coatings is largely dictated by the required sheet resistance for the film, which itself is a function of the window dimensions, the contacting/termination approach, and the supply voltage applied. In the common 12 V systems, the resulting ITO film thickness will have a considerable reddish color in reflection (and particularly at an angle), which is aesthetically undesirable. However, thin film based windshield systems avoid the "starburst" phenomenon typical of microwire solutions, where the diffraction of the light from the headlights of an oncoming vehicle at night creates an irritating diffraction pattern in the driver's eye. While direct-on-glass-coated ITO films for this functionality have been commercially implemented for a long time, an alternative approach for defrosting a windshield has come to market that uses the conductive silver layer in an IR-reflecting interlayer in a similar fashion but with the benefit of more aesthetically pleasing color.

20.7.1.2 Perceived passenger comfort versus energy conservation

The spectral property of an automotive window is only one of many factors that determine passenger comfort, and thus makes for a complex discussion. The IR radiation into the cabin can increase the absolute cabin temperature, but even at a

moderate cabin temperature, sun exposure (whether with a high or low IR dosage) onto bare skin generates a different temperature perception. In addition, the radiated heat from absorptive surfaces (dashboard, tinted windows) further adds to the radiative heat load that alters the perceived temperature. Finally, the influence of forced or natural air circulation in the cabin can be significant, is more user-controllable through ventilation controls, and thus the improvement of air circulation (even at the expense of added fans and electrical load) competes with improved thermal control coatings in the automotive sector.

20.7.1.3 Dimmable windows/sunroofs

A few luxury vehicles also feature dynamic glazing in the form of electrochromic windows for privacy and shading control. Such coatings can mostly be found on sunroofs and also on some rear sidelights. These electrochromic coatings are directly derived from similar products in the architectural markets, and thus have similar performance characteristics and operating constraints. However, a distinction between architectural and automotive electrochromic glazing systems is in the desired switching speed, which should be in the subminute range for cars, whereas slower switching is acceptable in architectural uses. In automotive applications, integration into the control system based on a 12 V operating voltage is a particular hurdle, which is often solved by designing the window surfaces into sufficiently small segments so that the overall electrical resistance of the coating and the resulting operating voltage are acceptable. While electrochromic glazing allows "on-demand" variation of a very notable bright/dark state, there are also examples for aftermarket options that may not offer notable bright/dark variations but clear/opaque (hazy) transitions for privacy (such as liquid-crystal-based solutions), or passive systems such as thermochromic or photochromic systems. It is important to recognize that many of these solutions are aftermarket products that should be selected carefully for compliance with vehicle codes and automotive OEM warranty conditions.

An often-voiced concern about the use of electrically conducting coatings in motor vehicles is the potential attenuation of radio signals. It has indeed been shown (California Air Resources Board, 2009) that the use of metallic spectrally selective coatings attenuates the signal of cellular phones and global positioning system (GPS) receivers (and possibly also toll collection transceivers and garage door openers), but technological alternatives such as the use of deletion zones (e.g., near the rear view mirror, where rain sensors or other sensors are already placed) or exterior antennas (already common for satellite radio or preinstalled GPS receivers) are available and can resolve the "Faraday Cage" effect while still enabling the energy-conservation benefits of implementing solar-selective coatings that can reduce carbon emissions in automobiles. Another approach to resolve the RF signal attenuation of conductive coatings is the substitution with all-dielectric (nonconductive) coating stacks. However, such Fabry-Perot filters require very thick overall coating designs, significantly higher layer counts, show a high sensitivity to color variations when viewed at an angle, and thus are complex, expensive, and not a solution that has found commercial implementations.

Modern glass forming capabilities have extended the design envelope for automotive glazing, and it is now common to include complex curvatures in car windows. Beyond simple cylindrical glass bending, so-called "cross-curvatures" (biaxial bending of glass over a three-dimensional mold) allow for a more refined contour integration. Bent glass poses a significant challenge for glass coaters. Among common thin film coating processes, only some CVD coating processes are truly omnidirectional (and allow the coating of virtually any geometry, including hollow structures), but solar control coatings are predominantly deposited with magnetron sputtering, which is highly directional. Therefore, the shape of the substrate directly influences the coating thickness uniformity. Coating uniformity can be modeled fairly well for a given deposition process, and some process variables can be adjusted to extend the capability range, but generally windows with any significant curvature are difficult to coat without noticeable color gradations (the result of nonuniform film thickness).

One solution to the problem of applying spectrally selective coatings on curved glass is to coat the glass prior to bending with a coating that tolerates the subsequent bending temperatures. Pyrolytic coatings are the best candidates for this process. Another solution is the lamination of a plastic film that is coated with a spectrally selective coating. The latter approach lends itself especially to the manufacture of windshields, which need to be laminated anyway for safety regulation compliance, so including the plastic film and a second layer of PVB lamination adhesive can be accommodated rather easily. Pyrolytic coatings as well as plastic films allow a certain degree of cross-curvature.

20.7.2 BUILDING APPLICATIONS

In architectural glazing, a specific coating or glazing solution is constrained by market conditions that quickly go beyond the simple question of which coating type or spectral performance is optimal to satisfy a certain application profile. It is important to understand the additional motivations or constraints the market imposes on a certain glazing solution.

The purpose of a building determines many aspects of its glazing solution. A big distinction is the difference between commercial and residential dwellings, or the difference in motivation from economic incentives that may differ between the operator owning versus renting/leasing the building.

In an unregulated market, the owner/operator distinction highlights the different motivations of owners and operators: owners want to minimize construction cost, whereas operators want to minimize operating cost. The resulting discrepancy between minimizing glazing cost and choosing an energy-efficient window is increasingly being resolved by regulatory requirements for energy efficiency, or—as is the case in Germany, for example—the need for a landlord to disclose the energy consumption of a rental building (especially residential).

Another application related distinction between commercial and residential construction is the size of individual windows. Residential windows tend to be smaller and of much more varied size and operator type compared to commercial

construction, which tends to be more standardized for a given building and generally of larger size.

Another distinguishing concept of commercial buildings is the trend toward "curtain wall" construction (especially in high-rises), which has a very different mounting system (the windows can become load-bearing members, so the structural integrity is important), and usually is fixed (nonopening). Commercial windows can also incorporate design elements where the exterior glass pane extends beyond the window opening to cover structural elements of the curtain wall structure or spandrels, which requires special window manufacturing techniques to accommodate the large setbacks (for multipane windows, removal of silver-containing low-e coatings, or additional printed aperture frames). Residential windows, in comparison, still follow the "hole-in-the-wall" paradigm, are smaller, and typically require to be opened for ventilation by the use of slider or turn/tilt operator types. It is important to recognize that the frame-to-aperture ratio influences the thermal properties of the overall window—multipane glazing can achieve significantly higher thermal insulation than common window frame systems, and for passive house windows that rely on large apertures, larger windows are desirable. This may sometimes create design conflicts—sliding windows typically have higher frame cross sections than turn/tilt windows of similar window aperture, or historicizing muntins or grids that are embedded inside multipane cavities add to shadowing and can create undesirable thermal bridges that negate the benefits of advanced energy-efficient glazing coatings.

20.7.2.1 Integration of coatings into multifunctional glazing requirements

A recent trend in window technology diversification is the combination of glazing with additional functionality such as photovoltaics (PVs) or dimmable/switchable glazing.

Building-integrated photovoltaics (BIPVs) offer many opportunities to utilize the building envelope for solar electricity generation.(Pagliario et al., 2010) The combination of PV structures with (typically semi) transparent glazing is a niche technology that is often a compromise between the desire for solar energy generation and design goals, most often shading (but possibly also IR-blocking—from the transparent conductors in a PV element—and UV-blocking from the use of suitable laminating adhesives) because a semitransparent solar cell will not utilize the full amount of available photons for energy conversion. Amorphous and crystalline silicon are the most common PV elements, and dye-sensitized cells (DSCs) may have future potential but currently show very small conversion efficiencies. Considering the significant "balance of system" expense and infrastructure for converters and wiring, a strong architectural design justification is typically driving such implementation, while a more conversion-efficient PV function can be obtained with opaque building components (some curtain wall structures may combine clear non-PV windows with adjacent opaque PV panels). Another design constraint for BIPV windows is the lack of standardized window sizes, as the solar panels are very difficult and expensive to build in custom formats. Therefore, installations tend to favor curtain

wall designs that take advantage of the standardized formats of the PV cells but demonstrate the creative potential, for example, by laminating with colored and screen-printed glass (e.g., a semitransparent amorphous silicon solar panel in an office building staircase façade) (Massek, 2005).

Switchable glazing (or "smart windows") is an attractive way to dynamically control the spectral properties of windows and resolve the changing optical requirements during the day or the seasons (Lampert, 1998; Lynam and Agrawal, 1990). Although the fundamental concept of electrochromism is well established, development into robust, reliable, and lasting consumer products has been hampered by technical hurdles (mostly reliability for the two leading technical embodiments, thin film solid-state devices, and electrolyte exchange polymer-based devices), which translate into relatively high consumer prices that have moved little and relegate electrochromic windows to niche applications. The need for electrical controls and thus supply of electrical power to windows is another hurdle that hinders broad adoption. Electrochromic windows, with their multilayer structures of transparent conductors, allow easy integration of several energy-efficiency functions beyond just-switchable shading (which primarily affects the visible spectrum), such as IR reflection or ultraviolet blocking.

20.8 CONCLUSION

Optical coatings play a significant role in the design of modern windows for buildings and automobiles. The important contributions of low-emissivity and solar selective coatings have long been implemented to improve the energy efficiency of windows in the building envelope, and a broad range of options of how coatings can be integrated into windows allows architects to adapt to regional climate conditions and additional functional building requirements as well as design preferences. The integration of "active" functionalities such as electrochromics or BIPVs is emerging, but is currently confined to a high-cost niche market.

For automotive applications, optical window coatings have been implemented on a much smaller scale compared to architectural glazing, primarily due to design constraints (e.g., visibility requirements for windshields, coating curved window surfaces), but also due to a different cost/benefit profile for the implementation of energy-saving coatings in vehicles. Only recently have there been some regulatory efforts to promote the broader adoption of spectrally selective (IR-reflective) coatings (along with other approaches to improve energy efficiency by reducing air-conditioning loads).

It is expected that regulatory conditions will increase the demand for low-emissivity and spectrally selective coatings to improve the energy efficiency, not only for buildings (where it is a well-established part of modern code requirements), but also in the automotive sector where it is relatively new.

20.9 FUTURE TRENDS

Improvements in energy efficiency will continue to be a primary motivator for the development of optical coatings for glazing. Emerging economies are expected to adopt energy-efficient glazing technologies much sooner and faster through regulation than has historically been demonstrated by developed countries. China, for example, is setting rather ambitious energy conservation goals for buildings in the recent 5-year plan that calls for a 20% reduction in energy intensity through various initiatives (Levine et al., n.d.), with a large focus on new construction and building retrofits. This will force adoption of modern coating technologies, expansion of production capacity, and cost reduction, similar to what has resulted from energy efficiency regulation in Europe and the United States. The shift from energy efficiency as an optional/high-end product function to a mandated, broadly adopted standard will continue to drive the competition between competing technologies, and those that cannot realize major cost reduction will be left behind. One example might be electrochromic windows which, despite significant capacity expansion and government support in the United States, have not been able to demonstrate significant end-consumer price reductions, and may stand the risk of losing the "adoption race" against, for example, a combination of improved insulating windows in combination with the replacement of incandescent lighting with energy-efficient lighting which responds to the energy-efficiency goal of dynamic glazing. The urgency of cost reduction for broad adoption of new technologies is likely to increase due to regulatory mandates. Modern energy modeling programs already enable a thorough analysis of the complete energy footprint of a specific building, and the case scenario with the most attractive adoption cost will become more transparent.

For automotive glazing, it remains to be seen if energy conservation standards translate into direct regulation of the thermal performance of windows. Although eventually not implemented, the recent Californian "Cool Cars" initiative (California Environmental Protection Agency Air Resources Board, n.d.) called for a solar control function in car windows starting with the 2012 model year, but until the 2015 model year only the windshield might have an IR-reflective coating in response to concerns about electromagnetic signal transmission, and subsequent implementation stages allowing for various glazing solutions. This is an example of the more complex balance of functionalities in automotive glazing resulting in less stringent regulatory mandates. Another market motivation may come from the electric vehicle sector—if the driving range reduction that results from the energy consumption to heat and cool an electric vehicle becomes a notable argument, it may indirectly drive the demand for energy-efficient vehicle glazing. The anticipated proliferation of autonomous vehicles may also motivate drastic changes in the role of automotive glazing. It is conceivable that glazing surfaces may transform into displays for entertainment, information exchange, or ambiance modification when a vehicle is in autonomous mode. However, technological advances in this direction would need to be accompanied by significant regulatory changes in the function of

automotive glazing, and it may well be that the regulatory environment will pace rapidly faster developing glazing technology innovation.

A specific hurdle for "active" glazing components (electrochromic or BIPV glazing) that will need to be overcome is the market expectation for customized window formats and short lead times. In the residential window market, this especially calls for innovative fabrication and interconnect techniques that compete with the practice in passive glazing of single-day turnaround for IGUs and fully automated manufacture of freely definable window sizes and configurations.

20.10 SOURCES OF FURTHER INFORMATION AND ADVICE

- US Department of Energy Efficient Windows Initiative: http://www.efficientwindows.org/
- National Fenestration Rating Council (NFRC): http://www.nfrc.org
- National Glass Association: https://www.glass.org
- European Glass and Glazing Association (UEMV): https://www.uemv.org
- Insulating Glass Industry Association (IGMA): https://www.igmaonline.org
- Glass Association of North America (GANA): http://www.glasswebsite.com
- American Architectural Manufacturers Association (AAMA): https://www.aamanet.org
- "Residential Windows: A Guide to New Technologies and Energy Performance (Third Edition)" by Dariush Arasteh, John Carmody, Lisa Heschong and Stephen Selkowitz (2007), W. W. Norton & Company, ISBN 978–0393732252
- "Window Systems for High-Performance Buildings" by Dariush Arasteh, John Carmody, Eleanor S. Lee and Stephen Selkowitz (2004), W. W. Norton & Company, ISBN 978–0393731219
- Glasstec trade show, Düsseldorf, Germany: https://www.glasstec-online.com
- Glass Processing Days trade show/conference: http://www.gpd.fi

ACKNOWLEDGMENTS

I want to thank my colleagues and especially Rich Wipfler for sharing their insights and expertise in the area of optical coatings for glazing applications.

REFERENCES

California Air Resources Board, 2009. Evaluation of Electromagnetic Interference Due to Automotive Reflective Glazing. Emission Research Section, Mobile Source Control Division, El Monte, CA.

California Environmental Protection Agency Air Resources Board, Cool Cars and Reflective Glazing. http://www.arb.ca.gov/cc/cool-cars/cool-cars.htm.

Kleinhempel, R., Wahl, A., Böhme, T., Thielsch, R., 2011. Einfluss der Oberflächenmorphologie auf die Performance von Low-E Schichtsysteme (Influence of surface morphology on the performance of low-e coating systems). German, Vakuum in Forschung und Praxis 23 (1), 35–39.

Lampert, C., 1998. Smart switchable windows for solar energy and daylighting control. Sol. Energy Mater. Sol. Cells 52, 207–221.

Levine, M., Price, L., Zhou, N., Fridley, D., Aden, N., Lu, H., McNeil, M., Zheng, N., Yining, Q., Yowargana, P., Assessment of China's Energy-Saving and Emission-Reduction Accomplishments and Opportunities During the 11th Five Year Plan. Publication LBNL-3385E. http://china.lbl.gov/sites/china.lbl.gov/files/LBNL_3385E.Ace_Study_Report_FINAL.pdf.

R. Lizardo and R. O'Shaughnessy, Method of manufacturing a multiple-pane insulating glass unit, United States Patent 4,335,166 (1982).

Lynam, N.R., Agrawal, A., 1990. Automotive applications of chromogenic materials. In: -Lampert, C.M., Granquist, C.G. (Eds.), Large Area Chromogenics: Materials & Devices for Transmittance Control. Optical Engineering Press, Bellingham, Washington.

Massek, T., 2005. In: Transparent Amorphous Silicon PV-Façade as part of an integrated concept for the energetic rehabilitation of an office building in Barcelona.Proc. 20th European Photovoltaic Solar Energy Conference, 6–10 June 2005, Barcelona, Spain.

Pagliario, M., Ciriminna, R., Palmisano, G., 2010. BIPV: merging the photovoltaic with the construction industry. Prog. Photovolt. Res. Appl. 18, 61–72.

Poirazis, H., Kragh, M., Hogg, C., 2009. In: Energy modelling of ETFE membranes in building applications.Proc. 11th International IBPSA Conference, Glasgow, Scotland, 23–30 July.

Standard UN/ECE R-43, 'Uniform provisions concerning the approval of safety glazing materials and their installation on vehicles', Available from: http://treaties.un.org/Pages/ViewDetails.aspx?src=TREATY&mtdsg_no=XI-B-16-43&chapter=11&lang=en European Standard ECE R-43.

US Department of Energy, 2009. Recovery Act: Advanced Energy Efficient Building Technologies', Funding Opportunity Announcement DE-FOA-0000115. .

US Federal Motor Vehicle Safety Standard 205 (49 C.F.R Part 571.205), SAE ANSI Z26.1–1996.

Valkonen, E., Karlsson, B., Ribbing, C.G., 1984. Solar optical properties of thin films of Cu, Ag, Au, Cr, Fe, Co, Ni and Al. Sol. Energy 32 (2), 211–222.

This page intentionally left blank

CHAPTER

Transparent conductive thin films

21

Clark I. Bright
Bright Thin Film Solutions LLC, Tucson, AZ, United States

21.1 INTRODUCTION

Transparent conductive thin films (TCTFs) are widely used in electronic devices by almost everyone. Smartphones, tablets, computer displays, and TVs are just a few examples of devices with TCTF. Tin-doped indium oxide (ITO) is the most commonly used TCTF and is one of a family of materials called transparent conductive oxides (TCO). There is considerable interest in alternative TCO to replace or be an alternative to ITO because of the high cost of ITO (indium) and concerns about the availability of indium (Schwarz-Schampera and Herzig, 2002). This chapter discusses ITO, alternative TCO, and some other TCTF alternatives. One non-TCO example of TCTF discussed in this chapter is optically enhanced (matched) metallic thin films. These antireflective metallic thin films can exhibit excellent optical/electrical properties, and can be very flexible (Bright, 2010b).

Examples of transparent conductive materials not discussed in this chapter are graphene, nanotubes, nanowires, and conductive polymers. While there is considerable interest in universities and elsewhere in these alternatives they are still emerging technologies and is considered beyond the scope of this chapter.

There is growing interest and demand for applications of thin films and electronic and optoelectronic devices on flexible substrates. This chapter will focus on the electrical and optical properties obtainable with TCTF on flexible substrates and their applications. However, the properties of TCTF for temperature-tolerant substrates, which are often rigid, for example, glass, will be discussed for benchmarking what is achievable and for comparison with the properties achieved for temperature-sensitive substrates, such as plastics. In addition, often little or no information is available in scientific publications for these TCFT and applications on temperature-sensitive substrates, particularly plastics. The TCTF on metal foil substrates will not be discussed here. Generally, they are considered "bendable" but not "flexible," and, of course, they are not transparent. The TCTF on "flexible glass" substrates will also not be discussed in this chapter; it too is considered "bendable" but not "flexible," and results on rigid glass substrates are included as

Optical Thin Films and Coatings. https://doi.org/10.1016/B978-0-08-102073-9.00021-7
Copyright © 2018 Elsevier Ltd. All rights reserved.

appropriate. Because of the chosen focus on optical and electrical properties and applications, mechanical properties of TCTF and plastic substrates are not discussed. A limited discussion of the mechanical properties of TCTF and references to other work in this area can be found in Bright (2006, 2007), Cairns et al. (2000), and Leterrier et al. (2003).

21.1.1 TRANSPARENT CONDUCTIVE OXIDES

The transparent conductive oxides (TCO) are a class of materials, which have the unusual capability of being both transparent and electrically conductive. Today, there are no rules for identifying which metal oxides can be TCO (there are some empirical rules of thumb for dopants). Rather, TCO have been identified experimentally over many years. Examples of binary metal oxide compounds shown to be TCO when doped by defects, either extrinsic or intrinsic, are indium oxide (In_2O_3), tin oxide (SnO_2), cadmium oxide (CdO), and zinc oxide (ZnO). These hosts have been shown to be acceptable TCO with many different dopants and have been widely discussed (see, e.g., Ginley and Bright, 2000). Table 21.1 lists many TCO and dopants, which achieved good performance including these classic binary metal oxide hosts. The most widely known binary TCO is In_2O_3:Sn, commonly known as ITO. Doping of TCO is discussed in Section 21.2.

Table 21.1 TCO semiconductors for thin-film transparent electrodes

Material	Dopant or compound
SnO_2	Sb, F, As, Nb, Ta
In_2O_3	Sn, Ge, Mo, F, Ti, Zr, Hf, Nb, Ta, W, Te
ZnO	Al, Ga, B, In, Y, Sc, F, V, Si, Ge, Ti, Zr, Hf
CdO	In, Sn
ZnO-SnO_2	Zn_2SnO_4, $ZnSnO_3$
ZnO-In_2O_3	$ZnTln_2O5$, Zn_3In_2OG
In_2O_r-SnO_2	$In_4Sn_3O_{12}$
CdO-SnO_2	Cd_2SnO, $CdSnO_3$
CdO-In_2O_3	$CdIn_2O_4$
$MgIn_2O4$	
$GaInO_3$, $(Ga, In)_2O_3$	Sn, Ge
$CdSb_2O_6$	Y
ZnO-$In_2O_3SnO_2$	$Zn_2In_2O_5$-$In_4Sn_3O_{12}$
CdO-In_2O_3-SnO_2	$CdIn_2O_4$-Cd_2SnO_4
ZnO-CdO-$In_2O_3SnO_2$	

From Minami, T., 2005. Transparent conducting oxide semiconductors for transparent electrodes. Semicond. Sci. Technol. 20, D35–S44.

Table 21.2 Typically achieved electrical and optical properties for ITO: ($90\%In_2O_3/10\%SnO_2$)

	High-temperature process (glass)	Low-temperature (RT) process (plastic)
Resistivity (ρ) (Ωcm), $\%T$ visible transmittance	$1–2 \times 10^{-4}$, $\geq$[a]85%–88%	$5–8 \times 10^{-4}$, $\geq$[a]80%–85%

[a]*Includes substrate losses, plastic is PET, "Transmission" often given without these losses.*
Courtesy: Bright, C. I., 1995–2012. ITO and other transparent conductive coatings: fundamentals, deposition, properties, and applications. In: Class C-304, Annual Technical Conference of the Society of Vacuum Coaters.

The optical and electrical (O/E) performance achieved by ITO with high- and low-temperature processes is summarized in Table 21.2. The values listed are typical values that can be achieved in industry with volume production, not the best values that can be achieved in the laboratory on small samples. Because ITO is one of the most widely used TCO, its performance will be used as the comparison baseline for alternative TCO. Note in the table the significant volume resistivity difference ($\sim 4\times$) between the high-temperature and the low-temperature processed ITO; the reason for this difference will be discussed in Section 21.2.2. Table 21.3 illustrates typical values of sheet resistance and the corresponding optical transmittance for ITO made by high-and low-temperature processes. Generally, the O/E performance of other binary host TCO, even with the preferred dopant, at best, may equal the performance of ITO but is generally inferior.

Less well known are ternary and multicomponent TCO, which have also been investigated, typically by blending known binary TCO with or without defect dopants. Most often a mixture results but occasionally "new" compounds are formed

Table 21.3 Typically achieved sheet resistance and optical transmittance for ITO: ($90\%In_2O_3/10\%SnO_2$)

	High-temperature process (glass)	Low-temperature process (plastic)
Sheet resistance (R_s) $\approx$	10 Ω/sq	50 Ω/sq
Physical thickness, $d \approx$	128 nm ($\lambda/2$ optical thickness)	135 nm ($\lambda/2$ optical thickness)
$T \approx$	[a]85%–88% luminous transmittance	[a]80%–85% luminous transmittance

[a]*Includes substrate losses. Plastic is PET.*
Courtesy: Bright, C. I., 1995–2012. ITO and other transparent conductive coatings: fundamentals, deposition, properties, and applications. In: Class C-304, Annual Technical Conference of the Society of Vacuum Coaters.

(see Table 21.1). Some of these compounds are excellent TCO while others are poor TCO. For example, cadmium stannate (Cd_2SnO_4), CTO, is an excellent TCO (Haacke, 1976) comparable or superior to ITO; while zinc stannate (Zn_2SnO_4) is a poor TCO. Another zinc stannate compound identified is $ZnSnO_3$, but its O/E properties are inferior even to those of the other zinc stannate compound, Zn_2SnO_4 (Minami, 1999). Another cadmium stannate compound ($CdSnO_3$) is also known but it is inferior to CTO. Conversely, certain mixtures of indium oxide and zinc oxide have produced TCO with good performance including a zinc indate compound ($Zn_2In_2O_5$) and related compounds, with equal atomic percentages of Zn and In (Minami et al., 1995).

Multicomponent TCO have been made from mixtures of multiple binary or ternary TCO and sometimes with additional metal oxides, for example, gallium oxide (Ga_2O_3) and magnesium oxide (MgO). The most successful multicomponent TCO to date are made from the following systems:

- Zn-In-Sn-O
- Zn-Ga-Sn-O
- In-Ga-Zn-O and
- these three systems with various dopants.

Some of these multicomponent TCO, particularly IGZO, will be discussed in more detail when transparent oxide electronics applications are discussed. Multicomponent materials have, so far, become more important as semiconducting materials than TCO.

21.1.2 TRANSPARENT METALLIC THIN FILMS

Metals are highly conductive and when deposited as a very thin film can become semitransparent to highly transparent. Noble metals and alloys, particularly silver (Ag)-based, are widely used as TCTF. Single-layer metallic thin films such as Ag and Au are typically semitransparent with significant reflectance. However, when antireflection (AR) coating by a high-index layer is applied on either side of the metallic thin film, the three-layer stack produces an optically enhanced metallic thin film, which is highly transparent. This three-layer construction was originally called an induced transmission filter (Berning and Turner, 1957), and more information about their designs can be found in Macleod (2001). More current literature often refers to these constructions as dielectric-metal-dielectric (DMD), insulator-metal-insulator (IMI), or by listing the metal oxide used, irrespective of whether it is an insulator or TCO, for example, ITO-Ag-ITO, or similar. Metallic thin films with enhanced nucleation can exhibit excellent O/E properties, and the stack can be very flexible, as recently reported by Bright (2010b), when (high index) polymers are used as the matching layers in a DMD design (Table 21.4).

Table 21.4 Optical/electrical performance summary for ultra-transparent conductive materials (U-TCM): polymer/metal/polymer design on plastic film

ID	Ω/Sq	$\%T_{lum}$ (μm)	$\%^{a}R_{lum}$ (μm)	$\%T_{ave}$ (450–650 nm)	$\%T_{ave}$ (400–700 nm)	$\%^{a}R_{ave}$ (450–650 nm)	Color	
							x	*y*
2817 Ag	10.20	87.20	5.37	86.90	85.60	5.60	0.311	0.331
2810 Ag/Au	30.30	88.60	5.70	88.39	87.60	5.82	0.313	0.331
2690A Ag/Au	36.66	91.41	3.75	91.19	90.25	3.72	0.313	0.331
2703B Ag	23.71	91.62	4.10	91.15	90.81	4.11	0.313	0.331

Notes*: Transmittance values include PET substrate losses.*
[a]*The spectrometer-measured reflectance values are intermediate between the first surface (coating) and total (two surfaces) values.*
Courtesy: Bright, C.I., 2010b. TCM 2010. In: 3rd International Symposium on Transparent Conductive Materials, 17–21 October 2010, Analipsi, Hersonissos, Crete, Greece.

21.2 CONDUCTIVITY FUNDAMENTALS

The classical free electron model explains the properties of metals based on the motion, that is, the kinetic properties, of the conduction electrons. As will be shown later, some optical properties of metals can be successfully explained with classical theory. However, classical physics is unable to explain all the interactions of electrons with electromagnetic (EM) waves. Understanding these interactions is important to explain the dependence of some optical properties (e.g., the bandgap) on the conductive properties of metals and TCO. Both the classical and quantum theory models are used in the following discussion.

21.2.1 METALS

The electrical properties of a metal are fundamentally related to its atomic structure. Highly conductive metals such as copper, silver, and gold, have a single free electron per atom. For copper, it is the 4s electron, for silver, 5s electron, and for gold it is the 6s electron, where the number represents the principal quantum number (n). In these metals their conduction band is formed by these ns electrons. Recall that (Bright, 1995a–2012) by definition, in a metal the highest energy band, the conduction band, is only partly filled with electrons. The highest filled energy state in the conduction band is called the Fermi level (E_f). The conduction band wavefunction is formed from the separate "s-state" electron wavefunctions of the atom; hence, these metals are often called "s-band metals" In a noble metal there is also a filled "d-band," where the electrons are bound. The bound electrons of the metal ion core cannot carry an electrical current. This filled band below the conduction band is called the valence band.

Other effects, which occur, include broadening of the energy bands caused by disorder in the atomic structure of the solid, and excitation of an electron into the empty "p-band" (the band above the conduction band) by absorption, that is, interaction with an EM wave.

In metals, electrical conductivity, σ, or its reciprocal resistivity, ρ, is a function of just two variables: the carrier (electrons) concentration per unit volume, N, and the mobility of the carriers, μ. However, the mobility is frequency (wavelength) dependent and so is the conductivity (resistivity). The conductivity can be represented by the following equations (Bright, 1995a–2012):

$$\sigma(\omega) = Ne\mu(\omega) \quad \text{and} \quad \text{forDC} \quad (\omega = 0),\ \sigma = Ne\mu = \frac{Ne^2\tau}{\varepsilon_0 m^*} = \omega_p^2\tau \tag{21.1}$$

where ω is angular frequency, N is the number density of electrons, e is the electronic charge, τ is the electron scattering time, ε_0 is the dielectric constant of free space, m^* is the electron effective mass, and ω_p is the plasma angular frequency. The plasma frequency will be discussed further when the optical properties of TCO are discussed. From Eq. (21.1) is clear that mobility is directly proportional to scattering time and is inversely proportional to electron effective mass.

21.2.2 DOPING

While metals have a partially filled conduction band and a filled valence band, by definition, semiconductors have an empty conduction band and a filled valence band. For example, stoichiometric indium oxide is shown in Fig. 21.1A (a, left). However, when semiconductors are doped, with a suitable impurity atom, for example, Sn, a donor state is created below but near the conduction band. As doping is increased these states eventually merge (Mott's criterion) and become part of the conduction band, see Fig. 21.1A (b, right), with Sn providing a free (conduction) electron. In such heavily doped semiconductors, there is a partially filled conduction band, and changes in the band structure occur with shifts of both the conduction band and the valence band (Hamberg and Granqvist, 1986). When this occurs, a semiconductor is called degenerate. Degenerate *n*-type semiconductors behave electrically

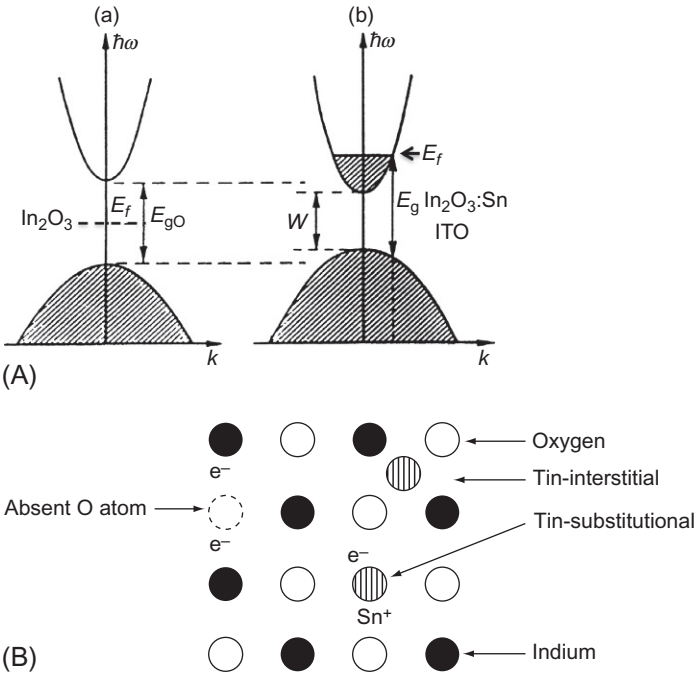


FIG. 21.1

(A) Assumed band structure for undoped (a) direct bandgap $E_{gO} \sim 3.75\,eV$, and tin doped (b) bandgap $E_g > E_{gO} > W$. Indium oxide shaded areas indicate occupied states. k is the wavevector amplitude and $\hbar\omega$ is photon energy. (B) Basic physics of transparent conductive coatings. Oversimplified crystal structure and doping model for indium tin oxide (actual crystal structure of indium oxide is much more complicated).

Modified from (A) Hamberg, I., Granqvist, C.G., 1986. Evaporated Sn-doped In_2O_3 films: basic optical properties and applications to energy-efficient windows. J. Appl. Phys. 60, R123; (B) Granqvist, C.G., 1989. Spectrally selective surfaces for heating and cooling applications. Tutorial Texts in Optical Engineering, vol. TT 1, SPIE Optical Engineering Press, SPIE—The International Society for Optical Engineering, Bellingham, WA.

like metals. Because all highly conductive TCO are degenerate *n*-type semiconductors, the expression for σ in TCO is the same as that for metals shown in Eq. (21.1).

In a semiconductor, the conduction electrons are created by impurity doping as explained above, or by a lack of stoichiometry (defects). For ITO and other TCO there is a "threshold temperature," which is required to activate the impurity metal dopant ($\sim$200°C for Sn in ITO). Most industrial ITO deposition processes for temperature-tolerant substrates such as glass, use substrate temperatures of $\geq$200°C to promote Sn replacing In substitutionally in the indium oxide lattice (see Fig. 21.1B). However, even in ITO, the conduction electrons are usually created *primarily* by defects, oxygen deficiencies ("vacancies"), not by tin doping (substitutional) (Fraser and Cook, 1972).

Deposition of ITO or other TCO on temperature-sensitive substrates such as plastics, at or near room temperature, results in virtually all of the conduction electrons being created by oxygen deficiencies, and virtually none by Sn substitutional doping. An oversimplified schematic drawing for these two doping processes is shown in Fig. 21.1B. Because oxygen deficiency is the major cause of conductivity (and absorption), its control during deposition and any postprocessing is critical.

These two doping mechanisms, shown for ITO in the oversimplified Fig. 21.1B, are not completely independent. Two (nearby) substitutional Sn atoms bound to an oxygen interstitial atom can form a neutral cluster and do not contribute to conductivity. However, processing at low oxygen partial pressure can cause breakup of this cluster, with the loss of the interstitial oxygen. This results in two, now unbounded, Sn cations, each contributing an electron to conduction. (Frank and Kostlin, 1982).

For any given TCO deposition process, there is a resistivity minimum. At low doping levels, the film resistivity is increased by lack of conduction electrons. At high doping levels, the resistivity is increased by electrons scattering from oxygen "vacancies" and tin ions (ionized impurity scattering), causing reduced mobility. The minimum resistivity occurs when scattering caused by doping is comparable to scattering caused by all other mechanisms (Bright, 1995a–2012, 2010a, 2014–2018).

A plot of resistivity versus doping will generate a curve demonstrating this relationship, which has been named the "resistivity-well" (Bright, 1995a–2012, 2010a, 2014–2018), Fig. 21.2A. The resistivity-well will be discussed much further in Section 21.2.3 and used extensively in the discussion on control of optoelectronic properties in Section 21.3.

21.2.3 OPTICAL PROPERTIES RELATED TO CONDUCTIVITY

Of course, the optical properties of a material are related fundamentally to its atomic structure. A given material, for example, an insulating metal oxide, will absorb radiation in selected wavelength regions because of its structure. The absorption coefficient, $\alpha(\lambda)$, or for convenience simply α, varies with wavelength, and is given by.

$$\alpha = \frac{4\pi k}{\lambda} \tag{21.2}$$

where k is the extinction coefficient and λ is the wavelength.

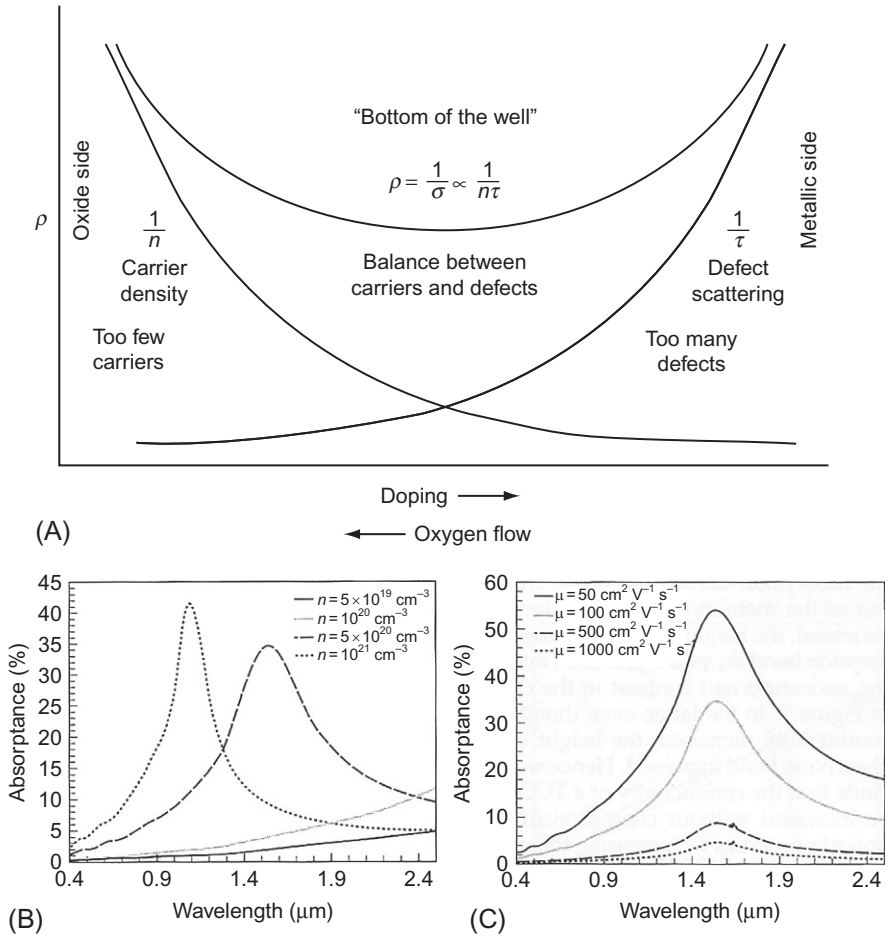


FIG. 21.2

(A) Resistivity versus doping and the origin of the "resistivity-well" TCO deposition process (Bright, 1995a–2012, 2014–2018). (B) Modeled free-carrier absorptance for carrier concentration of 5×10^{19}, 10^{20}, 5×10^{20}, and $10^{21}\,cm^{-3}$. The mobility was $100\,cm^2\,V^{-1}\,s^{-1}$, high-frequency permittivity was 4, the effective mass of the carriers was assumed to be 0.3 m_e and the film thickness was 0.5 μm. (C) Modeled free-carrier absorptance of films with a carrier concentration of $5 \times 10^{20}\,cm^{-3}$. The mobility was varied between 50 and $1000\,cm^2\,V^{-1}\,s^{-1}$. *From Coutts, T.J., Young, D.L., Li, X., 2000. Characterization of transparent conducting oxides. MRS Bull. 25 (8), 59, absorption Figs. 3 and 4.*

21.2.3.1 Transparent conductive oxides

However, if the same metal oxide is doped and becomes electrically conductive, additional wavelength regions of selective absorption occur. Therefore, in TCO some optical properties are related to the conductivity. In the near-infrared (NIR)

region, the optical properties are related to the conductivity, and can be modeled using classical Drude theory by the following equations. The plasma frequency is related to the conductivity, as shown above, by the following equations:

$$\sigma = Ne\mu = \frac{Ne^2\tau}{\varepsilon_0 m^*} = \omega_p^2\tau \quad (21.1), \quad \text{then} \quad \omega_p^2 = \frac{Ne^2}{\varepsilon_0 m^*} \tag{21.3}$$

and

$$\omega_p = \frac{\left(Ne^2\right)^{1/2}}{\left(\varepsilon_0 m^*\right)^{1/2}} \tag{21.4}$$

or

$$\lambda_p = 2\pi c \frac{\left(\varepsilon_0 m^*\right)^{1/2}}{\left(Ne^2\right)^{1/2}} \tag{21.5}$$

where λ_p is the plasma (linear) wavelength and c is the speed of light in vacuum.

The free carriers needed for conduction in TCO will absorb incident EM radiation. The NIR absorption of photons by free carriers (A_e) is given by.

$$A_e = \frac{\lambda^2 e^3 N d}{4\pi^2 c^3 n m^{*2} \mu} \tag{21.6}$$

where d is the film thickness and n is the real part of the refractive index. A_e is directly and linearly proportional to the carrier concentration (Chopra et al., 1983): however, free-carrier absorption is also inversely and linearly proportional to the mobility (μ). Because conductivity is directly proportional to the product of N and μ and absorption is inversely proportional to μ, it is better to increase optically the conductivity by increasing μ rather than increasing N (Coutts et al., 2000). Eq. (21.6) demonstrates that the characteristic spectral optical properties of TCO are inherently related to its conductivity.

When an EM wave is incident on a TCO the conduction electrons, as a group, will be influenced by the electric field component of the wave. In general, the motion of the electrons will either lead or lag the variations of the EM wave. However, at a specific frequency/wavelength, a resonance will occur. This is the plasma frequency/wavelength. At the plasma frequency/wavelength, strong free-carrier absorption of the EM wave occurs (see Fig. 21.2B and C (Coutts et al., 2000, Figs. 3 and 4)). Note in Fig. 21.2B that a higher carrier (electron) concentration increases the peak absorption (Eq. 21.6) and moves the peak (plasma wavelength) to shorter wavelengths (Eq. 21.5) (Coutts et al., 2000). Beyond the plasma wavelength, the group of electrons act as a screen and reflect the EM wave as shown by the high optical reflectance (see Fig. 21.4).

A schematic representation of the optical properties of TCO in three regions is shown in Fig. 21.3. The above discussion applies near the plasma wavelength and to the region shown as "Reflecting" beyond the plasma wavelength. The spectral region shown as "Transmitting" is typically the visible wavelength region, and the spectral region shown as "Absorbing" is typically in the ultraviolet spectral region. The Absorbing region is a function of the TCO bandgap (see Fig. 21.1A).

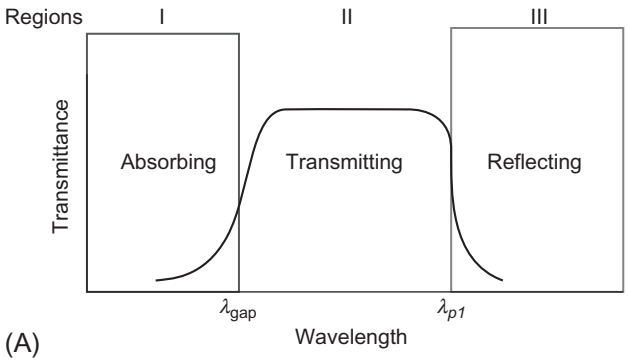


FIG. 21.3

Basic physics of transparent conductive coatings. (A) Optical properties related to conductivity (classical Drude theory). (B) Three optical regions (Bright, 1995a–2012, 2014–2018).

Modified from Simonis, F., et al., 1979. Physics of doped tin dioxide films for spectral-selective surfaces. Solar Energy Mater. 1, 221–231.

The spectral transmittance and reflectance for ITO determined by optical modeling for different N values is shown in Fig. 21.4. As shown in the figure the location of the plasma wavelength, determined by Eq. (21.6), moves to shorter wavelengths with increasing N values. The location of the absorbing region due to the bandgap of ITO also moves to shorter wavelengths due to the Bernstein-Moss effect (Burstein, 1954) (see Fig. 21.1A).

21.2.3.2 Metals

Similarly, the optical properties of metals are determined by its atomic structure. Also the optical properties of metals are described by Eqs. (21.1)–(21.6) as discussed for TCO. However, in a metal the carrier concentration, N, is roughly two orders of magnitude greater that than in TCO. Consequently, the plasma wavelength is located in the visible or ultraviolet regions. For example, gold has its plasma wavelength located in mid-visible region causing the characteristic color of the metal. For silver, the plasma wavelength is located in the ultraviolet region and it reflects highly over the entire visible region (and infrared regions) with a neutral "silver" color. A major difference between metals and TCO is that metals have a fixed N value but the N value for TCO are determined by doping (deposition process), that is, *TCO are engineered materials whose optical properties are controlled by their electrical properties.*

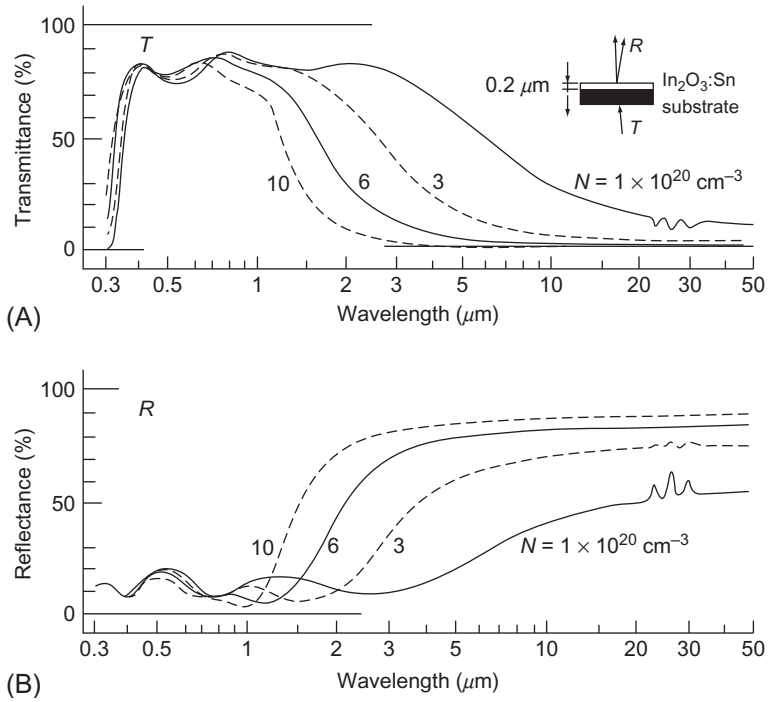


FIG. 21.4

Optical properties related to conductivity: optics of TCO (ITO) thin films. Graphs showing change in spectral properties of ITO at bandgap and plasma wavelengths as a function of carrier density (N) (Granqvist, 1989).

Thin film metals exhibit optical characteristics of their materials; however, the optical properties can be modified by interference effects due to film thickness or interference effects of the optical construction, for example, the three-layer stack described previously. Of course, TCO films can exhibit interference effects as well, even as a single layer.

Because the optical properties of TCO and metals are related to their conductivity, a compromise is always required between high optical transmittance and high conductivity (low resistivity). The TCO, for example, ITO or metals, have optical transmittance that is fundamentally limited by absorption and the amount of visible absorption depends on carrier concentration. As explained above, the visible transmittance and reflectance of conductive thin films are wavelength dependent (dispersive). Further, the optical performance can be generalized by conductor type (i.e., metal, TCO or semiconductor) and by waveband [UV, Vis, NIR, midwave IR, and longwave far infrared (FIR)].

21.3 CONTROL OF OPTOELECTRONIC PROPERTIES

Process conditions have the largest effect on the O/E properties of TCO, for example, ITO films. For a typical vacuum deposition process, the most important process variable is oxygen partial pressure (flow rate) because this will control the amount of doping by oxygen deficiency, that is, "vacancies" (Zunger, 2003). As explained previously, oxygen deficiency is the major reason for free-carrier generation.

Substrate temperature during deposition is also a very important process parameter. As discussed in Section 21.2.2, substitutional doping with an impurity cation requires an activation energy, which is typically achieved by heating.

Of course, all of the typical process parameters that are important in thin film deposition such as deposition rate, vacuum level (pressure), gas or plasma conditions. and deposition geometry, all influence film properties, for example, quality, as they would for a dielectric thin film. They do not directly affect the electrical and optical properties except in terms of the film quality, for example, crystallinity or microstructure, which can affect electron mobility, and therefore, conductivity and optical absorption (see Eq. 21.6).

As explained in Section 21.2.2, for any given TCO deposition process, there is a resistivity minimum; at low doping levels, the film resistivity is increased by lack of conduction electrons and at high doping levels, the resistivity is increased by electron scattering from oxygen vacancies and dopant ions (ionized impurity scattering). The minimum resistivity occurs as shown in Fig. 21.2A, when scattering caused by doping is comparable to scattering caused by all other defects.

Consider, for example, the magnetron sputter deposition of an ITO film onto a plastic film substrate held at a near room temperature in a roll-to-roll deposition process. After determining the sputter deposition conditions in argon, oxygen is added to the plasma. The oxygen flow rate is varied to create the resistivity-well as shown in Fig. 21.5. The O/E properties of the samples made with differing oxygen flow conditions are measured and plotted. By overlaying the O/E values on the resistivity-well (bottom curve) chart the functional relationship between the optical properties, for example, percent transmittance, *%T (top curve)*, versus doping (oxygen flow rate) can be determined (Fig. 21.5). Resistivity, ρ, (ohm-cm) should be used as the *Y*-axis, not sheet resistance (ohms/square) because the thickness of the TCO films typically varies with the change in process conditions (oxygen).

These optical and electrical relationships versus oxygen flow rate are very useful in controlling the deposition process to achieve the desired tradeoff between electrical and optical properties of the TCO. If unsuccessful with the original conditions, one can repeat the generation of these curves with different starting sputtering conditions and attempt to produce TCO thin films of differing optoelectronic properties, for example, transmittance, thickness, and sheet resistance (ohms per square) (Bright, 1995a–2012, 2012a, 2014–2018).

A vacuum sputter deposition process, which is most common for TCO, was described, but the same principles apply for other physical vapor deposition (PVD),

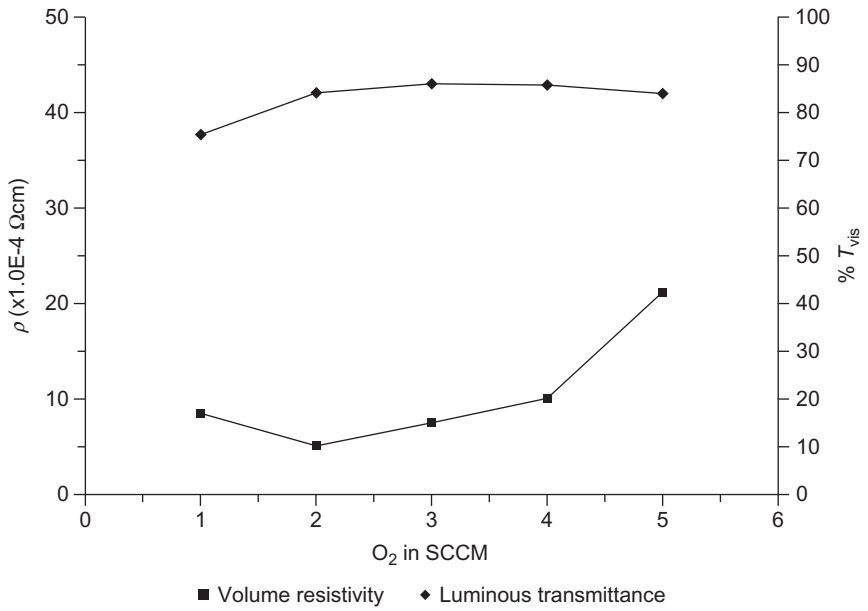


FIG. 21.5

Optical and electrical properties relationship of ITO thin films versus oxygen flow rate.

chemical vapor deposition (CVD), or solution deposition processes but the control of the variables, for example, oxygen may be different and even indirect (Bright, 1995a–2012, 2010a).

21.4 BEYOND OPTOELECTRONIC PROPERTIES

While the optoelectronic properties of TCO are of paramount importance in many applications, other characteristics of the film also may be required. For example, in applications where the film will be deposited on flexible substrates and flexibility is required in the application, clearly the mechanical properties of the TCO are important. In some applications, for example, organic light emitting diodes (OLEDs), the work function of the TE is critical for efficient charge injection. In many applications, durability of the TCO, for example, abrasion resistance and resistance to humid conditions may be required. In such applications the selection, design, and deposition of the TCO must accommodate these requirements. In the following section, applications of TCO will be discussed and the requirements of each application, both optoelectronic and other requirements, will be addressed.

21.5 TRADITIONAL APPLICATIONS

There are a surprisingly large and growing number of applications for TCTF. In the next three sections many applications are described, which for the context are divided into three categories: Traditional (Section 21.5), Recent (Section 21.6), and Future (Section 21.7). The format of the discussion in the text is to provide an overview and methodology for designing a TCTF for each application. An associated example ("figures/tables") demonstrates the detailed design of a TCTF meeting the specific example's requirements. This format provides the reader with a "handbook" of TCTF coating application examples, yet allows the reader to focus quickly on the details of an application of current interest.

21.5.1 HEATERS

One of the earliest significant applications of TCO was for electrical heating of aircraft windshields during World War II. Doped tin oxide, SnO_2:Sb, was produced from a tin chloride solution containing antimony, by pyrolysis on heated glass substrates (McMaster, 1947). Electrical heating of windshields and windows of an aircraft and other vehicles is still a significant application of TCO today.

The pertinent design parameters for heated windows are the "terminal resistance" R_T, i.e., the resistance, in Ohms, measured at the buss bar contacts to the window TCTF heater coating, the power density W, the voltage V, and the optical transmittance $\%T$. Formulae useful for designing a heated window are summarized in Fig. 21.6. A design example for a heated window, using a low-voltage source, to provide deicing/defogging capability and transmitting at several wave bands is summarized in Example 21.1. As shown, once the voltage source is known, the terminal

- Power, $P = W \times A$, where W, is the power density (W/in.^{2}) and A, is the total heated area
- $P = \frac{V^2}{R_T}$, where V is the applied voltage and R_T is the resistance of the heater coating and $R_T = R_{\text{sheet}} \frac{S}{L}$
- $A = A_{\text{TRI}} + A_{\text{RECT}}$ where $A_{\text{TRI}} = \frac{1}{2}$ [$L1x(S2–S1)$] and A_{RECT} = [$L1$ X $S1$]
- S' is effective bussbar spacing and L' is the projected bussbar length
- $R'_{\text{sheet}} = \frac{v^2}{w(s')^2}$ and $S' = \frac{A}{L'}$ or if uncurved, $S' = \frac{s1+s2}{2}$
- the sheet resistance at any location, X, $R_{x\ \text{sheet}} = R'_{\text{sheet}} \times \left(\frac{s^1}{s_x}\right)^2$ and the power density is $W = \frac{V^2}{R_{\text{sheet}} S^2}$

FIG. 21.6

Basic heater formulae (Bright, 1995a–2012).

Requirements:

- Heater specifications:

  Power density of 1.4 W/in^2 from a 25 V, DC power source

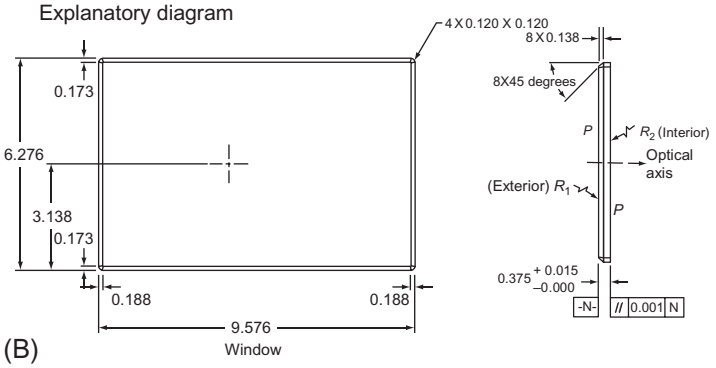
- Coated window transmittance:

T visible	> 84% from 525 to 625 nm
T average	> 83% between 700 and 900 nm
T laser	> 82% at 1070 nm

- Laser damage resistant (36 mW/cm^2, 20 ns FWHM, 20 pps)
- Durability to Mil-C-48497

(A)

Explanatory diagram



(B)

Approach:

- Choose materials and deposition process for high durability (metal oxides and high temperture)
- Try two layer ITO/SiO_2 coating design to meet optical requirements
- Use halfwave (or multiples) SiO_2 thickness to minimize laser damage
- Adjusted optical design for electric field control at interfaces
- Select ITO thickness for optical requirements
- Adjust ITO deposition process parameters to produce nominal sheet resistance at thick-ness determined by optics

(C)

Determining coating parameters:

- From window drawing, requirements and basic formulae
- The separation (S) between bussbars is 6.0″ (bussbar width of 0.138″)
- The total heated area, $A = S \times L = 6.0'' \times 9.20'' = 55.2$ in.^{2}
- With a power density, $W = 1.4$ W/in.^{2} and $A = 55.2$ in.^{2}, the power is $P = W \times A = 77.3$ watts
- The nominal sheet resistance is given by
- $R_{SHEET} = \dfrac{V^2}{WS^2} = \dfrac{(25)^2}{1.4 \times (6.0)^2} = 12.4\ \Omega/\square\ (+/-1.8\ \Omega/\square = 10.6 - 14.2\ \Omega/\square)$
- R_T is the resistance of the heater coating and $R_T = R$ Sheet $\dfrac{S}{L}$
- $R_T = \dfrac{12.4 \times 6.0''}{9.20''} = 8.1\ \Omega\ (+/-1.2 = 6.9 - 9.3\ \Omega)$

(D)

EXAMPLE 21.1

A design example for antiicing of TV laser window: (A) requirements; (B) explanatory diagram; (C) approach; and (D) determining coating parameters (Bright, 1995a–2012).

resistance can be calculated to achieve the required power density. From the terminal resistance and the window geometry, the sheet resistance of the coating, either TCO or thin metal film, can be determined. Knowing the sheet resistance, the corresponding optical transmittance must be achieved by selecting the coating type and by deposition process control. The measured electrical and optical performance for the window of the design example is shown in Fig. 21.7 (Bright, 1995a–2012, 2010a).

21.5.2 ELECTROMAGNETIC INTERFERENCE SHIELDING

Another traditional application of TCTF is electromagnetic interference (EMI) shielding. Any active electronic device, which has a display, is a likely candidate for an EMI shield. Because the display must have some type of transparent opening or window for viewing, radiation can escape from or be incident through this aperture. The rest of the device can, typically, be contained in an opaque conductive enclosure. To complete the "Faraday cage" shield, the viewing aperture of the device must be covered by transparent conductive material. Often a TCTF like ITO or a metallic thin film is chosen for the EMI shield.

The equations for far field EMI shielding effectiveness (SE) are shown in Fig. 21.8. As shown the SE is proportional to the logarithm of the inverse of the sheet resistance. Therefore, the lower the resistance or the higher the conductivity, the higher is the shielding. A design example for a device requiring 20 dB of SE and visible transmittance of $\geq$85% is summarized in Example 21.2. From the calculation of SE the required sheet resistance is $\leq 20\,\Omega$/sq. Any TCTF of $20\,\Omega$/sq or less and a corresponding transmittance of 85% or greater can meet the design requirements (Bright, 1995a–2012, 2010a).

21.5.3 ANTISTATIC FILMS

Another early application of TCTF was as an antistatic film. The function of an antistatic film is the nondestructive discharge of a static electric charge. Therefore, the electrical requirement on the film is for a "leaky" film rather than a highly conductive film. One early application for this type of film was to bleed off the static charge created on cathode ray tube (CRT) displays by the scanning electron beam. The resistance to ground of the coating can be high and still achieve adequate discharge-often in the kiloohm or even megaohm region. Because the coating ohms/square value can be high and easily achieved, the primary TCTF requirement is usually an attendant high transmittance (Bright, 1995a–2012, 2010a).

21.5.4 TRANSPARENT ELECTRODES

21.5.4.1 Type I

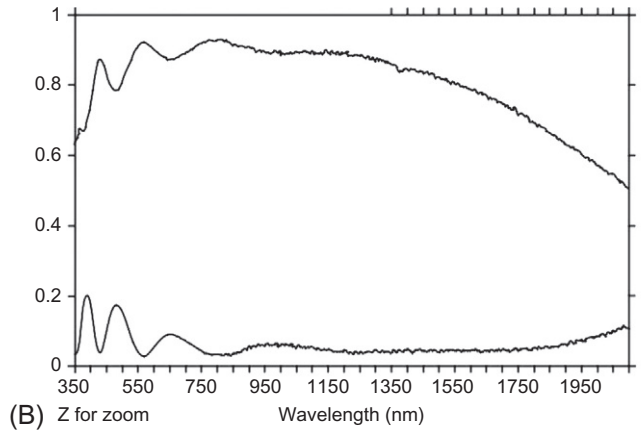
Today, the most common use of TCO is as a TE for a display device. Every device with an electrical flat-panel display uses one or more TEs. The most common type of display today is a liquid crystal display (LCD) and most LCD devices have an ITO

- Heater coating resistance = 7.9 Ω (6.9 –9.3 Ω)
- Coating sheet resistance = 11.3 Ω/□ (10.6 –14.2 Ω/□)
- Window transmittance

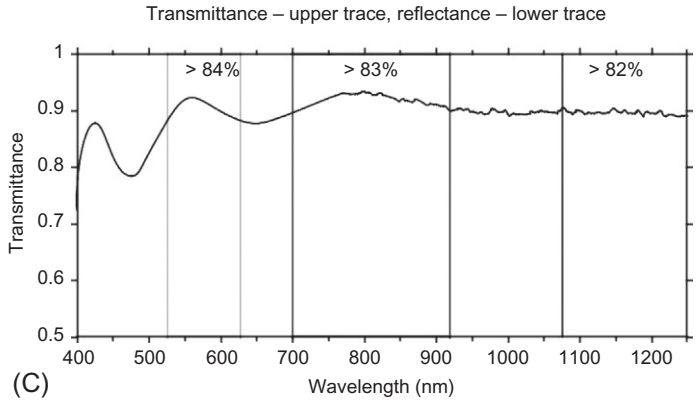
T visible	525–625 nm	=	88%	(> 84%)
T average	700–910 nm	=	92%	(> 83%)
T laser	1070 nm	=	89%	(> 82%)

- Passed laser damage testing at 22.5–36.0 mW/cm$_2$
- Passed durability tests of Mil-C-48497

(A)



(B)



(C)

FIG. 21.7

Measured electrical and optical performance for the window of the design example: (A) measured TCO performance and (requirements); (B) graph showing measured spectral reflectance and transmittance performance with a resistive heater coating for antiicing TV and laser window; and (C) graph showing measured optical performance for coated antiicing TV and laser window versus waveband requirements (Bright, 1995a–2012).

- Shielding effectiveness (SE) is a figure-of-merit for the performance of a shield in reducing interfering incident electromagnetic radiation
- Shielding effectiveness (SE) can be defined as the reduction in (transmitted) field intensity by losses (e.g., reflections) which occur after inserting the shield
- SE = $-20 \log_{10} E_{TRANS}/E_{INC}$ in same medium (impedance), where E_{TRANS} is the transmitted electric field and E_{INC} is the incident electric field
- SE = $20 \log_{10}[1 + \eta_0 /2R_{FILM}] = 20 \log_{10}[1 + 188.5/R_{FILM}]$ where $\eta_0 = (\mu_0\varepsilon_0)^{1/2}$ = 377 Ω (free space)
- (This formula assumes the substrate is one-halfwave, or multiples, in optical thickness or a free standing film)

FIG. 21.8

Basic formulae for far field EMI shielding effectiveness (Klein, 1990).

Requirements:

- shield effectiveness (SE) of 20 dB minimum (far field)
- transmittances of ≥ 80% at both 1.06 and 1.54 μm
- laser damage resistant
- mil-spec durability

(A)

Basic EMI formulae (far field): $SE = 20 \log_{10}[1 + \frac{188.5}{R_{film}}]$ dB

Shielding effectiveness (dB)	R_{film} Ω/sq
4.2	300
9.2	100
13.5	50
20.4	20
26.0	10
31.8	5
45.6	1

(B)

Approach:

- SE requires coating surface resistivity ≤ 20 Ω/sq
- Plasma wavelength must be longer than near infrared wavelength (1.54 μm) for required transmittance
- Use **indium oxide** (IO) low loss TCO on heated glass substrate (≥ 250°C) coating process for low optical loss, laser damage resistance and durability
- Use deposition process (oxygen flow) to control carrier concentration and locate plasma wavelength beyond longest wavelength (1.54 μm)
- Assure TCO minimum thickness meets coating surface resistivity (sheet resistance) requirement
- Adjust TCO optical thickness to locate halfwave-multiples at laser wavelengths (1.06 and 1.54 μm) to achieve transmittance

(C)

EXAMPLE 21.2

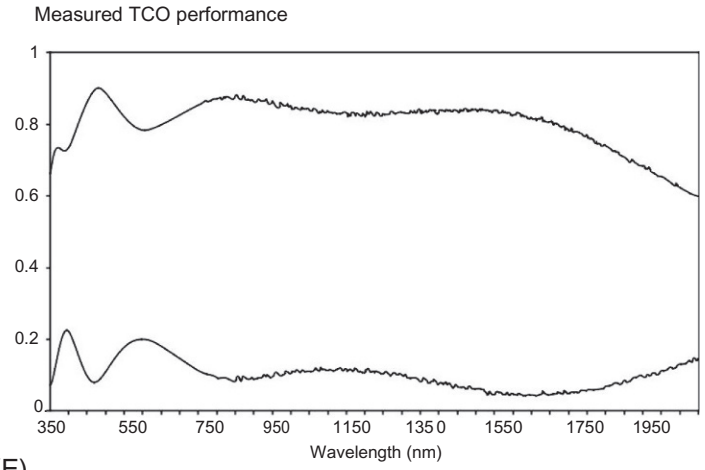
EMI shield for dual laser (1.06 and 1.54 μm) range finder window: (A) requirements; (B) basic EMI formulae (far field);

(Continued)

Determining coating parameters:

- *Determine carrier concentration to locate plasma wavelength beyond* 1.54 *μm,* N ~ 3×10^{20} ($\sigma = Ne\,\mu$, $\omega_p = [Ne^2/\varepsilon_0 m^*]^{1/2}$, $\lambda_p = 2\pi c[\varepsilon_0 m^*/Ne^2]^{1/2}$)
- *Calculate minimum* ***IO*** *thickness to meet coating surface resistivity requirement*, assume μ, from process data, or find emperically μ, then $\rho(1/\sigma)$ is known, find $d = \rho/r$
- *Calculate* ***IO*** *optical thickness to locate halfwave-multiples at laser wavelengths* (*1.06 and 1.54 μm*), $(x)\lambda/2$ and $(x-1)\lambda/2$
- *Surface resistivity* ≤ 20 Ω/□ requirement
- $\sigma = Ne\,\mu$, N ~ 3×10^{20}cm^{-1}, μ ~ 48.7 cm^2/Vs, $\rho = 4.3\times10^{-4}$ Ωcm, d = 242 nm, $r = \rho/d$, r = 17.7 Ω/□

(D)



(E)

Measured TCO performance: requirements

• Surface resistivity	=	17.7Ω/□	(≤ 20 Ω/□)
• Shield effectiveness	=	≥ 21.3 dB	(≥ 20 dB)
• Transmittance at 1.54 μm	=	83.5%	(≥ 80%)
•			(without adding AR layers)
• Transmittance at 1.06 μm	=	83.5%	(≥ 80%)

- Passed laser damage resistance
- Passed durability requirement of Mil-C-48497

(F)

EXAMPLE 21.2, cont'd

(C) approach; (D) parameters; (E) measured TCO performance; and (F) tabulated measured TCO performance versus (requirements) (Bright, 1995a–2012).

electrode. Because an LCD is an electric field-effect device, it requires an electric field for operation but current drawn is very low. This type of TE is defined here as Type I. Another example of devices using Type I TE is electrophoretic displays like that made by E ink©. Type II TEs defined here are for current-carrying devices and will be discussed in the following section.

For field effect display devices the requirements for the TE are very high transmittance, but a relatively high ohm per square value is acceptable. Typical coatings like ITO on glass would transmit nearly 90% in the visible region with the corresponding sheet resistance of 1000 Ω/sq or greater. For small devices the sheet resistance can easily be in the high kiloohms per square range. Large devices could require lower sheet resistance but often, for example, TV, the display is formed from small pixels and each is contacted by an "electronic switch" so that significant voltage drop due to the path length through the TCO to a pixel is avoided (see also Section 21.6.3). Thus, the technical requirements on TCO for an LCD are not demanding; often, cost considerations are paramount.

21.5.4.2 Type II

A Type II TE is required in current-carrying devices such as OLEDs or photovoltaic (PV) cells. Because current carrying is required, the ohms per square value must be low to avoid electrical losses and nonuniformity. Common requirements for the TE in a small display are a sheet resistance of $\leq 10\,\Omega$/sq with a transmittance of $\geq 85\%$. Depending on the type and size of the device, the required sheet resistance may be even lower. Thus, the O/E requirements for Type II TEs are technically much more challenging than for Type I TE. Fig. 21.9 shows a cross-sectional schematic drawing of an OLED emissive display. The requirements for a TE for this generic OLED device are listed in Fig. 21.10. The electrical requirements for the TE can vary depending on the type of addressing scheme used for the OLED display. Today, most displays use an active matrix (AM) addressing method, particularly for larger displays, which mitigates somewhat the requirements for a very low resistance TE. A high carrier concentration, $\sim 10^{21}\,\mathrm{cm}^{-3}$ for the chosen TCO, will typically be used to achieve low sheet resistance. Corresponding visible transmittance should be as

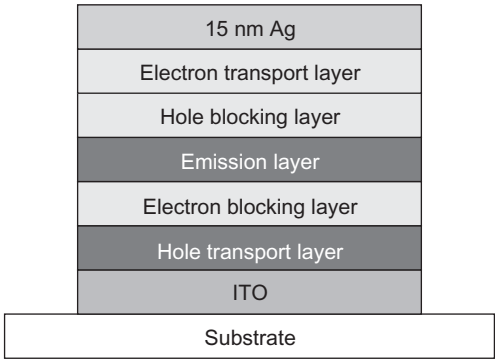


FIG. 21.9

Transparent electrodes—Type IIA; current devices (injecting). Cross-sectional schematic drawing of an organic light-emitting device (OLED) display.

Modified from May, C., Mogck, S., Amelung, J., 2009. Roll-to-roll deposition for OLED lighting devices. In: 52nd SVC TechCon, pp. 701–704.

Requirements:

- Low surface resistivity (sheet resistance) ≤ 10 Ω/sq
- High transmittance (T_{vis}) ≥ 85%
- Low surface roughness (rms and peak) ≤ few nm
- Match organic layer work function

Approach:

- Single layer ITO coating
- ITO anode work function should match (homo) organic (hole) layer
- High carrier density (~ 10^{21} cm^{-3}) for low surface resistivity (≤ 10 Ω/sq)
- ITO thickness of halfwave (or multiple) for high visible transmittance

(A)

Deposition process parameters:

- Magnetron sputter deposit ITO from ceramic target (low defects)
- High substrate temperature for tin doping and high durability
- Control oxygen flowrate (partial pressure) near ITO resistivity-well minimum for high conductivity (low surface resistivity) but maintaining high transmittance
- Control sputtering parameters for smooth ITO surface
- Oxygen plasma or UV surface post treatment for high ITO work function

(B)

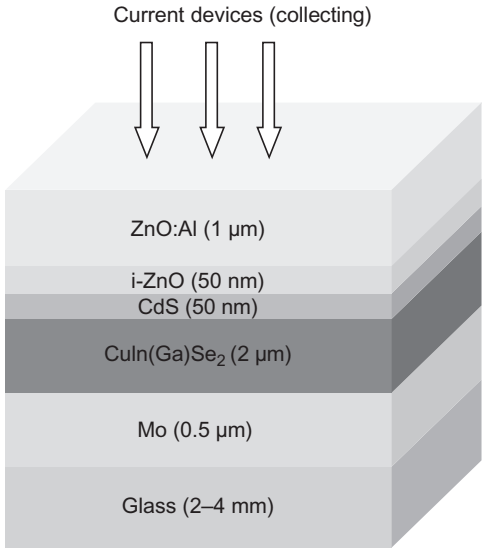
FIG. 21.10

Charge injecting transparent electrode (anode) for OLED device: (A) requirements and approach; (B) deposition process parameters (Bright, 1995a–2012).

high as possible while achieving the required low sheet resistance. Typical values for visible transmittance of the chosen TCO on a thin glass substrate are ≥85%. Generally, ITO is the selected candidate from the TCO for OLED applications (Bright, 1995a–2012, 2010a).

There are several requirements of the TE beyond the O/E requirements for OLED devices. For example, the TE surface roughness must be very low, typically less than a nanometer, because very thin layers are deposited on it to make an OLED. Also, generally the TE work function must be matched to the neighboring organic layer for proper charge injection. The TE is typically an anode in an OLED, and to match common organic materials used, a work function of about 5.0 eV is desired. The ITO can achieve a work function close to this value (Kim et al., 1999).

Another example of a device with a Type II TE requirement is shown in Example 21.3, a cross-sectional schematic view of a thin film PV cell. In this example, a TE for a CIGS ($Cu(In,Ga)Se_2$) cell is selected. The electrical requirement for the TE in this PV cell is typically specified as ≤10 Ω/sq. However, a lower sheet resistance is desirable, particularly in larger area cells, but the requirement must be a compromise with the optical requirement. The transmittance requirement is based on the absorption characteristics of the active material in the PV cell. The spectral absorption characteristics of CIGS cells of two compositions are shown in Fig. 21.11. From the example it can be seen that the spectral transmittance of the TE must be from about 400 to 1100 nm. This broad spectral transmittance band will put limits on



CIGS ($Cu(In,Ga)Se_2$) type thin film solar cell stack

EXAMPLE 21.3

Cross-sectional schematic view of a thin film PV cell: another example of a device with a Type II transparent electrode requirement (Ochs et al., 2009).

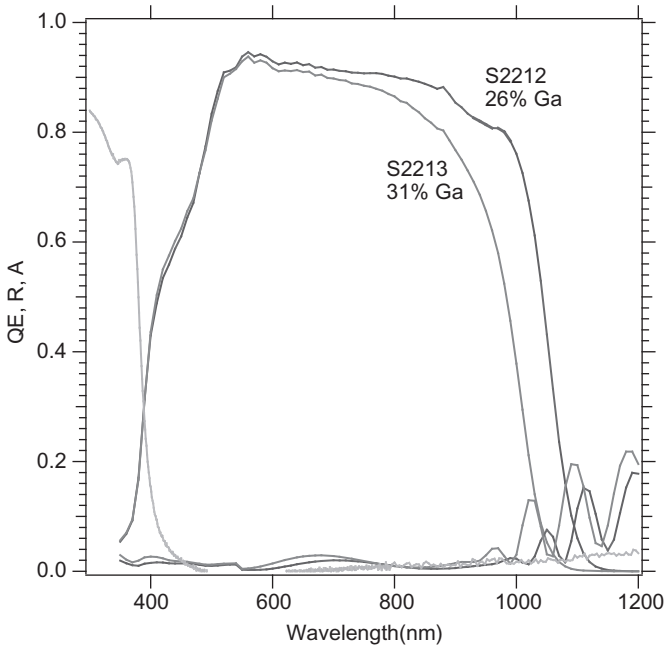


FIG. 21.11

Transparent electrode for PV device; properties of high efficiency CIGS thin film solar cells. *From Noufi, R., Romero, M.J., Jiang, C.-S., Yan, Y., Abu-shama, J., Ramanathan, K., NREL Invited Presentation, 2004. Why do CIGS-based solar cells have superior performance? Insight into the properties of grain boundaries and the surface as influenced by the growth dynamics. In: European MRS Meeting, Thin Film Chalcogenide Symposium.*

- Locate plasma wavelength, $\lambda_p \geq 1100$ nm for high transmittance to solar cell
- Calculate maximum allowed AZO carrier density, N, from

$$\lambda_p = 2\pi c \frac{(\varepsilon_0 m^*)^{1/2}}{(N e^2)^{1/2}} \quad \text{(see Section 21.2.3)}$$

- maximum $N \leq 6\times10^{20}\text{cm}^{-3}$ needed for $\lambda_p \geq 1100$ nm
- for low surface resistivity (sheet resistance) and high transmittance, high mobility, μ, desirable (≥ 20 cm^2/Vs)
- calculate AZO minimum thickness, d, for surface resistivity, r, $\leq 10\ \Omega$/sq,
  [using $\sigma = n\ e\ \mu$, $\rho = 1/\sigma\ \Omega$ cm, $r = \rho/d$]
  - $\sigma = 6\times10^{20}$ cm$^{-3}\times 20$ cm^2/Vs $\times\ e = 1920$ S/cm, then $\rho \approx 5\times10^{-4}\ \Omega$ cm
  - $d = 500\ \mu\Omega$ cm/10 Ω/sq $= 5\times10^{-5}$ cm $= 500$ nm

FIG. 21.12

Transparent electrode for CIGS PV device: AZO film requirements (Bright, 1995a–2012).

the allowed carrier concentration. The calculation of the allowed plasma wavelength (see Section 21.2.3) and the corresponding N is shown in Fig. 21.12 along with the other required characteristics of the TE. In this example, zinc oxide doped with aluminum, commonly called AZO, was selected. The result is a TCTF with $N \leq 6\times10^{20}\,\text{cm}^{-3}$, a mobility of $20\,\text{cm}^2\,\text{V}^{-1}\,\text{s}^{-1}$, and a thickness of ≥ 500 nm for a sheet resistance of $\leq 10\,\Omega$/sq (Bright, 1995a–2012, 2010a).

21.5.5 ENERGY-EFFICIENT WINDOWS

Energy-efficient windows are also addressed in Chapters 8 and 20 and the reader is referred to these chapters for more detailed discussions related to controlling thermal radiation from surfaces and in automotive and building glazing. The purpose of brief discussion here is to provide sufficient understanding of the application requirements so that appropriate TCTF can be selected and designed (see Sections 21.2.3 and 21.3).

21.5.5.1 Low-emissivity windows

There are, fundamentally, two types of energy-efficient coatings for window applications. The first type of coating is for energy conservation windows where the dominant concern is to conserve heat loss from the interior and to harvest solar heating. These TCTF coatings are sometimes called "winter films" because they are most useful in cold climates. When the temperature on the outside of the window is lower than that on the inside of the window, heat is radiated out from the interior of the building. To reduce this heat loss a low emissivity or "low-e" coating can be applied to the window. Recall that over a spectral interval, the sum of the transmittance (T), reflectance (R), and absorption (A) must equal one, that is,

$$T + R + A = 1 \quad \text{or rearranging} \quad A = 1 - R - T \tag{21.7}$$

and by Kirchhoff's law, $A = \epsilon$, where epsilon or "e" is the emissivity. Further, for metallic thin films and TCO on glass in the FIR region because $T \approx 0$,

$$\varepsilon = 1 - R \tag{21.8}$$

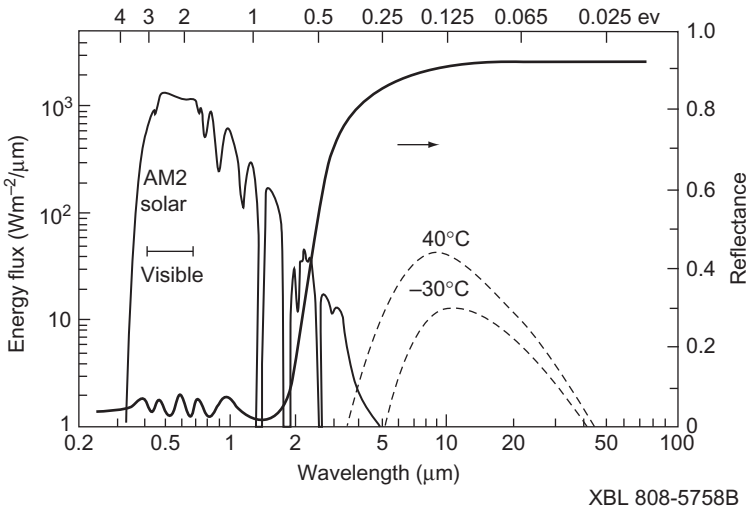


FIG. 21.13

Low-ε "winter film" window with TCO coating (Lampert, 1981).

Therefore, low-ε (or more commonly called "low-e") properties can be accomplished with a TCTF having high FIR reflectance.

To achieve heating of the interior requires that the visible and near-infrared solar energy be transmitted by low-e coating and by the window. This concept is illustrated in Fig. 21.13 showing the solar spectral energy distribution and the desired spectral characteristics of the low-e coating. Solar heat gain is better achieved with TCO than with most metallic thin films. The spectral characteristics of the metallic thin films are determined primarily by the choice of metal, that is, by its atomic structure, whereas with TCO these characteristics can be controlled by doping. By suitable doping of TCO the plasma wavelength can be located at the desired wavelength for the change from transmittance to reflectance. An example of the design process for matching the low-e application requirements is detailed in Example 21.4 (Bright, 1971, 1995a–2012).

21.5.5.2 Solar control coatings

The second type of energy-efficient coatings for windows is called solar control coatings. These coatings are used in hot regions to reject solar energy before entering through the window to the interior. These types of TCTF coating are also called "summer films." Fig. 21.14 shows a plot of the solar spectral energy distribution. An ideal solar control coating would transmit all the light visible spectral range (dashed area in Fig. 21.14) and reflect all of the light infrared spectral range. To reject maximum amount of nonvisible solar radiation the plasma wavelength of the TCTF should be located at the long-wavelength extreme of the visible region, that is, about

Requirements:

- Solar transmittance (≤ 2 μm) (TE) ≥ 50%
- Low emissivity in FIR waveb and ($\lambda \geq 5$ μm), for $\varepsilon \leq 0.20$, $R \geq 1 - \varepsilon = 0.80 = 80\%$
- Visible (eye weight) transmittance (T_{vis}) ≥ 70%

Approach:

- TCO with low carrier concentration
- Fluorine doped tin oxide TCO for high mobility (SnO_2:F)
- Pyrolitic deposition process, low cost and high durability

Determine coating parameters:

- Single layer tin oxide coating doped for low carrier density, $\sim 3 \times 10^{20}$ cm^{-3}, to locate plasma wavelength for high NIR transmittance
- High mobility ≥ 40 cm^2/Vs for steep slope in IR reflectance
- Low surface resistivity for high (≥ 80%) FIR reflectance
- Minimum thickness ≥ skin depth of ~200 nm (0.2 μm) at 20 μm wavelength, for high IR reflectance (low emissivity)
- Thickness multiple of halfwave for visible transmittance

EXAMPLE 21.4

Design of low-ε winter films.

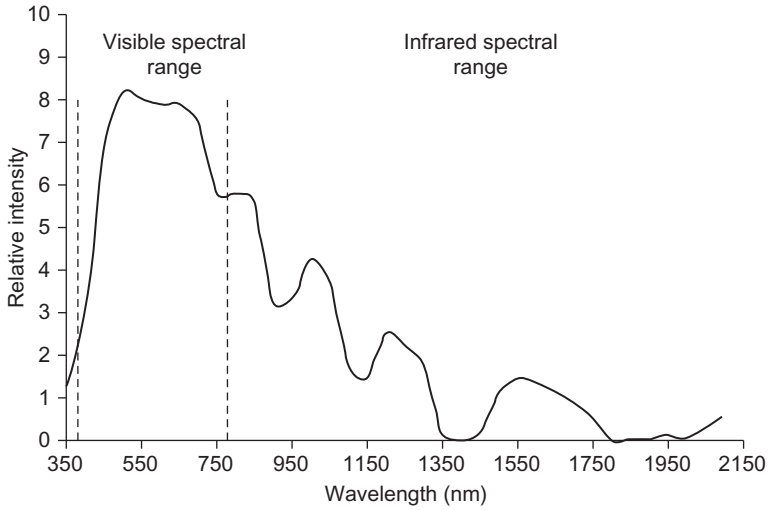


FIG. 21.14

"Summer film" window with metal coating (American Society for Testing and Materials (ASTM), https://www.astm.org).

700 nm. Because of the short wavelength required for the plasma wavelength, thin film metals are generally superior to TCO for this application. The TCO cannot generally achieve a carrier concentration greater than about $10^{21}\,\text{cm}^{-3}$ whereas noble metals typically have N values of about $10^{23}\,\text{cm}^{-3}$.

If additional heat rejection is desired some reduction in visible light will be required. Almost half of the incident solar energy is in the visible region, so a compromise will be required between achieving greater heat rejection and maintaining transparency. Typical values of visible transmittance for reflecting solar control films are from about 40% to 75%T. A detailed example of the design of a solar control film is given in Example 21.5 (Bright, 1971, 1995a–2012).

21.6 RECENT APPLICATIONS

21.6.1 CONDUCTIVE AR

Thin films for AR are widely used in optical displays, eyeglasses, smartphones, tablets, and many more. Today, most AR coatings are multilayer thin film stacks based on optical interference designs. Additional functionality can be incorporated in AR coatings by using TCTF. Including one or more TCTF in the AR stack can provide antistatic, EMI shielding or if patterned, can provide touch sensing capability. The use of TCTF for touch sensing applications will be discussed in Section 21.6.2.

Because the eye is not equally sensitive to all visible wavelengths, one important set of parameters for displays are eye-weighted, that is, photopic or luminous, transmittance, and reflectance values. However, for color displays, transmittance and reflectance values over a broad band in the visible region are often used also for performance specifications. A common spectral band specified is the wavelength region from 450 to 650 nm. The optical requirements for a conductive AR coating on a flexible plastic substrate for use with displays are summarized in Example 21.6.

In addition to meeting difficult optical requirements, a wide range of other requirements must be met by the conductive AR coatings including abrasion resistance, chemical and environmental durability, antistatic, and EMI shielding performance. In addition, it must be produced at low cost. These requirements are also summarized in Example 21.6.

A four-layer optical coating (based on a classical three-layer, Quarter-Half-Quarter design with a two-layer equivalent first layer), with alternating layers of ITO as the high index material and SiO_2 as the low index material was chosen for meeting the requirements of this example. An optical design program was used to optimize the layer thicknesses. The preferred thicknesses are shown in the cross section schematic drawing (Fig. 21.15).

An AR coating exceeding the requirements was produced by the roll-to-roll (web) coating method using a PET plastic film substrate with an organic SiO_2 particle loaded hardcoat. DC magnetron sputtering was used for the ITO layers and AC dual magnetron sputtering for the SiO_2 layers. A liquid fluorocarbon coating was applied to the AR stack to provide antifingerprint capability and increased scratch resistance. Typical optical and electrical performance for the four-layer

Design of solar control "summer" film

Requirements:

- Solar control "summer film" for existing window
- Visible transmittance ≥ 75% (coated film only)
- Solar reflectance ≥ 25% (~ solar IR reflectance ≥ 50%)

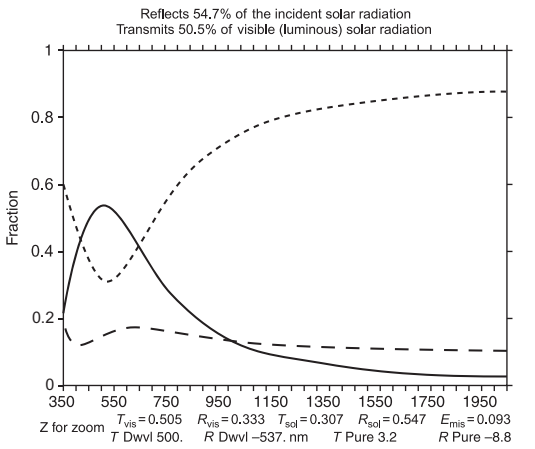
Approach:

- Optically enhanced metal on plastic film
- Indium oxide-silver-indium oxide coating stack
- Magnetron sputter indium oxide and silver layers in roll-to-roll (web) coating process

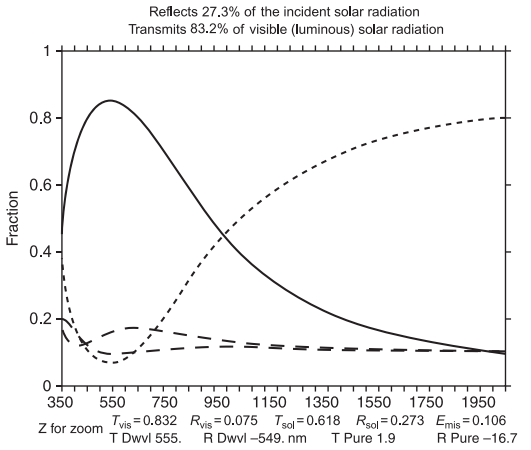
Determine coating parameters:

- Computer optical design program for layer thickness
- Trade-off required between visible transmittance and solar IR reflectance
- Silver surface resistivity (thickness) controls solar IR reflectance
- Surface resistivity ≤ 10 Ω/sq (see figures)

(A)



(B)



(C)

EXAMPLE 21.5

Detailed example of the design of a solar control film: (A) design of solar control "summer" film; (B) optically enhanced silver (5Ω/sq); (C) optically enhanced silver (Bright, 1995a–2012).

Optical requirements:

- Average reflectance from 450–650 nm: ≤0.7%
- Maximum reflectance at 450 and 650 nm: 2.0%
- AR bandwidth: ≥ 1.4
  (long wavelength ÷ short wavelength for R = 1.0%)
- luminous reflectance: ≤0.6%

Other requirements:

- Abrasion resistant to 3H (1000 g) pencil, mechnical pencil (200 g) and #0000 steel wool (200 g/cm^2)
- Chemical and environmental (temperature/humidity) durability
- Antistatic and moderate EMI shield (≤ 200 Ω/sq)
- Low cost (few dollars/square feet)

EXAMPLE 21.6

Requirements for the conductive AR coating of displays (Bright, 1995b).

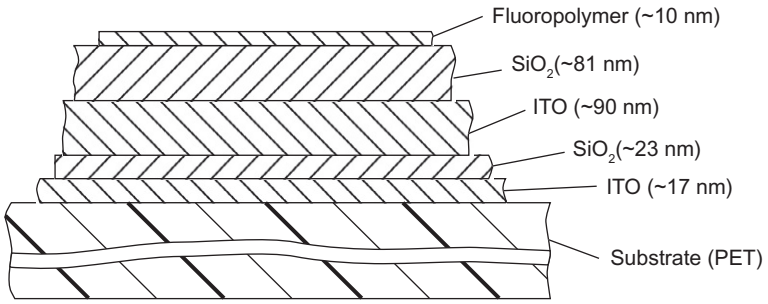


FIG. 21.15

Cross-sectional schematic of conductive AR coating (Bright et al., 1998).

- Average reflectance (450–650 nm) 0.46%
- Maximum reflectance (450, 650 nm) 1.1%, 0.3%
- Bandwidth (1% wavelengths) 1.5
- Luminous reflectance 0.44%
- Surface resistivity 200 Ω/sq

FIG. 21.16

Conductive AR coating for displays: typical measured optical and electrical performance (Bright, 1995b).

coating is summarized in Fig. 21.16 and spectral performance is shown graphically in Fig. 21.17. Durability requirements are summarized in Fig. 21.18. For more detail on the optical design, deposition process, performance, and testing, see Bright (1995b) and Bright et al. (1998).

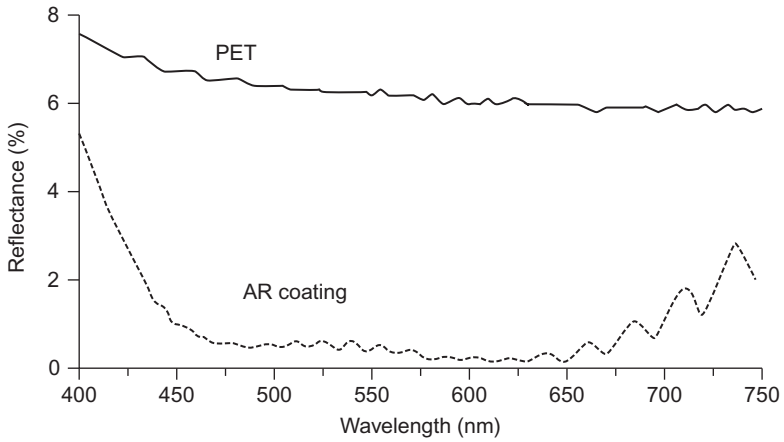


FIG. 21.17

Conductive AR coating for displays: typical measured spectral optical performance (Bright et al., 1998).

- 3H pencil hardness ≥ 1 kg load
- Mechanical pencil resistant at ≥ 200 g load
- Steel wool (#0000) 30 cycles at 200 g/cm^2 load
- Resists "all" common household and office chemicals
- Passes 48 h at 50°C and 98% humidity
- Unaffected by temperature cycling from –40°C to 71°C (5 cycles)

FIG. 21.18

Conductive AR coating for displays: typical measured durability performance (Bright, 1995b).

21.6.2 TOUCH SENSORS

21.6.2.1 Analog resistive

There are many different types of touch sensor technologies; however, only two mainstream technologies will be described. The first type is analog resistive touch, which has been used for many years, and is based on having two conductive coatings, at least one of which is applied to a flexible substrate. When the flexible coated film is touched ("pushed"), it makes physical (electrical) contact with the opposite conductive coating, say on glass (see Fig. 21.19) (Walker, 2010). This electrical contact completes a circuit and allows sensing of that location.

For example, the voltage applied across the (second) conductive coating on glass could be in the x direction and because of the resistance of that coating, a voltage gradient is created. When the conductive coating on the flexible substrate touches the coating with the voltage gradient, it measures the voltage at that location and thus senses the x direction. Similarly, a voltage across the flexible conductor could be applied in the y direction and because of the resistance of that coating a voltage

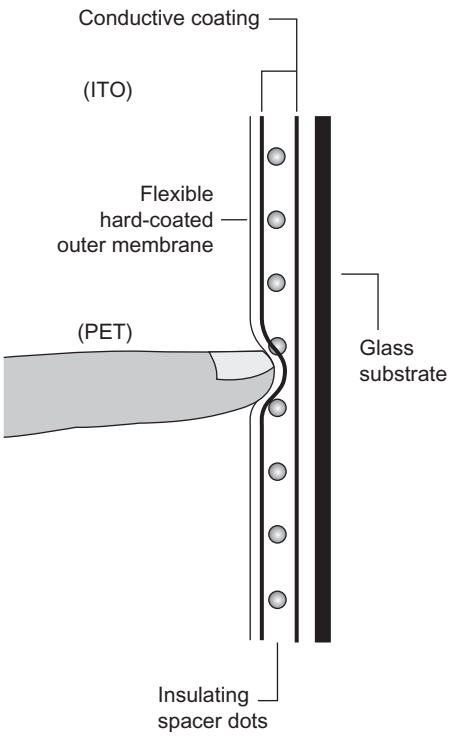


FIG. 21.19

Resistive touch (Walker, 2010).

gradient is again created. When the voltage gradient is across the conductive coating on the flexible substrate (*y* direction) and it comes in contact with (touches) the coating on the glass, the voltage of the coating on the flexible substrate is measured and the location sensed. Now both the *x* and *y* directions at the point of touch are known. This method of resistive touch screen sensing (four-wire) is shown in Fig. 21.20 (Walker, 2010). For display applications where the touch sensor is in the field of view, of course, both conductive coatings and their substrates must be transparent.

For resistive touch applications, the sheet resistance of the TCTF is relatively high, typically 200–500 Ω/sq so that a significant voltage drop, that is, gradient, is produced across the coating. Because sensing is based on this voltage gradient the conductive coatings must be very uniform in resistance to cause a very linear voltage drop to correlate accurately with location. The contact resistance between the two conductive coatings upon touching should be low and constant at all locations to avoid introducing sensing errors. Durability against contact, "abrasion resistance," for the two TCTF coatings is also a requirement for resistive touch sensing applications. The ITO is most commonly used for resistive touch sensing and display applications, and because of this durability requirement, crystalline ITO is preferred.

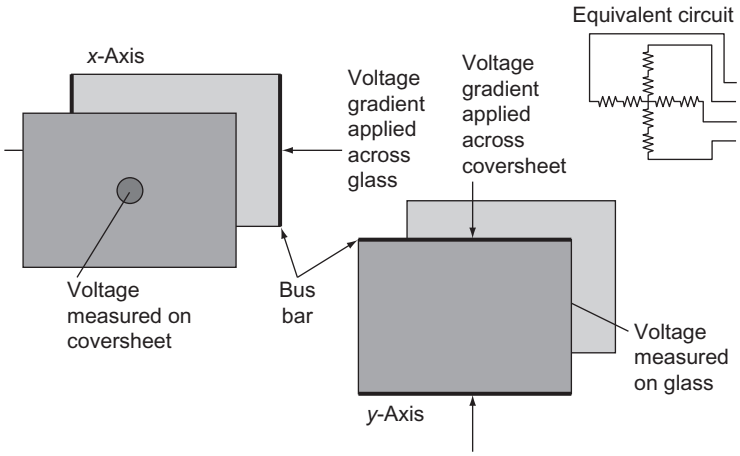


FIG. 21.20

Four-wire resistive touch sensing (Walker, 2010).

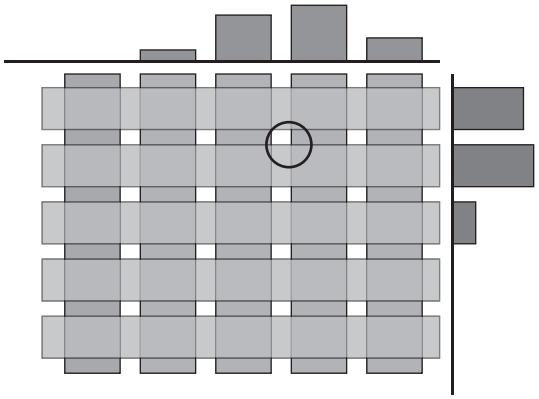


FIG. 21.21

Schematic grid-line structure for *x* and *y* sensing (Walker, 2010).

21.6.2.2 Projected capacitive

Projected capacitive touch technology is the fastest growing touch sensor method, since Apple introduced the iPhone in 2007. Apple was not the first to use this touch sensor method but it has added many capabilities to the original technology and popularized its use. Like resistive touch technology, projected capacitive touch uses two conductive coatings for sensing, one for sensing in the *x* direction and the other for sensing in the *y* direction; however, there is no physical contact between the two coatings for sensing. Also, the two coatings are patterned typically in some type of a grid-line structure (magnified, not to scale) as shown in Fig. 21.21. Typically, the two coatings are of ITO and may be deposited on both sides of a single substrate

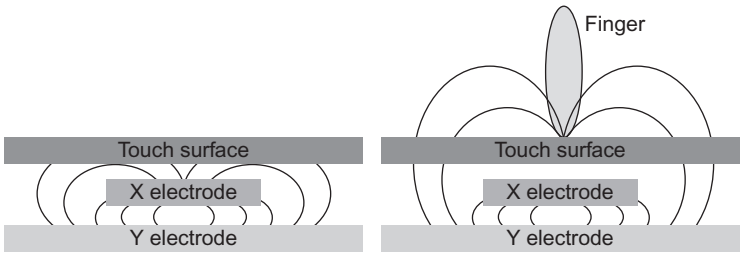


FIG. 21.22

Projected capacitive sensor (Walker, 2010).

or on one side of the two substrates. The space between the two patterned coatings is dielectric and thus a capacitor is formed wherever the two coatings separated by a dielectric overlap each other. Usually, for protection another substrate, which is touched with a finger by the user, is placed above the sensor substrate(s). When a voltage is applied to the two patterned ITO coatings an electric field is generated between them, which extends beyond the conductive grid line into the space between lines and further into the insulating touch substrate as shown in Fig. 21.22. When a finger touches the surface of the insulating substrate, charge is drawn to the finger (to ground) from the nearest conductive patterned area, changing the capacitance between the X and Y electrodes in that area. This change in capacitance is sensed by electronic circuitry to identify the touched area. There are many different schemes for sensing this touch and for applying the voltage to the X and Y electrodes but all rely on the electric field being projected beyond the electrodes and interaction with the finger causing a change in the capacitance.

The requirements on the TCTF are for high transmittance and low reflectance so that the patterned electrodes are not readily visible, the ability to be patterned accurately, and having an appropriate sheet resistance such that the resistance of a grid line does not reduce the signal significantly before electronic processing. The actual value of sheet resistance required will depend on the construction details and the electronics of the device; however, a typical value of sheet resistance for handheld devices such as smartphones is about 100 Ω/sq for the ITO (Bright, 1995a–2012, 2010a).

21.6.3 OLED LIGHTING

Technically, the use of a TCTF for OLED lighting is also a Type II, current-carrying, TE application as discussed for OLED displays. However, OLED lighting is an emerging application and has some differences in requirements compared with AM displays, that is, AMOLED. For example, an OLED lamp is in essence a single

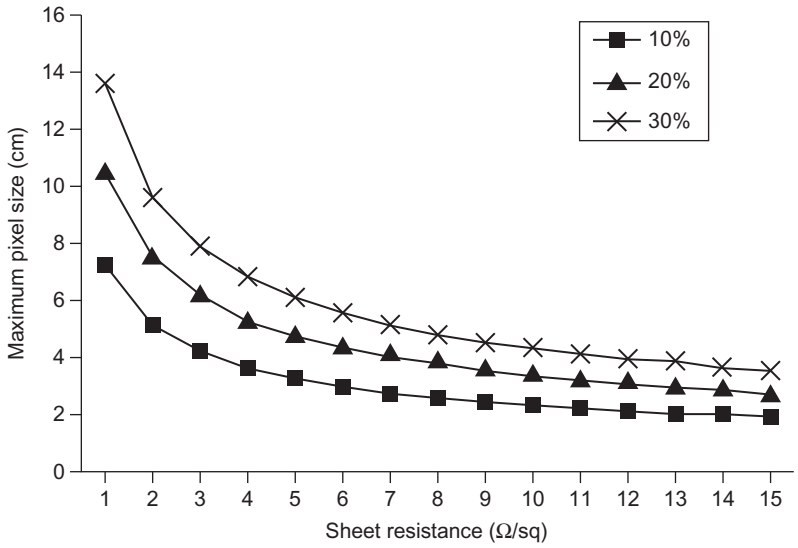


FIG. 21.23

Percentage nonuniformity as a function of pixel size and TE (TCTF) ohms/square (Ma et al., 2011).

pixel display. Thus, a patterned TE and a method of deriving the *x* and *y* addressing lines as in a display is not required. However, the TE must be capable of supplying significant current without significant voltage drop across the entire OLED lamp. If the resistance (sheet resistance) of the TE is too high the voltage drop across the lamp will cause a drop in the illumination spatially across the lamp, which can be detected by human eye. In fact, today, the size of an OLED lamp is limited by the TE electrode resistance, as shown in Fig. 21.23 (Ma et al., 2011). For this OLED lamp example with an ITO TE sheet resistance of 15 Ω/sq, to limit the nonuniformity to 10% (30%) the lamp dimension can't be larger than about 2 cm (4 cm). Prototype OLED lamps typically use ITO as TE; however, the resistance is higher than desired and the cost of the ITO is a concern. Alternative TE solutions including hybrid electrodes, for example, a wire or deposited metal mesh, or silver nanowires plus a continuous TCO, or conductive polymer layer to bridge between individual conductors, are being sought for this application in particular. As in the OLED display example, all the additional non-O/E requirements apply to OLED lighting, but the major requirements are low resistance and very low cost for which no preferred TE solution has yet been found.

21.6.4 TRANSPARENT OXIDE ELECTRONICS

Transparent oxide electronics represents both a traditional and a new use for TCO (Facchetti and Marks, 2010). The traditional application of TCO is as a TE or transparent contact. The new "TCO" use is as a true semiconductor. As explained in

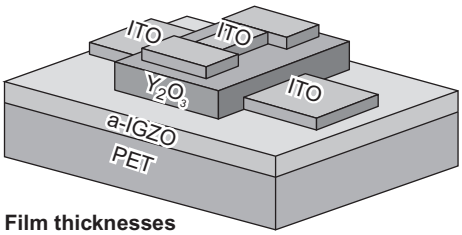


FIG. 21.24

Structure of first TTFT deposited on a flexible substrate (Nomura et al., 2004).

Section 21.2.2, all common high performance TCO are *n*-type degenerate semiconductors, that is, electrically equivalent to metals. However, in this application a true semiconductor is also required, that is, labeled as transparent semiconductive oxides (TSO) for clarification, which is used for the channel of a thin film transistor (TFT), that is, a field-effect transistor (FET).

A typical TFT (FET) structure is shown in Fig. 21.26. In a typical TFT (FET), current flows from the source through the channel to the drain when the gate electrode is activated. The TFTs are widely used as "switches" in AM addressing electronics for displays. Nomura et al. (2004) demonstrated the first transparent TFT (TTFT) deposited on a flexible substrate, PET. The ITO was the selected TCO used as a TE for the source, gate, and drain (Fig. 21.24). The TSO used for the semiconducting channel was amorphous indium gallium zinc oxide, a-IGZO. This TSO is currently the preferred material for the channel of TTFT because of its high field effect mobility and amorphous structure. Many TCO materials have been used to make TSO channel layers in TFT and TTFT. However, there are significant issues with making TSO from binary and ternary TCO materials, particularly on low-temperature substrates like plastics (Bright, 2010a). An interesting history of TFT and TTFT is reported in a recent book (Fortunato et al., 2010). Applications of oxide electronics are growing rapidly and they are in use in the current generation of TVs and pad/tablet devices from some major manufacturers.

21.7 FUTURE APPLICATIONS

21.7.1 BEYOND TFT

While current transparent oxide electronics are entering industry, and the use of TFT and TTFT will be very large because of the display industry, *p*-type TCO and TSO are required to make *p*-*n* junction-type devices. Much progress has been made in recent years in developing crystalline *p*-type TCO and TSO, and some

p-n junction-type devices have been demonstrated (Kudo et al., 1999; Kawazoe et al., 2000). However, to make practical electronic devices beyond TFT and TTFT "switches" much work is needed. New and improved *p*-type materials must be found and developed with superior O/E properties.

The breakthrough, which caused the Renaissance search for *p*-type semiconducting materials, occurred in 1997 (Kawazoe et al., 1997) with the investigation of copper aluminum oxide, $CuAlO_2$. This success spawned investigation of many other delafossites and then spinel materials. Several materials have been found which demonstrate *p*-type properties, for example, copper gallium oxide, $CuGaO_2$, and strontium copper oxide, $SrCu_2O_2$. Also, copper indium oxide, $CuInO_2$, was developed as a *p*-type material (Yanagi et al., 2001). The first transparent bipolar *p-n* homojunction ($CuInO_2$;Mg/$CuInO_2$:Sn) was fabricated based on this material (Yanagi et al., 2001).

After the success with delafossites, chalcogenide materials with copper were also investigated and *p*-type semiconductors demonstrated, for example, α-$BaCu_2S_2$. However, the chalcogenide materials will not have high transparency in the visible region. Next chalcogenide oxide (and fluoride) materials were investigated for wider bandgaps. These materials have a stacked, alternating two-layered structure, which exhibits two-dimensional like electronic properties. Degenerate *p*-type conduction was exhibited in LaCuOSe doped with magnesium with mobility of $\sim 4\,cm^2\,V^{-1}\,s^{-1}$. All the *p*-type materials discussed in this section have been epitaxially grown. The performance of polycrystalline or amorphous samples, where attempted, has been much poorer.

Another *p*-type discovered, which operates fundamentally differently (polarons) than these copper-based materials, is nickel cobalt oxide, $NiCo_2O_4$; this material has demonstrated some quite interesting properties including IR transmittance and the ability to be magnetic (Exarhos and Zhou, 2007).

Binary *p*-type oxides of copper (Cu_2O) and nickel (NiO:Li) have been known for decades but the O/E performance is too low. Of course, there have been many efforts to make *p*-type materials from known binary *n*-type TCO such as zinc oxide. Generally, this has been unsuccessful or controversial although there have been some convincing reports of making ZnO *p*-type material (Ryu et al., 2003; Tsukazaki et al., 2004).

However, none of these materials has demonstrated *p*-type performance comparable to elemental semiconductors, adequate for a *p*-channel layer, or comparable with *n*-type TCO (see Section 21.8 for more discussion on *p*-type materials).

21.7.2 TRANSPARENT OLED

Transparent displays are expected to enter the market in 2012. This new application for displays, for example, OLED, LCD, and PDP, is predicted to grow rapidly to an $87.2 billion market by 2025 (Displaybank, 2012).

The use of TCO as a TE for OLED displays was discussed in Section 21.5.4 and for lighting in Section 21.6.3. A future application is using more than one TCTF with

OLED to produce a transparent display or lamp. The same general O/E requirements and considerations as discussed previously would apply for this new application; however, now two TEs would be required. In fact, transparent OLEDs have already been demonstrated (Gu et al., 1996). However, the performance and TE characteristics were not optimized for an intended application. Simply choosing to make an OLED with two single-layer ITO electrodes will not make an efficient device because for ohmic contacts the work function of the TE should match the work function of the organic layers, separately for electron and hole injection. Clearly, different work functions are required for the two cases.

Traditionally, the cathode electrode is metallic whereas the anode is typically ITO (TCO). Generally, metal layers used as electrodes are opaque but thin layers can be made semitransparent. Transparent OLEDs of this type have been demonstrated but the percentage transmittance of the full structure is not adequate for most applications (Gu et al., 1996; Riedl, 2010). For example, for either display or lighting applications, high light transmittance is required for efficient operation. Therefore, a different approach is needed which will meet the electrical requirements while also satisfying the demanding optical requirements. There have been many attempts to use TCO, particularly ITO, as the cathode for an OLED (Dobbertin et al., 2003; Kowalsky et al., 2007) by adding additional layers to better match the work function of the organic layer. However, the preferred deposition process for ITO, sputtering, is well known as being damaging to organic layers. Therefore adding a very thin buffer layer, which will protect the organic layer during sputtering yet have acceptable hole injection, and which can be deposited by a low-energy evaporation process has been attempted. This approach has been demonstrated successfully using transition metal oxides, for example, tungsten oxide, WO_3, as the buffer layer. However, the added layers and processes bring additional complexity and cost concerns for such a device construction, particularly in large area applications (Riedl, 2010).

Another possibility for the cathode TE is to use a very thin metallic film between optical matching layers (see Section 21.2.1). As recently demonstrated by Bright (2010b), these constructions can have very high transmittance and high conductivity. Perhaps the optical matching layers could be thin enough to allow charge injection yet still increase transmittance. Alternatively, the matching layers could be made of transition metal oxides or organic materials with known, good hole injection properties.

Once a practical construction for transparent OLEDs is demonstrated it can be combined with transparent oxide electronics, for example, TTFT, to enable large area transparent displays.

21.7.3 TRANSPARENT PV (SOLAR) CELLS

The idea of having a transparent solar cell at first seems contradictory. One would think that collecting the maximum amount of solar radiation to which the cell is sensitive would be a requirement, and typically it is for opaque cells. However, even though almost half of the energy arriving from the sun is at visible wavelengths, solar

control coatings for windows, which allow significant transmittance of visible light for viewing and reject infrared radiation, are still energy efficient and very useful (see Section 21.5.5). Similarly, a transparent solar cell used as a window can provide dual use as an energy-efficient compromise between energy generation and energy conservation. Actually, this idea is not new and was proposed at least as early as in the 1970s by Bright in a patent application, and perhaps earlier.

There are multiple ways to implement a transparent PV cell. One way is to use an inorganic thin film for the construction of PV cell such as CIGS, cadmium telluride (CdTe), or amorphous or polycrystalline silicon; alternatively, organic polymer photovoltaic (OPV) device constructions could be used (Huang et al., 2010). Conceptually, even dye-sensitized solar cells could be used. For the compromise in visible transmittance, basically the absorbing layer of the PV cell is made thinner to achieve the desired transmittance.

The spectral transmittance band for the two required TEs will depend on the type of cell chosen and its spectral sensitivity, which will set the limit on the allowed carrier concentration, N. The calculation of the allowed carrier concentration for a CIGS PV cell was described in Section 21.5.4.

For all of these implementations, two TCTFs (or alternatives) will be required as TEs for the transparent PV cell. The choice of TCTF, for example, TCO or metallic thin film, will depend on several factors. Because the transparent PV is a current device the TE electrical requirements will be determined in a way similar to that previously described for a Type II TE. Because of the very large size of windows, for example, in commercial buildings, some types of very high conductivity busbars will be required to periodically collect current from the PV window to avoid unacceptable losses occurring in the TCTF. This situation also occurs in standard opaque PV solar cell modules. It is also similar to the voltage drop problem discussed for OLED lighting. Because of this issue early implementations of transparent PV windows may look more like a "French door" with muntin bars between what appears to be individual small windows. Smaller size windows and skylights are also candidates for transparent PV cells.

21.7.4 TRANSPARENT ELECTROCHROMIC WINDOWS

Another application incorporating TCTFs and expected to find commercial use in the future is electrochromic (EC) windows. The EC devices can vary in the optical properties between a clear transmitting state and a darkened state achieved by reflection, absorption, or both. One of the primary applications foreseen for EC devices is in active energy efficient windows, that is, "smart windows." The application of TCTF in passive energy efficient windows was described in Section 21.5.5. The benefits of having an active EC window are that the transmittance and reflectance/absorption of the window can be modified as appropriate for interior lighting needs, the time of day or season of the year, resulting in reduced energy usage for lighting, heating, and cooling.

Modern EC cells are typically based on metal oxide EC materials. Obviously for a transparent EC device two TEs are required. In addition, one electrode must be in contact with an EC material and the other TE must be in contact with an ion storage layer, which also may be an EC material. In addition, there must be an ion transport layer between these layers. In operation, when a voltage is applied, charge is transported between the EC material and the ion storage material which causes the change in optical transparency. The full transparency of the EC cell can be restored by reversing the voltage polarity (Granqvist, 2010).

Current EC technology has advanced to being compatible with roll-to-roll fabrication wherein each "half" of the cell is deposited on a separate plastic substrate then laminated together with polymer layers used for the ion transport (see Granqvist, 2010 and references therein). This flexible laminate could then be installed or laminated between two pieces of glass. Commercial use of EC windows with this construction is underway in Europe for architectural glazing. Of course the application of EC technology is not limited to architectural glazing or even auto glazing but these two applications are early market entries.

The basic function of the TCTF for EC applications would again be a TE. However, for EC applications the function of the TE is neither purely Type I nor Type II. Electrically, an EC cell is similar to a battery. When the EC cell is switched on there is current flow and the requirements of the TE are similar to Type II. However, when the EC cell is in the darkened or the transparent state no current flow is required to maintain that state (assuming no leakage). This condition is more like an antistatic application but is not exactly like either Type I or Type II functionally, but has attributes of both types depending on the EC Cell state. However, because of the large area covered in many window applications the same size-related concerns discussed in Section 21.7.3 for transparent PV cells in window applications would apply for transparent EC windows. Spectral consideration for the TEs will depend on the specifics of the application and also on the ability of the chosen EC technology to modulate not only visible transmittance but also infrared reflectance and emissivity properties.

One can envision combining several of the applications discussed, for example, transparent PV and transparent EC characteristics in a given window application, or one or both of these along with passive solar control or energy efficient coatings. A multifunctional window might also have display capabilities. Future applications for TCTF is likely be quite varied and challenging optically and electrically and also require many other features and attributes both technology and business related.

21.8 CONCLUSION

The section has three subsections. Because of the large difference in the state of development and the underlying physics, *n*-type and *p*-type TCTF are discussed separately. The first subsection addresses *n*-type TCTF, followed by the *p*-type TCTF discussion. Because of the specialized nature of the TCTF topic, there is not a single

or few obvious sources for information; therefore, the final subsection provides some advice on sources of further information. The intent of this section is to provide some perspective for expectations of future developments, rather than provide conclusions, per se. Further, there always may be some surprising developments, which alter the performance expectations discussed here and even the character of future TCTF.

21.8.1 FUTURE DEVELOPMENTS AND OUTLOOK FOR *N*-TYPE TCTF

Recently, Bright (2007) discussed the outlook for improved O/E properties in (*n*-type) TCO. Today that discussion is still relevant and is paraphrased and quoted here, but updated where experimental advances or improved knowledge have occurred. The "theoretical limit" for conductivity (resistivity) in classical TCO was calculated following Bellingham et al. (1992). Using nominal values for the ITO material properties, an estimated resistivity value of $\sim 4\text{–}5 \times 10^{-5}\,\Omega\,\text{cm}$ was calculated as the "theoretical limit." Fig. 21.25 shows the calculated theoretical resistivity limit, plotted with the measured performance reported, at that time, for various TCO and updated by Szyszka et al. (2006).

However, there are two exceptions to the assumptions by Bellingham, which were reviewed by Bright (2007) that could allow further improvement in the resistivity of certain TCO. The first exception is that some "multicomponent TCO with layered structures achieve spatial separation of the carrier donors and carrier transport layers; thus, alleviating scattering on the dopants" (Kawazoe et al., 1994). To the extent that scattering of ionized impurities is reduced beyond standard theory, a commensurate reduction in the theoretical limit for resistivity would be allowed. On the contrary, however, to date no multicomponent TCO of any type has achieved experimentally, equal, or better conductivity than classical binary TCO, for example, ITO.

The second exception is that using transition metals, magnetically mediated dopants, with new or traditional binary TCO hosts can reduce the "traditional TCO theoretical limit" by a factor of $2\times$, to $\sim 2\text{–}3 \times 10^{-5}\,\Omega\,\text{cm}$, because conduction electrons of only one spin direction, instead of both, are scattered (Medvedeva, 2006a,b). To date this approach has resulted in high mobility TCO with good O/E performance. But a resistivity of $\sim 10^{-5}\,\Omega\,\text{cm}$ has not been demonstrated because, even though the mobility is high, carrier concentrations achieved by transition metal doping are in the low $\times\, 10^{20}\,\text{cm}^{-3}$.

Cage-structured materials have been suggested as a new class of TCO with the possibility of not compromising optical properties to achieve good conductivity (Hayashi et al., 2002). Theoretical band structure analysis (Medvedeva, 2006a,b) supports this possibility although experimental results to date have not achieved this goal. Examples of cage-structured materials are the $CaO\text{-}Al_2O_3$ family, in particular, $12CaO{\cdot}7Al_2O_3$, abbreviated as 12A7 (see Fig. 21.26) (Hosono, 2010). The unit cell can be represented by the chemical formula $[Ca_{24}Al_{28}O_{64}]^{4+} + 2O^{2-}$. The bracketed quantity represents the "cage framework" and the two additional oxygens are considered "free oxygen ions." The nanostructure of these cage-structured materials

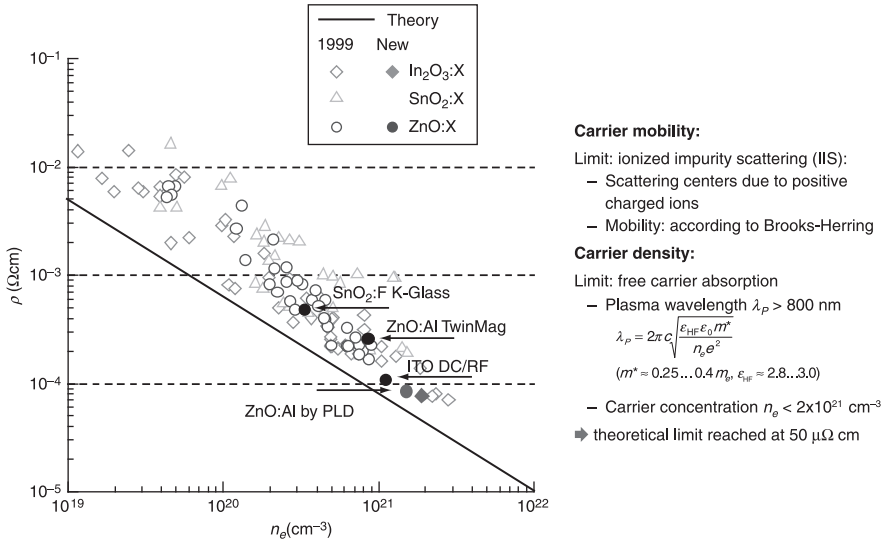
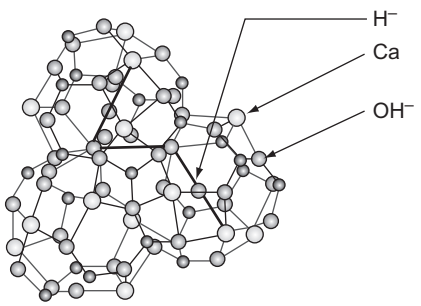


FIG. 21.25

Intrinsic performance limits for TCO (Szyszka et al., 2006).

Based on Bellingham, J.R., Phillips, W.A., Adkins, C. J., 1992. Intrinsic performance limits in transparent conducting oxides. J. Mat. Sci. Lett. 11, 263.



Crystal structure of H-doped $12CaO \cdot 7Al_2O_3$
(only three of the 12 cages in the unit cell are shown)

FIG. 21.26

Example of cage-structured materials of $12CaO{\cdot}7Al_2O_3$: crystal structure of H-doped $12CaO{\cdot}7Al_2O_3$ (only three of the 12 cages in the unit cell are shown) (Medvedeva, 2006a).

leads to unique doping opportunities (Hosono, 2010 and references therein). Substitution of hydrogen ions (H^-) for the free oxygen ions created a hydrogen-doped material (C12A7:H^-). However, this doped material remained an electrical insulator until irradiated with UV light, causing conductivity as high as $1\,S\,cm^{-1}$ but which also created new absorption bands imparting a green color to the previously colorless

material. Further experiments were able to replace all of the free oxygen in the cages with electrons by a reduction process (Hosono, 2010 and references therein). This material is considered an "electride" and has achieved conductivity as high as $1000\,S\,cm^{-1}$, without requiring UV illumination/radiation. The new material with complete replacement of the free oxygen ions can be represented by chemical formula $[Ca_{24}Al_{28}O_{64}]^{4+}+4e^{-}$, and is considered a "new type of inorganic electrode" with metallic conduction and mobilities from about ~ 0.1 to $4\,cm^2\,V^{-1}\,s^{-1}$ with strong dependence on the electron carrier concentrations (Hosono, 2010 and references therein). Cooling the material to very low temperatures (0.2–0.4 K), causes a metal to superconductor transition at ambient pressure, a first for an s-metal material (Hosono, 2010 and references therein).

Bright (2007) also suggested for developing TCO with improved E/O properties (versus ITO), systematic exploration of the full periodic table should be undertaken rather than limiting studies to (host) materials in neighboring columns IIB and IIIA (except for Sn in IVA, which isn't a "high performance" TCO host).

"The surprise discovery of TiO_2:Nb (Furubayashi et al., 2006) shows the value of a broader investigation (column IVB), rather than "mixing" of the known binary TCO." These single crystalline films of anatase TiO_2:Nb (TNO) were grown by pulsed laser deposition (PLD) and achieved resistivity of $2–3\times10^{-4}\,\Omega\,cm$, with an internal transmittance of 97%, that is, 3% absorption. Since that discovery considerable work has been done on this material system at several laboratories and achieved similar performance for epitaxial films. In all the cases the rutile phase of TiO_2 shows significantly poorer O/E properties than the anatase phase (Zhang et al., 2007). The growth temperature was high ($\sim$600°C) for all of these TNO epitaxial films. More recently, magnetron sputtered films were deposited on unheated glass or 150°C heated glass but were subsequently postannealed at 500°C or 600°C in a hydrogen atmosphere (Hitosugi et al., 2008; Sato et al., 2008). Polycrystalline films on glass have exhibited a resistivity of about 4.5×10^{-4} to $1.5\times10^{-3}\,\Omega\,cm$. Clearly, after only a few years of study with a new material, achieving this type of O/E performance is very promising but more recent work has not shown significant improvement.

21.8.2 FUTURE DEVELOPMENTS AND OUTLOOK FOR *P*-TYPE TCTF

Since the discovery of *p*-type copper aluminum oxide, $CuAlO_2$, substantial progress has been made in developing new *p*-type oxide materials. Conductivities as high as $900\,S\,cm^{-1}$, mobility near $10\,cm^2\,V^{-1}\,s^{-1}$, and high visible transmittance, all have been achieved (Tate and Keszler, 2010). However, this level of performance requires epitaxial films, typically grown at very high temperatures. It is desirable to have polycrystalline or even more preferable to have amorphous *p*-type materials which are processable on glass or ideally on flexible plastic substrates.

For fabrication it is very desirable to have a bipolar material for making *p-n* junction devices but to date only $CuInO_2$ (*p-n*) and co-doped ZnO (also *p-i-n type*) materials have been used successfully, and neither has the characteristics desired for transistor- or TFT-type devices (Hosono, 2010; Tate and Keszler, 2010). Even for

heterojunction-type devices no satisfactory *p*-type transparent oxide material suitable for practical use has been found. Further, no *p*-type materials have been demonstrated which could be satisfactory as a *p*-channel in TFT and TTFT devices (Tate and Keszler, 2010). If a transparent material adequate for *p*-channel TTFT devices could be found, complementary metal-oxide-semiconductor (CMOS) field effect devices could be developed. For *p*-type semiconductor materials, developing suitable transparent oxide contacts, that is, *p*-type TCO, to achieve proper hole injection with an ohmic contact, or at least a low injection barrier, is another requirement.

The challenges in developing *p*-type, wide bandgap semiconductors, that is, *p*-TSO, are different than those for *n*-TSO. Because holes carrier movement is in the valence bands, carriers have inherently lower mobility in comparison to electrons in a conduction band generated by diffuse and spherical s orbitals. Valence bands are typically highly directional p or d orbitals and are narrower with less spatial overlap of atomic orbitals. Because of this inherent lower mobility higher doping is needed to achieve a high carrier concentration for a given amount of conductivity, which leads to higher ionized impurity scattering (Tate and Keszler, 2010). Further, obtaining high carrier concentrations is not always possible due to the development of "killer defects" causing "pinning" of the Fermi level (Zunger, 2003). Maintaining transparency of the material by avoiding causing absorption at visible wavelengths when doping in the valence band, also is very challenging. Clearly, there are many difficult hurdles to be overcome for achieving satisfactory transparent *p*-TSO and *p*-TCO (Tate and Keszler, 2010).

21.8.3 OTHER REVIEW ARTICLES

Today, with access to so much information sometimes it is hard to know where to start. Here are some suggested sources of further information based on my personal knowledge. Certainly, this list is far from inclusive but represents some sources I am aware of and which are generally useful to me. Of course, the usual thin film journals such as Thin Solid Films (TSF), the Journal of Vacuum Science and Technology (JVST) and many others are appropriate but cover many topics. Occasionally, journals will have a special issue, which covers the TCTF topic. For example, the MRS Bulletin, August 2000 issue focused on TCO and is still recommended. Other examples are special issues of TSF and JVST, which document selected papers from focused conferences.

Excellent sources of information on TCTF are review articles. Of course, by their nature they represent the knowledge base relevant to the time of the article. However, even quite old review articles still can be quite useful and authoritative. For example, the review by Chopra et al. (1983) is still recommended as a good way to efficiently review prior work on TCTF. It is particularly strong in reviewing solution-coated TCO. Already mentioned is the MRS bulletin of August 2000, which is based on a TCO workshop with contributors from many different countries and representing universities, institutes, and industry. More recent, recommended TCTF reviews are the reviews by Granqvist and Hultaker (2002), Granqvist (2007), and Exarhos and Zhou (2007).

Similarly, there are many good conferences to attend such as American Vacuum Society (AVS) held annually in November and the Materials Research Society (MRS) held in spring and fall, but these are very large conferences and, again, cover many topics. The content in these two conferences are also heavily weighted toward academic presentations. If you are looking for the latest research results from a university or institution these could be good sources.

Alternatively, if you are looking for thin film results representative of industry and technology applied on a large scale, the Society of Vacuum Coaters (SVC) conference is suggested. In addition to the excellent technical conference there is an associated exhibit with companies representing most major and specialty vacuum and thin film equipment, materials and related services. The SVC has a few parallel sessions, which cover several technology and market segments of vacuum and thin film coatings. The TCTF papers may be in more than one sessions including, for example, Large Area Coatings, for example, glass and glazing, and Web Coating for roll-to-roll coating primarily on plastics. In addition, there will be one or two annual theme topics which focus on papers in a particular area like PV and Clean Technologies.

Another good US conference, which includes TCTF on flexible substrates, is 20xxFLEX associated with SEMI, the global association for electronics manufactures, previously FlexTech Alliance, and previously called the United States Display Consortium (USDC), conference focused on flexible displays and electronics and held annually in February.

Specialty conferences for TCTF include the biannual TOEO (Symposium on Transparent Oxide Thin Films for Electronics and Optics) held in even numbered years in Japan, and the Symposium on Transparent Conductive Materials, TCM20XX, conference, formerly Symposium on Transparent Conductive Oxides, TCO20XX, held in Crete, Greece in even numbered years.

Finally, of course there are many websites with helpful information on TCTF; the websites for the professional societies and conferences previously mentioned are recommended as well as the websites of universities, institutes, and companies active in TCTF work. In the United States, National Laboratory websites may also be useful, for example, the National Renewable Energy Laboratory (NREL), at https://www.nrel.gov/. Also one should not forget patents and patent applications as a source of detailed TCTF information. Both the US patent office (USPTO) and the European patent office (EPO) are excellent sources of information available online, as are patent offices of other countries.

REFERENCES

Bellingham, J.R., Phillips, W.A., Adkins, C.J., 1992. Intrinsic performance limits in transparent conducting oxides. J. Mater. Sci. Lett. 11, 263.

Berning, P.H., Turner, A.F., 1957. Induced transmission in absorbing films applied to band pass filter design. J. Opt. Soc. Am. 47, 230–239.

Bright, C., 1971. Solar Shielding Performance of Sierracin Coating. Sierracin Corporation, Sylmar, CA. RDR-13–71, 1971.
Bright, C.I., 1995a. In: ITO and other transparent conductive coatings: fundamentals, deposition, properties, and applications. Class C-304, Annual Technical Conference of the Society of Vacuum Coaters.
Bright, C., 1995b. Conductive antireflection coatings on plastic films. AVS, Southern California Chapter, Vacuum Coating Workshop, 1995.
Bright, C.I., 2006. Fundamental Issues with TCO on Plastic Substrates. 1st International Symposium on Transparent Conductive Oxides, Crete, Greece, Conference Proceedings, C6, 62 (2006).
Bright, C.I., 2007. Review of Transparent Conductive Oxides (TCO). In: Mattox, D., Harwood-Mattox, V. (Eds.), 50 Years of Vacuum Coating Technology and the Growth of the Society of Vacuum Coaters. Society of Vacuum Coaters, Albuquerque, NM, pp. 42–50.
Bright, C.I., 2010a. Deposition and performance challenges of transparent conductive oxides on plastic substrates. In: Facchetti, A., Marks, T.J. (Eds.), Transparent Electronics from Synthesis to Applications. Wiley, Chichester.
Bright, C.I., 2010b. TCM 2010. 3rd International Symposium on Transparent Conductive Materials, 17–21 October 2010, Analipsi, Hersonissos, Crete, Greece.
Bright, C.I., 2014–2018. ITO and Alternative TCO: from fundamentals to controlling properties. Class C-337, Annual Technical Conference of the Society of Vacuum Coaters.
Bright, C. I., Woodard, F. E., Pace, S. J. and Kozak, J.G. (Southwall technologies Inc) (1998). Antireflective coatings comprising a lubricating layer having a specific surface energy. US patent 5,744,227, 28 April 1998.
Burstein, E., 1954. Anomalous optical absorption limit in InSb. Phys. Ther. Rev. 93, 632.
Cairns, D.R., Wittell, R.P., Sparacin, D.K., Sachsman, S.M., Paine, D.C., Crawford, G.P., Newton, R.R., 2000. Strain-dependent electrical resistance of tin doped indium oxide on polymer substrates. Appl. Phys. Lett. 76, 1425.
Chopra, K.L., Major, S., Pandya, D.K., 1983. Transparent conductors—a status review. Thin Solid Films 102, 1–46.
Coutts, T.J., Young, D.L., Li, X., 2000. Characterization of transparent conducting oxides. MRS Bull. (25 August 2000).
Displaybank, I.H.S., 2012. Transparent Display Technology and Market Forecast. San Jose, CA, Available from: http://www.displaybank.com/_eng/research/report_view.html?id=768&cate=6 (Accessed 19 November 2012).
Dobbertin, T., Werner, O., Meyer, J., Kammoun, A., Schneider, D., Riedl, T., Becker, H., Johnnes, H., Kowalsky, W., 2003. Inverted hybrid organic light-emitting device with polyethylenedioxythiophene-polystyrene sulfonate as an anode buffer layer. Appl. Phys. Lett. 83, 5071.
Exarhos, G.J., Zhou, X.-D., 2007. Discovery-based design of transparent conducting oxide films. Thin Solid Films 515, 7025–7052.
Facchetti, A., Marks, T.J. (Eds.), 2010. Transparent Electronics from Synthesis to Applications. Wiley, Chichester.
Fortunato, E., Barquinha, P., Goncalves, G., Pereira, L., Martins, R., 2010. Oxide semiconductors: from materials to devices. In: Facchetti, A., Marks, T.J. (Eds.), Transparent Electronics from Synthesis to Applications. Wiley, Chichester.
Frank, G., Kostlin, H., 1982. Electrical properties and defect model of tin-doped indium oxide layers. Appl. Phys. Solids Surf. 27, 197.

Fraser, D.B., Cook, H.D., 1972. Highly conductive transparent films of sputtered $In_{2-x}Sn_xO_{3-y}$. J. Electrochem. Soc. 119, 1368.

Furubayashi, Y., Hitosugi, T., Yamaoto, Y., Hirose, Y., Kinoda, G., Inaba, K., Shimada, T., Hasegawa, T., 2006. Novel transparent conducting oxide: anatase $Ti_{1-x}Nb_xO_2$. Thin Solid Films 496, 157–159.

Ginley, D.S., Bright, C.I., 2000. Transparent conducting oxides. Guest Editors, MRS Bull. 15–18.

Granqvist, C.G., 1989. Spectrally selective surfaces for heating and cooling applications. In: Tutorial Texts in Optical Engineering. Vol. TT 1. SPIE Optical Engineering Press, SPIE—The International Society for Optical Engineering, Bellingham, WA.

Granqvist, C.G., 2007. Transparent conductors as solar energy materials, a panoramic review. Sol. Energy Mater Sol. Cells 91 (13), 1529–1598.

Granqvist, C.G., 2010. Oxide-based electrochromics. In: Facchetti, A., Marks, T.J. (Eds.), Transparent Electronics from Synthesis to Applications. Wiley, Chichester.

Granqvist, C.G., Hultaker, A., 2002. Transparent and conducting ITO films: new developments and applications. Thin Solid Films 411, 1–5.

Gu, G., Bulovic, V., Forrest, S.R., 1996. Transparent organic light-emitting devices. Appl. Phys. Lett. 85, 3911.

Haacke, G., 1976. New figure of merit for transparent conductors. J. Appl. Phys. 47 (9), 4086.

Hamberg, I., Granqvist, C.G., 1986. Evaporated Sn-doped In_2O_3 films: basic optical properties and applications to energy-efficient windows. J. Appl. Phys. 60, R123.

Hayashi, K., Matsuishi, S., Kamiya, T., Hirano, M., Hosono, H., 2002. Light-induced conversion of an insulating refractory oxide into a persistent electronic conductor. Nature 419, 462.

Hitosugi, T., et al., 2008. Electronic band structure of transparent conductor: Nb-doped anatase TiO_2. Appl. Phys. Express. 1, 111203.

Hosono, H., 2010. Transparent oxide semiconductors: Fundamentals and recent progress. In: Facchetti, A., Marks, T.J. (Eds.), Transparent Electronics from Synthesis to Applications. Wiley, Chichester.

Huang, J., Li, G., Li, J.-H., Chen, L.-M., Yang, Y., 2010. Transparent solar cells based on organic polymers. In: Facchetti, A., Marks, T.J. (Eds.), Transparent Electronics from Synthesis to Applications. Wiley, Chichester.

Kawazoe, H., Ueda, N., Un'no, H., Omata, T., Hosono, H., Tanoue, H., 1994. Generation of electron carriers in insulating thin film of $MgIn_2O_4$ spinel by li+ implantation. *J. Appl.* Phys. 76, 7935.

Kawazoe, H., Yanagi, H., Ueda, K., Hosono, H., 2000. Transparent p-type conducting oxides: design and fabrication of p-n heterojunctions. MRS Bull. 25, 28–36.

Kawazoe, H., Yasukawa, M., Hyodo, H., Kurita, M., Yanagi, H., Hosono, H., 1997. P-type electrical conduction in transparent thin films of $CuAlO_2$. Nature (London) 389, 939–942.

Kim, J.S., Cacialli, F., Granstrom, M., Friend, R.H., Johanson, N., Salaneck, W.R., Daik, R., Feast, W.J., 1999. Characterisation of the properties of surface-treated indium-tin oxide thin films. Synth. Met. 101, 111.

Klein, C., 1990. Microwave shielding effectiveness of EC coated dielectric slabs. IEEE Trans. Microwave Theory Tech. 38, 321–324.

Kowalsky, W., Gorrn, P., Meyer, J., Kroger, M., Johannes, H., Riedl, T., 2007. See-through OLED displays. Proc. SPIE 6486, 64860L.

Kudo, A., Yangi, H., Hosono, H., Kawazoe, H., Yano, Y., 1999. Fabrication of transparent p–n heterojunction thin film diodes based entirely on oxide semiconductors. Appl. Phys. Lett. 75 (18), 2851–2853.

Lampert, C.M., 1981. Heat mirror coatings for energy conserving windows. Solar Energy Mat. 6(1).

Leterrier, Y., Medico, L., Demarco, F., Manson, J.-A.E., Bouten, P.C.P., de Goede, J., Nisato, G., 2003. Mechanical properties of transparent functional thin films for flexible displays. 46th Annual Technical Conference Proceedings of the Society of Vacuum Coaters, May 3–8, 2003 San Francisco, CA, pp. 169–174.

Ma, R., Levermore, P.A., Mandlik, P., Pang, H., Brown, J.J., 2011. In: Technology gap analysis of vacuum coated materials for flexible OLED display and lighting applications. 54th Annual Technical Conference Proceedings. Society of Vacuum Coaters, Chicago, IL. 16–20 April 2011.

Macleod, H.A., 2001. Thin-Film Optical Filters, third ed. Institute of Physics Publishing, Bristol/Philadelphia.

McMaster, M. A. (1947) (Libby-Owens-Ford) (filed 5 October 1942) U.S. Patent 2,429,420, issued 21 October 1947, (see other McMaster US and British patents too).

Medvedeva, J.E., 2006a. Unconventional approaches to combined optical transparency with electrical conductivity. 1st International Symposium on Transparent Conductive Oxides, Crete, Greece, Conference Proceedings, FC4–1–FC4–2.

Medvedeva, J.E., 2006b. Magnetically mediated transparent conductors: In_2O_3 doped with Mo. Phys. Rev. Lett. 97, 086401.

Minami, T., 1999. Transparent and conductive multicomponent oxide films prepared by magnetron sputtering. J. Vac. Sci. Technol. A 17 (4), 1765.

Minami, T., Sonohara, H., Kakumu, T., Takata, S., 1995. Highly transparent and conductive $Zn_2In_2O_5$ thin films prepared by RF magnetron sputtering. Jpn. J. Appl. Phys. 34 (Part 2), L971–L974.

Nomura, K., Ohta, H., Takagi, A., Kamiya, T., Hirano, M., Hosono, H., 2004. Room-temperature fabrication of transparent flexible thin-film transistors using amorphous oxide semiconductors. Nature 432, 488–492.

Ochs, D., Rozanski, P., Ozimek, P., 2009. In: Progressive DC power for TCO deposition. 52nd Annual Technical Conference Proceedings, Santa Clara, CA, 9–14 May 2009, P60–63.

Riedl, T., 2010. Transparent OLED displays. In: Facchetti, A., Marks, T.J. (Eds.), Transparent Electronics from Synthesis to Applications. Wiley, Chichester.

Ryu, Y.R., Lee, T.S., Leem, J.H., White, H.W., 2003. Fabrication of homostructural ZnO p–n junctions and ohmic contacts to arsenic-doped p-type ZnO. Appl. Phys. Lett. 83, 4032.

Sato, Y., Akizukia, H., Kamiyamab, T., Shigesatoa, Y., 2008. Transparent conductive Nb-doped TiO_2 films deposited by direct-current magnetron sputtering using a TiO_{2-x} target. Thin Solid Films 516, 5758–5762.

Schwarz-Schampera, U., Herzig, P.M., 2002. Indium-Geology. Springer, Mineralogy and Economics.

Szyszka, B., Ruske, F., Sittinger, V., Pflug, A., Werner, W., Jacobs, C., Ulrich, S., Kaiser, A., 2006. Transparent conductive oxides for large area applications by in-line magnetron sputtering. 1st International Symposium on Transparent Conductive Oxides, 23–25 October 2006, FORTH Crete, Greece.

Tate, J., Keszler, D.A., 2010. p-type wide-band-gap semiconductors for transparent electronics. In: Facchetti, A., Marks, T.J. (Eds.), Transparent Electronics from Synthesis to Applications. Wiley, Chichester.

Tsukazaki, A., Ohtomo, A., Omuma, T., Ohtani, M., Makino, T., Sumiya, M., Chichibu, S., Fuke, S., Segawa, Y., Ohno, H., Koinuma, H., Kawasaki, M., 2004. Repeated temperature modulation epitaxy for p-type doping and light-emitting diode based on ZnO. Nat. Mater. 5, 42.

Walker, G., 2010. In: Touch technologies tutorial. 2010 Flexible Electronics & Displays Conference, Phoenix Arizona, USA, 1–4 February 2010.

Yanagi, H., Hase, T., Ibuki, S., Ueda, K., Hosono, H., 2001. Bipolarity in electrical conduction of transparent oxide semiconductor $CuInO_2$ with delafossite structure. Appl. Phys. Lett. 78, 1583–1585.

Zhang, S.X., Kundaliya, D.C., Yu, W., Dhar, S., Young, S.Y., Salamanca-Riba, L.G., Ogale, S.B., Vispute, R.D., Venkatesan, T., 2007. Niobium doped TiO_2: Intrinsic transparent metallic anatase versus highly resistive rutile phase. J. Appl. Phys. 102, 013701.

Zunger, A., 2003. Practical doping principles. Appl. Phys. Lett. 83 (1, 7), 57–59.

SOURCES OF FURTHER INFORMATION AND ADVICE

Dawar, A.L., Joshi, J.C., 1984. Review—semiconducting transparent thin films: their properties and applications. J. Mat. Sci. 19, 1–23.

FURTHER READING

Bright, C., 2008. In: Alternative Transparent Conductive Oxides (TCO) to ITO. 51st Annual Technical Conference Proceedings of the Society of Vacuum Coaters, pp. 840–850.

Minami, T., 2005. Transparent conducting oxide semiconductors for transparent electrodes. Semicond. Sci. Technol. 20, D35–S44.

Noufi, R., Romero, M.J., Jiang, C.-S., Yan, Y., Abu-shama, J., Ramanathan, K., NREL Invited Presentation, 2004. Why do CIGS-based solar cells have superior performance? Insight into the properties of grain boundaries and the surface as influenced by the growth dynamics. European MRS Meeting, Thin Film Chalcogenide Symposium.

Yanagi, H., Ueda, K., Ohta, H., Orita, M., Hirano, M., Hosono, H., 2002. Fabrication of all oxide transparent p-n homojunction using bipolar $CuInO_2$ semiconducting oxide with delafossite structure. Solid State Commun. 121, 15–17.

CHAPTER

Optical coatings in the space environment☆

22

Denny Wernham*, Angela Piegari†

*The European Space Agency (ESA), Noordwijk, The Netherlands** *Optical Coatings Group, ENEA, Rome, Italy†*

22.1 INTRODUCTION

The environment in space is a particularly harsh one for optical coatings. For porous coatings, the space vacuum causes a spectral shift and a change in stress due to water release. Atomic oxygen (ATOX) present in low earth orbits (LEOs) causes erosion of coatings. Space also has a harsh radiation environment which can cause absorptive losses in optics due to color center activation or polymerization of organic contaminants of the surface of optics. Coatings exposed to solar radiation are subject to ultraviolet (UV) fixation of outgassing contaminants. Similarly, high-power laser irradiation of coatings in the presence of contaminant outgassing sources results in laser-induced contamination (LIC), high absorption, and, in the worst case, laser damage. An important effect for high-power laser optics is the reduction of the laser-induced damage threshold (LIDT) of porous coatings in vacuum. An additional factor is the often high thermal excursion coatings can experience in space, typically ranging from −50°C to +80°C, notwithstanding deep space missions involving cryogenic temperatures, where coatings have to withstand −270°C and missions to the inner planets, or solar missions where coatings may have to survive temperatures in excess of 300°C. This chapter attempts to give a general overview of the effects of the space environment on optical coatings with some examples from tests carried out on ground and on space missions.

22.2 THE SPACE ENVIRONMENT

The space environment may induce a degradation of performance of optical coatings, which are exposed to high-energy particulate and electromagnetic radiations, high-energy ATOX, high vacuum, and large temperature excursions simultaneously.

☆Chapter originally authored by D. Wernham and revised by A. Piegari.

Optical Thin Films and Coatings. https://doi.org/10.1016/B978-0-08-102073-9.00022-9
Copyright © 2018 Elsevier Ltd. All rights reserved.

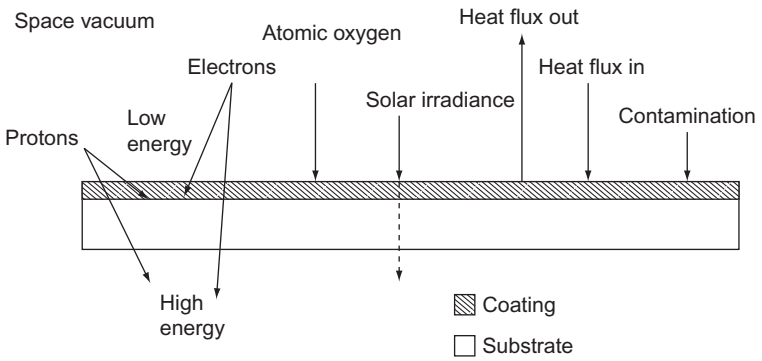


FIG. 22.1

The schematic gives an overview of the main environmental components of space that can have an impact on optical coatings and their performance.

The schematic of Fig. 22.1 gives an overview of the main environmental components of space that can have an impact on optical coatings and their performance.

The space environment effects are briefly described in the following sections along with some examples of the impacts that they can have on space optics. A good overview of the space environment is given by Fortescue et al. (2004) and in the relevant European Co-operation for Space Standardization (ECSS) standard (ECSS-E-ST-10-04C, 2008).

22.2.1 GENERAL OVERVIEW OF OPTICS IN SPACE

Optics are used extensively on spacecraft, not only for optical instrumentation, where almost all conceivable coating types are utilized. These range from the very large—for example, the primary mirrors of space-borne telescopes such as the Hubble Space Telescope and the Herschel and Planck satellites, which can be several meters in diameter—to the very small—for example, laser optics, which can be a few millimeters in diameter, necessarily minimized due to the severe weight and volume constraints placed on satellite payloads. Cover glasses protect solar cells, the main form of power generation on most satellites, from the harsh solar environment. Optical solar reflectors (second surface mirrors) on radiators and the outer surfaces of the satellite form the key means of thermal control of the satellite via radiative heat exchange with space. In these cases, the optical function is to have a high emissivity of the heat conducted from the satellite to space, while minimizing absorptance of radiation sources impinging upon the satellite. Multilayer insulation (MLI) is used in order to thermally isolate sensitive equipment from heat sources or to keep equipment temperatures high enough for proper operation via alternating low emissivity metal coatings and low thermal conductance between the layers. Telescopes which look at the very cold universe have reflective coatings which minimize emissivity in order to increase measurement sensitivity.

High-power laser optics with unique challenges have been developed for LIDAR instruments. Not only do they need sufficient margins with respect to laser damage threshold, but also they are particularly sensitive to optical degradation via the mechanism of LIC, particularly at the short laser wavelengths (UV).

One of the major issues surrounding space optics is that if degradation does occur, there is usually no way to fix the problem in orbit (a famous exception to this was the Hubble Space Telescope, but even then there were very large cost and mission downtime implications). Hence, the basic approach is that prevention is better than cure. The above necessitates a very high level of functional performance testing on ground in order to guarantee the performance in orbit. Since typical satellite mission durations range from 3 to 15 years, there is also a fundamental problem in testing for sufficient durations in order to make proper predictions on the end-of-life (EOL) performance. This has necessitated forms of accelerated testing which may not be completely representative. Another issue is the synergistic effect when multiple space environment effects are present at the same time. Good examples of this are the presence of contaminants together with UV radiation or high-intensity laser radiation.

22.2.2 IMPACT OF SPACE VACUUM

Space vacuum involves pressures below 10^{-8} mbar for a typical satellite LEO environment and pressures lower than this for higher orbits and planetary missions. Planetary landing missions for bodies such as Mars or Titan, which have atmospheres, will have different operational constraints.

For a highly densified coating, vacuum has little impact but for porous coatings the shift of the spectral response of the coating to lower wavelengths is typically observed. Despite the fact that this is a well-known phenomenon, porous coatings are present in many of the instruments being manufactured today. Fig. 22.2A shows the cross-sectional transmission electron micrograph (TEM) of a fully dense coating deposited using an assisted sputtering technique. The corresponding TEM for a conventional electron beam evaporated coating is shown in Fig. 22.2B. It is clear from a comparison of the micrographs of the two coatings that the sputtered coating has a much less porous structure. Conversely, the classical unassisted e-beam evaporated coating clearly shows a large degree of porosity, particularly at the interfaces and within the high index material. Air-to-vacuum spectral shifts of a dense and porous coating are shown in Plates 22.1 and 22.2 (see color section), respectively.

The impacts on instrument performance caused by the air-vacuum shift can be significant. In the case of the ALADIN laser, payload on the ADM-Aeolus satellite (ESA), the air-vacuum shift of a dielectric polarizer within the master oscillator of the laser, caused a complete failure due to an increase in the passive losses of the laser cavity. It is clear that coatings in space should be fully densified to avoid this effect, in addition to allowing representative performance testing on ground that can be related to in-orbit performance. The lesson learned in this case is to test the air-vacuum shift on the coatings that will be exposed to space vacuum, and not to

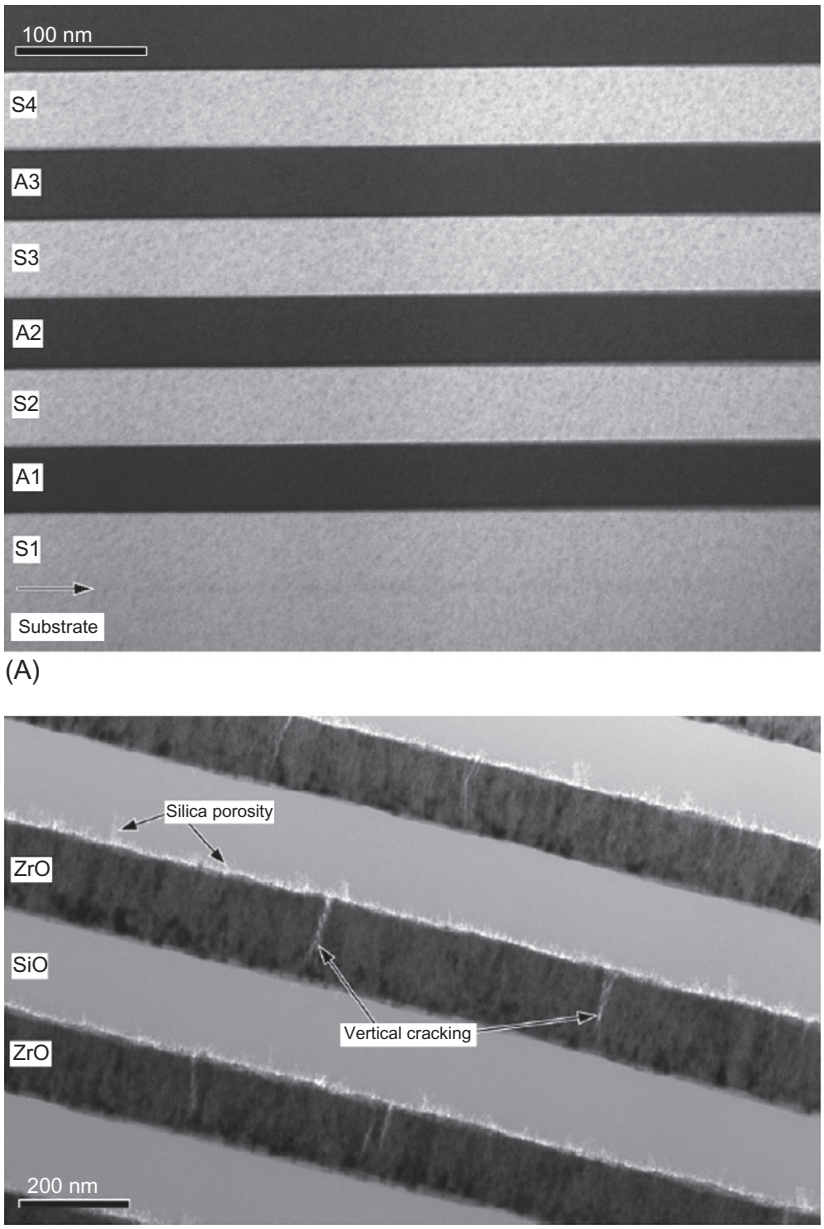


FIG. 22.2

(A) Cross-sectional transmission electron micrograph (TEM) of a fully dense coating deposited using an assisted sputtering technique; (B) corresponding TEM for a conventional electron beam evaporated coating.

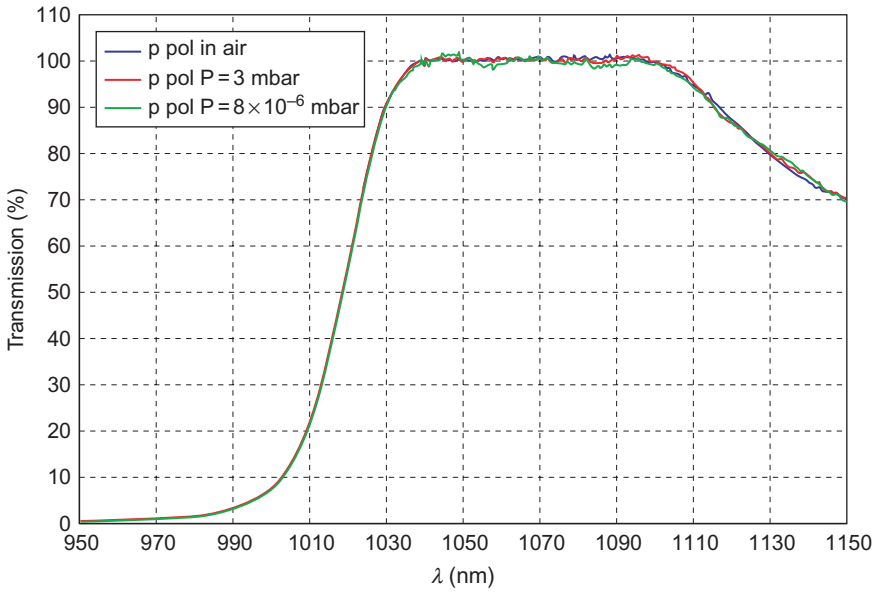


PLATE 22.1

Air-to-vacuum spectral shift of the transmission curve of a dense coating.

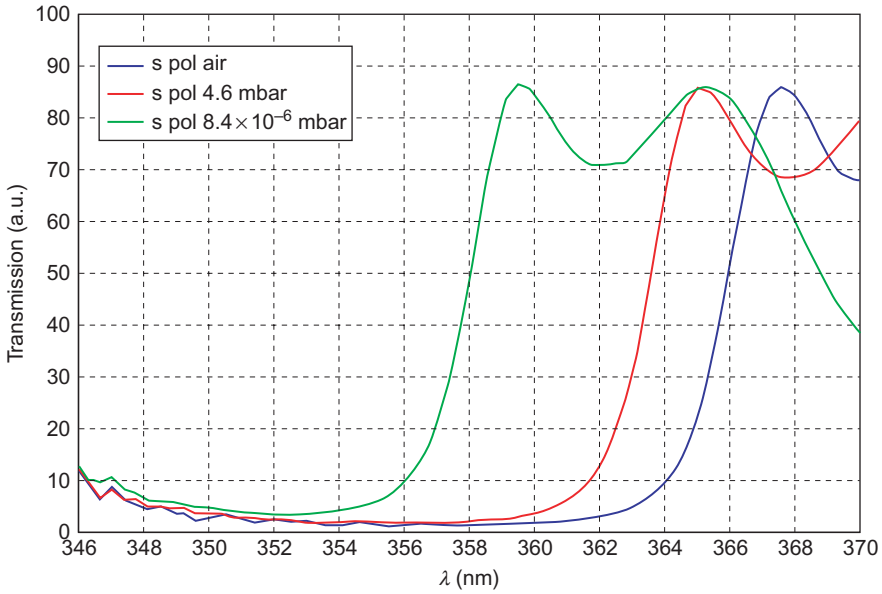


PLATE 22.2

Air-to-vacuum spectral shift of the transmission curve of a porous coating.

simply accept from the manufacturer that coatings are vacuum compatible. Special attention has to be given to narrow band coatings, edge filters, and dielectric polarizers where small vacuum shifts can have a large impact on the coating and instrument performance.

Another impact of the loss of water from porous coatings is the change in the overall stress of the coatings. In general, a change in stress from compressive to tensile is observed. For instruments containing alignment-sensitive focal planes, this can cause an unacceptable level of defocusing due to the induced deformation of the substrate.

There is also an impact of water release on the laser damage threshold for laser coatings where a decrease in the LIDT in tests performed under vacuum conditions compared to tests of the same samples in air is observed (Riede et al., 2007). This is analogous to the toughening of glass where a thin compressively stressed layer is induced at the surface, either thermally or chemically, in order to increase the fracture toughness, at the expense of more tensile stresses in the bulk. Fig. 22.3A shows the LIDT results of an S-on-1 test procedure (multiple laser shots per site) on a coating sample prepared by conventional, unassisted electron beam evaporation in air and in vacuum. For comparison, air and vacuum LIDT test results for a fully densified coating prepared by ion assisted deposition are shown in Fig. 22.3B. The results of the test show a significant reduction in the LIDT of the porous coating of approximately a factor of 5 $\times$.

This decrease is only observed on coatings which have a significant level of porosity. In the case of dense coatings, there is no decrease in the LIDT from air-to-vacuum. In order to demonstrate that this effect was due to the release of water and the resulting increase in the tensile stress of the coating, Riede et al. used a thin cover glass lamina substrate and measured the deflection of the coating in vacuum. The results of the test are shown in Fig. 22.4. The deflection is fully reversible when going from air-to-vacuum and back again. Tests of uncoated lamina did not show any bend, isolating the effect to the porous coating. Tests conducted in He atmospheres gave similar results to N_2, indicating that the thermal conductance was not a major effect (Allenspacher et al., 2005).

22.2.3 THERMAL CYCLING IN VACUUM

As well as the vacuum effects described above, coatings in space are often cyclically subjected to large thermal excursions. Generally speaking, optical instruments, especially those which are alignment sensitive, are contained within environments which are thermally controlled by means of heaters and radiators in order to minimize the impact of thermal variations. Optics are still, however, subjected to nonoperational thermal cycles during orbit acquisition, and when the satellite goes into safe mode as a result of an operational failure. This will typically involve eight or more thermal cycles in the range of -40°C to +50°C for the qualification of optics operating in an LEO. Solar array cover glasses are designed to be directly exposed to the sun and are thus exposed to 1 solar constant, sometimes referred to as air mass zero (1 AM0),

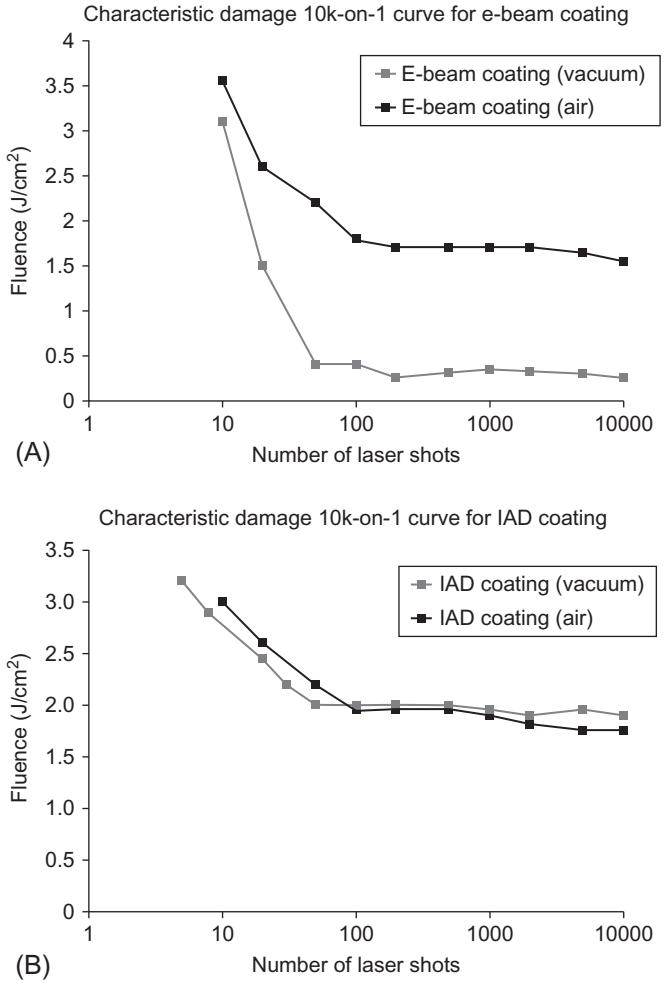


FIG. 22.3

(A) Results of an S-on-1 test on a coating sample prepared by conventional, unassisted electron beam evaporation in air and in vacuum; (B) air and vacuum LIDT test results for a coating prepared by ion assisted deposition (IAD).

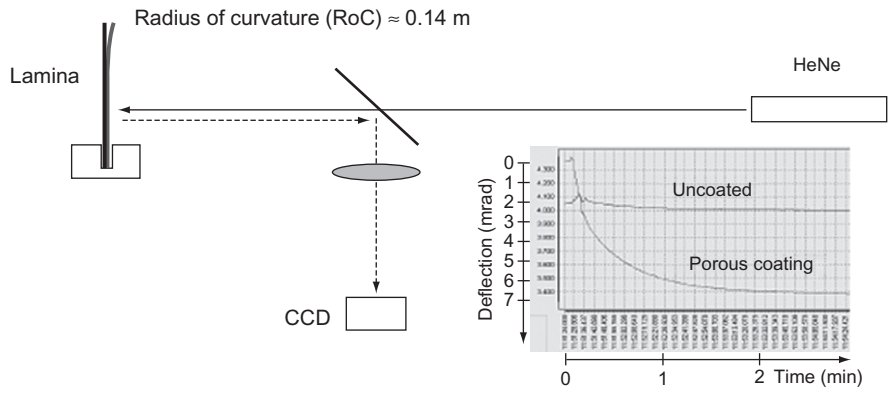


FIG. 22.4

Results of a test using a thin coated lamina measuring the deflection in vacuum.

amounting to some 1375 W m^{-2} of solar flux. This typically means that they will be exposed to thermal cycles between −40°C and +120°C. Coatings that are on inner planet or solar missions can experience much higher thermal excursions as they are exposed to up to 20 solar constants (several 100°C) and extremely low temperatures during eclipses (−150°C). Optics that are designed to look into deep space, or cryogenic detectors, contain coatings which have to operate at even lower temperatures. An example of the spectral behavior of a metal-dielectric filter during the thermal cycle is shown in Plate 22.3 (see color section). The test has been carried out in vacuum with eight cycles between −100°C and +45°C and with a temperature gradient of 2°C/min. A shift of 2 nm toward short wavelengths can be noticed at the lowest temperature, but the optical performance is recovered, returning to ambient temperature.

In addition to temperature-induced changes in the refractive index of the coating materials, the layers may suffer dimensional changes. Failures of coatings due to vacuum thermal cycles occur frequently, due to the change in stress caused by water release as well as the stresses caused by the different coefficients of thermal expansion of the materials which make up the layers of the coating and the substrate. The selection of the substrate is important because the change in substrate dimensions caused by temperature changes could be the dominant factor. A typical failure due to the vacuum thermal cycle of a space optic is shown in Fig. 22.5A. A high magnification image of the failure is shown in Fig. 22.5B, indicating that this was

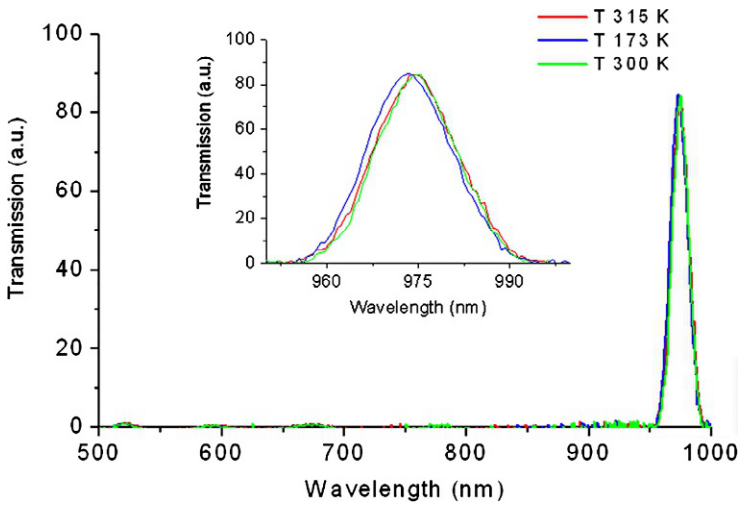
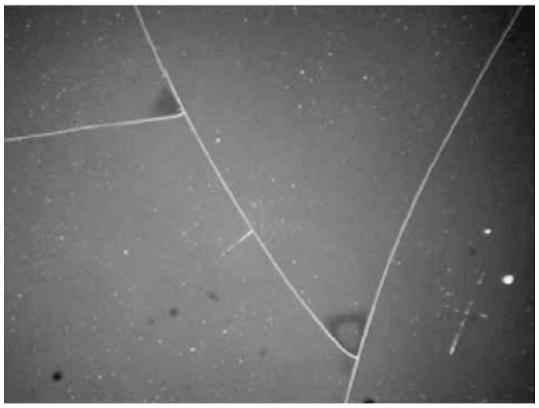


PLATE 22.3

Transmission curve of a metal-dielectric filter (21 layers) measured in vacuum (10^{-6} mbar) during the thermal cycle (eighth cycle), starting from the highest temperature and ending at ambient temperature.



(A)



(B)

FIG. 22.5

(A) Typical failure due to the vacuum thermal cycle of a space optic; (B) high magnification image of the failure, indicating that this was a stress failure.

a stress failure. The key for these coatings is to ensure that they are qualified with sufficient margins (generally $\pm 10°C$ of the nominal values), paying attention to the potential rate of change of the thermal cycles in addition to the actual temperature levels. It is important to differentiate between thermal cycling in vacuum and thermal cycling carried out under ambient pressure conditions, as coatings that survive in the latter can often fail under vacuum testing. It is still common practice for suppliers to test thermal cycling under ambient pressure nitrogen conditions to save costs, only to find that there are failures during subsystem or satellite level vacuum thermal cycle tests where the rectification of the problem is far more costly. Coatings that are designed to operate in vacuum should be tested in vacuum.

22.2.4 SOLAR IRRADIANCE

The main impact from the solar spectrum comes from the higher energy UV wavelengths which can cause darkening of coatings due to color center formation or polymerization of organic contaminants. The general characteristic of the degradation is that there is typically an increase in the absorption of the coatings at the UV end of the spectrum which becomes less prevalent at longer wavelengths.

This degradation in performance is particularly serious for solar cell cover glasses and optical solar reflectors used in radiators. In the former case, there can be a significant reduction in the conversion efficiencies of the cells and a resulting loss in power generation of the array, potentially leading to parts of the satellite payload being shut down before its nominal mission lifetime has been reached. In the latter case, there is a loss in the efficiency of the radiator resulting in excessive heating and potential loss of the thermal control of the satellite. Degradation of a solar cell cover glass tested with UV irradiation in vacuum is shown in Plate 22.4 (see color section). Note that the optic is made of a coating on an aluminum mirror in order that both reflective and transmissive losses could be measured during the test. There is an annealing effect which can reverse the degradation caused by UV exposure in vacuum when the optics are reexposed to ambient conditions. This, of course, does not happen in space, meaning that performance degradation effects can easily be underestimated if an in situ measurement is not used during testing. It should be noted that great care is required in performing vacuum testing for space optics where chamber contamination due to outgassing has to be minimized as far as possible, as this can cause a similar degradation in the spectral performance.

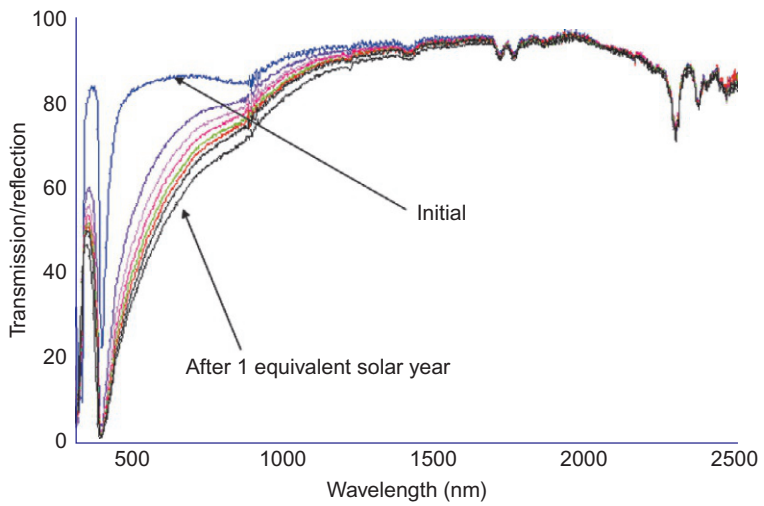


PLATE 22.4

Degradation of a solar cell cover glass tested with UV irradiation in vacuum.

For optical solar reflectors, degradation leads to an increase in the solar absorptance of the coating, meaning that the radiative efficiency (proportional to absorptance and emissivity) is degraded, leading to an overall increase in the temperature of the satellite.

22.2.5 PARTICULATE RADIATIONS

For optics in space, the main concern is caused by protons and electrons. The galactic cosmic rays are composed primarily of high-energy protons (89%) but they also include alpha particles (10%) and heavier nuclei (1%), while the solar wind consists of charged particles, mainly protons and electrons with energy ranging from a few tens of keV to GeV. These particles can be qualitatively defined as low energy (<1 MeV) and high energy (>1 MeV). For coatings, low-energy particulate radiations are the most critical as the energy from these can be completely absorbed within the thin coating layers, whereas higher energy radiations are only partially absorbed and are more of a problem for the substrate. Protons with energies from a few keV to some hundreds keV can cause particularly severe degradation due to the fact that the majority of damage occurs where the protons stop in the material.

The degradation effects caused by particulate radiations are generally similar to those caused by UV irradiation inasmuch as there is typically more degradation in optical performance at shorter wavelengths, which gets gradually less at longer wavelengths. In some cases, depending on the degradation mechanism, there is an annealing effect, which reverses the degradation when optics are reexposed to ambient conditions. Thus, the optical performance should be measured in situ during the test, in order to make a proper evaluation of the in-orbit performance.

An example of degradation of an optic exposed to various equivalent doses of low-energy protons (240 keV) is shown in Plate 22.5 (see color section). As in the previous example, the optic has been placed on an aluminum mirror in order that both reflective and transmissive losses could be measured during the test. Another example of transmission change detected in a dielectric filter, exposed to 60 keV protons with fluence of 10^{13} p/cm^2, is shown in Plate 22.6 (see color section). The filter is made of 29 alternating layers of SiO_2 and HfO_2, the transmission peak is centered in the UV, and a shift in the peak wavelength has been detected after irradiation, which seems to be caused by a modification of the refractive index of the SiO_2 material (Di Sarcina et al., 2014). Low-energy protons could be also responsible for changes in the coating morphology as shown by Pelizzo et al. (2011) for extreme UV coatings (Si/Mo multilayer structures).

Electrons induce similar degradation effects, although care has to be taken to ensure that the proper dose is applied to the test article due to the much larger stopping distances of electrons compared to protons (Russell and Jones, 2003). Experiments with gamma rays (Baccaro et al., 2005) and alpha particles (Nardello et al., 2013) have been also carried out on optical coatings and variations of optical properties have been found in some materials.

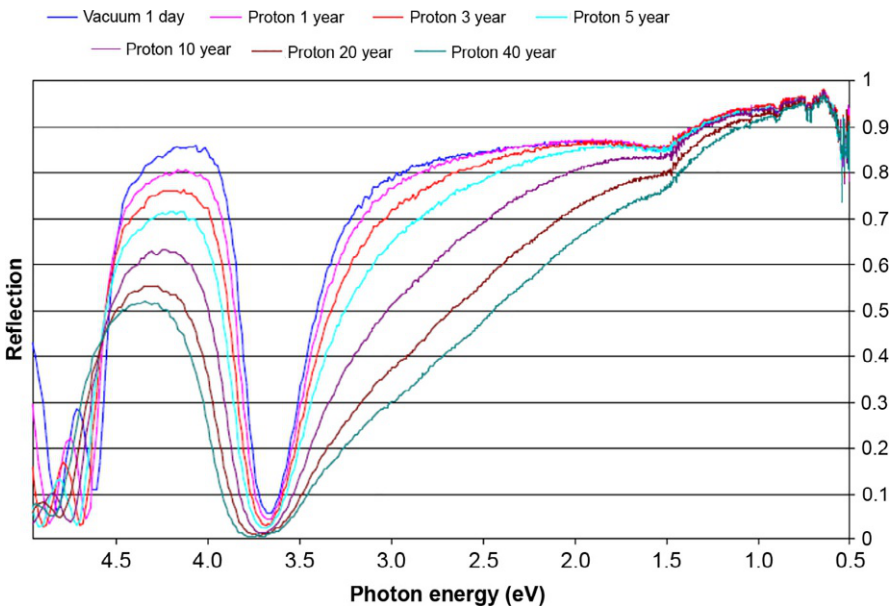


PLATE 22.5

An example of degradation of an optic exposed to various equivalent doses of low-energy protons (240 keV).

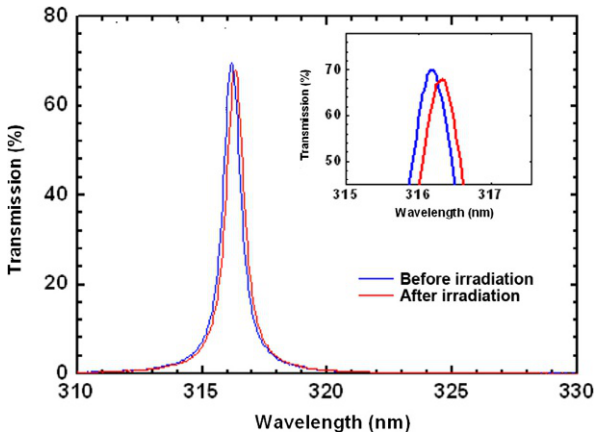


PLATE 22.6

Transmission curve of a multilayer dielectric filter (SiO_2/HfO_2) measured before and after exposure to low-energy (60 keV) protons.

Several data on material behavior in space have been collected during the NASA MISSE (Materials International Space Station Experiments—https://www.nasa.gov/mission_pages/station/research/experiments/72.html) that are important to analyze synergistic effects. Some results of testing of coatings on MISSE-7 have been reported by Pellicori et al. (2014).

The susceptibility to particulate radiation-induced degradations can be mitigated by suitable dopants. An example is the cerium doping used in solar cell cover glasses or radiation resistant glasses where the glass is protected by the redox reaction of Ce^{3+} being converted to Ce^{4+} and vice versa (Haynes, 1970). Unprotected glasses such as BK7 show a rapid darkening if they are not properly doped and should generally be avoided for use in space applications (Gusarov et al., 2007). Note that the radiation-hard glasses doped with Cerium, even though remaining transparent, may show a variation of the refractive index over the irradiated area when exposed to gamma rays and a consequent variation of the optical path difference (OPD). This effect could degrade the wavefront of the transmitted beam (Doyle, 2017).

22.2.6 ATOMIC OXYGEN

ATOX is the main atmospheric component present in LEOs up to altitudes of 700 km. The main effect of ATOX is reactive sputtering and erosion of surfaces, particularly those surfaces which contain elements that react with oxygen. The main effect of ATOX is the erosion caused by the relative velocity of approximately 8 km s^{-1} between the oxygen atoms and the spacecraft due to the orbital velocity of the spacecraft. Thus, the main impact occurs in the RAM direction of the spacecraft. Silver is particularly prone to ATOX degradation (De Rooij, 1985) and is sometimes used as a reflector coating on satellite telescope optics. Although protective layers are usually applied, care should be taken due to the presence of pinholes and other defects in the protective coating layers, and testing should always be carried out for any optics which are exposed to ATOX.

22.3 CONTAMINATION

Contamination is a major concern for satellite optical payloads, especially those which have multiple surfaces. The contamination can come from the assembly process, during integration, and during verification testing, from the launch and in orbit, over the mission lifetime of the instrument. This section gives a brief introduction to the various contamination sources that typically affect space optics.

22.3.1 TERRESTRIAL CONTAMINATION

Terrestrial contamination is an ever-present problem for optical components being sent into space. The main contributors are particulate contamination and molecular contamination. The general guidelines of contamination control are similar to those

employed for radiation protection for personnel who work with radioactive materials, that is, time, distance, shielding, and monitoring. Good practice is to minimize the time for which the parts are exposed to any contaminant sources, maximize the distance from sensitive items to contamination sources, use physical barriers, for example, protective covers or positive pressure gas purges to shield sensitive items, and always monitor the contamination levels. The contamination control methodologies to be used for space equipment are described in detail in the relevant ECSS standard (ECSS-Q-ST-70-01C, 2008).

The main source of particulate contamination in clean rooms is usually from people working in the proximity of the optics, from dead skin flakes, fibers from clothing, and contamination transferred from footwear. It is thus important to have appropriate contamination controls in place and, in particular, to have a clear demarcation between "clean" and "dirty" areas, to define the acceptable levels of particle contamination, and to monitor the contamination levels during the production of the optics. Typical methods of monitoring contamination are to place a clean witness sample which follows the optics through the entire assembly, integration, and testing phases. In addition to this, periodic particle counting should be performed in order to determine if a contaminating event has occurred and to check the levels against the required values.

The general particulate contamination monitoring in clean rooms relies upon airborne measurements of the particle concentrations. It should be noted that for space optics, the main concern is the particle "fallout," that is, those particles which are heavy enough to fall under the influence of gravity onto the sensitive surfaces. Only a small quantity of these particles is detected by airborne particle counters which are thus regarded as a warning system for potential contaminating events. It is also worth noting that a vertical surface will generally have a factor of $10\times$ less contamination than a horizontal one. Particle contamination can be particularly severe for laser optics where it can cause a significant reduction of the laser-damage threshold, or in optical systems which are very sensitive to stray light. In general, it is a sensible precaution to have a qualified cleaning procedure that can be used on optics in the event that the contaminant levels are deemed to be outside the required levels. Fig. 22.6 shows the impact of high particulate contamination on a laser optic which has been irradiated. From the figure, it can be seen that standing waves have been "written" into the coated surface from the interference generated by the particles.

The main source of molecular contamination on optical surfaces is generally from the offgassing of organic materials, that is, the release of volatile, low molecular weight species under ambient pressure conditions. It is important to avoid organic contamination on optics, which could subsequently darken due to the polymerization of the contaminants in the space environment caused by UV and particle irradiation. As with particulate contamination, a contamination budget should be defined beforehand, and monitored with a witness sample which follows the flight optics and is periodically measured. The typical contaminants encountered are hydrocarbons, silicones, and esters which can usually be identified from their infrared absorption spectrum. There is a dedicated ECSS standard

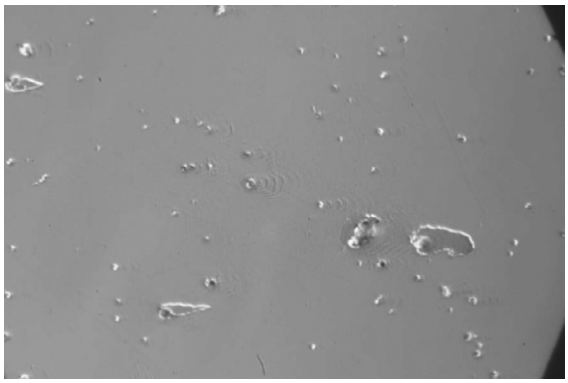


FIG. 22.6

An example of the impact of high particulate contamination levels causing laser damage on an optic.

(ECSS-Q-ST-70-05C, 2009) which describes how the monitoring of organic contamination is performed for space optics. It pays to have a qualified cleaning process in order to mitigate an unacceptable level of molecular contamination.

Another source of contamination is when the optics are incorporated into component-, system-, or satellite-level vacuum bakeouts or tests. Here the vacuum chamber, along with ground support equipment within it, can often be the source of contaminants. In this case, it is always best practice to check the vacuum compatibility of materials within the chamber, to incorporate a cold trap, and to perform a quartz crystal monitored bakeout of the vacuum chamber along with the ground support equipment at elevated temperature. This should be followed by a quartz crystal monitored blank test of the chamber at the test temperature prior to the flight optics being installed. Care should be taken when re-pressurizing the vacuum chamber. The chamber should be re-pressurized with dry nitrogen prior to cold traps or shrouds being warmed up in order to prevent redeposition of contaminants onto the sensitive optics.

There are also contaminants which can be present as part of the actual manufacturing of the optic itself which can have a severe impact when the optic is exposed to the space environment. Small concentrations of impurities in optical glasses and optical coatings can form color centers which can be subsequently activated by radiation in space. Care has to be taken with the purity of the substrates and raw materials used for the manufacture of optical coatings to be used for space and they should always be linked to a dedicated certificate of composition from the supplier and, if necessary, periodically checked by techniques sensitive to trace contaminant levels. Contaminants can also be introduced in the coating process itself, which could have an impact on the performance of the optic in space, such as the incorporation of crucible materials in the coatings for electron beam evaporated coatings or contaminants caused by arcing during sputtered coating deposition.

22.3.2 SPACE CONTAMINATION EFFECTS

The vacuum of space causes the efficient outgassing of nonmetallic materials which are unavoidably used in the construction of spacecraft. Some examples of these are adhesives; MLI used for spacecraft thermal control; carbon fiber reinforced plastic (CFRP) used for structures; cable insulation on electrical harnesses; and potting compounds and conformal coatings applied to electronics, to name a few. Great care is usually taken to reduce the outgassing levels of these materials as far as practically possible, via the use of high temperature, vacuum bakeouts of materials, subsystems, and at satellite level, prior to flight. However, some long-term outgassing flux will still remain which can accumulate over the many years of a typical satellite lifetime. There are standard methods for the screening of materials to be used in space vacuum which are described in the relevant ECSS standard (ECSS-Q-ST-70-02C, 2008).

Outgassing is particularly hazardous for cold space optics, where the efficiency of condensation of outgassing contaminants is significantly increased. Of course, even if extensive vacuum bakeouts have been undertaken, it is almost impossible to prevent readsorption of atmospheric moisture on the materials used in the satellite. The main preventative methods are therefore good instrument design (ensuring that view factors of the sensitive optics are restricted as far as possible from outgassing sources) and ensuring that the cold detector optics are the last ones to be cooled down. Lastly, heaters are often installed which allow recovery of performance via re-evaporation.

22.3.2.1 UV fixation of contaminants

The fixation of contaminants on surfaces which are also exposed to UV radiation has been studied by a number of groups (Tribble and Haffner, 1991; Pereira et al., 2003) which have shown that the deposition of outgassing contaminants on optical surfaces is greatly increased compared to the situation when no UV is present. This is due to UV-activated polymerization of contaminants, an increase in the molecular weight, and a consequent increase in the residence time on the surface of the optic. This effect highlights the sometimes insidious, synergistic effects that can occur in space, which are not always properly accounted for in qualification test campaigns.

22.3.2.2 Laser-induced contamination

A similar example to the UV fixation of contaminants is LIC, where highly absorbing deposits are formed in the areas of laser optics exposed to the high-intensity irradiation in nonoxidizing environments (Hovis et al., 1994). This has been studied extensively for the ALADIN and ATLID instruments (payloads on the ADM-Aeolus and EarthCARE satellites, respectively) which both contain high-intensity lasers operating at 355 nm (Riede et al. 2005; Tighe et al., 2008). An example of a fluorescing LIC deposit formed during a laser test is shown in Fig. 22.7A. A microscope image of an LIC deposit is shown in Fig. 22.7B. The degradation in performance can be dramatic. During a vacuum test of an ALADIN laser, the energy dropped by a factor of $2\times$ in 6 h due to LIC on the UV optics. LIC has also been implicated in the failure of the

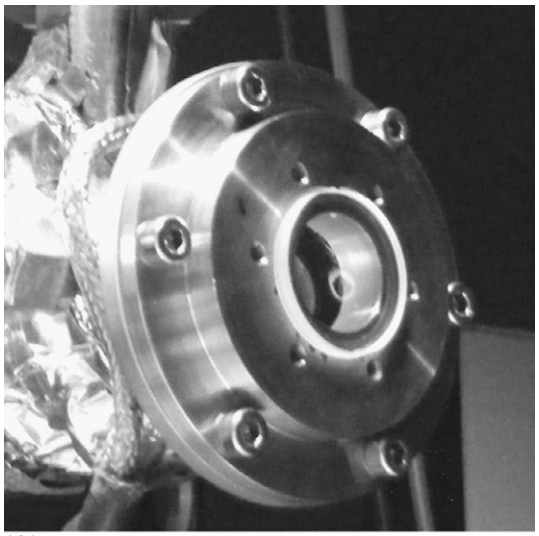


FIG. 22.7

(A) Example of a fluorescing LIC deposit formed during a laser test; (B) microscope image of an LIC deposit.

GLAS lasers on ICESAT (NASA), as well as in the rapid degradation observed on the LITE instrument which flew on the space shuttle (Winker et al., 1996).

Normal methods of mitigation against LIC, such as screening of "bad actor" materials, high-temperature vacuum bakeouts, reduction of view factors by baffling, and molecular absorbers, are only partially successful in eliminating LIC. One mitigation method which has proved to be successful is the implementation of a low-pressure oxygen environment which is used on the ALADIN instrument (Wernham et al., 2010). A much better method is to ensure that high-power lasers

are pressurized and that the number of vacuum exposed optics surfaces is minimized, which is the approach adopted for the ATLID laser (ESA) and has been successfully implemented on CALIPSO mission (NASA).

22.4 PRODUCT ASSURANCE FOR SPACE COATINGS

The general principles of space product assurance relevant to space optics are to properly define and control the materials and processes used in the manufacture, assembly, integration, and test of the components; to verify that the component meets its operational requirements with sufficient margins to account for any uncertainties ensuring performance over the lifetime; and to formally track any nonconformances and ensure that these do not have an unacceptable impact on the final performance. These are usually defined beforehand in a dedicated product assurance plan for the deliverable item.

22.4.1 END TO END TRACEABILITY

It is of particular importance for space equipment that the quality chain from source materials to finished product remains unbroken and includes all of the materials and processes in between. The main principle behind this is that, if a problem does occur during subsequent testing phases, or in orbit, this problem is traceable and the root cause for any anomaly can be determined and corrected efficiently (or, at the very least, not repeated). Thus, all of the materials used for the manufacture of optics and coatings should have a valid certification of composition which is traceable to the batch used. This is usually tracked with a declared materials list (DML) which is supplied to the customer along with the finished optics. This should include materials which are used in the manufacture and then removed such as waxes, rosins, pitch, and polishing compounds used in the formation of optical substrates, along with the solvents used to remove them. It is also important to review the packaging materials used for the transportation and containment of space optics to ensure that these are compatible, particularly given the long durations that optics often reside in the packaging container prior to being integrated into instrument or satellite assemblies.

Residual contaminants from organic compounds, if not properly removed, can result in subsequent failure of the optics in humidity, thermal vacuum, and adhesion tests. They can also darken in the space environment via the interaction with the radiations described previously. Residual polishing compounds such as cerium dioxide can have a detrimental effect on the damage threshold of high-power laser optics, especially at shorter wavelengths where they can have significant absorption. It is often the case that materials which are used in the manufacturing process and which are subsequently removed are omitted from the DML, only to be found later on during an anomaly investigation.

Certain materials are not permitted for use in space due to their incompatibility with the vacuum environment. These include mercury, cadmium, and zinc due to their propensity to evaporate in vacuum, PVC which contains a large proportion of plasticizers which are released in vacuum, and pure tin which can grow tin whiskers in space. Silicones should generally be avoided for space optics due to the fact that they are very difficult to remove and will darken if exposed to UV or particle irradiation.

It is usually the responsibility of the goods receiving party, for example, coating manufacturer receiving a substrate, to have the same level of product assurance in their supply chain, and so on. For example, if there is a delamination failure of a coating, it is all too often the case that the failure cannot be attributed to problems at the coating manufacturer or the substrate supplier, because the quality chain has been broken and both the substrate and the coating are potentially implicated in the failure.

22.4.2 PROCESS CONTROL

The DML is usually cross-referenced with a declared process list (DPL), which uniquely identifies all of the processes used for the manufacture of the optics. This includes cleaning processes and measurement and verification processes. Log books and plant maintenance files are complementary documents to the DML and the DPL. Some of the most important aspects to track are engineering changes, which are often implemented by experienced coating engineers, in order to stabilize or rectify drifts in coating plant performance. It is often the case that the materials are defined by the coating manufacturer in a process identification document (PID) and the various processes and measurements performed are recorded in a "traveler" which follows the product through its entire manufacturing life cycle. These documents can often take the place of the DPL.

22.4.3 NONCONFORMANCE CONTROL

Nonconformances, defined as any breach of a requirement, either from the customer-defined specification of the delivered product or from the internal specifications defined by the manufacturer for the manufacturing processes, should be traced and subjected to formal processing. Generally speaking, nonconformances are divided into major and minor depending on their degree of severity. Major nonconformances should be reported to the supplier as they are usually in a better position to make an assessment of the potential impacts at system level and judge whether they are acceptable or not. The nonconformance process usually comes under the responsibility of the quality assurance or product assurance departments, which raise a nonconformance report (NCR) and then chair the subsequent nonconformance review boards (NRBs) until the issue is closed. For space products, any nonconformances associated with a product are considered to be an inherent part of its configuration. Thus, all NCRs are usually reviewed at the point of the delivery of the product, as part of the overall acceptance process.

The nonconformance control process should be regarded by the supplier as beneficial, inasmuch as it often provides valuable inputs for improvements to manufacturing processes, and eventual yield of good-quality components, along with efficient identification and rectification of recurring manufacturing problems.

22.4.4 SPACE QUALIFICATION

Qualification is the verification that the equipment meets its requirements with sufficient margins. Qualification can be by design; by analysis; by test; via similarity to components made using the same design, materials, and processes, as one that has a demonstrated space heritage; or a combination of the above. The majority of space optics are qualified by test and similarity. It should be noted that in the latter case, it is often difficult to obtain direct performance data of optics from operational satellites due to the fact that the performance is often not directly measured, that the degradation cannot easily be traced to a single cause, and that satellite operators often do not provide detailed performance degradation data. In addition, depending on the particular satellite mission and orbit, any qualification by similarity argument has to ensure that the operation environment, for example, orbit and mission lifetime, for the component is completely enveloped by the heritage satellite. The fact that optics are flying on a particular satellite is not a demonstration that they are performing to requirements applicable to another mission, and therefore that cannot be used as an argument for qualification in isolation. Thus, a certain amount of verification testing should be performed in order to augment the heritage argument and ensure that there has been no process or material changes in the interim period which could affect the performance.

For optical coatings, witness samples are often used for qualification testing. Care has to be taken that these witness samples are not "hostile" to and are truly representative of the actual flight optic that will be produced. There have been several cases where witness samples have passed tests and the flight optics subsequently failed. Common differences are geometry, for example, when the witness sample is planar and the flight optic is curved; the thermal environments that in the coating plant are different between the witness sample and the flight optic due to geometry or tooling differences; materials and processing where different processes or materials are used for the witness sample and the flight optic; or the witness sample is in a different coating run to that of the flight optic. For space optics, qualification is preferably at the coating lot level unless there is evidence of process stability over a statistically significant number of coating runs. For critical components which can cause a single point failure for the satellite instrument, such as those for high-power lasers, or where a small number of failures randomly distributed with a large number of components can have a large overall impact on system performance, for example, solar cell assemblies for solar arrays, qualification at the coating lot level is even more important. Clearly, the qualification methodology should be based upon an assessment of the potential severity of the eventual performance impacts at system level and be agreed between the customer and supplier beforehand.

22.5 CONCLUSION

The general impact of the space environment on optics has been briefly described in the preceding text along with a description of the product assurance principles that are applied to space optics. Clearly, space is a harsh environment for optics with many physical interactions leading to potentially severe degradation of optical performance. The main lessons learned are summarized below:

- In almost all cases, it is not possible to repair the degradation of optics in orbit. This necessitates a comprehensive terrestrial test campaign, and product assurance process for space optics, in order to guarantee their eventual performance. Space optics should always be presumed "guilty" until proven "innocent."
- Testing of space optics should be as representative as possible to the actual environment they will be exposed to. In situ performance measurements during testing should be implemented where possible in order to ensure that performance degradations are not missed due to annealing effects. In other words: "test as you fly."
- Coatings used for space optics should be highly densified in order to reduce a number of degradation effects caused by porosity such as optical performance changes due to water release and the resulting changes in the stress of the coatings.
- A careful and detailed assessment of the risk and impacts of contamination on space optics should always be carried out, especially if the optics are exposed to UV or high-power laser irradiation, and if the optics are cold compared to their surroundings. Coatings which are operated at temperatures below −150°C, and thus subject to water-ice contamination in vacuum, should be cooled down after the rest of the satellite, and heating should be implemented in order to decontaminate if necessary.
- Better test facilities are needed in order to investigate the synergisms of space environmental effects on space optics as performance degradation can be significantly underestimated if only individual effects are tested.
- The impacts of accelerated tests need to be compared with the data from long-term exposure tests in order to construct better predictions of in-orbit performance.

ACKNOWLEDGMENTS

The authors are grateful to many colleagues, both in ESA and in industry, for their contributions. It is through constructive collaboration and the dissemination and understanding of many different test results that a successful satellite mission is made possible. In this chapter, the most important effects that the space environment has on space optics have been introduced but it is by no means a comprehensive review of a rather vast topic.

REFERENCES

Allenspacher, P., Riede, W., Wernham, D., Capanni, A., Era, F., 2005. Vacuum laser damage test bench. Proc. SPIE Laser-Induced Damage in Optical Materials, vol. 5991. p. 599128.

Baccaro, S., Cecilia, A., Di Sarcina, I., Piegari, A., 2005. Effect of γ irradiation on optical components. IEEE Trans. Nucl. Sci. 52 (5), 1779–1784.

De Rooij, A., 1985. The degradation of metal surfaces by atomic oxygen. Proc. 3rd European Symposium on Spacecraft Materials in Space Environment. ESA SP-232, p. 99.

Di Sarcina, I., Grilli, M.L., Menchini, F., Piegari, A., Scaglione, S., Sytchkova, A., Zola, D., 2014. Behavior of optical thin-film materials and coatings under proton and gamma irradiation. Appl. Opt. 53 (4), A314–A320.

Doyle, D., 2017. The Space Environment and its Effects on Optics. International School of Space Optics. ESA-ESTEC, http://www.isso2017.org.

ECSS-E-ST-10-04C, 2008. Space Engineering—Space Environment. ECSS Secretariat, ESA-ESTEC, Requirements & Standards Division, Noordwijk. Available to download from, http://www.ECSS.nl.

ECSS-Q-ST-70-01C, 2008. Space Product Assurance, Cleanliness and Contamination Control.

ECSS-Q-ST-70-02C, 2008. Space Product Assurance, Thermal Vacuum Outgassing Test for the Screening of Space Materials.

ECSS-Q-ST-70-05C, 2009. Space Product Assurance, Detection of Organic Contamination of Surfaces by Infrared Spectroscopy.

Fortescue, P., Stark, J., Swinerd, G. (Eds.), 2004. Spacecraft Systems Engineering, third ed. Wiley, ISBN 0-471-61951-5.

Gusarov, A., Doyle, D., Glebov, L., Berghmans, F., 2007. Comparison of radiation-induced transmission degradation of borosilicate crown optical glass from four different manufacturers. Opt. Eng. 46, 043004.

Haynes, G., 1970. Effect of radiation on cerium-doped solar-cell coverglass. In: NASA TN D-6062. National Aeronautics and Space Administration, Washington, DC, p. 20546.

Hovis, F., Shepherd, B.A., Radcliffe, C.T., Bailey, A.L., Boswell, W.T., 1994. Optical damage at the part per million level. Proc. SPIE 2114, 145–153.

Nardello, M., Zuppella, P., Polito, V., Corso, A.J., Zuccon, S., Pelizzo, M.G., 2013. Stability of EUV multilayer coatings to low energy alpha particles bombardment. Opt. Express 21, 28334–28343.

Pelizzo, M.G., Corso, A.J., Zuppella, P., Windt, D.L., Mattei, G., Nicolosi, P., 2011. Stability of multiplayer coatings to low energy proton bombardment. Opt. Express 19, 14838–14884.

Pellicori, S.F., Martinez, C.L., Hausgen, P., Wilt, D., 2014. Development and testing of coatings for orbital space radiation environments. Appl. Opt. 53 (4), A339–A350.

Pereira, A., Roussel, J.-F., van Eeesbeek, M., Guyt, J.M., Schmeitzky, O., Faye, D., 2003. Study of the UV enhancement of contamination. Proc. 9th International Symposium on Materials in a Space Environment, Noordwijk, The Netherlands, 16–20 June. ESA SP-540, 2003.

Riede, W., Allenspacher, P., Shroder, H., Wernham, D., Lien, Y., 2005. Laser-induced hydrocarbon contamination in vacuum. Proc. SPIE Laser-Induced Damage in Optical Materials, vol. 5991. pp. 59910H1–13.

Riede, W., Allenspacher, P., Wernham, D., 2007. Laser qualification testing of space optics. 38th Annual Boulder Damage Symposium 2006, Proc. SPIE, vol. 6403. p. 64030T.

Russell, J., Jones, G., 2003. Radiation testing of coverglasses and second surface mirrors. Proc. 9th International Symposium on Materials in a Space Environment, Noordwijk, The Netherlands,16–20 June. ESA SP-540, 2003.

Tighe, A.P., Pettazzi, F., Alves, J., Wernham, D., Riede, W., Schroeder, H., Allenspacher, P., Kheyrandish, H., 2008. Growth mechanisms for laser induced contamination on space optics in vacuum. Proc. SPIE. 7132, 71321L.

Tribble, A.C., Haffner, J.W., 1991. Estimates of photochemically deposited contamination on the GPS satellites. J. Spacecraft 28 (2), 222–228.

Wernham, D., Alves, J., Pettazzi, F., Tighe, A.P., 2010. Risk mitigation for laser-induced contamination on the ADM-Aeolus satellite. Proc. SPIE 7842, 78421E-1–12.

Winker, D.M., Crouch, R.H., McCormick, M.P., 1996. An overview of LITE: NASA's lidar in-space technology experiment. Proc. IEEE 84 (2), 164–180.

This page intentionally left blank

Index

Note: Page numbers followed by *f* indicate figures, *t* indicate tables and *p* indicate plates.

A

Abney's law, 404
Abrasion resistance, 545
Absorbent materials, 294–298, 324–325, 334
Absorption coefficient, 294, 309*f*, 612, 748
Absorption edges, 306–309
Absorption spectrum, 494, 497–500, 499–500*f*, 503*f*
Active materials, 652–654
Active matrix (AM) addressing method, 761–762
Active monochromatic monitoring strategies, 75–85
Active remote sensing, 273–274
Adaptive mirrors, 702
Adhesion
  acrylic case, 521
  plasma treatment, 520
  tests, 547–549, 549*f*
  thermal and stress-related effects, 522–523, 524*f*
ADM-Aeolus satellite, 791–794
AG coating. *See* Antiglare (AG) coating
Air mass zero, 794–796
Air-to-vacuum spectral shifts, 791–794, 793*p*
ALADIN laser, 791–794, 804–806
ALD. *See* Atomic layer deposition (ALD)
Alkali metals, 157–159, 303, 303*t*
All-dielectric filter, 636–638, 637*f*, 647*f*
All-dielectric MMs, 144, 146–147
Alloys, 157–160
All-silicon tandem solar cell, 601–602, 602*f*
Alternating ion plating, 12–13, 13*f*
Aluminium, 303
Aluminum-doped zinc oxide (AZO) film, 616–617, 764*f*
Ambient temperature, 366, 794–796, 796*p*
American Vacuum Society (AVS), 784
Amorphous Titania, 496–497
Analog resistive touch sensors, 770–771, 771–772*f*
Anderson localization, 156
Angular selection filter (ASF), 574, 576–579
  for blue light, 581
  design of, 577
  at incident angles, 580*f*
  luminance with and without, 580–581, 581*f*
  simulated and experimental spectra, 579–580
  transmittance of green light by, 576*f*
Annealing effect, 798–799, 809
Anomalous scattering (AS), 276–278
Anticounterfeiting, 633–634, 642–643, 652
Antiglare (AG) coating, 726
  flat panel display, 566
  glass substrates, 728
Antiicing, TV laser window, 756*f*, 758*f*
Anti-reflection (AR) coatings, 425–426, 517, 521, 522*f*
  AR-hard, 526, 527*f*
  conductive, 767–769, 769–770*f*
  double CM, 671–672
  flat panel display, 565–568
  with improved sunlight resistance, 521
  light-emitting diode, 586–588
  for ophthalmic glasses, 25
  photovoltaic solar cells, 600
  projectors, 568–569
  single-layer, 398–399
  tilted-front-interface CM, 673
  transparent metallic thin films, 744
  vacuum deposited, 526–527
  wet-chemical, 531–532
Antireflective structures (ARS), 528–531, 529–530*f*
Antistatic films, 757
Aperture mode, 400–401
Apollon laser, 700
Architectural coatings, 374
Architectural glazing
  test methods, 545
  thin film applications in, 540*f*
AR coatings. *See* Anti-reflection (AR) coatings
Aspecular angle, 412
Assisted sputtering technique, 791, 792*f*
Astronomy, 702
Asymmetric single SRRs (ASRs), 151
Atmospheric moisture, 6, 804
Atmospheric windows, 377–383
Atomic force microscopy (AFM), 163
Atomic layer deposition (ALD), 17–18, 328–329
Atomic number, 304, 313
Atomic oxygen (ATOX), 789, 801
Atomic scattering factors, 303–306

Attenuated total reflectance (ATR) measurement, 163
Attosecond Science, 688
Automotive glazing, 719, 737–738
  applications, 732–734
  evaluation, 545
  functional thin films and coatings, 541*f*
  polycarbonate, 557–559, 559–560*f*
  thermal control in, 720–723
Automotive head-up display, 583–586

B

Backprojection algorithm, 278
Back-side-coated CM, 673, 673*f*. *See also* Chirped mirror (CM)
a,b-Band-emittance, 365–366
Band engineering, 159
Band gap, 300–301
  energy, 299, 302*f*
  photonic, 364
  TCO, 750
s-Band metals, 746
Band-pass filtering, 150–151
BBAAR coating. *See* Broadband, broad-angle AR (BBAAR) coating
Beam current, 5
Beam splitter
  chromatic discrimination ellipse, 587*f*
  dichroic, 570
  head-up display, 584–586, 585*f*
  polarization, 569–570, 572*f*
Beer-Lambert law, 294, 316
Bergman-Milton representation, 166
Bernstein-Moss effect, 751
Bethe-Salpeter equation, 187–188, 247–248, 253–257, 273
Bidirectional reflectance spectral distribution function (BRDF), 411, 411*f*
Bidirectional transmittance spectral distribution function (BTDF), 411, 411*f*
BK7 glass, 500*f*, 680, 801
Blackbody radiation, 358–362, 360–361*f*
Black chrome, 371–372
Black silicon, 487, 600
Blue asbestos, 394–396
Boats, 5
Boltzmann constant, 148
Boltzmann distribution, 35
Bose–Einstein distribution, 359
Bragg's law, 192–194, 324, 670–671
Brewster angle, 333–334, 672–673, 672*f*. *See also* Chirped mirror (CM)
Brewster, David, 394, 396*f*
Broadband, broad-angle AR (BBAAR) coating, 39–40
Broadband lasers, 274
Broad Band Monitor (BBM), 66–69, 89–92, 103–105
  application of, 110–111
  design stability in production processes, 120–125
  online measurement system, 116
  precision, 111
  specifications, 108–110, 110*t*
  technical implementation, 110–111
  in transmission mode, 108
  transmittance spectrum, 111*f*
  VDP device, 116–117
Broad-beam ion sources, 6–7, 7*f*
Building integrated photovoltaic (BIPV), 612–613, 735–736
Bulk heterojunction (BHJ) devices, 604–607
Bulk plasmon, 143–144

C

Cadmium sulfide (CdS), 615–616
Cage-structured materials, TCO, 780–782, 781*f*
Calar Alto Observatory, 701
Calibration factor, 68–69, 93
CAMFR, Ses Cavity modeling framework (CAMFR)
Canonical boundary-value problem, 449–450, 454, 477
  metal/rugate-filter interfaces, 457–460, 458–459*f*
  metal/SNTF interface, 460–462, 461–462*f*
  theoretical formulation, 454–457
Carbide coating, 373–374
Carbon fiber reinforced plastic (CFRP), 804
Cathodic arc evaporation, 15
Cauchy principal value, 314
Cavity modeling framework (CAMFR), 43
CdSe/ZnS quantum dots, 496–497. *See also* Quantum dots (QDs)
  absorption spectrum, 497–498, 499*f*, 503, 503*f*
  luminescence, 500–501, 503, 503*f*
  reflectance spectra, 508, 509*f*
  refractive index, 505, 507*t*
  transmission electronic microscopy, 497, 498*f*
  transmittance spectrum, 497–498, 498*f*
Centre for Advanced Laser Applications (CALA), 688
Ceramic matrix, 147–156
Cerium dioxide, 806
Cermet, 371–372

Chalcogenide materials, thin-film solar cells, 611–618, 613*f*
Characteristic material parameters (CMP), 168
Charge-coupled device (CCD), 66, 110–111, 111*f*
Charge transport, 608
Chemical colors, 389
Chemical-deposition techniques, 452
Chemical interface damping, 148
Chemical silvering, 3–4
Chemical vapor deposition (CVD), 16–17, 383, 430
  initiated, 440–441
  nonplasma-activated, 438–441
  plasma-enhanced, 434–438, 435–438*f*
Chiral sculptured thin film (STF), 450–451, 453
Chirped mirror (CM), 669
  back-side-coated, 673, 673*f*
  Brewster-angle, 672–673, 672*f*
  complementary pair, 674, 675*f*
  tilted-front-interface, 673–674
Chirped-pulse amplification (CPA), 688–690
Chromaticity diagram, 402–403, 406
  CIE 1931, 405*f*, 418*f*, 572–573, 575*f*
  CIE 1964, 405*f*
CIE. *See* Commission Internationale de l'Éclairage (CIE)
CIGSSe solar cell, 612
  absorber layer deposition, 614–615, 615*f*
  back contact electrode, 613–614
  buffer layer, 616
  manufacturers, 617
  scanning electron microscope, 613, 613*f*
  substrate configuration, 612–613
  window layer, 616
CILAS, 700*f*, 708, 712
Clausius-Mossotti relation, 166–167
Closed-field magnetron sputtering, 13
Cloud, 39
Clustering methods, 36–37
CM. *See* Chirped mirror (CM)
CMFs. *See* Color-matching functions (CMFs)
Coating-based window heating applications, 732
Coating systems, 542–543
  containing metasurfaces, 155–156
  for control of radiative exchange with the atmosphere, 377–383
  glass substrate, 552
  materials, 375
  multifunctional coatings, 553–556
  numerical simulation, 553, 554*f*
  optical properties of, 550–551
  polycarbonate substrate, 552–553, 553*f*
  stress distribution, 555*f*
  testing methods, 544–545
    adhesion tests, 547–549, 549*f*
    haze measurement, 551, 551*f*
    sand trickling test, 546
    scratch test, 546, 547–548*f*
    Taber abraser test, 545, 546*f*
    testing methods, 544–551
    weathering test, 549–550
  for thermal solar collectors, 367–374
Co-deposition processes, 126–127, 130, 135–136
Coefficient of thermal expansion (CTE), 726, 728
Co-evaporation techniques, 618
  organic solar cell, 606–607
  perovskite-based solar cells, 622
Coherent backscattering
  random medium
    with random rough interfaces, 271–272
    with two planar interfaces, 267–271
  semiinfinite medium, 266–267
Coherent Potential Approximation (CPA), 255
Color-appearance colorimetry, 410
Color constancy, 409
Color filters
  flat panel display, 567
  robustness, 39
Colorimetry, 389–390, 399, 400*t*
  classical computations, 413–418, 413*f*, 415–418*f*
  gonio-apparent color, 410–412
  psychometric, 400, 408–410
  psychophysical, 400–408, 402*f*, 405*f*
Color matching, 400–401
Color-matching functions (CMFs), 401, 402*f*, 403, 647–648
Color rendering index (CRI), 407
Color shifting
  all-dielectric filters, 636–638
  American banknotes, 634
  British Columbia, 634
  magnetic film, 648, 649*f*
  technologies of, 651–652
Color wheel
  LCoS projector, 570–571, 573*f*
  phosphor, 576*f*, 582, 582*f*
Columnar thin film (CTF), 453
Commission Internationale de l'Éclairage (CIE), 389–390, 408, 412
  CIE 1924 standard observer, 405*f*
  CIE 1931 standard observer, 402*f*, 403–406, 405*f*, 409, 418, 418*f*
  CIE 1964 standard observer, 403, 405*f*, 406, 409
  colorimetries with, 400*t*
  illuminants, 406–407

Commission Internationale de l'Éclairage (CIE) *(Continued)*
models, 410
psychometric system, 409
reflectance-factor measurement recommended, 407–408
Complementary color, 390, 567
Complex materials
in multilayers, 168–172
optical characterization techniques for, 163–164
Composites
organic layers, 441–442, 442–443*f*
organic optical coatings, 429, 441–442, 442–443*f*
random elements, 154–155
thin film, 441, 442*f*
Comprehensive search, 26–27
Compton scattering, 312
Computational manufacturing, 39, 114–115
Conduction band, 300–301
Conductivity, 746
AR coating, 767–769, 769–770*f*
doping mechanisms, 747–748
metal, 746
optical properties related to, 748–752, 751–752*f*
Cone-beam algorithm, 278
Contamination, 801
laser-induced, 789, 804–806, 805*f*
terrestrial, 801–803
UV fixation of, 804
Continuous refractive index variation, 125–134
Convection, 384, 723
Conventional evaluation techniques, 103–104
Cooling-dominated region, 721–722, 724*f*
Core polarizability, 145–146
Corundum coating, 543
Counterfeiting, 633–634. *See also* Anticounterfeiting
Crack onset strain (COS), 426
coating toughness, 547, 549*f*
determination, 427*f*
layer materials on polycarbonate substrates, 428*f*
PECVD, 436*f*
thin film composites, 441, 442*f*
CRI. *See* Color rendering index (CRI)
Critical angle, 226, 298, 317
Crystalline dielectrics, 300–301
CTF. *See* Columnar thin film (CTF)
Cumulative effect of thickness errors
direct optical monitoring, 68
elimination, 83
estimating, 81–82
examples, 90–91
indirect monitoring strategies, 68–69, 92–93
layer thickness monitoring, 67
minimizing, 82–83*f*
observation, 92
online reoptimization, 92
Current-to-light coupling, 156
CVD. *See* Chemical vapor deposition (CVD)

D

Dark exciton, 503
Dark mirror, 369, 370*f*
Daylight simulation coating, 588–589, 589*f*
DBR. *See* Diffraction Bragg reflector (DBR)
DC-magnetron sputtered (DCMS) ITO coatings, 556–557
DC magnetron sputtering, 13–14, 373*f*
Deb-type ECD, 656
Declared materials list (DML), 806–807
Declared process list (DPL), 807
Deformable mirror, 700–701, 700*f*
Degradation mechanism
optical solar reflectors, 798–799
particulate radiations, 799–801, 800*p*
solar cell cover glasses, 798, 798*p*
Delano's Q-function, 29
Deposition control
of coating systems, 125–134
of rugate filters, 132–134
Deposition techniques, 3–4, 115–116, 426, 429–430
adhesion improvement by plasma treatment, 441
atomic layer deposition, 17–18
cathodic arc evaporation, 15
chemical vapor deposition, 16–17
early processes, 4–6
energetic processes, 6–15
etching, 18–19
ion-assisted deposition, 6–8
ion plating, 8–10
nonplasma-activated chemical vapor deposition, 438–441
plasma-enhanced chemical vapor deposition, 434–438, 435–438*f*
processes for deposition, 4–6
pulsed laser deposition, 15–16
sol-gel processes, 18
sputtering, 10–15, 432–434, 433–434*f*
thermal evaporation, 430–432, 431*f*
Design stability in production processes, 120–125
Detector technology, 274
Deterministic production, 105–107

Dichroic beam splitter, 570
Dielectric(s), 160–162, 381
  band gap energy, 299
  coatings, 4–5, 369–370, 690
  filter, transmission curve, 799, 800*p*
  substrate, 224–229
  transparency cutoff of, 300–301
Dielectric film
  1D rough surfaces, 189–200
  planar interface, 224–229
  2D randomly rough surface, 216–229
Dielectric-metal-dielectric (DMD), 744
Differential reflection coefficient, 193, 195*f*, 196, 199*f*, 209, 216, 221, 223
Diffraction Bragg reflector (DBR), 586–588, 588*f*
Diffractive optically variable image devices (DOVIDs), 649
Digifeiting, 633–634
Digital light processing (DLP), 572–573, 573*f*
  band pass filter, 575*f*
  digital micromirror device, 570–571, 574*f*
  red laser diodes in, 574*f*
Digital micromirror device (DMD), 570–571, 574*f*
Dipping process, 566–567
Direct broadband optical monitoring, 89–92
Direct current (DC) magnetron sputtering, 432, 767–769
Direct online correction tools, 118–120
Discrete dipole approximation (DDA), 165
Dispersive mirror (DM), 667–669. *See also* Double-angle DM
  complementary pairs, 675*f*, 676
  damage threshold, 690, 690–691*f*
  design approaches, 669–670, 670*f*, 674*f*
  in high-intensity lasers, 687–690
  production of, 679–680
  pulse compression with, 680–683, 683–684*f*
  time-domain approach, 676
DLP. *See* Digital light processing (DLP)
DML. *See* Declared materials list (DML)
Doping mechanisms, 747–748
Double-angle DM. *See also* Dispersive mirror (DM)
  design approaches, 677, 680–681
  physical thicknesses of layers, 681*f*
  pulse compression, 680–683, 683–684*f*
  reflectance and GDD, 675*f*, 682*f*
Double-chirped mirror, 671–672, 671*f*. *See also* Chirped mirror (CM)
Double images, 583–586
Downward radiation, 379–380, 379*f*
DPL. *See* Declared process list (DPL)
Drude theory, 297*f*, 301–303, 749–750, 751*f*
DSSC. *See* Dye-sensitized solar cell (DSSC)
Dual-ion-beam sputtering (DIBS), 704–705, 705*f*
Dual magnetron sputtering, 11–12
Dyakonov-Tamm waves, 454, 479
Dye-sensitized solar cell (DSSC), 598, 618–619, 778
Dyson equation, 247–248, 256–257

E

Ebanol, 369
E-beam deposition systems, 126–127
E-beam lithography, 154
EDFA. *See* Erbium-doped fiber amplifiers (EDFA)
Effective macroscopic parameters, 166–168
Effective mass approximation (EMA), 488–489, 493–494
Effective mass model, 489–493
Effective medium approximation (EMA) model, 155, 166, 169
Effective medium theory, 276–278
Effective permittivity, 255–256
Eggshell effect, 552
Einstein's photon hypothesis, 393
Electrical conductivity
  of coating, 550–551
  metals, 746
Electrical insulation, 381
Electrochemical etching, 657
Electrochromic device (ECD), 654–656, 655*f*
Electrochromic (EC) windows, 778–779
Electromagnetic field distribution, 608–609
Electromagnetic Interference (EMI) shielding, 757
  for dual laser, 759–760*f*
  effectiveness, 759*f*
Electromagnetic theory, 487
Electromagnetic (EM) waves, 291, 746, 750
Electron beam evaporated coatings, 791, 792*f*, 803
Electron-beam heating, 5
Electron energy loss spectroscopy (EELS), 318
Electron gun evaporation, 703–704
Electron microscopy, 389
ELI. *See* Extreme Light Infrastructure (ELI)
Ellipsometry, 111–112, 317, 488, 497, 505
Embedded nanostructures, 147–156
Embossing process, 528
Emissivity, 362–367. *See also* Low-emissivity (low-E) coatings
End to end traceability, 806–807
Energetic processes, 6–15
Energieeinsparverordnung (EnEV), 720–721
Energy conservation, 732–733

Energy-efficient glazing, 719, 735, 737
automotive windows, 723
cooling-dominated applications, 722
low-emissivity coating, 764–765
solar control coatings, 765–767
thermal control coatings, 720–721
Energy-efficient window coatings, 367, 374–377
Energy saving, 374, 586–588
Energy Star, 720–721
Epsilon-near-zero (ENZ) media, 155–156
EQE. *See* External quantum efficiency (EQE)
Erbium-doped fiber amplifiers (EDFA), 39–40
Error self-compensation effect, 69–75
Etching process, 18–19
European Co-operation for Space Standardization (ECSS) standard, 790, 802–804
European Space Agency (ESA), 701–702
European Strategic Forum for Research Infrastructure (ESFRI), 688
European Synchrotron Radiation Facility (ESRF), 698
European X-ray free-electron laser (European XFEL), 699
EUV lithography (EUVL), 321–322
Excitons, 607
diffusion of, 607
dissociation, 608
Exner's coefficients, 404
External quantum efficiency (EQE), 50–51, 503, 504*f*, 505
Extinction coefficient, 294
Extra high reflection coating, 508
Extreme light infrastructure (ELI), 687–688, 699–701
Extreme ultraviolet (EUV)
absorption, 306–307
Drude model in, 303
HR coatings, 321–322, 323*f*
material behavior, 291–292
natural low-absorption bands, 319
reflective ML coatings in, 321–322
transparent materials, 316–318
wavelengths, 327
Eyeglasses, 518, 526

F

Fabrication process, 154, 612, 702
Fabry-Perot (FP) filtering, 156, 429, 635–636, 640
active materials, 652
high-/low-index, 725
metal-dielectric filters, 638
configurations, 639*f*
metamerism, 645, 646*f*
optically variable pigments, 643
optical monitoring strategies, 69, 70*f*, 72
upconverting nanoparticles, 652–654, 653*f*
Far ultraviolet (FUV), 291–292, 299–300
alkali metals, 303
extending, 334
high-reflectance coatings, 321
narrow-band filters, 319
reflectance, 328–329, 329*f*
transmission filters, 318–319
FDTD method. *See* Finite-difference time-domain (FDTD) method
Federal Aviation Administration (FAA), 633
Feldkamp algorithm, 278
Fermi level, 146, 746
Fermi surface, 157, 158*f*
Ferrell modes, 143, 170–171
Feynman diagrams, 262, 264
Field-effect transistor (FET), 774–775
Fine Guidance System (FGS), 701
Finite-difference time-domain (FDTD) method, 37, 165, 167
Finite element method, 553
First extremum, 87
Flat panel display (FPD), 565–568
Flip-flop Q-function, 34
Flip-flop technique, 26–27
Floquet-Bloch theorem, 192
Floquet-Lyapunov theorem, 456
Floquet-type representation, 167–168
Fluorine, 8, 11, 531–532
Fluorine-doped tin oxide (FTO) coating, 543–544, 544*f*
Focused ion-beam, 144–145, 154
Forward atomic scattering factor, 304
Fourier coefficient, 193
Fourier transform infrared spectroscopy (FTIR), 520
Fourier transform-limited pulse (FTLP), 676
Fourier transform (FT) method, 27–30
FPD. *See* Flat panel display (FPD)
Fraunhofer Institute for Surface Engineering and Thin Films (IST), 426
Free electron metals, 301–303, 746
French Laboratory Laboratoire des Matèriaux Avancés (LMA), 704–705, 713, 715
Fresnel reflectivity, 229
Fresnel's coefficients, 295–296, 298, 414
Fresnel's laws, 398–399, 413
FT method. *See* Fourier transform (FT) method

Full width at half maximum (FWHM), 681
high reflectance zone, 578
at incident angle, 579–580, 579–580*f*
Functional coatings, 539–540
automotive sector, 541*f*
plasma- and ion-based deposition, 540–544
Fused silica
full-bandwidth measurement, 685–687, 687*f*
threshold fluencies, 690*f*

G

Gain flattening filters, 39–40
Gain modified filter (GMF), 588–589, 589*f*
Galactic cosmic rays, 799
Gamma-ray interaction processes, 311–312*t*
Gas flow sputtering (GFS), 558
Gaussian random process, 190, 210–211, 214, 230
Gauss-Legendre method, 263
Gemini Observatory, 702
Genetic algorithms, 35–36
German Aerospace Center's Solar Research, 703
Ghost image, 3–4, 583–584
Giant Magellan Telescope, 702
Gires-Tournois interferometer (GTI), 669–671
Glancing-angle deposition (GLAD), 19, 657
Glass substrate
antiglare coatings, 728
coating systems, 552
low-emissivity coatings, 727–728
Glazing
antiglare coatings, 728
automotive applications, 732–734
building applications, 734–736
durable coatings, 542
low-emissivity coatings, 727–728
polymer substrates, 729–731
sources, 738
thermal control in, 720–723
types, 726–727
Global optimization, 34–37
GMF. *See* Gain modified filter (GMF)
Gonio-apparent color, 389, 410–412
Gradient coatings, 552–553
Gradual evolution, 26–27
Gradual evolution mode, 32–33
Grassmann's laws, 400–401
Grating-coupled configuration, 449–450, 462, 477
advantages, 478
metal/rugate-filter interface, 462–467, 463*f*, 465*t*, 466–467*f*
metal/SNTF interface, 467–470, 469–470*f*
time-averaged Poynting vector, 467*f*, 470*f*
Gravitational wave interferometric detectors (GWIDs), 713
Green function, 248–250, 254, 259
Green tensors, 259–265, 273
Group delay (GD), 112, 667–669, 684–687, 685*f*
Group delay dispersion (GDD), 112, 667–668
back-side-coated CM, 673, 674*f*
Brewster-angle CM, 672–673, 672*f*
chirped-pulse amplification, 688–689
complementary pairs, 674, 675*f*, 676
dispersive mirror, 678–683
double-angle DM, 675*f*, 677, 682*f*
double-chirped mirrors, 671–672
GTI approach, 670–671
highest possible value of, 678–679, 679*f*
GTI. *See* Gires-Tournois interferometer (GTI)
Guided-mode resonance (GMR) effect, 150

H

Hagen–Rubens relation, 369
Hard X-rays (HXR), 292–293
Haze measurement principle, 551, 551*f*
Head up display (HUD), 583–586
architecture, 585*f*
beam splitter, 585*f*
Heater, transparent conductive thin films, 755–757, 755*f*
Heat mirror, 369, 370*f*
Heaviside unit step function, 193–194, 220
Heavy-alkali-fluoride postdeposition treatment, 614
Helios sputtering system, 13
Hering's hypothesis, 409
Herschel and Planck satellites, 790
Herschel Space Observatory, 701
Hewlett-Packard, 654–655
High-contrast gratings, 150
High-dispersive mirrors (HDMs), 690
Higher energies, 309–314
High Field Science, 688
High-intensity lasers
CILAS, 700*f*
dispersive mirror in, 687–690
High power impulse magnetron sputtering (HiPIMS), 13–14, 543, 544*f*, 552, 556–557
High Power Laser Energy Research (HiPER) facility, 699
High reflection (HR) coating, 321–332, 323*f*, 586–588
High-resolution 3D imagery, 275
High-voltage ion plating, 8–9

HIPIMS. *See* High power impulse magnetron sputtering (HIPIMS)
Holeraum, 363–364
Hollow cathode activated deposition (HAD), 557–558
Homogenization approach, 166, 276–278, 487, 504
Horizontal polarization, 231–232
HR coating. *See* High reflection (HR) coating
Hubble Space Telescope, 701, 790
HUD. *See* Head up display (HUD)
Huygens-Fresnel principle, 649
Hybrid design
  solar cells, 48–52
  structured coatings, 44–47
  waveguide facet coatings, 41–44
Hybrid thickness monitoring, 112–114
Hydrophobic coatings, 542–543, 566–567
Hydrothermal method, 496–497

I

IAD. *See* Ion-assisted deposition (IAD)
Illuminating Engineering Society of North America (IES), 407
Impurity potential operator, 253
Incidence angle, 295
Incidence plane, 295–296
Incoherent intensity, 259–265
Incoherent scattering, 312
Indirect optical monitoring strategies, 92–96, 95*f*
  calibration factors, 68–69, 93
  of coating production, 66
  layer thicknesses, 67
  monitoring spreadsheet, 94*t*
  specifications, 76
  witness chips, 95*f*
Indium tin oxide (ITO), 48–49, 598, 742. *See also* Transparent conductive oxide (TCO)
  DC-magnetron sputtered, 556–557
  doping mechanisms, 748
  on glass substrate, 611*f*
  HiPIMS, 544*f*, 552, 556–557
  low-emissivity coatings, 727–728
  OLED lighting, 773–774
  optical and electrical properties, 743*t*, 754*f*
  sheet resistance and optical transmittance, 743*t*
  spectral transmittance and reflectance, 751
Induced transmission filter, 156, 725, 744
Infrared attenuated total reflectance (IR-ATR) spectra, 436–438, 437*f*
InGaAs array, 110–111, 111*f*
Inhomogeneous refinement, 30–34
Inhomogeneous surface coatings, 371–372
Initiated CVD (iCVD), 440–441. *See also* Chemical vapor deposition (CVD)
Injection molding, 517–518
In-line magnetron sputtering technique, 706*f*
Institut de Lumière Extrême (ILE), 700–701
Institut Laue-Langevin (ILL), 698
Instrumental reference frame, 403
Insulated glazing units (IGUs), 723, 728
Intensity, 294
  and Bethe-Salpeter equations, 253–255
  and cross section, 248–252
  incoherent, 259–265
  operator, 256–259
Interference-based security devices (ISDs), 633–634, 656–657
  diffraction and, 649–650
  electrochromic device and, 655–656, 655*f*
  feature of, 634–635
Interference color, 389–390, 397*p*, 410–411
  Brewster, David, 394, 396*f*
  colorimetric evaluation (*see* Colorimetry)
  lens optical coatings, 398–399
  Lippmann, J.F.G., 398
  Michel-Lévy, Auguste, 394–397
  Newton, Isaac, 390–392, 391*f*
  Nobili, Leopoldo, 393–394, 395*f*, 396*p*
  soap bubbles, 398
  thin film anticounterfeiting coatings, 399
  Young, Thomas, 392–393
Interference filters, 25
Interferometers, 317
  Gires-Tournois interferometer, 669–671
  Michelson interferometer, 684–687, 713
  white light, 684–687, 685*f*
Interferometric autocorrelation, 683, 684*f*
Intermetallics, 157–160
Internal quantum efficiency (IQE), 50–51
Ion-assisted deposition (IAD), 6–8, 7*f*, 105–107. *See also* Plasma-ion-assisted deposition (PIAD)
  functional coatings, 540–544
  large optical coatings, 704*f*, 707
  LIDT test, 795*f*
Ion-assisted filtered cathodic arc evaporation (IFCAD), 15
Ion beam assisted chemical vapor deposition (IBA-CVD), 555–556
Ion-beam sputtering (IBS), 14–15, 14*f*, 104–105, 107–108
  deposition process, 109*f*
  dispersive mirror, 668–669, 679–680

large optical coatings, 704–705, 713, 714*f*
polytetrafluoroethylene, 434
with zone target, 127–130, 128*f*
Ion plating, 8–10
IQE. *See* Internal quantum efficiency (IQE)
Iridescent colors, 394, 410–411
ISDs. *See* Interference-based security devices (ISDs)
IVB transition metal nitrides, 376–377

J

Jahoda-Velický dispersion relations, 315–316
James Webb Space Telescope (JWST), 701
Japanese-led Japan Aerospace Exploration Agency, 702
Journal of Vacuum Science and Technology (JVST), 783

K

Kaufman source, 7
Këserite cells, 617–618
Kirchhoff approximation method, 229–230
Kirchhoff's law, 363–364
Kramers–Kronig relations, 29, 32, 164, 307*f*, 314–315, 503–504
Kretschmann configuration. *See* Turbadar–Kretschmann–Raether (TKR) configuration
Krönig-Penney model, 491

L

Laboratory-scale deposition, 372–373
Lacquer technique, 557–558
Laminated glazings, 727, 730
Langmuir-Blodgett techniques, 19
Large optical coatings, 697
domains of applications, 697–698
astronomy, 702
laser, 699–701
scientific large instruments, 698
solar plants, 702–703
space industry, 701–702
large magnetron sputtering facility, focus on, 708–711
Laser Megajoule project, 711–712, 712*f*
sputtering technique, 704–706, 705–706*f*
thermal and electron gun evaporation, 703–704
thin-film uniformity, 706–708
Virgo project, 713–715, 714*f*
Laser, 699–701. *See also specific lasers*
chain amplifier, 712, 712*f*
electromagnetic wave, 275–276
imaging systems, 274
Ti:sapphire, 681–683, 690
Laser-induced contamination (LIC), 789, 804–806, 805*f*
Laser-induced damage threshold (LIDT), 127–130, 129*f*, 690, 789, 794, 795*f*
Laser Interferometer Gravitational-Wave Observatory (LIGO), 713, 715
Laser Megajoule (LMJ) project, 699, 711–712, 712*f*
Laser pulses, 667
Laser radar technology, 275
Laser technology, 103
Last extremum, 87
Lawrence Berkeley National Laboratory (LBNL), 721
LCoS projectors. *See* Liquid crystal on silicon (LCoS) projectors
Leadership in Energy and Environmental Design (LEED), 720
LED. *See* Light-emitting diode (LED)
Lens optical coatings, 398–399
Level monitoring, 66, 75–85
LIC. *See* Laser-induced contamination (LIC)
LIDT. *See* Laser-induced damage threshold (LIDT)
Light-emitting diode (LED), 407, 565–566, 568
angular selection filter, 580–581
colors of, 576*f*
optical coatings, 586–589
projectors using, 571–583, 583*f*
quantum dots, 507–508
Lightness, definition, 409
Light-to-current coupling, 156
Light trapping
organic solar cell, 608
electromagnetic field distribution, 608–609
implement periodic structures in multilayer stack, 609–610
plasmons for increasing absorption, 610–611, 611*f*
photovoltaic solar cells, 600–601, 601*f*
LIGO. *See* Laser Interferometer Gravitational-Wave Observatory (LIGO)
Linear polarizers, 332–341
Lipmann emulsion, 3–4, 19
Lippmann, J.F.G., 398
Liquid crystal display (LCD), 565
transmission-type projectors, 568–569, 568*f*
transparent conductive oxide, 757–761
Liquid crystal on silicon (LCoS) projectors
color wheel, 573*f*
reflection-type projectors, 569–570, 569*f*, 571*f*
Lithium fluoride (LiF), 291–292

LMJ project. *See* Laser Megajoule (LMJ) project
Localized SP resonances (LSPRs), 144, 148
Localized SPs (LSPs), 147
Long wavepass filter (LPF), 572–573
Lorentz oscillator model, 160–161
Lotus effect, 530
Low-emissivity (low-E) coatings, 374–377, 542–544, 723, 727
  design of, 766*f*
  glass substrates, 727–728
  metallic coating, 381
  polymer substrates, 729
  silver-based, 731
  transparent conductive oxide, 764–765, 765*f*
  on windshield, 556–557, 558*f*
Low-voltage ion plating, 9–10, 9*f*
Luminescence, quantum dots, 500–503, 501–504*f*

M

Macroscopic parameters, effective, 166–168
Macula lutea, 400
Magnetic films, 648, 649*f*
Magnetron sputtering, 107, 126–127, 520
  coatings, 372–373
  deposition techniques, 11–14
  direct current, 432
  dispersive mirror, 668–669, 679–680
  high power impulse, 543, 557
  in-line configuration, 706, 706*f*
  large size deposition machine, 708–711, 709*f*
  PACA2M, 708, 712
Manufacturability issues, 37–40
Markov-Chain Monte Carlo (MCMC) method, 35
Masking techniques, 707, 714
Material behavior, over spectrum, 291–293
Material mixtures, production of, 126–131
Material properties, 363
Material-radiation interaction, 299–314
Materials International Space Station Experiments (MISSE), 801
Materials Research Society (MRS), 784
Matrix-assisted pulsed laser evaporation (MAPLE), 432
Maxwell-Garnett theory (MGT), 166, 255–256, 504
Maxwell's boundary conditions, 168
Maxwell's electromagnetism theory, 393
Maxwell's equations, 28, 44–45, 165, 233, 248–250, 503–504
Metal
  conductive properties, 746
  multilayer, 375
  optical properties, 751–752
Metal-dielectric filter
  Fabry-Perot-like, 639–640*f*, 645, 646*f*
  for security, 636, 638–643
  thermal cycling, 794–796, 796*p*
Metal fluorides, 132–134
Metallic mirrors, 707, 710
Metallocromia, 393–394, 395*f*, 396*p*
Metal oxides, 425–426
Metamaterials (MMs), 144–145
  alloys and intermetallics, 157–160
  bianisotropy description, 167–168
  coatings containing metasurfaces, 155–156
  composites of random elements, 154–155
  effective macroscopic parameters, 166–168
  nanoclusters in periodic arrays, 149–154
  optical characterization techniques, 163–164
  resonating inclusions, 156–162
  semiconductors and dielectrics, 160–162
  small random disorders and imperfections, 154
  subwavelength inclusions, 145–147
Metamerism, 402, 644–648
  all-dielectric filter, 647*f*
  metal-dielectric Fabry-Perot-like filters, 646*f*
Metasurface (MS), 149–150, 155–156
Methyl methacrylate (MMA), 436
Michel-Lévy, Auguste, 394–397
Michel-Lévy Interference Color Chart, 396–397
Michelson interferometer, 112, 684–687, 713
Microprojector, 591, 591*f*
Mid-frequency sputtering, 11–12
Mid-InfraRed Instrument (MIRI), 701
Mid-latitude winter model, 379–380, 379*f*
Mie theory, 158*f*
Mie-type resonances, 146–147
Mirrors
  Brewster-angle CM, 672–673, 672*f*
  complementary pair of CM, 674, 675*f*
  deformable, 700–701, 700*f*
  dispersive mirrors, 669–670, 670*f*, 674*f*
  double-angle DM, 675*f*, 677, 681*f*
  double-chirped mirrors, 671–672, 671*f*
  Gires-Tournois interferometer, 670–671
  pulse compression and analysis, 677–678, 678*f*
  tilted-front-interface CM, 673–674
  time-domain DM, 676
MLI. *See* Multilayer insulation (MLI)
m-lines technique, 488, 505, 507*t*
Modified Drude approximation, 145
Modified Long Wavelength Approximation (MLWA), 165
Molecular contamination, 801–803

Monochromatic monitoring (MM) strategies, 66–69
Monolithic glass, 726–727
Most sensitive monitoring wavelengths, 78
Moth eye effect, 125–126
MRS Bulletin, 783
Mueller matrix, 236–238, 273, 276–278, 282–283
Multiangle spectrophotometry, 412, 412*f*
Multicavity glazing, 731
Multi-GTI mirror, 671
Multilayer (ML) coatings
  complex materials and ultrathin metals in, 168–172
  reflectance enhancement, 332*f*
  retarders, 340–341
  for short wavelengths, 318–341
Multilayer insulation (MLI), 790, 804
Multilayer–metasurface device, 47, 48*f*
Multiple exciton generation (MEG), 604
Multiple multipole method, 165
Multiple-scattering theory, 187–188, 273

N

Nanoclusters in periodic arrays, 149–154
Nano-imprint lithography (NIL), 528
Nanoparticles (NPs), 144
Nanostructured materials, 165–166
Nanowires, photovoltaic solar cells, 601–604
National Ignition Facility (NIF) Project, 699
The National Institute for Standards and Technology (NIST), 314
National Renewable Energy Laboratory, 611
National Research Council of Canada (NRC), 29–30, 634
Near-InfraRed Camera (NIRCam), 701
Near-InfraRed Spectrometer (NIRSpec), 701
Needle method, 32–34
Newton, Isaac, 390–392, 391*f*
Newton-Raphson method, 457
Newton's color series, 391*f*, 397
NIL. *See* Nano-imprint lithography (NIL)
Nobili, Leopoldo, 393–394, 395*f*, 396*p*
Nonconformance control process, 807–808
Non-iridescent material (NIM), 647–648, 647*f*
Nonplasma-activated chemical vapor deposition, 438–441
Non-vacuum sol–gel techniques, 566–567
N-type transparent conductive thin films, 780–782
Nyquist sampling theorem, 198

O

Octafluorocyclobutane (C_4F_8)
  deposition rate, 438*f*
  refraction index, 436–438, 437*f*
ODR coating. *See* Omnidirectional reflecting (ODR) coating
OIC. *See* Optical Interference Coatings (OIC)
Oil crisis, 719
OLEDs. *See* Organic light emitting diodes (OLEDs)
Oliver and Pharr method, 544–545
Omnidirectional reflecting (ODR) coating, 586–588, 588*f*
One-dimensional photonic crystal, 364
1D randomly rough interface, 189–200
1D randomly rough perfectly conducting surface, 196–200
1D randomly rough vacuum-dielectric interface, 190–196
1D rough surface, p- and s- polarized light, 200–213
Online error detection and correction tools, 118–120
Online measurement system, 116
Open-source software tool, 43
Optical broadband monitoring, 107–112
Optical characterization techniques, 163–164
Optical Coating Laboratory, Inc. (OCLI), 634
Optical coatings. *See also specific optical coatings*
  applications of, 425–426
  colorimetry (*see* Colorimetry)
  color of (*see* Interference color)
  film functionality/structurally controlled, 656–658
  lens, 398–399
  at short wavelengths, 318–341
Optical constants
  experimental determination of, 315–318
  of materials at short wavelengths, 299–314
Optical Interference Coatings (OIC), 36–37, 39–40, 52–53
Optically selective coatings, 367–383
Optically variable devices (OVDs), 633–634, 641–642, 656–657
Optically variable ink (OVI), 634, 643
Optically variable pigments (OVPs), 643, 644*f*
Optical monitoring strategies
  classification of, 67–69
  direct broadband optical monitoring, 89–92
  error self-compensation effect, 69–75
  indirect optical monitoring strategies, 92–96
  level monitoring, 75–85
  monitoring by swing values, 85–88
  subdivisions, 68*f*
  turning point optical monitoring, 69–75
Optical perfection, 372–373
Optical properties, 309–314

Optical solar reflectors, 790, 798–799
Optical technology, 372–373
Optoelectronic properties, TCO, 753–754
Organic light emitting diodes (OLEDs), 426, 428–429, 754, 776–777
  buffer layers, 436
  diffusion barriers, 429
  emission layers in, 430–431
  transparent conductive thin films, 773–774
  transparent electrode, 761–762, 761–762*f*
Organic optical coatings, 425–426, 429
  composites, 429, 441–442, 442–443*f*
  deposition techniques, 429–430
    adhesion improvement by plasma treatment, 441
    nonplasma-activated chemical vapor deposition, 438–441
    plasma-enhanced chemical vapor deposition, 434–438, 435–438*f*
    sputter deposition, 432–434, 433–434*f*
    thermal evaporation, 430–432, 431*f*
  properties, 426–429
Organic photovoltaic (OPV) cells, 428–429, 598
Organic solar cell (OSC), 598, 604–605
  charge separations, 608
  exciton diffusion, 607
  inverted structure, 606–607, 606*f*
  light trapping strategies, 608–611
  periodic structures in multilayer stack, 609–610
  plasmons for increasing absorption, 610–611, 611*f*
  power conversion efficiency, 604–605
  traditional structure, 606*f*
  working principles, 605–608
Organometallic perovskite-based solar cells, 598, 618–623, 620–621*f*
ORION, 699
Outward radiation, 379–380, 379*f*

P

Pair production, 312
Particle in-a-box (PIB) model, 488–489
Particle swarm optimization (PSO), 37
Particulate contamination, 802, 803*f*
Particulate radiations, 799–801
Parylene, 438–439
  deposition setup for, 440*f*
  polymerization process, 439, 439*f*
Pass band filters, 318–319
Passenger comfort, 732–733
Passive house, 721, 735
Passive monochromatic monitoring strategies, 75–85
Path length enhancement factors, 600
PBSs. *See* Polarization beam splitters (PBSs)
PCE. *See* Power conversion efficiency (PCE)
Percentage luminance factor, 406
Percus-Yevick distribution, 256, 259
Per frequency, 360–361
Periodic arrays, 149–154
Perovskite solar cells, 618–623, 620–621*f*
Per wavelength unit, 360–361
PET film. *See* Polyethylene terephthalate (PET) film
Phase diagram, 150
Phase monitoring, 112
Phase retarders, 332–341
Phosphor color wheel, 576*f*, 582, 582*f*
Photocatalytic decomposition process, 429
Photodetectors, 487
Photodiode arrays, 66
Photoelectric absorption, 312
Photometry, 404
Photon absorption, 607
Photonic bandgaps, 364
Photonic crystal, 150, 487, 609–610, 610*f*, 654
Photons–matter interaction, 299–300
Photopic vision, 399
Photovoltaic solar cells
  advantages, 595
  chalcogenide materials in, 611–618, 613*f*
  classes of, 596
  conversion efficiency, 597*t*
  drawbacks, 595–596
  inorganic nanostructures, 599–604
  light trapping and photo-carrier collection, 600–601, 601*f*
  nanowires and quantum dots, 601–604
Physical-deposition techniques, 452
Physical vapor deposition (PVD), 144–145, 540–541
  flat panel display, 566–567
  low-emissivity coatings, 728
  sculptured thin film, 453
Physics-based model, 275–276
PIAD. *See* Plasma-ion-assisted deposition (PIAD)
PICVD. *See* Plasma impulse chemical vapor deposition (PICVD)
Piecewise-uniform-approximation method, 456
Planar interface, dielectric film with, 224–229
Planar metal substrate, 216–229, 222*f*
Planar vacuum-dielectric interface deposition, 196–200

Planck's constant, 302–303, 315, 363
Planck's law for oscillators, 359
Plasma-assisted vacuum coating process, 525–526
Plasma-based deposition, 540–544
Plasma-enhanced chemical vapor deposition (PECVD)
  coatings on plastics, 541–542
  gradient coatings, 552–553
  organic layers, 434–438, 435–438*f*
  UV-protective coating, 557–558
Plasma etching
  ARS nanostructure, 528, 529–530*f*, 531
  PMMA surfaces, 428
Plasma frequency, 302
Plasma impulse chemical vapor deposition (PICVD), 16, 541–542
Plasma-ion-assisted deposition (PIAD), 520–523, 540–541. *See also* Ion-assisted deposition (IAD)
Plasma polymerization, RF-excited, 541–542
Plasma sputtering technology, 705
Plasma treatment
  adhesion, 441, 520
  vacuum deposited AR coatings with, 532–533
Plasma wavelength, of alkali metals, 303*t*
Plasmonic conductors, 144
Plasmonics, 610–611
Plasmon polariton (PP), 143–144
Plastic optics, 517–518
  antireflective structures, 528–531, 529–530*f*
  thermoplastics, 519*t*
  transparent polymer materials, 517–519
  vacuum coating, 518*f*, 520–526
  vacuum deposited AR coatings, 526–527
  wet-chemical AR coatings, 531–532
Plateau problem, 398
PLD. *See* Pulsed laser deposition (PLD)
Pleochroic effect, 394–396
Pleochroism, 394–396
PMMA. *See* Poly(methyl methacrylate) (PMMA)
Polarization beam splitters (PBSs), 569–570, 572*f*
Polarization state of radiation, 332–341
Polarized light, scattering of, 247–273
Polarizers, 334–338
Poly(methyl methacrylate) (PMMA), 18–19
  antireflective nanostructures, 528–530, 529*f*
  plasma etching, 428
  polar component of surface energy, 521*f*
  quantum dots, 504*f*
    absorption spectrum, 497–498, 499–500*f*, 500, 503*f*
    luminescence spectra, 500–501, 501*f*, 503, 503*f*
    realization process, 495–497, 496*f*
    refractive index, 505, 506*f*, 507*t*
  single-layer coating for, 531–532
Poly-bisphenol-A-carbonate, 521
Polycarbonate (PC), 521
  adhesion tests, 547–548
  automotive glazing, 557–559, 559–560*f*
  coating systems, 552–553, 553*f*
  crack onset strain, 547
  multifunctional coatings, 553–556
  optical properties, 550
  protective coating, 539–541
  weathering test, 549–550
Polyethylene terephthalate (PET) film, 729–730
  laminated glazing, 729–730
  multicavity glazing, 731
  retrofit applications, 731
Polymerization process, 439, 439*f*
Polymer substrates, glazing coatings on, 729–731
Polytetrafluoroethylene (PTFE), 432–434, 433–434*f*
Power conversion efficiency (PCE), 51
  organic solar cell, 604–605
  perovskite solar cells, 619
Power spectral density, 2-dimensional, 298
P-polarization, 192, 195*f*
  electromagnetic fields, 191
  reduced Rayleigh equations for, 200–213
  two guided waves in, 221
Preproduction investigation, 39, 90
Prismatic colors, 389
Prism-coupled configuration. *See* Turbadar–Kretschmann–Raether (TKR) configuration
Process control, space coatings, 807
Process identification document (PID), 807
Process-tracing algorithm, 116–117
Production strategy
  coated optical components, 106*f*
  continuous refractive index variation, 125–134
  design stability, 120–125
  deterministic production, 105–107
  direct online correction tools, 118–120
  hybrid thickness monitoring, 112–114
  optical broadband monitoring, 107–112
  virtual deposition system, 114–118
Projected capacitive touch technology, 772–773, 773*f*
Projection television (PTV), 565, 571–572

Projectors, 568–571
reflection-type, 569*f*, 571*f*
transmission-type, 568*f*
using LED, 571–583, 583*f*
Propagating SPs (SPPs), 147
Protective coating
applications, 544, 556–559
polycarbonate, 539–541
Pseudo-Brewster angle, 334
PSO. *See* Particle swarm optimization (PSO)
Psychometric colorimetry, 400, 408–410
Psychophysical colorimetry, 400
color stimuli, 400–406, 402*f*, 405*f*
light sources and nonself-luminous surfaces, 406–408
PTV. *See* Projection television (PTV)
P-type transparent conductive thin films, 782–783
Pulse compression, 668*f*, 669–670
analysis, 677–678, 678*f*
double-angle DM, 680–683, 683–684*f*
Pulsed laser deposition (PLD), 15–16
PulvérisAtion CAthodique de 2 Mètres (PACA2M), 708, 712
PVD. *See* Physical vapor deposition (PVD)
Pyrolysis technology, 543–544
Pyrolytic coatings, 727–728, 734

Q

Q-function, 29
Q-phase optimization alone, 29
Quantum dots (QDs), 487–488, 488*f*
absorption spectrum, 494, 497–500, 499–500*f*, 503*f*
band energy, 493–494
CdSe, 494, 495*f*
of copper sulfide, 162
lighting and displays, 507–508
luminescence, 500–503, 501–504*f*
materials with, 148–149
optical properties, 494–495
photovoltaic solar cells, 601–604
realization process, 495–497, 496*f*
reflectance spectra, 497–500, 508, 509*f*
refractive index, 503–505, 506*f*, 507*t*
solar cell efficiency, 505–507
transmission electronic microscopy, 496–497, 498*f*
transmission spectrum, 497–500, 498*f*
Quantum wells (QWs), 488–493, 491–493*f*
Quarter-wave retarders, 338–339
Quartz crystal monitoring, 65
Quartz deposition controller, 439
Quasicrystalline approximation (QCA), 255–256
Quasicrystalline coherent potential approximation (QC-CPA), 255–256
Quasirugate filter approach, 126

R

Radiant heating, 4–5
Radiation irradiance, 294
Radiative exchange with atmosphere, 377–383
Radical-assisted sputtering (RAS), 13
Radio frequency (RF) sputtering, 432–433, 433*f*
Random elements, composites of, 154–155
Randomly rough surface, 238–239
Random medium
with random rough interfaces, 271–272
scattering of polarized light, 247–273
with two planar interfaces, 267–271
RAS. *See* Radical-assisted sputtering (RAS)
RCWA. *See* Rigorous coupled-wave approach (RCWA)
Reactive low-voltage ion plating, 9–10, 9*f*
Reactive sputtering, 11–12
Reduced Rayleigh equation, for scattering of light
from dielectric films with 1D rough surfaces, 189–200
P- and S-polarized light, 200–213
2D randomly rough penetrable surface, 213–216
Refinement techniques, 25–26, 33–34
Reflectance measurement
over large spectrum at near-normal incidence, 316
at various angles of incidence, 316
Reflectance spectra, quantum dots, 497–500, 508, 509*f*
Reflectance/transmittance extrema, 65–66
Reflection
in absorbent materials, 294–298
retarders, 339
Reflection-type projectors, 569–570, 569*f*, 571*f*
Reflective polarizers, 335, 337–338
Refraction, 317
Refractive index
into complex number, 294
decrement, 305
deposited layer materials, 427*f*
m-lines technique, 488, 505, 507*t*
octafluorocyclobutane, 436–438, 437*f*
parylene, 440
quantum dots, 503–505, 506*f*
thin film composites, 441, 442*f*
variation, 125–134

Refractory oxides, 7–8
Relativistic quantum mechanics, 314
Resistive touch sensors, 770–771, 771–772*f*
Resistivity-well, 748, 749*f*
Resonant gratings, 44–47, 53
Resonating inclusions, 156–162
Reststrahlen band, 381
Retarders, 338–341
Retrofit applications, 731
Reverse engineering tool, 135
RF sputtering. *See* Radio frequency (RF) sputtering
Ricatti differential equation, 28
Rigorous coupled-wave approach (RCWA), 464, 477
Root-mean-square (RMS), 29–30, 298
Roughness, and scattering, 296–298
Rugate filters, 126, 449–450, 452
  canonical boundary-value problem, 457–460, 458–459*f*
  deposition control of, 132–134
  grating-coupled configuration, 462–467, 463*f*, 465*t*, 466–467*f*
  TKR configuration, 471–476
Rushton's univariance principle, 401
Rutherford Appleton Laboratory's Central Laser Facility, 699

S

Sand trickling test, 546
Sarid configuration, 451, 457–458
Satellite peaks
  analysis, 187–188
  reduced Rayleigh equations, 189–190
Satellite ring formation, 223
Scanning near-field optical microscopy (SNOM), 163
Scanning probe microscopy (SPM), 163
Scanning tunneling microscopy (STM), 163
Scattering
  anomalous scattering, 276–278
  atomic scattering factors, 303–306
  Compton scattering, 312
  incoherent scattering, 312
  roughness and, 296–298
Scattering amplitude
  Floquet-Bloch theorem, 192
  natural extension of, 241
  reduced Rayleigh equation, 191–192, 197, 208, 216
  single integral equation for, 208
  single 2D integral equation, 201–202
  2D randomly rough surface, 214
Scattering matrix
  definition of, 230–233, 232*f*
  for single rough surface, 281–282
Scattering of light
  applications, 273–280
  3D film with randomly rough surfaces, 229–247
  from dielectric film, 216–229
  dielectric films with 1D rough surfaces, 189–200
  2D randomly rough penetrable surface, 213–216
  P- and S-polarized light, 200–213
  theoretical methods for, 247–273
Schrödinger's "Helligkeit" equation, 404
Scratch-resistant coatings, 531
Scratch test, 546, 547–548*f*
Sculptured nematic thin films (SNTFs), 449–454
  canonical boundary-value problem, 460–462, 461–462*f*
  grating-coupled configuration, 467–470, 469–470*f*
  TKR configuration, 476–477
Sculptured thin film (STF), 452–454
Security devices, 644
  active materials, application, 652–654
  all-dielectric filter, 636–638, 637*f*, 647*f*
  Bank of Canada, 634, 641–642
  color shifting technology, 651–652
  combining interference and diffraction, 649–651, 650*f*
  electrochromic materials, 654–656, 655*f*
  features, 634
  film functionality/structurally controlled, 656–658
  magnetic films, 648, 649*f*
  metal-dielectric filters, 636, 638–643, 639–640*f*, 646*f*
  metamerism, 644–648, 646–647*f*
  optically variable pigments, 643, 644*f*
  principles, 634–643, 635*f*
Selective emittance, 379–380
Sellmeier model, fused silica, 685–687
Semi-analytical approaches, 26
Semiconductors, 160–162, 569–570
Semiinfinite medium, 238–239, 266–267
Sequential algorithm, 118–119
Short wave infrared (SWIR) band, 274
Short wavelengths
  optical coatings at, 318–341
  optical constants of materials, 299–314
Signal swing, monitoring by, 85–88, 85*f*
Silica sol–gel dip coating, 566–567
Silicium quantum dots, 495–496, 496*f*

Silicon nanowire (SiNW) array fabrication process, 603
Silver-based coating, advantage, 702
Simulated annealing, 35
Single rough surface, scattering matrices for, 281–282
Small-perturbation method (SPM), 187–188, 229–230
  for slabs with randomly rough boundaries
    applications, 243–246
    formulation, 240–243
  for 2D rough surface
    formulation, 233–236
    Mueller matrices, 236–238
    semiinfinite media, 238–239
Small-slope approximation (SSA), 187–188, 229–230
  for slabs with randomly rough boundaries
    applications, 243–246
    formulation, 240–243
  for 2D rough surface
    formulation, 233–236
    Mueller matrices, 236–238
    semiinfinite media, 238–239
Snell's law, 295, 413–414
SNTFs. *See* Sculptured nematic thin films (SNTFs)
Soap bubbles, interference color, 398
Society of Vacuum Coaters (SVC), 784
Soft X-rays (SXR), 292–293, 321–322, 323*f*
Solar cells, 48–52. *See also specific solar cells*
  co-evaporation techniques, 606–607, 618, 622
  concepts of, 599–600
  cover glass, 790, 798, 798*p*, 801
  efficiency, quantum dots, 505–507
  perovskite, 618–623, 620–621*f*
  tandem, 601–602, 602–603*f*
  unconventional, 596–598
Solar control coatings, 765–767, 766*f*, 768*f*
Solar Frontier, 616–617
Solar irradiance, 798–799
Solar photon absorption (SPA), 51, 51*f*
Solar plants, 702–703
Solar screens, 374
Solar selectivity, 368–369
Solar spectrum, 361
Solar thermal absorbers, 367–369
Sol–gel process, 18, 543, 706
  AR coating on plastics, 531–532
  dip coating, 566–567
Solid-state effects, 307–308
Solvent vapor annealing (SVA), 606–607
S-on-1 test procedure, LIDT, 794, 795*f*
SPA. *See* Solar photon absorption (SPA)
Space contamination, effects, 804–806
Space environment, 789–791
  atomic oxygen, 801
  components, 789–790, 790*f*
  particulate radiations, 799–801
  solar irradiance, 798–799
  space vacuum, impact of, 791–794
  thermal cycling, 794–797, 797*f*
Space industry, 701–702
Space Infrared Telescope for Cosmology and Astrophysics (SPICA) mission, 702
Space product assurance, 806
  end to end traceability, 806–807
  nonconformance control, 807–808
  process control, 807
  qualification testing, 808
Spacer layer, 69–75
Space vacuum
  impact of, 791–794, 795*f*
  thermal cycling, 794–797, 797*f*
Spatial harmonic analysis (SHA), 169
Special-effect colors, 389, 410–411
Specific intensity
  and Bethe-Salpeter equations, 253–255
  and cross section, 248–252
Spectral reflectance factor, 407–408
Spectral selectivity, window coating, 724–725, 724–726*f*
Spectral transmittance, 71–72, 75–76, 75–76*f*
Spectral transmittance factor, 408
Spectrophotometry, 357, 358*f*, 550
Spectro-Polarimetric High-contrast Exoplanet Research (SPHERE), 698
Spectrum
  locus, 402–403
  material behavior over, 291–293
  shift at incident angle, 578–579, 578–579*f*
Spin coating, 495–496, 528–530
Spinning process, 566–567
Split ring resonator (SRR)-based oscillators, 151, 159
S-polarization, 191–192, 195*f*
  reduced Rayleigh equations for, 200–213
  two guided waves in, 221
SPP. *See* Surface plasmon-polariton (SPP)
Sputter deposition, 432–434, 433–434*f*
  contamination, 803
  ITO film, 753
Sputtering, 10–15, 105–107. *See also specific sputtering*
  large optical coatings, 704–707, 705–706*f*
  photovoltaic thin films, 618
  in pulsed DC, 709–710, 710*f*

Statistical search, 26–27
Stefan–Boltzmann equation, 362
Stevens' power law, 409
Stoichiometric indium oxide, 747–748, 747*f*
Stokes vector, 248–250
Stress-related effects, 522–523, 523*f*
Structural colors, 389
Structured coatings, 44–47
Structure zone model, thin film, 657
Subquarterwave MLs (SQWMs), 330–332, 330*f*
Substrate configuration, CIGSSe device, 612–613
Subwavelength inclusions
  ceramic matrix with embedded nanostructures, 147–156
  characterization, 162–172
  physics of classes, 145–147
  resonating inclusions, 156–162
Summer films. *See* Solar control coatings
Supermirrors, 327
Surface-enhanced Raman spectroscopy (SERS), 163
Surface multiplasmonics, 449, 479. *See also* Surface plasmon-polariton (SPP)
  historical development, 450–452
  STFs types, 453
Surface plasmon (SP), 143–144
Surface plasmon frequency, 297
Surface plasmon-polariton (SPP), 143–144, 449–450, 477–479
  canonical boundary-value problem, 454–462
  dispersion equation, 457
  effects on efficiency of thin-film solar cells, 480
  with finite sources, 479
  historical development, 450–452
  periodically nonhomogeneous dielectric materials, 452–454
  rating-coupled configuration, 462–470
  resources, 480
  Turbadar–Kretschmann–Raether configuration, 471–477, 471*f*
Surface profile function, 193–194
Surface-relief grating, 462–464, 466–467*f*, 466*t*, 467, 477, 479–480
Surface scattering, 247–273
Swing values, 85–88, 85*f*
Switchable glazing, 736
Synthesis techniques, 25–26

T

Taber abraser test, 545, 546*f*, 556–557
Tandem solar cell
  all-silicon, 601–602, 602*f*
  conversion efficiency, 603*f*
Tang's statistical search, 26–27
Target poisoning, 11–12
TCO. *See* Transparent conductive oxide (TCO)
TCTFs. *See* Transparent conductive thin films (TCTFs)
TDMAH. *See* Tetrakis-[dimethylamido]-hafnium (TDMAH)
TE. *See* Transparent electrode (TE)
Teaching–learning-based optimization (TLBO), 37
Telescope, 790. *See also specific telescope*
Tensor, 248–250, 282–283
Ternary oxides
  co-deposition processes, 126–127
  as material mixtures, 135–136
  of reproducible stoichiometry, 104–105
Terrestrial contamination, 801–803
Tetrakis-[dimethylamido]-hafnium (TDMAH), 17–18
Thermal control, in glazing, 720–721
  automotive window energy efficiency, 722–723
  building window energy efficiency, 721–722
Thermal cycling
  metal-dielectric filter, 794–796, 796*p*
  in vacuum, 794–797, 797*f*
Thermal effects, vacuum coating, 522–523, 523*f*
Thermal evaporation, 4–5, 19–20
  large optical coating, 703–704
  organic layers, 430–432, 431*f*
Thermal radiation
  blackbody radiation, 359–362
  emissivity, 362–367
  optically selective coatings, 367–383
Thermal solar collectors, 358–359, 367–374
Thermoplastics, 518, 519*t*
Thin film
  anticounterfeiting coatings, 399
  applications in architectural glazing, 540*f*
  automotive sector, 541*f*
  SPP waves effects, 480
  structure zone model, 657
  uniformity, 706–708
Thin-film photovoltaic solar cells
  advantages, 595
  chalcogenide materials in, 611–618, 613*f*
  classes of, 596
  conversion efficiency, 597*t*
  drawbacks, 595–596
  inorganic nanostructures, 599–604
  light trapping and photo-carrier collection, 600–601, 601*f*
  nanowires and quantum dots, 601–604
  OSC (*see* Organic solar cell (OSC))
  silicon, 596–598
  Type II transparent electrode, 762–764, 763*f*

Thin films containing quantum dots, 508
absorption spectrum, 494, 497–500, 499–500*f*, 503*f*
luminescence, 500–503, 501–504*f*
realization process, 495–497
reflectance spectra, 497–500, 508, 509*f*
refractive index, 503–505, 506*f*, 507*t*
transmission electronic microscopy, 496–497, 498*f*
transmission spectrum, 497–500, 498*f*
Thin film transistor (TFT), 774–776
Thin island film (TIF) theory, 171–172
Thin metal layers, 155–156
Thin Solid Films (TSF), 783
Thirty-Meter Telescope, 702
Thomas-Reiche-Kuhn sum rule, 304, 315
3D film with randomly rough surfaces, 229–247
3D reconstruction algorithm, 275, 280*f*
Tightly bound electrons, 303–306
Tilted-front-interface CM, 673–674. *See also* Chirped mirror (CM)
Time-averaged Poynting vector
Cartesian components, 458–459
grating-coupled configuration, 467*f*, 470*f*
TKR configuration, 467*f*, 475–476
Time-domain DM, 676
Tinted glass, 722, 726, 728
Tinuvin 360, 430–431
Ti:sapphire laser, 681–683, 690
Titanium dioxide, 13–14
Titanium oxide, 17–18
TKR configuration. *See* Turbadar–Kretschmann–Raether (TKR) configuration
Total electron yield, 318
Total-internal-reflection ellipsometry (TIRE), 163
Total radiance, 362
Touch sensors
analog resistive, 770–771, 771–772*f*
projected capacitive touch technology, 772–773, 773*f*
Transition-metal nitrides, 162
Transmission
in absorbent materials, 294–298
phase retardation on, 340*f*
Transmission electron microscopy (TEM), 163
assisted sputtering technique, 791, 792*f*
conventional electron beam evaporated coating, 791, 792*f*
quantum dots, 496–497, 498*f*
Transmission filters, 318–321
Transmission spectrum
non-iridescent material, 647–648, 647*f*
quantum dots, 497–500, 498*f*
Transmission-type projectors, 568–569, 568*f*
Transmissive retarders, 339
Transmittance polarizers, 338
Transparency cutoff of dielectrics, 300–301
Transparent conductive oxide (TCO), 161, 542, 741–744
cage-structured materials, 780–782, 781*f*
flat panel display, 567–568
intrinsic performance limits, 781*f*
liquid crystal display, 757–761
optical properties, 749–751, 751–752*f*
optoelectronic properties, 753–754
photovoltaic solar cells, 616–617
thin-film transparent electrodes, 742*t*
Transparent conductive thin films (TCTFs), 741
antistatic films, 757
conductive AR coating, 767–769, 769–770*f*
electrochromic windows, 778–779
EMI shielding, 757, 759–760*f*
flexible substrates, 741–742
heaters, 755–757, 755*f*
low-emissivity coatings, 764–765, 765–766*f*
n-type, 780–782
OLED, 773–774, 776–777
p-type, 782–783
solar control coatings, 765–767, 768*f*
sources of information, 783–784
thin film transistor, 775–776
touch sensors, 770–773, 771–773*f*
transparent conductive oxides, 742–744, 742*t*
transparent electrodes, 757–764, 761–764*f*
transparent metallic thin films, 744–745
transparent oxide electronics, 774–775
transparent solar cell, 777–778
Transparent electrode (TE)
CIGS PV device, 764*f*
OLED device, 762*f*
pixel size and, 774*f*
PV device, 763*f*
Type I, 757–761
Type II, 761–764, 761*f*, 763*f*
Transparent metallic thin films, 744–745
Transparent OLEDs, 776–777
Transparent oxide electronics, 774–775
Transparent polymer materials, 517–519
Transparent solar cells, 777–778
Transparent TFT (TTFT), 775–776, 775*f*
Transversal electric (TE), 295–296

Transverse magnetic (TM) modes, 43, 295–296
Trapped rainbow effects, 149–150
Triangular algorithm, 118–119
Trichromacy, 400–401
Tris-[dimethylamino]-silane (3DMAS), 17–18
Tristimulus space, 400–401, 402*f*
Tristimulus values, 400–401, 403–406
Turbadar–Kretschmann–Raether (TKR) configuration, 449–450, 457–458, 471, 471*f*
  absorptance *vs.* incidence angle, 473*f*
  advantages, 478
  incidence angle and relative wavenumber, 473–474*t*
  metal/rugate-filter interface, 471–476
  metal/SNTF interface, 476–477
  time-averaged Poynting vector, 467*f*, 475–476
Turning point optical monitoring, 66, 69–75, 70*f*
TV laser window, antiicing, 756*f*, 758*f*
2D randomly rough interface, 224–229
2D randomly rough penetrable surface, 213–216
2D randomly rough surface deposition, 216–229, 222*f*

U

Ultrafast optics, 667–669
Ultrathin metals
  layers, 155–156
  multilayers, 168–172
Ultra-transparent conductive materials (U-TCM), 745*t*
United States Department of Energy, 719, 721
United States Display Consortium (USDC), 784
Universal law, 393
Upconverting nanoparticles (UCNPs), 652–654, 653*f*
US Environmental Protection Agency (EPA), 721
UV-BBM system, 108–110
UV fixation of contamination, 804
UV–IR cut filter, 569, 570*f*
UV-protective coating, 521, 539, 552, 553*f*, 557–558

V

Vacuum coating process, plastics, 517, 518*f*
  defects, 524*f*
  interaction with emissions from plasma, 520–521
  plasma-assisted processes, 525–526
  thermal and stress-related effects, 522–523, 523*f*
  water absorption/desorption, 523–525, 524–525*f*
Vacuum deposition, 3–4, 429. *See also* Chemical vapor deposition (CVD)
  adhesion in, 441
  antireflection coatings, 526–527
  gas discharge plasma, 438
Vacuum-dielectric interface, 190–196
Vacuum-free deposition, 618
Valence band, 300–301, 746
Vertical polarization, 231–232
Very large research infrastructures (VLRIs), 698
Very Large Telescope (VLT), 698, 698*f*, 702
Viavi Solutions Inc., 643
Virgo project, 698, 704–705, 713–715, 714*f*
Virtual deposition process (VDP), 39, 105, 114–118, 115*f*
  application example for, 117–118
  design stability in production processes, 120–125
  interfaces of, 116–117
Visible spectral range (VIS)-NIR-region, 372
Vision Ease Lens Inc., 531–532
Vulcan laser, 699

W

Waveguide facet coatings, 41–44, 41*f*
Wavelength division multiplexing (WDM) applications, 66, 73
  error sensitivity analysis, 74*f*
  vs. optical thickness, 74*f*
Wavelength shift, 579–580
Weathering test, 549–550
West-O'Donnell power spectrum, 198, 220–223
Wet-chemical antireflection coatings, 531–532
White light interferometers (WLIs), 684–687, 685*f*
Wide angle reflection (WAR) filter, 582, 582*f*
Wiener bounds, 155–156
Wien peak position, 361
Wien's displacement law, 359–360
Window coating, 719, 723
  antiglare, 726
  low emissivity, 723
  spectral selectivity, 724–725, 724–726*f*
Winter films. *See* Low-emissivity (low-E) coatings

X

X-plate
  in projectors, 583, 583*f*
  reflection filter, 583, 584*f*
X-ray absorption fine structure (XAFS) spectroscopy, 308–309, 308–309*f*
X-ray absorption near-edge spectroscopy (XANES), 308–309, 308*f*, 310*f*
X-ray absorption spectroscopy (XAS), 308
X-ray attenuation and absorption for materials of dosimetric interest database (XAAMDI), 314

X-ray diffraction (XRD), 496–497
X-ray free-electron laser (XFEL), 699
X-ray optical devices, 698
X-ray photoelectron spectroscopy (XPS), 308, 520

Y

Yamaguchi dipolar model, 171–172
Young, Thomas, 392–393

Z

Zeonex, 520
  AR-hard coating on, 526, 527*f*
  plasma-etched AR nanostructure, 528, 529–530*f*, 531
  polar component of surface energy, 521*f*
Zero-order diffraction (ZODs) gratings, 651
Zone melting approach, 35

- Provides a thorough review of applications of optical coatings including laser components, solar cells, glazing, and lighting
- One-stop reference that addresses the deposition techniques, properties, and applications of optical thin films and coatings
- Novel methods, suggestions for analysis, and applications make this a valuable resource for experts in the field

Optical Thin Films and Coatings provides an overview of thin-film materials, the properties, design and manufacture of optical coatings, and their use across a variety of application areas.

Optical Thin Films and Coatings is a technical resource for researchers and engineers working with optical thin films and coatings, professionals in the security, automotive, space, and other industries requiring an understanding of these topics, and for academics interested in the field.

Dr Angela Piegari is Head of the Optical Coatings Group at ENEA (Italian National Agency for New Technologies, Energy, and Sustainable Economic Development), Italy.

Angela Piegari has been working for 30 years in the field of optical thin-film coatings at ENEA. She has collaborated with many Institutes in the frame of international projects and has acted as evaluator of both National and European research proposals. She is a fellow of the European Optical Society and a member of various technical committees, author of more than 150 papers in the field of thin-film optics and coauthor of two books.

François Flory is Professor Emeritus at Ecole Centrale Marseille and performs his research at the Institut Matériaux, Microélectronique et Nanosciences de Provence, France.

François Flory's field of research is thin films, micro/nanostructured materials, and components for optoelectronics. Editor and coeditor of two books, he is also the author of more than 200 papers, patents, book chapters, and conferences. He is an expert for different research agencies and a reviewer for several international scientific journals. He is a coeditor of the journal OPTIK.

ISBN 978-0-08-102073-9

9 780081 020739

ELSEVIER

WP WOODHEAD PUBLISHING

An imprint of Elsevier

elsevier.com/books-and-journals